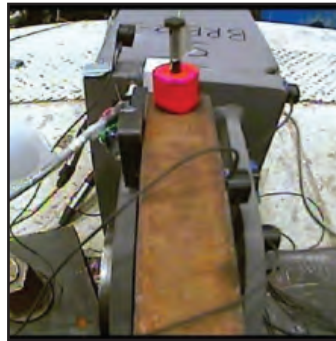# MCEER
EARTHQUAKE ENGINEERING TO EXTREME EVENTS

Buckling Restrained Braces Applications for Superstructure and Substructure Protection in Bridges

by

Xiaone Wei and Michel Bruneau

NOTICE

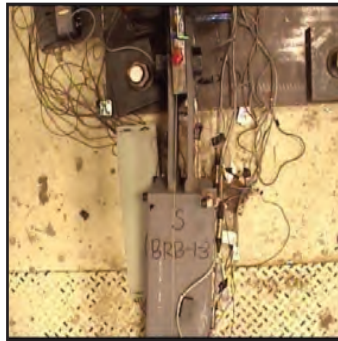# Buckling Restrained Braces Applications for Superstructure and Substructure Protection in Bridges

by

Xiaone Wei[1] and Michel Bruneau[2]

MCEER Thrust Area 1: Infrastructure and Public Policy

1   Research Assistant, Department of Civil, Structural and Environmental Engineering, University at Buffalo, State University of New York
2   Professor, Department of Civil, Structural and Environmental Engineering, University at Buffalo, State University of New York

MCEER
University at Buffalo, State University of New York
212 Ketter Hall, Buffalo, NY 14260
E-mail: *mceer@buffalo.edu*; Website: *http://mceer.buffalo.edu*

Preface

MCEER is a national center of excellence dedicated to the discovery and development of new knowledge, tools and technologies that equip communities to become more disaster resilient in the face of earthquakes and other extreme events. MCEER accomplishes this through a system of multidisciplinary, multi-hazard research, in tandem with complimentary education and outreach initiatives.

Headquartered at the University at Buffalo, The State University of New York, MCEER was originally established by the National Science Foundation in 1986, as the first National Center for Earthquake Engineering Research (NCEER). In 1998, it became known as the Multidisciplinary Center for Earthquake Engineering Research (MCEER), from which the current name, MCEER, evolved.

Comprising a consortium of researchers and industry partners from numerous disciplines and institutions throughout the United States, MCEER's mission has expanded from its original focus on earthquake engineering to one which addresses the technical and socio-economic impacts of a variety of hazards, both natural and man-made, on critical infrastructure, facilities, and society.

The Center derives support from several Federal agencies, including the National Science Foundation, Federal Highway Administration, Department of Energy, Nuclear Regulatory Commission, and the State of New York, foreign governments and private industry.

This report considers two applications of implementing Bucking Restrained Braces (BRBs) as structural fuses into new and existing bridge structures: (i) added between columns of a bridge bent, and (ii) inserted in the end-diaphragms of slab-on-girder steel superstructures. Design procedures are proposed for designing BRBs in both applications based on analytical and experimental results. Dynamic nonlinear time history analyses were performed on the bridge models to investigate their global behavior after adding the BRBs, and to understand the magnitude of local demands on the BRBs and other bridge members. Analytical and experimental studies are conducted for BRB's gusset plates welded to CFT columns to investigate the connection strength for seismic applications. Quasi-static experiments are performed to subject two types of BRBs to a regime of relative end displacements representative of the displacement demands when BRBs are implemented in ductile diaphragms. The use of BRBs in these applications was found to enhance the seismic performance of bridges.

ABSTRACT

Two prospective applications of implementing Buckling Restrained Braces (BRBs) as Structural Fuses (SFs) into new and existing bridges structures are considered: (i) added between columns of a bridge bent, and; (ii) inserted in the end-diaphragms of slab-on-girder steel superstructures. The objective of the SF is to protect the bridge's structural elements, such as to leave these other structural elements with minimal damage or even intact in the event of the earthquake. After the earthquake, the intent is that a SF should be relatively easily removed and replaced.

A design procedure is proposed for designing BRBs inserted in bridge bents. Two design configurations are considered, including: (i) a two-column bent with BRBs in single-inclined and inverted-V configurations (which provide SF only in the bridge's transverse direction and would have to be combined with other energy dissipating devices in the longitudinal direction), and; (ii) four-column box piers with BRBs in both the transverse and longitudinal directions. Nonlinear pushover and time history analyses are performed on the bridge bents to verify the effectiveness of adding BRBs to the bridge bents in reducing the seismic demands. Connection details are investigated to connect the BRBs to other members of the bridge bent (to establish feasibility when using certain conventional types of connections). Analytical and experimental studies are conducted for gusset plates welded to Concrete Filled steel Tube (CFT) columns, to investigate the connection strength for seismic applications.

For BRBs to be implemented in the End Diaphragm Systems (EDS), parametric nonlinear time history analyses are conducted on benchmark skew and nonskew bridges, which allows investigating the impact of these parameters on global behavior, as well as understanding the magnitude of local demands and the extent of bi-directional displacements that the BRBs must be able to accommodate while delivering their ductile response. The long-term service life of BRBs installed across expansion joints and subjected to bridge thermal expansion histories is also investigated. Quasi-static experiments are performed to subject the BRBs to a regime of relative end-displacements representative of the results predicted from the parametric analytical studies. Two types of BRBs are designed, and four specimens of each type of BRB are tested under different combinations of displacement protocols. The protocols include the bi-directional displacement histories applied to the specimens for the cyclic inelastic test, and the uniaxial displacement histories for the low-cycle fatigue test due to temperature changes. The BRB's hysteretic behaviors under different displacement protocols are studied and compared. A recommended design procedure for the EDSs in both nonskew and skew bridges is developed based on the paramedic analysis and experimental results.

ACKNOWLEDGEMENTS

TABLE OF CONTENTS

TABLE OF CONTENTS (CONT'D)

TABLE OF CONTENTS (CONT'D)

TABLE OF CONTENTS (CONT'D)

TABLE OF CONTENTS (CONT'D)

TABLE OF CONTENTS (CONT'D)

TABLE OF CONTENTS (CONT'D)

LIST OF FIGURES

LIST OF FIGURES (CONT'D)

LIST OF FIGURES (CONT'D)

LIST OF FIGURES (CONT'D)

LIST OF FIGURES (CONT'D)

LIST OF FIGURES (CONT'D)

LIST OF FIGURES (CONT'D)

LIST OF FIGURES (CONT'D)

LIST OF FIGURES (CONT'D)

LIST OF FIGURES (CONT'D)

LIST OF FIGURES (CONT'D)

LIST OF FIGURES (CONT'D)

LIST OF FIGURES (CONT'D)

LIST OF FIGURES (CONT'D)

LIST OF FIGURES (CONT'D)

LIST OF FIGURES (CONT'D)

LIST OF FIGURES (CONT'D)

LIST OF FIGURES (CONT'D)

LIST OF FIGURES (CONT'D)

LIST OF FIGURES (CONT'D)

LIST OF FIGURES (CONT'D)

LIST OF TABLES

LIST OF TABLES (CONT'D)

SECTION 1
INTRODUCTION

1.1   Objectives and scope of work

In recent earthquakes throughout the world, many existing bridges designed and built in compliance to obsolete design provisions (and particularly bridges built before the 1970's in North America) showed their seismic vulnerability when subjected to strong earthquake ground motions. These bridges suffered severe damage or even collapsed due to their poor detailing or the deficient design philosophies used at the time when they were built (Priestley et. al., 1996). Such bridges can put people's lives at risk and their loss could lead to significant economic losses due to their damage and closure in the immediate aftermath of an earthquake. In that regard, modern bridge design specifications have greatly improved the seismic performance of bridges, by introducing seismic design procedures that result in structural elements able to achieve higher ductilities, to prevent the collapse of bridges. However, it remains that the inelastic deformations concentrated in these structural elements may be significant and could be irreparable, which often requires temporary closure of the bridge for days or even weeks to bring the bridge back to service condition.

The research presented here investigates some strategies to implement Structural Fuses (SFs) into new and existing bridges structures, in order to minimize the structural damage and loss in the event of the earthquake. Since the SF concept can be implemented in a number of ways in various structural systems, for the current applications considered here, the SF is typically an energy dissipation element that can be inserted in the load resisting system in the vulnerable part in the bridge, which can be either the superstructure or the substructure. The objective of the SF is to protect the other structural elements; therefore, because of its high effectiveness in dissipating hysteretic energy, it should be designed such as to leave these other structural elements with minimal damage or even intact. After the earthquake, the intention is that a SF should be relatively easily removed and replaced. Therefore, the SF concept is also of benefit from a post-earthquake perspective, meeting the objectives of Accelerated Bridge Construction (ABC), which implies the ability to expedite bridge repairs, and if possible, execute those repairs while keeping the bridge open, or at worse limiting disturbance by requiring only short duration closures (typically, accomplishing work at night). In the perspective of this report, two prospective applications of the SF concept in bridges are considered: (i) as added in between columns of a bridge bent, and; (ii) inserted in the end-diaphragms of slab-on-girder steel superstructures. Both concepts can be applicable to existing bridge retrofits, as well as new bridge designs.

For bridges with reinforced concrete columns that are designed per the current design standards, the columns can provide the lateral load resistance while achieving ductile response in the lateral direction during an earthquake. However, as columns are also part of the gravity load resisting system, inelastic deformations in the columns may compromise the stability of a bridge during an earthquake, or result in permanent damage that is beyond repair afterwards. For well detailed ductile reinforced concrete columns, prevention of the bridge's total collapse can be achieved, but the seismic damage sustained could be irreparable, or cost a lot to repair. One of the objective in the research presented here is to investigate whether SFs could be implemented in typical California bridges with concrete box girder (or types of bridges that would be compatible with Caltrans' practice), to address the relevant performance issues, and develop the necessary new knowledge to achieve effective implementations. Different types metallic devices, including Buckling Restrained Braces (BRBs), Steel Plate Shear Walls (SPSWs), and Triangular Added Damping and Stiffness Devices (TADAS), were considered as possible practical solutions, but the focus of the work presented here is on BRBs.

For the bridges with slab-on-girder steel superstructure, the AASHTO Guide Specifications for LRFD Seismic Bridge Design (2011) includes provisions for the design of steel bridges having specially detailed ductile diaphragms to resist loads applied only in the bridge transverse direction. Ductile diaphragms can be viewed as a special implementation of the SF concept. Implementations of the ductile diaphragm concept remain limited (or rare), because the ductile diaphragms covered by the AASHTO (2011) are only specified for bridges without skew, and only provide resistance to earthquake excitations acting in the direction transverse to the bridge axis. Without addressing the issues of skew and bi-directionality, this is a most serious limitation and a real impediment to the implementation of ductile diaphragms, which is most unfortunate because ductile diaphragms are a low cost seismic solution compared to other alternatives. A bi-directional ductile end diaphragm concept proposed by Celik and Bruneau (2010) was used to implement ductile end diaphragms in straight or skew bridge superstructures, to resist bidirectional earthquake excitations. In this bi-directional concept, the SFs are arrayed in the end diaphragms such as to provide ductile response to horizontal earthquake excitations acting from any direction. However, Celik and Bruneau (2010) did not investigate the adequacy of the concept when subjected to earthquake excitations. Therefore, BRBs are further explored here as possible solutions to serve as ductile seismic fuses in bridge end-diaphragms. By providing an analytically and experimentally proven solution for ductile diaphragms able to explicitly address the fact that earthquake simultaneously shake a bridge in all horizontal directions (not just transversely to the bridge axis), and by making this solution also applicable to skew bridges (a large percentage of all bridges), this research is therefore poised to make ductile diaphragms a commonly used seismic-resistance solution for most short and

medium span steel bridges in all seismic regions (i.e. in regions exposed to low levels of seismicity, ranging up to those exposed to more severe earthquakes). Again here, BRBs are used for this purpose.

Note that, in the above-mentioned two prospective applications of using the SFs to protect bridges, BRBs have been considered as the most promising hysteretic device to achieve the design objective, which is to concentrate the damage to SFs and protect the rest of ýj g'bridge's structural elements. 'BRBs can exhibit stable hysteretic behaviors and sustain a large number of displacement cycles at high ductility demands. Various kinds of BRBs have been developed, studied and implemented in numerous building structures for seismic designs. Though a few implementations of BRBs have been used in bridges, efforts are still needed to study how BRBs can be utilized to help the bridge system achieve appropriate seismic performance, especially in those two prospective SFs applications for protection of the bridge's substructures and superstructures.

1.2   Outline

Section 2 provides a brief summary of the literature related to the SF concept, focusing especially on past research and implementations of ductile diaphragms in steel bridges. Some of the past analytical and research work on BRBs is presented, followed by examples of BRBs' implementations in actual bridges and outdoor structures.

The design concept for a few SF systems is presented in Section 3, along with a preliminary study conducted to investigate how various types of SFs could be implemented as energy dissipation devices in a representative California bridge bent with Reinforced Concrete (RC) columns; the feasibility of implementing each system with a different type of SF is assessed based on the results from this study. Several metallic hysteretic damping devices are investigated in the preliminary study, for their possible use in a Reinforced Concrete (RC) bridge bent. Also presented in Section 3, in a preliminary way, are a few different types of details proposed to connect SFs to the bridge columns.

Building on the findings in Section 3 that BRBs provide the most practical SF solution, with a wider range of possible applications compared to the others devices considered, a design procedure to implement BRBs in California bridge bents is formulated and presented in Section 4. To facilitate the design of the SF system and connection of BRBs to the columns, Concrete Filled steel Tubes (CFT) columns are used. In that study, BRBs are sized to meet the structural fuse objectives under the governing seismic lateral loads for two proposed bridge bent configurations, comparison of theoretical and actual

pushover curves obtained using nonlinear push-over analysis is performed, and seismic and service load demand checks on the CFT columns are conducted.

Section 5 presents results from nonlinear time history analyses of all the previously designed bridge bents with BRBs, subjected to spectra-compatible synthetic ground motions. The displacement demands of the system with BRBs are compared with the bare bridge bents without BRBs to prove the benefit of adding BRBs into the bridge bents. These nonlinear time history analysis results also allow to verify the bridge bent displacements predicted from the design procedure.

Given that BRBs can be added to an existing bridge bent to implement the structural fuse system, details of how BRBs could potentially be connected to transfer their loads to CFT columns, foundations and cap beams, are investigated in Section 6. Primary focus is on connection to CFT columns by welding of the gusset plate of the BRB directly to the steel shell of a CFT column. Based on the results of the analytical and experimental studies conducted for this type of connection, the feasibility of using the gusset plate connected to the CFT column's steel shell is contemplated. Details using concrete anchor bolts or anchor rods to connect BRBs to the foundation or cap beam are also studied, with possible connections details developed.

In Section 7, proposed ductile End Diaphragm Systems (EDS) are designed for benchmark skew and nonskew bridges and analyzed using nonlinear time history analysis to examine their seismic performance. Variations in skew, fundamental period of vibration, and earthquake excitation characteristics are also considered. These dynamic analyses allow investigating the impact of these parameters on global behavior, as well as understanding the magnitude of local demands and the extent of bi-directional displacements that the BRBs must be able to accommodate while delivering their ductile response. The long-term service life of BRBs installed across expansion joints and subjected to bridge thermal expansion histories is also investigated and a minimum ratio of the BRB's core over the whole bridge length ratio is recommended.

Section 8 describes the quasi-static experiments conducted to subject BRBs to a regime of relative end-displacements representative of the results predicted from the parametric analytical studies in Section 7. The test set-up that was developed for this purpose is described, together with the displacement protocols used, which include the bi-directional displacement histories applied to the specimens for the cyclic inelastic test, and the uniaxial displacement histories for the low-cycle fatigue test due to temperature changes. Two types of BRBs were designed, and four specimens of each type of

BRB were tested under different combinations of displacement protocols. The BRB's hysteretic behaviors under different displacement protocols are studied and compared.

The investigations on the BRB connection test results are presented in Section 9. The observations of the BRB specimens after their failure are described, followed by two methods for quantifying the BRB's hysteretic behaviors in the tests, namely, cumulative inelastic deformations and low-cycle fatigue life. A recommended design procedure for the EDSs in both nonskew and skew bridges is developed based on the parametric analysis and experimental results.

Section 10 presents a design example for a multi-span simply supported bridge, implemented with the proposed bidirectional ductile diaphragms. Nonlinear time history analyses are performed on this bridge to illustrate how its seismic behavior can be improved.

Section 11 summarizes the research work and provides conclusions, as well as recommendations for future work.

SECTION 2
LITERATURE REVIEW

2.1   General

There have been numerous analytical and experimental studies investigating the structural fuse concept using various devices in the past. In this Section, a brief summary of literature on the structural fuse concept is first presented in Section 2.2. As a special implementation of the structural fuse concept in bridges, past research and implementations of ductile diaphragms in steel bridges are presented in Section 2.3. Although many types of hysteretic devices have been used in past structural fuse systems, the more immediate focus here is on the application of BRBs in bridges; as such, a brief overview of BRBs in this context is presented in Section 2.4. Some of the past analytical and research work on BRBs is presented in Section 2.4.2, followed by examples of BRBs' implementations in actual bridges in Section 2.4.3. Since there is an aspect of using BRBs in outdoor applications that could be relevant given that bridges are exposed to the environment, a brief overview of the few related outdoor implementations of BRBs is provided in Section 2.4.4. For BRBs' implementation in bidirectional ductile diaphragm, there is a need for the BRB to accommodate both in-plane and out-of-plane displacement demands. Therefore, Section 2.4.5 provides a brief review on past research studying the out-of-plane stability of BRBs.

2.2   Structural Fuse

The terminology "ductile fuse" has long been used in the literature, going back at least to Roeder and Popov (1977) who used this term to describe the links of Eccentrically Braced Frames (EBF), promoted at that time as a mean to increase the hysteretic energy dissipation capacity of steel frames by concentrating energy dissipation primarily in specially detailed shear links that are integral to the frame itself. In other examples, Fintel and Ghosh (1981) used the term "structural fuse" to describe the capacity design concept in which beams are intentionally designed as weaker members that would yield by plastic hinging, to protect columns and walls which are considered more crucial for the structure to remain elastic.

The above examples use the terminology "fuses" generically for system designed in compliance with capacity design principles. However, for the case of interest here, "fuses" is a term used when damage is controlled by using parallel systems, as discussed below.

Wada et al. (1992) proposed the concept of "damage-controlled structures" schematically explained in Fig. 2-1. Such a structure consists of two separate primary components, namely the main moment frame structure and a system of passive energy dissipation elements. In this cited study, the moment frame

"

resists 80% of the lateral loads while the secondary fuse system withstands the loads resulting from strong ground motions (various ratios have been considered in other studies). This damage-controlled concept was further investigated and improved following the 1995 Northridge and 1995 Hyogoken-Nabu earthquake by Conner et al. (1997). The study demonstrated that by adjusting the distribution of stiffness and hysteretic damping, it is possible to control the seismic response of a building to limit repair costs. A schematic relationship between repair cost and earthquake intensity for conventional and damage-controlled structures is presented in Fig. 2-2. Damage-controlled structures were deemed more efficient in terms of cost reduction for larger earthquakes. Relevant extensive studies about this concept can also be found in Shimizu et al. (1998), Wada and Huang (1999), and Huang et al. (2002).

(a) (b) (c)
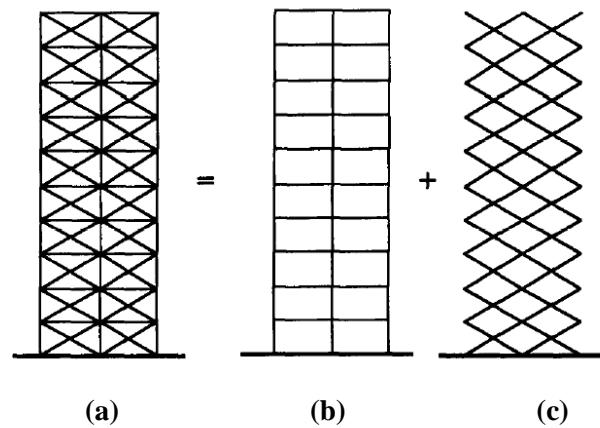
Figure 2-1 Damage-controlled Structure: (a) Total Structure; (b) Gravity Support Structure; (c) Seismic-Resistant Structure (Wada et al., 1992)
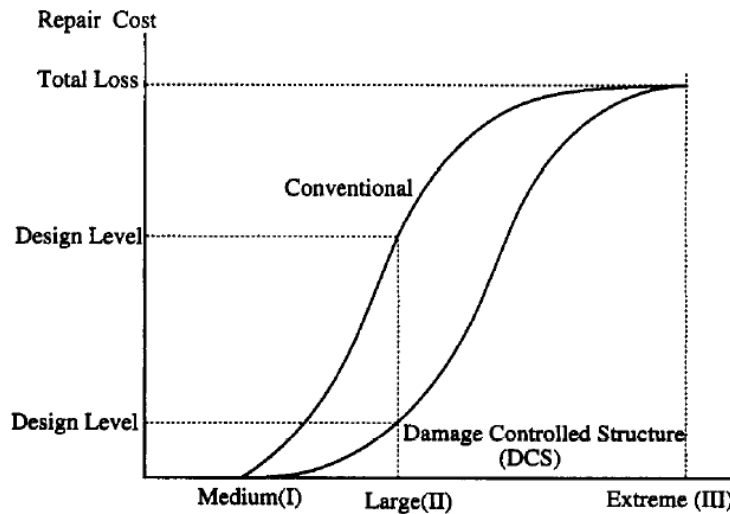
Figure 2-2 Repair Cost vs Earthquake Intensity (Conner et al., 1997)

The ideal Structure Fuse (SF) implementation would be one in which the fuse a disposable and replaceable structural element introduced into the structure system specifically to provide all of the needed seismic energy dissipation. Only limited research to date has focused on achieving this ideal objective, particularly with regard to easy replaceability (and thus expedient repairs) following the earthquakes.

Vargas and Bruneau (2006a, 2006b) described the SF concept in a parametric formulation, considering the behavior of nonlinear Single Degree of Freedom (SDOF) systems subjected to synthetic ground motions. A general pushover curves for a SDOF structure is shown in Fig. 2-3. The SF concept requires that yield deformation of the damping system Δ_{ya} be less than the yielding deformation corresponding to the bare frame Δ_{yf}. A systematic and simplified design procedure was put forward to achieve and implement SF concept that would limit damage to disposable structural elements for any general building. The procedure without the need for complex analyses was based on identifying regions of admissible solutions for the SF concept using nonlinear time history analyses. Metallic dampers such as BRBs, Triangular Added Damping and Stiffness (TADAS) and Shear Panels were implemented in both SDOF and Multi-Degree-of-Freedom (MDOF) systems to ensure the adequate seismic performance. A following experimental project tested a three-story building frame designed with BRBs as a proof of concept of the developed design procedure. Furthermore, the research reported the impact of introducing SF on floor accelerations and velocities (which has impact on seismic performance of nonstructural components).

(a)   (b)
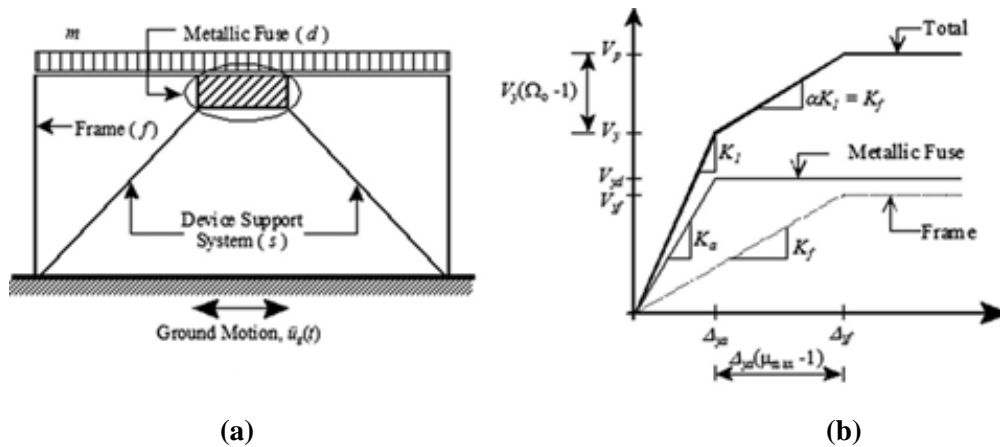
Figure 2-3 (a) Sample Model of a SDOF System with Metallic Fuses; (b) General Pushover Curve (Vargas and Bruneau, 2006a)

A wide range of passive hysteretic energy dissipation devices can be used to enhance the stiffness and strength of the structure to meet the structural fuse concept. Note that hysteretic energy dissipation

9

systems are sometimes called metallic yielding dampers if their only purpose is to provide hysteretic behavior of metals in the inelastic range. These are also called "rate or displacement dependent dampers" because their response is not sensitive to the frequency of loading. The resisting force of such dampers, therefore, depends on the nonlinear stress-strain characteristics of the materials. The amount of damping they provide is somewhat proportional to the magnitude of their inelastic deformations. However, in the present context, the perspective taken includes any solution that can achieve the structural fuse objectives stated above, and consequently, the design procedure followed is not based on structural damping analogies but rather on conventional stiffness and strength analyses.

A partial list of possible type of SF elements that could be constructed for potential use in bridge applications, includes standard Buckling Restrained Braces (BRBs) (Wada et al. 1992, AISC 2010), short specialty BRBs (El-Bahey and Bruneau 2010), shear links (Nakashima M. 1995, Tanaka et al. 1998, Goodyear & Sun 2003), steel plate added damping and stiffness device (Whittaker et al. 1991, Tsai et al. 1993), Steel Slit Dampers (Sugiyama 1998, Chan et al. 2007), Steel Plate Shear Link (El-Bahey and Bruneau 2010), and steel plate shear wall (Keller and Bruneau 2009, AISC 2010), to name a few. Different types of fuses may work best for different bridge topologies. Information on these various kinds of hysteretic devices' implementation is provided in detail in Wei and Bruneau (2013).

A noteworthy implementation of the SF concept in a bridge is the built-up wide-flange shear links implemented in the tower of the new San Francisco-Oakland Bay (SFOBB) suspension cable bridge. The main bridge tower in Fig. 2-4 consists of four closely spaced columns connected by a series of steel shear links designed per AISC seismic provisions. Details of the shear links installed between the columns are shown in Fig. 2-5. Each column is a hollow, semi-elliptical cross section with an interior steel liner that tapers from the tower head to the base. The shear links help form a transverse structural frame system with a greater number of redundant ductile elements. Goodyear and Sun (2003) compared the capacity of the tower with and without links by using nonlinear pushover analysis as shown in Fig. 2-6. The pushover curve of the tower with shear links showed no inelastic demand in the concrete tower element until well beyond the Safety Evaluation Earthquake (SEE) demand displacement. And all inelastic demand for the single tower was confined to the steel links.

Another special implementation of the structural fuse concept in bridges is the ductile diaphragm concept, for which specially detailed ductile diaphragms in bridge steel superstructures on elastic substructures are used to help achieve ductile response. Design using the ductile diaphragm is listed as Type 2 global seismic design strategy for bridge system by AASHTO (2009). Since the context in later Sections

specifically investigate the idea of bi-directional ductile end diaphragm, a summary of past research and implementations of ductile diaphragms is presented in Section 2.3.
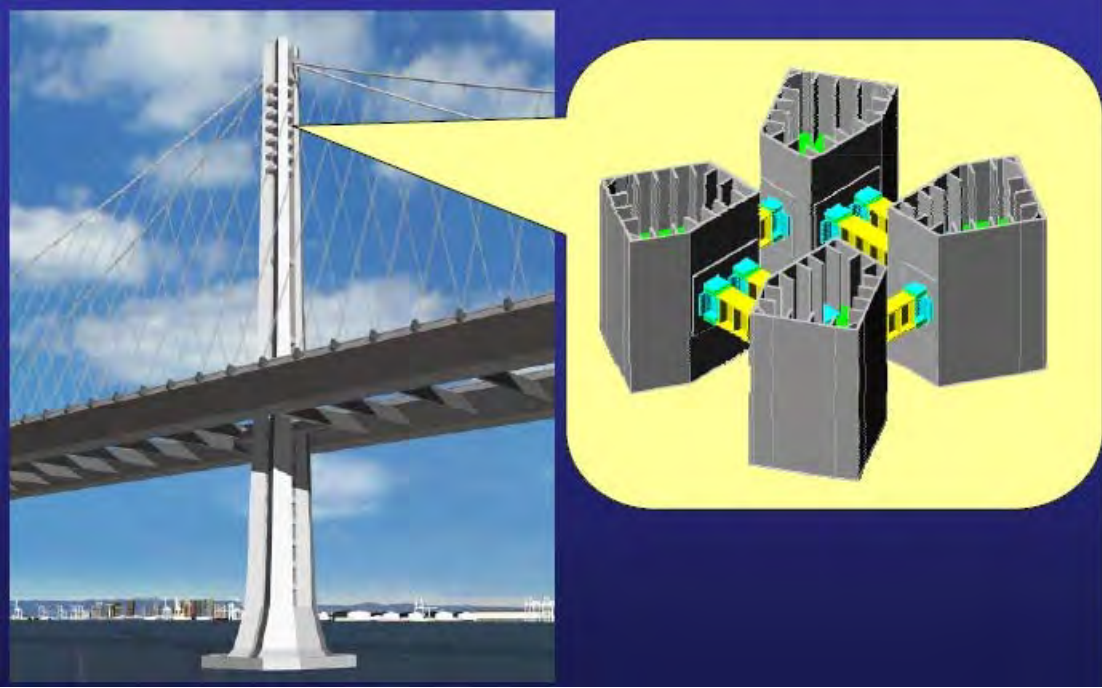
Figure 2-4 Bay Bridge Towers with shear links (El-Bahey and Bruneau, 2010)
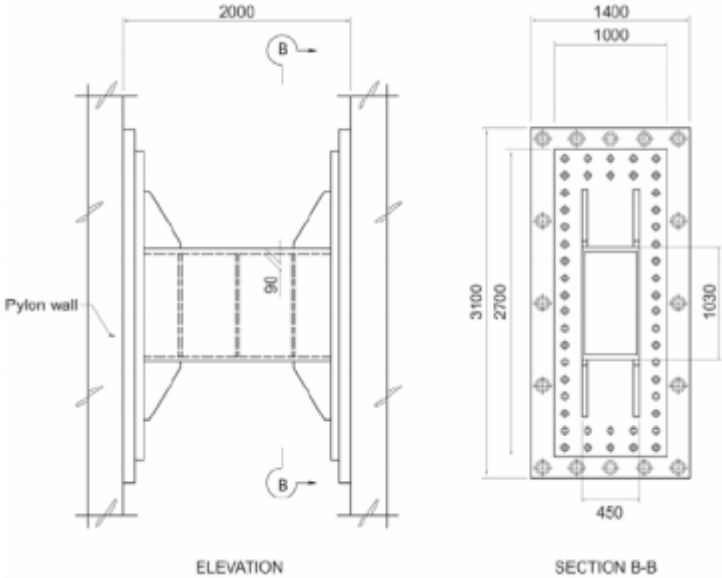
Figure 2-5 Shear link dimensions in SFOBB (Goodyear and Sun, 2003)
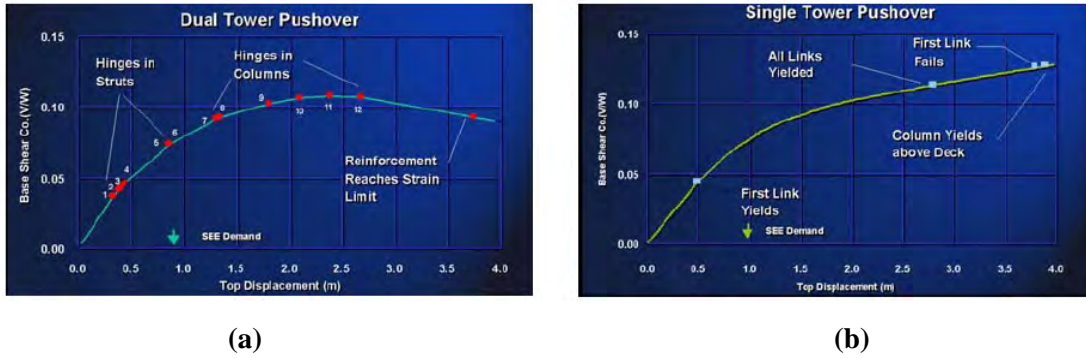
<div align="center">(a)   (b)</div>

Figure 2-6 Pushover curves for the tower: a) with shear links; b) without shear links

(Goodyear and Sun, 2003)

In the context of the current study, although many types of hysteretic devices have been used in past structural fuse systems, the more immediate focus here is on the application of BRBs in bridges; Section 2.4 provided a brief summary of research and analytical studies on BRB, followed by examples of BRB's application in bridges and outdoor structures.

2.3　Ductile Diaphragm

To investigate the behavior of steel bridges during earthquakes, Zahrai and Bruneau (1998) investigated the role of the diaphragms on the seismic behavior of slab-on-girder bridges with different length by comparing the behavior of bridges with and without diaphragms through pushover analysis. In Zahrai and Bruneau (1999a), ductile end diaphragms to be installed in the steel superstructure of slab-on-girder steel bridges was proposed as a seismic retrofit strategy. A design procedure for ductile end diaphragms was proposed using either shear links (Fig. 2-7a), Triangular-plate Added Damping and Stiffness Devices (TADAS) (Fig. 2-7b), or Eccentric Braced Frame (EBF) (Fig 2-7c) placed in an inverted Y-bracing configuration in the ductile diaphragm.

Zahrai and Bruneau (1999b) presented experimental results on full-scale ductile diaphragm specimens having the three proposed configurations and subjected to conventional reversed cyclic inelastic loading as well as pseudo-dynamic testing. The specimens with shear link and TADAS are shown in Figs. 2-8a and 2-8b, respectively. The ductile diaphragm systems reached drifts of around 3%, 3%, and 3.8% for the shear link, EBF and TADAS. The resulting hysteretic curves of the specimen showed good energy dissipation.

(a)   (b)

(c)
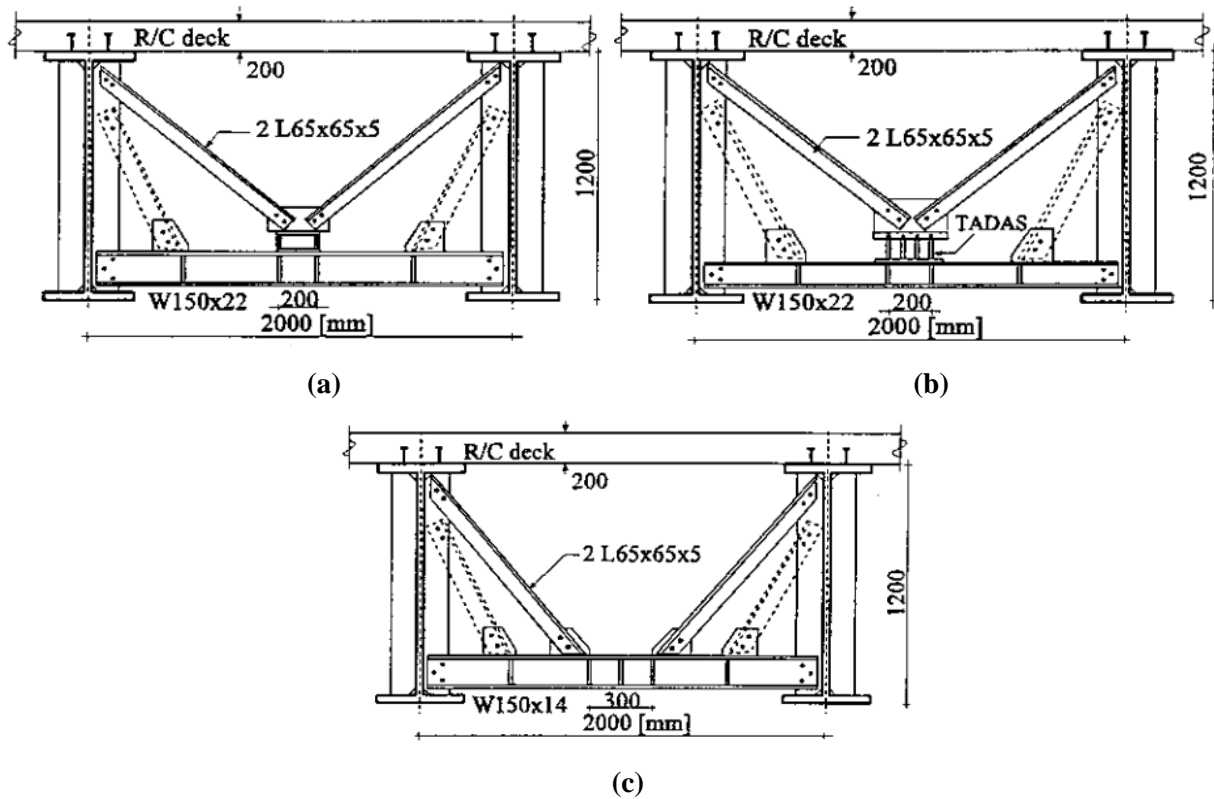
Figure 2-7 Ductile end diaphragm using: (a) shear link; (b) TADAS; (c) EBF (Zahrai and Bruneau, 1999a)

(a)   (b)

Figure 2-8 Specimen with: (a) deflected shear link having visible buckling in the flanges; (b) TADAS having significant flexure at 2% drift (Zahrai and Bruneau, 1999b)

Alfawakhiri and Bruneau (2000) used a generalized Single Degree of Freedom (SDOF) model to study the interaction of superstructure and support/substructure flexibility on the seismic response of simply

supported bridges under transverse ground motion. The closed-form expression for the modal shapes of the bridge was found to depend on a dimensionless stiffness index, which is the relative stiffness ratio between the superstructure and support/substructure. The accuracy of the numerical solution was proved to well capture the dynamic response of the bridge, as demonstrated by analyses of three different multiple degree of freedom bridge models.

For the simply supported bridge with a given global ductility demand when subjected to ground motions in its transverse direction, Alfawakhiri and Bruneau (2001) further studied the local ductility of the ductile member designed in the ductile diaphragms on top of the support/substructure considering the flexibility of the superstructure. Close-formed expressions were derived to predict the local and global ductility demands of the bridge, and how the span-to-substructure relative flexibility affects the ductility demand in the bridge support/substructure.

For deck-truss bridges, Sarraf and Bruneau (1998a) proposed a ductile seismic retrofit solution to improve its seismic vulnerability by introducing special ductile diaphragms to replace the end cross-frames and the flower lateral braces panels adjacent to the support. Similar to the ductile diaphragms introduced in slab-on-girder bridges, the energy dissipation in this retrofit solution is mainly concentrated in the ductile diaphragms, such as to eliminate (or limit) damage in the superstructure or substructures. Computer simulation of the retrofitted deck-truss bridge model subjected to severe ground motions proved that the proposed end ductile diaphragm significantly enhanced the seismic performance of deck-truss bridges. In Sarraf and Bruneau (1998b), a performance based design procedure of the ductile diaphragm in deck-truss bridges was proposed using shear links, TADAS, and EBF. Considering the constraints on limits of global drifts and ductility demands, as well as other constraints related to the specific type of devices used, ductile diaphragms having TADAS devices were found to have less constraints and thus to be simpler to design. Following this analytical work, pseudo-dynamic tests (Sarraf and Bruneau, 2002, 2004) were conducted on a 27 ft-long deck-truss bridge retrofitted with EBF and shear links. Both system performed well in terms of the hysteretic behavior of the device and the dissipated seismic energy, and the strategy worked well to prevent damage in other members of the bridge.

Bruneau et al. (2002) presented a step-by-step design procedure for specially detailed ductile diaphragms in slab-on-girder bridges and deck-truss bridges, based on the analytical and experimental work originally developed for retrofitted bridges in Zahrai and Bruneau (1998, 1999a, 1999b), Alfawakhiri and Bruneau (2000, 2001), and Sarraf and Bruneau (1998a, 1998b, 2002, 2004). Design equations were provided for the systems with shear links, EBF and TADAS devices, and it was mentioned that other types of devices

14

could also be used for this implementation as long as they possess accurately-assessed yield strength and could sustain repetitive cycles of inelastic deformations without significant strength degradation.

Carden et al. (2006a, 2006b) evaluated the performance of ductile end cross frames using single angle X and BRBs in a straight single-span two-girder bridge model with a scale factor of 0.4 from a bridge prototype. Fig. 2-9 shows the typical X-brace and BRB used in the specimen for the large shake table experiment. This specimen was an implementation of the ductile diaphragm concept developed by Zahrai and Bruneau (1999), but with different types of energy dissipating devices. Both bridge models were tested: (1) using two actuators acting at the deck level of the bridge model by conducting reversed static load in its transverse direction; (2) using shake table testing for increasing amplitudes of the 1940 El Centro earthquake ground motion applied in the transverse direction.

Bridge model with both types of end diaphragms showed satisfactory ductile seismic response with maximum drift of 5.3% and 6.6% obtained for the system with X-brace and BRB, respectively.

2.4 BRB
2.4.1 General

BRBs were initially developed in Japan by the Nippon Steel Corporation in the mid-1980s, and were then called as Unbounded Braces (UBs). Watanabe et al. (1988) presented a summary of some of the early development of BRBs. This system has been well received by Japanese designers after the 1995 Kobe Earthquake and implemented in numerous buildings. In North America, BRBs have been studied and implemented since the late 1990's and are becoming widely used in steel buildings, with at least three commercial suppliers of BRBs in the United States. For more than 30 years, BRBs with various materials and geometries have been developed and studied all over the world. A more thorough review of the development of BRBs can be found in Uang et. al. (2004) and Bruneau et. al (2011).

A BRB generally consists of a central core surrounded by a tube that restrains the core from axially buckling in compression. The space between the core and the tube is filled with mortar. Unbonded material covers the steel core to isolate it and allow it to deform freely in the axial direction. The unbonding material should be thin enough to avoid local buckling of the core, and yet thick enough to accommodate lateral expansion of the core due to Poison's effects. The steel core is usually of rectangular or cruciform cross section shapes. Fig.2-10 shows the components of a typical BRB and some detailed configurations.

15

(a)   **(b)**
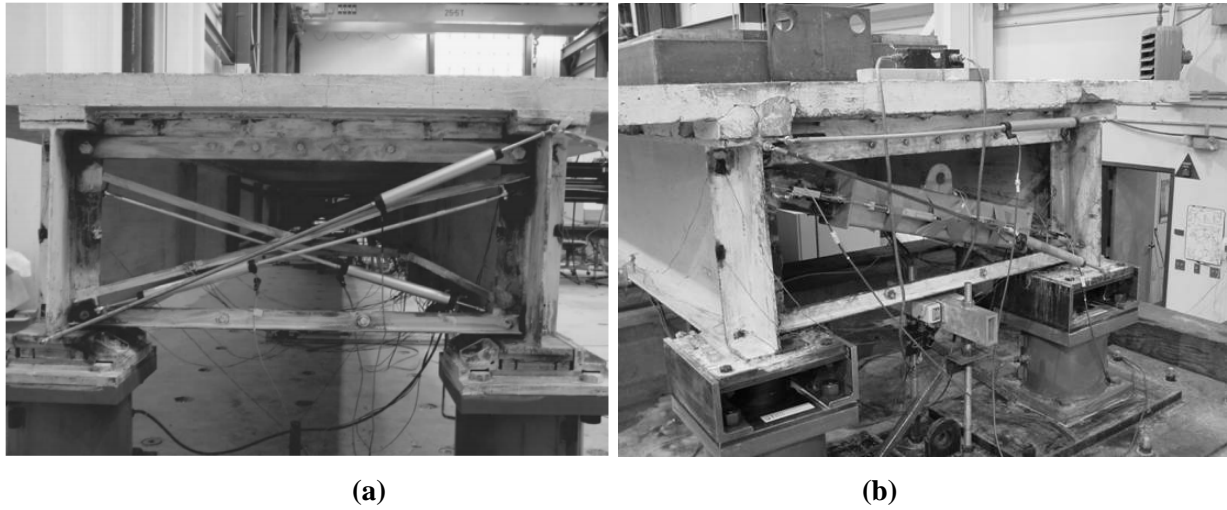
Figure 2-9 End ductile cross Frame of the plate girder bridge with (a) X brace; (b) BRB

(Carden et al., 2008)
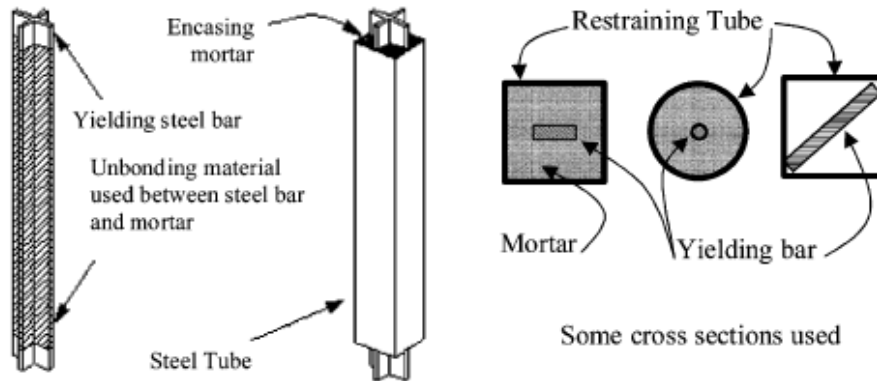
Figure 2-10 Some Schematic Details Used For BRB in Sabelli et al.(2003)

Since BRBs prevent global buckling of the steel core by encasing it over its length, they exhibit a better force-displacement hysteretic behavior as shown in Fig. 2-10, and can overcome many of the problems associated with the hysteretic behavior of concentrically braced special frames. A description of the mechanics of the BRBs with fully detailed design examples are presented in Lopez and Sabelli (2004). Most importantly, BRBs have a superior resistance to low-cycle fatigue, being typically able to sustain a large significant number of hysteretic cycles at large ductility demands. The large maximum ductility μ_{max} (BRB maximum deformation divided by BRB yield deformation) and cumulative ductility μ_c (sum of BRB plastic deformation over BRB yield deformation) capability can be observed in Table 2-1.

16
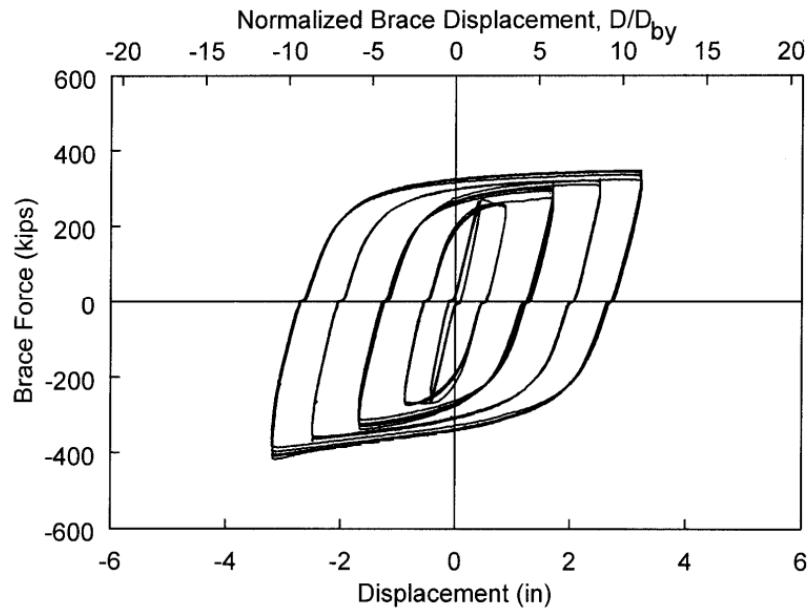
Figure 2-11 The cyclic behavior of a typical BRB (Merritt et al., 2003)

Table 2-1 Ductility Demands for Isolated BRB Tests (Fahnestock et al.,2007)

Reference	Designation	μ_{max}	μ_c
Watanabe et al. (1988)	[a]	10[b]	50[b]
Black et al. (2002)	99-1	20	324
	99-2	10	879[c]
	99-3	10	279
	00-11	15	1,045
	00-12	15	538
Merritt et al. (2003)	1	15	900[c]
	2	15	600[c]
	3	10	1,600
	4	15	1,100
	5	15	1,300
	6	15	800
	7	10	1,000
	8	10	1,000
Usami et al. (2003)	[a]	25[b]	400[b]
Tsai et al. (2003a)	T2_420SN_A	48.4[d]	[a,c]
	T3_350	42.3[d]	[a,c]

[a]Not reported.
[b]Estimated from published plot.
[c]Core fracture due to low-cycle fatigue.
[d]Tension only.

BRBs have been used extensively in Japan since 1987 in nearly 200 buildings. The first installation of BRBs in US is the Plant and Environmental Science Building at the University of California, Davis,

17

which was a new steel structure (Clark et al., 2000). Implementations of BRBs has dominantly been in steel buildings, as the details to connect BRBs to steel frames are naturally similar to those to connect braces in concentrically braced frames. However, implementations in concrete buildings are interesting here, given that BRBs implemented in RC bridge bents are likely to be connected to RC columns. Known BRB implementations in RC buildings include: the Martin County Civic Center (Shaw et al., 2000), the Wallace Bennett Federal Building (Aiken et al., 2001), the Hildebrand Hall (Morgan et al., 2004; Anagnos T., 2011), the Webb Tower (Islam et al.,2006), to name a few. More details on the above BRB's applications in concrete buildings are provided in Wei and Bruneau (2013).

Section 2.4.2 below presents selected findings from some of the past analytical and experimental research that has been conducted on BRBs that can be somewhat relevant as they address some issues that are relevant from the perspective of implementing BRBs in between the columns in substructures, and also in bi-directional diaphragms. Sections 2.4.3 and 2.4.4 focus on BRB's implementations in bridges and outdoor structures.

2.4.2   Analytical and Experimental Research

Analytical research has been performed extensively for BRB's implementations in building structures since 1990s all over the world (e.g., Sabelli 2001; Lopez et al. 2002; Tremblay and Bouatay 2002; Black et al. 2002; Iwata et al. 2003; Sabelli et al. 2003; Mayes et al. 2004; Higgins and Newell 2004). Experiments have been conducted on various BRB specimens (Watanabe et al.1988; Clark et al. 2000; Black et al. 2002; Usami et al. 2003; Merritt et al. 2003a, b; Tsai et al. 2003b, Romero et al.2007). Tests were also performed with plane frame i.e. one-story one-bay subassembly with BRBs (Tremblay et al. 1999; Aiken et al. 2001; Uriz 2005; Christopolus 2005), and for 3-dimensional multi-story multi-bay structure with BRBs (Tsai et al. 2003a; Fahnestock et al. 2007; Tsai et al. 2008 ; Tsai and Hsiao 2008).

Design guideline for Buckling Restrained Braced Frames (BRBFs) is provided in AISC 341 (2010). BRBs are normally designed to connect to the framing elements (beams and columns) using gusset plates. The most common BRB-gusset plate connections are the bolted and pinned connections, as shown in Fig.2-12.

BRBs were found to typically perform well and can withstand large displacement demands. However, the gusset plates in some large-scale tests of BRB planar subassemblies and BRBF 3-dimensional systems have exhibited poor performance at story drifts between 2% to 2.5% (Fahnestock et al. 2007). The gusset

plate increased the beam-column-brace connection region, where large deformation demands happened and caused potential gusset plate instability at large storey drifts (Lopez et al. 2002).
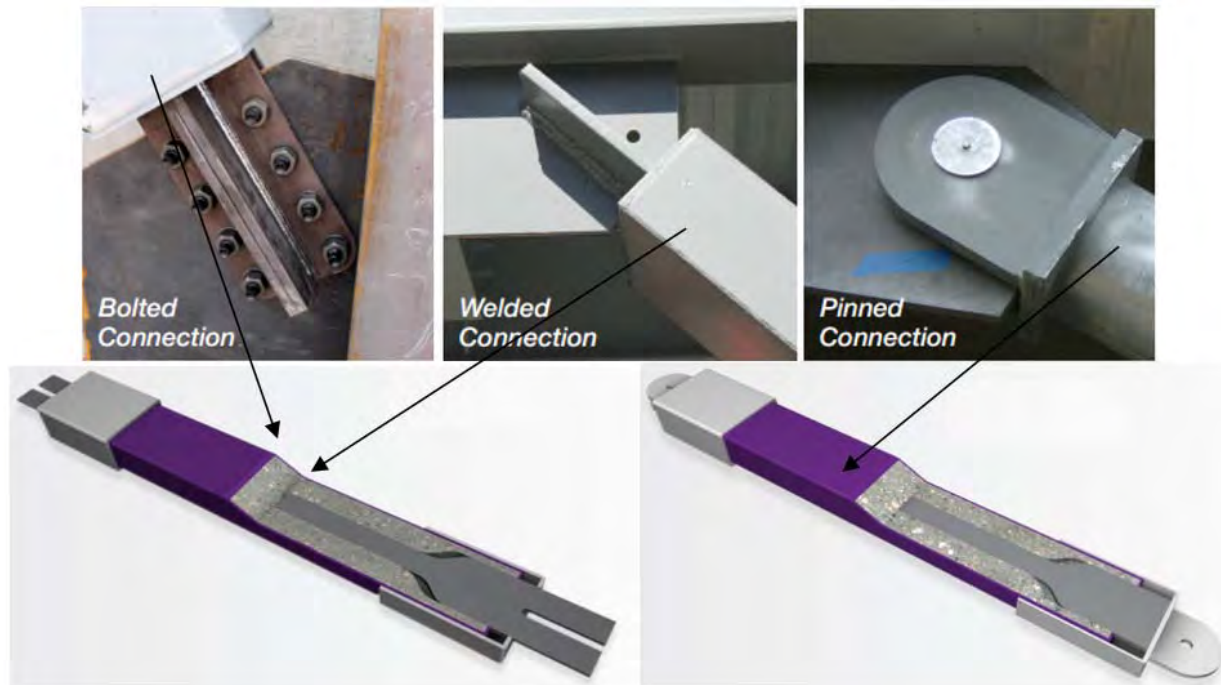
Figure 2-12 Different BRBs end connections (Star Seismic, 2016a)

Fahnestock et al. (2007) performed a large-scale experimental test of BRBFs using a hybrid pesudodynamic testing method to simulate earthquake ground motions. The four story BRBF with scale factor of 0.6 had BRBs in chevron configurations, as shown in Fig.2-13a. A special connection detail for between the beam-column-brace, as shown in Fig. 2-13b, was used to improve system performance and prevent undesirable problems in the connection details. The BRBF sustained story drifts of 4.8%, with the BRB's reaching maximum ductility demands of more than 25 without strength or stiffness degradation. Yielding in the beam flange at the full penetration welds was observed, but there was no distortion or damage in the gusset plates.

For the quasi-static cyclic test performed on the BRBF after the pesudodynamic test, the BRBs failed at cumulative ductility demands ranging from 372 to 453, with maximum ductility demand greater than 22. The failed BRB, presented in Fig. 2-14, exhibits a visible bulge in its collar and concrete filled tube. The inside damaged concrete around the fractured core plate is also shown in that figure. Note that these BRBs manufactured by Star Seismic, LLC of Park City, Utah, are similar to those of the specimens that will be presented in Section 8.
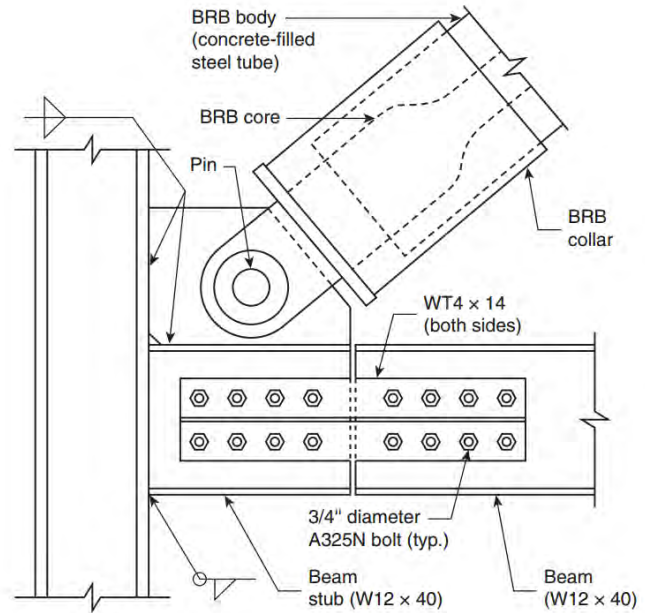
Figure 2-13 Large scale experimental test (a)Testing frames; (b) Improved connection detail (Fahnestock et al. 2007)

Note that the above frame systems were only tested unidirectionally (Tsai et al. 2003a; Fahnestock et al. 2007; Tsai et al. 2008; Tsai and Hsiao 2008). More recently, Palmer et al. (2013) tested a full three-dimensional two-story frame, with one-bay BRBFs in each direction, having BRBs manufactured by Star Seismic as shown in Fig. 2-15a. The BRBs were also pin-connected to the BRBF as shown in Fig. 2-15b. The BRBF were subjected to the bidirectional "cloverleaf" test protocols shown in Fig. 2-16. Although the BRBs' core plates failed at 3.6% and 4.2% storey drifts, significant inelastic deformations and damage happened to the framing member of the system and the gusset plates. Note that, in this specimen, the ability of the BRBs in the BRBF to resist bidirectional loading relies on the bending flexibility of the gusset plates to which the BRBs were connected.

<p align="center">(a)   (b)</p>

<p align="center">(c)   (d)</p>

Figure 2-14 BRB specimen removed from BRBF story 1 north after the test: (a) north end bulge in collar; (b) north end bulge in concrete filled tube under collar; (c) damaged concrete inside the tube; (d) fractured core plate (Fahnestock et al., 2007)
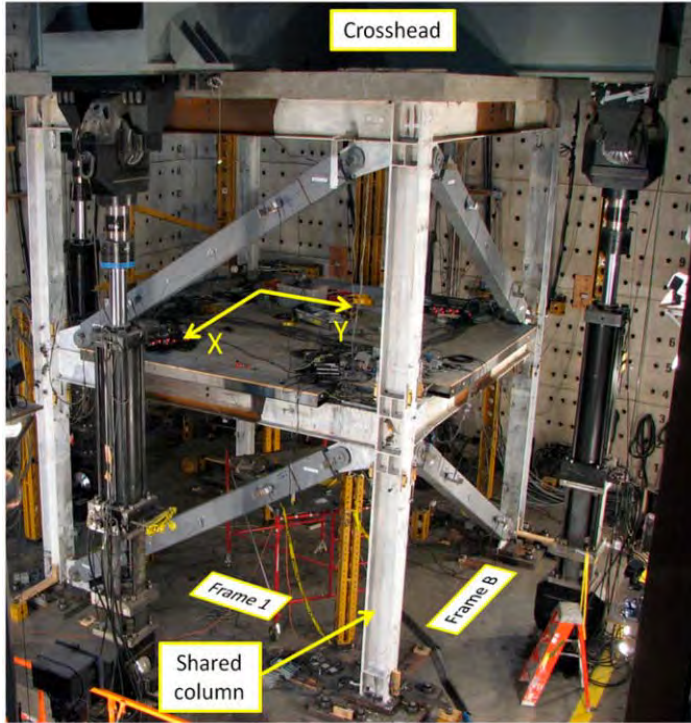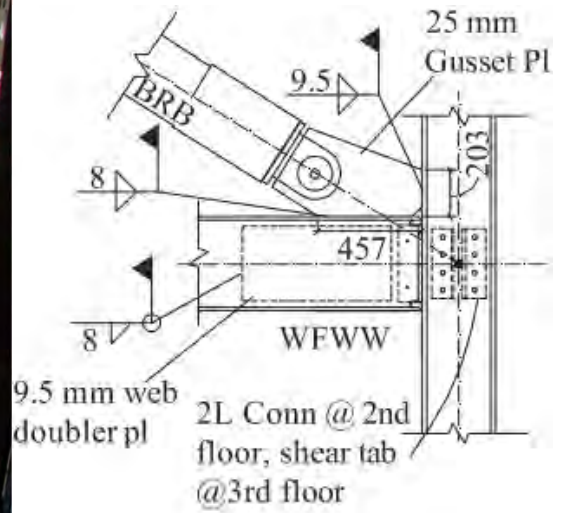
(a)   (b)

Figure 2-15 BRBF subjected to bidirectional testing protocols: (a) testing frame; (b) BRB and frame connection (Palmer et al. 2013)
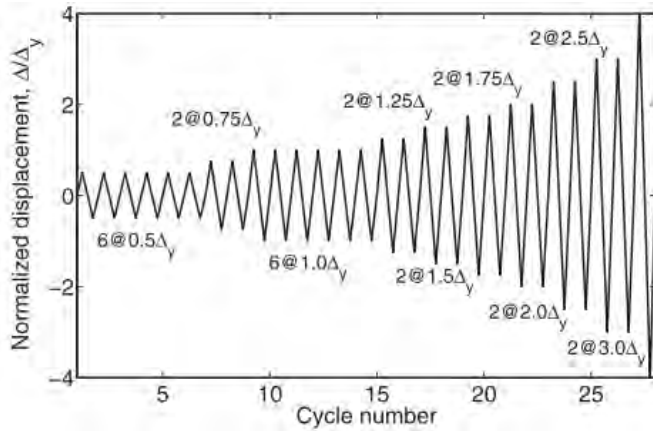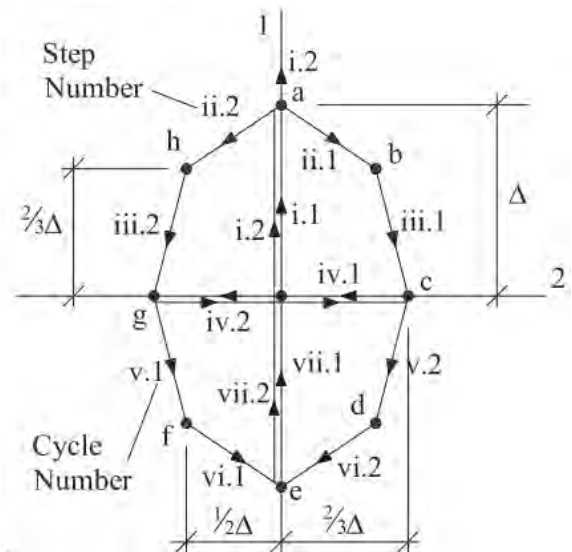
(a)   (b)

Figure 2-16 BRBF test protocol: (a) unidirectional ; (b) bidirectional cloverleaf displacement history (Palmer et al. 2013)

The above-mentioned research focus on BRBs more used in the context of reducing the inelastic deformations of the existing building frames. There are also a lot of work has been done to study the application of BRBs in bridges. Usami et al. (2005) studied the implementation of BRBs in steel arch bridges for seismic upgrading. The bridge was composed of reinforced concrete deck slab, steel girders and arch ribs as shown in Fig.2-17. Nonlinear time-history analysis of the bridge showed that its seismic performance in the transverse direction was inadequate. Two retrofit plans considered replacing some lateral members and diagonals by BRBs. In Fig. 2-18, lateral braces of the pier as well as twelve diagonals near the two arch rib bases were replaced by BRBs. The addition of BRBs at the arch ribs decreases the strain demand at the arch rib base to elastic range. The maximum strain demand in BRBs is below the capacity and stable behavior is ensured.

An analytical study by Celik and Bruneau (2011) used BRB in a bidirectional ductile diaphragm system to help the bridge resist bidirectional earthquake effects in straight and skewed steel slab-on-girder bridge. Two schemes of the bidirectional end diaphragm system were proposed, and closed-form expressions were derived for both schemes to express stiffness, yield strength, yield displacement, and hysteretic energy dissipation as a function of a given ductility level. The effect of changing certain parameters in the closed-form hysteretic model was studied based on static pushover analyses. Note that while the Celik and Bruneau (2011) explains the bidirectional ductile end-diaphragm concept, and contains an exploration of behavior for bridges subjected to progressively increasing static lateral loads, it is a conceptual paper that provides equations useful to "weed-out" some bad solutions and that provided valuable insights on where to focus further research efforts needed to develop and validate this concept to a point where it ready for implementation.
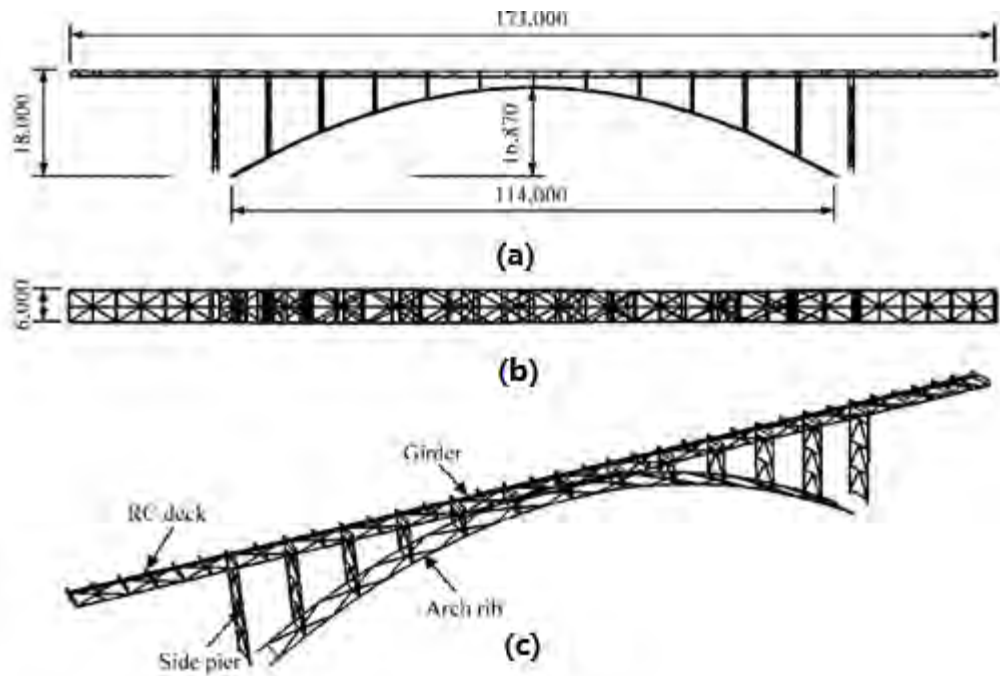
Figure 2-17 Layout of the Steel Arch Bridge to be retrofitted: (a) Elevation; (b) Plan; and (c) 3-D View (Usami et al., 2005) (Unit:mm) (Usami et al., 2005)
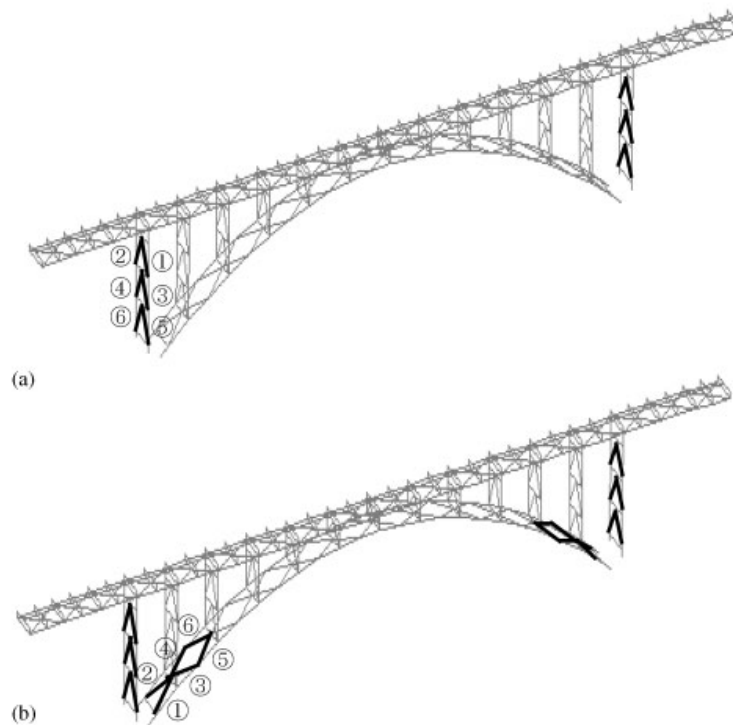
Figure 2-18 Location of BRBs in the Two Retrofit Proposals (Usami et al., 2005)

El-Bahey and Bruneau (2010) considered using an inverted chevron BRB brace system to retrofit general RC bridge bents. Governing parameters defining the behavior and design of the fuse system were identified. Seismic response was verified through parametric analyses of the studied systems and the results were refined and validated using non-linear time history analyses. A step-by-step design procedure was also proposed. That study was analytical and assumed that connection of the BRBs to concrete columns was possible. In related experiment, although using composite columns, special purpose short BRBs were inserted between twin closely-spaced segmental columns and over the whole height of the columns, as shown in the configuration in Fig. 2-19. The twin columns were subjected to a series of quasi-static cyclic tests. Analytical investigation was also conducted to replicate the experimental results. Hysteretic curves obtained during the full bridge column specimen tests reflected the behavior of the entire system, and were complemented by uniaxial BRB tests to verify the effectiveness of the newly proposed BRB device developed for this application.
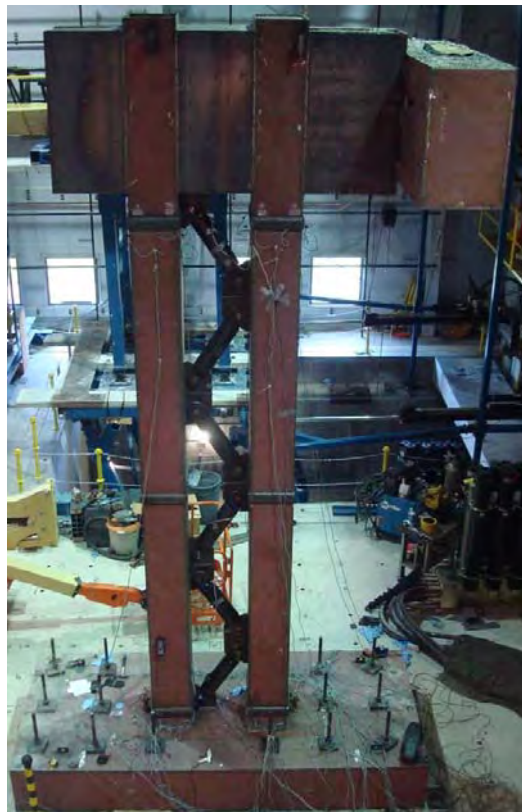
Figure 2-19 Twin Column Specimen S2-1 with BRBs Prior to Testing (El-Bahey and Bruneau, 2010)

Lanning et.al. (2015b) investigated replacing viscous dampers with BRBs for retrofitting the Vincent Thomas suspension bridge in Long Beach, California. Viscous dampers had been installed between the

suspended structure, the adjacent towers and cable bents, with the intent to mitigate their impact by reducing relative motions during a possible future significant seismic event caused by the Palo Verdes Fault. Unfortunately, the wearing of the viscous damper under service conditions induced loss of the viscous fluid and the damper solution could not be made effective for a future earthquake event without significant long-term regular maintenance costs. The study by Lanning et al. (2015b) showed that it was possible for alternative BRB designs (using current commercially available BRB) to provide sufficient bridge seismic response mitigation. An analytical model of the bridge and proposed BRB locations is shown in Fig. 2-20. Note that the displacement demands caused by a near-fault pulse type design earthquake applied to the bridge model were used to generate the loading sequences for testing the BRBs (Lanning el.al. 2015a). The simulated peak strain rates were, on average, 17% larger than those used for typical BRB testing rates. The BRB used in this case was deemed to be resilient in terms of inelastic deformation and energy dissipation capability.
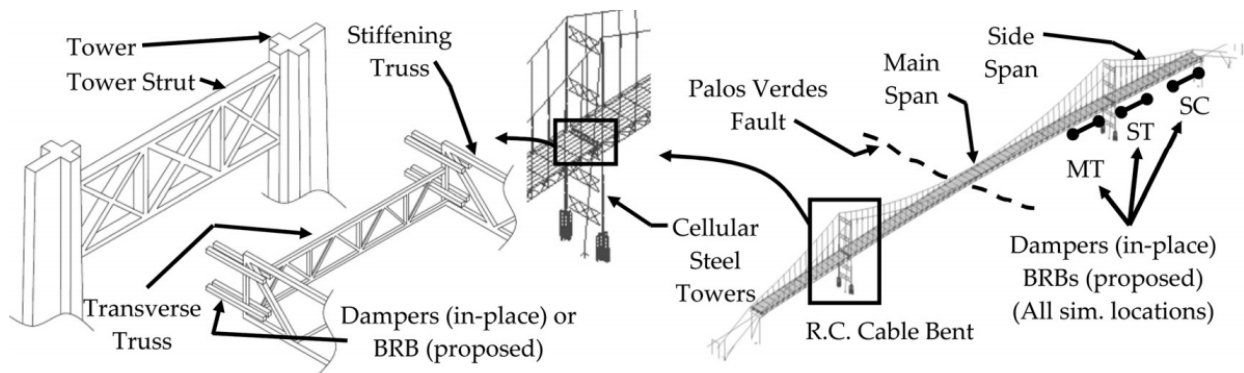
Figure 2-20 Locations of the proposed BRBs to replace the viscous dampers in the Vincent Thomas Bridge (Lanning, 2015)

Dusicka et.al. (2015) investigated the cyclic performance of a half-scale reinforced concrete bridge bent with RC columns retrofitted using BRB in a diagonal configuration as shown in Fig. 2-21. Retrofitted and unretrofitted bridge bents were both tested using quasi-static cyclic loading protocols generated based on subduction zone earthquake displacement demands. Two BRB designs were considered in the study in an effort to assess the influence of BRB stiffness on the overall structural performance. Both BRBs were connected to the foundation and the cap beam using classic bolted connections as shown in Fig. 2-22. Note that there is no direct gusset-to-RC column connection in Fig. 2-22; this was done to avoid inducing the BRB forces into the columns. The experimental results showed that utilizing BRBs as a SF in the bridge bent can help the retrofitted structure achieve high displacement ductility, and the damage of

the reinforced concrete bent can be controlled to satisfy the design performance levels. After the BRB was removed, no damage was observed in the gusset plates.
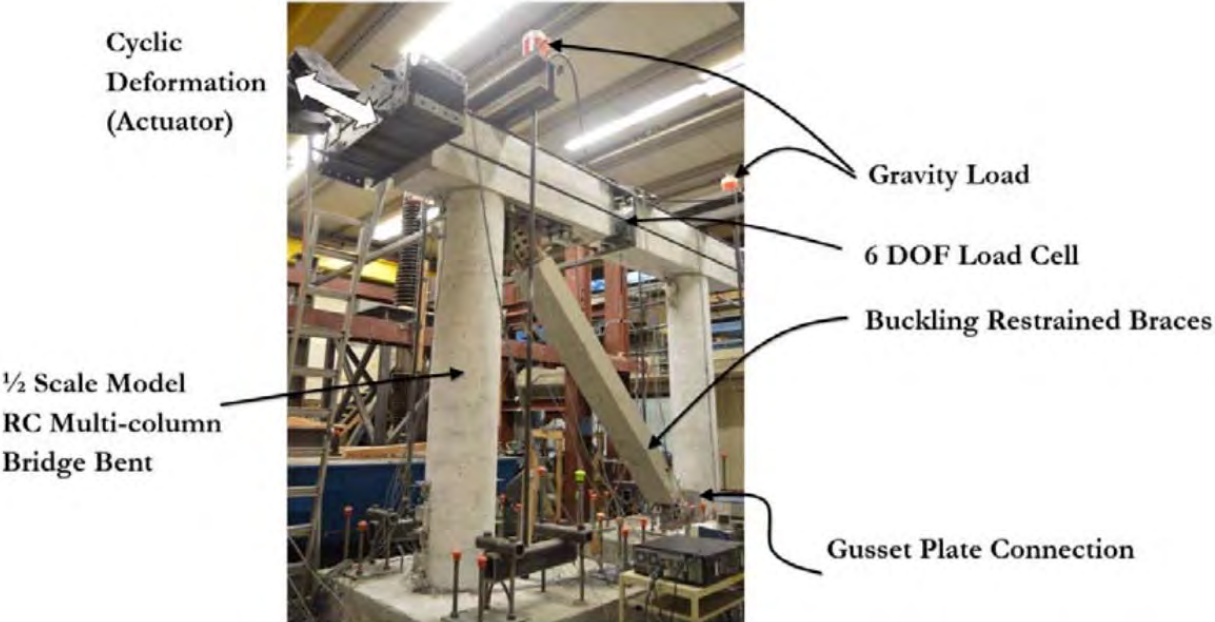
Figure 2-21 Test setup of the half-scale concrete bridge bent with BRBs (Dusicka et.al., 2015)

| (a) | (b) |

Figure 2-22 Gusset plate to bridge bent connection: (a) bottom connection; (b) top connection

2.4.3 Application and Installation in Bridges

Applications of BRBs in bridges have been recently contemplated, and in a few cases implemented. Following are example applications of BRBs in bridges to improve their seismic performance.

(1) Minato Bridge, Osaka, Japan

The Minato Bridge is a long-span truss bridge whose center span length is 510m, ranked as the world's 3rd truss bridges (Hamada et al., 2007). The analytical model of the entire bridge is shown in Fig. 2-23. The bridge needed to be retrofitted in order to accommodate the Japanese seismic performance level 2, described in Table 2-2. This was achieved by installing BRBs on the cross frames of the main tower and on the lower lateral bracing near the main tower, as shown in Fig. 2-24. In addition, one of the lower lateral bracing panels on the side of the center span was also replaced with BRBs. In order to use BRBs in this bridge retrofit, BRBs used mainly in retrofitting buildings were modified to make them lighter members and suitable to coupled with the existing gussets. Kanaji et al. (2005) reported that analyses of the retrofitted bridge proved that BRBs were effective to reduce the strain energy of lower chord members near the tower. Adequate damping to the entire bridge was provided by BRBs and buckling or yielding of main members can be avoided. A photo of the BRB installed in the bridge is shown in Fig. 2-25.

Table 2-2 Functions Required for Bridge and Performances Required for Members

Level	Functions required for bridge (Basic performances required for bridge)	Performances required for members
Performance level 1	To protect human lives (to alleviate bridge collapse) To allow transport of emergency and general vehicles (to necessitate inspection after earthquake but in principle not to necessitate repair)	Elastic behavior of all members Demonstration of hysteretic damping by damage-control members and devices
Performance level 2	To protect human lives (to alleviate collapse) To allow transport of emergency and general vehicles (to necessitate reinforcement of non-main frame and inspection and monitoring during reinforcement period)	Elastic behavior of main members Allowance of damage of non-main members Demonstration of hysteretic damping by damage-control members and devices
Performance level 3	To protect human lives (to alleviate collapse but to allow large-scale repair and reinforcement)	Allowance of damage of main frames within the range in which they do not lead to collapse Allowance of damage of non-main members Demonstration of hysteretic damping by damage-control members and devices
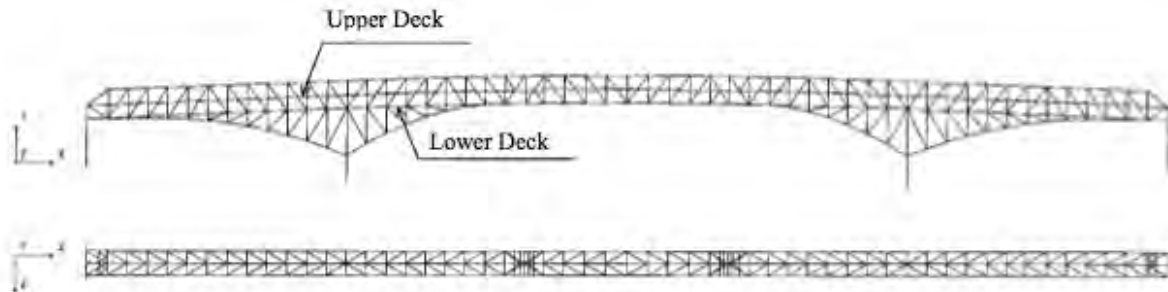
Figure 2-23 Analytical Model of Minato Bridge (Kanaji et al. ,2005)
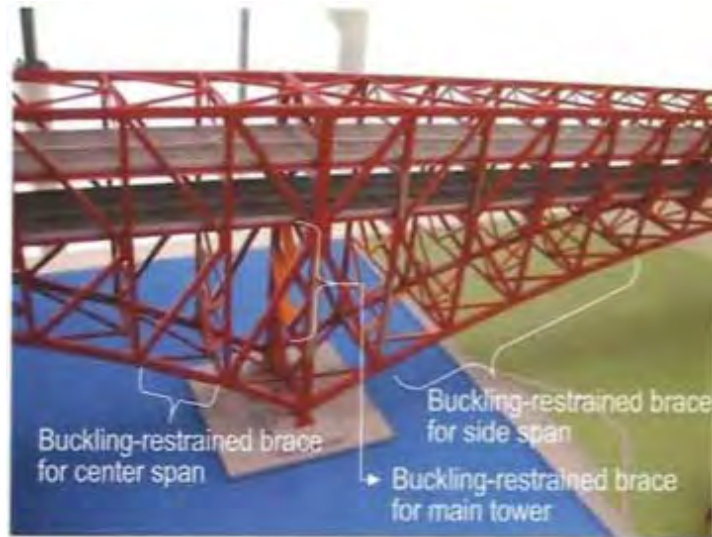
Figure 2-24 Location of BRBs in the Bridge (Hamada et al., 2007)

Figure 2-25 BRB Installed in the Bridge (Hamada et al., 2007)

(2) Auburn-Foresthill Road Bridge, Northern California

The Auburn-Foresthill Road Bridge, in northern California (Fig. 2-26), was built by the Bureau of Reclamation in 1973. The superstructure is a parabolic haunched deck truss bridge that has fracture-critical, high-strength steel (100ksi) main members. There are two locations of the BRBs being installed. Longitudinal anchor plates at abutments were attached with link plates, as shown in Fig. 2-27. These longitudinal anchor plates will experience forces and strains that significantly exceed their capacity, which leads to longitudinal instability of the bridge. Yielding and damage in the anchor plates anchored in the concrete at the abutment was also not desirable because of the irreplaceability. So the geometry of

the link plates at the abutment was changed to reduce their capacity so that yielding occurs in the link plates rather than the anchor bars. And then BRBs were added at the abutment about the centerline of the bridge to provide longitudinal stability. When the link plates fail at the prescribed strain 0.4 during earthquake events, BRBs will take over the load so that the system can stabilize and later the bridge be inspected and repaired. Fig. 2-28 shows the plan view of the planned BRBs installation.

(a)   (b)
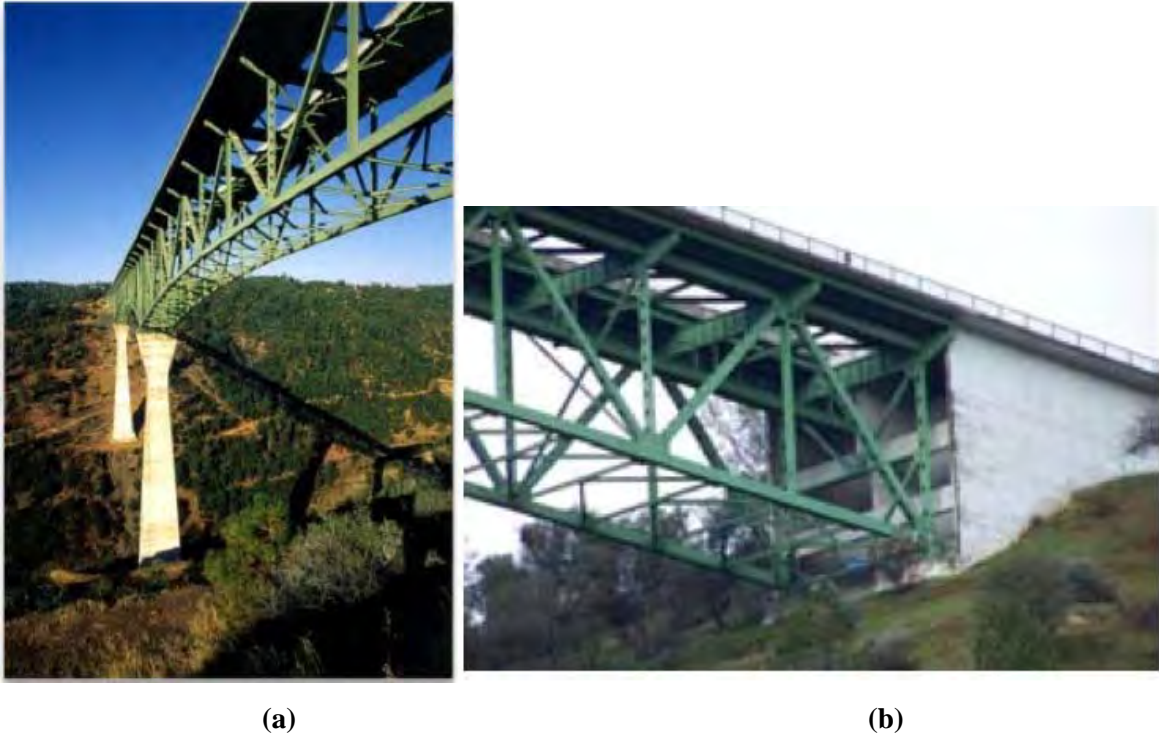
Figure 2-26 Auburn-Foresthill Road Bridge: (a) general view of the deck truss; (b) abutment (Reno and Pohll, 2010b)

(a)   (b)
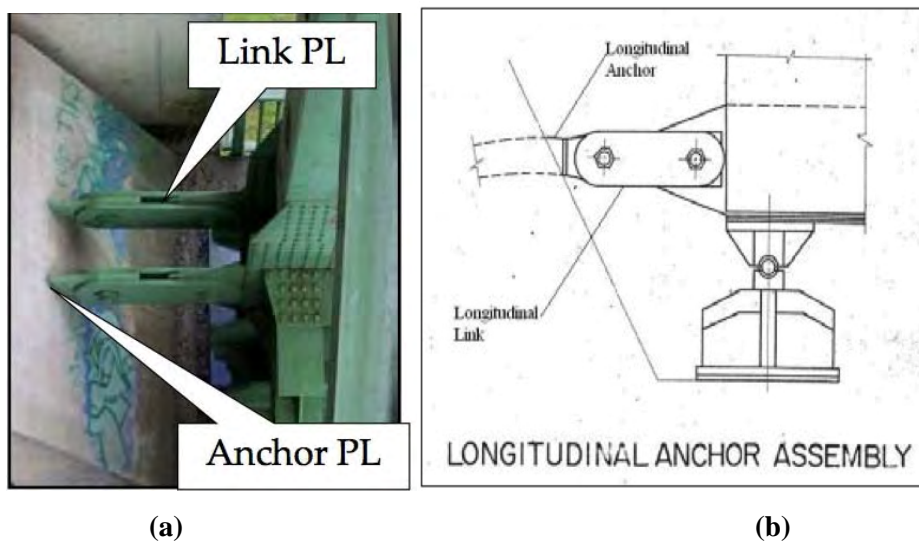
Figure 2-27 Longitudinal anchors assembly to the abutment (Reno and Pohll, 2010a)

30
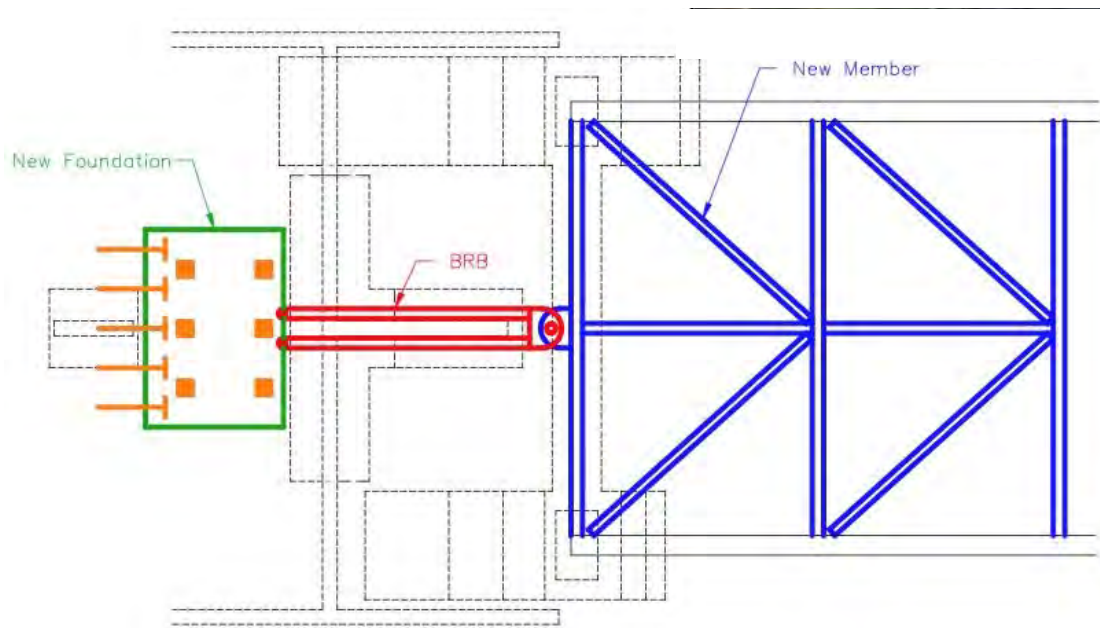
Figure 2-28 Plan View of installed BRB at location 1 (Reno and Pohll, 2010b)

Horizontal chevron bracing members near the abutment have strain demands surpass the design criteria, as shown in Fig. 2-29. The members were replaced by BRBs, together with new longitudinal struts, in order to take conservative loads into the critical load path system, as shown in Fig. 2-30. Proof tests were conducted at the University of California, San Diego to quantify the right type of BRBs supplied by the manufacturer. The loading cycles history was not as severe as those tests of BRBs used in buildings.

Figure 2-29 Lower Horizontal Bracing Near Abutment

PLAN AT TOP OF LOWER CHORD
⅛"=1'-0"
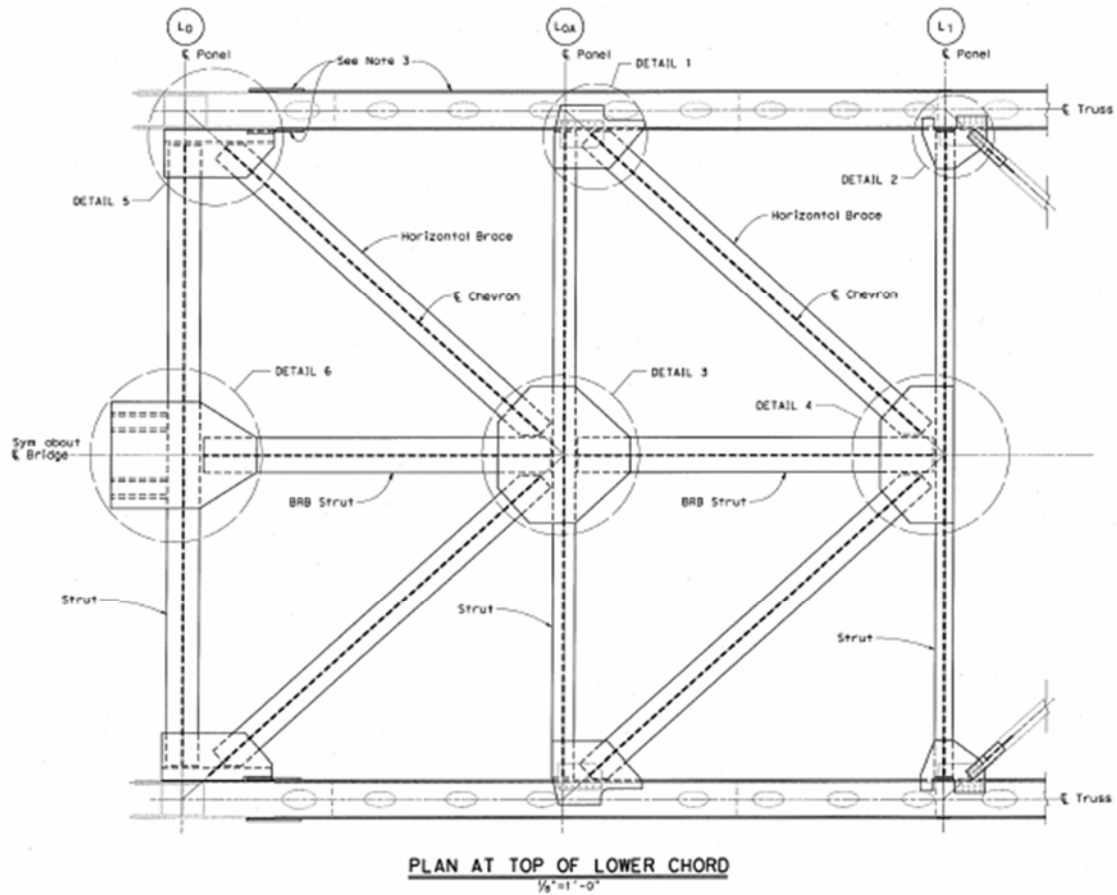
Figure 2-30 Plan View of BRBs Installed in Location 2 (Reno and Pohll, 2010a)

(3) Araku-bashi Bridge, Japan

The Araku-bashi Bridge is a rigid frame bridge with knee brace. The length of the bridge is 80.0 m. The distance between the fulcrums in Fig. 2-31 is 28.0 m. A new type of BRBs, which using two steel mortar planks welded together as the buckling restraining parts to keep the core plate being under axial forces and exhibit plastic behavior, were implemented (Fig. 2-32).

| (a) | (b) |
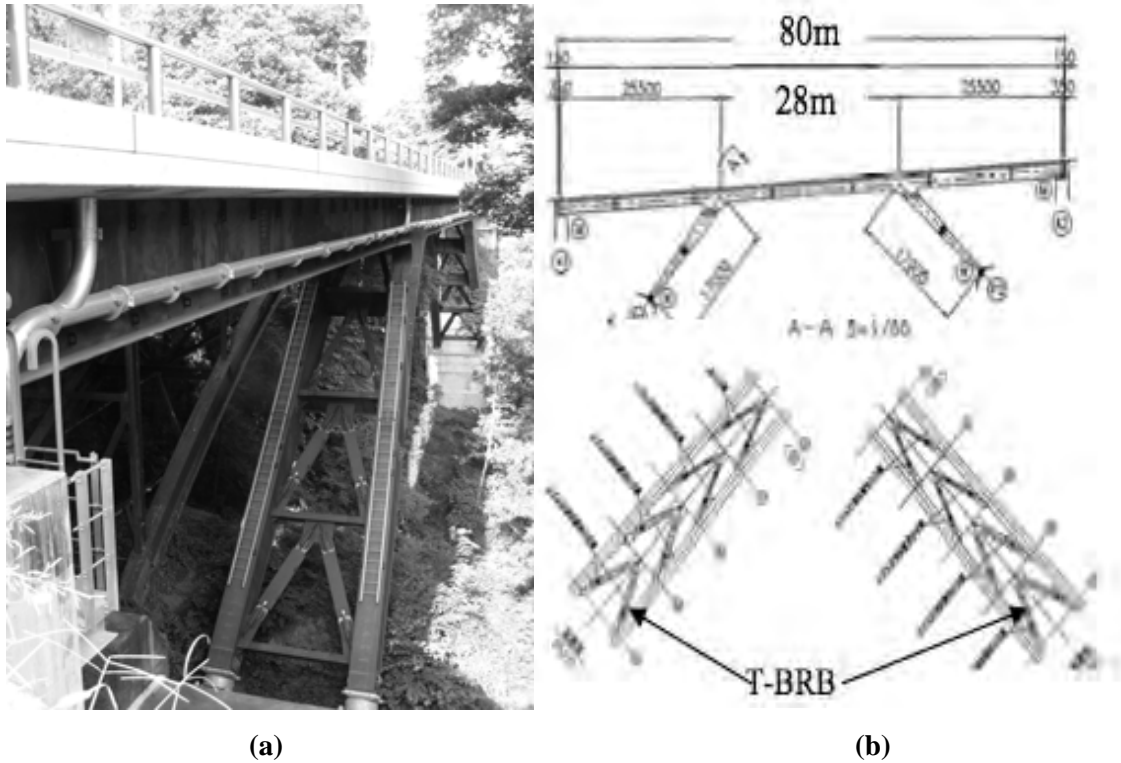
Figure 2-31 Layout of BRBs Installed in the Bridge (Oya et al., 2009): (a) photo view; (b) drawing of the T-BRB in the bridge
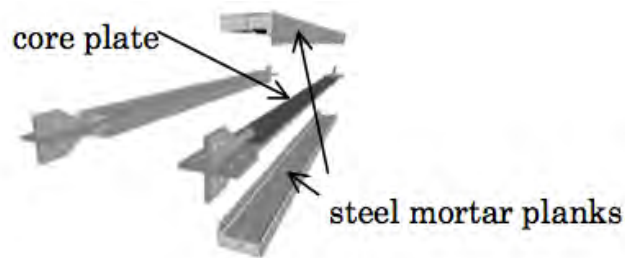
Figure 2-32 T-BRB Configuration (Oya et al., 2009)

(4) Other bridge

There possibly exist many other applications of BRBS in bridges. For example, it has been observed that BRBs have been implemented in the ductile diaphragm of a bridge in Japan as shown in Fig. 2-33. In that example, the BRBs are connected to floor beams and to the top of the bridge columns. A complete list of all applications of BRBs in bridges does not exist, but the objective here was not to present a comprehensive overview of all such instances, but rather to show the increasing interest of the bridge engineering community to use BRBs in bridges.

Figure 2-33 BRB application in transverse ductile diaphragm (Courtesy of H.B.Ge, Meijo University, Japan)

2.4.4 Application and Installation in other structures

Mircowave communication towers usually been placed on the top of buildings. These high-rise steel truss structures with pipe sections have been basically designed to withstand wind forces. Such structures would also be likely to undergo serious damage when subjected to large seismic forces. Some seismic retrofit projects have been carried out that the critical truss members are replaced with BRBs to avoid the structure collapse due to buckling of members. The BRBs installed exposed to the elements are shown in Fig. 2-34 and 2-35.

Figure 2-34 A Telecommunication Tower in Japan (Courtesy of Ian Aiken, Seismic Isolation Engineering, Emeryville, California)

Figure 2-35 Close Look of BRBs Installed in the Communication Tower (Courtesy of Ian Aiken, Seismic Isolation Engineering, Emeryville, California)

Many exterior installations of BRBs have been completed in the US. The following Table 2-3 is a brief summary of where they have been used and how the BRBs are protected against harsh environmental problems by StarSeismic. Figs. 2-36 and 2-37 show the pictures of some of the BRB applications in the Table 2-3.

Table 2-3 Exterior Applications of BRBs by StarSeismic (Courtesy of Steve Powell, StarSeismic, Park City, Utah)

Project Name	Location	Industry	Protection of BRBs
John Wane Airport Parking Garage	Tustin, CA	Transportation	Galvanized
Casad Dam	Bremerton, WA	Utility, Power & Water	Stainless Steel
Rio Tinto Soccer Stadium	Salt Lake City Utah	Stadium	Painted
BART Dublin Transit Station	San Francisco CA	Transportation	Painted
Harborside Pedestrian Bridge	San Diego CA	Transportation	Painted
San Francisco International Airport, Terminal 2 Renovation	San Francisco CA	Transportation	Painted
Plum Point Power Plant	Osceola, Arkansas	Utility, Power & Water	Painted

(a)

(b)

(c)

Figure 2-36 BRBs application in Rio Tinto Soccer Stadium (Star Seismic, 2016b)

Figure 2-37 BRBs Installed in Casad Dam (Star Seismic, 2016b)

2.4.5   Out-of-plane stability of BRBs

BRBs can develop stable hysteresis when subjected to in-plane cyclic loading, provided the BRB's end connections are designed to ensure that BRBs can reach their design axial strength in the core plate without first having instability issues at their ends. The out-of-plane instability of the BRB has been observed in several BRBF tests (Aiken et al., 2002; Roeder et al., 2006; Tremblay et al., 2006, Tsai et al., 2008). Tsai et al. (2008) reported the out-of-plane buckling of the gusset plate that connected a BRB to a column when a full-scale 3-story 3-bay BRBF reached 2% drift, as shown in Fig. 2-38. Tsai and Hsiao (2008) described the details of a gusset plate stiffened by adding edge stiffeners to improve the seismic performance of the BRBF. This paper also suggested that the effective length factor, K, used to design the gusset plate, should be 0.65 and 2 as in Fig. 2-39, for the cases with and without edge stiffeners, respectively.

Figure 2-38 Buckling of a BRB gusset plate (Tsai et al, 2008)
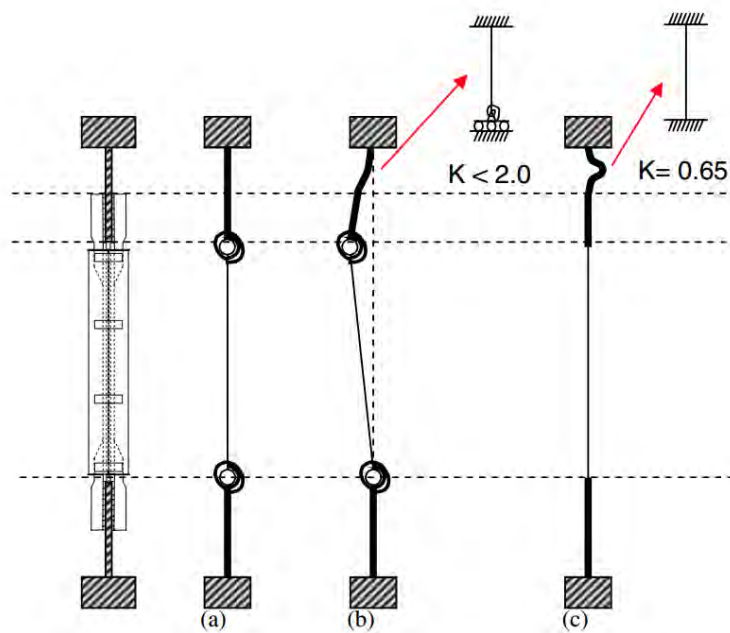
Figure 2-39 Buckling shapes and boundary conditions of gusset plates (Tsai and Hsiao., 2008)

Hikino et al. (2011) performed shake table tests on a single-story, single bay BRBF with BRBs in a chevron configuration as shown in Fig. 2-40a. Near-fault ground motions with increasing amplitude were applied to the test frame. The gusset plates with adequate stiffening had negligible distortion, and the first-order, out-of-plane buckling BRB model in Fig. 2-40b was assumed. Two types of BRBs with different embedment length of the transition segment inside the steel casing were used in the test. The BRB with a transition segment embedment length of 1.5 times the depth of the yielding segment did not

buckle and exhibited excellent hysteretic behavior, whereas the other one with only 0.4 times the depth of the yielding segment developed out-of-plane buckling. Fig. 2-41 shows the kinking deformation at both ends of the BRBs
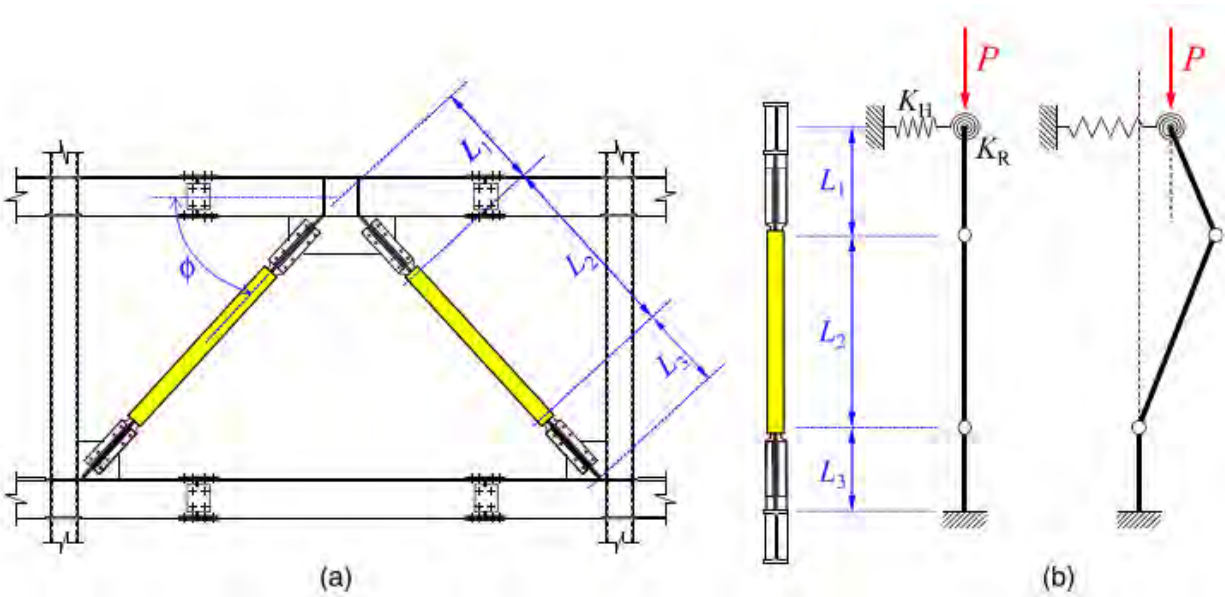
Figure 2-40 Test frame with chevron BRBs and model used for designing the connections
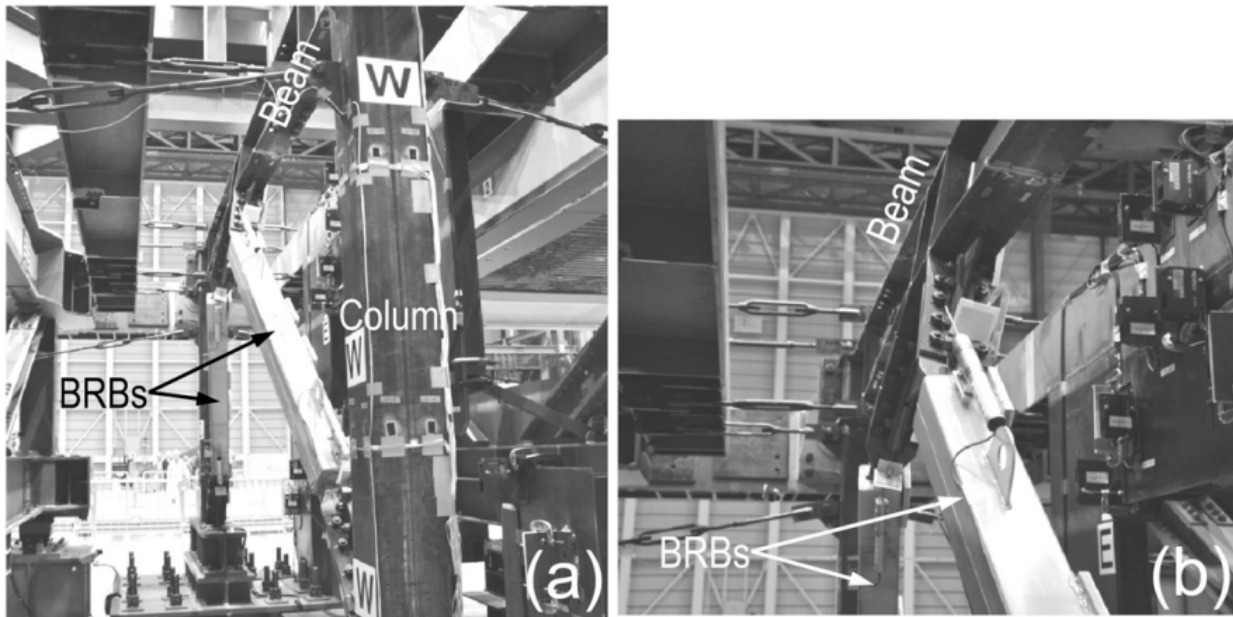
Figure 2-41 Buckling of the second type of BRB in the test frame under 120% ground motion;(a) overall view; (b) close-up view

The AIJ Recommendations for stability design of steel structures (2009) contains two models that must be considered for preventing the global instability of BRBs as shown in Fig. 2-42. The rationale for these two models is best explained by Koetaka et al. (2008) and Takeuchi et al. (2014) who investigated the stability of BRB per these two concepts, respectively.
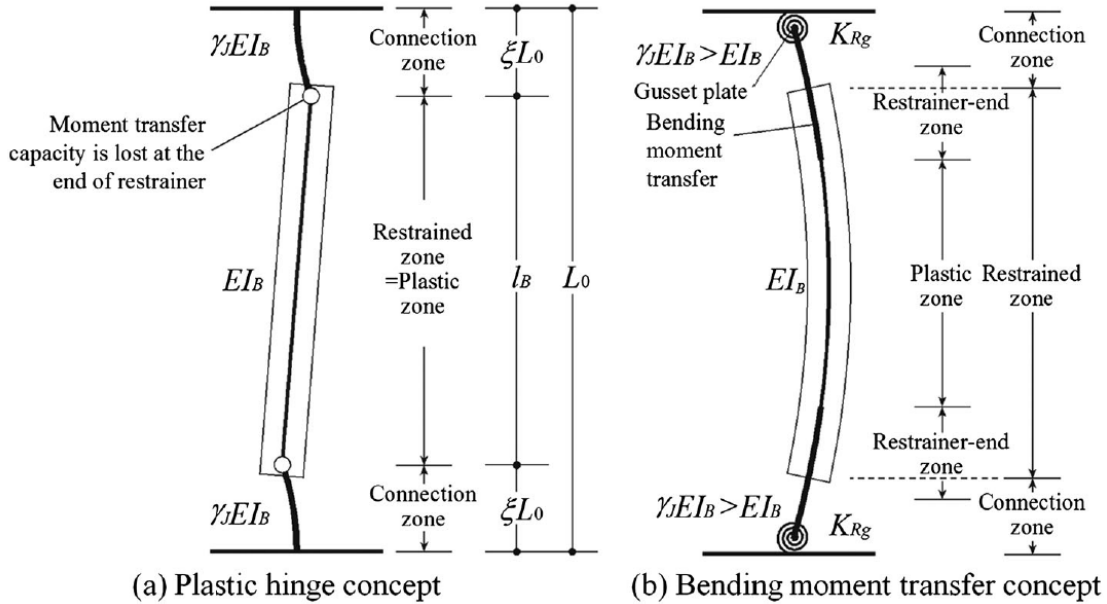
Figure 2-42 BRB stability condition concepts (AIJ, 2009)

For the first concept in Fig. 2-42a, Koetaka et al. (2008) proposed a design criteria for BRBs' restrained and connection zones to prevent out-of-plane buckling when installed in either a single diagonal or chevron bracing configuration in BRBF. Differential equations for the compression member were formulated and the boundary conditions shown in Fig. 2-43 were used to obtain the buckling strength of the entire BRB/connection system. The resulting solution indicated that the connection zone should satisfy Equation 2-1 to avoid the undesired out-of-plane instability:

$$\frac{(1-2\xi)\pi^2\gamma_J EI_B}{(2\xi L_0)^2} > N_{cu}$$

(2.1)

where N_{cu} is the maximum axial strength of the core plates, normally estimated as 1.2-1.5 of the yield strength of the core plate considering strain hardening; $\gamma_J EI_B$ is the bending stiffness of the connections; L_0 is the total length of the BRB, and; ξL_0 is the length of the connection zone on each side of the core plate.
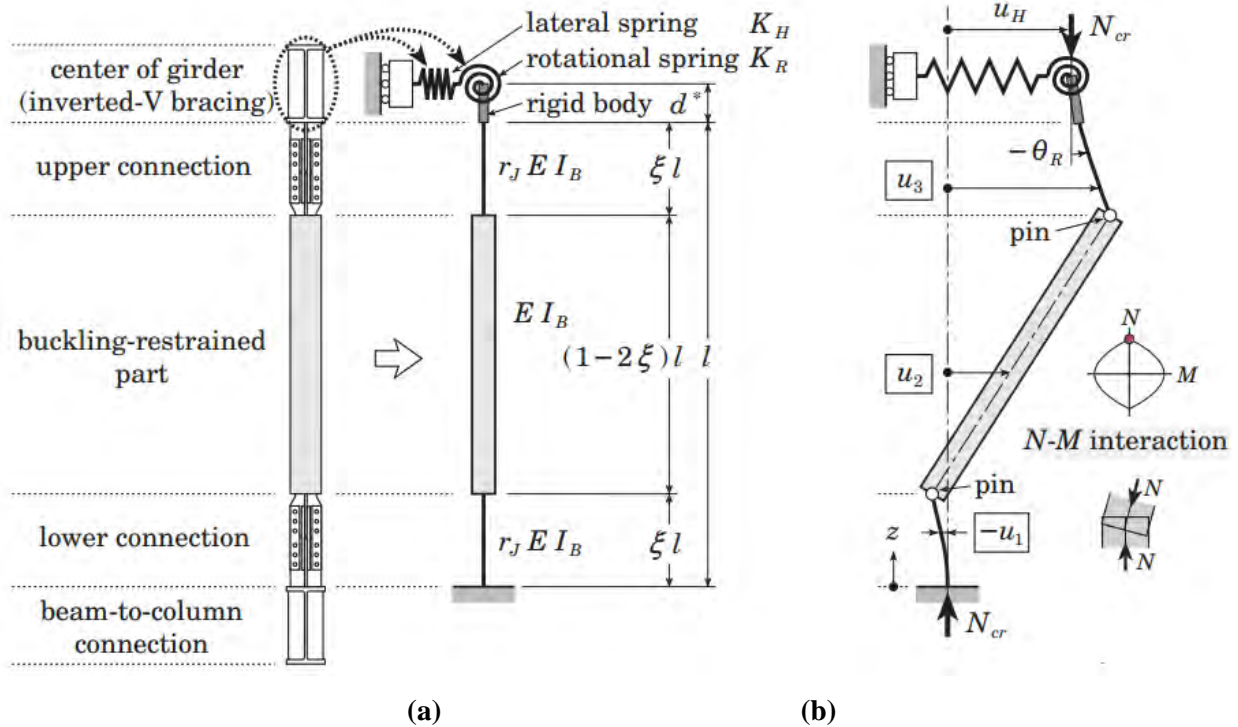
Figure 2-43 Analysis model and buckling mode of the BRB (Koetaka et al. 2008)

For the second concept in Fig. 2-42b, the bending moment transfer capacity between the core section and the restrainer tube end is provided. For BRBs having end connections as shown in Fig. 2-44, Takeuchi et al. (2014) used the model in Fig. 2-45 to study the stability of the restrained and connection zones. In this paper, equations to ensure the BRB's stability were proposed considering the boundary conditions of the three BRB models shown in Fig. 2-45a, b, c, respectively. The buckling strength was found to depend on the moment capacity at the restrained end zone, rotational stiffness at the gusset plate ends, and the clearance between the core plate and the restrained tube. The complex individual equations that captured the behavior corresponding to the three mechanisms are presented in Takeuchi et al (2014). The resulting predicted ultimate strength of the BRB was verified through cyclic loading tests on full-scale BRBs in which the initial out-of-plane drifts and various connection stiffnesses were considered. The study suggested using longer insert zones and smaller clearance in the BRBs, and noted that stiffened gusset plates would help improve the BRB's out-of-plane instability for the type of BRBs considered in Fig.2-44.

41
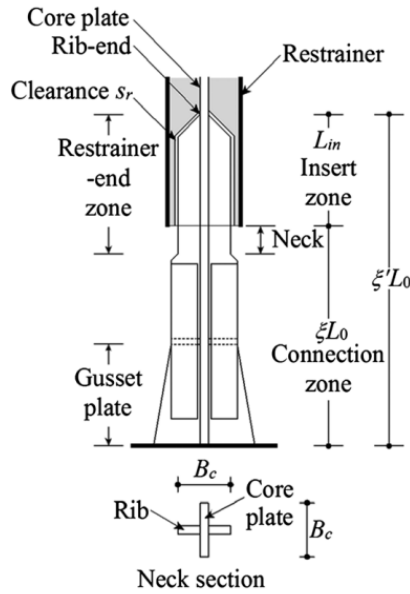
Figure 2-44 Illustration of the BRB's end connections (Takeuchi et al., 2014)

(a)   (b)   (c)
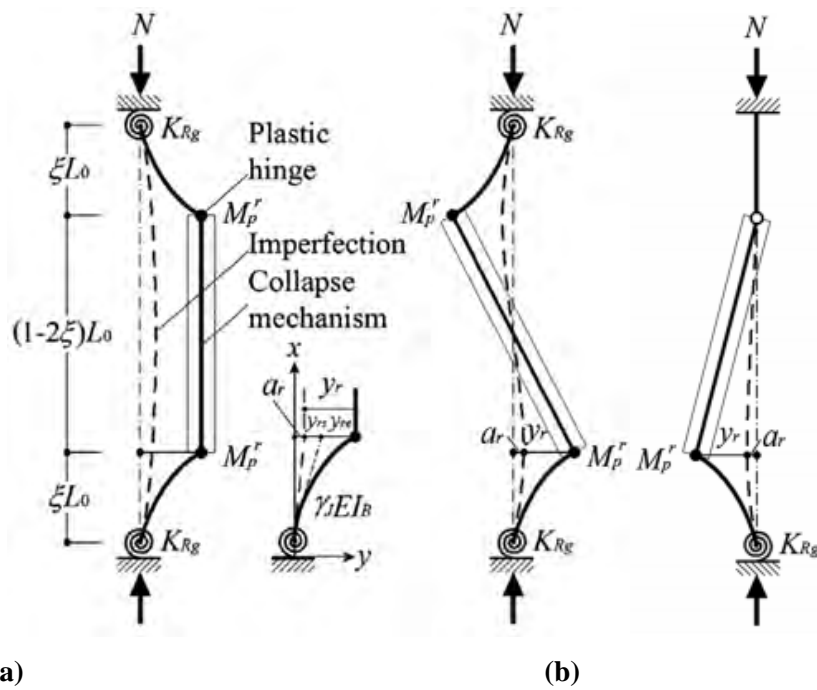
**Figure 2-45 Possible mechanism used to calculate the ultimate strength: (a) symmetric; (b)
asymmetric; (c) one sided (Takeuchi et al., 2014)**

The above research focused on BRBs having bolted connections of the type shown in Fig. 2-12. For
BRBs with pin-ended connections, Zhao et al. (2011) tested an all-steel BRBs having four combined

angle steels forming a cruciform-shape yielding core, as shown in Fig. 2-46. The primary failure mode of the BRBs was due to the compression-flexure failure of the steel core projection region (which consists of the part of the steel that project outside of the core, as shown by the label in Fig 2-47). To obtain the flexural demand in the core projection region of this type of BRB, Zhao et al. (2012) used equilibrium equations based on the free body diagram shown in Fig 2-47, considering the pinned connectors as rigid bodies, and the core stiffening segments and the casings as flexural members. The three different failure modes shown in Fig. 2-47 were considered to obtain the different boundary conditions and deformation compatibility, and to develop corresponding equations. The analytical flexural demand on the steel core projection region relies on the end rotation modes, initial eccentricity, initial deflection of casing and clearance between the core and casing for different deflected shapes. Once this flexural demand is obtained, it is combined with the axial demand, and the design criteria of the BRB's end connection consist in ensuring that yielding doesn't occur at the extreme fiber of the cross section. The study indicated that reducing the clearance between the core and casing, or increasing the constrained length of the core stiffening segment, were both effective to reduce the bending effect on the core projection region.
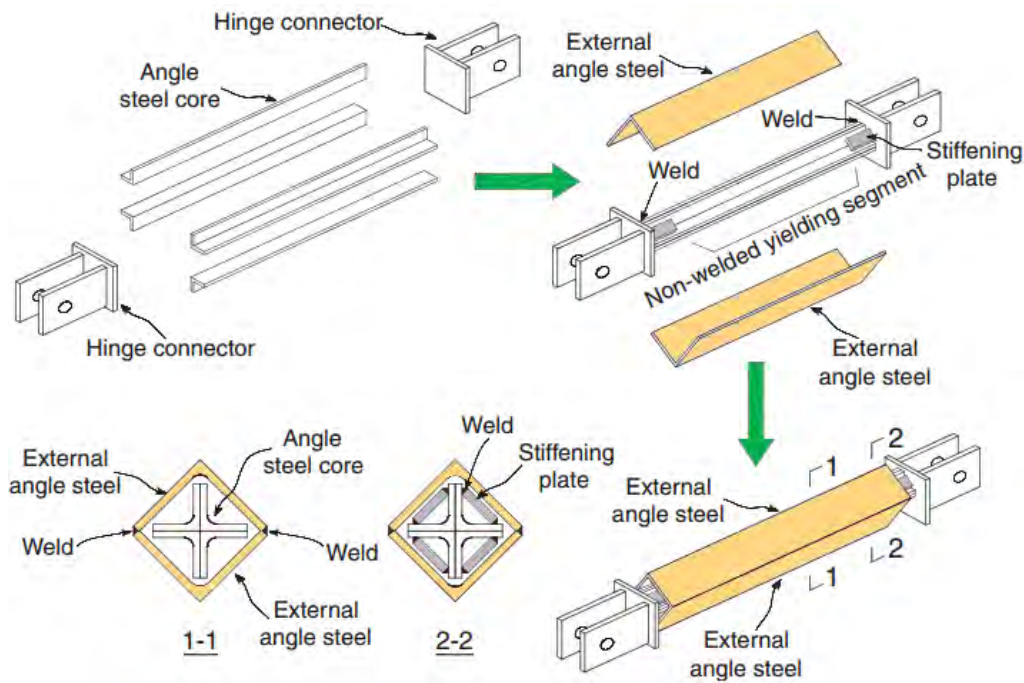
Figure 2-46 Main components of the novel all-steel BRB (Zhao et. al., 2011)
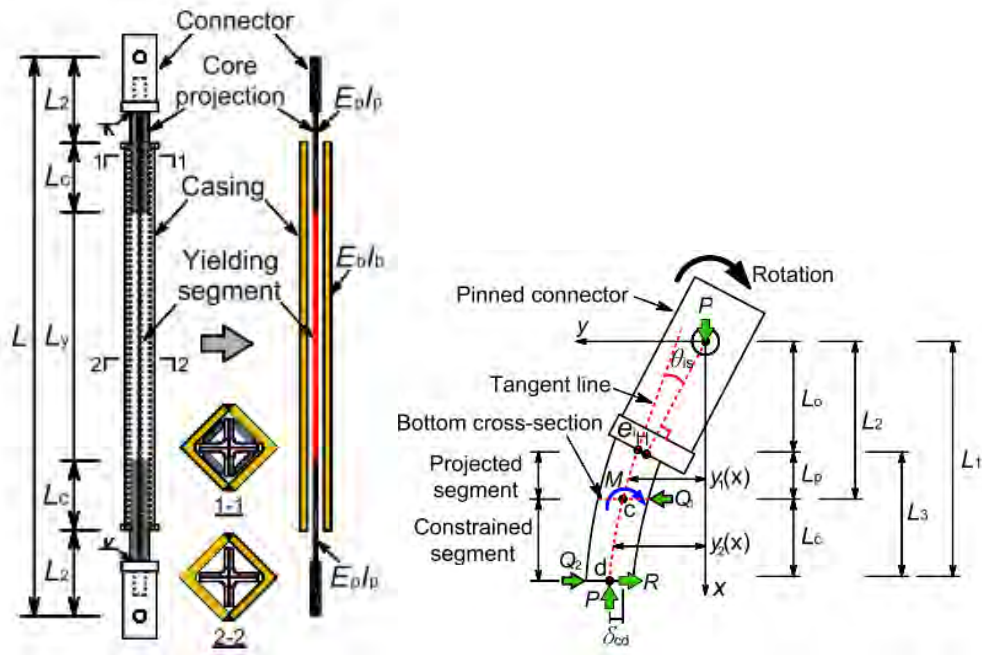
Figure 2-47 BRB and free body diagram for core stiffening segment with connector (Zhao et. al., 2012)
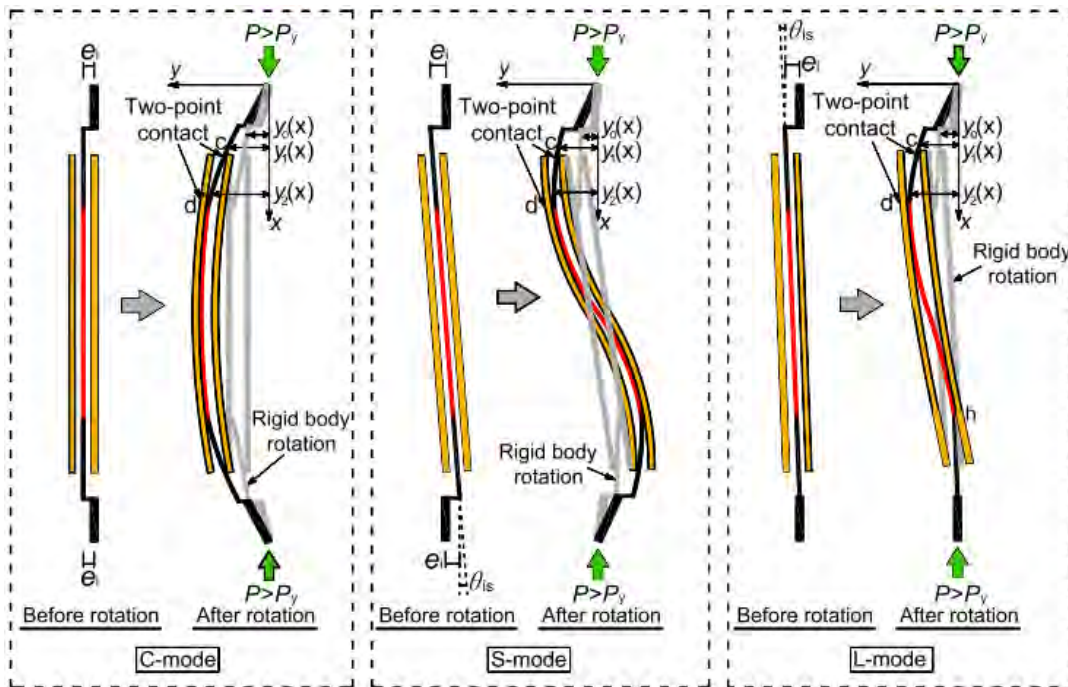
Figure 2-48 Failure modes in the flexural demand analysis of the core projection region of the BRB (Zhao et. al., 2012)

SECTION 3
""""""STRUCTURAL FUSE CONCEPT AND PRELIMINARY UVWF[

3.1   General

This Section illustrates examples of possible options for implementing structural fuses in bridges – either as retrofit of existing bridges, or as possible solutions for consideration in new bridges. The benefit of using structural fuses and its design objectives are first introduced. Possible structural fuses are listed, primarily focusing on the types of metallic hysteretic energy dissipation devices that have been most studied in the literature. The results of a case study investigating how various structural fuses could be implemented in an ordinary California bridge are presented. A following generic bridge case study also examines applicability of the various structural fuses considered to help narrow down the viable choices that will be further studied in subsequent (and more thorough) analyses.

3.2   Structural Fuse Concept

3.2.1   General

In seismic design, structures are typically designed to undergo inelastic deformations during severe earthquake. In those instances, most of the seismic energy is dissipated through hysteretic behaviors of the structural members, which provide the lateral load resistance. Ductile detailing strategies exist to ensure that the stability of a structure is not compromised if the inability of structural elements to accommodate these inelastic deformations, especially for critical load resisting components. However, even for the most ductile members, permanent system deformation and damage following an earthquake could make repairs expensive, or in some cases impossible. Thus concentrating earthquake damage in a certain part of a structure is desirable, but special design and detailing approaches are needed to facilitate achievement of such a goal.

Among the many strategies proposed in the past to dissipate earthquake energy and improve structural performance of bridges by minimizing inelastic demands on the primary lateral load resisting elements, the use of hysteretic energy dissipating devices (sometimes called hysteretic dampers) is the approach taken here, combined with a design strategy to limit system displacement such as to concentrate all inelastic demands into the devices.

3.2.2 Structural fuse design objectives

A structural fuse system can be divided into two parts, namely, the frame that is intended to remain elastic (i.e., the bridge bent in the case at hand), and the structural fuse that is the hysteretic energy dissipating element. Key parameters that define the proposed structural fuse system are its stiffness, displacement, and lateral shear strength. In addition, ductility factors and strength ratios are important to evaluate the effect of adding structural fuses to the bridge bent. A brief summary of the various parameters that drives the design of structural fuse systems is presented in this section. Most of the information here is a summary of work presented in Vargas and Bruneau (2006a, b) and El-Bahey and Bruneau (2010).

In a generic sense, the overall stiffness of the bridge bent, K_{tot} , is equal to the sum of the lateral stiffness, K_s, provided by the SF, and the lateral stiffness of the bare bridge bent, K_f. Correspondingly, a stiffness ratio, , is defined as the ratio between K_s and K_f such that:.

$$K_{tot} = K_f + K_s \qquad (3.1)$$

$$\alpha = \frac{K_s}{K_f} \qquad (3.2)$$

Most efficient use of SF is achieved when the difference between bare bent and fuse yield displacement is maximized. Other useful non-dimensional parameters related to the strength of the system include: the seismic demand of the total system, V_e, if the system behaved elastically up to the corresponding expected displacement, δ_e; the yield strength of the bare bent, V_{yf}, which is the force resisted by the bare bent when the yield displacement of the column is reached, and; the yield strength of the SF, V_{ys} , which is the force resisted by the fuse after the fuse yields. The maximum displacement ductility that the bridge bent needs to withstand is given by the ductility ratio calculated at the system displacement reached for the maximum credible earthquake (expected displacement), δ_e. When the expected displacement δ_e is in the constant velocity region of the spectrum:

$$\delta_e = \frac{V_e}{K_{tot}} \qquad (3.3)$$

For the SF system to be effective, the expected displacement δ_e should be larger than the yield displacement Δ_{ys} that the bent reaches when the SF yields, while smaller than the yield displacement Δ_{yf} corresponding to yielding of the bent columns. Among all the parameters defined above, the ductility factor μ_D and the stiffness ratio α can be thought of as those that govern the design of the structural fuses for the system. The push-over force-displacement curves are shown in Fig. 3-1 for the bare bent, the SF, and the total SF system, with the displacement and force notation defined above.
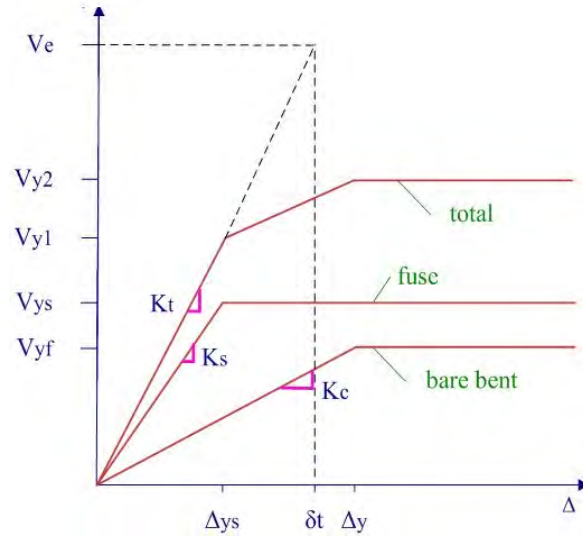
Figure 3-1 General Pushover Curve for the Bridge Bent System with Structural Fuses

For the structural fuse system to be effective, the expected displacement δ_e should be larger than the yield displacement Δ_{ys} that the bent reaches when the structural fuse yields, while smaller than the yield displacement Δ_{yf} corresponding to yielding of the bent columns. Among all the parameters defined above, the ductility factor μ_D and the stiffness ratio α can be thought of as those that govern the design of the structural fuses for the system.

Vargas and Bruneau (2006a) recommended that the ductility factor μ_D be no less than 5 to ensure the elastic behavior of the bent, based on results from a parametric study conducted using nonlinear dynamic analysis for a steel building prototype. Along those lines, Bahey and Bruneau (2010) plotted the fuse strength ratio V_e/V_{ys} with respect to the stiffness ratio α for a certain target structural fuse ductility μ_D. The study showed that a slight change in the stiffness ratio α, for values smaller than 2, would significantly affect the structural fuse strength ratio needed to achieve a target the structural fuse ductility, μ_D. When α is larger than 2, such a sensitivity is not present. In order to more easily achieve $\delta_e < \Delta_{yf}$, which correspond to elastic behavior of the frame, the suitable range for μ_D should be $\mu_D \geq 5$. For the sections later used to study the applicability of various kinds of structural fuses, α of 3 and μ_D of 5 are used. However, numerical analysis of typical bridge bents is required to verify the admissible ranges of these parameters to ensure the desired system behavior.

There is actually no fixed relationship between the bare bent strength V_{yf} and the fuse strength V_{ys}. Figure 3-1 is just a schematic to illustrate that there will be a difference between the bare bent and fuse strength.

3.2.3   Structural fuse configurations for bridges

Adding structural fuse to the bridge bents could mitigate damage to those bridges by keeping the gravity supporting elements (mainly the columns) intact and concentrating the damage on the fuses. Moreover, if the bare bridge bent remains elastic after the earthquake, self-centering of the bridge would occur once the ductile fuse devices are removed, and the bridge would return to its original undeformed position. For inspection purposes, the fuses and their connections would be visible. The following is a sample of applicable structural fuses using metallic hysteretic damping devices, for bents with either largely or closely spaced columns. Note that further details on each of the metallic hysteretic fuses mentioned are presented in the literature review in Wei and Bruneau (2013).

3.2.3.1 Bent with largely spaced columns

(a) BRB systems

A structural fuse system can be achieved by inserting a pair of Buckling Restrained Brace (BRBs), an inverted-V chevron configuration, into a general Reinforced Concrete (RC) bridge bent, as shown in Fig. 3-2. While a sensitivity analysis was performed by El-Bahey and Bruneau (2010) for a single bridge geometry similar to the case investigated here (Fig. 3-2) to find how some parameters affect the bridge's seismic performance, that work cannot be used to establish the effectiveness of using BRBs as structural fuses for a broad range of heights and diameters of bridge columns and bent aspect ratio, or for other structural fuse configurations (for example, as diagonal single braces).
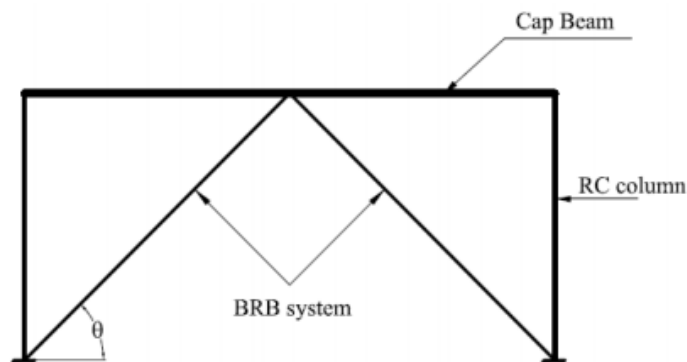
Figure 3-2 Layout of BRB Retrofit Scheme (El-Bahey and Bruneau, 2010)

(b) Eccentrically braced systems

Eccentrically braced systems have been frequently used in steel buildings. For the structural fuse approach taken here, the transformation from traditional bracing to a eccentrically braced system

could be achieved by inserting special hysteretic energy dissipative devices between the point of intersection of the diagonal brace members (purposely located below the bent-beam) and the bent-beam itself, as shown in Fig. 3-3. The inverted Y-Shaped assembly could have various types of metallic dampers installed between the braces and the overlying concrete bent cap beam. The link connection at mid-span of the RC beam would require special detailing; an example of how the link could be connected to braces and anchored to the RC beam is shown in Fig. 3-4. Horizontal forces are transferred to the brace members through bending and shear forces developed in the ductile steel link, which is sized to dissipate energy at forces lower than those that would produce buckling of the brace members. In other words, while plastic deformations occur in the dissipative device, the diagonal braces have to remain elastic both in tension and compression. Note that, per the structural fuse concept, the connection at the link ends must be detailed to allow easy removal of a link damaged after a severe seismic event.
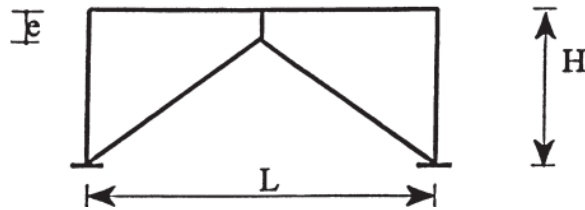
Figure 3-3 RC Bridge Bent Frame with Eccentric Bracing Systems (Ghobarah et al ,2001)
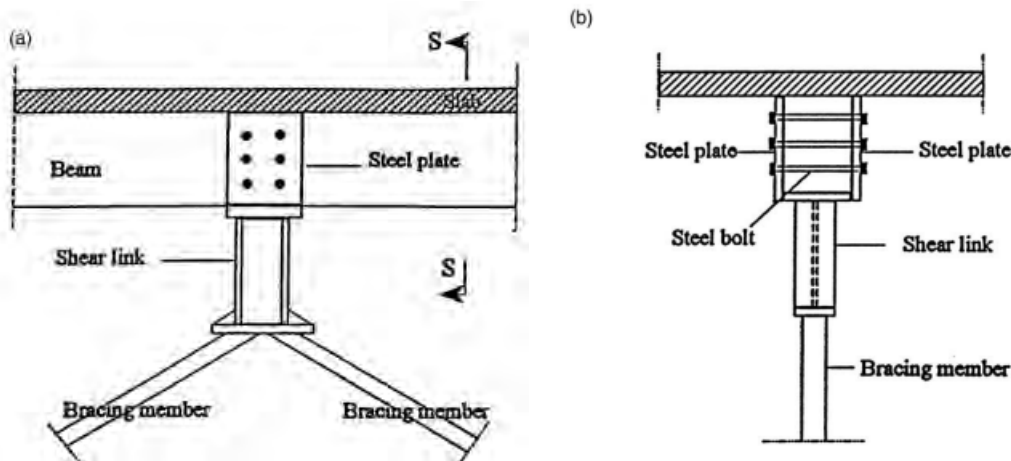
Figure 3-4 Connection Details of a Vertical Steel Link: (a) Elevation, and (b) Section S-S (Ghobarah et al., 2001)

The types of ductile links that could be used in this eccentric bracing scheme to provide a stable source of energy dissipation include (among many possibilities):

(1) Steel plates triangular added damping and stiffness (TADAS) device

(2) Steel Shear Panel Links

49

(3) Steel Slit Dampers

Section 3.4 discusses the applicability of these above mentioned devices as structural fuses.

3.2.3.2 Bent with closely spaced columns

When structural fuses are added between two closely spaced RC columns, the total pier behaves like a cantilever beam with the columns acting as flanges and the fuses acting as webs as shown in Fig. 3-5. The expected system behavior before yielding of the structural fuses results in one column being in compression while the other one is in tension. When the fuses yield while the columns remain elastic, behavior changes from the single cantilever system to a moment frame behavior. Each column then behaves independently and the fuses resist part of the lateral loads. For the structural fuse concept, the fuses can be designed to improve the bridge pier performance when subjected to earthquakes.

(a)   (b)
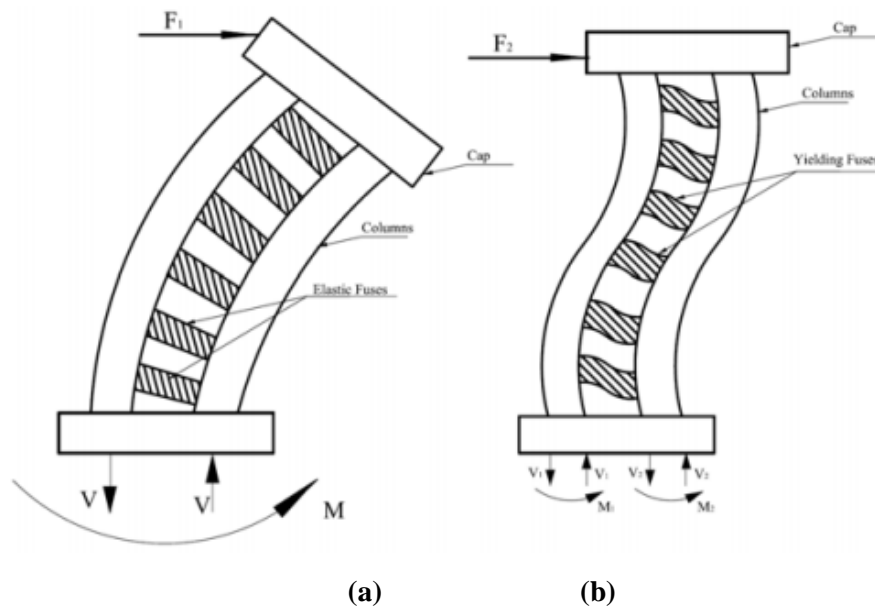
Figure 3-5 Total System Behavior, (a) Before Yielding of Fuses, (b) After Yielding of Fuses
(El-Bahey and Bruneau, 2010)

The types of links that could be inserted between such closely spaced columns to form a unit pier system capable of dissipating hysteretic energy include (among many):

(1) Steel Plate Shear Links (SPSLs)

(2) Short BRBs

(3) Steel plates added damping and stiffness device

(4) Shear Panel Devices

Section 3.4 also discusses the applicability of these devices as structural fuses.

3.2.3.3 Steel plate shear wall

The multi-hazard bridge pier proposed by Keller and Bruneau (2009) can also be used here to develop a pier system similar in concept to steel plate shear walls (SPSWs), as shown in Fig. 3-6.
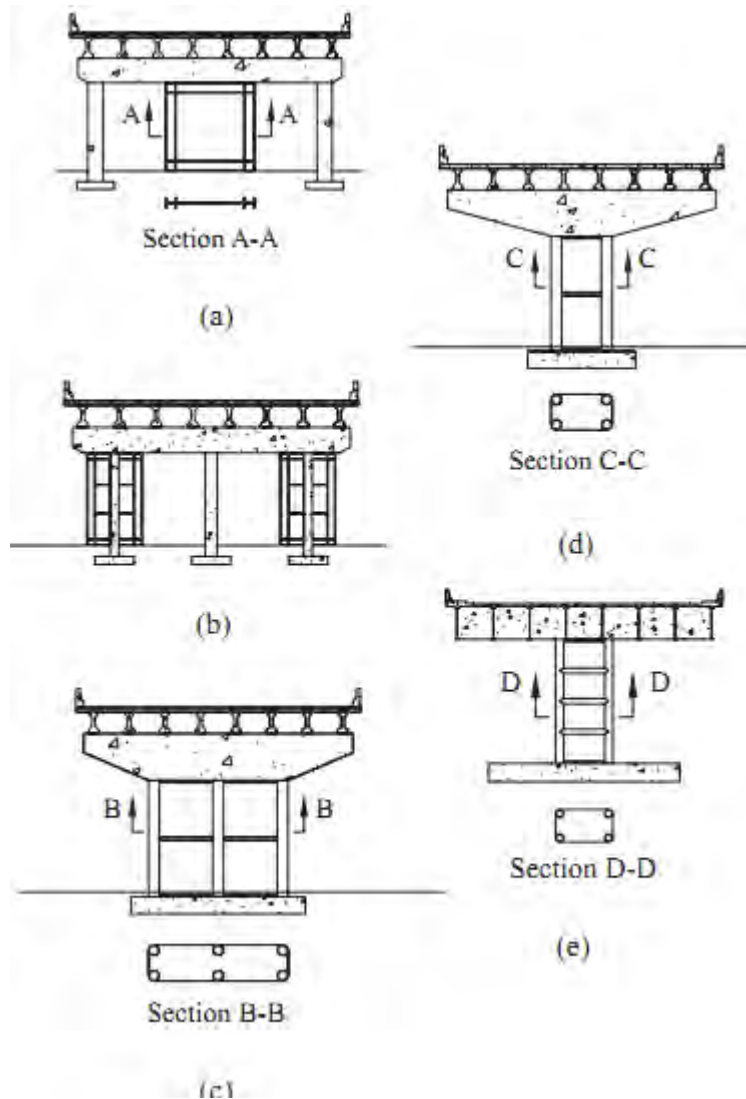
Figure 3-6 Multi-hazard Resistant SPSWs Bridge Pier Concept (Keller D., Bruneau M., 2009)

SPSWs add significant redundancy and strength to the system, as well as a substantially ductile behavior. To achieve the objectives of the structural fuse concept, the vertical boundary elements (VBEs) must remain elastic when subjected to earthquake loads, while the steel plates connected to them yield through tension field action developing over the pier height (by using suitable size of bridge pier and steel connecting beams, tension field action can be achieved across the entire web plates). In development of the full sway plastic mechanism, plastic hinges would develop at the ends of the HBEs; these plastic

mechanisms help mitigate deformation and therefore damage in the columns (VBEs). The sketch in Fig. 3-7(a) provides a 3-D view of the structural system in Fig. 3-6(e). An exploded view is shown in Fig. 3-7(b). A careful detailing can make the system aesthetically pleasing, while keeping the yielding elements visible for inspection purposes.

(a)   (b)
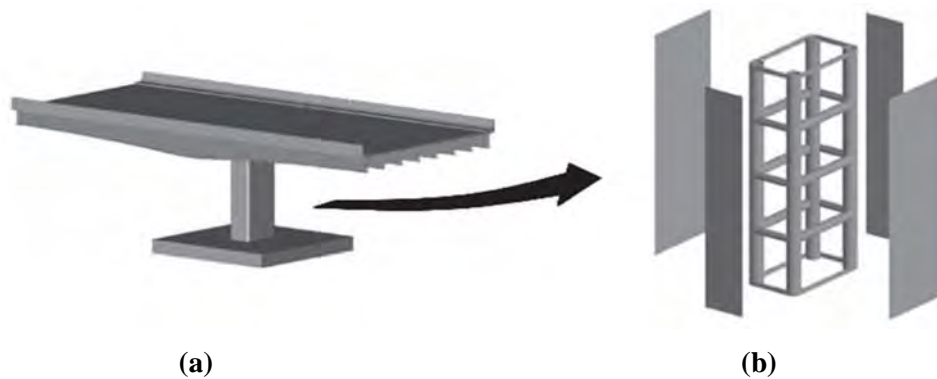
Figure 3-7 Final Box Pier with SPSWs Configuration (Keller and Bruneau, 2008)

3.3   Caltrans concrete bridges with fuses

Before going into generic bridge investigations of applicable structural fuses for different bridge schemes proposed, a case study investigating how various structural fuse concepts could be implemented in an ordinary California bridge was first conducted. This chosen case study bridge was the Caltrans generic bridge "Ordinary Standard Bridge 1" (OSB1, revision date 07-21-2011), for which drawings were provided by Caltrans for this purpose. This two span continuous bridge has a total abutment-to-abutment length of 300 ft and is supported on an integral two-column bent at mid-span, as shown in Fig. 3-8.

Note that the case study bridge provided by Caltrans, and described in the "Ordinary Standard Bridge" drawings, had an integral bent. For the non-integral bent, the bare bent stiffness would be smaller than the integral bent (the non-integral bent would be considered free at the top of the cap beam, contrary to the integral bent system which was considered fixed at that location), and the stiffness of the BRB needed to achieve the structural fuse design objective would be different. Comparison of the results obtained using different types of boundary conditions was not part of the scope of this project. However, the methodology presented remains valid, and the structural fuse concept would still be applicable to the type of California bridges considered in this study.

(a)

(b)
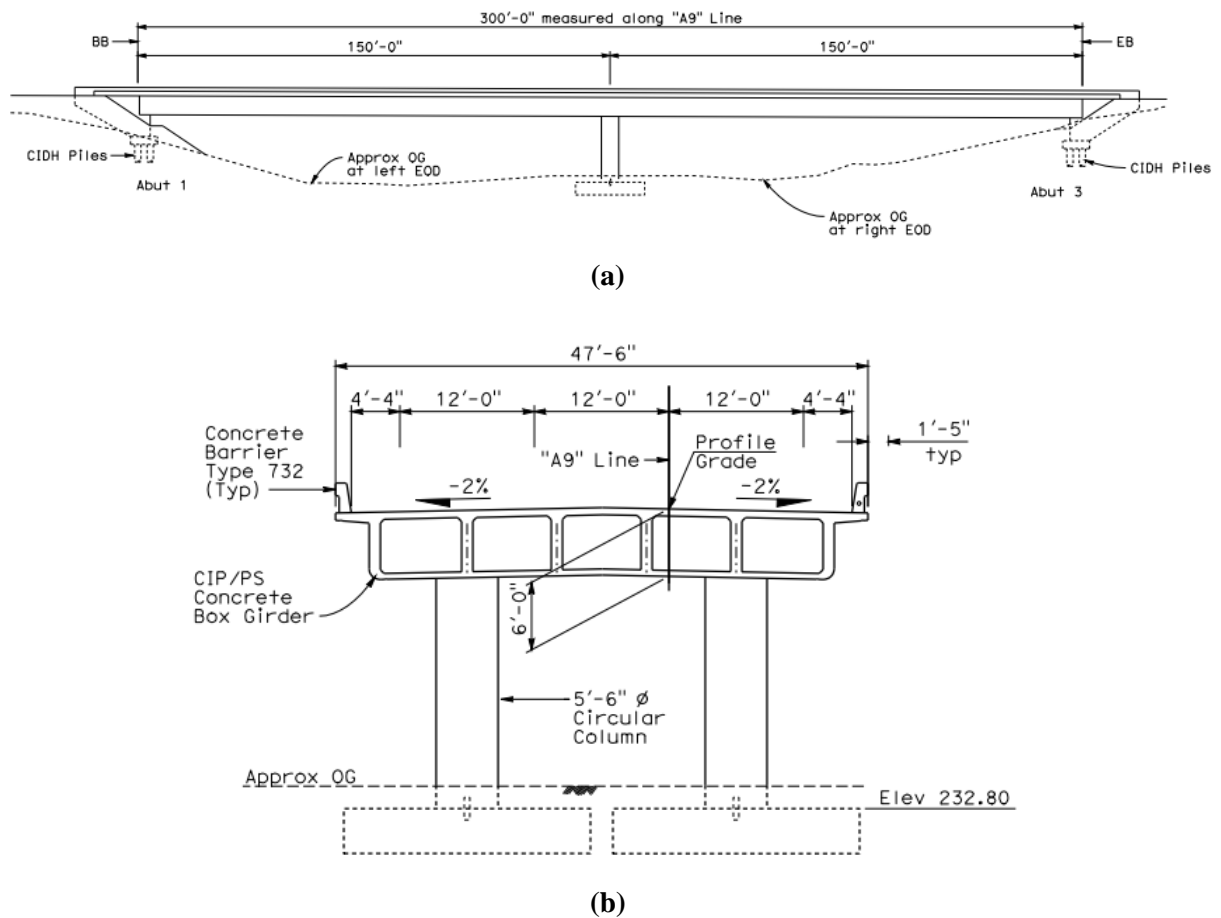
Figure 3-8 Caltrans ordinary standard bridge 1: (a) elevation (b) bridge bent at the center of the bridge span (note: unit = ft; OG = original ground; EOD = edge of deck; CIP = case in place; PS = prestressed)

3.3.1 Retrofitted bridge bent

For the provided ordinary standard bridge with two RC columns of 5.5 ft in diameter, eight structural fuse schemes have been considered as possible retrofit scenarios, namely:

- BRBs implemented as: (1) Inverted chevron BRB frame, or; (2) Single inclined BRB frame configuration
- SPSWs considered, as: (1) Supplementary SPSW system; or; (2) SPSW Integral with RC Columns
- Eccentrically Braced systems, with vertical links consisting of either: (1) TADAS devices; (2) Added Damping and Stiffness Devices (ADAS); (3) Slit Dampers; (4) Shear Panel Devices

53

The stiffness ratio of the structural fuses to the bare bridge bent was arbitrarily chosen to be 3, while the structural fuses yield displacement was chosen to be 1/5 of the yielding displacement of the columns in the bent without fuses. Reasons for choosing these parameters are mentioned in a previous section, recognizing that other values can also provide satisfactory implementations. The structural fuse concept is achieved when the columns in the bridge bent do not yield while the structural fuses yield over a range of displacements smaller than the yielding displacement of the columns. Ductility of the structural fuses after yielding helps the system dissipate energy while keeping the bridge columns elastic.

The bridge bents were designed using the acceleration response spectrum shown in Fig. 3-9. The expected displacement of the bridge bent with fuses was taken equal to the yield displacement of the RC column. The fuses were designed to provide the required strength based on the pushover curve in Fig. 3-1.
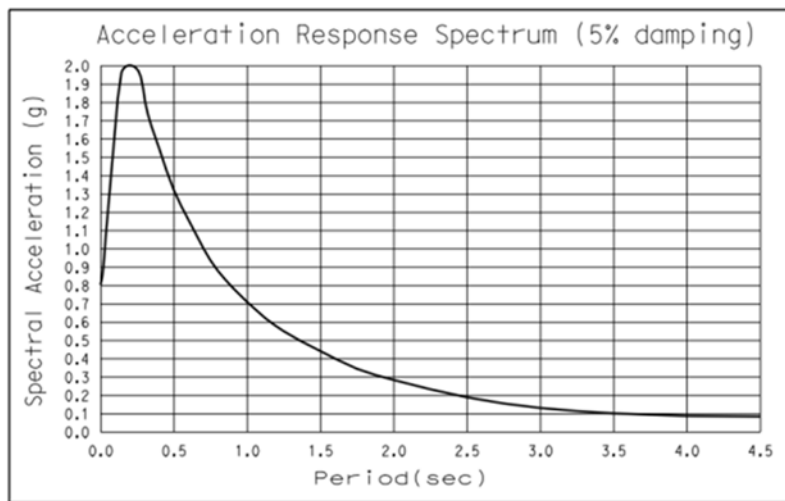
Figure 3-9 Acceleration Response Spectrum with 5% Damping

Trial designs showed that BRBs and SPSWs could be designed to implement the structural fuse concept, but that eccentrically braced system with vertical links consisting of either TADAS, ADAS, or Slit Dampers would have required steel plates of impractical thicknesses or an excessive number of plates (or both). While the use of Shear Panels Devices might have been possible, their length was long to the extent that their stability would be an issue.

3.3.2 New bridge bent

In addition to the above, structural fuse schemes are also possible for new bridges. To allow comparison of results with the designs for the retrofitted case, the stiffness of the Caltrans bridge bent was kept the same when multi-column bents were considered (note that to achieve this, the diameter of the columns in a multi-column bent would not be the same as in a two column bent). With respect to dynamic properties of these new bridges, the weight of the columns was assumed to be only a small part of the total weight of the bridge, and the period of these bridges (without the fuses) was still taken to be the same as that of the case study bridge. The same target design spectrum was therefore used for the new-bridge case studies. The additional systems considered that would likely be only applicable to new bridges include:

- Bridge bents with closely spaced columns, linked with: (1) Steel Plate Shear Links (SPSLs); (2) Short BRBs; (3) SPSWs-type plates; (4) ADAS
- Bridge with box pier relying on SPSWs action.

Trial designs showed that the thickness of the SPSLs and ADAS plates would have been excessive, to the point that these systems were deemed impractical. On the contrary, the trial designs showed that BRBs and SPSWs could be designed to work for new bridges.

Note that the case study bridge provided by Caltrans seemed to have columns somewhat larger than those in bridges designed based from the onset to be part of a structural fuse concept. When column diameters are large, it is more difficult to size practical structural fuses to provide stiffness equal to 3 times that of the concrete bridge bent. It should be kept in mind that having the benefit of structural fuses to provide resistance to lateral seismic forces would normally allow the diameter of bridge columns to be less than those considered in the case study, which would help make the structural fuses concept more broadly applicable.

3.4   Generic RC bridge study with fuses

After a specific study of the Caltrans bridge with RC bents, a generic bridge with columns of different heights was studied to investigate how structural fuses would perform in a broader range of configurations, with structural elements sized based on simple assumptions. The bridge column heights considered for that purpose were selected to range from 12 ft to 44 ft, because Priestley and Seible (1996) reported this range to encompass most columns encountered in practice. To estimate column stiffness, a relationship for the diameter of RC columns, D, as a function of column height was first developed.

The effect of key parameters on the column yielding curvature, such as longitudinal reinforcement ratio and axial load ratio was described by Priestley et al. (2007) for typical bridge columns. Data from analyses to determine yielding curvature, Φ_y, were plotted in dimensionless form in Fig. 3-10. The dimensionless yield curvature, Φ_{Dy}, is expressed as $\Phi_y D/\varepsilon_y$, where $\varepsilon_y = f_y/E$ is the flexural reinforcing steel yield strain. As observed in Fig. 3-10, the yielding curvature for circular sections does not vary much for different axial forces. The average dimensionless curvature of 2.25, along with lines at 10% above and 10% below this average, is shown in that figure. Though the data is generated for a specific column size and material strengths, the dimensionless results are expected to apply, with only insignificant errors, to other column sizes and material strengths within the normal range expected for standard design (Priestley et al. 1997), leading to the following equation for circular columns:

$$\Phi_y D = 2.25\varepsilon_y \pm 10\% \tag{3.4}$$
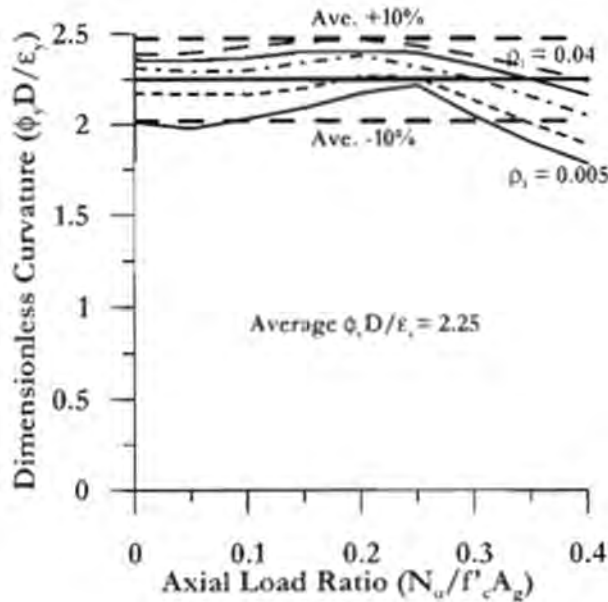
Figure 3-10 Dimensionless Yield Curvature for Circular Bridge Columns (Priestley et al., 2007)

An estimate of column yielding displacement of $\Delta_y = 0.005H$ was used (Priestley et al. 1997). By relating the yielding displacement and curvature of the column, an estimate of the diameter of circular RC column, D, was obtained as a function of its height, H. The stiffness of the bridge bent column can be related to the column diameter D, as the inertia of the section I can be expressed as $\pi D^4/64$.

For cantilever column,

$$K = \frac{3EI}{H^3} \tag{3.5}$$

For fixed-fixed column,

56

$$K = \frac{12EI}{H^3} \tag{3.6}$$

Bridges with both cantilever and fixed-fixed end columns were considered. The same values of structural fuse design parameters were chosen as for the Caltrans bridge, namely, 3 for the stiffness ratio of the structural fuses to bare bridge bent, and 5 for the yielding displacement of the column to the structural fuses. Therefore, the required stiffness and yielding displacement of the fuse can be derived regarding to the height of the bridge bent.

Bridges that needed retrofit and new bridge construction were both considered in this generic bridge study. For two RC columns braced by a single inclined BRB, it could be demonstrated using the above equations that the strength of the BRB is proportional to the square of height H^2. There is no known factor that could limit the strength of a BRB. However, because this is a relatively new structural system, building specifications require full scale testing of BRBs to demonstrate satisfactory performance before implementation, unless tests results are already available for BRBs of equivalent strength from the same manufacturer. At the time this parametric study was conducted, it was assumed that the largest BRBs that had been previous tested had a strength 2155kN (485kips), based on information provided by Aiken et al. (2001). Subsequent personal communications with BRB suppliers revealed that BRBs of up to 2000 kips have been tested to date, but the information below is nonetheless valuable in illustrating the range of column heights for which structural fuses can be implemented for a given limit on BRB strength (note that for stronger BRBs, problems will arise as connections will become progressively more difficult to accomplish). Note that bridge bents with fixed-fixed columns would require smaller BRBs than the ones with cantilever columns. Structural fuse calculations indicated that the required BRBs strength would be less than 485 kips for the case of a bridge bent with fixed-fixed column if the height of the columns did not exceed 16.5 ft. However, all BRBs for the comparable bents having cantilever columns (i.e., fixed-pin ends) required a strength exceeding 485 kips. Theoretically, nothing prevents the fabrication of stronger BRBs. However, the real challenge lies in the development of connections to transfer those loads to existing concrete columns.

For the case of RC bridge bent having a vertical link between the cap beam and chevron brace, the possible use of TADAS, ADAS, Slit Dampers, and Shear Panel Devices were investigated to serve as potential vertical links. It was found that either the thickness of the required steel panel was excessive, or the design required an impractically large numbers of steel panels. The stability of the vertical link would also be an issue making the implementation of vertical hysteretic links difficult.

As mentioned previously, structural fuses can also be installed between closely spaced columns in bridge bents. The distance between such closely spaced columns in this study was assumed to be equal to the diameter of the column, recognizing that other values could also be used. Assuming that SPSLs of up to 0.5" thickness were acceptable, such SPSLs could be used in bridge bent having fixed-fixed columns of up to 27 ft. No such solution was found for bridges with cantilever columns. The use of ADAS plates between the columns was also considered but found to require too many plates to be practical. Note that connections of SPSLs or ADAS plates to the RC columns would require steel-and-concrete connection all over the columns' height. The option of introducing BRBs between the columns was also considered. If BRBs' strength of up to 485 kips could be developed (within their short length), BRB could be a solution for cantilever bridge column shorter than 24 ft, and for fixed-fixed bridge columns ranging from 12 ft to 44 ft.

For bridge bents with supplementary SPSWs system of the type shown in Fig. 3-6a, assuming a steel plate width equal to twice the column diameter, solution was found possible for column height ranging between 20 ft and 42 ft for cantilever columns and fixed-fixed end columns, respectively, providing the SPSWs' thickness did not exceed 0.5 in. For SPSWs that do not fill in the full space between the columns, additional steel column acting as Vertical Boundary Elements would be required, so this didn't prove to be an attractive solution.

For the case of SPSWs inserted between closely spaced RC columns, for various ratios of the wall width-to-column diameter, the required thickness of the SPSWs plate is inversely proportional to the width of the SPSWs for a given column height. For SPSWs system integral with RC columns in Fig. 3-6b, it requires two steel columns on each side of the RC column. For a certain ratio of steel plate widths to column diameter, the thickness of SPSWs is proportional to the bridge height.

The required thickness of the SPSWs in a box-pier configuration, as in Fig. 3-6e but with two box piers, is half of that for the SPSW system integral with the RC columns. If the ratio between the wall's steel plate width and the column diameter is 2 in all these three cases, it was found possible to limit the thickness of the SPSWs steel plate to less than 0.5 in for columns ranging from 12 ft to 44 ft tall for both cases of cantilever and fixed end columns. Note that for SPSWs, link beams serve as horizontal boundary elements and need to be designed to ensure that the force demand on the columns remain within their capacity.

In conclusion, BRBs and SPSWs are more easily implemented as structural fuses in RC bridge bents, given the assumptions stated above. No other options were found to be practical. Note that, the stiffness ratio and the fuse ductility were arbitrarily chosen for the generic study. These two parameters are not exactly independent. More studies need to be done to establish appropriate admissible ranges for cases where this dependency exists for fuses to be implemented in each of the above configuration.

3.5   Connections

For structural fuses to be effective when added to existing concrete bents, connection concepts must be formulated to transfer these forces to the concrete bridge components. Three different strategies were investigated for the fuse-column connections, namely: (i) steel plates wrapped around concrete columns ("jacketed columns") to which other elements can be connected; (ii) anchor bolts embedded in the concrete columns; and (iii) through-columns anchor rods. This section only investigates the inverted-V chevron BRBs and inserted SPSWs between closely spaced columns for the typical Caltrans bridge bent configurations described in Section 3.2. The connection of SPSW's steel plates to RC columns needed anchor rods through the entire height of the columns, while the BRBs only requires anchor rods connections at the two ends where BRBs were connected to the columns.

3.5.1   Steel Jacketing

Steel jacketing is an external encasement of columns achieved by welding prefabricated steel shells in situ. It has commonly been implemented as a seismic retrofit approach for RC column bridges. Here, it is solely considered as a detail to facilitate the connection of hysteretic energy device (via steel plates) to RC columns. In this application, the steel plates transferring the forces developed in the structural fuse are welded to the steel jacket, which is itself wrapped around the concrete columns.

The steel jackets that have been typically used in the retrofit of RC columns are slightly oversized and the gap between the jacket and column is usually filled with cement-based grout to ensure composite action between the jacket and column. Fig. 3-11 shows the schematic seismic retrofit of a RC bridge column using steel jacketing. Its purpose in seismic applications is to enhance the flexural and shear performance of deficient bridge columns (Chai et al., 1994).

Note that steel jacketing is typically not extended into the foundation or cap beam of the column, as vertical gaps are left between the steel jacketing and the foundation and cap beam, such as to not increase the column flexural demands on those adjacent structural elements. The enhancement to the bridge

column is in terms of greater flexural ductility, as well as to prevent shear failures. The steel jacketing does not help the RC column resist additional axial compression force or moment induced by lateral displacement.
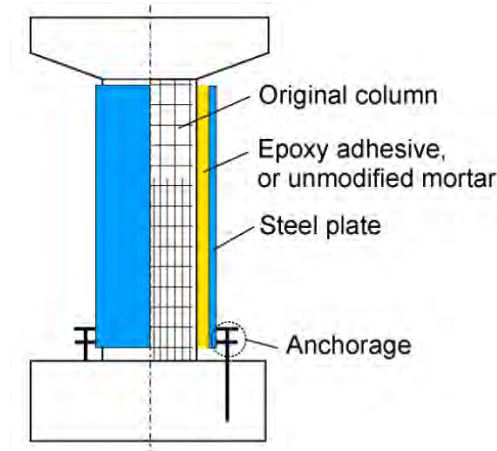
Figure 3-11 Steel jacketing of a RC column (Zhang et al., 2009)

When a steel jacket is subjected to the axial tension from a steel plate perpendicular to its surface (i.e. a "branch plate"), the concrete columns inside of the jacket helps the side faces of the steel jacket from getting close to each other, as shown in Fig. 3-12. Therefore, the perpendicular pulling forces N that can be resisted by such steel jackets may be larger than on a Circular Hollow Section (CHS) of same thickness and diameter.

(a)   (b)
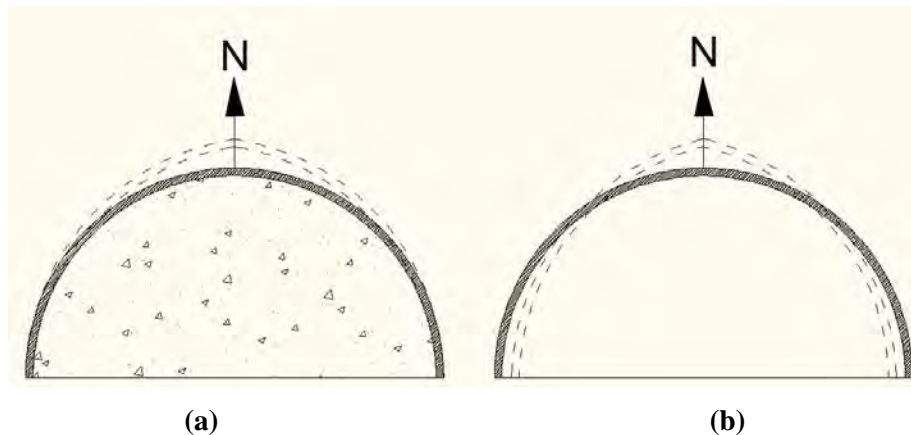
Figure 3-12 (a) Concrete column wrapped with steel jacketing under perpendicular tension loading; (b) CHS section under perpendicular tension loading

For the branch plate to CHS connection shown in Fig. 3-13a, relevant design equations for calculating the pulling force N have been given in Wardenier et.al. (2010). The ultimate connection resistance is related to two governing limit states for the CHS: CHS plastification (with excessive deformation) and CHS

punching shear. Filling the chord with concrete or grout is mentioned in Wardenier et. al. (2008) as a viable stiffening method to increase the static capacity of existing joints or to reduce the stress concentration as shown in Fig. 3-13b. Equation 3.7 from Wardenier et.al., (2008) is suggested for calculating the concrete-filled CHS connection strength based on the punching shear strength, when the branch plate is loaded by a perpendicular tension force:

$$N_1^* = 0.72 f_{y0} l_1 t_0 \tag{3.7}$$

where: f_{y0} is the yield strength of the steel material of the CHS, l_1 is the length of the branch plate, and t_0 is the thickness of the CHS.

(a) **(b)**
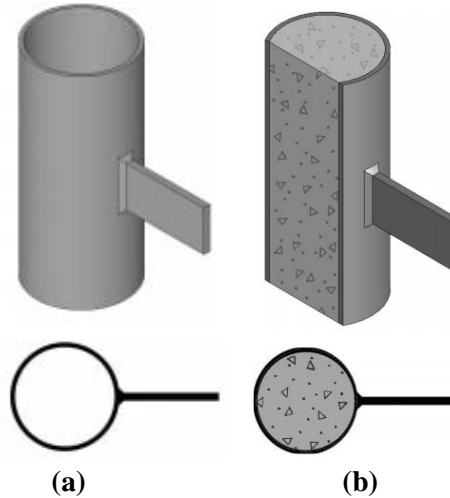
Figure 3-13 Branch plate connection to: (a) CHS; (b) CHS filled with concrete (Voth, 2010)

Voth (2010) investigated the increase of connection strength after adding the concrete infill to the CHS and found Equation 3.7 above to be too conservative. Instead, Voth recommended using Equation 3.8 for calculating the punching shear for unfilled CHS since both the experimental and analytical results indicated that the actual strength when the connection failed in punching shear was closer to value calculated per that equation.

$$N_2^* = 1.16 f_{y0} l_1 t_0 \tag{3.8}$$

Note that because of the size of the RC columns in bridges, concrete-filled CHS created by the steel jacketing in this application would be comparatively larger than the CHS considered by Wardenier (2008) and Voth (2010). Given the limited experimental and analytical results available regarding the behavior and strength of this connection to concrete-filled CHS (only one specimen was studied by Voth (2010), it is hard to assess the ultimate strength and failure mode of this kind of connection and more research needs to be conducted. Therefore, this connection's behavior, particularly with regard to yielding and punching shear of the concrete-filled CHS, was studied analytically in Section 6, along with experimental

verifications for a few sizes of concrete-filled CHS. A design example for a BRB's gusset plate connecting to the concrete-filled CHS will be provided in Section 6.

In the interim, using the above equations, it was found that the required length of the BRB's gusset plate is substantial if a BRB is only connected to the bottom of the column rather than also to the foundation. It was also found that the steel shell thickness required to resist the tensile force typically developed by SPSWs would be unpractical.

3.5.2 Anchor Bolts

Headed steel studs, as cast-in anchors, are usually welded to a steel endplate and encased in concrete for connections. It has been the most common method for transferring forces between steel and concrete in composite constructions. The failure modes of such anchors bolts are shown in Fig.3-14. The strength corresponding to each failure mode is provided in ACI 318. Various limit states of "in-field" anchors (defined as the case when the edge distance of the anchor to the free side of the concrete member is greater than a specified value such that edge failure cannot develop) are listed below.

(1) Steel strength of anchors in tension (Fig. 3-14 (a)i);

(2) Steel strength of anchors in shear (Fig. 3-14 (b)i);

(3) Concrete breakout strength of anchors in tension (Fig. 3-14 (a)iii);

(4) Concrete pullout strength of anchors in tension (Fig. 3-14 (a)ii);

(5) Concrete pryout strength of anchor in shear (Fig. 3-14 (b)ii)

(i) Steel failure   (ii) Pullout   (iii) Concrete breakout
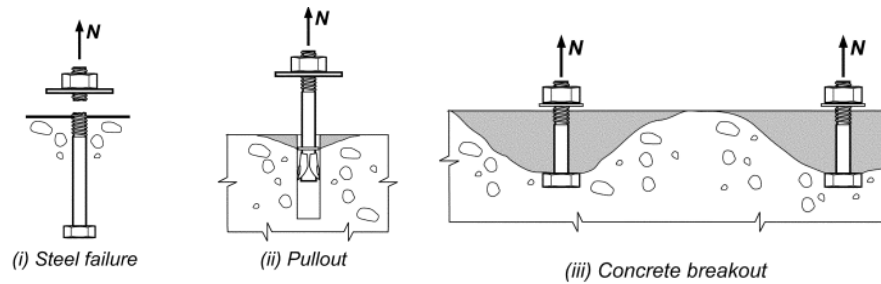
(a) Failure modes for anchors in tension

(i) Steel failure preceded by concrete spall   (ii) Concrete pryout for anchors far from a free edge
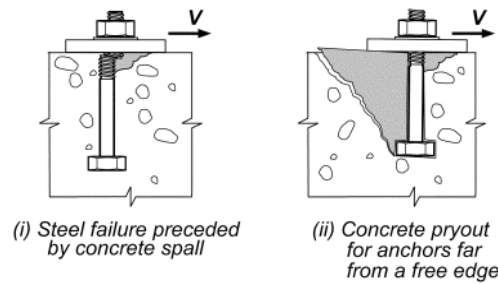
(b) Failure modes for anchors in shear

Figure 3-14 Failure modes of anchors under different conditions (ACI 318 Appendix D Commentary RD.4.1)

A generic configuration of the headed studs that connect a steel endplate to a RC column is shown in Fig. 3-15. The anchors are welded to the steel endplate, to which the structural fuse can be connected to. There can be several rows and columns of headed studs.

A case study of specified headed studs was performed to obtain their strength under tensile and shear forces using equations provided in ACI 318 and PCI (2004). The cast-in headed studs with the largest available shank diameter, d_0, of 7/8" (per PCI 2004) were used. The shear and tensile strength of these studs was evaluated as a function of the embedded length of headed studs. Group effect was excluded by providing the code-required distance between each headed stud. Simple connections of SPSWs and BRBs were evaluated using the largest strength that can be developed by a single headed stud. The available contact area between the concrete column and steel endplate was less than necessary for the studs to develop the needed strength (in both cases, the required number of headed studs was found to be impractical).

(a)   (b)
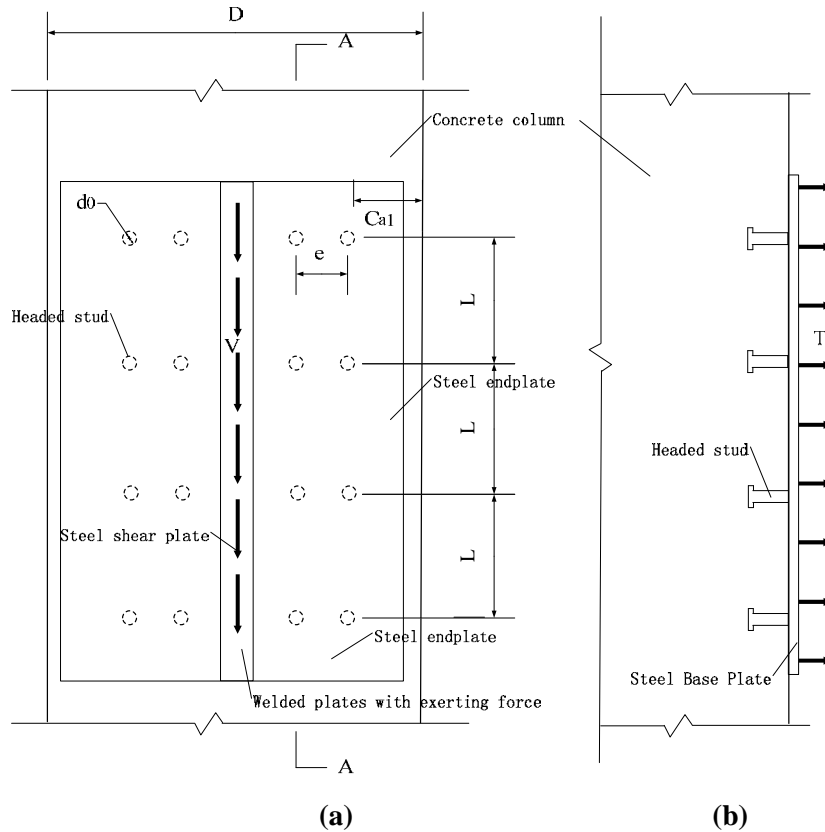
Figure 3-15 (a) A group of anchors loaded in shear parallel to the side edge and illustrated dimensions (b) View of Section A-A in (a)

3.5.3 Anchor Rods

The connections of steel plates to RC columns can also be accomplished using bolted endplates, using the layouts shown in Fig. 3-16. Concrete or grout can be used to fill the space between the endplates and the circular RC columns. The anchor rods are installed in conduits prior to casting RC columns, or in ducts drilled in the existing RC columns. Then the anchor rods are fixed by the nuts at each ends.

Different types of cast-in-place anchor rods are shown in Fig. 3-17. These include anchor rods with a head, threaded rods with nut, threaded rods with a plate washer, hooked bars or U-bolts. The most common anchor rods are type c in Fig. 3-17.   Anchor rods are supplied in conformance with ASTM F1554 "Standard Specification for Anchor Bolts, Steel, 36, 55, and 105 ksi Yield Strength." ASTM F1554 recommends the use of a standard Grade 36 rod, ¾ in diameter, for most practical cases. However, when more strength is required, it is possible to increase the rod's diameter up to about 2 in for ASTM F1554 Grade 36 steel before switching to a higher-strength material grade.

64
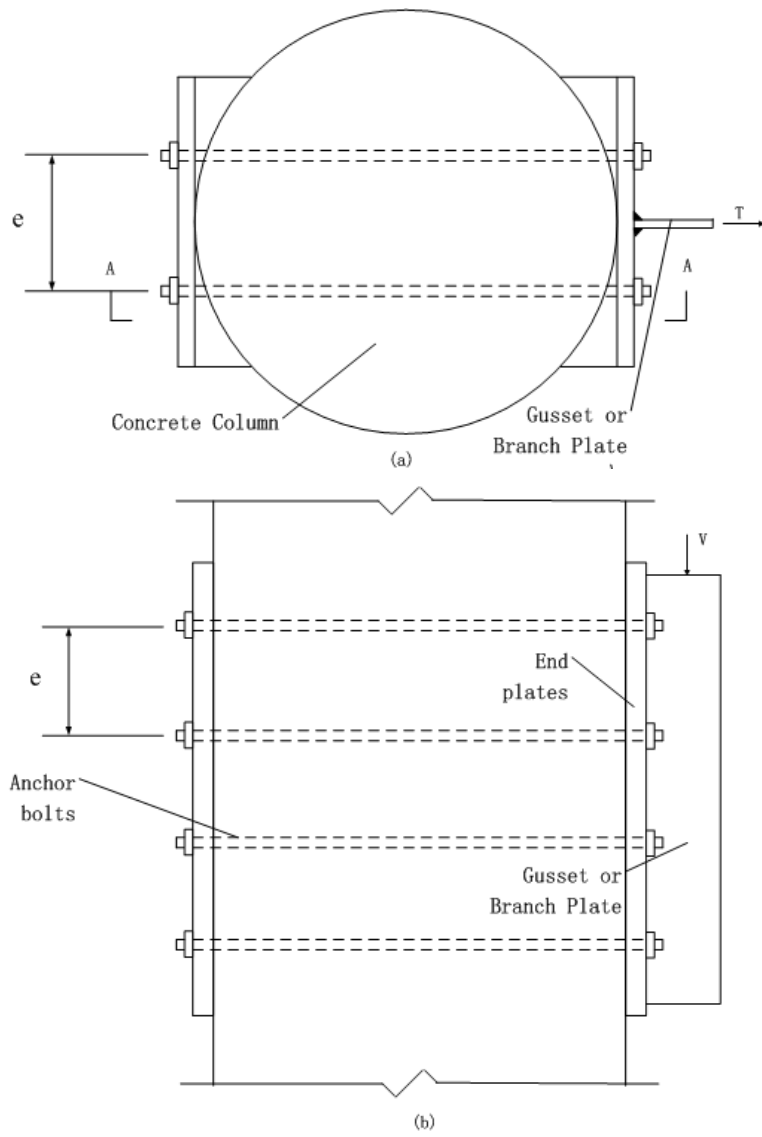
Figure 3-16 (a) Connections of steel plates with circular concrete columns using anchor bolts (b) Section view of A-A
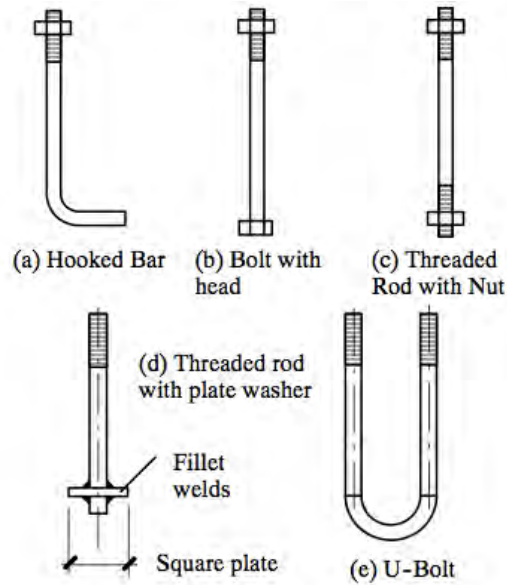
Figure 3-17 Types of Anchor Bolts (Hogan and Thomas, 1994)

The endplate thickness, anchor holes' size and the distance between the anchor rods must be designed to ensure transfer of the force from the endplate to the anchor rods and allow an even redistribution of forces. The design of the end plate is not considered here. Simple connections of SPSWs and BRBs were designed based on strength of single anchor rods (i.e., neglecting strength reduction for group effect), but connecting to columns using anchor rods was found to be not practical due to the limited space available.

3.5.4 Comparison

For the two bridge bent configurations considered for the typical Caltrans bridge investigated, none of the three details considered was found to be fully satisfactory to connect the fuse to RC columns. The three types of connections considered required the RC columns to have an added steel component to achieve connection: either a steel jacket or a bolted end-plate, to which the structural fuses could be connected. This observation suggests that Concrete Filled steel Tube (CFT) columns would be an effective substitute for RC columns in new bridge construction, relying on the CFT's steel shell to facilitate connections. This type of column is considered in Sections 4 and 5 for the study of structural fuses added to bridge bents. In Section 6, the strength that can be developed by the shell of a CFT under a perpendicularly applied tensile force is investigated more specifically, and the example is provided for connection that consists of a plate welded to the shell of CFT column, together with alternate connection designs using anchor rods and headed studs' details for comparison purposes.

Note that comparing details required to connect SPSWs and BRB to columns, it was found that SPSWs required connection over the entire column height, while BRB connections could be located to the locations at their ends, which might be more cost effective to implement (although such effectiveness was not calculated).

3.6   Conclusions

Based on preliminary studies using both a specific Caltrans standard bridge and generic RC bridge, BRBs and SPSWs were found as the most practical energy dissipating systems for the implementation of structural fuses in a bridge bent. SPSWs, because they require the design of link beam (Horizontal Boundary Element) and overall assessment of the SPSWs yielding force demand on the columns, are more complicated to implement than BRBs. Besides, SPSWs require to be connected through the entire height of the columns, whereas the connections of BRBs are only needed at the location where they are connected to the columns at the two ends.

The above results show challenges in connecting structural fuses to some RC columns (when neglecting the possibility of partially connecting to the footing). Work on connections indicated the advantage of using steel jackets around columns compared to other types of details considered. Based on that observation, for applications of the SF concept in new bridges, the following Sections focus on the BRBs design in bridge bents with CFT columns. Such CFT columns are also able to provide the needed strength with a smaller stiffness, which helps achieve the SF objectives.

SECTION 4

""""DESIGN EXAMPLES OF STRUCTURAL FUSE IN DTĸF I G̅U

""""USING BRBS

4.1   General

Per discussion in Section 3, the design procedure for structural fuses in bridge bents were developed focusing on BRBs, for the two bent configurations described in this Section. Then, the two bridge bents with BRBs were analyzed uing SAP2000 to verify that the force demands from seismic and service load did not exceed the capacity of the columns. The same Caltrans Ordinary Bridge geometry described in Section 3.3 was used here. Recall that the bridge bent is located at the center of that bridge.

Two scenarios having different column layout were considered. First, a two-column bent with BRB fuses and having the same column spacing as Caltrans' Ordinary Bridge example was studied. Concrete Filled Tube (CFT) columns were used, and single inclined BRB and inverted-V BRBs configurations were both considered.   Response of the bent to seismic excitations in the transverse direction was studied, understanding that this implementation of the fuse strategy would have to be coupled with another system in the longitudinal direction (which could be structural fuses in-series with Lock-up Devices connecting the bridge deck to the abutments, for example).

Second, a box-pier configuration concept that allows implementation of BRBs to resist earthquake excitations in both transverse and longitudinal directions was studied. In this concept, the BRBs are inserted between closely spaced CFT columns to form the box-pier configuration.

In both cases, although the use of RC columns was considered in the early phases of the study, the final designs were conducted with concrete-filled steel tube columns, as this provided many advantages for the current application. Figures of the two bridge cases are shown in analysis models in later sections.

4.2   Design procedure

This section provides a general overview of the design procedure followed to design the structural fuse system, and summarizes the underlying assumptions made in the process. The flow-chart in Fig. 4-1 summarizes this procedure, recognizing that the process was iterative. Following that flow-chart, the design procedure can be broken down in the following steps:
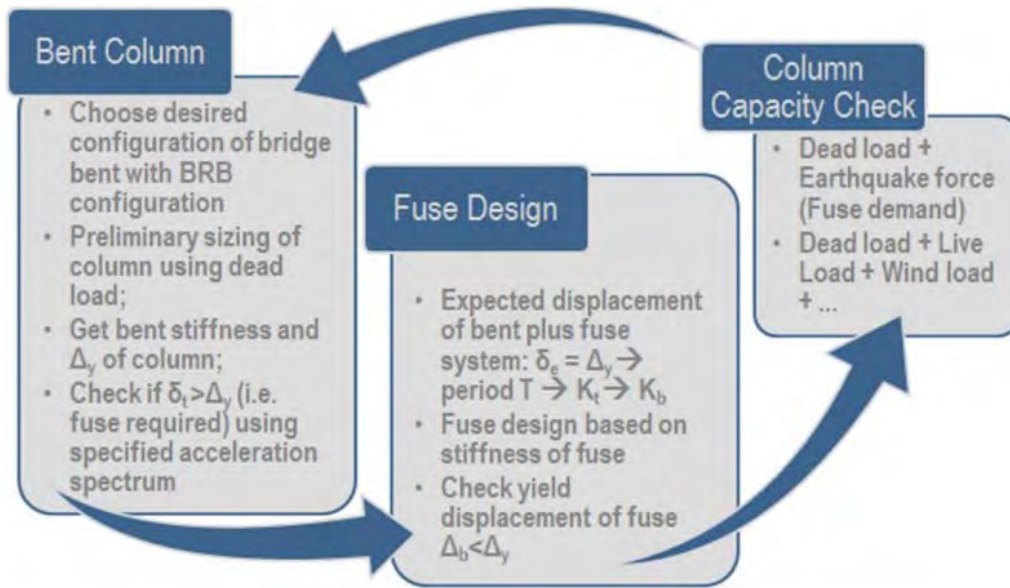
Figure 4-1 Design Flow-chart of Bridge Bent with BRBs

Step 1: Calculations of the bent target displacement and bare bent stiffness

The maximum displacement permissible with the SF concept is set equal to the yield displacement of the column (also called the "expected displacement" in subsequent steps). This can be calculated knowing the stiffness of the bare bent. For preliminary design, to size column's diameter, the gravity dead load of the bridge's superstructure tributary to the column bent was assumed to be distributed equally to each column of the center bridge bent, and dead load demand was taken to be approximately 5% of the overall axial strength of each CFT column. Note that CFT columns have no reinforcement in the concrete infill and that their properties and strengths (in particular, their cross-section axial compressive and tensile strength, flexural strength, and yielding curvature) were obtained through fiber analysis using the program Section Designer in *SAP2000 Version 14*. The buckling compressive strength of the column was checked using equations in AISC (2010) for composite members. The yield displacement, Δ_y, and the effective stiffness of the CFT column, K_{col}, were calculated as:

$$\Delta_y = 2\varphi_y \frac{(\frac{h}{2})^2}{3} \tag{4.1}$$

$$K_{col} = \frac{2M_y}{h\Delta_y} \tag{4.2}$$

where: φ_y is the yield curvature of the CFT section; h is the height of the CFT column, and; M_y is the yield strength of the CFT column. Note that bridge OSB1 has an integral bent with columns fixed at the top of the cap beam. For a non-integral bent, the bare bent stiffness would be smaller and the stiffness of

70

the BRB needed to achieve the SF design objective would be different, but the design methodology remains the same.

Step 2: Calculation of required fuse stiffness

The required fuse stiffness is selected to be the minimum value required to prevent column yielding. For this purpose, the expected displacement of the bridge bent with BRBs, δ_e, was calculated based on the assumption of "equal elastic and inelastic displacements for a given period" commonly used in earthquake resistant design. As mentioned in Step 1, it was set to be equal to the yield displacement of the column, Δ_y. The provided acceleration spectrum gives a relationship between the maximum acceleration, S, and period, T, by Equation 4.3. The total stiffness of the bridge bent with BRBs was derived for the given superstructure weight, W_{super}, in Equation 4.4, assuming that no lateral resistance was provided by the abutments. The self-weight of the columns was ignored since it is typically small compared with that of the superstructure. The expected displacement of the bare bridge bent, δ_t, was calculated using Equation 4.5, and checked to be larger than the columns' yield displacement Δ_y, thus making the addition of BRBs worthwhile in reducing the displacement demand.

$$\delta_e = S_a T_s^2 \frac{g}{4\pi^2} = \Delta_y \tag{4.3}$$

$$K_t = \frac{W_{super} 4\pi^2}{386 T_s^2} \tag{4.4}$$

$$\delta_t = S_b T_1^2 \frac{g}{4\pi^2} \tag{4.5}$$

where: S_a and S_b are the accelerations from the target spectrum and respectively corresponding to the period of the bridge bent with BRBs, T_s, and period of the bare bridge bent, T_1, which is equal to $\sqrt{\frac{W_{super} 4\pi^2}{386 K_c}}$; and, K_t, K_c, are, respectively, the stiffness of the total bridge bent with BRBs, and of the bare bridge bent;

Step 3: BRB design

BRB was designed to reach a strain limit of 1.5% in the yield core when the columns reach their yield displacement, Δ_y. Note that strains up to 3% can be typically developed in BRBs and that such a limit could have been used instead, resulting in smaller BRB sizes. Fig. 4-2 schematically illustrates the composition of a BRB, identifying three specific zones: the yield core at the center of the BRB restrained from buckling; the buckling restrained transition segments, and; the non-yielding unrestrained end zones at the two ends.
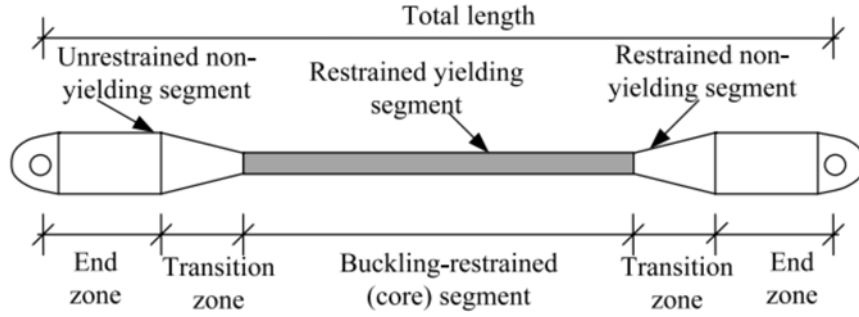
Figure 4-2 Typical section of a BRB (Sahoo and Chao, 2010)

For the two general bridge configurations, namely, two-column bent with BRBs and box-pier bent with BRBs, the area and length ratio of the required BRBs were designed differently.

(i) Two-column bent with BRBs

Behavior of this system depends on the length ratio of the yield core length to the entire BRB length, c_b (given by Equation 10), and the angle of the BRB from the horizontal, θ, which differs for the single inclined BRB and inverted-V BRBs case, as shown in Fig. 4-3..

$$c_b = \frac{\Delta_y}{\varepsilon_{bm}L_{brb}}$$

(4.6)

where: ε_{bm} is the strain limit of BRB's yielding core, and; L_{brb} is the length of BRB.

(a)   (b)
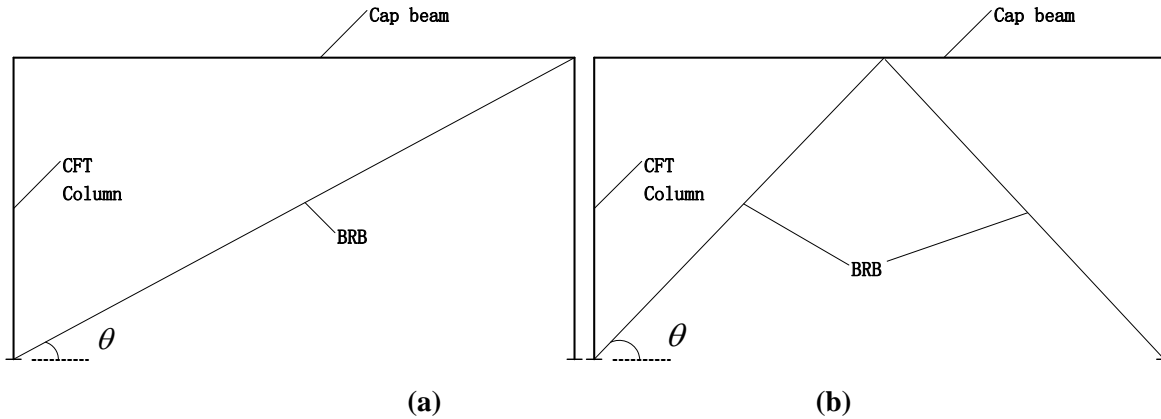
Figure 4-3 Two-CFT-column bent with BRBs: (a) Single Brace of Two-column Bent; (b) Inverted Chevron of Two-column Bent

The displacement of the bent corresponding to the yielding of BRB, Δ_b, as a minimum requirement for the SF concept to work, must be smaller than the expected displacement of the bridge bent, δ_e. This is expressed by Equation 4.7:

$$\Delta_b = \frac{f_{yb}c_b L_{brb}}{E_s cos\theta} < \delta_e$$

(4.7)

where: f_{yb} is the yield strength of the steel used in BRB's core, assumed in this case study to be A36 with an expected yield strength of 42 ksi. Based on the required BRB stiffness obtained from Step 2, the stiffness of each BRB is K_b, which equals to $K_t - K_c$, for single inclined BRB case, and $(K_t - K_c)/2$, for inverted-V BRBs case. Therefore, the cross sectional area of each BRB, A_{brb} ,is:

$$A_{brb} = \Delta_b \frac{K_b}{f_{yb}\cos\theta}$$

(4.8)

(ii) Box-pier bent with BRBs

The typical geometry of a box-pier bent with BRBs is shown in Fig. 4-4. The number of BRBs between the closely spaced CFT columns in the composite box-pier can be generically taken as n. For example, for the bridge bent in Fig. 4-4, n equals 4.
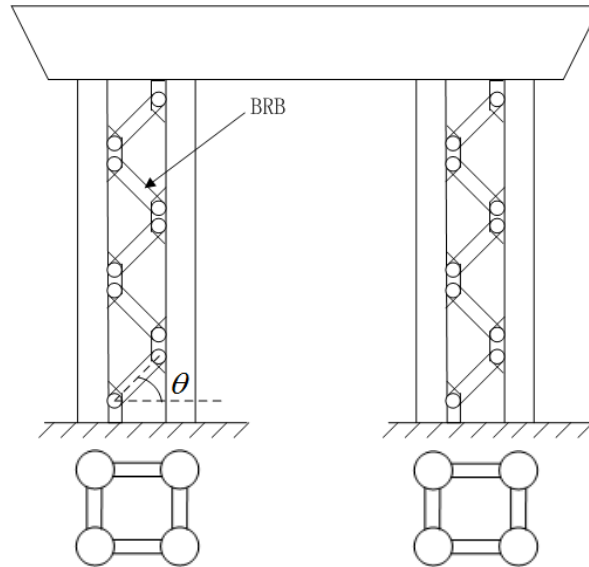
Figure 4-4 Box pier with BRBs in the transverse direction having four BRBs between closely spaced columns

In this case, the length ratio of BRB, c_b, is

$$c_b = \frac{\Delta_y \cos\theta}{n\varepsilon_{bm}L_{brb}}$$

(4.9)

Again, the displacement of the bent corresponds to the yielding of the BRB, Δ_b, must be smaller than the expected displacement of the bridge bent, δ_e

$$\Delta_b = \frac{nf_{yb}c_bL_{brb}}{E_s\cos\theta} < \delta_e$$

(4.10)

The total stiffness of BRBs K_b equals to $K_t - K_c$, based on calculation from Step 2. The cross sectional area of the BRB, A_{brb}, is:

$$A_{brb} = \frac{\Delta_b K_b h}{4 n f_{yb} sin\theta L_c}$$

(4.11)

where: L_c is the clear distance between the closely spaced CFT column in the box-pier bent case

In both two-column bent and box-pier bent with BRBs cases, the BRB's yield strength F_{ybrb} is

$$F_{ybrb} = f_{yb} A_{brb}$$

(4.12)

After the BRB yields, strain hardening is assumed to develop in the yielding core. The largest compressive strength P_{ybrb} and tensile strength T_{ybrb} that will develop in the BRB at a given strain must be considered, particularly for capacity design purposes. Those strengths are given by:

$$P_{ybrb} = \omega\beta f_{yb} A_{brb}$$

(4.13)

$$T_{ybrb} = \omega f_{yb} A_{brb}$$

(4.14)

where: β and ω are strain hardening factors, which vary with BRB size and suppliers, and assumed here to be $\beta = 1.11$ and $\omega = 1.35$ at 1.5% strain per the backbone curve in Fig. 4-5 (Lopez and Sabelli, 2004).

Step 4: Column Capacity Check and Design Iteration

Once a tentative design has been reached, the column capacity at the expected displacement, δ_e , must be checked to ensure that the column axial, flexural and shear strength are not exceeded, considering both the seismic and service load demands (including the expected yield forces coming from BRBs per capacity design principles). Details of such calculations are presented in Section 4.3 and 4.4 for the two design bridge configurations. If column strength is exceeded under the lateral force loading on the bent and the yielding forces coming from BRBs (from capacity design), the column must be redesigned. Design iteration must continue until a column of satisfactory strength is found.
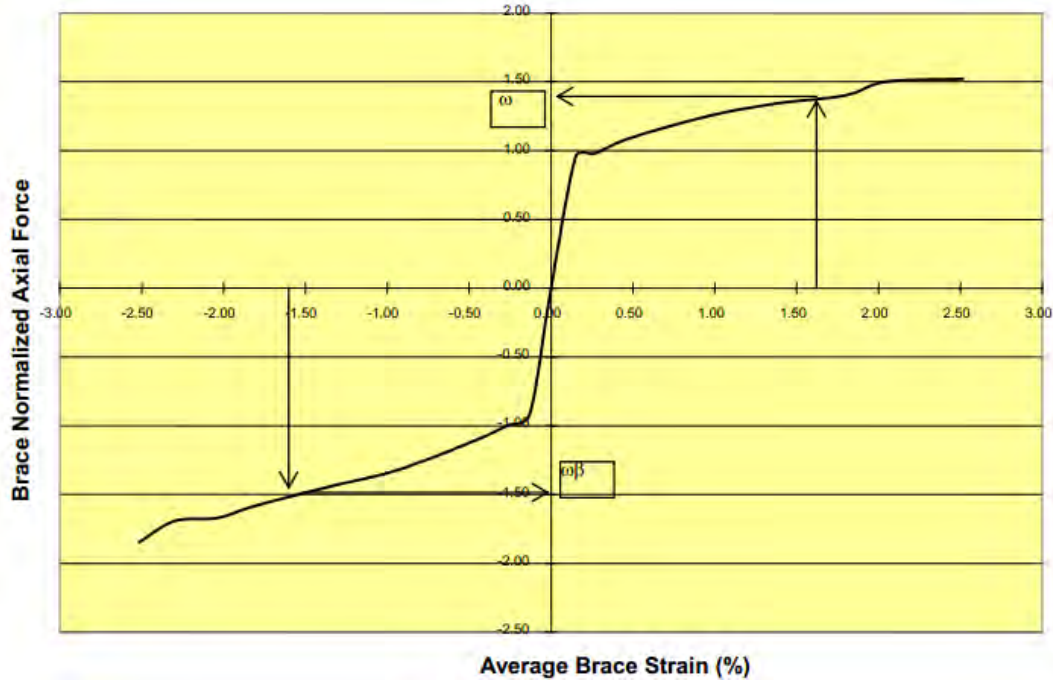
Figure 4-5 Strain hardening factors vs brace strain for an example BRB (Lopez and Sabelli, 2004)

4.3   Two-CFT-Column Bent with BRBs Capacity Check

Following the design procedures in Section 4.2, the two-CFT-column bent with (a) single inclined BRB and (b) inverted-V chevron BRBs are designed. The calculations are shown in Appendix A.

In this section, the seismic and service load check is presented. Firstly, an analytical model built in SAP2000 to verify the bridge behavior. The force demand of the columns in the pushover analysis is checked at the target displacement, which is obtained from elastic response spectrum analysis. Pushover curve from analysis result is plotted and compared with the theoretical one developed from the structural fuse concept. Sections 4.3.1.1 to 4.3.1.6 focus on the case of a bridge bent having a single inclined BRB. Sections 4.3.1.7 to 4.3.1.10 are for the case of a bent with inverted-V (a.k.a. inverted-chevron) BRBs.

Secondly, it was observed during the process of implementing structural fuses in this bridge that the design of the bridge columns was governed by the seismic load cases. However, to illustrate that this is the case, Section 4.3.2 presents the results of bridge analysis under the gravity dead and live load, as well as for wind loads.

4.3.1 Bent pushover analysis

4.3.1.1 Model information-bent with single BRB

Instead of performing a 3-D global analysis of the bridge, a local analysis of the bent in the middle of the bridge is considered adequate and is performed to verify the structural fuse concept. In order to model the clear distance between the adjacent CFT columns where the BRBs are added to the bent, the bridge bent is modeled as the bold lines shown in Fig. 4-6. The CFT columns are fixed at the top to the cap beam, and at the bottom to the ground. The footing is not modeled. The BRBs are designed to be pin connected to the columns (i.e. moments are released at both ends of the beam elements used to model the BRBs). The overhang of the box girder at each side of the bridge bent is 9 ft, which is 1.5 times of the height of the box pier.
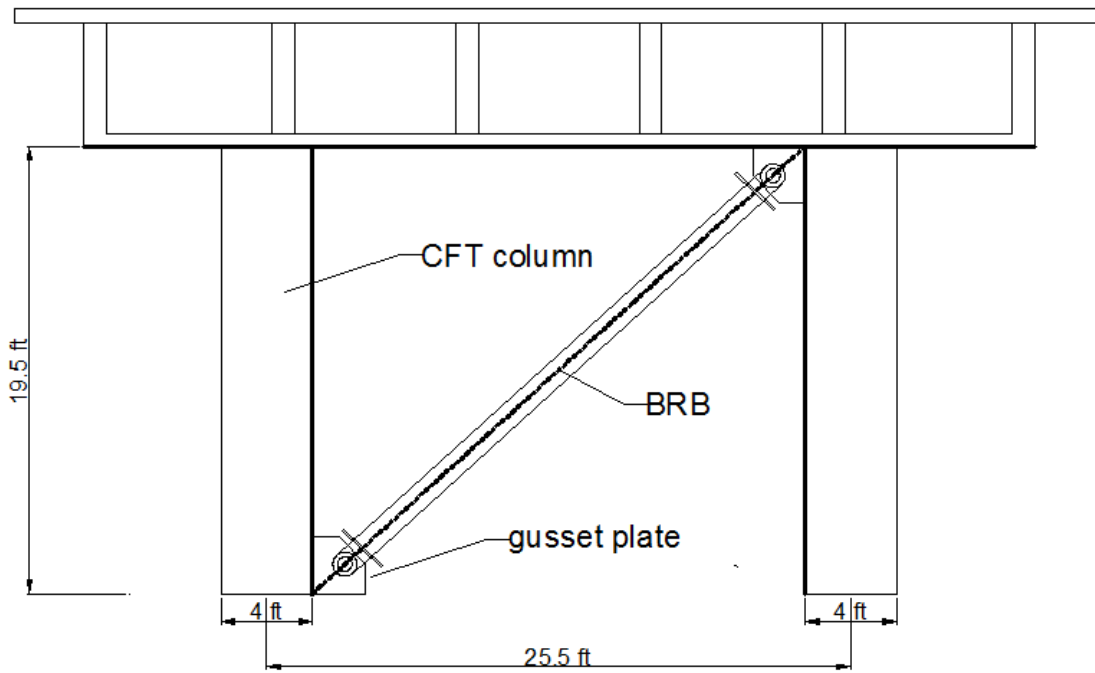
Figure 4-6 Transverse bridge bent with a single inclined BRB

4.3.1.1.1   Material

Table 4-1 lists the materials used for the cap beam, CFT column, and the BRB. Concrete in the CFT columns has the same strength as in the cap beam.

Table 4-1 Materials for different members in the model

Member	Material
Cap beam	Concrete 4 ksi (unconfined)
CFT column	Steel shell A572 Grade 60
	Concrete 4 ksi (confined)
BRB	A500Gr. B with yielding strength requirement of 42 ksi

Concrete in the cap beam is defined as having an ultimate unconfined strain capacity of 0.005. The uniaxial compressive strength and the corresponding strain of the unconfined concrete are f_c' and ε_c' as shown in Fig. 4-7. The value ε_c' is usually around the range of 0.002-0.003. A representative value 0.002 is normally used. When the concrete is subjected to laterally confining pressure, the uniaxial compressive strength f_{cc}' and the corresponding strain ε_{cc}' are much higher than the unconfined concrete. The ultimate strain of the confined concrete is about 11 times of ε_{cc}'. The strain capacity of the confined concrete in the CFT columns is correspondingly increased to 0.02.
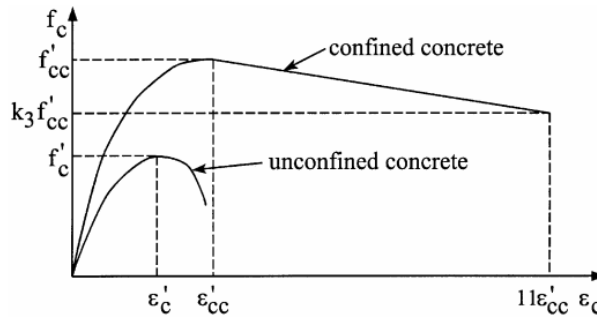
Figure 4-7 Stress-strain curve for concrete (Hu et.al., 2005)P77

The BRB in the SAP2000 model yields over its entire length. In the real case, however, the deformation of the BRB is concentrated in the yielding core. The calculated yielding length ratio, c, is calculated to be 0.101 in Appendix A. To make the overall deformation of the BRB in the SAP2000 model match that of the actual BRB, the modulus of elasticity of A500 Gr.B (42 ksi) is increased to

$E_s = 29000/0.101 = 287129$ ksi.

The idealized nonlinear material model for A500 Gr.B (42 ksi), shown in Fig. 4-8, has been "calibrated" to match the BRB properties shown in Fig. 4-4. As such, at strains of 1.5%, the material reaches its maximum compressive stress of 63 ksi, corresponding to a strain hardening factor of 1.5, and maximum tensile stress of 56.7 ksi, corresponding to a strain hardening factor of 1.35.
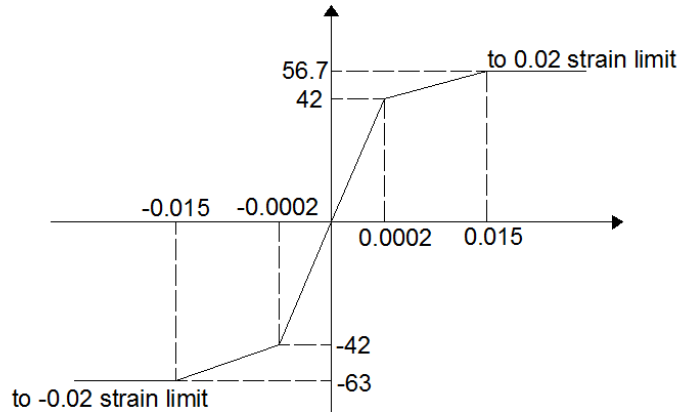
Figure 4-8 Stress-strain curve of A500 Gr.B (42 ksi) (not to scale)

4.3.1.1.2   Section property

According to Caltrans Seismic Design Criteria (2010) Section 7.4.2.1, the minimum cap width, B_{cap}, is calculated to be the diameter of the column plus 2 ft. Therefore, the bent cap section is modeled as rectangle of 6'(width) by 6'(depth). For expediency, the cap beam is modeled as "infinitely rigid" relative to the columns by making the moment of inertia 1000 times larger than that corresponding to a 6' by 6' beam (to reflect the fact that flexure of the cap-beam would also engage the flexural rigidity of the box-girder in that direction).

The CFT column in the analytical model is built using SAP2000's Section Designer. The diameter of the section is 48". The thickness of the steel shell is 1.25". A grid of 20 by 20 fibers is used for calculating the capacity of the section and plastic hinge analysis. The BRB has a cross section of 22.39 in^2.

4.3.1.1.3   Fiber hinge assignment

The columns are modeled in four segments. Fiber P-M2-M3 hinges are used at the ends of each segment. Each fiber hinge length is 10% of the length of the member. A fiber P-M2-M3 hinge locates in the middle of each BRB. However, because moments are released at the ends of the BRB (pin-ends), the fiber P-M2-M3 hinge is only used to model the nonlinear axial behavior. As such, it is equivalent to a fiber P hinge model (which could also have been used for that matter), and it was only used to model the nonlinear axial behavior (resulting in a trilinear behavior). Kinematic strain hardening was used in the fiber hinge of BRB. Note that, Rossi (2015) has compared the behavior of single-story BRB frames, analyzed considering both isotropic and kinematic hardening, as well as smooth hysteretic curves versus bi-linear curves. The differences in results obtained when using the various models was found to depend on the selected level of maximum ductility demand. Based on the results presented in that paper, variations in the maximum displacement demands obtained using the various hysteretic models should be

no greater than 20% for the high ductility demands of BRB used here, given that the peak ground acceleration of the nine synthetic ground motions falls in the range 0.7-1.0g.

4.3.1.2 Load assignment

The dead loads are applied on the cap beam as point load where the webs of the box-girder are located (See Fig. 4-9). The dead loads are applied on the bent as a starting step of the non-linear pushover analysis. The lateral load used for the pushover analysis in the transverse bent consists of a horizontal load applied at the center of the cap beam. The lateral load is applied from right to left in order to put the BRB brace in compression and thus get the largest axial force in the column. The horizontal displacement of the cap beam is the monitored displacement used in the displacement-control method in the pushover analysis. P-delta or second order effect was not considered.
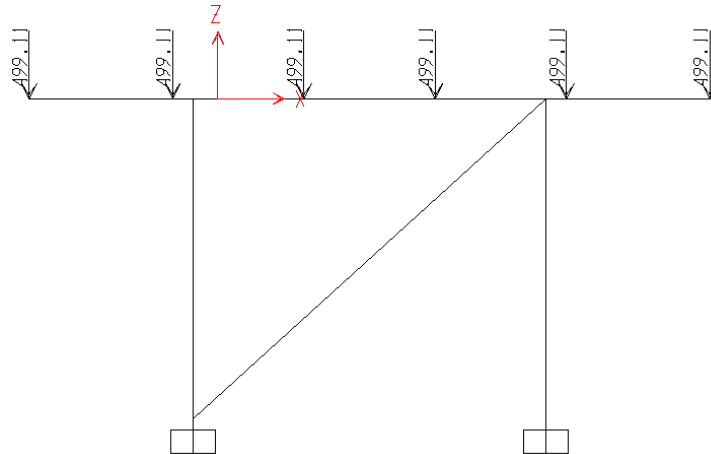
Figure 4-9 Dead loads applied to the bridge bent before push-over analysis in the transverse direction (Unit: kips)

4.3.1.3 Response spectrum analysis

The elastic demand of the bridge model is obtained from a simple response spectrum analysis to assess the displacement and force demand of the bent. The seismic force capacity check of the columns will be examined when the bridge bent reach the elastic displacement demand. In order to be consistent with the time history analysis in Section 5, the modified NEHRP 2003 response spectrum in Fig. 4-10 is used. For comparison, the black solid line and red dotted lines, respectively, correspond to the Caltrans design acceleration spectrum specified for the Ordinary Standard Bridge and the NEHRP 2003 target design acceleration spectrum with design spectral accelerations of $S_{Ds} = 2g, S_{D1} = 0.6g$.
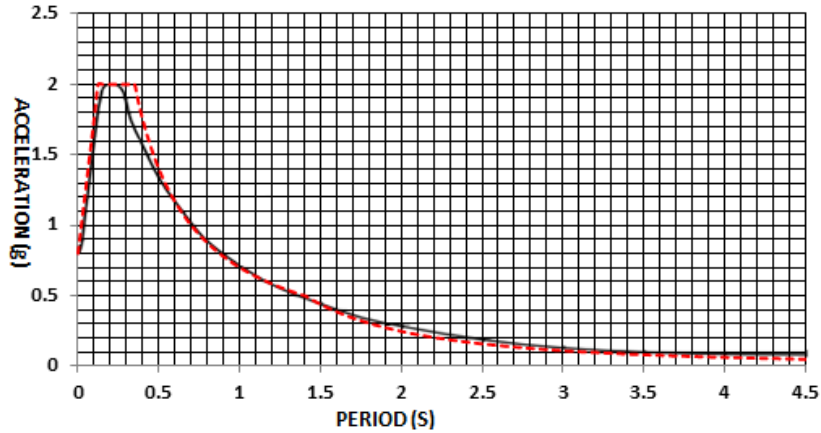
Figure 4-10 Caltrans acceleration response spectrum and corresponding NEHRP 2003 target design spectrum

The displacement demands of the two-CFT-column bent with BRBs are shown below in Table 4-2. The column yielding displacement is assumed to be the target displacement at the top of the bent in the design hand calculation. The difference in results obtained for the design assumption and response spectrum analysis cases is caused by the slightly different bent stiffness considered in the SAP2000 analyses. The designed strength and stiffness were obtained by assuming that the columns developed their yield moment, M_y, at both of their ends (assuming an infinitely rigid superstructure). The corresponding shear resistance of the frame at yield is $2M_y/h$, where h is the height of the column. In the SAP2000 model, the superstructure was not modeled as infinitely rigid, resulting in a more flexible bent overall, and the moment at the top of the columns M_{top} is less than M_y, when M_y is reached at the column bases (i.e., $V = (M_{top}+M_y)/h$).

Table 4-2 The displacement demand comparison of the two-CFT-column bents

Two-CFT-column with	Design	Analysis (Response Spectrum)	Difference
Single inclined BRB	0.71"	0.94"	24%
Inverted-V BRBs	0.71"	0.81"	12%

4.3.1.4 Two-CFT-column bent with single inclined BRB analysis results

When the bridge bent reach the expected elastic displacement at the cap beam level of 0.94" in the pushover analysis, the moment demand in the columns is shown in Fig. 4-11(a). The axial tensile and compressive force is shown in Fig. 4-11(b). The reactions at the bottom of the CFT columns are shown in Fig. 4-11(c).

(a)

(b)

(c)
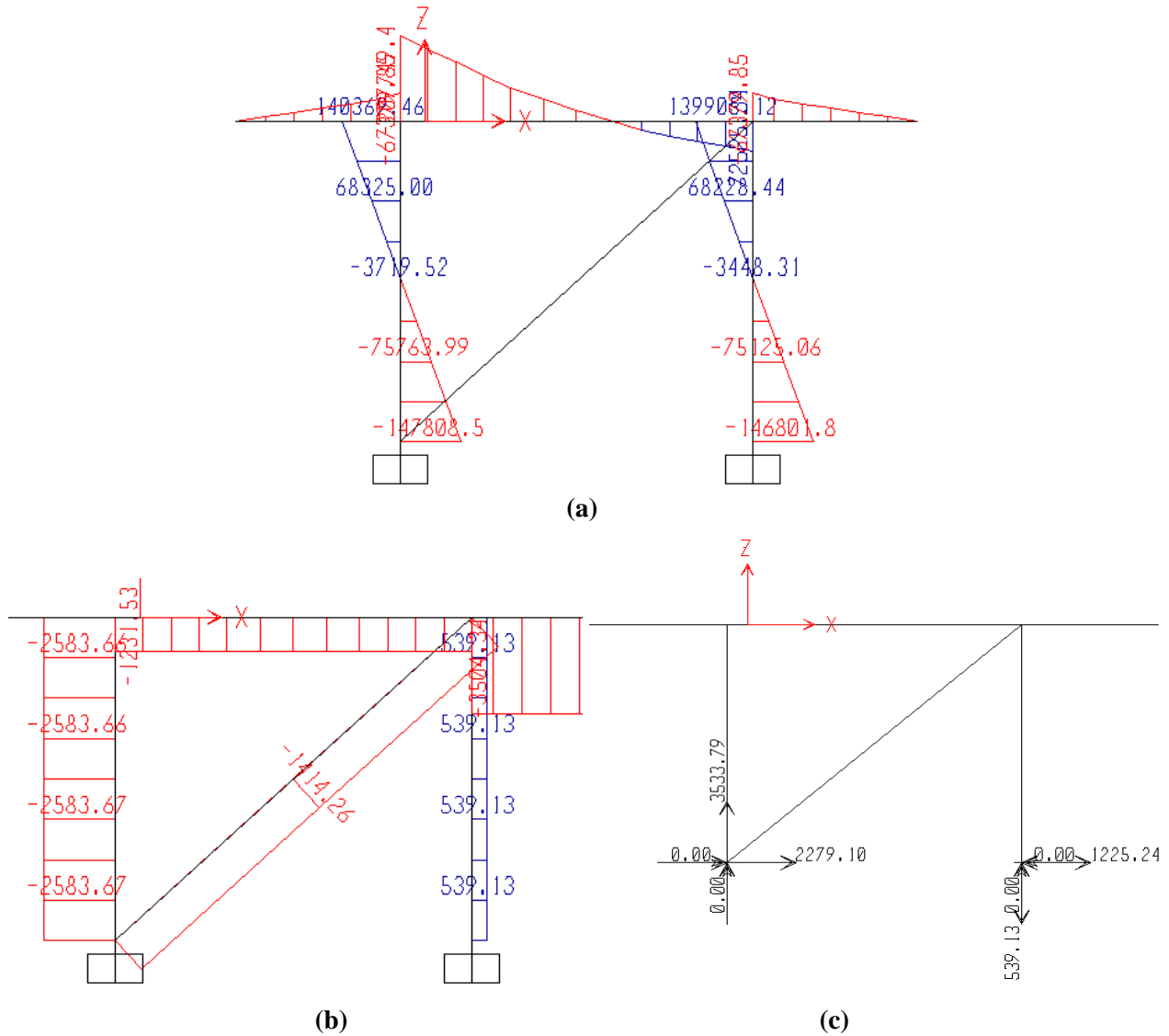
Figure 4-11 (a) Moment diagram of the bent with single inclined BRB when the expected displacement is reached in the transverse direction (unit: kip-in); (b) Corresponding axial forces in the members of the bent (unit: kips); (c) Corresponding reactions at the bottom of the CFT columns (unit: kip-in)

The reaction forces are used here to check the column capacities, in which case the eccentricity between the point where the brace and column workline meet around the foundation exist, as shown in Fig. 4-12a. The maximum forces used would be larger than the corresponding forces when the eccentricity does not exist in Fig. 4-12b, since the forces in the braces goes to the ground.
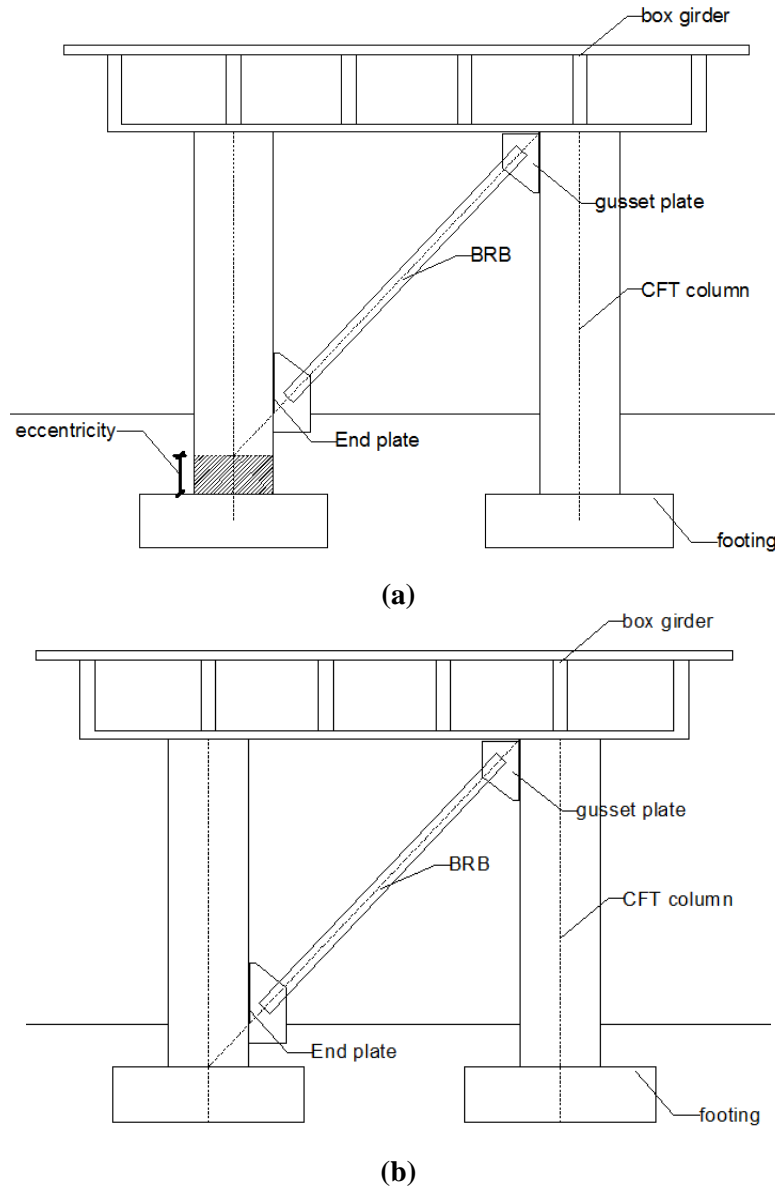
Figure 4-12 The bridge bent with single inclined braces in the transverse direction (a) considering a possible eccentricity, *e* (b) no eccentricity

The moment and axial force demands shown in Fig. 4-11 are compared against the provided member strengths, as shown in Table 4-3. The flexural plastic strengths and yield strength obtained from Section Designer are listed in Table 4-4. The plastic flexural strength of column is the full composite flexural strength. The resistance reduction factors Φ for the strength values from Section Designer are all 1.0. Checking the plastic strength and axial strength interaction at that drift gives an indication of the columns' reserve strength beyond the first yielding. The ratios are all smaller than 1.0. This indicates that the

columns have sufficient strength to resist the forces at the target displacement. Note that the interaction equation used in Table 4-3 for the axial force and plastic flexural strength is a simple linear relationship.

Table 4-3 Summarized force demands in the columns for bent with single inclined BRB

Column Type	Moment Demand M_u (kip-in)	Reaction Force Demand P_u (kips)	Plastic Strength ΦM_n (kip-in)	Axial Strength ΦP_n (kip)	$M_u/\Phi M_n$ $+P_u/\Phi P_n$
Tension	147,809	539	185,621	11,020	0.84
Compression	146,802	-3534	185,621	-164,37	1.00

The interaction diagram is equivalent to what is shown in Fig. 4-13 for a B factor of 1.0. In reality, for CFT columns, B is typically less than 1.0, which provides for further reserve strength. Note that all the above are interaction equations based on cross-section strength. Columns were designed considering the actual column slenderness. However, as shown in Appendix A, the columns are quite stocky and slenderness has a minimal impact of strength for this particular example.
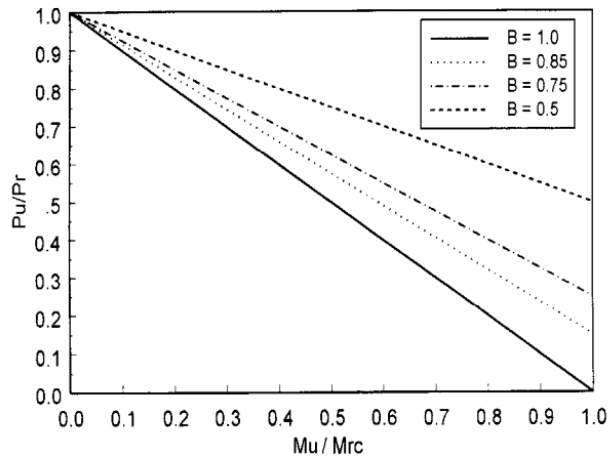
Figure 4-13 Interaction curve for CFT column (AASHTO, 2011, figure C7.6.1-1)

It is conservative to use that linear interaction equation here, instead of the interaction equations provided in the AASHTO LRFD Seismic design specification (2011) Section 7.6.1 for axial compression and moment (which uses a calculated B value, typically less than 1.0). Note that there exists no equation in AASHTO for the axial tensile and flexural interaction of CFT sections. Following is an arbitrary example to show the difference in the strength calculated from the AASHTO equation and the value obtained from Section Designer given the axial force. The AASHTO compression-flexure interaction equation for CFT gives:

$$\frac{P_u}{P_n} + B\frac{M_u}{M_n} \leq 1 \tag{4.15}$$

where: $M_u/M_n \leq 1$; $B = 1 - P_{rc}/P_n = 1 - \varphi_{c1}f_cA_c/P_n = 0.70$; $\varphi_{c1} = 0.75$

The resulting ratio $BM_u/M_n + P_u/P_n$ for the column in compression is 0.65, providing a greater reserve strength.

4.3.1.5 Pushover curve for two-CFT-column bent with single inclined BRB

Fig. 4-14 shows the theoretical pushover curves of lateral shear resistance versus top displacement of the column for the frame, BRB, and the combined system, obtained using a bilinear force deformation relationship for the columns (yielding at a moment of M_y=126,891 kip-in) and tri-linear relationship for BRBs yielding at 42 ksi and strain hardening to 63 ksi at a strain of 0.015). The purple line of the theoretical BRB shows the yielding of the BRB at the displacement of 0.069", and point where the maximum strain hardening considered is reached at 0.71". The target displacement of the bent is reached when the BRBs have the largest strain hardening. The theoretical frame curve in navy blue dash lines shows that the frame yields at the displacement of 0.71". The two parts add up to the total theoretical curve for the combined system plotted in red dash lines. The left green vertical dash dotted line represents the expected displacement for the structural fuse system. The right pink vertical dash dotted line shows the expected displacement for the bent frame alone (without the BRB) if using the same acceleration spectrum.

Fig.4-15 overlays, on top of the results from Fig. 4-14, the pushover curve obtained from the SAP2000 analysis (in solid lines). The solid blue line shows the total base shear versus lateral displacement at top of the bent. By subtracting the lateral forces resisted by the BRBs (equal to the horizontal component of the forces in the BRB) shown in solid green line, the solid brown line gives the portion of the base shear forces resisted by the frame itself.

Fig. 4-16 shows the target displacement demand of 0.94" from response spectrum analysis as the orange vertical line. Note that SAP2000 analyses consider strain hardening of the columns as well as the BRBs. In Fig. 4-16, the push-over analysis results indicate that column yield is first reached at the bottom of the right column; the orange lower horizontal dotted line identifies the base shear resisted by the columns when that happens (which incidentally happens in a CFT column in tension). The middle grey light blue upper horizontal dotted lines show the starting of the strain hardening of the same section. For

comparison, the upper blue dotted line is shown for the reaching shear resistance of the frame V corresponding to the $2M_p/h_{column}$ calculated, where M_p equals to 187,851 kip-in obtained from SAP2000 Section Designer.
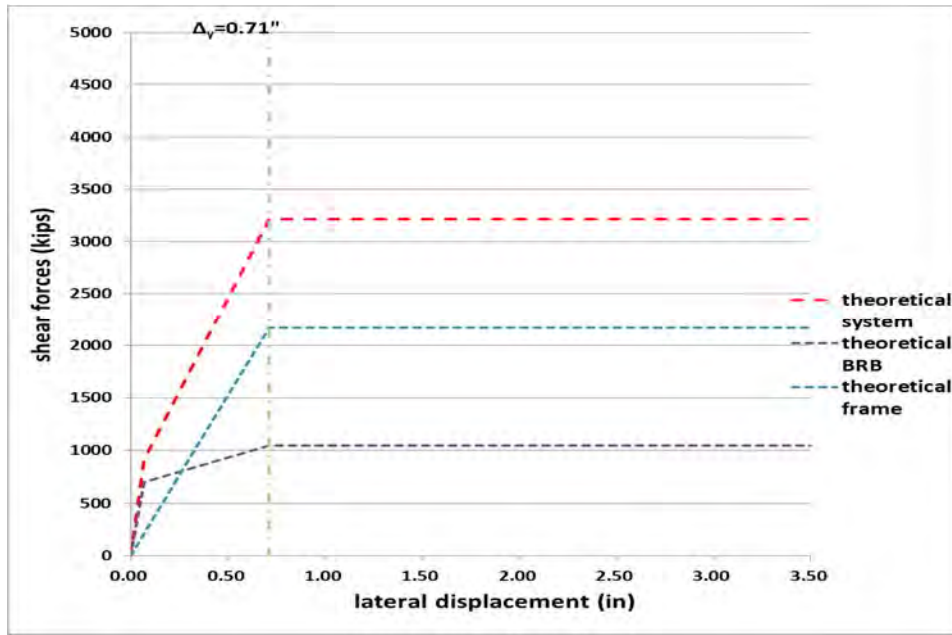
Figure 4-14 Theoretical pushover curves of the frame, BRB and the combined system for the single inclined BRB case
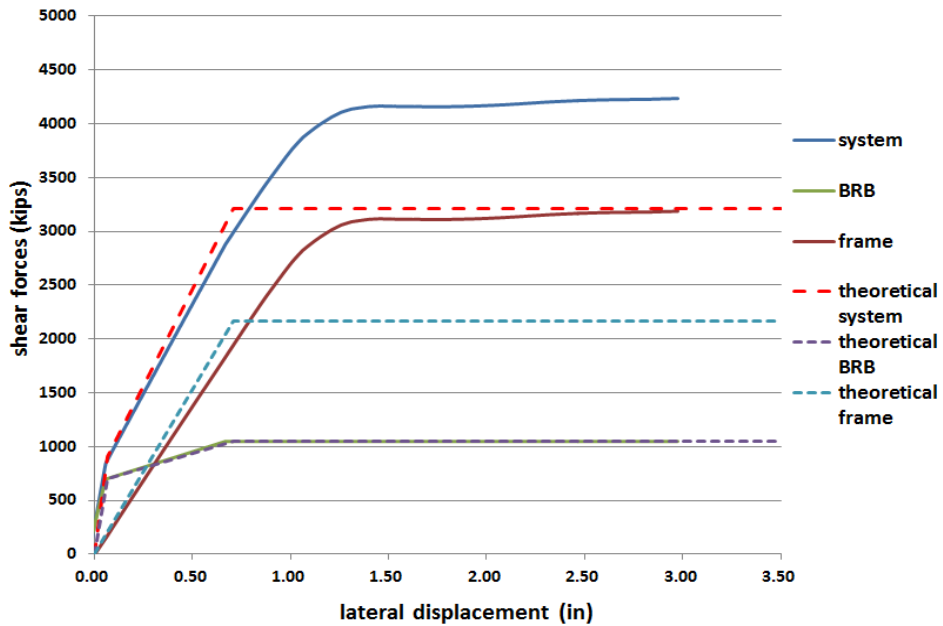
Figure 4-15 Comparison between the theoretical curve and the analytical curve for the single inclined BRB case

85
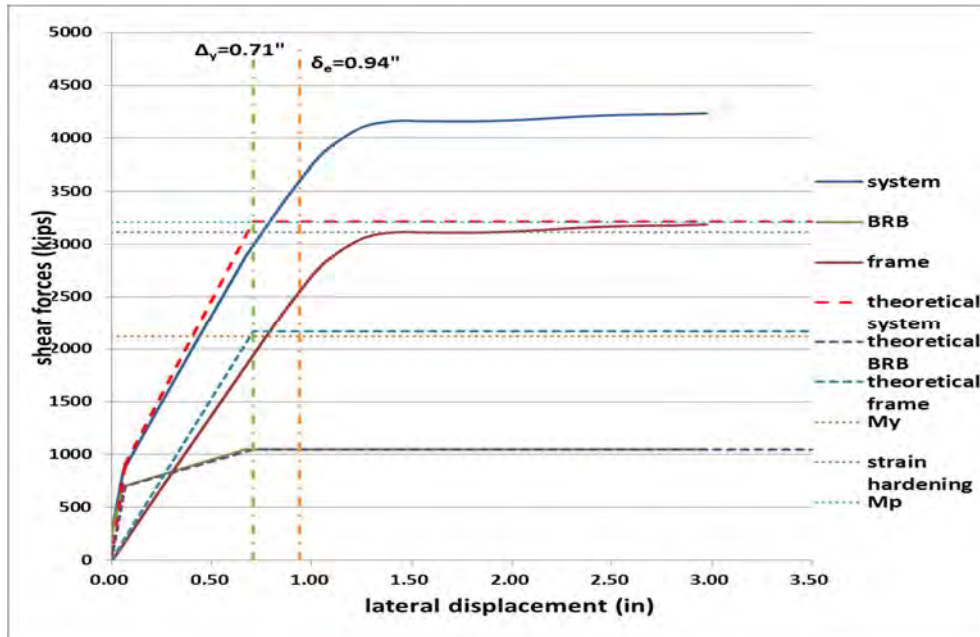
Figure 4-16 Pushover curve comparison between the analysis result and theoretical design value for the single inclined BRB case

The sequence of yielding at top and bottom of the CFT columns (i.e. the point when the extreme fiber yields) and reaching the capacity (i.e. from which strain hardening starts to develop at each of those locations) is tabulated in Table 4-4. As an example of the notation used in that table, "R_b" stands for bottom ("b") of the right ("R") column. Note that the yielding (and onset of strain hardening) in these column is not happening at the same time, but they are doing so over small increases of frame drift. However, what happens beyond the onset of frame yielding is of some interest, but is not expected to happen since the structural fuse will limit displacements to prevent frame yielding. Fig. 4-16 shows that limiting the column demands to M_y, to prevent any column yielding, is conservative. The use of a more liberal design limit is arguably possible.

4.3.1.6 BRB design details for two-CFT-column bent with single inclined BRB

BRBs and their gusset plates used for the connections are usually designed by the BRB manufacturers. BRBs can be pin connected to the CFT columns, and this is the option that has been considered in this report. Equation 4-16 can be used to design BRB pins.

$$P_n = 0.6 \times 0.75 \times pin\_areaa \times F_u(pin) \times 2(two\_shear\_plane) \qquad (4.16)$$

where: F_u equals to 115 ksi for pin diameter greater than 2.5" and 125 ksi for pin diameter of 2.5" or less.

86

Table 4-4 Displacement and shear forces resisted by the frame when the yielding strength is reached and when the capacity of the section is reach before strain hardening happen

Member	Yielding Disp. (in)	Yielding Force (kips)	Capacity Disp. (in)	Capacity Force (kips)
R_b	0.77	2120.67	1.53	3113.63
R_t	0.81	2222.38	1.70	3110.19
L_b	0.89	2419.59	1.80	3110.35
L_t	0.93	2530.43	2.03	3122.80

Therefore, for a BRB to develop the strain hardened loads of 1414.26 kips calculated above, a pin of 4.25" would be necessary (note that BRBs having strengths of 2000 kips have already been implemented in many instances). A BRB supplier (StarSeismic) indicated that a 1.5" thick gusset plate can be used for the BRB connection to resist the forces. Distance from the pin to the edge of the gusset would be 9".

4.3.1.7 Model information for two-CFT-bridge bent with inverted-V BRBs

For the Inverted-V BRBs with the same bridge columns design, the bridge columns are still modeled with the clear distance as shown in the bold lines in Fig. 4-17. This section only shows the part of the modeling and results that are different from the bridge bent with single inclined BRB case. The calculated yielding length ratio is only 0.085 for the BRBs designed in the inverted-V configuration. To make the overall deformation of the BRB in the SAP model match that of the actual BRB, the modulus of elasticity of A500 Gr.B (42 ksi) is increased to $E_s = 29000/0.085 = 341176$ ksi. BRB has a cross section of 17.178 in^2.

4.3.1.8 Two-CFT-column bent with inverted-V BRBs analysis results

The expected displacement of the bent at the cap beam level Δ_y=0.81" is reached, the moment demand in the columns is shown in Fig. 4-18(a). The corresponding axial tensile and compressive forces are shown in Fig. 4-18(b). The reactions at the bottom of the CFT columns are shown in Fig. 4-18(c).

The moment and axial force demands shown in Fig. 4-18 are compared against the provided member strengths, as shown in Table 4-5. The plastic and yield strengths listed in Table 4-5 are from Section Designer. With the ratio less than 1.0, the columns are proved sufficient to resist the forces under the plastic strength and axial strength interaction check.
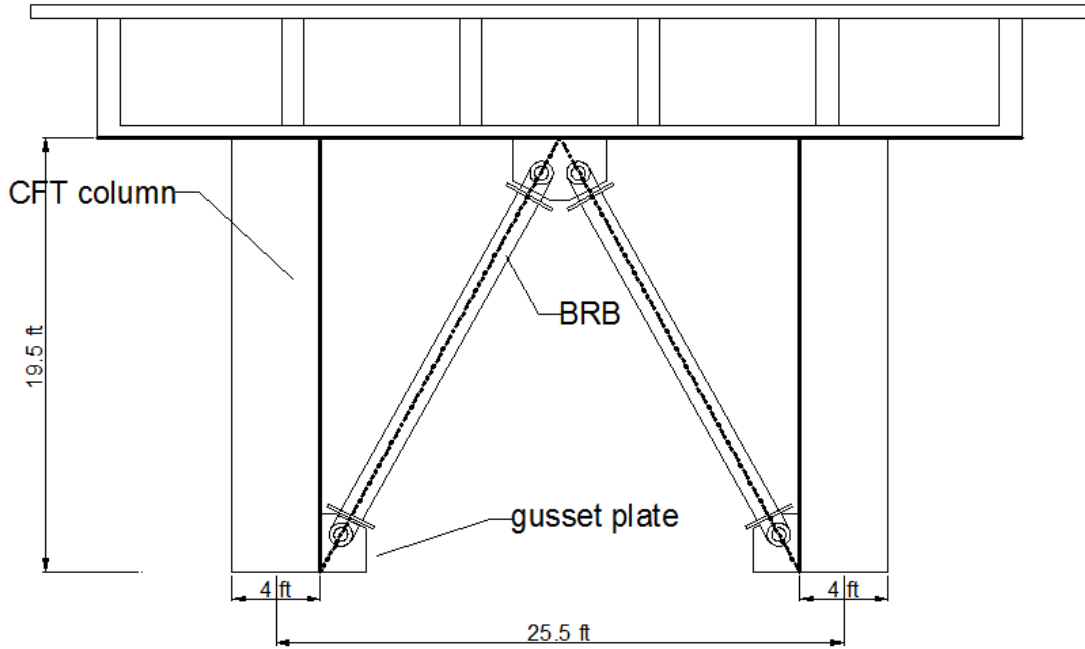
Figure 4-17 Transverse bridge bent with BRBs in inverted-V configuration

Table 4-5 Summarized force demands in the columns for bent with inverted-V BRB

Column Type	Moment Demand M_u (kip-in)	Reaction Force Demand P_u (kips)	Plastic Strength ΦM_n (kip-in)	Axial Strength ΦP_n (kip)	$M_u/\Phi M_n$ $+P_u/\Phi P_n$
Tension	135,884	404	185,621	11,020	0.77
Compression	133,468	-3399	185,621	-16,437	0.93

Following is an arbitrary example to show the difference in the strength calculated from the AASHTO equation and the value obtained from Section Designer given the axial force. The AASHTO compression-flexure interaction equation for CFT (i.e. Equation 4.15) gives a *B* factor of 0.7. The resulting ratio $BM_u/M_n + P_u/P_n$ for the column in compression is 0.71, providing a greater reserve strength.
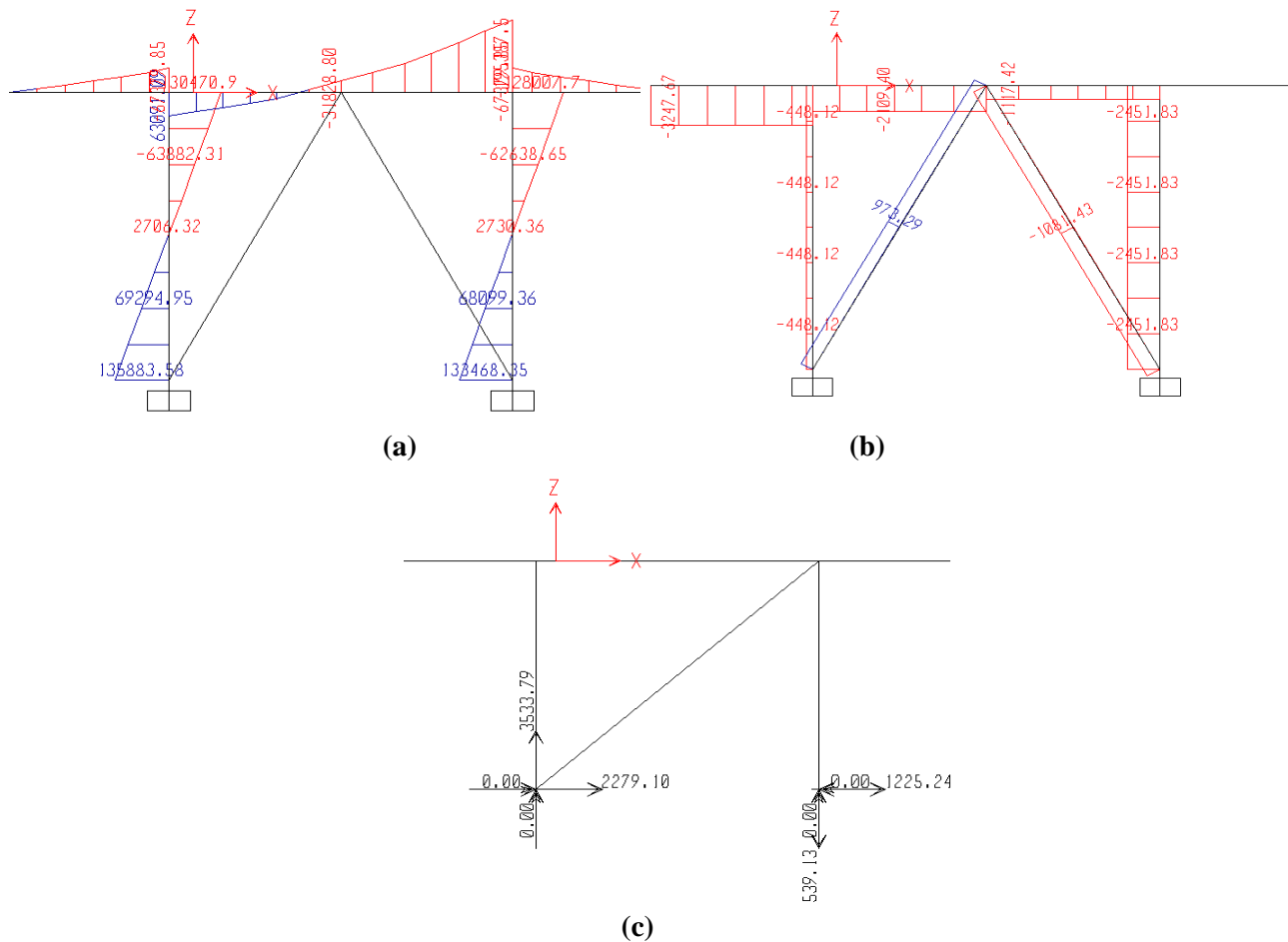
Figure 4-18 (a) Moment diagram of the bent with inverted-V BRBs when the expected displacement is reached in the transverse direction (unit: kip-in); (b) Corresponding axial forces in the members of the bent (unit: kips); (c) Corresponding reactions at the bottom of the CFT columns (unit: kips)

4.3.1.9 Pushover curve for two-CFT-column bent with inverted-V BRBs

The overall comparison of the pushover curve between the analysis result and the theoretical ones is directly shown in Fig. 4-19. The theoretical curves are the same as in the single inclined BRB case. The purple dash line of the theoretical BRB shows the yielding of the BRB at the displacement of 0.069", and point where the maximum strain hardening considered is reached, at 0.71". The theoretical frame curve in navy blue dash lines shows that the frame yields at the displacement of 0.71". The two parts add up to the total theoretical curve for the combined system plotted in red dash lines. The pushover curves obtained from SAP2000 analysis overlay on top of the theoretical results as solid lines. The solid blue line shows the total base shear versus lateral displacement at top of the bent. By subtracting the lateral forces resisted by the BRBs (equals to the horizontal component of the forces in the BRBs) shown in solid green line, the

89

solid brown line gives the portion of the base shear forces resisted by the frame alone. The target displacement demand of 0.81" from response spectrum analysis is shown as the orange vertical line.

The pushover analysis results indicate that column yielding is first reached at the bottom of the left column where the tension and flexure interaction exists. The orange lower horizontal dotted line identifies the base shear resisted by the columns when that happens. The middle grey light blue upper horizontal dotted lines show the starting of the strain hardening of the same section. For comparison, the upper blue dotted line is shown for the reaching shear resistance of the frame V corresponding to the $2M_p/h_{column}$ calculated, where M_p equals to 187851 kip-in obtained from SAP2000 Section Designer.

The sequence of yielding at top and bottom of the CFT columns (i.e. the point when the extreme fiber yields) and reaching the capacity (i.e. from which strain hardening starts to develop at each of those locations) is tabulated in Table 4-6. As an example of the notation used in that table, "R_b" stands for bottom ("b") of the right ("R") column. Note that the yielding (and onset of strain hardening) in these column is not happening at the same time, but they are doing so over small increases of frame drift.
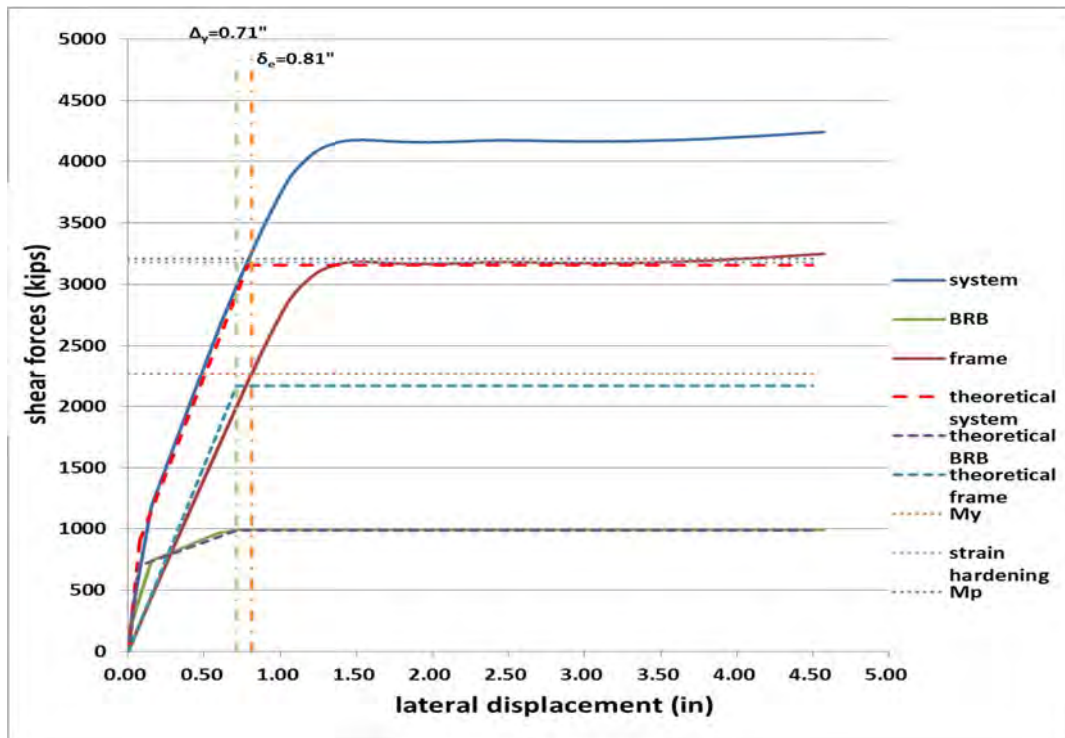
Figure 4-19 Pushover curve comparison between the analysis result and theoretical design value for the Chevron Inverted-V BRB case

90

Table 4-6 Displacement and shear forces resisted by the frame when the yielding strength is reached and when the capacity of the section is reached before the strain hardening happens

Member	Yielding Disp. (in)	Yielding Force (kips)	Capacity Disp. (in)	Capacity Force (kips)
L_b	0.81	2272.01	1.63	3180.71
L_t	0.84	2356.72	1.78	3170.68
R_b	0.88	2457.41	1.81	3169.54
R_t	0.92	2552.48	1.98	3166.37

4.3.1.10 BRB design details for two-CFT-column bent with inverted-V BRBs

BRBs and the gusset plates used for the connections are usually designed by the BRB manufacturers. Using the same equation as shown in Section 4.3.1.5, for BRB to develop the strain hardened loads of 1081.43 kips, a pin of 3.75" would be necessary. A BRB supplier (StarSeismic) indicated that a 1.5" thick gusset plate can be used for the BRB connection to resist the forces. Distance from the pin to the edge of the gusset would be 9".

4.3.1.11 Two-CFT-column bent with BRBs analysis summary

The CFT columns, designed in Appendix A, are found to have adequate strength to reach the force demands when the bridge bent reaches the target displacement (elastic displacement demand from response spectrum analysis, which is larger than the yielding displacement of the column assumed in the design process). Note that the demand versus capacity check were performed considering the reaction forces and the moment demand in the columns, as this would be the more critical case if there was an eccentricity between the point where the work-lines of the column and BRB intersected and the foundation. Table 4-7 shows the force demand on the foundation for the two cases from Figs. 4-11c and 4-18c. For the inverted-V BRBs case, the force demand is 134.9 kips less than the single inclined BRB case, for both the compressive and tensile columns.

Table 4-7 Force demand on the foundation for the two cases in the two-CFT-column bent

	Compression (kips)	Tension (kips)
Single inclined BRB	-3533.79	539.13
Inverted-V BRB	-3398.89	404.23

In absence of that eccentricity, for the single BRB case, only slightly smaller results would be obtained considering the axial and flexural forces acting on the columns. For the inverted-V BRBs case, the axial force in the columns would be considerably smaller compared with the single BRB case, since the

reaction for the vertical component of the BRB force would not appear in the column. Therefore, a smaller column section might be sufficient for this structural fuse design example using inverted-V BRBs. The difference between the single BRB case and the inverted-V BRBs case also lies in the resulting smaller BRB sizes needed in the latter case (and correspondingly, smaller force demands on the connections). Compared with the single inclined BRB case, the force demand in the BRBs is reduced by 24% in the inverted-V BRBs case.

4.3.2 Service Load Check for Two-CFT-column Bent with BRBs
4.3.2.1 Global bridge model

The global model developed in SAP2000 is used to determine the forces in the columns due to the dead load, live load and wind load. Note that since the design of the superstructure may need to be revised because of the locations of the new columns and the fact that they are CFTs (instead of RC columns), the permanent loads due to secondary prestress forces, creep, and shrinkage are not calculated here. As mentioned above, the abutments allow longitudinal movement of the superstructure, limited only by the width of the gap between the superstructure and the abutment back wall (which is not considered to be a limiting factor here). The support provided by the abutment is assumed to be fixed against translation in the vertical and transverse directions and fixed against rotation about the longitudinal axis. The bent resists all the seismic force in the longitudinal direction while in the transverse direction part of the lateral force is taken by the abutments. The behavior of the bridge under the lateral load in the transverse directions is shown in Fig. 4-20. In the SAP2000, the bridge superstructure is modeled analyzed as a line element (i.e. spine) located at mid-width of the bridge deck.
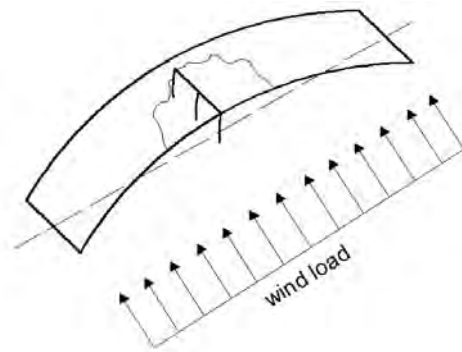
Figure 4-20 Wind load applied to the bridge in the transverse direction

A 3-D view of the spine bridge model is shown in Fig. 4-21. The braces are assumed to not take the gravity load. So the bridge is modeled without the BRBs. The service load check for the single inclined BRB and inverted-V Chevron BRBs case is the same.

92
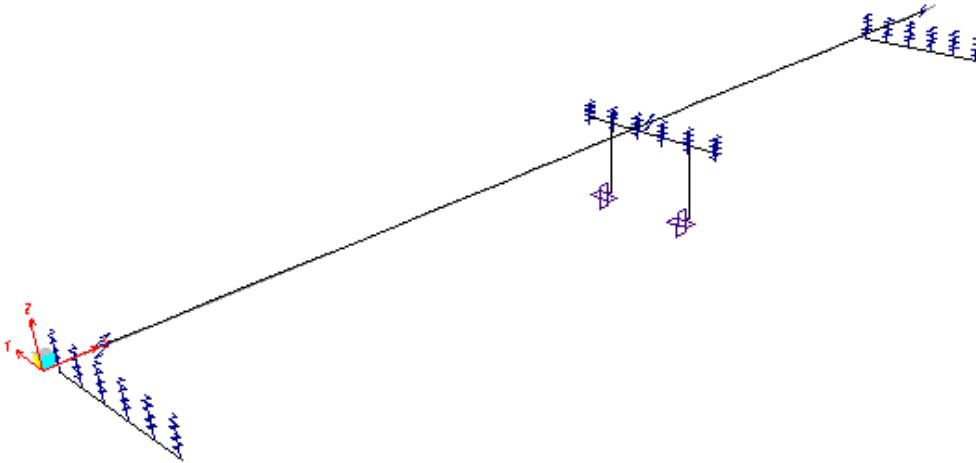
Figure 4-21 Global spine model of the bridge in 3-D view

The number of design lanes should be determined by taking the integer part of the ratio *w*/12.0, where *w* is the clear roadway in ft, between curbs or barriers. The top width of the box girder between the barriers is 44.67 ft. Therefore, the bridge deck is modeled with three lanes, each having 12 ft in width. Details for the dead loads, live loads, and wind loads considered in the "service" load analyses are provided in the following sections.

4.3.2.2 Bridge loads
4.3.2.2.1　　Dead load

Dead load includes the gravity loading from structural components and nonstructural attachments (DC), as well as that from wearing surfaces and utilities (DW), where DC and DW are the respective AASHTO (2014) parameters used to refer to those loads. The area of the concrete box girder is $81.7\ ft^2$. The unit weight of the concrete girder is $0.15\ kip/ft^3$.. Concrete barrier type 732 was also used, with a distributed weight of 0.41 kip/ft per barrier. With one barrier on each side of the bridge, the applied load is 0.82 kip/ft. The total DC loading is therefore 13.07 kip/ft.

The self-weight of the superstructure is automatically calculated by the program for the provided geometry of the box-girder and column's cross section, and material densities. Only the additional 0.82 kip/ft loads is therefore be applied directly on the bridge. An allowance for a wearing surface of 35 psf was assumed. The top width of the concrete box girder between the barriers is 44.67 ft. Two bridge rails also give the distributed load of 0.5 kip/ft on each side of the bridge. The total DW loading is therefore 2.56 kip/ft.

4.3.2.2.2   Live load

There are two vehicular load types considered here: (1) The standard vehicular live load condition for the roadways of the bridges, designated as HL-93 in the AASHTO bridge design specification (2014), and equivalent to HS 20-44 in the Caltrans bridge specification (2012); (2) The permit truck load P15.

In SAP2000, vehicle classes are defined; these may include any number of individual vehicles. The maximum and minimum force and displacement response quantities for a vehicle class will be the maximum and minimum values obtained for any individual vehicle in that class. Only one vehicle ever acts at a time. For the standard truck HL-93 load class, three vehicles standard type HL-93K, HL-93M, and HL-92S are used. For the permit truck load class, the P15 is used. HL-93K load consists of the code-specified design truck and its related design lane load. HL-93M represents a design tandem truck and its related design lane load. HL-93S contains two code-specified design trucks and the design lane load, all scaled by 90%. The axle spacing for each truck is fixed at 14 feet. The spacing between the rear axle of the lead truck and the lead axle of the rear truck varies from 50 feet up to the length of the lane.

The static effects of the design truck or tandem are increased by a dynamic magnification factor of 33%. The force effect from the design lane load is not subject to a dynamic load allowance. The dynamic load allowance factor must be included in the live wheel load. The truck wheel-line load can be placed in the design lane such that the center of any wheel load is not closer than 2' from the edge of the design lane or 1' from the edge of an overhang barrier. The live load force effect shall be determined by considering each possible combination number of loaded lanes multiplied by a corresponding multiple presence factor to account for the probability of simultaneous lane occupation by the full truck design live load. The multiple presence factors are listed in Table 4-8. The vehicular loads are applied on the bridge lanes as shown in Fig. 4-22 to illustrate the location of the live truck wheel load.

Table 4-8 Multiple presence factor for multi-lane truck load (AASHTO, 2014)

Number of loaded lanes	Multiple presence factors m
1	1.20
2	1.00
3	0.85
>3	0.65
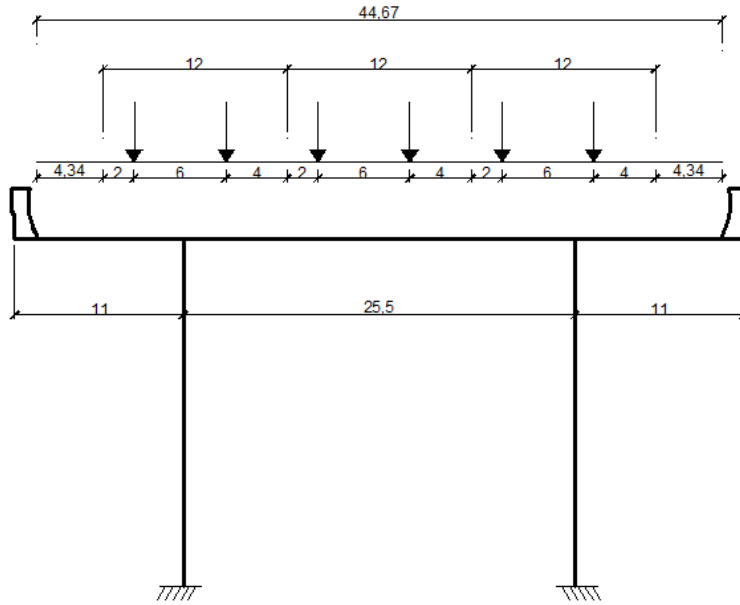
(a) Live load for three lanes
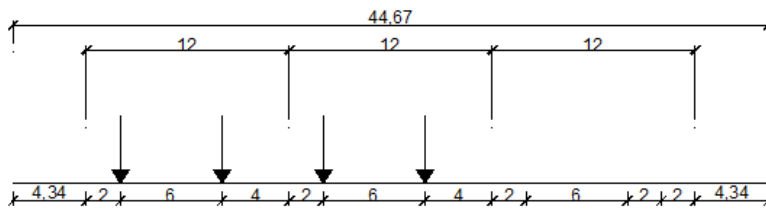
(b) Live load for lane 1 and 2

(c) Live load for lane 1 and 3

(d) Live load for lane 2 and 3

(e) Live load for lane 1

(f) Live load for one lane 2
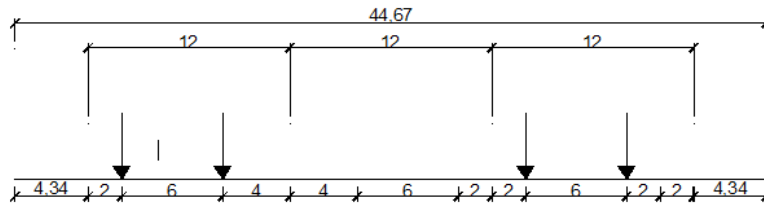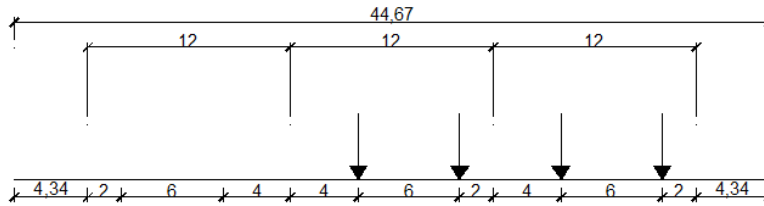
(g) Live load for one lane 3
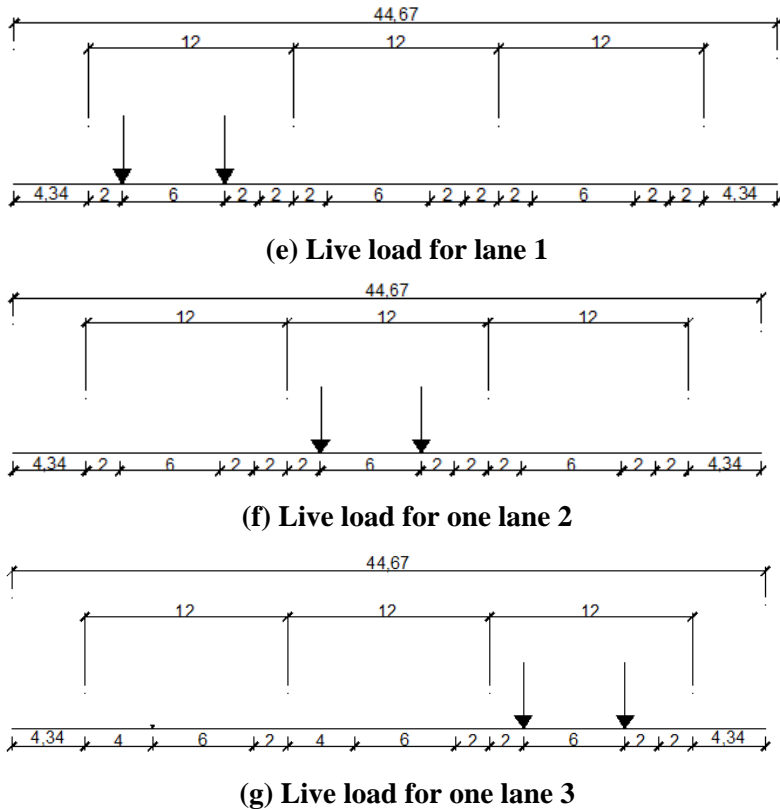
Figure 4-22 Live load distribution on different road lanes (Unit: ft)

4.3.2.2.3   Wind load

The wind is assumed to act uniformly on the bridge area exposed to the wind. The exposed area is the sum of the areas of all components, as seen in elevation taken perpendicular to the assumed wind direction. The skew angle is measured from the perpendicular to the longitudinal axis and the assumed wind direction shall be that which produces the maximum stress in the substructure. The transverse and longitudinal forces shall be applied simultaneously at the elevation of the center of gravity of the exposed area of the superstructure. Wind pressure is assumed to be caused by a base design wind velocity V_B of 100 mph. The bridge height is within 30.0' above the ground; as a result, the design wind velocity does not need to be adjusted for height. The base wind pressure corresponding to the design wind velocity V_B of 100 mph on the box girder is 0.05 ksf per Table 4-9. The total wind loading shall not be taken less than 0.30 kip/ft on the beam or girder spans. The height of the barrier is 32 in.

The total height of the superstructure is 8.67 ft. The controlling distributed transverse wind load is 0.43 kip/ft, which is larger than 0.30 kip/ft. The corresponding longitudinal load is zero.

Table 4-9 Base wind pressure for various angles of attack and V_B = 100 mph (AASHTO , 2014)

	Trusses		Girders	
Skew Angle of Wind	Lateral Load	Longitudinal Load	Lateral Load	Longitudinal Load
Degrees	PSF	PSF	PSF	PSF
0	75	0	50	0
15	70	12	44	6
30	65	28	41	12
45	47	41	33	16
60	24	50	17	19

4.3.2.3 Axis of member

The indication of the global and local axis in the bridge model is shown in Fig. 4-23.
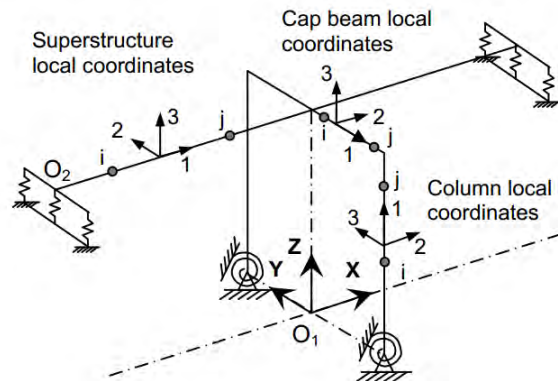
Figure 4-23 Global and local coordinate indication for cap beams and columns (Aviram, Mackie and Stojadinovic, 2008)

4.3.2.4 Service load analysis results

The critical forces in the columns are shown in Table 4-9 for the considered load cases. The numbering of the column element is shown in Fig. 4-24. The combination load cases that are considered for column design are: Strength I, III, V, listed in AASHTO bridge design specification (2014).

Strength I= 1.25 DC + 1.50 DW + 1.75LL

Strength III = 1.25 DC + 1.50 DW + 1.40 WS

Strength V= 1.25 DC + 1.50 DW + 1.35 LL + 0.4WS

The governing forces resulting from these load combinations, and used to verify the adequacy of the design of columns, are presented in Table 4-11.

Figure 4-24 Element locations in the transverse bent

Table 4-10 Analysis result of all the service load cases

Load cases	Element	P (kips)	V_2 (kips)	V_3 (kips)	M_2 (kip-in)	M_3 (kip-in)
DC	34	-1431.7	-0.29	0	0	36.36
	35	-1469.71	-0.29	0	0	-21.12
	36	-1431.7	0.29	0	0	-36.36
	37	-1469.71	0.29	0	0	21.12
DW	34	-223.68	-0.05	0	0	7.08
	35	-223.68	-0.05	0	0	-4.08
	36	-223.68	0.05	0	0	-7.08
	37	-223.68	0.05	0	0	4.08
Wind	34	-22.75	0	-28.00	2460.24	0
	35	-22.75	0	-28.00	-3083.52	0
	36	22.75	0	-28.00	2460.24	0
	37	22.75	0	-28.00	-3083.52	0
Live maximum compression	34	-653.85	0	-0.31	-492.72	-14514.7
	35	-653.85	0	-0.31	-288.96	-14514.7
	36	-311.25	0	-0.26	-513.24	-14514.7
	37	-311.25	0	-0.26	-292.8	-14514.7
Live maximum tension	34	7.21	0	0	531.48	8708.88
	35	7.21	0	0	303.96	8708.88
	36	7.21	0	2.30	0	8708.88
	37	7.21	0	2.30	0	8708.88
Live Moment	34	-615.91	0	-1.89	-418.8	-18506.3
	35	-615.91	0	-1.89	-245.64	-18506.3
	36	-615.91	0	-1.75	-436.2	-18506.3
	37	-615.91	0	-1.75	-248.88	-18506.3

The axial force and flexural moment interaction is checked for the columns strength in Table 4-12, where P_u and M_u are the force demand in the columns, P_n and M_n are the axial and flexural plastic strength of the CFT column obtained from Section Designer respectively, without considering the resistance factors. The results from the interaction equation confirm that column capacity to resist all non-seismic load combinations considered is sufficient.

Table 4-11 The controlling force to design the bridge columns

Governing Load cases	Element	P (kips)	V_2 (kips)	V_3 (kips)	M_2 (kip-in)	M_3 (kip-in)
Strength I, maximum column moment	35	-3250.5	-0.4375	-3.3075	-429.87	-32418.5
Strength I, maximum column axial force	34	-3269.38	-0.4375	-0.5425	-862.26	-25344.7

Table 4-12 Capacity check for the CFT column

Case	Axial load P_u (kips)	Moment Demand M_u (kip-in)	Flexural Strength M_n (kip-in)	Axial strength P_n (kips)	P_u/P_r $+M_u/M_r$
Strength I, maximum column Moment	-3250.5	32,421.39	185,621	-16,437	0.37
Strength I, maximum column axial force	-3269.38	25,359.32	185,621	-16,437	0.34

4.4 Box-pier bents with BRBs capacity check

This section describes the analytical model built in SAP2000 to verify the bridge behavior of the box-pier bents with BRBs. The capacity of the columns is checked. Pushover curves from analysis result is plotted and compared with the theoretical one developed from the structural fuse concept. Section 4.4.2 presents the results of bridge analysis under the gravity dead and live load, as well as for wind loads.

4.4.1 Bent pushover analysis
4.4.1.1 Model information

The box-pier bridge configuration is shown in Fig. 4-25. There are total eight CFT columns. The number of BRBs inserted between the columns is 16. Instead of performing a 3-D global analysis of the bridge, local analyses of the bent are considered adequate and are performed to verify the structural fuse concept in both the transverse and longitudinal directions.
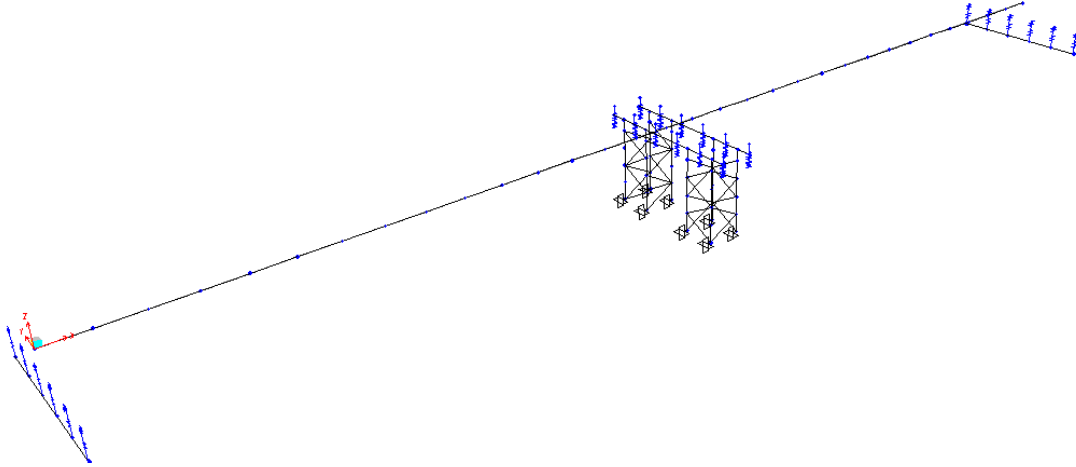
Figure 4-25 3-D bridge model of the bridge system

A close-up view of the bridge bent in the middle is shown in Fig. 4-26. There are two bents with four columns and four BRBs between the adjacent columns in the transverse direction. Only one of them is modeled in Fig. 4-27 (with column number of 187,189,191 and 193). The bridge bent is modeled as the bold lines as shown in Fig. 4-26 for the BRBs to working within the clear distance of the CFT columns. The CFT columns are fixed at top to the cap beam, and at bottom to the ground. The footing is not modeled. The BRBs are designed to be pin connected to the columns (i.e. moments are released at both ends of the beam elements used to model the BRBs). The overhang of the box girder at each side of the bridge bent is 3 ft. The brace layout in the transverse bridge bent is symmetric; therefore only one pushover analysis of the bent in the transverse direction is needed.

A similar model of one of the four longitudinal parallel bent frames with BRBs is also built to investigate the behavior of the bent in the pushover analysis for the longitudinal direction (with column number of 187 and 196). The elevation view of the longitudinal bent is provided in Fig. 4-28, and the longitudinal bridge bent is built as the bold lines shown. In order to represent the restraint of the bent from the bridge box girder in the longitudinal direction, the cap beam level is restrained from rotation by providing a rigid body constraint in the vertical direction of the cap beam.
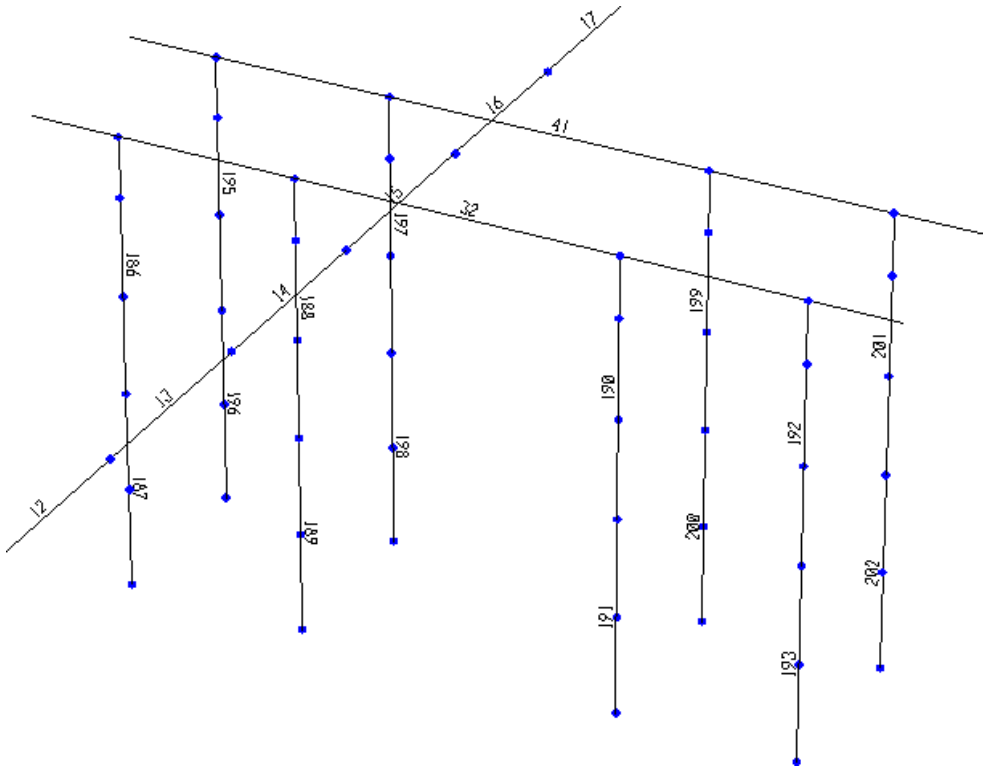
Figure 4-26 Enlarged 3-D view of the bridge bents in the middle of the bridge (with column numbers)
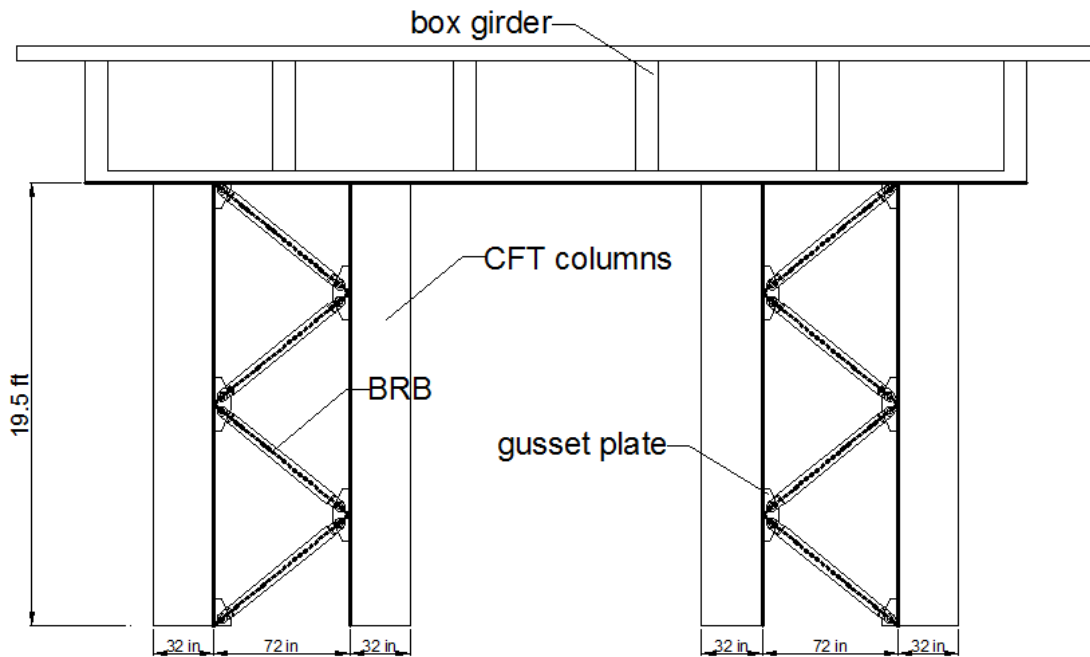
Figure 4-27 Transverse bridge bent with inserted BRBs

101
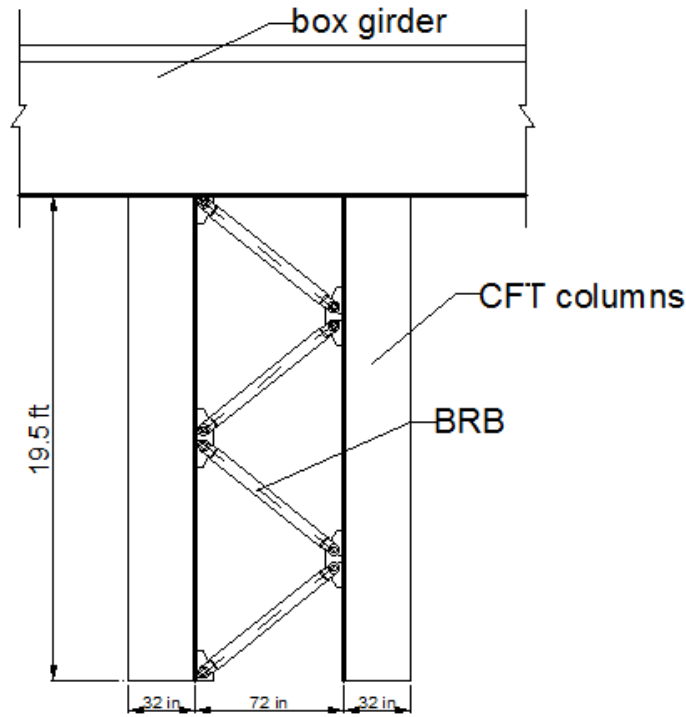
Figure 4-28 Longitudinal bridge bent with inserted BRBs

For the longitudinal direction, it is conceivable that all top BRBs could be in compression, or all in tension, depending on the overall layout used and direction of seismic loading. For a two-column bent, forces in columns were affected by the direction of loading (as BRBs in compression develop more force than in tension at the same drift). To investigate whether this is still the case here, two "layouts" are considered, namely Layout A and Layout B. For the frame shown in Fig. 4-28, Layout A corresponds to the case of having a lateral load applied from left to right. Layout B corresponds to the same frame, but with the load applied from right to left. In the analyses presented in Section 4.4.2, loads will always be applied from left to right, so the mirror image of the frame shown in Fig. 4-28 will be used as Layout B. Arguably, it may have been easier to simply refer to direction of loading while presenting results, but since the direction of lateral loads applied is not shown in the moment and axial force diagrams obtained from SAP2000, "Layouts" are used instead to differentiate between the two cases.

The same materials of the cap beam, CFT column, and the BRB as in the two-CFT -column bent with BRBs. The calculated yielding length ratio, c, is calculated to be 0.147 for the box-pier bent with BRBs. To make the overall deformation of the BRB in the SAP model match that of the actual BRB, the modulus of elasticity of A500 Gr.B (42 ksi) is increased to $E_s = 29000/0.147 = 197279$ ksi. BRB has a cross section of 5.22 in^2.

According to Caltrans Seismic Design Criteria (2010) Section 7.4.2.1, the minimum cap width, B_{cap}, is calculated to be the diameter of the column plus 2 ft. Therefore, the bent cap section is modeled as rectangle of 5'(width) by 6'(depth). For expediency, the cap beam is modeled as "infinitely rigid" relative to the columns by making the moment of inertia 1000 times larger than that corresponding to a 5' by 6' beam (to reflect the fact that flexure of the cap-beam would also engage the flexural rigidity of the box-girder in that direction). The CFT column in the analytical model is built using SAP2000's Section Designer (which provides cross-section properties and moment-curvature strength using a fiber analysis). The diameter of the section is 32". The thickness of the steel shell is 0.75". A grid of 20 by 20 fibers is used for calculating the capacity of the section and plastic hinge analysis. The same fiber hinge assignment for both the CFT column and BRB is also the same as the two-CFT-column bent with BRBs.

4.4.1.2 Load assignment

The dead loads are applied on the cap beam as point load where the webs of the box-girder are located (See Fig. 4-29) for the bent model in the transverse direction. The dead loads are applied on the bent as a starting step of the nonlinear pushover analysis.
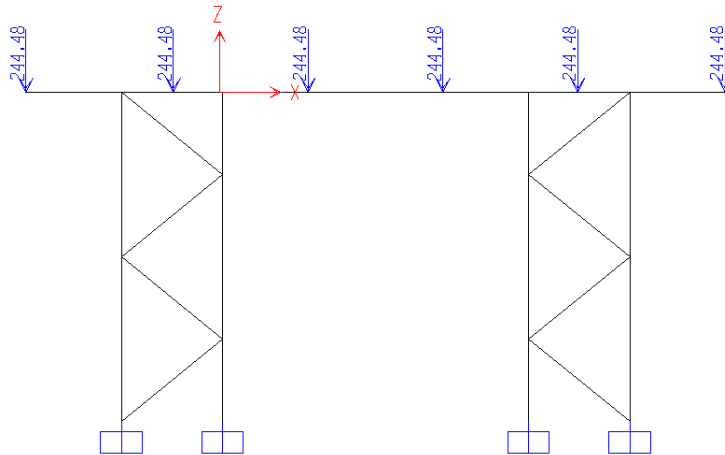
Figure 4-29 Dead loads applied to the bridge bent before pushover analysis in the transverse direction (Unit: kips)

The analysis result of the dead load applied to the transverse bent is shown in Fig. 4-30. Note that the BRBs resist a negligible amount of dead loads, which justifies the design assumption of neglecting their contribution to resist gravity forces. Axial force ranging from 362 to 368 kips are resisted by the columns. The largest axial force of 368.03 appears in the middle column, which would be directly used as the point dead load applied to the longitudinal bent as shown in Fig. 4-31.

103
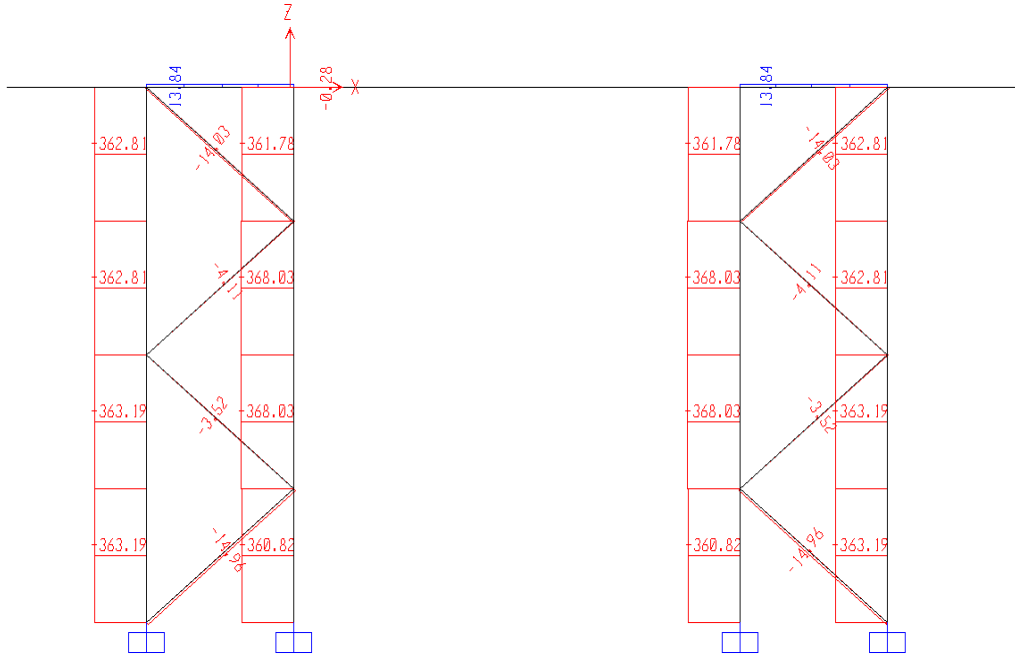
Figure 4-30 Axial loads in the transverse bridge bent members when the dead loads in fig. 4-28 is applied on the cap beam (Unit: kips)

The lateral load used for the pushover analysis consists of a horizontal load applied at the center of the cap beam. The lateral load is applied from left to right. The horizontal displacement of the cap beam is the monitored displacement used in the displacement-control method in the pushover analysis.
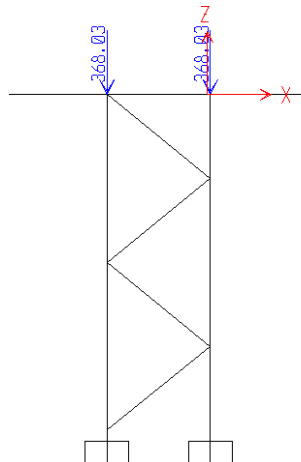
Figure 4-31 Dead loads applied to the bridge bent before push-over analysis in the longitudinal direction (Unit: kips)

4.4.1.3 Bent pushover analysis

4.4.1.3.1   Response spectrum displacement demand

As for the two-CFT-column bent case, the seismic force demand of the bridge model is assessed in the pushover analysis at the bent displacement value obtained from response spectrum analysis. The displacement demands of the box-pier bent with BRBs are shown below in Table 4-13. Smaller stiffness of the box-pier bent in both transverse and longitudinal directions can be observed, for the same reasons as those already presented in Section 4.3.1.3.

Table 4-13 The displacement demand comparison of the box-pier bents

Box-pier bents	Design	Analysis (Response Spectrum)	Difference
Transverse direction	1.05"	1.28"	18%
Longitudinal direction	1.05"	1.17"	10%

4.4.1.3.2   Transverse direction

When the bridge bent has a lateral displacement at the expected displacement of 1.28", the moment demand in the columns is shown in Fig. 4-32(a). The axial tensile and compressive forces in the columns are shown in Fig. 4-32(b). The reactions at the bottom of the CFT columns are shown in Fig. 4-32(c). The reaction forces are used to check the column strengths for the case when an eccentricity exists between the point where the bottom brace and column workline meet around the foundation.
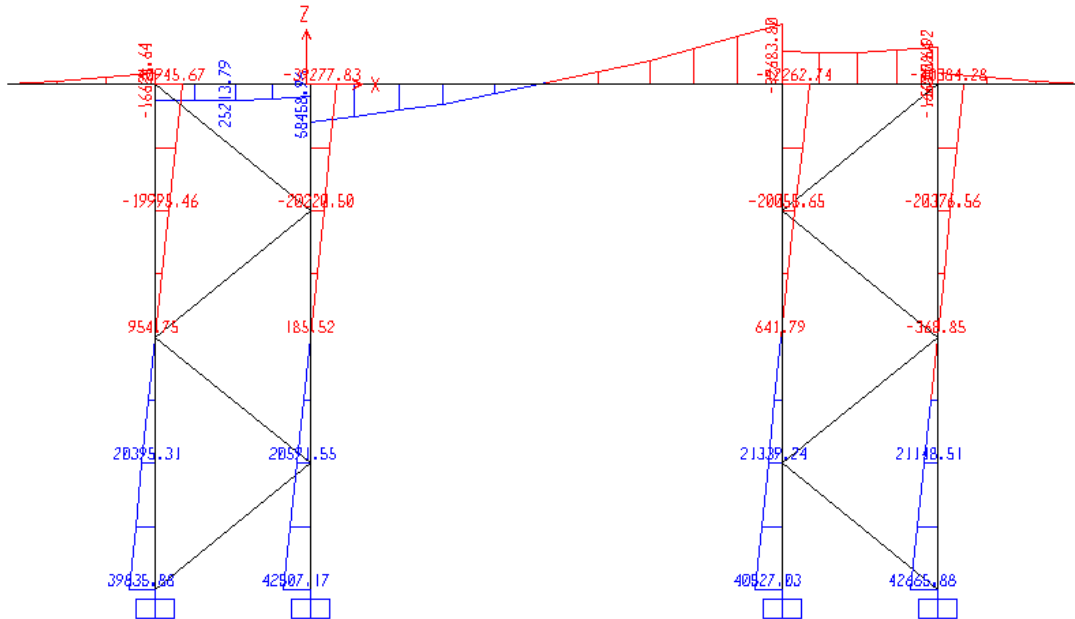
(a) Moment diagram of the bent when the expected displacement is reached at the top of the bent in the transverse direction (Unit: kip-in)
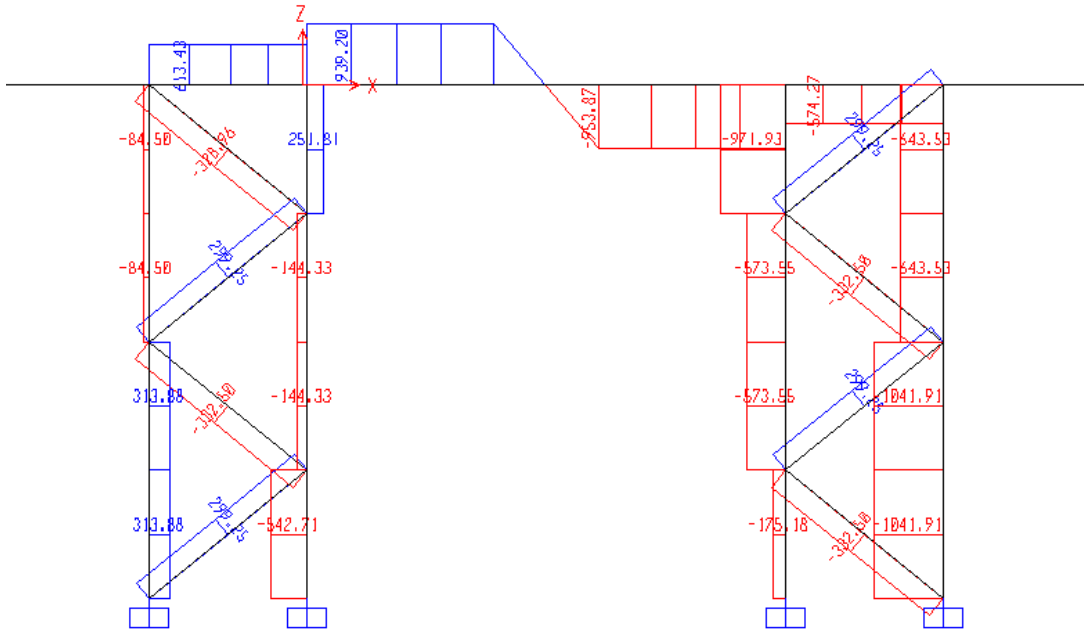
(b) Corresponding axial forces in the members of the bent (Unit: kips)
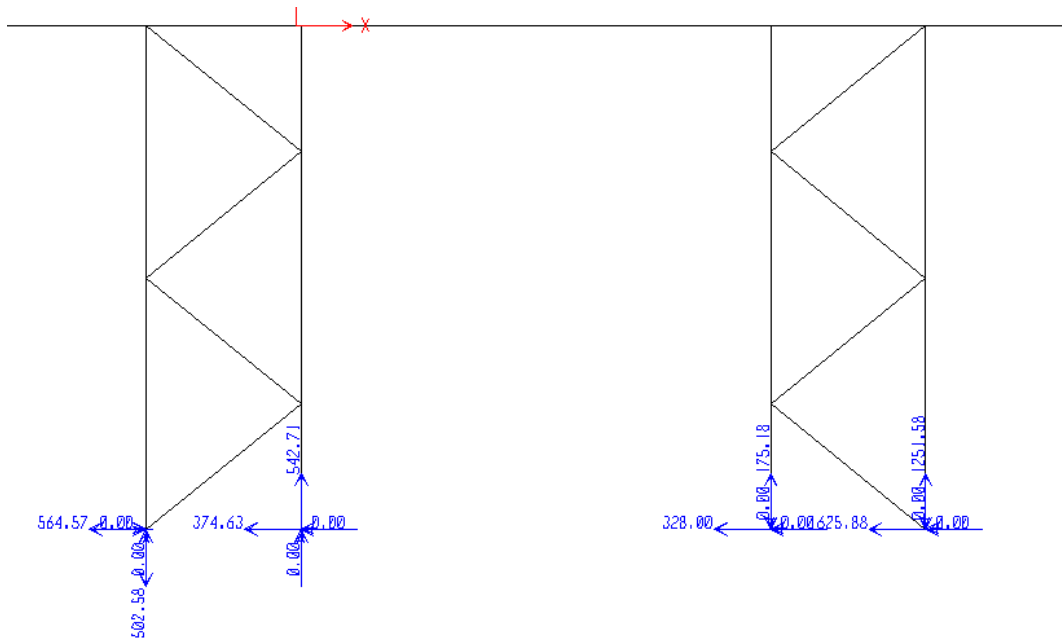
(c) Corresponding reactions at the bottom of the CFT columns (Unit: kips)

Figure 4-32 Force and moment demand of the transverse box-pier

For the directional combination of the forces in the transverse and longitudinal directions, the reactions at the base of the columns are decomposed into three parts: (1) the overturning effect of the lateral load; (2) the forces applied by the yielding BRBs; and (3) the dead load. As demonstrated in Table 4-14 by

106

subtracting the axial forces added by the BRBs and the dead loads, the axial forces left in the columns are those solely induced by the lateral forces. The compressive forces in the columns have minus signs.

Table 4-14 Components of the reaction at the bottom of the CFT in the transverse direction

Reaction force location of corresponding column number	Analysis result (kips)	Dead loads (kips)	BRBs (kips)	Lateral load (kips)
187	502	-363	795	70
189	-543	-361	-795	613
191	-175	-361	795	-609
193	-1252	-363	-795	-94

4.4.1.3.3   Longitudinal direction

There are two longitudinal frames model required for the pushover analysis.

1) Layout A

At the expected displacement 1.17", the moment demand in the columns is shown in Fig. 4-33(a). The corresponding axial tensile and compressive forces are shown in Fig. 4-33(b). The reactions at the bottom of the CFT columns are shown in Fig. 4-33 (c).

2) Layout B

The force diagrams shown in Fig. 4-34 are obtained at the same expected displacement 1.17".

Same as what is done for the case of lateral loading applied in the transverse direction, the reactions at the base of the CFT columns in the longitudinal direction are also broken down in Table 4-15 into the various contributions to those reactions, for both layout A and B.
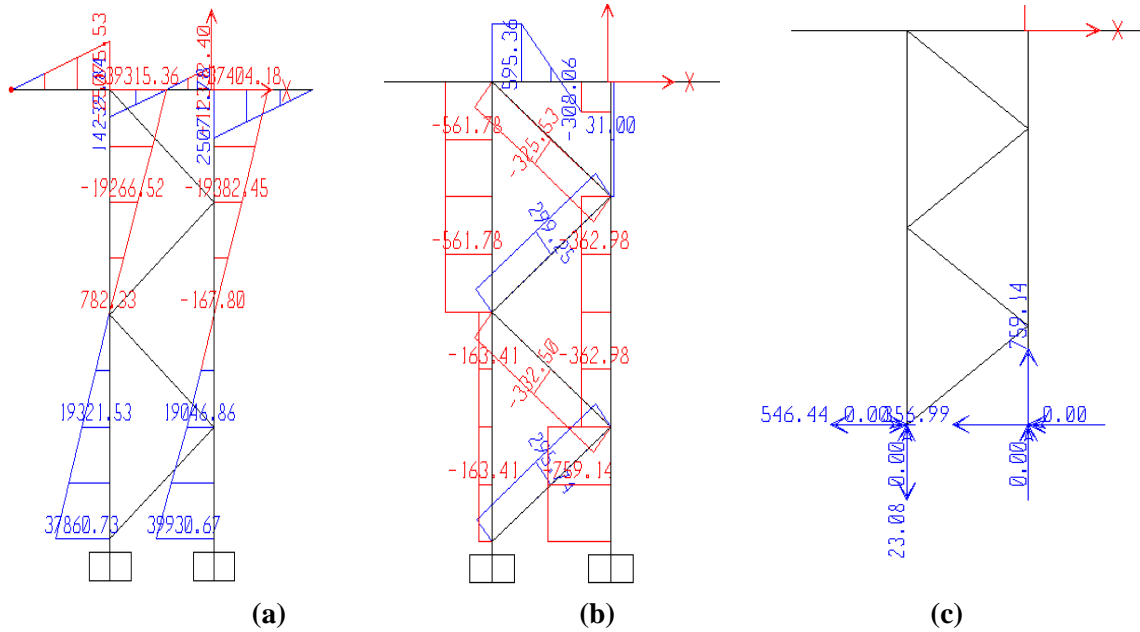
Figure 4-33 Layout A in the longitudinal direction: (a) Moment diagram of the longitudinal bent in layout A when the expected displacement at the top of the bent is reached (Unit: kip-in); (b) Corresponding axial forces in the members of the bent (Unit: kips); (c) Corresponding reactions at the bottom of the CFT columns (Unit: kips)
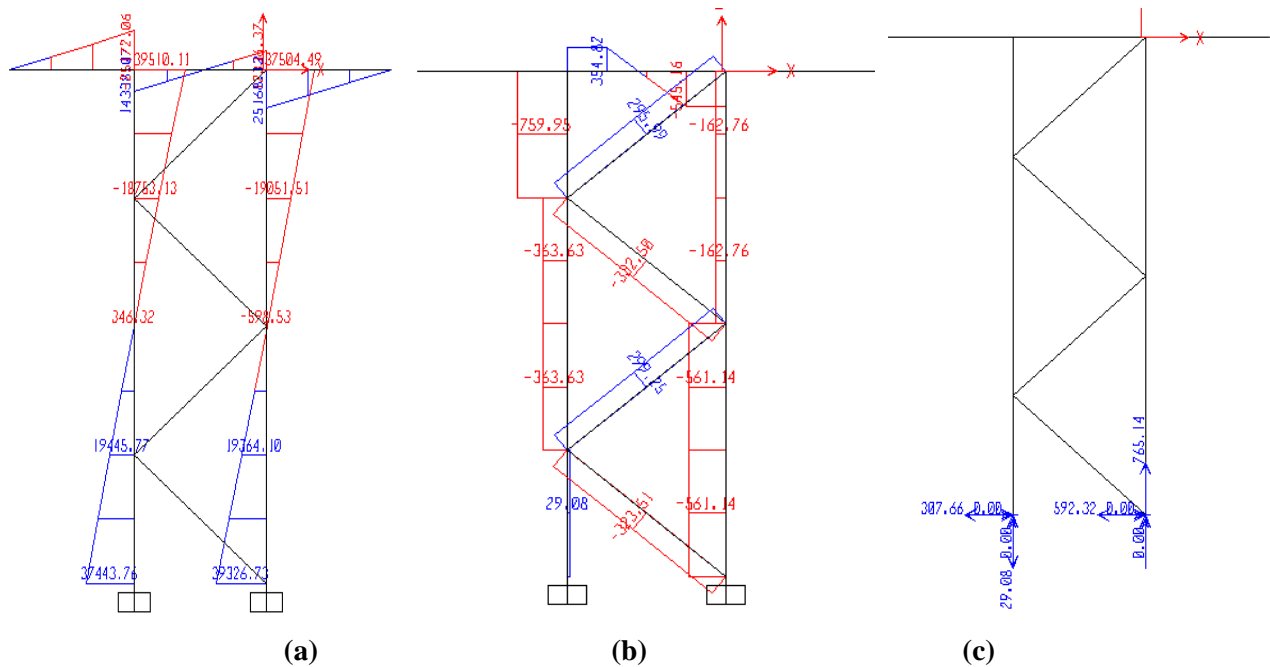
Figure 4-34 Layout B in the longitudinal direction:(a) Moment diagram of the longitudinal bent in layout B when the expected displacement is reached at the top of the bent (Unit: kip-in); (b) Corresponding axial forces in the members of the bent (Unit: kips); (c) Corresponding reactions at the bottom of the CFT columns (Unit: kips)

Table 4-15 Components of the reactions at the bottom of the columns in the longitudinal direction

Reaction force location of corresponding column number	Analysis result (kips)	Dead loads (kips)	BRBs (kips)	Lateral load (kips)
A-187	23	-368	790	399
A-196	-759	-368	-790	-399
B-187	29	-368	790	393
B-196	-765	-368	-790	-393

4.4.1.3.4   Directional combination

In an actual earthquake, the seismic forces are simultaneously applied to the bent in difference directions. Therefore, given that the structural fuse concept is intended to be effective for seismic excitation in any horizontal direction, the bi-direction combination of the force demand in the transverse and longitudinal direction is considered here. This section performs the capacity check for axial force and flexure interaction, and shear as well.

1) Axial force and flexure interaction

The moment demands in both directions, shown in Figs. 4-32, 4-33 and 4-34 are listed in Table 4-16. Table 4-17 presents the critical controlling vertical reactions at the bottom of the CFT column. The reaction induced by the dead loads is conservatively taken as the largest column axial force appearing in the columns as shown in Fig. 4-30.

Table 4-16 Moment demand at the base of the column in both directions

	Column number	Moment demand (kip-in)		
		Transverse	Longitudinal Layout A	Longitudinal Layout B
Bent 1	187	39,837	37,861	37,444
	189	42,507	37,861	37,444
	191	40,527	37,861	37,444
	193	42,666	37,861	37,444
Bent 2	196	39,837	39,931	39,327
	198	42,507	39,931	39,327
	200	40,527	39,931	39,327
	202	42,666	39,931	39,327

Note: The two parallel bent seen from the transverse direction as shown in Fig. 4-26.

Table 4-17 Components of the controlling vertical reactions at the base of the columns considered for the combination

Column number		Longitudinal lateral force induced axial load (kips)	Transverse lateral force induced axial load (kips)	BRB induced axial load in transverse direction (kips)	BRB induced axial load in longitudinal direction (kips)	Dead load induced axial load (kips)
Layout A	187	399	70	795	790	-368
	189	-399	613	-795	-790	-368
	191	399	-609	795	790	-368
	193	-399	-94	-795	-790	-368
Layout B	196	393	70	773	752	-368
	198	-393	613	-773	-752	-368
	200	393	-609	774	752	-368
	202	-393	-94	-774	-752	-368

It is clear from Tables 4-14, 4-15, and 4-16, that results from Layout A and Layout B are nearly identical, for all practical purposes. Therefore, direction of lateral loading is not significant in this case as far as member forces are considered. However, for the case where there would be an eccentricity between the foundation and the intersection of the worklines of the column and the lower BRB, the demands at the lowest segment of the columns would be different for Layouts A and B.

The Caltrans Seismic Design Criteria (2010) section 2.1.2 requires that the earthquake effects shall be determined from horizontal ground motion applied by one of two possible methods. The method used here consists of applying the ground motion in two orthogonal directions along a set of global axes, where the longitudinal axis is typically represented by a chord connecting the two abutments: two cases must be considered

● Case I: Combine the response resulting from 100% of the transverse loading with the corresponding response from 30% of the longitudinal loading
● Case II: Combine the response resulting from 100% of the longitudinal loading with the corresponding response from 30% of the transverse loading

The above rule was expressed in terms of force combinations for elastic analyses, in fact, it also combines probable simultaneous displacements. Here, the overall moment demand at base of the columns is decided based on the square root of the sum of the squares of 100% of the moment in one direction plus 30% of

the moment in the other direction. The total controlling reaction forces at the base of the CFT columns are calculated to be the maximum of:

(1) 100% of longitudinal + 30% of transverse + BRB (transverse + longitudinal) + dead; or

(2) 30% of longitudinal + 100% of transverse + BRB (transverse + longitudinal) + dead.

where: "BRB (transverse + longitudinal)" means that the BRBs have yielded in both directions, and that the corresponding forces at their strain-hardening level of 1.5% strain have been added together. Note that this is somewhat conservative, as the 1.5% strain may not necessarily be reached in the direction in which 30% of the lateral load is applied.

The moment and axial load demands with directional combination are tabulated in Table 4-18. As an example of the notation used in this table, "L_A" stands for longitudinal ("L") analysis for layout A ("A").

Table 4-18 Summarized force demands at the base of the columns

Column type		Moment Demand M_u (kip-in)	Vertical Reaction Demand P_u (kips)
187	(100%T+30%L_A)	41424.6	1406.7
	(30%T+100%L_A)	39702.4	1637
	(100%T+30%L_B)	41390.5	1404.9
	(30%T+100%L_B)	39305.0	1631
189	(100%T+30%L_A)	43998.4	-1220.3
	(30%T+100%L_A)	39950.9	-1370.1
	(100%T+30%L_B)	43966.2	-1222.1
	(30%T+100%L_B)	39555.9	-1376.1
191	(100%T+30%L_A)	42088.6	727.7
	(30%T+100%L_A)	39765.2	1433.3
	(100%T+30%L_B)	42055.0	725.9
	(30%T+100%L_B)	39368.4	1427.3
193	(100%T+30%L_A)	44152.0	-1927.3
	(30%T+100%L_A)	39966.1	-1582.2
	(100%T+30%L_B)	44120.0	-1929.1
	(30%T+100%L_B)	39571.3	-1588.2
196	(100%T+30%L_A)	41599.2	1107.3
	(30%T+100%L_A)	41681.1	779
	(100%T+30%L_B)	41547.3	1109.1
	(30%T+100%L_B)	41102.8	785
198	(100%T+30%L_A)	44162.8	-1399.7
	(30%T+100%L_A)	41917.8	-2108.1
	(100%T+30%L_B)	44113.9	-1397.9
	(30%T+100%L_B)	41342.8	-2102.1
200	(100%T+30%L_A)	42260.4	429.3
	(30%T+100%L_A)	41740.9	576.3

Column type	Moment Demand M_u (kip-in)	Vertical Reaction Demand P_u (kips)	Column type
200	(100%T+30%L$_B$)	42209.4	431.1
	(30%T+100%L$_B$)	41163.5	582.3
202	(100%T+30%L$_A$)	44315.8	-2107.7
	(30%T+100%L$_A$)	41932.3	-2321.2
	(100%T+30%L$_B$)	44267.2	-2105.9
	(30%T+100%L$_B$)	41357.6	-2315.2

The flexural yield strength M_y, plastic strength M_p, tensile axial strength P_{nt}, and compressive axial strength P_{nc} are obtained from SAP2000 Section Designer fiber analysis and listed in Table 4-19. The controlling moment and axial forces are checked for the axial force and moment interaction. No resistance reduction factors are applied. Also note that reactions are used for the axial forces, again accounting for the possibility of an eccentricity between the foundation and the intersection of the worklines of the column and the bottom BRB. If that eccentricity doesn't exist, the corresponding results are shown in Table 4-20.

Table 4-19 Column capacity checking (case with eccentricity)

Column Type	Moment Demand M_u (kip-in)	Reaction Demand P_u (kips)	Plastic Strength M_n (kip-in)	Axial Strength P_n (kips)	M_u/M_n +P_u/P_n
Tension	41424.6	1406.7	49,687	4389.5	1.15
Compression	44267.2	-2105.9	49,687	-6857.7	1.20

Table 4-20 Refined column axial and flexure interaction capacity checking

Column Type	Moment Demand M_u (kip-in)	Reaction Demand P_u (kips)	Plastic Strength M_n (kip-in)	Axial Strength P_n (kips)	M_u/M_n + P_u/P_n
Tension	41424.6	1031.5	49,687	4389.5	1.07
Compression	44,152	-1692.2	49,687	-6857.7	1.14

The plastic moment and axial force interaction check gives values slightly larger than 1.0 for some cases. However, it is recognized that using a linear interaction diagram is a conservative approximation; results are compared below with the actual interaction diagram for CFT columns.

The interaction equation used in Table 4-19 and 4-20 for the axial force and plastic flexural strength is a simple linear relationship. It is equivalent to the interaction diagram shown in Fig. 4-12, for a B factor equal to 1.0. In reality, for CFT columns, in compression, B is typically less than 1.0, which provides for further reserve strength.

It is conservative to use that linear interaction equation here, instead of the interaction equations provided in the AASHTO LRFD Seismic design specification (2011) section 7.6.1 for axial compression and moment (which uses a calculated B value, typically less than 1.0). Note that there exists no equation in AASHTO for the axial tension and flexural interaction of CFT sections. The AASHTO compression-flexure interaction equation for CFT gives the axial-flexure interaction check for compression column considering the *B* factor in Table 4-21. There is no B factor check for tensile columns.

Table 4-21 Refined column capacity checking considering B factor for compression column

Column Type	Moment Demand M_u (kip-in)	Axial Load Demand P_u (kips)	Plastic Strength M_n (kip-in)	*B* factor	Axial Strength P_n (kips)	BM_u/M_n $+P_u/P_n$
Compression	44,152	-1692.2	49,687	0.68	-6857.7	0.85

Note that all the above are interaction equations based on cross-section strength. Columns were designed considering the actual column slenderness. However, as shown Appendix A, the columns are quite stocky and slenderness has a minimal impact of strength for this particular example.

2) Shear force

The horizontal reaction forces from Figs. 4-31c, 4-32c and 4-33c are listed in Table 4-22.

Table 4-22 Column shear capacity check

Column number		Transverse horizontal reaction (kips)	Largest Longitudinal horizontal reaction (kips)	Square root of reactions from two directions
Layout A	1	565	546	588
	2	375	546	557
	3	328	546	554
	4	626	546	647
Layout B	1	565	592	616
	2	375	592	603
	3	328	592	600
	4	626	592	651

The shear forces are not divided based on the origin of the shear force as done for the large axial force. Given that the column's cross section is circular; a square root combination of the demands in the two orthogonal directions is conservatively carried out, which gives the vectorial resultant shear force acting on the columns (the largest of corresponding to a 100% and 30% combination of seismic forces), when the eccentricity exists between the point where the bottom brace and column workline meet around the foundation. The shear strength calculated based on the equations provided by AISC (2010) and AASHTO Bridge Design Specifications (2014) is 1192.5 kips with the resistance factor 0.9. The shear force demands calculated are all within this strength limit.

Note that these large shear forces would reduce the column flexural strength. Since there is currently no equations provided in AASHTO or AISC quantifying the magnitude of this interaction for CFT columns under the combined shear and flexural strength, the strength check for the column is only performed for the axial and flexural combination.

4.4.1.4 Pushover curve

The pushover curve verification is done for the transverse bent and longitudinal bent in layout A.

4.4.1.4.1   Transverse bent

Fig. 4-35 shows the theoretical pushover curves of lateral shear resistance versus top displacement of the column for the frame, BRB, and the combined system, obtained using a bilinear force deformation relationship for the columns (yielding at a moment of M_y=34199) and tri-linear relationship for BRBs yielding at 42 ksi and strain hardening to 63 ksi at a strain of 0.015). The purple line of the theoretical BRB shows the yielding of the BRB at the displacement of 0.101", and point where the maximum strain hardening considered is reached, at 1.05". The target displacement of the bent is reached when the BRBs reaches the strain hardening value of 1.5% strain. The theoretical frame curve in navy blue dash lines shows that the frame yields at the displacement of 1.05". The two parts add up to the total theoretical curve for the combined system plotted in red dash lines. The left green vertical dash dotted line represents the expected displacement for the structural fuse system.

The pushover curve obtained from the SAP2000 analysis (in solid lines) overlays on top of the results from Fig. 4-35 in Fig. 4-36. The solid blue line shows the total base shear versus lateral displacement at top of the bent. By subtracting the lateral forces resisted by the BRBs (equal to the horizontal component

of the forces in the BRB) shown in solid green line, the solid brown line gives the portion of the base shear forces resisted by the frame. Note that the SAP2000 analyses consider both yielding and strain hardening of the BRBs and columns.
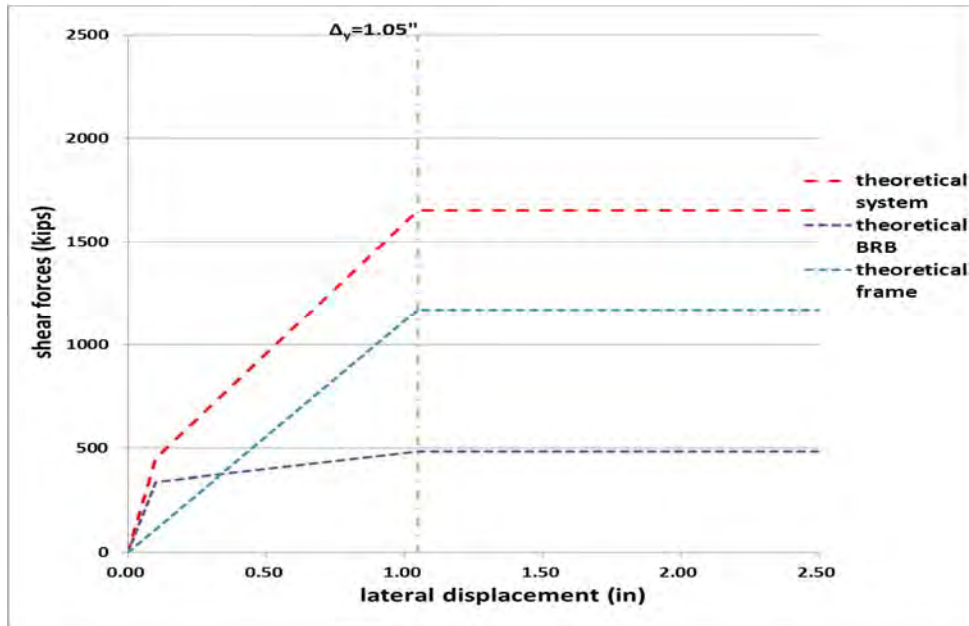
Figure 4-35 Theoretical pushover curves of the frame, BRB and the combined system in the transverse direction
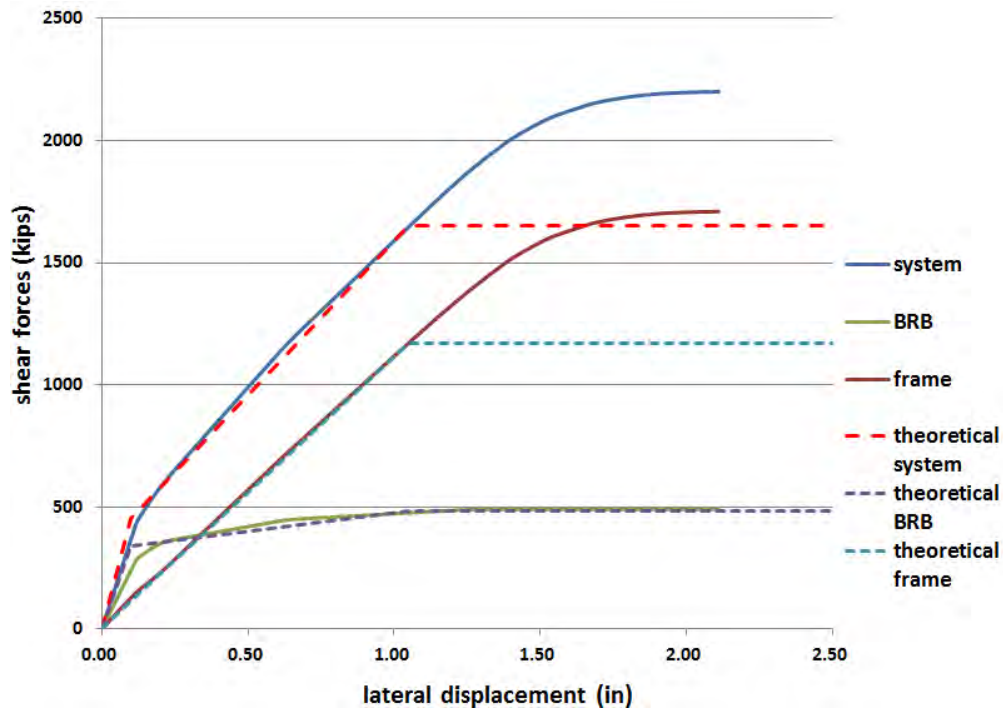
Figure 4-36 Comparison between the theoretical curve and the analytical curve in the transverse direction

In Fig. 4-37, the target elastic displacement demand of 1.28" from response spectrum analysis is shown as the orange vertical line. The pushover analysis results in Fig. 4-37 indicate that column yielding is first reached at bottom of the left column; the orange lower horizontal dotted line identifies the base shear resisted by the columns when that happens (which incidentally happens in a CFT column in tension). The upper blue dotted line is shown for the reaching shear resistance of the frame V corresponding to the $2M_p/h_{column}$ calculated, where M_p equals to 49687 kip-in obtained from SAP2000 Section Designer.
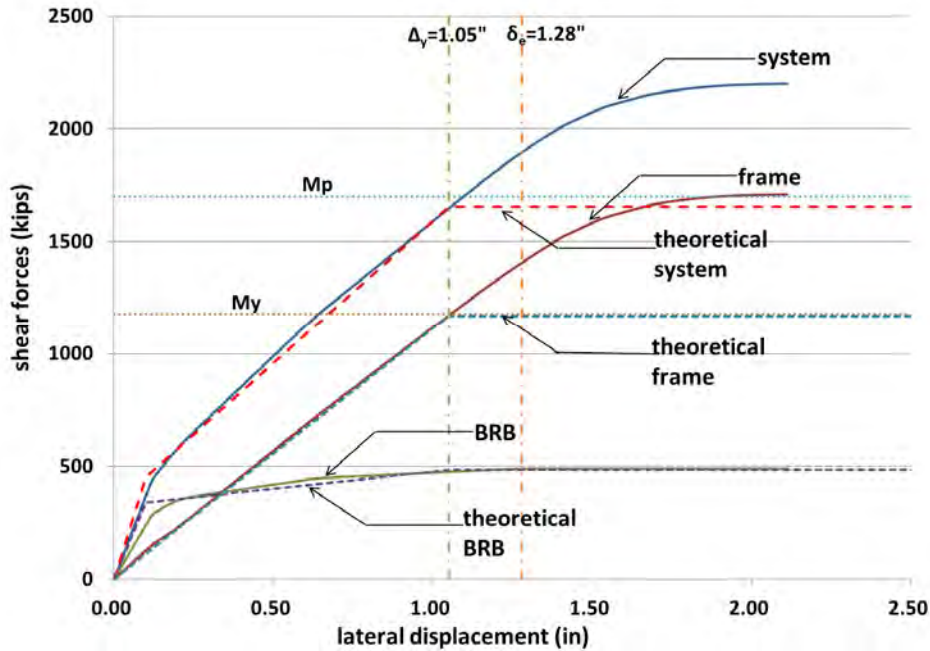
Figure 4-37 Pushover curve comparison between the analysis result and theoretical design value for the box-pier with BRBs in transverse direction

The sequence of yielding at top and bottom of the CFT columns (i.e. the point when the extreme fiber yields) is tabulated in Table 4-23. The column numbers are shown in Fig. 4-26. As an example of the notation used in that table, "187$_b$" stands for bottom ("b") of the column ("187"). Note that the yielding in these columns is not happening at the same time, but they are doing so over small increases of frame drift. If anything, Fig. 4-37 shows that limiting the column demands to M_y, to prevent any column yielding, is conservative. The use of a more liberal design limit is arguably possible.

4.4.1.4.2   Longitudinal bent (layout A)

The overall comparison of the pushover curve between the analysis result and the theoretical ones is directly shown in Fig. 4-38 (note that nearly identical results are obtained for Layout B, and are therefore

not presented here). The dashed purple line of the theoretical BRB shows the yielding of BRBs at the displacement of 0.101", and point where the maximum strain hardening considered is reached, at 1.05". The theoretical frame curve in navy blue dash lines shows that the frame yields at the displacement of 1.05". The two parts add up to the total theoretical curve for the combined system plotted in red dash lines. The pushover curves obtained from SAP2000 analysis overlay on top of the theoretical results as solid lines. The solid blue line shows the total base shear versus lateral displacement at top of the bent. By subtracting the lateral forces resisted by the BRBs (equals to the horizontal component of the forces in the BRBs), shown in solid green line, the solid brown line gives the portion of the base shear forces resisted by the frame. The target elastic displacement demand of 1.17" from response spectrum analysis is shown as the orange vertical line.
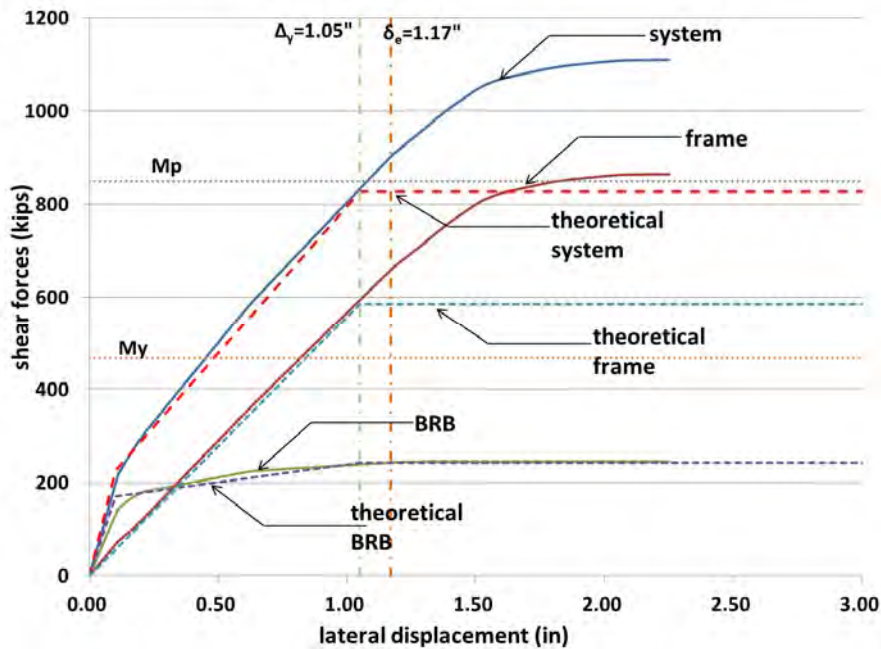
Figure 4-38 Pushover curve comparison between the analysis result and theoretical design value for the longitudinal bent layout A

The pushover analysis results indicate that column yielding is first reached at the bottom of the left column where the tension and flexure interaction exists. The orange lower horizontal dotted line identifies the base shear resisted by the columns when that happens. The upper blue dotted line is shown for the reaching shear resistance of the frame V corresponding to the $2M_p/h_{column}$ calculated, where M_p equals to 49687 kip-in obtained from SAP2000 Section Designer. The sequence of yielding at top and bottom of the CFT columns (i.e. the point when the extreme fiber yields) is tabulated in Table 4-24. As an example of the notation used in that table, "L_b" stands for bottom ("b") of the left ("L") column. The

117

yielding in these columns is not happening at the same time, but they are doing so over small increases of frame drift. If anything, Fig. 4-38 shows that limiting the column demands to M_y, to prevent any column yielding, is conservative. The use of a more liberal design limit is arguably possible.

Table 4-23 Displacement and shear forces resisted by the frame when the yielding strength is reached

Critical section	Yielding Displacement (in)	Yielding Force (kips)
187_b	1.06	1178
188_t	1.07	1197
186_t	1.11	1238
191_b	1.15	1273
189_b	1.18	1307
193_b	1.20	1331
190_t	1.22	1350
192_t	1.27	1396

Table 4-24 Displacement and shear forces resisted by the frame when the yielding strength is reached

Critical section	Yielding Displacement (in)	Yielding Force (kips)
L_b	1.13	638
R_b	1.18	664
L_t	1.17	660
R_t	1.10	619

4.4.1.5 BRB design details for box-pier bent with BRBs case

BRBs and the gusset plates used for the connections are usually designed by the BRB manufacturers. Using the same equation as shown in section 4.4.1.5, for BRB to develop the strain hardened loads of 332.50 kips, a pin of 2" would be necessary. A BRB supplier (Star Seismic) indicated that a 0.75" thick gusset plate can be used for the BRB connection to resist the forces. Distance from the pin to the edge of the gusset would be 6".

4.4.1.6 Pushover analysis summary

The CFT columns, designed in Appendix A, are found to have adequate strength to reach the force demands when the bridge bent reaches the target displacement (the elastic displacement demand from response spectrum analysis). Conservatively, the demand versus capacity check were performed considering the reaction forces and the moment demand on the column, as this would be the more critical

case if there was an eccentricity between the point where the work-lines of the column and BRB intersected and the foundation. In absence of that eccentricity, smaller results would be obtained considering the axial and flexural forces acting on the columns. The box pier design was also shown to be satisfactorily for simultaneous earthquake demands from both the transverse and longitudinal directions.

4.4.2 Service load check for box-pier bent with BRBs
4.4.2.1 Global bridge model

The global model developed in SAP2000 is used to determine the forces in the columns due to the dead load, live load and wind load. Note that since the design of the superstructure may need to be revised because of the locations of the new columns and the fact that they are CFTs (instead of RC columns), the permanent loads due to secondary prestress forces, creep, and shrinkage are not calculated here.

As mentioned above, the abutments allow longitudinal movement of the superstructure, limited only by the width of the gap between the superstructure and the abutment back wall (which is not considered to be a limiting factor here). The support provided by the abutment is assumed to be fixed against translation in the vertical and transverse directions and fixed against rotation about the longitudinal axis. The bent resists all the seismic force in the longitudinal direction while in the transverse direction part of the lateral force is taken by the abutments. In the SAP2000, the bridge superstructure is modeled analyzed as a line element (i.e. spine) located at mid-width of the bridge deck.

The braces are assumed to not take the gravity load. For the live load analysis, the brace would affect the results since they link the two bridge bents together. So the bridge is modeled with the BRBs. Similar to the two-CFT-column bent with BRBs, the bridge deck is modeled with three lanes, each having 12 ft in width. Details for the dead loads, live loads, and wind loads considered in the "service" load analyses are provided in the following sections.

4.4.2.2 Bridge loads
4.4.2.2.1   Dead loads
Same as the two- CFT-column bent with BRBs case.

4.4.2.2.2   Live loads
The vehicular loads are applied on the bridge lanes as shown in Fig. 4-39 to illustrate the location of the live truck wheel load.
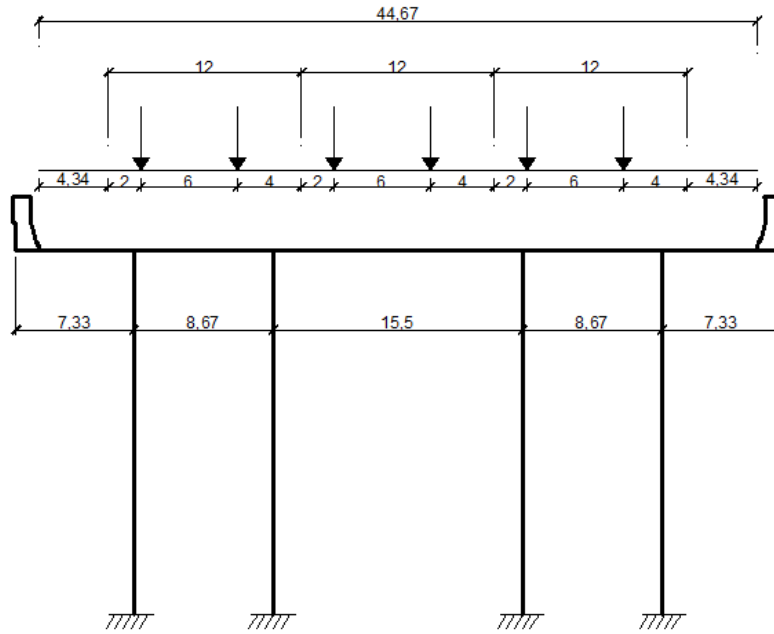
(a) Live load for three lanes
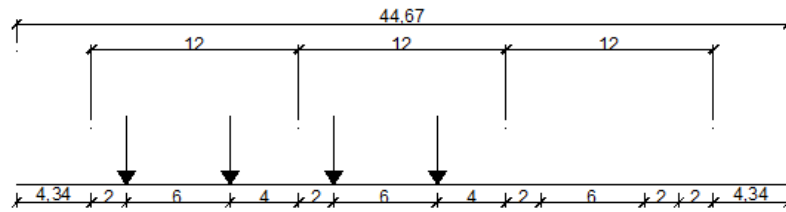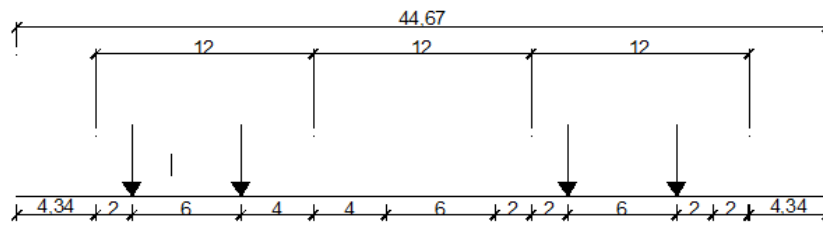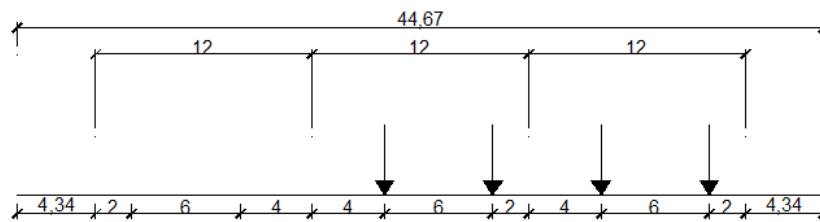
(b) Live load for lane 1 and 2

(c) Live load for lane 1 and 3

(d) Live load for lane 2 and 3
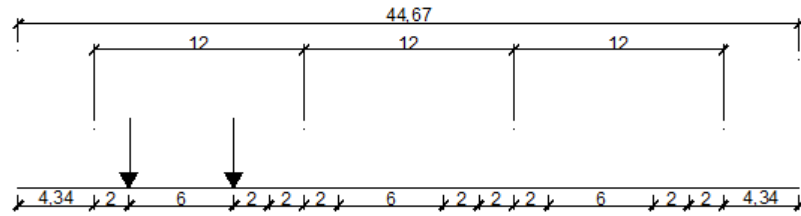
(e) Live load for lane 1
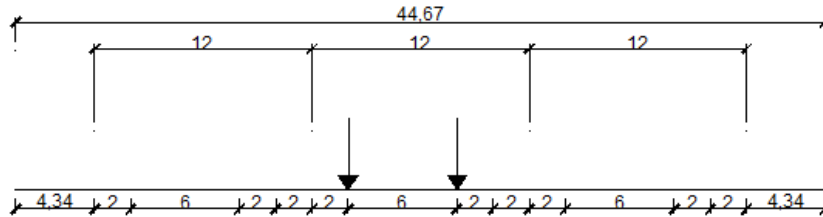
(f) Live load for one lane 2
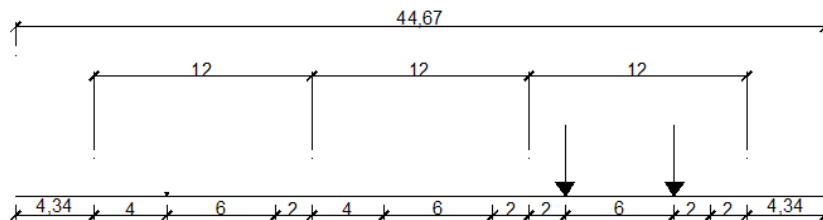
(g) Live load for one lane 3

Figure 4-39 Live load distribution for different lanes (Unit: ft)

4.4.2.2.3 Wind loads

Same as the two-CFT-column bent with BRBs case.

4.4.2.3 Service load analysis results

The critical forces in the columns are shown in Table 4-25 for the considered load cases. The numbering of the column element is shown in Fig. 4-26, for the columns in the parallel bent frames. Only the columns with the possible largest axial force or moment are listed here.

Table 4-25 Analysis result of all the load cases for critical members

Load cases	Element	P (kips)	V2 (kips)	V3 (kips)	M2 (kip-in)	M3 (kip-in)
DC	186	-424.3	143.4	6.4	-56.4	-3934.8
	187	-414.3	-15	-2.0	-122.4	-518.4
	192	-378.0	-143.4	6.5	-62.4	6736.8
	193	-419.2	18.3	-2.1	-132	776.4
	195	-424.3	143.4	-6.4	56.4	-3934.8
	196	-414.3	-15	2.0	122.4	-518.4

121

Load cases	Element	P (kips)	V2 (kips)	V3 (kips)	M2 (kip-in)	M3 (kip-in)
DC	201	-378.0	-143.4	-6.5	62.4	6736.8
	202	-419.2	18.3	2.1	132	776.4
DW	186	-64.3	24.5	1	-8.4	-674.4
	187	-59.3	-2.5	-0.3	-18	-86.4
	192	-56.4	-24.5	1	-9.6	1153.2
	193	-60.1	2.8	-0.3	-19.2	120
	195	-64.3	24.5	-1	8.4	-674.4
	196	-59.3	-2.5	0.3	18	-86.4
	201	-56.4	-24.5	-1	9.6	1153.2
	202	-60.1	2.8	0.3	19.2	120
Wind	186	-4.5	0.1	-1.8	-5.3	4.6
	187	-20.3	-0.1	-2.7	-326.9	-4.5
	192	4.5	-0.1	-12.8	-5.3	-4.6
	193	-20.3	0.1	-2.8	-326.9	4.5
	195	-4.7	-0.1	-1.8	-5.3	-5.8
	196	20.6	0.6	-2.8	-326.9	23.8
	201	4.7	0.1	-1.8	-5.3	5.8
	202	20.6	-0.1	-2.8	-326.9	-23.8
Live maximum compression	186	-644.4	-1.8	-8.0	-145.5	-3845.5
	187	-657.1	-6.6	-3.2	-118.3	-450.2
	192	-644.4	-1.8	-11.8	-97.3	-3845.5
	193	-657.1	-6.6	-2.2	-176.4	-450.2
	195	-629.8	-65.3	-7.6	-150.7	-337.5
	196	-658.3	-0.1	-3.4	-121.9	-1425.1
	201	-629.8	-65.3	-11.5	-99.6	-337.5
	202	-658.3	-2.3	-0.1	-185.4	-1425.1
Live maximum tension	186	435.1	29.1	2.4	176.3	1229.3
	187	437.4	0.2	2.2	176.3	1229.3
	192	435.1	29.1	1.6	118.3	1229.3
	193	437.4	0.2	3.2	118.3	1229.3
	195	435.1	6.8	2.6	185.4	808.0
	196	436.5	7.8	2.3	153.6	1101.9
	201	435.2	6.8	1.6	121.9	808.0
	202	436.8	6.8	3.4	121.9	808.0
Live maximum moment	186	-644.4	-1.8	-8.0	-145.5	-3845.5
	187	437.4	0.2	2.2	176.3	1229.3
	192	-644.4	-1.8	-11.8	-97.3	-3845.5
	193	437.4	0.2	3.2	118.3	1229.3
	195	414.8	0.4	11.5	99.6	4593.7
	196	-658.3	-0.1	-3.4	-121.9	-1425.1
	201	414.8	0.4	7.6	4593.7	150.7
	202	-658.3	-2.3	-0.1	-185.4	-1425.1

The combination load cases that are considered for column design are: Strength I, III, V, listed in AASHTO bridge design specification (2014) as mentioned in Section 4.3.2.4 for the two-column bent cases. The governing forces resulting from these load combinations, and used to verify the adequacy of the design of the column, are presented in Table 4-26.

Table 4-26 The controlling force to design the bridge columns

Element	P (kips)	V_2 (kips)	V_3 (kips)	M_2 (kip-in)	M_3 (kip-in)
186	-1754.5	-4.5	212.9	-12659.7	-337.7

The axial force and flexural moment interaction is checked for the columns strength in Table 4-27, where P_u and M_u are the force demand in the columns, P_n and M_n are the axial and flexural strength of the CFT column obtained from Section Designer respectively, without considering the resistance factors. The results from the interaction equation confirm that column capacity to resist all non-seismic load combinations considered is sufficient.

Table 4-27 Capacity check for the CFT column

Axial load P_u (kips)	Moment Demand M_u (kip-in)	Flexural Strength M_n (kip-in)	Axial strength P_n (kips)	$P_u/P_n+ M_u/M_n$
-1754.5	-12659.7	49,687.0	-6857.7	0.51

SECTION 5

'''''''''''''''NONLINEAR TIME HISTORY ANALYSES OF BENTS '''''''''''''''''''''

INSERTED WITH BRBS

5.1   General

In order to validate the system responses previously obtained for the bridge bents using response spectrum and pushover analysis, nonlinear time history analysis of all the previously designed bridge bents with BRBs have been performed using SAP2000. Nonlinear dynamic time history analysis can account for the nonlinearities in different members of the bridge bent and ground motion characteristics. The nonlinear time history analysis results allow assessing the effectiveness of adding the structural fuse to limit displacements by comparing them with those for the bare bridge bents without BRBs.

5.2   Ground Motions and Analysis Setting
5.2.1   Ground Motion Selections

The Target Acceleration Spectra Compatible Time Histories (TARSCTHS) Program (Pagageorgiou et al, 2000) was used to generate spectra-compatible synthetic ground motions. That program is set up to match ground motions to the NEHRP 2003 design acceleration spectrum as a target. Therefore, the acceleration response spectrum provided by Caltrans in the drawing of the Ordinary Standard Bridge was replaced by an equivalent NEHRP 2003 spectrum shape, as shown in Fig. 4-10. The black solid line and red dotted lines, respectively, correspond to the Caltrans design acceleration spectrum and the NEHRP 2003 target design acceleration spectrum with design spectral accelerations of $S_{Ds} = 2g$, $S_{D1} = 0.6g$.

Given that location of the Ordinary Standard Bridge is not provided, the distance to the earthquake epicenter and the possible earthquake moment magnitude are unknown. Both of these two parameters are required to obtain synthetic ground motions in the program TARSCTHS. Therefore, a few combinations of earthquake epicentral distances and moment magnitudes were used in TARSCTHS to generate the synthetic ground motions. The resulting motions that yielded an acceleration response spectrum that best matched the target one were chosen. The final set of nine spectral-compatible ground motions generated in TARSCTHS is shown in Fig. 5-1. The lengths of the synthetic time histories are all 25 seconds. The numbers in the parenthesis above each ground motion correspond to earthquake moment magnitude, epicentral distance, and an identifier for each individual run of this combination. For example, (7 5-2) is the second ground motion generated for a site located 5km from a magnitude 7 earthquake.

'''''''

(a)

(b)

(c)

(d)

(e)

(f)

(g)

(h)

126
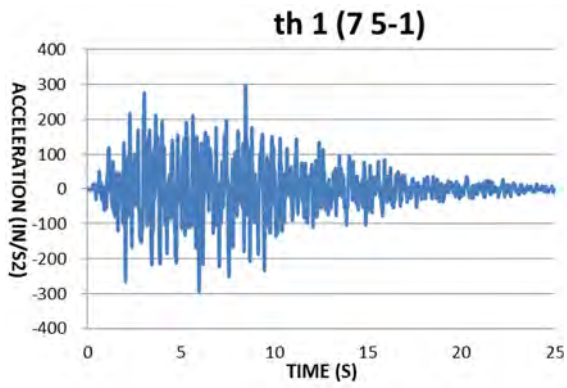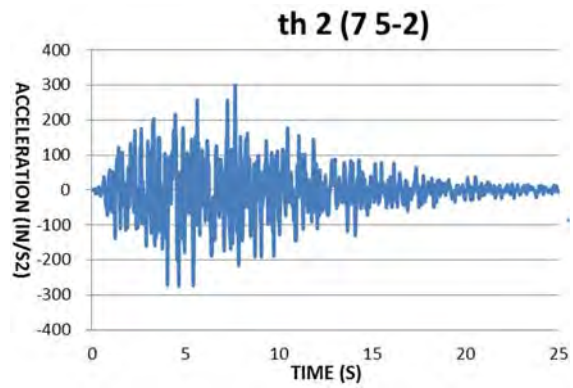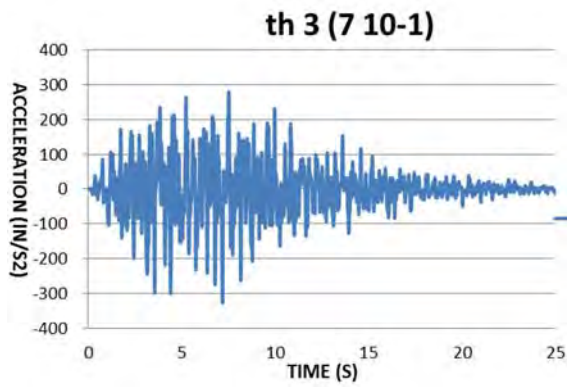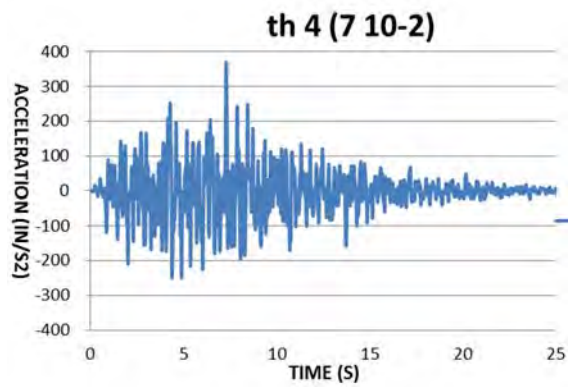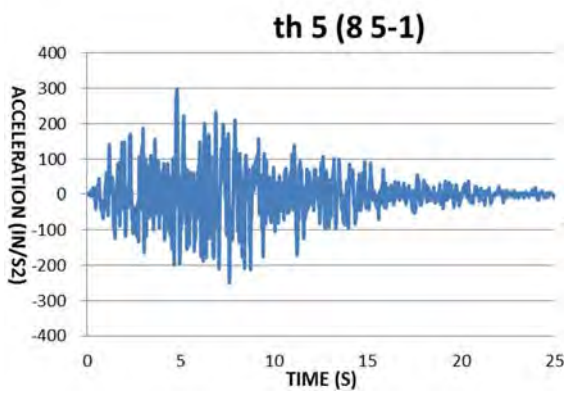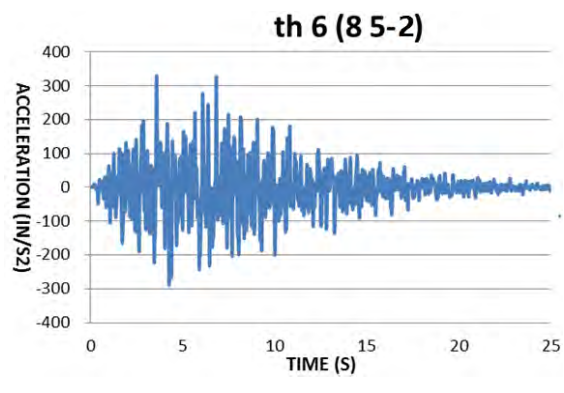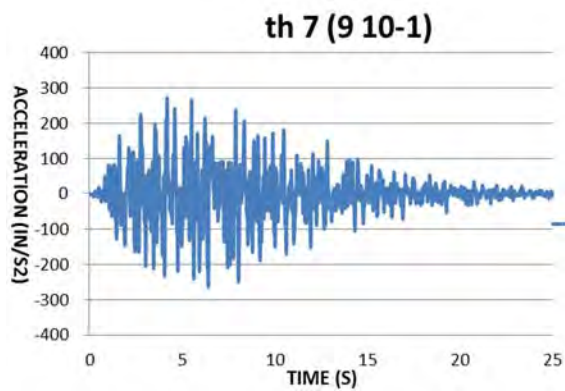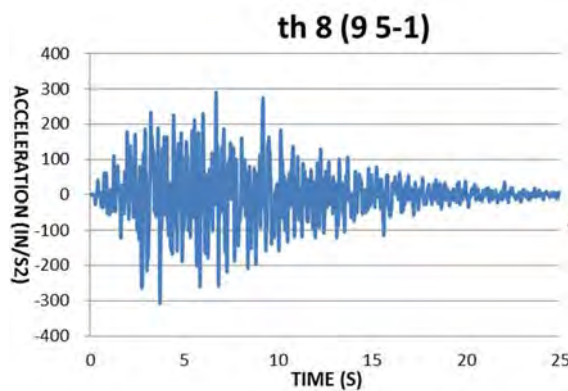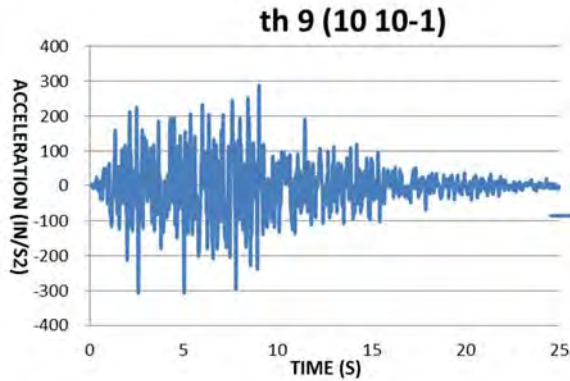
(i)

Figure 5-1 Nine ground motions used in the nonlinear time history analysis

Section 2.1.5 of Caltrans SDC (2010) requires that a 5% elastic response spectrum be used for determining seismic demand in Ordinary Standard Concrete Bridges. In Fig. 5-2, the acceleration spectra of the nine ground motions are shown to match with the target response spectrum with 5% damping.
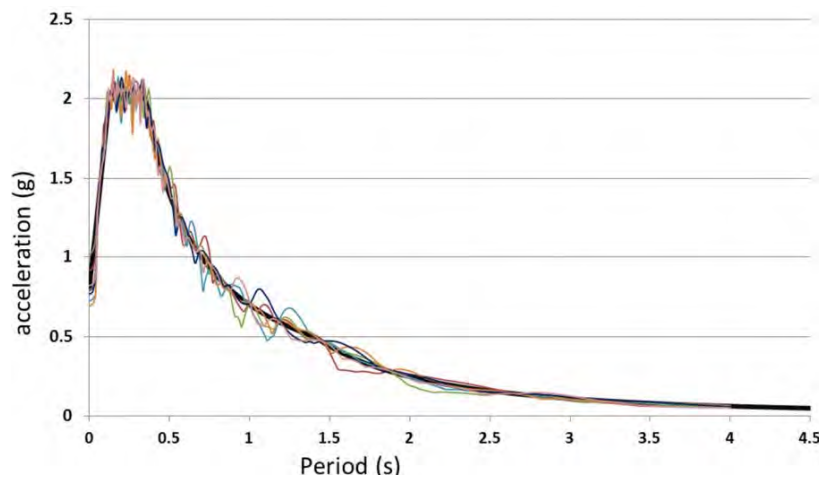
Figure 5-2 Acceleration response spectra of the nine synthetic ground motions (damping = 5%)

5.2.2 Nonlinear Time History Analysis Setting

The nonlinear time history analysis has been performed for the 2-D bridge bent instead of the 3-D entire bridge. The 2-D bent analysis makes it easier to compare with the pushover analysis results for the same bent. Out-of-plane displacements of the bent are restrained in this model. The mass of the bridge is assigned as a linearly distributed mass on the cap beam. The self-weight of the assigned mass is not accounted into the dead load since the mass is only used to apply the lateral seismic load to the bridge bent under the ground motions. The dead load is applied directly to the column before nonlinear time

history analysis is conducted. Hinge properties and assignments are defined the same way as done for the pushover analysis (see Section 4.4 and 4.5).

In the nonlinear time history analysis, direct integration was used to solve the dynamic equilibrium equations for the bridge bent at discrete time steps. The selection of the integration method was based on the desire for stability and accuracy of the results. Direct implicit integration was chosen. It is computational demanding, since it requires iteration at each time step to achieve equilibrium, but it allows consideration of any type of damping and nonlinearity. Certain parameters, if chosen well, can make the direct implicit integration tolerate larger time step due to unconditional stability. Among all implicit integration methods, the Hilbert-Hughes-Taylor (HHT) method was used for this direct integration time history analysis (SAP2000 reference manual, 2016). In these analyses, ground acceleration was applied in the bridge's transverse direction, which corresponds to excitations applied in the plane of the 2-D bridge bent model. The output time step is 0.002 second. P-delta or second order effect is not considered in the analysis. From the modal analysis, the mass participating ratio is more than 90% for the first two modes. Rayleigh damping was used, with coefficients corresponding to 5% damping for the first and second modal periods here.

5.3   Analysis Results
5.3.1   Two-CFT-Column Bent

The two-CFT-column bridge bent with BRBs have two configurations: single inclined BRB and inverted-V chevron BRBs. Referring to Appendix B, the theoretical fundamental period of the two-CFT-column bent designed with BRBs is 0.19 s. The bare bridge bent without BRBs is also analyzed to compare with the two designed bridge bents with BRBs. The first two periods of the three bridge bent are presented in the Table 5-1 (these were the periods used to setting the Rayleigh damping of 5% coefficients). The modal shapes of the bridge bents are shown in Fig. 5-3. The first modal periods of the two designed bridge bents with BRBs are close to the theoretical period of 0.19 s, and substantially smaller than the bare bent without BRBs. The first modal shape of all the bridge bents considered corresponds to a sway mode of vibration (i.e. bents moving laterally). The second modal shape of the bridge bents with BRBs have the columns elongating on one side and compressing on the other, while the bare bridge bent without BRBs have both columns elongating and compressing at the same time. The mass participating ratio is more than 90% for the first two modes.

(a) Single inclined BRB first mode

(b) Single inclined BRB second mode

(c) Inverted –V chevron BRBs first mode

(d) Inverted –V chevron BRBs second mode

(e) No BRB first mode
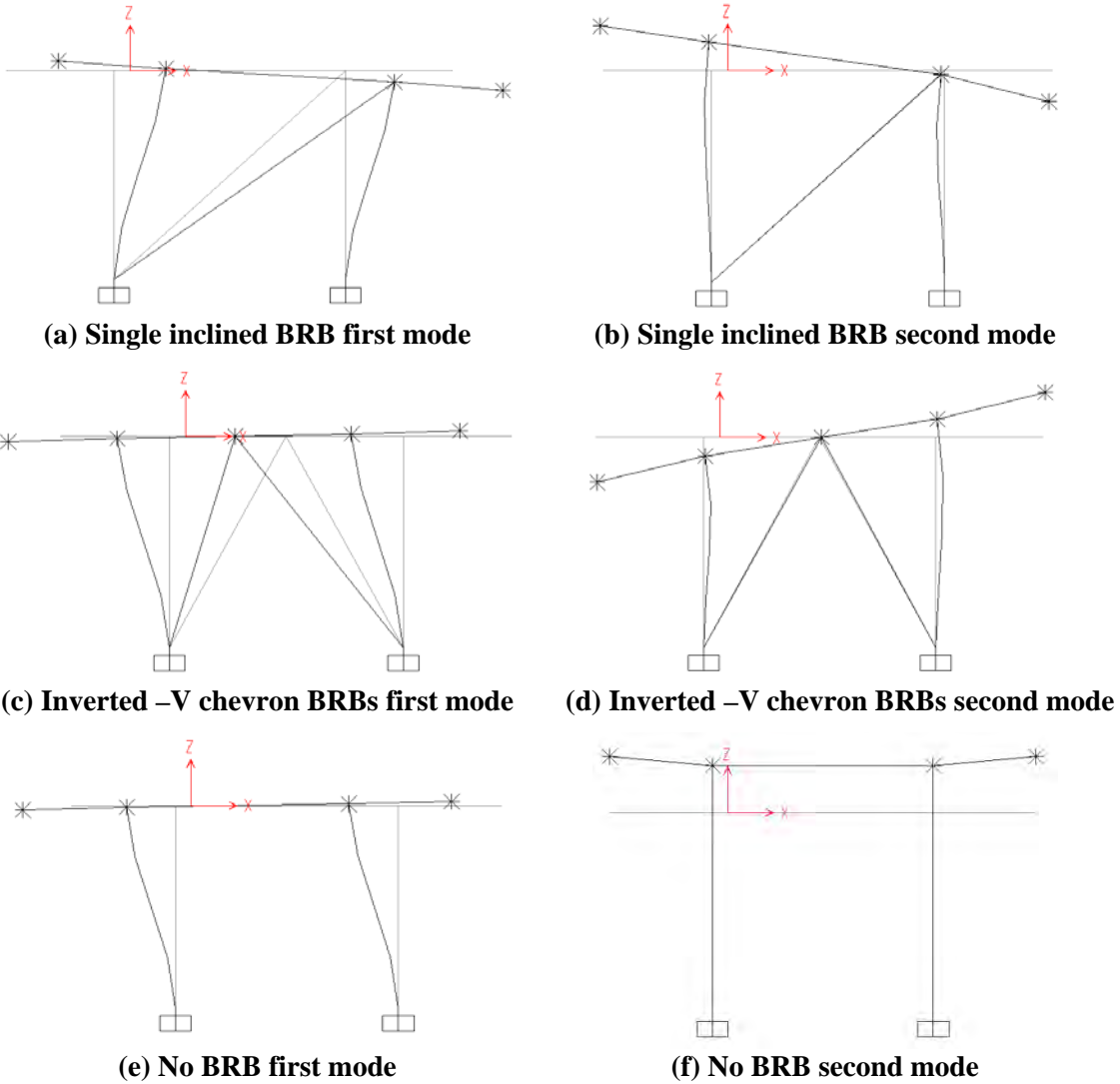
(f) No BRB second mode

Figure 5-3 The mode shapes of the two-CFT-column bent with and without BRBs

Table 5-1 First and second modal periods of the two-CFT-column bent

Period (s)	Single inclined BRB	Inverted-V BRBs	No BRB
First mode	0.225	0.202	0.406
Second mode	0.089	0.097	0.080

The maximum displacements in positive and negative in-plane transverse directions (X directions) of all the two-CFT-column bents resulting from the nine ground motions are presented in Table 5-2. The averages of the maximum displacements are in bold.

Table 5-2 Displacement demands at top of the two-CFT-column bents

		th1	th2	th3	th4	th5	th6	th7	th8	th9	Ave.
Single inclined BRB (in)	max	1.012	1.123	1.122	1.117	0.851	0.991	1.047	1.160	1.000	1.130
	min	-1.117	-1.075	-1.116	-0.992	-1.138	-1.208	-0.977	-1.297	-0.829	
Inverted-V chevron BRBs (in)	max	0.999	1.076	1.051	1.064	0.808	0.933	0.982	1.085	0.944	1.095
	min	-1.085	-1.017	-1.092	-0.965	-1.124	-1.229	-0.919	-1.262	-0.815	
Bare bent with no BRB (in)	max	3.175	1.880	1.766	1.584	1.957	1.315	1.101	1.759	1.941	2.139
	min	-1.495	-1.757	-1.716	-1.744	-2.099	-2.399	-2.218	-2.027	-1.385	

The average maximum absolute lateral displacement of the two-CFT-column bent with no BRB is 2.139 in. The bridge bent with single inclined BRB has an average maximum displacement of 1.13 in, which corresponds to 52.8% of the bare bridge bent value. The bridge bent with inverted-V chevron BRBs case has an average maximum displacement of 1.095 in, equal to 51.2% of the bare bridge bent value.

The base shear forces for the three bridge bents are compared in Table 5-3. The average maximum absolute base shear forces of the bridge bents with single inclined BRB and the inverted-V chevron BRBs case are 3916.5 kips and 3904.7 kips, respectively, which are 20.7% and 20.3% higher than the no BRB case of 3245.8 kips. Note that this 20% increase in base shear strength produced a reduction of approximately 50% of the lateral displacement for the designed two-CFT-column bents with structural fuses, which is a significant gain in drift reduction for a relatively modest increase in base shear demands.

Table 5-3 Base shear demands of the two-CFT-column bents

		th1	th2	th3	th4	th5	th6	th7	th8	th9	Ave.
Single inclined BRB (kips)	max	3917.1	3827.7	3936.6	3689.0	3969.4	4035.1	3628.9	4139.4	3234.0	3916.5
	min	-3763.3	-3880.9	-3911.7	-3918.5	-3378.8	-3725.8	-3787.9	-3964.9	-3663.4	
Inverted-V chevron BRBs (kips)	max	3902.0	3750.6	3912.8	3656.5	3973.9	4106.5	3628.9	4135.1	3251.9	3904.7
	min	-3732.8	-3866.8	-3846.8	-3869.3	-3326.5	-3681.2	-3787.9	-3916.7	-3588.1	
Bare bent with no BRB (kips)	max	3160.1	3164.2	3242.5	3219.7	3249.8	3258.7	3237.4	3264.7	3039.5	3245.8
	min	-3290.2	-3209.5	-3143.4	-3207.3	-3195.0	-3149.3	-2947.5	-3260.4	-3240.1	

The nonlinear response of the two bridge bents under ground motion TH5 (Fig. 5-1) are shown below as examples. Displacement time histories at top of the cap beam are plotted in Fig. 5-4 for the two-CFT-column bent with (a) no BRB, (b) single inclined BRB, and (c) inverted-V chevron BRBs. The yield displacement of the CFT column is 0.71 in, marked by the horizontal red lines. The elastic yielding demand is not marked for each case here. Note that all three bridge bents reach a maximum displacement larger than yield displacement of the columns, meaning that columns undergo inelastic deformations. As shown in Table 5-2, for that particular ground motion, the two-CFT-column bent with a single inclined

BRB has a maximum displacement of 1.14 in, which is equal to 54.3% of the corresponding value for the two-CFT-column bent with no BRB case. For the inverted-V chevron BRBs case, the displacement demand is 1.12", i.e., 53.3% of that for the two-CFT- column bent with no BRB case.

(a)   **(b)**

(c)
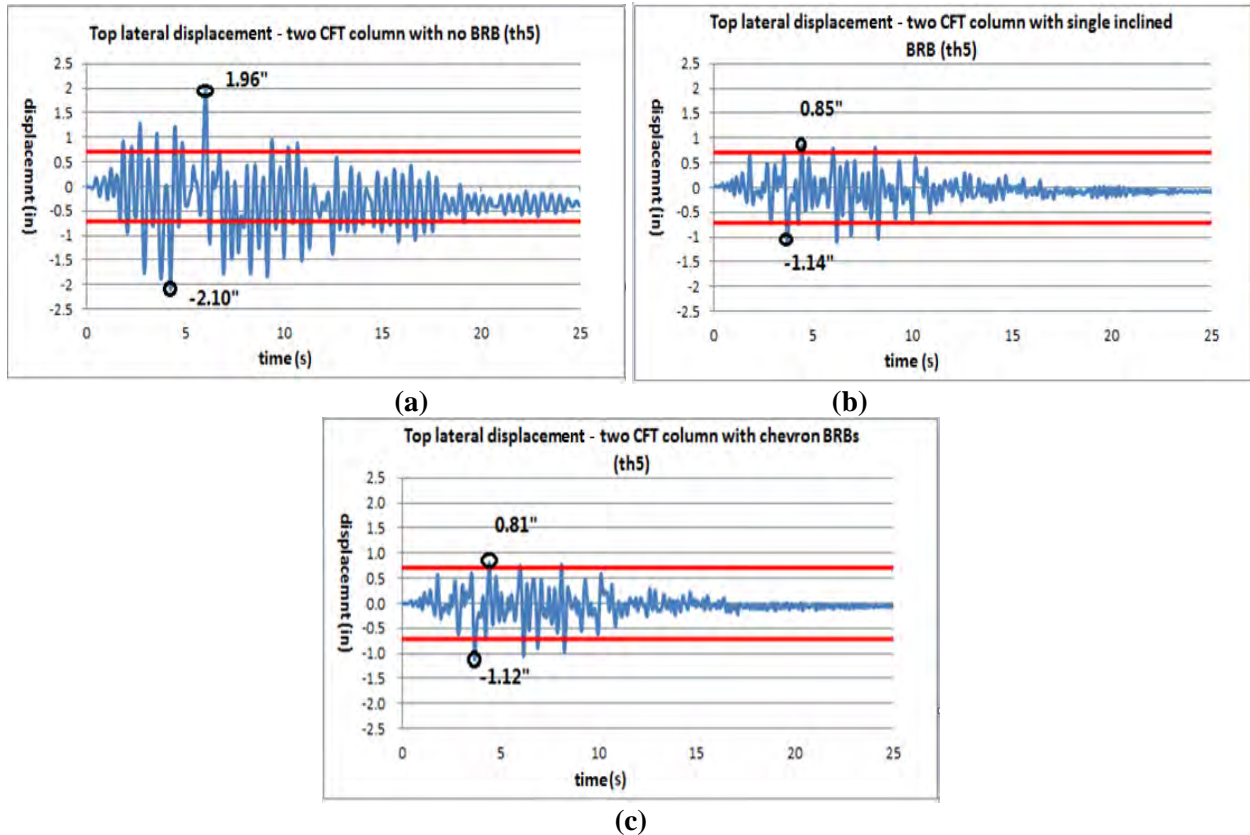
Figure 5-4 Displacement demands of the two column bridge bents under ground motion TH5

The base shear force time histories resisted by the three bents are plotted in Fig. 5-5. Note that, the maximum base shear forces are 21.1% and 22.3% larger, respectively, for the single inclined BRB and the inverted-V chevron BRBs case, compared to the no BRB case. Note that no strain hardening in the columns was assumed.

In all cases considered, P-M_2-M_3 fiber hinges (as defined in Section 4.3.1.1.3) were located at top and bottom of the CFT columns. Moment rotation history for the hinge at bottom of the right column, found to develop the maximum rotation, is shown in Fig. 5-6. The maximum rotation for the single BRB case and the inverted-V chevron BRBs case is 0.0013 rad and 0.00092 rad, respectively, which is only about 20% of the corresponding value for the no BRB case which has a 0.005 rad maximum rotation. Note that,

131

from Fig. 5-6, the yield rotation for the column (under its specific axial loads) is graphically estimated to be approximately 0.0005 rad. The yielding in the column is deemed acceptable.

(a)

(b)

(c)
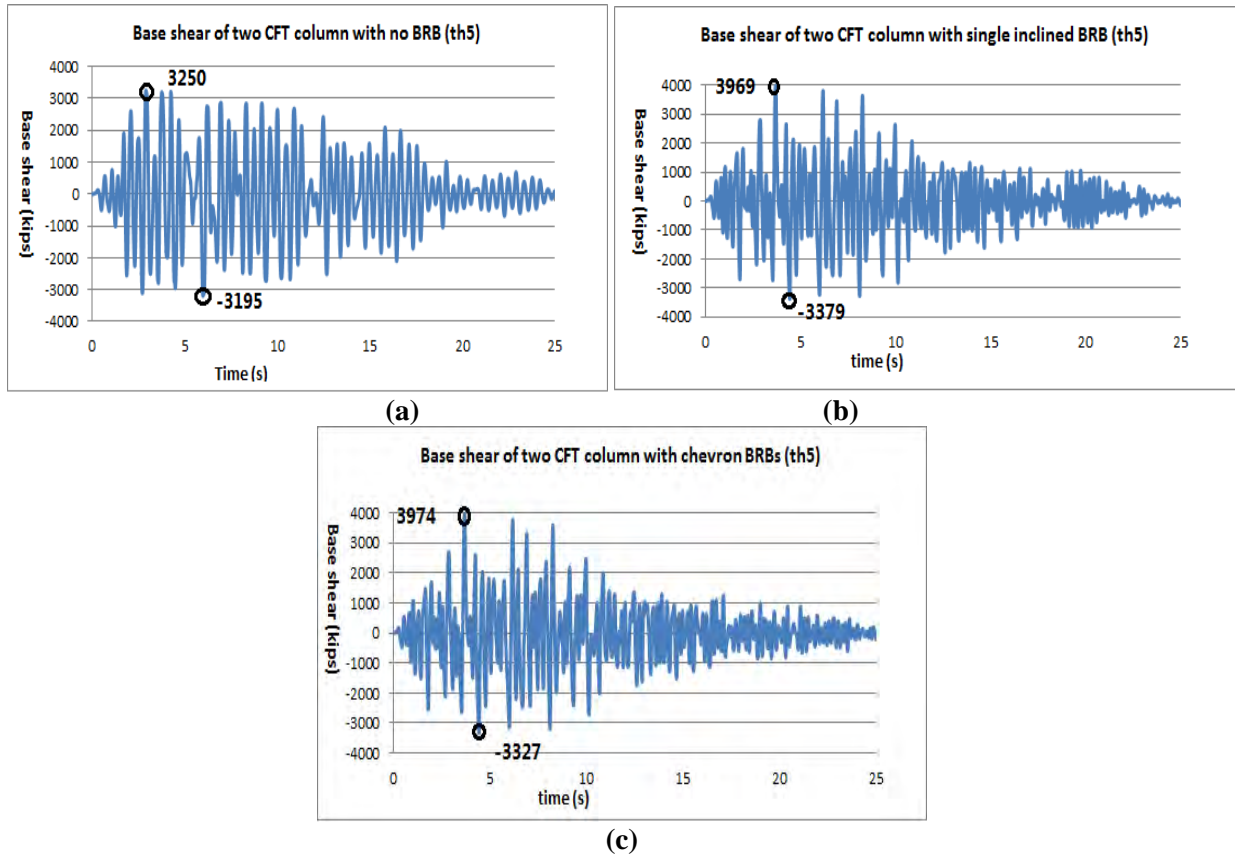
Figure 5-5 Base shear demands of the two column bridge bents under ground motion TH5

In Fig. 5-7, the BRBs in the (a) single inclined BRB case have reached a compressive strength of 1411 kips and tensile strength of 1270 kips (after strain hardening). Also, BRBs in the (b) inverted-V chevron BRBs case have reached a compressive strength of 1082 kips and tensile strength of 973 kips (after strain hardening). This corresponds to maximum ductility of 10 and 15.2, respectively, for the single inclined BRB case and inverted-V chevron BRBs case.

(a)

(b)

(c)
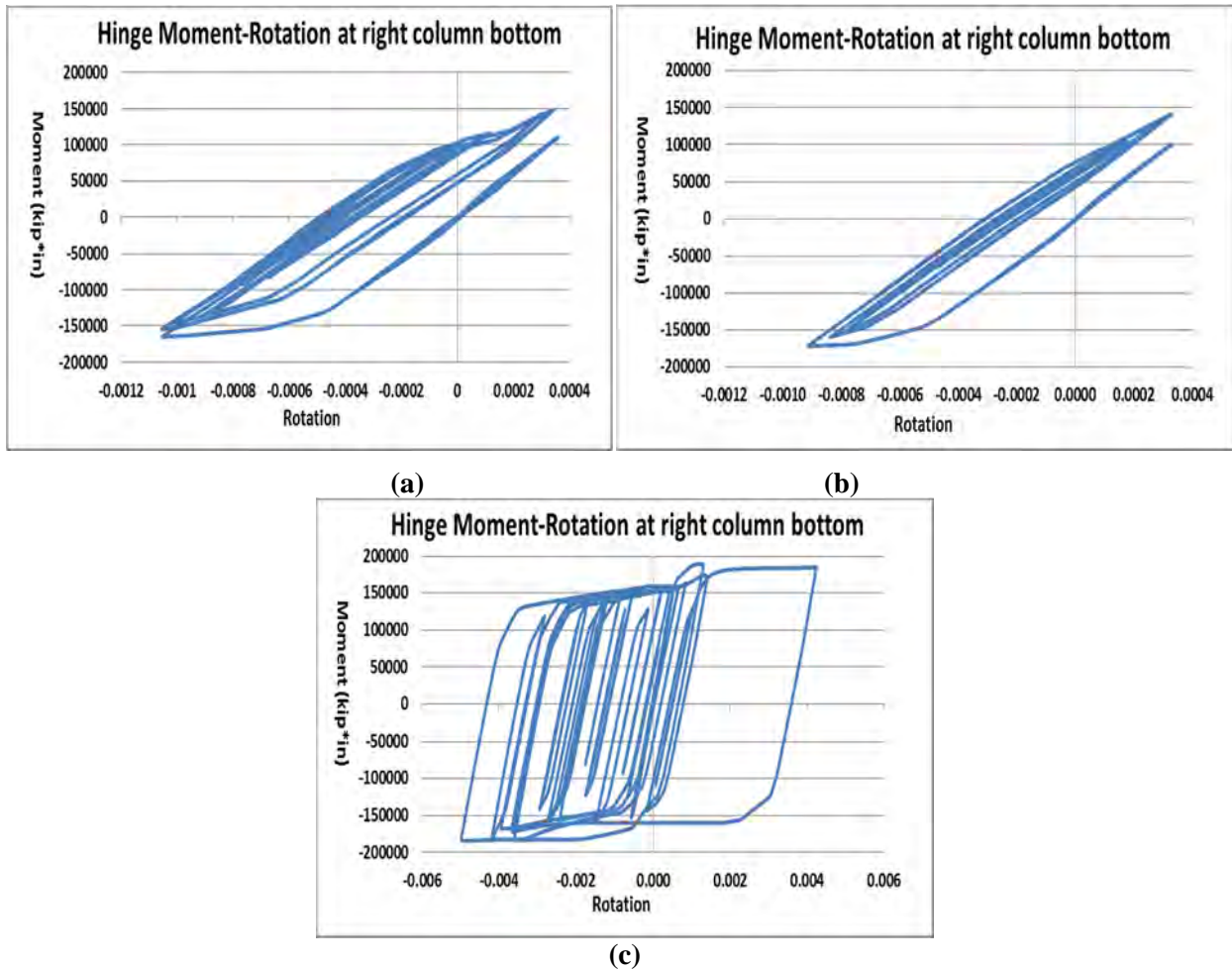
Figure 5-6 Moment-rotation plot of the PM$_2$M$_3$ hinge at bottom of the right column for : (a) single inclined BRB case (b) inverted-V chevron BRBs case, and (c) no BRB case

5.3.2   Box-pier bent

The box-pier bridge bent was analyzed separately in the transverse and longitudinal direction. Referring to Appendix A, the theoretical fundamental period of the bridge bent with BRBs in both the transverse and longitudinal direction is 0.23 s. The bare bridge bent was also analyzed to compare with box-pier bent with BRBs in both directions. To note, the bare bent for the box-pier configuration is purely academic because the box-pier system would never be used without BRBs. The first two periods of the box-pier bents with and without BRBs are presented in the Table 5-4 (these are the periods used in setting the Rayleigh damping coefficients). The modal shapes of the bridge bents are shown in Fig. 5-8. The first modal periods of the box-pier bridge bents with BRBs are close to the theoretical period of 0.23 s, i.e., smaller than the period of the bare bent without BRBs. The first modal shape of all the bridge bents considered corresponds to a sway mode of vibration. The second modal period of the box-pier bent with

133

BRBs does not differ much from the no-BRB case in each direction. The second modal shape of the bridge bents in the transverse direction have one side compressed and the other elongated; the same behavior is observed in the longitudinal direction.

(a)

(b)

(c)
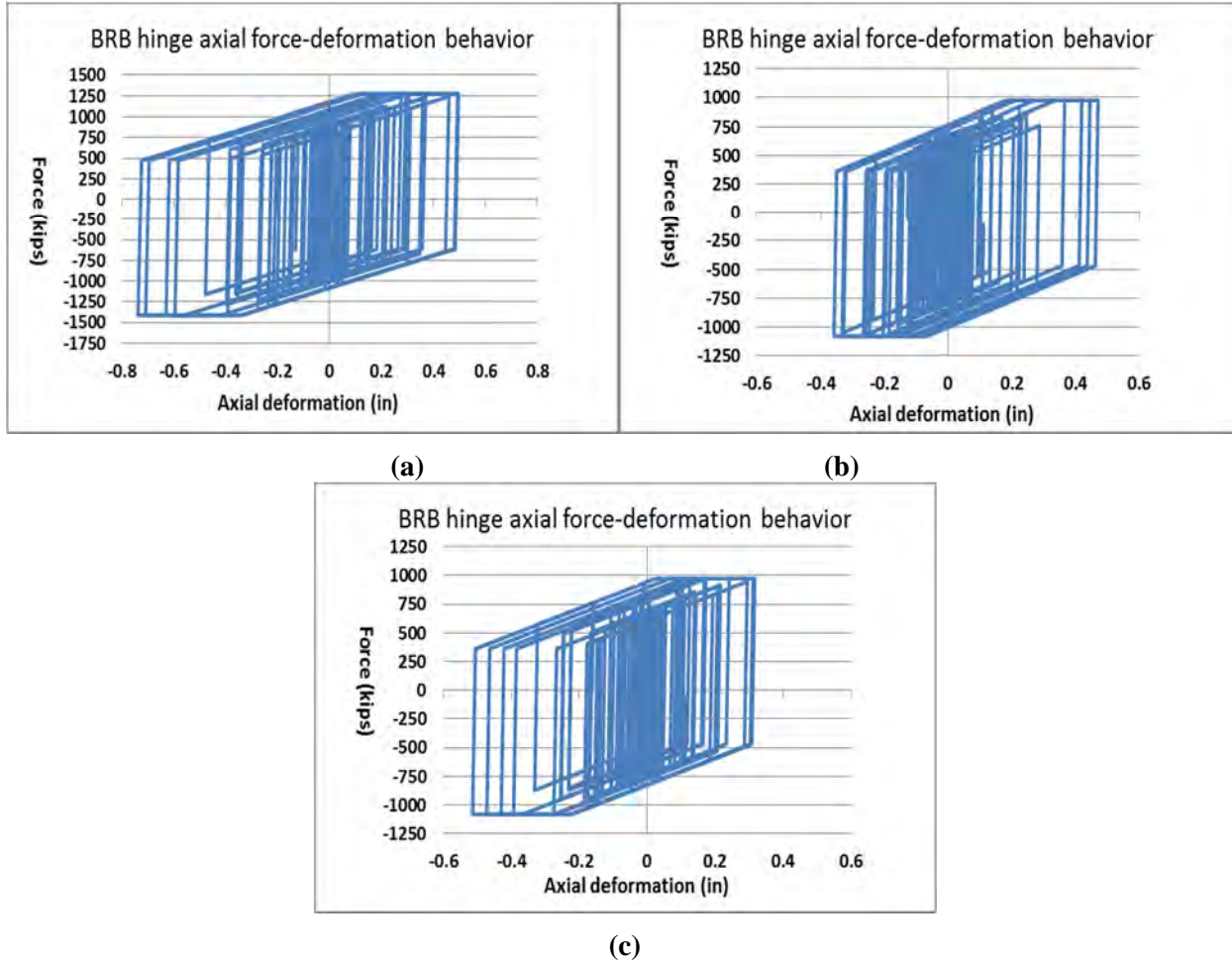
Figure 5-7 BRB hinge axial force-deformation plot for the bridge bents: (a) single inclined BRB case; (b) left BRB in the inverted-V chevron BRBs; and (c) right BRB in the inverted-V chevron BRBs

Table 5-4 First and second modal periods of the box-pier bents

Period (s)	Transverse with BRBs	Transverse no BRBs	Longitudinal with BRBs	Longitudinal no BRBs
First mode	0.256	0.455	0.244	0.444
Second mode	0.062	0.063	0.059	0.059
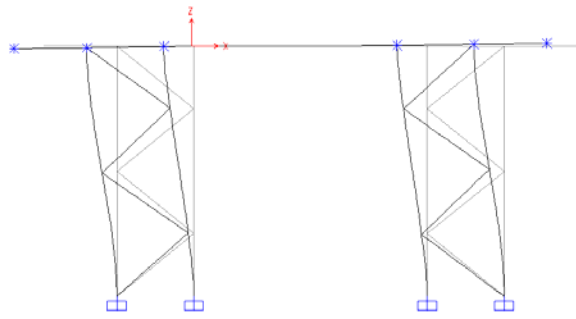
(a) Transverse with BRBs first mode   **(b) Transverse with BRBs second mode**
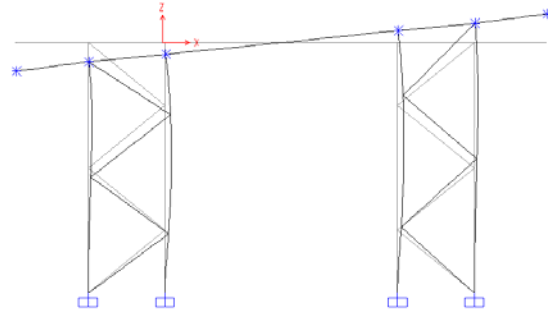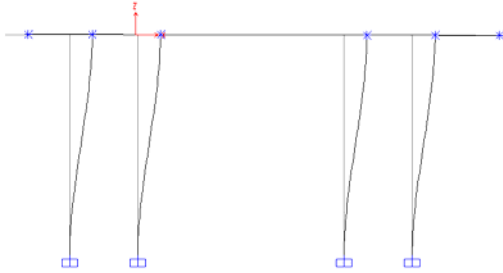
(c) Transverse no BRBs first mode   **(d) Transverse no BRBs second mode**
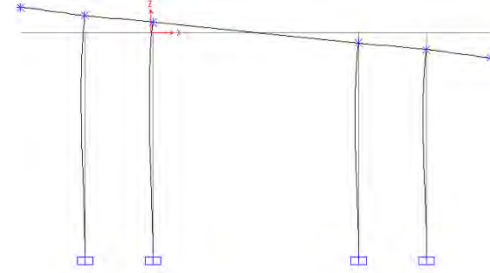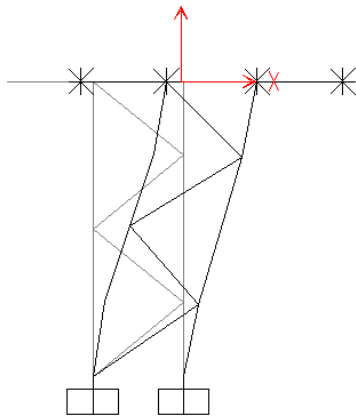
(e) Longitudinal with BRBs first mode   **(f) Longitudinal with BRBs second mode**
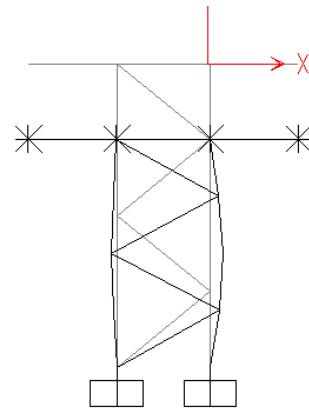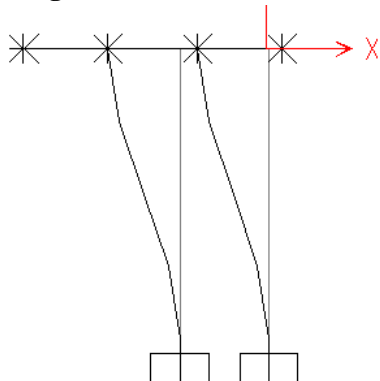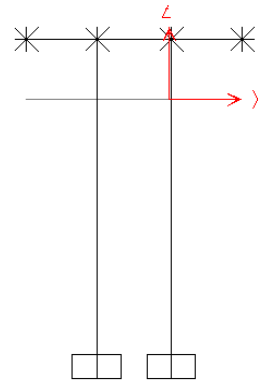
(g) Longitudinal no BRBs first mode   **(h) Longitudinal no BRBs second mode**

Figure 5-8 The mode shapes of three two-CFT-column bents

The maximum displacements in positive and negative in-plane transverse directions (X directions) of the box-pier bents with and without BRBs are presented in Table 5-5. The averages of the maximum displacements are in bold.

Table 5-5 Displacement demands at top of the box-pier bents

		th1	th2	th3	th4	th5	th6	th7	th8	th9	Ave
Transverse with BRBs (in)	max	1.256	1.340	1.397	1.301	1.084	1.184	1.241	1.234	1.052	**1.317**
	min	-1.314	-1.369	-1.247	-1.212	-1.270	-1.308	-1.181	-1.601	-1.049	
Transverse no BRBs (in)	max	2.789	2.893	1.558	2.116	2.758	1.421	1.298	1.756	1.943	**2.617**
	min	-2.109	-1.892	-2.800	-1.556	-1.897	-3.110	-2.724	-2.417	-1.688	
Longitudinal with BRBs (in)	max	1.154	1.302	1.323	1.255	1.157	1.022	1.149	1.194	1.024	**1.259**
	min	-1.250	-1.260	-1.220	-1.157	-1.277	-1.227	-1.095	-1.520	-0.969	
Longitudinal no BRBs (in)	max	2.747	2.738	1.610	2.149	1.365	2.549	1.396	1.890	2.049	**2.505**
	min	-2.020	-1.874	-2.710	-1.467	-2.666	-1.953	-2.572	-2.364	-1.554	

The average maximum absolute lateral displacement of the box-pier bent with no BRB in the transverse direction is 2.617 in. The average maximum displacement of the box-pier bent with BRBs in the transverse direction is 1.317 in, which corresponds to 50.3% of the bare bridge bent value. The box-pier bent with no BRB in the longitudinal direction has an average maximum displacement of 2.505 in. The average maximum displacement of the box-pier bent with BRBs in the longitudinal direction is 1.259 in, equal to 50.3% of the bare bridge bent value.

The base shear forces for the four bridge bents are compared in Table 5-6. The average maximum absolute base shear forces of the box-pier bent are 1930.2 kips and 950.6 kips in the transverse and longitudinal direction, which are 10.2% and 7.8% higher than the no-BRB case in both directions. Note that this 10% increase in base shear strength produced a reduction of approximately 50% of the lateral displacement for the designed box-pier bents with BRBs. Similar to the two column bridge bents with BRBs, a significant gain is also observed in drift reduction for a relatively modest increase in base shear demands.

Table 5-6 Base shear forces of the box-pier bents

		th1	th2	th3	th4	th5	th6	th7	th8	th9	Ave.
Transverse with BRBs (kips)	max	1946.1	1970.0	1885.1	1842.9	1896.5	1933.6	1804.5	2135.7	1644.5	**1930.2**
	min	-1900.9	-1958.3	-2015.2	-1929.4	-1698.5	-1821.7	-1879.1	-1862.4	-1666.1	
Transverse no BRBs (kips)	max	1750.1	1600.7	1738.5	1613.7	1716.0	1785.0	1771.5	1758.1	1674.1	**1750.9**
	min	-1749.1	-1747.0	-1605.0	-1737.5	-1762.6	-1556.0	-1486.3	-1710.8	-1708.2	
Longitudinal with BRBs (kips)	max	954.7	951.7	941.2	906.5	961.5	940.5	868.1	1063.2	789.5	**950.6**
	min	-912.3	-969.1	-988.1	-953.2	-905.0	-824.0	-902.7	-923.5	-822.8	
Longitudinal no BRBs (kips)	max	875.2	821.5	876.7	811.1	891.6	867.7	887.4	884.7	817.8	**882.0**
	min	-893.8	-878.5	-835.7	-875.2	-760.0	-884.1	-763.5	-867.3	-865.6	

The nonlinear response of the box-pier bridge bents under ground motion TH5 (Fig. 5-1) are shown below as an example. Displacement time histories at top of the cap beam are plotted in Fig. 5-9 for the box-pier bent cases (1) transverse with BRBs, (2) transverse no BRBs, (3) longitudinal with BRBs, and (4) longitudinal no BRBs. The yield displacement of the frame is 1.05 in, marked by the horizontal red lines. The elastic yielding demand is not marked for each case here. Note that the CFT columns of all four bridge bents undergo inelastic deformations since the largest lateral deformations are all larger than 1.05". As shown in Table 5-5, for that particular ground motion, the box-pier bent with BRBs in the transverse direction has a maximum displacement of 1.27 in, which is reduced to 46% from the box-pier bent with no BRB case of 2.76 in. For the longitudinal direction, the displacement demand is 1.28", i.e., 48% of that for the box-pier bent with no-BRB case of 2.67 in.

The base shear force time histories resisted by box-pier bents are plotted in Fig. 5-10. Note that, the maximum base shear forces are only increased by 10.2% and 7.8% for the box-pier in the transverse and longitudinal directions, if comparing them with the no-BRB case. Note that no strain hardening in the columns was assumed.

For all the box-pier bent cases considered, P-M_2-M_3 fiber hinges (as defined in Section 4.3.1.1.3) are located at top and bottom of the CFT columns. Moment rotation history for the hinge at bottom of the right column, found to develop the maximum rotation, is shown in Fig. 5-11.

137
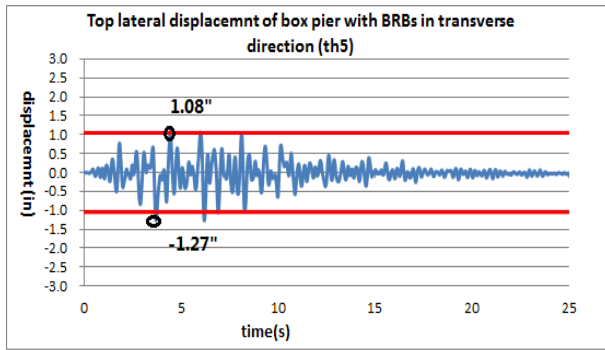
(a)
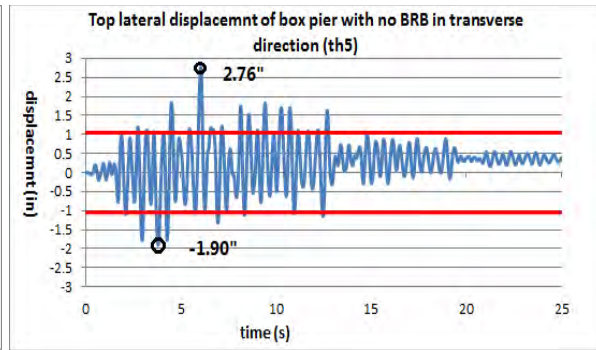
(b)
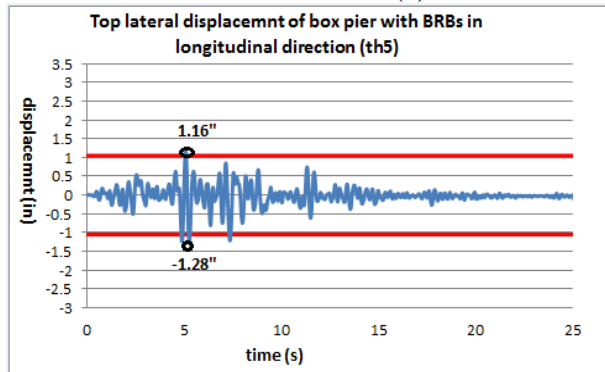
(c)
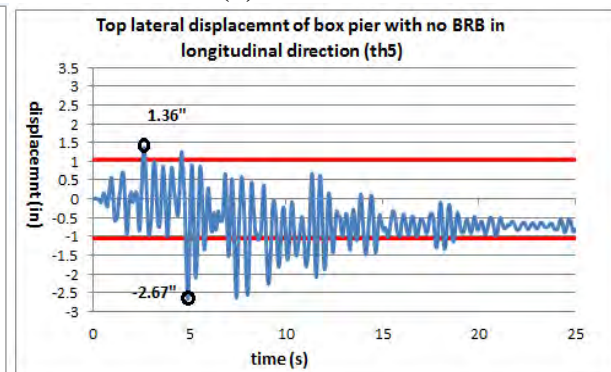
(d)

Figure 5-9 Displacement demands of the two column bridge bents under ground motion TH5
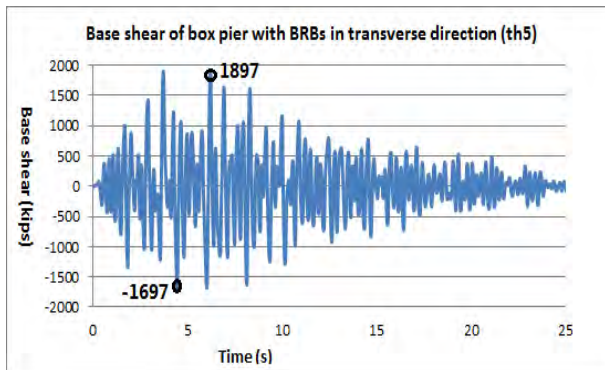
(a)
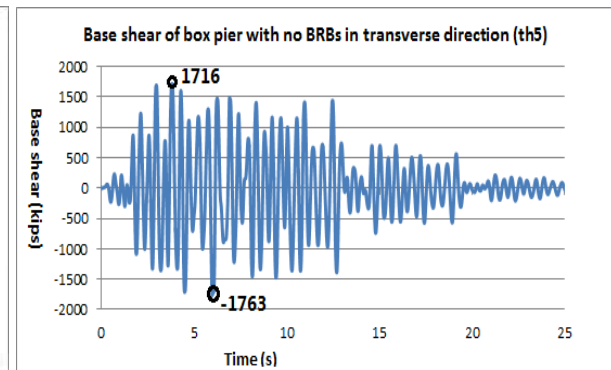
(b)
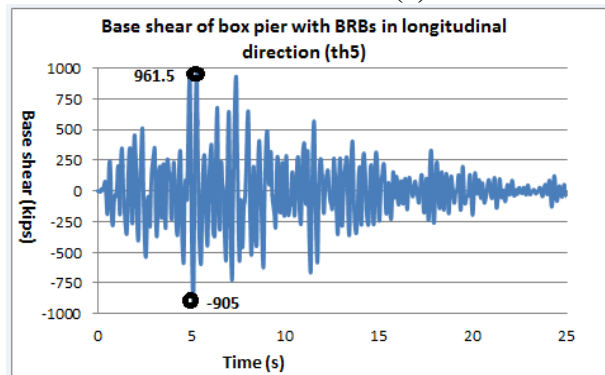
(c)
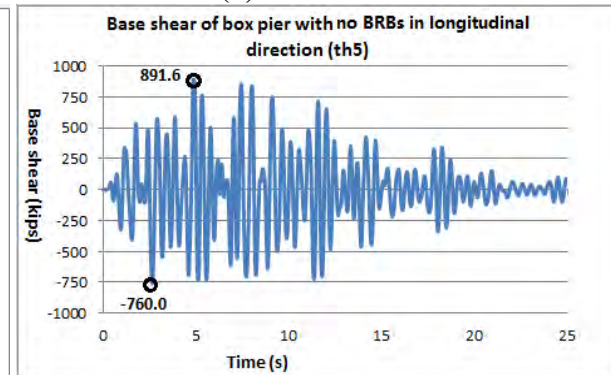
(d)

Figure 5-10 Base shear demands of the box-pier bents under ground motion TH5

138
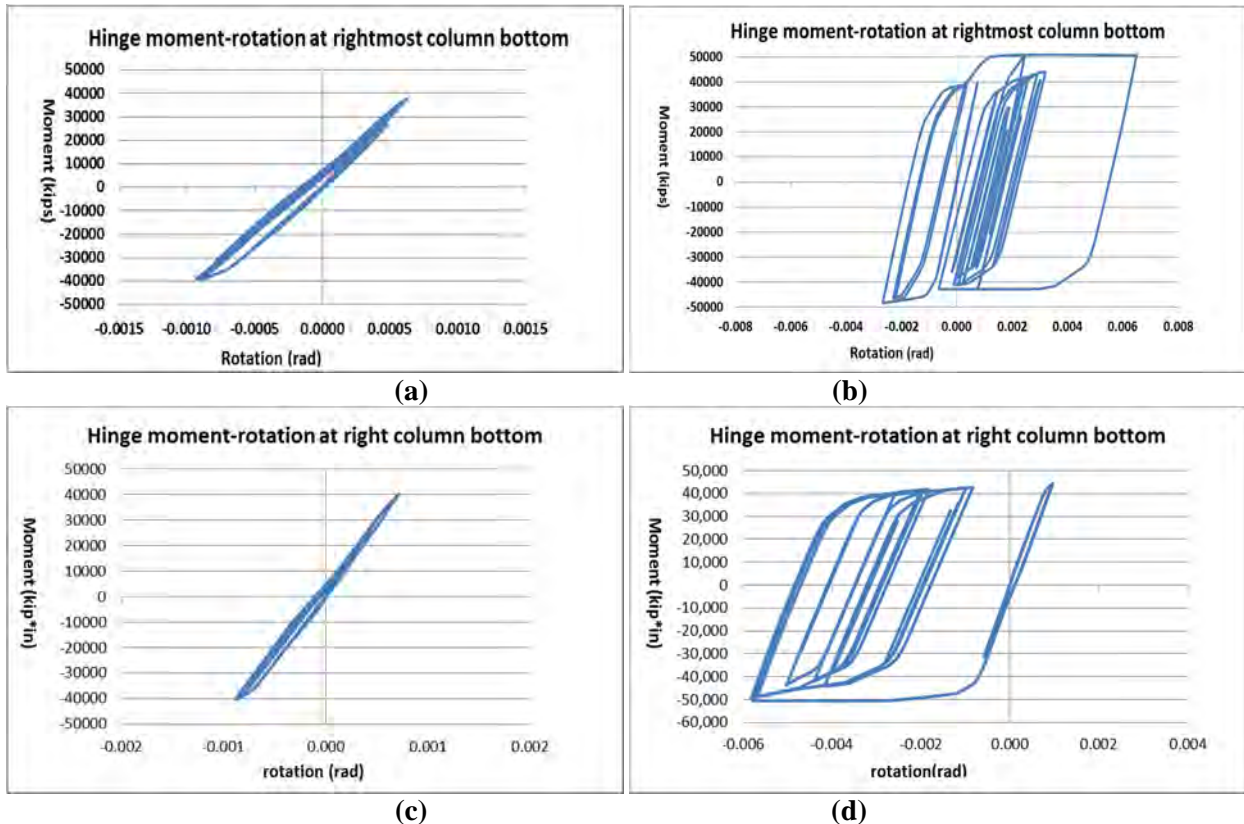
Figure 5-11 Hinge behaviors at bottom of the rightmost column of the box-pier bent: (a) transverse with BRB, (b) transverse no BRB, (c) longitudinal with BRB and (d) longitudinal no BRB

The hinge behaviors in the transverse box-pier bent with and without BRBs are shown in Figs 5-12 (a) and (b). The maximum rotation of the hinge is 0.0009 rad, which is only about 14% of the no-BRB case which has a 0.0065 rad maximum rotation. For the box-pier bent with and without BRBs in the longitudinal direction, the hinge behaviors at bottom of the rightmost column are shown in Figs 5-12 (c) and (d). The maximum rotation of the hinge is 0.0017 rad, which is only about 20% of the no-BRB case, which has a 0.0085 rad maximum rotation. Note that, from Fig. 5-12, the yield rotation for the column (under its specific axial loads) is graphically estimated to be approximately 0.0006 rad. The slight amount of yielding that develops in the column is deemed acceptable for the box-pier bent with BRB in both directions. Note that the column hinge behaviors were obtained for the bents analyzed independently for both transverse and longitudinal directions, and the rotation could be bigger if the whole box-pier bent was applied with orthogonal ground motions simultaneously in both directions.

Fig.5-12 shows the hinge axial force-deformation behavior for the four BRBs located between the left two columns in the transverse direction box-pier model. The BRBs between the right two columns have similar behaviors. For the box-pier bent in the longitudinal direction, the axial force-deformation plots

139

are shown in Fig. 5-13. In both directions, the BRBs did not yield to the same extent. The middle two BRBs have developed more ductility than the top and bottom ones. Note that a compressive strength of 332 kips and tensile strength of 299 kips (after strain hardening) developed in the BRBs at maximum ductility of 15 and 12.5, respectively, for the box-pier bent in the transverse and longitudinal direction, respectively.

(a)   (b)

(c)   (d)
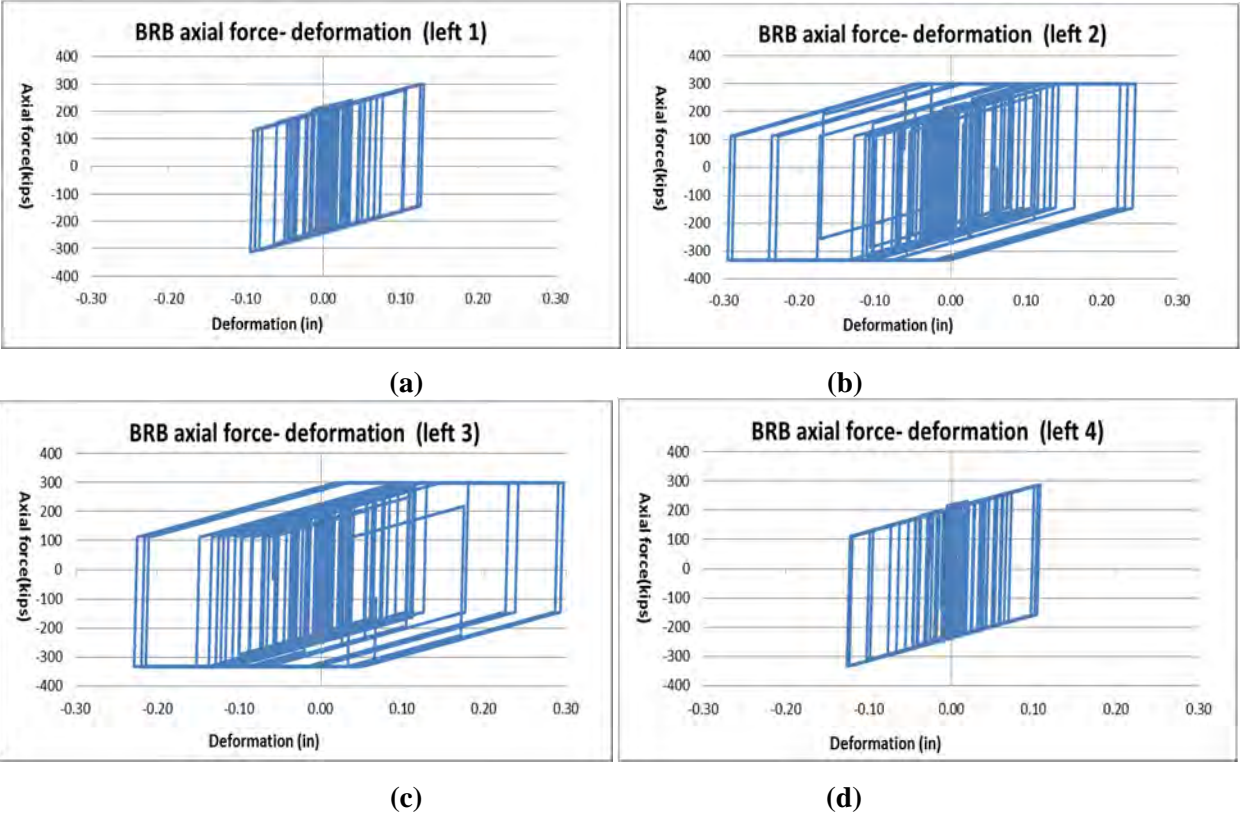
Figure 5-12 BRB hinge axial force-deformation plot for the box-pier bridge bent in the transverse direction (between left two columns, numbered from 1 to 4 top to bottom)
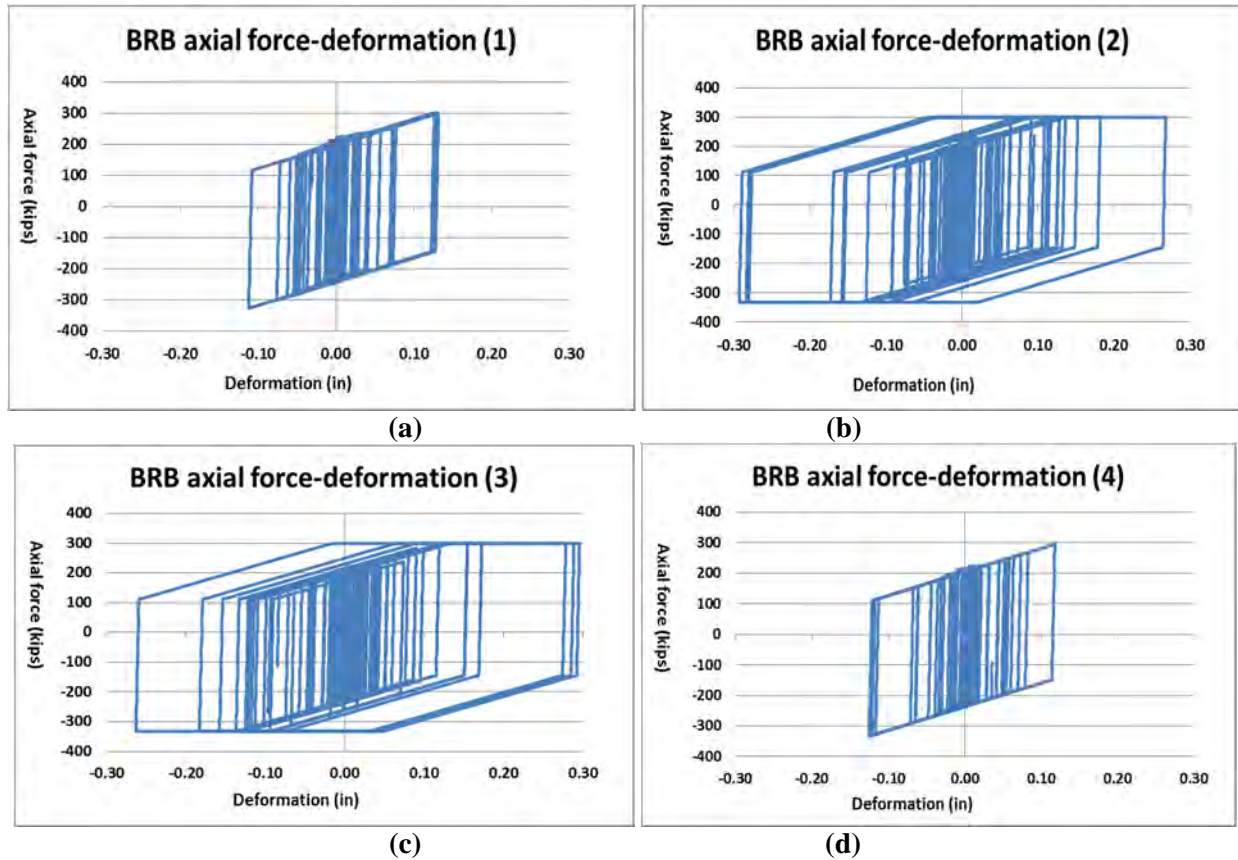
Figure 5-13 BRB hinge axial force-deformation plot for the box-pier bridge bent in the longitudinal direction (numbered from 1 to 4 top to bottom)

5.3.3 Verification with SDOF Nonlinear Time History Analysis

Vargas and Bruneau (2006a, 2006b) described the Structural Fuse (SF) concept in a parametric formulation, considering the behavior of nonlinear Single Degree of Freedom (SDOF) systems subjected to synthetic ground motions. A systematic and simplified design procedure was developed to achieve and implement the SF concept in generic buildings, in a way that ensure that damage only occurs in disposable structural elements. The procedure, intended to eliminate the need for complex analyses, relied on the use of regions of admissible solutions for the SF concept, pre-determined using nonlinear time history analyses. Response of a Single Degree of Freedom (SDOF) system with structural fuses was presented in terms of normalized parameters, as shown in Fig. 5-14. These dimensionless charts are normalized with respect to a number of key parameters, namely, the stiffness ratio α (equal to the ratio between the frame stiffness K_f and the total initial stiffness K_t), maximum displacement ductility ratio μ_{max} (i.e., the ratio of the frame yielding displacement Δ_{yf} and the fuse yielding displacement Δ_{yb}),

frame ductility μ_f, fuse ductility μ, and the strength-ratio η defined as the ratio of the yielding strength of the system V_y over the maximum ground force applied during the ground motion $m\ddot{u}_{gmax}$.
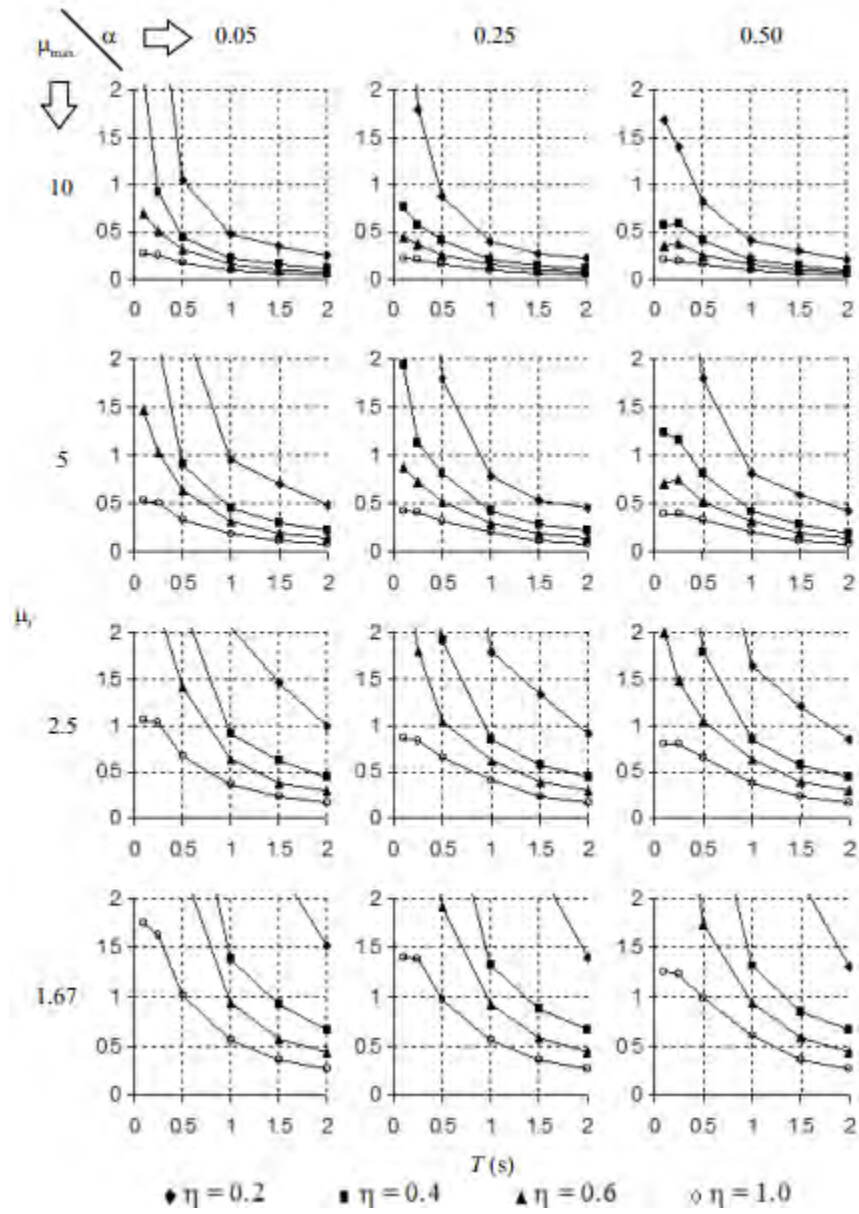
(a)
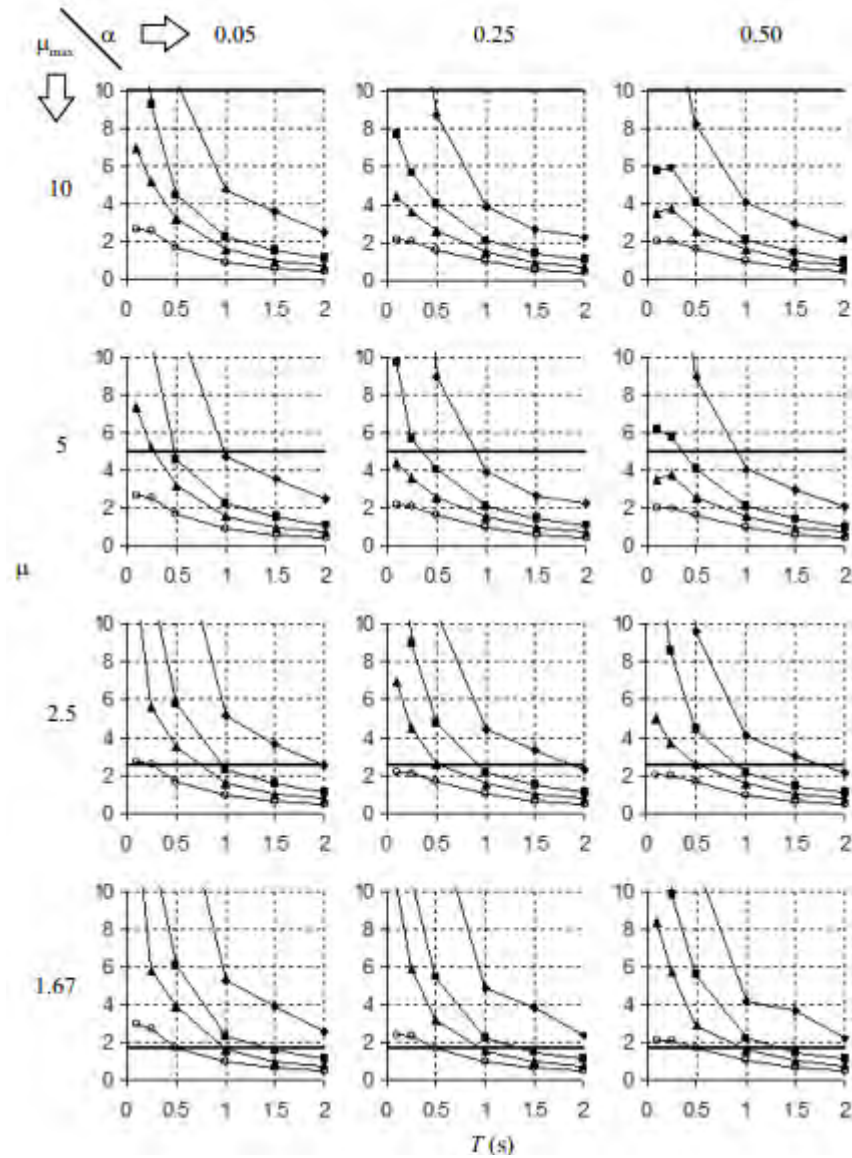
(b)

Figure 5-14 Nonlinear time history analysis response plots of a Single Degree of Freedom (SDOF) system with structural fuses

Referring to Section 3 for the two-CFT-column bent with BRBs systems considered, the period is 0.19 second. The stiffness ratio α, the maximum displacement ductility ratio μ_{max} and the yielding strength of the system V_y are:

$$\alpha = \frac{K_f}{K_t} = 0.231 \tag{5.1}$$

$$\mu_{max} = \frac{\Delta_{yf}}{\Delta_{yb}} = 10.29 \tag{5.2}$$

$$V_y = (K_f + K_b)\Delta_y = 912.18 \text{ kips} \tag{5.3}$$

143

Table 5-7 shows the strength ratio α , the frame ductility μ_f and the fuse ductility μ ,under for the nine ground motions considered for the two-CFT-column bents with BRBs.

Table 5-7 Strength ratios of the two-CFT-column bent with BRBs under the nine ground motions

		TH1	TH2	TH3	TH4	TH5	TH6	TH7	TH8	TH9	Ave
$\ddot{\mu}_{gmax}$ (in/s²)		117.3	118.6	110.4	145.7	117.5	129.7	107.4	114.4	113.5	119.4
η		0.25	0.25	0.27	0.20	0.25	0.23	0.28	0.26	0.26	0.25
Single BRB	μ_f	1.53	1.52	1.54	1.50	1.58	1.73	1.38	1.78	1.33	1.54
	μ	15.72	15.59	15.83	15.42	16.29	17.81	14.23	18.29	13.68	15.87
Chevron BRBs	μ_f	1.57	1.58	1.58	1.57	1.60	1.70	1.47	1.83	1.41	1.59
	μ	16.18	16.28	16.26	16.18	16.50	17.51	15.18	18.79	14.49	16.37

With the stiffness ratio α of 0.23 and the maximum displacement ductility ratio μ_{max} of 10.3, the charts in Fig. 5-14 can be consulted to obtain an estimate of expected response. Note that the closest SDOF system corresponding to the two-CFT-column bent with BRBs would be the one whose behavior is represented by the second chart in the first row of Fig. 5-14. Here, the average strength ratio η for the bridge bents with BRBs is 0.25, i.e., between 0.2 and 0.4 (which would require interpolation). The frame ductility μ_f of 1.54 for the single inclined BRB case and 1.59 for the inverted-V chevron BRBs case are both between the 0.65 and 2.0 cases in Fig. 5-14 (a). And it is hard to verify if the previously calculated fuse ductility μ of 15.87 for the single inclined BRB case and 16.37 for the inverted-V chevron BRBs case can be predicted by the data in Fig. 5-14 (b), since the value to be read would be out of range.

The second case considered in this section is the box-pier bent. The period of the box-pier bent with BRBs is 0.23 second. The stiffness ratio α, the maximum displacement ductility ratio μ_{max} and the yielding strength of the system V_y are:

$$\alpha = \frac{K_f}{K_t} = 0.25 \tag{5.4}$$

$$\mu_{max} = \frac{\Delta_{yf}}{\Delta_{yb}} = 10.41 \tag{5.5}$$

$$V_y = (K_f + K_b)\Delta_y = 901.93 \text{ kips} \tag{5.6}$$

Table 5-8 shows the strength ratio α , the frame ductility μ_f and the fuse ductility μ ,under for the nine ground motions considered for the box-pier bents with BRBs in both transverse and longitudinal directions.

Table 5-8 Strength ratios of the box-pier bents with BRBs under the nine ground motions

		TH1	TH2	TH3	TH4	TH5	TH6	TH7	TH8	TH9	Ave
$\ddot{\mu}_{gmax}$ (in/s^2)		117.3	118.6	110.4	145.7	117.5	129.7	107.4	114.4	113.5	119.4
η		0.25	0.25	0.26	0.20	0.25	0.23	0.27	0.26	0.26	0.25
Transverse direction	μ_f	1.25	1.30	1.33	1.24	1.21	1.24	1.18	1.52	1.00	1.25
	μ	13.01	13.56	13.83	12.88	12.58	12.95	12.29	15.85	10.41	13.04
Longitudinal direction	μ_f	1.62	1.54	1.42	1.38	1.43	1.58	1.40	1.76	1.32	1.49
	μ	16.81	16.00	14.74	14.38	14.86	16.48	14.61	18.30	13.76	15.55

With the stiffness ratio α of 0.25 and the maximum displacement ductility ratio μ_{max} of 10.4, the closest SDOF system corresponding to the box-pier bent with BRBs would also be the one whose behavior is represented by the second chart in the first row of Fig. 5-14. Here, the average strength ratio η for the bridge bents with BRBs is 0.25, i.e., between 0.2 and 0.4 (which would require interpolation). The frame ductility μ_f of 1.25 for the transverse direction and 1.49 for the longitudinal direction is between the 0.55 and 2.0 case in Fig. 5-14 (a). This makes it hard to verify if the previously calculated fuse ductility μ of 13.04 for the transverse direction and 15.55 for the longitudinal direction can be predicted by the data in Fig. 5-14 (b), since the value is out of the range.

Note that the above examples illustrate that, in some instances, structural fuse implementations in bridges could have combination of parameters that fall outside the range covered in Fig. 5-14. This could be even more so for bridge with different fuse and column designs, or subjected to different severity of earthquake ground motions. Therefore, a broader parametric study of SDOF structures with fuses may be required to obtain charts to predict the behavior of bridge systems with fuses.

5.4   Bridge performance comparison

5.4.1 Displacement

The displacement demand at top of the column obtained by the design hand calculation (yielding displacement of the column), the elastic response spectrum analysis, and the inelastic nonlinear time history analysis, are compared in Table 5-9. Due to the smaller stiffness in the SAP2000 model for the columns (their restraint being less than for the fixed end condition assumed in the design hand calculation), the elastic displacement demand in the response spectrum analysis is larger than the design hand calculation.

The averages of the maximum displacements in positive and negative in-plane transverse directions of the two-CFT-column bents and both directions of the box-pier bents, with and without BRBs, resulting from the nine ground motions are presented in Table 5-9. Results show that in all cases, displacements of the bents with BRBs have average maximum absolute lateral displacements less than 50% of the values for cases without BRBs. The design displacements and the elastic displacement demands from response spectrum analyses are also shown for comparison. Note that both the design displacement and displacement demands from response analyses of the bare bent is larger than that of the bent with BRBs cases because of less lateral stiffness and larger period.

Table 5-9 Displacement of bare bent and bent with BRBs for different systems in theoretical design, response spectrum analysis, and nonlinear time history analysis

Case	Design Target Displacement			Response Spectrum Analysis			Nonlinear Time History		
	Bare bent	Bent with BRBS	Dif.	Bare bent	Bent with BRBs	Dif.	Bare bent	Bent with BRBs	Dif.
Two-CFT-column bent with single inclined BRB	2.30"	0.71"	69.2%	2.81"	0.94"	66.6%	2.14"	1.13"	47.2%
Two-CFT-column bent with inverted-V BRBs	2.30"	0.71"	69.2%	2.81"	0.81"	71.2%	2.14"	1.10"	48.8%
Transverse box-pier bent	2.85"	1.05"	63.2%	3.13"	1.28"	59.1%	2.62"	1.32"	49.7%
Longitudinal box-pier bent	2.85"	1.05"	63.2%	3.06"	1.17"	61.8%	2.51"	1.26"	49.7%

The inelastic displacement demands of the bridge bents are larger than the elastic response spectrum demand. This is due to the fact that design was based on the "equal displacement" assumption (i.e., assuming that displacements resulting from inelastic analysis are approximately equal to those obtained from a linear elastic analysis). This is usually a reasonable assumption, except for short period structures for which it is not conservative (AASHTO Seismic Design Specification, 2011). Recognizing this exception, a modification factor R_d is typically prescribed to magnify the maximum elastic displacements of short-period structures and estimate the actual maximum inelastic response. R_d as defined by MCEER-ATC 49 (2003), is equal to:

$$R_d = \frac{\Delta_{inelastic}}{\Delta_{elastic}} \tag{5.7}$$

The modification factor R_d when the bridge period is smaller than $1.25T_s$ is given by Equation 5.8, from the MCEER-ATC 49 (similar to AASHTO 2011):

$$R_d = \left(1 - \frac{1}{R}\right)\frac{1.25T_s}{T} + \frac{1}{R} \geq 1 \tag{5.8}$$

where: T is the period of the bridge bent; T_s is the period at the end of the acceleration response spectrum plateau; R is the ratio between design elastic lateral force and the lateral strength of the bent, which is conceptually similar to the maximum local displacement ductility demand, μ_D, in AASHTO (2011) (conservatively, the upper limits for μ_D in AASHTO could have been used here instead of the actual value of this ratio, but this would have resulted in larger values of R_d).
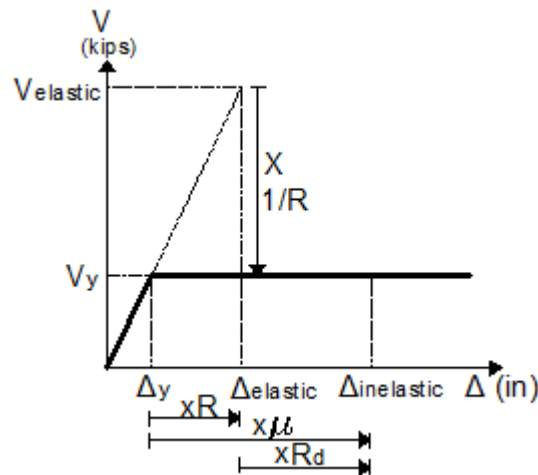
Figure 5-15 Lateral strength vs displacement plot for trilinear system

The ratio R_{design} in Table 5-10 is the ratio between the design elastic force demand and the design lateral strength of the bent as assumed in the design bilinear pushover curve, as illustrated in Fig.5-15. The corresponding value R_d calculated from Equation 5.8, using T_s of 0.35s from the acceleration response spectrum is shown in Fig. 4-10 and the theoretical fundamental periods T_{design}. These actual R_d values from analyses are smaller than the value predicted by Equation 5.8, which indicates that Equation 5.8 is conservative for this particular application. The validation of Equation 21 for the trilinear system as shown in Fig. 3-1 for the total bent system remains to be investigated, since it has been originally developed based on nonlinear time history results of bilinear system.

Table 5-10 Elastic and inelastic base shear demand ratio and displacement amplification factor

Bridge bent case	R_{design}	R_d (equation)	T_{design} (s)	R_d (analysis)
Two-CFT-Column bent with single inclined BRB	2.92	1.85	0.19	1.47
Two-CFT-Column bent with inverted-V BRBs	2.92	1.85	0.19	1.49
Transverse box-pier bent with BRBs	2.84	1.57	0.232	1.5
Longitudinal box-pier bent with BRBs	2.84	1.57	0.232	1.5

5.4.2 Base shear force

The base shear forces for the frame base shear from the bent pushover analysis at the target elastic displacement of response spectrum analysis, as well as the base shear demand from elastic response spectrum analysis and the inelastic nonlinear time history analyses, are compared in Table 5-11.

Table 5-11 Base shear force of bare bent and bent with BRBs for different systems in theoretical design calculation, pushover analyses, and nonlinear time history analysis

Case	Design Calculation			Pushover			Nonlinear Time History		
	Bare Bent	Bent with BRBs	Dif.	Bare Bent	Bent with BRBs	Dif.	Bare Bent	Bent with BRBs	Dif.
Two-CFT-column bent with single inclined BRB	2169	2994	38%	3178	3600	13.3%	3246	3917	20.7%
Two-CFT-column bent with inverted-V BRBs	2169	2989	38%	3175	3258	2.6%	3246	3905	20.3%
Transverse box-pier bent	1169	1654	41%	1709	1897	11%	1751	1930	10.2%
Longitudinal box-pier bent	585	827	41%	864	902	4.4%	882	951	7.8%

SECTION 6

'''''''''''''''STUDY ON BRBS' CONNECTION TO BRIDGE BENT

6.1   General

For structural fuse connections to RC columns, three types of connections have already been briefly introduced in Section 3 (Section 3.4). In this Section, primary focus is on connection to CFT columns by welding of the gusset plate of the BRB directly to the steel shell of a CFT column. Analytical and experimental studies have been conducted here for this type of connection, and this work is presented in Sections 6.1 to 6.4. A "Ring" model was first investigated in Section 6.2. In Section 6.2.2, theoretical equations for this connection strength were developed based on the Ring model. In Section 6.2.3, the Ring model of the branch plate's connection to the CFT shell was built in SAP2000 using beam elements, to predict the design strength of the connections. Finite element Ring models were built in Abaqus *Version 6.14.*, to compare with the SAP2000 analytical results, and findings are presented in Section 6.2.4. Section 6.3 describes tests undertaken on branch plates welded to CFT to investigate the behavior and strength of this connection. Quasi-static monotonic and cyclic tests were performed on specimens having various CHS diameters. Finite element models of the specimens were built in Abaqus and analysis results were compared with the test results. Conclusions and design recommendations are made for the design strength of gusset plates welded to CHS columns from a seismic application perspective. In Section 6.4, a design example is provided for the BRB's connections using gusset plates welded to CFT columns. Information on the design of alternative BRB's connections using headed studs and anchor rods are provided in Sections 6.5 and 6.6, respectively. A summary of findings for the connection design details investigated is presented in Section 6.7.

6.2   Study of Ring Model

6.2.1   General

Recall that, in Section 3, two governing limit states were considered in calculating the strength of a plate connected to a concrete-filled CHS, namely: CHS plastification (with large axial and flexural plastic deformations) and CHS punching shear. The suggested equations for punching shear are provided by Wardenier (2008) and Voth (2010) in Equation 3.8 and 3.9. Here, focus is on the strength of the CHS connection at first-yielding of the CHS, for reasons that become apparent in Section 6.3.

"

When applying a tension force to the branch plate welded to the CHS, the branch plate will produce a three-dimensional pattern of deformation locally around its connection to the CHS, as shown in Fig. 6-1. In that figure, the effective length B_1 is meant to represent the length where the CHS is separating from its infilled concrete. To obtain the strength of that connection, a complete analytical yield line model based on the connection's plastic behavior is difficult to formulate due to the curved connection geometry. In such cases in the past, the connection geometry has been simplified by using the "Ring" model, which replaces the three dimensional connection surfaces and curved yield lines with a two dimensional ring. Calculations of connection strengths for CHS based on the Ring model were first established by Togo (1967). Later, the derivation of the connection capacity was refined by Mäkeläinen (1988), Paul (1992), and presented by Van der Vegte (1995) based on the equations of equilibriums of the Ring model when plastic hinges developed along the ring.
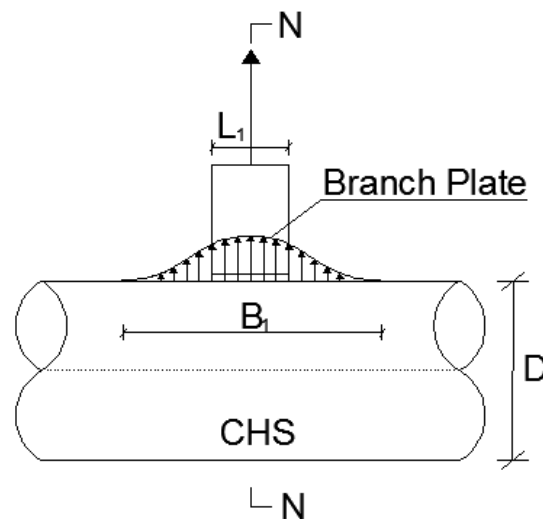
Figure 6-1 Branch plate connection to CHS under tensile force

The same methodology is adopted here by considering a unit width CHS, as shown in Fig. 6-2, which is obtained from the section cut N-N in Fig. 6-1. Note that this Ring model neglects the possible contribution of yield lines extending along the steel shell beyond the end of the branch plate, which is slightly conservative for long branch plates. This Ring model could be representative of the case when a gusset plate applied along the entire length of the CHS is uniformly loaded in tension. Note that the Ring model also neglects the presence of axial stresses simultaneously acting along the longitudinal axis of the CHS (in the case when the CFT column is subjected to gravity load of the bridge). This is a reasonable assumption provided that the steel shell of the CFT column is not near yielding in that longitudinal direction (based on the von Mises yield criteria).

150
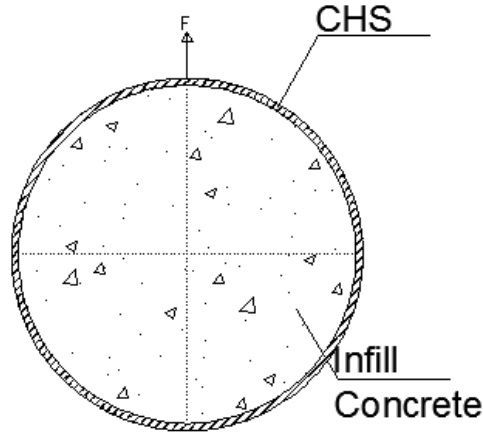
Figure 6-2 Ring model from N-N section cut (from Fig.6-1)

Section 6.2.2 presents theoretical calculated first-yield strength determined based on the Ring model. The behavior of the analytical Ring models in SAP2000 and Abaqus are studied in Sections 6.2.3 and 6.2.4, respectively, where the comparisons of the results obtained from analytical and numerical models of the Ring are provided. Sections 6.2.3 and 6.2.4 presents results for a Ring model having a specific size, whereas more general comparisons made between the theoretical calculations and the analytical results are provided in Section 6.2.5 for CHS sizes corresponding to the specimens tested (for which results are presented later this Section). Note that the axial load acting on the steel shell of the CFT column may affect the analytical and experimental results obtained in this Section. The axial load and the pulling force coming from the gusset plate needs to be considered together under different loading conditions to access the connections' behavior, which was out of the scope of work presented here.

6.2.2   Theoretical First-Yield Strength and Deformation Calculation

A simple derivation of stresses under flexure using the Ring model is considered here based on the classic mechanics of material solution for curved beams. For this derivation, the curved beam shown in Fig. 6-3 is subjected to bending moments. To establish the relationship between the stress in a single fiber in the cross section related to the corresponding moment applied at that section, the section c-b in Fig.6-3 is used. Section c-b is at an angle of $d\theta$, from the centerline of the ring. The cross section which is a plane before bending remains a plane after bending. The neutral axis is at a line of zero stress and strain.

Three radii are marked in Fig. 6-3, extending from the center of the curvature of the member. They are listed individually below:

$\bar{r}$ is the location of the centroid of the cross sectional area, which is $\frac{R_1+R_2}{2}$;

R is the location of the neutral axis;

r is the arbitrary point of area element dA on the cross section
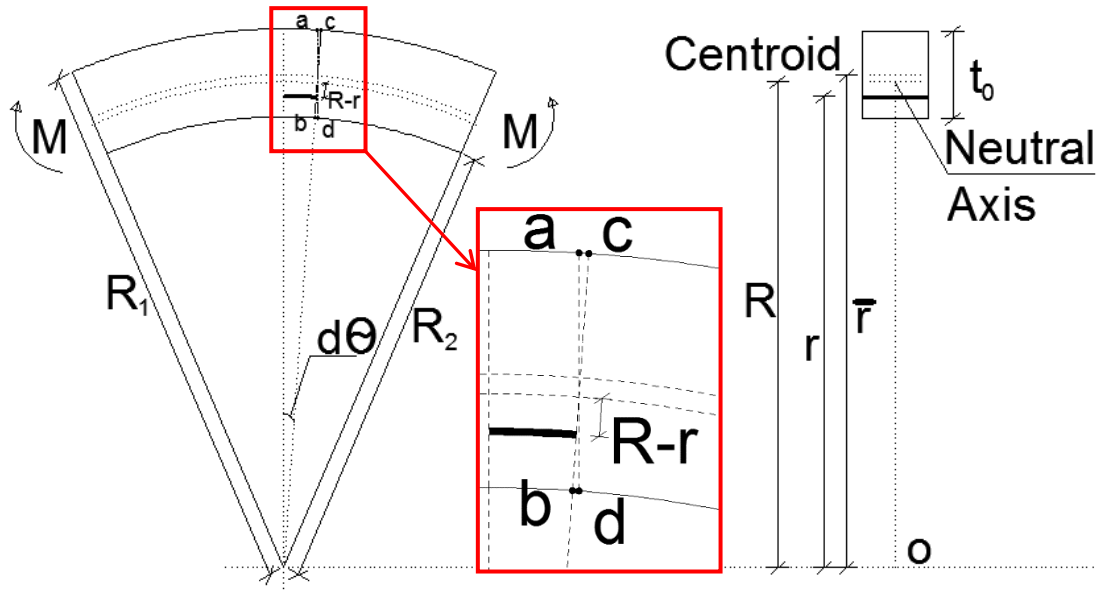
Figure 6-3 Section analysis of curved beam under pure moment

The area element dA in section c-b corresponds to an angle of $d\theta$. The arbitrary fiber at location r has the original length of $rd\theta$. The distance of the fiber to the neutral axis is *R-r*. The framed zoomed view in Fig.6-3 shows that after the cross section rotates by an angle of $\delta\theta$, section b-c changes to section a-d. The length change of the same fiber is (R-r) $\delta\theta$.

The normal strain in the fiber is therefore

$$\varepsilon = \frac{(R - r)\, \delta\theta}{rd\theta} \tag{6.1}$$

The normal stress in the fiber is

$$\sigma = E\frac{(R - r)\, \delta\theta}{rd\theta} \tag{6.2}$$

Force equilibrium equations can be used at location R (radius of the neutral axis), such that:

$$\int dF = \int \sigma dA = E\frac{\delta\theta}{d\theta}\left(R\int \frac{dA}{r} - \int dA\right) = 0 \tag{6.3}$$

Therefore:

$$R = \left(\int dA\right)/(\int \frac{dA}{r}) = A/(\int \frac{dA}{r}) = \frac{t_0}{\ln(R_1/R_2)} \tag{6.4}$$

Assume *y* is the distance of a fiber to the neutral axis, then the value of y would be expressed as:

$$y = R - r \tag{6.5}$$

The moment at section a-d is therefore

$$M = \int \delta M = \int y\sigma \delta A = E\frac{\delta\theta}{d\theta}\int (R-r)\frac{R-r}{r}\delta A = E\frac{\delta\theta}{d\theta}\left(R^2\int\frac{dA}{r} - 2R\int dA + \int r dA\right)$$

$$= E\frac{\delta\theta}{d\theta}A(\bar{r}-R) \tag{6.6}$$

The stress in the fiber at location *y* is

$$\sigma = \frac{Md\theta}{EA(\bar{r}-R)\delta\theta}\frac{E(R-r)\,\delta\theta}{rd\theta} = \frac{M(R-r)}{Ar(\bar{r}-R)} = \frac{My}{A(R-y)e} \tag{6.7}$$

where

$$e = \bar{r} - R = \frac{R_1 + R_2}{2} - \frac{t_0}{\ln(R_1/R_2)}$$

Note that the above equations to find the neutral axis and calculate the stress resulting from the moment applied on a curved beam can be found in books related to mechanics of materials (for example, in Hibbeler, 2011). These results can be expanded as follows:

When there is an axial force, *F*, present, the axial stress can be superposed to the bending stress in Equation 6.7, and the resulting stress in the fiber becomes:

$$\sigma = \frac{F}{A} + \frac{My}{A(R-y)e} \tag{6.8}$$

The extreme fiber is the cross-section point farthest from the neutral axis, at a distance of:

$$y = \frac{t_0}{2} + \frac{R_1 + R_2}{2} - \frac{t_0}{\ln(R_1/R_2)} \tag{6.9}$$

Based on observations from the analyses performed on the SAP2000 model (presented in Section 6.2.3), and as intuitively expected, the moment along the entire Ring model only exists locally where the load is applied because the infilled concrete prevents deformations of the ring beyond a certain distance from the applied load. Therefore, the entire Ring model in Fig. 6-2 can be simplified to the half Ring model shown in Fig. 6-4a (the concrete infill is not shown in that figure). In that model, flexural deformations (and moment) in the ring only exist between point C and C', which are located at an angle β from the centerline. This angle is related to the ratio of D/t_0 of the CHS, per a relationship that will be studied in

153

Section 6.2.3.3 based on results from SAP2000 analyses. Fig. 6-4b shows a free body diagram of the ring from the centerline to point C' in Fig. 6-4a.

(a)
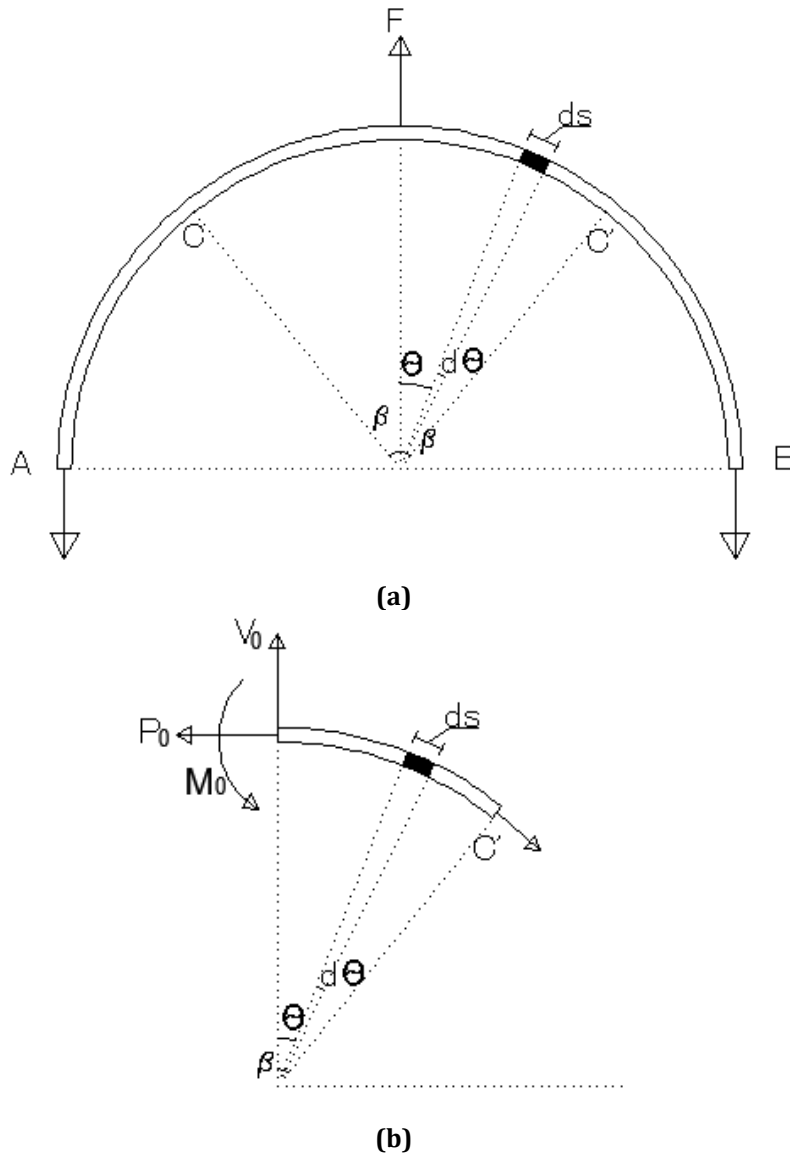
(b)
Figure 6-4 Equilibrium in the Ring model: (a) half ring model; (b) segment with developed moment

According to Castigliano's theorem, when a body is elastically deflected by any combination of loads, the deflection at any point and in any direction is equal to the partial derivative of strain energy with respect to a load located at that point and acting in that direction. Stored strain energy for the member from A to B in Fig 6-4a is

$$U = \int_{-\frac{\pi}{2}}^{\frac{\pi}{2}} [P^2 L/(2EA) + M^2 L/(2EI) + 3V^2 L/(5GA)] ds \qquad (6.10)$$

From the free-body diagram in Fig. 6-4b, the bending moment at any point located at angle θ is

154

$$M = M_0 + P_0\bar{r}(1 - \cos\theta) - V_0\bar{r}\sin\theta \qquad (6.11)$$

Given that there would be no relative rotation between point A and B, because the filling concrete would prevent such rotation, therefore, according to Castigliano's theorem,

$$\frac{\partial U}{\partial M_0} = \int_{-\frac{\pi}{2}}^{\frac{\pi}{2}} \frac{M}{EI} \frac{\partial M}{\partial M_0} ds = 0 \qquad (6.12)$$

Knowing that between the arch of AC and BC' (within the angle of β from the centerline), the moment is zero because of the filling concrete, and the following equation can be obtained from taking the derivative of Equation 6.11.

$$\frac{\partial M}{\partial M_0} = 1 \qquad (6.13)$$

By inputting Equation 6.13 into Equation 6.12, Equation 6.12 can be derived as:

$$\frac{\partial U}{\partial M_0} = \int_{-\beta}^{\beta} \frac{1}{EI}(M_0 + P_0\bar{r}(1 - \cos\theta) - V_0\bar{r}\sin\theta)ds = 0 \qquad (6.14)$$

Since

$$ds = \bar{r}d\theta$$

The integration in Equation 6.14 gives

$$(M_0 + P_0\bar{r})\beta - P_0\bar{r}\sin\beta = 0$$

Therefore, the moment at the point along the ring where the load is applied is

$$M_0 = P_0\bar{r}(\frac{\sin\beta}{\beta} - 1) \qquad (6.15)$$

The shear force V_0 can be obtained from Equation 6.11, when M is zero at point C as

$$V_0 = \frac{M_0 + P_0\bar{r}(1 - \cos\theta)}{\bar{r}\sin\theta} \qquad (6.16)$$

The pulling force F is

$$F = 2V_0 \qquad (6.17)$$

When the flexural first-yielding happens at the point where the pulling force F is applied, the extreme fiber in the section reaches the yield stress of the steel material. Using Equations 6.8 and 6.15, the moment and axial force corresponding to that condition can be obtained for a given angle β. The shear force V_0 and puling force F can also be calculated using Equations 6.16 and 6.17.

To calculate the deformation at the load application point, the illustration in Fig 6-5 is used. Due to the moment M on *ds* at point D only in Fig.6-5, the length OD is rotated by an angle

$$d\gamma = \frac{Mds}{EI} \tag{6.18}$$

Point O moved to O' and the length OO' is

$$OO' = ODd\gamma \tag{6.19}$$
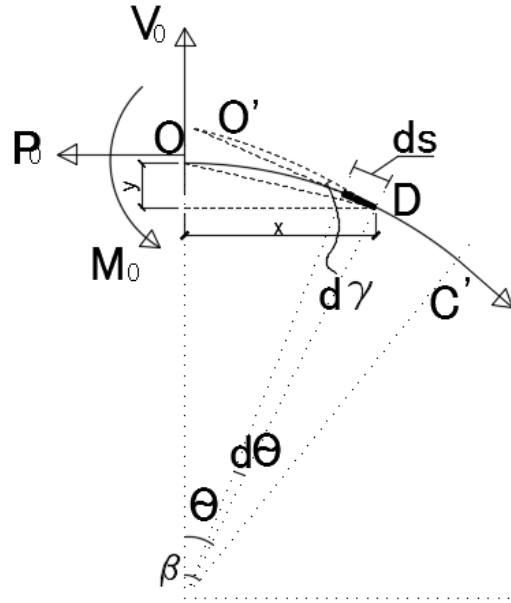
Figure 6-5 Contribution to deformation at load application point due to moment acting at section ds, illustrated for a segment along the curved beam

The vertical deflection at point O due to the moment at point D is

$$OO'\cos\theta = OD\cos\theta d\gamma = xd\gamma = \frac{Mxds}{EI} = \frac{Mx\bar{r}}{EI}d\theta \tag{6.20}$$

The moment between C'B along the ring in Fig. 6-4a is zero. Therefore, due to the bending of all the ds along the curve of OC', the vertical deflection at point O is integrated over the curved length of OC':

$$d_y = \int_0^\beta \frac{Mx\bar{r}}{EI}d\theta = \int_0^\beta \frac{M\bar{r}^2}{EI}\sin\theta d\theta \tag{6.21}$$

After inputting Equation 6.11 into Equation 6.21, the vertical deflection at point O becomes

$$d_y = \int_0^\beta \frac{Mx\bar{r}}{EI}d\theta = \frac{\bar{r}^2}{EI}\int_0^\beta [M_0 + P_0\bar{r}(1-\cos\theta) - V_0\bar{r}\sin\theta]\sin\theta d\theta \tag{6.22}$$

156

6.2.3 SAP2000 Ring Model

A SAP2000 model replicating the conditions of the CHS with infilled concrete was built to investigate the load carrying capacity of the steel shell to transfer tension loads acting perpendicularly to CFT columns. Section 6.2.3.1 introduces the modeling of the Ring model in SAP2000. The analysis of the Ring model is presented in Sections 6.2.3.2 and 6.2.3.3, using an example size of the CHS in the concrete-filled CHS tests presented in Section 6.3. In Section 6.2.3.4, observations of the location where the moment becomes zero along the perimeter of the Ring model are made based on results of analyses for CHS having various dimensions.

6.2.3.1 SAP2000 Ring Model Description

In this SAP2000 model, only half of the CHS was modeled, similarly to what is shown in Fig. 6-4a. To capture the location and sequence of plastic hinging in the CHS due to the applied tensile load, the arch was divided into multiple beam elements, as shown in Fig. 6-6. Each beam had plastic hinges assigned at each end. At the joint of each beam, a gap link was used to account for the presence of concrete resisting inward deformations of the steel tube. The gap link element was set to have zero stiffness when the gap was larger than zero, which allowed the steel shell to separate from the infilled concrete columns under tensile load. The stiffness of the gap link was set to be large (arbitrarily set to be 100,000 kips/in) when the gap closed and resisted compression, which kept the steel jacket from moving inward. The width of the section in this ring model was arbitrarily taken as 1 in (unit length).

Pushover analysis was conducted (by displacing the load application point away from the CFT surface) to determine the plastic mechanism, i.e. to capture development of plastic hinges at any location in the steel shell due to the applied tensile load. The corresponding tensile force resisted by the CFT at the development of the yielding flexural strength and plastic flexural strength at the first hinge is obtained. Note that the geometric nonlinearity setting in pushover analysis was not considered, i.e. small displacement was used, which is used to compare with the theoretical calculation results. The analytical results from the SAP2000 model considering large displacement and P-delta effect in the geometric nonlinearity are presented in Section. 6.2.3.3.

The Ring model in SAP2000 was divided into 60 beam elements as shown in Fig. 6-6. Using more beam members along the perimeter typically provides more resolution as to the possible location of plastic

hinges and actual strength of the system; with hinges located at two ends of each member in the model, results were found to converge when using 60 elements.

6.2.3.2 Example of CHS with 9.625" diameter and 0.233" thickness

The CHS of 9.625" diameter and 0.233" thickness in the concrete-filled specimen tests presented in Section 6.3 is used in this section as an example for the SAP2000 analysis performed. The diameter of the Ring model was 9.625", with a rectangular cross section of 0.233 in (thickness) by 1 in (unit length). The steel was A500 Gr.B with yield strength of 42 ksi. The bilinear stress-strain curve shown in Fig. 6-7 for that material was considered. SAP2000 beam elements were used, with fiber P-M_2-M_3 hinges at both ends of each element, to account for the interaction of axial and flexural forces in plastic hinges. The nonlinear static pushover analysis using displacement control was performed.
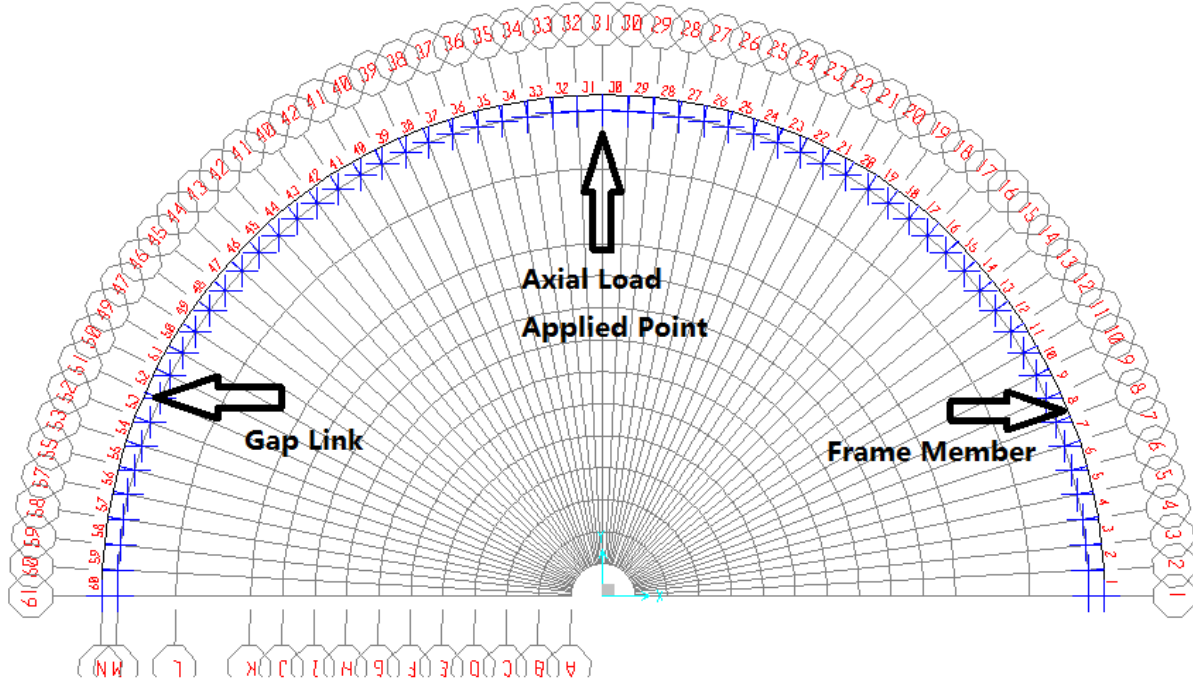
Figure 6-6 Ring model in SAP2000

ε_y	1.448E-03
ε_h	2.000E-03
ε_{su}	0.23
f_{sy}	42.
f_{su}	42.
ε_{sb}	0.24
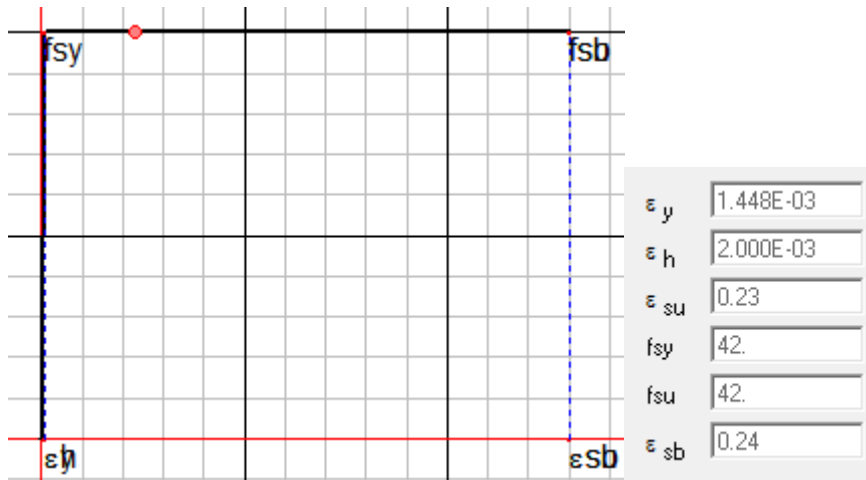
Figure 6-7 Steel stress-strain curve without the strain hardening

The force versus displacement at the load point resulting from the pushover analysis of the Ring model with 60 frame element is shown in Fig. 6-8. Since the pushover analysis is conducted by applying a displacement at the point where the tension load would be applied, the corresponding force is obtained by summing the vertical reactions for the model (labeled "base reaction" in Fig. 6-8).
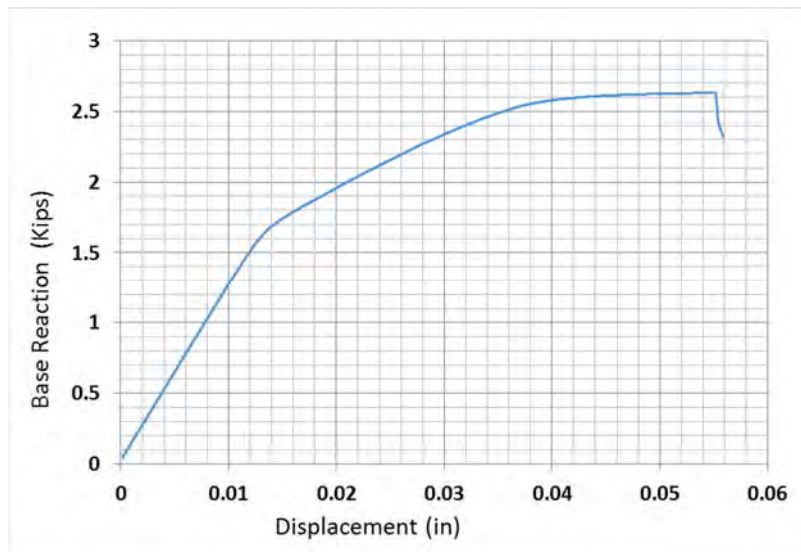
Figure 6-8 Pushover curve of the arch structure for bilinear steel material

The moment diagram shown in Fig. 6-9a corresponds to the case when the extreme fiber in the section reached the yield stress at load application point, i.e. the apex of the arch, where frame members 30 and 31 meet (frame element numbers are labeled in Fig. 6-6). Note that significant moments only developed in ten frame elements on each side from the point where the load was applied (the moment in the other frame elements is negligible). The corresponding force applied to the Ring model in Fig.6-9a is 1.045

159

kips, with a displacement at the loading point of 0.008 in when first yielding of the section happened. The force applied to the Ring model in Fig.6-9b is 1.763 kips, with a displacement at the loading point of 0.015 in, when the largest moment at the section at the load application point was reached. Note that afterwards, the moment at the apex section of the ring drops as shown in Fig. 6-11, for reasons explained later in this section. After the first plastic hinge appeared at the top where the load was applied, the next plastic hinges to develop upon increased loading occurred at the intersection of frame elements 23 and 24, and, symmetrically, at frame elements 35 and 36, as shown in Fig. 6-10. The corresponding force applied to the arch is 2.635 kips, with a displacement at the loading point of 0.045 in.

Note that the small decrease in the value of the plastic moment in the first hinge was due to moment-axial force interaction and to changes in axial forces in the arch (this phenomenon can be observed by comparing the plastic moment values in Fig. 6-9a, b and Fig. 6-10c). To illustrate this phenomenon, the moment and axial force in the first hinge were plotted in Fig. 6-11 against the displacement at the apex point where the load was applied. A decrease of the hinge moment capacity is observed to occur as the applied load increases after the section has reached its moment capacity.
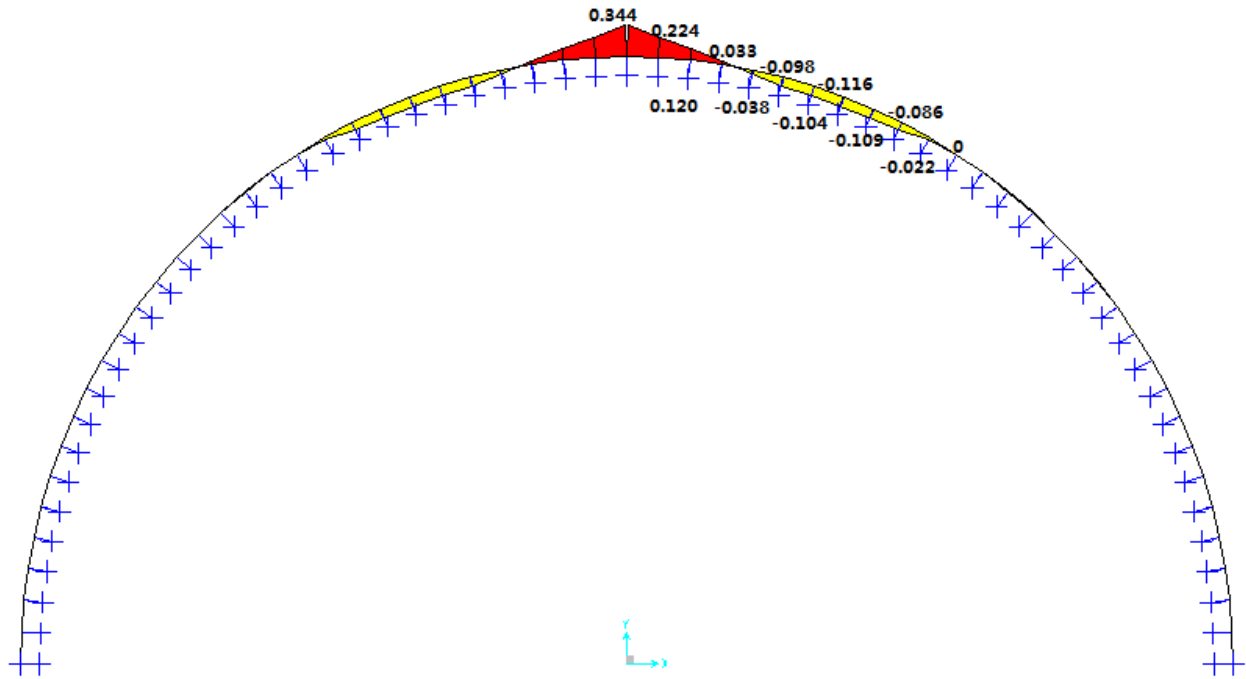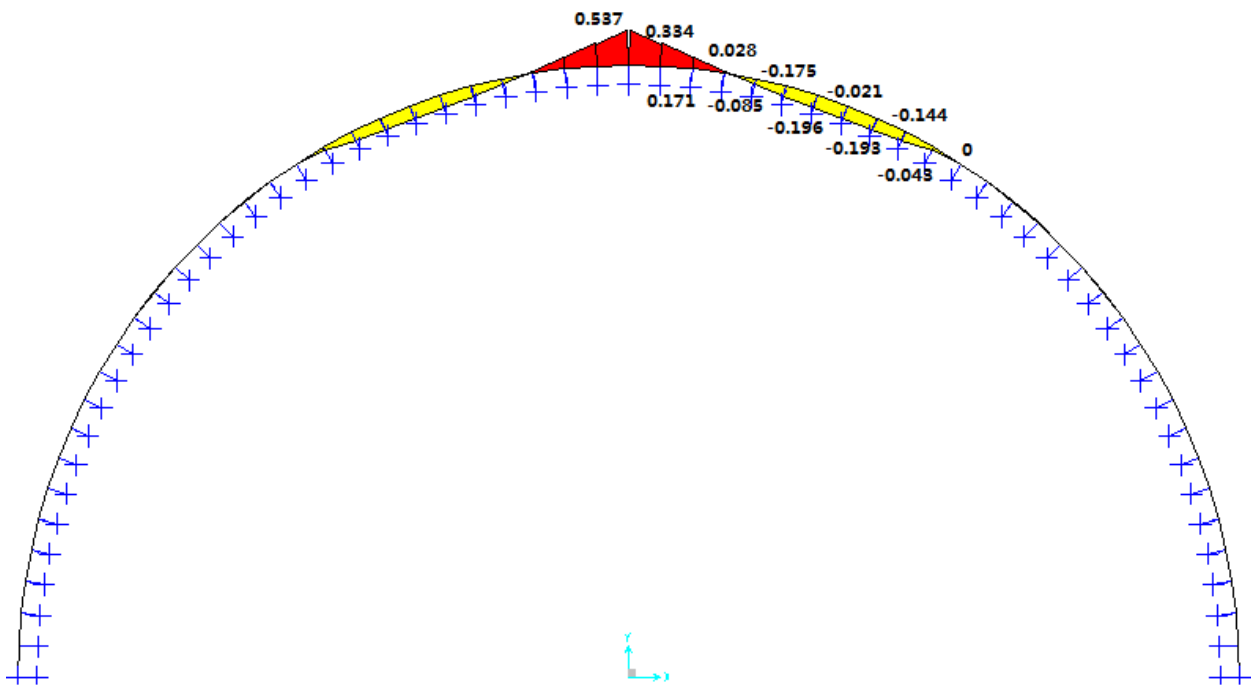
Figure 6-9 Moment diagram along the ring model: (a) the first yielding at the location of the first hinge; (b) maximum moment at the location of the first hinge
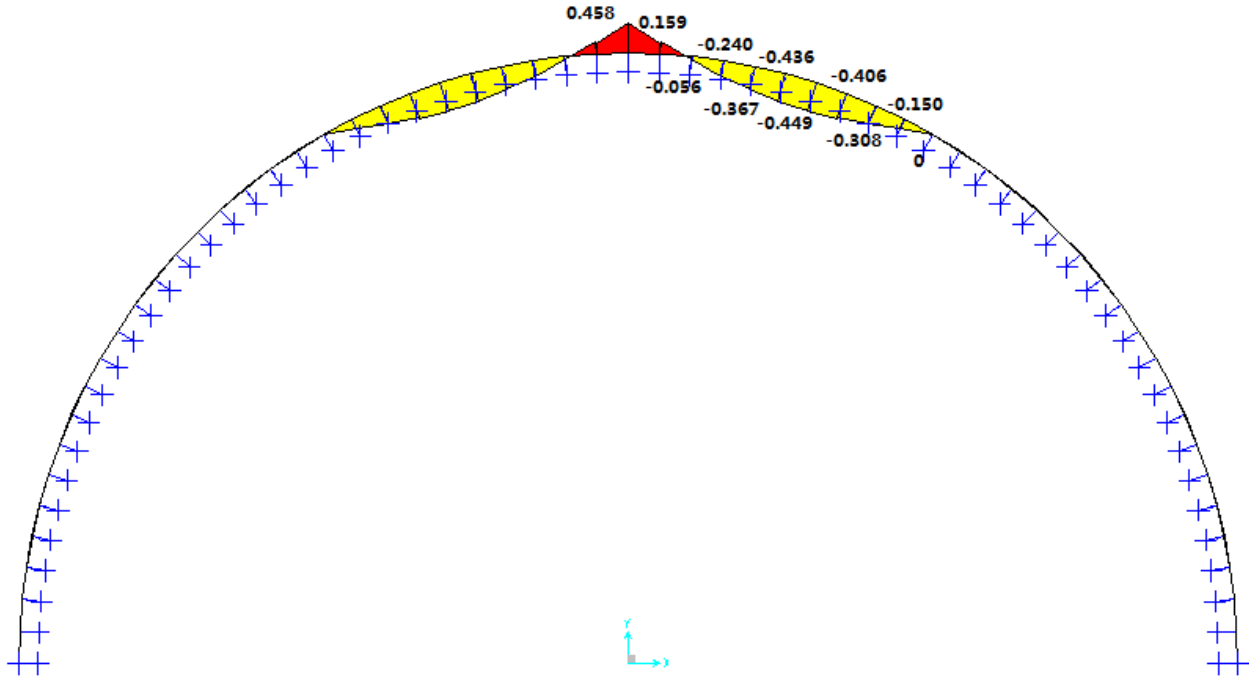
Figure 6-10 Moment diagram of the arch model corresponding to the end of the pushover analysis

The comparison of the SAP2000 Ring model and the theoretical calculations at first yielding at the location of the first hinge in Section 6.2.2 is shown in Table 6-1. Note that the angle β in Fig. 6-4 is 30 degrees, obtained from the SAP2000 model analysis.

Table 6-1 Ring model comparisons between the theoretical calculations and the SAP2000

	Moment	Axial force	Shear Force	Displacement	Strength
Theoretical	0.312	1.474	0.528	0.006	1.056
SAP2000	0.344	1.256	0.490	0.008	1.045

Note that when the plastic hinge appeared at the top, at the location where the pulling force was applied, the strength achieved corresponds to development of a plastic mechanism. Attempts were made to calculate this strength, but the results obtained for the plastic mechanism considered did not match the maximum strength obtained from the SAP2000 model (even when considering axial-flexure interaction in calculating plastic hinge strength and when considering both axial and flexural plastic internal work). Possible reasons for this discrepancy may relate to the fact that simple plastic theory is based on small displacement theory and that the large-displacement flexural behavior of the Ring model is largely affected by the axial force developed along the perimeter of the Ring model (the larger the deformation of

the Ring model, the larger the axial force), but this line of inquiry was not pursued further for reasons that will become obvious in subsequent sections.
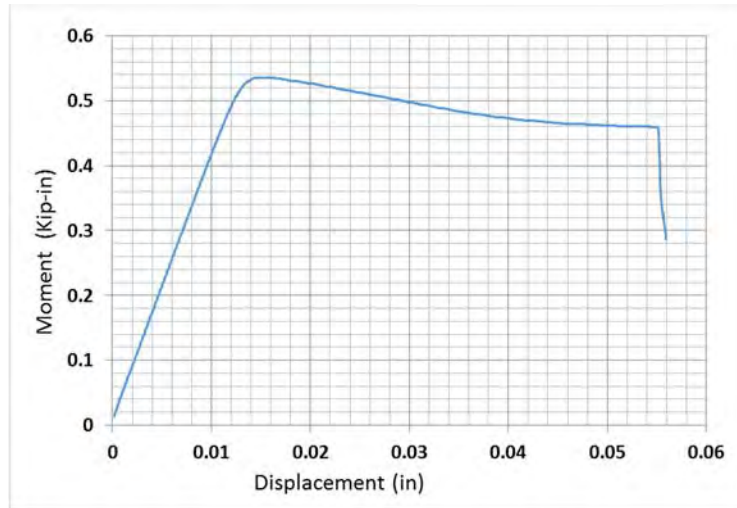
(a)
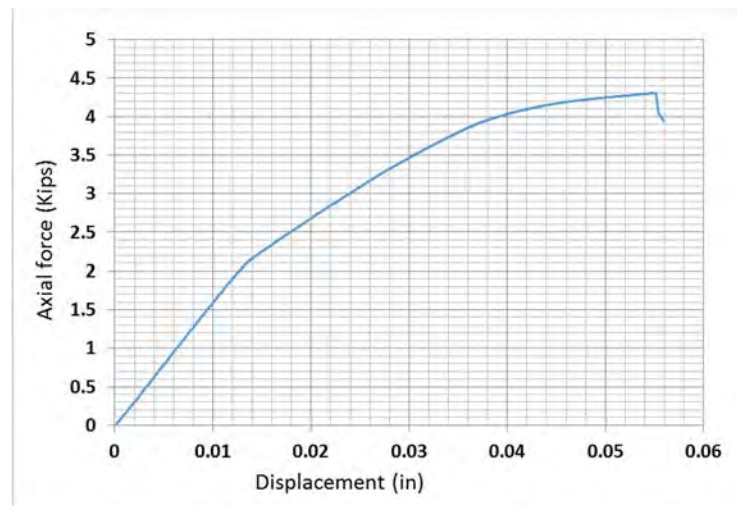
(b)

Figure 6-11 (a) Moment-rotation relationship of the plastic fiber hinge at apex of ring; (b) corresponding axial load in the hinge

6.2.3.3 Results Comparisons Considering Changes in SAP2000 Ring Models

To compare analytical results with experimental ones, the steel material properties of the tested material would have to be taken into account, which implies considering strain hardening and also different yield strength than in the assumed bilinear material used in the above SAP2000 model. The stress-strain curve for one such actual steel material is shown in Fig. 6-12, which was obtained from the tensile test of a

163

coupon cut from a CHS with diameter of 9.625" and thickness of 0.233" (the details of the coupon test is presented in details in Section. 6.3). The yield strength of that steel, obtained per the 0.2% offset method, is 47.9 ksi, which is larger than the assumed yield strength of 42 ksi. When the actual steel material in Fig. 6-12 was used in the SAP2000 model, the pushover curve previously obtained for the bilinear material changed to the solid line shown in Fig. 6-13. The plateau, in the pushover curve from the Ring model using the bilinear material (dashed line), no longer exists. The force applied to the model is 1.689 kips with a displacement of 0.0137", when first yielding happened at the top of the Ring model where the load was applied. The increase of the first-yield strength from the SAP2000 model with bilinear material is 61%. The force applied to the model is 3.369 kips with displacement of 0.0464", when the maximum moment is reached at the top of the Ring model where the load was applied. The maximum-moment strength reached, compared to the results from the SAP2000 model with bilinear material, is 91% greater. Note that it takes more displacements for the actual material with strain hardening to reach its maximum flexural strength than for the one with bilinear material (incidentally, this is also true for the results obtained with the Abaqus Ring model analyses results presented later, in Section 6.2.4). The maximum force could be applied to the model was 3.574 kips, reached at a corresponding displacement of 0.061", and this strength is 35.6% more than what was obtained in the analysis considering bilinear material.

Note that for comparison purpose, when the yield strength of 47.9 ksi is considered for the actual steel material, the theoretically calculated strength per the equations in Section 6.2.2 is 1.204 kips, which is 28% smaller than the SAP2000 analyses results with actual steel material.
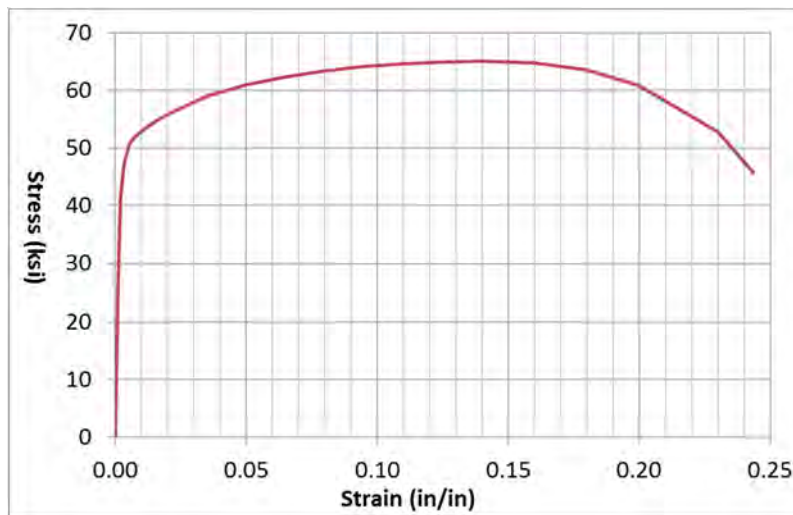
Figure 6-12 Stress-strain curve from actual steel material with the strain hardening from coupons taken from a CHS with diameter of 9.625" and thickness of 0.233"
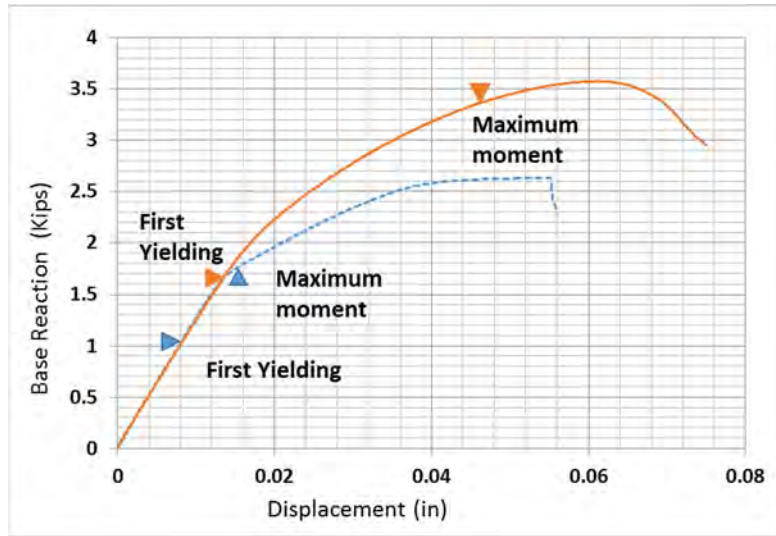
Figure 6-13 Pushover curve of the ring model with actual material from coupon test (Solid Line) compared with the model with bilinear material (Dashed line)

All the above analyses in SAP2000 considered small displacement theory. When the geometric nonlinearity, considering P-delta and large displacement theory, was used in the analyses of the SAP2000 for the Ring model with actual material, the resulting pushover curve is shown in Fig. 6-14 in dashed line.
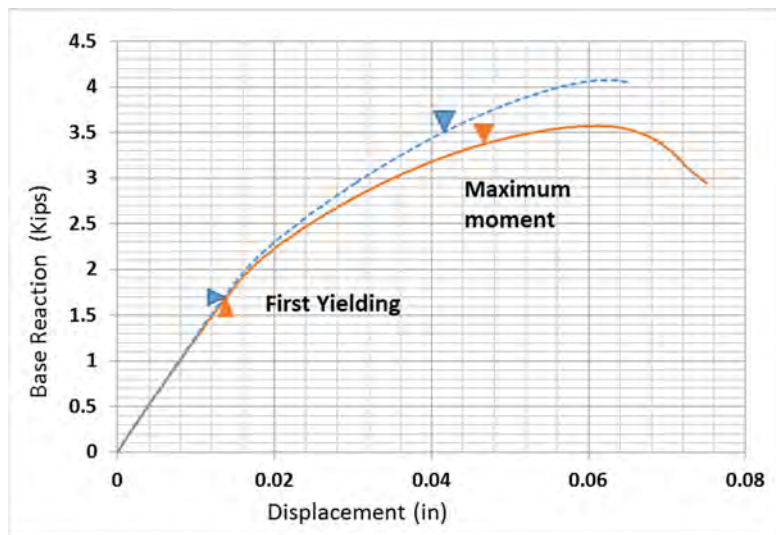
Figure 6-14 Comparisons of pushover curve of the ring model with actual material: small displacement (Dashed line) versus large displacement (Solid Line)

The force applied to the model is 1.691 kips with corresponding displacement of 0.0134", when first yielding happened at the apex section of the Ring model where the load was applied. This first-yield strength value is negligibly 0.1% greater than the one obtained from the SAP2000 model with small displacement theory. The force applied to the model is 3.523 kips with corresponding displacement of

0.0419", when the maximum moment was reached at the top of the Ring model where the load was applied. This maximum-moment strength is 4.6% greater than the one obtained from the SAP2000 model with small displacement theory. In both cases, the increases in strengths obtained using large displacement theory are negligible, and these strengths were developed at a smaller displacement compared with the model using small-displacement theory.

6.2.3.4 Prediction of Zero-moment Point in the Ring Model

From the analyses of the SAP2000 Ring models, it was observed that the moment in the Ring model only concentrated within an arc segment of the CHS, subtended by a certain angle from the centerline, as shown by the angle β in Fig.6-4. Various SAP2000 Ring models of CHSs with different diameters and thicknesses were built to investigate this angle. Table 6-2 summarizes the angle β obtained for some of the CHS sizes provided in AISC (2010), considering different ratio between the diameter and thickness. Fig.6-15 shows the plots of $\bar{r}/t_o$ versus β, and the approximate logarithmic trendline is

$$\beta = -12.97 \ln\left(\frac{\bar{r}}{t_o}\right) + 79.7 \tag{6.23}$$

This trendline can be used to predict the angle β for the theoretical calculations of the Ring model in Section 6.2.2.
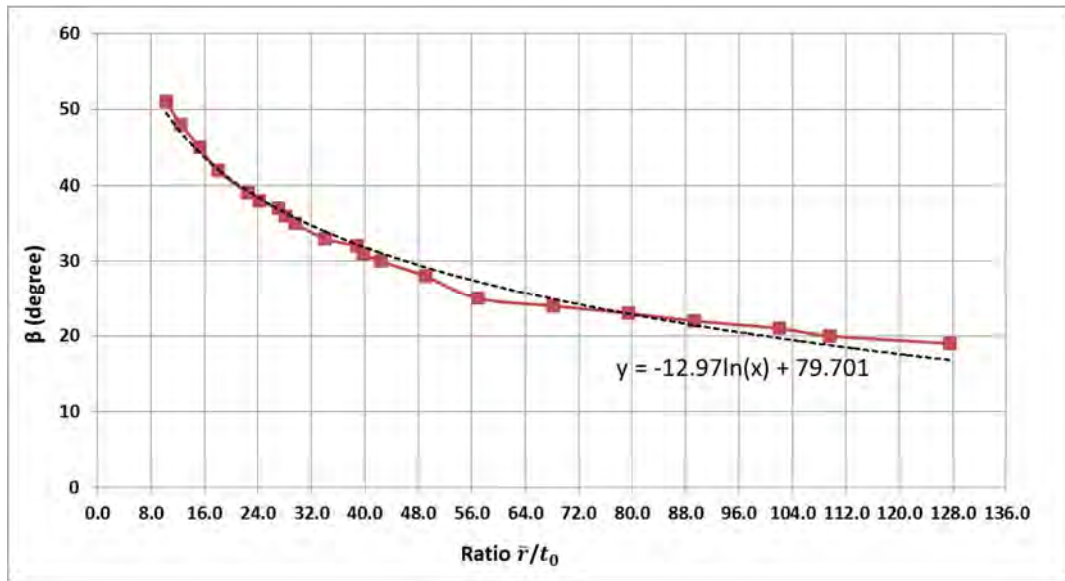
Figure 6-15 Plot of the relationship between uplifting angle β and the CHS size

Table 6-2 Summary of uplifting angle β obtained from various SAP2000 Ring models

R_1	t_o	$\bar{r}/t_o$	β
5	0.465	10.253	51
4.5	0.349	12.394	48
6	0.465	12.403	48
5.5	0.349	15.259	45
8.625	0.465	18.048	42
5	0.233	21.459	40
4	0.174	22.489	39
8.625	0.349	24.213	38
16	0.581	27.039	37
10	0.349	28.153	36
14	0.465	29.608	35
6	0.174	33.983	33
16	0.407	38.812	32
7	0.174	39.730	31
9.625	0.233	41.309	30
10	0.233	42.418	30
8.625	0.174	49.069	28
10	0.174	56.971	25
16	0.233	68.170	24
20	0.25	79.500	23
28	0.312	89.244	22
32	0.312	102.064	21
24	0.218	109.592	20
48	0.375	127.500	19

6.2.4   Abaqus Ring Model

The Abaqus Ring model in Fig. 6-16 was created to be equivalent to the SAP2000 Ring model, to investigate the strength of the concrete-filled CHS using an alternate finite element analysis approach. Bilinear material setting was first used in the Abaqus Ring model. In Section 6.2.4.1, the geometry modeling (element definition), material setting, meshing, contacts between different parts, boundary conditions, loading, and parameters used to perform the stable numerical finite element analysis of the Ring model are first explained. The analyses results of the Abaqus Ring model with bilinear material are presented in Section 6.2.4.2. In Section 6.2.4.3, additional results for different Abaqus Ring models are presented, considering: (1) the friction between the concrete and the CHS; (2) the steel and concrete's actual material properties; (3) geometric nonlinearity.
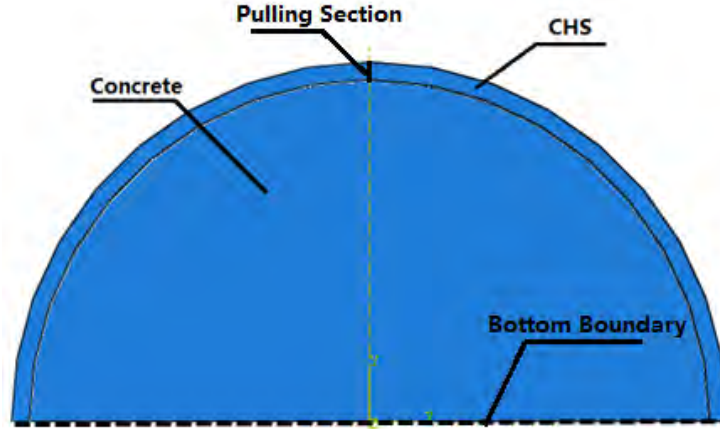
Figure 6-16 Abaqus Ring model

6.2.4.1 Abaqus Ring Model Description

The CHS and the infilled concrete were modeled separately using the general purpose solid element C3D8R, which is an 8-node linear brick with reduced integration element having hourglass control and three displacement degrees of freedom per node (Abaqus, 2014). Since the SAP2000 model had 30 fibers throughout the thickness of the CHS, the Abaqus Ring model was set to have the same number of layers across its thickness of 0.233 in.; the number of the layers used across the Ring width of 0.05" is 6 (resulting in 180 solid elements per cross-section). Smaller mesh for the model was analyzed and convergence of the solution was reached (i.e. the model with a finer mesh gave the same non-linear results as the one with coarser mesh). The mesh technique used is termed "Structured" by Abaqus, and the element shape is called "Hex". Note that results were verified to be the same (per unit width) when using Ring model having width of 0.2 in and 1.0 in.

Abuqus defines the stress and strain for the material in terms of true stress and strain. The stress and strain obtained from regular steel coupon tests are nominal stress and strain. The change in the cross section of the coupon during the tensile tests needs to be included to calculate true stress and strains. Under tensile loading, the specimen's cross section reduces. The true values can be calculated from the nominal (engineering) values, which are based on the original specimen dimensions. The conversion from the nominal stress, σ_{nom}, nominal strain, ε_{nom}, to the true stress, σ_{true}, and true strain, ε_{true}, follows the equations below:

$$\sigma_{true} = \sigma_{nom}(1 + \varepsilon_{nom}) \qquad (6.24)$$

$$\varepsilon_{true} = ln(1 + \varepsilon_{nom}) \qquad (6.25)$$

168

Per Equations 6.23 and 6.24, the bilinear material with engineering values used in the SAP2000 model was converted to true stress and strains, which were then used in the Abaqus Ring model. In order to simulate the rigid infilled concrete in the SAP2000 model, the concrete in the Abaqus Ring model was set to have a very large young's modulus of 1×10^8 ksi. Note that the Abaqus Ring model with concrete material was modeled and analyzed, and the result is presented in Section 6.2.4.3.

Contacts was set as general contacts between the inside surface of the CHS part and the outside surface of the infilled concrete part. The friction formulation in the contact property options' tangential behavior was set to be frictionless, since both the Ring models in the theoretical calculations in Section 6.2.2 and SAP2000 analyses in Section 6.2.3 do not consider the friction. Analysis results of the Abaqus Ring model considering friction are compared with the one without friction to show the difference in Section 6.2.4.3. The default contact pressure-overclosure of "hard" contact was used (per Abaqus terminology), which implies that the surfaces transmit no contact pressure unless the nodes of the slave surface contact the master surface. Furthermore, for this model, there is no penetration of one surface into the other surface once the two surfaces contact each other (Abaqus, 2014).

The Ring model was restrained at the bottom boundary in the y-direction, as shown in Fig. 6-16. Displacement control was used to gradually apply the displacement at the center of the CHS (where the tension load would be applied), until failure of the model occurred when the ultimate strain provided in the material model was reached at this apex section.

In the analyses, when the geometric nonlinearity option was "turned-off", the Abaqus Ring model only considered small-displacement theory. Note that the Abaqus Ring model with geometric nonlinearity "turned-on" was also analyzed, and the results are presented in Section 6.2.4.3. In all cases, "Full Newton" was selected as the solution technique. The displacement increment was automatically adjusted so that the time increment in each step would permit convergence of results without unstable responses, and the range of the increments remained within a reasonable range to ensure that equilibrium can be found. The minimum and maximum increment was set to be 1×10^{-7} and 0.01 for this case, respectively.

6.2.4.2 Example of CHS with 9.625" diameter and 0.233" thickness

Here, the CHS specimen of 9.625" diameter and 0.233" thickness tested as described in Section 6.3 is used as an example of the Abaqus analysis results obtained. The dashed line in Fig.6-17 shows the pushover curve from the Abaqus Ring model analysis, which is compared with the pushover curve

previously obtained from SAP2000 Ring model analysis with bilinear material. The first-yielding strength of the Abaqus Ring model is 1.172 kips, with the displacement at the load application point of 0.0079".
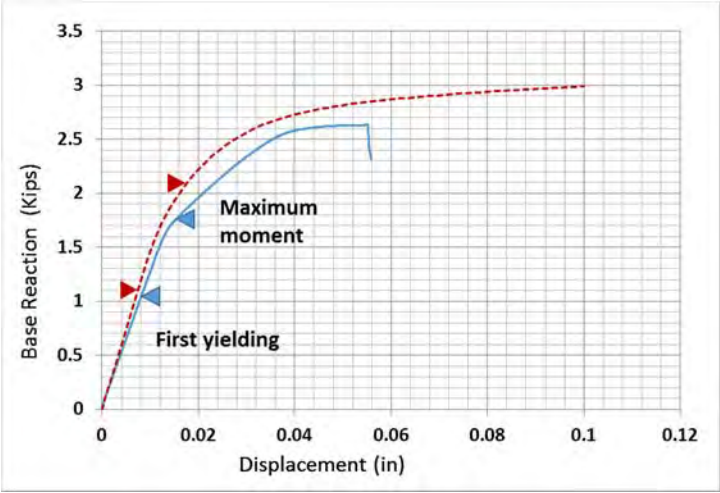
Figure 6-17 Comparison of pushover curves from Abaqus and SAP2000 ring model with bilinear material

Fig 6-18a shows the von-Mises stress contour of the Abaqus strip model when first yielding happened at the load application point, with an enlarged view showing the separation of the CHS from the infilled concrete in Fig. 6-18b. The strength of the Abaqus Ring model is 2.136 kips, when the maximum moment developed at the load application point, with a corresponding displacement of 0.018".

(a)

(b)
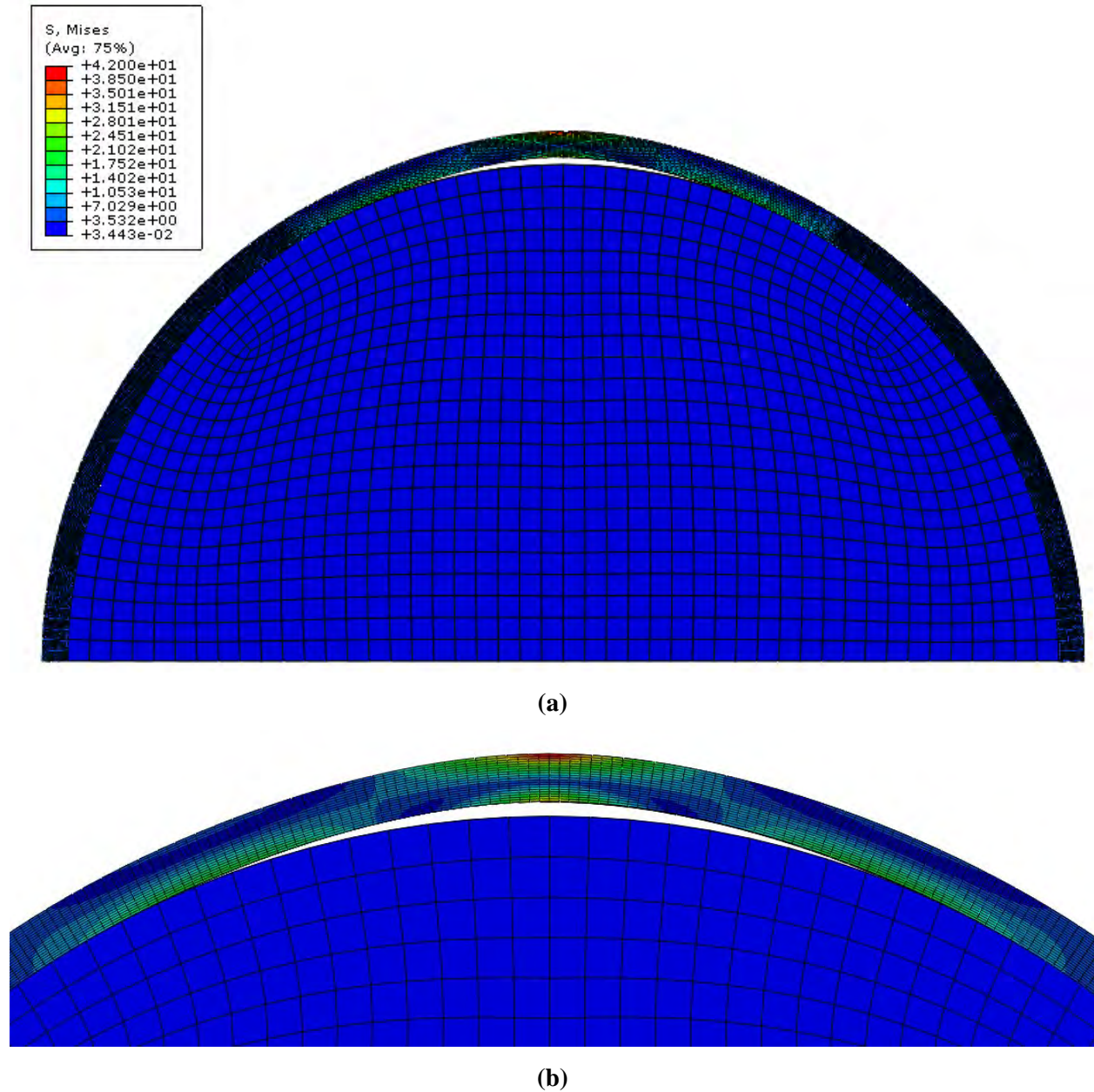
Figure 6-18 Von-Mises stress contour of the Abaqus ring model when the first yielding happened at the load application point: (a) entire model; (b) enlarged view at the top

Similarly, Fig. 6-19 shows the von-Mises stress contour of the Abaqus Ring model when the maximum moment happened in the apex section at load application point. Note that the deformations in Figs. 6-18 and 6-19 are magnified by a scale factor of 10. The increase of the first-yield strength and maximum-moment strength reached in the Abaqus model is 12% and 21%, respectively, compared to the results from the SAP2000 model with bilinear material.

S, Mises
(Avg: 75%)
+4.200e+01
+3.851e+01
+3.501e+01
+3.152e+01
+2.802e+01
+2.453e+01
+2.104e+01
+1.754e+01
+1.405e+01
+1.055e+01
+7.060e+00
+3.566e+00
+7.196e-02

(a)

(b)
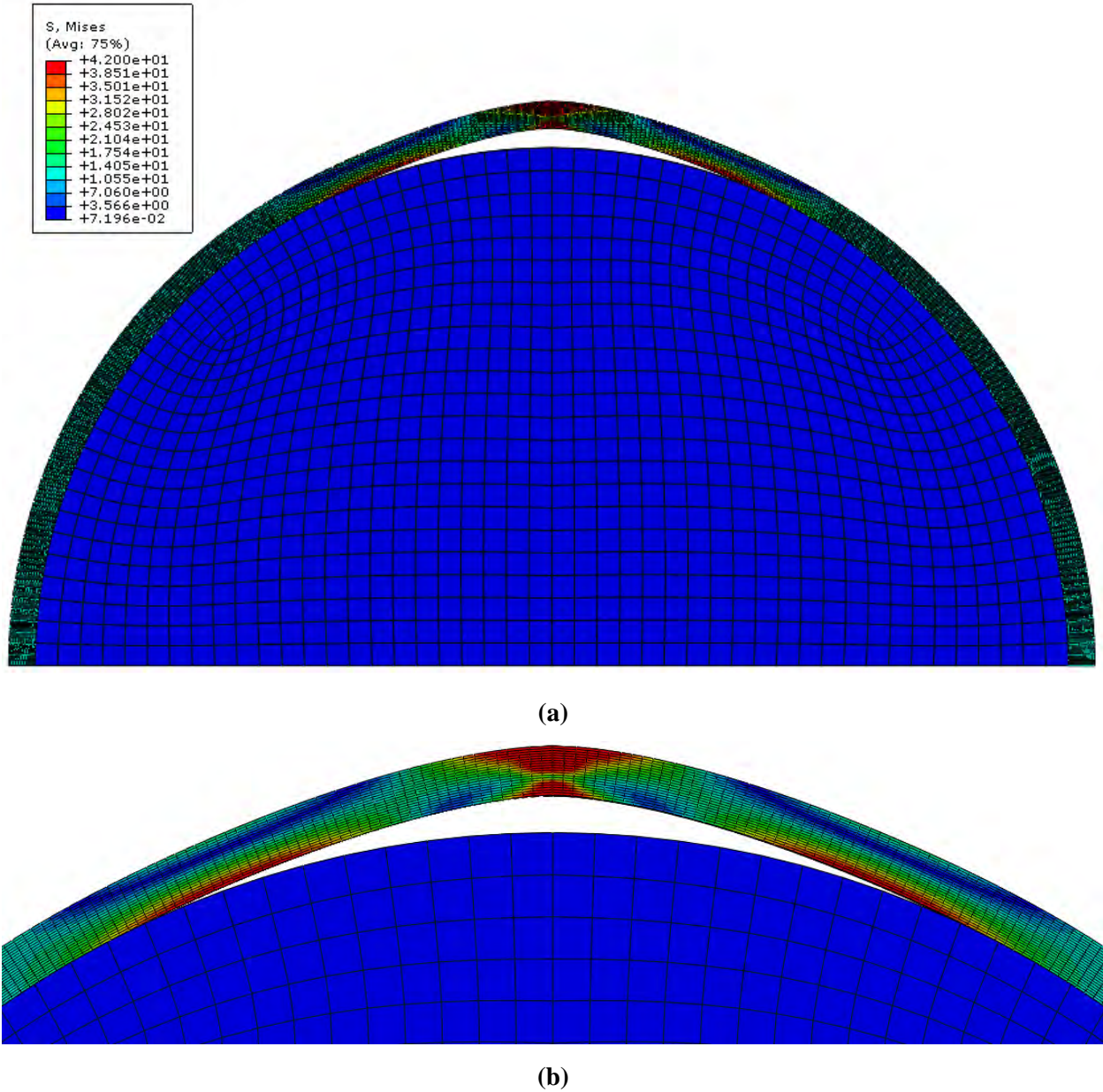
Figure 6-19 Von-Mises stress contour of the Abaqus ring model when the maximum moment reached at the load application point: (a) entire model; (b) enlarged view at the top

6.2.4.3 Results comparisons considering changes in modeling in Abaqus

The effect of friction in the obtained strength for the Abaqus Ring model was also investigated. The friction formulation was set to be "penalty", for which the directionality was chosen as "isotropic", i.e. the same in all directions. The friction coefficient between the infilled concrete and steel was set to be 0.57, as recommended by Rabbat and Russell (1985). The solid line in Fig.6-20 shows the pushover curve

172

from the Abaqus Ring model analysis with friction considered, and the dashed line represents the no friction case. For the Abaqus model with friction, the first-yielding strength of the Abaqus Ring model is 1.307 kips, reached at a corresponding displacement of 0.0079" at the load application point; the strength of the Abaqus Ring model is 2.273 kips with a corresponding displacement of 0.018", when the maximum moment happened in the apex section at the load application point. The difference of the first-yielding and maximum-moment strength is 11.5% and 6.4% larger than the case with no friction considered.
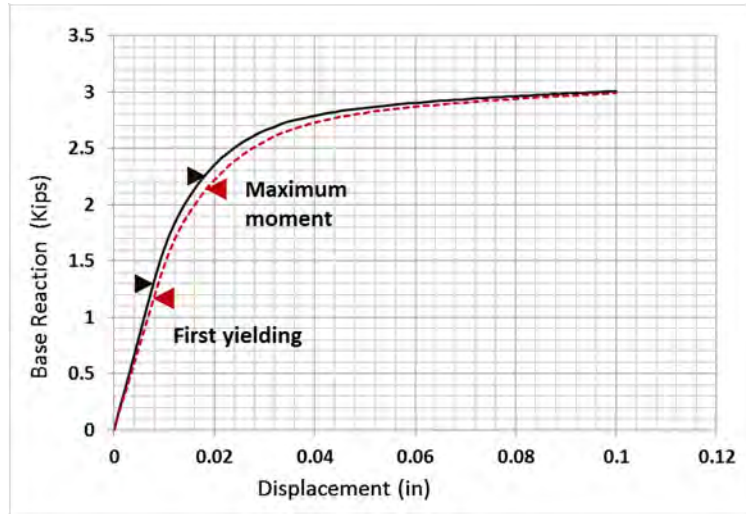
Figure 6-20 Comparisons of pushover curve of the Ring model with bilinear material: (a) no friction (dashed line); (b) with friction (solid line)

Abaqus Ring model was also built to consider the actual steel material (friction considered in this case). Note that the concrete material properties remained as specified in Section 6.2.4.1. The resulting pushover curve is shown in dash-dot line in Fig.6-21 for the model with actual steel material; the solid line representing the pushover curve from the Abaqus model with bilinear material is also shown in Fig 6-21. For the Abaqus model with steel material, the force applied to the model is 1.620 kips with a corresponding displacement of 0.010" at the apex of the ring, when first yielding happened at the top of the Ring model where the load was applied. This first-yield strength (actual steel material) is 24% larger than the first-yield strength obtained from the Abaqus model with bilinear material. When the maximum moment of the apex section at the load application point was reached in the Abaqus Ring model, the force applied to the model is 4.42 kips, with the corresponding displacement of 0.194"at the load application point. This strength is 94% larger than the strength obtained from the Abaqus Ring model with bilinear material. Recall that this difference caused by the material properties used in the model also happened in the SAP2000 Ring model as explained in this Section 6.2.3.2.
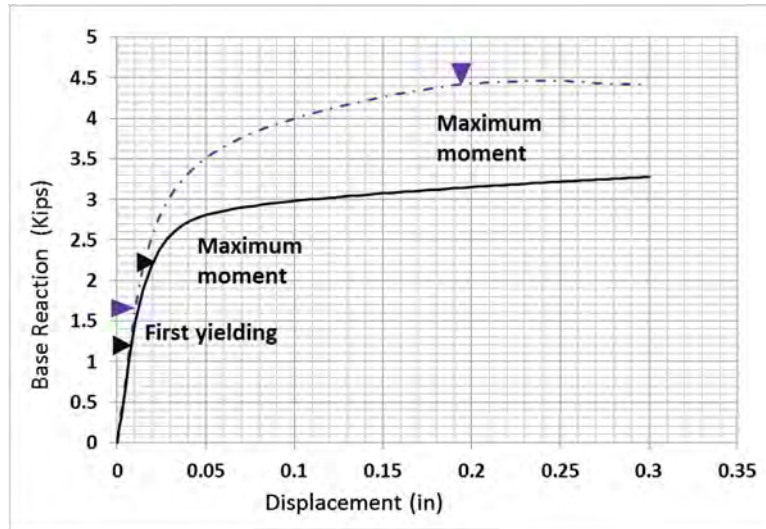
Figure 6-21 Pushover curve of the ring model with actual material from coupon test (dash-dot Line) compared with the one with bilinear material (solid line)

All the above analyses in Abaqus considered small-displacement theory. When the geometric nonlinearity setting is active in the Abaqus Ring model with actual material (friction considered in this case), the resulting pushover curve is shown in Fig. 6-22 in solid line, compared with the one using small-displacement analyses in dash-dot line. The force applied to the model is 1.670 kips with a corresponding displacement of 0.01" at the load application point, when first yielding happened at the apex section of the ring model where the load was applied. This first-yield strength is 3% larger than the first-yield strength obtained from the Abaqus model using small displacement theory. The force applied to the model is 4.182 kips with a corresponding displacement of 0.0596" at the load application point, when the maximum moment is reached in the apex section at the top of the ring model where the load was applied. This maximum-moment strength is 5.3% larger than the maximum-moment strength obtained from the Abaqus model using small displacement theory. The change in these strength considering geometric nonlinearity is small, however these strengths were developed at a smaller displacement compared with the model using small displacement theory. This change is also observed when the results from the SAP2000 Ring model analysis were compared for the cases with and without geometric nonlinarity considered, as described in Section 6.2.3.3.

Note that all the above models mentioned in this section assumed that the concrete infill is rigid. In the test specimen, the concrete is not infinitely rigid and may crack under the pushing force of the CHS. Therefore, to investigate if considering this flexibility would significantly change the above results, another Abaqus analysis was conducted using a model that considered the actual concrete material

properties. The concrete material was defined with an elastic modulus of 3605 ksi and a Poisson ratio of 0.2. The compressive strength of the concrete f_c' was taken as 4.05 ksi, as obtained from the concrete material test mentioned later in Section 6.3.2. The tensile strength of the concrete was calculated by the ACI-318-14 equation, $f_t = 6.5\sqrt{f_c'}$, which gave 0.41 ksi. The concrete damage plasticity (CDP) material model was used. The two main failure mechanisms were defined as tensile cracking and compression crushing. The modified concrete backbone curve that was used to define the concrete material behavior is shown in Fig. 6-23.
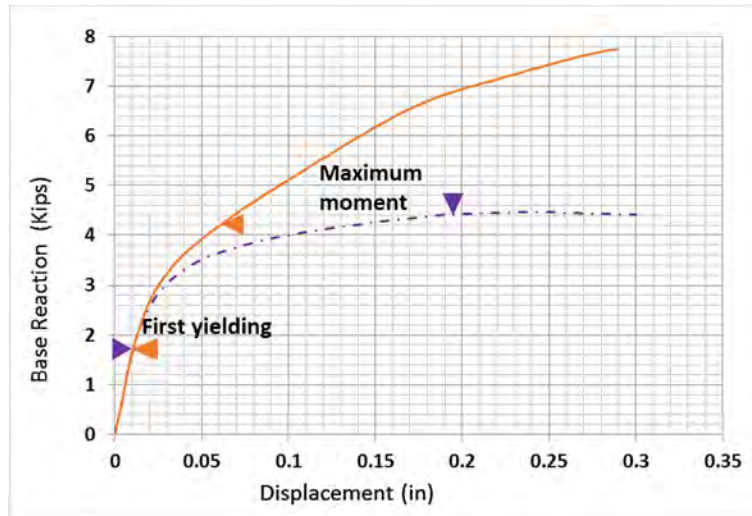
Figure 6-22 Comparisons of pushover curve of the Ring model with actual material: small displacement (Dash-Dot line) versus large displacement (Solid Line)

The CDP model used in Abaqus has the following parameters which affect the shape of the yield surface as recommended in the Abaqus User manual:

(a) The ratio, K_c, of the distances between the hydrostatic axis and the compression and tension meridian in the deviatoric cross section, taken as 0.67

(b) The plastic potential eccentricity factor, which represents the length of the segment between the vertex of the hyperbola and its center, taken as 0.01

(c) The ratio between the strength of the concrete in the biaxial state of stress, f_{bo}, and the uniaxial state of stress, f_{co}, taken as 1.16

(d) The dilation angle, taken as 38°

(e) The viscosity parameter, taken as 0.002.
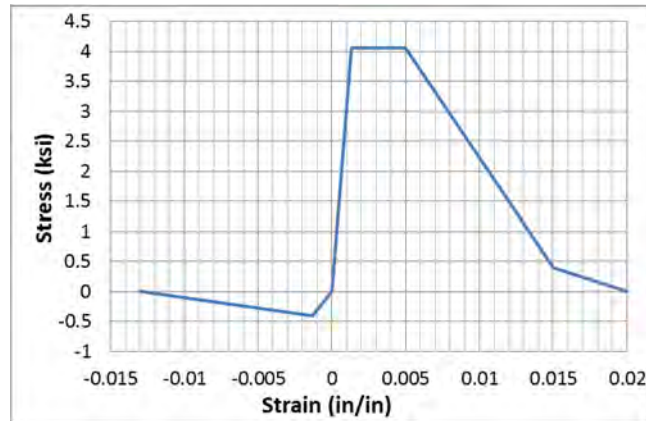
Figure 6-23 Stress-strain curve of concrete material used in the Abaqus Ring model

The resulting pushover curve is shown in Fig. 6-24 in solid line for the Abaqus Ring model, compared with the Abaqus Ring model using rigid concrete material setting in dash-dot line. In both cases, no geometric nonlinearity, steel actual material, and friction, are considered in the analysis. For this Abaqus model with actual concrete material properties, the force applied to the model is 1.59 kips with a corresponding displacement of 0.011", when first yielding happened at the apex of the ring model where the load was applied. The difference in first-yield strength between the Abaqus models with rigid and actual concrete setting is 2%. When the maximum moment was reached at the apex section of the Ring model where the load was applied, the pulling force is 4.41 kips with a corresponding displacement of 0.201". This maximum-moment strength is 0.2% different from the maximum-moment strength obtained the Abaqus model with rigid concrete. This shows that using the actual concrete material in this Abaqus Ring model only result in a negligible difference in the first-yield and maximum-moment strength, and that using rigid concrete in the prior analyses was an appropriate assumption.
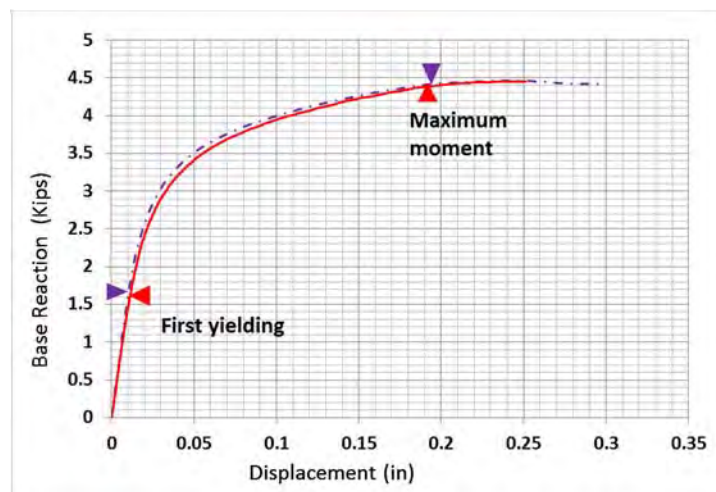
Figure 6-24 Comparisons of pushover curve of the Ring model: actual concrete material

(Dash-Dot line) versus rigid concrete material (Solid Line)

176

Note that the above comparisons were provided to indicate how strengths calculated using the Abaqus Ring model changed when various factors (friction, geometric nonlinearity, actual steel and concrete material) were considered. In Section 6.3, these Abaqus Ring model results will be compared with test results and with Abaqus results for models that consider the 3-D geometry of the connection for specific specimens, such as to more accurately capture the design strength of the branch plate welding to concrete-filled CHS connections.

6.2.5   Results comparisons between theoretical calculation and analyses models

In this section, the analytical results from the Ring model in both SAP2000 and Abaqus are compared to those obtained from the theoretical equations in Section 6.2.2, for the CHS sizes that were used in the tests presented later in Section 6.3. The comparisons here are for the bilinear material with yield strength of 42 ksi. The resulting first-yielding strength and displacement are presented from: (1) the theoretical calculation; (2) SAP2000 Ring model; and (3) Abaqus Ring model. Results are presented in Table 6-3. It is observed from those results that the theoretically first-yielding strength calculated per the equations in Section 6.2.2 is within 10% of the SAP2000 and Abaqus results. The resulting strength and displacement reached when the maximum moment was developed at the load application point is also presented for the SAP2000 and Abaqus Ring model in Table 6-3.

6.3   Concrete-filled CHS tests
6.3.1   General

In this section, the test setup, testing protocols, and test results are presented for the tests performed on various concrete-filled CHS. The design of the test specimens, the test set-up and the instrumentations are described in Section 6.3.2. The general test protocols are explained in Section 6.3.3. Section 6.3.4 provides the modeling of the testing specimens in Abaqus, along with analyses results presented for selected specimens. The detailed test results for each specimen are presented in Section 6.3.5. The applied force and deformation of all specimens were recorded and the resulting curves of the applied force versus the specimen's deformation are compared with the analytical results from the Abaqus analyses. Conclusions based on the test results and the analytical work for the concrete-filled CHS is provided in Section 6.3.6.

Table 6-3 Ring model comparisons between the theoretical calculations, model in SAP2000 and Abaqus with bilinear material

CHS Shape	16×0.25	10.75×0.188	14×0.375	9.625×0.25	5×0.25
Design Wall Thickness(in)	0.233	0.174	0.349	0.233	0.233
D/t_0	68.67	61.78	40.11	41.31	21.46
First-Yielding displacement -Theoretical (")	0.01053	0.00630	0.00845	0.00602	0.00286
First-Yielding Force -Theoretical (kips)	0.793	0.728	1.621	1.056	1.537
First-Yielding displacement- SAP2000 (")	0.01521	0.00956	0.01158	0.00802	0.00367
First-Yielding Force -SAP2000 (kips)	0.772	0.742	1.561	1.045	1.554
Difference of First-Yielding Force (Theoretical&SAP2000)	-2.65%	1.92%	-3.70%	-1.04%	1.11%
First-Yielding displacement -Abaqus (")	0.01284	0.00879	0.00965	0.00787	0.00354
First-Yielding Force -Abaqus (kips)	0.768	0.730	1.518	1.171	1.700
Difference of First-Yielding Force (Theoretical & Abaqus)	-3.15%	0.27%	-6.35%	10.89%	10.61%
Displacement at maximum moment-SAP2000 (")	0.02876	0.01821	0.0221	0.01510	0.00677
Force at maximum moment -SAP2000 (kips)	1.301	1.208	2.669	1.763	2.601
Displacement at maximum moment -Abaqus (")	0.02965	0.02244	0.0246	0.01837	0.0639
Force at maximum moment -Abaqus (kips)	1.568	1.436	3.229	2.136	3.197

6.3.2 Test specimens and test set-up

In this section, the design of the test setup and specimens are presented in Sections 6.3.2.1 and 6.3.2.2, respectively. Section 6.3.2.3 focuses on the coupon tests conducted to obtain the steel material properties of the CHS with different diameters. The instrumentation for the CHS specimen tests is described in Section 6.3.2.4.

6.3.2.1 Test set-up information

The concrete-filled CHS specimens were designed to be tested using the test setup shown in Fig. 6-25. The reaction frame in SEESL was used in the test setup to provide adequate support for the actuator which was used to apply load to the specimen. The actuator was bolted to the column in the reaction frame. One side of the specimen was connected to the actuator, and the other side was connected to the reaction block, which was itself bolted down to the floor beam of the reaction frame using threaded bars. The connection between the specimen to either of the actuator or the reaction block used one line of slip-resistant A490 bolts to connect the plates extending from the specimen (branch plates) to double sets of plate (tab plates), as shown in Fig. 6-25. The head of the actuator was connected to a thick steel block, which had two tab plates welded to it. The two tab plates on the opposite side of the specimen were welded to the reaction block. A wood block was used between the specimen and the floor beam in the reaction frame to support specimen's gravity load. A PTFE/Teflon plastic sheet was used between the wood block and the specimen to reduce the possible friction between the CHS and the supporting block. Note that the height between the actuator and the tab plates from the floor beam did not change during the test. When specimens of smaller sizes were tested, higher supporting blocks made up with several wood blocks were used, however, the Teflon sheet was always in contact with the CHS.

Due to the limits in the stroke of the actuator, the reaction blocks had to be moved horizontally along the floor beam in the reaction frame to accommodate specimens with different diameters. This relocation of the reaction block was intended to ensure that the specimens could be applied to the required displacement demands to fail them. The specimen was also secured by guiding blocks on each side to avoid instability of the test setup in the out-of-plane loading direction. The two guiding blocks were fixed to the floor beam by two beam clamps.

(a)
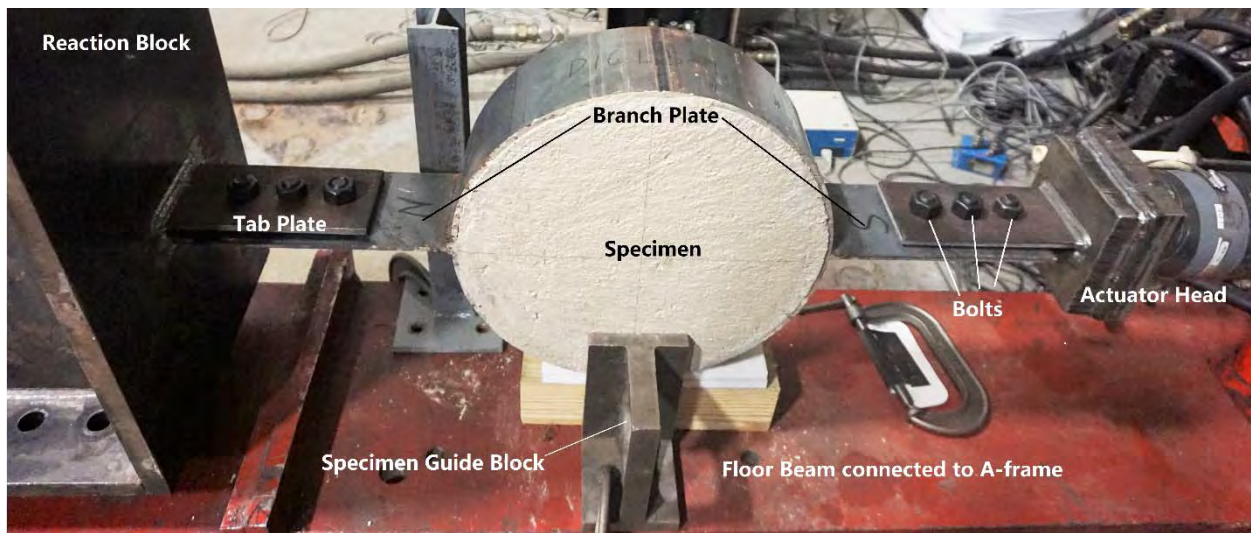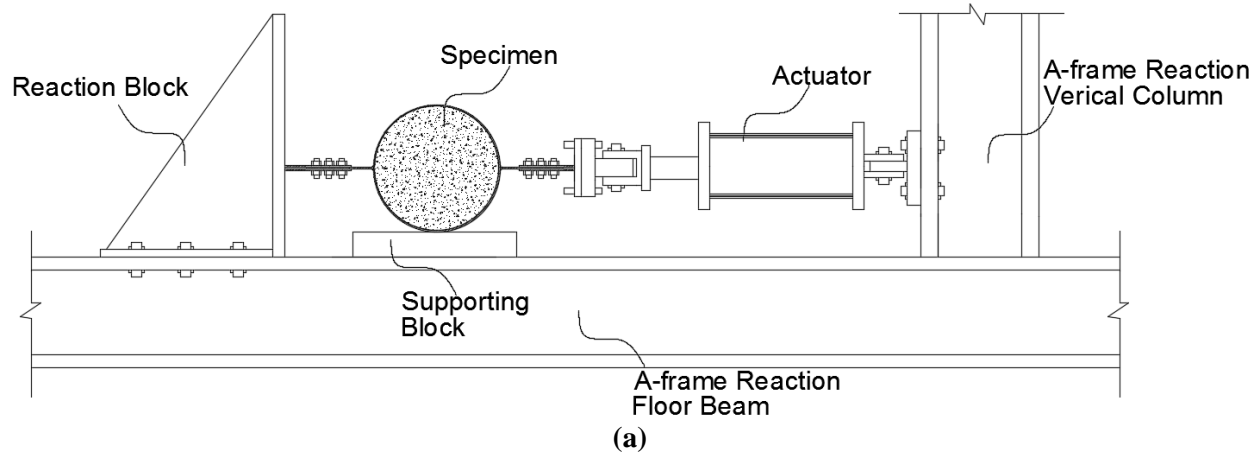
(b)

Figure 6-25 CHS with infilled concrete specimen test set-up: (a) top view; (b) side view

6.3.2.2 Design of Test Specimen and Set-up

The designs of the test specimens and set-up involved: (1) bolt connections between the reaction block to the floor beam in the reaction frame using threaded bolts; (2) bolt connections between the tab plates and the branch plate; (3) fillet welds between the tab plates and reaction block (or the steel blocks connected to the actuator side); (4) fillet welds between the branch plate and the concrete-filled CHS.

At the time when the test set-up and specimen was designed, the plan was to use a Parker servo-controlled static rated actuator with a load capacity of 70 kips and 4-in stroke. The reaction block was designed to have six Grade 8 threaded bolts with a diameter of 1-1/8" (only three on one side of the reaction block are shown in Fig. 6-25a). The threaded bolts were pre-tensioned, and the bolted connection was capable to

resist a force of 100 kips from the tab plates that were connected to the specimen. The tab plates were welded to the reaction block (or the steel block connected to the actuator head) using fillet welds, and the welds are able to resist a force of 86 kips.

Fig. 6-26 shows the bolt connections between the tab and branch plates, as well as the fillet welds between the branch plate and the CHS. The bolts connecting the tab and branch plates were A490 bolts with a diameter of 3/4". They were pre-tensioned to create a slip-resistant connection with a strength of 89 kips. The branch plates were welded to the CHS by double-sided fillet welds. Initially, the maximum strength developed by the Ring models in Section 6.2 was used to design the branch plate and fillet welds. A safety factor of 2 was used to choose the preliminary width of the CHS. Note that in the Ring model, tensile force was applied at the apex of the CHS; in the actual test, the force from the branch plate was applied to the CHS through the fillet welds of the branch plate to the CHS. Therefore, in the actual test, the branch plate was pulling over an area of the CHS, rather than a point as in the Ring model (the thicker the branch plate, the larger the fillet weld size, and the wider this area would be). It was recognized that the strength of the specimen would be affected by these two factors. Therefore, it was decided to build another Abaqus model of the specimen to better estimate the strength of the infilled-concrete CHS by considering different sizes of branch plate and fillet welds. Trial analyses were performed on the Abaqus specimen model (described in detail in Section 6.3.4), which proved that the strength of the model was much larger than the value predicted from the width of the CHS times the maximum unit-length strength obtained by the previously considered Ring model. Therefore, CHS with smaller width than predicted from the Ring model had to be used to account for this increase so that the specimen could be failed before reaching the maximum actuator force of 70 kips. The thickness of the branch plate and the fillet weld size also had to be carefully chosen to make sure that the specimen could fail in the CHS. To minimize the fact that the bolted connections might apply a non-uniform load to the CHS through the branch plate, the distance from the CHS-to-branch plate fillet weld to the nearest bolt was chosen to be the same as the length of the fillet weld.
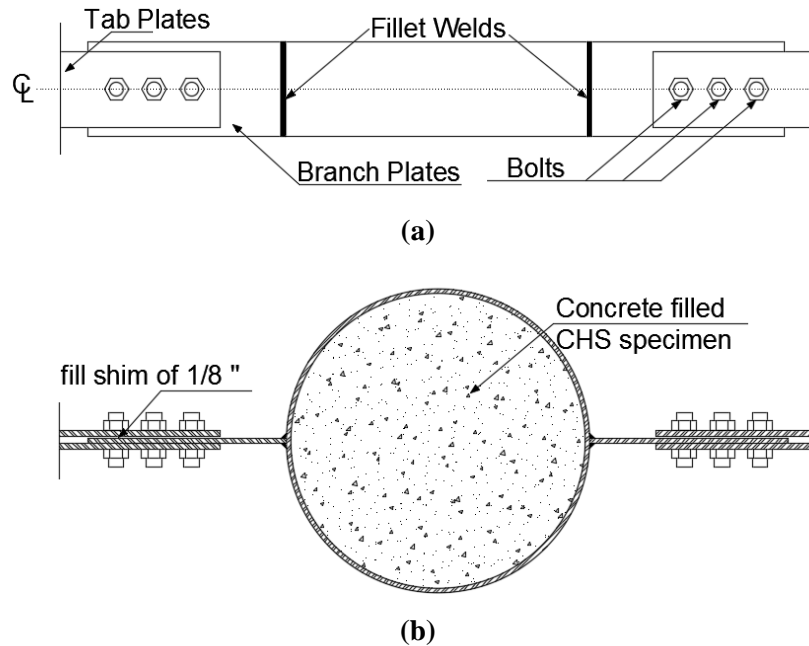
Figure 6-26 Tab plates, branch plates and CHS connections for specimen with CHS diameter of 16": (a) top view; (b) side view

Since no coupon test data from the CHS were available when designing the specimen, the material used in the trial Abaqus model was A500Gr.B steel with yield strength of 42 ksi and ultimate strength of 58 ksi. In interpreting the results, the strength at failure was considered reached when strains reached an ultimate value of 0.24 at any point on the mesh. Note that this strength was obtained when the maximum strain was reached on a small part of the CHS, and while the actual strength at failure of the CHS could be different in the tested specimen, this could not be accurately assessed at that time. However, it was recognized that this difference between the strength predicted by this initial Abaqus analysis (with the improved specimen model) and the actual strength of the specimen in the test could be also affected by differences between assumed material properties/geometries and actual values.

The specimen with all the considered CHS diameters are shown in Figs. 6-27 to 6-31. A summary of all final specimen dimensions is presented in Table 6-4. The name for each type of specimen, "D-i-L-j", indicates that the diameter and width of the CHS used in the specimen are "i" and "j" in, respectively. More than one of each specimen type was built such that both monotonic and cyclic tests could be performed on each type of specimens (as indicated in Table 6-4). The purpose of performing the cyclic tests was to access the behavior of this type of connection from the perspective for a seismic application, if it ever was to yield, since the connection detail is intended for connecting bridge columns to a BRB used for seismic protection. For the specimens having CHS diameter of 9.625", three different widths of

182

the CHS were tested to investigate how strength increase as a function of the width of the CHS, which were not welded to the branch plate.

Table 6-4 Summary of concrete-infilled CHS test specimens

Specimen Name	D16L5	D14L3	D10.75L5	D9.625 L3	D9.625 L6	D9.625 L7	D5L3
CHS Shape	16×0.25	14×0.375	10.75×0.188	9.625×0.25			5×0.25
Specimen Total Number	4	2	2	2	2	2	2
Design Wall Thickness(")	0.233	0.349	0.174	0.233			0.233
CHS width (")	5	3	5	3	6	7	3
Branch plate connecting width (")	5	3	5	3			3
Branch plate length (")	10.5	8.5	10.5	8.5			8.5
Branch plate thickness (")	0.25	0.375	0.25	0.375			0.375
Fillet Weld size (")	0.25	0.375	0.25	0.375			0.375

Note that for specimens with CHS diameter of 16" and 10.75", the thickness of the branch plate is 0.25", which is 1/8" thinner than the thickness of 0.375 for the rest of the specimens. Because the branch plate was to be inserted between the tab plates, and the space between the plates was a constant 0.375" (and not-adjustable because they were welded to either the reaction block or the steel block connected to the actuator's head), shims of 1/8" thick were originally designed to fill the gap between the branch plate and the tab plates for these specimens.

The branch plate used for the specimens with CHS diameter of 14", 9.625", and 5" was tapered, as shown in Figs. 6-28, 6-30 and 6-31. If the branch plate's width had been taken as the same as the width of the CHS, the branch plate's strength would have been controlled by net section ultimate strength, which would have been smaller than the failure strength predicted by the Abaqus analyses of the corresponding specimen model. Therefore, tapering of the branch plates was done to provide a larger width and compensate for the cross sectional loss at the bolt holes. Example Mathcad calculations for the design of the test set-up and for the specimen D9.625L3 is presented in Appendix F.

The CHSs used in the test specimens were manufactured and supplied by Atlas Tube, JMC Steel Group of Chicago, Illinois. The CHSs were cut into the length used in the specimen listed in Table 6-4. The branch plate was fillet welded to the CHS before the concrete was poured into the CHS. The concrete was cured for 28 days before the tests.

Note that the test setup and some of the specimen details have been revised based on the performance of the specimen in the first few tests. Changes are listed as follows: (1) the actuator was eventually replaced

by one with a larger force capacity of 250 kips (see Section 6.3.5.2.1); (2) the branch plates for certain specimens was strengthened following undesired failure of a branch plate (see Section 6.3.5.2.2); (3) cover plates were added to one specimen to prevent results being affected by non-representative concrete crushing (see Section 6.3.5.5).

(a)

(b)
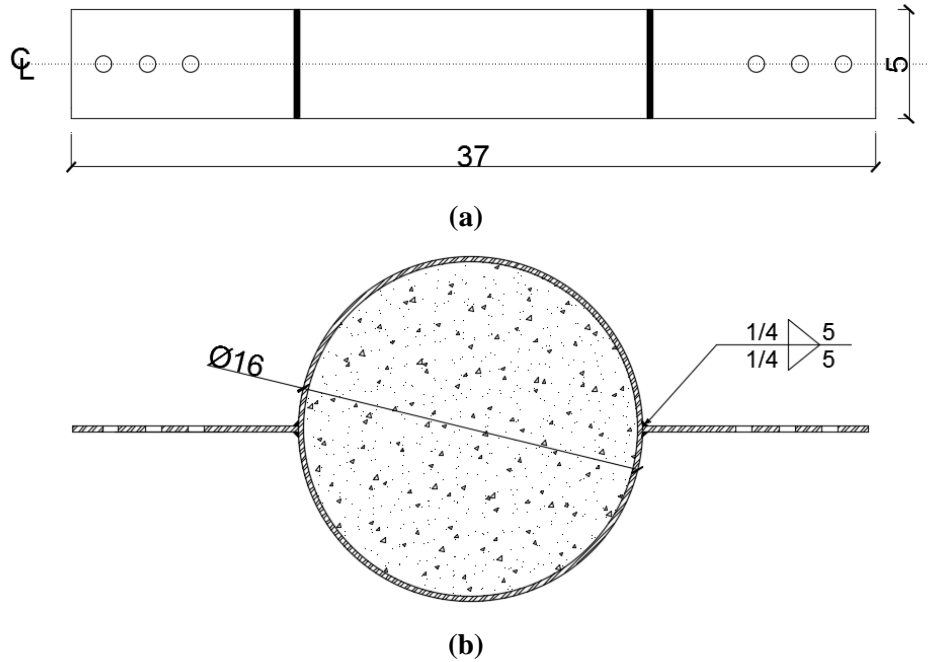
Figure 6-27 Test specimens D16L5: (a) top view; (b) side view (unit: in.)

(a)

(b)
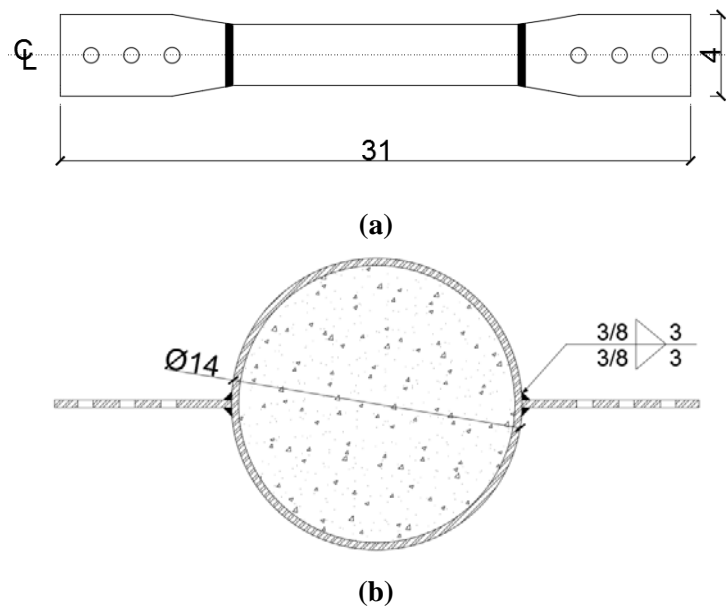
Figure 6-28 Test specimens D14L3: (a) top view; (b) side view (unit: in.)

184

(a)

(b)
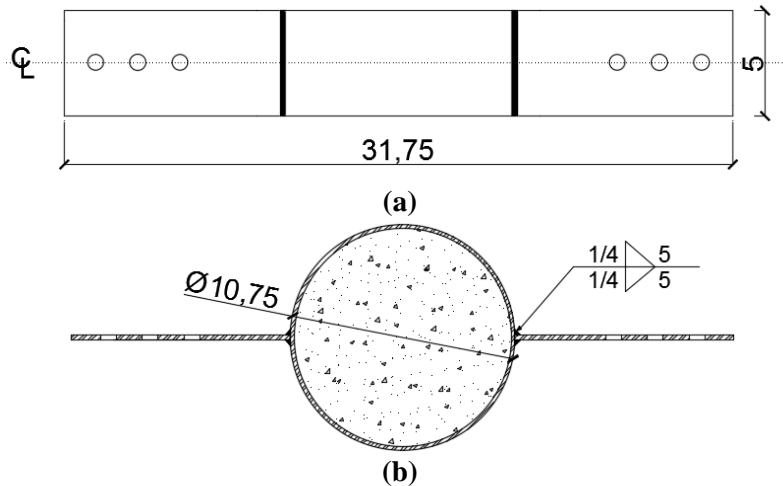
Figure 6-29 Test specimens D10.75L5: (a) top view; (b) side view (unit: in.)

(a)

(b)

(c)

(d)
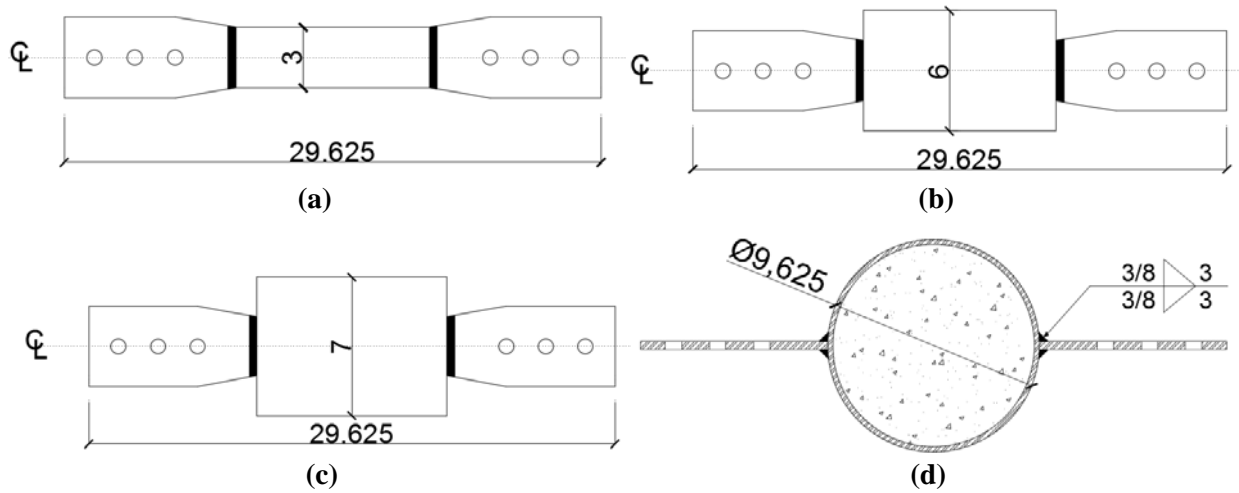
Figure 6-30 Test specimens with CHS of 9.625" diameter: top view of (a) Specimen D9.625L3; (b) Specimen D9.625L6; (c) Specimen D9.625L7; side view of (d) Specimen D9.625L3, D9.625L6 and D9.625L7 (unit: in.);

(a)

(b)
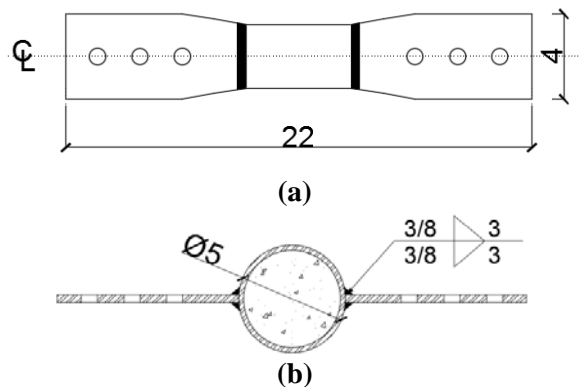
Figure 6-31 Test specimens D5L3: (a) top view; (b) side view (unit: in.)

185

6.3.2.3 Material Property Tests

The material assumed for the CHS in all finite element analyses of the Ring model and Abaqus specimen model was A500Gr.B with yield strength of 42 ksi, and ultimate strength of 58 ksi. Actual values for the CHSs would evidently be different and needed to be obtained from coupon tests. Therefore, three coupons were taken from each type of CHS used for the specimens. All coupons were tested under monotonic tensile force using the MTS universal test machine in the SEESL. A MTS extensometer with 2" gage length was mounted on the coupons to record the axial deformations, which were then used to calculate the strains. The forces were monitored by the internally mounted load cell in the MTS universal test machine. The resulting average yield strength, ultimate strength, and coupon maximum strain are tabulated in Table 6-4. The stress-strain curve of the coupon, which has the properties closest to the average value among the three coupons for each type, is shown in Fig. 6-32. The resulting stress-strain relationship of the material was used in the analyses of the Ring model (both SAP2000 and Abaqus) in Section 6.2.3 and the Abaqus specimen model in Section 6.3.4. Note that the stress-strain curve of the Specimen with CHS of 9.625" diameter has already been presented in Section 6.2.3.3.

Three standard 6×12 in concrete cylinders, made from the same concrete cast in the specimen, were tested to obtain the compressive strength. The cylinders were cured for 28 days in accordance with ASTM C31 (2015a) and tested in accordance with ASTM C39 (2015b) on the 37th day. The concrete compressive strength f_c' for the three cylinders are 4.26, 3.82, 4.08 ksi, and the average compressive strength of 4.05 ksi was used. The concrete material properties are used in the Abaqus model in Section. 6.3.4. Note that although the actual concrete-filled CHS specimens were tested at times ranging from 92 to 185 days after the concrete was cast, and concrete strength in the actual specimen would slightly exceed the cylinder strength, this small different in concrete strength does not have a significant impact on the results.

Table 6-5 Steel material properties from tests of coupons cut from various CHS

CHS diameter	F_y(ksi)	F_u (ksi)	Maximum strain (in/in)	F_u/F_y
5	64.5	71.6	0.315	1.11
9.625	47.9	65.0	0.244	1.37
10.75	48.4	61.6	0.251	1.27
14	56.0	76.1	0.329	1.36
16	50.9	70.0	0.284	1.38
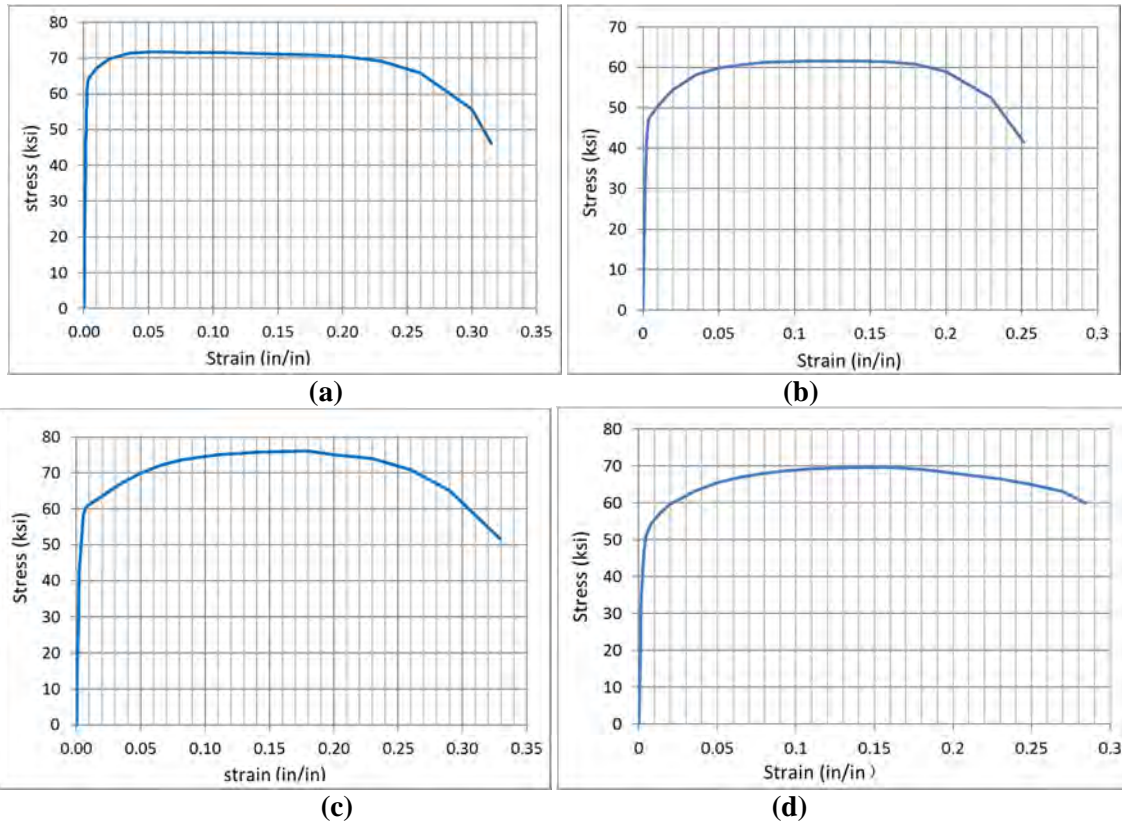
Figure 6-32 The material stress- strain curve of coupons taken from specimens with CHS diameter of: (a) 5"; (b) 10.75"; (c) 14"; (d)16"

6.3.2.4 Instrumentation

The concrete-filled CHS tests were performed using displacement control and the displacement was applied to the branch plates through the bolted connection with the tab plates. For the Parker servo-controlled static rated actuator mentioned in Section 6.3.2.2, the force was measured using an in-house custom built load cell and displacement was measured using external displacement transducers. For the reasons mentioned later in Section 6.3.5.2.1, the actuator was later changed to a Miller servo-controlled static rated actuator with a load capacity of 250 kips and stroke of 8 in. The force was measured using the manufacturer-supplied internal load cells and the displacement of the actuator's head was measured using internally mounted Linear Variable Differential Transformers (LVDTs).

To measure the deformation of the CHS in the specimen, the Krypton dynamic measurement machine was used. It has three sensitive infrared cameras mounted on a moveable frame, Light-Emitting Diodes (LEDs), and a data acquisition system. The LEDs are 1" in diameter and can be attached to any location visible to the cameras. The three cameras would capture the locations of the LEDs in a user defined

coordinate system. Accuracy of the krypton measurement is of the order of 0.004" and can be as high as 0.002", depending on the relative distance between the camera and the LEDs. The window of the Krypton camera in this test set-up was able to accommodate the entire concrete-filled CHS specimen, the reaction block, the actuator and part of the reaction frame.

The Krypton camera was placed in front of the specimen. It was used to capture the complete kinematics of the specimen, the reaction block and the actuator, by recording the 3D movement of LEDs attached to them. The layout and numbering of the LEDs used for testing specimen D16L5 is shown in Fig. 6-33. The LEDs were all facing the Krypton camera. The first 12 LEDs were at the following specified locations in the test set-up. LED 1 was used to measure the movement of the reactions blocks at the height of the tab plates. LEDs 2 and 6 were glued to the tab plates, while LEDs 3 and 7 were glued to the branch plates. The displacement of LED 2 and 3, 6 and 7 in the x-direction in Fig. 6-33 can be used to calculate the slippage between the branch and tab plates. Comparisons of the x-direction displacements of LED 1 and 2, 7 and 8 were used to obtain the elongation of the branch plates. The displacements of LED 9 and 10 in the x-direction can be used to calculate if rotation of the specimen occurred. LEDs 8, 9, and 10 were used to monitor the displacement of the actuator in 3-D space. Comparisons of the displacements of LED 3 and 10, as well as 4 and 10 in the x-direction, were used to monitor the deformation of the CHS, i.e. the separation of the CHS from the infilled concrete.

The largest deformation of the CHS was theoretically expected to happen at the CHS-to-branch plate connection points, which are on opposite sides of the specimen. The "CHS's Deformation-A" is defined here as the peak deformation of the CHS on the side close to the actuator, which is calculated as the displacement difference in the x-direction between LEDs 3 and 12 in Fig.6-33. Similarly, the "CHS's Deformation-R" corresponds to the peak deformation of the CHS on the side close to the reaction block, and the value is obtained from the displacement difference in the x-direction between LEDs 5 and 12 in Fig.6-33. Note that the terms CHS's deformation used throughout the text from here on refer to the above measures. The letters "A" and "R" will be used to represent the words "Actuator" and "Reaction Block", respectively.

In addition to the first 12 LEDs described above, a number of LEDs were glued to the CHS's perimeter to capture the separation of the CHS from the infilled-concrete across the perimeter of the tube. These were evenly spread on the surface over a distance defined by an angle ranging +/- 45 degrees from the horizontal, as shown in Fig. 6-33, which was expected to span the radius over which separation of the CHS from the concrete was anticipated, based on results from the Abaqus finite analyses of the specimen

model. The numbering of these LEDs started from 13 and increased in a clockwise direction. Note that the total numbers of LEDs for specimens of various diameters, since CHS with smaller diameters could not accommodate the same numbers of LEDs as the larger ones. For example, specimen D16L5-1 in Fig 6-34 had 24 LEDs attached along its perimeter, whereas D9L3-1 only had 12.
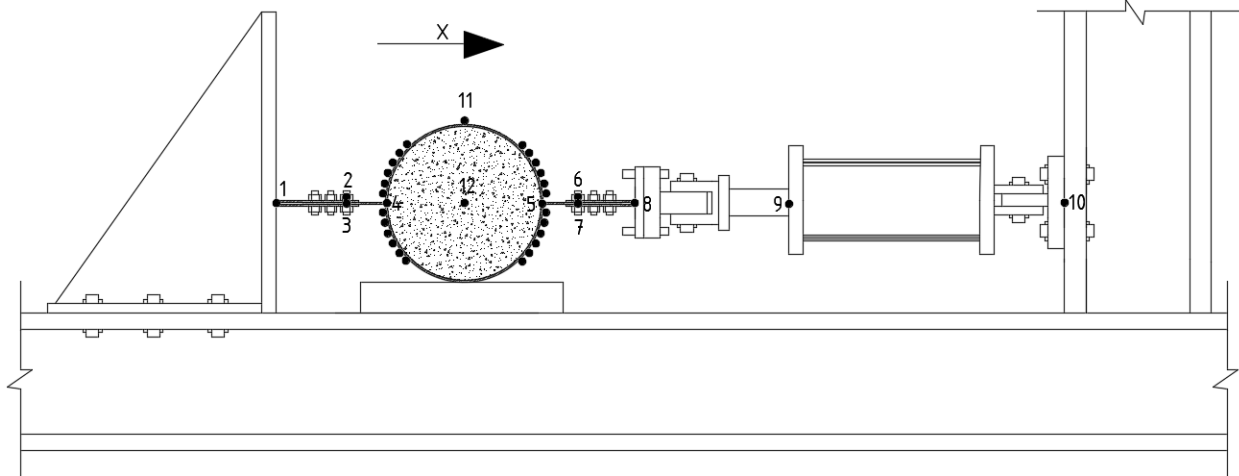
Figure 6-33 LED layout in the concrete-infilled CHS specimen test set-up

Figure 6-34 LED layout for specimen D16L5-1

The movement of the LEDs captured by the Krypton camera provided more accurate measurements of deformations of the CHS, but this data required post-processing after completion of the test and could not be used in real-time during the test. Therefore, String Potentiometers (SP) were also used during the test to monitor the real-time movement of the reaction block and the specimen. A vertical post was clamped to the flour beam in the reaction frame, to provide the magnetic attachment point for the SPs. The locations of the SPs are shown in Fig.6-35. SP1 and SP2, which were attached at the center level of the

specimen (i.e. the level of the actuator applying the load), were used to measure the displacement of the specimen and the reaction block. SP3 was placed at the bottom close to the base of the reaction block to capture any slippage between the reaction block from floor beam.
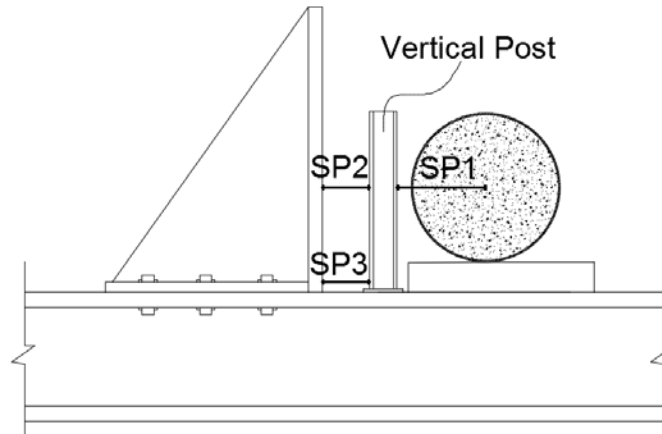
Figure 6-35 Positions of the string potentiometers in the test set-up

In order to monitor the stress change of the CHS during the test, the specimens were instrumented with strain gauges as shown in Fig. 6-36. In particular, two strain gauges, named "SG-A" and "SG-R", were attached to the CHS at the location corresponding to the point along the circumference where the SAP2000 Ring model analyses in Section 6.2.3.4, predicted that the moment diagram would end (defined by the zero-moment angle β shown in Fig. 6-36), where "A" and "R" refer to the strain gauge closer to the Actuator and the Reaction Block, respectively.
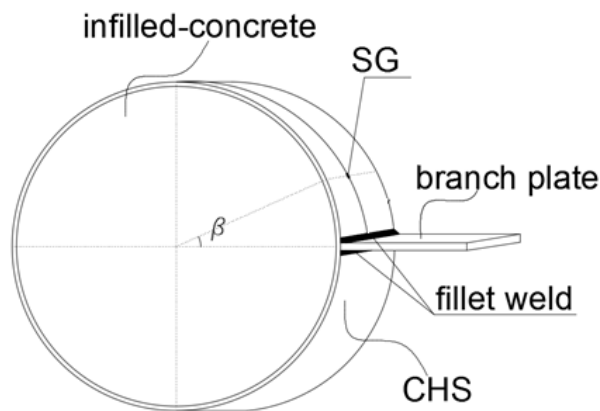
Figure 6-36 Positions of the strain gauges for the specimen

Digital videos were recorded for all the tests. Each test was documented using standard definition cameras to record the global and local view of the BRB specimens' behaviors during the tests. A high definition camera was used to focus on one side of the branch plate-to-CHS connection to capture the

190

failure of the connection. All videos were accelerated by post-processing to help provide a better understanding of the behavior of the specimens being tested.

6.3.3 Test Protocols

The general test protocols for testing the specimens monotonically and cyclically are presented in Sections 6.3.3.1 and 6.3.3.2, respectively. The details of the specific displacement protocols for each specimen will be presented later in Section 6.3.4, together with the test results of the specimen. A summary of the test performed on each specimen is provided in Section 6.3.3.3.

6.3.3.1 Monotonic pulling test

The monotonic pulling test used the actuator to apply pulling forces to the specimen, which separated the CHS from the infilled concrete. The actuator was displacement-controlled and its head moved at the speed of 0.1"/min, which is considered small enough for the quasi-static purpose of these tests. The displacement applied to the specimen started from zero and increased until it failed.

6.3.3.2 Incremental Cyclic Test

The incremental cyclic test protocol used for testing the concrete-filled CHS specimens was adapted from the protocol in Fig. 6-37, which was originally developed for testing steel structures in ATC-24 (ATC-24, 1992). In this protocol, Δ_{yield} represents the yield displacement of a component, a sub-assembly, or even the structural system. The ATC-24 protocol contains at least 6 elastic cycles (amplitude$<\Delta_{\text{yield}}$), followed by three cycles of amplitude Δ_{yield}, $2\Delta_{\text{yield}}$, $3\Delta_{\text{yield}}$, followed by pairs of cycles whose amplitude increases increments of Δ_{yield} until severe cyclic deterioration occurs.

For the incremental cyclic tests mentioned later in Sections 6.3.4, the cyclic protocol shown Fig. 6-38 was used. The incremental cyclic test of all the concrete-filled CHS specimens started from the zero displacement position, when the CHS was in contact with the concrete. The direction, in which the CHS was pulled and separated from the infilled concrete, corresponded to the positive displacement in this test protocol. After reaching the target displacement of the yield displacement (i.e., Δ_y), the displacement direction of the actuator reversed. The displacement would then decrease to zero displacement to complete the first cycle. Negative displacements were not applied to the specimen, because in that direction the branch plate would push on the concrete infill. At the displacement level of Δ_y, a total of

three cycles were applied. Then the displacement level increased proportionally to $2\Delta_y$, $3\Delta_y$, $4\Delta_y$, $5\Delta_y$, $6\Delta_y$, $7\Delta_y$, etc., and three cycles at each displacement level were applied to the specimen until it failed. Note that the shape of the protocol was also smoothened into a half-sine-wave shape to prevent sudden vibration or instability when the actuator reversed the direction of the applied displacement. The incremental cyclic tests were performed at a constant test rate, which was 0.4"/min and four times larger than the rate for the monotonic test with the purpose of trying to reduce the testing time. Note that the yield displacement for specimens with different CHS diameter is different. The detail of how it was obtained for each specimen is explained in detail in Section 6.3.5.2.4, using D16L5-4 as an example. Table.6-6 provides the yield displacement for the different specimens on which incremental cyclic tests was performed. The complete test protocols and specific displacement values for the individual specimens are presented in Section. 6.3.5 together with the test results.
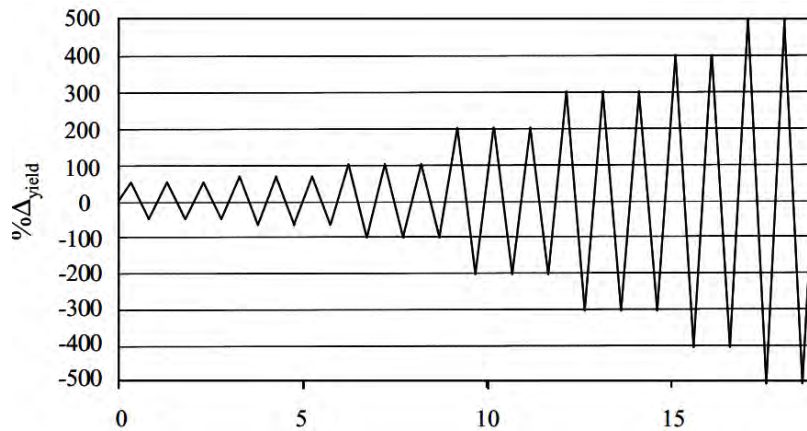
Figure 6-37 ATC-24 protocol for cyclic testing of steel structures (ATC-24, 1992)
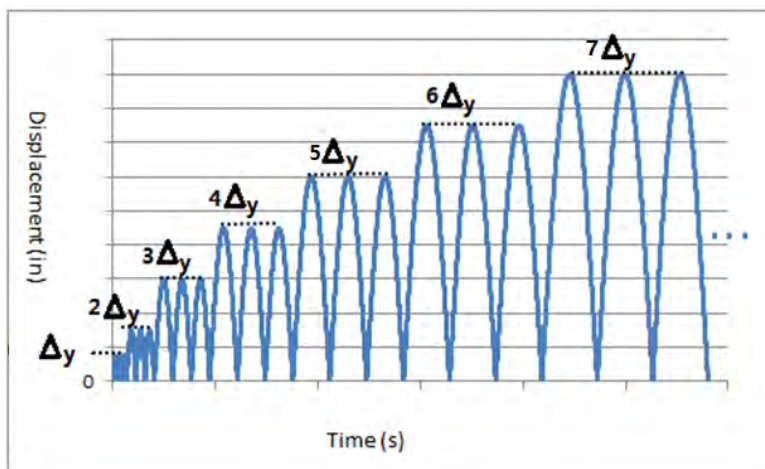
Figure 6-38 Cyclic test protocols for concrete-filled CHS specimen

192

Table 6-6 Yield displacement used in the test protocol for the incremental cyclic tests

Specimen Name	D16L5	D10.75L5	D9.625L3	D9.625L6	D9.625L7
Δ_y	0.0752"	0.0648"	0.0626"	0.0626"	0.0626"

6.3.3.3 Summary of Test protocols

Table 6-7 presents the summary of the test protocols for each specimen in Section 6.3.4. For each type of specimen listed in Table 6-4, the specimens are numbered as "D-i-L-j-k", which is the k-th specimen of the specimen type "D-i-L-j" (already described in Section. 6.3.2.2). A brief description of all the tests performed in Section 6.3.4 is presented below:

- Specimen D16L5-1 was tested monotonically, and failed in the branch plate. After strengthening the branch plates of specimen D16L5-2 as mentioned in Section 6.3.5.2.2, a monotonic test was performed on the specimen and it failed in the CHS close to the welds connecting the branch plate. In anticipation, to prevent a repeat of the undesirable branch plate failure, the branch plates of specimens D16L5-3 and D16L5-4 were also strengthened prior to testing, using the same reinforcement detail as for specimen D16L5-2. Specimen D16L5-3 was subjected to multiple cycles at a constant displacement amplitude in the cyclic test (named as "cyclic-2" in Table 6-7), until it failed. For this purpose, the displacement amplitude used was arbitrarily taken as the actuator head's displacement, when the force applied to specimen D16L5-2 reached 60 kips (76% of the maximum force reached in specimen D16L5-2 at 79.2 kips). Specimen D16L5-4 was tested with the incremental cyclic test protocol in Fig. 6-36.

- For the specimens D9.625L3, D9.625L6, D9.625L7, D10.75L5, for each specimen diameter, one of the specimens was used for the monotonic test and the other was used for the incremental cyclic test with the protocols in Fig. 6-36.

- Specimen D5L3-1 was tested monotonically. The infilled concrete crushed and the CHS deformed freely and fractured. After strengthening specimen D5L3-2 by using cap plates on both sides of the specimen, as shown in Section 6.3.5.5, to prevent the concrete from "popping out" when the CHS deformed, a monotonic test was performed on specimen D5L3-2 and it failed in the CHS close to the welds connecting the branch plate.

- Specimen D14L3-1 was tested monotonically. Since there were defects in the concrete for specimen D14L3-1 (the concrete was chipped at a location close to the branch plate during installation of the specimen in the test set-up), the infilled concrete was damaged before the specimen failed in the CHS as mentioned in Section 6.3.5.6. Therefore, Specimen D14L3-2 was also tested monotonically.

193

Specimen D14L3-2 failed in the concrete again because of a sudden vibration that shook the specimen when bolt slippage occurred.

Table 6-7 Summary of concrete-infilled CHS test protocols

	Specimen															
CHS Diameter (in)	5		9.625		9.625		9.625		10.75		14		16			
CHS width (in)	3		3		6		7		5		3		5			
Numbering	1	2	1	2	1	2	1	2	1	2	1	2	1	2	3	4
Monotonic Test	×	×	×		×		×		×		×	×	×	×		
Incremental Cyclic Test				×		×		×		×						×
Cyclic-2 Test															×	

6.3.4 Abaqus model of the specimen

Abaqus specimen models were built and subjected to tensile forces pulling on the branch plate. Only monotonic tensile loading was simulated in the analyses. The predicted failure strength for each type of specimen was obtained, along with the failure mode of the specimen. Specimen D16L5 is used as an example in Section 6.3.4.1 to present the modeling details of the Abaqus specimen model followed by presentation of the analyses results in Section 6.3.4.2. Specimen D16L5 is representative of specimens having a CHS's width equal to that of the branch plate. The modeling and analyses results of specimens D9.625L3, D9.625L6 and D9.625L7 are presented in Section 6.3.4.3. The behavior of these specimens, having different CHS width and the same branch plate is also compared there.

The Abaqus specimen models were initially built with assuming A500Gr.B steel (yield strength of 42 ksi and ultimate strength of 58 ksi) for the CHS. The strength of each type of specimens was used to design the specimens and the test setup, as mentioned earlier in Section 6.3.2. After obtaining the material property from the tests mentioned in Section 6.3.2.3, analyses of all specimens were re-performed using the specimen's actual material properties; it is the result of those analyses that are presented in this section.

6.3.4.1 Modeling details of specimen D16L5

The Abaqus specimen that was modeled includes the branch plate, the fillet weld and the concrete-filled CHS, as shown in Fig. 6-39a. Since the specimen is symmetric, only 1/8 of the specimen was modeled to reduce the computational demand. The bolted connection between the tab and branch plates was not

modeled, and uniform area loads were applied at the tip of the branch plate. Each component of the Abaqus specimen model in Fig. 6-39a was modeled using the general purpose solid element C3D8R. The fillet weld was modeled in contact with both the CHS and the branch plate, using tie constraints as shown in Fig. 6-39b. The discretization method for the tie constraints was "surface to surface", for which the master and slave surface must be defined. For the tie constraints between the branch plate and fillet weld, the surface of the branch plate and the fillet weld served as the master and slave surface, respectively. Similarly, for the tie constraints between the CHS and fillet weld, the surfaces belonging to the fillet weld and CHS served as the master surface and slave surface, respectively. Thus, model replicated the fact that, in the fabricated experimental connection detail, the load was transferred from the branch plate to the CHS through the fillet weld. General contact between the inner surface of the CHS and the outer surface of the concrete infill was used, and the friction setting was the same as for the Ring model in Section 6.2.4.1. The converted true stress and strain material properties of the actual CHS, and concrete were used for the Abaqus specimen model. The steel in the branch plate was taken as A572Gr60 with yield strength of 60 ksi and ultimate strength of 75 ksi. The fillet weld used matching electrode E80 with yield and ultimate strength of 68 and 80 ksi, respectively. For the Abaqus specimen models, the same mesh technique of "structured" and element shape of "hex" as in the prior Abaqus Ring model were used.
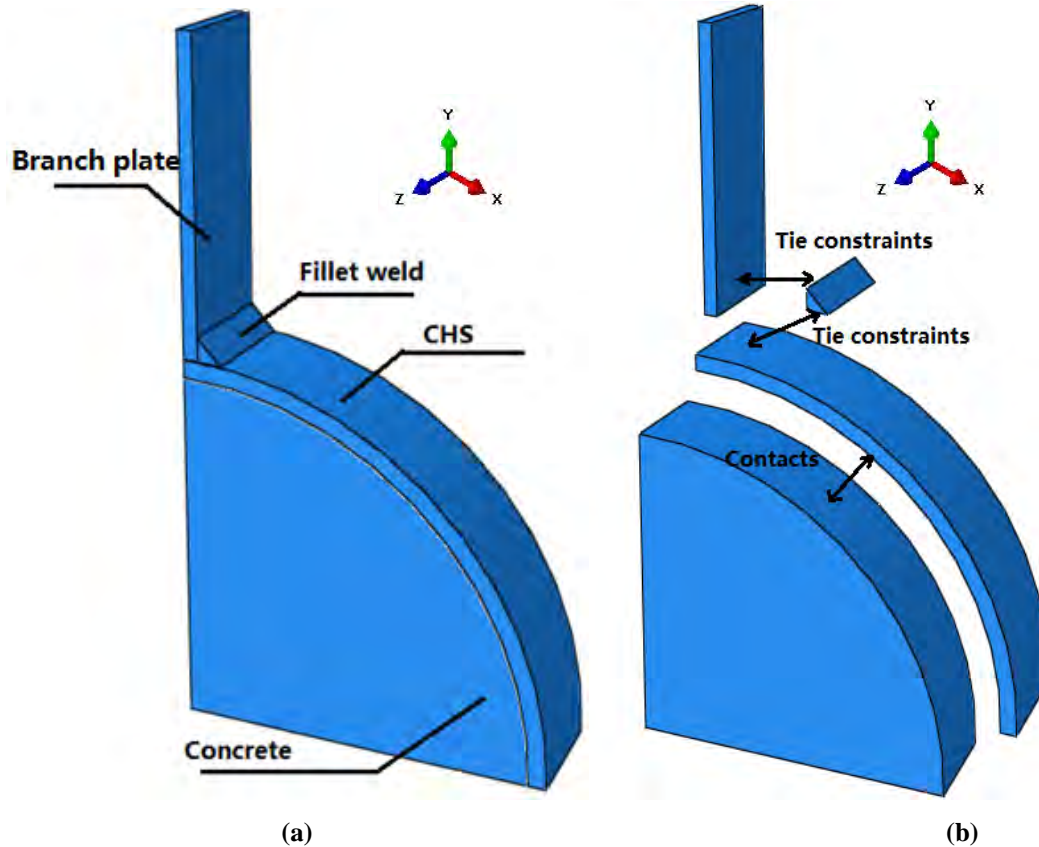
Figure 6-39 Abaqus specimen model: (a) names of parts in the model; (b) contacts and constraints between different parts

Fig. 6-40 shows the mesh for specimen D16L5. The mesh used through the thickness of the CHS divided itself into 12 layers. The branch plate, CHS, and the fillet weld had a mesh size of 0.075" along the direction of z, and the number of mesh elements was 33. The mesh size along the perimeter of the Abaqus specimen model was 0.1". The leg of the fillet weld was set to have a mesh size of 1/32", resulting in a total number of 39 elements in the cross section of the fillet weld. Convergence of the analysis results was achieved with these chosen mesh size after trial and error on the Abaqus model.
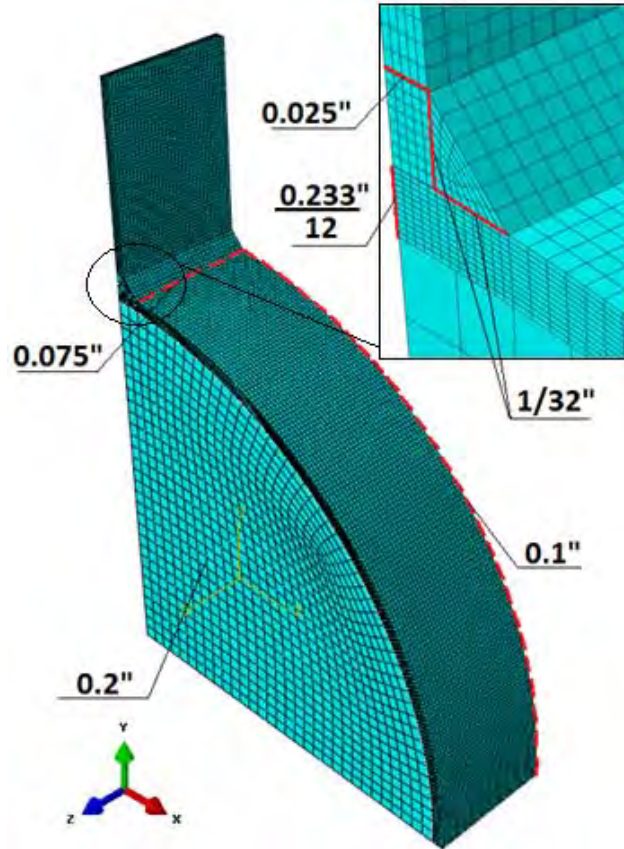
Figure 6-40 Mesh size for different parts of the Abaqus specimen model

Since only 1/8 of the specimen was modeled, the Abaqus specimen model was restrained as shown in Fig. 6-41, where for each of the blown-up surface of the model shown in that figure, the directions in which modes on those surfaces have been restrained. Displacement control was used to gradually apply displacements at the branch plate, until failure of the model, which was considered to have occurred when the ultimate strain provided in the material model was reached in the CHS.

In the analyses, geometric nonlinearity was considered. A "Full Newton" solution technique was selected. The displacement increment was automatically adjusted so that the time increment in each step would permit convergence of results without unstable responses, and the range of the increments remained within a reasonable range to ensure that equilibrium could be found. The minimum and maximum increment was set to be 1×10^{-7} and 0.01 for this case, respectively.
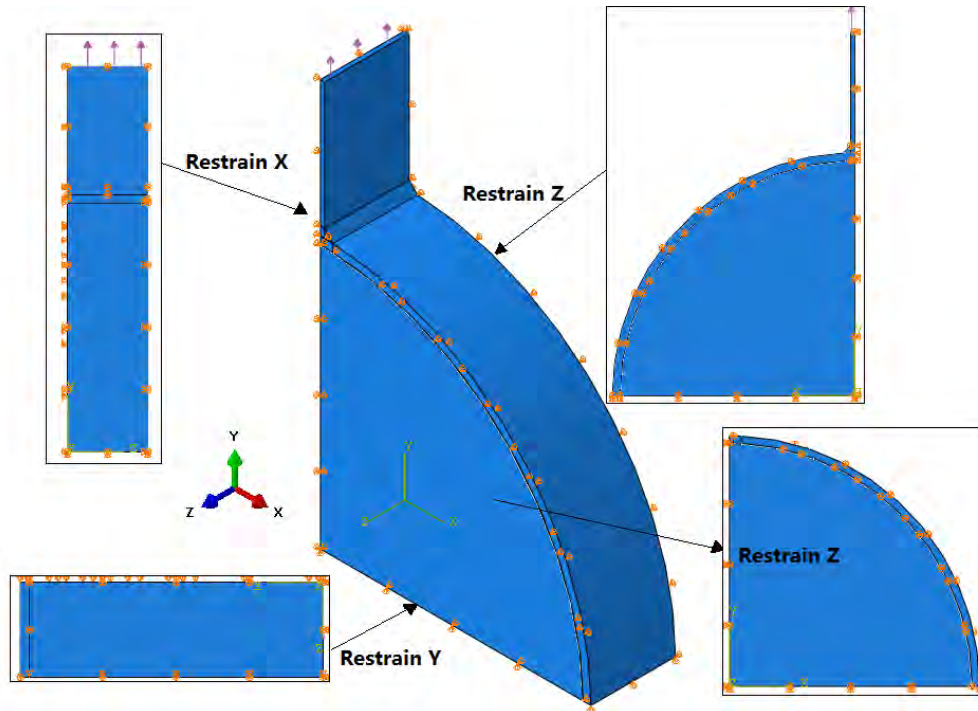
Figure 6-41 Mesh size for different parts of the Abaqus specimen model

6.3.4.2 Analyses results of D16L5

The behavior and analyses results for the Abaqus model of specimen D16L5 are presented in this section. In the end, the specimen model was deemed to have failed when the ultimate strain was reached in the CHS section close to the weld, as shown in the enlarged view in Fig. 6-42. Recall, from Section 6.3.2.3, that a yield strength f_y of 50.9 ksi was obtained for the coupons of the CHS used in Specimen D16L5. The first yielding strength of the specimen was therefore defined as the point when the extreme fiber of the CHS reached this yield stress. The corresponding Von-Mises stress contours for the specimen are shown in Fig. 6-42a. A force of 10.59 kips was applied to the specimen at first yield, with a corresponding peak CHS deformation of 0.028"; the location where first yield was observed is shown by the black dot on the CHS (in line with the branch plate) in the enlarged view in Fig 6-42. Note that this force is 4 times of the value obtained from Abaqus, because that latter one is obtained for the 1/8 model. This correction will be done consistently throughout the following presentation of results. The moment and axial force at the failure section were obtained and are shown in Fig. 6-43. Von-Mises stress contours for the specimen are also shown in Fig. 6-42b for the point when the moment at the failure section reached it maximum value (as identified in Fig. 6-43). The load applied to the specimen when that

198

maximum-moment was reach is 24.78 kips, with a corresponding peak CHS deformation of 0.066". Note that the deformations shown in Figs. 6-42 are presented with a scale factor of 1.

(a) **(b)**
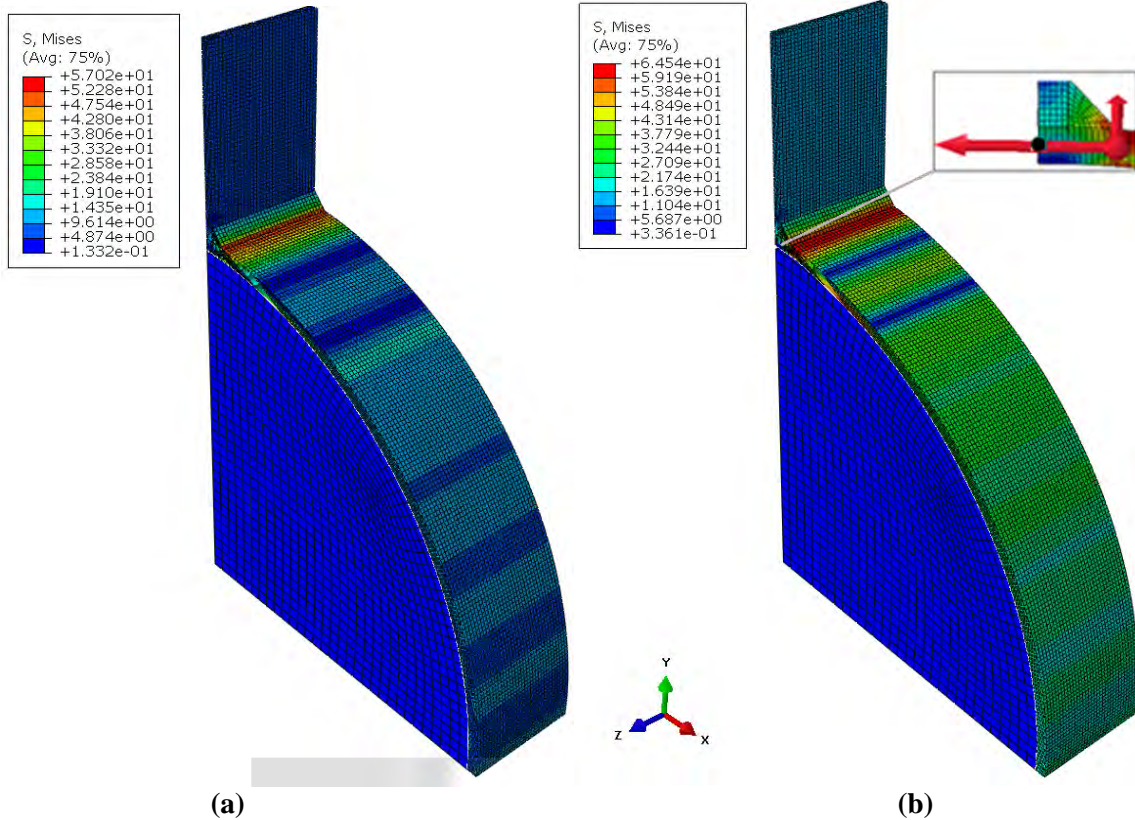
Figure 6-42 Von-Mises stress contour of the Abaqus specimen model: (a) first yielding reached at failure section; (b) maximum moment reached at failure section
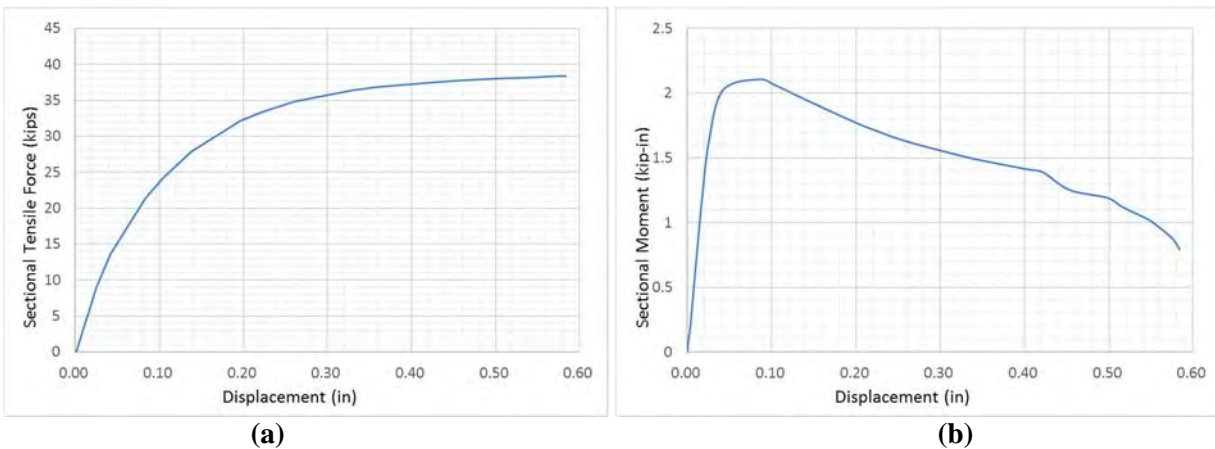
(a) **(b)**
Figure 6-43 The axial force and moment at the failure section: (a) axial force; (b) moment

The specimen's applied force versus peak CHS deformation curve is shown in Fig. 6-44. The points, which correspond to the state of the specimen in Figs. 6-42a and b, are marked out in Fig 6-44. Recall that in Section 6.3.2.3, a maximum engineering strain limit of 0.284 in/in was set, as this was the value

obtained from the coupon test of the CHS material for specimen D16L5. The corresponding logarithmic (true) strain is 0.25 in/in per Equation 6.24. When this maximum logarithmic strain was reached in the model at what was deemed to be the failure section, the strength of the model was 70.2 kips with a corresponding peak CHS deformation of 0.583".
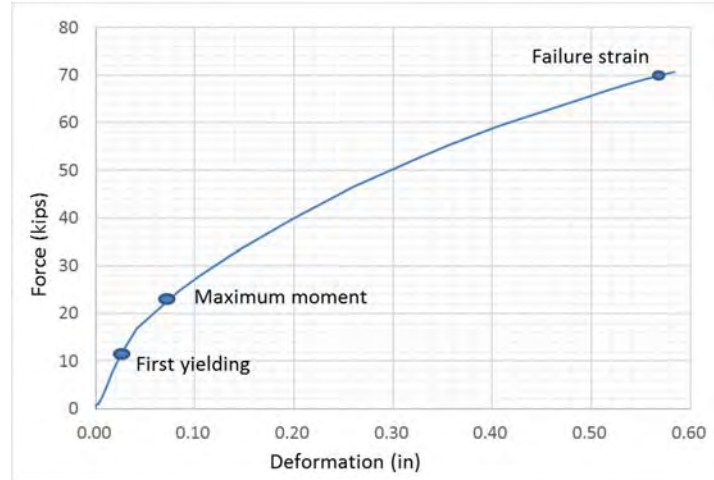
Figure 6-44 Applied force versus peak CHS deformation curve for Abaqus specimen D16L5

Note that the other specimens having CHS width equal to that of the branch plate behaved in a similar way. The applied force versus peak CHS deformation for each type of specimen is presented in Section 6.3.5 and compared with the corresponding test results.

6.3.4.3 Abaqus modeling and analyses results for specimens with CHS diameter of 9.625"

In this section, additional information related to the modeling of specimens with CHS diameter of 9.625" in Abaqus is presented. The behavior of specimens, having different CHS width and the same branch plate, were studied, and findings are reported in this section together with comparisons between results for these specimens. The mesh size of specimen D9.625L3 is shown in Fig. 6-45a for comparison. Similar to the mesh for specimen D16L5 in Fig. 6-40, the mesh size used through the thickness of the CHS divided itself into 12 layers. For the Abaqus model D9.625L3 in Fig. 6-45a, the mesh number along the width of the CHS were 30. The leg of the weld was set to have a mesh size of 3/64", which resulted in a total number of 48 elements in the cross section of the fillet weld. The global mesh size was set to be 0.075" and 0.2" for the CHS and the infilled concrete. The mesh of specimen D9.625L7 is shown in Fig. 6-45b. The mesh settings were kept the same as for the D9.625L3 model.

The three Abaqus models of D9.625L3, D9.625L6 and D9.625L7 failed in the CHS section close to the weld. Note that "failure" in these Abaqus analyses is defined here as the point, when the maximum engineering strain limit (obtained from the coupon test) was reached at any point in the CHS in the model. The maximum moment was taken at the failure section of D9.625L3 similar to D16L5, and the sectional moment and force were also obtained from the section of D9.625L6 and D9.625L7 at the same location as marked in the enlarged view in Fig. 6-45b.

(a)   (b)
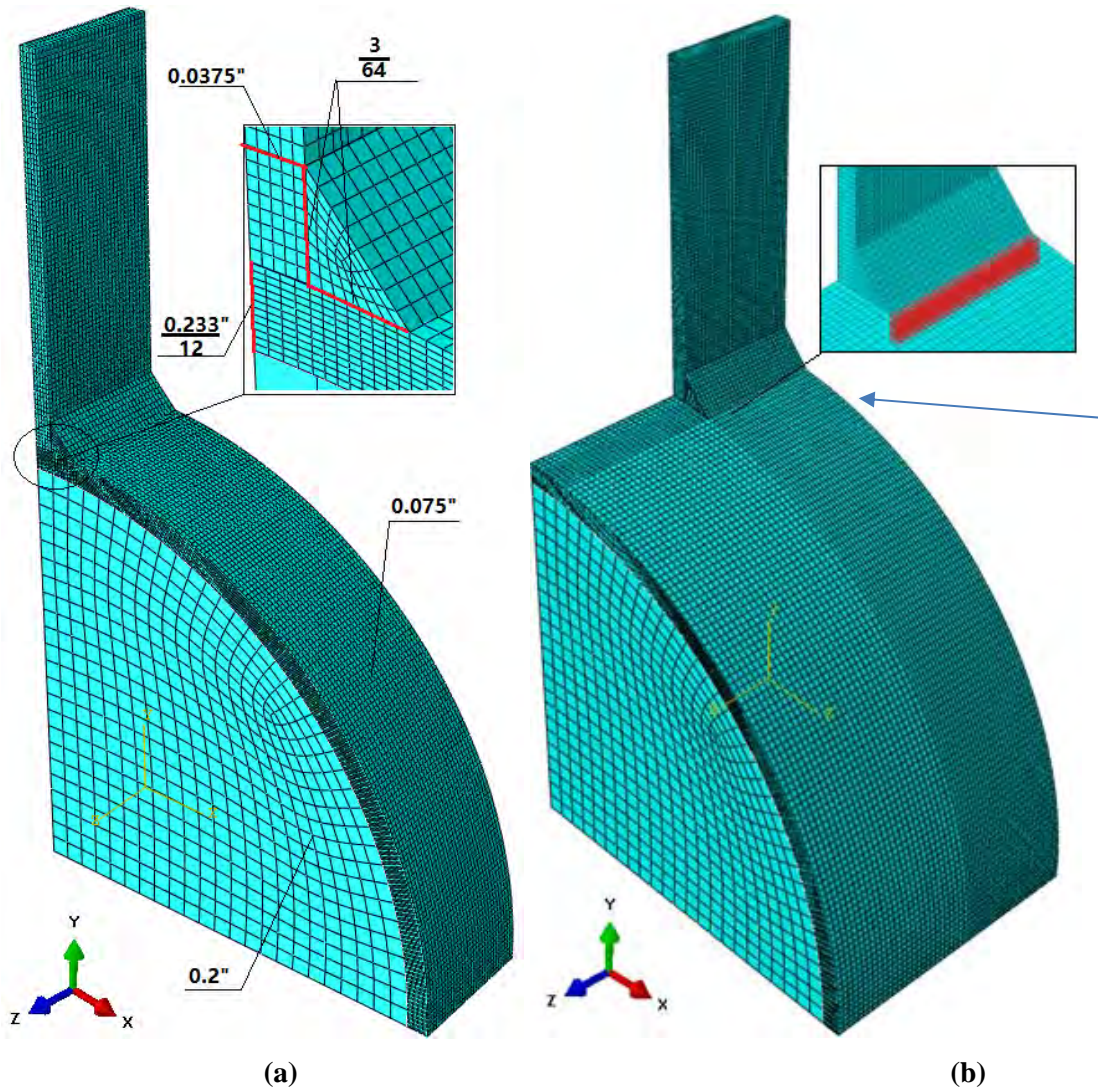
Figure 6-45 Mesh size for different parts of the Abaqus specimen models

The peak CHS deformation of D9.625L3 was taken at the similar location as the D16L5 model, i.e. at the middle of the CHS thickness (in line with the branch plate). For specimen D9.625L6 and D9.625L7, the corresponding location was taken at a similar location, at the surface pointed by the arrow in Fig. 6-45b. The resulting applied force versus peak CHS deformation curve obtained for these three Abaqus models

are plotted in Fig. 6-46. Note that the difference between the model D9.625L6 and D9.625L7 is minimal. Note that the CHS widths of 6" and 7" were chosen for the test specimens D9.625L6 and D9.625L7 on the basis of this analyses result, to verify that there is a limit of how much the extra width of the CHS (beyond the width of the branch plate) could contribute to the overall strength of the specimen, when the specimens have different CHS width and the same branch plate.
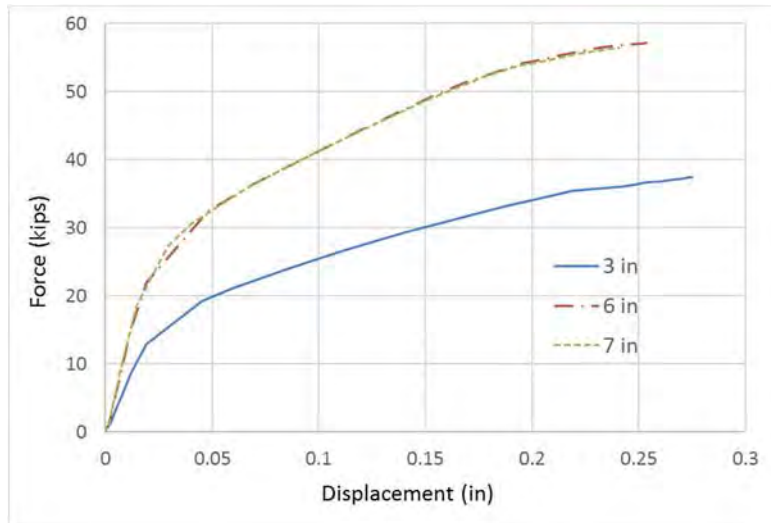
Figure 6-46 The applied force versus peak CHS deformation curve comparison of Abaqus specimen with CHS diameter of 9.625", and widths of 3", 6" and 7"

The critical strengths obtained from the Abaqus models were tabulated in Table 6-8, which correspond to three states: (1) first yielding, defined as the point when the stress of the extreme fiber of the CHS reached the yielding strength of 47.9 ksi (obtained from the coupon test of the CHS material for specimen with diameter of 9.625"); (2) maximum moment, obtained when the moment at the failure section reached the maximum value; (3) maximum strain, corresponding to the maximum the logarithmic (true) strain of 0.218 in/in reached in the CHS at what was defined above as failure (the maximum engineering strain limit of 0.244 in/in was obtained from the coupon test).

Table 6-8 Comparison of forces obtained from specimens with diameter of 9.625" at different states

CHS width		Abaqus model		
		First yielding	Maximum moment	Maximum failure strain
3	Force reached (kips)	5.82	19.2	35.6
	Corresponding displ. (in)	0.0082	0.045	0.227
6	Force reached (kips)	6.01	26.9	44.2
	Corresponding displ. (in)	0.0036	0.033	0.119
7	Force reached (kips)	6.13	27.3	44.7
	Corresponding displ. (in)	0.0028	0.032	0.120

6.3.4.4 Comparisons between the Abaqus Ring and Specimen model

In this section, the analytical results from all the Abaqus Specimen models (tabulated in Table 6-9) are compared. Recall that Abaqus Ring models were built in Section 6.2.4 to determine the unit-width strength when first yielding happened, and when the sectional moment at the load application point reached the maximum. When the actual steel materials obtained from the coupon tests in Section.6.3.2.3 were used in the Ring model, the resulting first-yielding and maximum-moment strengths were obtained (as shown in Table 6-9). The predicted first-yielding and maximum-moment strength of the specimen can be calculated by multiplying the unit-width strength obtained from the Abaqus Ring model by the width of the branch plate. Comparisons were made in Table 6-9 with the results from Abaqus specimen models, and the differences observed indicate that the predictions from the Ring model were conservative. Note that the larger strengths obtained in the Abaqus specimen model were partly due to the fact that the branch plate was pulling over an area of the CHS, rather than at a point as in the Ring model, as mentioned in Section 6.3.2.2.

Table 6-9 Strength comparisons between the predicted values from Abaqus Ring model and analysis results from Abaqus Specimen model

CHS Shape	16×0.25	10.75×0.188	14×0.375	9.625×0.25	5×0.25
Design Wall Thickness(in.)	0.233	0.174	0.349	0.233	0.233
D/t_0	68.67	61.78	40.11	41.31	21.46
Width of the CHS (in.)	5	5	3	3	3
First-Yielding Force-Abaqus Ring model (kips)	1.52	1.218	3.08	1.67	3.76
Predicted specimen force at First-Yielding (kips)	7.60	6.09	9.24	5.01	11.28
First-Yielding Force-Abaqus Specimen model (kips)	10.59	7.48	14.9	5.82	13.5
Force difference at First-Yielding between the Ring model prediction and analysis results from Specimen model	39.3%	22.8%	61.3%	16.2%	19.7%
Force reached at sectional Maximum Moment -Abaqus Ring model (kips)	3.38	3.05	6.59	4.18	6.0
Predicted specimen force at sectional Maximum Moment (kips)	16.9	15.25	19.8	12.54	18.0
Force reached at sectional Maximum Moment -Abaqus Specimen model (kips)	24.78	21.4	28.8	19.20	25.7
Force difference at sectional Maximum Moment between the Ring model prediction and analysis results from Specimen model	46.6%	40.3%	45.5%	53.1%	42.8%

6.3.5 Detailed test protocols and test results

6.3.5.1 General

Specimens with 16" diameter were first tested, and the corresponding testing protocols and results obtained are presented in details in Section 6.3.5.2, along with a description of adjustments made to the test setup and specimens. Section 6.3.5.3 provides the test results for specimens with 9.625" diameter. The behavior of these specimens, having different CHS width and the same branch plate, are investigated. The test results for the specimens having diameters of 10.75", 5" and 14" are presented in sections 6.3.5.4, 6.3.5.5, and 6.3.5.6, respectively.

6.3.5.2 Specimen D16L5

6.3.5.2.1   Specimen D16L5-1

Three tests were performed on specimen D16L5-1. A tensile force was first applied to specimen D16L5-1 in test D16L5-1-A. The hydraulic pressure in the actuator was turned off after test D16L5-1, which left a residual out-of-roundness deformation to the specimen. In test D16L5-1-B, a compressive force was applied to the specimen to bring the CHS in the specimen to its original shape. The test set-up was adjusted after test D16L5-1-B. In test D16L5-1-C, specimen D16L5-1 was tested monotonically under tensile force, and the specimen failed due to net section fracture in the branch plate.

a)   Test D16L5-1-A

Specimen D16L5-1 was first tested monotonically. The specimen was located in the test set-up (Fig. 6-33) such that the stroke of the actuator allowed applying a maximum applied displacement of 3" in the positive-x direction. Due to an error with the settings of the data acquisition system, the actual displacement applied to the specimen turned out to be only half of what believed to be observed in real-time. Therefore, when the displacement was shown to reach 3", the test was stopped to avoid the possibility of damaging the actuator. However, in fact, the head of the actuator had only moved by 1.5" in this case, and the corresponding largest force obtained from the load cell was 60 kips. The force dropped to zero after the hydraulic pressure in the actuator was turned off. Fig 6-47 shows the obtained curve of the applied force versus the displacement of the actuator head.
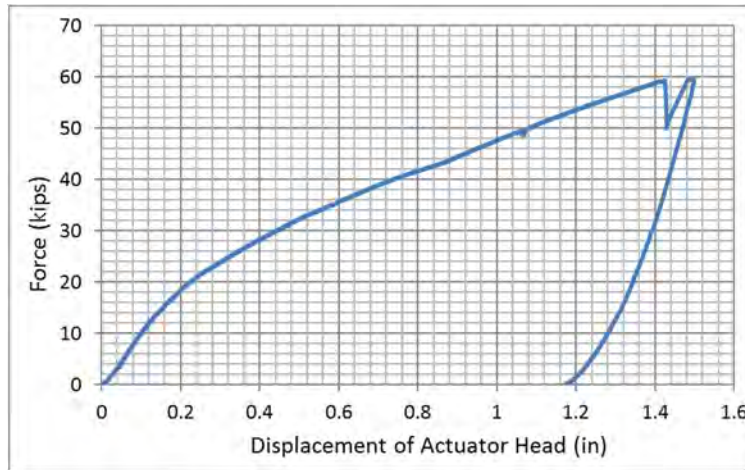
Figure 6-47 Applied force versus actuator's applied displacement curve for specimen D16L5-1 in test D16L5-1-A

During the loading process in test D16L5-1-A, the movement of the LEDs attached to the CHS was recorded and the peak CHS deformation were obtained after the post-processing. Fig.6-48 shows the applied force versus the peak CHS deformation, in which "A" and "R" represents the peak CHS deformation on the connections sides having branch plates connected to the "Actuator" and the "Reaction block", respectively. The procedure used to calculate the peak CHS deformations is explained in Section.6.3.2.4. The same notation for peak CHS deformations is used throughout this Section. Note that the peak CHS deformations are not exactly the same on both sides of specimen. Also note that the unloading process in Fig 6-48 was not captured by the LEDs on the CHS, since the recording of the Krypton data acquisition system was stopped after the hydraulic pressure in the actuator was turned off.

At the end of the loading process, the peak CHS deformation on both sides of the CHS added up to 0.78", which differed from the displacement of the actuator head of 1.5". The difference was due to:

(1) Bolt slippage between the tab and branch plates (slippage happened can be seen by the sudden drop in load in Fig. 6-47); note that the bolts used in the connection has not been designed to be slip-resistant at the that early time of this test;

(2) Insufficient anchorage of the reaction block to the floor beam in the reaction frame. The loading level of the actuator required the reaction block to be raised about 2.875" from the top of the floor beam in the reaction frame. Being so elevated, the originally designed anchor bolts for the reaction block could provide enough resistance for the applied overturning force from the specimen as they behaved not only in shear but also in flexure (which was not originally anticipated).
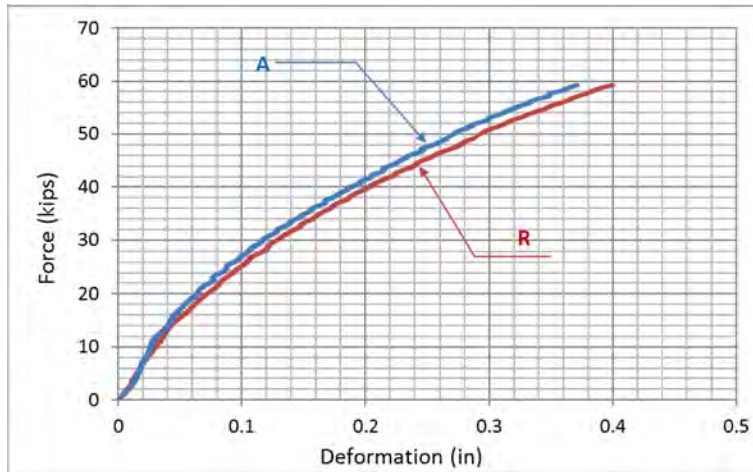
Figure 6-48 Applied force versus peak CHS deformation curve for specimen D16L5-1 in test D16L5-1-A

The experimentally obtained results in Fig.6-48 are compared with the analyses results from the Abaqus specimen model in Fig. 6-49. It is seen that the Abaqus analyses results generally match well with the test results.
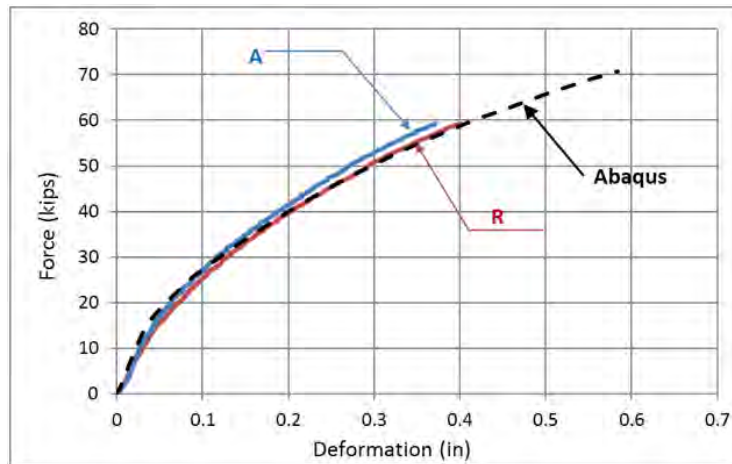
Figure 6-49 Comparison of the applied force versus peak CHS deformation curves between the Abaqus analyses and experiment results for specimen D16L5-1

b) Test D16L5-1-B

Specimen D16L5-1 was then subjected to a compressive force with the intent to push the CHS back to its original shape. The resulting curve for the applied actuator's force versus the displacement of the actuator head in test D16L5-1-B is shown in Fig 6-50 by the dotted line.

206

For comparison, Fig. 6-51 shows the applied force versus peak CHS deformations obtained from the Krypton on both side of the specimen. Since the deformation of the CHS was not recorded by the krypton system during the unloading process in test D16L5-1-A, the starting deformation of the CHS in Fig 6-51 used the final recorded peak CHS deformation in Fig. 6-47.
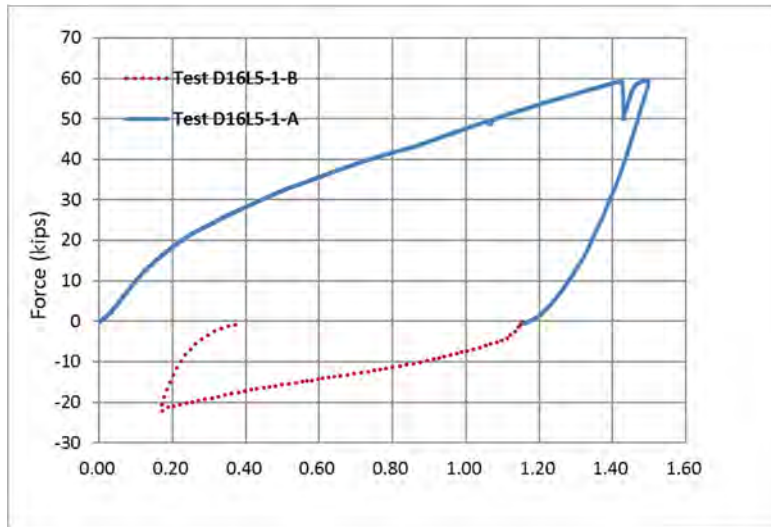
Figure 6-50 Applied force versus actuator's applied displacement curve for specimen D16L5-1 in test D16L5-1-B
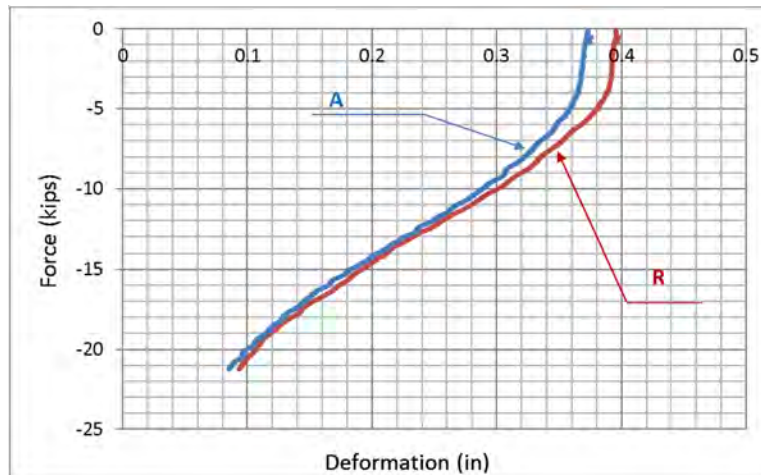
Figure 6-51 Applied force versus peak CHS deformation curve for specimen D16L5-1 in test D16L5-1-B

c) Test D16L5-1-C

Since the specimen did not fail at the force of 60 kips, there was a concerned that the actuator first used (mentioned in Section 6.3.2.2), with a force capacity of 70 kips, might not be able to fail the specimen. Therefore, the actuator in the test set-up was changed to a different one (the Miller servo-controlled static

rated actuator) with a load capacity of 250 kips and stroke of 8 in. The connecting location for the tab plates to the reaction block was lowered so that the reaction block would be in contact with the floor beam in the reaction frame during the test. The large displacement of the reaction block observed in Test D16L5-1-A could thus be reduced.

In test D16L5-1-C, specimen D16L5-1 was subjected to a monotonic tensile force again. The bolts between the tab and branch plates again slipped, at a force of 51 kips. After this slippage, the branch plate eventually yielded and fractured at the net section at the bolt hole. The displacements applied to the specimen were therefore mostly taken by the deformations in the branch plate. The applied force versus peak CHS deformation is not therefore not shown for test D16L5-1-C.

6.3.5.2.2   Specimen D16L5-2

Given that the branch plate in the previous specimen failed before the desired failure mode in the CHS could be reached, the branch plate for some of the subsequent tests needed to be strengthened. The thickness of the branch plate was 1/4" and the space between the tab plates was 3/8". Therefore, there was only space for a strengthening plate having the thickness of 1/8". Such a strengthening plate was welded to the branch plate with a 1/8" thick fillet weld as shown in Fig 6-52. The strengthening plate was wider than the branch plate, extending by 1.5" on both sides of the branch plate. The strengthening plate was first welded to the branch plate, and then (after the branch and strengthening plate cooled down), the bolt holes were drilled. Calculations for the design of the strengthening plate are provided in Appendix F. Both branch plates of the specimen were strengthened. Note that after strengthening of the branch plates proved effective during testing of specimen D16L5-2, the other specimens having 1/4" thick branch plates were all strengthened in the same way (including D16L5-3, D16L5-4, D10.75L5-1, and D10.75L5-2). The A490 bolts connecting the tab and branch plates were also pre-tensioned to provide the slip resistance during the test.

Specimen D16L5-2 was tested monotonically, and the resulting applied force versus peak CHS is shown in Fig. 6-53. Note that the peak CHS deformation shown in Fig 6-53 is only for the side close to the reaction block. The peak CHS deformation on the other side (close to the actuator) was not obtained due to a data acquisition error for the movement of LED 5 in Fig. 6-33. Specimen D16L5-2 failed at a force of 79.2 kips. The curve in Fig 6-52 does not show the part after the failure, because the LED 3 fell off the CHS due to the sudden vibration caused by the specimen failure.

208

(a)   (b)
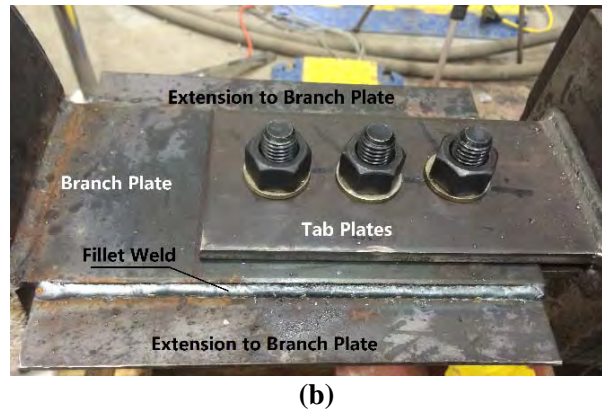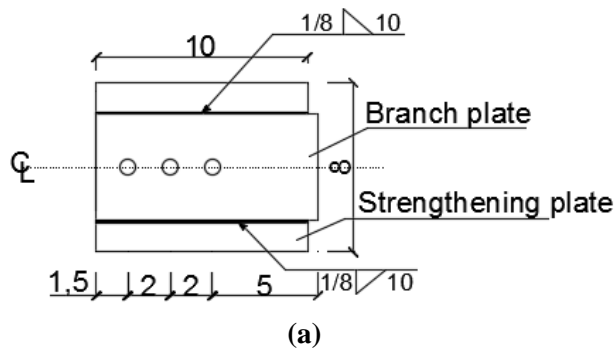
Figure 6-52 Branch plate welded with strengthening plate: (a) dimensions; (b) photo of strengthened branch plate with tab plate bolt connection
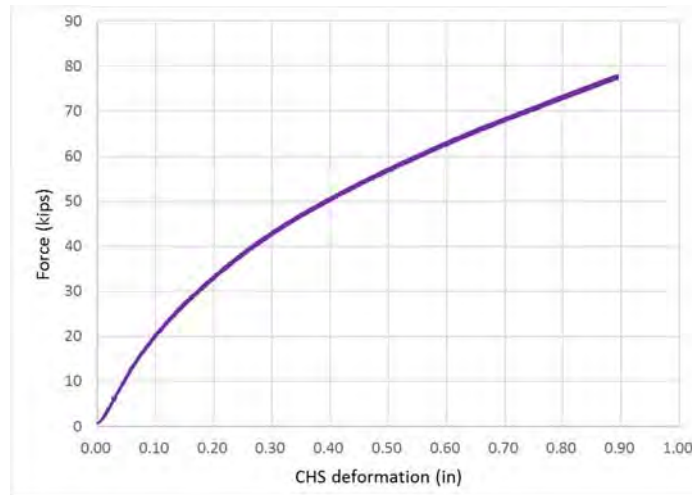
Figure 6-53 Applied force versus peak CHS deformation curve for specimen D16L5-2

The specimen failed in the CHS close to the weld connecting it to the branch plate, as shown in Fig. 6-54a, which was on top of the branch plate towards the actuator. Fig. 6-54b shows the view of the failure section of the CHS from the direction pointed by the arrow in Fig. 6-54a.

The curve in Fig.6-53 from the test was compared with the analysis results from the Abaqus specimen model, as shown in Fig. 6-55. The Abaqus analysis results give a specimen strength higher than the value from the test at the same peak CHS deformation.

(a)	**(b)**
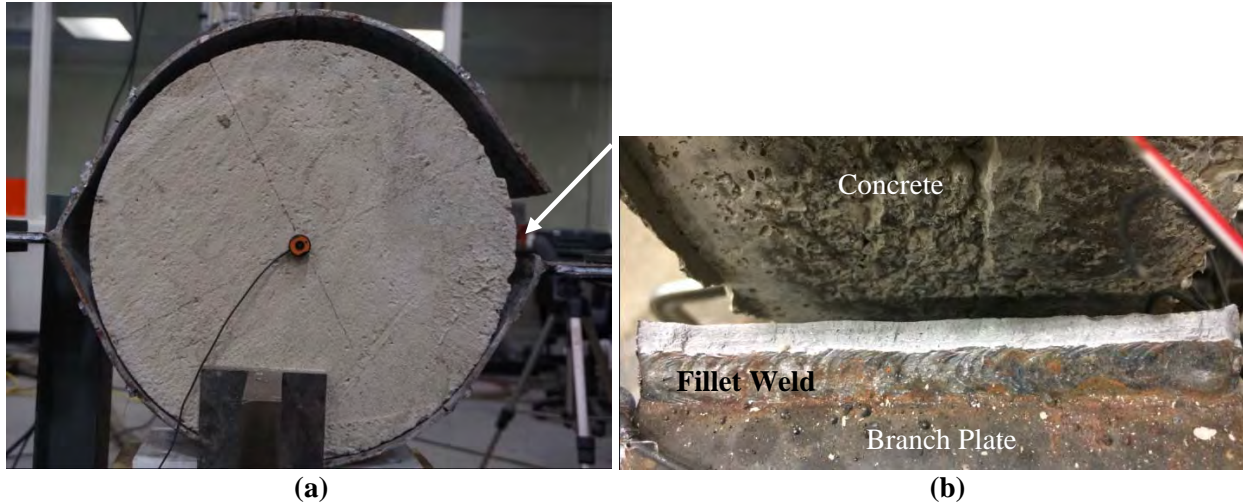
Figure 6-54 Failure of specimen D16L5-2
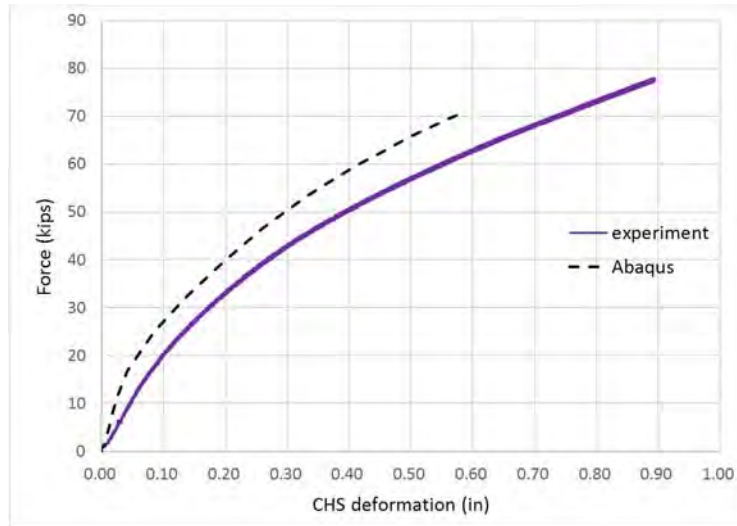
Figure 6-55 Comparison of the applied force versus peak CHS deformation curves between the Abaqus analyses and experiment results for specimen D16L5-1

The LEDs attached to the perimeter of the CHS were used to monitor the CHS deformation at those specific points shown in Fig.6-33. Recall that in Section. 6.3.4, three different states of the specimen under tensile loading were examined in the Abaqus analyses of D16L5. Strengths of 10.59, 24.78, and 70.2 kips were obtained corresponding to first yielding, maximum moment at the failure section, and maximum strain in the CHS (namely State 1, 2, and 3). Deformations of the CHS at the LED-monitored locations were obtained from the Abaqus specimen model analyses for these three states. Figs. 6-56 to 6-58 compares the experimentally and analytically-obtained deformations at the same locations along the CHS' perimeter, as the same three states respectively. Note that the CHS' deformation at these locations are only compared in the X direction (i.e., in the horizontal direction, it being the direction of the applied

210

loads). The left side of the CHS shown in Figs 6-56 to 6-58 corresponds to the CHS's side close to the reaction block. The peak CHS deformation on the actuator side are not shown here. Note that the CHS' deformations concentrated at locations close to the branch plate during States 1 and 2, and the CHS' deformation over the rest of the circumference remained zero and are therefore not shown in the figures. For State 3, the CHS' deformation started to develop more extensively towards the top and bottom of the CHS (i.e., away from the branch plates).

Recall from Section. 6.3.2.4 that strain gauges were attached to the CHS. The strain obtained from the strain gauges were converted to CHS surface stress. Fig. 6-59 shows the variation of surface stresses as a function of the force applied to the specimen as recorded by two strain gauges. The curves are compared with the curve obtained from the Abaqus analyses results at the same location. The general trend is the same for the three curves. Note that compressive stress first developed due to flexure in the CHS, but when the CHS continued to deform, the CHS plate became mostly in tension until the CHS section close to the weld failed.

(a) (b)
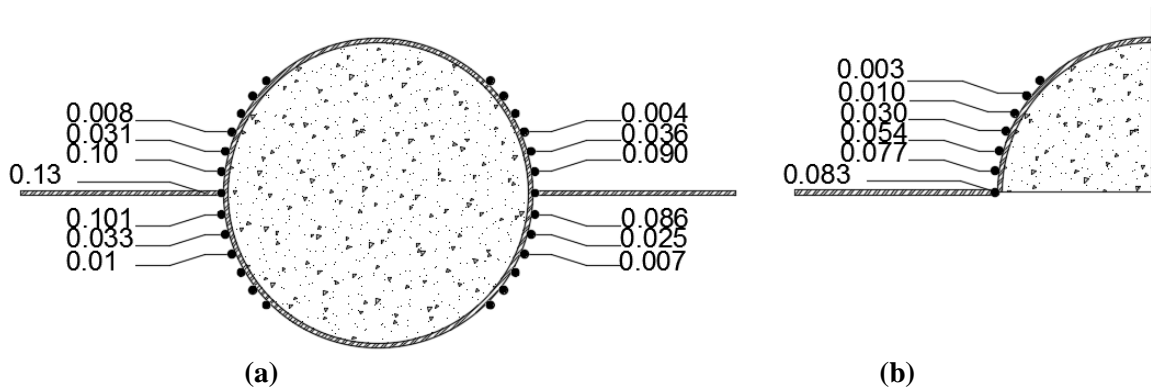
Figure 6-56 Comparison of the CHS' deformation at first yielding (state 1) from: (a) the test; (b) Abaqus analyses

(a) (b)
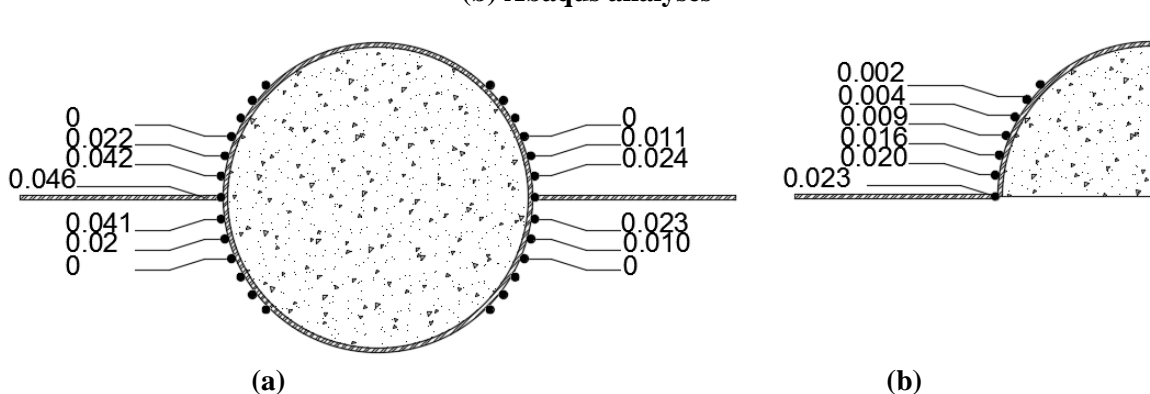
Figure 6-57 Comparison of the CHS' deformation at maximum moment of failure section (state 2) from: (a) the test; (b) Abaqus analyses

211
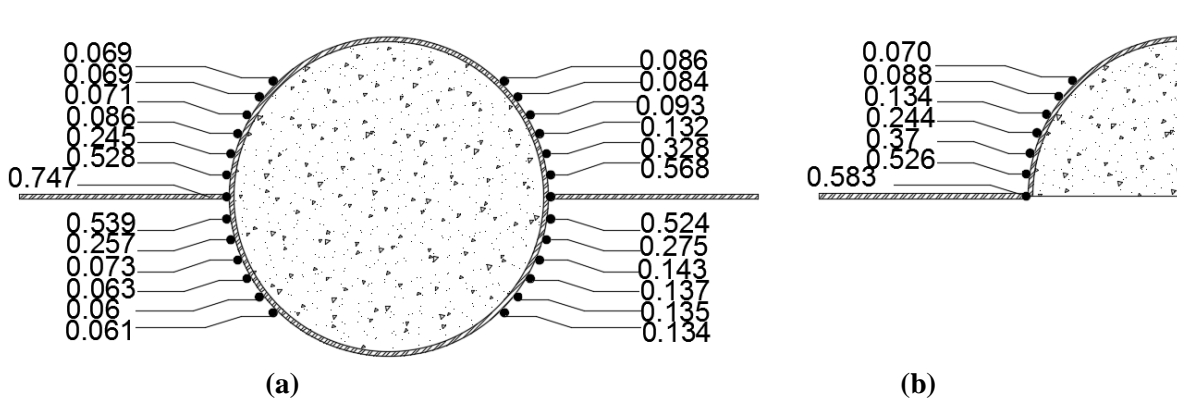
Figure 6-58 Comparison of the CHS' deformation at maximum strain of the CHS (state 3) from: (a) the test；(b) Abaqus analyses
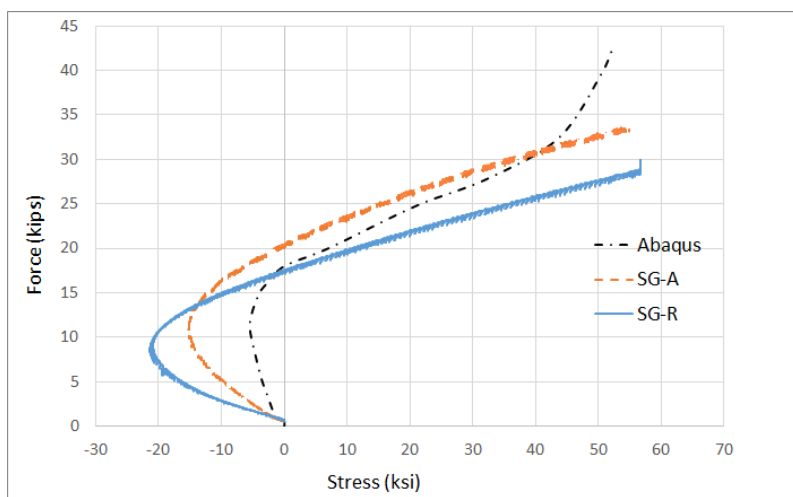
Figure 6-59 CHS surface stress comparison between the test and Abaqus analyses results

6.3.5.2.3   Specimen D16L5-3

Specimen D16L5-3 was subjected to multiple cycles with the same maximum displacement magnitude until it failed. This maximum displacement magnitude of 1.28" was taken from the displacement of the actuator head in the test of specimen D16L5-2, when the applied force was 60 kips. Note that this force value was arbitrarily chosen to determine the amplitude of displacement for the test protocol to test specimen D16L5-3 as shown in Fig. 5-60. Assuming specimens D16L5-2 and D16L5-3 have the same stiffness, specimen D16L5-3 was also expected to develop a force of 60 kips when the movement of the actuator head reached 1.28". The actuator's head moved at a speed of 0.4"/min, which was four times larger than the rate for the monotonic test of specimens D16L5-1 and D16L5-2. After completing the first three cycles, the specimen failed in the 4th cycle at a force of 30 kips, with a corresponding actuator's displacement of 1.2". The specimen failed in the CHS close to the weld connecting it to the branch plate.

212

The failure was similar to what is shown in Fig. 6-54a, but the fracture section was in the CHS below the branch plate close to the reaction block side. Fig. 6-61 shows the curve of the applied actuator's force versus the displacement of the actuator head. Note that the force drop in the curve was due to the slippage of the bolt connection between the tab and branch plates.
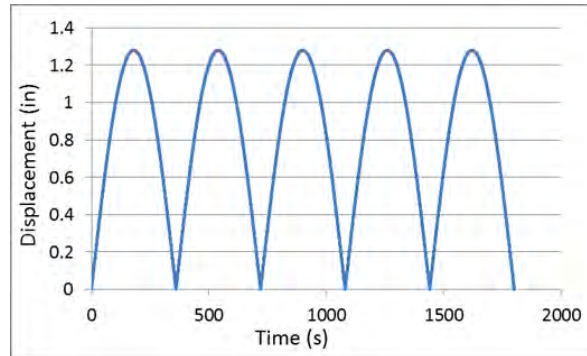
Figure 6-60 Cyclic testing protocol for specimen D16L5-3
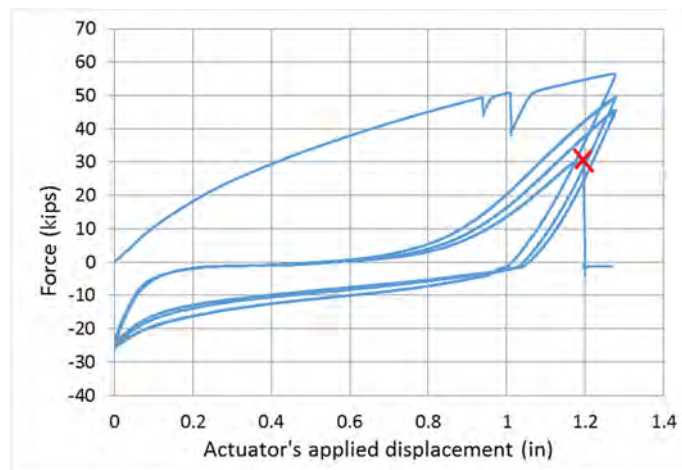
Figure 6-61 Actuator's force versus applied displacement for specimen D16L5-3

Fig. 6-62 shows the applied force versus peak CHS deformation obtained for specimen D16L5-3. Note that the peak CHS deformation on both sides of the specimen differed slightly. After the first half cycle, the displacement direction of the actuator head reversed its moving direction, and unloading took place in the specimen before compressive force was applied to it. The compressive stiffness of the specimen in the second half of the first cycle was much smaller, compared with the tensile stiffness in the first half cycle. In the following cycles, the force applied to the specimen remained close to zero until the CHS reached about 60% of the largest deformation attained in the previous cycle. Then, the force slowly increased as the CHS deformed and expanded more. The specimen in these following cycles showed a significant pinched behavior when compared with the first cycle. The maximum force resisted by the specimen at the maximum actuator displacement gradually decreased in each subsequent cycle.

213
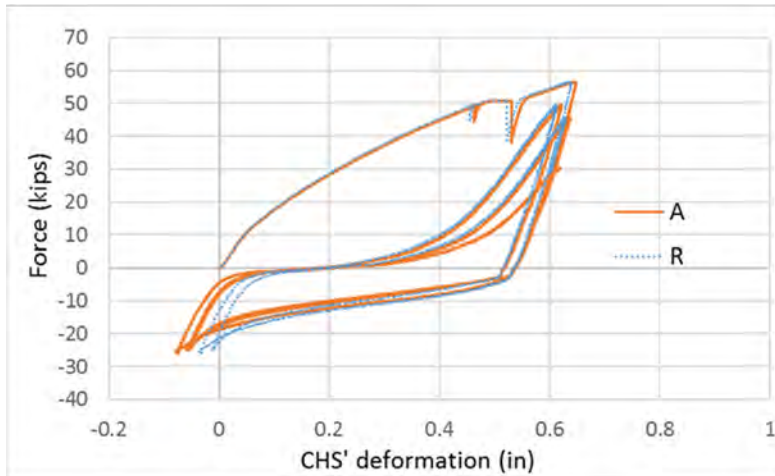
Figure 6-62 Applied force versus peak CHS deformation curve for specimen D16L5-3

The solid line in Fig. 6-63 shows the applied force versus the peak CHS deformation on the side close to the reaction block. The dash-dot curve in Fig. 6-63 was obtained from the monotonic test of specimen D16L5-2. It is observed that the stiffness shown in the first half cycle in the cyclic test of specimen D16L5-3 is lower than that of specimen D16L5-2 in the monotonic test. These two curves obtained from the tests are compared with the analyses results from the Abaqus specimen model in Fig. 6-63, and it is observed that the stiffness obtained from the analysis was higher than all experimentally obtained ones.
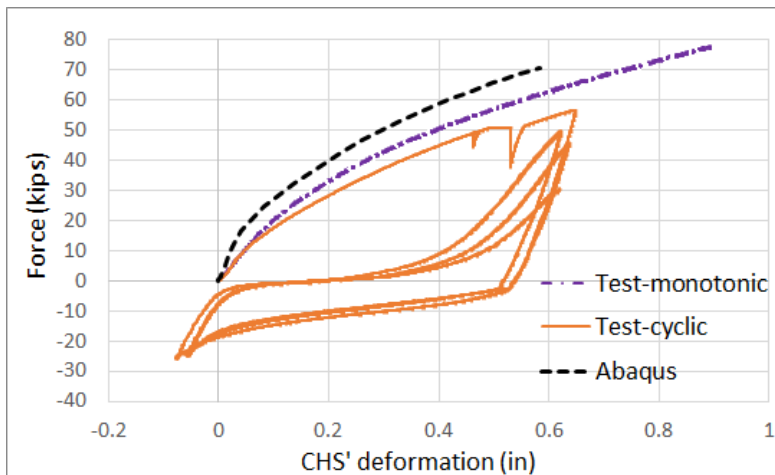
Figure 6-63 Comparisons of actuator's force versus peak CHS deformation curves from tests of specimens D16L5-2, D16L5-3, and Abaqus analysis results

6.3.5.2.4 Specimen D16L5-4

The incremental cyclic test mentioned in Section 6.3.3.2 was performed on Specimen D16L5-4. Recall, from Section 6.3.4.2, that the first-yielding strength predicted by the Abaqus model was 10.59 kips, with

a corresponding peak CHS deformation of 0.028". Since it was hard to identify when first-yielding happened in the specimen during the monotonic tests performed above, it was assumed that the specimen's first-yielding strength was 10.59 kips, even though the comparison between the Abaqus analysis and the test results showed differences in the curves in Figs. 6-49, 6-55, and 6-63. When this force of 10.59 kips was developed in specimen D16L5-2, the actuator head's displacement was 0.0752". Assuming that the stiffnesses of specimens D16L5-2 and D16L5-4 were the same, specimen D15L5-4 was expected to develop the same force when first yielding happened. The yield displacement defined in the incremental cyclic test protocol in Fig. 6-36 in Section 6.3.3.2 used 0.0752". The resulting actual displacement cyclic-displacement protocol applied to specimen D16L5-4 is shown in Fig. 6-64. The specimen failed when it reached a displacement of 7 times the yield displacement, equal to 0.81", as marked by the cross in Fig. 6-64.
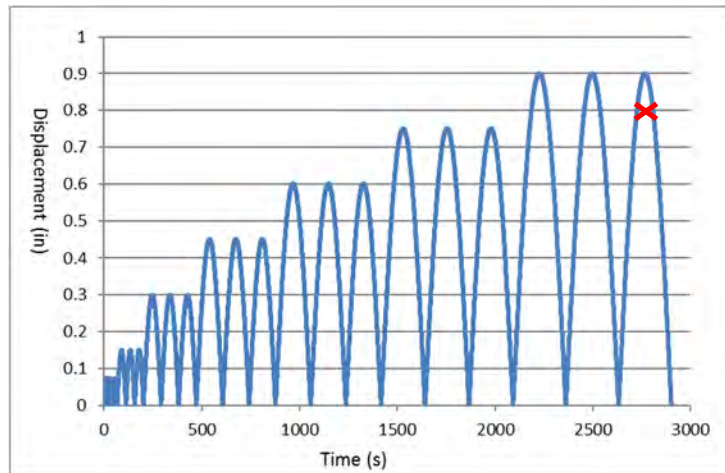
Figure 6-64 Cyclic testing protocol for specimen D16L5-4

Fig. 6-65 shows the hysteretic curve corresponding to the actuator's applied force versus the displacement of the actuator head for specimen D16L5-4. The specimen developed a maximum force of 45 kips, and the force was 27.8 kips when the specimen failed in the CHS close to the weld connecting it to the branch plate. The failure section was similar to what is shown in Fig. 6-49a, but it was located below the branch plate close to the reaction block.

Fig. 6-66 shows the applied force versus peak CHS deformation on both sides of specimen D16L5-4. Note that the deformations on the actuator and reaction block side were slightly different. Fig. 6-67 compares experimentally the obtained results from the monotonic test of specimens D16L5-2 and the incremental cyclic test of D16L5-4, with the Abaqus analysis results from the model. The peak CHS deformations close to the reaction block side were used for comparison in this figure. The backbone of

the hysteretic curve for specimen D16L5-4 during the first few cycles in tension matches well with the results from specimen D16L5-2 in the monotonic test. The stiffness obtained from the analysis was higher than all experimentally obtained ones.
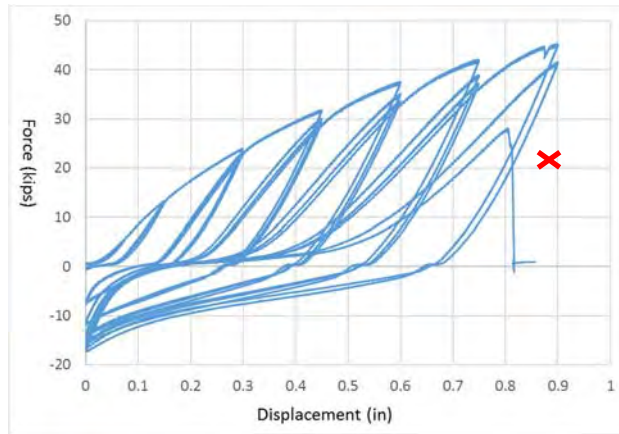
Figure 6-65 Actuator's force versus applied displacement curve for specimen D16L5-4
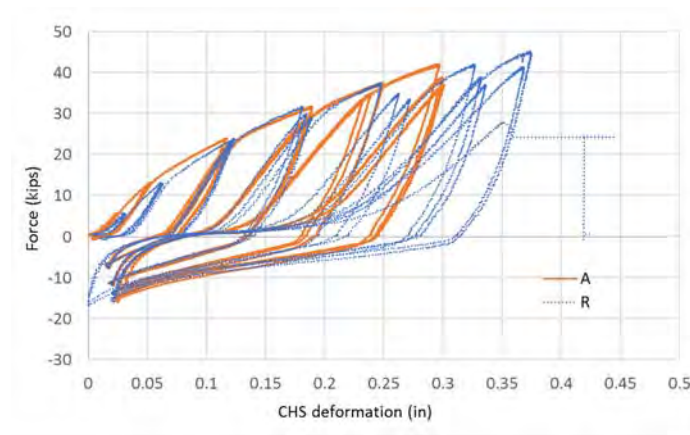
Figure 6-66 Actuator's force versus peak CHS deformation curve for specimen D16L5-4
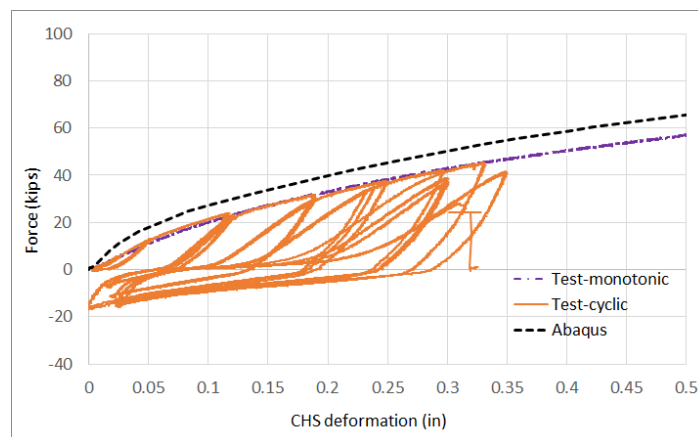
Figure 6-67 Actuator's force versus peak CHS deformation curve for specimen D16L5-4

216

6.3.5.3 Specimen D9.625L3, D9.625L6 and D9.625L7

6.3.5.3.1   General

Specimens with 9.625" diameter were tested, and the corresponding test protocols and results are presented in this section. The behavior of these specimens having different CHS widths and the same branch plate, are investigated. Section 6.3.5.3.2 shows the monotonic and incremental cyclic test results of the two specimens with CHS width of 3". Section 6.3.5.3.3 presents the test results of the four specimens with CHS width of 6" and 7".

6.3.5.3.2   Specimen D9.625L3

Specimen D9.625L3-1 was tested monotonically, and the curve for the applied actuator's force versus peak CHS deformations on both sides are shown as the solid and dash lines in Fig. 6-68. Note that the specimen failed in the CHS close to the weld to the branch plate, at the force of 44.9 kips.   The analytically obtained result of D9.625L3 is shown as the dash-dot line in Fig. 6-68, which has a larger stiffness than the test result.
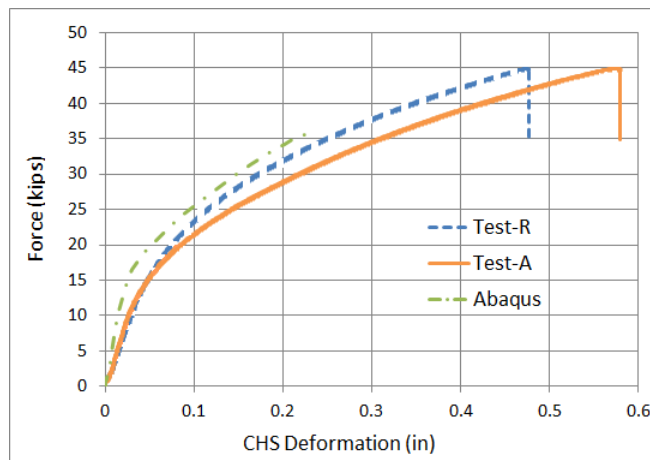
Figure 6-68 Applied force versus peak CHS deformation curve for specimen D9.625L3-1

The specimen failed in the CHS close to the weld connecting it to the branch plate, as shown in Fig. 6-69, which was below the branch plate towards the reaction block (in the circle).

The incremental cyclic test mentioned in Section 6.3.3.2 was performed on Specimen D9.625L3-2. Recall that in Section 6.3.4.3, the first-yielding strength of the Abaqus model was 5.82 kips, with a

corresponding peak CHS deformation of 0.0082". When this force of 5.82 kips developed in testing specimen D9.625L3-1, the actuator's applied displacement was 0.0625", which was used as the yield displacement in the displacement protocol applied to specimen D9.625L3-2. When the specimen was cycled to the third cycle at the displacement of 6 times the yield displacement, it failed at the displacement of 0.67". The maximum force resisted by the specimen was 32.5 kips, and force in the actuator was 28.9 kips when the specimen failed in the CHS close to the weld connecting it to the branch plate. The failure location is the same as for specimen D9.625L3-1. Fig. 6-70 shows the curve of the applied force versus peak CHS deformations on both sides of specimen D9.625L3-2, marked as the "Cyclic-R" and "Cyclic-A". These two curves are compared with the curve "Monotonic-A" obtained from the monotonic test of specimen D9.625L3-1, which matched well with the enveloped stiffness of the curves obtained from the incremental cyclic tests.

Figure 6-69 Failure of specimen D16L5-2
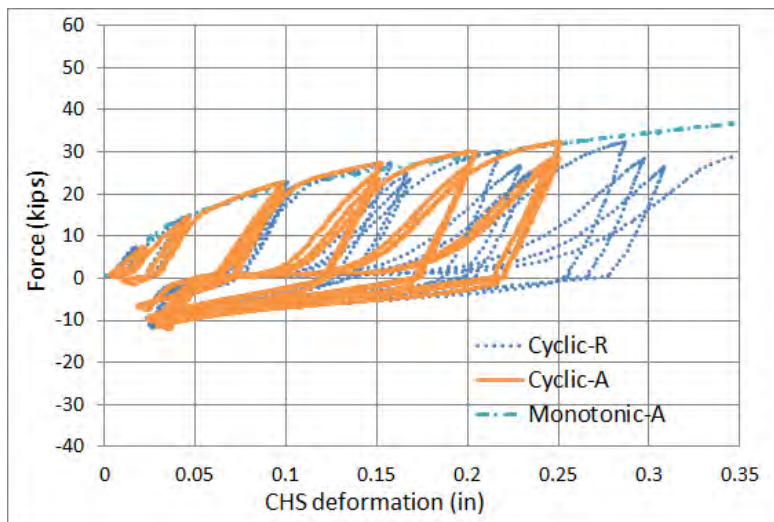
Figure 6-70 Comparisons of the actuator's force versus peak CHS deformation curves of specimens D9.625L3-1 and D9.625L3-2

218

6.3.5.3.3   Specimens D9.625L6 and D9.625L7

Similar to specimens D9.625L3-1 and D9.625L3-2, each of the two specimens, for specimen type D9.625L6 and D9.625L7, was subjected to monotonic and cyclic test, respectively. Since the width of the CHS is larger than the branch plate in specimens D9.625L6 and D9.625L7, the peak CHS deformations were obtained from two different locations at both sides of the specimen. LEDs were attached to them to record the CHS deformation. These two locations are marked by dots in Fig. 6-70, which shows half of the specimen D9.625L7. The location close to the branch plate is named as "Center" in Fig. 6-71. The other location, with the notation "Side", was on the outside perimeter of the CHS and in line with the branch plate. The comparison between displacements recorded at the "Center" and "Side" points indicates the difference in deformations close and away from the branch plate.
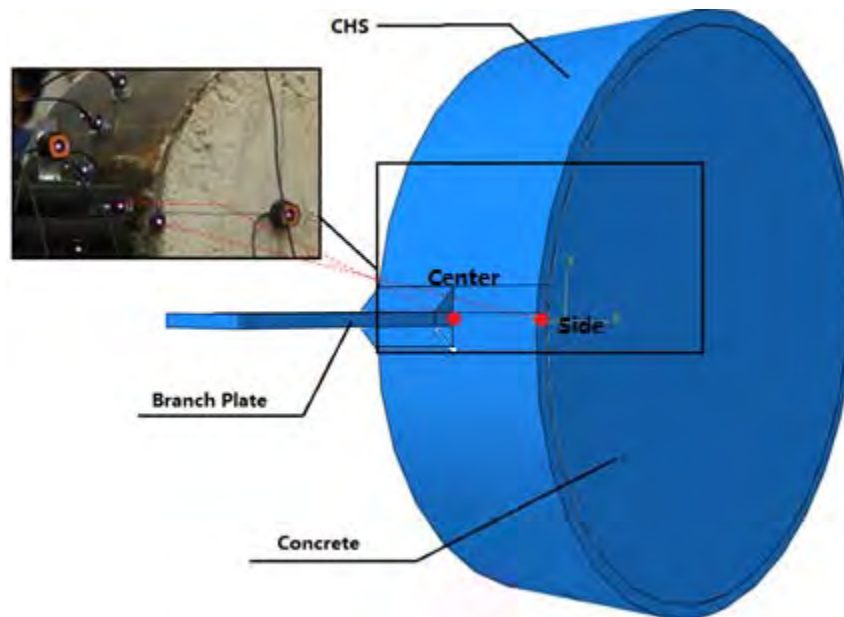
Figure 6-71 Locations of the LEDs used to obtain deformations of the CHS specimen D9.625L7

All four specimens failed in the CHS section close to the bottom of the branch plate connected to the reaction block. Fig. 6-72 shows a typical failure section from specimen D9.625L6-1. Note that this photo was taken after the specimen was removed from the test setup, and the specimen has been flipped to better observe the failure section.

In Figs. 6-73a and 6-73b, the applied force versus CHS deformation curves obtained from the monotonic test of specimen D9.625L6-1 are compared with the analytical results of the Abaqus specimen model D9.625L6. The notations of "Test-S-A" and "Test-C-A" in Figs. 6-73a and 6-73b indicate that the deformations were respectively taken from the "S" and "C" locations on the CHS close to the "Actuator"

or "Reaction block", where "S" and "C" refer to the "Side" and "Center" locations as mentioned above. The figures show that the CHS deformations reduced further away from the branch plate. Note that the early termination of the curve "Test-C-A" was because the LED, used to obtain this deformation, fell off the CHS.

Figure 6-72 Failure section of the CHS for specimen D9.625L6-1

| (a) | (b) |
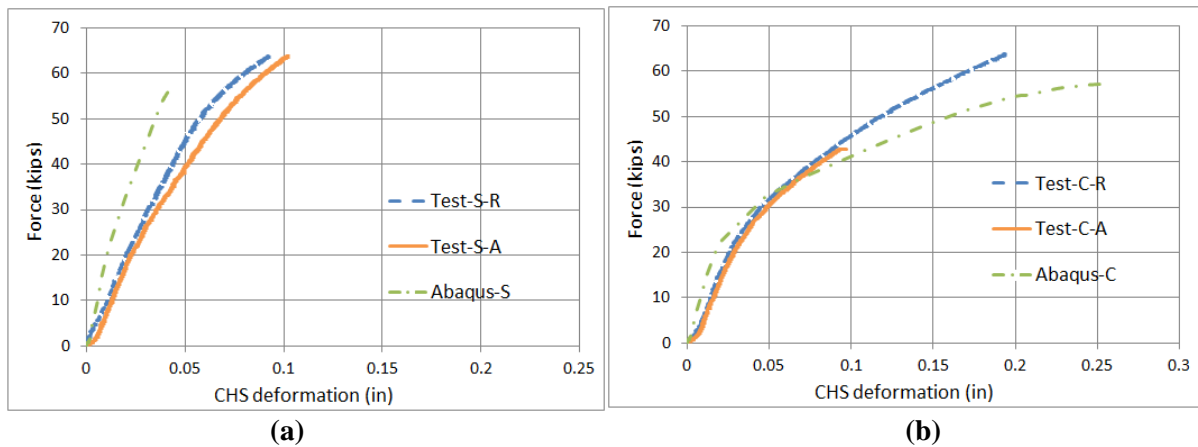
Figure 6-73 Applied force versus CHS' deformation curve for specimen D9.625L6-1: (a) deformation at CHS "Side"; (b) deformation at CHS "Center"

The displacement protocol for testing D9.625L3-2 was used in the incremental cyclic test of specimen D9.625L6-2 to facilitate comparisons between the two specimens. The specimen sustained the cyclic displacement history, as shown in Fig. 6-74, until the failure section in Fig. 6-72 developed. Note that during the third cycle at the displacement of 6 times the yield displacement, the force in the actuator suddenly dropped from 37.9 to 17.4 kips. This was due to the initial cracking of the CHS close to the weld connecting to the branch plate. During the first cycle at the displacement of 7 times the yield displacement, failure occurred at an actuator head's displacement of 0.65".
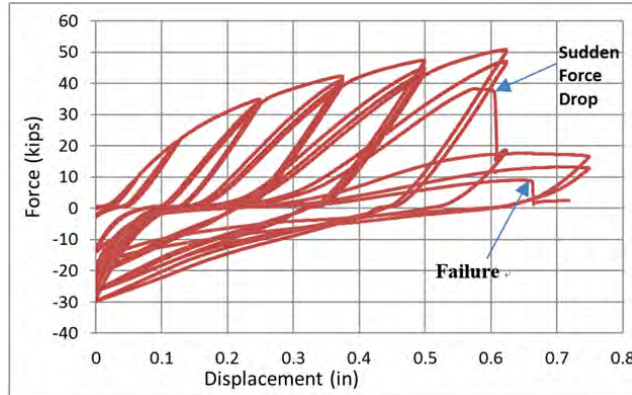
Figure 6-74 Applied force versus actuator's applied displacement for specimen D9.625L6-2

The experimentally obtained curves of the applied force versus CHS deformation are compared in Fig. 6-75 for specimens D9.625L6-1 and D9.625L6-2. The CHS deformations were both taken from the "Center" location, which was close to the branch plate connecting to the actuator. Note that the CHS deformation close to the branch plate, which was connected to the reaction block, was not obtained due to the data acquisition error for the LED at the "Center" location in Fig. 6-71. The CHS deformations captured by the LEDs only were obtained until the sudden force drop for specimen D9.625L6-2 in Fig. 6-74. The backbone of the hysteretic curve for specimen D9.625L6-2 during the first few cycles in tension matches well with the results from specimen D9.625L6-1 in the monotonic test.
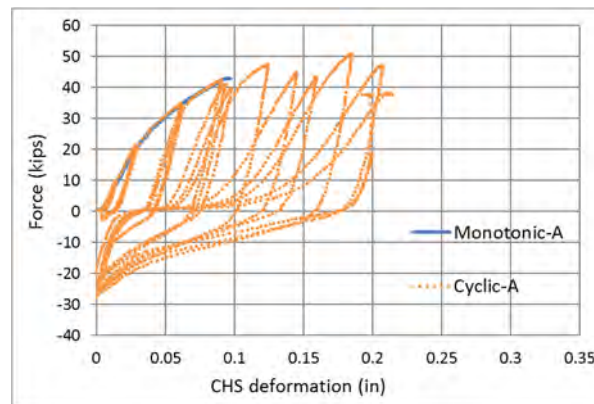
Figure 6-75 Applied force versus CHS' deformation curves for specimens D9.625L6-1 and D9.625L6-2

Monotonic and cyclic tests were performed on specimens D9.625L7-1 and D9.625L7-2, respectively. Fig 6-76 shows the applied force versus CHS deformation curves obtained from the monotonic test of specimen D9.625L7-1, as compared with the analytical result of Abaqus specimen model D9.625L7. When the specimen was cycled to the second cycle at the displacement of 6 times the yield displacement, the force in the actuator suddenly dropped from 46.5 kips to 17 kips, as shown in Fig. 6-77. The complete fracture of the cross section occurred where indicated by the arrow "Failure" in Fig. 6-77. The

221

experimentally obtained curves of the applied force versus CHS deformations were compared in Fig. 6-78 for specimens D9.625L7-1 and D9.625L7-2. The CHS deformation close to the branch plate on both sides of the specimen were plotted against the applied force. The backbone of the hysteretic curve for specimen D9.625L7-2 during the first few cycles in tension matches well with the results from specimen D9.625L7-1 in the monotonic test.

(a)   (b)
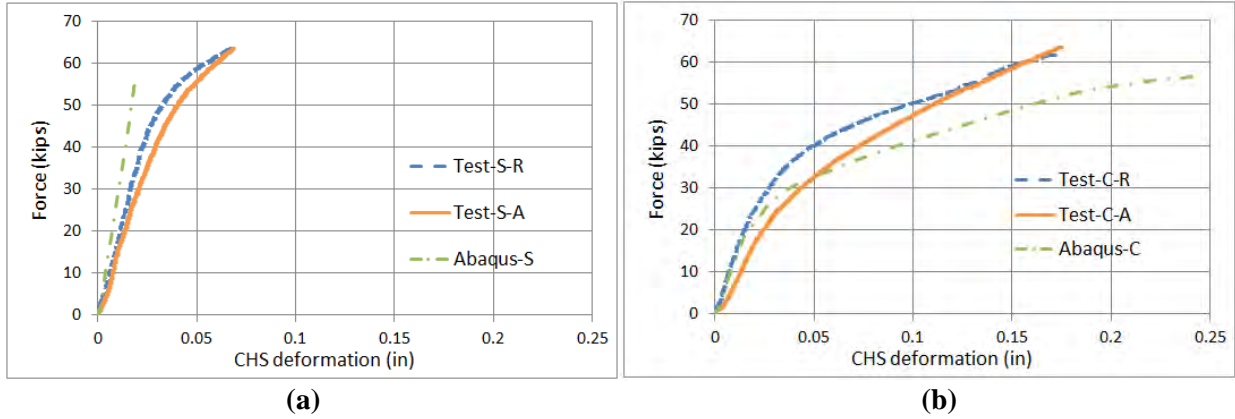
Figure 6-76 Applied force versus CHS' deformation curve for specimen D9.625L7-1: (a) deformation at CHS "Side"; (b) deformation at CHS "Center"
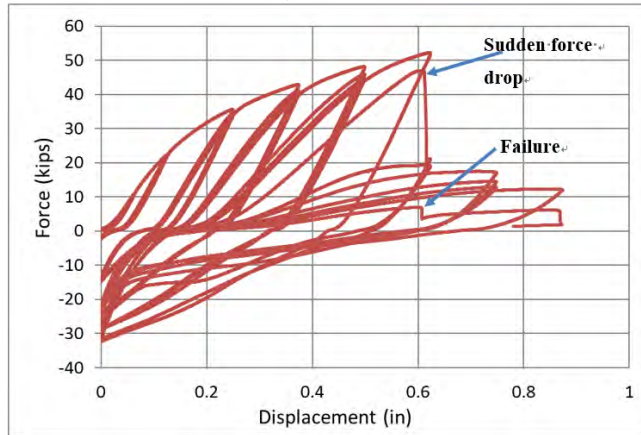
Figure 6-77 Applied force versus actuator's applied displacement for specimen D9.625L7-2
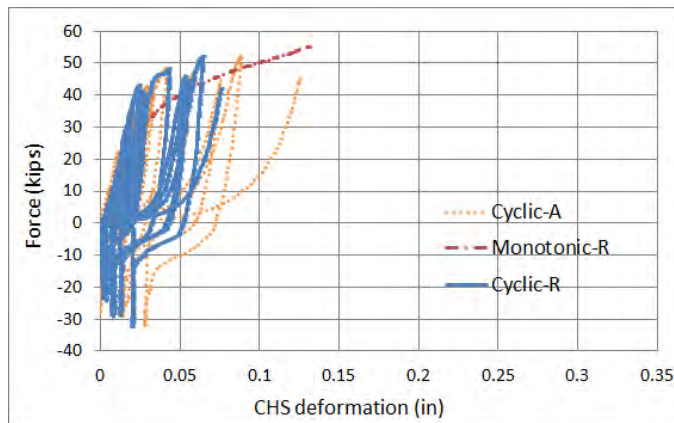
Figure 6-78 Applied force versus CHS' deformation curves for specimens D9.625L7-1 and D9.625L7-2

222

6.3.5.4 Specimen D10.75L5

Monotonic and cyclic tests were performed on specimens D10.75L5-1 and D10.75L5-2, respectively. Fig 6-79 shows the applied force versus peak CHS deformation curve obtained from the monotonic test of specimen D10.75L5-1, as compared from the analytical result of Abaqus specimen model D10.75L5. Note that the peak CHS deformation close to the reaction block's side was not obtained due to the data acquisition error as a consequence of the movement of the corresponding LED. The Abaqus analysis results give a specimen strength higher than the value from the test at the same peak CHS deformation.
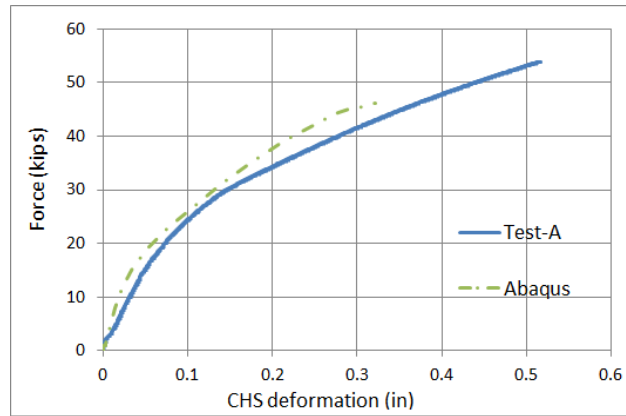
Figure 6-79 Actuator's force versus peak CHS' deformation curve for specimen D10.75L5-1

The incremental cyclic test mentioned in Section 6.3.3.2 was performed on Specimen D10.75L5-2. The first-yielding strength of the Abaqus model was 7.48 kips, with a corresponding peak CHS deformation of 0.013". When this force of 7.48 kips developed in testing specimen D10.75L5-1, the actuator's applied displacement was 0.065", which was used as the yield displacement in the displacement protocol in Fig. 6-36 in Section 6.3.3.2. When the specimen was cycled to the first cycle at the displacement of 7 times the yield displacement, it failed at the applied displacement of 0.65". The maximum force resisted by the specimen was 41 kips, and force in the actuator was 33 kips when the specimen failed in the CHS close to the weld connecting it to the branch plate. Fig. 6-80 shows the curve of the applied force versus peak CHS deformation on both sides of specimen D10.75L5-2, marked as "Cyclic-R" and "Cyclic-A". These two curves are compared with the curve "Monotonic-A" obtained from the monotonic test of specimen D10.75L5-1. The backbone of the hysteretic curve for specimen D10.75L5-2 during the first few cycles in tension shows higher force than that of specimen D10.75L5-1.

Both specimens failed in the CHS close to the weld connecting it to the branch plate, which was below the branch plate towards the reaction block. Fig. 6-69a shows the failed specimen D10.75L5-2 with the

failure section in circle. Fig. 6-81b shows the view of the failure section of the CHS from the direction pointed by the arrow in Fig. 6-81a.
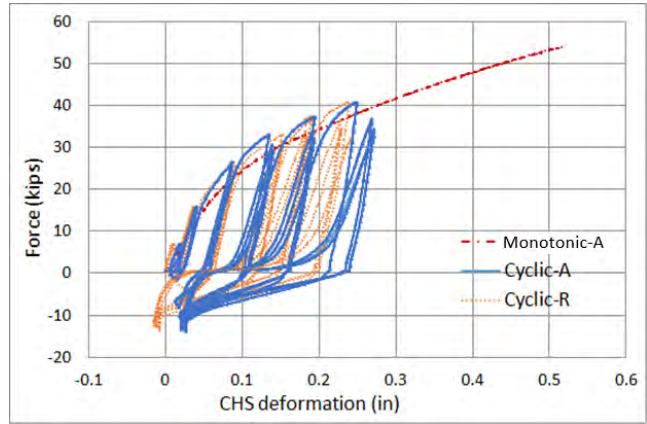
Figure 6-80 Comparisons of actuator's force versus CHS' deformation curves from tests of specimens D10.75L5-1 and D10.75L5-2

(a)   (b)
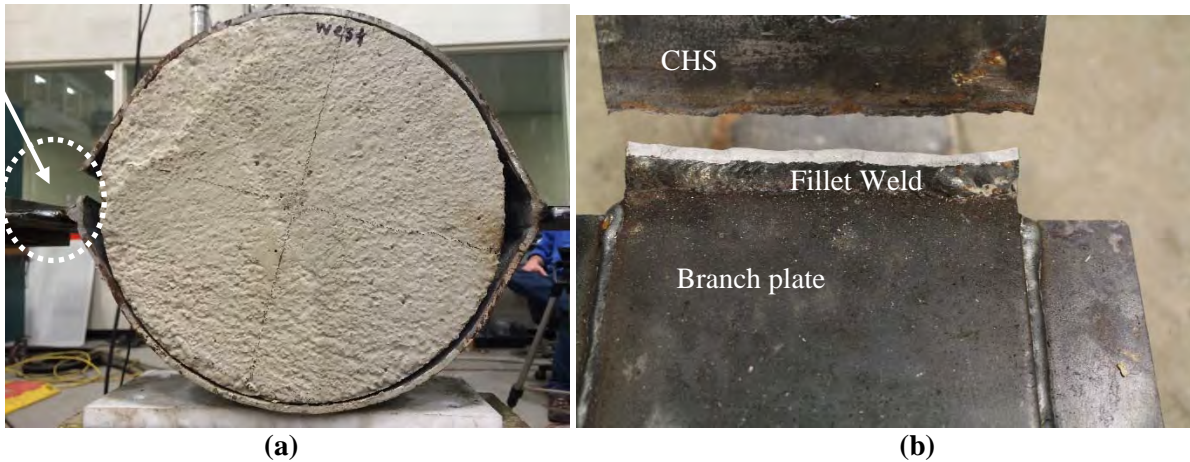
Figure 6-81 Failure of specimen D10.75L5-2

6.3.5.5 Specimen D5L3

Monotonic tests were performed on the specimens D5L3-1 and D5L3-2. The concrete inside the CHS crushed in specimen D5L3-1, and the CHS deformed freely and became oval. In the end, the specimen failed in tension in the CHS section close to the weld to the branch plate as shown in Fig. 6-82. To prevent the concrete from "popping out" as the CHS deformed, specimen D5L3-2 was strengthened using 1/4" thick cap plates on both side of the CHS, as shown in Fig. 6-83. The two cap plates were secured with a Grade 8 bolt of 5/8" with a pretension force of 20 kips. Teflon sheets were inserted between the CHS and cap plates so that the friction force between the CHS and cap plates could be minimized when the CHS deformed under the tensile force. Specimen D5L3-2 was tested monotonically, and failed in the

CHS section close to the weld as shown in Fig.6-84. After the test, the cap plates were removed and the concrete was found to have slightly crushed closed to the branch plate.
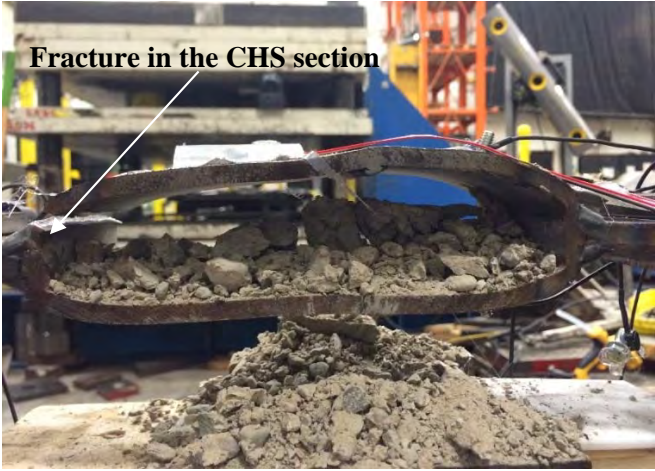
Figure 6-82 Failure of specimen D5L3-1
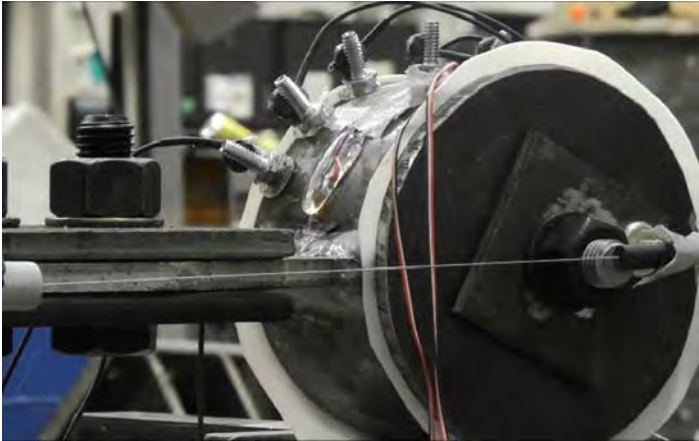
Figure 6-83 Modification of specimen D5L3-2 strengthened by cap plates with bolts

Figure 6-84 Failure of specimen D5L3-2

Fig. 6-85 shows the applied force versus peak CHS deformation on both sides of specimens D5L3-1 and D5L3-2. The Abaqus analysis result from the model D5L3 was also shown for comparison. Note that the Abaqus specimens have the concrete restrained as in Specimen D5L3-2. After strengthening the specimen, the failure strength increased by 75.7%. The initial stiffness of specimen D5L3-2 is close to the value obtained from the Abaqus specimen model.

(a)   (b)
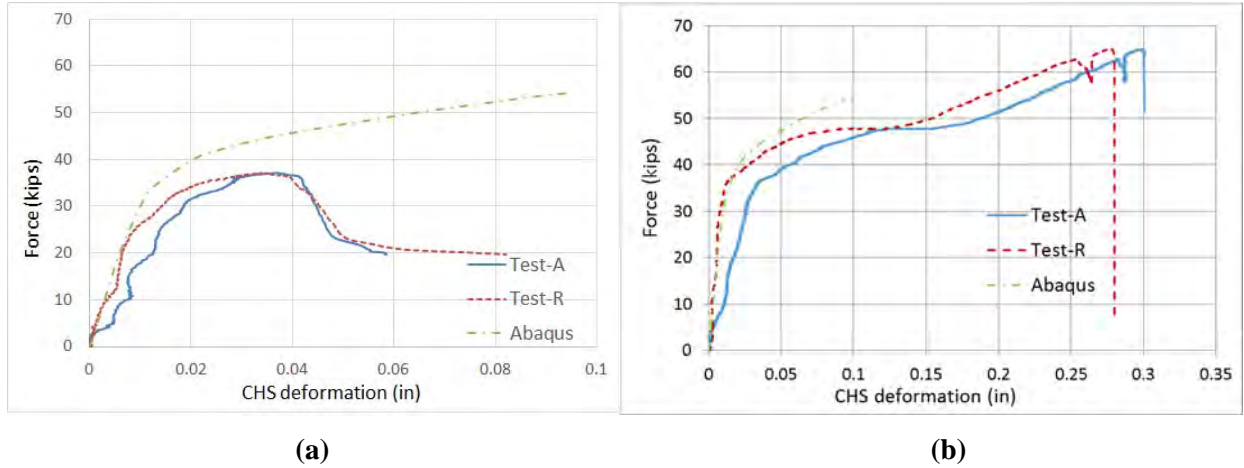
Figure 6-85 Actuator's force versus peak CHS deformation curve comparisons from the Abaqus analytical results and the tests of: (a) specimen D5L3-1; (b) specimen D5L3-2

6.3.5.6 Specimen D14L3

Monotonic tests were performed on the specimens D14L3-1 and D14L3-2. Both of these two specimen did not fail in the CHS. Towards the end of testing specimen D14L3-1, the applied force dropped suddenly and the tests were stopped due to loss of the concrete in specimen D14L3-1 in Fig. 6-86a. Since the concrete was chipped at a location close to the branch plate during installation of specimen D14L3-1 in the test set-up, the decision was made to test specimen D14L3-2 monotonically again. Specimen D14L3-2 sustained higher force than D14L3-1. The concrete popped out due to a sudden vibration caused by the slippage of the bolts, as shown in Fig. 6-86b.

Fig. 6-87 shows the applied force versus peak CHS deformations on both sides of specimens D14L3-1 and D14L3-2. The Abaqus analysis result from the model D14L3 is also shown for comparison. The stiffness of specimen D14L3-2 is higher than that of specimen D14L3-1.

(a)   **(b)**

Figure 6-86 Photos after the monotonic tests of specimens: (a) D14L3-1; (b) D14L3-2

(a)   **(b)**
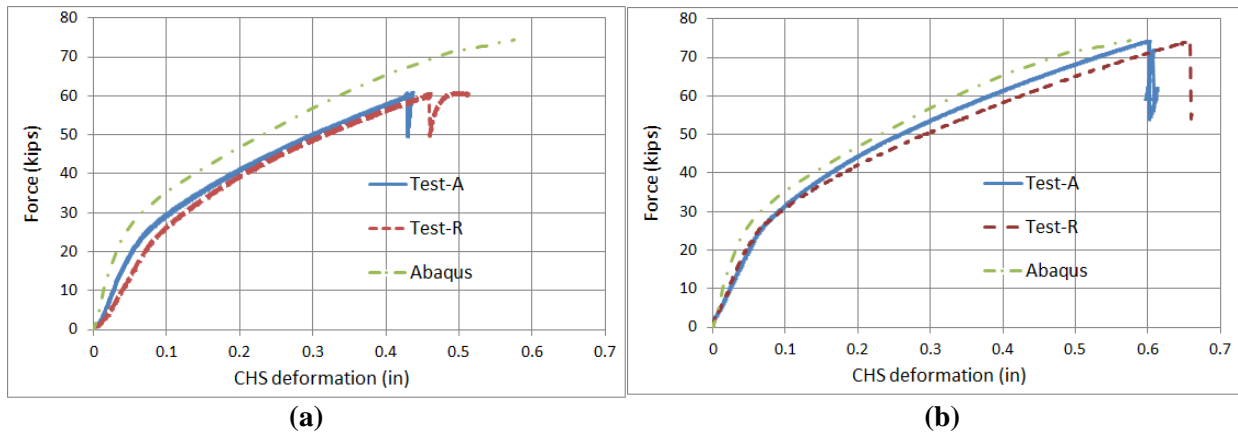
Figure 6-87 Actuator's force versus CHS' deformation curve comparisons from the test and the Abaqus analytical results for specimen: (a) D14L3-1; (b) D14L3-2

6.3.6   Overall observation on the test results

For the specimens tested under monotonic tests, the curves of the applied force versus CHS deformation obtained from analytical and monotonic test results were compared. The curves from the test results were found to generally match the analytical ones. The failure section of the specimens was typically located close to the fillet weld of the CHS to the branch plate. In two cases, namely for specimens D14L3 and specimens D5L3-1, failure occurred in the infill concrete, but the crushing or popping-out of the infill concrete out of the tested CHS ring would not occur in an actual column as concrete is laterally restrained in that case.

The failure strengths obtained from the monotonic tests were compared with the punching shear strength calculated based on Equation 3.8 and 3.9 in Section 3. Recall that in Section 3, the punching shear strength was calculated using Equations 3.8 and 3.9, proposed by Wardenier et. al. (2008) and Voth (2010), respectively. Voth (2010) recommended Equation 3.9, since Equation 3.8 is too conservative. Here in Table 6-10, the maximum strength developed by the specimen at failure in the monotonic tests is presented and compared with the punching shear strength calculated based on Equations 3.8 and 3.9. For comparison purposes, the specimens tested monotonically were divided based on whether or not the CHS and branch plate were of the same width.

For the specimens with CHS and branch plate of identical width, the failure strength was larger than the value predicted by both equations. The largest difference is 100% and 24% when comparing the failure strength with the values calculated based on Equations 3.8 and 3.9, respectively. Note that since none of the specimens D14L5 experienced a failure of the type expected in an actual CHS columns because of the popping-out of the infill concrete, the strength reached by the specimens D14L5 if that failure spurious mode had been prevented, would have been higher. Therefore, for the 14" diameter cases considered, for comparison purpose, it is the maximum force reached by specimen D14L3-2 before failure that was used in table 6-10.

Table 6-10 Comparisons between the predicted values from punching shear equations and failure strength

	Specimens						
	D5L3-1	D9.375L3-1	D10.75L5-1	D14L3-2	D16L5-2	D9.375L6-1	D9.375L7-1
Failure strength (kips)	65	44.9	54	73	79.2	63	64
f_{y0} (ksi)	64.5	47.9	48.4	56	50.9	47.9	47.9
l_1 (in)	3	3	5	3	5	3	3
t_0 (in)	0.233	0.233	0.174	0.349	0.233	0.233	0.233
Punching Shear strength (Per Equation 3.8) (kips)	32.46	24.11	30.32	42.22	42.69	24.11	24.11
Punching Shear strength (Per Equation 3.9) (kips)	52.30	38.84	48.85	68.01	68.79	38.84	38.84

For specimens D9.375L6-1 and D9.375L7-1 (in the last two columns of Table 6-10), the design punching shear strength indicated by Equations 3.8 and 3.9 was calculated using the width of the branch plate, which was less than the width of the CHS. For these two specimens, the strength obtained in the monotonic tests were up to 165% and 65% larger that the values calculated from Equations 3.8 and 3.9.

228

Note that in the tests of specimens with CHS diameter of 9.625", the strength of the specimen did not increase further when the width of the CHS not connected to the branch plate exceeded a specific value (6" in this case). This indicates that it is conservative to use the strength of the specimen only considering a CHS width equal to the branch plate width.

It was consistently observed that the specimens' strength under cyclic tests, beyond the first cycle, were smaller than the value obtained from the monotonic tests. Observed hysteretic behavior also most significantly revealed a deficient hysteretic energy dissipation upon repeated cycling. Recall that the purpose of the cyclic tests was to investigate the feasibility of using this type of connection from a seismic application perspective. On the basis of these observations, for seismic applications, this type of connections should be designed to remain elastic.

6.4   BRB connections using gusset plate welded to the CHS

The connection of the BRB to the CFT column considered in this section is assumed to be entirely accomplished through a gusset plate, welded to the CHS in the CFT column, and schematically as shown in Fig. 6-88.
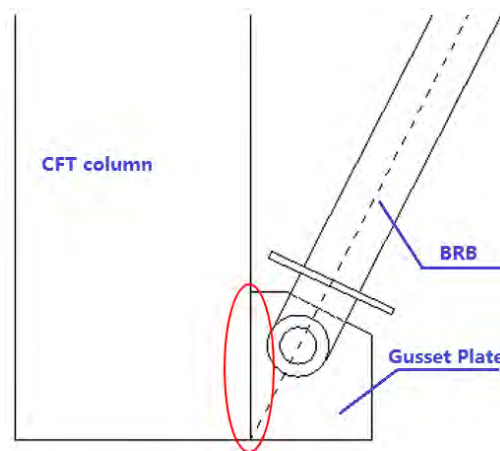
Figure 6-88 BRB connected with the CFT column through the gusset plate

(1) Two-CFT-column bent with BRBs

Recall from Section 4 for the single inclined BRB case considered in a two-CFT-column bent, that the largest tensile force produced by that BRB was 1270 kips. The corresponding horizontal and vertical force components were 941.07 kips and 853.44 kips, respectively. The CHS in the CFT column had a diameter of 48 in, with a thickness of 1.25 in. The steel grade used was A572Gr60 with the yield strength of 60 ksi. The zero-moment point in the Ring model predicted by Equation 6.22 for that CFT column is

41.72°, given that the ratio $\frac{\bar{r}}{t_o}$ is 18.7. The resulting unit-width strength at first yielding is 6.95 kips. The required length of the gusset plate to develop that force would be 11.2 ft, which is impractical.

For the two columns with chevron BRB case, the largest tension force in the BRB was 973.97 kips. The corresponding horizontal and vertical force components were 470.43 kips and 853.44 kips, respectively. A gusset plate length of 5.6 ft would be required in that case, which is also not feasible for implementation using this type of connections of the BRBs.

(2) Box-pier bent with BRBs

The largest tensile force produced by the BRB for the box-pier bent configuration was 295.8 kips. The corresponding horizontal and vertical force components were 229.54 kips and 186.65kips, respectively. The CHS in the CFT column had a diameter of 32 in, with a thickness of 0.75 in. The steel grade used was A572Gr60 with the yield strength of 60 ksi. The zero-moment point in the Ring model predicted by Equation 6.22 for that CFT column is 40.3°, given the ratio $\frac{\bar{r}}{t_o}$ is 20.8. The resulting unit-width strength at first yielding is 3.79 kips. The required gusset plate length in that case would be 5 ft, which is smaller, but still impractical.

Note that for the gusset connection described above, the CHS would also be subjected to shear forces. To account for the presence of the shear stress caused by the vertical component of the force from the gusset plate, the tensile strength of the CHS would need to be reduced.

As a consequence of the above observations, different techniques would be required to anchor the BRB to CFT columns. A few such alternatives are investigated here, purely from a theoretical perspective, to determine their practicality.

6.5   BRB connections using headed studs

In this section, first the strength of the head studs connection under tensile and shear loading is shown respectively. The numbers of headed studs are calculated for a specific connection, to investigate the applicability of this form of connection for the situation at hand.

Note that headed studs can be designed in accordance with ACI 318-14-Appendix D, PCI design handbook (2004) or AISC (2010). ACI 318-08 does not apply to reinforcement used as part of

embedment, therefore the strength calculated is based on the resistance from the concrete surroundings and the strength of the anchor itself.

6.5.1 General

There are mainly two types of headed studs. PCI (2004) specifies minimum tensile and yield strength for headed studs in Table 6-11. Type A headed studs are for general purpose of any type and size. Type A studs cannot be used in shear transfer of composite beam design and construction because of their lower capacity. The available diameters of type A headed-studs are 1/4" and 3/8". The shank diameters of type B shear studs are available in the range from 1/4" to 7/8". Dimensions of example anchor studs are shown in Table 6-12.

Table 6-11 Minimum Mechanical Property Requirements for Headed Studs (PCI Design Handbook, 2004)

Property (Diameter)	Type A (1/4 and 3/8 in.)	Type B (1/2 to 1 in.)
Tensile Strength (min.)	61,000 psi	65,000 psi
Yield Strength (0.2% offset)	49,000 psi	51,000 psi
Elongation (min. % in 2 in.)	17%	20%
Reduction of area (min.)	50%	50%

Table 6-12 Dimensions of headed studs (PCI Design Handbook, 2004)

$$h_{ef} = L + t_{pl} - t_{hs} - \tfrac{1}{8}"$$

Shank Diameter, d_o (in.)	Shank Area, A_{se} (in.^{2})	Head Diameter, d_{hs} (in.)	Head Thickness, t_{hs} (in.)	Bearing Area, A_{brg} (in.^{2})
1/4	0.05	1/2	3/16	0.15
3/8	0.11	3/4	9/32	0.33
1/2	0.20	1	5/16	0.59
5/8	0.31	1 1/4	5/16	0.92
3/4	0.44	1 1/4	3/8	0.79
7/8	0.60	1 3/8	3/8	0.88

The respective tensile and shear force capacity of single cast-in-place headed stud is first calculated, according to ACI 318-14 and PCI (2004). In order to get the largest capacity of one single anchor, the largest shank diameter d_0 of 7/8" of type B headed stud in Table 6-11 is used. The area of that steel stud is $0.6\ in^2$. The design compressive strength of normal weight, uncracked concrete f_c' is taken here as 5000 psi. The concrete density factor λ is 1. The headed studs are installed without supplementary reinforcements. The design ultimate strength of the anchor steel F_{ut} is 65 ksi, and the yield strength F_y is 51 ksi.

6.5.2 Strength Calculation

Effective embedment length is used as a controlled parameter to compare different strengths calculated below. The headed stud can be considered "in the field" for the current application. The tensile and shear force are assumed to be applied concentrically to the single headed stud. Equations using approaches from ACI-318-14 and PCI (2004) are calculated and compared. Different strength calculated below corresponds to the various types of steel and concrete failure modes defined in ACI 318 Appendix D for a single anchor.

(1) Steel anchor strength

$$F_s = A_{se}F_{ut} = 0.6 \times 65 = 39 \text{ ksi}$$

The reduction factors for steel failure are 0.75 for tension, and 0.65 for shear respectively. Therefore, the corresponding tensile and shear strength of the anchor failing in steel shank is 29.25 kips and 25.35 kips, respectively.

(2) Concrete breakout strength in tension per ACI 318-08

$$N_b = k_c\lambda\sqrt{f_c'}h_{ef}^{1.5} = 24 \times \sqrt{5000} \times h_{ef}^{1.5} = 1.70h_{ef}^{1.5}$$

where: $k_c = 24$ for cast-in anchors

(3) Concrete breakout strength in shear per ACI 318-08

$$V_b = 2 \times 7 \times \left(\frac{l_e}{d_0}\right)^{0.2}\sqrt{d_0}\ \lambda\sqrt{f_c'}(c_{a1})^{1.5} = 14h_{ef}^{0.2} \times \left(\frac{7}{8}\right)^{0.3} \times \sqrt{5000} \times (12)^{1.5} = 39.54h_{ef}^{0.2}$$

where: l_e = the load-bearing length of the anchor for shear, equal to h_{ef} for anchors with a constant stiffness over the full length of embedded sections

(4) Concrete pullout strength in tension per ACI 318-08

$$N_{pn} = 8A_{brg}f_c' = 8 \times 0.88 \times 5000 = 35.20 \text{ kips}$$

where: A_{brg}= the bearing area of the headed stud head in tension, as listed in Table 6-11;

(5) Pryout strength for anchors in shear per ACI 318-08

$$V_{cp} = k_{cp}N_b$$

232

where: k_{cp} =1.0 for $h_{ef} < 2.5$ in;

=2.0 for $h_{ef} \geq 2.5$ in.

(6) Concrete breakout strength in tension per PCI (2004)

$$N_b = 3.33\lambda\sqrt{\frac{f_c'}{h_{ef}}} \times 9h_{ef}^2 = 3.33\sqrt{\frac{5000}{h_{ef}}} \times 9h_{ef}^2 = 2.12h_{ef}^{1.5}$$

(7) Concrete breakout strength in shear per PCI (2004)

$$V_b = 87\lambda\sqrt{f_c'}(c_{a1})^{1.33}(d_0)^{0.75} = 87 \times \sqrt{5000} \times (12)^{0.75} \times \left(\frac{7}{8}\right)^{0.75} = 35.88 \text{ kips}$$

The side to edge distance of anchors loaded in shear parallel to the edge c_{a1} is taken as $6d_0 = 5.25''$.

(8) Concrete pullout strength in tension per PCI (2004)

$$N_{pn} = 11.2A_{brg}f_c' = 11.2 \times 0.88 \times 5000 = 49.28 \text{ kips}$$

(9) Pryout strength for anchors in shear per PCI (2004)

$$V_{cp} = 215\sqrt{f_c'} \times \psi_y \times (d_0)^{1.5} \times h_{ef}^{0.5} = 215 \times \sqrt{5000} \times 0.53 \times \left(\frac{7}{8}\right)^{1.5} h_{ef}^{0.5} = 6.59h_{ef}^{0.5}$$

and $h_{ef} \leq 4.5d_0$

where: $\psi_y = \frac{\sqrt{y}}{4d_0}$ for $\frac{y}{4d_0} \leq 20$, or =1.0 for y =0; y = center-to-center spacing of studs in direction of load,

which is the minimum center-to-center distance of the headed stud, taken as $4d_0 = 3.5''$

Fig. 6-89 plots the steel and concrete strength calculated per the above equations, for embedment lengths ranging from 0 to 8.75 in (10 times of the shank diameter). The steel strength of the anchor remains the same no matter how large h_{ef} is, while the concrete strength increases when the anchor is embedded deeper. The concrete strength shown are for a strength reduction factor (ϕ) of 0.7. The steel strength reduction factor is already included in the calculation.

For anchors strengths calculated per PCI (2004), the anchor is certain to fail in the steel shank if the embedment length is larger than 7.375 in under tensile force. Per ACI 318-14, the concrete breakout strength controls the strength for anchors loaded under tensile force for embedment length less than 7.75 in. Otherwise, the concrete pullout strength controls no matter how deep the embedment length is beyond 7.75 in. Anchors would fail in steel shank under shear forces, if the embedment length is larger than 4.875 in and 4 in per ACI 318-14 and PCI (2004), respectively.

Based on the values shown in Fig. 6-89, the strength of a single stud with 7/8 in diameter is summarized in Table 6-13 if the embedment length is larger than the specified length in the brackets in the table header. For ACI 318-08, the tension and shear strength of a single stud having embedment length greater

than 7.75" is 24.64 kips and 25.35 kips. For PCI (2004), the single stud with embedment length larger than 7.375" has the tensile and shear strength of 29.25 kips and 25.35 kips. The strengths from PCI (2004) will be used to design the layout of the headed studs.
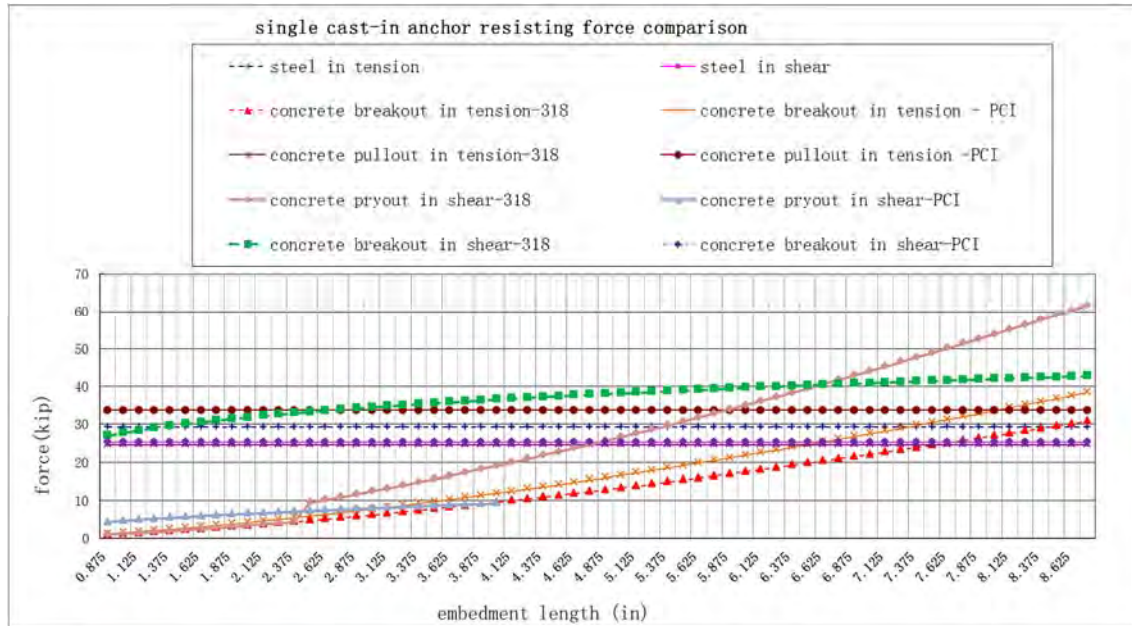
Figure 6-89 Single headed studs resisting strength comparison

Table 6-13 Shear and tension force sustained by headed-studs

	ACI 318-08 (Embedment length larger than 7.75 in)	PCI (2004) (Embedment length larger than 7.375 in)
Tension strength	24.64 kips	29.25 kips
Shear strength	25.35 kips	25.35 kips

6.5.3 Connection Evaluation

This section illustrates sample BRB connection designs using headed studs. The case of two columns with chevron BRBs and box-pier bent with BRBs are presented. The layout and geometry of the resulting connection is shown at the end of the connection design process.   The evaluation is for BRBs under tensile force, since the tension and shear force design for the connection with the foundation or the cap beam governs, rather than the combined compression and shear force.

(1) Two-CFT-column bent with chevron BRBs

a. Bottom BRB connection with the footing (BRB in tension)

The tensile force in the BRB to transfer is 973.97 kips. The corresponding horizontal and vertical force components are 470.43 kips and 853.44 kips, which would exert tensile and shear forces of 853.44 kips

and 470 kips, respectively, on the footing. It assumes that the entire force is to be transferred to the footing (e.g. none transferred to the column).

From the precious section, the tension and shear strength of individual headed stud are 29.25 kips and 25.35 kips, respectively. The interaction equation for tensile and shear forces acting on a headed stud in both ACI318-14 and PCI (2004), is:

$$(\frac{N_u}{\phi N_n})^{\frac{5}{3}} + (\frac{V_u}{\phi V_n})^{\frac{5}{3}} \leq 1.0$$

(6.26)

where: N_u is the applied tension force; V_u is the applied shear force; ϕN_n is the reduced tension force capacity; ϕV_n is the reduced shear force capacity

The resulting total number of headed studs needed to transfer the forces is calculated to be 40. Fig 6-89a illustrates the headed studs configuration at the connections, from a top view. A side view is shown in Fig. 6-90b. Note that the distance between the headed studs and the minimum side distance with the footing are identified in Fig. 6-90. The center-to-center stud distance is chosen based on the ACI 318-14 requirement of at least 3 times of the embedment length (to exclude the group effect of the headed studs). The side distance is 1.5 times of the embedment length.

The eccentricity of the loading to the headed studs is not considered here. The base plate is not designed. The welding between the BRB gusset plate and the base plate is not evaluated either.

The detail shown in Fig.6-90 indicate that an unrealistically high number of studs would be needed to transfer the BRB forces, making the use of headed studs impractical for connections in this application.

b. BRB connections with cap beam

The largest tensile and shear forces in the BRBs are 973.97 kips and 1083 kips, respectively. The resultant of these forces acting simultaneously at the point where both BRB meet at the underside of the bent cap would exert compression and shear forces of 95 kips and 992 kips, respectively. The compressive force is transferred to the bent cap directly without mobilizing the studs. Therefore, the connection need only resist the resultant shear force, and is designed based on the shear capacity of the headed studs of 25.35 kips.

The total number of headed studs needed is again 40, resulting in the same layout of the studs shown in Fig. 6-90. Again, for this connection design, the large a number of headed studs required for the connection design to work make it not feasible to implement.
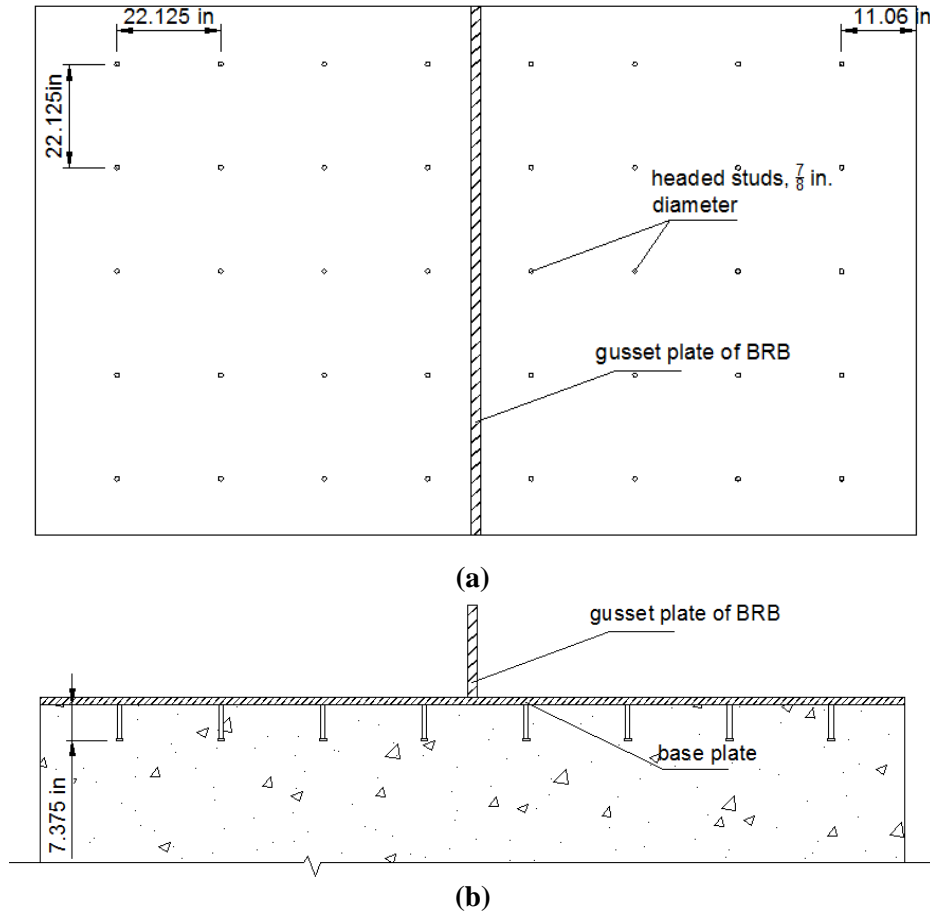
Figure 6-90 (a) Top view of BRB gusset plate connected with foundation (b) Side view

(2) Box-pier bent with BRBs

The largest tensile force in the BRB to transfer is 295.8 kips. The corresponding horizontal and vertical force component is 229.54 kips and 186.65kips, which would exert tensile and shear force of 186.65 kips and 229.54 kips, respectively on the footing. It assumes that the entire force is to be transferred to the footing (e.g. none transferred to the column).

Again, the tension and shear capacity of a single headed stud of 29.25 kips and 25.35 kips is used. Using the same interaction Equation 6.25, the total number of headed studs needed to transfer the forces is calculated to be 12. Fig. 6-91a illustrates the headed studs configuration at the connections, from top view. A side view is shown in Fig. 6-91b. Note that the distance between the headed studs and the minimum side distance with the footing are identified in Fig. 6-91. The center-to-center stud distance is chosen based on the ACI 318-14 requirement of at least 3 times of the embedment length (to exclude the group effect of the headed studs). The side distance is 1.5 times of the embedment length.
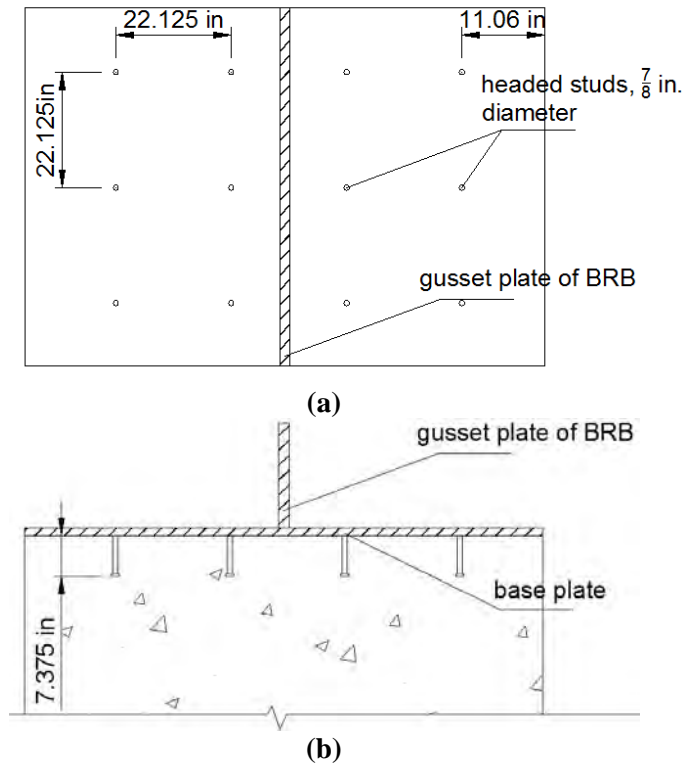
Figure 6-91 (a) Top view of BRB gusset plate connected with foundation (b) Side view

The eccentricity of the loading to the headed studs is not considered here. The base plate is not designed. The welding between the BRB gusset plate and the base plate is not evaluated either. The design is shown for the footing connection. For the cap beam connection, the design remains the same but upside down. For this connection design, the headed studs design works. However, the design is not complete, as the connection between the CFT column and the footing has not considered yet. Depending on the detail used, it might require adjusting the locations of the headed studs, leaving less space for the headed studs to be installed.

6.6   BRB connections using anchor rods

The connections of steel plates with concrete footing or cap beam can be accomplished with embedded anchor rods. This is similar to what is done with column base plate connection, when connecting a steel structure to its concrete foundation (as shown in Fig. 6-92).
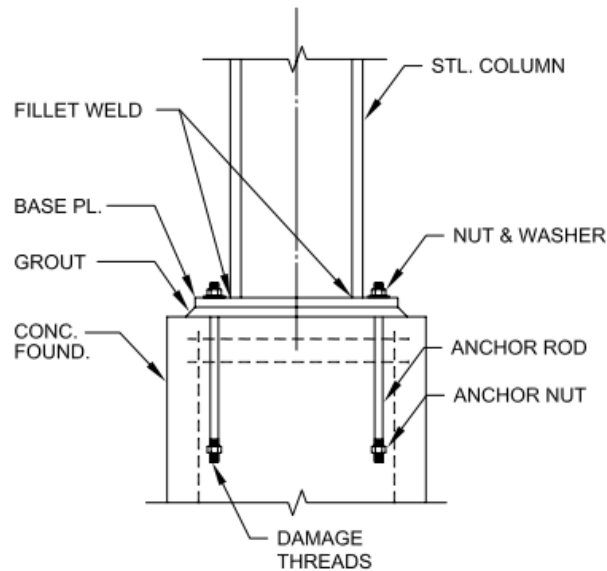
Figure 6-92 Column base connection components (Fisher, J.M. and Kloiber, L.A., 2006)

6.6.1 Materials and Types

Anchor rods are supplied in conformance with ASTM F1554 (2015c) "Standard Specification for Anchor Bolts, Steel, 36, 55, and 105 ksi Yield Strength." ASTM F1554 provides for three different grades of anchor rods: Grade 36, Grade 55, and Grade 105. The specified minimum yield strength (F_y) and specified minimum tensile strength (F_u) for each grade are given in Table 6-14.

Table 6-14 Tensile Properties for Anchor Rods

Tensile Property	ASTM F15544 Rod Grade 36	ASTM F15544 Rod Grade 55	ASTM F15544 Rod Grade 105
Minimum Yield Strength F_y (ksi)	36	55	105
Minimum Tensile Strength F_u (ksi)	58	75	125

The ASTM F 1554 Grade 36 rod of 0.75" diameter is recommended for most common applications. When more strength is required, increasing rod diameter up to about 2 in for ASTM F1554 Grade 36 is common practice before switching to a higher-strength material grade (Fisher and Kloiber, 2006). Anchor rod details typically provide ample threaded length, and it is recommended that threaded lengths be specified to be at least 3 in. The most common threaded anchor rods with nuts are used in this section to design the connections.

6.6.2 Connection Evaluation

This section illustrates simple design of BRBs connections using anchor rods for two cases: the two-column bent with chevron BRBs (with BRB force demand smaller than for the case of two-column bent with single BRB) and the box-pier bent with BRBs. Similar to the headed stud design, the design is only performed for the BRB in tension connected to the foundation, and for the top BRB in tension connected with the cap beam.

Note that the connection of the CFT column to the footing or bent cap beam can be designed in many different ways to ensure that the force demand can be achieved. Examples can be found in Roeder and Lehman (2008), Fujikura, Bruneau, and Lopez-Garcia (2008).

(1) Two-CFT-column bent with chevron BRBs

a. Bottom BRB connection only with the footing (BRB in tension)

For the chevron BRB case, the tensile force applied by the BRB is 973.97 kips. The corresponding horizontal and vertical force components are 470.43 kips and 853.44 kips, respectively. This corresponds to tensile and shear force on the foundation of 853.44 kips and 470 kips, respectively.

Appendix B presents detailed calculations for the design of anchor rods according to the equations provided in ACI318-14 and AISC (2010). The resulting layout and geometry of the connection is shown in Fig. 6-93a and b. Note that the plate thickness to allow engaging all anchor rods remains to be sized and would have to be much thicker than schematically shown in Fig. 6-93.

b. BRB connections with cap beam

The largest tensile and compressive forces in the BRBs are 973.97 kips and 1083 kips, respectively. The resultant of these forces acting simultaneously at the point where both BRB meet at the underside of the bent cap would exert compression and shear forces of 95 kips and 992 kips, respectively. The compression force is transferred to the bent cap directly without mobilizing the studs. Therefore, the connection need only resist the resultant shear force.

The calculation in Appendix B shows that the same anchor rod configuration as the BRB connected with the footing would be used, except that the distance of the anchor rod to the any edge would be 100 in instead of 90 in.
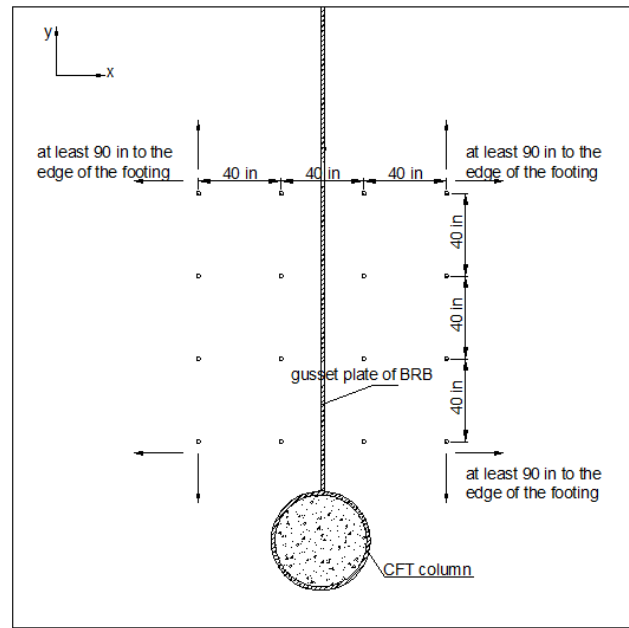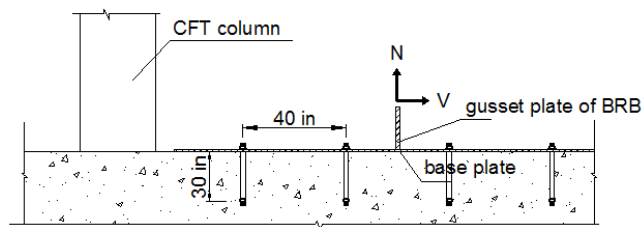
Figure 6-93 (a) Top view of BRB gusset plate connected with foundation (b) Side view

(2) Box-pier bent with BRBs

Similar to the headed stud design, the design is only performed for the BRB in tension connected to the foundation, and for the top BRBs in tension connected with the cap beam. The layout and geometry of the connection is shown in Fig. 6-93 for the BRB and footing connection. For the cap beam connection, the design remains the same but upside down.

The tensile force applied by the BRB is 295.8 kips. The corresponding horizontal and vertical force components are 229.54 kips and 186.65kips, respectively. This corresponds to tensile and shear force on the foundation of 186.65 kips and 229.54 kips, respectively.

Appendix B presented detailed calculation for the design of anchor rods according to the equations provided in ACI318-14 and AISC (2010). The resulting layout and geometry of the connection is shown in Fig. 6-94a and b.

(a)

(b)
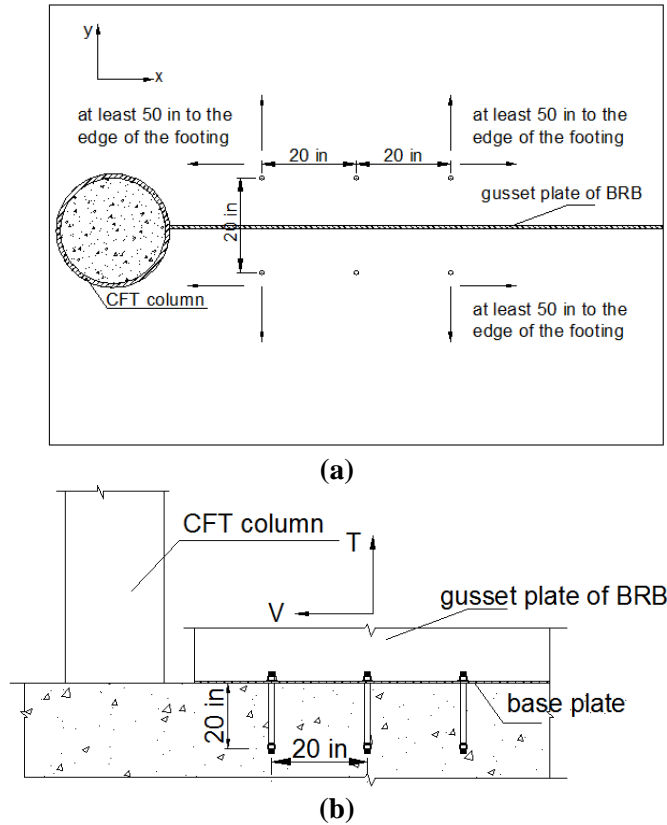
Figure 6-94 (a) Top view of BRB gusset plate connected with foundation (b) Side view

Note that for both cases, the plate thickness to allow engaging all anchor rods remains to be sized and would have to be thicker than schematically shown in Figs 6-91 and 6-92. The possibility of eccentricity of the loading to the anchor rods group is not considered here. The base plate has not been designed either. The welding between the BRB gusset plate and the base plate is not sized either. Not to mention that the above design is incomplete, as the connection between the CFT column and the footing has not been considered yet. Depending on the detail used, it might require adjusting the locations of the headed studs, leaving even less space for the anchor rods to be installed.

6.7   Summary

Three types of connections were used in this Section to investigate how BRBs could possibly be connected to different members of the bridge bent. Note that the latter two types of designs were more cursorily studies, and not evaluated from a seismic design perspective, nor experimentally.

For the connection directly welding to the shell of the CFT, the resulting design was found to be not feasible for both the two-column bent case and the box-pier case, since unrealistic long gusset plates are required. However, the analytical and experimental program conducted in support of this evaluation provided valuable information on both the monotonic and cyclic strength and behavior of this type of detail, which can prove useful in other applications.

The headed studs and anchor bolts were designed for BRBs to be connected to the foundation or the cap beam. Note that results were derived for the case of a chevron BRB frame configuration. It was found that an unrealistically high number of headed studs was required to transfer the BRB forces, making the use of headed studs impractical for connections in this application. Since the forces for the case of a single inclined BRB are larger than for the chevron BRBs for the two-CFT-column bent case, connections were not designed for that case. However, a headed stud connection was possible for the BRBs between the box pier columns (of the type presented in Section 6.5.3) due to the smaller BRB forces.

Using anchor rods to connect a BRB to a CFT column or to a footing or cap beam was found to be workable for both the chevron BRBs in the two-CFT-column bent case and the box-pier bent case (both presented earlier in Section 6.6). Note that eccentricity of the loading applied to the group headed studs or anchor rods group was not considered. Also note that investigation of techniques to connect the CFT column to the footing was beyond the scope of this work, as knowledge already exists on this topic.

Note that the exploratory works performed in this Section was conducted to access the feasibility of designing BRB connections to columns/foundations/cap beams using simple conventional methods. The connection designs considered here only serve as examples that investigated possible connection details that could have possibly worked or that would work in some specific situations. More elaborate research work is required to determine more complex connection details that would be more effective in resisting the demands from BRBs for the type of applications considered here.

SECTION 7

PARAMETRIC ANALYSIS OF BIDIRECTIONAL END DUCTILE DIAPHRAGM SYSTEM

7.1   General

In this Section, BRBs were implemented in the superstructure of a slab-on-girder steel bridge to improve its seismic performance, as explained in Section 7.2, such as to create a bidirectional ductile End Diaphragm System (EDS). Two types of EDS configuration (EDS-1 and EDS-2) were designed to provide benchmark skew and nonskew bridges, and the corresponding properties of these bridges are presented in Section 7.3. Ground motions were selected and scaled to be used to perform dynamic nonlinear time history analyses of the EDS-1 and EDS-2 bridges. The seismic performance resulting from those analyses are examined in Sections 7.4 and 7.5. Variations in skew angle, fundamental period of vibration, and earthquake excitation characteristics were also considered in the analyses of the bridge models, which allowed investigating the impact of these parameters on global behavior, as well as understanding the magnitude of local demands and the extent of bidirectional displacements that the BRBs must be able to accommodate while delivering their ductile response. In Section 7.6, the long-term service life of BRBs installed across expansion joints and subjected to bridge thermal expansion histories was also investigated and a minimum ratio of the BRB's core length over the whole bridge length was recommended.

7.2   Proposed bidirectional ductile end diaphragm system concept

The AASHTO Guide Specifications for LRFD Seismic Bridge Design (2011) already include provisions for the design of steel bridges having specially detailed ductile diaphragms, but these are only applicable to straight bridges without skew, and only provide resistance to earthquake excitations acting in the direction transverse to the bridge axis. This is a limitation and also an impediment to the implementation of ductile diaphragms. Without addressing the issues of skew and bi-directionality, implementations of the ductile diaphragm concept would remain limited (or rare), which is most unfortunate because ductile diaphragms are a low cost seismic solution compared to other alternatives.

A bidirectional ductile end diaphragm concept was proposed to implement ductile end diaphragms in straight or skew bridge superstructures, to resist bidirectional earthquake excitations (Celik and Bruneau, 2011). The proposed concept relies on hysteretic energy dissipation devices, which are structural fuses intended to be easily replaceable devices, arrayed such as to provide ductile response to horizontal

earthquake excitations acting from any direction. BRBs were chosen here as a possible solution to serve as the diaphragm's ductile seismic fuses (other hysteretic energy dissipation devices could equally work for this purpose). Two EDSs (i.e. geometrical layouts) are proposed, namely EDS-1 and EDS-2 (Fig. 7-1), described as follows:

•	EDS-1: Two pairs of structural fuses installed at each end of a span, in a configuration that coincides with the skew and longitudinal directions.

•	EDS-2: A single pair of structural fuses installed at each end of a span, at angles that do not coincide with the bridge longitudinal and skew directions.
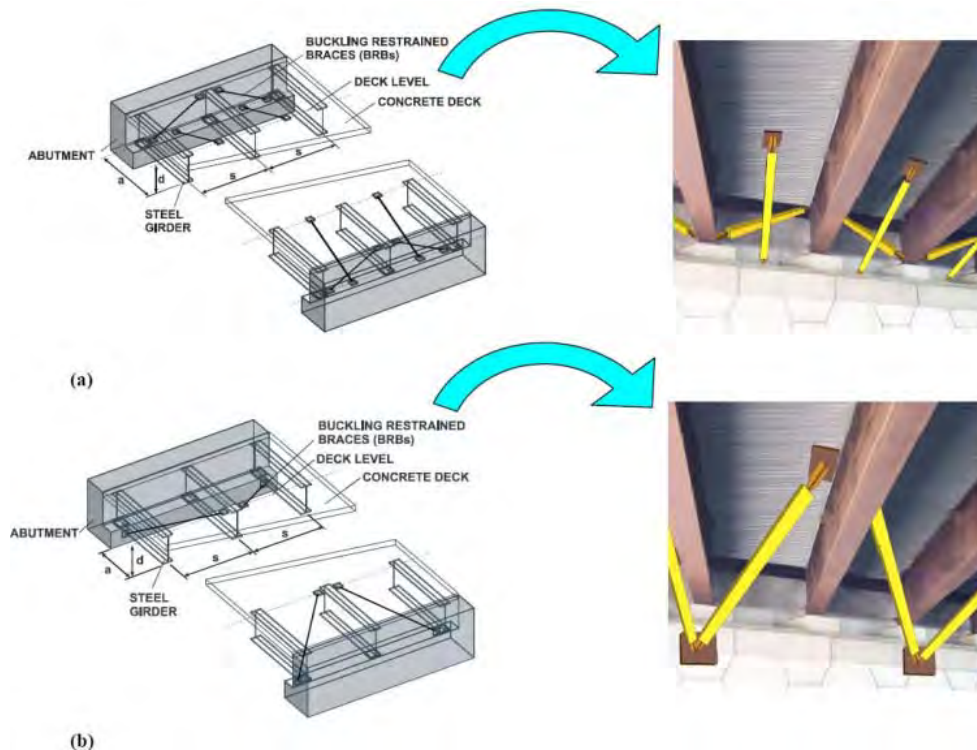
Figure 7-1 Proposed Schemes for Bridge Ductile End Diaphragms: (a) EDS-1; (b) EDS-2

(Celik and Bruneau, 2011)

## 7.3	Benchmark Simplified Bridge Models

Benchmark simplified bridge models with the above mentioned two EDSs have been developed in SAP2000 Version 14 and OpenSees Version 2.4.6. Section 7.3.1 describes the properties of the selected bridge, which was used to build the benchmark simplified model with the considered EDSs. Section 7.3.2 shows the layout and configurations of the benchmark simplified model with both EDSs in Section 7.3.2.1, followed by equations to design the benchmark simplified bridge model with both EDS configurations in Section 7.3.2.2. The benchmark simplified bridge models with both EDSs

configurations were designed using the proposed equations in Section 7.3.2 and their properties are summarized in Section 7.3.2.3. These properties will be used in later sections in the nonlinear time history analyses conducted to study dynamic behaviors of the bridge with the proposed EDSs.

7.3.1 Description and Properties of the Selected Bridge

A straight (nonskew) simply supported single-span steel slab-on-girder bridge is considered as the prototype bridge in this study. This bridge has girders spaced at 72" center-to-center. The height of the girder is also 72". The deck is assumed to be supported on bidirectional sliding bearings or other bearings with neglibible strength to horizontal deformations at the abutment. The bridge length is assumed to be 100 ft. The weight of the bridge (mg) is 2000 kips, and m is the mass of the bridge.

The bidirectional ductile diaphragms are implemented at both end of this benchmark bridge model. The corresponding benchmark simplified models consider a rigid bridge deck as a floating span. The flexibility of the girder and slab is neglected, as well as the stiffness contribution from the bearing web stiffeners. The details of the bridge modeling in OpenSees are explained in Appendix C.

Although multi-span simply supported steel bridges are known to be more vulnerable to earthquakes (e.g., Dicleli and Bruneau,1995; Priestley et al.,1996; Uang et al., 2014) their behavior is more complex when designed with bidirectional ductile diaphragms. As such, a fundamental understanding of simply-supported bridges with bidirectional ductile diaphragms is essential as a critical step towards addressing multi-span bridge. The effect of substructure stiffness and flexibility of the superstructure in multi-span bridges will be discussed in Section 10, along with example strategies for implementations in multi-span bridges.

7.3.2 Properties of Simplified Benchmark Bridge Model with EDS
7.3.2.1 Geometry and Configurations

The key dimensions of the EDSs are the girder skew spacing projection in the transverse direction, s, end diaphragm depth, d, which is approximately equal to the girder depth, and the horizontal longitudinal distance between connections of the longitudinal BRB at deck level and the abutment, a. The material in the steel core of BRB is assumed bilinear with yield stress, F_{yb}, and the Young's modulus, E.

7.3.2.1.1   EDS-1 skew and nonskew bridges

Fig. 7-2 shows the example benchmark skew bridge with EDS-1, having equal skew angle, φ, of 45 degrees at the two ends of the bridge span and enlarged view at one end. The stiffness of the diaphragms is K_L and K_S in the longitudinal and skew directions. The yielding core length ratio, c, is the length of the BRB restrained yielding steel core over the length of the entire BRB. In the EDS-1 configurations, c_{Lb} and c_{Sb} are for the longitudinal and skew BRBs, respectively.
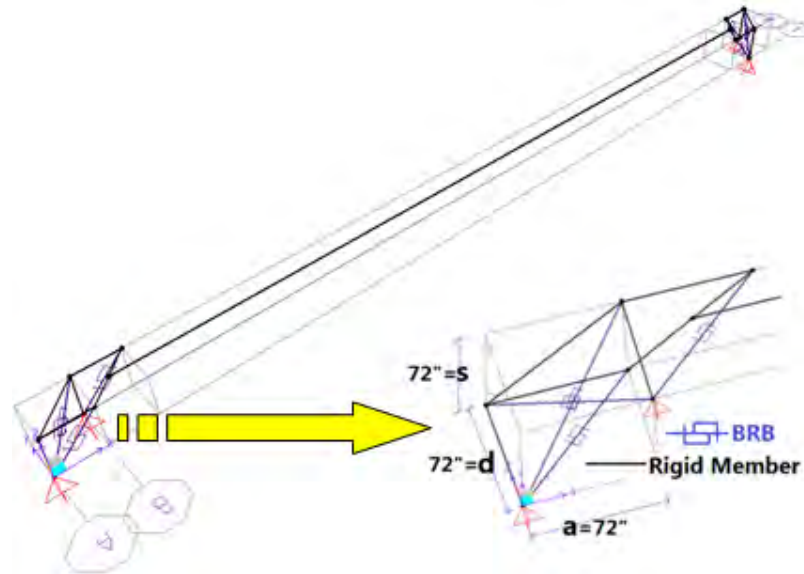
Figure 7-2 EDS-1 bridge diaphragms with BRBs and enlarged view at the end: skew 45°

Fig. 7-3 shows the example benchmark nonskew bridge with EDS-1 at the two ends of the bridge span and enlarged view at one end. The stiffness of the diaphragms is K_L and K_T in the longitudinal and transverse directions.

The length of the longitudinal BRBs is

$$L_{Lb} = \sqrt{a^2 + d^2}$$

(7.1)

The length of the skew BRBs is

$$L_{Sb} = \sqrt{(s/\cos\varphi)^2 + d^2}$$

(7.2)
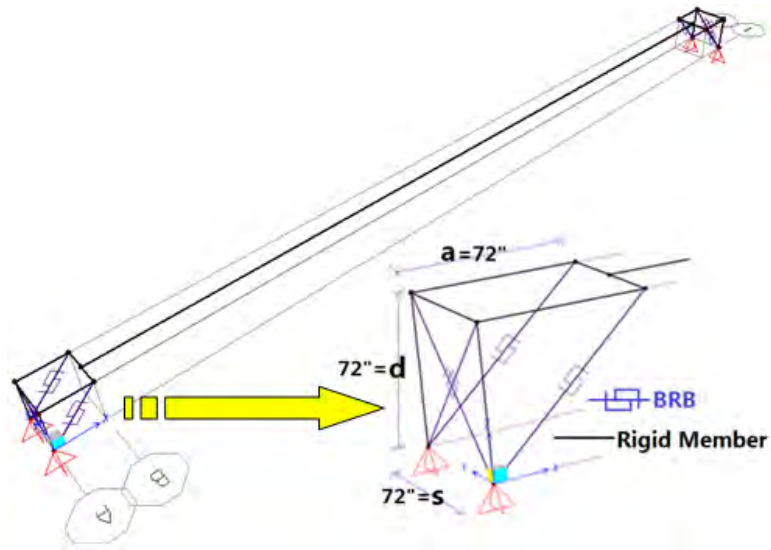
Figure 7-3 EDS-1 bridge diaphragms with BRBs and enlarged view at the end: skew 0°

7.3.2.1.2   EDS-2 skew and nonskew bridges

Fig. 7-4 shows the example benchmark skew bridge with EDS-2, having equal skew angle, φ, of 60 degrees at the two ends of the bridge span and enlarged view at one end. The stiffness of the diaphragms is K_L and K_T in the longitudinal and transverse directions. The yielding core length ratio of the BRBs in the EDS-2 configurations is c_L and c_S for the long and short BRBs, respectively. Similarly, Fig. 7-5 shows the example benchmark nonskew bridge with EDS-2 at two ends of the bridge span and enlarged view at one end.
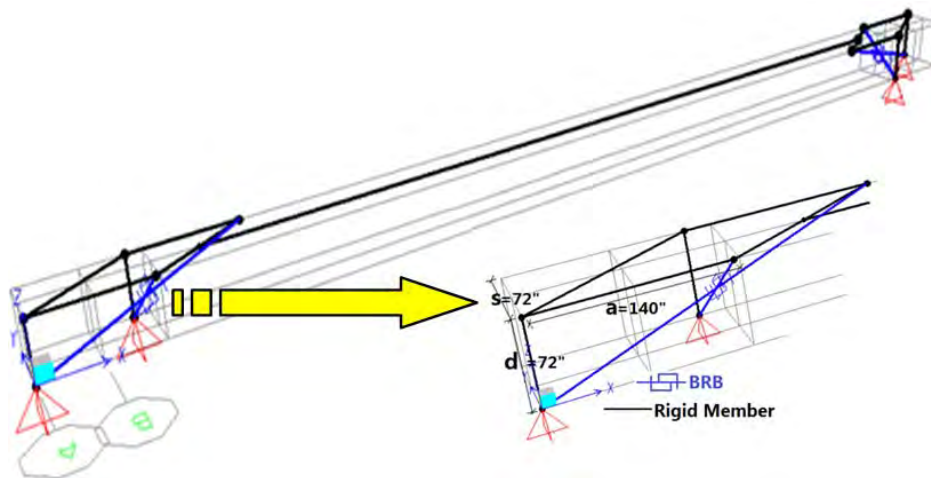
Figure 7-4 EDS-2 bridge diaphragms with BRBs and enlarged view at the end: skew 60 °

The length of the long BRBs is

$$L_L = \sqrt{(a + s \times \tan\varphi)^2 + s^2 + d^2}$$ (7.3)

The length of the short BRBs is

$$L_S = \sqrt{(a - s \times \tan\varphi)^2 + s^2 + d^2}$$ (7.4)
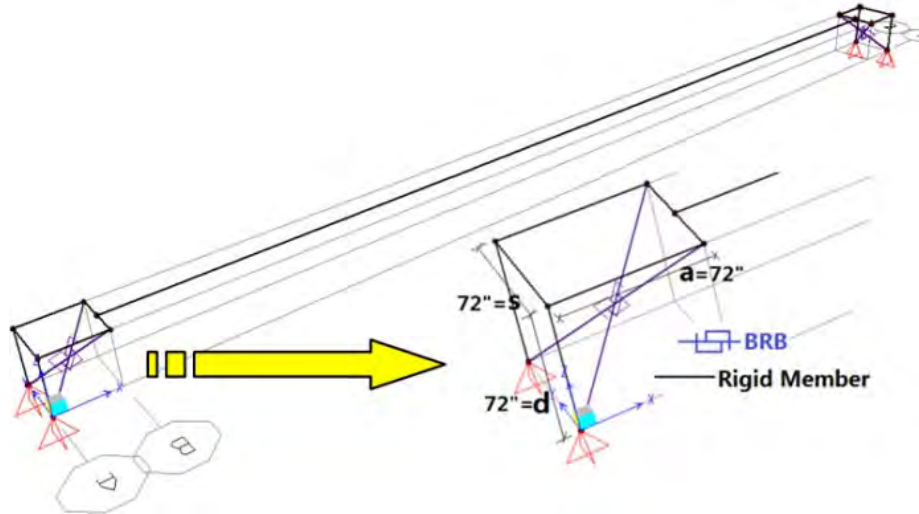
Figure 7-5 EDS-2 bridge diaphragms with BRBs and enlarged view at the end: skew 0°

7.3.2.2 Bi-directional EDS design

Note that Celik and Bruneau (2011) provided some insights into the seismic resistance of skewed steel bridges under bidirectional earthquake excitation for both EDS schemes through numerical nonlinear pushover analyses. To summarize: lateral earthquake loads were applied at the deck level on the diaphragm in both longitudinal and transverse directions; the yielding sequence of BRBs was related to the ratios of applied lateral loads, the skew bridge angle φ, and the ratios of EDS dimensions d/a and d/s, and; assuming equal areas of all the BRBs, the yield displacement and yield strength in both the longitudinal and transverse direction of the bidirectional EDS was expressed in terms of yield strength and displacement of individual BRB. No yield length ratios of the BRBs were considered in Celik and Bruneau (2011).

The purpose of this study is to investigate the seismic demands of the bridge with bidirectional EDSs, by performing nonlinear time history analyses. For the straight (i.e., nonskew) bridge, the seismic response in the longitudinal and transverse direction is uncoupled. Per the response spectrum at the bridge location, the applied ground motions can be scaled to match the seismic demand, which is related to the

period of the bridge in either of the longitudinal or transverse direction. Thus, the displacement demands of the bridge can be calculated separately in the transverse or longitudinal direction (detailed information is provided later in Sections 7.3.2.2.1 and 7.4.1). However, due to the complex skew bridge behavior related to the coupling of the response of the BRBs, the main vibration directions of the skew bridge are not in the longitudinal and transverse directions. An approach is taken here to design the skew bridges to have the same yield strength and yield displacement in the transverse and longitudinal directions as its equivalent nonskew bridge. The scaled ground motions used to analyze the nonskew bridge with EDSs were also used and applied to the skew bridges, and corresponding displacement demands in both the longitudinal and transverse directions were obtained. The magnifications factors of the skew bridges' displacement demands from the nonskew bridges were used in the prediction of the skew bridges' displacement demands in the design procedures proposed in Section 9.

For the proposed benchmark bridge diaphragm models with both EDSs, the difference in the translational vibration directions and corresponding periods is also identified below. The nonskew bridge vibrates translationally in the global longitudinal and transverse directions, while the skew bridges' translational periods and vibration directions depend on the skew angle of the bridge, the relative strength and stiffness between the longitudinal and skew BRBs for EDS-1 scheme, and the long and short BRBs for EDS-2 scheme.

7.3.2.2.1   EDS-1 skew and nonskew bridges

The periods of the nonskew equivalent bridge are first assumed in both the longitudinal and transverse direction as T_L and T_T, respectively. The stiffness of EDS-1 nonskew equivalent bridge in the longitudinal and transverse direction K_L and K_T are:

$$K_L = 2\pi\sqrt{m/T_L} \tag{7.5}$$

$$K_T = 2\pi\sqrt{m/T_T} \tag{7.6}$$

Note that for the specified design acceleration response spectrum at the bridge location, the elastic force demand of the bridge, mS_a, at the given period T can be obtained. Knowing the stiffness K calculated from the period T and the bridge mass m, the maximum displacement demand, δ_u, is equal to mS_a/K. Note that this maximum displacement demand is limited by: (1) the limit in the longitudinal directions, δ_{Lm}, which is typically either the gap between the bridge deck and abutment or the maximum seat width available, and; (2) the limit in the transverse directions, δ_{Tm}, which is the girder lateral yield displacement (for diaphragms with energy dissipator connected between girders), calculated based on the girder

properties for a given steel bridge. The displacement ductility demand, μ, can be assumed, and a maximum of value of 6 is recommended, as determined per Equation 4.3.3 in AASHTO (2011) for this application. Therefore, the yield displacement of the EDS-1 nonskew equivalent bridge is

$$\delta_y = mS_a/K\mu \tag{7.7}$$

The yield displacements of the EDS-1 nonskew bridge in either the longitudinal or transverse direction, δ_{yL} and δ_{yT}, can be calculated from Equation 7-7. The strength of the EDS-1 nonskew equivalent bridge in the longitudinal and transverse direction are P_L and P_T are:

$$P_L = K_L\delta_{yL} \tag{7.8}$$

$$P_T = K_T\delta_{yT} \tag{7.9}$$

For a skew bridge with EDS-1, when the longitudinal force is applied to the bridge as shown in Figs. 7-6a and 7-6b, the skew BRBs are not subjected to any force. The bridge's displacement occurs perpendicular to the skew direction. When the longitudinal BRB yields, the displacement in the global longitudinal direction is δ_{yL}. Due to the skewness, the corresponding displacement in the global transverse direction is

$$\delta_{T1} = \delta_{yL} \times tan\varphi \tag{7.10}$$

The yield length ratio of the longitudinal BRB can be obtained as

$$c_{Lb} = \delta_{yL} \times (E \times a)/(a^2 + d^2)/F_{yb} \tag{7.11}$$

Note that the yield length ratio is typically smaller than 1.0.

The yield displacement and strength in the transverse direction is dependent on the sequence of yielding of the BRBs, since the force applied in the transverse direction would put force in the BRBs in both the longitudinal and skew direction as shown in Figs. 7-6c and 7-6d. In the case considered here, the skew BRB was designed to yield first. When the skew BRB yield, the global transverse displacement is δ_{yT}. The corresponding displacement in the longitudinal direction is

$$\delta_{L1} = K_T\delta_{yT} \times tan\varphi/K_L \tag{7.12}$$

Note that this longitudinal displacement should be smaller than δ_{yT}.

The yield length ratio of the skew BRB is calculated as

$$c_{Sb} = \delta_{yT} \times Es \times (1 - K_T \times (tan\varphi)^2/K_L)/\big((s/\cos\varphi)^2 + d^2\big)/F_{yb} \tag{7.13}$$

252
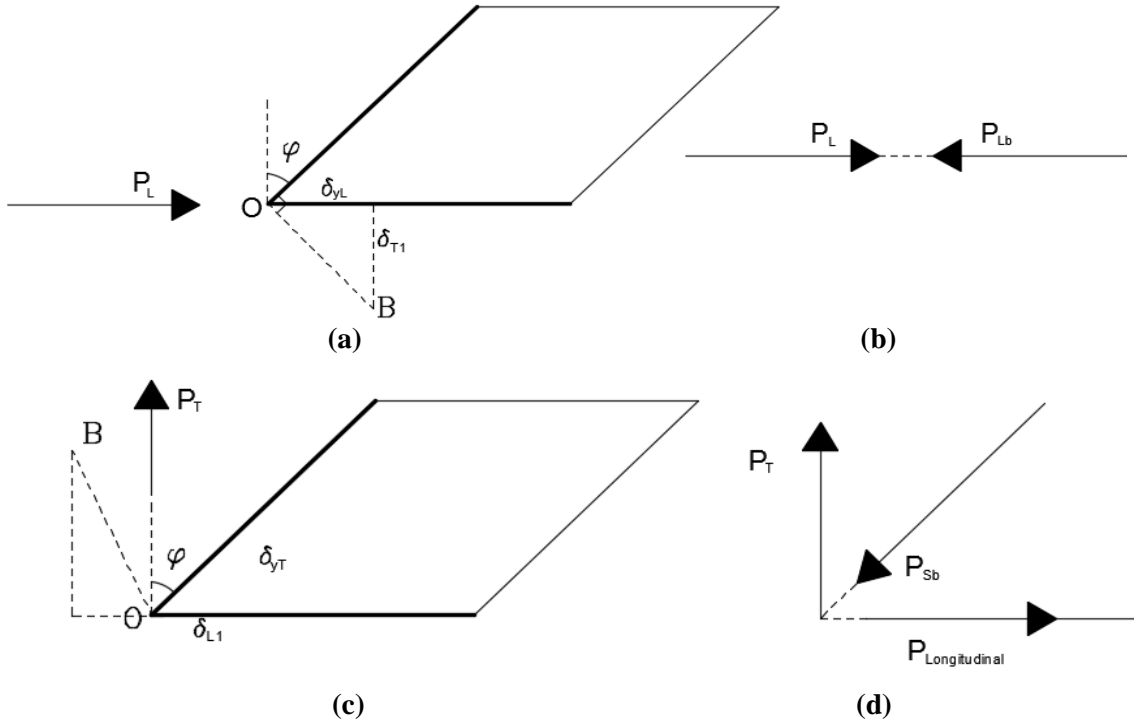
Figure 7-6 Displacement compatibility and force equilibrium illustrated for EDS-1 configurations: force applied in the longitudinal direction (a) displacement compatibility (b) force equilibrium; force applied in the transverse direction (c) displacement compatibility (d) force equilibrium;

The total number of BRBs, n, is assumed to be the same in the longitudinal and skew direction, respectively. For the benchmark bridge model, n equals to 4. Therefore, the yield strength of each longitudinal BRB is

$$P_{Lb} = P_L\sqrt{a^2 + d^2}/(4a) \tag{7.14}$$

The yielding strength of each skew BRB is

$$P_{Sb} = P_T\sqrt{(s/\cos\varphi)^2 + d^2}/(4s) \tag{7.15}$$

The corresponding yielding core area of the longitudinal and skew BRB would be P_{Lb}/F_{yb} and P_{Sb}/F_{yb}. The stiffness of the longitudinal and skew BRB are:

$$K_{Lb} = EP_{Lb}/(c_{Lb}F_{yb}L_{Lb}) \tag{7.16}$$

$$K_{Sb} = EP_{Sb}/(c_{Sb}F_{yb}L_{Sb}) \tag{7.17}$$

Fig. 7-7 shows the EDS-1 configurations with BRBs at one end of the bridge. The angle of the skew BRB with the horizontal plane is β_1. The angle of the longitudinal BRB's projection in the horizontal plane with the x-axis is β_2. The stiffness in the longitudinal and skew direction, K_L and K_S, shown in Fig. 7-8 can be calculated as:

$$K_L = 2K_{Lb}cos^2\beta_1 \tag{7.18}$$

$$K_S = 2K_{Sb}cos^2\beta_1 \tag{7.19}$$
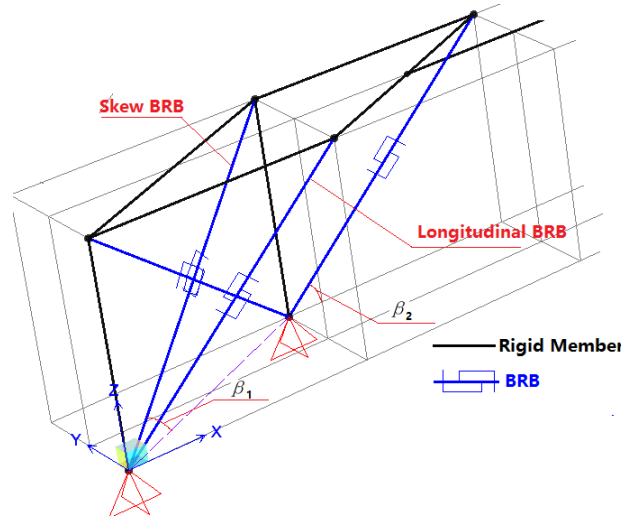
Figure 7-7 Illustration of directions in EDS-1 configuration
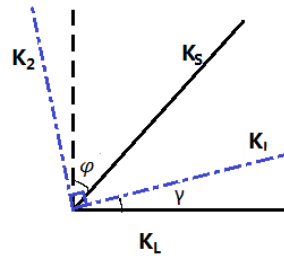
Figure 7-8 Illustration of directions in EDS-1 configuration

The ratio of the stiffness K_L and K_S in the longitudinal and skew directions of the benchmark bridge with EDS-1 is ρ. Fig. 7-8 shows the relative longitudinal and skew directions in the EDS-1 scheme with the solid black lines representing the longitudinal and skew direction, respectively. The dashed line indicates the transverse direction in the EDS-1 scheme. The first two main vibration directions of the benchmark bridge with EDS-1 are T_1 and T_2. The corresponding stiffness are K_1 and K_2, and the directions of which are illustrated in Fig.7-8 in dash-dot lines, which are perpendicular to each other. The angle γ, between the longitudinal and the main vibration direction corresponding to T_1, is $(\pi/2 - \varphi)/(1 + \rho)$.

The relationship between K_1, K_2 and K_L and K_S is given as follows:

$$K_1 = K_L \times (\cos((\pi/2 - \varphi)/(1 + \rho)))^2 + K_S \times (\cos((\pi/2 - \varphi)\rho/(1 + \rho)))^2 \tag{7.20}$$

$$K_2 = K_L \times (\sin((\pi/2 - \varphi)/(1 + \rho)))^2 + K_S \times (\sin((\pi/2 - \varphi)\rho/(1 + \rho)))^2 \tag{7.21}$$

The periods corresponding to K_1 and K_2 are

$$T_1 = 2\pi\sqrt{m/K_1} \tag{7.22}$$

$$T_2 = 2\pi\sqrt{m/K_2} \tag{7.23}$$

7.3.2.2.2 EDS-2 skew and nonskew bridge

The design of EDS-2 starts from the global yield strengths in the longitudinal and transverse direction, P_L and P_T, which are the same as for the EDS-1 nonskew equivalent bridge. Here, the number of long and short BRB at each end of the bridge in the EDS is taken as one. Note that the global yield strength in either the longitudinal or transverse direction is obtained when there are only forces applied on the bridge in that direction.

The assumption made for the design of the long BRB is that the long BRB would yield first and the short BRB would remain elastic under the longitudinal force applied to the bridge. Therefore, when the force of P_L is applied in the longitudinal direction of the bridge, the force demand on the long BRB will eventually reach its yield strength. This force that would produce yield of the long BRB (i.e., for which the BRB would need to be designed) is related to the longitudinal force by:

$$P_{Lb} = P_L \times L_L/(4 \times a) \tag{7.24}$$

The corresponding force in the short BRB is

$$P_{short} = P_L \times L_S/(4 \times a) \tag{7.25}$$

By using the principle of virtual work, the global yield displacement in the longitudinal direction is

$$\delta_{yL} = 2(P_{Lb}^2 c_L L_L/(P_L A_L) + P_{short}^2 c_S L_S/(P_L A_S))/E \tag{7.26}$$

Similarly, the short BRB would yield first and the long BRB would remain elastic under the transverse force applied to the bridge. When the force of P_T is applied in the transverse direction of the bridge, the force demand on the short BRB will eventually reach its yield strength. The force that would produce yield of the short BRB (i.e., for which the BRB would need to be designed) is related to the transverse force by:

$$P_{Sb} = P_T \times L_S \times (a + s \times \tan\varphi)/(4 \times s \times a) \tag{7.27}$$

The corresponding force in the long BRB is

$$P_{Long} = P_T \times L_L \times (a - s \times \tan\varphi)/(4 \times s \times a) \tag{7.28}$$

And, the global yield displacement in the transverse direction is

$$\delta_{yT} = 2(P_{long}^2 c_L L_L/(P_T A_L) + P_{Sb}^2 c_S L_S/(P_T A_S))/E \quad (7.29)$$

Note that P_{Long} and P_{short} are smaller than P_{Lb} and P_{Sb}.

With the yield displacements in the longitudinal and transverse direction known from the nonskew EDS-1 equivalent bridge, the yield length ratio of the long and short BRBs can be obtained from Equations 7-23 and 7-26.

The yielding core area of the long and short BRB would be P_{Lb}/F_{yb} and P_{Sb}/F_{yb} . The stiffness of the long and short BRB are:

$$K_{Long} = EP_{Lb}/(c_L F_{yb} L_L) \quad (7.30)$$

$$K_{Short} = EP_{Sb}/(c_S F_{yb} L_S) \quad (7.31)$$

In the benchmark bridge model with skew EDS-2 systems, the layout of long and short BRBs makes the response of the system coupled in the longitudinal and transverse direction. The equation of motions for the free vibration of this kind of system are shown below, where K_{xy} and K_{yx} are not zero:

$$\begin{bmatrix} m & 0 \\ 0 & m \end{bmatrix} \begin{Bmatrix} \ddot{u}_x \\ \ddot{u}_y \end{Bmatrix} + \begin{bmatrix} K_{xx} & K_{xy} \\ K_{yx} & K_{yy} \end{bmatrix} \begin{Bmatrix} u_x \\ u_y \end{Bmatrix} = \begin{Bmatrix} 0 \\ 0 \end{Bmatrix} \quad (7.32)$$

Solving the eigenvalue problem for the dynamic equation in Equation 7-32 would lead to the evaluation of the following equation:

$$Det \begin{bmatrix} K_{xx} - \omega^2 m & K_{xy} \\ K_{yx} & K_{yy} - \omega^2 m \end{bmatrix} = 0 \quad (7.33)$$

where: ω is the natural circular frequency of the system.

Equation 7-33 gives the natural frequencies of the system:

$$\omega = \sqrt{\left[(K_{xx} + K_{yy}) \pm \sqrt{(K_{xx} + K_{yy})^2 + 4(K_{xy}^2 - K_{xx}K_{yy})}\right]/(2m)} \quad (7.34)$$

Therefore, the corresponding first two periods of vibration for translational modes are:

$$T_1 = \sqrt{(8\pi^2 m)/\left[(K_{xx} + K_{yy}) + \sqrt{(K_{xx} + K_{yy})^2 + 4(K_{xy}^2 - K_{xx}K_{yy})}\right]} \quad (7.35)$$

$$T_2 = \sqrt{(8\pi^2 m)/\left[(K_{xx} + K_{yy}) - \sqrt{(K_{xx} + K_{yy})^2 + 4(K_{xy}^2 - K_{xx}K_{yy})}\right]} \qquad (7.36)$$

Similarly, in order to calculate the periods (T_1, T_2), the values in the stiffness matrix (K_{xx}, K_{yy}, K_{xy}) need to be obtained first. Fig. 7-9 shows the EDS-2 configurations with BRBs at one end of the bridge. The angle of the long BRB with the horizontal plane is θ_1. The angle of the long BRB's projection in the horizontal plane with the x-axis is θ_2. The angle of the short BRB with the horizontal plane is θ_3. The angle of the short BRB's projection in the horizontal plane with the x-axis is θ_4. The stiffness of the long and short BRBs are K_{Long} and K_{Short}, respectively.
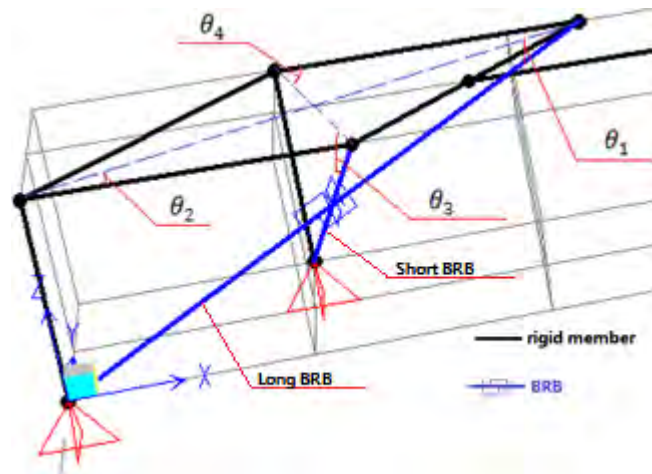
Figure 7-9 Illustration of angles in EDS-2 configuration at one end of the bridge

The stiffness K_{xx}, K_{yy}, K_{xy} in Equation 7-32 and 7-33 can then be expressed as:

$$K_{xx} = 2(K_{Long}cos^2\theta_1 cos^2\theta_2 + K_{Short}cos^2\theta_3 cos^2\theta_1 cos^2\theta_4) \qquad (7.37)$$

$$K_{yy} = 2(K_{Long}cos^2\theta_1 sin^2\theta_2 + K_{Short}cos^2\theta_3 cos^2\theta_1 sin^2\theta_4) \qquad (7.38)$$

$$K_{xy} = 2(K_{Long}cos^2\theta_1 cos\theta_2 sin\theta_2 - K_{Short}cos^2\theta_3 cos\theta_4 sin\theta_4) \qquad (7.39)$$

where: K_{Short} and K_{Long} is the axial stiffness of the short and long BRB, respectively.

7.3.2.3 Summarized Properties of skew bridge and equivalent nonskew bridges

In ease of the comparisons for the displacement demands obtained from the nonlinear time history analyses presented later in this Section, the skew bridge with EDS-1 schemes were designed to have the same yield strength and yield displacement in both the longitudinal and transverse directions as the nonskew bridge with EDS-1 scheme. The nonskew bridge is also the equivalent bridge of the skew

bridges of all skew angles. In Section 7.3.2.4.1, nonskew bridges were designed to have the bridge period of 0.2s for both EDS schemes. In Section 7.3.2.4.2, nonskew bridges were designed to have the period of 0.5s, 1.0s, and 1.5s, in order to investigate the effect of the period change when the period is not on the plateau of the acceleration response spectrum.

Note that skew and nonskew bridges with EDS-1 scheme were also designed to have different yield strength and displacement in both directions as presented in Appendix C. The bridges were modeled by assuming different ratios of stiffness in the longitudinal and transverse direction of the nonskew bridge with EDS-1 scheme. As the skew angle changed, the longitudinal stiffness stayed the same, and the skew stiffness in the skew EDS-1 bridge was kept the same as the transverse stiffness in the nonskew EDS-1 bridge. Therefore, skew bridges with different skew angles have its corresponding equivalent bridges. The bridges' dimensions, properties and also the comparison of the dynamic behaviors between the skew and nonskew bridges with EDS-1 are provided in Appendix C.

The total bridge length remains the same for all benchmark simplified bridge models, since the superstructure was assumed rigid and the length of the bridge does not affect the dynamic behavior of the bridges in this case. Modal and pushover analyses were performed in *SAP2000* and *OpenSees*, and verified with the equations that are used to calculate yield strength, yield displacement, and periods of the EDSs as presented in the tables in this section by using the equations in Section 7.3.2.2 and 7.3.2.3.

7.3.2.3.1   Equivalent nonskew bridge period of 0.2s

The skew angles of the bridges, φ, were changed at a 15-degree interval from 0 to 75 degree. For EDS-1 scheme shown in Fig. 7-2 and 7-3, the three dimensions a, d, s are kept the same for all skew bridge with different skew angles (including for the equivalent nonskew bridges). Only 15 and 30 degree skews were considered for the EDS-1 skew bridges, since skew bridges with skew angles beyond 45 degrees could not be designed to have the equal yield strength and yield displacement as their equivalent EDS-1 nonskew bridge. Dimensions and properties of the skew and nonskew bridge ductile diaphragms in the EDS-1 configuration are tabulated in Table 7-1. Note that, in the skew bridges, the cross section areas of the BRBs installed in the longitudinal and in the skew directions are not the same.

The skew and nonskew bridges with EDS-2 schemes were designed to have the same yield strength and displacement in both the longitudinal and transverse direction as the bridges with EDS-1 schemes. For the skew and nonskew bridges with EDS-2 shown in Fig. 7-3 and 7-7, the parameter s and d are the same,

while the parameter *a* changes as the skew angle changes, since the same *a* cannot be used to design the skew bridge with EDS-2 to have the same yield strength and displacement.

Table 7-1 Properties of benchmark simplified EDS-1 skew and nonskew bridges

Skew Angle (Degree)	0	15	30
First translational period T_1 (s)	0.20	0.22	0.25
Second translational period T_2 (s)	0.20	0.17	0.12
Stiffness in Longitudinal direction (kip/in)	5126.5	5126.5	5126.5
Stiffness in Skew direction (kip/in)	5126.5	5919.6	10253.1
Longitudinal BRB Cross Sectional Area (in^2)	9.00	9.00	9.00
Skew BRB Cross Sectional Area (in^2)	9.00	9.16	9.72
Global Yielding Displacement in both longitudinal and transverse directions (in)	0.209	0.209	0.209
Global Yielding Strength in both longitudinal and transverse directions (kips)	1069.1	1069.1	1069.1
Equivalent stiffness in both longitudinal and transverse directions (kip/in)	5126.5	5126.5	5126.5
Yielding length ratio of Longitudinal BRB	1.00	1.00	1.00
Yielding length ratio of Skew BRB	1.00	0.90	0.57

Dimensions and properties of the skew and nonskew bridge ductile diaphragms in the EDS-2 configuration are tabulated in Table 7-2. Note that in the skew bridges, the cross section areas of the long and short BRBs are not the same. It is acknowledged that, for skew bridge with skew angle beyond 60 degrees, the length of the BRBs may be too long to be practical; such large skew angles for EDS-2 were only considered here to show that EDS-2 systems can be theoretically designed to have equal yield displacement and yield strength in the longitudinal and transverse directions at large skew angles.

Table 7-2 Properties of benchmark simplified EDS-2 nonskew and skew bridges

Skew Angle (Degree)	0	15	30	45	60	75
a (in)	72	72	75	95	140	270
First translational period T_1 (s)	0.200	0.213	0.221	0.212	0.206	0.211
Second translational period T_2 (s)	0.200	0.186	0.180	0.186	0.193	0.188
Long-BRB Cross Sectional Area (in^2)	11.023	12.088	13.133	13.103	12.892	12.922
Short-BRB Cross Sectional Area (in^2)	11.023	12.850	14.723	16.220	17.208	17.958
Global Yielding Displacement in both longitudinal and transverse directions (in)	0.209	0.209	0.209	0.209	0.209	0.209
Global Yielding Strength in both longitudinal and transverse directions (kips)	1069.1	1069.1	1069.1	1069.1	1069.1	1069.1
Yielding Stress of Material in BRBs' Core in Both Directions(ksi)	42	42	42	42	42	42
Yielding length ratio of Long BRB	0.67	0.63	0.61	0.59	0.47	0.25
Yielding length ratio of Short BRB	0.67	0.87	0.99	0.99	0.99	1.00

7.3.2.3.2   Equivalent bridge of increased periods

Since the periods of the equivalent nonskew bridge in the above cases all fall on the plateau of the average acceleration response spectrum considered, the 30-degree skew bridges with both EDS schemes were redesigned to have equivalent nonskew bridge periods of 0.5s, 1.0s, and 1.5s, by keeping the same mass of the bridge and by changing the size of the BRBs. The properties of the benchmark simplified EDS-1 skew bridges of 30 degrees and corresponding equivalent nonskew bridges of 0.5s, 1.0s, and 1.5s periods are shown in Table 7-3. Case 1, Case 2, and Case 3 in Table 7-3 each include a skew bridge and its equivalent nonskew bridge with periods corresponding to 0.5s, 1.0 and 1.5s, respectively. Note that for each case of bridges in Table 7-3, the stiffness of the skew bridge is tabulated in the longitudinal and skew direction, and its stiffness in the longitudinal and transverse directions are the same as those for the nonskew equivalent bridge in the same directions.

The properties of the benchmark simplified EDS-2 skew bridges of 30 degrees and corresponding equivalent nonskew bridges of 0.5s, 1.0s, and 1.5s periods are shown in Table 7-4. Case 1, Case 2, and Case 3 in Table 7-4 each include a skew bridge and its equivalent nonskew bridge with periods corresponding to 0.5s, 1.0 and 1.5s, respectively.

Table 7-3 Properties of benchmark simplified EDS-1 skew 30 degree bridges and corresponding equivalent nonskew bridges

	Case 1		Case 2		Case 3	
	skew	nonskew	skew	nonskew	skew	nonskew
First translational period T_1 (s)	0.62	0.50	1.24	1.00	1.87	1.50
Second translational period T_2 (s)	0.31	0.50	0.61	1.00	0.92	1.50
Stiffness in Longitudinal direction (kip/in)	818.2	818.2	204.5	204.5	90.9	90.9
Stiffness in Skew (Transverse for nonskew) direction (kip/in)	1636.4	818.2	409.1	204.5	181.8	90.9
Longitudinal BRB Cross Sectional Area (in²)	1.44	1.44	0.36	0.36	0.16	0.16
Skew (Transverse for nonskew) BRB Cross Sectional Area (in²)	1.55	1.44	0.39	0.36	0.17	0.16
Global Yielding Displacement in both longitudinal and transverse directions (in)	0.209	0.209	0.209	0.209	0.209	0.209
Global Yielding Strength in both longitudinal and transverse directions (kips)	170.6	170.6	42.6	42.6	18.9	18.9
Yielding length ratio of Longitudinal BRB	1.00	1.00	1.00	1.00	1.00	1.00
Yielding length ratio of Skew BRB	0.57	1.00	0.57	1.00	0.57	1.00

25:

Table 7-4 Properties of benchmark simplified EDS-2 skew 30 degree bridges and corresponding equivalent nonskew bridges

	Case 1		Case 2		Case 3	
	skew	nonskew	skew	nonskew	skew	nonskew
First translational period T_1 (s)	0.55	0.50	1.10	1.00	1.65	1.50
Second translational period T_2 (s)	0.44	0.50	0.89	1.00	1.33	1.50
Stiffness in Longitudinal direction (kip/in)	818.2	818.2	204.5	204.5	90.9	90.9
Stiffness in Transverse direction (kip/in)	818.2	818.2	204.5	204.5	90.9	90.9
Long BRB Cross Sectional Area (in^2)	2.10	1.76	0.52	0.44	0.23	0.19
Short BRB Cross Sectional Area (in^2)	2.35	1.76	0.59	0.44	0.26	0.19
Global Yielding Displacement in both longitudinal and transverse directions (in)	0.209	0.209	0.209	0.209	0.209	0.209
Global Yielding Strength in both longitudinal and transverse directions (kips)	170.6	170.6	42.6	42.6	18.9	18.9
Yielding length ratio of Long BRB	0.61	0.67	0.61	0.67	0.61	0.67
Yielding length ratio of Short BRB	1.00	0.67	1.00	0.67	1.00	0.67

7.4   Nonlinear time history analysis of nonskew and skew bridges

Nonlinear time history analyses of the benchmark skew and nonskew bridges were conducted by inputting orthogonal components of the ground motions records in the global longitudinal and transverse direction of each bridge, to investigate their inelastic displacement demands. The EDS-1 nonskew bridges were first designed and an approach was used to calculate the maximum ground motions scaling factor corresponding to the target global displacement ductility as explained in Section 7.4.1. The inelastic displacement demands of the EDS-1 nonskew bridges with different periods were compared with the assumed target displacements in Section 7.4.2; results of this comparison were used to define the inelastic displacement magnification factor, R_{d1}. The same pairs of scaled ground motions were applied to EDS-1 skew bridges, and the displacement demands were then compared with the EDS-1 nonskew bridges to assess whether results from the EDS-1 equivalent nonskew bridge could be used to predict the global displacements of the actual EDS-1 skew bridge in Section 7.4.3.1. EDS-2 skew and nonskew bridges were also subjected to the same analysis using pairs of scaled ground motions, and inelastic displacements were also obtained and presented in Section 7.4.3.2. The displacement magnification factor for skew EDSs configurations from the displacement response of the equivalent nonskew EDSs, R_{d2}, was also defined for both EDS schemes in Section 7.4.3. The magnification factors will be used in the proposed design procedures in Section 9.

7.4.1 Ground motions and scale factors

For the nonskew bridge, the behaviors of the EDS in the two orthogonal directions are uncoupled and the system can be detailed to behave in the bilinear manner shown in Fig.7-10 (neglecting the lateral stiffness of the steel girders in that application). The EDSs' displacement limits in both directions can translate into maximum global ductility demand, μ, themselves related to yielding displacement of the BRB in the EDS. To ensure that those ductility demands are not exceeded during nonlinear time history analyses, relationships must be established between these values and the minimum yield strength of the system, V_y, itself related to $V_{elastic}/R$, where $V_{elastic}$ is the corresponding elastic force demand. Different relationships between R, μ, and the period T can be found in Miranda and Bertero (1994), such as in Equations 7-40 and 7-41 (referenced by MCEER/ATC49, 2003). For a certain ductility μ ranging from 2 to 6, the force reduction factor R varies as a function of T as shown in Fig. 7-11.

$$R = \frac{\mu - 1}{\phi} + 1 \geq 1 \tag{7.40}$$

$$\phi = 1 + \frac{1}{12T - \mu T} - \frac{2}{5T}\exp[-2(lnT - \frac{1}{5})^2] \tag{7.41}$$

The value R obtained from Equations 7-40 and 7-41 were used to scale the 44 ground motions specified in FEMA-P695 (2009) to perform the nonlinear time history analyses of the benchmark bridges. The elastic force demand at the bridge's modal period in each direction is V_yR. The average spectral acceleration of the scaled 44 ground motions, shown in Fig. 7-12, at the bridge modal period in each direction corresponds to the elastic force demand S_a. All the 44 ground motions use the same scale factor of $V_yR/(mS_a)$.
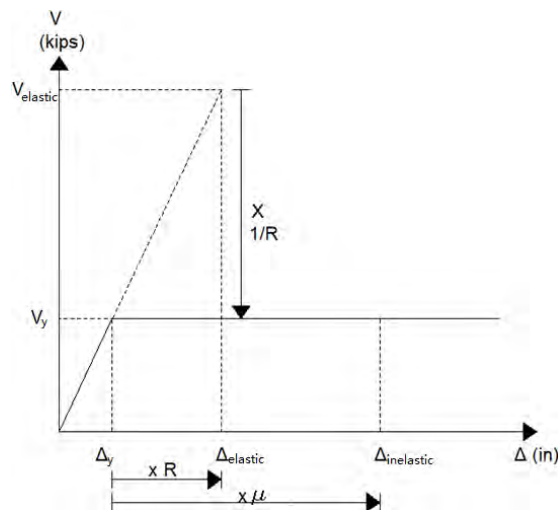
Figure 7-10 Illustration of displacement ductility and force reduction factor for bilinear system

262
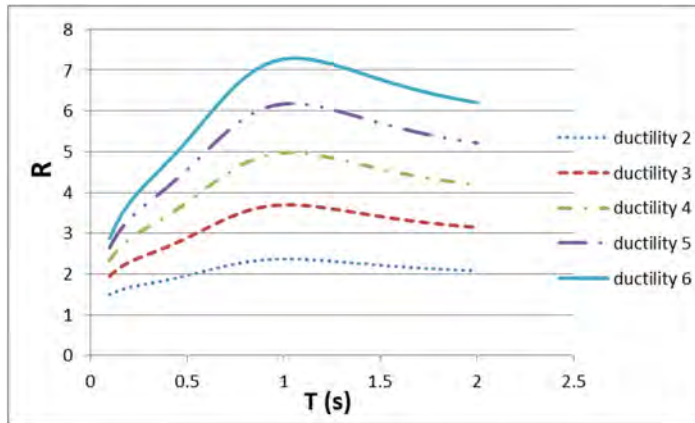
Figure 7-11 The relationship between R and T for a certain ductility (calculated from Miranda and Bertero ,1994)
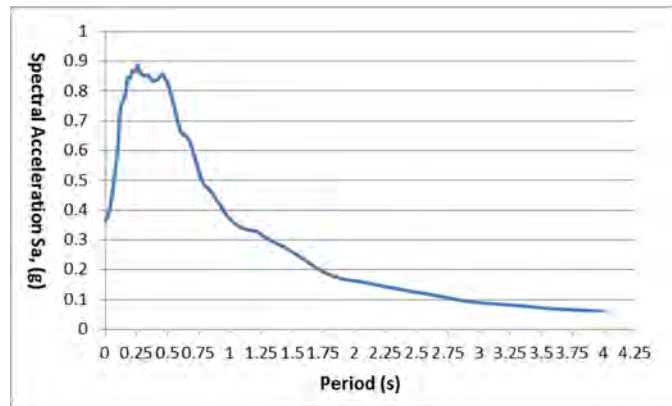
Figure 7-12 The average acceleration response spectrum of 44 ground motions

7.4.2 Assessing the relationship between R and μ

As mentioned above, the EDS-1 nonskew bridge's response in the transverse and longitudinal direction is uncoupled, therefore, the bilinear system behaviors in both directions as shown in Fig.7-8 were used to assess the relationship between R and μ. The scaled ground motions calculated above were applied to the EDS-1 equivalent nonskew bridge to investigate whether the displacement demand would exceed the assumed target displacement. Various nonskew equivalent EDS-1 with translational periods ranging from 0.2s to 1.5s were analyzed. Target ductilities from 2 to 6 were used. Table 7-5 shows the force reduction factor R corresponding to the ductilities for each period from the nonskew equivalent bridges with EDS-1s. For example, for the nonskew bridge with EDS-1 having the period of 0.3 s, the force reduction factor obtained from Equation 7-40 and 7-41 is 3.15 for the target ductility of 4. Note that the properties of the nonskew bridge with EDS-1 of 0.2s, 0.5s, 1.0s, and 1.5s periods are presented in Section 7.3.2.4. The

properties for the rest of the nonskew EDS-1 bridge details considered in Table 7-5 are presented in Appendix C.

Table 7-5 Force reduction factor R for each period from the nonskew equivalent bridges with EDS-1s

Ductility	Period (s)													
	0.20	0.21	0.26	0.28	0.30	0.35	0.45	0.50	0.53	0.66	1.00	1.07	1.32	1.50
2	1.67	1.68	1.73	1.75	1.76	1.81	1.90	1.96	2.00	2.16	2.37	2.36	2.29	2.22
3	2.29	2.32	2.41	2.46	2.48	2.57	2.77	2.89	2.95	3.27	3.70	3.69	3.55	3.41
4	2.85	2.90	3.04	3.11	3.15	3.28	3.58	3.76	3.86	4.32	4.97	4.97	4.77	4.58
5	3.34	3.40	3.59	3.69	3.75	3.93	4.33	4.56	4.69	5.30	6.17	6.18	5.94	5.70
6	3.73	3.82	4.06	4.18	4.26	4.49	4.98	5.27	5.43	6.18	7.27	7.29	7.04	6.77

Table 7-6 presents the design yield displacement of the nonskew equivalent bridge in the direction which corresponds to each period presented in Table 7-5. The resulting average of the maximum displacement demands were obtained from nonlinear time history analyses using 44 ground motions and tabulated for all the ductilities from 2 to 6.

The average displacement demands were compared to the displacement targets (taken as equal to the yield displacement times the target ductility μ in this case). Fig. 7-13 shows by how much (in percentage) the average displacements of the nonskew EDS-1 (for all 44 ground motions) exceeds from the assumed displacements limit of all ductility cases (from 2 to 6), as a function of the force reduction factor used. As the ductility increases, the percentage of exceedance typically increases. The smaller the force reduction factor, the smaller the percentage of exceedance of the resulting displacement from the estimated displacements. For periods around 1.0 s, the percentage of exceedance is generally larger than for the other periods. In all cases, the percentage of exceedance is less than 40% for the range of R between 1.5 and 7.5. This information was used to define the displacement magnification factor R_{d1}. This factor is similar to the displacement magnification for short period bridges provided by Equation 4.3.3 in AASHTO (2011), except that AASHTO gives much larger and more conservative values.

Table 7-6 Yield displacement and displacement demand from nonlinear time history analyses of nonskew equivalent bridges with EDS-1s (Unit: in)

Periods(s)	Yield Displacement	ductility				
		2	3	4	5	6
0.20	0.209	0.391	0.662	0.983	1.336	1.637
0.21	0.231	0.418	0.674	1.004	1.369	1.735
0.26	0.304	0.479	0.778	1.22	1.668	2.099
0.28	0.209	0.347	0.595	0.876	1.155	1.419
0.30	0.223	0.361	0.606	0.88	1.184	1.477
0.35	0.469	0.768	1.175	1.701	2.259	2.808
0.45	0.391	0.646	1.02	1.456	1.819	2.2
0.50	0.209	0.335	0.526	0.734	0.992	1.21
0.53	0.843	1.521	2.359	3.47	4.502	5.363
0.66	0.717	1.299	2.054	3.034	4.003	4.786
1.00	0.209	0.441	0.782	1.147	1.422	1.681
1.07	1.613	3.435	6.173	8.637	10.82	13.23
1.32	2.436	4.926	7.838	10.62	13.12	15.97
1.50	0.209	0.385	0.589	0.77	1.009	1.249
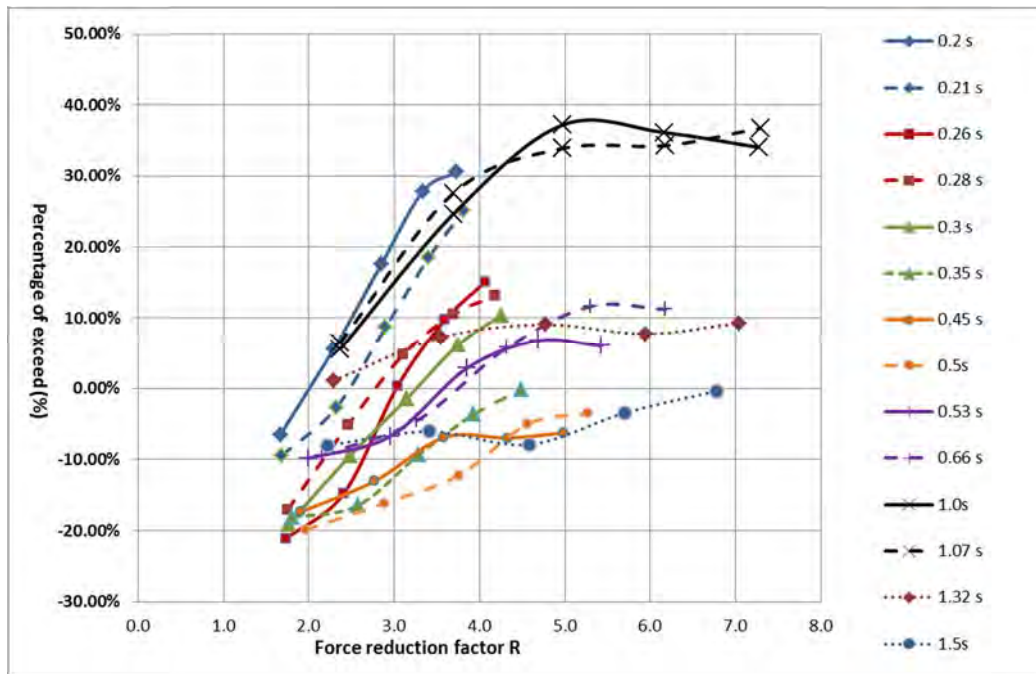
Figure 7-13 Percentage of exceedance of nonskew bridge displacements from displacement limits versus the force reduction factors for 44 ground motions at various periods

7.4.3 Comparison between skew and nonskew bridge displacements

7.4.3.1 EDS-1 skew bridges

The properties of the skew bridges with EDS-1 schemes are presented in Table 7-1. The ground motions applied in the longitudinal and transverse directions of the skew bridge were the same as those used for its equivalent nonskew bridge. The scaling of the ground motions applied to the nonskew bridges followed

the method mentioned in Section 7.4.1. The resulting average of the maximum displacements of the skew bridge from analyses using 44 ground motions are shown in Table 7-7. The skew bridges' displacement demands were compared with those from the EDS-1 nonskew bridge cases in Table 7-8. The resulting longitudinal displacements of the skew bridges are generally larger than those for the equivalent nonskew bridges. The difference between the transverse displacements is smaller than that in longitudinal directions. For greater skew angle, the difference in longitudinal displacements is larger, with values up to 36% greater for the skew bridge.

Table 7-7 Displacement demands of the EDS-1 skew bridge and their equivalent nonskew bridges of period 0.2s (Unit: in)

Ductility	Nonskew	Skew 15°		Skew 30°	
	Longitudinal &Transverse	Longitudinal	Transverse	Longitudinal	Transverse
2	0.391	0.415	0.397	0.531	0.418
3	0.662	0.677	0.646	0.853	0.666
4	0.983	0.982	0.914	1.199	0.973
5	1.336	1.300	1.250	1.509	1.276
6	1.637	1.571	1.556	1.757	1.583

Table 7-8 Displacement comparison between the EDS-1 skew bridge and their equivalent nonskew bridges of period 0.2s

Ductility	Skew 15°		Skew 30°	
	Longitudinal	Transverse	Longitudinal	Transverse
2	6.19%	1.56%	35.84%	6.98%
3	2.27%	-2.40%	28.84%	0.57%
4	-0.14%	-7.04%	21.95%	-0.99%
5	-2.71%	-6.44%	12.94%	-4.48%
6	-4.06%	-4.97%	7.32%	-3.29%

In the above comparison, an equivalent bridge period of 0.2s was used. The same comparisons were made to investigate the effect of period change on the difference in the displacement response between the EDS-1 skew and nonskew bridges in Table 7-3. All the resulting displacement demands are shown in Table 7-9 with Case 1, Case 2, and Case 3 corresponding to the skew bridges mentioned in Table 7-3. The difference between the displacement demands of the skew and nonskew bridge are tabulated in Table 7-10, which are smaller than those for the corresponding reference 30-degree skew bridge (i.e. with equivalent nonskew bridge period of 0.2s) in Table 7-8. Generally, the longitudinal displacement results for skew bridges exceeded those from the nonskew bridge, with smaller maximum exceedance percentage as the period increased. The comparison of transverse displacements exhibited no specific trends as the period changed. At a period of 1.0s, the percentage of transverse displacement response for skew that

266

exceeded that of their corresponding equivalent nonskew bridge was the largest of all the 30 degree skew cases considered.

Table 7-9 Displacement demands of the EDS-1 skew bridge and their equivalent nonskew bridges of increased periods (Unit: in)

| Ductility | Case 1 | | | Case 2 | | | Case 3 | | |
| | Nonskew | Skew | | Nonskew | Skew | | Nonskew | Skew | |
	Longi&Trans	Longi.	Trans.	Longi&Trans	Longi.	Trans.	Longi&Trans	Longi.	Trans.
2	0.335	0.347	0.342	0.441	0.453	0.523	0.385	0.359	0.403
3	0.526	0.512	0.545	0.782	0.751	0.893	0.589	0.560	0.615
4	0.734	0.701	0.752	1.147	1.044	1.262	0.770	0.731	0.810
5	0.992	0.897	0.964	1.422	1.328	1.567	1.009	0.931	1.032
6	1.210	1.083	1.140	1.681	1.625	1.789	1.249	1.109	1.245

Table 7-10 Displacement comparison between the EDS-1 skew bridge and their equivalent nonskew bridges for increased periods

| Ductility | Case 1: Skew 30° | | Case 2: Skew 30° | | Case 3: Skew 30° | |
	Longitudinal	Transverse	Longitudinal	Transverse	Longitudinal	Transverse
2	3.71%	2.19%	2.61%	18.55%	-6.84%	4.73%
3	-2.57%	3.57%	-3.98%	14.24%	-4.88%	4.45%
4	-4.45%	2.48%	-8.94%	10.00%	-5.05%	5.15%
5	-9.55%	-2.85%	-6.60%	10.22%	-7.69%	2.23%
6	-10.52%	-5.79%	-3.34%	6.40%	-11.24%	-0.29%

7.4.3.2 EDS-2 skew bridges

The EDS-2 nonskew bridges in Table 7-2 had the same translational period of 0.2s in the longitudinal and transverse directions as the EDS-1 nonskew bridges considered earlier. Therefore, the force reduction factors and ground motions' scale factors were the same as the EDS-1 bridges for all ductility considered. However, there is a slight difference between the EDS-2 and EDS-1 nonskew bridge displacements, as shown in Table 7-11.

Table 7-11 Displacement comparison between the EDS-1 and EDS-2 nonskew bridge of period 0.2s

Ductility Demand μ	Displacement Limit (in)	Displacement demand of EDS-1 nonskew bridge (in)	Displacement demand of EDS-2 nonskew bridge (in)	Difference [(EDS-2/EDS-1)-1]
2	0.417	0.391	0.385	-1.53%
3	0.626	0.662	0.699	5.59%
4	0.834	0.983	1.049	6.71%
5	1.043	1.336	1.368	2.40%
6	1.251	1.637	1.628	-0.55%

The EDS-2 skew bridges were analyzed by applying in the same directions the same scaled ground motion used with EDS-2 nonskew cases, and the resulting displacement demands are shown in Table

7-12. The displacements of the skew bridges are compared with those from the EDS-2 nonskew bridge cases in Table 7-13. The resulting longitudinal displacements of the skew bridges are generally less than those from the equivalent nonskew bridges, except for the 15 and 30-degree skew bridges. With increase of the skew angle, the displacements differences reduced, which is different than what was observed for the EDS-1 cases.   The greatest difference in the resulting displacements is 27.3% in the transverse direction for the 15-degree skew bridges.

Table 7-12 Displacement demands of the EDS-2 skew bridge corresponding to equivalent nonskew bridges of period 0.2s (Unit: in)

Ductility	Skew 15°		Skew 30°		Skew 45°		Skew 60°		Skew 75°	
	Longi.	Trans.	Longi.	Trans.	Longi.	Trans.	Longi.	Trans.	Longi.	Trans.
2	0.474	0.455	0.430	0.445	0.382	0.398	0.362	0.385	0.368	0.385
3	0.830	0.850	0.761	0.768	0.668	0.697	0.640	0.651	0.624	0.633
4	1.183	1.292	1.102	1.170	0.978	1.054	0.978	0.973	0.943	0.906
5	1.562	1.685	1.399	1.549	1.298	1.432	1.317	1.358	1.268	1.229
6	1.948	2.073	1.674	1.883	1.599	1.729	1.605	1.685	1.531	1.543

Table 7-13 Displacement comparison between the EDS-2 skew bridge and their equivalent nonskew bridges of period 0.2s

Ductility	Skew 15°		Skew 30°		Skew 45°		Skew 60°		Skew 75°	
	Longi.	Trans.	Longi.	Trans.	Longi.	Trans.	Longi.	Trans.	Longi.	Trans.
2	23.15%	18.24%	11.82%	15.68%	-0.66%	3.48%	-6.07%	0.05%	-4.31%	0.14%
3	18.73%	21.64%	8.91%	9.87%	-4.44%	-0.30%	-8.41%	-6.90%	-10.69%	-9.43%
4	12.77%	23.14%	4.97%	11.51%	-6.79%	0.44%	-6.76%	-7.30%	-10.18%	-13.65%
5	14.19%	23.12%	2.29%	13.20%	-5.12%	4.64%	-3.74%	-0.75%	-7.31%	-10.17%
6	19.63%	27.30%	2.79%	15.65%	-1.80%	6.18%	-1.45%	3.46%	-5.96%	-5.25%

Similarly, to what was done for the EDS-1 bridges, the displacement demands were obtained to investigate the effect of period change on the difference in the displacement response between the EDS-2 skew and nonskew bridges as shown in Table 7-14. Case 1, Case 2, and Case 3 in Table 7-9 each correspond to the bridges cases in Table 7-4. The same comparisons were made between the skew and equivalent nonskew bridges in Table 7-15. It is found that the resulting skew bridges displacements are all smaller than that of their corresponding nonskew bridges.

In general, the displacement magnification factor for skew bridge, to apply to the displacement response of the equivalent nonskew bridges, R_{d2}, vary for the different EDS schemes as a function of skew angles. The difference may be a consequence of the difference in the true period of the skew and nonskew bridges, which would cause the variability in the inelastic displacements. Results of the above parametric studies indicate that, for skew bridges with skew angles smaller than 15 degrees, R_{d2} could be taken as 1.1 and 1.3 for EDS-1 and EDS-2, respectively. For skew bridges with skew angles larger than 30 degrees,

R_{d2} could be taken as 1.4 and 1.15 for EDS-1 and EDS-2, respectively. For skew angle beyond 45 degrees, only the EDS-2 scheme is possible to achieve such that the yield strength and yield displacement of the skew and nonskew EDS are the same. Note that beyond 60-degree skew, the EDS-2 scheme would require BRB lengths that may not be practical.

Table 7-14 Displacement demands of the EDS-2 skew bridge and their equivalent nonskew bridges of increased periods (Unit: in)

Ductility	Case 1			Case 2			Case 3		
	Nonskew	Skew		Nonskew	Skew		Nonskew	Skew	
	Longi&Trans	Longi.	Trans.	Longi&Trans	Longi.	Trans.	Longi&Trans	Longi.	Trans.
2	0.359	0.333	0.334	0.496	0.481	0.487	0.426	0.421	0.387
3	0.544	0.517	0.516	0.872	0.832	0.823	0.634	0.651	0.610
4	0.805	0.762	0.727	1.186	1.176	1.165	0.851	0.862	0.833
5	1.056	0.994	0.940	1.519	1.469	1.436	1.102	1.068	1.033
6	1.305	1.218	1.150	1.847	1.753	1.665	1.343	1.273	1.232

Table 7-15 Displacement comparison between the EDS-2 skew bridge and their equivalent nonskew bridges for increased periods

Ductility	Case 1: Skew 30°		Case 2: Skew 30°		Case 3: Skew 30°	
	Longitudinal	Transverse	Longitudinal	Transverse	Longitudinal	Transverse
2	-7.30%	-6.90%	-3.12%	-1.94%	-1.11%	-9.12%
3	-5.00%	-5.15%	-4.54%	-5.60%	2.54%	-3.83%
4	-5.41%	-9.72%	-0.84%	-1.72%	1.36%	-2.13%
5	-5.83%	-10.91%	-3.26%	-5.43%	-3.11%	-6.30%
6	-6.62%	-11.78%	-5.07%	-9.83%	-5.16%	-8.20%

7.5   Effect of orthogonal ground motion applying directions on response of skew bridges with EDSs

Different maximum displacements in the longitudinal and transverse directions of both EDSs in skew bridges can be obtained by applying ground motions in different orthogonal directions with respect to the bridge longitudinal axis. In absence of knowledge on how significantly response would vary when considering various excitation directions, analyses were conducted investigate this matter. Three ways of applying the ground motion pairs were used in this section to investigate the sensitivity of displacement demands. These pairs of ground motions were applied in: (1) the bridge global longitudinal and transverse direction; (2) the skew direction and the direction perpendicular to it; (3) the principal vibration directions of the system (obtained from modal analysis). The analyses conducted in Section 7.4.3 for the skew bridges with EDSs corresponded to the first case of these three cases. For the remaining two cases, a simple spring-mass model was first analyses, followed by the benchmark bridge models with skew EDSs, and results are presented in Section 7.5.1 and 7.5.2, respectively.

7.5.1 Simple spring-mass model in SAP2000

A simple spring-mass model was first built, as shown in Fig. 7-14a, using longitudinal and skew springs linked to a concentric mass of 2000 lbs. The longitudinal and skew springs have the same stiffness of 1000 kip/in and yield strength of 300 kips. The yield strength and displacement in the longitudinal direction is 300 kips and 0.3", respectively. The yield strength and displacement in the transverse direction is 212 kips and 0.636", respectively. The considered skew angle φ for this spring-mass model is 45 degree. Per Equations 7-20 to 7-23 in Section 7.3.2.3.1, the periods of this model are 0.519s and 0.215s. The two main vibration directions corresponding to these two periods are perpendicular to each other. The intersection, γ, angle between the longitudinal (x) direction and one of the main vibration directions (corresponding to the period of 0.215s) is 22.5°. The three ways described above for applying the ground motions pairs are shown in Figs. 7-14b, 7-14c, and 7-14d, where the notation GM i-j refers to the j-th ground motion in the ground motion pair i.
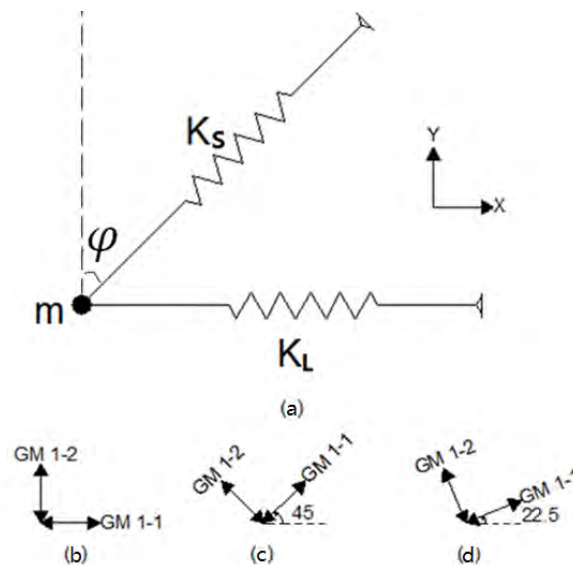
Figure 7-14 Simple spring-mass model: (a) two springs and concentric mass; and rotating directions of applying ground motions: (b) in the global longitudinal and transverse direction; (c) in the skew direction and the direction perpendicular to it; (d) in the principal vibration directions

Note that for nonskew bridges, it doesn't matter if the positive or negative directions of a ground motion are applied to the bridge (where "positive" is defined here as the direction in which the maximum displacement of response is obtained for a single-degree-of-freedom system subjected to that earthquake excitation). However, for skew bridge, because responses in the longitudinal and skew directions are coupled, this may not be the case. Hence, for the 44 ground motions considered and applied in 22 pairs, 88 time history analyses (i.e. 22 analyses for each of the four cases shown in Fig. 7-15) were performed for each skew bridge, rather than the corresponding 44 runs for each nonskew bridge. The scaling factors

are the same for the two ground motions in each of the 22 pairs of ground motions. Furthermore, all the 22 pairs of ground motions use the same scale factor as mentioned in Section 7.4.1.
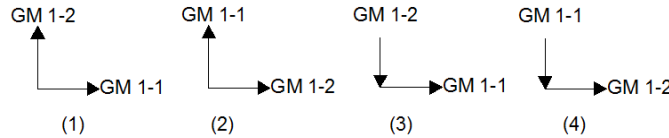
Figure 7-15 Inputting ground motions negatively for skew bridges

Note that the equivalent stiffness of the skew bridge in the longitudinal and transvers direction is not the same, and for scaling of the ground motions, the period of 0.487 s, corresponding to the longitudinal stiffness, was used. The acceleration demand in Fig. 7-11 for the average response spectrum of 44 ground motion is 0.853g. By choosing the scale factor (same for all the 44 ground motions) arbitrarily as 1.16, an elastic acceleration demand on the mass-spring system of 1g (corresponding to that period of 0.487 s) was obtained. Table 7-16 shows the average of the maximum displacements resulting from the 44 and 88 analyses run in the transverse and longitudinal directions. Case 1, 2 and 3 corresponds to Figs. 7-12b, 7-12c, and 7-12d, respectively, when the orthogonal ground motions pair was applied in the global longitudinal and transverse direction, skew and its perpendicular direction, and principle vibration directions, respectively. The displacements in the X and Y directions are tabulated, as well as the difference in response in both directions, which are all within 8%. Note that the displacement demands from the 88 time history analyses considered variations in the positive and negative directions of the ground motions. For the three cases shown in Table 7-16, displacements in the longitudinal direction are smaller after rotating the ground motions (i.e., Cases 2 and 3) compared to when the ground motions are applied in the bridge's global longitudinal and transverse direction (Case 1), while the transverse displacements are about 3% larger. In all cases, the differences are negligible.

Table 7-16 Displacements for spring-mass models subjected to various ground motion directions

	44 Average (in)		88 Average (in)		Difference	
	X	Y	X	Y	X	Y
case 1: original global longitudinal and transverse direction	1.997	3.183	1.885	3.269	-5.62%	2.71%
case 2: skew direction and its perpendicular direction	1.870	3.270	1.860	3.280	-0.45%	0.22%
case 3: principal vibration directions of the spring-mass model	1.702	3.278	1.826	3.238	7.28%	-1.23%

In a set of subsequent analyses, the scale factor used for the 44 ground motions in the global X and Y directions (Case 1 in Table 7-16) was changed from 1.16 to 0.87 and 1.45 (namely, a +/-25% percent difference in the scale factor) to investigate whether the previous results were sensitive to the severity of

inelastic displacements, as shown in Table 7-17. Again, the differences in the brackets remained within 8% after considering variations in the positive and negative directions.

Table 7-17 Displacements for spring-mass model subjected to ground motions with different scale factors

	44 Average (in)		88 Average (in)		Difference	
	X	Y	X	Y	X	Y
case 1 with scale factor of 1.16	1.997	3.183	1.885	3.269	-5.62%	2.71%
case 2 with scale factor of 0.87	1.397	2.212	1.293	2.237	-7.45%	1.12%
case 3 with scale factor of 1.45	2.676	4.441	2.652	4.501	-0.90%	1.36%

In another set of analyses, longitudinal stiffness was changed to twice that of the spring in the skew direction, and the scale factor of the ground motions stayed at 1.16. Results in Table 7-18 show that both the longitudinal and transverse displacements became smaller when the structure was subjected to ground excitations rotated from the original orthogonal directions. Differences in brackets were again on the order of 8% when comparing the average maximum displacements for the 44 and 88 analyses runs.

Table 7-18 Displacement for spring-mass model with different spring stiffness

	44 Average (in)		88 Average (in)		Difference	
	X	Y	X	Y	X	Y
case 1: original global longitudinal and transverse direction	1.402	2.923	1.36	2.966	-3.00%	1.49%
case 2: skew direction and its perpendicular direction	1.352	2.783	1.355	2.829	0.19%	1.64%
case 3: principal vibration directions of the spring-mass model	1.344	2.846	1.456	2.805	8.38%	-1.43%

Therefore, based on the results of this limited study, it appears that the ground motions used to investigate the behavior of skew bridges could be applied in the bridge's global longitudinal and transverse directions, without the need to consider: (1) applying ground motions in other orthogonal directions; (2) changing the "polarity" of the directions of each ground motion.

7.5.2 Benchmark skew bridges with EDS-1

After examining the behaviors of the simple spring-mass model, the benchmark skew bridge models in EDS-1 configuration were analyzed to compare with the above mentioned differences of displacement demands after rotating the directions of applied ground motions. The model used in for this purpose was the benchmark bridge in EDS-1 configurations having the same stiffness in the longitudinal and skew

directions (and further described in Appendix C). The properties of the skew EDS-1 bridge with 45 and 60-degree skew angles are presented in Table 7-19. The skew EDS-1 bridge had the same longitudinal and skew stiffness of 5126.5 kip/in. The yield stress of the steel core of all the BRBs was 42 ksi. The yield length ratio of the BRB was set to 1.0 for simplicity. Therefore, the principal vibration directions of the system were obtained after rotating the global axis half of the intersection angle between the longitudinal and skew direction, counterclockwise. The same analyses conducted in Section 7.4 for the skew bridges, with various ductility demands ranging from 2 to 6, were conducted here. The scale factors of the ground motions were obtained the same way as mentioned in Section. 7.4.1 for the equivalent nonskew EDS-1 bridge.

Table 7-19 Properties of benchmark EDS-1 skew bridges with skew angle of 45 and 60 degree

Skew Angle (Degree)	45	60
First translational period T_1 (s)	0.37	0.55
Second translational period T_2 (s)	0.15	0.15
Longitudinal BRB Cross Sectional Area (in^2)	9.00	9.00
Skew BRB Cross Sectional Area (in^2)	8.27	8.22
Global Yielding Displ. in longitudinal direction (in)	0.209	0.209
Global Yielding Displ. in transverse direction (in)	0.469	0.843
Global Yielding Strength in in transverse direction (kips)	801.9	617.3

The average values of the maximum displacements of the skew bridges for the skew angle of 45 degrees are compared in Table 7-20 for the three considered orientations of input ground motion directions. The displacement demands obtained in Case 2 and Case 3 are compared with Case 1 in the longitudinal and transverse direction, respectively. For these three cases shown in Table 7-20, most displacements in the longitudinal direction are smaller in Case 2 and Case 3 compared to Case 1, except for the target ductilities of 5 and 6 in Case 3. For Case 2, the transverse displacement demands are all larger than Case 1, with differences as large as 51%. For Case 3, the transverse displacement demands are all smaller than in Case 1.

The average values of the maximum displacement demands resulting from the 44 and 88 analyses run in the transverse and longitudinal directions are compared in Table 7-21. The differences in each direction indicate that the displacement increases for the 88 analyses run (after considering variations in the positive and negative directions) are within 14.5%.

273

Table 7-20 Displacement demands for simplified EDS-1 skew bridge model (45 degree) subjected to different orthogonal pairs of ground motions

Skew 45°			Ductility				
			2	3	4	5	6
Case 1 original global longitudinal and transverse direction	Longitudinal Displ. (in)		0.518	0.931	1.271	1.622	1.971
	Transverse Displ. (in)		0.844	1.018	1.724	2.235	2.728
Case 2 skew direction and its perpendicular direction	Longi.	Displ. (in)	0.505	0.853	1.161	1.530	1.872
		Difference	-2.51%	-8.38%	-8.65%	-5.67%	-5.02%
	Trans.	Displ. (in)	0.959	1.537	2.167	2.843	3.463
		Difference	13.63%	50.98%	25.70%	27.20%	26.94%
Case 3: principal vibration directions of system	Longi.	Displ. (in)	0.484	0.827	1.244	1.672	2.046
		Difference	-6.56%	-11.17%	-2.12%	3.08%	3.81%
	Trans.	Displ. (in)	0.448	0.705	0.970	1.287	1.623
		Difference	-46.92%	-30.75%	-43.74%	-42.42%	-40.51%

Table 7-21 Displacement demands for benchmark EDS-1 skew bridge model (45 degree) using 44 and 88 ground motions

Skew 45°				Ductility				
				2	3	4	5	6
Case 2: skew direction and its perpendicular direction	44 Ave. (in)	Longitudinal Displ. (in)		0.505	0.853	1.161	1.530	1.872
		Transverse Displ. (in)		0.959	1.537	2.167	2.843	3.463
	88 Ave. (in)	Longi.	Displ. (in)	0.524	0.837	1.175	1.506	1.818
			Difference	3.76%	-1.88%	1.21%	-1.57%	-2.88%
		Trans.	Displ. (in)	0.904	1.427	2.003	2.658	3.258
			Difference	-5.74%	-7.16%	-7.57%	-6.51%	-5.92%
Case 3: principal vibration directions of system	44 Ave. (in)	Longitudinal Displ. (in)		0.484	0.827	1.244	1.672	2.046
		Transverse Displ. (in)		0.448	0.705	0.970	1.287	1.623
	88 Ave. (in)	Longi.	Displ. (in)	0.481	0.787	1.147	1.579	1.953
			Difference	-0.62%	-4.84%	-7.80%	-5.56%	-4.55%
		Trans.	Displ. (in)	0.473	0.782	1.099	1.473	1.844
			Difference	5.58%	10.92%	13.30%	14.45%	13.62%

Similarly, the average values of the maximum displacements of the skew bridges for the skew angle of 60 degrees are compared in Table 7-22 for the three considered orientations of input ground motion directions. The displacement demands obtained in Case 2 and Case 3 are also compared with Case 1 in the longitudinal and transverse direction, respectively. For these three cases shown in Table 7-22, it is observed that displacements in the transverse direction are smaller for Case 2 and Case 3 compared to Case 1. For Case 2 and 3, the longitudinal displacement demands that are larger than the values in Case 1 for some ductilities.

The average values of the maximum displacement demands resulting from the 44 and 88 analyses run in the transverse and longitudinal directions are compared in Table 7-23. The differences in each direction indicate that the displacement increases for the 88 analyses run (after considering variations in the positive and negative directions) are within 11.5%.

Table 7-22 Displacements for simplified skew bridge model (60 degree) subjected to different orthogonal pairs of ground motions with different scale factors

Skew 60°			Ductility				
			2	3	4	5	6
Case 1 original global longitudinal and transverse direction	Longitudinal Displ. (in)		0.645	1.101	1.609	2.085	2.495
	Transverse Displ. (in)		1.461	2.427	3.493	4.455	5.410
Case 2 skew direction and its perpendicular direction	Longi.	Displ. (in)	0.505	0.853	1.161	1.530	1.872
		Difference	7.44%	2.09%	-2.73%	-4.65%	-1.72%
	Trans.	Displ. (in)	0.959	1.537	2.167	2.843	3.463
		Difference	-23.07%	-27.89%	-27.11%	-25.95%	-26.95%
Case 3: principal vibration directions of system	Longi.	Displ. (in)	0.484	0.827	1.244	1.672	2.046
		Difference	7.91%	3.27%	-1.99%	-1.92%	1.00%
	Trans.	Displ. (in)	0.448	0.705	0.970	1.287	1.623
		Difference	-71.59%	-73.09%	-72.00%	-71.02%	-70.54%

Table 7-23 Displacement demands for simplified skew bridge model (60 degree) using 44 and 88 ground motions

Skew 60°				Ductility				
				2	3	4	5	6
Case 2: skew direction and its perpendicular direction	44 Ave. (in)	Longitudinal Displ. (in)		0.693	1.124	1.565	1.988	2.452
		Transverse Displ. (in)		1.124	1.750	2.546	3.299	3.952
	88 Ave. (in)	Longi.	Displ. (in)	0.644	1.067	1.542	1.963	2.385
			Difference	-7.07%	-5.07%	-1.47%	-1.26%	-2.73%
		Trans.	Displ. (in)	1.100	1.801	2.637	3.381	4.017
			Difference	-2.14%	2.91%	3.57%	2.49%	1.64%
Case 3: principal vibration directions of system	44 Ave. (in)	Longitudinal Displ. (in)		0.696	1.137	1.577	2.045	2.520
		Transverse Displ. (in)		0.415	0.653	0.978	1.291	1.594
	88 Ave. (in)	Longi.	Displ. (in)	0.666	1.081	1.521	1.925	2.304
			Difference	-4.31%	-4.93%	-3.55%	-5.87%	-8.57%
		Trans.	Displ. (in)	0.45	0.727	1.087	1.428	1.775
			Difference	8.43%	11.33%	11.15%	10.61%	11.36%

Therefore, for the skew benchmark models with EDS-1, the input direction of the ground motions will cause a difference in the displacement demands, which is dependent on the ductility demand and skew angle. However, for all the analyses cases considered in this section, the difference is mostly less than 25%. To obtain more thorough observations on how the input directions of ground motions would affect the skew bridge's behavior with installed EDSs, additional analyses would be conducted, and that is out of the scope of the work contemplated here.

7.6   Thermal effect on low-cycle fatigue of BRBs

Thermal movements (elongation and shortening) of the bridge superstructure resulting from temperature changes would impose displacement demands on the longitudinal BRBs connecting the superstructure to the abutments across expansion joints. The concern was whether the longitudinal BRB can accommodate thermal expansion movements without the need for special detailing (i.e. in series with lock-up devices

that allow thermal expansion under normal conditions, but engage the BRBs during the earthquakes). This issue was investigated by calculating the low-cycle fatigue life of longitudinal BRBs due to thermal movements of the bridge superstructure resulting from temperature changes. That study also allowed determining the required minimum length of BRB located across an expansion joint to ensure that its low cycle fatigue life exceeds the 75 years' bridge design life specified by AASHTO (2011). Longitudinal BRBs shorter than this length would need to be designed in series with lock-up devices that allow thermal expansion. Alternatively, the BRB could be scheduled to be replaced before it reaches its expected fatigue life. The details of that study are presented in Appendix D. A summary of the methodology is presented in the rest of this section. Note that this study is focused on the low-cycle fatigue life of the BRB's core plate, the low/high temperature effect on changing the steel properties was not considered.

To consider the variability in temperature yearly fluctuations across North America, 9 cities in seismic regions were arbitrarily chosen to investigate a wide range of temperature variations within a year. They are Anchorage, Alaska; Boston, Massachussets; Charleston, South Carolina; Los Angeles, California; Memphis, Tennessee; Portland, Oregon; San Fransisco, California; Seattle, Washington, and; Quebec City, Canada. For each of those cities, daily temperature data were collected from Accuweather (2012). A simply supported bridge model was used here, with one end fixed and the other end connected with BRBs over the expansion joints. Recorded maximum and minimum temperatures within a day were transformed into strain histories for BRBs. Calculation of strain histories require specifying a reference temperature(T_r), defined as the temperature when the BRB was first installed. Analyses were conducted considering a number of reference temperatures, ranging between the maximum and minimum temperature at the specific bridge location, at intervals of 10°F. Note that the strains caused by the temperature-induced displacement history can be considered to concentrate over the length of the yielding core plate, as the rest of the BRB has much larger cross section area. Therefore, the ratios of BRB yielding core plate length over total bridge length (L_c/L) is what was actually considered in calculating BRB thermal strain and fatigue life, which were taken as 1% to 5% at intervals of 1% for each location.

The software program Fatiga Version 1.03 was chosen to calculate low-cycle fatigue life using the strain history and the fatigue properties of the BRB's core plate material (ASTM A36 steel material). The resulting strain histories were characterized as variable amplitude strain loading (because the amplitude of the strain ranges changed in each cycle instead of being of constant amplitude). Strain cycles were obtained using the Rainflow Counting method and the damage (i.e. the percentage of the total fatigue life) caused by cycles at each stress-range amplitude were accumulated using Miner's rule. The Smith-Watson and Topper (1970) method was used to calculate fatigue life, considering the tensile mean stress effect.

276

The damage done by all cycles in the temperature-induced strain history (i.e., for one year) can be obtained. Since the BRB fails when the cumulative damage reaches 1.0, therefore, the fatigue life is the reciprocal of the damage caused by the strain history for one year (i.e., a single application of the temperature-induced strain history). In other words, the fatigue life is the number of times that this strain history can be applied to the BRB before it fails.

In places where the yearly fluctuations of temperature were more severe (the most severe case being Memphis for all cities considered), the calculated fatigue life of the BRB was less compared to places where the yearly temperature variations were smaller. In general, a minimum length ratio BRB's yielding core plate of 3% proved to be sufficient to avoid low-cycle fatigue of the BRB due to 75 years of thermal changes on the bridge superstructure for all locations, for all the install temperatures and cities considered.

Note that, in this low-cycle fatigue study, the longitudinal BRB was considered to be installed horizontally aligned with the bridge's longitudinal axis. However, in both the EDS-1 and EDS-2 schemes, BRBs are installed at an angle with the bridge longitudinal axis, both vertically and horizontal. Considering this geometry effect would result in smaller minimum length demands for the BRBs to satisfy their low-cycle fatigue performance requirement. As a result, the recommended minimum yielding core plate length ratio of BRB of 3% is conservative and was kept for simplicity.

However, the above estimated fatigue life of BRBs obtained from Fatiga is solely based on the axial strain loading applied to its core steel (for ASTM A36 material). Note that the core plate of a BRB typically develops local buckling under the applied low-cycle strain loading (albeit of constrained amplitude). This local buckling produces additional flexural plastic deformations that add up to the pure axial strains. Therefore, a calibration factor was deemed necessary to account for the fact that the local buckling of BRBs may reduce the estimated low-cycle fatigue life results obtained based on metal properties.

Since little data is available for the low-cycle fatigue of BRBs under variable amplitude loading, prior to the tests conducted for this project (Section 8), a tentative calibration factor was contemplated based on the constant amplitude loading experiments by Usami et al. (2011), Wang et al. (2012), Akira et al. (2000) and Maeda et. al. (1998). The strain history applied to the BRBs up to failure in those tests was input to Fatiga to get the estimated fatigue life of each tested BRB. The damage calculated by Fatiga for each of these tests to failure is essentially equal to the calibration factor. Based on those results, the calibration factor was found to vary with the strain magnitude, ranging from 0.05 to 0.53. Note that this calibration

factor is also expected to depend on how the BRB is fabricated, as this would have an impact on the amplitude of the local buckling in the BRB core. Therefore, the minimum BRB's yielding core plate length ratio that is sufficient to avoid low-cycle fatigue of the BRB for 75 years of thermal changes on the bridge superstructure could be larger than 3%.

SECTION 8

""""BRB TEST PROTOCOLS AND EXPERIMENTAL'TGUWNVU

8.1   General

Quasi-static tests were performed on two types of BRBs using the shake table to apply displacement histories, to determine their ultimate inelastic cyclic performance when subjected to different scenarios of individual or sequential displacement protocols. In this Section, these experimental results are presented and the performance of each type of BRB is examined.

Section 8.2 describes the design of the test setup and presents information on the two types of BRB specimens, together with a description of their different behaviors expected during the tests.   A description of instrumentation of the BRB specimens is provided in Section 8.3. The initial test protocols are explained in Section 8.4, including the bidirectional and axial displacement histories. Section 8.5 presents the detailed test protocols for each BRB and adjustments made based on experimental results. The hysteretic behaviors of each BRB under different displacement histories are plotted. Section 8.6 summarizes and compares the inelastic cumulative displacements of each tested BRB.

8.2   Test Setup and Reaction Block Design
8.2.1   Test Set-up Plan

The test set-up consisted of connecting the BRB from the strong floor to a shake table in the SEESL, as shown in Fig. 8-1. One end of the BRB was connected to a reaction block, itself tied down to holes in the strong floor. The other end was connected to the shake table, which was then used to apply horizontal end-displacement demands to the BRB. The details of the reaction blocks will be explained later in this section.
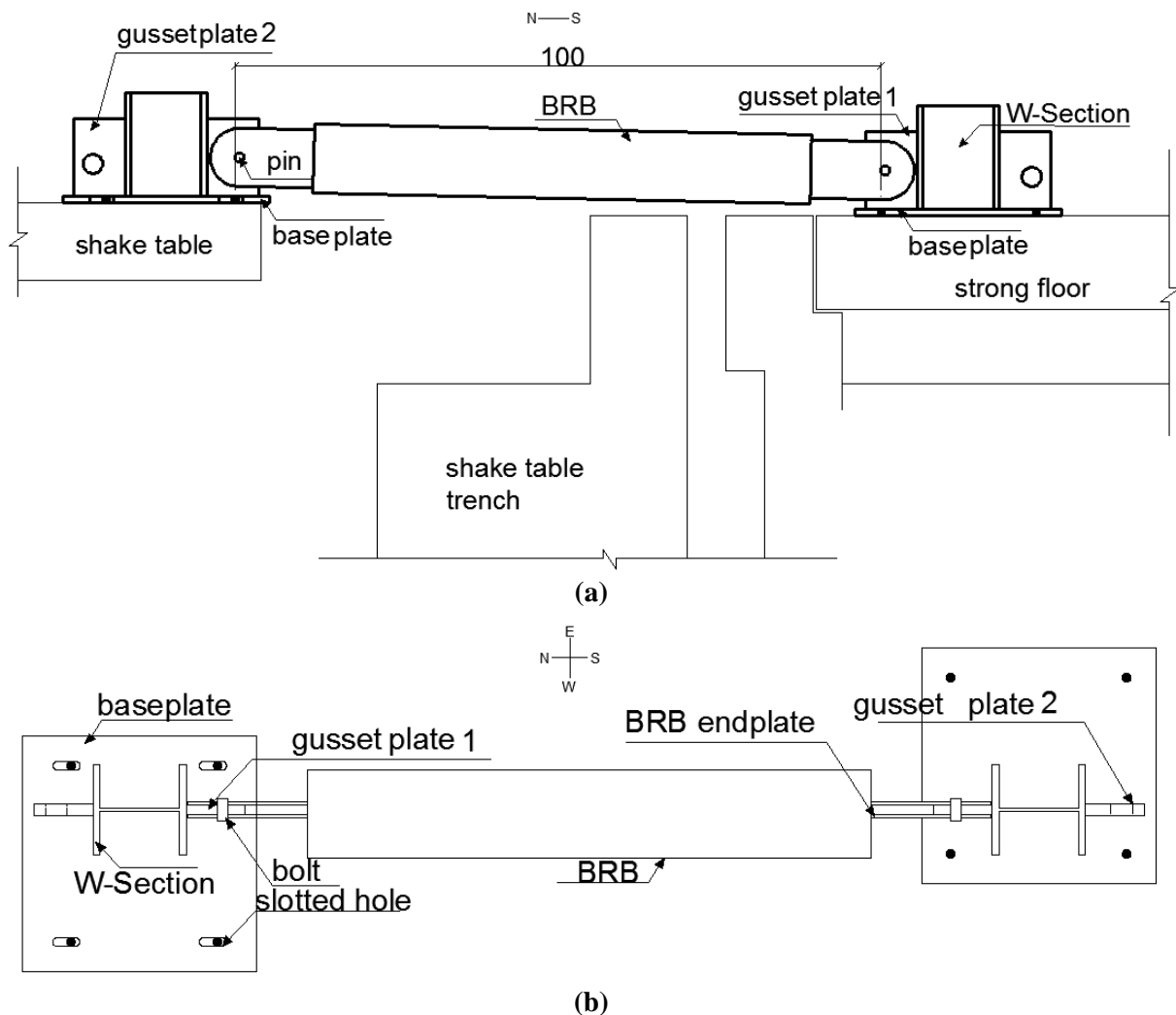
Figure 8-1 Test set-up layout with BRB; (a) side view (b) top view

The SEESL shake table has a horizontal force capacity of 120 kips, and an overstrength factor of 3 was considered in selecting the yield strength of the BRB. This factor was intended to account for a number of experimental contingencies, including the fact that the BRB steel core expected yield strength is greater than the specified minimum yield strength assumed in design, and allowing for the BRB to develop significant strain hardening (as accounted for by compressive and tensile strength adjustment factors $\omega\beta$ and β). Therefore, the design yield strength of the BRB to be tested was chosen to be 40 kips. A minimum BRB's length of 100" was required due to the distance between the location of the closest holes in the strong floor and shake table used to anchor the reactions blocks. The BRB length was also selected considering that the maximum displacements that can be applied by the shake table are ±7" in both horizontal directions, although this was not found to be a limiting factor.

Note that, due to the elevation difference of 2" between the shake table and the strong floor, the BRB was slightly inclined. This inclination is exaggerated in the figures of the test set-up, which are not drawn to scale. The slotted holes in the base plate of the reaction block on the shake table allowed adjustment of the location of the reaction block to make sure that the BRB was installed properly (and, most importantly, not preloaded when starting from the zero position). Also note that because the grid of holes in the strong floor and on the shake table did not line up, the location of the W-shape used in the reaction block was not centered on the base plate of the reaction blocks, as shown in Fig. 8-1. A photo taken from above the test setup in the SEESL is shown in Fig.8-2.
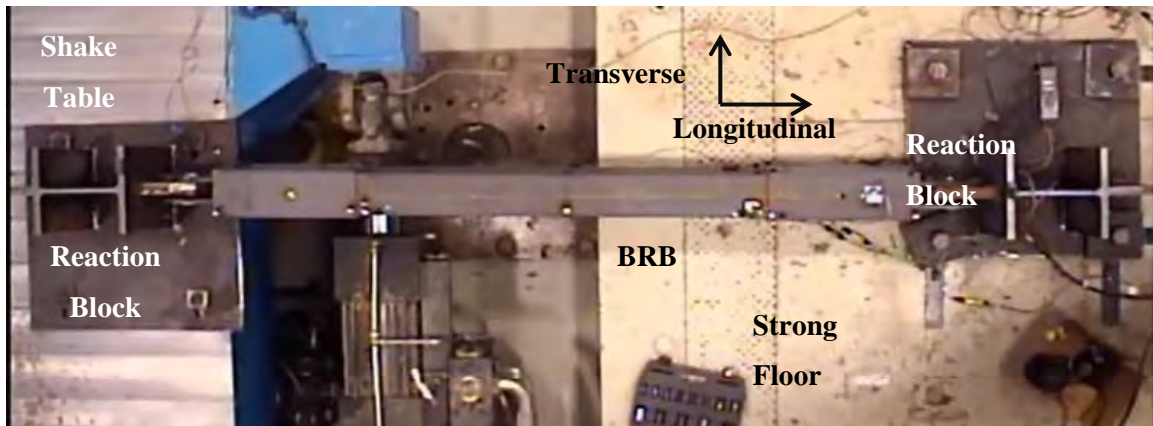
Figure 8-2 Quasi-static test setup with BRB-2

8.2.2   BRB Specimens

8.2.2.1 General

Two types of BRBs, namely BRB-1 and BRB-2, were designed and tested. They were manufactured and supplied by Star Seismic, LLC of Park City, Utah. Fig. 8-3 shows the side view of a typical BRB specimen and detailed drawings of BRB-1 and BRB-2 are provided in Appendix E.
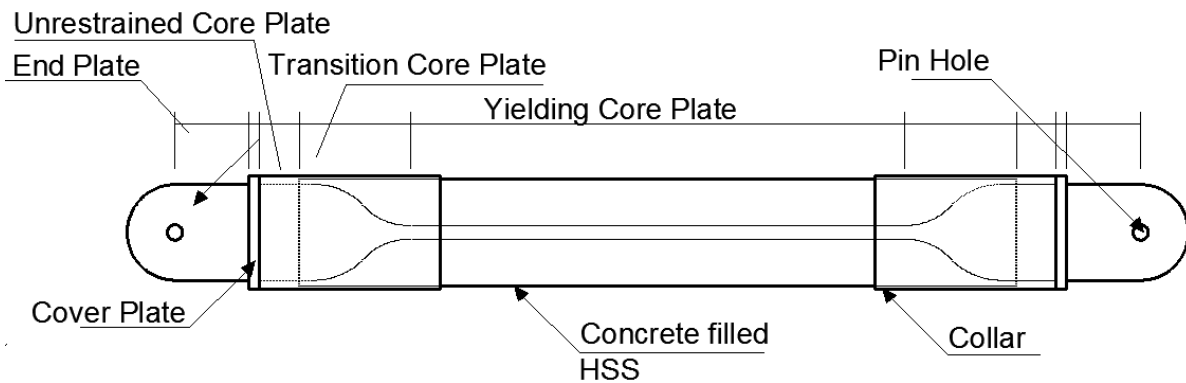
Figure 8-3 Side view of a typical BRB specimen

29;

Both BRBs have two flat end plates with holes at their end, designed such that the BRB could be pin-connected to gusset plates in the reaction blocks located on the strong floor or the shake table. The total pin-to-pin length of the BRB is 100 in, and their yield cores have a cross section area of 1.0 in². The material of the yielding steel core was specified as A36 with expected yield strength of 46 ksi. The BRB's core plate is encased in a concrete-filled steel hollow structural section (HSS). End Collars prevent instability of the core plate when it extends outside of the concrete restraining material.

The BRBs' end connections need to sustain the required displacement demands when installed in the ductile bridge diaphragm, especially the transverse displacement that could cause the flexural yielding of the end plates of the BRB beyond the target design displacement. The mechanisms for BRB-1 and BRB-2 to sustain the transverse displacements are shown in Fig.8-4 (not drawn to scale).

(a)

(b)
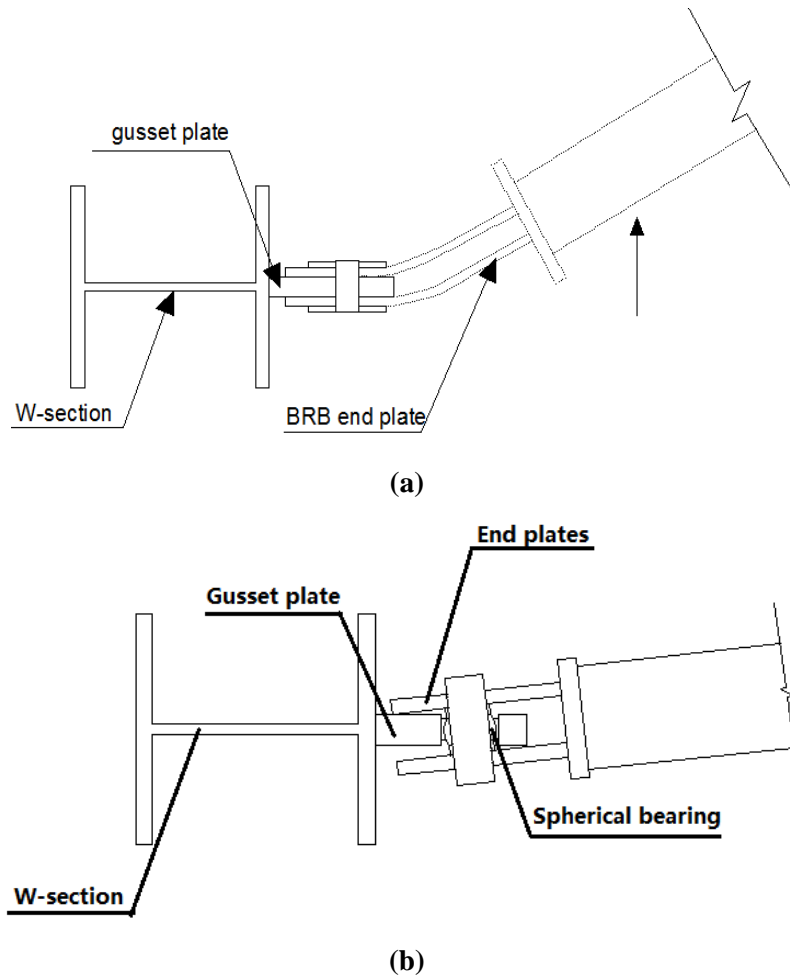
Figure 8-4 Schematic illustration of the mechanisms for the BRBs to accommodate the lateral displacement (base plate of the reaction block not shown)

282

The end plates of BRB-1 were designed to bend laterally to accommodate the required lateral displacement without developing instability. The BRB's end plates were sized such that the shake table's maximum displacement capacity could be used to test the BRB and examine the BRB's connection behavior beyond yielding and investigate its failure mode. Later in this Section 8.2.2.1, the details of how to design the end plates for BRB-1 are presented.

The end plates of BRB-2 were connected to a spherical bearing, itself kept in place in a pre-drilled hole in the gusset plates. Each spherical bearing works as a bi-directional hinge (similar to those that have been used by some dampers manufacturers). The maximum transverse displacement that BRB-2 can sustain depends on the design of the spherical bearing in the reaction block, for which details are provided in Section 8.2.3. It is recognized that special protection would be required when using spherical bearings in bridge applications, to prevent their corrosion.

Other differences between BRB-1 and BRB-2 are listed below:
- BRB-1 has a yielding core length of 46.5", while BRB-2's yielding core length is 50.2" (resulting in a yield length ratio of 0.46 and 0.5 for BRB-1 and BRB-2, respectively).
- The width of the unrestrained core plate part inside the BRB's collar is 5" and 9" for BRB-1 and BRB-2, respectively
- The distance between the pin hole and the point where the end plates are connected to the cover plate is 11.5" and 5" for BRB-1 and BRB-2, respectively.
- The clear distance between the two end plates of BRB-1 is 1.25", and the pin hole size is 1 17/32". In comparison, the clear distance between the two end plates of BRB-2 is 2.5", and a 2" pin hole is used in which the spherical bearing is fitted.

To be consistent, the expected yield strength of the BRB's core plate of 46 ksi was used to calculate the yield displacement of all BRBs. This yield strength is also equal to the experimentally obtained average value of yield strength based on observations of the first significant yielding of all tested BRBs presented later in this Section Incidentally, it is also close to the yield strength value obtained from coupon tests performed by the BRB manufacturer for a group of plates used to fabricate the BRBs, but individual coupon results could not be related to specific BRBs. The BRB's core plate's total length is composed of three parts as shown in Fig. 8-3, which are the yielding core length, L_{ys}, the transition core plate length, L_{ts}, and the unrestrained core plate length, L_{us}. The calculation of the BRB's yield displacement, Δ_{by}, was based on the total respective deformation of these three parts, Δ_{ys}, Δ_{ts}, Δ_{us}, as in equation 8-1. The corresponding calculated yield displacement Δ_{by} of BRB-1 and BRB-2 is 0.107" and 0.081", respectively.

$$\Delta_{by} = \Delta_{ys} + \Delta_{ts} + \Delta_{us} \qquad (8.1)$$

8.2.2.2 End Plate Design of BRB-1

For BRB-1, its transverse yield displacement, d_{yt}, is obtained when the end plate reaches its flexural yield strength at the bottom of the cantilevering end-plate under the BRB's maximum axial force. This transverse yield displacement should be larger than the target transverse displacement demand obtained from the bridge diaphragm analysis, making sure that BRB's end connection would not yield in flexure. Fig. 8-5 shows the end plate of a BRB with a pin connection. The end plate has a clear length, L_{end}, from the bottom of the pin hole to its base (Fig. 8-5). The width and thickness of the connecting end plate is b and t. The maximum force, P, considered applied through the pin connection is 90 kips, to account for strain hardening and material variability. The material for the end plates is assumed to be A36 with specified yield strength, f_{ye}, of 36 ksi.
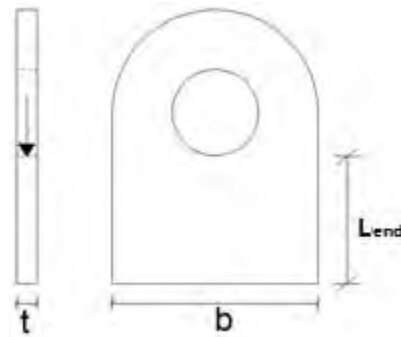
Figure 8-5 The dimension of the end plate of BRB-1

The BRB end plates were designed as beam-columns with K of 2 to remain elastic under the maximum axial force that the BRB can develop, by avoiding yielding in tension and buckling in compression. Eq. D2-1 and D2-2 specified in AISC 360-10(2010) were used to calculate the plates' tensile strength. The compressive strength (buckling considered) was calculated based on eq. E3-1, E3-2, E3-3 and E3-4 specified in AISC 360-10(2010). In preliminary design, possible width of the end plate for this particular application was considered over a range from 5" to 10". The above equations were used to determine the maximum possible length of end plate, L_e, for which buckling in compression would be prevented for a given end plate cross section of $b \times t$, where b and t are the width and thickness of the end plate, respectively. The maximum end plate length ratio is defined as $2L_e/L_{brb}$, where L_{brb} is the total pin-to-pin length of the BRB (accounting for both ends of the BRB). This maximum length ratio $2L_e/L_{brb}$ is plotted against the width of the connecting end plate for gusset plate thickness ranging from 1/8 to 1 in., at 1/8 in. intervals, in Fig. 8-6a.

The BRB's end plate was assumed to behave as a cantilever beam with cross section of $b \times t$ and length of L_e. For a lateral displacement applied to the BRB at its pin hole location, the cantilever beam would be under single curvature. The yield rotation of the end plate, θ_y, is obtained when the bottom of the end plate reaches its flexural yield strength. From the equation for a cantilever beam rotation at its free end under a lateral force, F_e, applied at its end, the relationship between θ_y and the curvature at the fixed end φ_{ye} can be obtained as follows:

$$\theta_y = \frac{F_e L_e^2}{2EI} = \frac{F_e L_e \times L_e}{2EI} = \frac{M_{ye} \times L_e}{EI \times 2} = \phi_{ye} \times \frac{L_e}{2} \tag{8.2}$$

where: M_{ye} is the flexural yield strength at the fixed end, and φ_{ye} is the yield curvature

Considering that the BRB is also subjected to an axial force P, equal to the BRB's core yield force when maximum demands are reached in both directions, the flexural yield strength is reduced accordingly, and the yield curvature ϕ_{ye} when the expected yield stress, f_{ye}, is reached, is given by the following equation:

$$\phi_{ye} = \frac{\varepsilon_{ybending}}{\frac{t}{2}} = \frac{\sigma_{ybending}}{E \times \frac{t}{2}} = \frac{f_{ye} - \frac{P}{2bt}}{E \times \frac{t}{2}} \tag{8.3}$$

The rotation θ_y vs the maximum length ratio $2L_e/L_{brb}$ plot is shown in Fig. 8-6b. In Fig. 8-6a and Fig. 8-6b, it is shown for the same BRB's end plate thickness that the wider the end plate, the larger the end plate's yield rotation, and the larger the maximum length of the end plate. As the thickness of the end plate increases, the maximum possible length of the end plate also increases.

(a)   (b)
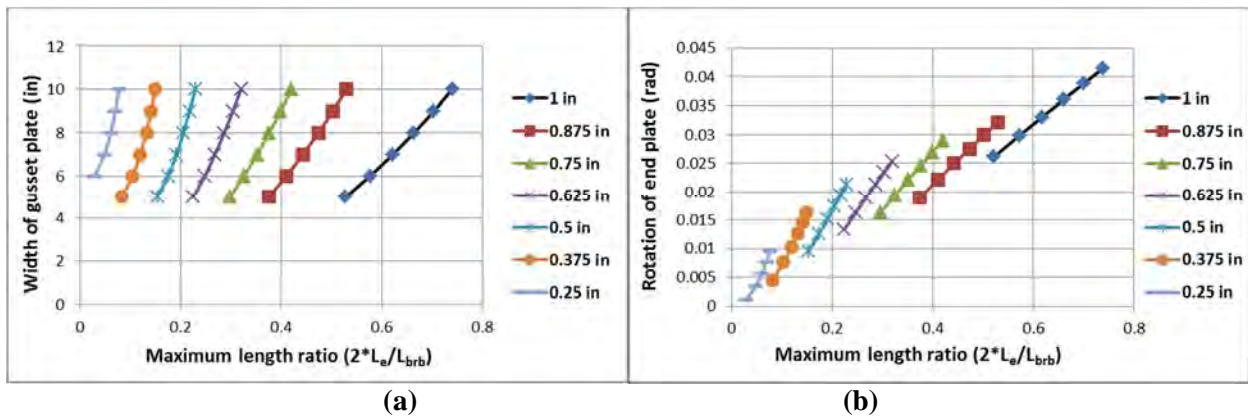
Figure 8-6 Occurrence of yield for gusset plates having different thicknesses, expressed in terms of: (a) End plate width vs maximum length ratio; (b) End plate's yield rotation vs maximum length ratio

The transverse yield displacement of the BRB d_{yt} is calculated as the product of the end plate's end rotation θ_y and the total pin-to-pin length of the BRB L_{brb} as shown in Fig.8-7. Given that the largest

expected transverse displacement demand (obtained from nonlinear time history analyses, as explained later in Section 8.4.1) on the BRB's end plate was 1.602", Fig. 8-8 shows the ratio of that value over the end plate's flexural yield displacement against the previously determined maximum length ratio $2L_e/L_{brb}$ controlled by buckling of the end plates (Fig. 8-6). The largest transverse displacement demand over the end plate's flexural yield displacement ratio should be smaller than 1.0 to keep the BRB's end connection elastic in flexure. It is shown that not all thicknesses considered over the range from 0.25" to 1" meet this requirement. For some end plates' thickness, unrealistic end plate length ratio would be needed to achieve this objective. As expected, thinner plates deflect more prior to yield and are more desirable in that perspective. However, this must be also balance by the fact that thinner plates are more prone to buckling.
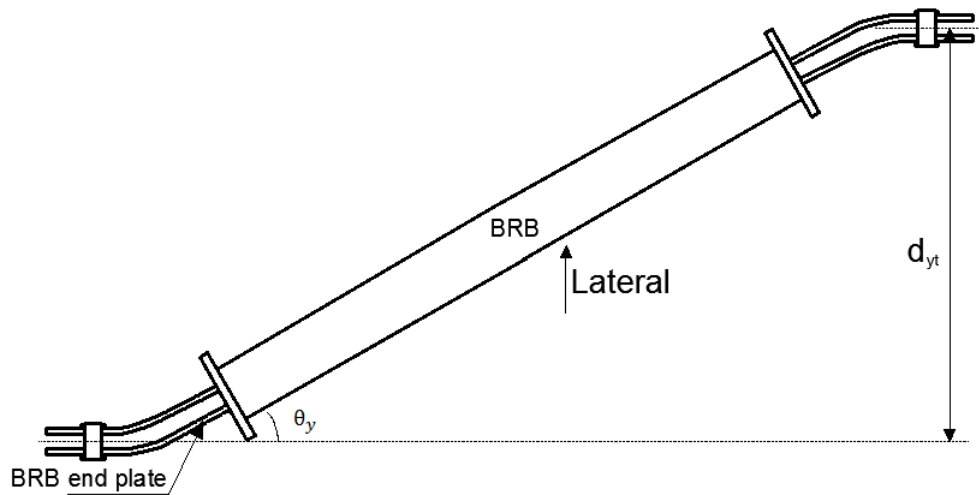
Figure 8-7. Illustration of the relationship between BRB's transverse yield displacement vs the end plate yield rotation
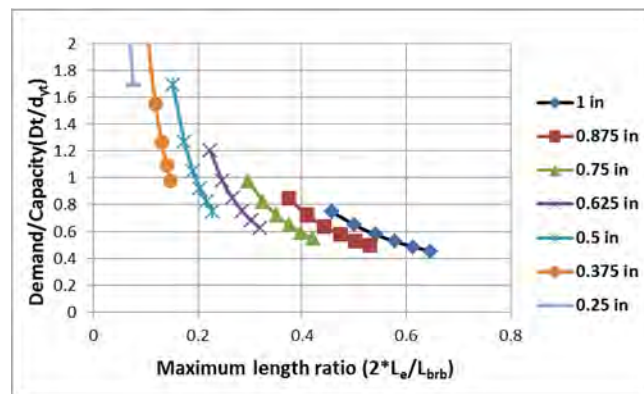
Figure 8-8. The transverse displacement demand over the end plate's flexural yield displacement ratio vs maximum length ratio at different gusset plate thickness

286

The following gives an example of satisfactory end plate design for BRB-1 based on the information provided above. In this example, the bolt hole size is 1-17/32", the end plate thickness, t, is 0.5", and the width of the end plates, b, is 9". The maximum axial force that BRB-1 would be expected to develop is 90 kips. From Fig. 8-6a, the maximum total end plate length ratio of the BRB $2L_e/L_{brb}$ is 0.217. For BRB-1 with a pin-to-pin length of 100", the corresponding maximum end plate's clear length L_e would be 10.85". For comparison, note that the BRB-1 specimens provided by Star Seismic had an end plate clear length of 10.75". For those specimens, the ratio of the largest transverse displacement of 1.602" over the end plate's flexural yield displacement is 0.83, confirming that the end plates would remain elastic at the maximum target displacement demands (predicted from the nonlinear time history analyses of the bridge diaphragm),

The shake table's displacement capacity was also compared with the BRB's transverse yield displacement to examine the possible ductility that could be developed when testing the connection beyond yielding of the end-plates. Note that one possibility during the tests was to examine the ductile performance and possible failure modes of the end plates (if no other failure mode occurred first). For the transverse displacement limit of the shake table of 7", the ratio of table displacement limit over BRB-1's end plate's flexural yield displacement is 3.62. This indicates that, beyond their elastic behavior within the expected range of response, the BRB end plates could be pushed to moderate ductility demands at the shake table maximum displacement.

8.2.3   Reaction block design

For the BRB with pin connections in the test layout shown in Fig. 8-1, reaction blocks were designed to tie the BRB to those reactions points. Each reaction block was made of a W-shape steel section, welded to a base plate, and gusset plates were welded to the W-shape and base plate. The reaction block located on the strong floor is shown in Fig.8-9. Note that because two different types of BRB were to be tested, two different types of gusset plates were needed to connect the BRBs to the reaction block. Instead of building two different reaction blocks, it was decided to build each reaction block with the gusset plates needed to connect the two different types of BRBs installed on opposite sides of the W-section. The reaction blocks only needed to be flipped 180 degrees when changing the type of BRB tested. The reaction block gusset plates were designed to remain elastically when resisting the maximum tensile and compressive forces expected to be developed by the BRB, without yielding or buckling. Both gusset plates were made of A572Gr.50 steel. The detailed design calculations of the reaction block are shown in Appendix E.
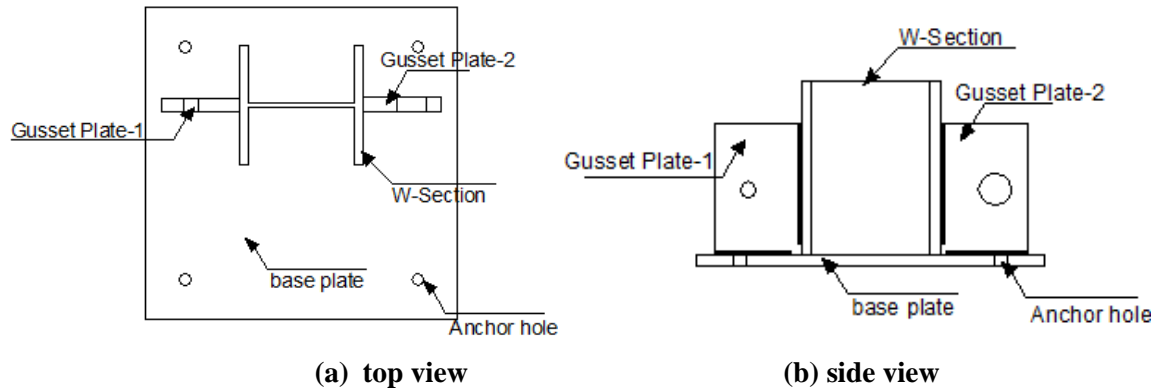
(a) top view   (b) side view

Figure 8-9: Reaction block on the strong floor

The gusset plate-1 (labeled "Gusset Plate-1 in Fig.8-9)" had a thickness of 1.25". To allow using a 1.5" diameter bolt to connect the BRB to the gusset plate, both the gusset plate and the BRB-1 end plates had 1-17/32" holes. The connection details of BRB-1 with gusset plate-1 in the reaction block using the bolt are shown in Fig.8-10, together with a side view photo in the test setup.
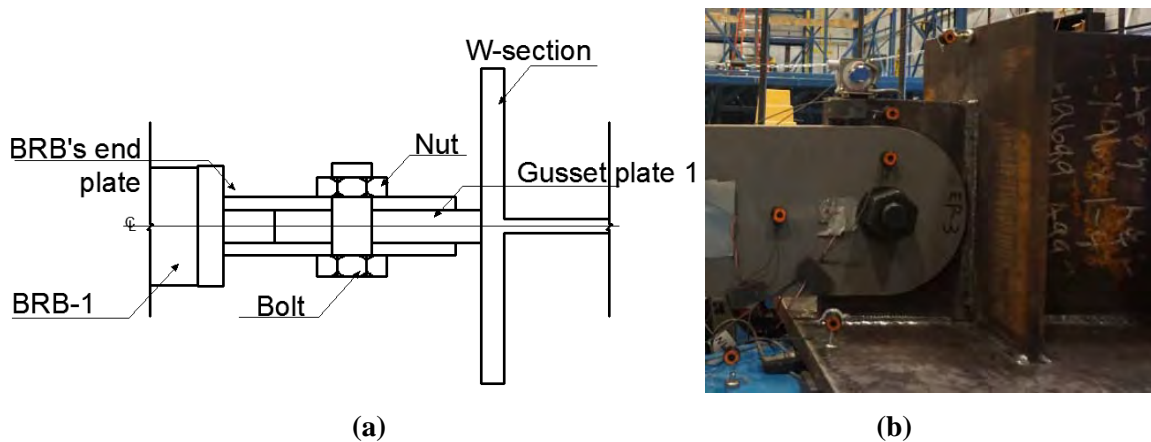
(a)   (b)

Figure 8-10: (a) Section cut view of the details of BRB-1 with gusset plate-1 in the reaction block using the bolt connections;(b) Side-view photo of BRB-1 with reaction block connection in test setup

In order to connect BRB-2 to the reaction block, a spherical bearing allowing multi-directional movement was inserted to fit in the hole in the other gusset plate (labeled "Gusset Plate-2" in Fig.8-9). The principal dimensions of the spherical bearing are shown in Fig. 8-11, based on the data provided by SKF Group for this type of spherical bearing, designated as SCF-50ES in the SKF design manual (2011). The basic static load rating is the maximum permissible load that a spherical bearing can take when there is no relative movement between the sliding contact surfaces at room temperature. The value of the static radial load

rating provided by SKF for this bearing is 93.3 kips, which is larger than the maximum axial force that was expected to develop in the BRB specimens. Note that, the basic rating life of the spherical bearing was not considered here since the contact surface, sliding velocity, temperature, and lubrication in the real bridge application was unknown.

1 Outer ring
2 Sliding contact surfaces
3 Seal
4 Inner ring
5 Lubrication hole
6 Lubrication groove

(a)   **(b)**
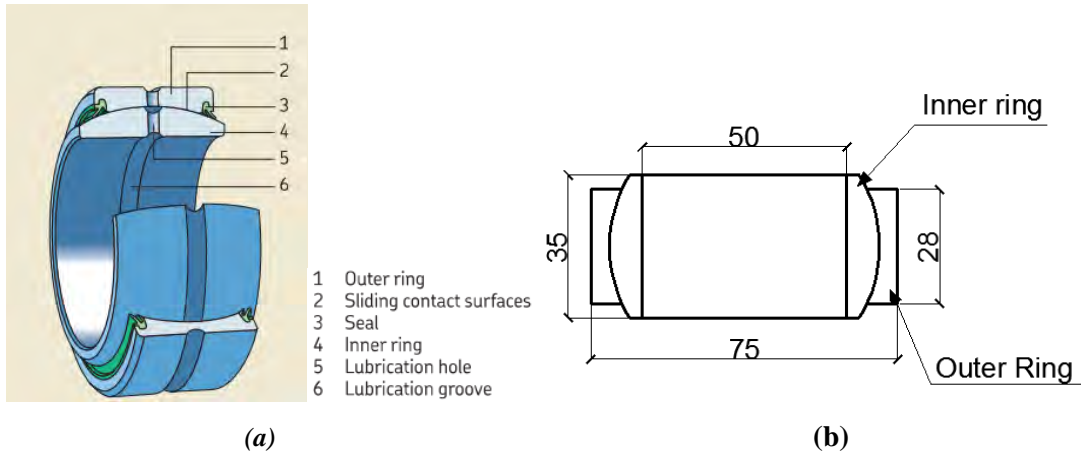
Figure 8-11: (a) SKF spherical bearing SCF-50ES (2011); (b)Section view of the spherical bearing with dimensions(units: mm)

A mounting pin with diameter of 1-31/32" (running through both the inner ring of the spherical bearing and the holes of the BRB plates) was used to connect the BRB the Gusset Plate-2 to the reaction block. The Gusset Plate-2 has a thickness of 1.625"; other dimensions are shown in Fig. 8-12a. The steel material used was A572Gr50. The diameter of the hole in the gusset plate was 3", to allow insertion of the spherical bearing into it; the 3" diameter of the bearing outer ring is shown in Fig.8-11b. Note that the gusset plate-2 itself had more than adequate strength to resist the axial tensile and compressive force of 90 kips from the BRB-2. The BRB-2's end plates' dimensions are shown in Fig. 8-12b. The pin hole in the BRB-2 was 2", which was the same as the inner ring diameter of the spherical bearing. The thickness of each end plate of BRB-2, t_e, was 0.5". The clear distance between the end plates of BRB-2, d_{cg} , was 2.5".

To keep the spherical bearing in place in the hole of gusset plate-2, two keeper rings were tack welded to the gusset plate on both side of the spherical bearing as shown in Fig. 8-13. Each keeper ring had a thickness of 3mm, with an inner diameter of 63mm and an outer diameter of 75mm.
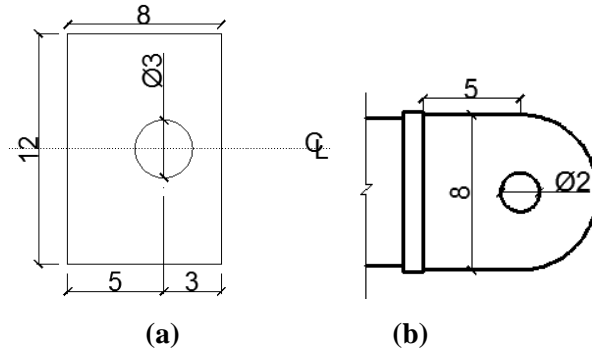
Figure 8-12 (a) Gusset plate dimensions; (b) BRB-2's end plate dimensions
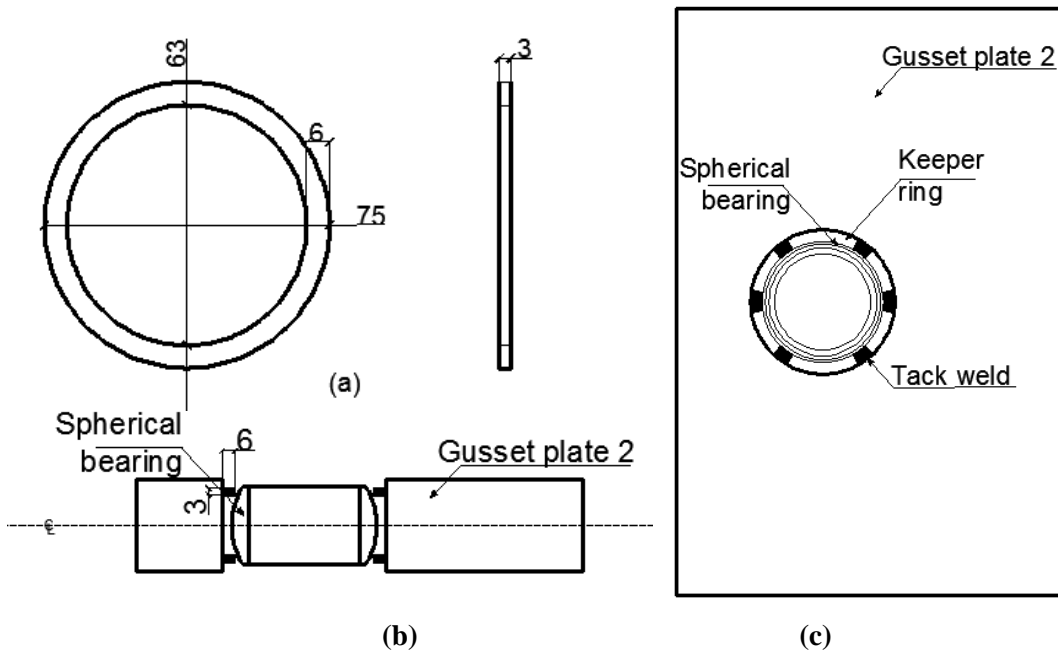
Figure 8-13: (a) Keeper ring dimensions (units: mm); (b) Front view of gusset plate-2 with spherical bearing and keeper ring; (c) Section view of gusset plate-2 with spherical bearing and keeper ring (units: mm)

Stainless steel shims, provided by the BRB manufacturers, were used on both sides of the spherical bearing to ensure that the gusset plate was centered in the clear space between the BRB's end plates as shown in Fig. 8-14a. A 1-15/16" diameter pin was specially made to go through holes in the BRB-2s' end plates and the inner ring of the spherical bearing as shown in Fig. 8-14b. Two threaded holes were drilled at both ends of the pin, and a bolt and washer was used at each end to secure the pin within the BRB's end plates and prevent it from sliding out during cyclic loading. A photo of the final connection's side view is shown in Fig.8-15.

28:

(a)   (b)
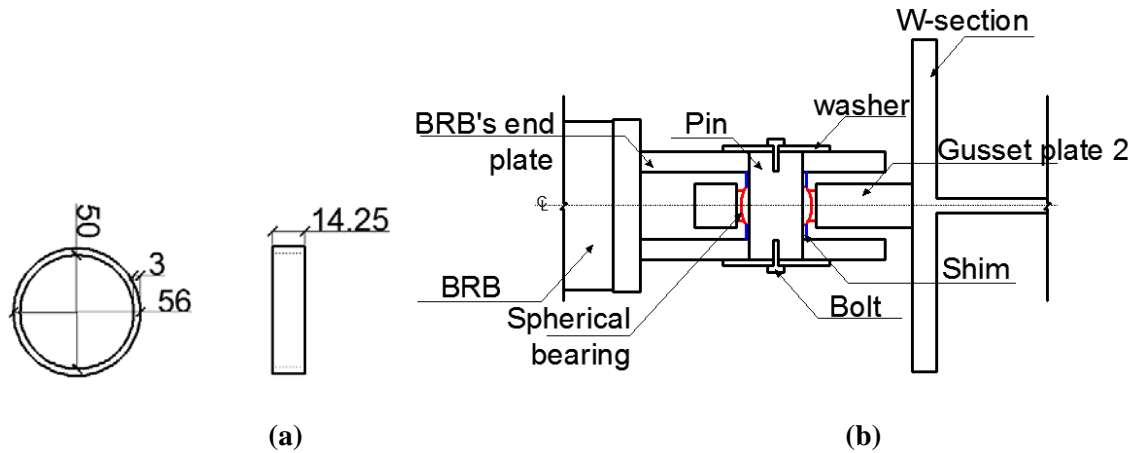
Figure 8-14: (a) Dimensions of shims that were used to keep the BRB connection centered (unit:mm); (b) Connection details of BRB-2 with gusset plate-2 in the reaction block

Figure 8-15: Side view of BRB-2 connecting to the gusset plate-2 with pin, washer, and bolts

The rotation capacity of the spherical bearing, α_s, is 0.102 rad, calculated the following equation that is provided in the SKF design manual (2011) .

$$\gamma = sin^{-1}\frac{W}{E_b} - sin^{-1}\frac{H}{E_b}$$

(8.4)

where: E_b is the diameter of the outer race; W is the ball width, and; H is the housing width as shown in Fig.8-15.

Furthermore, governing over the above limit in the current case, the maximum rotation that can be developed by the spherical bearing assembly is limited by the distance created between the BRB's end plates and the gusset plate by the bearing assembly geometry. In other words, the maximum rotation that can be developed is reached when the BRB's end plate becomes in contact with the gusset plate while the spherical bearing rotates; this rotation is labelled α_c here. This value need not be greater than the rotation capacity of the spherical bearing itself. Based on the geometric relationship in Fig.8-17 for the rotated

2: ;

BRB with gusset plate assembly, the maximum rotation capacity of this spherical bearing, α_c in Fig. 8-17a, is given in Eq. 8-5 as the difference between α_s and β_s., which are geometrically defined as shown in Fig. 8-17b and 8-17c:

$$\alpha_c = \alpha_s - \beta_s = \text{atan}\frac{d_{cg}}{w_e} - \text{asin}\frac{t_g}{2\sqrt{(\frac{d_{cg}}{2})^2 + (\frac{w_e}{2})^2}}$$

(8.5)

where: d_{cg} is the clear distance between the gusset plates; w_e is the width of the end plate; t_g is the thickness of the gusset plate-2.

(a) **(b)**
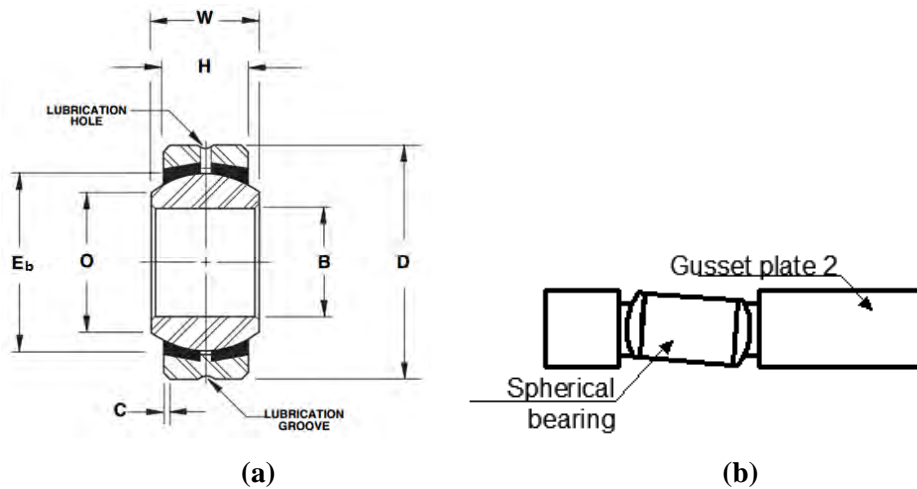
Figure 8-16: (a) Spherical bearing's principle dimensions (2011); (b) illustration of maximum rotation of the spherical bearing in gusset plate-2

The maximum rotation capacity α_c was 0.108 rad, which was larger than the spherical bearing's rotation limit α_s of 0.102 rad. Therefore, the bearing's rotation limit would be reached before the BRB's end plate touched the gusset plate-2. Note that, for the current pin-to-pin length of the BRB of 100", considering the displacement limits of the shake table of ±7" in both horizontal directions, the maximum possible rotational demand of the BRB in the transverse direction during the tests was limited to 0.07 rad. Therefore, based on the above calculations, for the planned series of tests using the shake table to apply BRB's transverse displacements, neither of the above rotation limits would be reached (i.e., the spherical bearing wouldn't reach their rotation limit and the gusset and end-plate would not come in contact).

Also note that the spherical bearing design here only investigated strength and geometry requirements. Longevity issues related to materials between the sliding surface and the protection needed for the BRB to perform well in an exposed environment across bridges expansion joints still remain to be addressed.
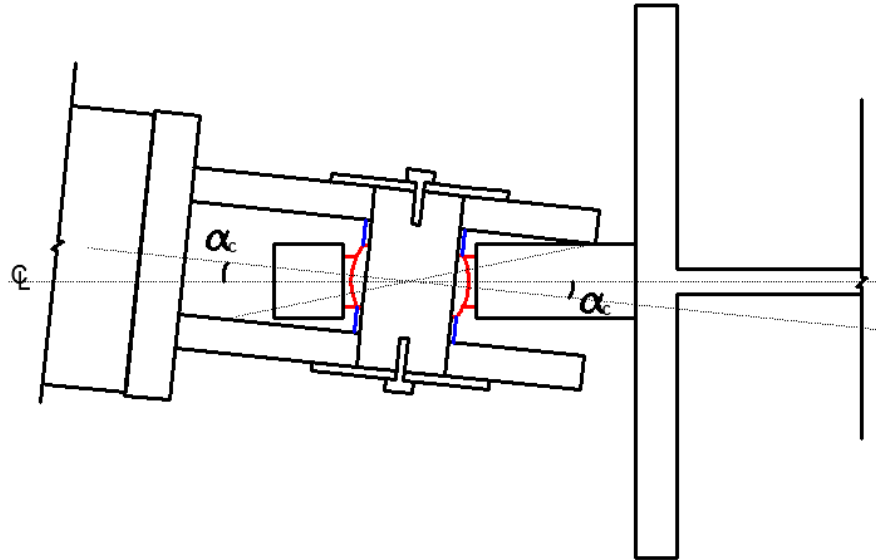
(a)
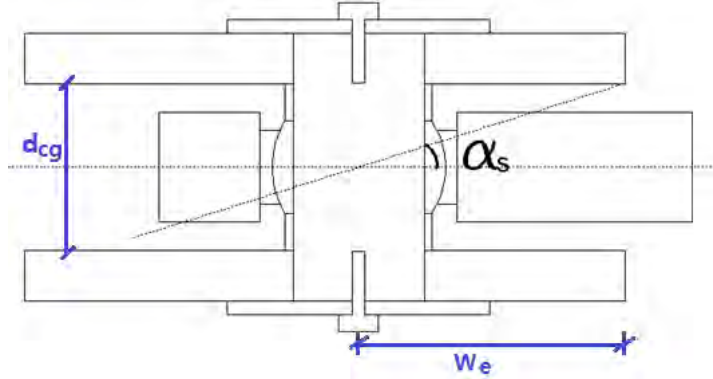
(b)
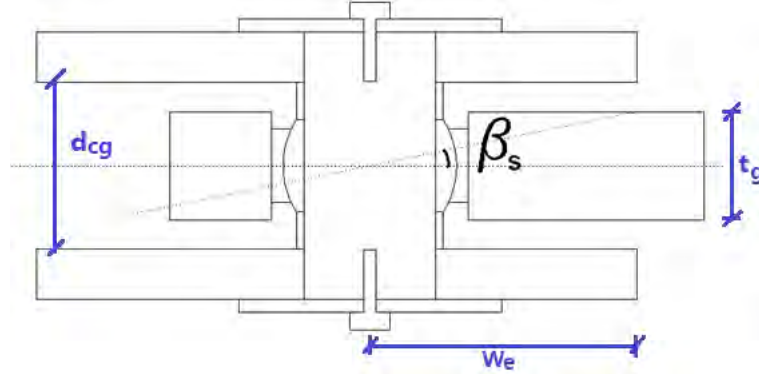
(c)

Figure 8-17: Illustration of the spherical bearing with maximum rotation when the end plate and gusset plates are in contact with angles marked for (a) α_c (b) α_s (c) β_s

8.3   Instrumentations

8.3.1   String Displacement Potentiometers

Two string displacement potentiometers (SPs) were placed at the top and bottom of every BRB. Each end of the string pots was at middle of the two end collars of the BRB as shown in Fig.8-17. These were intended to measure the axial deformation of the BRB. The difference between the two string pots would indicate the possible rotations (about the horizontal axis) of the collar against the concrete-filled HSS.
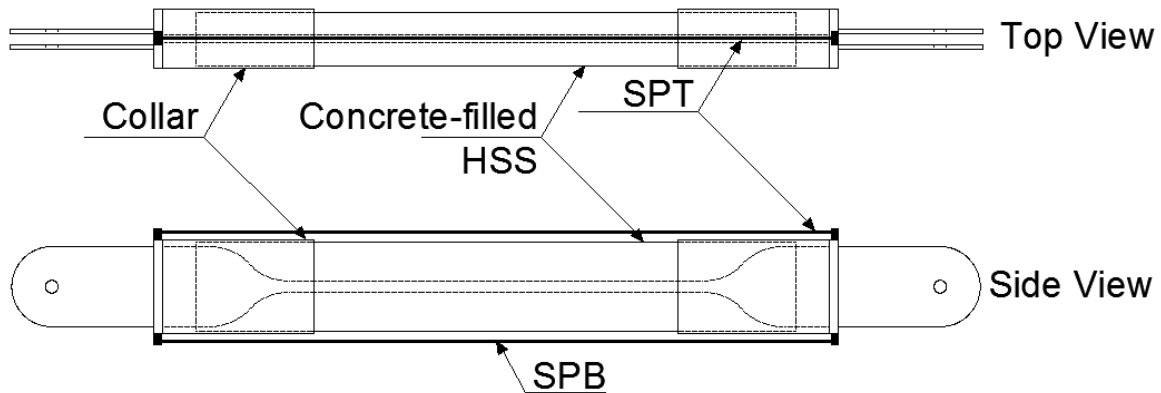
Figure 8-18: Illustrations of locations of SPs in BRB-1 specimen setup

8.3.2   Linear Displacement Potentiometers

A linear potentiometers (LP) was also installed at each BRB end to measure the displacement between the collar and the HSS sleeve of the BRB. They were positioned at the top middle of the BRB as shown in Fig.8-19. The sum of the measured deformations from the two LPs is related to elongation of the BRB yielding core, assuming no rotation of the collars. The readings from those LPs, with accuracy on the order of 0.01", were expected to be more accurate than the SPs.
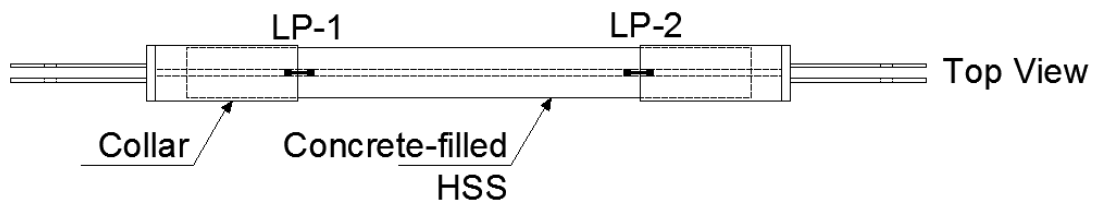
Figure 8-19: Illustrations of locations of LPs in BRB-1 specimen setup

Furthermore, after sliding of the reaction blocks was noticed during the first BRB test (as described in Section 8.5.1), additional LPs were placed at the corners of the base plates of the reaction blocks to

monitor the magnitude of this slippage on the strong floor and shake table (even though measures were taken to prevent such slippage in subsequent tests). These LPs were numbered as shown in Fig. 8-20, with "F" and "T", referring to the base plate on the strong floor and shake-table, respectively. The "NE", "NW", "WN", "WS", "SW" and "SE" labels following the hyphen indicate the location of the LP: the first letter refers to the face of the base plate where the LP was attached, and the second letter refers to the location where the LP was situated on that side. "N", "S", "W", and "E" stand for the cardinal directions North, South, West, and East, respectively. Table 8-1 summarizes all the potentiometers included in the BRB test setup.

(a)   (b)
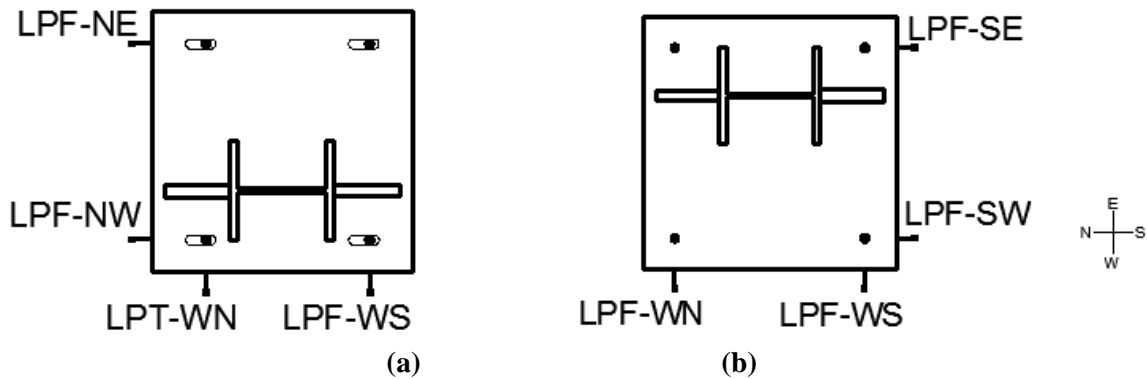
Figure 8-20: Illustrations of locations of LPs around the base plate of reaction block on (a) shake table; (b) strong floor

Table 8-1: Displacement Potentiometers and its corresponding locations

Name	Location of Linear Potentiometer
SPT	Top of BRB
SPB	Bottom of BRB
LP-1	BRB's end close to strong floor
LP-2	BRB's end close to shake table
LPF-SW	At the southwest corner of the base plate in the strong floor's reaction block
LPF-SE	At the southeast corner of the base plate in the strong floor's reaction block
LPF-WS	At the westsouth corner of the base plate in the strong floor's reaction block
LPF-WN	At the westnorth corner of the base plate in the strong floor's reaction block
LPT-NE	At the northeast corner of the base plate in the strong floor's reaction block
LPT-NW	At the northwest corner of the base plate in the strong floor's reaction block
LPT-WN	At the westnorth corner of the base plate in the strong floor's reaction block
LPT-WS	At the westsouth corner of the base plate in the strong floor's reaction block

8.3.3   Krypton Dynamic Measurement Machine

To capture the displacements of different parts in the BRB, the Krypton dynamic measurement machine mentioned in Section.6.3.2.4 was used. The window of the Krypton camera in this test set-up was able to accommodate the entire BRB specimen and part of the reaction blocks on each end. Krypton camera was placed on the east side of the BRB specimen. It was used to capture the complete kinematics of the various parts of the BRB by recording the 3D movement of 32 LEDs attached to the BRBs and the reaction blocks. The layout of the LEDs used is shown in Fig. 8-21, with their numbering also marked out. The LEDs were all facing the negative-y direction (with respect to the Krypton coordinate system).
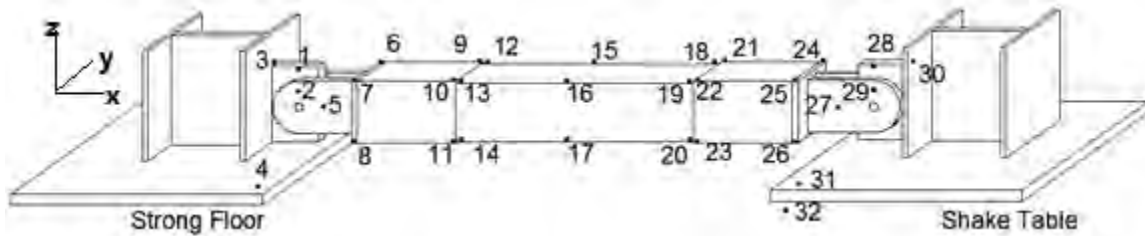
Figure 8-21: Illustrations of LED locations in the test setup

LED 4 and 31 on the base plates were used to measure the movement of the reactions blocks on the strong floor and shake table, respectively (since the shake table was also moving, LED 32, located on the shake table, was used as the reference for LED 31). The deformations of the reaction block's W-shape and gusset plates were captured by LED 3 and 30. Comparisons of the displacement of LED 1 and 2, 28 and 29 in the x-direction were used to monitor opening and closing of the gap in the bolt holes. The "BRB's axial deformation" is defined here, and calculated, based on the displacements between LED 2 and 29. In comparison, the "BRB's applied axial displacement" is defined here, and calculated, based on displacements between LED 1 and 28, which correspond to the sum of the "BRB's axial deformation" and the slippage of the pins (or bolts used as pins). Note that the terms BRB's axial deformation and BRB's applied axial displacement used throughout the text from here on refer to the above measures, which exclude and include slippage in the pins/bolts at the BRB ends, respectively.

Information from the displacements of LEDs 6, 7, 8, 9, 10, 11 in the x-y plane made it possible to monitor the rotation of the collar. Displacements of LEDs 21, 22, 23, 24, 25, 26 in the x-y plane were used to determine the collar's rotation at the other end of the BRB. The rotation of the BRB sleeve (i.e., the concrete-filled HSS) was calculated based on the displacements of LEDs 12, 13, 14, 15, 16, 17, 18, 19, 20 in the x-y plane. The displacements measured in the x-y plane corresponding to the BRB's axial deformation were also used as a redundancy, in case the potentiometers failed to perform. Since gaps

296

existed between the collars and the concrete-filled HSS, opening and closing of those gaps was measured by the LEDs closer to these gaps during the bidirectional test. Fig.8-22a shows a top view of the BRB with arrows indicating the points-of-view from which the photos shown in Fig. 8-22b and 8-22c were taken; these photos provide north-east and north-west side views of the north collar. In both photos, the gaps can be observed.

(a)

(b)   (c)
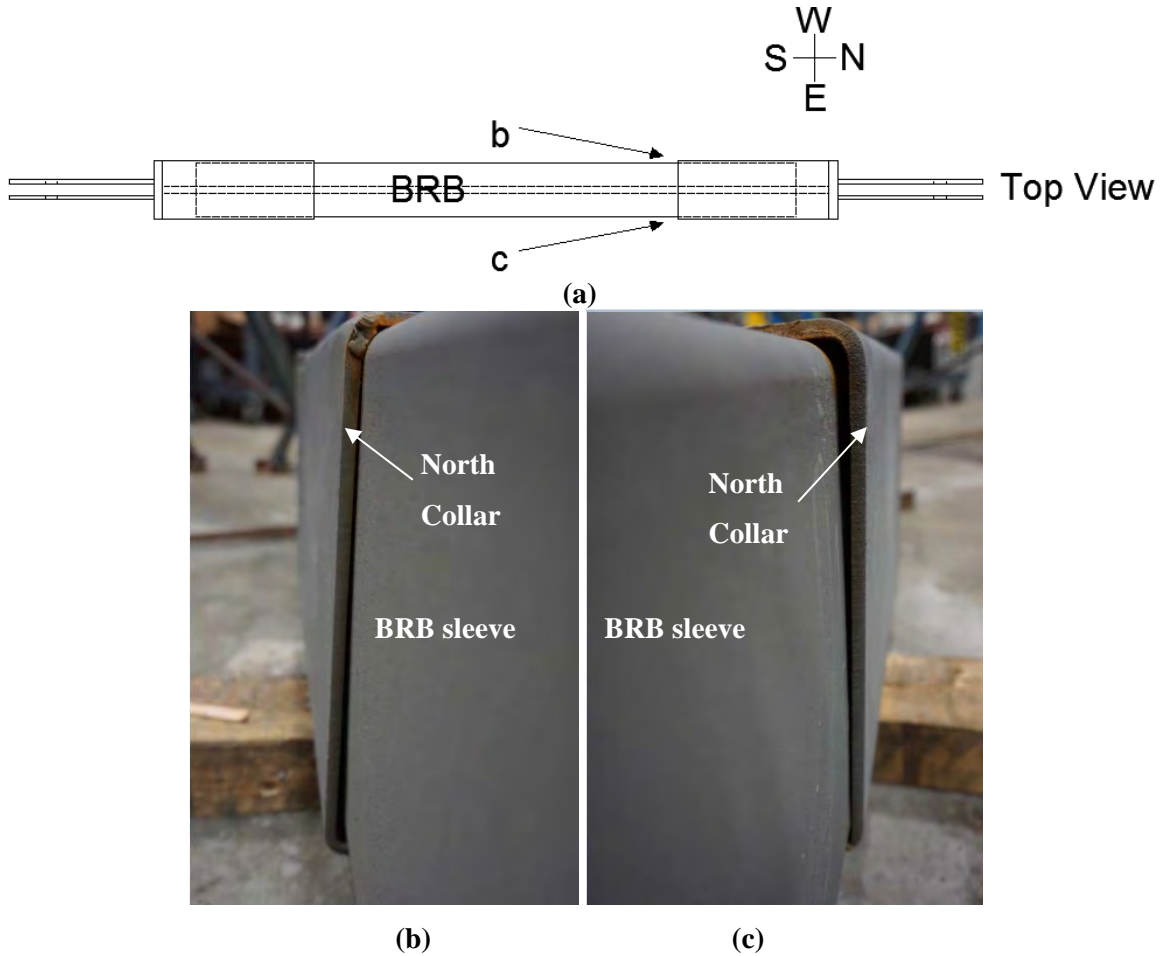
Figure 8-22: Gap between the collar and HSS casing of BRB-1-4: (a) top view of the whole BRB with the direction of taken photos (b) north-west side; (c) north-east side

In summary, the BRB's axial deformation was measured in three different ways: using SP, LP, and LEDs (Krypton system) as shown in Fig.8-23. Data from the SPs and LPs can provide real-time display of the BRB's deformations during the tests; the movement of the LEDs captured by the Krypton camera provided more accurate measurement of displacements at various locations along the BRB, but this data required post-processing after completion of the test and could not be used in real-time during the test. The combined data captured by the above instrumentation provided information on elongation of the

yielding core, relative rotation between the collar and HSS, rotation and lateral displacement of the BRB end plates, and slippage of the BRB pins in their holes.

Finally, data output from the shake table include the forces from the actuators driving the shake table, which can be summed to obtain the forced applied in the table's longitudinal and transverse directions (where the longitudinal direction is defined by the axis of the BRB in its original position); and the displacement of the shake table in those same longitudinal and transverse directions. The key parameter monitored in real-time during the test was the longitudinal force and displacement of the shake table; the other data had to be post-processed.
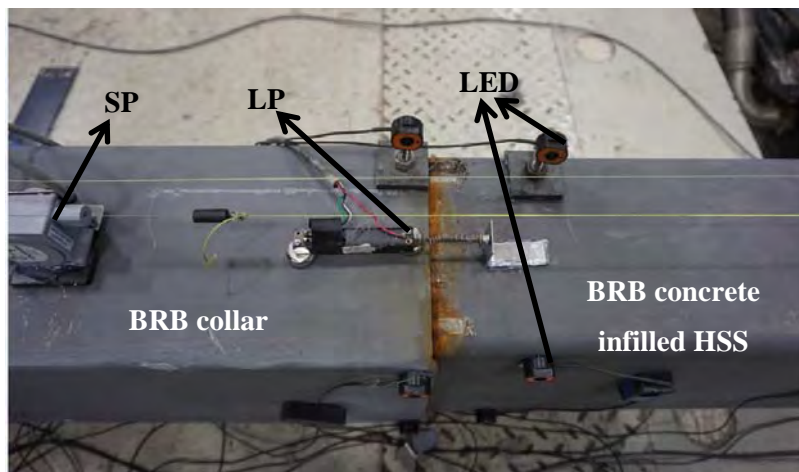
Figure 8-23:Instrumentations to measure the deformation of the BRB at one end

8.3.4 Strain Gauges

Some of the BRB-1 specimens, when subjected to transverse displacement demand, were also instrumented by stain gauges located on the end plates and the collar in an attempt to record their yielding. CAE-06-125-UW-120 strain gauges manufactured by Vishay Measurement Group Inc were used for this purpose. The strain gauges that were installed on BRB-1-3 are circled in red as shown in Fig.8-24.
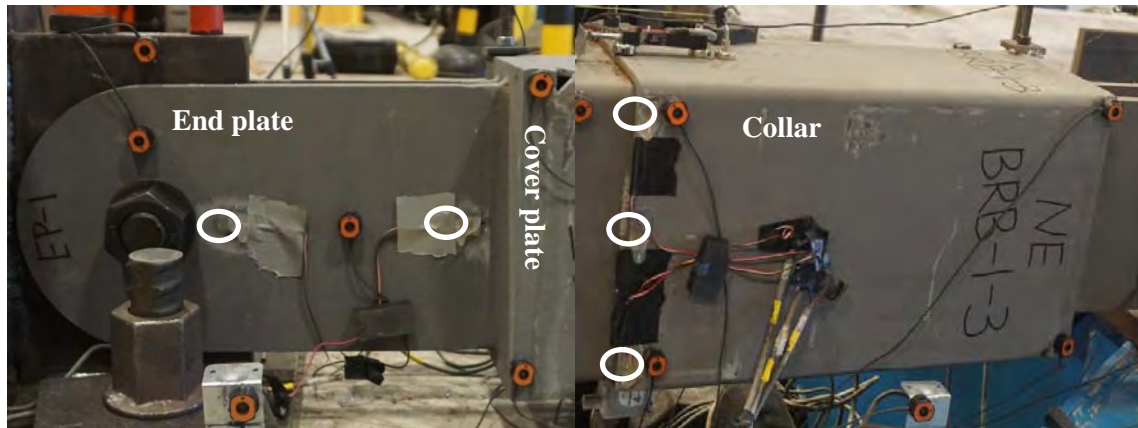
(a) (b)

Figure 8-24:Strain gauges attached to BRB-1-3: (a) end plate-1 on the south end; (b) east side of north collar

Two strain gauges were attached to each end plate, in line with the central axis of the BRB-1 as shown in Fig.8-23a (only the two end plates on the south end of BRB-1 had strain gauges). These two locations, one close to where the end plate's was welded to the collar's cover plate and one closer to the bolt, which were close to where maximum moments were expected in the plate. In addition, three strain gauges were placed at each vertical sides of each collar of the BRB (for a total of 12 gauges). Fig.8-23b shows the strain gauges on the east side at the top, middle and bottom of the north collar respectively. Table 8-2 summarizes all the strain gauges instrumented in the BRB-1 test setup.

Table 8-2: Strain gauges name and corresponding locations

Name	Note
SGE-ES	End plate on the southeast side close to the bolt
SGE-EN	End plate on the southeast side away from the bolt
SGE-WS	End plate on the southwest side close to the bolt
SGE-WN	End plate on the southwest side away from the bolt
SGC-SET	East side of south collar (top)
SGC-SEM	East side of south collar (middle)
SGC-SEB	East side of south collar (bottom)
SGC-SWT	West side of south collar (top)
SGC-SWM	West side of south collar (middle)
SGC-SWB	West side of south collar (bottom)
SGC-NET	East side of north collar (top)
SGC-NEM	East side of north collar (middle)
SGC-NEB	East side of north collar (bottom)
SGC-NWT	West side of north collar (top)
SGC-NWM	West side of north collar (middle)
SGC-NWB	West side of north collar (bottom)

8.3.5 Videos

Digital videos were recorded for all the tests. Each test was documented using standard definition cameras to record the global and local view of the BRB specimens' behaviors during the tests. All videos were accelerated by post-processing to help provide a better understanding of the behavior of the BRBs being tested.

8.4   BRB Displacement Demand and Test Protocols

When a BRB is installed spanning across an expansion joint in a bridge, axial strains in the BRB can be induced as a consequence of thermal movements of the bridge during regular service, or by an earthquake when (in this application) the BRB is subjected to cyclic bi-directional displacement demands. Both sources of strains can produce inelastic deformations that can accumulate to produce low cycle fatigue of the BRB's steel core plate. Consequently, the loading protocols developed for this project have taken both of these sources into consideration.

The seismic bi-directional demands from nonlinear time history analyses are first obtained in Section 8.4.1 and corresponding bi-directional test protocols to be applied to the specimens are developed in Section 8.4.2. Then the uniaxial displacement histories due to temperature fluctuations, to be used in the tests, are explained in the Section 8.4.3. The corresponding displacement protocols and sequence for applying them to each individual BRB is described in Section 8.5, along with the adjustment made based on test results and observations from prior tests.

8.4.1   Seismic Bi-directional Demand

To size the specimen and assess the design displacements to consider in its testing, nonlinear time history analyses were performed for the EDS-1 nonskew benchmark bridge having a longitudinal BRB of 100" in length and yield strength of 40 kips. The same EDS-1 simplified nonskew bridge diaphragm model from Section 7 was used. Rigid superstructure of the bridge was assumed. The longitudinal BRB was assumed to have an inclination angle of 45 degrees from the bridge deck. The yield length ratio factor of the BRB was assumed to be 0.5. The material of the steel core was assumed to be A36 with expected yield strength of 42 ksi. The cross sectional area of the BRB steel core was designed as 0.95 in^2. Note that at the time of analyzing this bridge model, the details of the BRB specimens to be tested was not known, the BRB's axial yield displacement, D_{by} was calculated only for the deformation at the yielding core length,

29:

which is 0.074". Note that this approximate calculation of the yield deformation has been used in Lopez and Sabelli (2004). When the plates outside of the core were significantly larger and their length significantly smaller, it is rational to take them as rigid for sake of stiffness calculations.

Orthogonal components of the ground motions records were inputted in the global longitudinal and transverse directions when performing the nonlinear time history analyses to investigate inelastic displacement demands of the BRB. The ground motions' scaling factor, corresponding to the target global displacement ductility, was calculated based on the design approach described in Section 7. Longitudinal and transverse displacements of the bridge diaphragm model were obtained from 44 time history analyses using the same 22 pairs of ground motions and these were scaled as described in Section 7.3.1.

Note that the BRBs to be tested have a yielding core area about nine times less than in the example bridge used in Section 7. Consequently, the ground motions that produced the target ductility in this case were comparably smaller. Rigorous scaling laws were not used here, as the purpose was not to establish a direct relationship with the prototype bridge considered in Section 7, but rather to investigate behavior of BRBs at target bidirectional displacements.

A BRB target ductility of up to 6 was originally contemplated, and the largest transverse displacement obtained from all 22 pairs of ground motions was 1.440", with a corresponding longitudinal displacement demand of 1.038". Since the bidirectional displacement protocols was mainly intended to test the BRB's transverse displacement capacity, target ductilities of 7, 8, 9, 10, 11 were also considered in order to explore greater possible transverse displacement demands. It turned out that the target ductility of 9 resulted in the largest transverse displacement of 1.602" among these ductilities, with a corresponding longitudinal displacement demand of 0.913" (i.e., approximately the same longitudinal displacement demands than for the target ductility of 6 case). Therefore, a ductility of 9 was chosen as the target ductility. The resulting average bidirectional displacement demand was 0.761" (same value in both directions), which was smaller than the global target displacement of 0.938" (corresponding to a ductility of 9).

The bidirectional displacement trace resulting from the ground motion that caused the largest transverse displacement of 1.602" obtained from all 22 pairs of ground motions is shown in Fig. 8-25 (with a corresponding longitudinal displacement demand of 0.913").
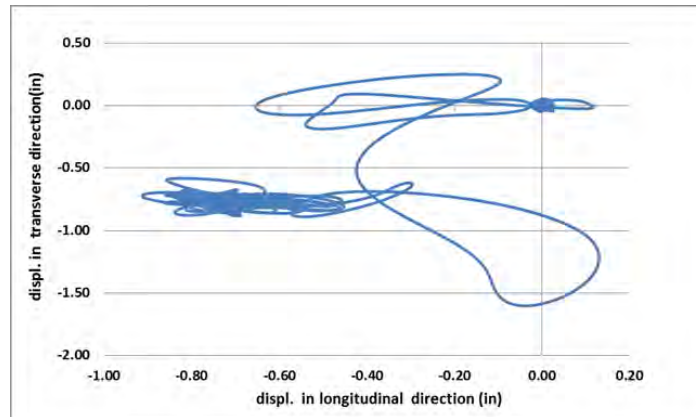
Figure 8-25:Displacement contour of the bridge with the EDS-1 bridge diaphragm

The corresponding axial displacement demand of the BRB is 0.646", which was obtained by converting the longitudinal displacement demand considering the longitudinal BRB's inclination angle. Note that, during execution of the project, this ground motion producing the largest displacement demands was selected as the "reference" motion. However, in the course of testing specimens, this decision was revisited and found to be inconsistent with BRB design practice. This is because BRBs are typically designed for twice the design displacements, and design displacements are representative of average response, with the multiplier of 2 allowing to account for maximum demands above the average. The displacement demand protocol was therefore revised accordingly, as described in Section 8.5.

Note that both types of the actual BRBs manufactured were expected to have slight difference in yield strength, cross section area and yielding core length from the generic BRB considered in the above model. This indeed turned out to be the case. To gage the difference between displacement demands predicted above for the generic BRB and those that would occur with the actual BRBs installed in the prototype bridge, the latter cases were re-analyses for the same 22 pairs of ground motions. The results of the displacement demands in both directions of the bridge having actual BRBs, for the earthquake excitation producing the largest demands, are shown in Table 8-3, together with those for the generic prototype. Longitudinal values are roughly 37% greater in the longitudinal direction, but only 10% larger in the transverse direction. Note that these displacement demands all corresponded to the target ductility of 9. Also note that because it was time consuming to perform the time history analyses with 44 ground motions for the changed bridge diaphragm model with different BRB properties, and because the tight scheduled "window" for testing in the SEESL lab could not allow a delay while waiting for the results of these analyses, the BRB-2 specimens, tested first, were subjected to the protocol considering the original displacements displacement values. However, the analyses were completed prior to the testing of the BRB-1 specimens, and changes were made to adjust the testing protocols for BRB-1 specimens.

In other words, the design displacements that were retained for the BRB-2 specimens to define their testing protocol were based on analyses for the generic BRB, namely 0.646" and 1.602", in the axial and transverse direction, respectively. These design displacements are denoted as D_{bmL} and D_{bmT}. The axial yield displacement, D_{by}, of the BRB is 0.074". Note that the axial design displacement is equal to about 9 times the axial yield displacement.

Table 8-3:Comparison of displacement demands for different BRB properties

	Transverse (in)	Corresponding Longitudinal (in)
Original (yield strength 42 ksi, cross section 0.95 in^2, yield length ratio 0.5)	1.602	0.913
BRB-1 (yield strength 46 ksi, cross section 1 in^2 , yield length ratio 0.465)	1.770	1.262
BRB-2 (yield strength 46 ksi, cross section 1 in^2 , yield length ratio 0.5)	1.751	1.247

8.4.2 Displacement Histories for Bi-directional Qualification Test

The standard test protocol used for the qualification test of BRBs is outlined in details in the AISC 341-10 Specifications (2010) as below:

(1) 2 cycles of loading at the deformation corresponding to 1.0 D_{by}

(2) 2 cycles of loading at the deformation corresponding to 0.5 D_{bmL}

(3) 2 cycles of loading at the deformation corresponding to 1.0 D_{bmL}

(4) 2 cycles of loading at the deformation corresponding to 1.5 D_{bmL}

(5) 2 cycles of loading at the deformation corresponding to 2.0 D_{bmL}

(6) Additional cycles of loading at the deformation corresponding to 1.5D_{bmL} as required for the brace test specimen to achieve a cumulative inelastic axial deformation of at least 200 times the yield deformation.

This protocol was developed for BRBs (tested alone and in sub-assemblies) principally subjected to axial displacements. Given that in the current proposed application in bi-directional diaphragms, BRBs are explicitly expected to be subjected to significant out-of-plane deformations in addition to axial ones, the existing test protocol had to be adapted.

Recall (from Section 8.2.2) that one of the design objectives was that the BRB's end plates (for BRB-1) must not yield due to out-of-plane bending before the transverse displacement D_{bmT} is reached. Furthermore, AISC specifies that the BRB's core plate must sustain progressively increasing axial

displacements until a value equal to twice the design displacement; it was therefore extrapolated here that it should also not fail at the twice the displacement demands in both directions during the bi-directional qualification test.

Therefore, the bi-directional BRB test was conducted by controlling the level of axial (longitudinal) and transverse deformations imposed on the BRB, and by adapting the AISC requirements for the cyclic testing of BRBs. Bi-directionality was introduced in the test protocol to investigate the BRB response by applying the biaxial S-type displacement pattern shown in Fig. 8-26. A complete large displacement loop is obtained by succession of the four small loops shown in Fig.8-26a, with movement of the shake table (looking from above) following the arrows. Each complete large loop in Fig. 8-26c was deemed equivalent to two of the cycles mentioned in the AISC test protocol because it imparted two full cycles of axial yield excursions. Therefore, at each displacement step of the AISC protocol outlined above, only one complete bi-directional large loop was needed. Following the AISC protocol, the displacement demands for each large loop are increased incrementally after completing the previous cycle.
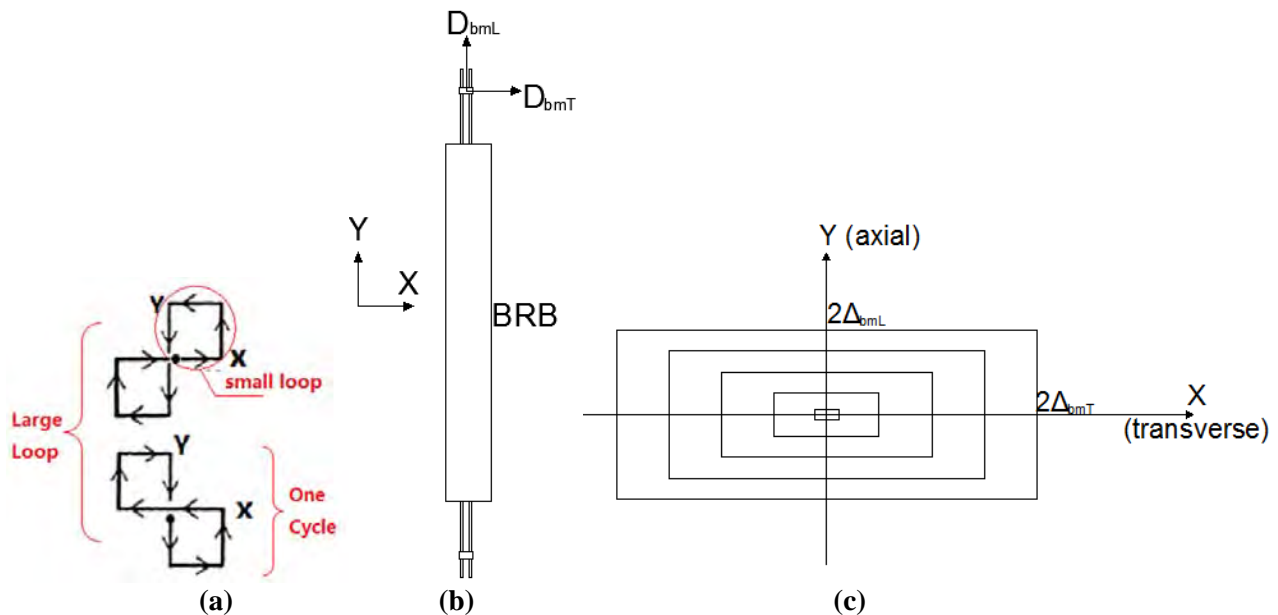
Figure 8-26: Bi-axial s-type displacement pattern (a) small loops with arrows of movement; (b) BRB's longitudinal and transverse demand; (c) movement of one end of the BRB (connected to the shake table)

The bi-directional qualification test protocol imposed displacements to the specimen until 2 D_{bmL} and 2 D_{bmT}, were reached in both directions. A constant strain rate of 1.3×10^{-3} /s was used for this test protocol. Note that this test rate slightly changed for the adjusted test protocols described in Section 8.5.

Note that due to the different core plate length for the two types of BRBs tested, the bi-directional loading protocols for BRB-1 differ from BRB-2 during the first cycles of loading when deformation targets are expressed as the yielding displacement; they are then identical when expressed as multipliers of design displacements. The corresponding displacement versus time history for the qualification test of BRB-2 is shown in Fig. 8-27a and 8-27b, for the longitudinal and transverse direction, respectively.

Note that, when the BRB is subjected to the transverse displacement demand (i.e., where the terms "transverse" and "longitudinal" refer to actual displacements of the shake table), as a result of the large amplitude of displacements, this would also impose additional axial displacement demands to the BRB. Therefore, if this bi-directional protocol has maintained a constant longitudinal displacement demand when the transverse displacements were applied, the BRB axial displacements would not have remained constant when it happened. To keep the axial BRB displacements constant (for sake of following the spirit of the test protocol), the longitudinal displacement of the shake table was adjusted, as shown in Fig.8-27a. For example, the displacement history in Fig. 8-28 is an enlarged view of Fig. 8-27a as time goes from 500 to 600 seconds, which corresponds to the small loop circled in red in Fig.8-26a.

(a)   (b)
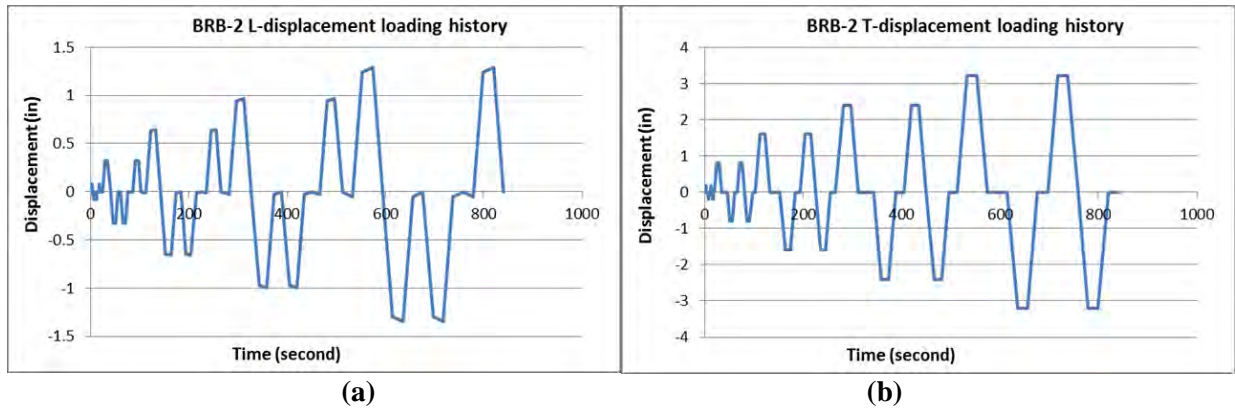
Figure 8-27:Bi-directional cyclic loading protocol for BRB-2 qualification test (a) longitudinal displacement vs time; (b) transverse displacement vs time
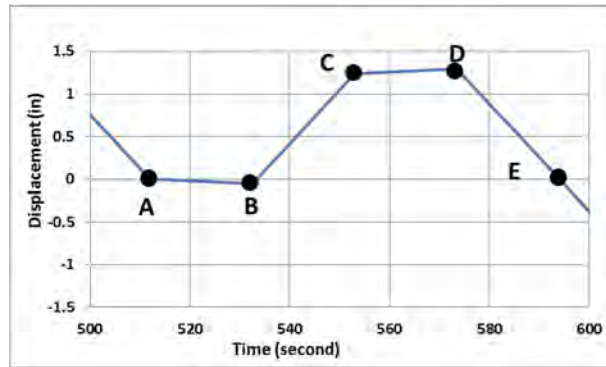
Figure 8-28: Enlarged view of longitudinal displacement history in Fig. 8-27 from 500 to 600s

Fig. 8-29 shows the BRB (in blue solid line) and its idealized prescribed displacement in the box (i.e., the black dash-dot line, matching the circled loop in figure 8.26a) for this loop. Points A to E in Fig 8-28 are marked in Fig. 8-29 to indicate the five positions that the BRB's end on the shake table would move to if following this idealized loop. The dotted red line in Fig. 8-29 shows the position where the BRB's end should be instead if it was to be kept at a constant axial length, which is a transverse displacement following the arc of a circle of diameter equal to the distance between the two BRB ends. Comparing the locations B and D where BRB's end would be if no adjustment was made with the locations following the arch that follows the BRB rotation, give the decrease and increase shown in Fig. 8-28 for the adjusted longitudinal displacement history demand. Note that this was done in the spirit of matching the AISC test protocol and that it may not reflect the BRB's actual response in the ductile diaphragm in the bridge when subjected to earthquakes (where a transverse displacement will indeed put additional axial strains into the BRB). Also note that, in some cases, the BRBs were tested under the bidirectional protocols without this longitudinal displacement adjustment, as discussed later in Section 8.5.
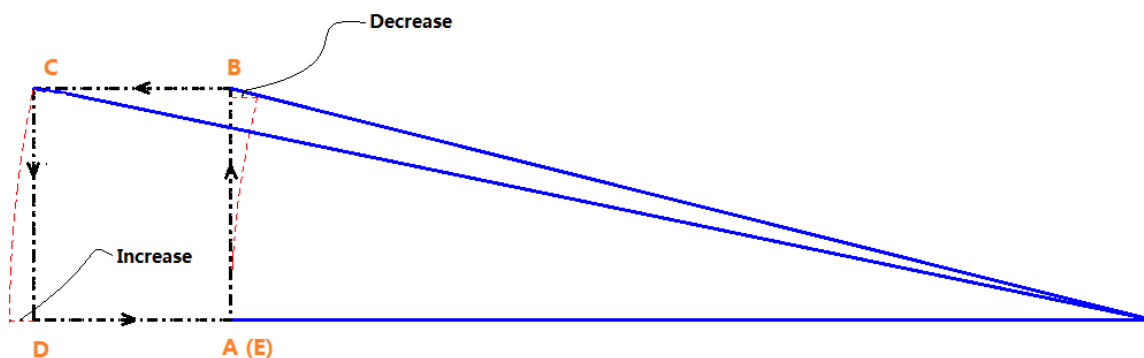
Figure 8-29:Movement of the BRB with the bidirectional displacement history

The magnitudes of displacements corresponding to the loading cycles in the longitudinal directions for BRB-1 and BRB-2 are shown in Table 8-4 and Table 8-5, respectively.

Table 8-4: Longitudinal displacement histories for bidirectional test of BRB-1

cycles	Axial displacement		Inelastic axial deformation	Cumulative inelastic axial deformation	Execution Time (s)
2	D_{by}	D_{by}	0	0	5
2	$0.5\ D_{bmL}$	$4.38\ D_{by}$	$27.04\ D_{by}$	$27.04\ D_{by}$	21.9
2	D_{bmL}	$8.76\ D_{by}$	$62.08D_{by}$	$89.12D_{by}$	43.8
2	$1.5\ \ D_{bmL}$	$13.13D_{by}$	$97.04D_{by}$	$186.16D_{by}$	65.7
2	$2\ D_{bmL}$	$17.52D_{by}$	$132.16D_{by}$	$318.32D_{by}$	87.6

Table 8-5: Longitudinal displacement histories for bidirectional test of BRB-2

cycles	Axial displacement		Inelastic axial deformation	Cumulative inelastic axial deformation	Execution Time (s)
2	D_{by}	D_{by}	0	0	5
2	$0.5\ D_{bmL}$	$4.06\ D_{by}$	$24.48\ D_{by}$	$24.48\ D_{by}$	20.3
2	D_{bmL}	$8.12\ D_{by}$	$56.96D_{by}$	$81.44D_{by}$	40.6
2	$1.5\ \ D_{bmL}$	$12.18D_{by}$	$89.44D_{by}$	$170.88D_{by}$	60.9
2	$2\ D_{bmL}$	$16.24D_{by}$	$121.92D_{by}$	$292.80D_{by}$	81.2

The execution time in the last columns in both tables is the time taken for applying each small loop as in Fig.8-26a. In that table, the term "inelastic axial deformation" refers to two cycles, and the inelastic deformation for each cycle was calculated as four times the axial displacement deformation minus the yield displacement. The difference between the two tables lies in the different yielding core length for the two types of BRBs. Note that the design displacements of the BRB in both directions are reached at the same time and, in all cases, the transverse displacements increase proportionally to those in the longitudinal direction. Also note that in the longitudinal direction, the BRB's test protocol follows the AISC standards. That test protocol specifies that a minimum cumulative inelastic axial deformation of at least 200 times the yield deformation be applied to the specimen, which, in this case, is already exceeded by the time twice the cycles at twice the design displacements are completed (this is not always the case when testing BRBs). Note that for the actual yield displacement calculated for the BRB including the deformation of the core plate outside the yielding core, the cumulative inelastic axial deformation for both BRBs would be 286.7 and 215.8, respectively, which is still larger than 200 times the yield deformation.

8.4.3 Low-cycle Fatigue Displacement History Due to Temperature Change

In the fatigue life studies described in Section 4.5 (for which details are presented in Appendix D), the temperature history for Memphis (for the year 2012) was found to be the most severe for the ten cities considered (in terms of producing a lesser fatigue life, because it produced the more severe strain demand

history on the BRB. Therefore, this temperature history (shown in Fig.8-30) was used here for the test protocol intended to represent yearly fluctuations of temperature. Note that the strain history chosen also corresponds to the worst case scenario for installation of the BRB, with installation at a temperature of 100 ºF, because doing so produces a temperature history that would put the BRB under mostly tensile strains, causing the BRB to approach fatigue faster, resulting in a lesser fatigue life.
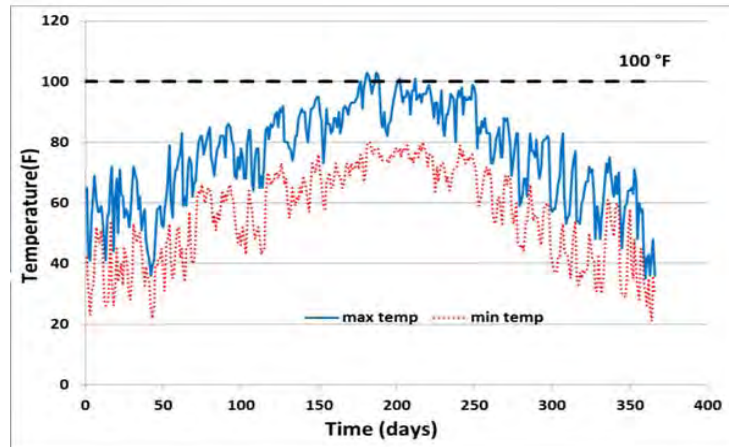
Figure 8-30:Recorded Temperatures at Memphis with BRB installation temperature of 100 ºF

Note that the study presented in Section 7.7 on the effect of temperature changes was conducted for a simply-supported bridge fixed at one end and free to move at the other end, where the longitudinal BRB spanned between the abutment and the bridge deck across the expansion joint at the free end. The chosen length was 100 ft of the simply-supported bridge model with a longitudinal BRB installed with an inclination angle of 45 degrees at one end. The horizontal projection length was 72 in, which was equal to 6% of the total bridge length. The yielding core length ratio is 0.5. The resulting axial displacement history and strain history of the BRB, corresponding to the yearly temperature loading described above, are shown in Fig. 8-31a and 8-31b, respectively. The magnitude of the largest displacement applied is 0.448", corresponding to a strain of 0.0096 and 0.0089 for BRB-1 and BRB-2 respectively. In principle, the number of times that the protocol in Fig 8-28 would be repeated before failure of a specimen gives the low-cycle fatigue life of that BRB, in years, for the worst case scenario considered.

Recall that in Section 7.7, the fatigue life under the temperature-induced strains was predicted by using the Fatiga software. The strain history in Fig. 8-31 was input in Fatiga and the resulting predicted fatigue life was 413 years. However, that theoretical calculation neglects the fact that the BRB's core plate will develop local buckling under the applied low cycle fatigue strain loading. This local buckling, even though limited and of small amplitude, produces additional flexural plastic strains that add to the pure axial strains. The above estimated fatigue life of 413 years, solely based on axial strains (for ASTM A36

material) needs to be adjusted. Using a preliminary calibration factor of 0.1 (obtained from the study described in Appendix D) to estimate the fatigue life for BRBs subjected to large strain ranges, the estimated fatigue life would become 41.3 years. However, note that the tests referenced in Appendix D to obtain this calibration factor were performed using various constant strain ranges, for BRBs from a different fabricator. Here, results from the tests will be assessed to obtain a revised calibration factor, as presented in Section 9.

| (a) | (b) |
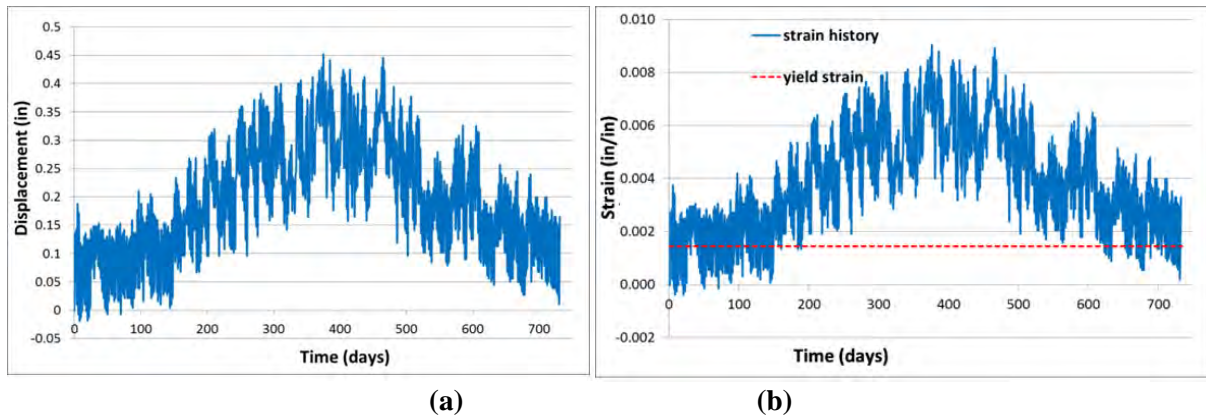
Figure 8-31: Axial deformation and strain history in the BRB core plate caused by one year of temperature changes (with respect with days in a year)

Recall that the simplified bridge diaphragm model mentioned in Section 8.4.1 and used for getting the bidirectional displacement demand due to earthquake excitations, corresponded to a bridge of 100 ft and had longitudinal BRBs at both ends. Therefore, for consistency, if the temperature histories were to correspond to a similar span having expansion joints at both ends, the axial deformation due to temperature change shown in Fig.8-29 would actually correspond to a prototype bridge of 200 ft. Therefore, the BRB-2s specimens, which were subjected to the above displacement history due to temperature, were effectively tested for twice the displacement demand due to the effect of temperature changes that would be experienced on a 100 ft span bridge. The adjusted correct displacement history for a 100 ft bridge was applied later to the BRB-1 specimens, as mentioned later in Section 8.5.

An additional complication arose due to the presence of gaps at the BRB's end connections; as a consequence of those gaps, the BRB's core plate deformations were smaller. This required other adjustments to the axial displacement history (to recognize this specific BRB's behavior, but also to generalize findings to cases where the gaps would be less or inexistent), which are discussed in Section 8.5.

The test speed at which to apply the displacement history shown in Fig. 8-31 also had to be determined. The ASTM E606 (2015) standard for strain-controlled fatigue testing specifies a strain rate of 10^{-3} sec^{-1} as an often used value. However, for the current testing program, at such a testing speed, subjecting a BRB specimen to 75 years of the temperature-induced displacement history would be have been too long (33.3 hours) and impractical to use. A higher strain rate was therefore desirable, but a concern arose that the BRB's core plate might overheat at such faster test speed under low-cycle fatigue. Finite element analyses were performed to estimate the heat build-up, but concerns arose that reliance on the models might not be sufficient, given the complexities of having the BRB's steel core plate encased in the concrete.

Tests were therefore conducted on two steel coupons designed to simulate a condition where heat transfer to the surrounding environment was prevented (as a limit case to the condition encountered inside a BRB). The selected material for the steel coupons was A36, to be the same as for the BRB's core plate. A thermocouple was attached to the middle of each coupon. Insulation foams were compressed and wrapped around the first coupon, and then secured with duct tapes as shown in Fig. 8-32. A constant amplitude cyclic displacement of 0.02" was applied to this coupon using the MTS universal testing machine in the SEESL. The test frequency was 0.25 Hz. For the coupon with a gauge length of 2", this corresponded to a testing strain rate of 10^{-2} sec^{-1}. For comparison, the other coupon had no insulations and was applied with the same cyclic displacement history. Both coupons were tested until low cycle fatigue happened. The results showed that the highest temperature reached by the coupon with insulation was 161 F, while that reached by the other one was 148 F. Both of the temperatures were far below the temperature level when the steel properties would change significantly.

Therefore, the testing strain rate of 10^{-2} sec^{-1} was chosen, the experimental duration of the strain and displacement history corresponding to one year's temperature loading is shown in Fig.8-33a and 8-33b. Note that at that strain rate, one year of temperature fluctuations is applied to the BRB in 165 Seconds.
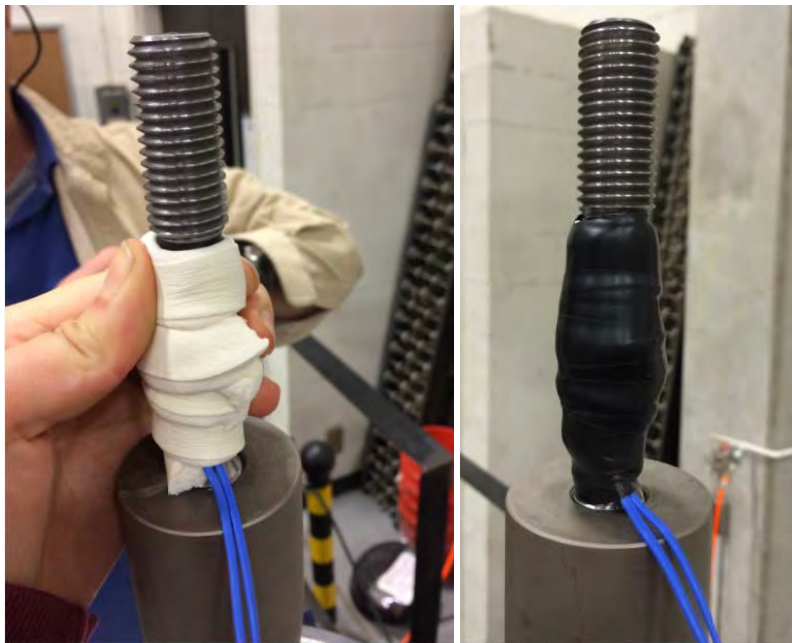
(a)   **(b)**

Figure 8-32:Photo of the coupon test with insulation foam and duct tape (a) before applying duct tape; (b) after applying duct tape
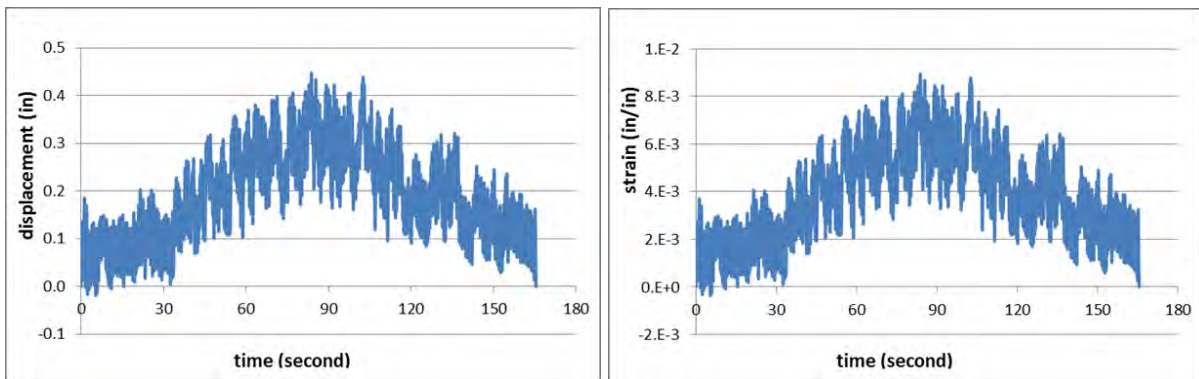
(a)   **(b)**

Figure 8-33: Axial displacement history and resulted strain history for one year of temperature fluctuations for BRB's low cycle fatigue test, in terms of actual experimental time

8.4.4   BRB Loading Protocols

While the test protocols described in Sections 8.4.3 and 8.4.4 served as "templates" for the bi-directional qualification testing and temperature cyclic histories, respectively, various combinations of those protocols were considered and combined as part of the complete test program. This was done to provide a broader understanding of behavior and expected service life for the two proposed type of BRBs considered.

30;

Four specimens of each type of BRB were tested. The different combinations of displacement protocols that were applied to them are summarized in Table 8-6. Note that the bidirectional qualification protocol labeled "(extreme displacement demand)" exactly corresponds to the one described Section 8.4.3. The other combinations and changes to all test protocols are presented in more details in subsequent sections below, following the order in which the tests were conducted.

Table 8-6:Summary of BRB test protocols

Specimen	Test protocol
BRB-2-1	Bi-directional qualification (extreme displacement demand)
BRB-2-2	Axial
BRB-2-3	Bi-directional qualification (extreme displacement demand) + axial
BRB-2-4	Axial + bi-directional qualification (extreme displacement demand)
BRB-1-1	Bi-directional qualification (average displacement demand)+ axial
BRB-1-2	Bi-directional qualification (average displacement demand) + axial
BRB-1-3	Bi-directional qualification (average displacement demand) + bi-direction (with increased transverse displacement demand)
BRB-1-4	Bi-direction (from non-linear seismic response of prototype model) + axial + bi-direction (from non-linear seismic response of prototype model)

The four BRB-2 specimens were first tested. Therefore, their test protocols are first explained below, along with experimental results. Some significant changes were made to the protocols after testing the BRB-2 specimens. More specifically, for testing of the BRB-1 specimens, the displacement demands in both directions in the bidirectional qualification test protocols were reduced based on the behavior of the BRB-2 tests.

Finally, the term "axial" in Table 8-6 refers to the axial displacement history applied repeatedly to the BRBs to simulate temperature cycles over different number of years in service.

In all tests, the number of cycles to which the BRBs were subjected prior to failure was recorded, with the goal of estimating their service life before failure. Note that because the axial displacement histories varied in amplitudes for the various BRBs tested, and the specific number of years of temperature cycles applied and the magnitude of the temperature-related displacement demands were also adjusted for various specimens, the specifics and rationale for those changes is described in the subsequent sections describing the tests performed on each individual specimen.

312

8.5   BRB Test Protocols and Test results

In this section, the test protocols for each BRB are presented, along with adjustments made to those protocols based on the previous BRB test results. The experimentally obtained hysteretic results and behaviors of the BRBs under bidirectional and axial displacement protocols are also presented. Since some adjustments made to the test setup and protocols were based on the test observations, they are explained in subsequent sections along with the test protocols and BRB specimens' hysteretic behaviors.

A list of the adjustments and changes done to the test set-up and protocols is summarized to provide clarifications provided in later sections, together with a cross-reference to the sections the details of those changes presented. These events that led to those changes can be described as follows:

- Because of insufficient friction resistance between the base plates in the reaction block and the Strong Floor and the Shake Table, the sliding of the reaction blocks reduced the actual displacement applied to the BRB (two separate set-up modifications to solve this problem are described in Sections 8.5.1 and 8.5.3.
- Still, elastic deformations and sliding (even though smaller in magnitude than before) of the reaction block under the BRB's force, as well as pin slippage in the BRB, combined to reduce the BRB displacement demand to less than originally desired with the initial protocol. Therefore, the original displacement histories for the extreme bidirectional qualification test and the temperature-induced axial test (described in Section 8.4) were increased to correct for this effect in Section 8.5.3.
- After obtaining the test results of BRB-1, upon further consideration, the bidirectional qualification displacement demands were judged to be excessively severe, as they corresponded to the extreme values of displacements obtained from all the ground motions considered. For the reason presented in Section 8.4.1 and further described in detail in Section 8.5.5, new nonlinear time history analyses were performed using the actual BRB properties and bridge characteristics. The average displacement demands resulting from those analyses were found and used in subsequent tests.
- A corrected axial temperature-induced test history (corresponding to 100-ft bridge) is shown in Section 8.5.5. The adjustments were made considering the deformation and sliding of the reaction blocks under the BRB's force and the bolt slippage.
- In subsequent tests of temperature histories, the axial displacement history was further modified, scaled such as to induce an inelastic deformation of 5 times the yield displacement when applied to the BRB-1-2, as described in Section 8.5.6. At that time, the output frequency of the shake table and potentiometers, and the duration of the axial displacement history due to temperature change

313

was increased, such as to provide reliable plots of the BRB's force versus axial deformation, as described in Section 8.5.6.

- In order to explore the magnitude of the maximum transverse displacement demand that can be applied to the BRB, the average bidirectional qualification test histories were modified to apply increased transverse displacements, as explained in Section 8.5.7.

- Finally, a BRB was subjected to simulated ground motions, using bidirectional displacement histories obtained from the new nonlinear time history analyses of the simplified bridge diaphragm model, with and without consideration of bolt slippage, as described in Section 8.5.8.

8.5.1   BRB-2-1

8.5.1.1 Overview of Parts of Test BRB-2-1

BRB-2-1 was used to investigate behaviors under only bidirectional displacement histories. BRB-2-1 was first subjected to the extreme bidirectional qualification displacement history described in Section 8.4.2 (and shown in Fig.8-27) in Test BRB-2-1-A, which stopped after finishing the cycle of the protocol corresponding to 1.5 times the design displacement. This interruption occurred due to slippage of the reaction block on the strong floor, which was fixed before the entire protocol was re-applied. This additional extreme bidirectional qualification displacement history, restarted from the beginning of the protocol, was applied in Test BRB-2-1-B. Since BRB-2-1 had still not failed after Test BRB-2-1-B, a new bidirectional displacement history was applied to BRB-2-1 with increased transverse displacement demand in Test BRB-2-1-C. The BRB-2-1 specimen finally failed during Test BRB-2-1-C.

8.5.1.2 Test BRB-2-1-A

BRB-2-1 was first subjected to the extreme bidirectional qualification displacement history described in Section 8.4.2 (and shown in Fig.8-27), but only until 1.5 times the design displacements in both directions. The test was stopped at that point (i.e., before the whole qualification test was finished) because of a large slippage that happened between the reaction block and the strong floor with a loud noise. The corresponding hysteretic curve of BRB-2-1 is shown in Figs.8-34a and 8-34b, in which the BRB's axial deformations were measured by the LPs and Krypton system respectively.

314
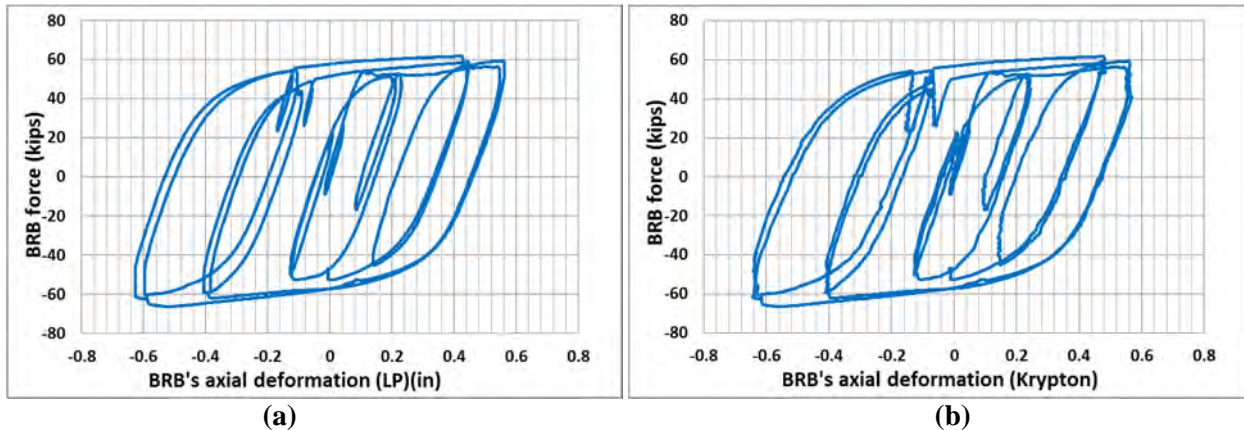
Figure 8-34: Hysteretic behavior of BRB-2-1 in Test BRB-2-1-A: force vs BRB's axial deformation measured by (a) LPs; (b) Kryptons;

Fig. 8-35 schematically illustrates (exaggerated, for clarity) the gaps in the pin holes of the BRB's end plates and gusset plates in the reaction blocks, and how the pins move within those gaps as cycling occurs. Fig. 8-36 shows the BRB's axial force versus the BRB's applied axial displacement as measured by Krypton system (recall Section 8.3.3); visual inspection of this figure reveals a slippage of the pin at zero load of approximately 0.06", which is close to a 0.0625" slip (i.e., 1/16"). Note that the magnitude of those slips in each direction could be estimated, knowing that there was a 1/32 difference between the pin and pin-hole diameters, but the magnitude of the initial development of that slip could not be predicted at the onset of the test as the initial setting locations of the pins in their holes (i.e., clearances on each side of the pins) were somewhat random.

Fig. 8-37a shows the slippage in the reaction block on the strong floor versus the BRB's axial force in Test BRB-2-1-A. Once the BRB's force was larger than 60 kips, the reaction block on the strong floor started to slide, and continued to slide in each subsequent cycles after that. The friction force to prevent slippage of the reaction block was directly related to the pretension force in the tie-down bolts between the reaction block's base plate and the strong floor and the friction coefficients. Considering the fact that the W-section was not centered on the base plate (as described in Section 8.2.1 and shown in Fig. 8-1), this created eccentric loading and the assumed friction resistance turned out to not be adequately conservative. The same thing also happened for the reaction block on the shake table as shown in Fig.8-37b. This is the main reason why the BRB's largest axial deformation turned out to be less than the desired displacement demand corresponding to 1.5 times design displacement of 0.998".

315
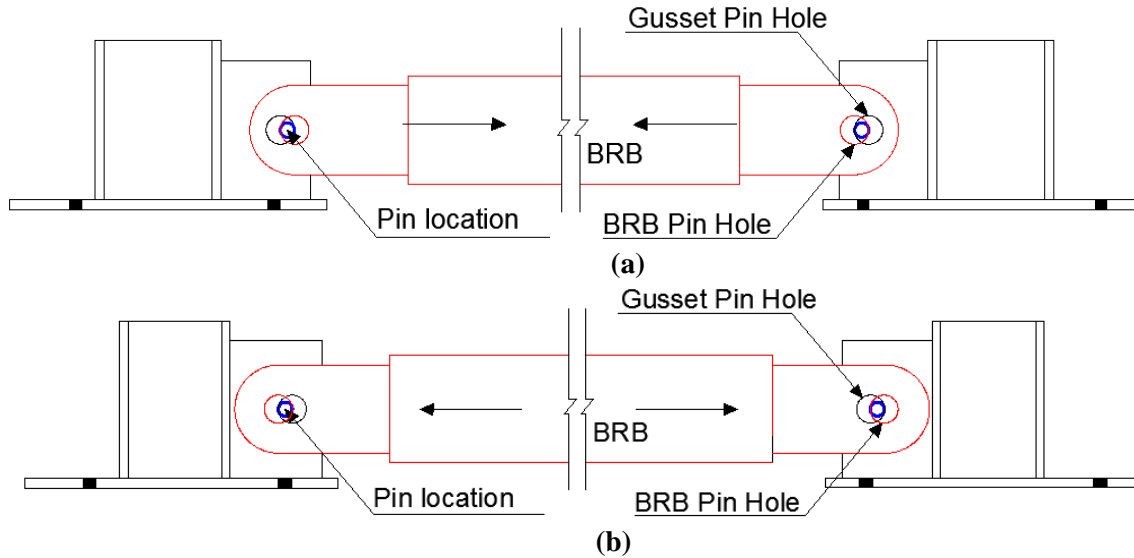
Figure 8-35: Illustration of the gaps in the pin holes of BRBs' end plates (in red) and gusset plates in the reaction blocks (in black): (a) BRB in tension; (b) BRB in compression
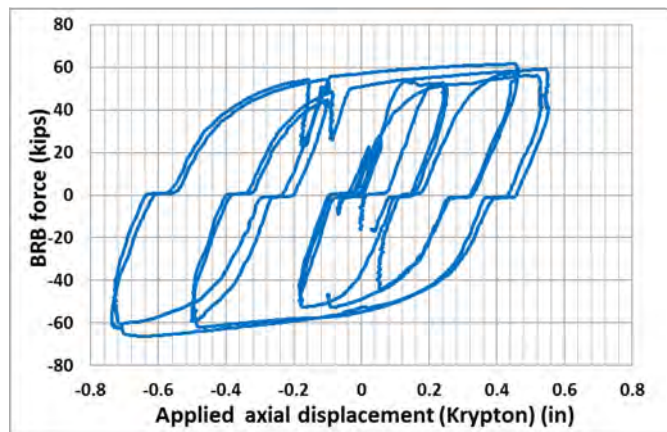
Figure 8-36: Hysteretic behavior of BRB-2-1 in Test BRB-2-1-A: forces vs BRB's applied axial displacement

For example, in Fig. 8-37, the maximum slippage of the reaction blocks on the strong floor and shake table was 0.09" and 0.13", respectively, when the BRB reached the maximum tensile force, which added up to 0.22" to the total displacement (i.e., sum of values in the negative and positive directions). The slippage of the reaction blocks on the strong floor and shake table was 0.34" and 0.07" when the BRB reached the maximum compressive force, which added up to 0.41". Therefore, the total slippage that happened when the BRB was loaded from maximum tension to compression was 0.63".

316

(a)   **(b)**
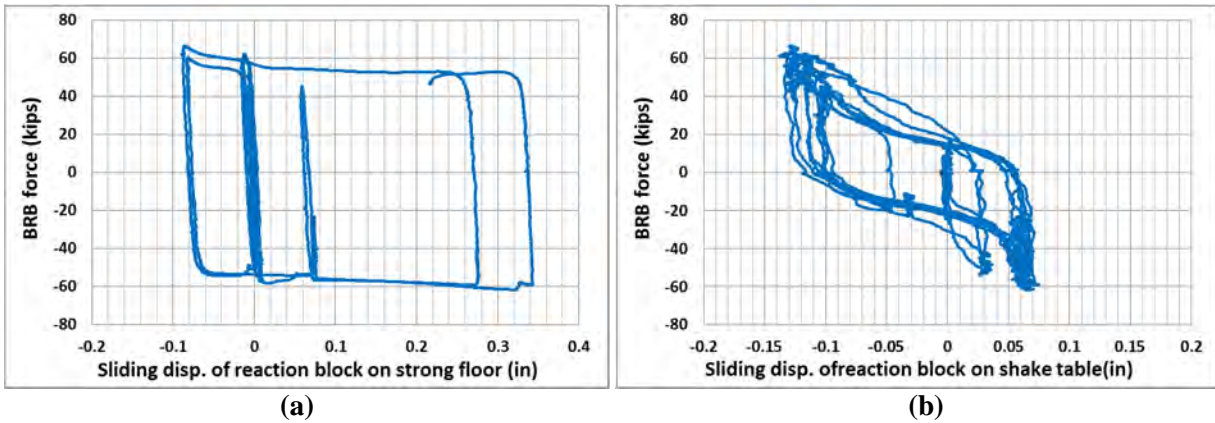
Figure 8-37:BRB-2-1's force vs sliding displacement of the reaction block (a) on the strong floor; (b)on the shake table

The reaction blocks also deformed under the BRB forces as shown in Fig. 8-38, in which the BRB's axial force is plotted against the reaction blocks' deformations on the strong floor and shake table. At maximum tensile force of the BRB, the elastic deformations of the reaction blocks on the strong floor and shake table were 0.026" and 0.009", respectively. At maximum compressive force of the BRB, the elastic deformations of the reaction blocks on the strong floor and shake table were 0.056" and 0.026", respectively. The total deformations of the reaction block were therefore 0.117". The BRB's largest tensile and compressive deformations were 0.56" and 0.64", as shown in Fig. 8-34. With the pin slippage of 0.0625" mentioned earlier, the total axial displacement becomes 2.015", which is approximately the magnitude of displacement that was applied axially to the BRB from its points of maximum tension to maximum compression force (i.,e, twice the displacement that was applied to the specimen for the cycle corresponding to 1.5 times the design displacement of 0.998", is 1.996").

(a)   **(b)**
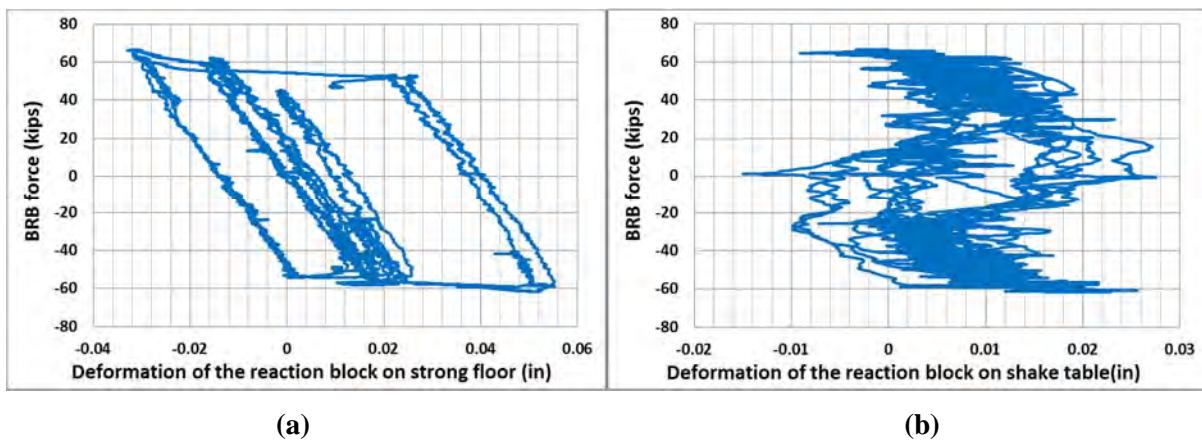
Figure 8-38: BRB-2-1's force vs deformations of the reaction block (a) on the strong floor; (b) on the shake table

Since the BRB-2-1 was under bidirectional displacement history, the illustration of how the reaction block's slippage and deformation, as well as the pin slippage, affect the BRB's axial deformation was not directly noticed during the test. It became more evident when the BRB was subjected to axial displacement history, as described in Section 8.5.2 for BRB-2-2. Therefore, the details of how this was addressed are presented in Section 8.5.2; note that because the magnitude of the displacements applied to BRB-2-2 was much smaller than for BRB-2-1, this made the sum of the above set-up corrections substantially more significant and non-negligible in that case, as described later.

8.5.1.3 Modification of anchorage on the strong floor

To achieve friction resistance of the reaction block on the strong floor, it had originally been originally connected by four 1-1/8" anchor rods (Grade 8) torqued to 600 ft-lbf (resulting in a theoretical pretension force of 32 kips in each anchor rod), for an original design that assumed a friction coefficient of 0.45 between the base plate and the concrete strong floor. In light of the above behavior, the anchor rods were replaced by four Dywigdag rods with diameter of 1-3/8" (yield strength of 150 ksi), each loaded to a pretension force of 100kips.

Recall that, as mentioned earlier, only the force and displacement output of the shake table in the longitudinal direction (i.e., in the BRB's axial direction) was monitored in real time during the test. It was therefore assumed that the stronger tie-down forces had solved the sliding problems, and that large sliding had only occurred on the strong floor side. It is only after post-processing of the data that slippage of the reaction block on the shake table was found to occur (without the large noise that had been heard when sliding occurred for the reaction block on the strong floor). Note that because BRB-2-2 was only subjected to temperature-induced axial displacement histories of smaller amplitude compared to the bidirectional displacement history, and that the BRB in that case developed only a force of 50 kips (as shown in Section 8.5.2), the slippage of the reaction block on the shake table was not very large for the BRB-2-1 test. As a result, it is only later during the test of BRB-2-3 that the large slippage of the reaction block on the shake table happened (in both bidirectional qualification and temperature-induced axial displacement test). The anchorage of the base plate on the shake table was therefore strengthened at that time (per details described in Section 8.5.3).

8.5.1.4 Test BRB-2-1-B

Since BRB-2-1 was not subjected to the entire extreme bidirectional qualification displacement history during test BRB-2-1-A (as illustrated in Fig. 8-27), the loading protocol was re-applied in its entirety to BRB-2-1 (i.e., restarting from the beginning of the protocol and increasing amplitude of cycles up to two times the design displacement demand).

The corresponding hysteretic curve of BRB-2-1's force versus axial deformation is shown in Figs 8-39a and 8-39b, for cases where the BRB's axial deformation was measured by the SP and Krypton system, respectively. Fig. 8-40 shows the BRB's axial force versus the applied axial displacement measured by the Krypton system, where the effect of the pin gaps at both ends of the BRB, adding up to a 0.0625" slip at zero load, can be observed. Note that the BRB's axial deformations measured by the Krypton system are not as accurate as the one measured by SP in Fig. 8-39. Fig. 8-39b is shown here only for comparison with Fig. 8-40, since the BRB's applied axial displacement can only be obtained through measurements by the Krypton system in Fig. 8-40, which includes the slippage of the pins at BRB's two ends.

(a)   (b)
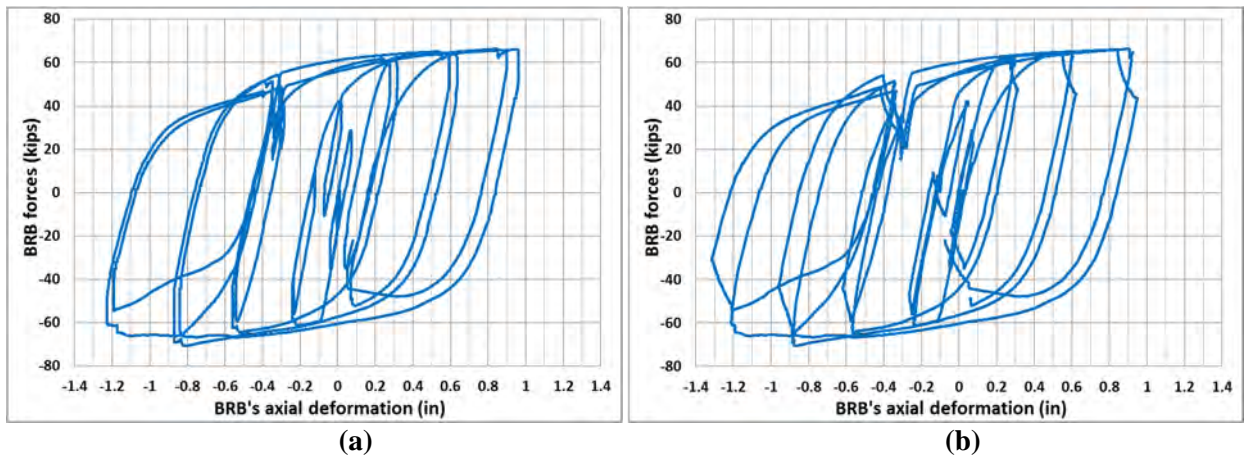
Figure 8-39: Hysteretic behavior of BRB-2-1 in Test BRB-2-1-B: force vs BRB's axial deformation measured by (a) SPs; (b) Kryptons;

Note that there is a difference between the largest tensile and compressive deformations reached in Fig. 8-39. This is mainly due to slippage of the reaction block on the shake table, which was non-symmetric, as shown in Fig. 8-41. In this case, the base plate slid more when the BRB was in tension than in compression, but the reverse could have been equally possible, as this depends on the original position of the anchor bolts inside their holes, which is somewhat random.
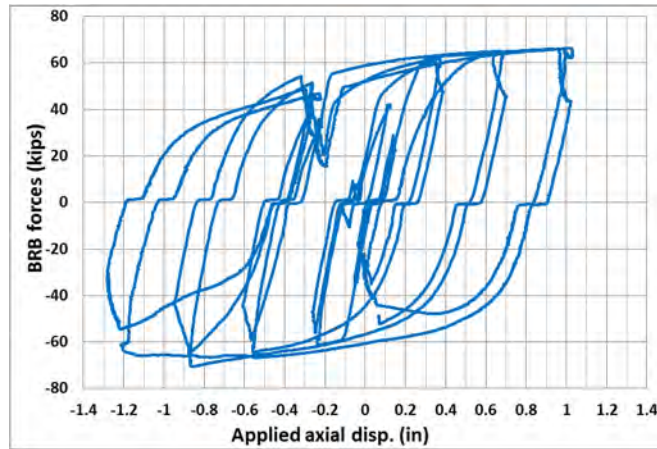
Figure 8-40:Hysteretic behavior of BRB-2-1 in Test BRB-2-1-B: forces vs BRB's applied axial displacement obtained from Krypton system
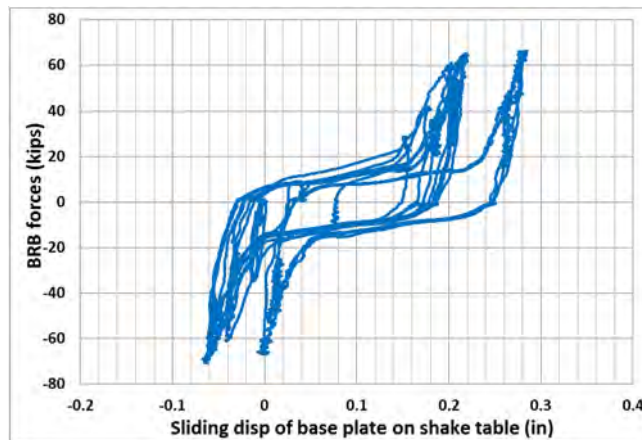
Figure 8-41:BRB-2-1's force vs sliding displacement of the reaction block on the shake table in test BRB-2-1-B

8.5.1.5 Test BRB-2-1-C

After completion of the first incomplete qualification test and the subsequent complete one, with the BRB still unfailed, BRB-2-1 was subjected to a new protocol of additional displacement histories to investigate the BRB's ultimate transverse displacement capacity. This new protocol was designed such that, in this added sequence of displacement histories, the transverse displacement demand would be increased incrementally from $2D_{bmT}$ up to $4D_{bmT}$ (if the specimen didn't fail before then) while the longitudinal displacement demand remained at $2D_{bmL}$. Therefore, the cycles of the displacement history corresponding to 2.5 D_{bmT} and $2D_{bmL}$ (shown in Fig. 8-42) were first applied to BRB-2-1. The specimen failed during the second cycle of transverse displacement demand in tension when the table was moving longitudinally toward the largest longitudinal displacement of $2D_{bmL}$, as shown in Fig.8-42, where the failure point is

31:

indicated by a red cross. Fig.8-43 shows the bidirectional movement of the shake table, with a red cross again marking the point when failure of BRB-2-1 occurred.

(a)   (b)
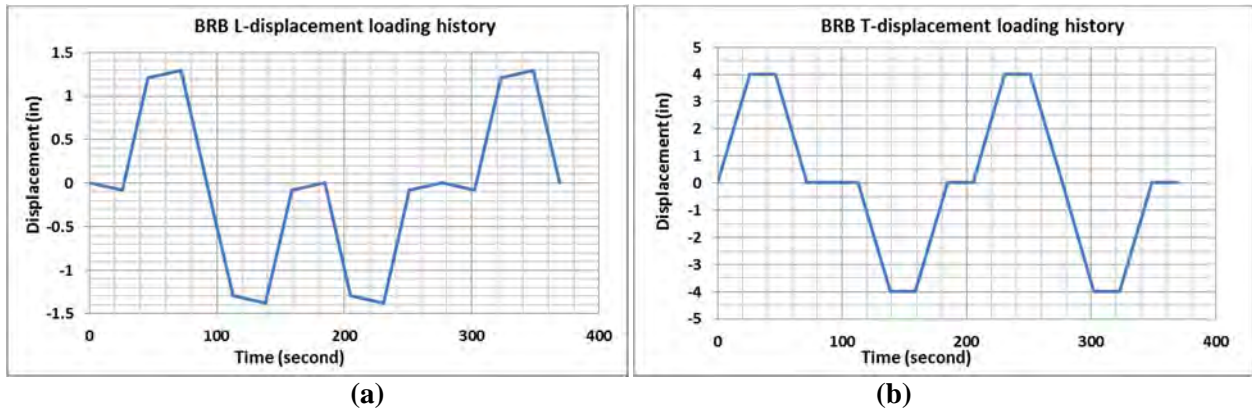
Figure 8-42:Test BRB-2-1-C with larger transverse displacement demand: (a) longitudinal displacement vs time; (b) transverse displacement vs time
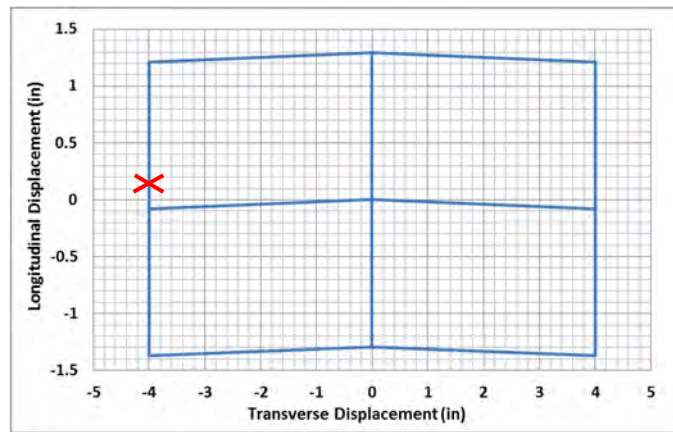
Figure 8-43: Displacement history in test BRB-2-1-C: transverse displacement vs longitudinal displacement

The corresponding hysteretic curve of BRB-2-1 is shown in Fig. 8-44 by the red dotted line (i.e., at 2.5 D_{bmT}), superposed on top of the largest displacement cycle (i.e., at 2 D_{bmT}) applied during the test BRB-2-1-B (in Fig. 8-39) for comparison. The failure of BRB-2-1 is indicated by the red cross in Fig. 8-44. Note that at the beginning of test BRB-2-1-C, the shake table was at zero position. However, because of the slippage of the reaction blocks from their original positions, the specimen had an initial residual deformation of 0.07" at the start of test BRB-2-1-C (i.e. after tests BRB-2-1-A and BRB-2-1-B).

Though the specimen successfully finished this qualification test without failing, due to the various slippage and deformations of the reaction set-up, the applied displacements did not reach the desired displacement demand in the test protocols. However, based on the fact that the bidirectional protocol was almost applied twice to the BRB, a better way to quantify the BRB's behavior is to compare the

cumulative inelastic displacements reached in all tests. This comparison is presented in Section 9 for all of the BRBs tested.
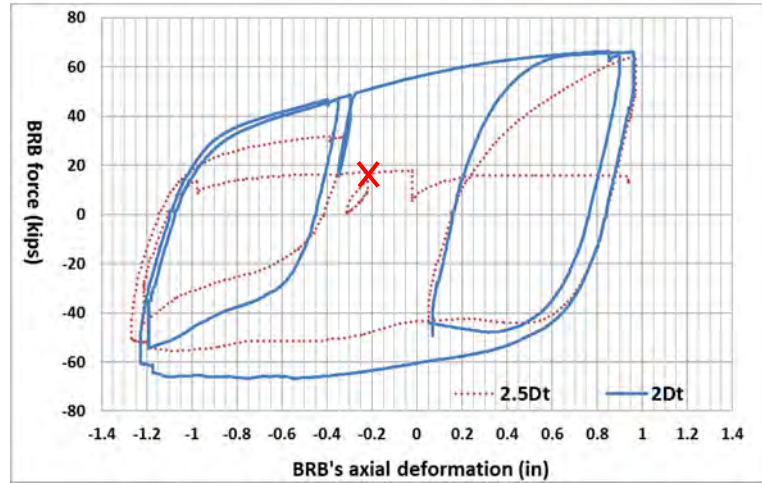
Figure 8-44: Hysteretic behavior of BRB-2-1 in the test BRB-2-1-C with larger transverse displacement demand

In all of the above testing for BRB-2-1, no end-plate failure or instability was observed. After the test, a visible bulge was observed on the northeast side of the BRB. The cause of that bulge and mode of failure of the BRB specimens will be discussed in details in Section 9.1.

8.5.2   BRB-2-2

8.5.2.1 Overview of Parts of Test BRB-2-2

BRB-2-2 was subjected only to temperature-induced axial displacement histories. The original axial displacement history due to temperature change shown in Fig.8-33a was first applied to the specimen in Test BRB-2-2-A.   BRB-2-2 successfully went through 85 cycles of this temperature-induced displacement history (i.e. corresponding to 85 years of temperature changes).   Since the target performance objective was to have the BRB be able to sustain 75 years of axial displacement demand (for the protocol illustrated in Fig.8-33a), BRB-2-2 successfully met and exceeded that limit. However, as most of that applied displacement history was accommodated by slippage of the pins, it was felt that the BRB should be subjected to a displacement history of larger amplitude, so that future results could also be safely generalized to specimens having proportionally smaller (or even no) gap at their pins. For sake of completing testing of the specimen already in place, the original axial displacement history was arbitrarily scaled up to1.5 times and successfully applied to the specimen for 10 cycles in Test BRB-2-2-B. After that, BRB-2-2 was subjected to further axial displacement history scaled up to 1.75 times in Test BRB-2-2-C. The specimen completed 9 cycles of this displacement history and failed in the 10th cycle.

8.5.2.2 Test BRB-2-2-A

BRB-2-2 was first subjected to the original axial displacement history due to temperature change shown in Fig.8-33a in Test BRB-2-2-A. Fig. 8-45a shows the hysteretic curve of the BRB-2-2's force versus the table's longitudinal displacement output, for the first 5 cycles of temperature-induced axial displacement histories (i.e., the results in Fig. 8-45a correspond to 5 years of temperature changes). Note that the table's longitudinal direction was the same as the BRB's axial direction. Except for the first cycle when the BRB was loaded from zero deformation and axial force, the rest four cycles follows the same shape as shown in Fig 8-45b.

(a)   (b)
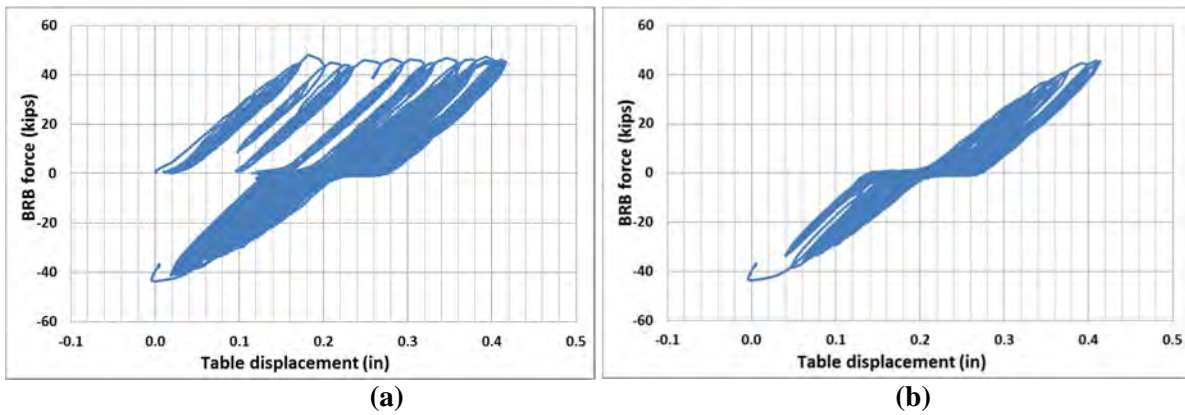
Figure 8-45: BRB-2-2's axial force vs longitudinal table displacement in Test BRB-2-2-A: (a) 10-cycles; (b) typical one cycle

At the time of the test, it was expected to be straightforward to plot the BRB's force versus axial deformation for the temperature-induced axial test. However, upon closer scrutiny of the collected data after its post-processing, it was found that, due to the fast speed of the input axial displacement history, the force output of the shake table was affected by the inertia of the shake table and could not reflect the force in the BRB in real time when using a data output frequency of 32 Hz. The reason why that 32 Hz frequency was chosen in the first place is because the maximum sampling rate of the Krypton system is 32 Hz. For consistency, the frequency of the data acquisition from the LPs and SPs was also kept at 32 Hz, which turned out to be not large enough to accurately capture the change in displacements. Therefore, the recorded hysteretic curves of the BRB's force versus axial deformation as shown in Fig. 8-46 could not reflect the BRB's real hysteretic behavior. This problem only occurred in the temperature-induced displacement histories, because the sampling rate was adequate for the bidirectional qualification test (which led to reliable plot of the BRB's axial forces vs axial deformation in that case). Given that it already took a whole day to apply the 85 cycles of axial displacement histories, it was decided that the plots of shake table's longitudinal displacement output versus the BRB's axial force would be sufficient

323

for BRB-2s when subjected to temperature-induced axial displacement history. However, a way to fix this problem was found by the time the BRB-1s were tested, as described in Section 8.5.6.
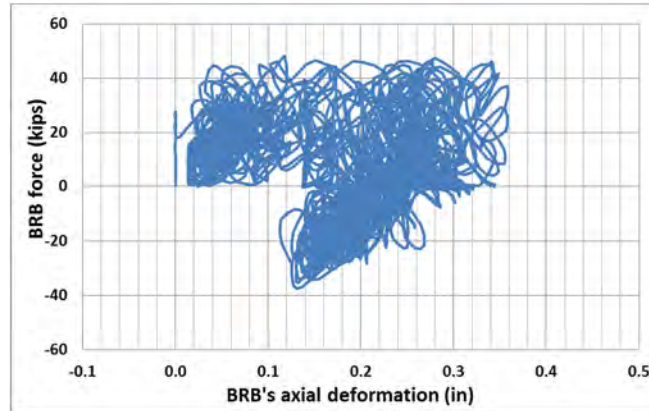
Figure 8-46: BRB-2-2's axial force vs axial deformation of the first cycle axial displacement history in Test BRB-2-2-A

Fig. 8-47a compares the table's longitudinal displacement output and the BRB's applied axial displacement under 5 cycles of axial displacement history. Fig. 8-47b compares the BRB's axial deformation and the BRB's applied axial displacement for the same five cycles.

The above difference happened as explained using the system shown in Fig.8-48, where the shake table, the strong floor, the reaction blocks, and the BRB system shown in Fig.8-1 is simplified. In this model, the displacements shown are the pin gap at each end of the BRB, Δ_g, and the sliding displacement of the reaction blocks on the strong floor, Δ_{bpf}, and the shake table, Δ_{bps}, respectively. The reaction blocks on the strong floor and the shake table can each be treated as a spring with stiffness, K_{rf} and K_{rs}, respectively. They deform under the BRB force, and the elastic stiffness of each reaction block can be calculated as the applied force divided by the blocks' deformation, itself obtained from the relative displacements of the LEDs attached to the reaction blocks (shown in Fig. 8-21). The displacement difference between LEDs 1 and 4 give the deformation of the reaction block with respect to the strong floor, Δ_{rf} ; and that between LEDs 28 and 31 corresponds to the deformation of the reaction block on the shake table, Δ_{rs}. The displacement applied to the BRB, Δ_{BRB}, can be expressed by the following equations. These relationships are illustrated in Fig.8-49, except for the sliding of the reaction blocks which is not shown in the figure:

$$\Delta_{BRB} = D_s - \Delta_{rf} - \Delta_{rs} - \Delta_{bpf} - \Delta_{bps} \text{ (for BRB is in tension)} \qquad (8.6)$$

$$\Delta_{BRB} = D_s + \Delta_{rf} + \Delta_{rs} + \Delta_{bpf} + \Delta_{bps} \text{ (for BRB is in compression)} \qquad (8.7)$$

where: D_s is the shake table's longitudinal displacement output

(a)

(b)
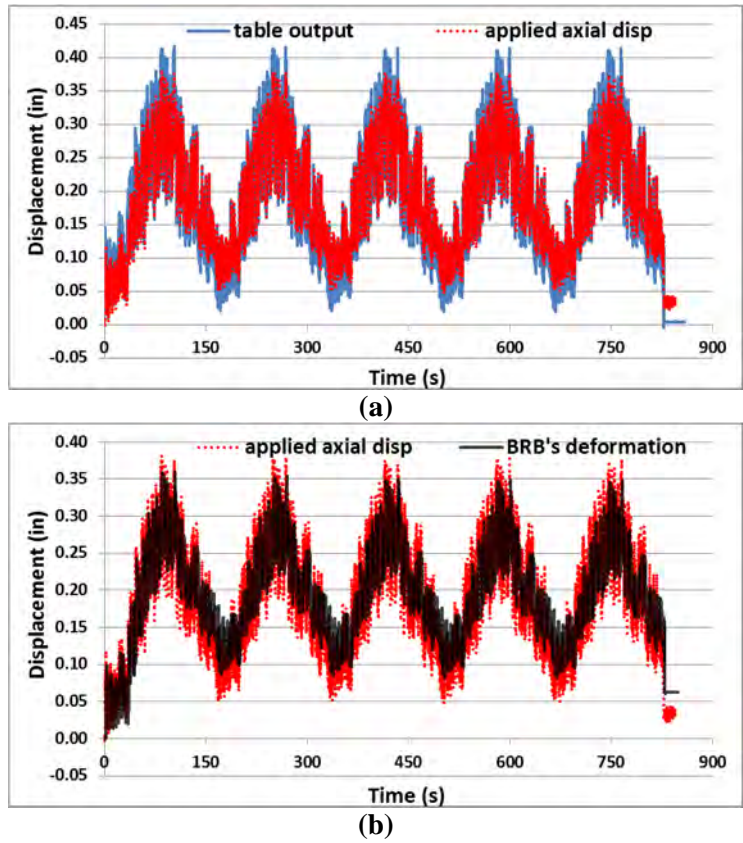
Figure 8-47: Displacement comparison in test BRB-2-2-A for the first 5 cycles of temperature-induced axial displacement history: (a) shake table's longitudinal displacement output and applied axial displacement; (b) axial deformation and applied axial displacement
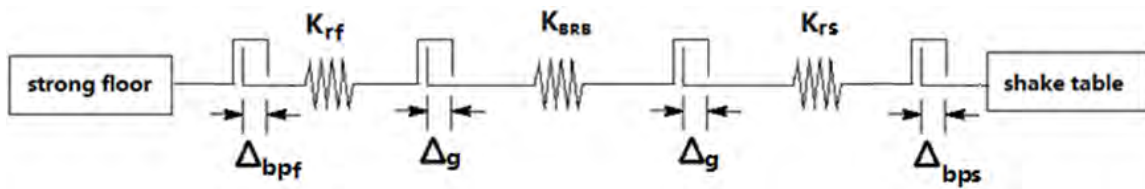
Figure 8-48: Spring and Gap model for the BRB test setup
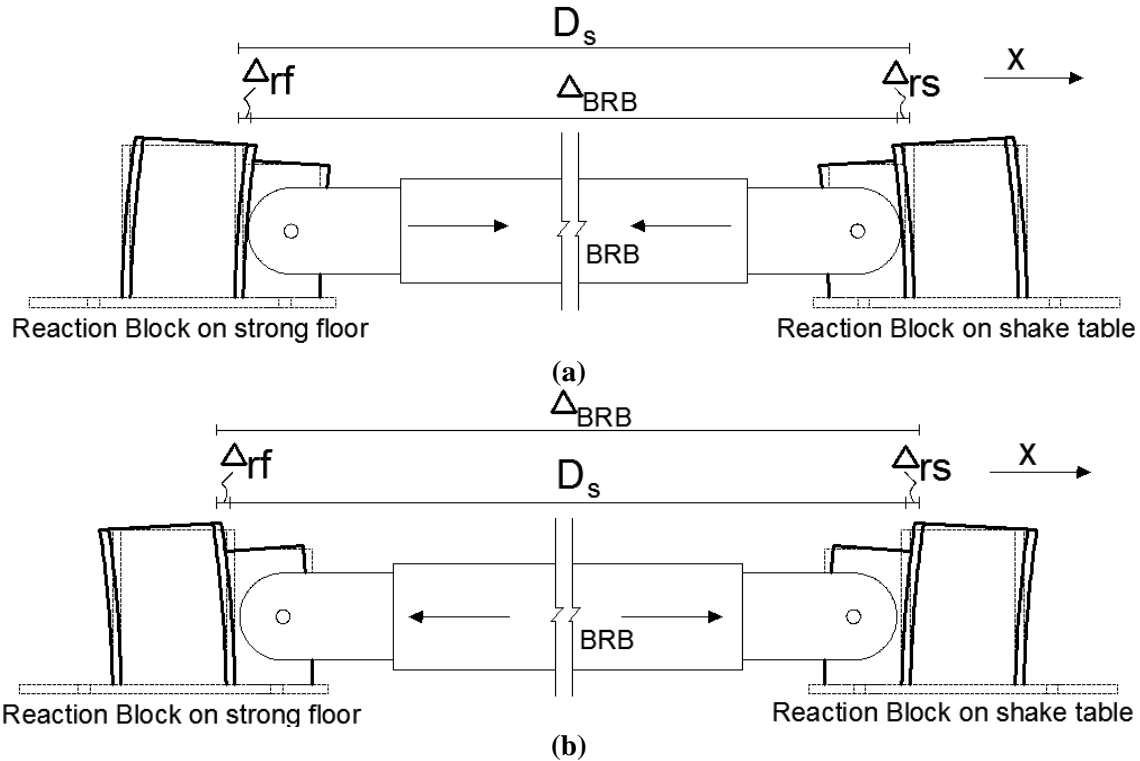
Figure 8-49: Illustration of the deformation of reaction blocks under the BRB axial force (a) BRB under tension force; (b) BRB under compression force

An example of the quantitative values in Equations 8-6 and 8-7 is provided here by using a typical cycle of the displacement history comparisons in Fig.8-47, as shown in Fig. 8-50 for more clarity.

At the time marked by the vertical dotted line, when the BRB reached its maximum tension force in Fig. 8-50a, a displacement difference of 0.048" was observed between the table's longitudinal displacement and the BRB's applied axial displacement, which can be broken down into the following parts (measured experimentally): the sliding displacement of the reaction block on the shake table and strong floor was 0.018" and 0.002", respectively, as shown in Fig.8-51; the corresponding deformation of the reaction block on the shake table and strong floor was 0.02" and 0.008", respectively, as shown in Fig.8-52. At the time marked by the vertical dash-dotted line, when BRB was in maximum compression force in Fig. 8-50a, a displacement difference of 0.025" between the table's longitudinal displacement and the BRB's applied axial displacement, can be observed, which can be broken down into the following parts: the sliding displacement of the reaction block on the shake table and strong floor was 0.004" and 0.001",respectively, as shown in Fig.8-51, and; the corresponding deformation of the reaction block on the shake table and strong floor was 0.01" and 0.01", respectively, as shown in Fig.8-52. The total

326

displacement difference at maximum tension and compression force is 0.073", which corresponds to the displacement range difference between the two histories in Fig. 8-50.

The displacement range difference between these two histories in Fig. 8-50b was 0.0625", which was due to the pin gap in the BRB's connections with the gusset plates in the reaction blocks. It is also the same as the magnitude of the pin gaps reported for BRB-2-1. As a consequence, for the tested BRB, the smaller displacements fluctuations that occur due to temperature cycles as part of the yearly cycle shown in Fig. 8-50 were for the most part "taken" by the slippage of the pin and did not apply force to the BRB.

Note that the stiffnesses of the reaction blocks, K_{rf} and K_{rs}, mentioned above were actually only calculated after later tests (i.e., those described in Section 8.5.3), because the temperature-induced axial displacement history had lots of small cyclic cycles that made it hard to process and calculate stiffnesses based on data of the reaction blocks' deformation processed from the Krypton system.
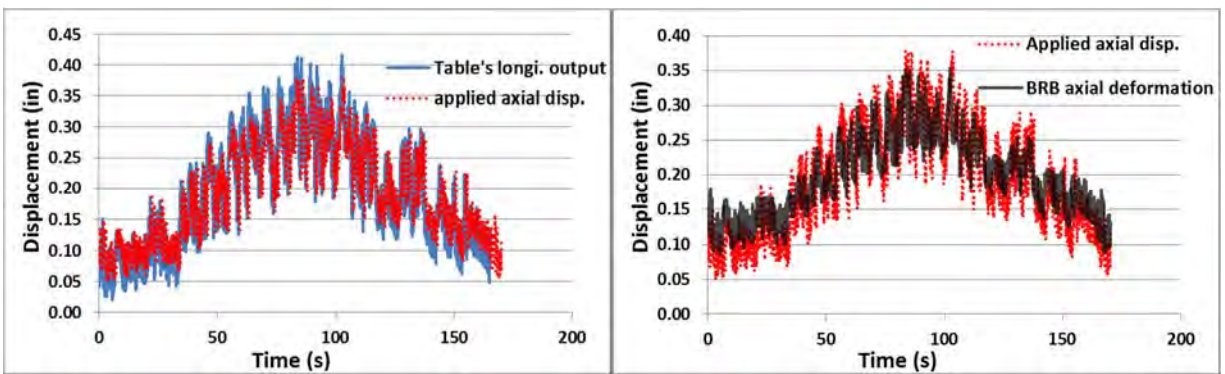
Figure 8-50: Displacement comparison in test BRB-2-2-A for the typical one cycle of temperature-induced axial displacement history: (a) shake table's longitudinal displacement output and axial applied displacement; (b) axial deformation and axial applied displacement

(a)   (b)
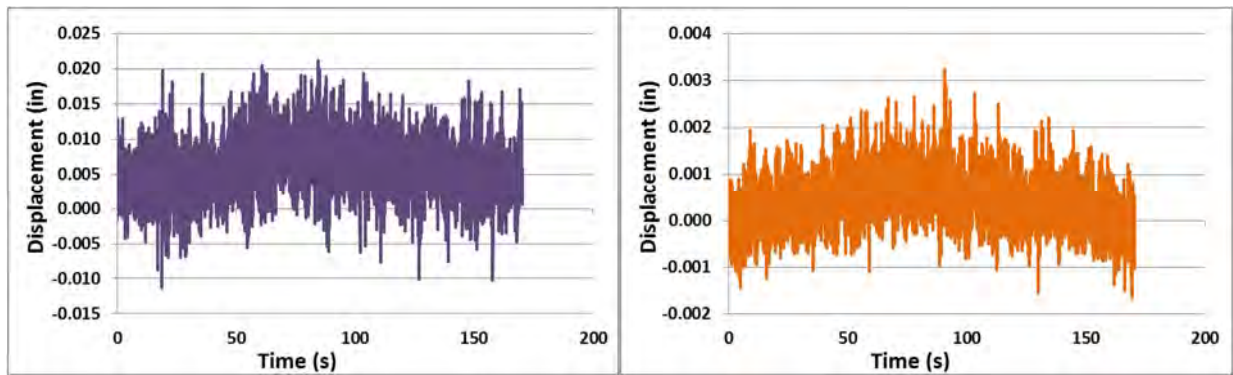
Figure 8-51: The sliding of the reaction block on the (a) shake table; (b) strong floor
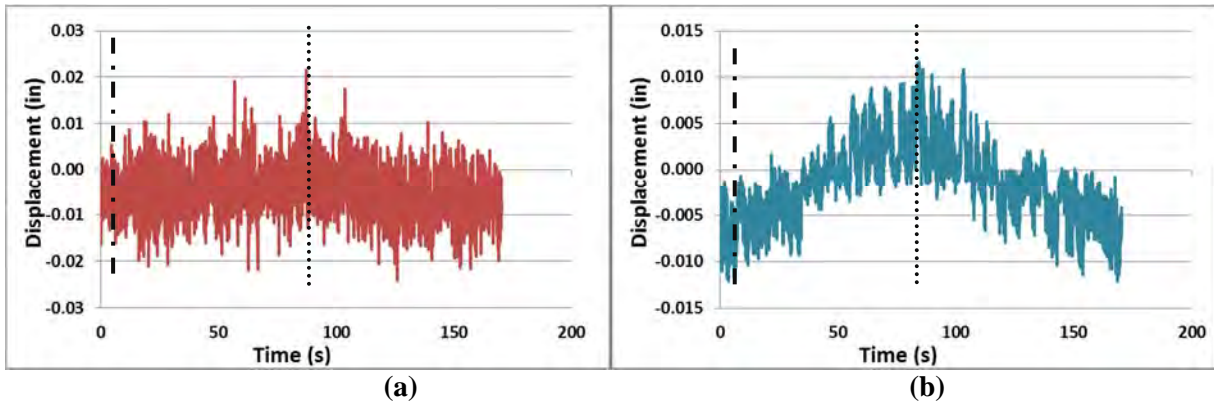
Figure 8-52: The deformation of the reaction block on the (a) shake table; (b) strong floor

8.5.2.3 Test BRB-2-2-B

Since the BRB-2-2 was unfailed after 85 cycles, the original axial displacement history was arbitrarily scaled up by 1.5 times (resulting in the history shown Fig.8-53) and successfully applied to the specimen for 10 cycles in Test BRB-2-2-B. The magnitude of this displacement history was 0.671".
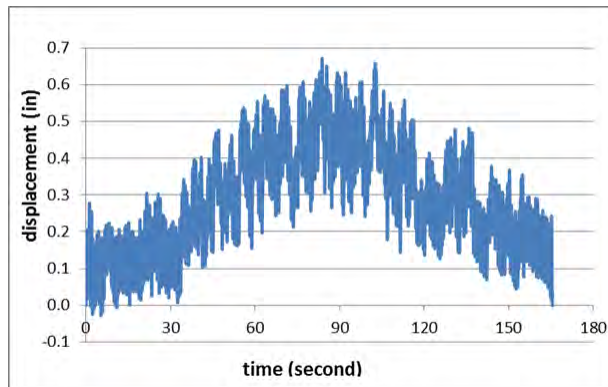
Figure 8-53: Temperature-induced axial displacement history used in test BRB-2-2-B corresponding to 1.5 times of original axial displacement history of one year's temperature fluctuations

The corresponding BRB force versus table's longitudinal displacement output for these 10 supplementary cycles is shown in Fig. 8-54a. Fig.8-54b shows the shape under such one cycle of displacement history.

Fig. 8-55a compares the table's longitudinal displacement output and the BRB's applied axial displacement. Fig. 8-55b compares the BRB's axial deformation and the BRB's applied axial displacement for these ten cycles. The same displacement range difference mentioned before can be observed in both figures.
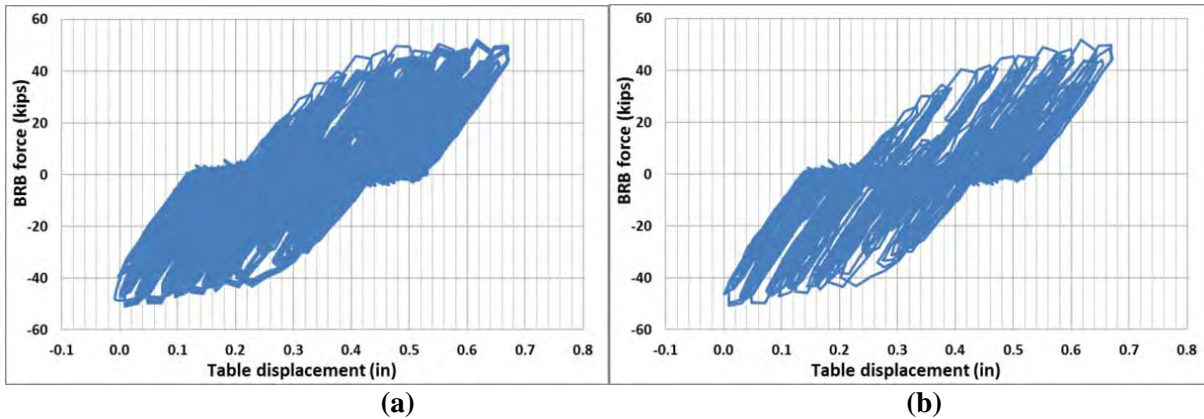
Figure 8-54: BRB-2-2's axial force vs table's longitudinal displacement output in test BRB-2-2-B: (a) 10-cycles; (b) typical one cycle

(a)

(b)
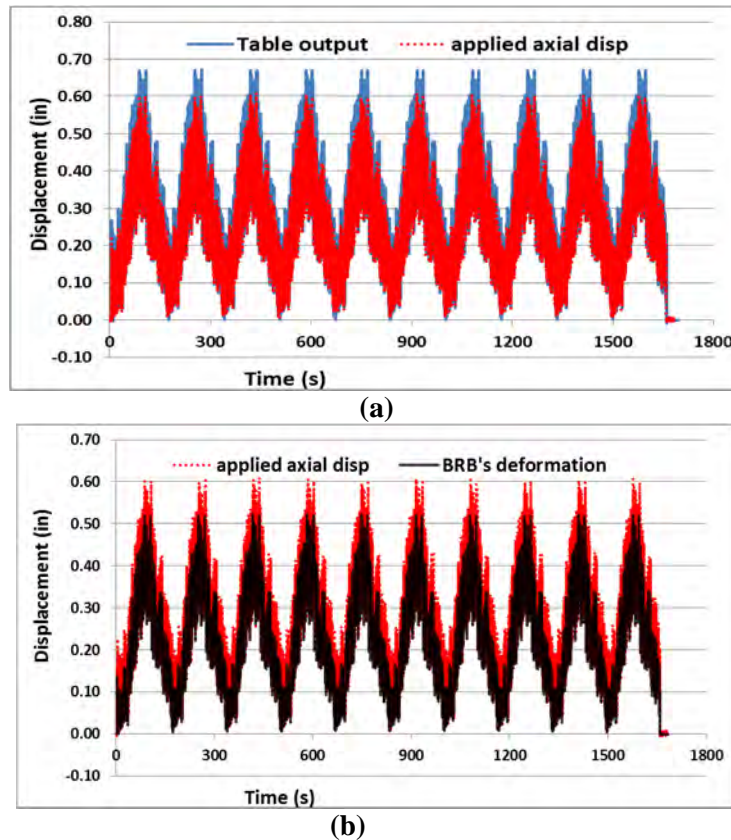
Figure 8-55: Displacement comparisons in the axial displacement test of BRB-2-2-B: (a) table's longitudinal displacement output and applied axial displacement; (b) axial deformation and applied axial displacement

8.5.2.4 Test BRB-2-2-C

Since BRB-2-2 did not fail after applying the supplementary displacement history in Fig. 8-53, the original axial displacement demand (shown in Fig.8-33a) was scaled up to 1.75 times the original

amplitude, with the intention of applying it to the specimen until failure. The resulting displacement history, with a maximum displacement magnitude of 0.783", is shown Fig.8-56.
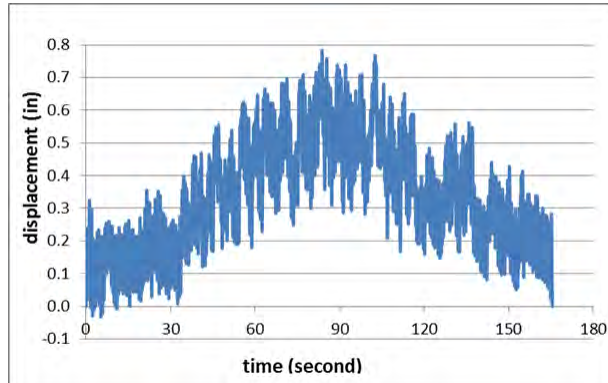
Figure 8-56: Temperature-induced axial displacement history used in test BRB-2-2-C corresponding to 1.75 times of original axial displacement history of one year's temperature fluctuations

BRB-2-2 sustained 9 cycles of this final temperature displacement history, and failed at beginning of the 10th cycle. The BRB force versus shake table's longitudinal displacement for these 9 cycles is shown in Fig. 8-57a. In the 10th cycle, BRB-2-2 failed at the displacement marked by the red cross as shown in Fig.8-57b.

| (a) | (b) |
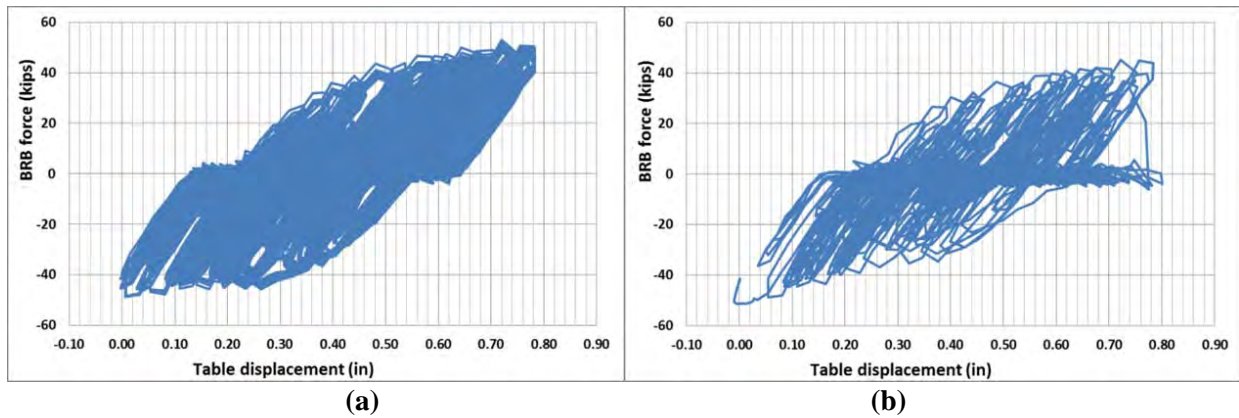
Figure 8-57: BRB-2-2's axial force vs longitudinal table displacement when subjected to supplementary displacement history (illustrated in Fig.8-55): (a) 9-cycles; (b) 10th cycle

Fig. 8-58a compares the table longitudinal displacement output and the BRB's applied axial displacement. Fig. 8-58b compares the BRB's axial deformation and the BRB's applied axial displacement for these five cycles. The same displacement range difference mentioned before can be observed in both figures. Note that, there was an initial axial deformation of the BRB because of the small slippage of the reaction blocks from their original position. However, to be able to compare the BRB deformations with the applied axial displacement history in Fig. 8-58, the BRB's deformation was zeroed at the beginning (only for plotting purposes, as the actual residual deformations of the BRB

continued to be tracked throughout the test sequence). Note that this will also be done for all subsequent BRB test results for the temperature-related bidirectional histories. In all of the above testing for BRB-2-2, no end-plate failure or instability was observed. No visible bulge was observed on the either side of the BRB.
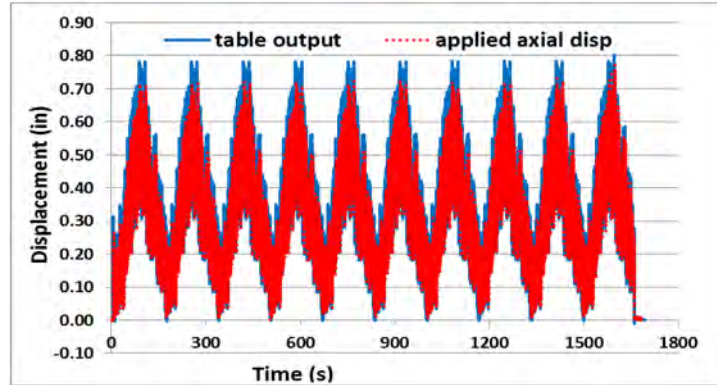
(a)
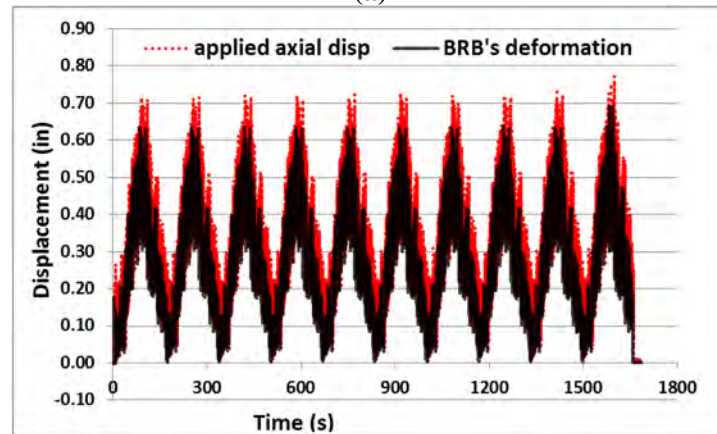
(b)

Figure 8-58: Displacement comparisons in the axial displacement test of BRB-2-2-C: (a) shake table's longitudinal displacement output and applied axial displacement; (b) axial deformation and applied axial displacement

8.5.3 BRB-2-3

8.5.3.1 Overview of Parts of Test BRB-2-3

BRB-2-3 was subjected to a bidirectional qualification test history, followed by temperature-induced axial displacement histories, with the intent to investigate how the seismic demands affected the service life of the BRB.

From the previous tests BRB-2-1 and BRB-2-2, it was observed that the reaction block's slippage and deformation, plus the pin slippages at the BRB's connections, reduced the actual displacement demand to

less than originally desired with the initial protocol. Therefore, the input displacement histories to the shake table were adjusted from the original bidirectional qualification displacement history and temperature-induced axial displacement history mentioned in Sections 8.4.2 and 8.4.3, respectively, by adding extra displacements to account for pin slippage and reaction block's slippage and deformation. The revised time histories were labeled "Extreme Bidirectional Qualification Displacement History-II" and "Temperature-Induced Axial Displacement History-II", respectively.

BRB-2-3 was first subjected to the Extreme Bidirectional Qualification Displacement History-II in test BRB-2-3-A. Then the Temperature-Induced Axial Displacement History-II was successfully applied to the specimen in test BRB-2-3-B for 5 cycles. The slippage of the reaction block on the shake table was found to be large and the anchorage of the shake table's reaction block was secured before continuing testing with more protocols. Test BRB-2-3-C was performed with an axial displacement history to verify that the sliding displacement of the reaction block on the shake table was small and that the anchorage was effective. Ten more cycles of the Temperature-Induced Axial Displacement History-II were then successfully applied to the specimen in test BRB-2-3-D. Since BRB-2-3 has not been subjected to the intended displacement demand at the bidirectional qualification test (as a consequence of slippage prior to the modified connection of the reaction block to the shake-table), the largest loop in the Extreme Bidirectional Qualification Displacement History-II (corresponding to 2 times the design displacement) was re-applied to the specimen in test BRB-2-3-E. Specimen BRB-2-3 failed during that last test.

8.5.3.2 Adjustments to the original test protocols

In revising the displacement protocol for testing BRB-2-3, three factors were taken into consideration, namely:
- To account for the elastic deformations of the reaction block, based on the fact that the maximum total deformations of the two reaction blocks was 0.048" when BRB-2-2 developed its maximum force of 50 kips, with the expectation that BRB-2-3 would reach its maximum design axial force of 90 kips, a total maximum elastic deformation of the reaction blocks of 0.086" was estimated, assuming that deformation is proportional to the applied force.
- The expected amount of slippage of the reaction blocks for test BRB-2-3 was harder to predict. Since this amount is small, and possibly reaching a limit after some displacement, the same total maximum slippage measured for the reaction blocks in test BRB-2-2 was used here, namely 0.025".

- The total pin slippage at both ends of the BRB-2 was 0.0625", as this occurs at zero loads and remains the same, irrespective of load applied.

By adding these three displacements (0.086", 0.025" and 0.0625"), the total displacement lost in the process of the BRB going from maximum tensile to maximum compressive force/displacement in the extreme bidirectional qualification test is 0.174". Half of that 0.174" displacement was added to the longitudinal displacement demand in each cycle of the original extreme bidirectional displacement history as mentioned in Section 8.4.2. The resulting increased displacement history was labeled "Extreme Bidirectional Qualification Displacement History-II". As a consequence of this change, the longitudinal displacement demand at twice the design displacement, which was 1.292" in the original extreme bidirectional displacement history, became 1.379" in the Extreme Bidirectional Qualification Displacement History-II. The resulting longitudinal displacement history in the Extreme Bidirectional Qualification Displacement History-II is shown in Fig.8-59 in solid red line, and compared with the original longitudinal displacement history in dotted black line. The transverse displacement history in the bidirectional test stayed the same as in Fig. 8-27.
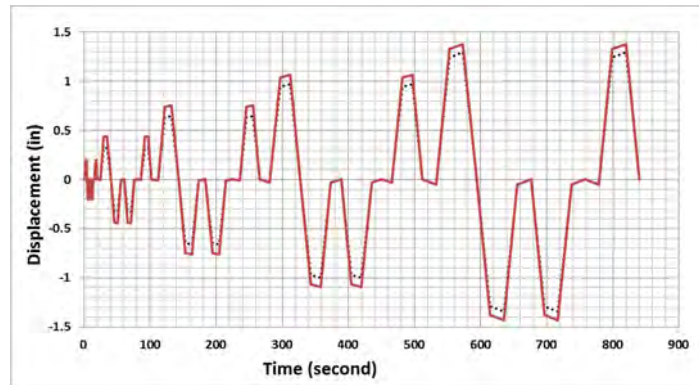
Figure 8-59: Longitudinal displacement history comparison in the Extreme Bidirectional Qualification Displacement History-II (solid line in red) and the original Extreme Bidirectional Qualification Displacement History (dotted line in black)

For the axial temperature-induced displacement history adjustment, BRB-2-2 was expected to develop a maximum force of 50 kips. Therefore, a displacement increase of 0.1355" (the sum of 0.048", "0.025", 0.0625") was added to the range of 0.447" used in the original axial temperature-induced displacement history (illustrated in Fig.8-33a in Section 8.3.3). By scaling up the original axial displacement history accordingly, the new axial displacement (referred to as "Temperature-Induced Axial Displacement History-II") has the range of 0.582" as shown in Fig.8-60.
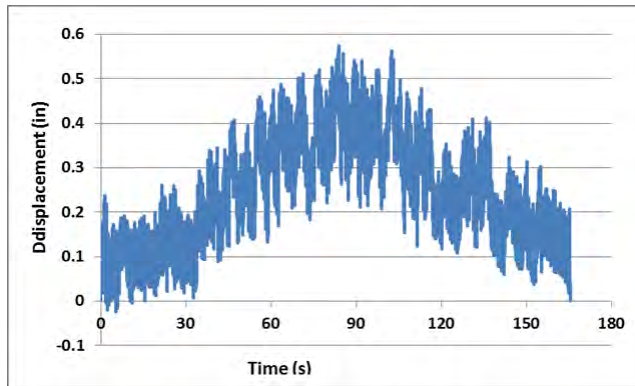
Figure 8-60: Temperature-Induced Axial Displacement History-II corresponding to one year's temperature change

8.5.3.3 Test BRB-2-3-A

BRB-2-3 was subjected to the Extreme Bidirectional Qualification Displacement History-II in test BRB-2-3-A and successfully passed it. Fig 8-61a shows the corresponding hysteretic curve for BRB-2-3's axial force versus axial deformation measured by the Krypton system. The BRB's applied axial displacement was also plotted against the BRB force to show the pin slippage (measured by the Krypton system) in Fig. 8-61b, where the effect of the pin gaps at both ends of the BRB, adding up to a 0.0625" slip at zero load, can be observed.

The BRB's applied axial displacement was not the same on the maximum compression and tension side for some of the cycles. This is due to the unequal slippage that happened between the reaction block and the shake table, as shown in Fig. 8-62a. The slippage of the reaction block on the strong floor, presented in Fig. 8-62b, was much smaller. Fig. 8-63 shows the plots of BRB's axial force versus the slippage of the reaction blocks in Fig. 8-62.

334
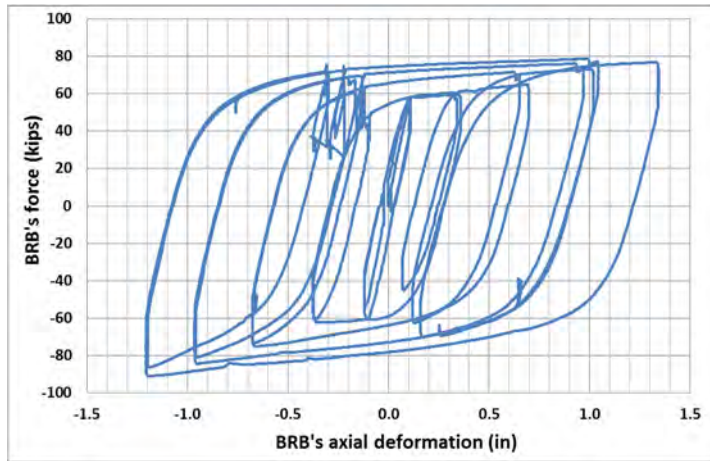
(a)
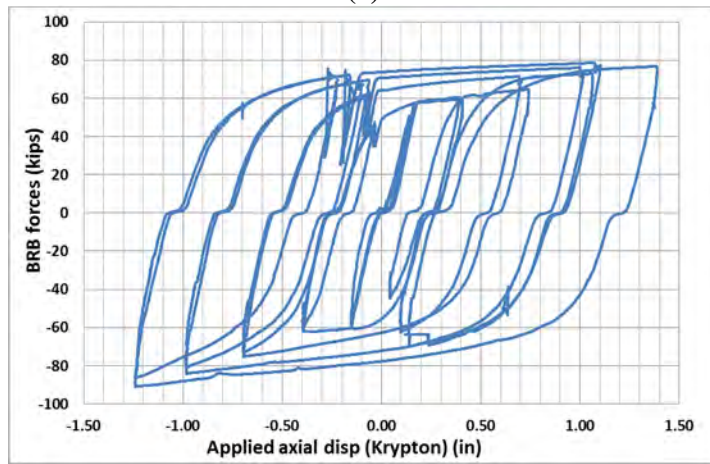
(b)

Figure 8-61: Hysteretic behavior in test BRB-2-3-A: (a) BRB-2-3's axial force vs axial deformation; (b) BRB-2-3's axial force vs applied axial displacement
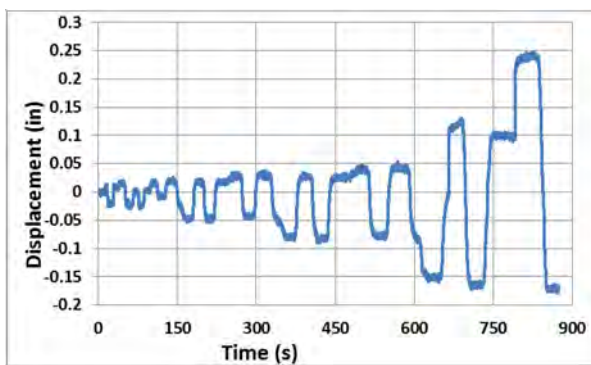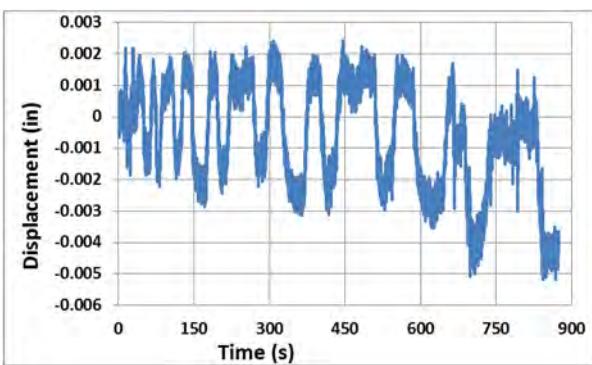
(a)   (b)

Figure 8-62: Slippage of the reaction block on (a) the shake table; (b) the strong floor

335

(a)   **(b)**
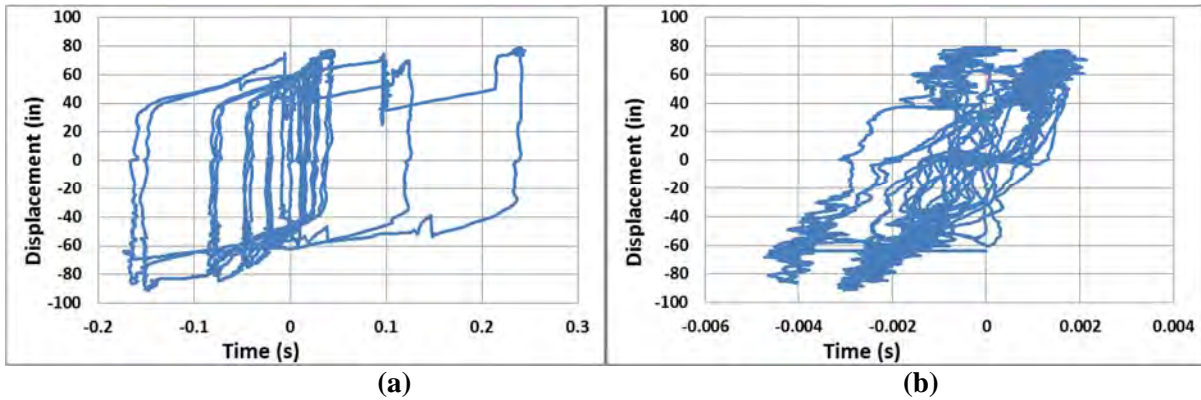
Figure 8-63: BRB's axial force vs slippage of the reaction block on (a) the shake table; (b) the strong floor

8.5.3.4 Test BRB-2-3-B

After the bidirectional qualification test, testing of BRB-2-3 continued with the temperature-induced axial test. The anchorage of reaction block to the shake table was not strengthened before this test because the BRB's force in this test was not expected to be as large as in the bidirectional test. The slippage of the reaction block on the shake table was expected to be similar to the value in the tests of BRB-2-2, and the correction in the Temperature-Induced Axial Displacement History-II already accounted for that slippage.

Five cycles of the displacement history shown in Fig. 8-60 were applied to the specimen in test BRB-2-3-B. The resulting hysteretic curve of BRB-2-3's axial force versus table's longitudinal displacement output for these 5 cycles is shown in Fig. 8-64a. The hysteretic curve under a typical one-cycle displacement history is shown in Fig. 8-64b.

(a)   **(b)**
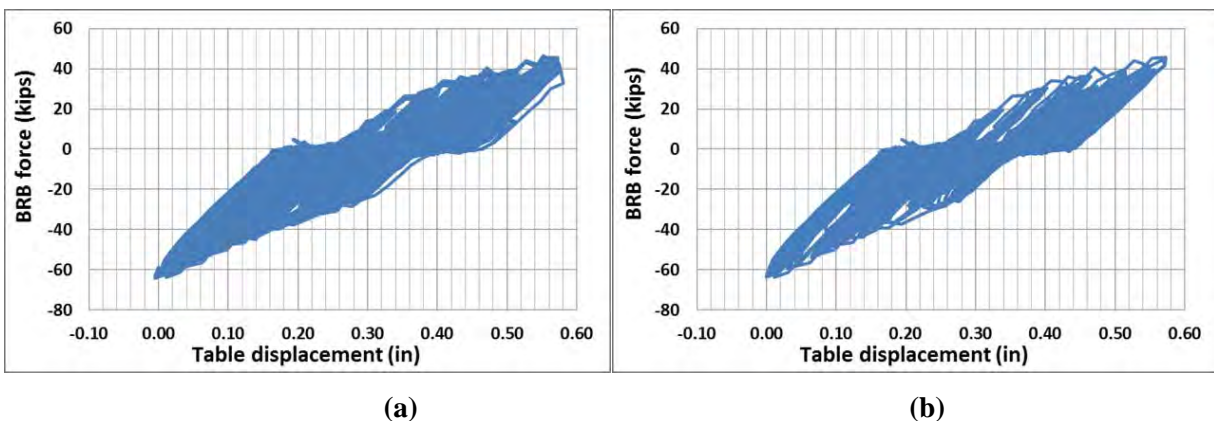
Figure 8-64: BRB-2-3's axial force vs table's longitudinal displacement in test BRB-2-3-B: (a) 5-cycles; (b) typical one cycle

Fig. 8-65 compares the table's longitudinal displacement output and the BRB's applied axial displacement, with a difference of 0.207" observed in the displacement range between the two. This difference was mainly caused by the sliding of the reaction block on the shake table, as shown in Fig. 8-66a, which amounted to approximately 58% of the 0.207" difference. Elastic deformation of the reaction blocks accounted for most of the remaining difference. The sliding of the reaction block on the strong floor in Fig. 8-66b remained very small.
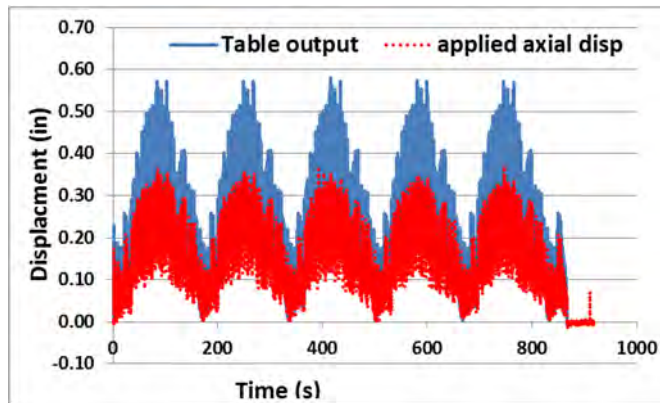
Figure 8-65: BRB-2-3's table's longitudinal displacement output and applied axial displacement in test BRB-2-3-B

Fig. 8-67 compares the BRB's axial deformation and BRB's applied axial displacement for these five cycles. The difference of 0.0625" in the displacement range of these two histories was again due to the pin slippage.

(a)   (b)
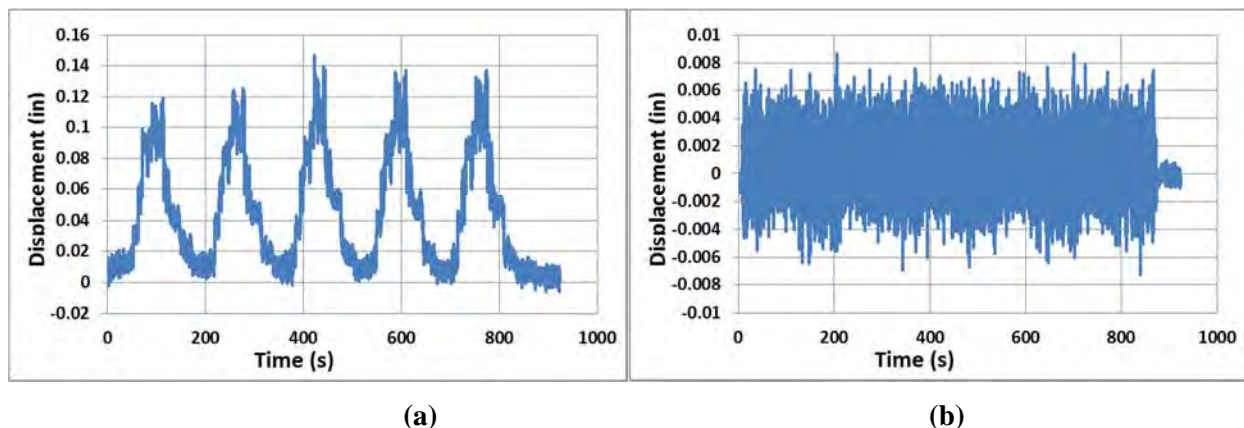
Figure 8-66: The sliding of the reaction block on the (a) shake table; (b) strong floor in test BRB-2-3-B
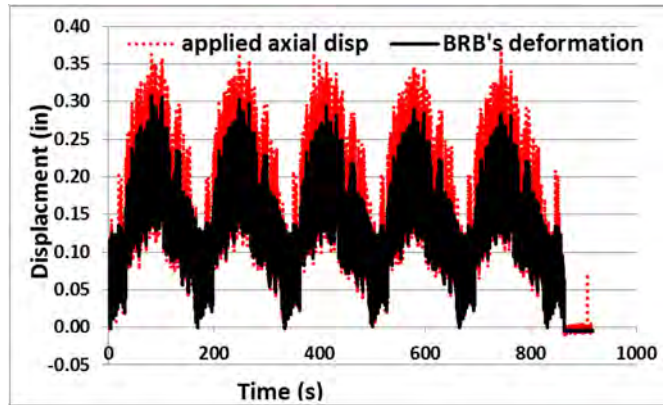
Figure 8-67: BRB-2-3's applied axial displacement and BRB's axial deformation in test BRB-2-3-B

8.5.3.5 Modification of anchorage on the shake table and test BRB-2-3-C

The testing program was interrupted to modify the anchorage of the reaction block on the shake table. The grid of tie-down holes in the shake tables has a center-to-center distance of 24" in both directions. To eliminate the eccentricity, the base plate was extended by welding another plate on its side to be able to engage another line of holes on the shake table to anchor the reaction blocks. To further strengthen the anchorage, two angles were welded to the base plate at one end and bolted down with three bolts each, to engage more holes in the shake table, as shown in Fig 8-68. A total of 10 bolts were used to anchor this reaction block.

To make sure that sliding of the reaction block on the shake table was reduced to an insignificant level by this new anchorage, the single cycle of displacement history shown in Fig.8-69 was applied to BRB-2-3 in the longitudinal (axial) direction. This was called test BRB-2-3-C. Results showed that the maximum slippage, shown in Fig. 8-70, was satisfactorily reduced to 0.03".

The hysteretic curve of BRB-2-3's axial force versus axial deformation is shown in Fig 8-71a. The pin slippage of 0.0625" is shown in Fig.8-71b in the plots of BRB's axial force versus applied axial displacements. Note that there is a residual deformation of 0.34" at the beginning of test BRB-2-3-C, even though the table was at its zero position. The slippage of the reaction blocks on the shake table from the beginning of test BRB-2-3-A and pin gaps accommodated this initial BRB deformation.

338

Figure 8-68 Reaction block on the shake table with modification of anchorage using bolted angles
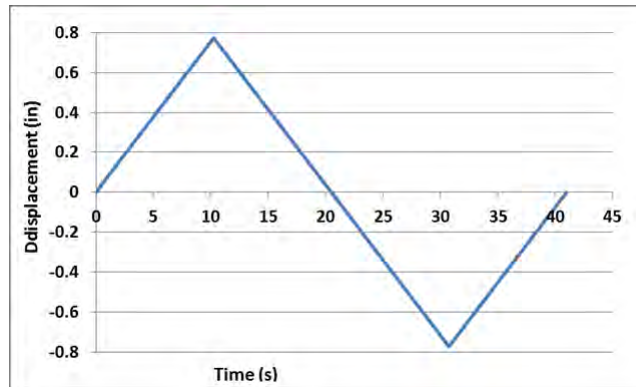
Figure 8-69 Longitudinal displacement history for test BRB-2-3-C
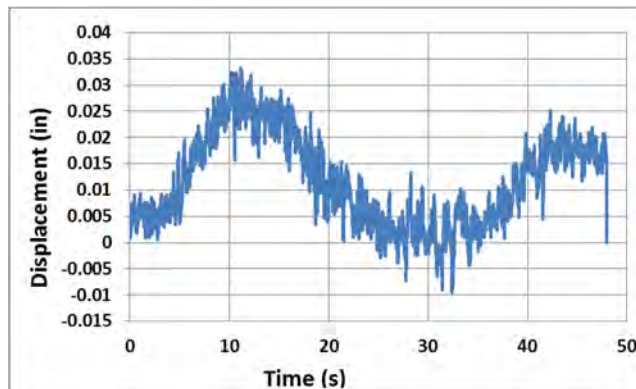
Figure 8-70 Sliding displacement of the reaction block on the shake table in test BRB-2-3-C

(a)   **(b)**
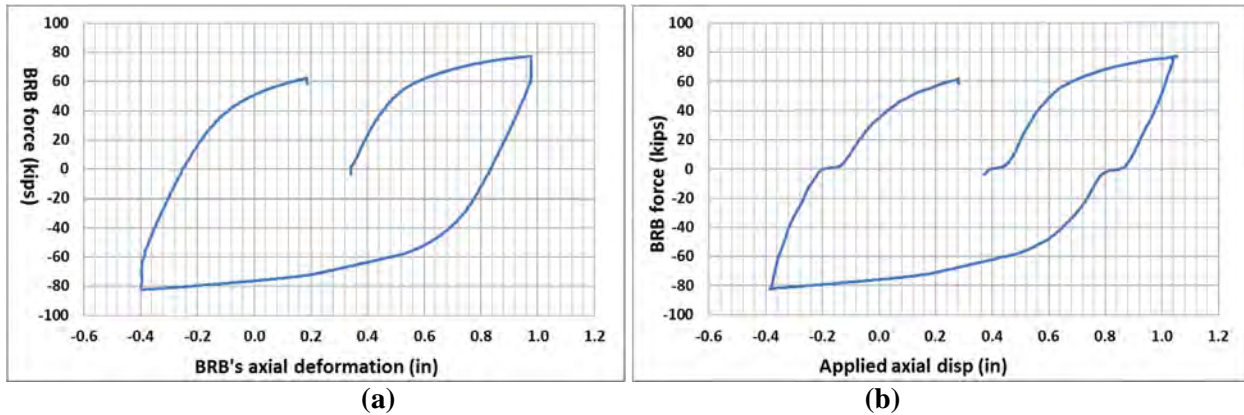
Figure 8-71 Hysteretic behavior of BRB-2-3 in test BRB-2-3-C: (a) axial force vs axial deformation; (b) axial force vs applied axial displacement

Figs. 8-71a and 8-71b show the BRB's axial force versus the deformation of the reaction blocks on the shake table and the strong floor, respectively. The stiffness of the reaction block in each case was obtained by drawing a straight line (black dotted line in Fig. 8-72. The stiffness on the shake table, K_{rs}, and strong floor K_{rf} of 4000 and 5300 kip/in, respectively, can be calculated. Note that accuracy of LEDs' displacements captured by the Krypton camera depends on the relative distance between the LEDs and the camera. Since the krypton camera was further away from the shake table's reaction block than the one on the strong floor, there is more noise in the deformation in Fig. 8-71a than in Fig. 8-71b.

(a)   **(b)**
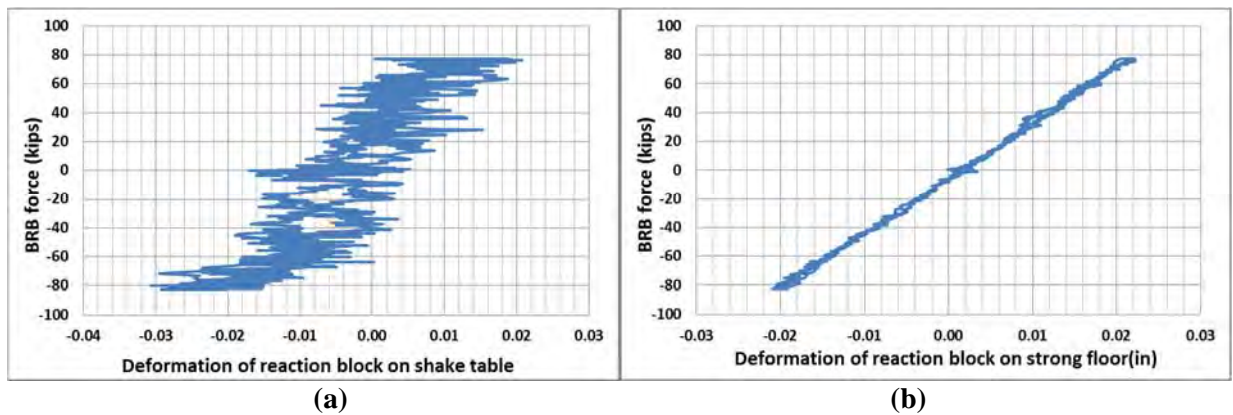
Figure 8-72 BRB's axial force vs deformation of reaction block on the (a) shake table (b) strong floor in test BRB-2-3-C

8.5.3.6 Test BRB-2-3-D

BRB-2-3 was then subjected to 5 supplementary cycles of the Temperature-induced axial displacement history-II (illustrated in Fig.8-60). The corresponding hysteretic curve of BRB-2-3's axial force versus

the table's longitudinal displacement output is shown in Fig 8-73. Note that, the residual force was 60 kips in the BRB after test BRB-2-3-C, and thus at the beginning of test BRB-2-3-D.

(a)   (b)
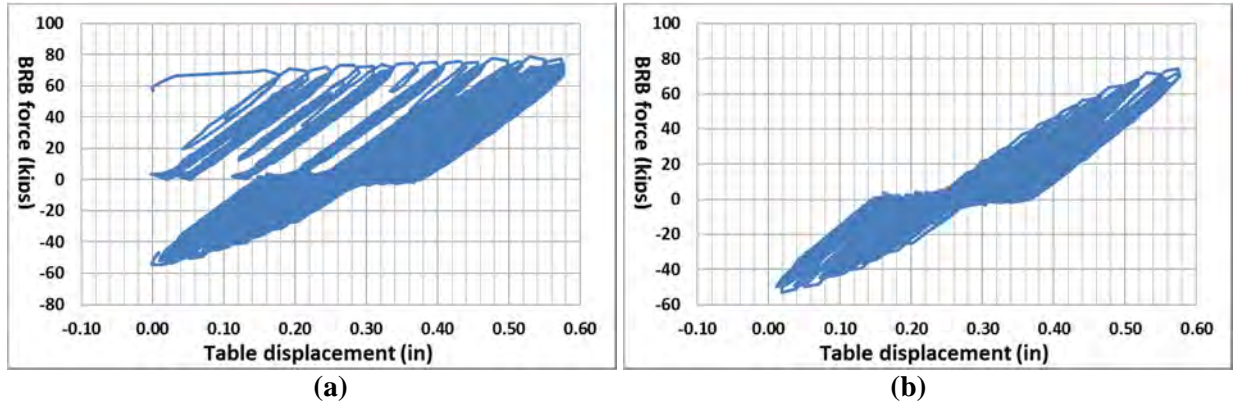
Figure 8-73 BRB-2-3's axial force vs table's longitudinal displacement in test BRB-2-3-D: (a) 5-cycles; (b) typical one cycle

Fig. 8-74 compares the table's longitudinal displacement and the BRB's applied axial displacement. The range difference of 0.073" between the two displacement histories can be observed, which was due to deformation of the reaction blocks (sliding of the block amounted to 0.03", where deformation contributed 0.043" to that difference). The sliding of the reaction blocks on the shake table is shown in Fig 8-75, which shows that the magnitude of sliding had been greatly reduced compared to the values from test BRB-2-3-B (in Fig. 8-66).
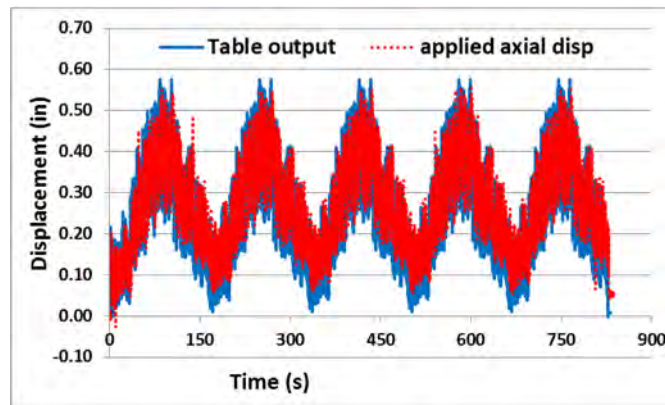
Figure 8-74 BRB-2-3's table's longitudinal displacement output and applied axial displacement in test BRB-2-3-D

35;
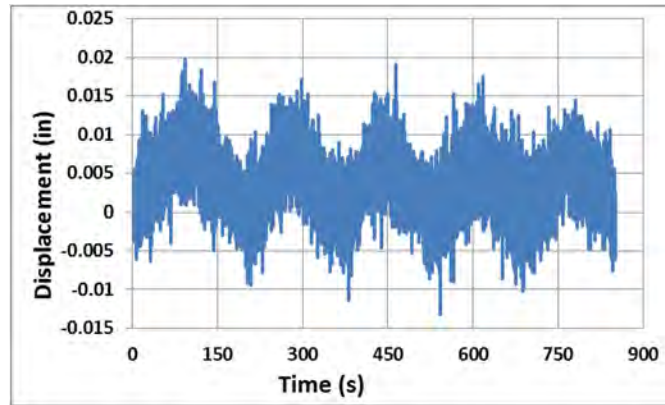
Figure 8-75 The sliding of the reaction block on the (a) shake table in test BRB-2-3-D

Fig. 8-76a compares the BRB's axial deformation and the applied axial displacement for these five cycles, with an enlarged view of the second cycle (included in the dotted box in Fig. 8-76a) presented in Fig. 8-76b to better show the relative responses more clearly. The difference of 0.0625" in the displacement range of these two histories was due to the pin slippage. Note that the magnitude of the BRB's deformation of 0.432" is close to the intended range of 0.447" in the original temperature-induced axial displacement history. Therefore, this proves that the adjustments to the displacement protocol described above were effective.

(a)   (b)
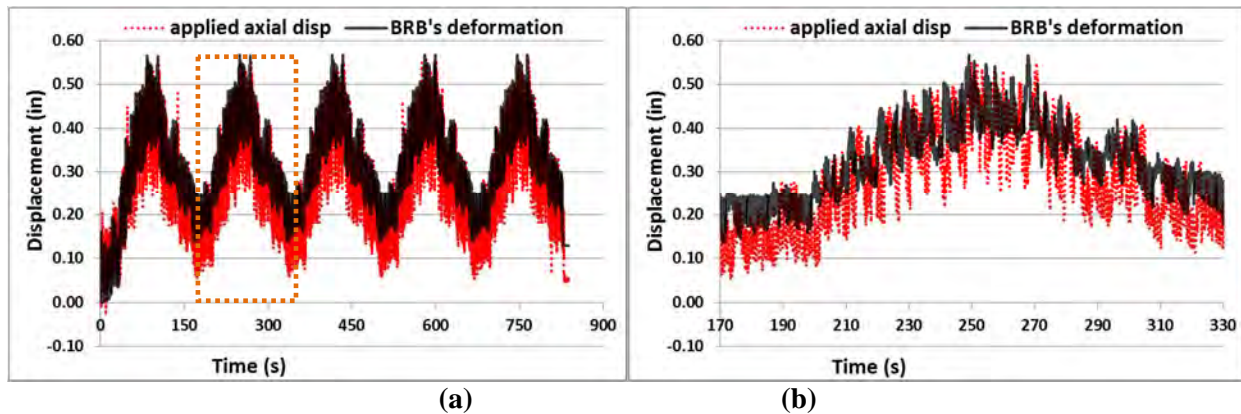
Figure 8-76 BRB-2-3's axial deformation and applied axial displacement in test BRB-2-3-D: (a) for 5 cycles ;(b) second cycle

8.5.3.7 Test BRB-2-3-E

Since BRB-2-3 was not subjected to the full magnitude of the intended displacement demand in the prior bidirectional qualification test, due to the slippage of the reaction block on the shake table, it was re-tested by adding a cycle at a displacement magnitude corresponding to 2 times the design displacement in the Extreme bidirectional qualification displacement history-II. This was labeled test BRB-2-3-E. BRB-2-3

342

failed in that test during at the second small loop in tension when the table was moving longitudinally to the largest displacement of $2D_{bmL}$, as shown in Fig.8-77 by the red cross.
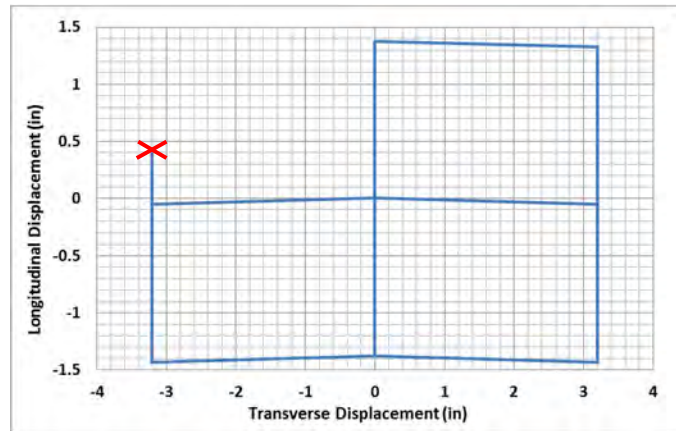
Figure 8-77 Shake table's movement in Test BRB-2-3-E before the specimen failed

The corresponding hysteretic curve of BRB-2-1's axial force versus axial deformation is shown in Figs 8-78a and 8-78b, for cases where the BRB's axial deformation was measured by the SP and Krypton system, respectively. Fig. 8-79 shows the BRB's axial force versus the applied axial displacement measured by the Krypton system, where the effect of the pin gaps at both ends of the BRB, adding up to a 0.0625" slip at zero loads, can be observed. Note that the BRB's axial deformations measured by the Krypton system are not as accurate as the one measured by SP in Fig. 8-78a. Fig. 8-78b is shown here only for comparison with Fig. 8-79, since the BRB's applied axial displacement can only be obtained through measurements by the Krypton system in Fig. 8-79, which includes the slippage of the pins at BRB's two ends. The failure of the BRB is indicated by the red marks as well in Figs. 8-78 and 8-79.

Recall that in Section 8.5.3.1, the axial displacement demand for the cycle corresponding to 2 times the design displacement in the original bidirectional qualification displacement history was 1.292". Since the transverse displacement demand at the cycle of twice the design displacement was 3.204", the axial displacement applied to the BRB was 1.34". Therefore, the total displacement demand of the BRB from maximum tension to maximum compressive should be 2.68". Note that due to the slippage of the reaction block on the shake table throughout all preceding tests in this sequence, there was an initial residual deformation of 0.392" at the start of test BRB-2-3-E. If the hysteretic curves of Fig. 8-78 were shifted to have a zero initial deformation, a maximum tensile and compressive deformation of 1.30" and 1.41" would be observed, respectively. The total applied displacement to the specimen in test BRB-2-3-E is 2.71", which is 1% larger than the desired displacement demand of 2.68". This verifies that the adjustments done to the protocols were effective.

343

Though the specimen successfully finished this qualification test with the bidirectional displacement history-II without failing, the slippage of the reaction block on the shake table caused it not reaching the desired displacement demand in the test protocols. In the supplementary bidirectional test BRB-2-3-E, the specimen was subjected to the intended displacement demand but failed before finishing the whole loop at two times the design displacement. Therefore, it is hard to say that the BRB passed the qualification test. Besides, BRB-2-3 was also applied axial temperature-induced displacement history-II for 10 cycles and the axial displacement history in test BRB-2-3-D. As mentioned in Section 8.5.1, a better way to quantify the BRB's behavior is to compare the cumulative inelastic displacements reached in all tests. This comparison is presented in Section 9 for all of the BRBs tested.

(a)   (b)
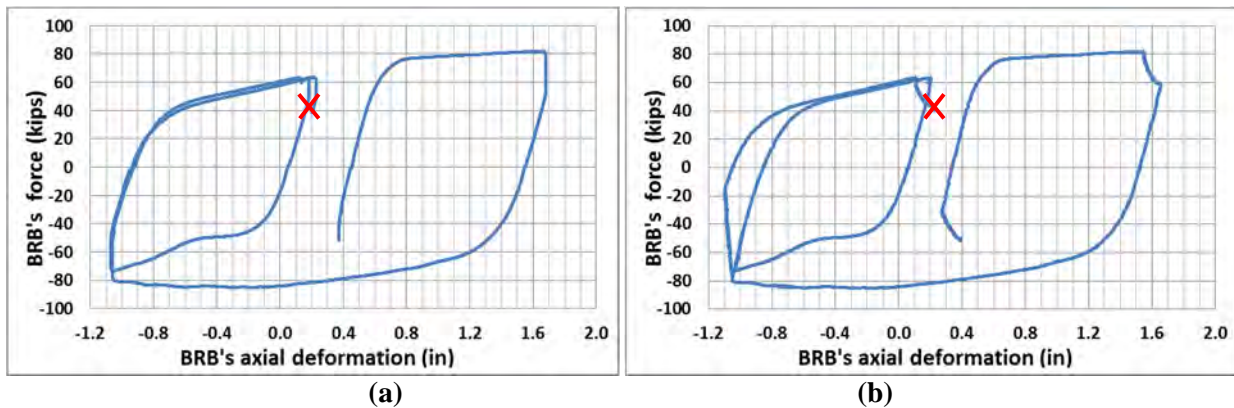
Figure 8-78 Hysteretic behavior of BRB-2-3 in test BRB-2-3-E: axial force vs axial deformation measured by: (a) LPs; (b) Krypton System
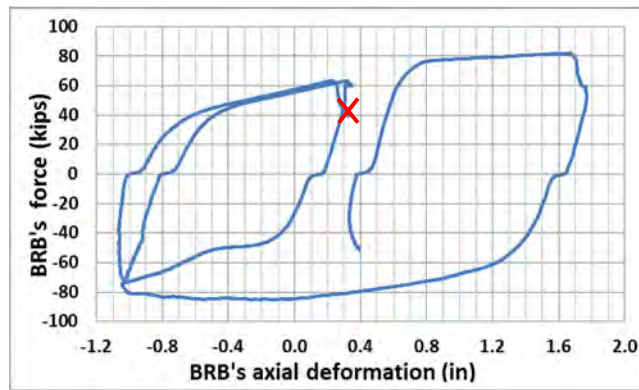
Figure 8-79 Hysteretic behavior of BRB-2-3's axial force vs applied axial displacement in test BRB-2-3-E

In all of the above testing for BRB-2-3, no end-plate failure or instability was observed. After the test, a visible bulge was observed on the northeast side of the BRB. The cause of that bulge and mode of failure of the BRB specimens will be discussed in details in Section 9.1.

8.5.4   BRB-2-4

8.5.4.1 Overview of Parts of Test BRB-2-4

BRB-2-4 was first subjected to a bidirectional displacement history and then a temperature-induced axial displacement history. For consistency, the same Extreme bidirectional qualification displacement history-II and Temperature-induced axial displacement history-II was used for testing BRB-2-4. However, the test sequence was changed from that of test of BRB-2-3 in order to investigate whether a BRB can resist the earthquake demand without failing after being in service for several years (and thus subjected to a history of temperature-induced deformations). A total of 15 cycles of Temperature-related axial displacement history-II was first applied to BRB-2-4 in test BRB-2-4-A. After that in test BRB-2-4-B, the specimen was subjected to the Extreme bidirectional qualification displacement history-II, but failed during the largest cycle corresponding to twice the design displacement.

8.5.4.2 Test BRB-2-4-A

In test BRB-2-4-A, 15 cycles of the Temperature-related axial displacement history-II (illustrated in Fig.8-60) was applied to the specimen. The corresponding hysteretic curve is shown in Fig 8-80a. Except for the first cycle when the BRB was loaded from zero deformation and axial force, the other 14 cycles followed the same hysteresis loop, as shown in Fig 8-80b.

(a)   (b)
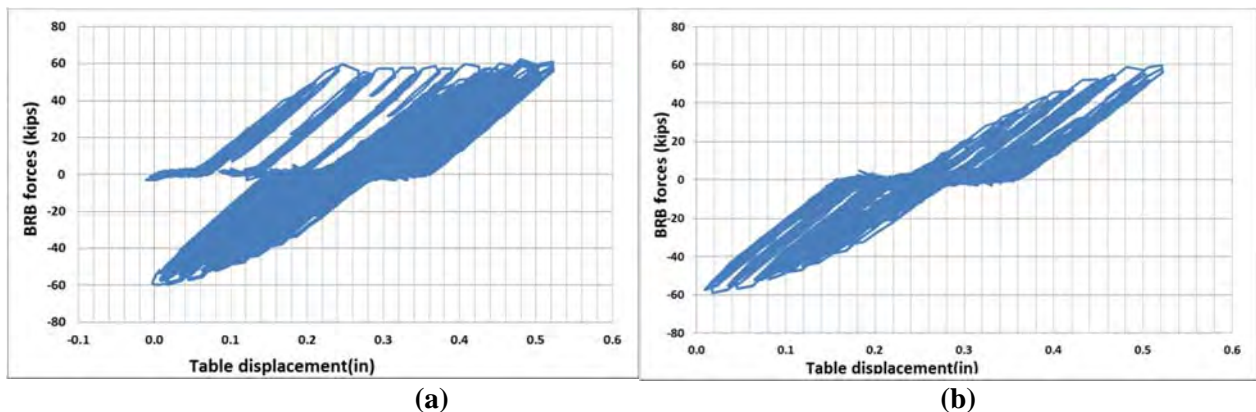
Figure 8-80 BRB-2-4's axial force vs longitudinal table displacement in Test BRB-2-4-A: (a) 15-cycles; (b) typical one cycle

Fig. 8-81a show the table's longitudinal displacement output and the BRB's applied axial displacement under 5 cycles of axial displacement history. The total displacement difference at maximum tension and compression force between the two histories is 0.076", which was caused by the reaction blocks' slippage

and deformation (this is close to the values observed in the test of the previous BRBs, after all corrections to the test set-up). Fig. 8-81b shows the BRB's axial deformation and the BRB's applied axial displacement for the same five cycles and the observed difference of 0.0625" caused by the pin slippage.
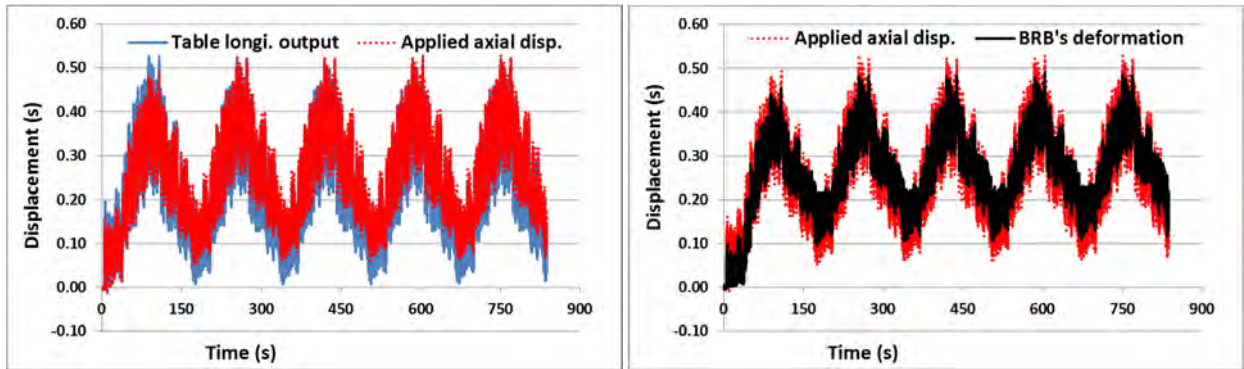
(a)   (b)

Figure 8-81 Displacement comparison in test BRB-2-4-A for 5 cycles of Temperature-induced axial displacement history-II: (a) shake table's longitudinal displacement output and applied axial displacement; (b) axial deformation and applied axial displacement

8.5.4.3 Test BRB-2-4-B

After the Temperature-induced axial displacement history-II was applied to BRB-2-4 for 15 cycles, the specimen was subjected to the Extreme bidirectional qualification displacement history-II in test BRB-2-4-B. It failed during the cycle at two times the design displacement (marked by the red cross) when the shake table was putting the BRB in tension, as shown in Fig.8-82.

The corresponding hysteretic curve of BRB-2-4's force versus axial deformation is shown in Figs 8-83a and 8-83b, for cases where the BRB's axial deformation was measured by the SP and Krypton system, respectively. Fig. 8-40 shows the BRB's axial force versus the applied axial displacement measured by the Krypton system, where the effect of the pin gaps at both ends of the BRB, adding up to a 0.0625" slip at zero load, can be observed. Note that the BRB's axial deformations measured by the Krypton system are not as accurate as the one measured by SP in Fig. 8-83. Fig. 8-83b is shown here only for comparison with Fig. 8-84, since the BRB's applied axial displacement can only be obtained through measurements by the Krypton system in Fig. 8-84, which includes the slippage of the pins at BRB's two ends.

The failure of BRB-2-4 was indicated by the red cross in Figs. 8-83 and 8-84. Apparent softening of the BRB's compression strength can be observed in the cycle at twice the design displacement demand before its failure.
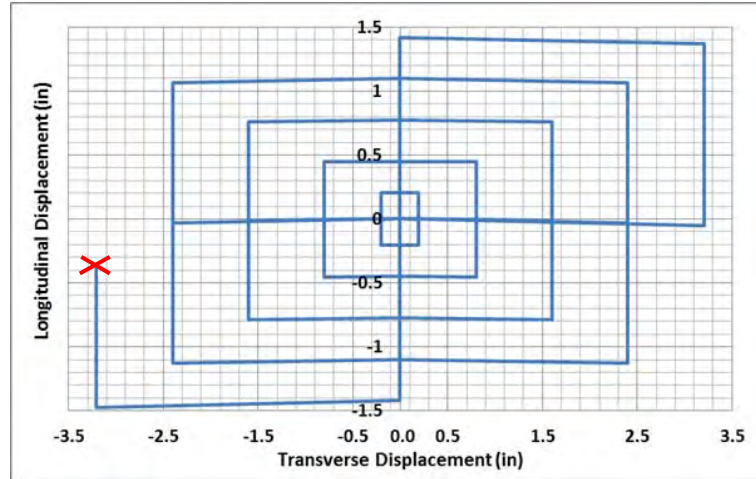
Figure 8-82 Test BRB-2-4-B with Extreme bidirectional qualification displacement history-II: transverse displacement vs longitudinal displacement
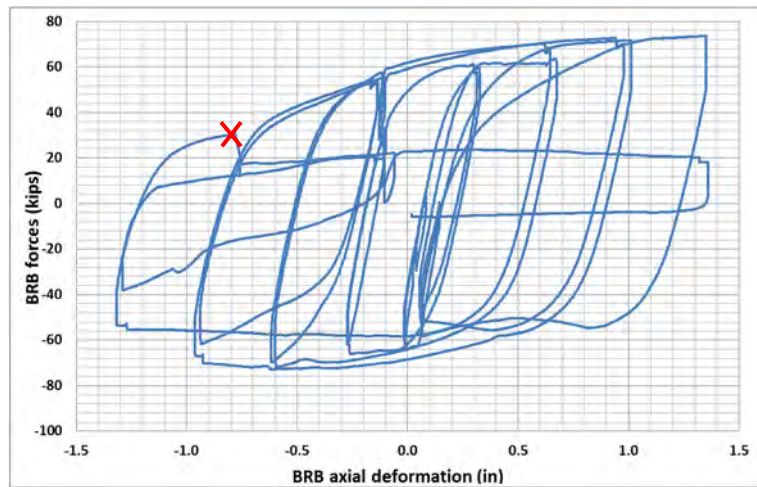
(a)
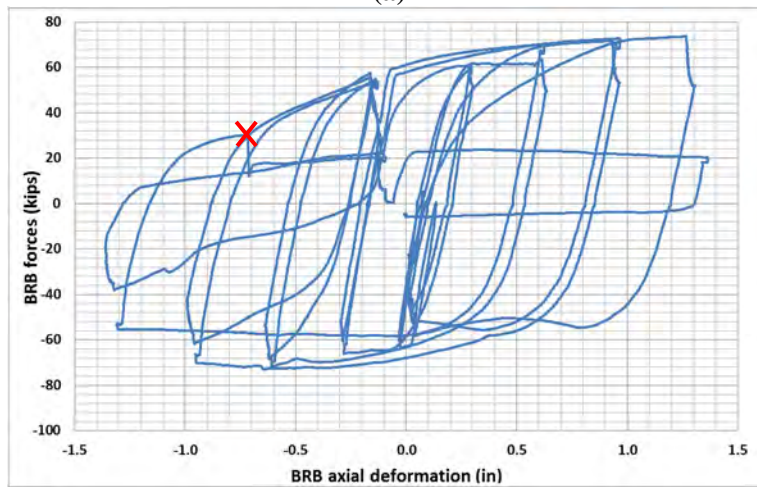
(b)

Figure 8-83 Hysteretic behavior of BRB-2-4 in Test BRB-2-4-B: force vs BRB's axial deformation measured by (a) SPs; (b) Kryptons;

347
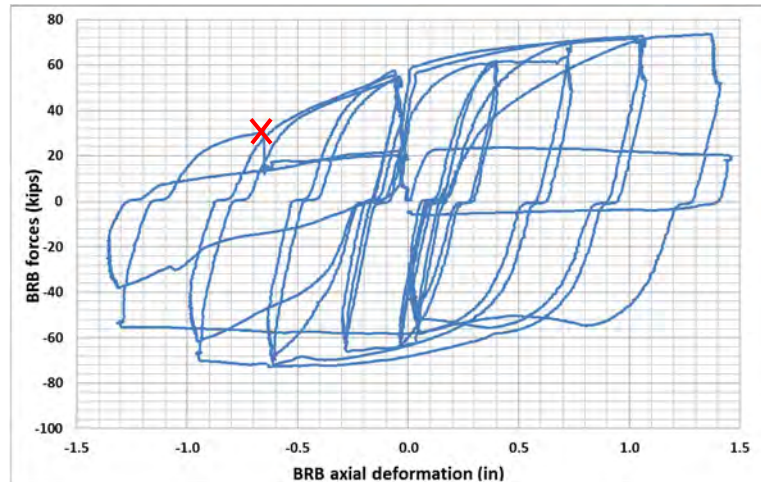
Figure 8-84 Hysteretic behavior of BRB-2-4 in Test BRB-2-4-B: forces vs BRB's applied axial displacement obtained from Krypton system

In all of the above tests for BRB-2-4, no end-plate failure or instability was observed. After the test, a visible bulge was observed on the northeast side of the BRB. The cause of that bulge and mode of failure of the BRB specimens will be discussed in details in Section 9.1.

8.5.5 BRB-1-1

8.5.5.1 Overview of Parts of Test BRB-1-1

BRB-1-1 was subjected to both bidirectional qualification and temperature-induced axial displacement history.

After reviewing the entire set of test results for BRB-2, upon further consideration, the bidirectional qualification displacement demands were judged to be excessively severe. For the reason presented in Section 8.4.1 and further described in detail in the next section (Section 8.5.5.2), a revised bidirectional qualification test protocol labeled "Average Bidirectional Qualification Displacement History" was developed and used in test BRB-1-1-A.

A corrected axial temperature-induced axial displacement history corresponding to a 100-ft bridge was also obtained, to be consistent with the bridge span used in getting the bidirectional displacement demand in Section 8.5.5.4. After accounting for expected reaction blocks elastic deformation and slippage obtained from test BRB-1-1-A (as described in Section 8.5.5.3), and slippage of the pins/bolts at the BRB connections, the resulting new temperature-induced axial displacement labeled "Temperature-Induced Axial Displacement History-III" was used applied to BRB-1-1 for 75 cycles, in test BRB-1-1-B.

348

To complete testing of the specimen already in place, the Temperature-Induced Axial Displacement History-III was arbitrarily scaled up to 1.37 times and applied to the specimen for 10 cycles in Test BRB-1-1-C. After that, BRB-1-1 was subjected to a further amplified axial displacement history, scaled up to 2.05 times from the Temperature-Induced Axial Displacement History-III and used in Test BRB-2-2-D. The specimen completed 3 cycles of this displacement history and failed during the 4th cycle.

8.5.5.2 Adjustments to the extreme bidirectional displacement history

Recall from Section 8.4.1 that the design displacement demand of the BRB in the original extreme bidirectional qualification test history in Fig. 8-27 corresponds to a design ductility of 9 for a design displacement taken as equal to the maximum displacement obtained for the bridge diaphragm model analyzed considering 22-pairs of ground motions. The decision of using the maximum displacement (resulting from all 22-pairs of ground motions) as the design target was revisited and found to be inconsistent with BRB design practice. This was because BRBs are typically designed for twice the design displacements, and design displacements are representative of average response, with the multiplier of 2 intended to account for maximum demands above the average. Therefore, it was decided to use the average displacement in subsequent analyses. This average displacement demands were obtained from new nonlinear time history analyses conducted with the actual BRB properties and bridge characteristics.

In these new analyses, the simplified bridge diaphragm model still had the same strength and stiffness in both the longitudinal and transverse direction. The resulting average displacement demand of the bridge diaphragm model obtained for the 22-pairs ground motions for ductility 9 was the same in both directions, namely 0.779". Since the tested BRB represents the inclined longitudinal BRB in the simplified bridge diaphragm model, the design longitudinal and transverse displacement demand to be imposed to the BRB during the test are 0.549" and 0.779". By using these demands, the corresponding bidirectional qualification displacement history would result in a cumulative inelastic displacement of $265.6D_{by}$ for BRB-1 at the end of the qualification test. This seemed excessive and suggested that the original idea of selecting a target ductility of 9 (which was originally done with the intent to similarly magnify the transverse displacements) was probably impacting unrealistic inelastic demands on the BRB. Therefore, to limit the cumulative inelastic displacements reduced to approximately $200\ D_{by}$ at the end of the qualification test, the target design ductility was reduced to 6, which gives the slightly smaller design longitudinal and transverse displacement demand of 0.438" and 0.619", respectively. The corresponding cumulative inelastic displacement of the qualification test with these displacement demands is $208D_{by}$.

Note that for the actual yield displacement calculated for BRB-1 including the deformation of the core plate outside the yielding core, the cumulative inelastic axial deformation would be 132Δ_{by}, which is smaller than 200 times the yield deformation.

Due to the bolt slippage, the elastic deformation and sliding of the reaction blocks, the BRB couldn't be applied with the intended longitudinal displacement in the bidirectional displacement history, in which adjustments were needed. Since no experimental data can give an estimation of the sliding of the reaction blocks, only two preliminary factors considered to obtain the corrected longitudinal displacement demand were listed as follows:

- Knowing the stiffness of the reaction block and expecting that the BRB will develop a maximum tensile and compressive force of 90 kips (based on results from BRB-1's temperature-induced axial test), the sum of the maximum deformation of the two reaction blocks at this force was calculated to be 0.0375". Since the BRB would be loaded from maximum tensile to compression force in the axial temperature-induced test, a total of 0.075" should be added to the range of the axial displacement history to compensate for these elastic deformations of the test set-up.

- The diameter of the pin holes in the BRB-1's end plates and the gusset plates of the reaction block were design to be 1 17/32" and 1.57", respectively. Therefore, the sum of the estimated gaps between the bolts and their holes are 0.263".

By adding these two displacements (0.075" and 0.263"), the total displacement lost in the process of the BRB going from maximum tensile to maximum compressive force/displacement is 0.338". Half of that 0.338" displacement was added to the longitudinal displacement demand in each cycle of the bidirectional displacement history. The resulting bidirectional qualification displacement history with average displacement demand labeled "Average Bidirectional Qualification Displacement History" is shown in Fig.8-85. Note that in order to keep the axial BRB displacements constant (for sake of following the spirit of the test protocol), the longitudinal displacement of the shake table was adjusted in the same way as what was done (as described in Section. 8.4.2) for the extreme bidirectional displacement history.
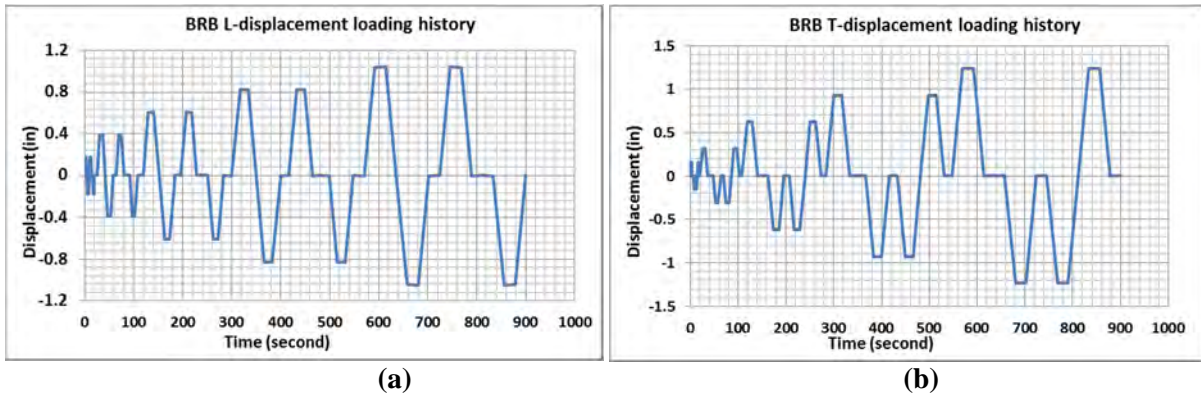
Figure 8-85 Average bidirectional cyclic loading protocol for BRB-1 qualification test: (a) longitudinal displacement vs time; (b) transverse displacement vs time

Note that the longitudinal displacement previously used in the extreme bidirectional qualification test of BRB-2 had loaded the BRB in a sequence of tension-compression-compression-tension, as shown in Fig.8-26a. To make the BRB's hysteretic curves consistent with those of unidirectional tests (which also makes them easier to read), the longitudinal displacement history shown in Fig.8-85a also differs from those used previously by putting the BRB in a tension-compression-tension-compression sequence, as shown in Fig. 8-86a. The corresponding revised loops of longitudinal versus transverse displacement for the average bidirectional qualification test displacement history are shown in Fig. 8-86b.
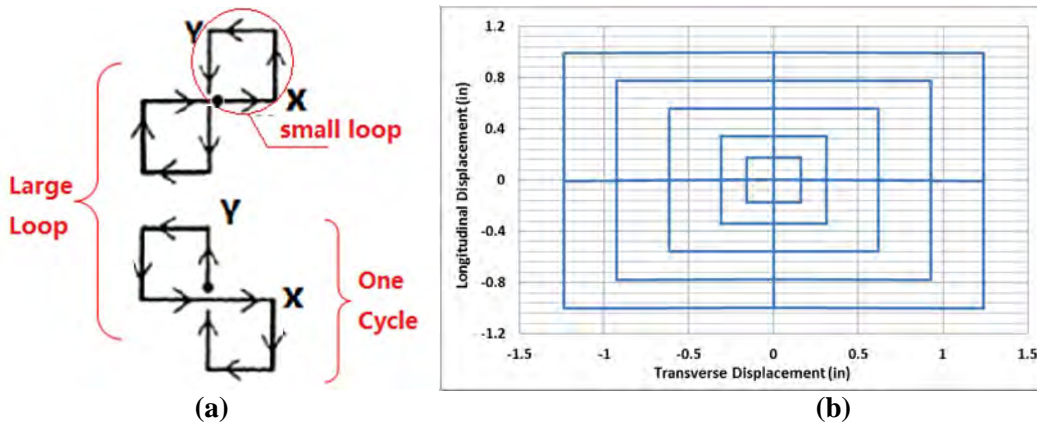
Figure 8-86 Average bidirectional qualification test history for BRB-1 test: (a) loading sequence; (b) longitudinal vs transverse displacement

8.5.5.3 Test BRB-1-1-A

BRB-1-1 was subjected to the Average Bidirectional Qualification Displacement History in test BRB-1-1-A. The resulting hysteretic curve of the BRB's axial force versus axial displacement is shown in Fig. 8-87a. The BRB force was plotted with applied axial displacements in Fig. 8-87b, which shows slippage at zero load to be approximately 0.27". Note that the BRB-1 was connected to the gusset plates in the

reaction blocks using bolts having a nominal diameter of 1.5" and actual measured diameter of 1.47". As mentioned before, the sum of the estimated gaps between the bolts and their holes for BRB-1 are 0.263", which is close to the 0.27" observed in Fig. 8-87.

(a)

(b)
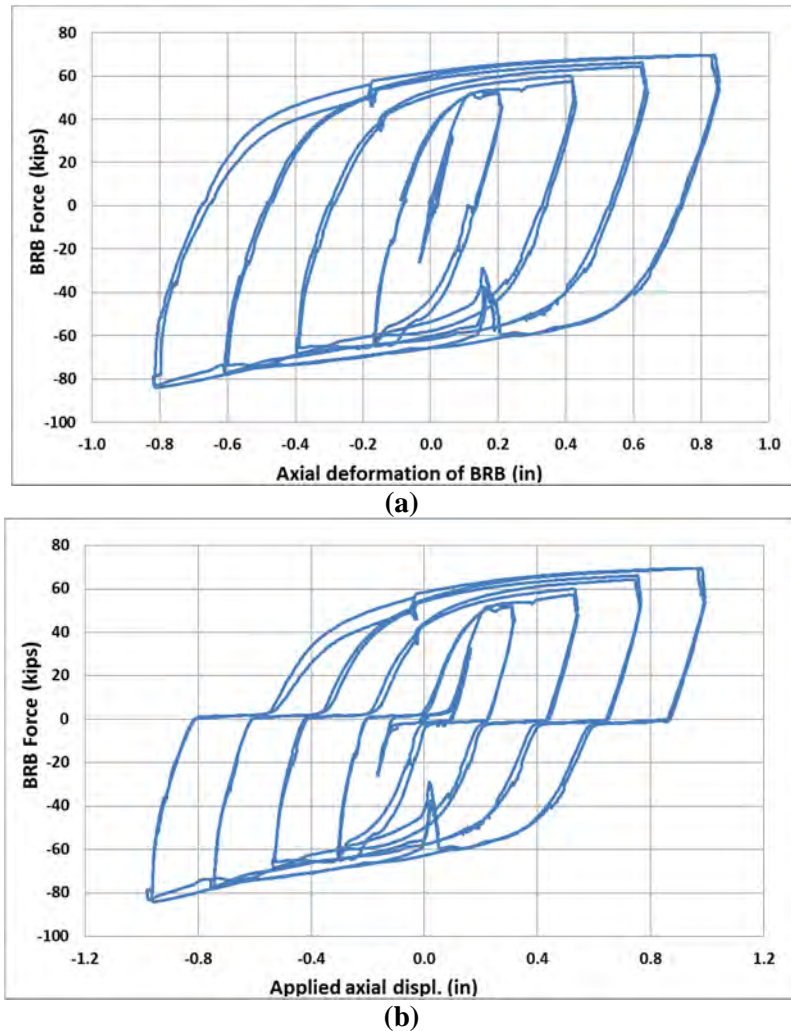
Figure 8-87 Hysteretic behavior of BRB-1-1 in test BRB-1-1-A: (a) axial force vs axial deformation; (b) axial force vs applied axial displacement

The sliding displacements of the reaction blocks were plotted against the BRB's axial force separately for the shake table and the strong floor, in Fig. 8-88. This is used later for determining the portion of the total displacement due to slippage of the reaction blocks, which will be added to temperature-induced axial displacement in subsequent tests.
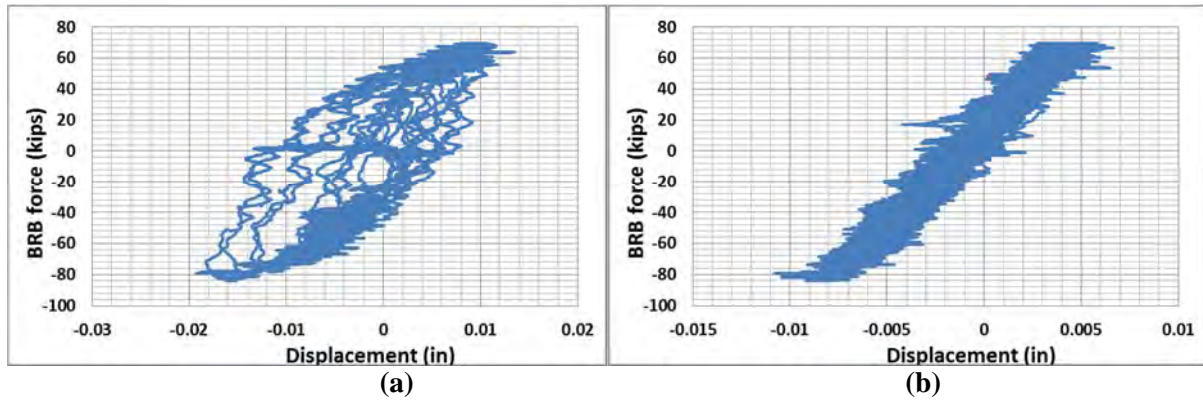
Figure 8-88 BRB-1-1's forces vs sliding displacement of the reaction blocks on (a) shake table; (b) strong floor in test BRB-1-1-A

BRB-1-1 was instrumented with strain gauges on the end plates at both BRB ends, as mentioned in Section 8.3.4. The strain gauge closer to the pin on both end plates in Fig.8-24a, underwent greater strain than the other one. Fig. 8-89a shows the transverse displacement applied to the BRB versus the strain measured by the gage close to the pin hole on the southeast endplate of the BRB (which was the one recording the largest strains). For comparison, the BRB's axial force versus strain from the strain gauge close to the cover plate on the same end plate of the BRB is shown in Fig. 8-89b. When the BRB was subjected to longitudinal displacement, the transverse displacement stayed unchanged, and the changes in the axial force of the BRB caused increases in strains, reflected in the horizontal part of the curve plotted in Fig.8-89a. When the longitudinal displacement remained the same, the strain in the plate changed proportionally with the applied transverse displacement. The maximum strain was 1.03×10^{-3} in/in, which indicates that the end plates remained elastic, as the yield strain of the steel material is 1.45×10^{-3} in/in.
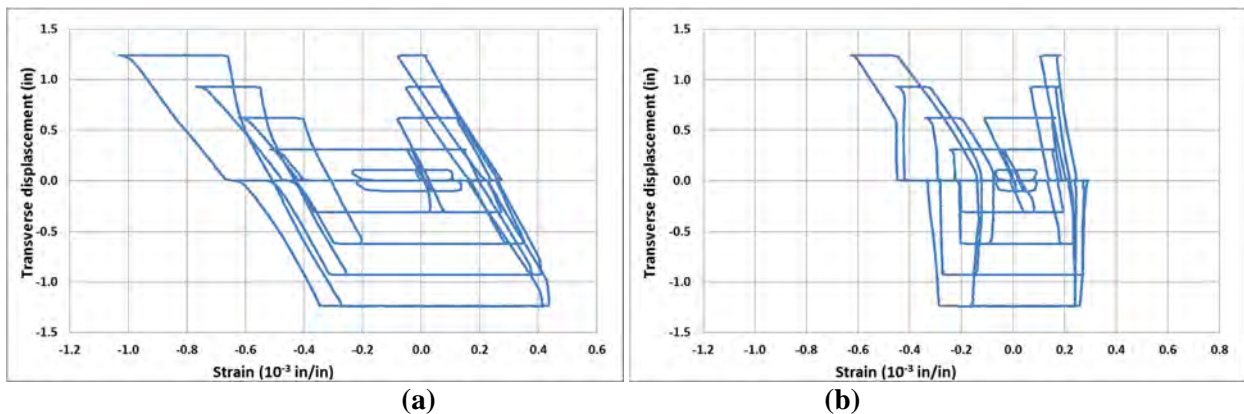
Figure 8-89 BRB-1-1's axial force vs strain recorded on the southeast end plate: (a) strain gauge close to the pin; (b) strain gauge close to the cover plate

353

8.5.5.4 Adjustments to the temperature-related axial displacement history

As mentioned in Section 8.4.3, the original temperature-induced axial displacement history (Fig. 8-33a) that had been used in testing the BRB-2s was actually developed for the case of a longitudinal BRB in a 200 ft long bridge. However, somewhat inconsistently, the displacement demands in the bidirectional qualification test were obtained for a BRB in a 100 ft long bridge. Therefore, to eliminate this discrepancy for all BRB-1 tests, a corrected temperature-induced axial history corresponding to that expected in a 100-ft bridge was obtained, with a magnitude of 0.224" as shown in Fig.8-89. Note that this amplitude is half of that shown in Fig.8-33a.
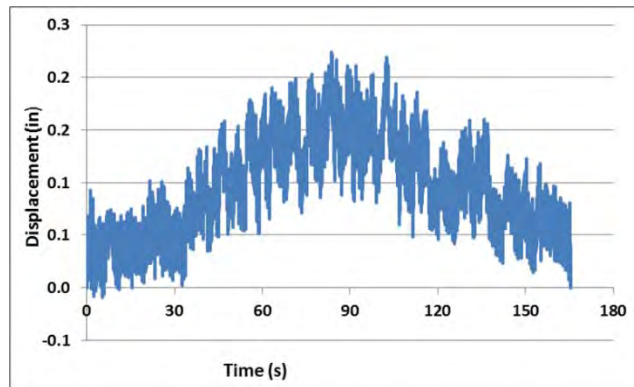
Figure 8-90 Axial displacement history of one year's temperature fluctuations corresponding to 100 ft long bridge

Furthermore, testing of BRB-2s showed that, because of the small displacement amplitude in the corrected temperature-induced axial displacement history corresponding to the 100-ft bridge, deformations of the test set-up (such as slippage and deformation of the reaction blocks) and slippage the pins/bolts at the BRB connections can be non-negligible. For example, the core of a BRB connected with pin undersized compared to their holes could be subjected to less strains (or even, for extremely large gaps between the pins and their holes, no strain at all) during the axial test due to temperature change. Given that not all BRBs are constructed with pinned ends, a new temperature-induced axial history was developed by scaling up the corrected axial displacement history (for the 100 ft long bridge), to strain the BRB core as if the original protocol had been applied to BRB connected in a manner that did not allow slippage at their ends, and to eliminate the loss in displacements applied to the BRB due to reaction set-up deformations.

Three factors are considered to obtain the corrected displacement history. Besides the elastic deformation of the reaction blocks and the bolt slippage, which were added to the Average Bidirectional Displacement History in Section 8.5.5.2, the sliding of the reaction blocks is also included. Recall from Fig.8-88 that

the sliding of the reaction block on the shake table was 0.011" and 0.016" at tensile and compressive forces of 60 kips, and that the sliding of the reaction block on the strong floor was 0.006" and 0.007" at the same tensile and compressive forces. The total sliding displacements considered in both reaction blocks was therefore 0.04". For this case, the bolt slippage part is 0.27" (close to 0.263" used in Section 8.5.5.2), as shown by the bidirectional test hysteretic curve in Fig.8-87b. The total elastic deformation of the reaction blocks is 0.05" considering a different maximum tensile and compressive force of 60 kips (based on results from BRB-1's temperature-induced axial test).

The three displacements (0.04", 0.27", and 0.05"), summed up to 0.36", were added to the displacement range of 0.224" in the corrected temperature-induced axial displacement history, to produce a revised displacement history having a magnitude of 0.584". The corrected temperature-induced axial history in Fig.8-90 was scaled up to have this range of 0.584" as shown in Fig.8-91 (named as "Temperature-Induced Axial Displacement History-III").
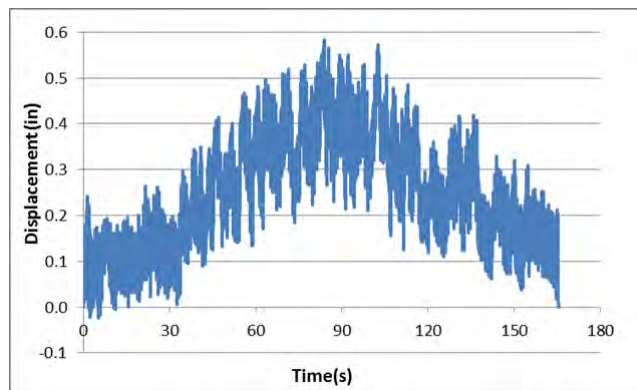
Figure 8-91 Temperature-induced axial displacement history-III considering the bolt gaps and reaction block's slippage and deformation

8.5.5.5 Test BRB-1-1-B

The Temperature-Induced Axial Displacement History-III was applied to BRB-1-1 for 75 cycles in test BRB-1-1-B. The corresponding hysteretic curve of BRB-1-1's axial force versus table's longitudinal displacement output for 10 cycles is shown in Fig 8-92.
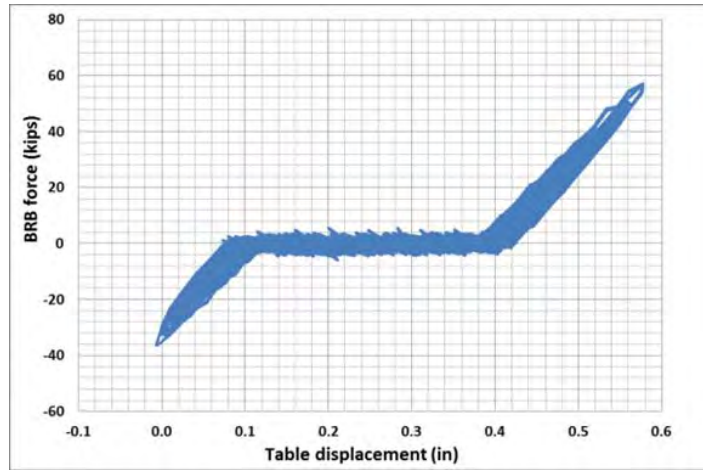
Figure 8-92 BRB-1-1's axial force vs longitudinal table displacement in Test BRB-1-1-B for10 cycles

Fig. 8-93a compares the table's longitudinal displacement output and the BRB's applied axial displacement under 10 cycles of axial displacement history. The total displacement difference at maximum tension and compression force between the two histories is 0.095", which was caused by the reaction blocks' slippage and deformation and is close to the observed values in the test of the previous BRBs. Fig. 8-93b compares the BRB's axial deformation and the BRB's applied axial displacement for the same ten cycles; the difference of 0.27" caused by bolt slippage at the ends of the BRB is observed.

| (a) | (b) |
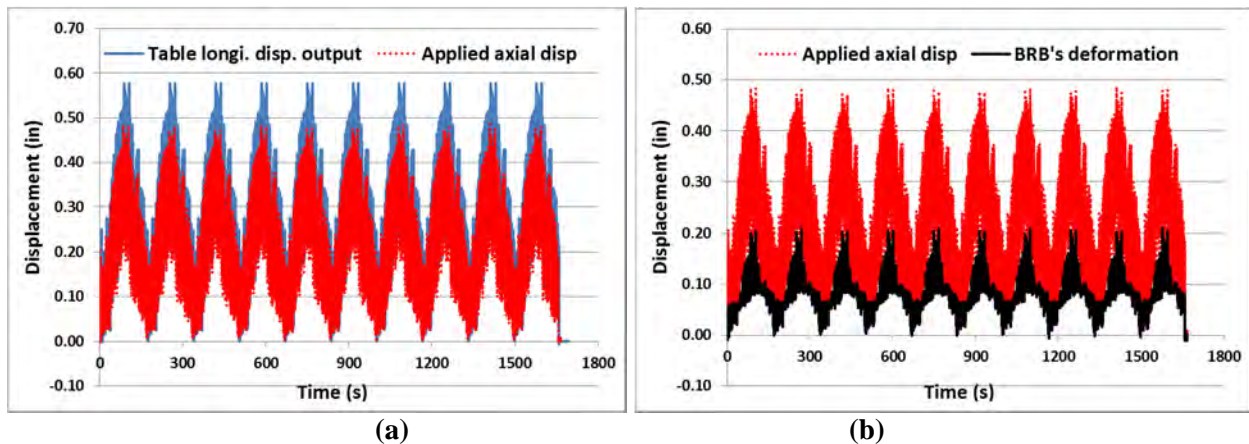
Figure 8-93 Displacement comparison in test BRB-1-1-B for 10 cycles of temperature-induced axial displacement history-III: (a) shake table's longitudinal displacement output and applied axial displacement; (b) axial deformation and applied axial displacement

The magnitude of deformation in the BRB is 0.213", which is close to the magnitude of the axial displacement history in Fig.8-90 corresponding to a 100 ft bridge. It is seen that the BRB remained essentially elastic under this loading history. Therefore, it could be subjected to substantially more than 75 years of temperature-induced history, and it was not practical to continue testing at that displacement

amplitude until fracture of the BRB (as elastic fatigue-related fracture typically occurs after hundreds of thousands of cycles).

8.5.5.6 Test BRB-1-1-C

Since BRB-1-1 did not fail after 75 years of repeated Temperature-Induced Axial Displacement History-III, the displacement history in Fig. 8-91 was arbitrarily scaled up to a displacement history of 0.8" (i.e., 1.37 times the magnitude of the previously applied history) and applied to the specimen for 10 cycles in test BRB-1-1-C. The corresponding plot of the BRB's axial force versus table's longitudinal displacement for these 10 cycles is shown in Fig.8-94a. Fig. 8-94b shows the results for one cycle of displacement history.

(a)   (b)
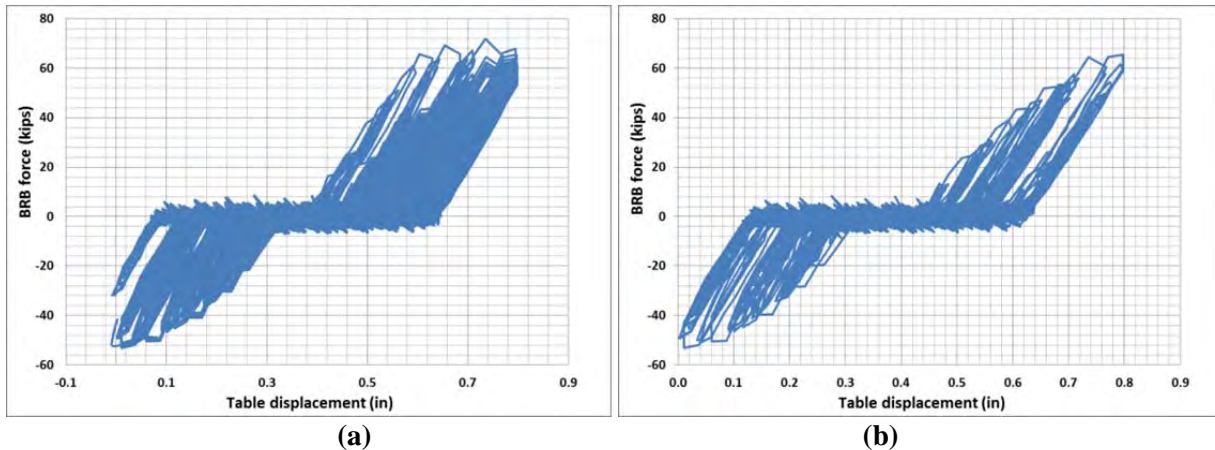
Figure 8-94 BRB-1-1's axial force vs table's longitudinal displacement output in test BRB-1-1-C: (a) 10-cycles; (b) typical one cycle

Fig. 8-95a compares the table's longitudinal displacement output and the BRB's applied axial displacement under 10 cycles of axial displacement history. Fig. 8-95b compares the BRB's axial deformation and the BRB's applied axial displacement for the same ten cycles. The same difference in displacement ranges mentioned before can be observed in both figures.

(a)   **(b)**
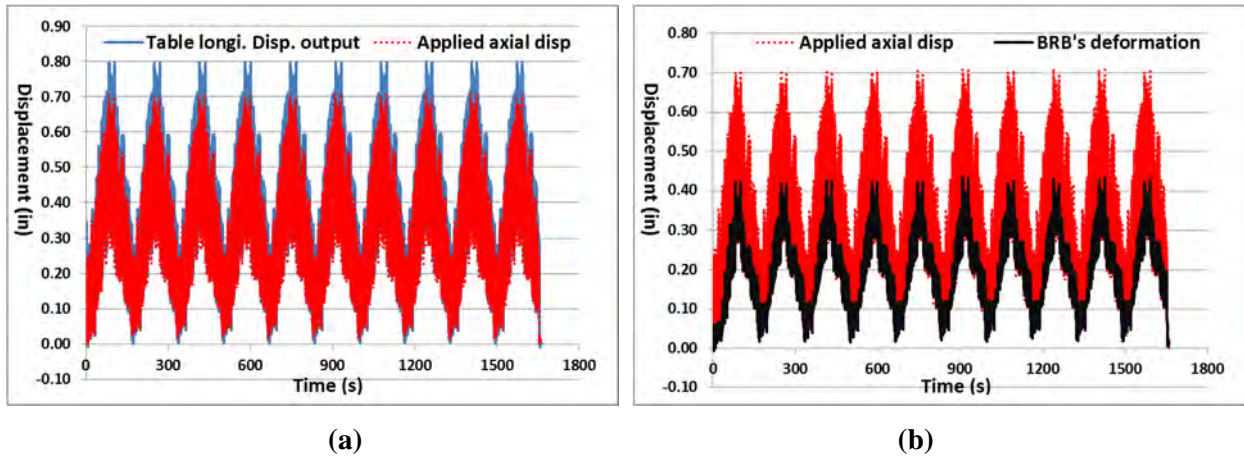
Figure 8-95 Displacement comparison in test BRB-1-1-C for 10 cycles:(a) shake table's longitudinal displacement output and applied axial displacement; (b) axial deformation and applied axial displacement

8.5.5.7 Test BRB-1-1-D

Since BRB-1-1 did not fail after applying the supplementary displacement history in test BRB-1-1-C, the temperature-induced axial displacement history-III was further scaled up to an arbitrary maximum displacement of 1.2" (i.e., 2.05 times the amplitude of 0.584"), with the intention of creating a sufficient amount of BRB inelastic deformations such that the specimen could be cycled until failure in a relatively small number of cycles.

This final displacement history was applied to BRB-1-1 in test BRB-1-1-D and the specimen failed during the 4th cycle, close to reaching the target displacement. The corresponding BRB's axial force versus table's longitudinal displacement for these 4 cycles is shown in Fig.8-96a, with the failure of BRB-1-1 marked by the red cross. Fig. 8-96b shows the shape for one typical cycle of displacement history.

Fig. 8-97a compares the table's longitudinal displacement output and the BRB's applied axial displacement under 4 cycles of axial displacement history. Fig. 8-97b compares the BRB's axial deformation and the BRB's applied axial displacement for the same 4 cycles. The same difference in displacement ranges mentioned before can be observed in both figures.
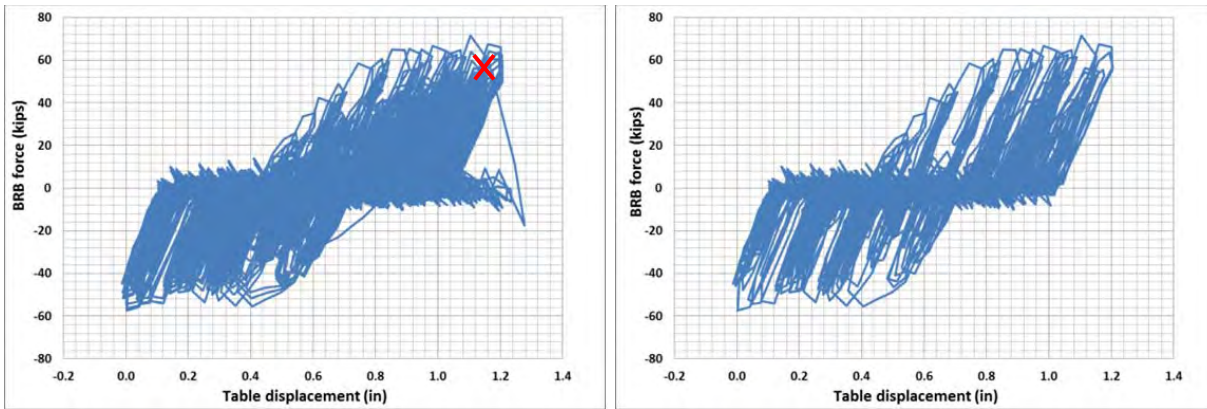
(a)   (b)

Figure 8-96 BRB-1-1's axial force vs longitudinal table displacement when subjected to 4 cycles during test BRB-1-1-D: (a) 4-cycles; (b) 3rd cycle
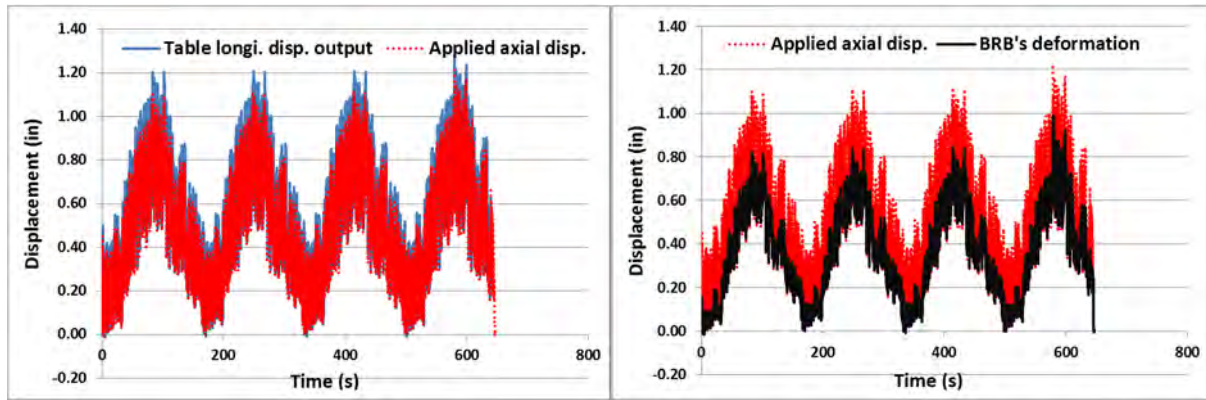
(a)   (b)

Figure 8-97 Displacement comparison in test BRB-1-1-D for 4 cycles of temperature-induced axial displacement history-III after scaling up to 2.05 times: (a) shake table's longitudinal displacement output and applied axial displacement; (b) axial deformation and applied axial displacement

In all of the above tests for BRB-1-1, no end-plate failure or instability was observed. After the test, a visible bulge was observed on the southeast side of the BRB. The cause of that bulge and mode of failure of the BRB specimens will be discussed in details in Section 9.1.

8.5.6 BRB-1-2

8.5.6.1 Overview of Parts of Test BRB-1-2

BRB-1-2 was first subjected to the Average Bidirectional Qualification Displacement History in test BRB-1-2-A. After this bidirectional qualification test, temperature-related displacement histories were applied to the specimen. In a first test, called BRB-1-2-B, for reasons mentioned in Section 8.5.2.2 and further discussed in Section 8.5.6.3, the sampling rate in the data acquisition system was increased and

359

BRB-1-2 was subjected to two cycles of Temperature-Induced Axial Displacement History-III. Upon studying the hysteretic curves of BRB's axial force versus axial deformation in test BRB-1-2-B, it was found that the total displacement magnitude of the axial displacement history mattered more than the small cycles (that mostly strain the BRB in elastic range). Therefore, a decision was made to increase the magnitude of the axial displacement history such as to produce an inelastic BRB deformation of approximately 2.5 times the yield displacement of the BRB for reasons explained in Section 8.5.6.3. After a bit of trial and error, the revised temperature-related axial displacement history was set with a range of 0.77". Then to achieve the intended BRB inelastic deformations and satisfactory data resolution, the test duration for that protocol was doubled and the resulting displacement history was applied to the specimen for one cycle, for verification, in test BRB-1-2-B.

This new displacement history, labeled "Temperature-Induced Axial Displacement History-IV", was applied to BRB-1-2 repeatedly until its failure at 33th cycle in test BRB-1-2-C.

8.5.6.2 Test BRB-1-2-A

The Average Bidirectional Qualification Displacement History in Fig. 8-85 was first applied to BRB-1-2. Fig.8-98a shows the corresponding hysteretic curve of BRB-1-2's axial force versus axial deformation. The BRB's axial force was plotted with applied axial displacements in Fig. 8-98b, which shows the bolt slippage of 0.27". Stable inelastic behavior is observed.

8.5.6.3 Test BRB-1-2-B and adjustment to the temperature-related axial displacement history

For reasons explained in Section 8.5.2.2, the BRB's axial force and deformation of the BRB-2 specimens could not be plotted to show the BRB's true hysteretic behavior, due to a combination of the speed of the axial displacement input in the shake table needed to achieve 75 years of temperature-induced deformations in less than one day of testing, and the available sampling rate of the data acquisition system. At the time, it was deemed desirable (for simpler post-processing) to set the sampling rate of all data acquisition systems to match the Krypton system upper limit of 32 Hz, even though the sampling rate of data acquisition for LPs and SPs and the shake table could still be increased. From here on, in all subsequent tests, it was decided that all systems sampling rates did not need to match, as this would allow better resolution in data acquisition and make it possible to plot other important relationships.
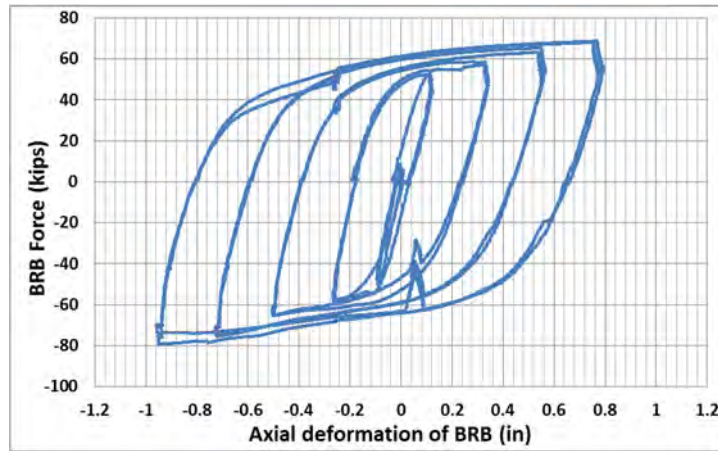
(a)
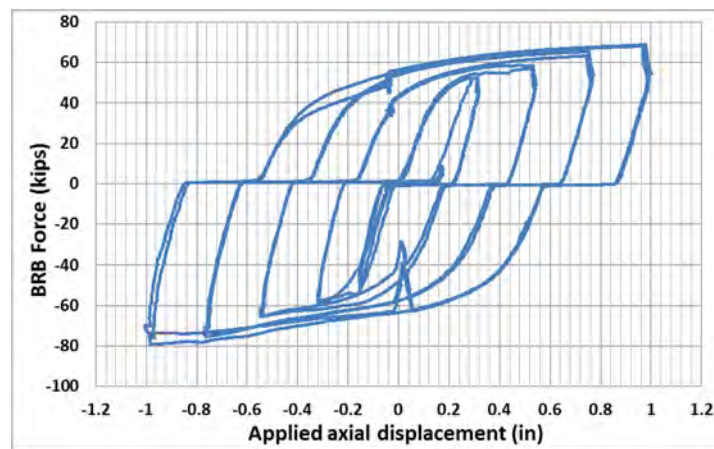
(b)

Figure 8-98 Hysteretic behavior of BRB-1-2 in test BRB-1-2-A: (a) axial force vs axial deformation; (b) axial force vs applied axial displacement

The Temperature-Induced Axial Displacement-III protocol (Fig. 8-91) was first applied to BRB-1-2 for one cycle, after doubling the sampling rate to 64 Hz in the data acquisition system for the LPs, SPs, and the shake table, to try to achieve improvements in the results. Fig. 8-99 shows the corresponding hysteretic curves of the BRB's axial force versus axial deformation (measured by LPs). Note that there is a residual deformation of 0.247" at the beginning of test BRB-1-2-B, even though the table was at its zero position. The gaps in the bolts accommodated this initial BRB deformation.
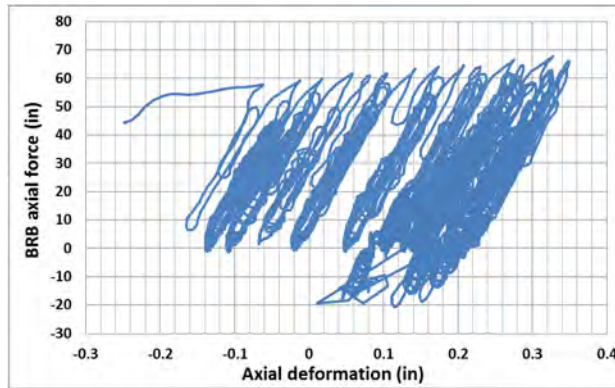
Figure 8-99 Hysteretic behavior of BRB-1-2 in test BRB-1-2-B with Temperature-Induced Axial Displacement-III with 64 Hz sampling rate in the data acquisition system

It can be observed that the total displacement magnitude of the axial displacement history mattered more than the small cycles (as those small cycles imposed mostly elastic strains to the BRB). Therefore, the magnitude of the temperature-related axial displacement history was increased to produce an inelastic BRB deformation of approximately 2.5 times the yield displacement of the BRB's core plate Δ_{by} in equation 8-1 when the BRB was loaded from zero to the maximum displacement. This amplitude was selected on the basis of the cumulative inelastic deformations achieved in previous tests (presented in Section 9) with the expectation that the BRB should be able to resist 35 years of this temperature-induced deformation history and still pass the bidirectional qualification protocol. By trial and error, the axial displacement histories in Figs.8-100a and 8-100b were accordingly scaled up from Fig.8-91 and each was applied to the BRB for one cycle, respectively, to find the correct displacement history. The corresponding hysteretic curves of the BRB's axial force versus axial deformation are shown in Fig. 8-101.

| (a) | (b) |
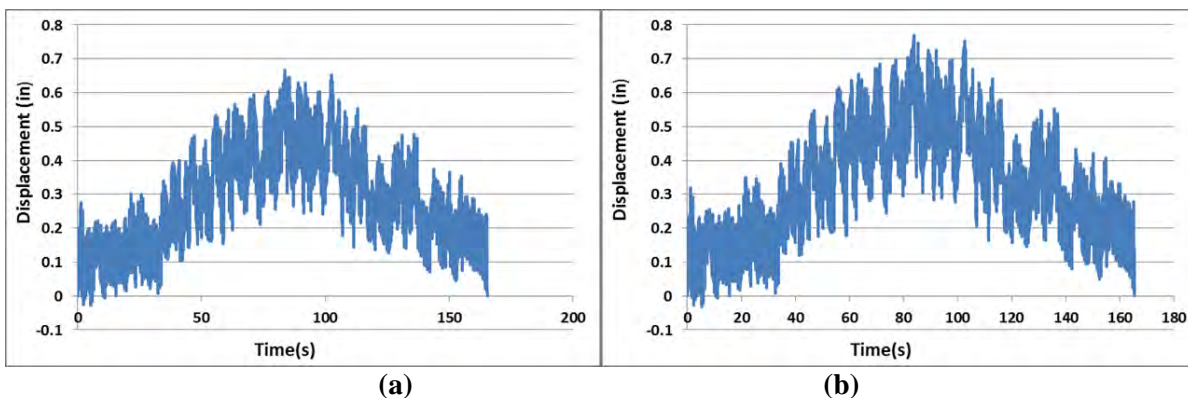
Figure 8-100 Trial axial displacement history of one year's temperature fluctuations for BRB-1-2's low cycle fatigue test: (a) range of 0.667"; (b) range of 0.77"

362
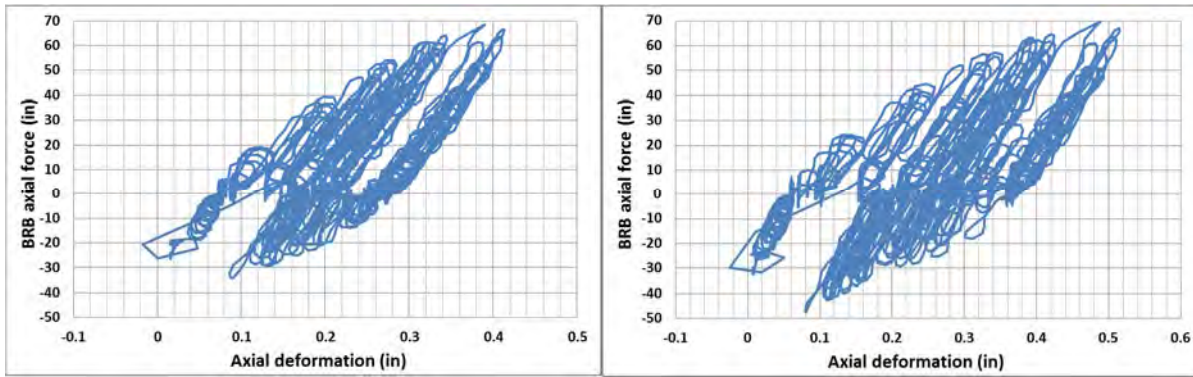
(a)   **(b)**

Figure 8-101 Hysteretic curves of BRB' axial force versus axial deformation corresponding to trial axial displacement history in Fig. 8-99: (a) range of 0.667"; (b) range of 0.77"

Since fewer than 75 years of temperature-induced displacement history at that displacement magnitude were expected to be applied to the BRB before its failure, it was deemed practical for subsequent tests to use a slower test speed. Therefore, in order to improve the resolution of the plots the BRB's axial force versus axial deformation in the temperature-induced axial test (to also better capture the force output from the shake table), the time duration of the axial displacement history in Fig 8-100b was doubled, as shown in Fig. 8-102 (called "Temperature-Induced Axial Displacement History-IV"). Note that the sampling rate of the output from LPs, SPs and the shake table remained 64 Hz. This protocol was applied to BRB-1-2 for one cycle and the corresponding hysteretic curve is shown in Fig. 8-103.
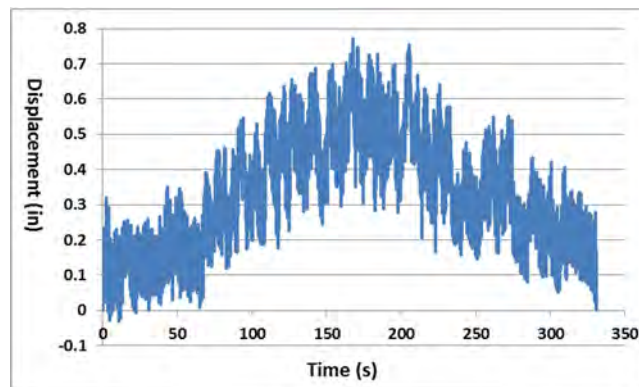
Figure 8-102 Temperature-Induced Axial Displacement History-IV of one year's temperature fluctuations for BRB-1 tests

The dashed red line on Fig. 8-103a indicates an approximate bilinear envelope for the resulting hysteretic curve. This envelope is shaped to match the slopes of the elastic deformation and peaks in the total deformation. The left and right lines match the elastic part with twice the yield displacement, and the upper and lower lines approximately connect the peaks of the elastic deformation. Fig. 8-103b shows the same hysteretic curve with a different dashed-line envelope that has two corners, where the BRB did not

363

reach those deformations. However, they allow to better envelope the hysteretic curves. Note that using the envelope in Fig.8-103a will give more conservative results when calculating cumulative inelastic deformations (i.e. smaller values), and it is the approach taken here.
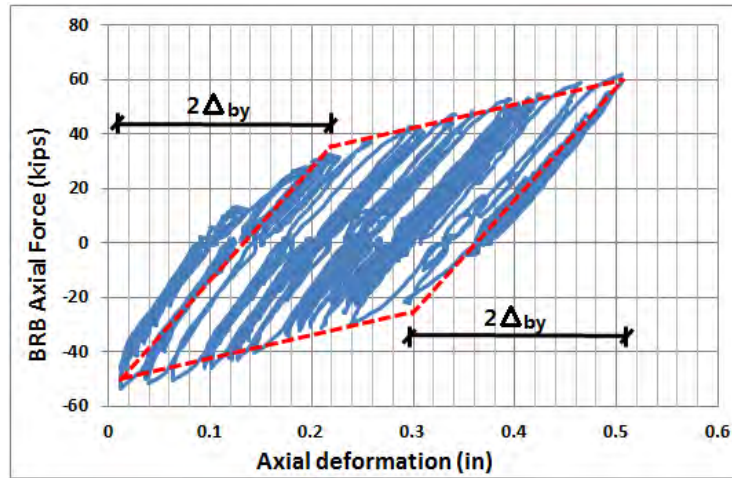
(a)
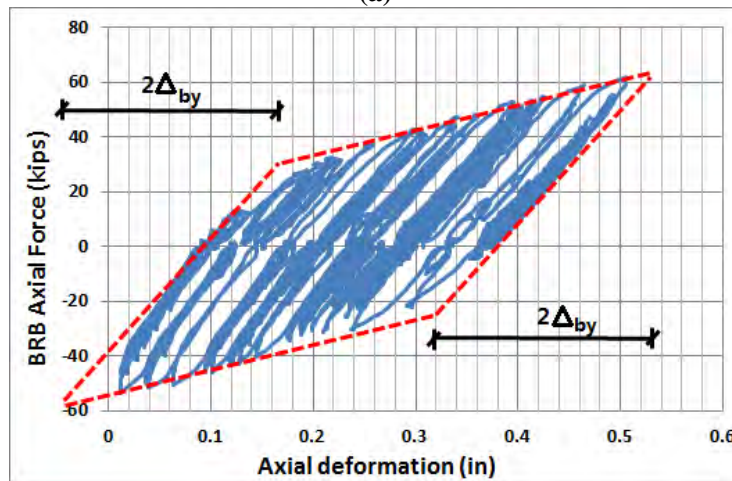
(b)

Figure 8-103 Hysteretic behavior of BRB-1-2 subjected to one-cycle Temperature-Induced Axial Displacement History-IV (a) approximate bilinear envelope; (b) bilinear envelope with adjusted vertical edges

In both cases, the elastic part of the equivalent bilinear hysteretic curve is shown as having a length of 0.214", which is equal to twice the yield displacement Δ_{by} of 0.107". The total magnitude of the BRB's deformation in Fig.8-103 is 0.5". Following this approach, the inelastic deformation caused by this axial displacement history is 0.286", which is 2.67 times the yield displacement and deemed to be equal to the target of 2.5 times the yield displacement. The total inelastic deformation that the BRB was subjected to under this one cycle of temperature-related displacement history is therefore twice of that, which is 5.34 times the yield displacement.

364

8.5.6.4 Test BRB-1-2-C

The Temperature-Induced Axial Displacement History-IV in Fig.8-102 was applied to BRB-1-2 until failure and the specimen failed at the 33th cycle when the displacement was at the maximum. The corresponding hysteretic curve of BRB-1-2's axial force versus axial deformation for a typical 5 cycles (cycles from 10 to 15) is shown in Fig 8-104.
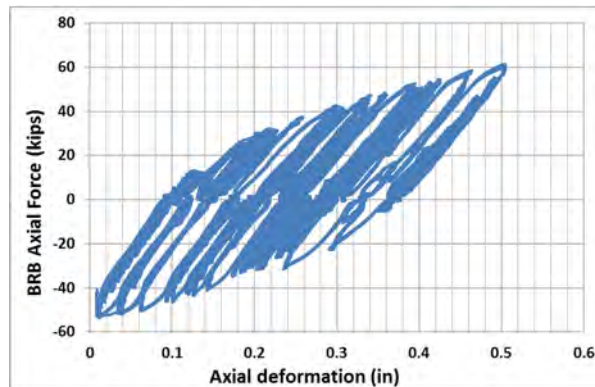
Figure 8-104 BRB-1-2's axial force vs axial deformation in Test BRB-1-2-C for typical 5 cycles

Figs. 8-105a and 105b shows the axial force and deformation of BRB-1-2 for the last 5 cycles. Note that the largest axial force in the specimen decreased from cycle to cycle (indicated by the inclined dash line) in Fig. 8-105b. The hysteretic curve of the BRB in the last cycle is shown in Fig. 8-106, with the red cross indicating its failure.

(a)   (b)
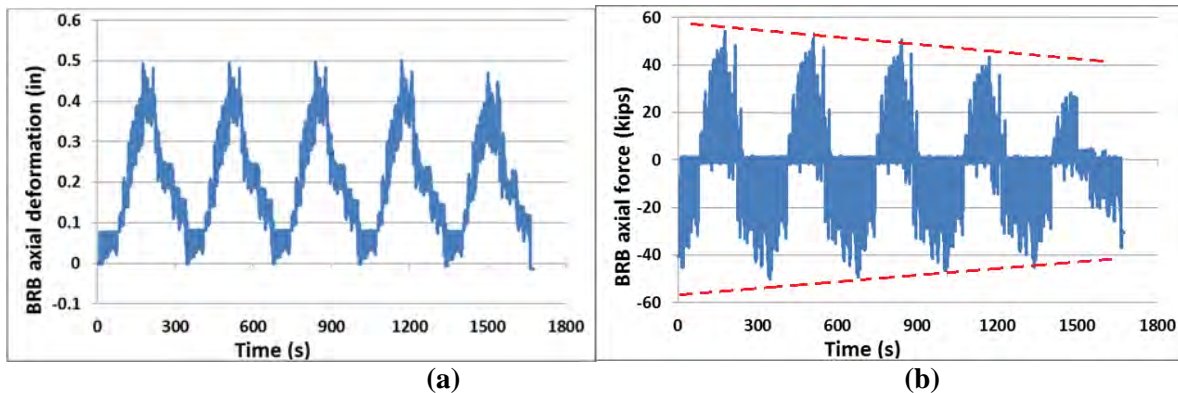
Figure 8-105 Test BRB-1-2-C for last 5 cycles: (a) axial deformation vs time; (b) axial force vs time
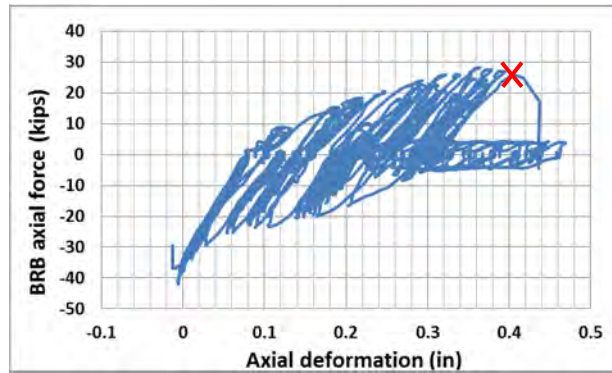
Figure 8-106 BRB-1-2's axial force vs axial deformation in Test BRB-1-2-C in the last cycle before it failed

Fig 8-107 shows the comparison of the qualification and temperature-induced hysteretic curves of BRB-1-2 in one figure. It can be observed that the displacement magnitude reached during the bidirectional qualification is significantly larger than the axial displacement history due to temperature change, even though the temperature-induced maximum displacement was 2.23 times larger than what was predicted for the actual prototype bridge (i.e., 0.5" versus 0.224").
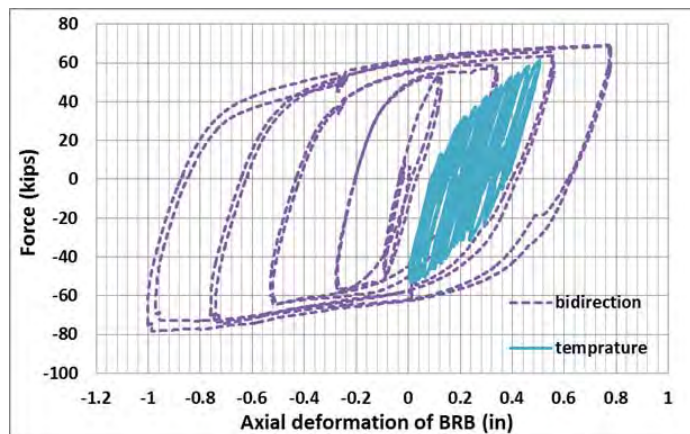
Figure 8-107 Hysteretic behavior of BRB-1-2 subjected to both bidirectional and temperature-induced axial displacement history

In all of the above testing for BRB-1-2, no end-plate failure or instability was observed. After the test, a visible bulge was observed on the northeast side of the BRB. The cause of that bulge and mode of failure of the BRB specimens will be discussed in details in Section 9.1.

8.5.7 BRB-1-3

8.5.7.1 Overview of Parts of Test BRB-1-3

BRB-1-3 was only subjected to bidirectional displacement histories. The longitudinal displacement adjustments, caused by the transverse displacement demand described in Section 8.4.2, were removed from the Average Bidirectional Qualification Displacement History, and the resulting displacement history labeled "Average Bidirectional Qualification Displacement History-II" was applied to BRB-1-3 in test BRB-1-3-A.

In order to explore the transverse displacement capacity of the BRB, the Average Bidirectional Qualification Displacement History-II was revised to impose arbitrary transverse displacement demands progressively increasing to 2", 4", and 6", while the longitudinal displacement demand remained at 1.5 times the design displacement, as explained in Section 8.5.7.3. The corresponding displacement histories corresponding to transverse displacement demands of 2", 4" and 6" were named as "BT2", "BT4", "BT6", respectively. In test BRB-1-3-B, BT2, BT4, BT6 were applied to the specimen sequentially, for one cycle each. To complete testing of the specimen already in place, BT6 was continuously applied to BRB-1-3 until the specimen failed during the 7th cycle at that magnitude of transverse displacement, in test BRB-1-3-C.

8.5.7.2 Adjustment to Average Bidirectional Qualification Displacement History

Recall that, in Section 8.5.5.2, the longitudinal displacement history was adjusted in Average Bidirectional Qualification Displacement History to match the longitudinal displacement demands of the AISC test protocol. This time, to reflect the BRB's actual response in the ductile diaphragm of the bridge when subjected to earthquakes (where transverse displacements indeed put additional axial strains into the BRB), and also to be consistent with the displacement histories with increased transverse displacement demand that were to follow (as described in Section 8.5.7.4), the longitudinal displacement adjustments were removed from the Average Bidirectional Qualification Displacement History. The resulted bidirectional displacement history, labeled "Average Bidirectional Qualification Displacement History-II", is shown in Fig.8-108.

8.5.7.3 Test BRB-1-3-A

The Average Bidirectional Qualification Displacement History-II was applied to BRB-1-3 in test BRB-1-3-A. The specimen successfully passed the qualification test and the corresponding hysteretic curve of BRB-1-3's axial force versus axial deformation is shown in Fig. 8-109a. The BRB force versus applied axial displacements (in Fig. 8-109b) shows the bolt slippage at zero loads of 0.27". Stable inelastic behavior is observed.

(a)   **(b)**
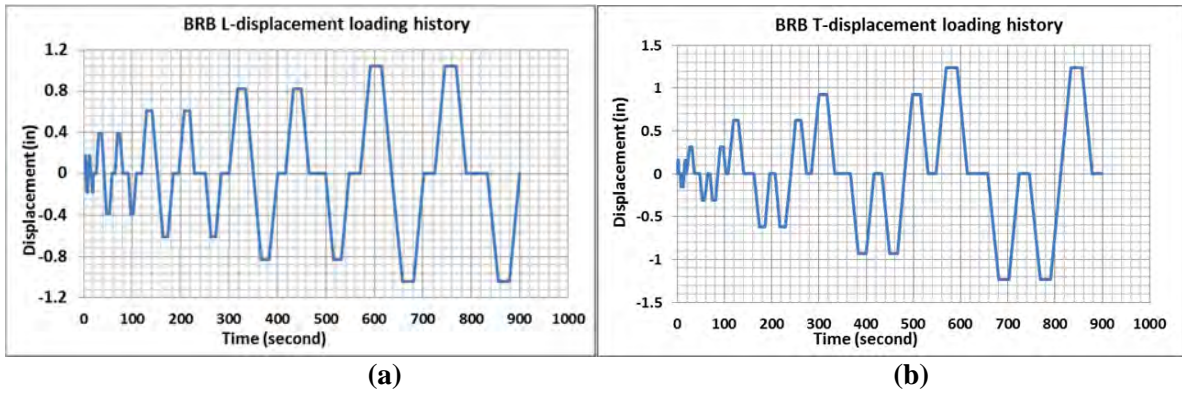
Figure 8-108 Average Bidirectional Qualification Displacement History-II for BRB-1-3 test (a) longitudinal displacement vs time; (b) transverse displacement vs time

(a)

(b)
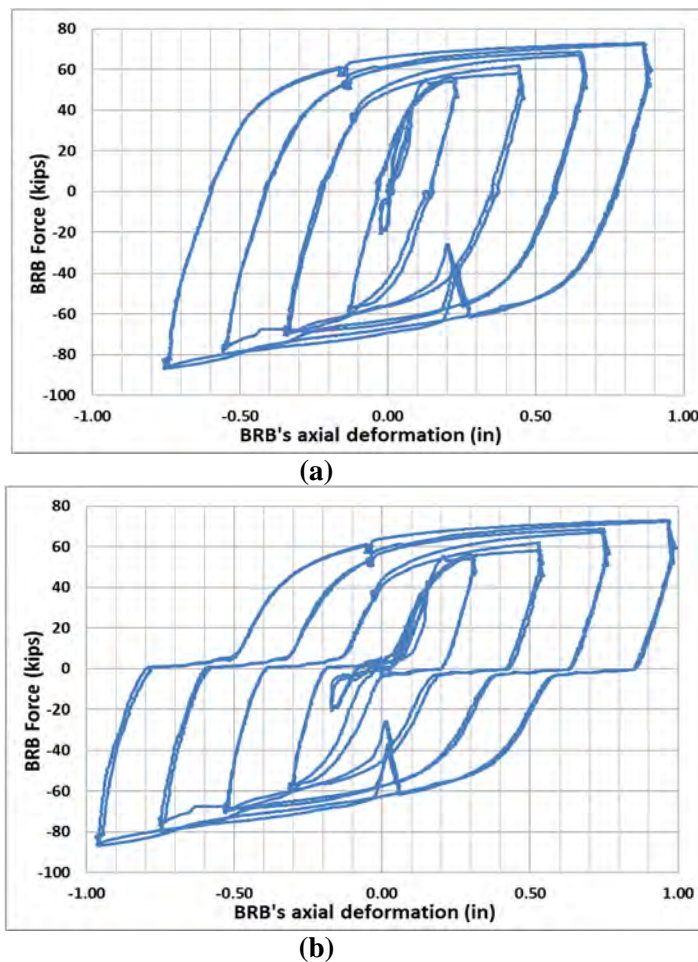
Figure 8-109 Hysteretic behavior of BRB-1-3 in test BRB-1-3-A: (a) axial force vs axial deformation; (b) axial force vs applied axial displacement

BRB-1-3 was instrumented with strain gauges both on end plates and collars. Two end plates at the south end of the BRB had four strain gauges, i.e. two on each end plate. Fig. 8-110a shows the transverse displacement applied to the BRB versus the strain measured by the gage close to the cover plate on the

369

southeast endplate of the BRB (which was the one recording the largest strains). The maximum strain was 0.9 $\times 10^{-3}$ in/in, which indicates that the end plates remained elastic, as the yield strain of the steel material is 1.45×10^{-3} in/in. For comparison, the BRB's axial force versus strain for the strain gauge close to the pin hole on the same end plate of the BRB is shown in Fig. 8-110b.

<div align="center">(a)   (b)</div>
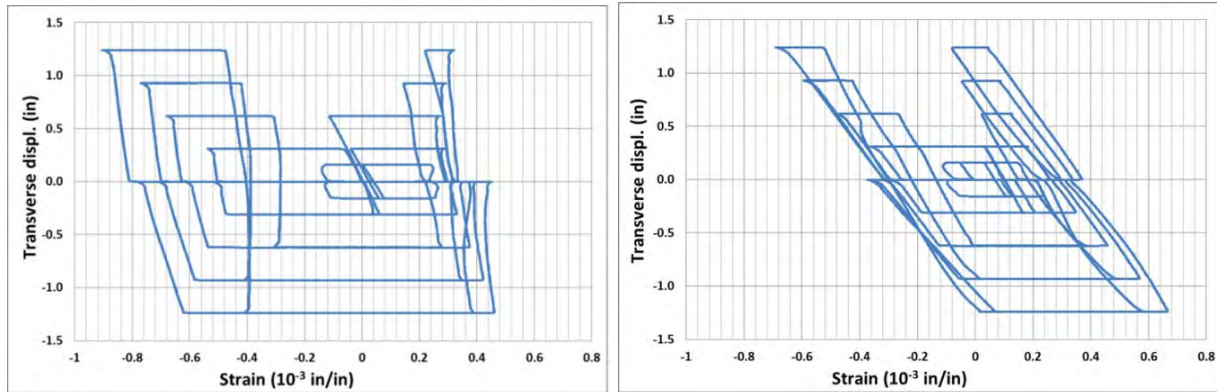
Figure 8-110 BRB-1-3's axial force vs strain recorded on the southeast end plate: (a) strain gauge close to the cover plate; (b) strain gauge close to the pin hole

BRB-1-3 was also instrumented with strain gauges at the two sides of each collar at the locations were mentioned in Section 8.3.4. Once the collars became in contact with the concrete-filled HSS under the applied increasing transverse displacements, both collars deformed under lateral forces. From the strains recorded by the gages at the side of each collar, the top and bottom locations (Fig.8-24b) were found to have larger strains than the middle one. During test BRB-1-3-A, a maximum strain of 2.06 $\times 10^{-3}$ in/in was recorded by the top strain gauge at the east side of the south collar, as shown in Fig. 8-111, which indicates that the collar has experienced localized yielding, as the yield strain of the steel material is 1.45×10^{-3} in/in. This yielding happened at 1.5 times the design transverse displacement demand of 0.929". This is the only one in the total 12 gages located around the collars where evidence of yielding happened at that value of transverse displacement.

Note that the strain gauge closer to the pin hole underwent smaller strains than the other one on the same end plate in Fig.8-110, which the opposite of what was observed for the bidirectional qualification test of BRB-1-1 in Section.8.5.5.3. This is attributed to variations in the gaps between the collar and the concrete-filled HSS, which were introduced during fabrication of the BRB specimen, and are expected to vary from specimen to specimen. Measures to tightly control the size of this gap might have been possible, but this was beyond the scope in this study. Note that to adequately capture the relative movements of the collar, concrete-filled HSS, and end plates, significantly more instrumentation would have been required all around the specimen and possibly also inside the BRB and collar gaps.
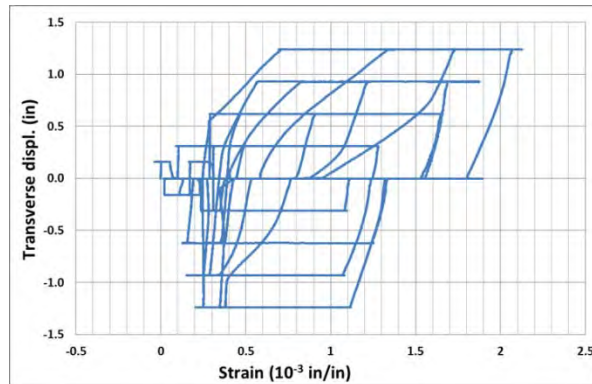
Figure 8-111 BRB-1-3's axial force vs strain recorded with the top strain gauge at east side of the south collar

8.5.7.4 Average Bidirectional Qualification Displacement History-II with increased transverse displacement demand

In order to investigate the transverse displacement capacity of the BRB, the Average Bidirectional Qualification Displacement History-II was revised to have larger transverse displacements of 2", 4" and 6", while the longitudinal displacement demand remained at 1.5 times the design displacement, as shown in Fig. 8-112. The longitudinal displacement demand was kept at 1.5 times the design displacement, to be consistent with the standard BRB qualification test protocols described in Section 8.4.2 for additional cycles after the BRB has been subjected to the cycles at twice the design displacement. Note that, since the pin-to-pin length of the BRB is 100 in, the bidirectional displacement histories at these three levels of transverse displacements correspond to drifts of 2%, 4% and 6%. They were labeled "BT2", "BT4", "BT6", respectively.

8.5.7.5 Test BRB-1-3-B

The bidirectional displacement histories BT2, BT4, BT6 were applied to BRB-1-3 sequentially, for one cycle each. The corresponding hysteretic behaviors of BRB-1-3 subjected to BT2, BT4, BT6 are shown in Figs 8-113a, 8-113b, 8-113c, with axial deformation measured by LPs and Krypton system in dotted and solid lines, respectively. Note that there is a residual deformation of 0.158" at the beginning of test BRB-1-3-B, even though the table was at its zero position. The gaps in the bolts accommodated this initial BRB deformation.
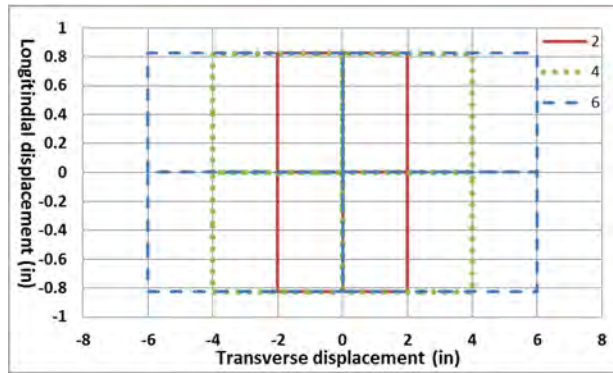
Figure 8-112 Loops of Average Bidirectional Displacement History with increased transverse displacement demand: solid line (BT2), dotted line (BT4), dashed line (BT6)

Note that in the third and fourth small loops in Fig.8-86, the BRB was moving from point C to O to D as shown in Fig. 8-114. Since there was no longitudinal displacement adjustment in BT2, BT4, and BT6, the transverse displacement demand at point C and D would increase the BRB's axial deformation. Therefore, the BRB experienced a small unloading and reloading when the table moved from C to O to D, which is indicated by the "indentation" of the hysteretic curves circles in Fig. 8-113. It was found that the axial deformation measurement from LPs tracked the response better than the Krypton system in this process. This phenomenon became more apparent as the transverse displacement demand became larger.

It is observed in Fig. 8-113 that the BRB did not have the same axial deformation when it reached its maximum displacement in tension at points A and B. This difference is progressively accentuated in Figs. 8-113b and 8-113c compared to Fig 8-113a. This could have been due to the unequal gaps between the collar and the concrete-filled HSS. As the BRB moved under the transverse displacement, the gaps on each side of the collars opened and closed. These collars deformed to a different extent when the BRB moved to point A and B, as presented later in this section. The exact cause for this observed behavior (which is, incidentally, not significant) could only be determined by constructing a BRB model able to capture the actual movements of the collars and HSS, and verified by additional instrumentations inside and outside around the gap area (which was not done, as considered to be beyond the scope of work).
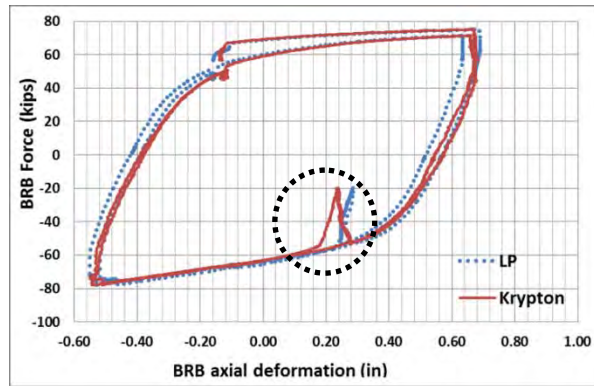
(a)
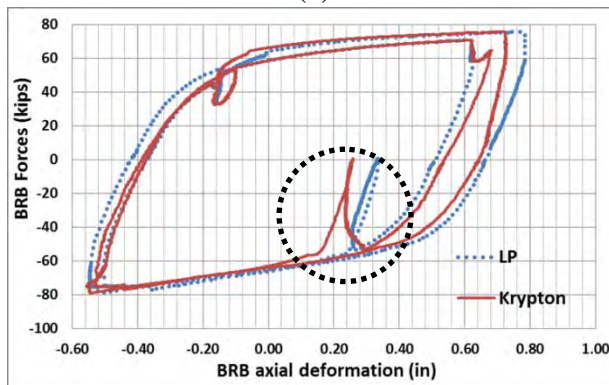
(b)
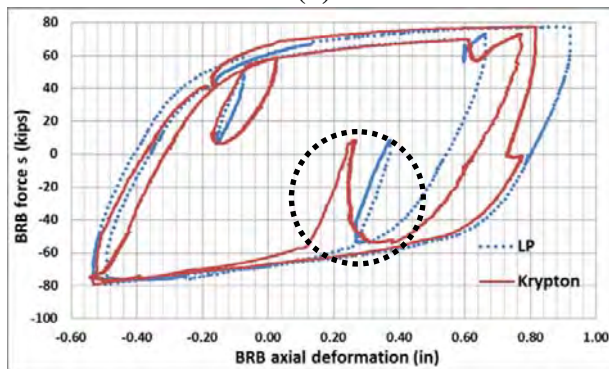
(c)

Figure 8-113 Hysteretic curves of BRB-1-3 subjected to (a) BT2, (b) BT4, and (c) BT6

Figs. 8-115a, 8-115b, 8-115c show the transverse displacement applied to the BRB versus the strain measured by the gage close to the bolt hole on the southwest endplate of the BRB (which was the one recording the largest strains), when BT2, BT4, and BT6 was applied to BRB-1-3, respectively.

373
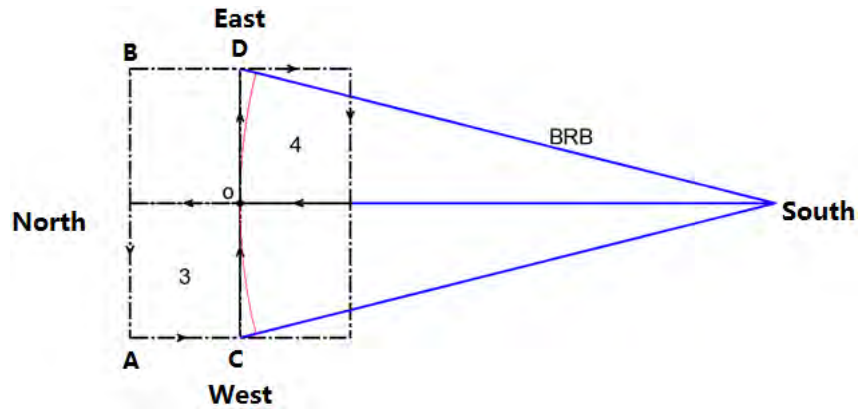
Figure 8-114 BRB and table movement for the third and fourth loops in BT2, BT4, and BT6

(a)

(b)

(c)
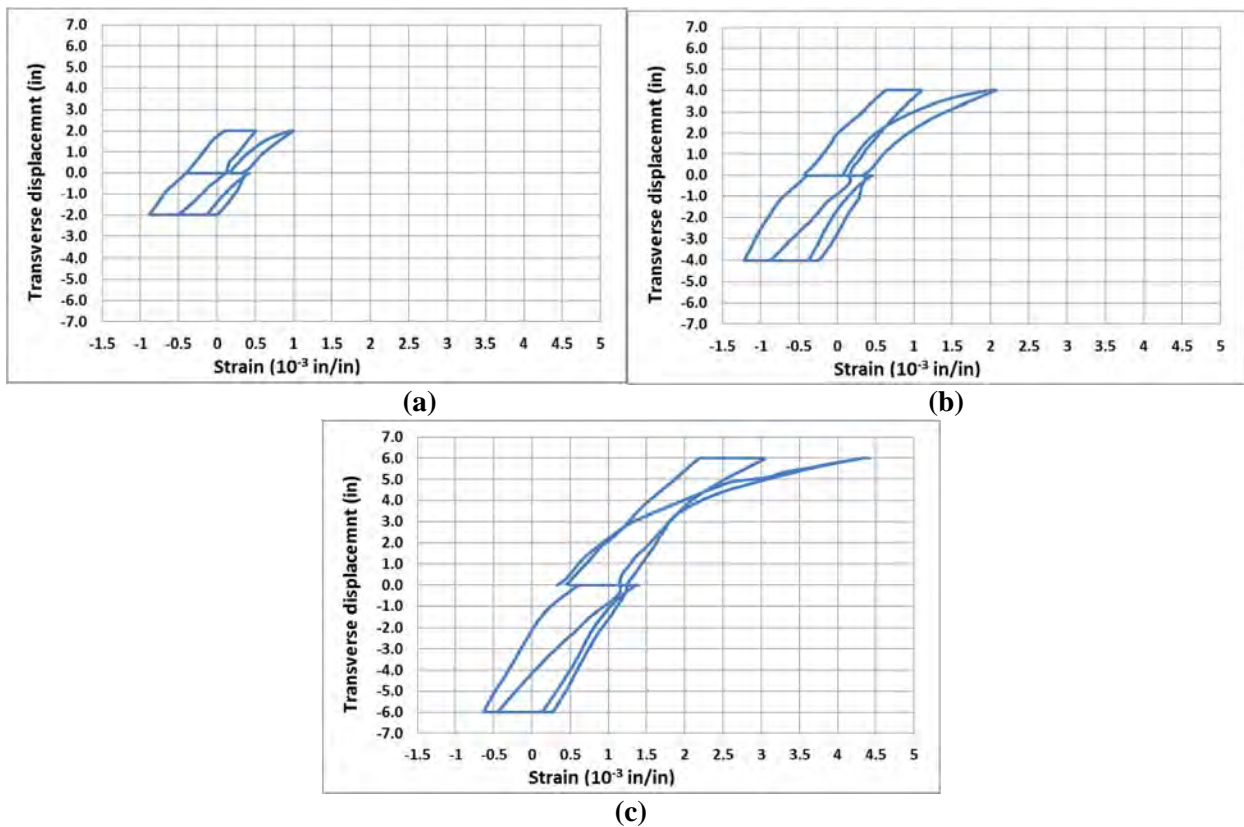
Figure 8-115 BRB-1-3's axial force vs largest strain recorded by the strain gauges on the end plates corresponding to: (a) BT2; (b) BT4; (c) BT6

No end plate yielding occurred at 2% drift, and the maximum strain of 0.98×10^{-3} in/in was recorded by the strain gauge close to the bolt hole on the west end plate. At 4% drift, yielding happened close to the bolt hole on the west endplate, with a maximum recorded strain value of 2.06×10^{-3} in/in. Note that the maximum strain close to the east endplate bolt hole was 1.43×10^{-3} in/in (i.e., close to yielding), while the strains in the other two strain gauges remained elastic. At 6% drift, the maximum strain of 4.41×10^{-3} in/in

374

happened close to the bolt hole on the west endplate. The strain gauges close to the cover plate on the southeast end plate and the other one close to the pin hole on the same end plate recorded a maximum strain of 1.76×10^{-3} and 2.36×10^{-3}, respectively. These three locations on the end plates all yielded except for the one close to the cover plate on the west endplate.

The largest strains recorded by the strain gauges at both side of each collar are shown in Figs. 8-116a, 8-116b, and 8-116c, when BT2, BT4, and BT6 was applied to BRB-1-3, respectively. The top and bottom locations (Fig.8-24b) were found to experience larger strains than the middle one. At 2% drift, the maximum strain of 2.55×10^{-3} in/in happened at the top-east side of south collar, which was the only one in the 12 gauges that showed localized yielding. At 4% drift, yielding happened at the top-east side of the south collar and at the top-west side of the north collar, with maximum strains of 3.86×10^{-3} and 1.8×10^{-3}, respectively. The strains in the other 10 strain gauges remained elastic at 4% drift. For 6% drift, yielding happened at the same locations for 4% drift, with maximum strains of 2.13×10^{-3} and 2.32×10^{-3} in/in, respectively, and the other 10 strain gauges also remained elastic.

(a)

(b)

(c)
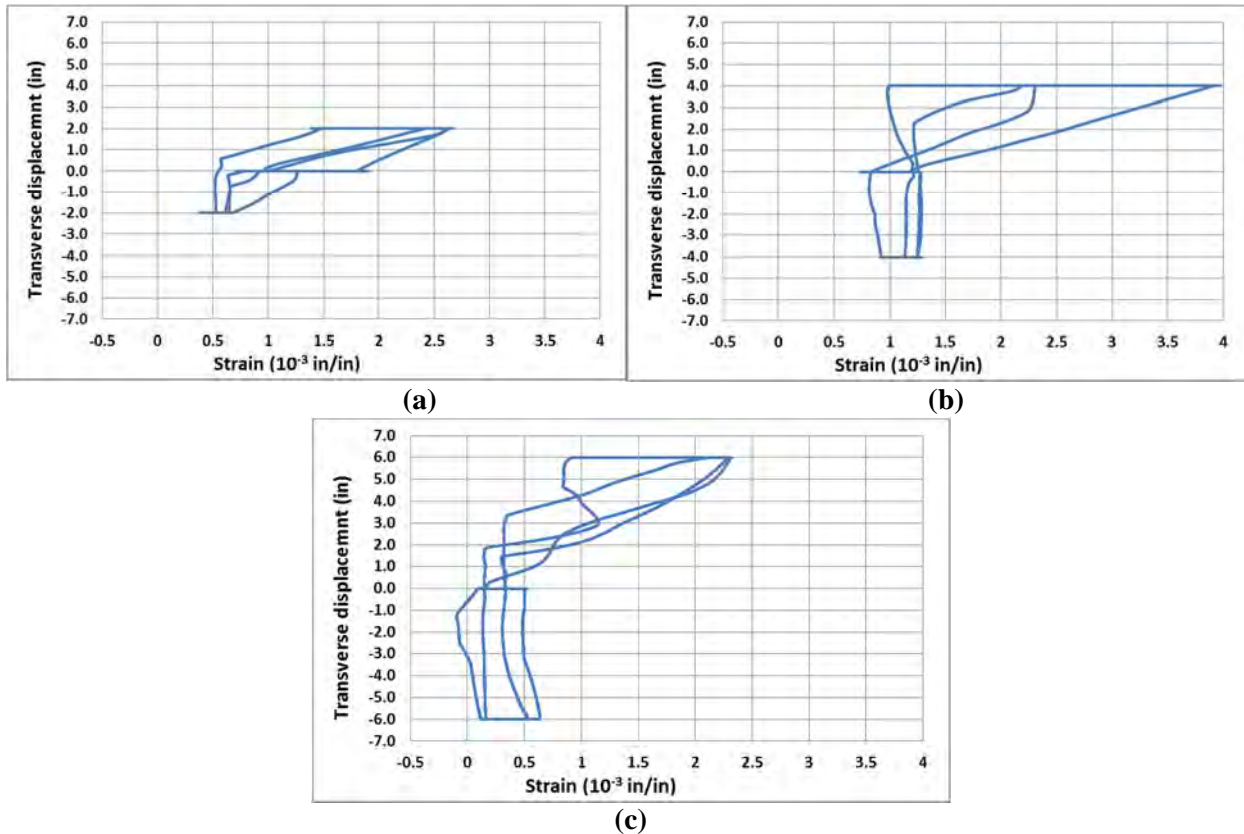
Figure 8-116 BRB-1-3's axial force vs largest strain recorded by the strain gauges at the side of collars corresponding to: (a) BT2; (b) BT4; (c) BT6

It is observed that the yielding at the east side of the south collar and the west side of the north collar are more than their corresponding opposite side on the same collar. This indicates that the collars experienced more deformation when the BRB's end on the shake table moved to west side, which also matched the hysteretic curves in Fig.8-113 when BRB had more deformation at Point B than Point A.

Fig 8-117 shows the BRB's hysteretic curves for four tests under the Average Bidirectional Qualification Displacement History-II, BT2, BT4, and BT6, in solid, dotted, dashed, and dash-dotted lines, respectively. Note that the BRB's axial deformation was measured by LPs in that case.
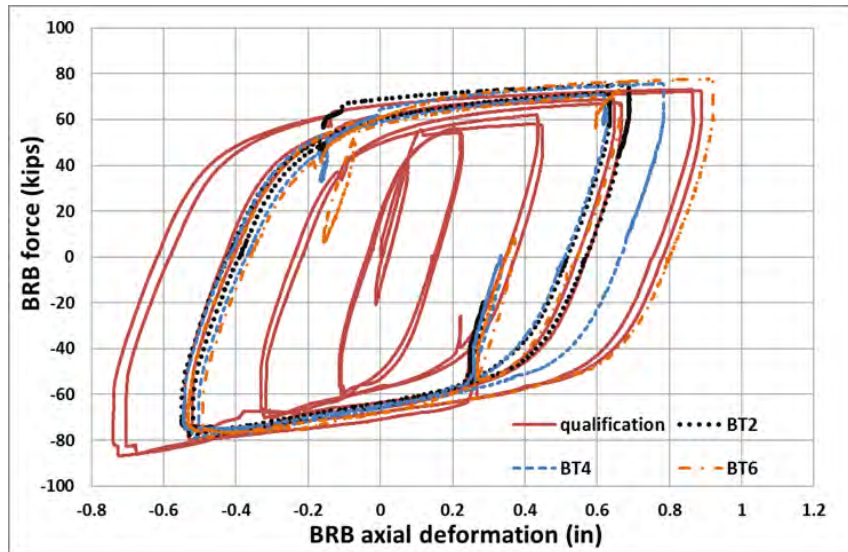
Figure 8-117 Hysteretic behavior of BRB-1-3 subjected to Average Bidirectional Qualification Displacement History-II, BT2, BT4 and BT6

8.5.7.6 Test BRB-1-3-C

Since BRB-1-3 successfully passed the bidirectional displacement history up to 6% drift in test BRB-1-3-B, a decision was made to continuously apply BT6 to BRB-1-3 until it failed in test BRB-1-3-C. Under this displacement history, BRB-1-3 failed at the beginning of the 7th cycle of BT6 that was applied to BRB-1-3 in test BRB-1-3-C. Note that this is in addition to the BT6 applied to BRB-1-3 in test BRB-1-3-B. The specimen failed when the table was close to its largest longitudinal displacement (point B in Fig. 8-114).

The hysteretic curves corresponding to the first four cycles of BT6 are identical to Fig. 8-113c, and therefore not shown here. The same discrepancies between the BRB's axial deformation measured by LPs and Krypton system also existed. Fig. 8-118 shows the last three cycles of BT6 applied to BRB-1-3

with axial deformation measured by LPs with solid line, dash-dot line and dotted line indicating the 5th, 6th and 7th cycle of BT6, respectively. The failure of BRB-1-3 is marked by the red cross in the 7th cycle.
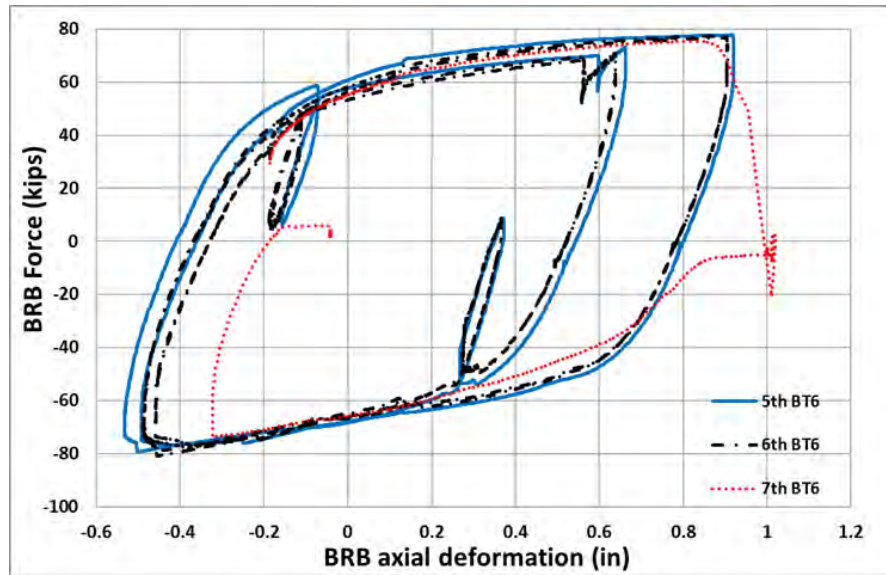
Figure 8-118 Hysteretic behavior of BRB-1-3 subjected to BT6 in the 5th , 6th and 7th cycle

The largest strain recorded by the strain gauges on the end plates in all the cycles of BT6 applied in BRB-1-3-C remained the same 4.41×10^{-3} in/in at the same location, which was close to the pin hole on the west end plate on the south side. The largest strain recorded by the strain gauges on the sides of the collars in all the cycles of BT6 applied in BRB-1-3-C remained the same 2.32×10^{-3} in/in at the same location, which was at top of west side of the north collar.

In all of the above tests for BRB-1-3, no end-plate failure or instability was observed. After the test, a visible bulge was observed on the southeast side of the BRB. The cause of that bulge and mode of failure of the BRB specimens will be discussed in details in Section 9.1.

8.5.8 BRB-1-4
8.5.8.1 Overview of Parts of Test BRB-1-4

BRB-1-4 was subjected to both bidirectional displacement histories and temperature-induced axial displacement history. The bidirectional displacement histories applied to all the BRBs tested before followed a rectangular shape. The ones applied to BRB-1-4 were new bidirectional displacement histories obtained directly from the response of the BRBs in the nonlinear analyses of the simplified bridge diaphragm model. The details on these bidirectional displacement histories, labeled "Bidirectional Seismic Response Displacement History", "Bidirectional Seismic Response with Gap Displacement

History-C", and "Bidirectional Seismic Response with Gap Displacement History-T" are presented in Section 8.5.8.2 and Section 8.5.8.6.

BRB-1-4 was first subjected to Bidirectional Seismic Response Displacement History in test BRB-1-4-A. Then Temperature-Induced Axial Displacement History-IV was applied to BRB-1-4 for 35 years in test BRB-1-4-B. The same Bidirectional Seismic Response Displacement History was again applied to BRB-1-4 in test BRB-1-4-C. This was followed by Bidirectional Seismic Response with Gap Displacement History-C and Bidirectional Seismic Response with Gap Displacement History-T, successively applied to the specimen in test BRB-1-4-D, alternating one after the other, until failure. BRB-1-4 failed during the 3rd repetition of the Bidirectional Seismic Response with Gap Displacement History-T (in other words, after three cycles of Bidirectional Seismic Response with Gap Displacement History-C and two cycles of Bidirectional Seismic Response with Gap Displacement History-T).

8.5.8.2 Bidirectional Displacement Protocols

The bidirectional displacement histories used for the previous BRB tests all followed a rectangular trace, sequentially applying longitudinal and transverse displacement, effectively enveloping the actual displacement response of the BRB in the simplified bridge diaphragm model when subjected to earthquakes. In the bidirectional test of BRB-1-4, the movement of the shake table followed the actual bidirectional displacement trace of the BRB's response to an actual ground excitation, instead of the rectangular envelope.

Recall that, in Section 8.5.5.2, the average displacement demand from the nonlinear time history analyses of the simplified bridge diaphragm model is 0.619", which corresponds to a target ductility of 6. Since the tested BRB represents the inclined longitudinal BRB in the simplified bridge diaphragm model, the design longitudinal and transverse displacement demand to be imposed to the BRB during the test are 0.438"and 0.619", respectively. Upon looking at the bidirectional demands resulting from all of the 44 time history analyses conducted for this purpose, one ground motion was identified as causing a maximum BRB longitudinal displacement of 0.448" as shown in the bidirectional history in Fig. 8-119, which was the closest to the design longitudinal displacement demand of 0.438" for all the ground motions considered.

(a)   **(b)**
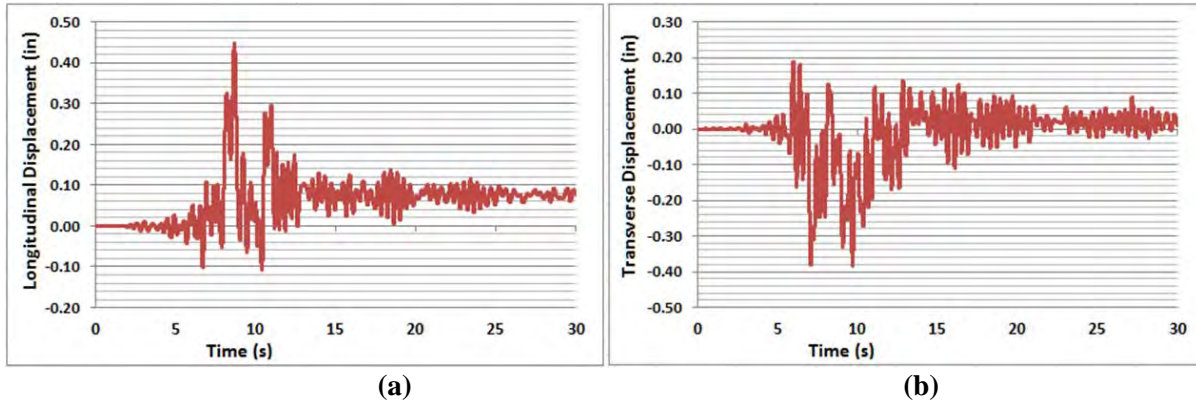
Figure 8-119 BRB-1-4 displacement demand subjected to the selected pair of ground motions in the nonlinear time history analysis (a) longitudinal; (b) transverse

To get the displacement history in Fig. 8-119, the ground motion shown in Fig.8-120a was applied to the bridge diaphragm model in the longitudinal direction, while the corresponding ground motion acting in the orthogonal direction (from the same pair of ground motions), shown in Fig.8-120b, was applied to the transverse direction of the bridge diaphragm model. The corresponding acceleration spectra for these two ground motions are shown in Fig. 8-121.

(a)   **(b)**
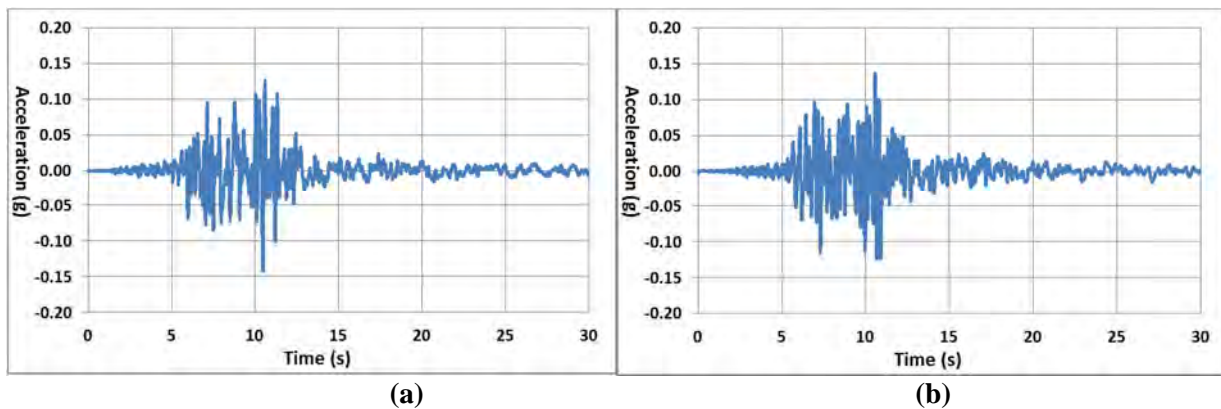
Figure 8-120 Selected pair of ground motions (a) component applied in longitudinal direction; (b) component applied in transverse direction

Note that the period of the bridge diaphragm model is 0.41s. Since the bridge model considered here was the same as in the parametric analyses in Section 7, large BRBs would have been required in that application. However, the shake table's maximum force that can could be applied to a specimen dictated that a smaller BRB be used for the tests. Therefore, the ground motions were proportionally scaled down to accommodate the BRB sizes available while still developing the target ductility demand of 6 in the tested BRB. This scaling factor was 0.372. Recall that the tested BRBs have a yielding core area about

nine times less than in the prototype bridge used in Section 7, which explains the low amplitude of the peak ground accelerations used in these analyses (for reasons described in Section 8.4.1).

(a)   (b)
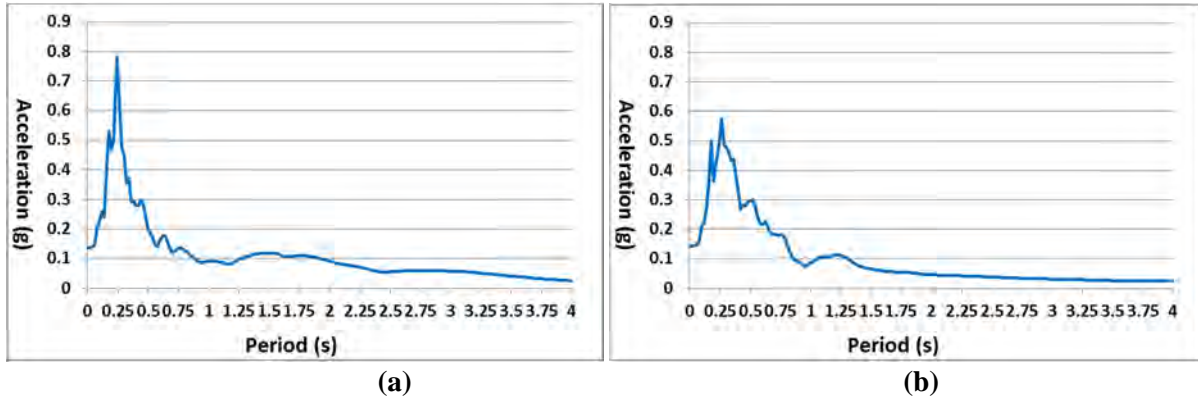
Figure 8-121 Acceleration spectra for selected pair of ground motions (a) component applied in longitudinal direction; (b) component applied in transverse direction

For the ground motion pair in Fig. 8-120 applied to the simplified bridge diaphragm model, the bidirectional displacement trace of BRB's actual response (corresponding to Fig. 8-119) is shown in Fig.8-122.
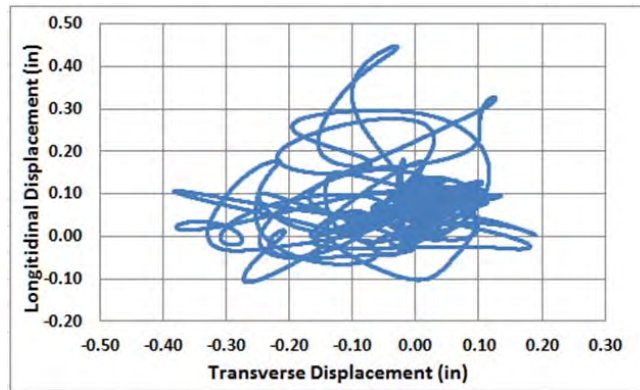
Figure 8-122 Trace of the bidirectional displacement history (illustrated in Fig. 8-119)

Note that the bidirectional displacement history protocol used in the previous tests of BRB-1s reached a maximum displacement demand of twice the design displacement; however, here, the bidirectional displacement history in Fig. 8-119 only develops the design displacement, by having a maximum displacement of 0.448". As observed in the temperature-induced axial tests of BRBs of similar amplitude (i.e., test BRB-1-1-B), most of this displacement was taken by the bolt slippage and reaction blocks' deformation and slippage, resulting in axial deformations in the BRB that were greatly reduced compared to the desired displacement demand. Therefore, corrected displacement histories were also created to generalize the results to BRBs that would not benefit from pin slippage to resist the applied displacements, and to eliminate test set-up deformations.

The same three factors considered to obtain the increased demand in Temperature-Induced Axial Displacement History-III in Section 8.5.5.4, were used here to calculate the adjustment to add to the bidirectional displacement history in Fig.8-119, except that the maximum tensile and compressive force of BRB considered to calculate those values was 90 kips instead of 60 kips. As a result, the total elastic deformation of the reaction block is 0.075", the total sliding of the reaction blocks at the maximum force is 0.048", and the bolt slippage is 0.27". These three values are summed up to be 0.393". Half of this 0.393" displacement was added to the maximum longitudinal displacement demand of 0.438" in the bidirectional displacement history in Fig.8-119. Therefore, the revised bidirectional displacement history needs to have a maximum displacement of 0.635".

The same pair of ground motions was therefore used to produce a new bidirectional displacement history intended to have the maximum tensile displacement demand of 0.635", by increasing the scale factors used in the new nonlinear time history analyses of the simplified bridge diaphragm. By trial and error, the scale factor was increased to 1.64 times of the value used to obtain the displacement history in Fig. 8-119, when the maximum tensile longitudinal displacement reached 0.635" in the new bidirectional displacement history shown in Fig. 8-123. Note that the maximum compressive longitudinal displacement was only 0.11" in Fig. 8-119a; however, with the new scaling factor and resulting new bidirectional displacement history, this maximum compressive displacement reached up to 0.745", as shown in Fig. 8-123a, which is larger than the maximum tensile displacement demand of 0.635" (which indicates that, arguably, a lower scaling factor could have been used).

(a)   (b)
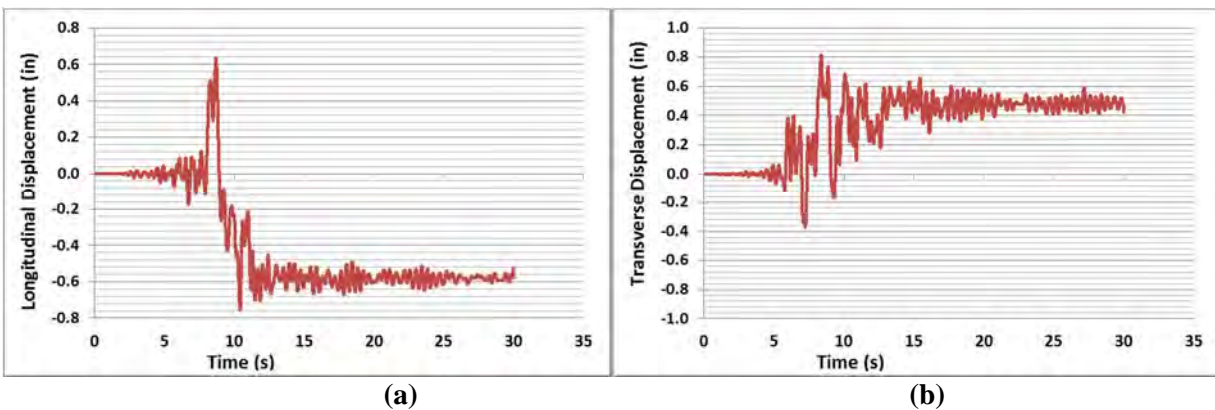
Figure 8-123 BRB-1-4 displacement demand subjected to the selected pair of ground motions in the nonlinear time history analysis with increased intensity

Finally, because the earthquake duration is relatively short compared to all other tests conducted as part of this testing program, the test speed was further reduced to better observe the specimen's behavior and

record the data. More specifically, the test duration to apply the bidirectional displacement history in Fig. 8-123 was increased from 30s to 300 s. The resulting bidirectional displacement history shown in Fig.8-123 is labeled "Bidirectional Seismic Response Displacement History"; its bidirectional trace is shown in Fig.8-124. Note that at the end of the bidirectional displacement history, the residual displacement was not zero. The shake table controllers require it to return back to the zero position after completion of a test. Therefore, to avoid sudden changes and vibrations to the BRB, a gradual decrease of the displacement, from the residual displacement value down to zero, was added to the end of the Bidirectional Seismic Response Displacement History in Fig. 8-123 (not shown here).
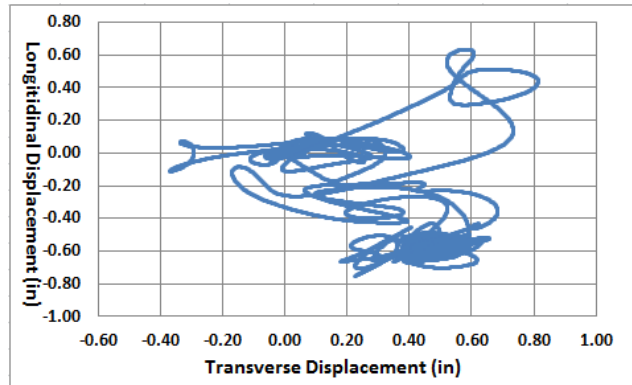
Figure 8-124 Traces of Bidirectional Seismic Response Displacement History

8.5.8.3 Test BRB-1-4-A

BRB-1-4 was subjected to the Bidirectional Seismic Response Displacement History in test BRB-1-4-A. The corresponding hysteretic curve of the BRB's axial force versus axial deformation (measured by Krypton system) is shown in Fig.8-125a. The BRB force was plotted as a function of applied axial displacements in Fig. 8-125b, which shows the bolt slippage of 0.27" at zero loads.

(a)   (b)
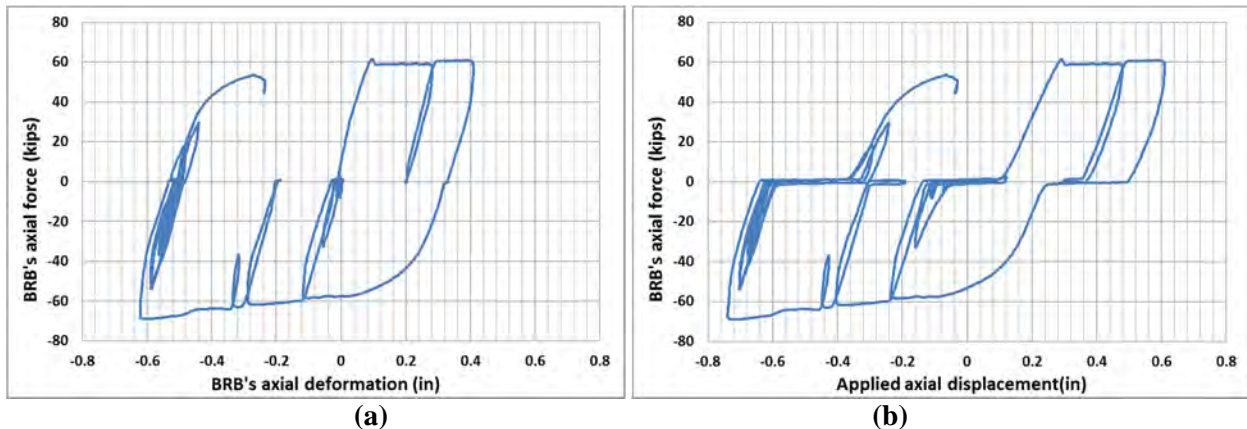
Figure 8-125 Hysteretic behavior of BRB-1-4 subjected to Bidirectional Seismic Response Displacement History in test BRB-1-4-A: a) axial force vs axial deformation; (b) axial force vs applied axial displacement

8.5.8.4 Test BRB-1-4-B

BRB-1-4 was then subjected to the Temperature-Induced Axial Displacement History-IV for 35 years. The hysteretic curve of BRB-1-4's axial force versus axial deformation subjected to the first cycle is shown in Fig.8-126a. Fig. 8-126b shows the typical hysteretic curve of BRB-1-4's axial force versus axial deformation in a typical cycle after the first one.

(a)   (b)
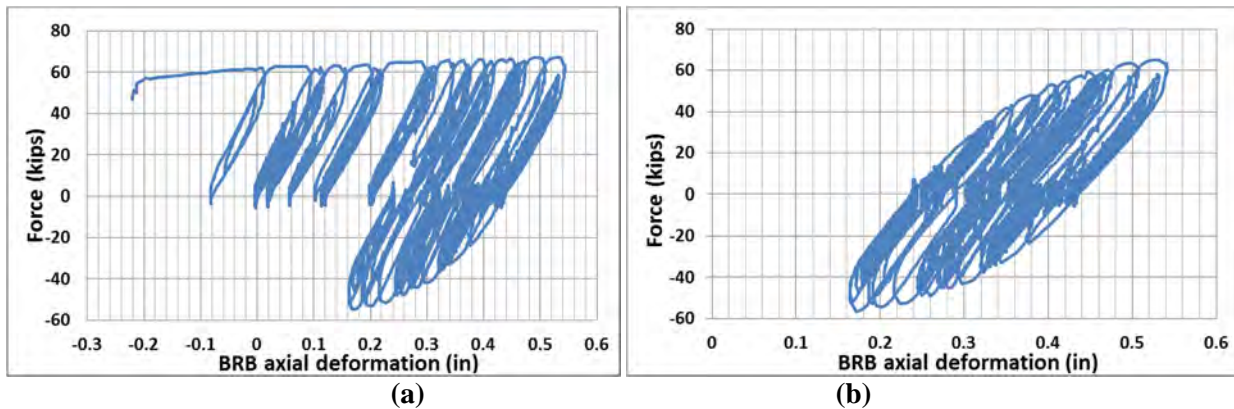
Figure 8-126 Hysteretic behavior of BRB-1-4 subjected to Temperature-Induced Axial Displacement History-IV: (a) first cycle (b) a typical cycle after the first one

8.5.8.5 Test BRB-1-4-C

BRB-1-4 was again subjected to the Bidirectional Seismic Response Displacement History in test BRB-1-4-C. The corresponding hysteretic curve of the BRB's axial force versus axial deformation (measured by Krypton system) is shown in Fig.8-127a. The BRB force versus applied axial displacements, in Fig. 8-127b, shows the bolt slippage of 0.27" at zero loads.

Note that the sum of tests BRB-1-4-A to BRB-1-4-C can be thought of as equivalent to subjecting the bridge to the design-level earthquake the day after the BRB was just installed, followed by 35 years of service (and movements of the bridge due to temperature changes), and another similar design-level earthquake after those years in service.

383

	(a)		(b)
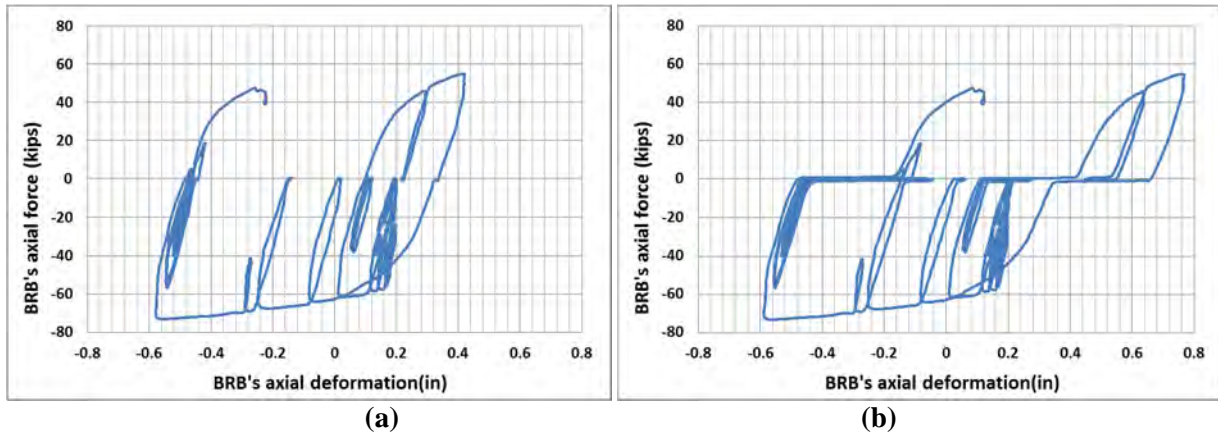
Figure 8-127 Hysteretic behavior of BRB-1-4 subjected to Bidirectional Seismic Response Displacement History in test BRB-1-4-C: a) axial force vs axial deformation; (b) axial force vs applied axial displacement

8.5.8.6 Bidirectional Displacement Protocols with Gaps

As observed in the previous tests of BRBs, the actual deformation of the BRB was different from the intended applied displacement, due to the bolt slippage. To investigate how the existence of the bolt gaps affect the dynamic response of the BRB, the bolt gaps were included in the simplified bridge diaphragm model, with the intent of obtaining a displacement history representative of the nonlinear response of the bridge that could develop when gaps were present at the pins. Re-analysis of the bridge was performed using the *OpenSees*. For this purpose, an Elastic-Perfectly Plastic Gap (EPPG) material was used to model the bolt gaps (together with the BRB), which replaced the bilinear material of the BRB. The resulting BRB force-deformation relationship obtained with this gap material setting is shown in Fig.8-128.
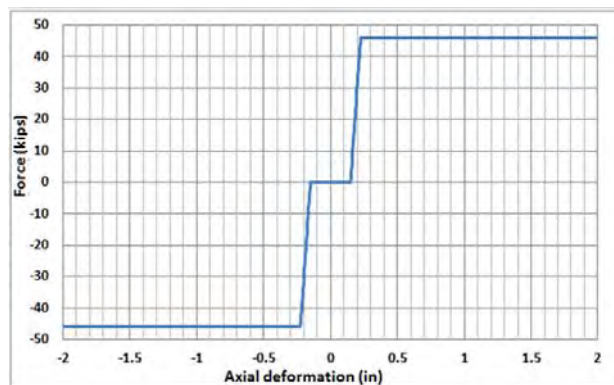
Figure 8-128 BRB's force-deformation relationship with the gap material setting in OpenSees

The same pair of ground motion and scale factor used to obtain the bidirectional displacement history in Fig. 8-123 was used in the new nonlinear time history analysis of the simplified bridge diaphragm model

384

that included the gap elements. Results shown in Fig.8-129 compare the BRB's bidirectional displacement demand in the bridge diaphragm model using EPPG material (solid line) with that for the bilinear material (dotted line). The responses are different in terms of frequencies and magnitude of the two displacement histories in each direction. As expected, larger displacements were observed for the bridge diaphragm model with the EPPG material in both directions.

(a)   (b)
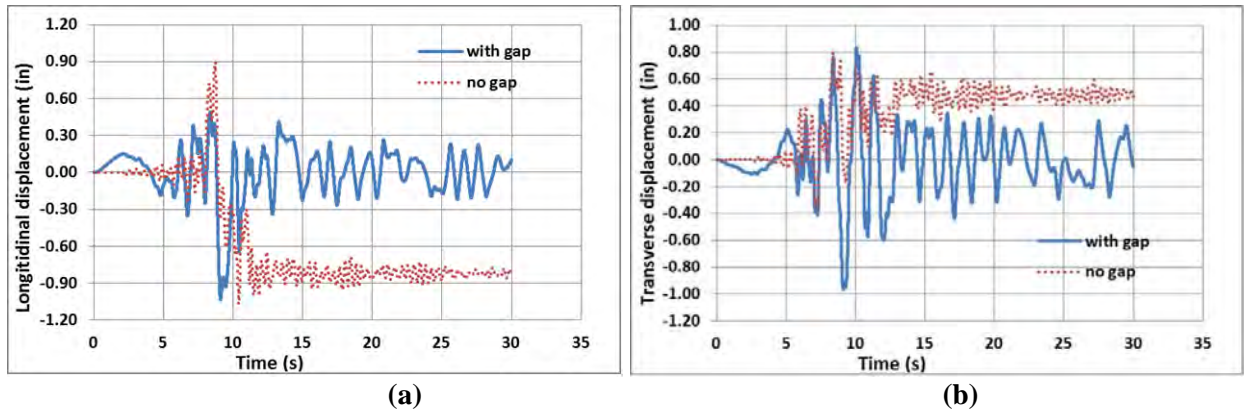
Figure 8-129 Displacement history comparisons of the bridge diaphragm model between bilinear material (no gap) and EPPG material (with gap): (a) longitudinal direction; (b) transverse direction

The BRB's hysteretic curve of axial force vs axial displacement in the bridge diaphragm model with the gap material is shown in Fig. 8-130. Note that the BRB modeled with the EPPG material did not exhibit full hysteretic loops. This was not the expected behavior of BRB including the bolt slippage (which should have compressive force on the tensile side, and vice versa). It can be observed in Fig. 8-130 that the length of the gap slippage crossed the point of zero deformation. It was expected that smaller displacement demands might have resulted if modeling the correct BRB hysteretic behavior. However, due to the tight schedule of testing BRB in the lab, there was no time to revise the nonlinear analysis, and the displacement history (solid line) in Fig. 8-129 was used for the BRB test. Note that it was not essential to have exact displacement history at that stage, as the BRB was expected to survive the ground motion multiple times. It was understood that this displacement history could be later be compared to that obtained using a corrected model of gap behavior.

After all the BRB tests were completed, the model with the correct BRB hysteretic behavior including the gap effects was built and analyzed. The desired hysteretic behavior of BRB with gap was achieved by modeling the gap element in series with the BRB so that the bilinear behavior of the BRB was separated from the gap slippage. For this revised nonlinear model, push-over analysis gave a force-deformation relationship (of the BRB in series with the gap) identical to the one shown in Fig. 8-128. The hysteretic

behavior of the BRB with gap is shown in Fig. 8-131 for the new bridge model under the same pair of ground motion and scale factor as mentioned before.
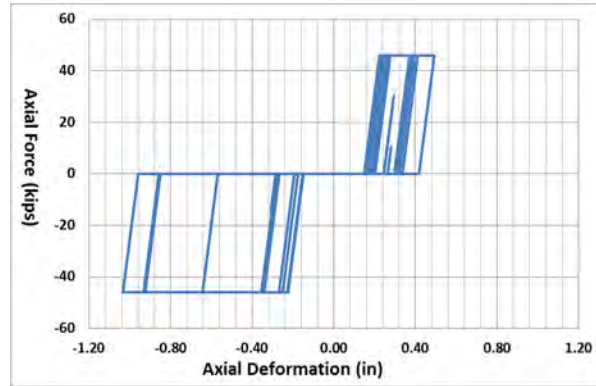
Figure 8-130 BRB hysteretic curve of axial force vs axial displacement in the bridge diaphragm model with EPPG material
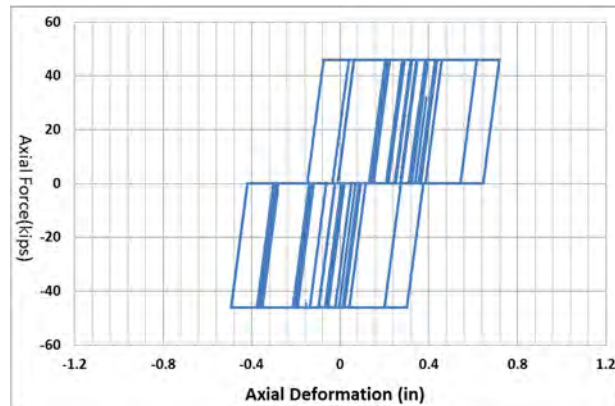
Figure 8-131 Correct BRB hysteretic curve of axial force vs axial displacement in the new bridge diaphragm model with gap

In Fig. 8-132, the corresponding BRB's displacement demand in this new model is shown to have maximum longitudinal and transverse demands of 0.711" and 0.937", respectively. They are 31% and 2.5% smaller than the longitudinal and transverse demands of 1.039" and 0.961" in the displacement history obtained using the EPPG material (i.e., the solid line in Fig. 8-129, to which the specimen was subjected). Therefore, the displacement history applied to the specimen was slightly more conservative than what was necessary, and the obtained results remain valid.

For consistency, the test duration to apply the bidirectional displacement history (solid line in Fig. 8-129) was also increased from 30s to 300 s as shown in Fig.8-133, which is labeled as "Bidirectional Seismic Response with Gap Displacement History-C" with the corresponding bidirectional trace shown in Fig. 8-

134. Note that the displacement history shown in Fig. 8-133 subjects the BRB to greater amplitude of displacement in compression than in tension.

(a)   (b)
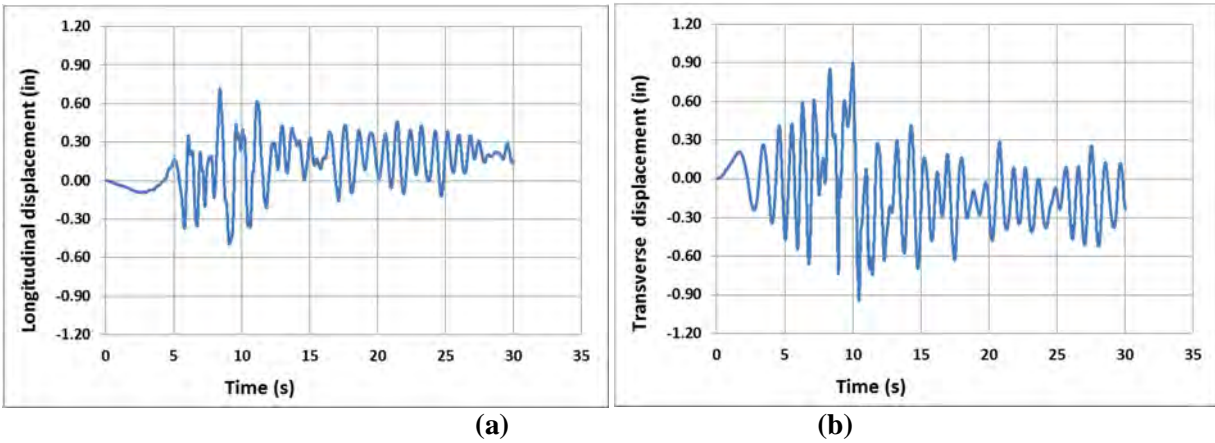
Figure 8-132 BRB's bidirectional displacement demand from the bridge diaphragm model with correct BRB hysteretic behavior

(a)   (b)
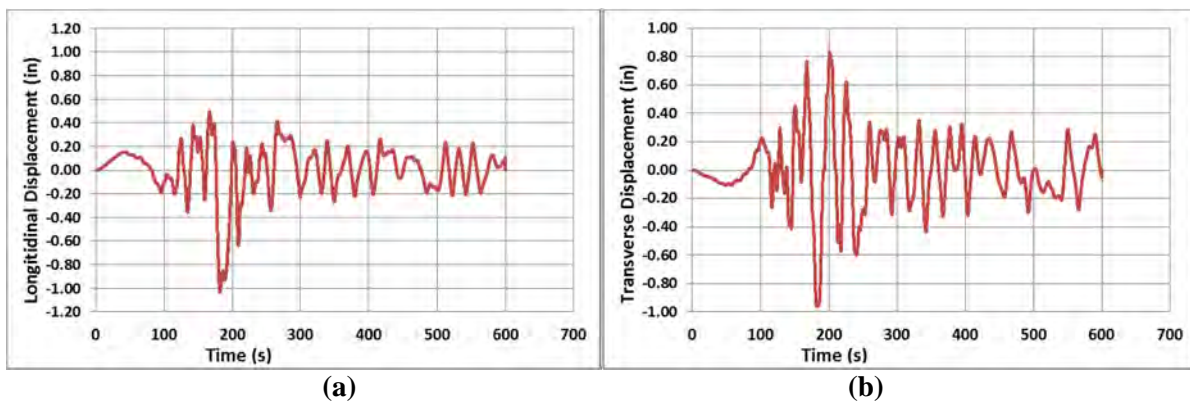
Figure 8-133 Bidirectional displacement history demand obtained from nonlinear time history analyses of bridge diaphragm model with EPPG material: (a) longitudinal; (b) transverse

Due to uncertainty in the direction of any input ground motion, the displacement demand history could equally have been the one shown in Fig. 8-135 (if the ground motions directions had been inverted), which subjects the BRB to more tension than compression. The bidirectional displacement history in Fig. 8-135 was named "Bidirectional Seismic Response with Gap Displacement History-T" and also used, as described below.

387
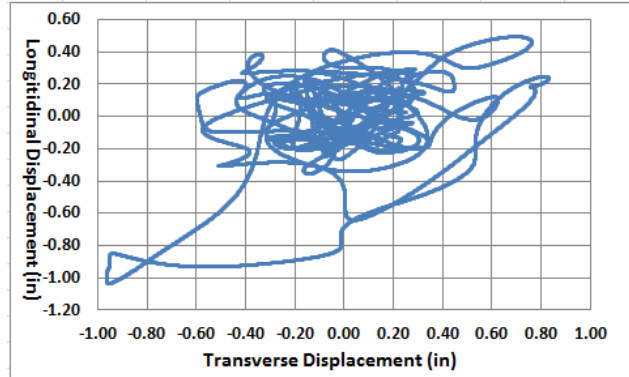
Figure 8-134 Traces of Bidirectional Seismic Response with Gap Displacement History-C
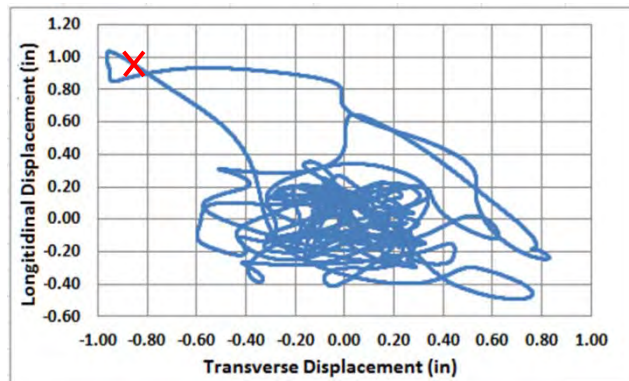
Figure 8-135 Traces of Bidirectional Seismic Response with Gap Displacement History-T

8.5.8.7 Test BRB-1-4-D

BRB-1-4 was subjected to Bidirectional Seismic Response with Gap Displacement History-C and Bidirectional Seismic Response with Gap Displacement History-T alternately in test BRB-1-4-D.

The hysteretic curve of BRB-1-4's axial force versus axial deformation (measured by Krypton system) under Bidirectional Seismic Response with Gap Displacement History-C is shown in Fig. 8-136a. The BRB force was plotted as a function of applied axial displacements under the same displacement history in Fig. 8-136b, which shows the bolt slippage of 0.27" at zero loads.

The hysteretic curve of BRB-1-4's axial force versus axial deformation (measured by Krypton system) under Bidirectional Seismic Response with Gap Displacement History-T is shown in Fig. 8-137a. The BRB force was plotted as a function of applied axial displacements under the same displacement history in Fig. 8-137b, which shows the bolt slippage of 0.27"at zero loads.

388

The comparisons of hysteretic curves of BRB-1-4 under these two bidirectional displacement histories obtained considering gap slippage in the non-linear analyses are shown in Fig. 8-138, with dotted line and solid line for Bidirectional Seismic Response with Gap Displacement History-C and Bidirectional Seismic Response with Gap Displacement History-T, respectively. Note that the axial deformations were measured by LPs in Fig.8-138.

(a)   (b)
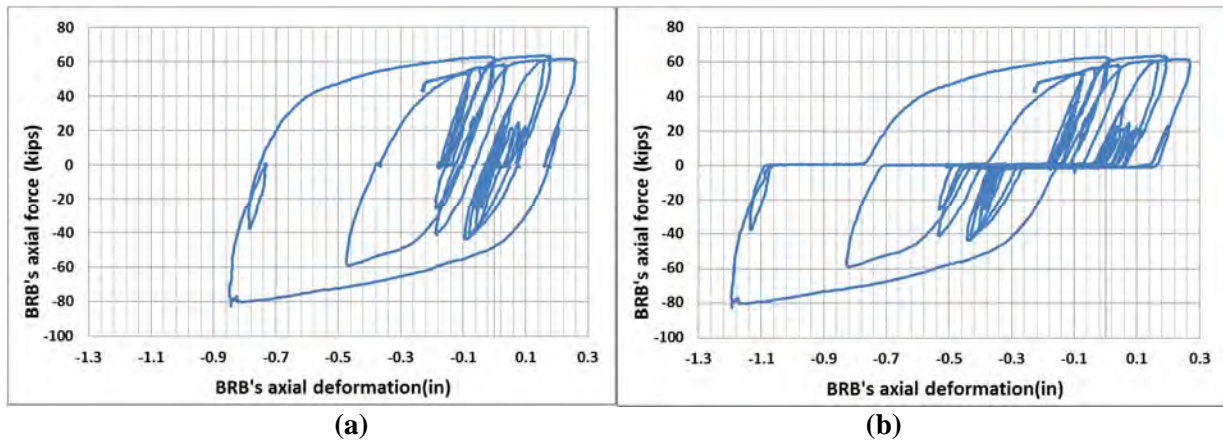
Figure 8-136 Hysteretic behavior of BRB-1-4 subjected to Bidirectional Seismic Response with Gap Displacement History-C in test BRB-1-4-D: a) axial force vs axial deformation; (b) axial force vs applied axial displacement

(a)   (b)
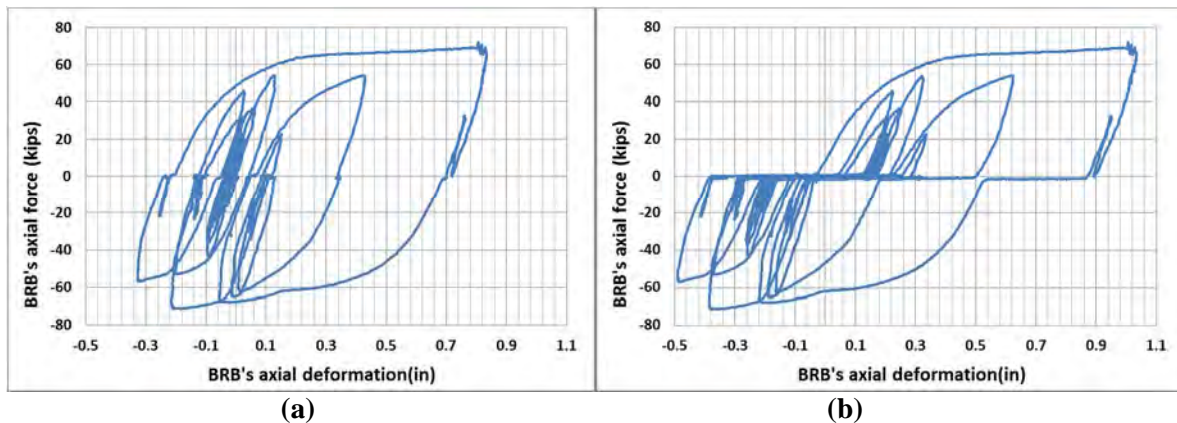
Figure 8-137 Hysteretic behavior of BRB-1-4 subjected to Bidirectional Seismic Response with Gap Displacement History-C in test BRB-1-4-D: a) axial force vs axial deformation; (b) axial force vs applied axial displacement

The Bidirectional Seismic Response with Gap Displacement History-C and Bidirectional Seismic Response with Gap Displacement History-T, were successively applied to the specimen in test BRB-1-4-D, alternating one after the other, until failure. BRB-1-4 failed during the 3rd repetition of the Bidirectional Seismic Response with Gap Displacement History-T (in other words, after three cycles of Bidirectional Seismic Response with Gap Displacement History-C and two cycles of Bidirectional

Seismic Response with Gap Displacement History-T). The failure of BRB-1-4 is indicated by the red cross in Fig. 8-135.
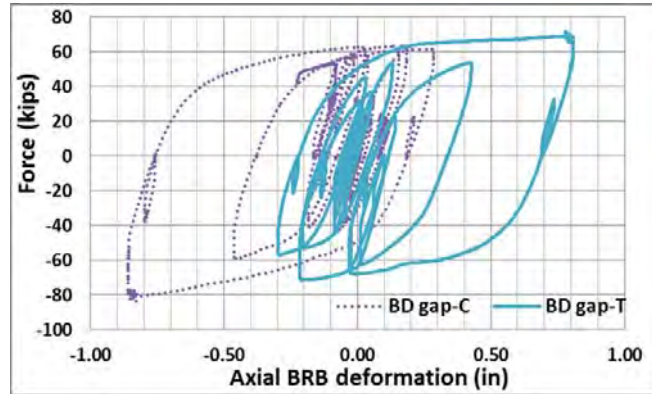
Figure 8-138 Hysteretic behavior of BRB-1-4 subjected to Bidirectional Seismic Response with Gap Displacement History-C and Bidirectional Seismic Response with Gap Displacement History-T

Fig. 8-139 compares the hysteretic curves under the bidirectional displacement history applied in test BRB-1-4-A ("BD no gap"), test BRB-1-4-D ("BD gap-C" and "BD gap-T") and the temperature-induced displacement history in test BRB-1-4-B ("Temp"). In all of the above testing of BRB-1-4, no end-plate failure or instability was observed. After the test, a visible bulge was observed on the southwest side of the BRB. The cause of that bulge and mode of failure of the BRB specimens will be discussed in details in Section 9.1.
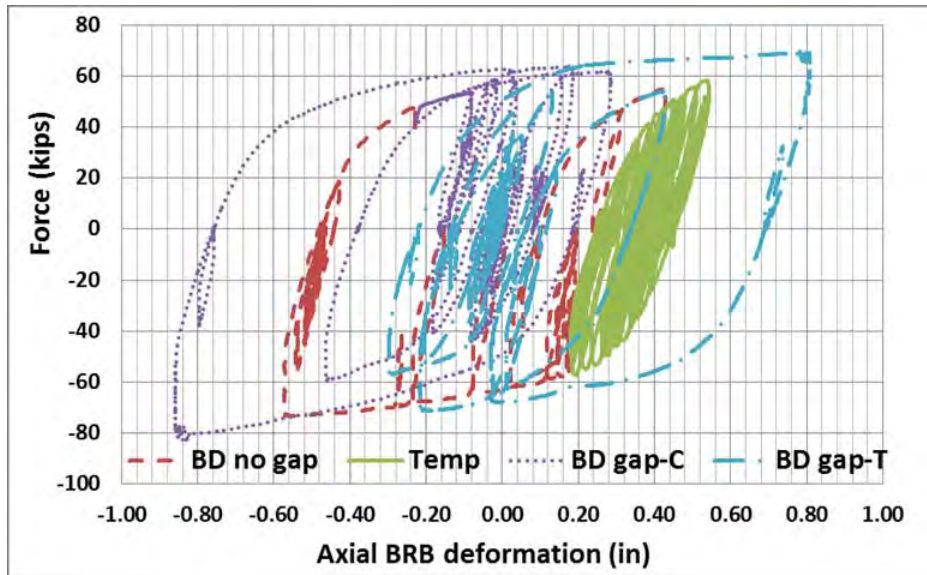
Figure 8-139 Hysteretic behavior of BRB-1-4 under all the applied displacement histories

SECTION 9

""""""INVESTIGATION ON BRB TEST RESULTS

9.1   General

In this Section, the observations of the BRB specimens after its failure are described in Section 9.2. In order to provide guidance on how to estimate BRB's damage under bidirectional and temperature-induced axial displacement history, each BRB specimen's hysteretic behaviors in different tests are quantified by the cumulative inelastic deformations and low-cycle fatigue damage calculated using Fatiga Software in Sections 9.3 and 9.4, respectively.   Section 9.5 provides additional information of the BRB's displacement demands when actual hysteretic behavior of the BRB material was used in the nonlinear time history analyses of the simplified bridge diaphragm model. Predictions about the BRB's expected behaviors in this bridge ductile diaphragm application are presented in Section 9.5, based on the all the tests results in Section 8 and calculations done in Sections 9.3 and 9.4.

9.2   Observations on BRBs' Failure

As expected, all the BRBs failed in tension after extensive cycles of inelastic deformation, irrespective of whether the BRB was subjected to bidirectional or temperature-induced axial displacement histories. No end-plate failure or instability was observed. After the test, a visible bulge at one end of the BRB was observed in almost all BRBs, except for BRB-2-2, which was only subjected to uniaxial displacement histories due to temperature change. Fig. 9-1a shows a typical bulge at the northeast side of BRB-2-3, when viewed from the direction shown by the arrow in Fig. 9-1b. For different BRBs, the bulges occurred on different sides (east and west) and ends (north and south) of the BRBs, as documented in Table 9-1 (in that table, "NE", "SE", and "SW", stands for the north-east, south-east, and south-west sides of the BRB, and "N/A" means no apparent bulge was observed).   After opening some BRB specimens (cutting the casing with a cutting torch, and chipping the concrete with a small hammer and a chisel), it was found that the bulge was produced by the core plate's buckling inside the concrete and HSS at that location.

Looking from the same direction as shown in Fig. 9-1b, the bulge that occurred on the NE side of BRB-2-4's concrete-filled HSS is shown in Fig. 9-2. That HSS casing was then cut open where the bulge was the largest, revealing the displaced (and cracked) concrete inside, as shown in Fig. 9-3.

'"'

(a)
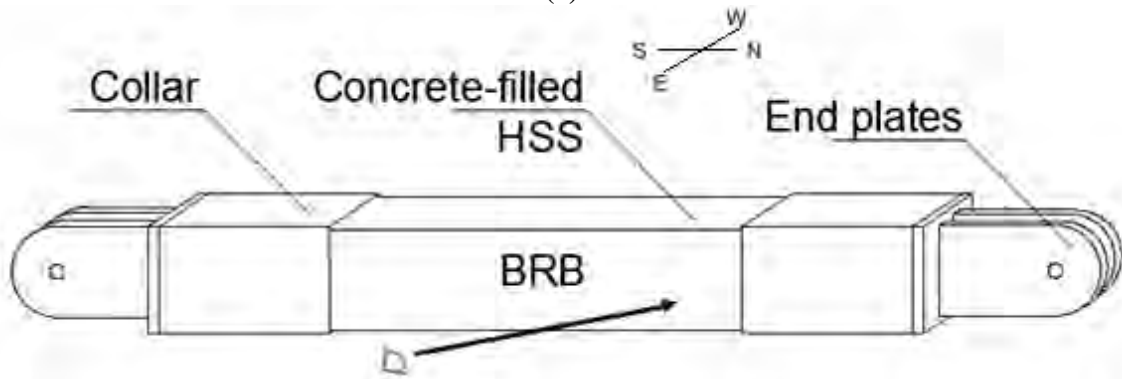
(b)
Figure 9-1 Bulge on the NE side of the HSS of BRB-2-3

Table 9-1 Summary of BRB bulges after the failure

BRB	2-1	2-2	2-3	2-4	1-1	1-2	1-3	1-4
Side	NE	N/A	NE	NE	SE	NE	SE	SW

That cracked concrete was then partly removed to reveal the steel core. Fig. 9-4a shows the fractured core plate, when viewed from the direction shown by the arrow in Fig. 9-4b. Visibly, significant out-of-plane displacement of the core plate had occurred and was the cause of the observed bulges.

After completely removing the collar, HSS casing, and encased concrete, the entire core plate was revealed. Fig. 9-5 shows part of the core plate in the vicinity of where it fractured. That fracture occurred at the tip of a severe and isolated local buckle. The circled part of the core plate shown in Fig. 9-5 is similarly circled in Fig. 9-6 to show that failure typically occurred in the part of the core plate close to the transition zone (typically at one of the two locations as shown in Fig. 9-6). Note that when fracture

392

occurred at one of the two circled location in Fig. 9-6, at the opposite location close to the other transition part of the core plate, significant out-of-plane deformation of the core plate also happened, but it had smaller amplitude than where failure occurred. Specific manufacturing details of the tested BRB (that cannot be revealed) were found to explain why the BRB core plate could more easily buckle at those two locations, and recommendations were made to the BRB manufacturers that could enhance the low fatigue life of the BRB (although one must keep in mind that the BRBs already all exhibited considerable cumulative ductilities, as shown in Section 9.3.3 below). Note that except for these two circled part in Fig. 9-6, the rest of the core plate remained mostly straight (as verified using a straight edge).
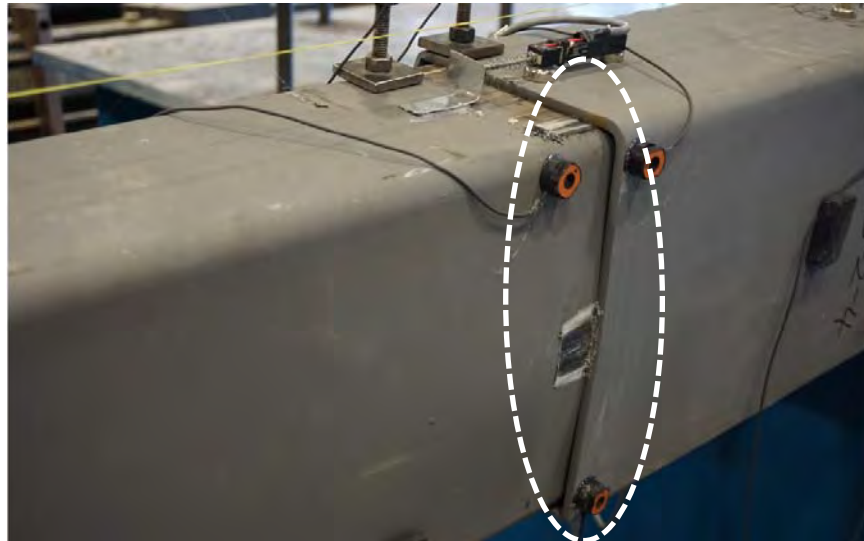
Figure 9-2 Bulge on the NE side of the HSS of BRB-2-4

Figure 9-3 Concrete fractured around the broken core plate of BRB-2-4

(a)
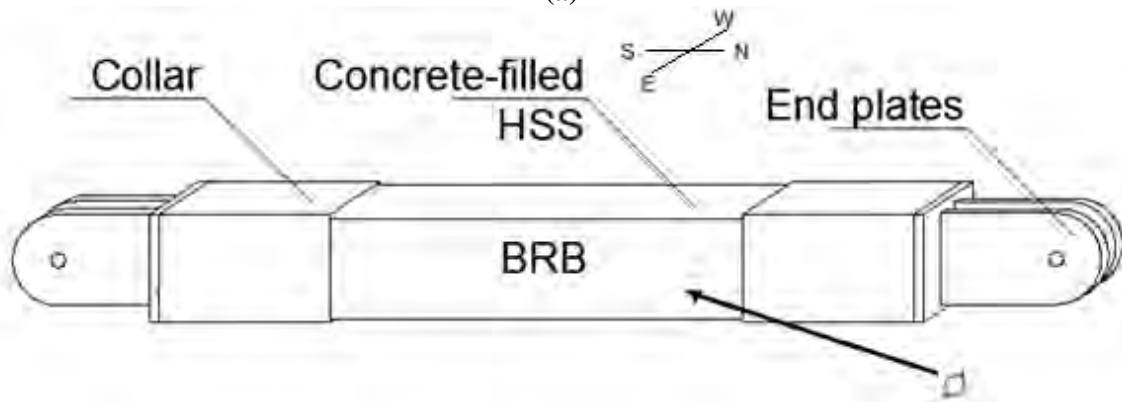
(b)

Figure 9-4 Broken section of BRB-2-4's core plate

Figure 9-5 Part of the core plate of BRB-2-4 with the fracture
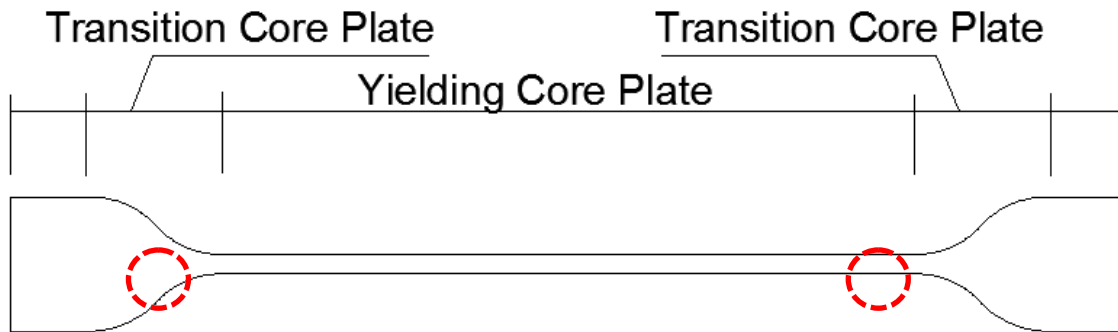
Figure 9-6 Buckling locations of the core plate of BRB-2-4

9.3 Cumulative Inelastic Deformations

A commonly used approach to quantify the severity of each BRB's inelastic response under different displacement history in each test is to examine the cumulative inelastic deformations that the BRB experienced. The cumulative inelastic deformations are quantified in terms of the axial yield displacement of the BRB, Δ_{by}. Recall from Section 8.2.2.1 that the yield displacements Δ_{by} are 0.107" and 0.081" for BRB-1 and BRB-2, respectively. Representative examples of how the BRB's cumulative inelastic deformations are calculated from the test results are shown separately for bidirectional and temperature-induced axial displacement history in Sections 9.3.1 and 9.3.2, respectively. The summarized cumulative inelastic deformations for all BRBs are presented in Section 9.3.3.

9.3.1 Bidirectional Displacement History

Three examples are provided below to illustrate how the cumulative inelastic deformations were calculated for BRBs subjected to bidirectional displacement history. The hysteretic curves used in this section are from test BRB-1-1-A, BRB-1-3-B, and BRB-2-3-E, in which the BRB had different initial starting force, as this affects how the inelastic deformations are calculated.

The hysteretic curve of BRB-1-1 in test BRB-1-1-A in Fig. 9-7a is used to illustrate how to obtain the inelastic deformations for the typical bidirectional displacement history, in which the BRB's starting force is zero. Recall from the test protocol described in Section 8.4.2 that the displacement demand in each of the cycles applied to this BRB in the bidirectional displacement history corresponded to (successively) the yield displacement D_{by}, half the Design Displacement (D_{bm}), D_{bm}, 1.5 D_{bm} and 2 D_{bm}, as indicated in Fig. 9-7a. Note that there are two cycles at each displacement demand. The dashed lines matching the elastic slopes in Fig 9-7b indicate the range of the elastic deformations. There was no inelastic deformation in

the BRB in the D_{by} cycle. The BRB started to have inelastic deformations in the $0.5D_{bm}$ cycle. The inelastic deformation for the first cycle at $0.5D_{bm}$ is calculated as $2(\Delta_{tmax} + \Delta_{cmax}) - 5\Delta_{by}$, where Δ_{tmax} and Δ_{cmax} are the maximum deformation at tensile and compressive side, respectively. For the second cycle at $0.5\ D_{bm}$ and the following cycles at other displacement demand, the inelastic deformation is calculated as $2(\Delta_{tmax} + \Delta_{cmax}) - 4\Delta_{by}$, which is different from the previous case because this cycle does not have the initial Δ_{by} that occurred during first loading. Table 9-2 shows the total cumulative elastic deformations of 120.54 Δ_{by} calculated based on the BRB-1-1 hysteretic loops shown in Fig.9-7b.
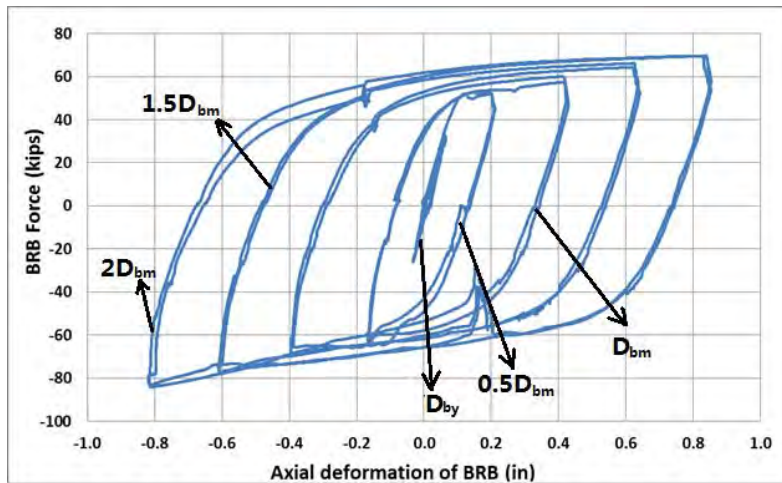
(a)
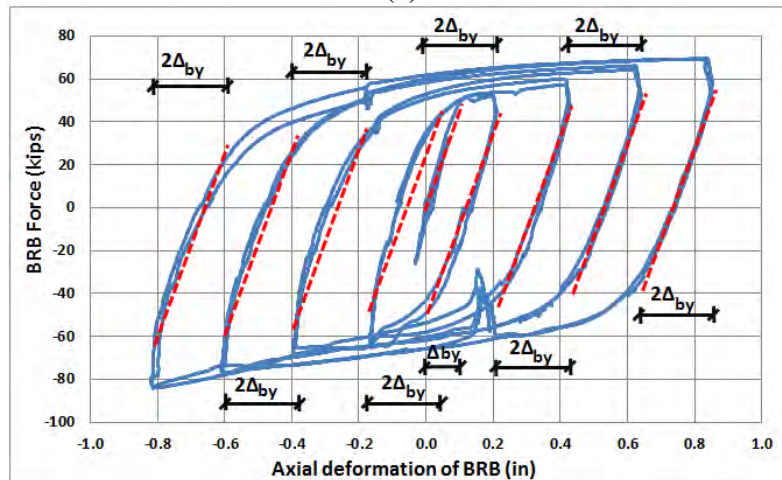
(b)

Figure 9-7 Hysteretic behavior of BRB-1-1 in test BRB-1-1-A: (a) labeling specific loops in the hysteretic curves; (2) marked elastic deformations

Note that, as described in Section 8, some tests ended leaving a residual force in the BRB. This had to be taken into account when calculating cumulative deformations in bidirectional displacement histories conducted after such tests. The hysteretic curve of BRB-1-3 in test BRB-1-3-B at 2% drift is shown in

Fig. 9-8, in which the BRB was already yielded in tension at the start of this bidirectional displacement history. The dashed lines are drawn in the same way as in Fig. 9-7b to indicate the elastic deformation. The inelastic deformations per cycle is calculated as $2(\Delta_{tmax} + \Delta_{cmax}) - 4\Delta_{by}$, which is $19.16\Delta_{by}$. These two cycles shown in Fig. 9-8 are similar to the cycles after the first cycle at $0.5D_{bm}$ in Fig 9-7b. The total inelastic deformation corresponding to two cycles in Fig. 9-8 is $38.32\Delta_{by}$.

Table 9-2 Inelastic deformations of BRB-1-1 in test BRB-1-1-A

Cycles	Inelastic Deformation				
	Δ_{max}	Δ_{min}	Per cycle(Δ_{by})	Total	Cumulative
2@ D_{by}	0.061"	-0.032	0	0	0
2@0.5 D_{bm}	0.210"	-0.166"	1@2.02&1@3.02	5.05	5.05
2@ D_{bm}	0.421"	-0.400"	2@11.34	22.69	27.74
2@1.5 D_{bm}	0.631"	-0.612"	2@18.24	38.48	66.22
2@2 D_{bm}	0.850"	-0.817"	2@27.16	54.32	120.54
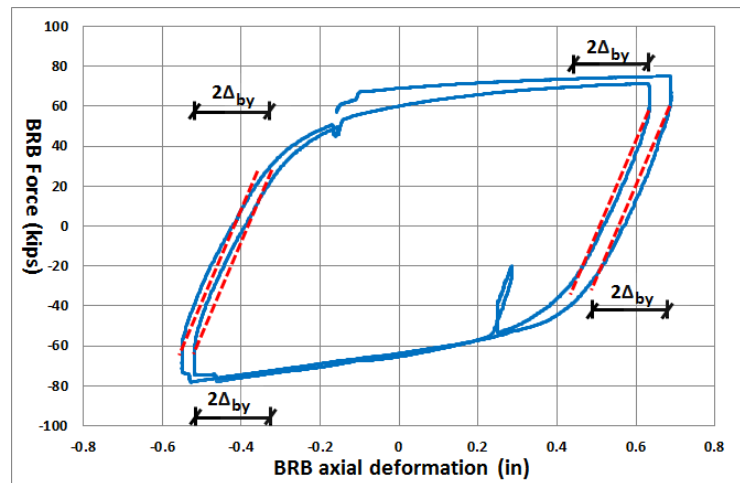
Figure 9-8 Hysteretic curve of BRB-1-3 in test BRB-1-3-B with marked elastic deformations

Conversely, some BRB tests also started with an initial compressive force as in the hysteretic curve of BRB-2-3 from test BRB-2-3-E shown in Fig. 9-9. Note that the BRB in this test followed a tension-compression-compression-tension loading sequence, which is not the same as the BRB-1s in Fig. 9-7 and 9-8. Recall that, as described in section 8.5.2, the loading sequence had been changed in the Average Bidirectional Displacement History used for BRB-1.

In that case when the BRB started from the compressive force, an elastic deformation of $2\Delta_{by}$ occurred before tension yielding (as the BRB had to first be unloaded from that compressive force before undergoing tension). Except for this initial elastic range, the other four elastic ranges are defined the same

way as before (note that the left-most part of the figure has two superposed elastic curves on top of each other). Note that BRB-2-3's yield displacement $\varDelta_{by}$ of 0.081" is smaller than BRB-1's yield displacement of 0.107". The total deformation of the BRB in Fig. 9-9 is 8.55". By subtracting the elastic deformations $10\varDelta_{by}$ of 1.07", the remaining deformation is the cumulative inelastic deformations of 7.48", which is equal to 69.9 $\varDelta_{by}$.
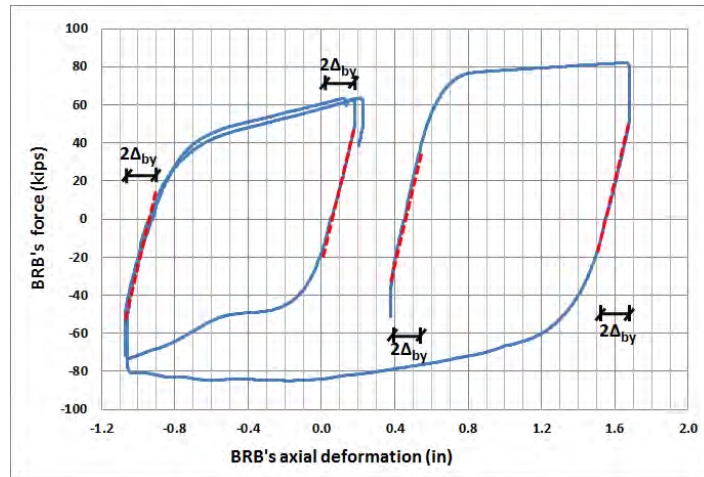
Figure 9-9 Hysteretic curve of BRB-2-3 in test BRB-2-3-E with marked elastic deformations

9.3.2 Axial Temperature-Induced Displacement History

This section presents three examples of how the cumulative inelastic deformations were calculated for BRBs subjected to axial temperate-induced displacement histories. The hysteretic curves used in these examples are from tests BRB-2-2-A and BRB-2-3-D, in which the BRB also had different initial starting forces.

The approach taken to calculate the inelastic displacement for each half of a hysteretic cycle was explained in Section 8.5.6.3. It was shown there that for one year of temperature-induced axial displacement (shown in Fig. 8-103), the inelastic displacement was calculated as twice the total deformation range minus the elastic deformation of $4\varDelta_{by}$ of the BRB. This is due to the fact that for the hysteretic curves obtained from the temperature-induced axial displacement history, the total displacement magnitude was shown to matter more than the small cycles (as those small cycles imposed mostly elastic strains to the BRB). The same approach is used here to calculate the cumulative inelastic deformations for other BRBs, for which hysteretic curves of axial force versus axial deformation were available.

Note that for the tests conducted before BRB-1-2, when temperature-induced axial displacement histories were applied, the hysteretic curves of the BRB's axial force versus axial deformation cannot be well represented, for the reasons mentioned in Section 8.5.6.3. For example, Fig. 9-10 shows the BRB's axial force versus the shake table's longitudinal displacement for a typical cycle after the first cycle in test BRB-2-2-A. From this plot, the BRB's force developed during the test can be seen to correspond to displacements that are larger than the BRB's actual axial deformation shown in Fig. 9-11 (refer to the comparison between the table's longitudinal displacement, applied BRB's axial displacement, and axial deformation in Fig.8-50 for more information). However, it is possible to obtain the cumulative inelastic deformations from figures such as Fig. 9-11. The maximum and minimum axial deformation Δ_{max} and Δ_{min} is 0.353" and 0.086", respectively, reached at maximum tensile and compressive forces of 46 kips and -41kips in Fig. 9-11. The magnitude of BRB's deformation Δ_{max}-Δ_{min} is therefore 0.267". The inelastic deformation of the BRB under this one-year temperature-related displacement history is calculated as $2(\Delta_{max}$-Δ_{min}-$2\Delta_{by})$, which is 0.21" (2.6 Δ_{by}).
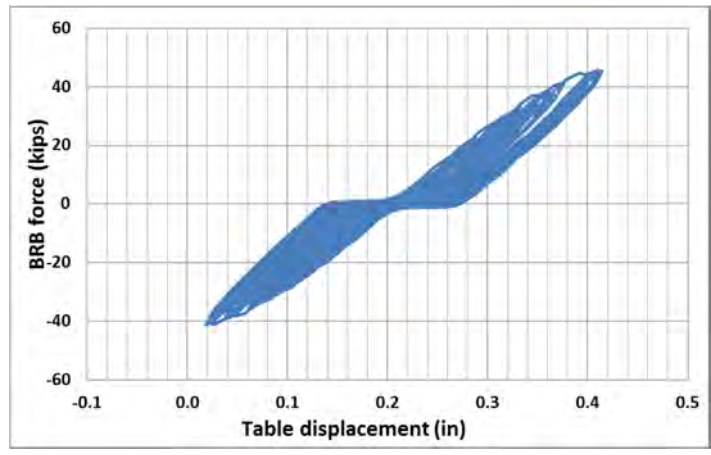
Figure 9-10 BRB-2-2's axial force vs table's longitudinal displacement for a typical cycle in test BRB-2-2-A
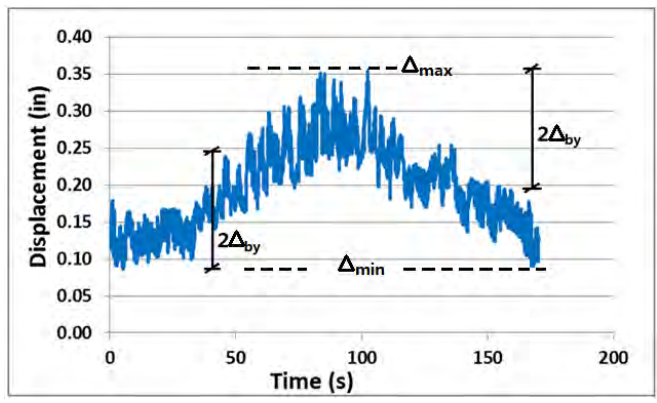
Figure 9-11 Axial deformation of BRB-2-2 for a typical cycle in test BRB-2-2-A with marked elastic deformation

399

The hysteretic curve of BRB-2-2 subjected to the first year of temperature-induced displacement history in the same test BRB-2-2-A is shown in Fig. 9-12. Note that it differs from the typical cycle in Fig. 9-10. The corresponding axial deformation of the BRB in this first cycle is shown in Fig. 9-13. The initial force of the BRB is zero at the beginning of the test; the elastic deformation is Δ_{by} when the BRB undergoes tension from 0 to 48 kips. The corresponding BRB's initial minimum deformation Δ_{min1} and maximum deformation Δ_{max} are 0" and 0.364" as shown in Fig. 9-13. The inelastic deformation corresponding to that yield excursion is Δ_{max}- Δ_{min1}-Δ_{by}, which is 0.283" ($3.5\Delta_{by}$). When the BRB was compressed from the maximum tensile force of 48 kips to the maximum compressive force of -38 kips in Fig. 9-12, the BRB's maximum deformation Δ_{max} of 0.364" decreased to the minimum deformation Δ_{min2} of 0.09" in Fig. 9-13. The corresponding inelastic deformation in that case is Δ_{max}- Δ_{min2}-$2\Delta_{by}$, which is 0.112" ($1.38\Delta_{by}$). The resulting total inelastic deformation of the BRB under this one-year temperature-related displacement history is 4.88 Δ_{by}.
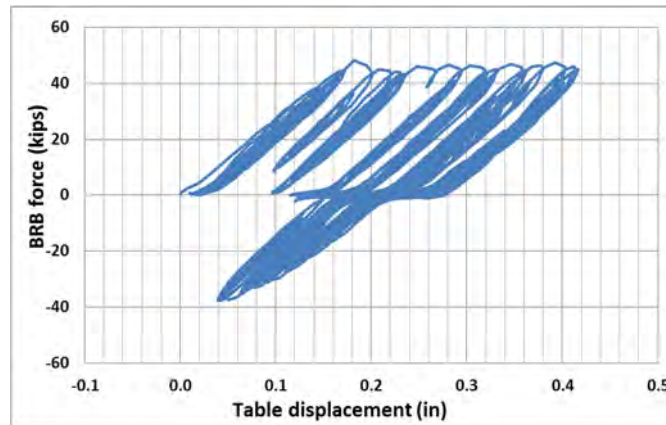
Figure 9-12 BRB-2-2's axial force vs table's longitudinal displacement for the first cycle in test BRB-2-2-A
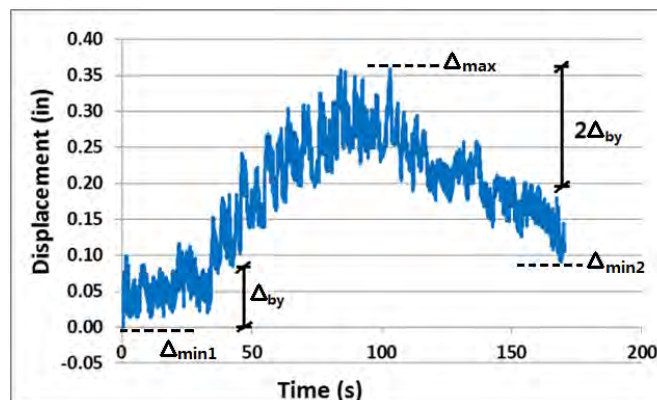
Figure 9-13 Axial deformation of BRB-2-2 for the first cycle in test BRB-2-2-A

Note that the initial force of the BRB can also be tensile as in the hysteretic curve of BRB-2-3 subjected to the first year of temperature-induced displacement history in test BRB-2-3-D, as shown in Fig. 9-14. The corresponding axial deformation of the BRB in this first cycle is shown in Fig. 9-15. The BRB was already in the inelastic range of response at the beginning of that test when the BRB was at the minimum deformation $\varDelta_{min1}$ of 0", as shown in Fig. 9-15. Therefore, in that case, when the BRB reached the maximum deformation $\varDelta_{max}$ of 0.58", the inelastic deformation is $\varDelta_{max}$- $\varDelta_{min1}$, which is 0.58" (7.16 $\varDelta_{by}$). When the BRB was compressed from 79 kips to -54 kips (Fig. 9-14), the BRB's deformation changed from $\varDelta_{max}$ of 0.58" to $\varDelta_{min2}$ of 0.13" (Fig. 9-15). The elastic deformation is $2\varDelta_{by}$, and the inelastic deformation is $\varDelta_{max}$- $\varDelta_{min1}$-$2\varDelta_{by}$, which is 0.288" (3.56 $\varDelta_{by}$). Therefore, the total BRB's deformation is 10.72 $\varDelta_{by}$.
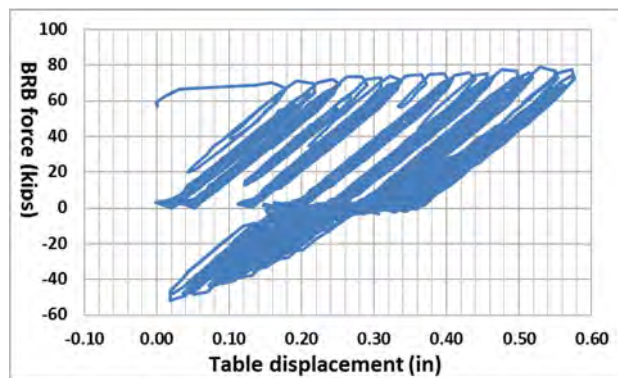
Figure 9-14 BRB-2-3's axial force vs table's longitudinal displacement for the first cycle in test BRB-2-3-D
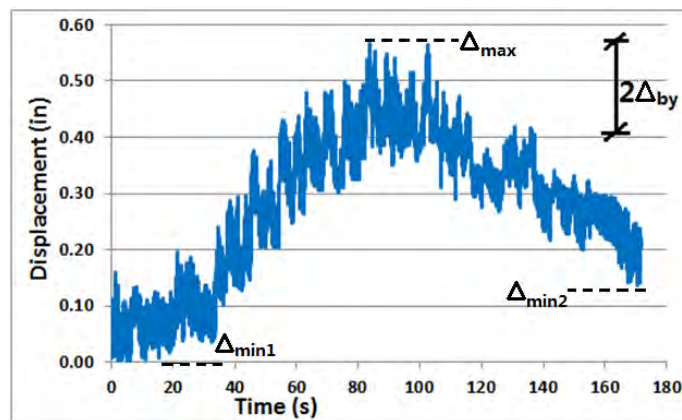
Figure 9-15 Axial deformation of BRB-2-3 for the first cycle in test BRB-2-3-D

9.3.3 Summary of cumulative inelastic displacements for all BRBs

The cumulative inelastic deformations of each BRB are calculated and shown in Table 9-3 in terms of the yield displacement of the BRB $\varDelta_{by}$.

Table 9-3 Summary of BRB's cumulative inelastic deformations in terms of yield displacement Δ_{by}

Specimen	Bidirectional	Axial	Total
BRB-2-1	306 Δ_{by}	0	306 Δ_{by}
BRB-2-2	0	343 Δ_{by}	343 Δ_{by}
BRB-2-3	363 Δ_{by}	44 Δ_{by}	407 Δ_{by}
BRB-2-4	200 Δ_{by}	60 Δ_{by}	260 Δ_{by}
BRB-1-1	120 Δ_{by}	102 Δ_{by}	222 Δ_{by}
BRB-1-2	141 Δ_{by}	191 Δ_{by}	332 Δ_{by}
BRB-1-3	475 Δ_{by}	0	475 Δ_{by}
BRB-1-4	144 Δ_{by}	106 Δ_{by}	250 Δ_{by}

All the BRBs developed cumulative inelastic displacement of more than 200 Δ_{by}, which is a threshold of inelastic performance specified as part of the acceptance criteria in AISC 341-10 Specifications (#). Note that the different test protocols used for the various specimens tested (and sequence in which these protocols were applied) partly explain the differences in cumulative inelastic displacements recorded for each of the BRBs in Table 9-1.

The following observations can be made based on the comparisons of cumulative elastic deformations between different BRBs:

- When comparing results for BRB-1-3 and BRB-2-1, which were both only subjected to bidirectional displacement histories (i.e., without temperature-induced cycling), it is observed that BRB-1-3's cumulative inelastic deformation is larger than that for BRB-2-1. Given that the bidirectional test displacement histories for BRB-1 generally had smaller amplitude than for BRB-2, this indicates that the BRBs failed after fewer cycles of inelastic deformations when those cycles were of a larger amplitude, which resulted in smaller cumulative inelastic deformations.

- When comparing results for BRB-1-1 and BRB-1-2, which were both first subjected to essentially the same bidirectional displacement history, followed by different axial temperature-induced displacement histories until failure, it is observed that the BRB subject to larger amplitude of axial displacement history failed at a smaller cumulative inelastic deformation. A larger amplitude of axial displacement history was used at the end in test BRB-1-1-D to fail the BRB specimen. The maximum amplitude of the axial displacement history used for BRB-1-2 was 64% of BRB-1-1, and it sustained 86% more of inelastic deformation under the axial temperature-induced displacement.

- BRBs were observed to fail at smaller cumulative inelastic deformation values if they experienced many years of the small temperature-induced axial displacement demand before the bidirectional displacement demands from the earthquake was applied to it. This can be seen by comparing results

for BRB-2-3 and BRB-2-4. Recall that a temperature-induced displacement history (corresponding to $60\Delta_{by}$) was first applied to BRB-2-4 before the extreme bidirectional displacement history (corresponding to $200\Delta_{by}$) was applied to it. In the test of BRB-2-3, the BRB was first subjected to a bidirectional displacement history (corresponding to $245\ \Delta_{by}$), followed then by the same temperature-induced axial displacement history but with a different number of cycles (corresponding to $44\ \Delta_{by}$), and ended with more cycles of bidirectional displacement history (corresponding to $118\ \Delta_{by}$). BRB-2-3 reached 156% more cumulative inelastic deformation than BRB-2-4. This result suggests that the sequence in which the different displacement histories are applied could matter.

However, note that more tests would be needed to provide a statistical basis to validate the above observations. Although the BRBs were identical in their design, some subtle (but not easily visible) differences in how they were fabricated could also be responsible for the observed differences.

Note that all the BRBs reached cumulative inelastic deformations of $250\Delta_{by}$, except for BRB-1-1. In BRB-1-1, which reached only $222\Delta_{by}$, the temperature-induced axial displacement history was scaled up to a large magnitude at the end of the test, with the intention to fail BRB-1-1 quicker, and it is possible that this has reduced the fatigue life.

From a design perspective, the above information could be used to assess how many years a BRB could remain in service while retaining its ability to provide adequate seismic response. For example, for a bridge with the length, L, in Memphis installed with longitudinal BRBs having a steel core length of 6% with no inclination (i.e., installed horizontally) at each end in the EDS, the number of years depends on BRB's design displacement demand from the earthquake (which is chosen to correspond to a ductility, μ_B, of 6 in this example). Note that the cumulative inelastic deformation in the AISC axial qualification test protocol equals to $8\times(5\mu_B-4)$, which gives $208\ \Delta_{by}$ for ductility 6. If the maximum cumulative inelastic deformation of the BRB of $250\Delta_{by}$ is used here, this leaves $42\Delta_{by}$ available for the cumulative inelastic deformations of the BRB subjected to the temperature displacement history. For a BRB's steel core plate having yield strength and Young's modulus of 46 ksi and 29000 ksi, the yield displacement of the BRB based on deformation only in the core length, Δ_{by}, equals to $9.52\times10^{-5}L$ (i.e.=$46/29000\times0.06L$). For the case at hand (Memphis), the maximum and minimum yearly temperatures are 102ºF and 20 ºF, and the temperature range, ΔT, is 82 ºF (for 2012, from Fig. 17a). Assuming that the bridge's concrete slab governs its thermal expansion, and using the coefficient of thermal expansion of concrete, α_c, of 0.000006 in/in/°F to calculate the one-year temperature displacement history applied to the BRB as $0.5\alpha_c L\Delta T$ (the tributary length of the bridge for each longitudinal BRB is $0.5L$). The corresponding inelastic

deformation of the BRB is $\alpha_c L\Delta T\text{-}4\Delta_{by}$, equaling to $1.17\Delta_{by}$. Therefore, the number of years that the BRB can be installed in the EDS of this bridge is approximately 35 years. Note that the number of years in service would be greater if gaps in the end connections of the BRB absorbed some of these thermal displacements.

9.4   Low-cycle Fatigue Analyses
9.4.1   General

Recall, from Section 7.7, that the fatigue life of the BRB can be predicted by using the Fatiga Software, using as input the strain history calculated from displacements applied to the BRB due to the temperature changes of the bridge. The fatigue life is equal to the reciprocal of the "damage" caused by the strain history (with "damage" taken here in the context of low-cycle fatigue calculations, as no physical damage would be visible). Note that the fatigue damage computed by Fatiga was based on base metal properties and the axial strain calculated based on the entire core plate length. It is expected that BRBs will fail before the life that Fatiga predicted, since the local buckling strain would have added significant strains to the core. A calibration factor is therefore required to relate the base-metal low-cycle failure to that of a BRB which will ultimately fracture due to repeated local buckling of the core plate.

In this section, the fatigue life and damage are studied based on the experimental results. Section 9.4.2 first provides additional information on the fatigue damage calculated by Fatiga for the displacement protocols that were originally intended to be applied to the BRBs. Section 9.4.3 gives the fatigue damage values obtained from Fatiga based on the experimental results.

9.4.2   Damage Prediction of Intended Applied Displacement History

Recall that for the strain history that resulted from the original axial temperature-induced displacement history (shown in Fig. 8-33, in Section 8.4.3), the fatigue life calculated using the software Fatiga was 413 years. The corresponding fatigue damage is 0.0024. However, the original temperature-induced displacement history amplitude was calculated for a 200 ft bridge, and that history was corrected (amplitude reduced) to correspond to the prototype 100-ft bridge in Section 8.5.5.4. For this corrected corresponding axial strain history, a revised fatigue damage of 0.00023 was calculated by Fatiga. Note that this fatigue life is about 10 times longer than the one corresponding to the 200-ft bridge (which is expected, as fatigue life calculations are logarithmic in nature).

Fatiga was then used to calculate the fatigue damage caused by the axial strain obtained from the various applied bidirectional displacement histories considered in Section 8. The original Extreme Bidirectional Displacement History (Fig. 8-27 in Section.8.4.2) and the Average Bidirectional Displacement History (Fig.8-85 in Section 8.5.5.2) are divided by the yielding core length to obtain the corresponding histories of axial strains in the core plate, as shown in Figs. 9-16a and 9-16b.

(a)   (b)
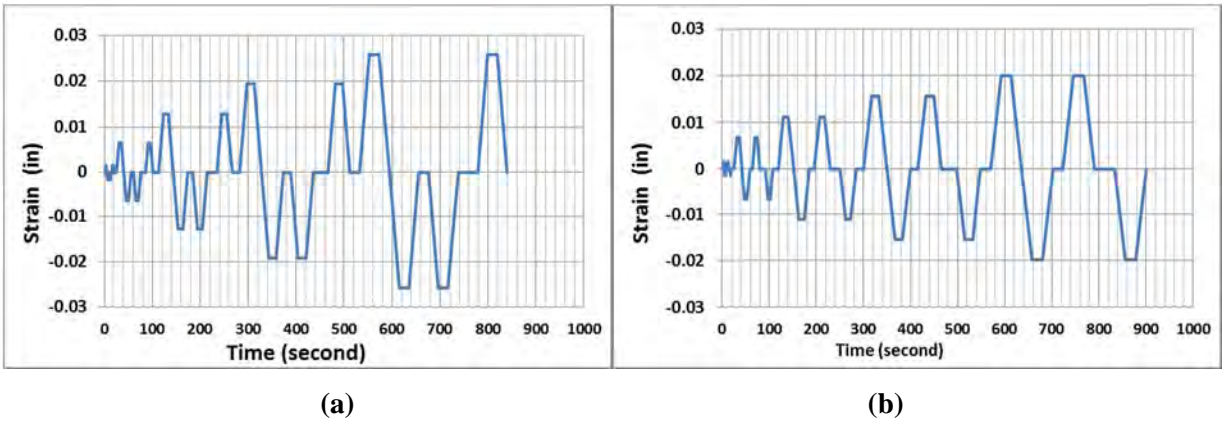
Figure 9-16 Axial strain history used in the fatigue damage calculation: (a) original bidirectional displacement history; (b) Average Bidirectional Displacement history

It is observed that Fig. 9-16b has different amplitude and loading sequence from Fig. 9-16a. The corresponding schematic stress excursions of the BRB under the displacement history are shown in Figs. 9-16a and 9-16b, with the different loading cycles shown in dashed lines.

(a)   (b)
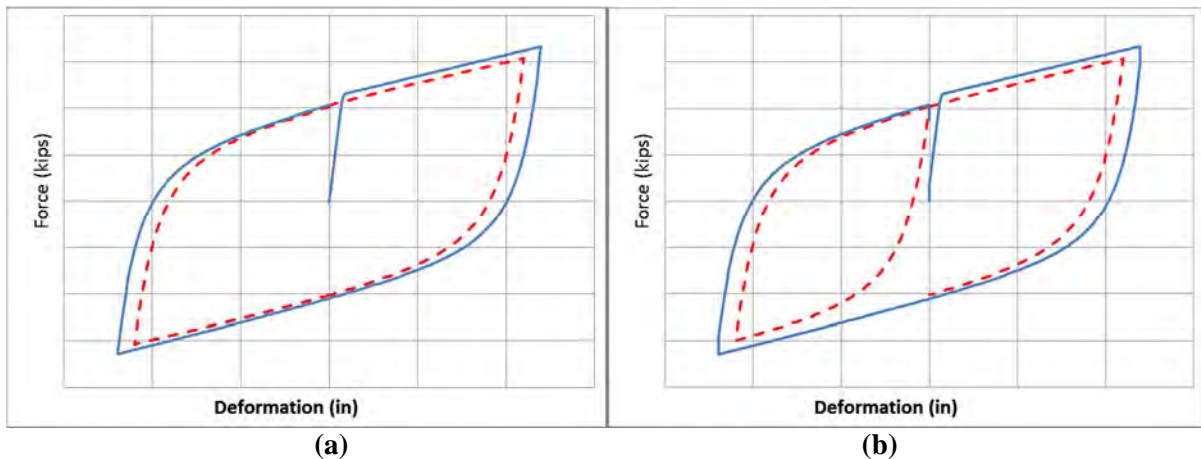
Figure 9-17 Schematic stress excursion corresponding the displacement histories (illustrated in Fig. 9-16): (a) original bidirectional displacement history; (b) Average Bidirectional Displacement history

405

The fatigue damages resulting from the cycles shown in Figs. 9-16a and 9-16b were calculated using Fatiga and are tabulated in Tables 9-4 and 9-5 with the corresponding total fatigue damage of 0.0168 and 0.011, respectively. The reciprocal of the total fatigue damage indicates that the strain history in Figs. 9-16a and 9-16b could each be respectively applied to a BRB for 59 and 88 times before it fails.

Table 9-4 Fatigue damage calculation of strain history (illustrated in Fig. 9-16a)

Number	ε_{max}	ε_{min}	Damage
1	0.025763	-0.02576	6.77E-03
1	0.025763	-0.01932	5.31E-03
1	0.019322	-0.01288	2.48E-03
1	0	-0.02576	0.00E+00
1	0.019322	0	9.52E-04
1	0.012881	-0.00644	7.71E-04
1	0	-0.01932	0.00E+00
1	0.012881	0	3.52E-04
1	0	-0.01288	0.00E+00
1	0.006441	-0.00159	9.10E-05
1	0.006441	0	5.74E-05
1	0	-0.00644	0.00E+00
2	0.001586	0	1.23E-06
1	0	-0.00159	0.00E+00
		Total Damage :	1.68E-02

Table 9-5 Fatigue damage calculation of strain history (illustrated in Fig. 9-16b)

Number	ε_{max}	ε_{min}	Damage
2	0.018839	-0.01884	6.55E-03
2	0.014129	-0.01413	3.32E-03
2	0.009419	-0.00942	1.24E-03
2	0.00471	-0.00471	2.07E-04
2	0.001586	-0.00159	7.47E-06
		Total Damage :	1.13E-02

The difference of total fatigue damage between those two displacement histories is due to the differences in magnitude and in the loading sequence. Note that the damage is zero for the cycles corresponding to the compressive strain range (shaded rows in Table 9-4). To investigate the effect of the loading sequence, the strain history in Fig. 9-16a was changed to become the one in Fig. 9-18, which has the same magnitude in each cycle as in Fig.9-16a but follows a loading sequence identical to the one in Fig. 9-16b. The corresponding total fatigue damage caused by the strain history in Fig. 9-18 is 0.0236 as tabulated in Table. 9-5, which is larger than the fatigue damage from Fig. 9-16a. The difference is due to the way

cycles are defined in fatigue calculations (note that compression excursions to not contribute to fatigue damage).
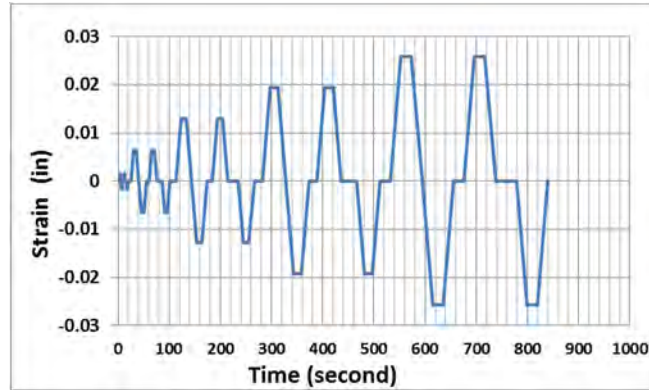
Figure 9-18 Changed loading sequence of the axial strain history corresponding to original bidirectional displacement history

Table 9-6 Fatigue damage calculation of strain history (illustrated in Fig. 9-18)

Number	ε_{max}	ε_{min}	Damage
2	0.025763	-0.02576	1.35E-02
2	0.019322	-0.01932	6.95E-03
2	0.012881	-0.01288	2.66E-03
2	0.006441	-0.00644	4.75E-04
2	0.001586	-0.00159	7.47E-06
		Total Damage :	2.36E-02

9.4.3   Damage Calculation Based on Experimental Results

The deformations output from the LPs were divided by the yielding core plate length to obtain the strain history of the core plate during each test. These strain histories were input in Fatiga individually to get the corresponding fatigue damage. The resulting fatigue damage for each BRB are presented in Table 9-5. Contributions from the bidirectional and temperature (axial) were calculated separately and summed to obtain the total damage (see Table 9-5). Since the BRB failed after applying these displacement histories, technically, the total damage factor should be 1.0. However, that is not the case because the fatigue damage values in Table 9-5 are those resulting from theoretical fatigue calculation using a fatigue model based on the base metal properties, which does not consider the additional strains due to the effect of local buckling. Therefore, the total damage factors of all BRBs are smaller than 1.0 in Table 9-5, ranging from 0.0122 to 0.0486 with an average of 0.0363. These total damage values effectively correspond to the calibration factor that should have been used in calculations to obtain a damage value of 1.0 at failure, as mentioned in Section 7.7 and Section 8.4.3.

Recall that, as described in Appendix D, from the existing literature, for BRBs tested to failure under various constant amplitudes, calibration factors ranging from 0.05 to 0.53 were reported. For strain ranges comparable to those reached during the tests described in Section 8, these factors from past experiments ranged from 0.05 to 0.11. The BRBs calibration factors obtained as part of the research conducted here are smaller than those reported in the literature. However, one must keep in mind that fatigue damage is dependent on the magnitude of the strain ranges and the cycling sequence in the strain history, but also on the type of BRB tested because different BRB detailing can lead to the development of different types of local buckling of the steel core.

Here, the reported calibration factors can be used to allow predicting the fatigue life of the BRB from a low-cycle fatigue perspective. However, more experimental works would be needed to provide a statistical basis to generate generic predicting calibration factors for BRBs, based on the type of BRB specimen, as well as the magnitude and sequence of the applied strain history.

Table 9-7 Summary of BRB's fatigue damage

Specimen	Bidirectional	Axial	Total Damage
BRB-2-1	0.0122	0	0.0122
BRB-2-2	0	0.0486	0.0486
BRB-2-3	0.0225	0.0100	0.0325
BRB-2-4	0.0085	0.0050	0.0135
BRB-1-1	0.0097	0.0275	0.0372
BRB-1-2	0.0103	0.0248	0.0351
BRB-1-3	0.0416	0	0.0416
BRB-1-4	0.0104	0.0351	0.0455

9.5   BRB's Bidirectional Displacement Demand Regarding to Real BRB Hysteric Material

Recall from Section 8.4.1 that the BRB modeled in the simplified bridge diaphragm in *OpenSees* used bilinear material. In fact, the BRB's actual hysteretic behavior exhibited a more complex behavior, including strain hardening and Bauschinger effect, as shown in the experimentally obtained hysteretic curves shown in Section 8. To investigate how sensitive the seismically-induced bidirectional displacement demands would change if nonlinear response of the bridge was computed using a more realistic material model, a material modeling able to replicate the actual BRB's hysteretic behavior (i.e., model Steel02 in *OpenSees*) was used to replace the bilinear material previously used in the simplified

bridge diaphragm model. New nonlinear time history analyses were performed and corresponding bidirectional displacement demands were obtained.

The Steel02 material in *OpenSees* allows to construct a uniaxial steel material object with isotropic strain hardening. Here, the Steel02 material was specified to have a yield strength of 46 ksi and Young's modulus of 29000 ksi, which are the same as the bilinear material of the BRB used before. The other parameters in the Steel02 material were obtained by trial and error to match the experimentally obtained BRB hysteretic behavior. These parameters include the strain hardening ratio, b, the parameters that control the transition from elastic to plastic branches (R_0, CR_1, CR_2), and the isotropic strain hardening parameters (a_1, a_2, a_3, a_4). Fig. 9-18a shows the comparison of BRB-1-1's hysteric behavior in test BRB-1-1-A with the results obtained with the Steel02 material, when b, R_0, CR_1, CR_2, a_1, a_2, a_3, a_4 were set equal to 0.03, 20, 0.0935, 0.15, 0.065, 1,0.05, 1, respectively. A similar comparison is shown in Fig. 9-18b for BRB-1-2 in test BRB-1-2-A with the same parameters for the Steel02 material. Generally, the two hysteretic curves are well matched, except at the corners, which may be because the analytical model cannot capture specific aspects of the BRBs construction details (such as gaps at collars) that may slightly influence response under the bidirectional displacement history.

Recall from Section 8.5.5.2 that the scale factors of the 22 pairs of ground motions is 0.372, which corresponds to the ductility of 6 used to obtain the Average Bidirectional Displacement History. The same 22 pairs of ground motions and scale factors were used in the new analyses of the simplified bridge model with Steel02 material. The resulting average displacement demand obtained for those analyses with the revised material model is 0.423", which is 31.7% smaller than the average displacement demand of 0.619" used in the Average Bidirectional Displacement History. Therefore, it is found that it was conservative to use the larger displacement demands to test the BRB.
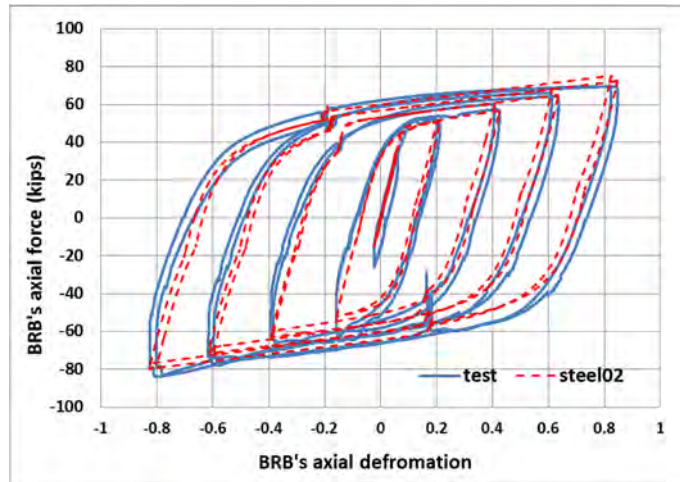
(a)
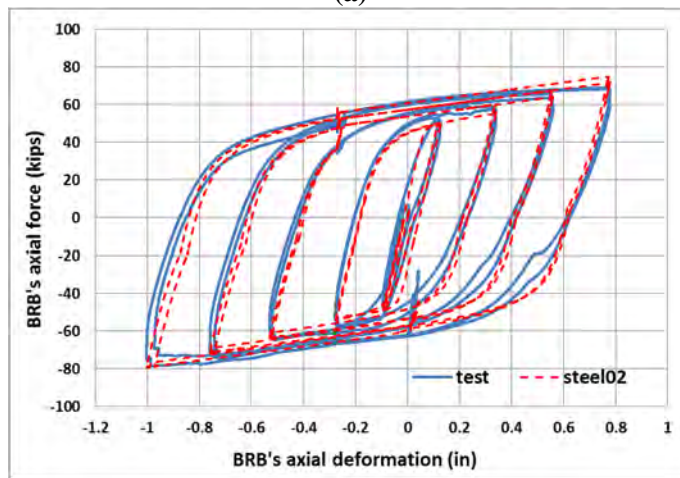
(b)

Figure 9-19 BRB's actual hysteretic behavior in bidirectional tests vs hysteretic behavior of steel02 material: (a) BRB-1-1; (b) BRB-1-2

9.6   Design procedures

On the basis of the above findings, the following procedure is proposed to design bidirectional bridge end diaphragms for a given bridge at a known location:

a. Assume an initial value for the fundamental period of the EDS, T_{eff}. In this procedure, the EDS period is the same for the longitudinal and transverse direction. For a skew bridge, that would be the value for an equivalent nonskew EDS.

b. For the specified design acceleration response spectrum at the bridge location, which gives the elastic force demand of the bridge, mS_a, at its fundamental period, T_{eff}, choose a desired displacement ductility of the nonskew bridge EDS, μ, the maximum of which can be taken as 6

per Equation 4.3.3 in AASHTO (2011); calculate the corresponding force reduction factor, R according to Equations 1 and 2 in Section 4.2.1.2.1.

c. The yield strength of the nonskew EDS, V_y, is mS_a/R, and the stiffness, K_{eff}, is $4\pi^2 m/T_{eff}^2$, and the yield displacement of the EDS, δ_y, is V_y/K_{eff}. The resulting inelastic displacement demand of the nonskew EDS is the elastic spectral displacement, $\delta_y\mu$, times the inelastic displacement magnification factor, R_{d1}, specified in Section 4.2.1.2.2.

d. Determine the displacement limits of the EDS: (1) the limit in the longitudinal directions, δ_{Lm}, is the gap between the bridge deck and abutment or the maximum seat width available; (2) the limit in the transverse directions, δ_{Tm}, is the girder lateral yield displacement(for diaphragms with energy dissipator connected between girders), calculated based on the girder properties for a given steel bridge. Changes to the bridge design can be made to ensure that these two values are greater than the displacement demands calculated in Step c. Alternatively, iterations over steps a to c may be needed until the resulting displacement demands δ_u in both directions are smaller than the limit.

e. For the bridge with skewness, the skew EDS is designed to have the same yield strength and displacement as its equivalent nonskew EDS designed following steps a to d. The displacement demand of the skew EDS, δ_u, is calculated as $\delta_y\mu R_{d1}R_{d2}$, where R_{d2} is a displacement magnification factor,R_{d2}, relating the expected maximum displacement response of skew bridge to that of its equivalent nonskew bridge, and specified in Section 4.2.1.2.4.

f. Determine the local displacement demand of the BRB based on the above displacement demand of the EDS, δ_u.

g. Design the BRB in the EDS following either of the three approaches presented below in item (1), (2), and (3), while satisfying the requirements in item (4) and (5):

  1) Implicit Design: Select the minimum length of the longitudinal BRB's steel core to be at least 6% of the total length of the bridge (one longitudinal BRB at each end of the bridge). Based on the above findings (i.e., BRB having maximum cumulative inelastic deformations of 250 times the yield deformation as described in Section 4.3.5.3), this BRB can be left in service for 35 years and expected to resist the seismic demand corresponding to the ductility of 6. This value can be modified to take into account the inclinations of the BRBs to reduce the length of the BRB yielding core as a percentage of total bridge length (see Section 4.2.2).

  2) Explicit Design: Select a longitudinal BRB yielding steel core length, such that the sum of the cumulative ductilities corresponding to temperature-induced displacement demand and cyclic testing protocol (both calculated following the example in Section 4.3.5.2) does not exceed

$250\Delta_{by}$. This may require iterations varying the length of BRB steel core, the desired number of years in service, and the expected BRB's ductility to resist the seismic demand).

3) Qualification Testing (to be used if the above cumulative inelastic displacement limit of $250\Delta_{by}$ is deemed too restrictive): BRB specimens can be qualified by subjecting one BRB to: (i) the BRB standard test protocols (following AISC 341-10), followed by; (ii) the temperature-induced axial displacement history protocols applied repetitively for the number of years of service that the BRB is expected to provide in addition to the satisfactory seismic response; and a second identical BRB subjected to the same protocols (i) and (ii) but applied in the reverse order (i.e., (ii) followed by (i)). Qualification testing approach would be of benefit for BRBs of different fabrication/detailing (and possibly sizes) than those considered in this research project.

4) Determine the BRBs' end connections by: (i) design the end plates of the BRB to bend laterally to accommodate the required lateral displacement without developing instability; (ii) connecting the end plates of the BRB to a spherical bearing (that special protection would be required to prevent corrosion of the spherical bearings).

5) Design the BRB connecting gusset plate to resist 1.5 times the BRB yield strength. Limitations for the maximum gusset plate length and corresponding thickness are provided to ensure that the BRB can sustain the displacements demands without flexural yielding of the gusset plate connection.

SECTION 10

""""""""BIDIRECTIONAL DUCTILE DIAPHRAGMS IN

MULTI-SPAN BRIDGE WITH FLOATING SPANS

10.1   General

In this section, bidirectional ductile diaphragms were implemented in nonskew multi-span bridge with simply-supported floating spans. In this case, the flexibility of the substructures in the transverse and longitudinal direction of the bridge needs to be considered when designing the bidirectional ductile end diaphragms. In Section 10.2, a design of bidirectional ductile diaphragms in an example multi-span bridge is presented. A corresponding analytical model of the bridge was built in SAP2000. In Section 10.3, pushover and nonlinear time history analyses were performed on the SAP2000 bridge model, and corresponding results are presented. Based on the analytical results, the design of the longitudinal ductile diaphragms in the end spans connecting to the abutment was changed, in order to study its effect on the bridge's dynamic performance. A summary of this study on multi-span bridges is presented in Section 10.4.

10.2   Designs of bidirectional ductile diaphragms
10.2.1 General

Fig. 10-1 shows a typical nonskew simply-supported bridge with three floating spans, which are supported on neoprene bearings, bidirectional sliding bearings or other bearings with negligible strength to horizontal deformations. For this bridge with the implemented bidirectional EDS-1 scheme mentioned in Section 7, Fig. 10-2a and 10-2b provide a schematic view showing the BRBs in the transverse and longitudinal ductile diaphragms, respectively. The transverse BRBs in Fig. 10-2a are located between the steel girders, and the BRBs can be pin-connected to the web stiffeners of the girders (which are not shown in Fig. 10-2a). Fig. 10-2b shows the longitudinal BRBs connected between the cap beams of the bent or the abutment to the top of the steel girders (i.e. bottom of the concrete slab). Note that the number of BRBs used in the EDS-1 scheme in Fig. 10-2 can change based on different bridge configurations and strength/stiffness demand provided by the BRBs. Also note that the connections details of the BRBs to different components in the bridge structures are not discussed here. The connection types presented in Section 6 of BRBs connecting to concrete may be considered, but this is not the focus of the study here and remains to be investigated.

"

Figure 10-1 A simply supported three-span bridge with floating spans

(a)

(b)

Figure 10-2 Illustration of the BRBs in the bidirectional ductile diaphragms in the three-span bridge: (a) transverse direction; (b) longitudinal direction

The design of the bidirectional ductile diaphragms in the multi-span bridge needs to consider the strength and stiffness contribution of the bridge bents in both the longitudinal and transvers directions. Fig. 10-3 illustrates the dynamic response of the multi-span bridge in the transverse and longitudinal directions when subjected to ground motions. The solid and dashed lines represent the undeformed and deformed shape of the bridge in both figures, respectively. The BRBs in the bidirectional diaphragms are intended

to yield and deform inelastically, absorbing and dissipating the seismic energy while keeping the rest of the structure elastic during the earthquake.

(a)
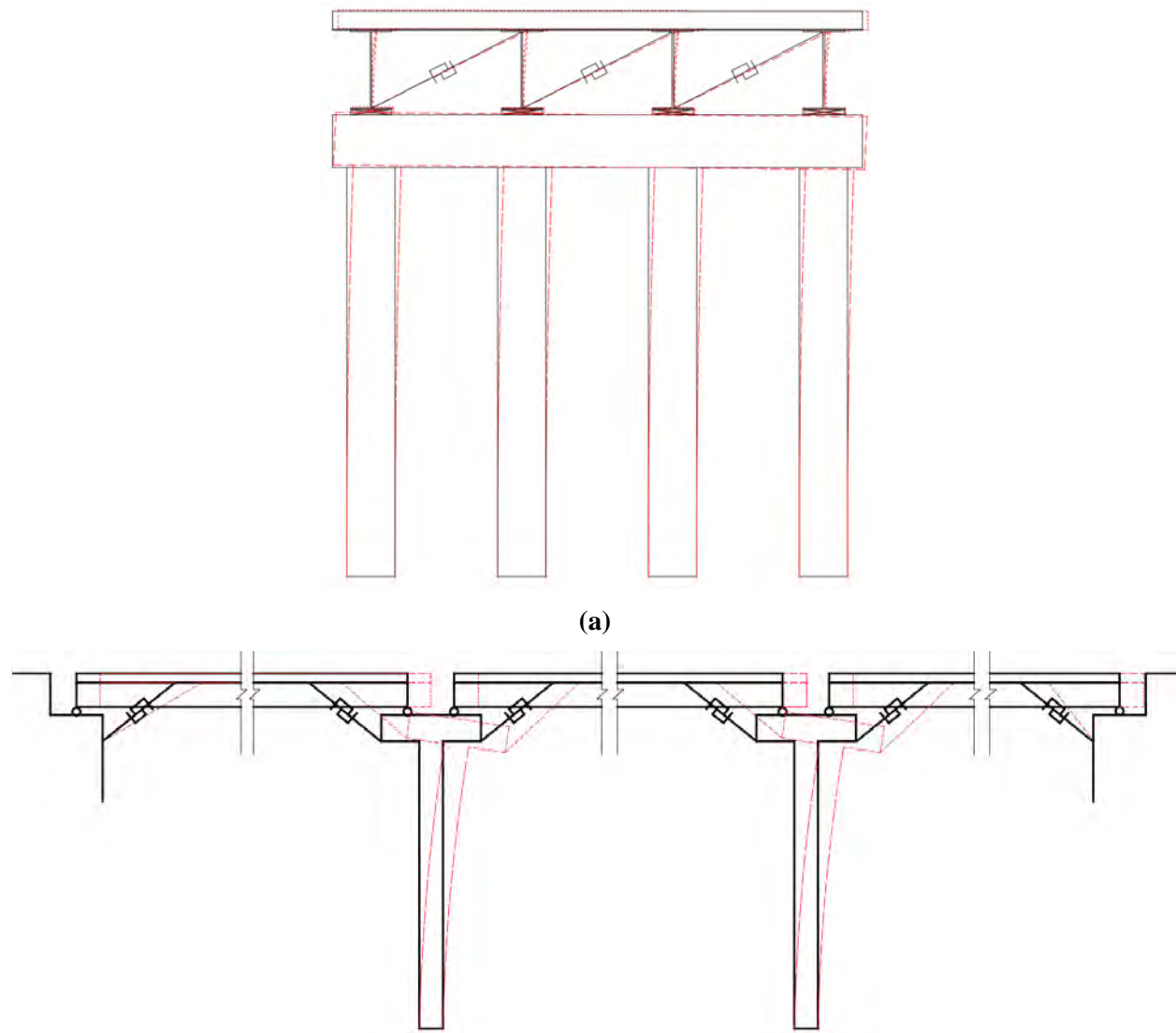
Figure 10-3 Illustration of the dynamic response of the multi-span bridge: (a) transverse direction; (b) longitudinal direction

The mass of each span of the bridge is M (including the mass of the nonstructural elements). The span length is L. The superstructure's moment of inertia is, I, which considers the slab and girders acting as a unit about a vertical axis perpendicular to the deck in the transverse direction. The bent stiffness in the transverse and longitudinal direction is K_{bt} and K_{bl}. The transverse and longitudinal stiffness of the bidirectional diaphragm at each end of the span is K_{dt} and K_{dl}. The stiffness of the girder stiffeners in the bridge's transverse direction is K_g, which is the total stiffness of the web bearing stiffeners of all girders.

The dynamic behaviors of the bridge in the transverse and longitudinal directions are discussed in Sections 10.2.2 and 10.2.3, in which equations used in the design calculations are introduced. Section 10.2.4 presents the design spectrum for the bridge and briefly stated the corresponding design parameters used in the design example and calculations presented in Appendix G. Section 10.2.5 shows the bridge model built in SAP2000, which was used in the pushover and nonlinear time history analyses presented in Section 10.3.

10.2.2 Bridge behavior in the transverse direction

The two end spans of the bridge are supported on the abutment at one end, and the bridge bent at the other end. The middle span of the bridge is supported on the bridge bent at both ends. Comparing the three spans, the behavior of the bridge in the transverse direction would be affected by the flexibility of the bridge bent (substructure) more at the middle span than at the end spans. Therefore, the designs of the BRBs in the transverse diaphragms in the middle span were the focus in this section.

The middle span of the bridge with transverse ductile diaphragms at both ends can be simplified as the beam with length L, uniform mass, M/L, and uniform stiffness, EI, supported on elastic spring groups as shown in Fig. 10-4. Since each bent supports the two adjacent spans, the stiffness K_{et} in Fig. 10-4 is not the entire transverse stiffness of the bridge bent, K_{bt}. Here, as a simplification, K_{et} is assumed to be half of K_{bt}. Note that the abutment supporting the end spans has much larger stiffness than the bents, this ratio of K_{et}/K_{bt} for the middle span is subjected to change for different transverse bent stiffness K_{bt}.
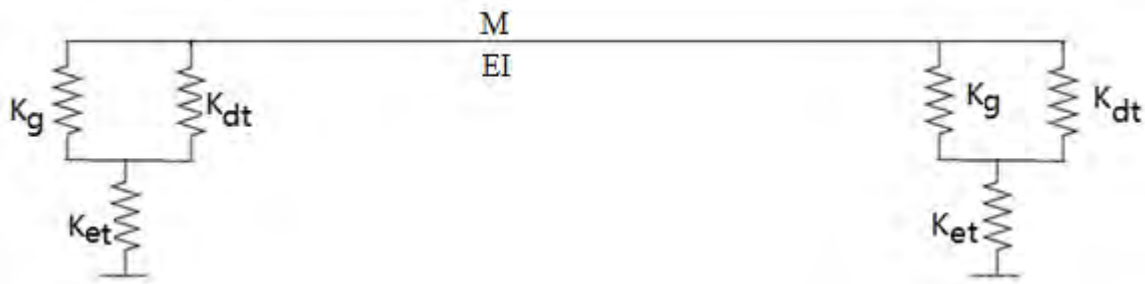
Figure 10-4 Simply supported transverse beam model on elastic springs

Therefore, this beam model can be viewed as simply-supported at the ends by springs with elastic stiffness, K_{nt}. The stiffness K_{nt} can be expressed as:

$$K_{nt} = \cfrac{1}{\cfrac{1}{K_{et}} + \cfrac{1}{K_g + K_{dt}}} \tag{10.1}$$

where: $K_{et}{=}0.5K_{bt}$

Alfawakhiri and Bruneau (2001) provides Equations 10.2 to 10.5, which indicate the dynamic parameters for the first mode of the beam model as shown in Fig. 10-5. The shape function for this first mode is:

$$\varphi_1(x) = \frac{3.2(xL^3 - 2x^3L + x^4 + 12BL^4)}{L^4(1 + 38.4B)} \tag{10.2}$$

where: the factor B is:

$$B = \frac{\frac{EI}{L^3}}{K_{nt}} \tag{10.3}$$

The period of the first mode is:

$$T_1 = 2\pi \sqrt{\frac{M(30B^2 + B + 31/3024)}{K_{nt}B(60B + 1)}} \tag{10.4}$$

The generalized mass is

$$M_1^* = \frac{M(60B + 1)^2}{60(60B^2 + 2B + 31/1512)} \tag{10.5}$$
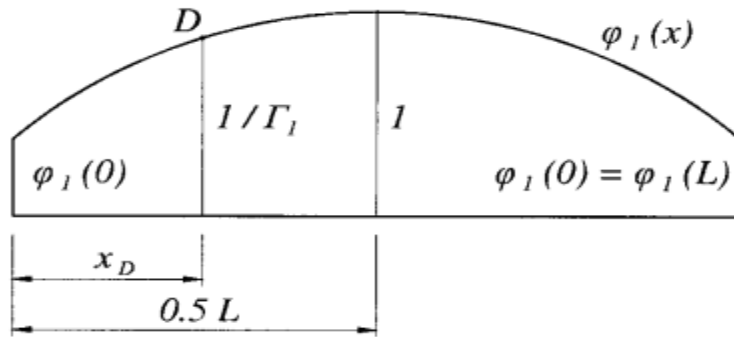
Figure 10-5 First mode of vibration of the beam model

The spectral displacement of the corresponding SDOF system of the transverse beam model in Fig.10-3 is:

$$\delta_{ut} = \frac{V_{sat}}{M_1^*\omega_1^2} = \frac{MS_{at}}{M_1^*\omega_1^2} = \frac{MS_aT_1^2}{M_1^*4\pi^2} \tag{10.6}$$

where: V_{sat} is the elastic force demand based on the spectral acceleration, S_{at}, corresponding to the period T_1.

The yield strength of the spring group at one end is V_{yt}, which is designed to correspond to the yielding of the BRBs in the transverse ductile diaphragms. When the yield force is reached in the transverse BRBs in

the ductile diaphragm, the girder bearing stiffeners and the column should remain elastic. And the yielding displacement of the spring group, δ_{yt}, is:

$$\delta_{yt} = \frac{V_{yt}}{K_n} \tag{10.7}$$

The ductility of the spring group, μ_{dt}, is

$$\mu_{dt} = \frac{\delta_{ut}}{\delta_{yt}} \tag{10.8}$$

The ductility of the beam system, μ_e, is defined as the ratios of the maximum displacements, δ_{ut}, at the center of the beam and the displacement of the spring group when corresponding to the yielding of the spring system, δ_{yt}. The relationship between the ductility of the beam system and the spring group is given in the Equations 10.9-10.11 below provided by Alfawakhiri and Bruneau (2001):

$$\mu_e = 1 + \frac{\mu_{dt} - 1}{\varphi_1(0)\Gamma_1} \tag{10.9}$$

where:

$$\varphi_1(0) = \frac{38.4BL^4}{L^4(1 + 38.4B)} \tag{10.10}$$

$$\Gamma_1 = \frac{(1 + 38.4B)(60B + 1)}{38.4(60B^2 + 2B + 31/1512)} \tag{10.11}$$

Based on the displacement and force relationship in the individual spring in the spring group, the local ductility of the individual transverse BRB is derived as:

$$\mu_{BT} = \mu_{dt}\left(1 + \frac{k_{dt} + k_g}{k_{et}}\right) - \frac{k_{dt} + k_g}{k_{et}} \tag{10.12}$$

By first assuming the stiffness of the transverse ductile diaphragm K_{et}, the acceptable ductility of the BRB can be determined by trial and error using the above Equations. Recall in Section 7.3.2.2, the design parameters of the individual BRB can be obtained for the nonskew EDS-1, based on the transverse yield strength and stiffness provided by the transverse BRBs.

10.2.3 Bridge behavior in the longitudinal direction

Similar to the bridge beam model of the middle span in the transverse direction, the middle span with longitudinal diaphragms at both ends can also be simplified as a beam model supported on the spring group as shown in Fig. 10-6. The stiffness K_{el}, representing the stiffness contribution from of the bridge

bent in the longitudinal direction, is also only a portion of the entire bent's longitudinal stiffness, K_{bl}. And the ratio between K_{el} and K_{bl} is assumed as 0.5, which is also subjected to change for different longitudinal bent stiffness K_{bl}.

Figure 10-6 Simply supported longitudinal beam model on elastic springs

The total stiffness of the spring group at each end, K_{nl}, in Fig. 10-6 can be expressed as:

$$K_{nl} = \frac{1}{\frac{1}{K_{el}} + \frac{1}{K_{dl}}} \tag{10.13}$$

where: $K_{el} = 0.5K_{bl}$

The period of the vibration mode in the longitudinal direction is:

$$T_2 = 2\pi \sqrt{\frac{M}{2K_{nl}}} \tag{10.14}$$

The spectral displacement of the corresponding SDOF system of the longitudinal beam model in Fig.10-6 is:

$$\delta_{ul} = \frac{V_{sa}}{M\omega_1^2} = \frac{MS_{aL}}{M\omega_1^2} = \frac{S_a T_1^2}{4\pi^2} \tag{10.15}$$

where: V_{sal} is the elastic force demand based on the spectral acceleration, $S_{al}L$, corresponding to the period T_2.

The yield strength of the spring group at one end is V_{yl}, which is designed to correspond to the yielding of the BRBs in the longitudinal ductile diaphragms. When the yield force is reached in the longitudinal BRBs, the column remains elastic. And the yielding displacement of the spring group, δ_{yl}, is:

$$\delta_{yl} = \frac{V_{yl}}{K_{nl}} \tag{10.16}$$

The ductility of the spring group, μ_{dl}, is

$$\mu_{dl} = \frac{\delta_{ul}}{\delta_{yl}} \tag{10.17}$$

The ductility of the spring group is the same as the ductility of the beam system in Fig. 10-6. The local ductility of the individual longitudinal BRB is derived as:

$$\mu_{BL} = \mu_{sdl}\left(1 + \frac{k_{dl}}{k_{el}}\right) - \frac{k_{dl}}{k_{el}}$$

(10.18)

By first assuming the stiffness of the transverse ductile diaphragm K_{el}, the acceptable ductility of the longitudinal BRB can be determined by trial and error using the above Equations. Similar to the transverse BRBs, the design parameters of the individual BRB can be obtained for the nonskew EDS-1 in Section 7.3.2.2 based on the longitudinal yield strength and stiffness provided by the longitudinal BRBs.

10.2.4 Design details of the example multi-span bridge

The example multi-span bridge, taken from Zahrai and Bruneau (1999a), has three spans with span length of 131 ft. Each span was simply-supported on the reinforced concrete bents, which have four columns of 35.4 in. diameter and 16.4 ft. height. The mass of the bridge in each span is 630 lbs. Four WWF47x224 steel girders were used with a girder-to-girder spacing of 78.75". The middle span in this multi-span bridge was used to determine the design parameters of the BRBs in the bidirectional ductile diaphragms at its two ends. The end spans used the same transverse and longitudinal BRBs as designed for the middle span. The location of the bridge was chosen at Memphis, TN with latitude 35.15° N, and longitude 90.17° W. The site soil is class C. The target response spectrum in Fig. 10-7 was obtained from USGS (2016) with the 2014 USGS National Hazard Map for a 7% probability of being exceeded in 75 years (or 975 years return period). The damping ratio considered in this design spectrum is 5% of the critical damping. The following are the spectral response acceleration parameters: S_{ds}=0.74g and S_{d1}=0.365g.
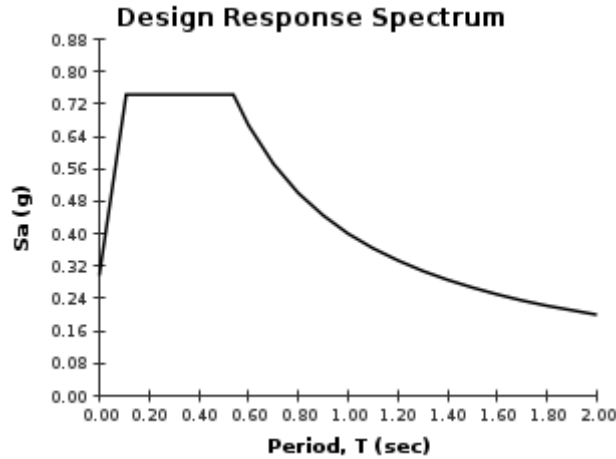
Figure 10-7 Design response spectrum from Memphis, TN

The Mathcad design calculations of the bidirectional ductile diaphragm designs for the middle span are shown in Appendix G. The bidirectional ductile diaphragms have the same yield strength and stiffness in both directions. The stiffness of the ductile diaphragm is 500 kip/in in both the transverse and longitudinal directions. The yield displacement of the ductile diaphragm (i.e. the relative displacement between the top and bottom) is 0.102", when the BRBs yield. The stiffeners at the end of each girder were made from two plates placed on each side of the girder's web. The original stiffener plates from the bridge example were used here, and each has the height of 47.25", width of 3.93" and thickness of 0.395". The total transverse stiffness provided by all the stiffeners at the end of the girders is 68.5 kip/in. The entire bridge bents' stiffness K_{bt} and K_{bl} are 1713 and 428 kip/in in the transverse and longitudinal direction, respectively. Note that the longitudinal stiffness of the bent is only 1/4 of that in the transverse direction. By adding the displacement of the bridge bent, the transverse and longitudinal displacements of the middle span at both ends δ_{yt} and δ_{yl}, where the bidirectional ductile diaphragm is located, are 0.170" and 0.341", when the transverse and longitudinal BRBs yield, respectively. Two transverse BRBs and one longitudinal BRB were used in the bidirectional ductile diaphragm at one end of the bridge's middle span. The steel material used in the BRB core plate is assumed to be A500 Gr. B with yield strength of 46 ksi. The inclination angle of the transverse BRB is 31 degrees from the deck, which is dependent on the girder height and spacing. The length of the transverse BRB is 91.8 in. The yield length ratio of the transverse BRBs is 0.6. The cross sectional area of the yield core in the transverse BRB is 0.65 in², resulting in a yield force of 30 kips. The axial yield displacement of the transverse BRB is 0.087". The longitudinal BRB has the length of 61.5 in, with an inclination angle of 50.2 degrees from the deck. The yield length ratio of the longitudinal BRBs is 0.67. The cross sectional area of the yield core in the longitudinal BRB is 1.74 in², resulting in a yield force of 80 kips. The axial yield

43;

displacement of the longitudinal BRB is 0.066". The girder stiffeners at each end of an individual girder has the lateral yield strength of 5 kips and yield displacement of 0.293". Note that the BRBs can be designed differently as long as the stiffness and strength provided by them are the same as the BRB designs used here.

The isolated middle span supported on the bridge bent has the resulting periods of 0.333 and 0.464 s in the transverse and longitudinal direction, respectively. Note that half of the bridge bents' stiffness in both the transverse and longitudinal direction was used for the middle span's bridge bent. Both periods fall on the plateau of the design response spectrum in Fig. 10-7. The spectral displacement δ_{ut} in the transverse direction is 0.827", which result in the ductility μ_{dt} of 4.86 in the transverse spring group. The bridge's transverse displacement ductility μ_e at the middle of the span is 5.4. And the corresponding transverse BRB ductility μ_{BT} is 7.2. The spectral displacement δ_{ul} in the longitudinal direction is 1.535", which results in the longitudinal displacement ductility μ_{dl} of 4.56. And the corresponding longitudinal BRB ductility μ_{BL} is 12.8. Note that bidirectional ductile diaphragms were only designed for the middle span in this design example. The end spans used the same BRBs in their bidirectional ductile diaphragms. The dynamic behavior will be assessed for the entire bridge with three spans, having bidirectional ductile diaphragms at each end, and compared with the ductility demand predicted above.

10.2.5 SAP2000 bridge model

The above designed multi-span bridge is modeled in SAP2000 as shown in Fig. 10-8. This bridge model is a three-dimensional spine bridge structure with line elements, representing the slab and girders in the superstructure, which is similar to the benchmark model in Section 7. To differentiate the ductile end diaphragms used in this example, the bidirectional End ductile Diaphragm System (EDS) is the one located on top of the abutments at the two end spans, and the bidirectional Intermediate ductile Diaphragm System (IDS) is the one located on top of the bents for the end and middle spans. There are two IDSs on top of each bent. The EDS and IDS are numbered as shown in Fig. 10-8. Fig. 10-9 shows the enlarged view of EDS-1 on top of Abutment-1 at the left end of Span-1. EDS-2 on top of Abutment-2 at the right end of span 2 is the mirror image of EDS-1. The longitudinal BRB, i.e. BRB-L-1, was built horizontally in line with the girder in both EDSs. This horizontal longitudinal BRB still provides the same stiffness and strength to the bridge structures as the inclined longitudinal BRBs in Fig. 10-2b in the longitudinal direction. Two BRBs were designed and modeled in the transverse ductile diaphragms, along with three girder stiffener links. Note that since there are four girders, four girder end stiffeners are present at the end of the bridge span. Three inclined links were modeled (i.e., one between each pair or

girders) to have the same lateral/transverse stiffness and strength as the four girder stiffeners, as G-1 to G-3 in Fig. 10-9. Two transverse BRBs, i.e. BRB-T-1 and BRB-T-2, were placed parallel to the girder stiffener links G-1 and G-3 in Fig. 10-9.
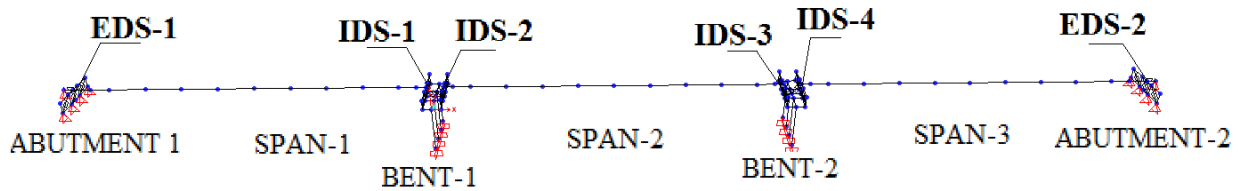
Figure 10-8 SAP2000 model of the multi-span bridge
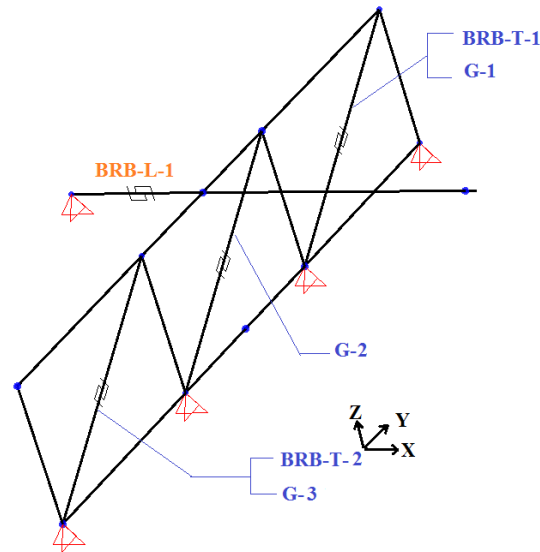
Figure 10-9 Enlarged view of the EDS-1 on top of Abutment-1

Fig. 10-10 shows the enlarged view of IDS-2 and IDS-3 (in Fig. 10-7) on top of Bent-1. Similarly, IDS-3 and IDS-4 on top of Bent-2 are the mirror image of IDS-1 and IDS-2 on top of Bent-1. The transverse ductile diaphragms in IDS-1 and IDS-2 are separated so that the longitudinal BRBs can be modeled connecting the superstructure spine line to the bridge bents. The spacing between the two ductile diaphragms on top of the bent is built to be the same as the girder spacing. Therefore, the longitudinal BRBs in IDS-1 and IDS-2, i.e. BRB-L-2 and BRB-L-3, has the inclination angle of 50.2 degrees from the deck, which is the same as the design inclination angle of the longitudinal BRBs designed in Section 10.2.4. The IDSs have the same transverse BRBs and girder stiffener links layout as the EDSs. Fig. 10-11 shows the enlarged view the IDS-1 with columns in Bent-1.

The line elements representing the superstructure (deck and girders) were defined with uniform mass, M/L, and uniform stiffness, EI. The BRBs and girder stiffener links were modeled as bilinear links using the Wen Plasticity property, as defined in SAP2000 reference manual (2016). The columns were modeled as frame elements and divided in four segments. Fiber P-M2-M3 hinges were used at the ends of each segment. Each fiber hinge length was set as 10% of the length of the member. The rest of the bridge structure elements were modeled as rigid elements, similar to the setting of the rigid members in the benchmark bridge model in Section 7. Details of the modeling can be found in Appendix C.

Since the bridge model is symmetric, therefore, the BRBs and the girder stiffener links are categorized into the following groups in Table 10-1. The BRBs and girder stiffener links are numbered from left to right in Fig. 10-7. The representative members identified in that Table are used in the following section for explaining the analyses results.
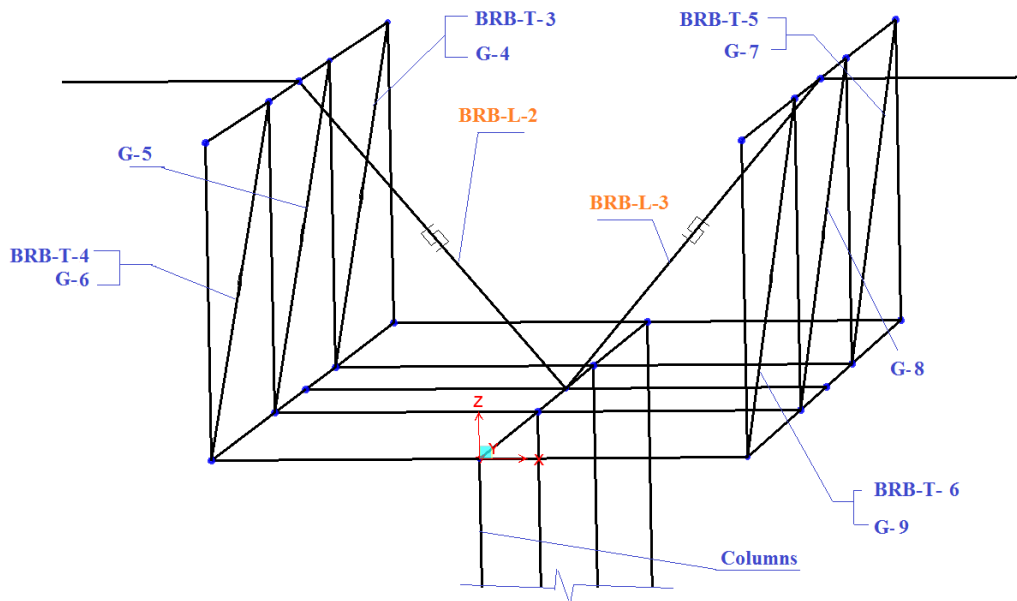
Figure 10-10 Enlarged view of the IDS-1 and IDS-2 on top of Bent-1
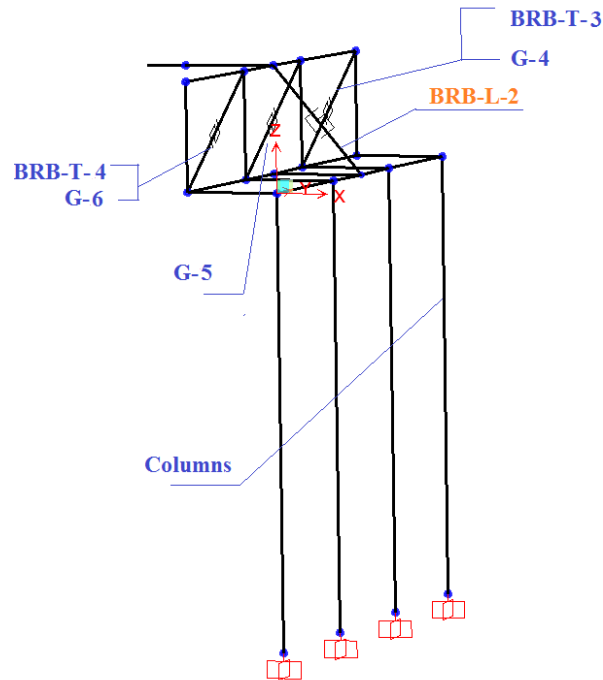
Figure 10-11 Enlarged view of the IDS-1 on top of Bent-1

Table 10-1: List of BRBs and girder stiffener links in the SAP2000 model

	Representative Member	Location	BRBs with the same response (Location of the BRB)
Longitudinal BRB	BRB-L-1	EDS-1	BRB-L-6 (EDS-2)
	BRB-L-2	IDS-1	BRB-L-5 (IDS-4)
	BRB-L-3	IDS-2	BRB-L-4 (IDS-3)
Transverse BRB	BRB-T-1	EDS-1	BRB-T-2 (EDS-1) BRB-T-11,12 (EDS-2)
	BRB-T-3	IDS-1	BRB-T-4 (IDS-1) BRB-T-9,10 (IDS-4)
	BRB-T-5	IDS-2	BRB-T-6 (IDS-2) BRB-T-7,8 (IDS-3)
Girder stiffeners	G-1	EDS-1	G-2,3 (EDS-1) G-16,17,18 (EDS-2)
	G-4	IDS-1	G-5,6 (IDS-1) G-13,14,15 (IDS-4)
	G-7	IDS-2	G-8,9 (IDS-2) G-10,11,12 (IDS-3)

Table 10-2 below shows a summary of the properties used for the BRBs and girder stiffener links in the SAP2000 bridge model in Fig. 10-7.

425

Table 10-2: BRBs and girder links summary in the SAP2000 bridge model

	Longitudinal BRB		Transverse BRBs	Girder stiffener links
	horizontal	inclined		
Numbers	2	4	12	18
Yield strength (kips)	51.0	79.6	29.7	7.8
Yield displacement (in.)	0.102	0.066	0.087	0.251

10.3 Pushover and nonlinear time history analyses of the multi-span bridge with bidirectional ductile diaphragms

10.3.1 General

In this section, static nonlinear pushover and dynamic nonlinear time history analyses were performed on the multi-span bridge with bidirectional ductile diaphragms model shown in Section 10.2.5 and corresponding results are presented. Section 10.3.2 shows the Pushover analyses results of the bridge model in the longitudinal and transverse directions, respectively. Section 10.3.3 describes the 7 pairs of ground motions chosen to perform the nonlinear time history analyses. Section 10.3.4 presents the analyses results of the SAP2000 model subjected to these chosen ground motions. Based on the analyses results in Section 10.3.4, a new multi-span bridge model was built by adding a longitudinal BRB in both EDSs in Fig.10-8 to double strength and stiffness in the longitudinal EDSs. The 7 pairs of ground motions in Section 10.3.3 were scaled accordingly and applied to the new bridge model in the nonlinear time history analyses. Comparisons were made between the two bridge models in the longitudinal direction to assess the effect of changing the longitudinal stiffness and strength of the EDSs.

10.3.2 Pushover analyses

Pushover analyses were performed on the SAP2000 bridge model in the longitudinal and transverse directions, respectively. Displacement control was used and the monitored displacement was at the middle of the bridge (i.e. middle of Span-2). Point load was applied to the bridge at the level of the bridge deck along the bridge in both directions. The resulted pushover curves of the bridge model are shown in Fig. 10-12 for the transverse and longitudinal direction, respectively. The first and second stiffness change points in Fig. 10-12a, corresponding to the transverse displacement of 0.189" and 0.398" at the middle of Span-2, when the transverse BRBs and girder stiffener links yielded, respectively. The first and second stiffness change points in Fig. 10-12b, corresponding to the longitudinal displacement of 0.154" and 0.562" at the middle of Span-2, when the longitudinal BRBs in the EDS and IDS yielded,

respectively. Note that after the longitudinal BRBs in the EDSs yielded, the force in the EDS BRBs of the end spans (Span-1 and Span-3) stopped increasing, but those spans could displace together with the middle span. As further displacement was applied to the middle span, the forces in the longitudinal BRBs in the IDSs at the ends of the middle spans increased until they also yielded. The pushover curve in Fig. 10-12a would have be different, if the longitudinal BRBs in the IDSs yielded first instead of the ones in the EDSs, or if the monitored displacement in the longitudinal pushover analysis was in the end spans.

(a)   (b)
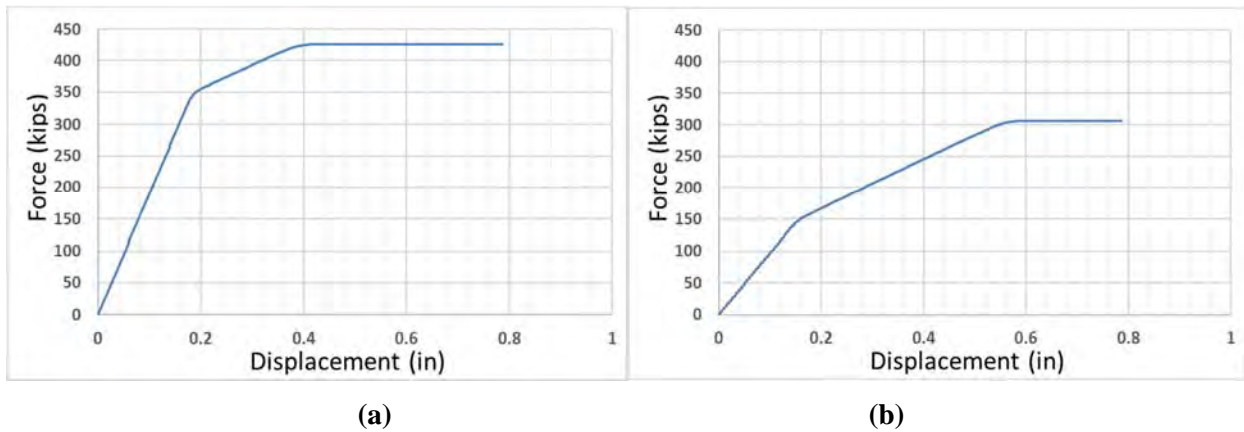
Figure 10-12 Pushover curves of the multi-span bridge model in the: (a) transverse; (b) longitudinal direction

Pushover analyses were also performed on the individual bent with four columns in the longitudinal and transverse directions. The yield displacements at the top of the bents are 0.906" and 0.522" in the longitudinal and transverse directions, respectively, when the hinge at the bottom of the columns yielded.

10.3.3 Ground motions

Seven pairs of ground motions were arbitrarily selected from the 44 pairs of ground motions specified in FEMA-P695 (2009). Each pair of ground motions has different duration and time steps. The seven pairs of ground motions are shown in Fig. 10-13. Per the naming convention adopted here for the ground motions, "GM-i-j", refers to the j-th ground motion in the i-th pair of ground motions. The corresponding response spectrum with 5% damping for these seven pairs of ground motions are shown in Fig. 10-14.

The first and second periods of the bridge model are 0.41 and 0.307 s, which correspond to the bridge's longitudinal and transverse direction, respectively. At both of these two periods, the response spectrum of the 14 ground motions (i.e. 7 pairs) do not match the design response spectrum in Fig. 10-12. Therefore, each ground motion was scaled in order to have the same spectral acceleration as the design response

spectrum at the period corresponding to the direction in which the ground motion was applied. This also means that the two ground motions in the same pair were scaled differently, due to the different periods in the longitudinal and transverse direction of the bridge. Since the behaviors of the bridge in the longitudinal and transverse directions of the nonskew bridge are independent from each other, this is a reasonable approach. The scale factors for these ground motions are presented in Table 10-3. For example, the scale factors of 0.913 and 0.66 were used for GM-1-1 and GM-1-2 in the first pair of ground motions, respectively, when they were applied to the bridge model in the longitudinal and transverse directions, and the scale factors of 0.986 and 0.583 were used for GM-1-1 and GM-1-2 in a second dynamic non-linear analysis when GM-1-2 was applied in the longitudinal direction and GM-1-1 in the transverse directions.
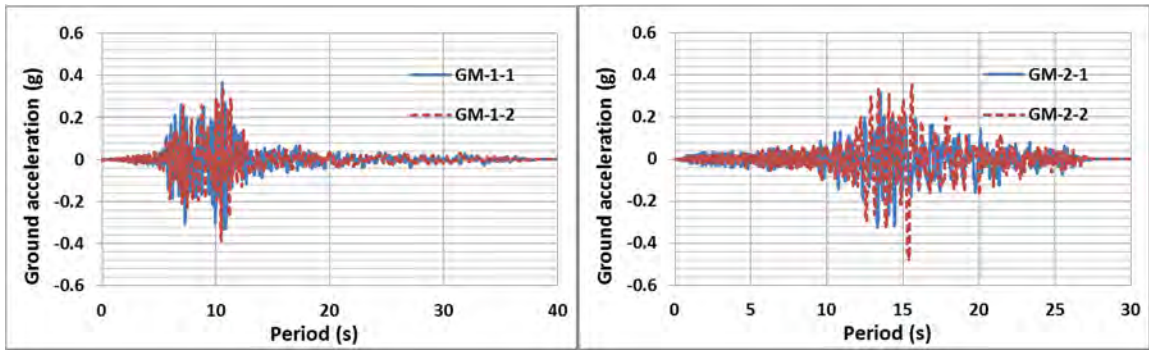
(a)

(b)
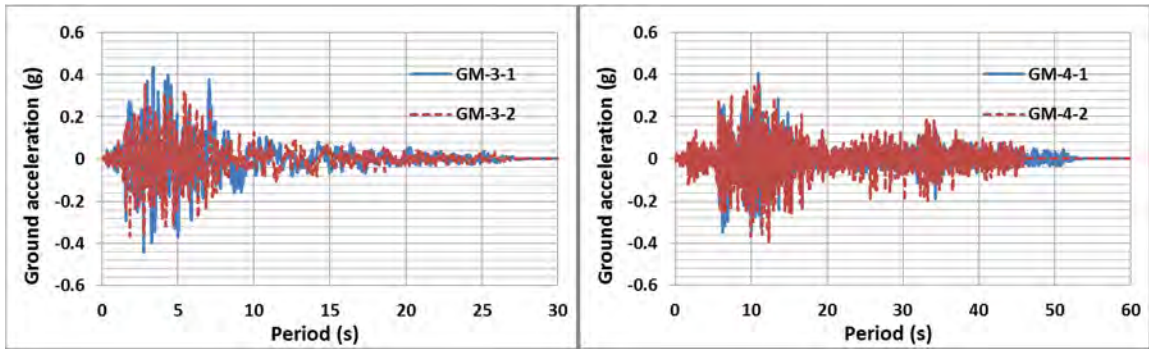
(c)

(d)
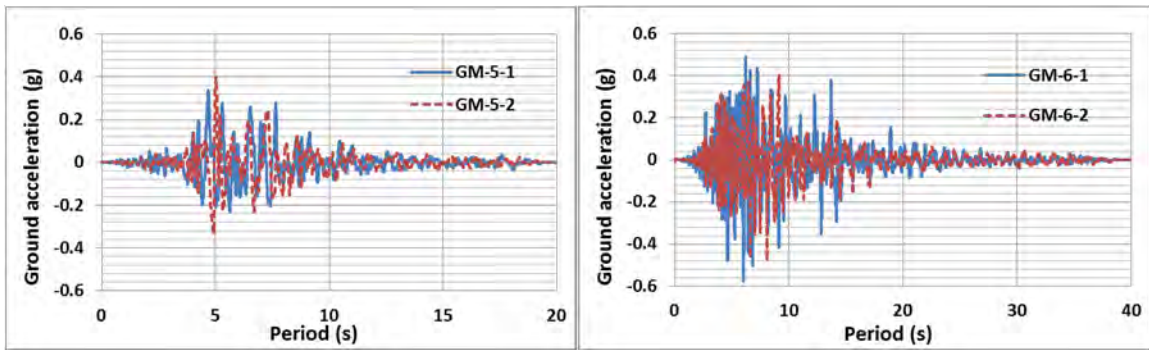
(e)

(f)
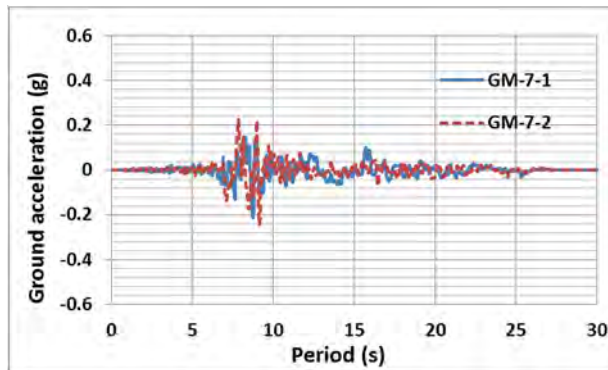
(g)

Figure 10-13 Seven pairs of ground motions from FEMA-P695 (2009)

429
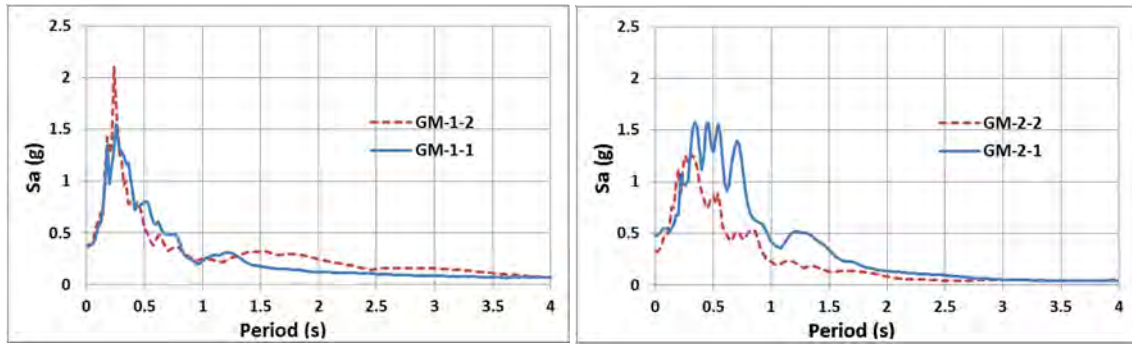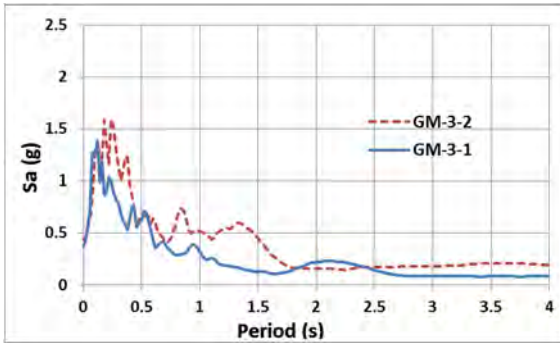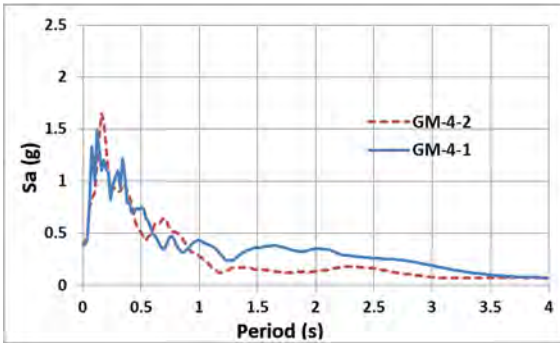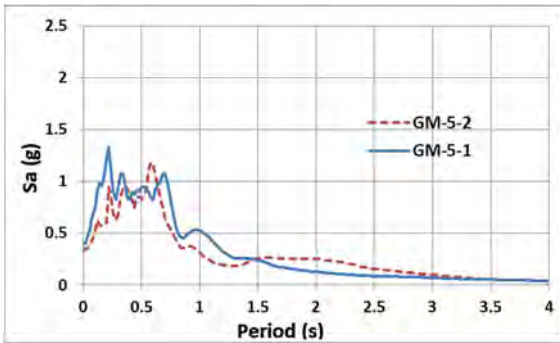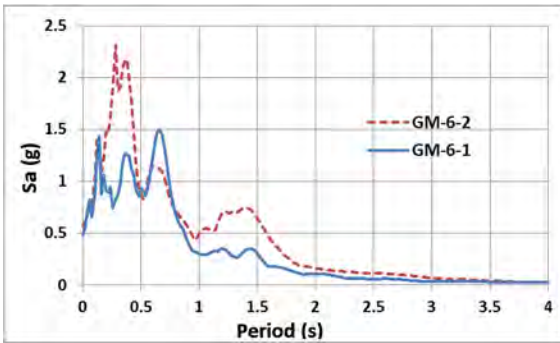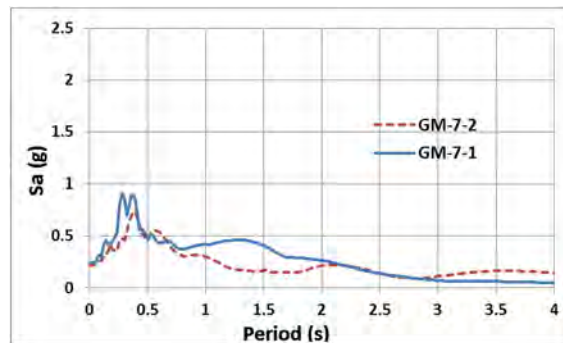
Figure 10-14 Response spectrum corresponding to the seven pairs of ground motions

Table 10-3: Scale factors for the seven pairs of ground motions

	Longitudinal	Transverse
GM-1-1	0.913	0.583
GM-1-2	0.986	0.66
GM-2-1	0.625	0.54
GM-2-2	0.85	0.591
GM-3-1	1.071	0.981
GM-3-2	0.815	0.679
GM-4-1	0.984	0.709
GM-4-2	0.906	0.819
GM-5-1	0.631	0.815
GM-5-2	0.395	0.393
GM-6-1	1.007	0.917
GM-6-2	1.082	1.508
GM-7-1	0.858	0.738
GM-7-2	0.87	0.975

10.3.4 Time history analyses and results

A total of 14 nonlinear time history analyses were performed using the 7 pairs of scaled ground motions mentioned above. Rayleigh damping was used in the time history analyses considering a damping ratio of 5% of the critical damping.

Table 10-4 shows the maximum forces, displacements, and ductilities of the transverse BRBs obtained from the analyses in which each ground motion was applied to the bridge model in the transverse direction. Note that the other ground motion from the same pair was simultaneously applied in the longitudinal direction of the bridge. The response of the longitudinal BRBs are presented in Table 10-6 later in this section. All transverse BRBs have yielded under all these ground motions. The displacements in BRB-T-5 are the largest. Note that, only the responses of the representative BRB are shown here, and the other BRBs in the same category in Table 10-1 had the same responses. The average ductilities obtained for the transverse BRBs are 7.0, 6.1, 7.4 for BRB-T-1, BRB-T-3, BRB-T-5, respectively. The ductilities for these BRBs at different locations along the bridge are relatively close to each other. Recall that in the design calculation presented in Section 10.2.4, the expected ductility of the transverse BRB in the ductile diaphragms at the middle span was 7.2, which is 18% larger than the average ductility obtained for BRB-T-3.

Table 10-4: Response of the transverse BRBs

		BRB-T-1			BRB-T-3			BRB-T-5		
		Max. Force	Max. Displ.	Ductility	Max. Force	Max. Displ.	Ductility	Max. Force	Max. Displ.	Ductility
GM-1	1	29.7	0.381	4.4	29.7	0.303	3.5	29.7	0.517	5.9
	2	29.7	0.292	3.3	29.7	0.223	2.6	29.7	0.256	2.9
GM-2	1	29.7	0.882	10.1	29.7	0.800	9.1	29.7	1.014	11.6
	2	29.7	0.283	3.2	29.7	0.227	2.6	29.7	0.283	3.2
GM-3	1	29.7	0.206	2.4	29.7	0.156	1.8	29.7	0.264	3.0
	2	29.7	1.127	12.9	29.7	1.059	12.1	29.7	0.926	10.6
GM-4	1	29.7	0.567	6.5	29.7	0.497	5.7	29.7	0.724	8.3
	2	29.7	0.305	3.5	29.7	0.225	2.6	29.7	0.318	3.6
GM-5	1	29.7	0.683	7.8	29.7	0.596	6.8	29.7	0.983	11.2
	2	29.7	0.757	8.7	29.7	0.680	7.8	29.7	0.745	8.5
GM-6	1	29.7	0.201	2.3	29.7	0.134	1.5	29.7	0.357	4.1
	2	29.7	1.224	14.0	29.7	1.109	12.7	29.7	1.248	14.3
GM-7	1	29.7	1.315	15.0	29.7	1.211	13.9	29.7	1.003	11.5
	2	29.7	0.391	4.5	29.7	0.301	3.4	29.7	0.461	5.3
Average		29.7	0.615	7.0	29.7	0.537	6.1	29.7	0.650	7.4

Table 10-5 shows the maximum forces, displacements, and ductilities of the girder stiffener links obtained from the analyses in which each ground motion was applied to the bridge model in the transverse direction. The displacements of the girder stiffener links are the same as the transverse BRB at the same location. The average ductilities of the girder stiffener links are 2.4, 2.1, 2.6 for G-1, G-4, G-7, respectively. Note that the girder stiffener links have larger yield displacements than the transverse BRB as indicated in Table 10-2. Therefore, the ductilities in Table 10-5 are different from that in Table 10-4 for the transverse BRB. Note that ductility values smaller than 1.0 indicate that the girder stiffener links have not yielded.

Table 10-6 shows the maximum forces, displacements, and ductilities of the longitudinal BRBs obtained from the analyses in which each ground motion was applied to the bridge model in the longitudinal direction. All longitudinal BRBs have yielded. The displacements in BRB-L-1 are the largest. The average ductilities of the longitudinal BRBs are 13.1, 8.5, 10.1 for BRB-L-1, BRB-L-2, BRB-L-3, respectively. Recall that in the design calculation presented in Section 10.2.4, the expected ductility of the longitudinal BRB in the ductile diaphragms at the end of the middle span was 12.8, which is 26% larger than the average ductility obtained for BRB-L-3.

Table 10-5: Response of the girder stiffener links

		G-1			G-4			G-7		
		Max. Force	Max. Displ.	Ductility	Max. Force	Max. Displ.	Ductility	Max. Force	Max. Displ.	Ductility
GM-1	1	7.8	0.381	1.5	7.8	0.303	1.2	7.8	0.517	2.1
	2	7.8	0.292	1.2	6.9	0.223	0.9	7.6	0.256	1.0
GM-2	1	7.8	0.882	3.5	7.8	0.800	3.2	7.8	1.014	4.0
	2	7.8	0.283	1.1	7.0	0.227	0.9	7.8	0.283	1.1
GM-3	1	6.4	0.206	0.8	4.8	0.156	0.6	7.7	0.264	1.0
	2	7.8	1.127	4.5	7.8	1.059	4.2	7.8	0.926	3.7
GM-4	1	7.8	0.567	2.3	7.8	0.497	2.0	7.8	0.724	2.9
	2	7.8	0.305	1.2	6.9	0.225	0.9	7.8	0.318	1.3
GM-5	1	7.8	0.683	2.7	7.8	0.596	2.4	7.8	0.983	3.9
	2	7.8	0.757	3.0	7.8	0.680	2.7	7.8	0.745	3.0
GM-6	1	6.2	0.201	0.8	4.2	0.134	0.5	7.8	0.357	1.4
	2	7.8	1.224	4.9	7.8	1.109	4.4	7.8	1.248	5.0
GM-7	1	7.8	1.315	5.2	7.8	1.211	4.8	7.8	1.003	4.0
	2	7.8	0.391	1.6	7.8	0.301	1.2	7.8	0.461	1.8
Average		7.6	0.615	2.4	7.1	0.537	2.1	7.8	0.650	2.6

Table 10-6: Response of the longitudinal BRBs

		BRB-L-1			BRB-L-2			BRB-L-3		
		Max. Force	Max. Displ.	Ductility	Max. Force	Max. Displ.	Ductility	Max. Force	Max. Displ.	Ductility
GM-1	1	51.0	0.800	7.9	79.6	0.311	4.8	79.6	0.239	3.7
	2	51.0	1.197	11.7	79.6	0.457	7.0	79.6	0.579	8.9
GM-2	1	51.0	0.643	6.3	79.6	0.151	2.3	79.6	0.135	2.1
	2	51.0	3.156	31.0	79.6	1.701	26.1	79.6	1.419	21.8
GM-3	1	51.0	2.852	28.0	79.6	1.571	24.1	79.6	1.549	23.7
	2	51.0	0.636	6.2	79.6	0.119	1.8	79.6	0.452	6.9
GM-4	1	51.0	0.912	8.9	79.6	0.282	4.3	79.6	0.322	4.9
	2	51.0	1.010	9.9	79.6	0.353	5.4	79.6	0.815	12.5
GM-5	1	51.0	1.819	17.8	79.6	0.885	13.6	79.6	0.889	13.6
	2	51.0	1.592	15.6	79.6	0.427	6.5	79.6	0.742	11.4
GM-6	1	51.0	1.305	12.8	79.6	0.536	8.2	79.6	0.812	12.5
	2	51.0	0.729	7.1	79.6	0.173	2.6	79.6	0.309	4.7
GM-7	1	51.0	0.725	7.1	79.6	0.201	3.1	79.6	0.400	6.1
	2	51.0	1.270	12.5	79.6	0.564	8.6	79.6	0.604	9.3
Average		51.0	1.331	13.1	79.6	0.552	8.5	79.6	0.662	10.1

Table 10-7 presents the displacements of the points taken along the bridge as shown in Fig. 10-15. The name for these points, "S-i-j", refers to the location of the points in Span-i, in which "i" ranges from "1" to "3" for the bridge's three spans. The "L", "R", and "M" labels following the hyphen as "j" correspond to the points located at the "Left" or "Right" ends, or "Middle" of the span, respectively. Since the bridge is symmetric, only displacements of points along the bridge's left half are tabulated in Table 10-7. In the first and second columns in Table 10-7, the ground motions applied to the bridge model are indicated for the longitudinal and transverse directions, respectively. The maximum transverse displacement of the bridge model occurred at the middle of Span-2 (i.e. point S-2-M in Fig. 10-15), and the corresponding average transverse displacement at point S-2-M is 0.875". Recall from the transverse pushover analyses in Section 10.3.2, that the transverse displacement of the point S-2-M is 0.189" when the transverse BRB first yields. The resulting ductility is 4.63, which is smaller than the value of 5.4 predicted from the design calculation in Section 10.2.4. The maximum longitudinal displacement of the bridge model occurred in Span-1. Note that the difference of the longitudinal displacements of points S-1-L and S-1-R is negligible, since the axial stiffness of the bridge deck and girders are very large. The corresponding average longitudinal displacement at Span-1 is 1.332". The average longitudinal displacement of the middle span (Span-2) is 1.47". Recall from the longitudinal pushover analyses in Section 10.3.2, that the longitudinal displacement of the point S-2-M is 0.154", when the longitudinal BRB first yields. The resulting ductility is 9.5, which is smaller than the value of 4.56 predicted from the design calculation in Section 10.2.4.

In addition to the displacements taken at the level of the bridge deck, the displacements at top of the bent in both longitudinal and transverse direction are also tabulated. The maximum longitudinal and transverse displacement at the top of the bridge bent are 0.413" and 0.099", respectively, which are smaller than the bents' yield displacements of 0.906" and 0.522" obtained from the pushover analyses. This indicates that the bridge columns remained elastic.

Table 10-7: Displacements of the multi-span bridge model (unit: in.)

Longitudinal GM	Transverse GM	S1-L		S1-R		S2-L		S2-M		Bent top	
		Longi.	Trans.	Longi.	Trans.	Longi.	Trans.	Longi.	Trans.	Longi.	Trans.
GM-1-1	GM-1-2	0.800	0.444	0.795	0.450	0.745	0.692	0.745	0.702	0.376	0.101
GM-1-2	GM-1-1	1.197	0.340	1.195	0.350	1.377	0.376	1.375	0.396	0.430	0.088
GM-2-1	GM-2-2	0.643	1.029	0.643	1.028	0.707	1.276	0.706	1.285	0.361	0.104
GM-2-2	GM-2-1	3.156	0.362	3.155	0.358	2.694	0.420	2.693	0.429	0.504	0.093
GM-3-1	GM-3-2	2.852	0.241	2.855	0.264	2.831	0.379	2.828	0.403	0.435	0.084
GM-3-2	GM-3-1	0.636	1.314	0.633	1.329	1.177	1.172	1.178	1.184	0.446	0.105
GM-4-1	GM-4-2	0.913	0.662	0.909	0.674	0.980	0.937	0.982	0.949	0.394	0.101
GM-4-2	GM-4-1	1.010	0.355	1.014	0.348	1.648	0.460	1.645	0.465	0.402	0.093
GM-5-1	GM-5-2	1.818	0.796	1.816	0.791	1.855	1.228	1.857	1.236	0.436	0.109
GM-5-2	GM-5-1	1.592	0.883	1.591	0.885	1.624	0.963	1.624	0.972	0.409	0.101
GM-6-1	GM-6-2	1.305	0.234	1.309	0.244	1.722	0.503	1.727	0.515	0.417	0.087
GM-6-2	GM-6-1	0.729	1.428	0.730	1.389	0.963	1.548	0.963	1.550	0.361	0.110
GM-7-1	GM-7-2	0.725	1.534	0.725	1.509	0.912	1.263	0.910	1.277	0.400	0.110
GM-7-2	GM-7-1	1.270	0.456	1.277	0.446	1.349	0.630	1.342	0.639	0.407	0.097
Average		1.332	0.720	1.332	0.719	1.470	0.846	1.470	0.857	0.413	0.099
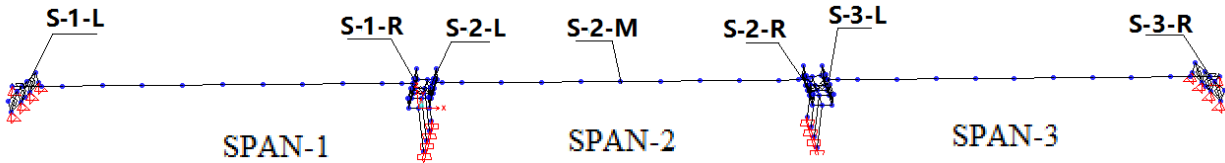
Figure 10-15 Locations of the points along the bridge spans where the displacements were monitored

Table 10-8 shows the total maximum base shear forces obtained from the longitudinal and transverse directions of the multi-span bridge model. The average longitudinal and transverse shear forces obtained from the 14 time history analyses are 362 and 464 kips, respectively. Note that these base shear forces are larger than the maximum forces shown in the pushover analyses, and this is due to the damping forces added to the total base shear forces. Recall that the damping ratio of 5% was considered in the Rayleigh damping setup in the time history analyses. In order to prove this, trial analyses were performed on the bridge model using Rayleigh damping ratio setting of zero, and the maximum base shear forces matched exactly with the maximum forces obtained from the pushover analyses. Note that the forces in the BRBs are not affected by this damping ratio.

Table 10-8: Base shear forces of the multi-span bridge model (unit: kips.)

Longitudinal GM	Transverse GM	Base shear force	
		Longitudinal	Transverse
GM-1-1	GM-1-2	328	472
GM-1-2	GM-1-1	368	418
GM-2-1	GM-2-2	322	480
GM-2-2	GM-2-1	460	441
GM-3-1	GM-3-2	389	397
GM-3-2	GM-3-1	325	496
GM-4-1	GM-4-2	344	476
GM-4-2	GM-4-1	354	441
GM-5-1	GM-5-2	380	515
GM-5-2	GM-5-1	379	470
GM-6-1	GM-6-2	370	406
GM-6-2	GM-6-1	327	520
GM-7-1	GM-7-2	350	520
GM-7-2	GM-7-1	372	449
Average		362	464

10.3.5 Adding longitudinal BRBs in EDSs

As noticed in Table 10-6, the longitudinal BRBs in the EDSs (i.e. BRB-L-1) have an average ductility of 13.1, and the ductility of the longitudinal BRBs in the ductile diaphragms at the end of the middle span is 26% larger than the average ductility obtained from design calculations. In order to reduce the ductility demand on the longitudinal BRBs in the EDSs, the longitudinal stiffness/strength of both EDS in the multi-span bridge was doubled by adding another longitudinal BRB identical to BRB-L-1. The effect of this change on the bridge's dynamic behavior in the longitudinal direction was investigated in this section. The EDS at the left end of Span-1 in the new bridge model is shown in Fig. 10-16. Note that in this revised design, the IDSs remained the same as in the original bridge model. The longitudinal BRBs in this new bridge model are also categorized into three groups as shown in Table 10-9.

Table 10-9: List of longitudinal BRBs in the new SAP2000 bridge model

Longitudinal BRB representative	Location	BRBs with the same response (Location of the BRB)
BRB-L-1	EDS-1	BRB-L-2 (EDS-1) BRB-L-7,8 (EDS-2)
BRB-L-3	IDS-1	BRB-L-6 (IDS-4)
BRB-L-4	IDS-2	BRB-L-5 (IDS-3)
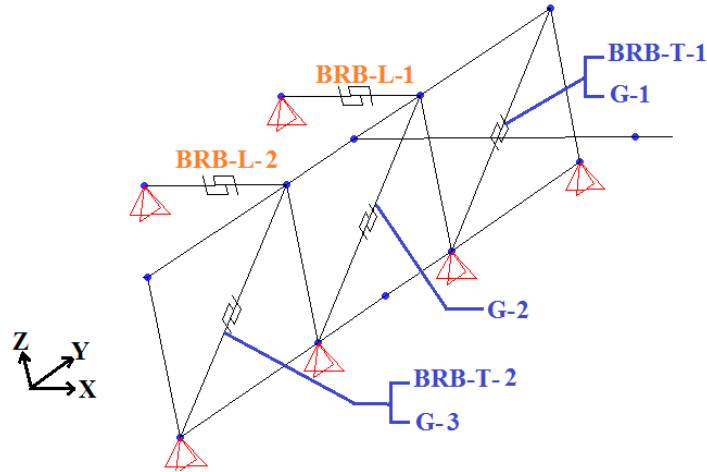
Figure 10-16 EDS-1 with two longitudinal BRBs on top of Abutment-1 in the new multi-span bridge model

The longitudinal period of this new bridge model is 0.365 s, which is smaller than the period of 0.41s of the original bridge model (with only one longitudinal BRB in the EDSs), and the transverse period stays the same as before. The ground motions were scaled the same way as mentioned in Section 10.3.3, and the resulting scale factors for the ground motions applied to the new bridge model are tabulated in Table 10-10. Note that the scale factors in the transverse direction remained the same as for the original bridge model.

Table 10-10: Scale factors for the seven pairs of ground motions

	Longitudinal	Transverse
GM-1-1	0.650	0.583
GM-1-2	0.936	0.66
GM-2-1	0.500	0.54
GM-2-2	0.674	0.591
GM-3-1	1.286	0.981
GM-3-2	0.600	0.679
GM-4-1	0.742	0.709
GM-4-2	0.778	0.819
GM-5-1	0.586	0.815
GM-5-2	0.342	0.393
GM-6-1	0.824	0.917
GM-6-2	1.051	1.508
GM-7-1	0.799	0.738
GM-7-2	0.778	0.975

Table 10-11 shows the maximum forces, displacements, and ductilities of the longitudinal BRBs obtained from the analyses in which each ground motion was applied to the new bridge model in the longitudinal direction. All longitudinal BRBs have yielded. The average ductility of the longitudinal BRBs is 5.4, 3.0,

437

11.1 for BRB-L-1, BRB-L-3, BRB-L-4, respectively. The displacements in BRB-L-4 in the IDS are the largest. Recall that in the original bridge model, the longitudinal BRB in the EDS had an average ductility of 13.1; this ductility demand has been reduced by 59% in this new bridge after adding another longitudinal BRB in the EDS in the new bridge model. The average ductility demand in the longitudinal BRB in IDS-2 was reduced by 65%. The average ductility demand in the longitudinal BRB in IDS-3 has slightly increased by 10%.

Table 10-11: Response of the longitudinal BRBs in the new bridge

		BRB-L-1			BRB-L-2			BRB-L-3		
		Max. Force	Max. Displ.	Ductility	Max. Force	Max. Displ.	Ductility	Max. Force	Max. Displ.	Ductility
GM-1	1	51.0	0.298	2.9	79.6	0.096	1.5	79.6	0.342	5.2
	2	51.0	0.644	6.3	79.6	0.193	3.0	79.6	0.800	12.3
GM-2	1	51.0	0.209	2.1	79.6	0.079	1.2	79.6	0.217	3.3
	2	51.0	1.054	10.3	79.6	0.348	5.3	79.6	0.654	10.0
GM-3	1	51.0	1.810	17.8	79.6	0.903	13.8	79.6	2.411	37.0
	2	51.0	0.219	2.1	79.6	0.078	1.2	79.6	0.350	5.4
GM-4	1	51.0	0.426	4.2	79.6	0.140	2.1	79.6	0.546	8.4
	2	51.0	0.479	4.7	79.6	0.201	3.1	79.6	0.697	10.7
GM-5	1	51.0	0.580	5.7	79.6	0.159	2.4	79.6	1.345	20.6
	2	51.0	0.496	4.9	79.6	0.122	1.9	79.6	0.942	14.4
GM-6	1	51.0	0.519	5.1	79.6	0.098	1.5	79.6	0.751	11.5
	2	51.0	0.237	2.3	79.6	0.060	0.9	79.6	0.226	3.5
GM-7	1	51.0	0.194	1.9	79.6	0.057	0.9	79.6	0.319	4.9
	2	51.0	0.566	5.6	79.6	0.197	3.0	79.6	0.502	7.7
Average		51.0	0.552	5.4	79.6	0.195	3.0	79.6	0.722	11.1

The longitudinal displacement demands were also obtained from the same points as indicated in Fig. 10-15 along the bridge. Table 10-12 shows the longitudinal displacements obtained from the new multi-span bridge model subjected to the 7 pairs of ground motions. The longitudinal displacements are compared with the results for the original bridge model in Section 10.3.4. The average longitudinal displacement for end spans and the middle span reduced by 63% and 23%, respectively. The longitudinal displacement at top of the bent was also reduced by an average of 33%.

Table 10-12: Longitudinal displacements of the multi-span bridge model (unit: in.)

Longitudinal GM	Transverse GM	S1-L		S1-R		S2-L		S2-M		Bent top	
		Longi.	%	Longi.	%	Longi.	%	Longi.	%	Longi.	%
GM-1-1	GM-1-2	0.298	63%	0.300	62%	0.686	8%	0.687	8%	0.191	49%
GM-1-2	GM-1-1	0.644	46%	0.646	46%	1.507	-9%	1.515	-10%	0.351	18%
GM-2-1	GM-2-2	0.209	67%	0.213	67%	0.408	42%	0.407	42%	0.178	51%
GM-2-2	GM-2-1	1.054	67%	1.048	67%	1.581	41%	1.582	41%	0.412	18%
GM-3-1	GM-3-2	0.668	77%	0.665	77%	0.676	76%	0.680	76%	0.443	-2%
GM-3-2	GM-3-1	0.219	66%	0.224	65%	0.633	46%	0.630	46%	0.159	64%
GM-4-1	GM-4-2	0.426	53%	0.426	53%	1.000	-2%	1.005	-2%	0.272	31%
GM-4-2	GM-4-1	0.479	53%	0.484	52%	1.253	24%	1.253	24%	0.283	30%
GM-5-1	GM-5-2	0.580	68%	0.582	68%	2.309	-25%	2.313	-25%	0.328	25%
GM-5-2	GM-5-1	0.496	69%	0.494	69%	1.603	1%	1.605	1%	0.306	25%
GM-6-1	GM-6-2	0.519	60%	0.520	60%	1.329	23%	1.330	23%	0.335	20%
GM-6-2	GM-6-1	0.237	67%	0.235	68%	0.538	44%	0.539	44%	0.172	52%
GM-7-1	GM-7-2	0.194	73%	0.201	72%	0.662	27%	0.659	28%	0.158	60%
GM-7-2	GM-7-1	0.566	55%	0.568	56%	1.088	19%	1.081	19%	0.343	16%
Average		0.471	63%	0.471	63%	1.091	23%	1.091	23%	0.281	33%

Table 10-13 shows the total maximum longitudinal base shear forces of the new multi-span bridge model, which were compared with the longitudinal maximum shear forces of the original bridge model in Table 10-8 with the difference shown in percentages. The average longitudinal shear force obtained from the 14 time history analyses is 383 kips, which is 5% larger than the average longitudinal shear forces of the original bridge model in Table 10-8.

Table 10-13: Base shear forces of the multi-span bridge model (unit: kips.)

Longitudinal GM	Transverse GM	Base shear force	
		Longitudinal	%
GM-1-1	GM-1-2	306	-7%
GM-1-2	GM-1-1	429	17%
GM-2-1	GM-2-2	306	-5%
GM-2-2	GM-2-1	498	8%
GM-3-1	GM-3-2	516	33%
GM-3-2	GM-3-1	302	-7%
GM-4-1	GM-4-2	373	8%
GM-4-2	GM-4-1	377	6%
GM-5-1	GM-5-2	414	9%
GM-5-2	GM-5-1	395	4%
GM-6-1	GM-6-2	408	10%
GM-6-2	GM-6-1	314	-4%
GM-7-1	GM-7-2	304	-13%
GM-7-2	GM-7-1	415	12%
Average		383	5%

In the new bridge model, the longitudinal stiffness and strength in the EDSs was arbitrarily doubled, and it proved effective in reducing the ductility demands in the longitudinal BRBs in the EDSs and IDSs at the end of end spans (Span-1 and Span-2), but not necessarily the ductility demand of the longitudinal BRBs in the IDSs of the middle span (which increased from 10.1 to 11.1). Work could be done to determine how to distribute the longitudinal BRBs' stiffness and strengths across the various spans such as to achieve more uniform ductility demands in all the BRBs, but that would be the subject of future research.

10.4   Summary

The dynamic behavior of multi-span nonskew bridge with bidirectional ductile diaphragms was investigated in this section. The response of the substructure was included in examining the multi-span bridge designed with bidirectional ductile diaphragms. The BRBs in the ductile diaphragms proved to be able to develop ductile behaviors, while keep the substructures (columns in the bridge bents) elastic in both directions.

In the transverse direction, the same stiffness and strength of the ductile diaphragms was used in the EDSs and IDSs, and the ductility demands in the transverse BRBs from the dynamic analyses results at different locations were close to the design ductility. The longitudinal ductile diaphragms were designed to have

the same stiffness and strength as the transverse ones. Since the bridge bents are weaker in the longitudinal direction, the ductility demand in the longitudinal BRBs were larger than the transverse ones, as both indicated in the design calculations and dynamic analyses results. Increasing the stiffness and strength of the longitudinal EDSs on top of the abutment in the end spans can be effective in reducing the longitudinal BRB's ductility in the end spans, as well as the longitudinal displacement demand of the bridge and bent columns.

SECTION 11

'''''''SUMMARY, CONCLUSION AND

'RECOMMENDATIONS FOR FUTURE WORK

11.1 Summary

Research was conducted to investigate using Buckling Restrained Braces (BRBs) as Structural Fuses (SF) either in bridge's substructure or superstructure as a mean to protect bridge structures from damage during earthquakes, as summarized in more details in Sections 11.1.1 and 11.1.2.

11.1.1 BRBs added in substructures

BRBs were first proposed to be added in the substructure between columns of a bridge bent. Two scenarios having different column layout were considered. First, a two-column bent (considering single inclined BRB and inverted-V BRBs configurations) was studied. For that case, the SF concept modifies response of the bent to seismic excitation only in the transverse direction, which can be used in the retrofitting of old bridges or implemented as a design strategy in new bridge constructions. This would have to be coupled with another system in the longitudinal direction (which could be SFs in series connecting the bridge deck to the abutments, for example). While satisfactory design could be obtained for both BRB layouts considered, the difference between the single BRB case and the inverted-V BRBs case lies in the resulting smaller BRB sizes needed in the latter case (and correspondingly, smaller force demands on the connections). For example, for the case considered, compared with the single inclined BRB case, the force demand in the BRBs was 24% less in the inverted-V BRBs case. The inverted-V brace configuration was also found to be more beneficial because the forces developed in the BRBs are not transferred to the columns, thus resulting in smaller column sizes (unless column sizes is governed by non-seismic load conditions). Note that the BRB forces still have to be resisted by the foundations, but the force demand on the foundation in the inverted-V BRBs case is also smaller than that for the single inclined BRB case. Second, a box-pier configuration with BRBs was considered. This design concept, applicable to new bridges, allows implementing SFs to resist earthquake excitations in both the longitudinal and transverse directions. Smaller BRBs were designed and installed between closely spaced columns.

To facilitate the design of the SF system and connections of BRBs to the columns, concrete-filled tube (CFT) columns were used in both layouts. The seismic force demands on the columns in the two-bent and box-pier cases were obtained from the pushover analyses at the target displacement. The seismic

demands on the CFT columns were checked for the interaction of axial and flexural strength; it was found that the columns were adequate to resist the force demands obtained from pushover analyses at the target elastic displacement (obtained from response spectrum analysis). A comparison of theoretical and actual pushover curves in both the two-CFT-column and box-pier column cases showed good results, which indicates that bridge bent behavior in both cases was consistent with that predicted by the SF concept. To verify that the design of the BRB and bridge bent was governed by the seismic loads in the above case studies, the bridge bents were also analyzed for service loads, including dead load, live load and wind load; results confirmed that seismic demands governed design.

Nonlinear time history analysis was performed on the bridge bents with and without BRBs to verify their response predicted by the design procedure, elastic response spectrum, and pushover analysis. The displacements at bent cap beam level and base shear force demand were compared for the bridge bents with BRBs in each case with their corresponding bare bent. Results from the above case studies showed that: (i) The two-CFT-column with BRBs case had a 20% larger base shear strength, together with an approximately 50% lower bent lateral displacement, than for the bare bent case, and; (ii) For the case of the box-pier bent in both transverse and longitudinal direction, the base shear strength was 10% larger and displacement were approximately 50% smaller than for the case without BRBs (although that latter comparison is purely academic because the box-pier system would never be used without BRBs). This indicated that, for all the bents designed with BRBs, a significant gain in drift reduction for a relatively modest increase in base shear demands can be achieved. Displacement demands were found to slightly exceed predictions. This was a consequence of using a constant strength reduction factor as part of the design procedure (which is a phenomenon known to result in greater inelastic displacement for structures having short periods). Recommendations have been provided to modify the design procedure to account for this effect. Nonetheless, it remains that displacement of the bridge bents with BRBs cases were still significantly reduced from those of the corresponding bare bridge bents.

Connections details have been investigated to connect the BRBs to other members of the bridge bent (to establish feasibility when using certain conventional types of connections, recognizing that other details are also possible). Three types of BRBs connections to the bridge bents were examined, namely. using gusset plates welded to the steel shell of the CFT columns, using headed studs and anchor rods to connect the BRBs with the cap beams or the foundations. Analytical and experimental studies have been conducted for gusset plates welded to CFT column connections, and the monotonic test results were found to generally match the finite element analyses for specimens with various configurations. For seismic applications, this type of connection should be designed to remain elastic, as the hysteretic

behavior of the connection revealed deficient hysteretic energy dissipation upon repeated cycling. Design of BRBs to the cap beam and foundation using anchor bolts or anchor rods was also investigated, and found to be practical only for small BRBs (investigated only based on strengths under static loads).

11.1.2 BRBs added in superstructures

BRBs were also proposed to be inserted in the end-diaphragms of slab-on-girder steel bridges. Two types of bidirectional end diaphragm systems, EDS-1 and EDS-2 (i.e. with different geometrical layouts), were implemented in both skew and nonskew bridges. An approach was taken to design the skew bridges to have the same yield strength and yield displacement in the transverse and longitudinal directions as their equivalent nonskew bridges. Parametric nonlinear time history analyses were performed on benchmark skew and nonskew bridges designed with both EDSs to examine their seismic performance. Variations in skew, fundamental period of vibration, and earthquake excitation characteristics were considered. The inelastic displacement demands of nonskew and skew bridges with both types of EDSs were compared in both the longitudinal and transverse directions. The magnification factors of the nonskew and skew bridges' displacement demands from the elastic spectral displacement of nonskew EDS-1 bridge were obtained, and used in the proposed design procedures of bidirectional ductile diaphragms to predict the skew bridges' displacement demands. The long-term service life of BRBs installed across expansion joints and subjected to bridge thermal expansion histories was also investigated. A minimum ratio of 3% for the BRB's yielding core length's ratio over the whole bridge length was recommended to avoid low-cycle fatigue of the BRB due to thermal effects. Note that this ratio is based on the worst scenario of temperature changes found considering a total of nine locations across North America, for the longitudinal BRB horizontally installed at one end of the bridge. This value is subject to change if implemented at locations with more critical thermal variations than considered in the study.

Following the parametric studies, quasi-static experiments were conducted using the shake table to subject BRBs to a regime of relative end-displacements representative of the results predicted from the analytical studies. Two types of BRBs with flat end plates and unidirectional pinholes were designed. The end plates in the first type of BRB were designed to bend laterally to accommodate the required lateral displacement. The end plates in the second type of BRB were connected to a spherical bearing in the gusset plate in the reaction blocks. Four specimens of each type of BRB were tested, and different combinations of displacement protocols were applied to them. The BRB's hysteretic behaviors under different displacement protocols were studied and compared. All the BRB specimens tested developed cumulative inelastic deformations of more than 200 times the BRB's axial yield displacement value.

More significantly, the specimens were able to sustain multiple years of severe temperature cycles in addition to meeting the prequalification criterion. Ultimately, as expected, all the BRBs failed in tension after extensive cycles of inelastic deformations. No end-plate failure or instability was observed (which would have been undesirable failure modes). Following the tests, some BRBs were opened. It was found that fracture typically occurred where the BRB's core plate locally buckled the most.

Detailed analyses of cumulative inelastic deformations and low-cycle fatigue life of all BRBs using data from the experiments were performed. The cumulative inelastic deformations were used in a design example, which could be applied to assess how many years a BRB could remain in service while retaining its ability to provide adequate seismic response. A recommended design procedure for the EDSs in both nonskew and skew bridges was developed based on the paramedic analysis and experimental results.

A case study was performed on a straight three-span simply-supported bridge with floating spans, implemented with bidirectional ductile diaphragms at each end. The dynamic behavior of the bridge's superstructure, as well as the response of the substructure, were investigated. The BRBs designed in the bidirectional ductile diaphragms proved to be able to develop ductile behaviors, while keeping the substructures (columns in the bridge bents) elastic in both directions.

11.2   Conclusions

From the analytical and experimental work presented in this report, the following conclusions are made:

1. Bridge bents using BRBs inserted between the CFT columns can be designed and be effective in improving seismic behavior per the procedures presented in this report. A conservative design objective of full elastic column response was considered in this study by limiting demands in columns to their yield moment (M_y). While this made design of the SFs more challenging, it remained possible to implement such fuses in the bridge bent to resist earthquake excitations from the transverse direction (or from two orthogonal directions when a box-pier configuration with BRBs was considered). For all the bents designed with BRBs per the design procedures, drift reduction of at least 50% were accompanied by modest increase in base shear demands no greater than 20%, when compared with the same bridge bents without BRBs.

2. For gusset plates welded to steel shell of CFT column connections in seismic applications, this type of connection should be designed such that the steel shell remains elastic.

3. Quasi-static tests have demonstrated that BRBs having specially designed end connection details (such as having either long end plates designed to provide adequate buckling resistance, or spherical bearing) are able to sustain extensive cycles of inelastic deformations without end-plate failure or

instability. Tests up to low-cycle fatigue failure on eight BRBs have demonstrated that the BRB specimens developed cumulative inelastic deformations of more than 200 times the BRB's axial yield displacement value, under different sequences of bidirectional and temperature-induced axial displacement test protocols designed to simulate demands when used in bidirectional ductile diaphragms.

4. The analytical and experimental work has demonstrated the feasibility of implementing bidirectional ductile diaphragm in both skew and nonskew bridges using BRBs. A corresponding design procedure has been formulated to design BRBs in ductile diaphragms, and to establish when they should be replaced during the life of the bridge, using the cumulative ductililty of 250 times the yield displacement as a performance basis. However, the design procedure also specifies a test protocol that can be used to extend this limit, as it is foreseen that other BRBs designs/detailing could allow reaching significantly greater cumulative ductilities.

11.3 Recommendations for future research

Beyond the research work presented in this report, further investigations are suggested as follows:
1. For the designs of the BRBs inserted in the bridge bents:
   a) Seismic performance of designs using the proposed modified strength reduction factors (applicable in short period range of design spectra) must be determined, to verify that it better controls predictions of maximum column deformations.
   b) As BRBs become smaller, their contribution to the initial stiffness becomes less dominant, and the design procedure may need to be revisited to ensure that maximum displacements predicted based on initial stiffness can still be achieved (or are corrected accordingly).
   c) Measures to reduce total base shear must be investigated, which can be achieved by allowing limited inelastic deformation of columns, or by allowing BRBs to develop up to 3% strain in their yielding core, or both.
   d) Connections details of BRBs to the bents need to be re-evaluated with unconventional types of designs to ensure satisfactory performance of BRBs in the bridge bent.
2. For the BRBs designed in the bidirectional ductile diaphragms:
   a) The testing of a scale-model of a complete bridge span using a shake table is recommended to verify the dynamic response of a complete system in which the bi-directional ductile diaphragm concept is implemented.

b) BRBs designs from various suppliers should be sequentially tested as part of this shake-table test series, to broaden the understanding of how various BRB details could impact system response.

c) It is also recommended to investigate more thoroughly the implementation of the bidirectional diaphragm concept in various configurations of multi-span bridges, especially for those with skewness.

3. Long-term performance of BRBs exposed to various harsh environments (i.e. as installed in bridges) needs be investigated to ensure sustained satisfactory service.

SECTION 12

REFERENCEU

1. Abaqus Version 6.13 [Computer software]. Dassault Systèmes

2. ABAQUS (2014). "ABAQUS 6.13 Analysis User's Manual". Online Documentation Help: Dassault Systèmes.

3. AccuWeather. (2012). Retrieved from http://www.accuweather.com/

4. ACI 318-14, building Code Requirements for Structural Concrete and Commentary. American Concrete Institute: Detroit, MI, 2014

5. Aiken, I.D., Clark, P.W., Tajirian, F.F., Kasai, K., Kimura, I., and Ko, E. (2001), "Unbonded braces in the united states — design studies, large-scale testing and the first building application," Proceedings, Japan Passive Control Symposium, Tokyo Institute of Technology, Japan

6. Aiken, I. D., Mahin, S. A., and Uriz, P. (2002). "Large-scale testing of buckling-restrained braced frames." Proc., Japan Passive Control Symp., Tokyo Institute of Technology, Tokyo, 35e44.

7. AISC (2010a). "Seismic provisions for structural steel buildings." ANSI/AISC 341-10 and ANSI/AISC 341s1-10. American Institute of Steel Construction, Chicago, Illinois.

8. AISC. (2010b). "Specification for Structural Steel Buildings" ANSI/AISC 360-10 and ANSI/AISC 360s1-10. American Institute of Steel Construction, Inc., Chicago, IL

9. Akira, W. (2000). "Fatigue properties of practical-scale unbonded braces." Nippon steel technical report, 82(0).

10. American Association of State Highway and Transportation Officials (AASHTO). (2014). "AASHTO LRFD Bridge Design Specifications (7th Ed.)." Washington, DC

11. American Association of State Highway and Transportation Officials (AASHTO). (2011). "AASHTO Guide Specifications for LRFD Seismic Bridge Design (2nd Ed.)." Washington, DC

12. Anagnos T., (2011), "Risk Mitigation for older Concrete Buildings Presentation,", May 2, 2011

13. Alfawakhiri, F., Bruneau, M. (2000). "Flexibility of Superstructures and Supports in the Seismic Analysis of Simple Bridges", Journal of Earthquake Engineering and Structural Dynamics, Vol.29, No.5, pp.711-729.

14. Alfawakhiri, F., Bruneau, M. (2001). "Local versus Global Ductility Demands in Simple Bridges", ASCE Journal of Structural Engineering, Vol. 127, No.5, pp.554-560.

15. Architectural Institute of Japan: Recommendations for stability design of steel structures, Sec. 3.5 Buckling-Restrained Braces, 2009, 74–79.

16. ASTM (2015a) "ASTM C31 / C31M-15ae1, Standard Practice for Making and Curing Concrete Test Specimens in the Field" , ASTM International, West Conshohocken, PA, 2015, www.astm.org

17. ASTM (2015b) "ASTM C39 / C39M-16, Standard Test Method for Compressive Strength of Cylindrical Concrete Specimens" , ASTM International, West Conshohocken, PA, 2015, www.astm.org

18. ASTM (2015c) "ASTM F1554-15e1, Standard Specification for Anchor Bolts, Steel, 36, 55, and 105 ksi Yield Strength" , ASTM International, West Conshohocken, PA, 2015, www.astm.org

19. ASTM (2015D) "ASTM E606 / E606M-12, Standard Test Method for Strain-Controlled Fatigue Testing" , ASTM International, West Conshohocken, PA, 2015, www.astm.org

20. ATC, (1992), "Guidelines for cyclic seismic testing of components of steel structures." Report ATC-24, Applied Technology Council, Redwood City, CA

21. Aviram A., Mackie K.R., Stojadinović B. (2008), "Guidelines for nonlinear analysis of bridge structures in California" , Pacific Earthquake Engineering Research Center, 2008

22. Black C.J., Makris N., and Aiken I.D. (2002), "Component Testing, Stability Analysis and Characterization of Buckling Restrained 'Unbonded' Braces," *Technical Report PEER 2002/08, Pacific Earthquake Engineering Research Center*, University of California, Berkeley, CA.

23. Bruneau, M., Uang., C.M., Sabelli, R. (2011). "Ductile Design of Steel Structures - 2nd Edition", McGraw-Hill, New York, NY, 921p.

24. Bruneau, M., Sarraf, M., Zahrai, S.M. and Alfawakhiri, F. (2002) "Displacement-Based Energy Dissipation Systems for Steel Bridges Diaphragms", Journal of Constructional Steel Research, Vol.58, No.5-8, pp.801-817.

25. California Department of Transportation (Caltrans). (2010). "Caltrans Seismic Design Criteria (Version 1.6)." Sacramento, CA

26. California Department of Transportation (Caltrans). (2012). "Caltrans Bridge Design Specifications." Sacramento, CA

27. Carden, L.P., Itani, A.M. and Buckle, I.G. (2006a) "Seismic Performance of Steel Girder Bridges with Ductile Cross Frames Using Single Angle X Braces", Journal of Structural Engineering, ASCE, Vol.132, No.3, pp.329-337.

28. Carden, L.P., Itani, A.M. and Buckle, I.G. (2006b) "Seismic Performance of Steel Girder Bridges with Ductile Cross Frames Using Buckling-Restrained Braces", Journal of Structural Engineering, ASCE, Vol.132, No.3, pp.338-345.

29. Carden, L., Itani, A., and Buckle, I. (2008) "Seismic performance of steel girder bridge superstructures with ductile end cross frames and seismic isolators", Technical Report MCEER-08-0002, MCEER, University at Buffalo, Buffalo, NY.

30. Celik, O., Bruneau, M., (2011). "Skewed Slab-on-Girder Steel Bridge Superstructures with Bidirectional-Ductile End Diaphragms," ASCE J。 of Bridge Engineering, Vol.16, No.2, pp.207-218.

31. Christopolus, A. S. "Improved seismic performance of buckling restrained braced frames," MS thesis, Civil and Environmental Engineering Dept., University of Washington, Seattle, WA, 2005.

32. Chan R.W.K., Albermani F. (2007), "Experimental study of steel slit damper for passive energy dissipation," Engineering Structures, 30,1058-1066

33. Clark, P., Aiken, I., Kasai, K., and Kimura, I. (2000) "Large-scale testing of steel unbonded braces for energy dissipation." Proceedings of the Structural Congress, Philadelphia, Pennsylvania.

34. Computers & Structures Inc. (2016) "CSI Analysis Reference Manual for SAP2000", CA

35. Connor, J.J., Wada, A., Iwata, M., and Huang, Y.H. (1997). "Damage-controlled structures. i: preliminary design methodology for seismically active regions." Journal of Structural Engineering, Volume 123, No. 4, ASCE, pp. 423-431.

36. Dargush G.F., Soong T.T. (1995) "Behavior of metallic plate dampers in seismic passive energy dissipation systems". Earthquake Spectra, Volumn 11, No.4

37. Dicleli, M. and Bruneau, M. (1995). "Seismic Performance of Single-Span Simply Supported and Continuous Slab-on-Girder Steel Highway Bridges." J. Struct. Eng., 10.1061/(ASCE)0733-9445(1995)121:10(1497), 1497-1506.

38. Dusicka, P., Bazaez. R., and Knoles. S. (2015), "Bridge seismic retrofit measures considering subduction zone earthquake", Tech. Rep. FHWA-OR-RD-16-01, Oregon Department of Transportation. Portland State University, Portland, OR, 2015

39. El-Bahey, S., Bruneau, M., (2010). "Analytical development and experimental validation of a structural-fuse bridge pier concept", Technical Report MCEER-10-0005, MCEER, University at Buffalo, Buffalo, NY.

40. Fahnestock. L., Ricles. J., and Sause. R. (2007). "Experimental evaluation of a large-scale Buckling-Restrained Braced frame." J. Struct. Eng., 10.1061/(ASCE)0733-9445(2007)133:9(1205), 1205-1214.

41. Fatiga Version 1.03 [Computer software]. Fatec Engineering, Bergschenhoek, Netherlands

42. FEMA (2000b), FEMA 356, "prestandard and commentary for the seismic rehabilitation of buildings", Building Seismic Safety Council for the Federal Emergency Management Agency, Washington, DC

43. FEMA P-695, (2009), "Quantification of building seismic performance factors", prepared by Applied technology council for the federal emergency management agency, Washington DC

44. Fintel, M., and Ghosh, S.K. (1981). "The structural fuse: an inelastic approach to seismic design of buildings." Civil Engineering. Volume 51, No. 1, ASCE, pp. 48-51.

45. Fisher, J.M. and Kloiber, L.A. (2006) "Base Plate and Anchor Rod Design," American Institute of Steel Construction Inc, Second Edition

46. Ghobarah A, Abou Elfath H. (2001), "Rehabilitation of a Reinforced Concrete Frame using Eccentric Steel Bracing" Engineering Structures, 23, 745-755

47. Goodyear, D., and Sun, J. (2003). "New developments in cable-stayed bridge design, San Francisco." Structural Engineering International, 13(1), 59-63.

48. Hamada N., Nishioka T., and Kanaji H.,(2007), "Seismic retrofitting of long-span truss bridge-minato bridge using damage-control technologies," Steel Construction Today & Tomorrow, No.19, pp.12-16

49. Hibbeler. R. C. (2011). "Mechanics of Materials.8th ed in SI units (8th ed.). Singapore: Pearson.

50. Higgins, C., and Newell, J. 2004. "Confined Steel Brace for Earthquake Resistant Design." Engineering Journal, AISC, 4th Quarter, 187–202.

51. Hikino, T.,Okazaki, T.,Kajiwara, K., and Nakashima, M. (2013). "Out-of-Plane Stability of Buckling-Restrained Braces Placed in Chevron Arrangement." J. Struct. Eng., 10.1061/(ASCE)ST.1943-541X.0000767, 1812-1822.

52. Hogan, T.J. and Thomas, I.R., "Design of structural connections," Fourth Edition, Australian Institute of Steel Construction, 1994

53. Hu H.T., Huang C.S. and Chen Z.L. (2005), "Finite element analysis of CFT columns subjected to an axial compressive force and bending moment in combination", Journal of Constructional Steel Research, Vol. 61, Issue 12, Page 1692-1712,

54. Huang, Y.H., Wada, A., Iwata, M., Mahin, S.A., and Connor, J.J. (2002). "Design of damage-controlled structures." Innovative Approaches to Earthquake Engineering, WIT Press, pp. 85-118.

55. Islam, S., Skokan, M., and Huang, S. (2006) "Innovative Hi-tech Solution for a Concrete Residential High Rise Tower."

56. Iwata, M., Kato, T. and Wada, A. [2003], "Performance Evaluation of BucklingRestrained Braces in Damage-Controlled Structures," Behavior of Steel Structures in Seismic Areas, Proceedings of the 4th International Conference STESSA 2003, Mazzolani, F. (ed.), Naples, Italy, June 9-12, pp. 37-43.

57. Kanaji, H., Kitazawa, M., Suzuki, N., (2005). "Seismic retrofit strategy using damage control design concept and the response reduction effect for a long-span truss bridge", US-Japan Bridge Workshop

58. Keller, D. and Bruneau, M. (2008), "Development of a Steel Plate Shear Wall Bridge Pier System Conceived from A Multi-hazard Perspective" Technical Report MCEER-08-0030, MCEER, University at Buffalo, Buffalo, NY.

59. Keller, D. and Bruneau, M. (2009), "Multi-hazard resistant steel plate shear wall bridge pier concept" Taylor & Francis Group, London, ISBN 978-0-415-56326-0

60. Koetaka Y, Kinoshita T, Inoue K, IItani K. (2008), "Criteria of buckling-restrained braces to prevent out-of-plane buckling", Proceedings of 14th World Conference on Earthquake Engineering, Beijing, China.

61. Lanning, J.,Benzoni, G., and Uang, C.M(2016a). "Using buckling-restrained braces on long-span bridges. i: full-scale testing and design implications." J. Bridge Eng., 10.1061/(ASCE)BE.1943-5592.0000781, 04016001.

62. Lanning, J., Benzoni, G., and Uang, C.(2016b). "Using buckling-restrained braces on long-span bridges. ii: feasibility and development of a near-fault loading protocol." J.Bridge Eng.,10.1061/(ASCE)BE.1943-5592.0000804, 04016002.

63. Lopez, W., Gwie, D., Saunders, M., and Lauck, T. (2002) "Lessons learned from large-scale tests of unbonded braced frame subassemblage." Proceedings 71st Annual Convention, Structural Engineers Association of California, Sacramento, California, 171-183.

64. López, W.A., and Sabelli, R. (2004). "Seismic design of buckling-restrained braced frames." Steel Tips Report. Structural Steel Educational Council.

65. Maeda, Y., Nakata, Y., Iwata, M., and Wada, A. (1998). "Fatigue properties of axial-yield type hysteresis dampers." J.Struct.Constr.Eng., 503, 109-115.

66. Mäkeläinen, P.K. (1988). "Strength, stiffness and non-linear behavior of simple (multi-braced) welded tubular joints." T.N.O. Report B1-87-72/63.6.1098, Delft, The Netherlands

67. Mayes, R.L., Goings, C., Wassim, N., Harris, S., Lovejoy, J., Fanucci, J.P., Bystricky, P. and Hayes, J.R. (2004), Proceedings of the 13th World Conference on Earthquake Engineering, Vancouver, B.C., Canada, Paper No. 2887.

68. MCEER-ATC 49 (2003). "Recommended LRFD Guidelines for the Seismic Design of Highway Bridges." Tech. Rep. MCEER-03-SP03, MCEER, Uni. at Buffalo, Buffalo, NY.

69. Merritt, S., Uang, C.M. and Benzoni, G. [2003a], "Subassemblage Testing of CoreBrace Buckling-Restrained Braces," Structural Systems Research Project, Report No. TR-2003/01, University of California, San Diego.

70. Merritt, S., Uang, C.M. and Benzoni, G. [2003b], "Subassemblage Testing of Star Seismic Buckling-Restrained Braces," Structural Systems Research Project, Report No. TR-2003/04, University of California, San Diego.

71. Miranda E. and Bertero V.V, (1994), "Evaluation of strength reduction factor for earthquake-resistant design", Earthquake Spectra, Vol. 10, No.2, 1994

72. Morgan, T., and Walters, M. (2004). "Innovative Approaches to Performance-based Seismic Rehabilitation of Concrete Buildings." Pacific Earthquake Engineering Research Center, College of Engineering, University of California, Berkeley

73. Nakashima, M. (1995). "Strain-Hardening Behavior of Shear Panels Made of Low- Yield Steel. I: Test." Journal of Structural Engineering, Volume 121, No. 12, ASCE, pp. 1742-1749.

74. OpenSees Version 2.4.6 [Computer software]. University of California, CA

75. Oya, T., Fukasawa, T. Fujiwara, M. et al. (2009). "Practical study on a new type Buckling-Retrained-Brace," Proceeding of the International Association for Shell and Spatial Structure (IASS) Symposium 2009, Vlencia

76. Palmer, K.,Roeder, C.,Lehman, D.,Okazaki, T., and Shield, C.(2013). "Experimental Performance of Steel Braced Frames Subjected to Bidirectional Loading." J. Struct. Eng., 10.1061/(ASCE)ST.1943-541X.0000624, 1274-1284.

77. Papageorgiu, A., Halldorsson, B. and Dong, G. (2000), "Strong Motion Simulation Code for Eastern North America, User Manual Version 1.0", Engineering Seismological Laboratory, Department of Civil, Structural and Environmental Engineering, University of Buffalo. Downloaded from Internet.

78. Paul, J.C. (1992). "The ultimate behavior of multiplanar TT- AND KK-joints made of circular hollow sections." Ph.D. thesis, Kumamoto University, Kumamoto, Japan

79. PCI (2004). "PCI design handbook, 6th ed.", Prestressed Concrete Institute PCI,2004, Chicago, IL

80. Priestley, M. J. N., Seible, F. and Calvi, G. M. (1996), Seismic Design and Retrofit of Bridges, John Wiley & Sons, New York, USA

81. Priestley M.J.N., Seible F., Calvi G.M. and Kowalsky M.J. (2007) "Displacement-Based Seismic Design of Structures", IUSS Press, Pavia, Italy, ISBN 978-88-6198-000-6

82. Rabbat, B. and Russell, H. (1985). "Friction Coefficient of Steel on Concrete or Grout." J. Struct. Eng., 10.1061/(ASCE)0733-9445(1985)111:3(505), 505-515.

83. Reno, M. and Pohll, M. (2010a). "Seismic Retrofit of California's Auburn-Foresthill Bridge" J. Transportation Board, TRB, 2201/2010, pp.83–94.

84. Reno, M. and Pohll, M. (2010b). "Incorporating Buckling Restrained Braces (BRB) as part of the Arburn-Foresthill bridge seismic retrofit " Retrieved from http://www.pwri.go.jp/eng/ujnr/tc/g/pdf/29/29-4-3_Reno.pdf

85. Roeder, C., and Popov, E. (1977). "Inelastic Behavior of Eccentrically Braced Steel Frames under Cyclic Loadings." Report No. UCB-77/17, Earthquake Engineering Research Center, University of California, Berkeley.

86. Roeder, C. W., Lehman, D. E., and Christopulos, A. (2006). "Seismic performance of special concentrically braced frames with buckling restrained braces." Proc., 8th U.S. National Conf. on Earthquake Engineering, Curran Associates, San Francisco

87. Romero P., Reaveley L., Miller P., and Okahashi T., "Full Scale Testing of WC Series Buckling-Restrained Braces," U of Utah, Salt Lake City, UT, Tech. Rep. Final Report to Star Seismic, 2007.

88. Rossi, P. (2015). "Importance of Isotropic Hardening in the Modeling of Buckling Restrained Braces." J. Struct. Eng.,141(4), 04014124.

89. Sahoo D.R. and Chao S.H. (2010) "Performance-based Plastic Design Method For Buckling-Restrained Braced Frames" Engineering Structures, 32, page 2950-2958

90. SAP2000 Version 14 [Computer software]. Computers & Structures. Inc, CA

91. SKF Group (2011) "SKF spherical plain bearings and rod ends", PUB BU/P1 06116/1 EN, September 2011

92. Star Seismic. (2016a) "Star Seismic BRBs". Retrived from http://www.starseismic.net/star-seismic-brbs/

93. Star Seismic. (2016b) "Star Seismic projects". Retrieved from http://www.starseismic.eu/projects

94. Sabelli R. (2001), "Research on Improving the Design and Analysis of EarthquakeResistant Steel Braced Frames," *The 2000 NEHRP Professional Fellowship Report*, Earthquake Engineering Research Institute, Oakland, CA.

95. Sabelli, R., Mahin, S., and Chang, C. (2003). "Seismic demands on steel braced buildings with Buckling-Restrained Braces." Engineering Structures, Elsevier Science Ltd., Volume 25, No. 5, pp. 655-666.

96. Sarraf, M., Bruneau, M. (1998). "Ductile Seismic Retrofit of Steel Deck-Truss Bridges. I: Strategy and Modeling", ASCE Journal of Structural Engineering, Vol.124, No.11, 1998, pp.1253-1262.

97. Sarraf, M., Bruneau, M. (1998). "Ductile Seismic Retrofit of Steel Deck-Truss Bridges. II: Design Applications", ASCE Journal of Structural Engineering, Vol.124, No.11, 1998, pp. 1263-1271.

98. Sarraf, M. and Bruneau, M. (2002) "Seismic Performance of a Ductile Retrofitted Deck-Truss Bridge", 7th National Conference on Earthquake Engineering, Boston, July, on CD-ROM.

99. Sarraf, M. and Bruneau, M. (2004) "Performance Tests of Innovative Ductile Steel Seismically Retrofitted Deck-Truss Bridges", 13th World Conference on Earthquake Engineering, Vancouver, Canada, August, CD-ROM, Paper # 1803.

100. Shaw, A., and Bouma, K. (2000) "Seismic Retrofit of the Marin County Hall of Justice Using Steel Buckling-Restrained Braced Frames." Proceedings, 69th Annual Convention, Structural Engineers Association of California, Sacramento, California.

101. Shimizu, K., Hashimoto, J., Kawai, H., and Wada, A. (1998). "Application of damage control structure using energy absorption panel." Paper No. T105-2, Structural Engineering World Wide 1998, Elsevier Science, Ltd.

102. Smith, K.N., Watson, P., and Topper, T.H. (1970). "A stress-strain function for the fatigue of metals." Journal of Materials ASTM, 5, 767-778.

103. Sugiyama, S. (1998). "Application of Hysteresis Steel Dampers to Tall Building." Paper No. T190-5, Structural Engineering World Wide 1998, Elsevier Science, Ltd.

104. Tanaka, K., Torii, T., Sasaki, Y., Miyama, T., Kawai, H., Iwata, M., and Wada, A. (1998). "Practical application of damage tolerant structures with seismic control panel using low-yield-point-steel to a high-rise steel building." Paper No. T190-4, Structural Engineering World Wide 1998, Elsevier Science, Ltd.

105. Takeuchi, T., Ozaki, H., Matsui, R. and Sutcu, F. (2014), Out-of-plane stability of buckling-restrained braces including moment transfer capacity. Earthquake Engng Struct. Dyn., 43: 851–869. doi:10.1002/eqe.2376

106. *Target Acceleration Spectra Compatible Time Histories (TARSCTHS) Version 1* [Computer software]. Papageorgious A., Halldorsson B. and Dong G., Univ. at Buffalo, Buffalo, NY

107. Tsai K.C., Chen H.W., Hong C.P., Su Y.F.(1993), "Design of Steel Triangular Plate Energy Absorbers for Seismic-Resistant Construction," Earthquake Spectra, Volume 9, No.3

108. Tsai, K.C., Hsiao, B.C., Lai, J.W., Chen, C.H., Lin, M.L. & Weng, Y.T. [2003a], "Pseudo Dynamic Experimental Response of a Full Scale CFT/BRB Composite Frame," Proceedings of the Joint NCREE/JRC Workshop on International Collaboration on Earthquake Disaster Mitigation Research, Tapei, Taiwan.

109. Tsai K.C., Loh C.H., Hwang Y.C., and Weng C.S. (2003b), "Seismic Retrofit of Building Structures with Dampers in Taiwan," Symposium of Seismic Retrofit of Buildings and Bridges with Base Isolation and Dampers, Kyoto University, Japan.

110. Tsai, K. C, Hsiao, P. C., Wang, K. J., Weng, Y. T., Lin, M. L., Lin, K. C., Chen, C. H., Lai, J. W., and Lin, S. L. (2008). "Pseudo-Dynamic Tests of a Full-Scale CFT/BRB Frame-Part I: Specimen Design, Experiment and Analysis."Earthquake Engineering & Structural Dynamics, vol. 37, no. 7, 1081–1098.

111. Tsai, K. C., and Hsiao P. C. (2008). "Pseudo-Dynamic Test of a Full-Scale CFT/BRB Frame-Part II: Seismic Performance of Buckling Restrained Braces and Connections." Earthquake Engineering & Structural Dynamics, vol. 37, no. 7,1099–1115.

112. Tremblay R., Degrange G., and Blouin J. (1999), "Seismic Rehabilitation of a Four Storey Building with a Stiffened Bracing System," *Proceedings of the 8th Canadian Conference on Earthquake Engineering*, Vancouver, British Columbia, Canada.

113. Tremblay R., and Bouatay, N. (2002), "Loading Protocols for the Seismic Testing of Ductile Bracing Members in Concentrically Braced Steel Frames," *Proceedings of the 12th European Conference on Earthquake Engineering*, Paper No. 480, London, September 9-13.

114. Tremblay, R., Bolduc, P., Neville, R., and DeVall, R. (2006). "Seismic testing and performance of buckling-restrained bracing systems." Can. J. Civ. Eng., 33(2), 183e198.

115. Uang, C.M., Nakashima, M. and Tsai, K.C. (2004), "Research and Application of Buckling-Restrained Braced Frames," *International Journal of Steel Structures*, The Korean Society of Steel Construction, 4 (4): 301-313.

116. Uang., C.M., Bruneau, M., K.C. Tsai, (2014). "Seismic Design of Steel Bridges", Chapter in "The CRC Handbook of Bridge Engineering - Seismic Design." CRC Press, Boca Raton, Florida, pp.301-336.

117. Uriz P., "Towards earthquake resistant design of concentrically braced steel structures," Ph.D. dissertation, Civil and Environmental Engineering Dept., University of California, Berkeley, Berkeley, CA, 2005.

118. Usami T., Kasai A., and Kato M. (2003), "Behavior of Buckling-Restrained Brace Members," Behavior of Steel Structures in Seismic Areas, Proceedings of the 4th International Conference STESSA 2003, Mazzolani, F. (ed.), Naples, Italy, June 9-12, pp. 211-216.

119. Usami, T., Wang, C., and Funayama, J. (2011). "Low-cycle fatigue tests of a type of buckling restrained braces." Procedia Engineering, 14, 956-964.

120. Usami, T., Lu, Z., and Ge, H. (2005). "A seismic upgrading method for steel arch bridges using Buckling-Restrained Braces." Earthquake engineering & structural dynamics, 34(4-5), 471-496.

121. USGS (2016) "U.S. Seismic Design Mpas". Retrived from http://earthquake.usgs.gov/designmaps/us/application.php?

122. Van der Vegte, G. J. (1995). "The static strength of uniplanar and multiplanar tubular T- and X-joints." Ph.D thesis, Delft University of Technology, Delft, The Netherlands

123. Vargas, R., Bruneau, M. (2006a), "Experimental investigation of the structural fuse concept", Technical Report MCEER-06-0005, Multidisciplinary Center for Earthquake Engineering Research, State University of New York at Buffalo, Buffalo, NY, 2006.

124. Vargas, R., Bruneau, M. (2006b), "Analytical investigation of the structural fuse concept", Technical Report MCEER-06-0004, Multidisciplinary Center for Earthquake Engineering Research, State University of New York at Buffalo, Buffalo, NY, 2006.

125. Voth, A. P. (2010). "Branch plate-to-circular hollow structural section connections." Ph.D. thesis, University of Toronto, Toronto, Canada.

126. Wada, A., Connor, J.J., Kawai, H., Iwata, M., and Watanabe, A. (1992). "damage tolerant structures." Proceedings of: Fifth U.S.-Japan Workshop on the Improvement of Structural Design and Construction Practices, ATC-15-4, Applied Technology Council, pp. 27-39.

127. Wada, A., and Huang, Y.H. (1999). "damage-controlled structures in japan." U.S.- Japan Workshop on Performance-Based Earthquake Engineering Methodology for Reinforced Concrete Building Structures, PEER Report 1999, Volume 10, pp. 279-289.

128.   Wada, A., Huang, Y.H., and Iwata, M. (2000). "passive damping technology for buildings in Japan." Progress in Structural Engineering and Materials, John Wiley & Sons, Ltd., Volume 2, No. 3, pp. 335-350.

129.   Wang, C.-L., Usami, T., and Funayama, J. (2012). "Evaluating the influence of stoppers on the low-cycle fatigue properties of high-performance buckling-restrained braces." Engineering Structures, 41, 167-176.

130.   Watanabe, A., Hitomi, Y., Saeki, E., Wada, A., and Fujimoto, M. (1988). "Properties of Brace Encased in Buckling Restraining Concrete and Steel Tube." Proceedings of Ninth World Conference on Earthquake Engineering, Tokyo-Kyoto, Japan, No. 6-7-4, Volume 4, pp. 719-724.

131.   Wardenier J., Kurobane Y., Packer J.A. etc. (2008), "Design guide for circular hollow section (CHS) joints under predominantly static loading," CIDECT, Section Edition

132.   Wei, X., Bruneau, M. (2013), "Resilient bridges: replaceable structural fuses for post-earthquake accelerated service, phase 1: analytical investigation", Tech. Rep. CA13-2296, Caltrans, CA

133.   Whittaker,A.S., Bertero, V.V., Thompson, C.L. and Alonso, L.J.(1991), "seismic testing of steel plate energy dissipation devices." Earthquake Spectra, 7(4), 563-604

134.   Zahrai, S.M., Bruneau, M. (1998). "Impact of Diaphragms on Seismic Response of Straight Slab-on-girder Steel Bridges", ASCE Journal of Structural Engineering, Vol.124, No.8, pp.938-947.

135.   Zahrai, S.M., Bruneau, M. (1999a). "Ductile End-Diaphragms for the Seismic Retrofit of Slab-on-Girder Steel Bridges", ASCE Journal of Structural Engineering, Vol.125, No.1, 1999, pp.71-80.

136.   Zahrai, S.M., Bruneau, M. (1999b). "Cyclic Testing of Ductile End-Diaphragms for Slab-on-Girder Steel Bridges", ASCE Journal of Structural Engineering, Vol.125, No.9, pp.987-996.

137.   Zhang G., Unjoh S., Hoshikuma J., and Sakai J. (2009), "Seismic Retrofit Techniques for Reinforced Concrete Bridge Columns with Combination of FRP Sheet and Steel Jacketing," the 25th U.S.-Japan Bridge Engineering Workshop Proceeding, Oct, 2009

138.   Zhao, J. X., Wu, B., and Ou, J. P. (2011). "A novel type of angle steel buckling-restrained brace: Cyclic behavior and failure mechanism." Earthquake Eng. Struct. Dynam., 40(10), 1083-1102.

139.   Zhao, J., Wu, B., and Ou, J. (2012). "Flexural Demand on Pin-Connected Buckling-Restrained Braces and Design Recommendations." J. Struct. Eng., 10.1061/(ASCE)ST.1943-541X.0000549, 1398-1415.

Appendix A Design CFT column bent with BRBs

A.1 Two CFT column bent with BRBs

This design example illustrates how BRBs are designed as structural fuses to limit damage to the bridge bent. The design procedure for two CFT columns with a single BRB, or BRBs in inverted-V, is shown below. The capacity of the CFT columns is checked at the end of this example.

CFT column properties

Start with a trial circular CFT column with the following properties

The height of the bent column	$h = 234$	in
The diameter of the CFT column	$D = 48$	in
The thickness of the steel tube	$t = 1.25$	in
The inside diameter of the concrete infill	$D_c = D - 2 \cdot t = 45.5$	in
The area of the steel tube	$A_s = \pi \cdot \dfrac{\left(D^2 - D_c{}^2\right)}{4} = 183.587$	in^2
The area of the concrete infill	$A_c = \dfrac{\pi \cdot D_c{}^2}{4} = 1.626 \times 10^3$	in^2
The area of the reinforcement in the infill concrete	$A_{sr} = 0$	in^2
The moment of inertia of the steel tube	$I_s = \pi \cdot \dfrac{\left(D^4 - D_c{}^4\right)}{64} = 5.019 \times 10^4$	in^4
The moment of inertia of the concrete infill	$I_c = \pi \cdot \dfrac{D^4}{64} = 2.606 \times 10^5$	in^4
The moment of inertia of the reinforcement in the concrete	$I_{sr} = 0$	in^4
The strength of the steel shell using A572 alloy steel plate Gr60	$F_y = 60$	ksi
	$F_u = 75$	ksi
The strength of the infill concrete	$f_c = 4$	ksi
The elastic modulus of concrete	$E_c = \dfrac{57000}{1000} \cdot \sqrt{f_c \cdot 1000} = 3.605 \times 10^3$	ksi
The elastic modulus of steel	$E_s = 29000$	ksi
EI of the CFT column	$EI = E_s \cdot I_s + E_s \cdot I_c = 9.012 \times 10^9$	in^4

Strength calculation

Axial Compressive and tensile strength

Per AISC 2010, the design compressive strength of the CFT section is calculated below using the LRFD approach. Additional information about why AISC equations instead of the AASHTO Bridge Design Specifications can be found in appendix A.

The stability limit using Width-to-thickness ratio is first checked according to table I1.1 A & B

$$\frac{D}{t} = 38.4 \qquad \text{smaller than} \qquad \lambda p_1 = 0.15 \cdot \frac{E_s}{F_y} = 72.5 \qquad \text{for compression}$$

$$\lambda p_2 = 0.09 \cdot \frac{E_s}{F_y} = 43.5 \qquad \text{for flexure}$$

The composite section is categorized as a compact section both under axial force and moment

To calculate the compressive strength, section I2.b is used per AISC2010

For circular section $\qquad C_2 = 0.95$

For compact section $\qquad P_p = F_y \cdot A_s + C_2 \cdot f_c \cdot \left(A_c + A_{sr} \cdot \frac{E_s}{E_c} \right) = 1.719 \times 10^4 \qquad$ kips

$$P_{n0} = P_p$$

To get the effective stiffness of the CFT section, the coefficient C3 is calculated

$$C_3 = 0.6 + 2 \cdot \left(\frac{A_s}{A_c + A_s} \right) = 0.803 \qquad \text{smaller than 0.9, ok}$$

The effective stiffness of the CFT section

$$EI_{eff} = E_s \cdot I_s + 0.5 \cdot E_s \cdot I_{sr} + C_3 \cdot E_c \cdot I_c = 2.21 \times 10^9 \qquad \text{in}^4$$

Check global buckling of the CFT column under axial compression load

The CFT column is fixed at both ends $\qquad K_c = 0.5$

The elastic critical buckling load is determined by using equatioin I2-5 (AISC,2010)

$$P_e = \pi^2 \cdot \frac{EI_{eff}}{\left(K_c \cdot h \right)^2} = 1.593 \times 10^6 \qquad \text{kips}$$

$$n_1 = \frac{P_{n0}}{P_e} = 0.011 \qquad \text{smaller than 2.25, OK}$$

The axial compression strength of the CFT column is calculated according to equation I2-2 (AISC,2010)

$$P_n = P_{n0} \cdot 0.658^{n_1} = 1.712 \times 10^4 \qquad \text{kips} \qquad \qquad \phi_c = 0.75$$

The axial tension strength of the CFT column is determined based on I2-8

$$T_n = F_y \cdot A_s = 1.102 \times 10^4 \qquad \text{kips} \qquad \qquad \phi_t = 0.9$$

The strength reduction factor for design is listed on the right side, and not included into the strength calculations at this stage.

Per AISC 2010, shear strength for filled composite members can be determined using the available shear strength of the steel alone. The nominal shear strength for round HSS per AISC 2010 Chapter G, is calculated using the equations listed below. The limit states of shear yielding and buckling is considered. The same equation is provided in the AASHTO Bridge Design Specifications (2010) section 6.12.1.2.3c

The critical shear stress is calculated to be the smaller of

$$F_{cr1} = 1.60 \cdot \frac{E_s}{\sqrt{\frac{h}{D}} \cdot \left(\frac{D}{t}\right)^{\frac{5}{4}}} = 219.845$$

$$F_{cr2} = 0.78 \cdot \frac{E_s}{\left(\frac{D}{t}\right)^{\frac{3}{2}}} = 95.06$$

$$F_{cr3} = 0.6 \cdot F_y = 36$$

therefore, $\quad F_{cr} = F_{cr3}$

The shear strength of the CFT section: $\quad V_n = F_{cr} \cdot \dfrac{A_s}{2} = 3.305 \times 10^3 \qquad$ kips

$$\phi_v = 0.9$$

Flexural strength calculation

Two approaches are identified as appropriate to calculate the flexural strength in AISC (2010), namely, (1) the plastic stress distribution, (2) the strain compatibility method. Per AASHTO Guide Specifications for LRFD Seismic Bridge Design (2009) section 7.6 , the design flexural strength of the composite section is calculated below using a method similiar to the plastic distribution method. β is the central angle formed between the neutral axis chord line and the center point of the steel shell found by the following recursive equation (unit: rad)

$$\beta = 2.443 \qquad \frac{A_s \cdot F_y + 0.2 \cdot D^2 \cdot f_c \cdot \left[\sin\left(\frac{\beta}{2}\right) - \left(\sin\left(\frac{\beta}{2}\right)\right)^2 \cdot \tan\left(\frac{\beta}{4}\right) \right]}{0.125 \cdot D^2 f_c + D \cdot t \cdot F_y} = \mathbf{I}\beta \qquad (7.6.2-8)$$
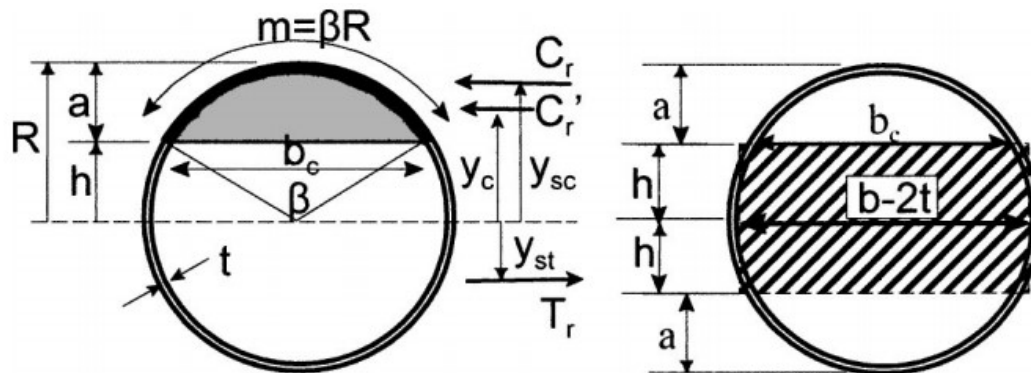
Figure A-1 Free body diagram to develop the flexural strength equation (Bruneau and Marson, 2004, similar to AASHTO Guide Specifications for LRFD Seismic Bridge Design (2009))

The following are parameters shown in figure a-1 for calculating the flexural strength of the CFT section

$$b_c = D \cdot \sin\left(\frac{\beta}{2}\right) = 45.101 \qquad\qquad (7.6.2-7)$$

$$a = \frac{b_c \cdot \tan\left(\dfrac{\beta}{4}\right)}{2} = 15.786 \qquad\qquad (7.6.2-6)$$

$$e_1 = b_c \cdot \left(\frac{1}{2 \cdot \pi - \beta} + \frac{1}{\beta}\right) = 30.206 \qquad\qquad (7.6.2-4)$$

$$e_2 = b_c \cdot \left[\frac{1}{2 \cdot \pi - \beta} + \frac{b_c^2}{1.5 \cdot \beta \cdot D^2 - 6 \cdot b_c \cdot (0.5 \cdot D - a)}\right] = 26.494 \qquad\qquad (7.6.2-5)$$

$$C_{r1} = F_y \cdot \beta \cdot D \cdot \frac{t}{2} = 4.397 \times 10^3 \qquad\qquad (7.6.2-2)$$

$$C_{r2} = f_c \cdot \left[\beta \cdot \frac{D^2}{8} - \frac{b_c \cdot \left(\dfrac{D}{2} - a\right)}{2}\right] = 2.073 \times 10^3 \qquad\qquad (7.6.2-3)$$

$$\phi_f = 1.0$$

Therefore the plastic strength of the CFT section is

$$M_n = \phi_f \cdot \left(C_{r1} \cdot e_1 + C_{r2} \cdot e_2\right) = 1.878 \times 10^5 \qquad\qquad \text{kips} \cdot \text{in}$$

Flexural strength, yielding displacement, and stiffness

The yielding flexural strength is obtained when the extreme point in the steel shell reaches the yielding strain of 0.002. Hand calculation is not performed here; instead this value is obtained from SAP2000 Section Designer. Details are shown in Appendix A3.

The yielding flexural strength of the section is $\qquad M_y = 126891 \qquad\qquad$ kips·in

The yielding curvature of the CFT column $\qquad \phi_y = 0.00007776 \qquad\qquad \text{in}^{-1}$

The yielding displacement of the CFT column $\qquad \Delta_y = 2 \cdot \phi_y \cdot \dfrac{\left(\dfrac{h}{2}\right)^2}{3} = 0.71 \qquad\qquad$ in

The effective stiffness of the CFT column $\qquad K_{col} = \dfrac{2 \cdot M_y}{h \cdot \Delta_y} = 1.528 \times 10^3 \qquad\qquad \dfrac{\text{kip}}{\text{in}}$

The gross stiffness of the CFT column based on the gross section properties $\qquad K_{gross} = 12 \cdot \dfrac{EI}{h^3} = 8.44 \times 10^3 \qquad\qquad \dfrac{\text{kip}}{\text{in}}$

The ratio of the effective stiffness over the gross stiffness is $\qquad \dfrac{K_{col}}{K_{gross}} = 0.181$

Fuse stiffness calculation

There are two CFT columns in the bridge bent, so the total stiffness of the bridge bent is

$$K_{bent} = 2 \cdot K_{col} = 3.057 \times 10^3 \qquad\qquad \frac{\text{kip}}{\text{in}}$$

Assuming the period of the bridge bent in the transverse direction is in the range of the design spectrum plateau, which is the largest value of the spectrum in Figure 4-10

$$S_a = 2 \quad g$$

The relationship between the expected displacement of the bridge δe , the acceleration Sa, and the period T is

The period of the bridge bent combined with the fuse can be calculated, assuming the expected displacement of the bridge bent to be the yielding displacement of the CFT columns Δy.

$$T_s = \sqrt{\Delta_y \cdot 4 \cdot \frac{\pi^2}{S_a \cdot 386}} = 0.19 \qquad s$$

The weight of the superstructure (includes all the dead loads calculated in chapter 4) is

$$W_{super} = 4692 \qquad kips$$

The total stiffness of the bridge required to make the period of the bridge in the transverse direction to be Ts is

$$K_t = \frac{W_{super} \cdot 4 \cdot \pi^2}{386 \cdot T_s^2} = 1.322 \times 10^4 \qquad \frac{kip}{in}$$

The required stiffness of the fuse is obtained by substracting the stiffness of the bent columns

$$K_{fuse} = K_t - K_{bent} = 1.017 \times 10^4 \qquad \frac{kip}{in}$$

The ratio of the stiffness of the fuse over the bent is

$$\frac{K_{fuse}}{K_{bent}} = 3.326$$

The following demonstrates the necessity of adding fuses to prevent column yielding

The period of the bridge for the bare bent alone is

$$T_b = 2 \cdot \pi \cdot \sqrt{\frac{W_{super}}{386 \cdot K_{bent}}} = 0.396 \qquad s$$

From the acceleration spectrum in Figure A-2, the spectrum acceleration

$$S_b = 1.77 \qquad g$$

The corresponding expected spectrum displacement is

$$\delta_t = S_b \cdot T_b^2 \cdot \frac{386}{4 \cdot \pi^2} = 2.717 \qquad in$$

which is much larger than the expected displacement Δy

$$\frac{\delta_t}{\Delta_y} = 3.829$$

This shows that the added structural fuse is effective to prevent the yielding of the bent columns.

Design of structural fuse for single BRB case

The configuration of the bridge bent with a single inclined BRB is shown in figure A-2 . Note that, the distance between the columns, the numbers of the BRBs, the columns size will vary from bridge to bridge.

The material used for BRB is A500Gr.B steel with yielding strength requirement of 42 ksi

$$f_{ybrb} = 42 \qquad ksi$$

The overhang of the bridge box girder is 6 ft, which is the same as the height of the box girder. The center-to-center distance between the two CFT columns is 25.5 ft. The clear distance between

the CFT columns is 21.5 ft in this case.

$$L_c = 21.5 \cdot 12 = 258 \qquad \text{in}$$

The length of the BRB is

$$L_{brb} = \sqrt{L_c^2 + h^2} = 348.31 \qquad \text{in}$$

The inclination angle of the BRB with the horizontal axis is

$$\theta = \text{atan}\left(\frac{h}{L_c}\right) = 0.737$$

$$\cos(\theta) = 0.741 \qquad \sin(\theta) = 0.672$$
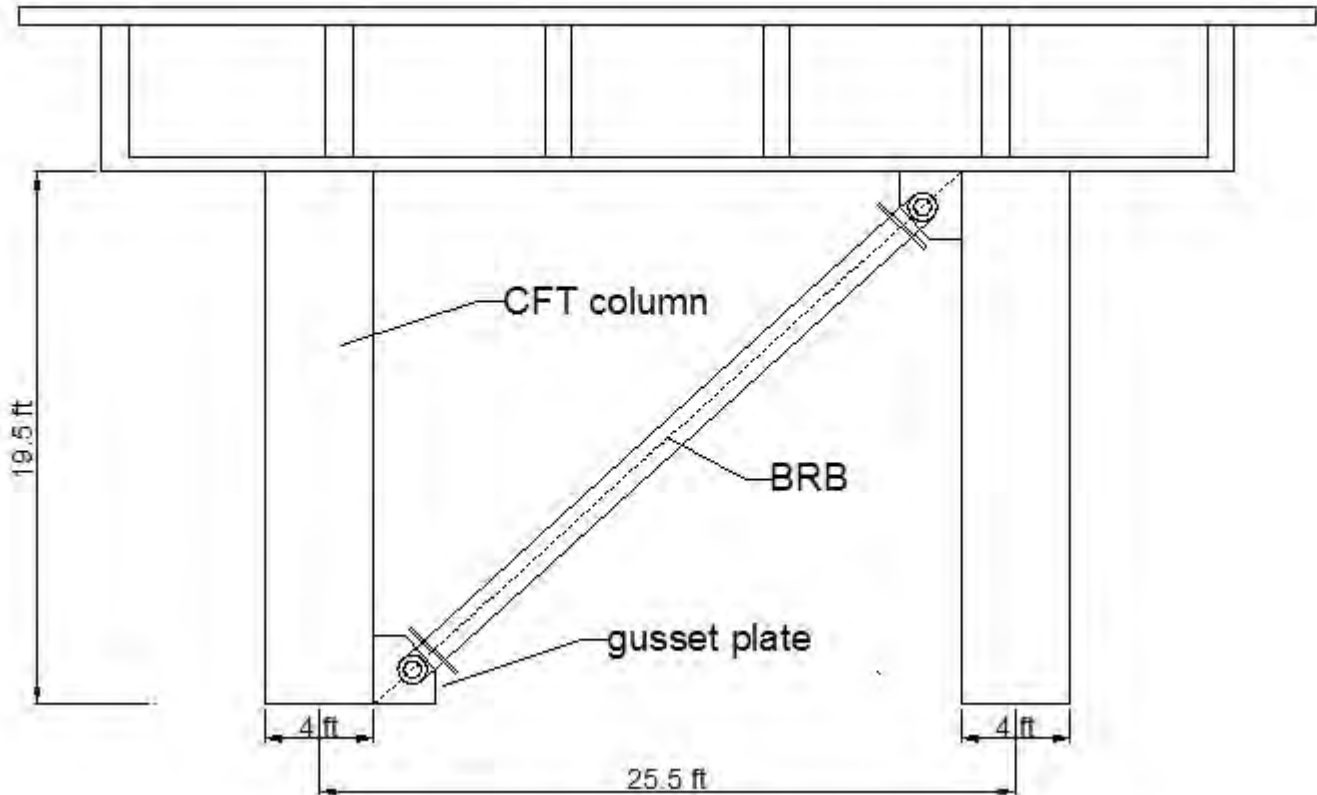
Figure A-2 The elevation of the bridge bent in the transverse direction with single BRB

A typical BRB consists of a yielding steel core encased to restrain buckling, non-yielding and buckling-restrained transition segments, and non-yielding and unrestrained end zones. When the BRB yields, yielding is limited to the buckling restrained yielding segment. The length of this yielding core is $c_{brb} * L_{brb}$, where c_{brb} is the yielding length ratio, which needs to be calculated.

The yielding length ratio of the BRB is obtained here by having the BRB strain limit to be attained, when the expected spectrum displacement at the top of the bent reach Δy. The corresponding displacement of the BRB is $\Delta_y \cos\theta$. Noting that 1.5% strain limit is assumed to be conservative here, and larger strain limit can be used. A small strain limit can also be used, however, this would result in a longer yielding core and thus a larger brace section and yielding force to achieve the same target brace stiffness.

$$c_{brb} = \frac{\Delta_y}{0.015 \cdot L_{brb}} \cdot \cos(\theta) = 0.101$$

The corresponding displacement of the CFT column when the BRB yields is

462

$$\Delta_{fuse} = \frac{f_{ybrb} \cdot c_{brb} \cdot L_{brb}}{E_s \cdot \cos(\theta)} = 0.069 \qquad\qquad \text{in}$$

The area of the BRB required to obtain the stiffness calculated above is

$$A_{brb} = \Delta_{fuse} \cdot \frac{K_{fuse}}{f_{ybrb} \cdot \cos(\theta)} = 22.392 \qquad\qquad \text{in}^2$$

The yielding force in the BRB is

$$f_{ybrb} \cdot A_{brb} = 940.455 \qquad\qquad \text{kips}$$

After the BRB yields, it will enter into the strain hardening stage. The axial force in the BRB will increase, and the strain hardening factors below are used to calculate the largest forces the BRB can develop under compression or tension forces. To note, strain hardening factors will vary with BRB size and suppliers.

$$\omega\beta = 1.5 \qquad \omega = 1.35$$

The largest force that can be developed in the BRB subjected to compressive force is

$$\omega\beta \cdot f_{ybrb} \cdot A_{brb} = 1.411 \times 10^3 \qquad\qquad \text{kips}$$

The largest force that can be developed in the BRB subjected to tensile force is

$$\omega \cdot f_{ybrb} \cdot A_{brb} = 1.27 \times 10^3 \qquad\qquad \text{kips}$$

The largest lateral load resistance provided by the single inclined BRB when it is under compression is

$$V_{bc} = \omega\beta \cdot f_{ybrb} \cdot \cos(\theta) \cdot A_{brb} = 1.045 \times 10^3 \qquad\qquad \text{kips}$$

The largest axial force added to the CFT columns by the single BRB under compression is

$$P_{bc} = \omega\beta \cdot f_{ybrb} \cdot A_{brb} \cdot \sin(\theta) = 947.718 \qquad\qquad \text{kips}$$

The largest lateral load resistance provided by the single inclined BRB when it is under tension is

$$V_{bt} = \omega \cdot f_{ybrb} \cdot \cos(\theta) \cdot A_{brb} = 940.428 \qquad\qquad \text{kips}$$

The largest axial force added to the CFT columns by the single BRB under tension is

$$P_{bt} = \omega \cdot f_{ybrb} \cdot A_{brb} \cdot \sin(\theta) = 852.946 \qquad\qquad \text{kips}$$

The lateral load resistance of the system in the transverse direction is provided by two parts: the shear resistance of the CFT columns and the horizontal component of the axial force in the single inclined BRB. When the expected displacement, a.k.a. the yielding displacement of the column, is reached, the shear force resistance from the CFT columns can be obtained. The moment at the end of the CFT columns are assumed to be the yielding strength of the column since the yielding displacement is reached. The frame action under the applied lateral seismic load will develop axial forces in the columns to resist the corresponding overturning moment. The axial force in the BRB would also adds to the column axial force. The axial strength of the columns are checked first. Then the shear strength of the CFT columns is also checked. The flexural strength of the section will be reduced because of the presence of additional axial force in the columns. The reduction of the flexural strength of the CFT section due to the presence of the larger axial force will be checked in chapter 4.

The lateral load resistance taken by the CFT columns is

$$V_{bent} = 2 \cdot \frac{2M_y}{h} = 2.169 \times 10^3 \qquad\qquad \text{kips}$$

The distance between the tension and compression resultant for the two CFT columns as in figure A-3 is

$$x = 21.5 \cdot 12 = 258 \qquad\qquad \text{in}$$

The resultant axial force F_{re} resulting from the lateral load applied to the frame alone (in absence of the BRB) is

$$F_{re} = \frac{(V_{bent} \cdot h - 2 \cdot M_y)}{x} = 983.651 \qquad\qquad \text{kips}$$

Under the lateral load when the single chevron BRB is in compression, the largest reaction at the base of both columns is

$$F_{oc} = F_{re} + P_{bc} = 1.931 \times 10^3 \qquad\qquad \text{kips}$$

Under the lateral load when the single chevron BRB is in tension, the largest reaction at the base of both columns is

$$F_{ot} = F_{re} + P_{bt} = 1.837 \times 10^3 \qquad\qquad \text{kips}$$
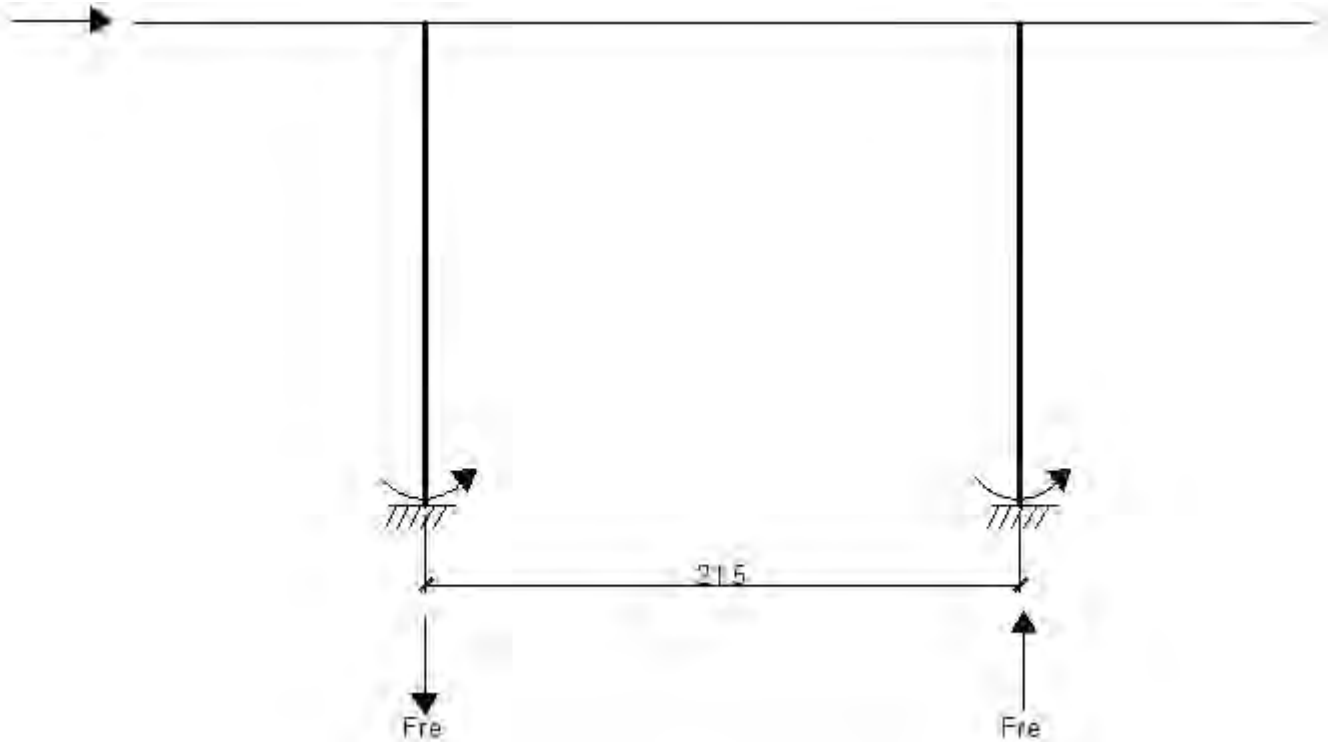
Figure A-3 Axial loads induced by the lateral loading on the bent in the transverse direction

The values resulting for the column axial force design due to the lateral load is shown in figure A-4a

and A-4b, for the BRB in tension and compression respectively.
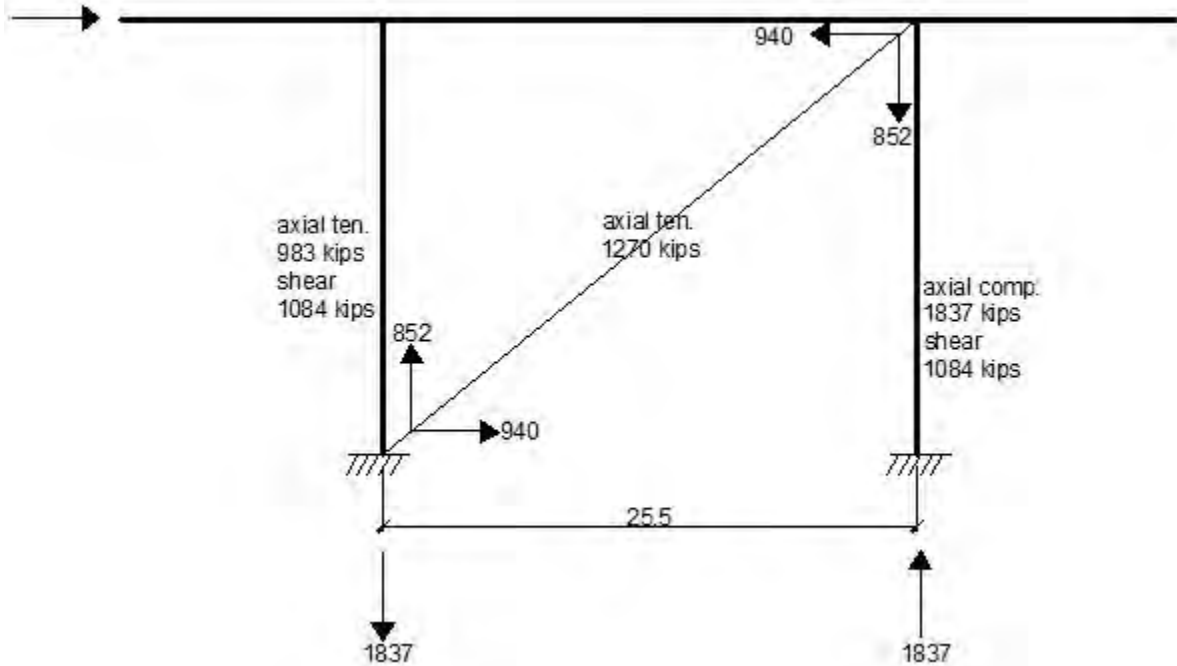
Figure A-4a Reactions at the base and forces in the bridge member when the BRB is in tension
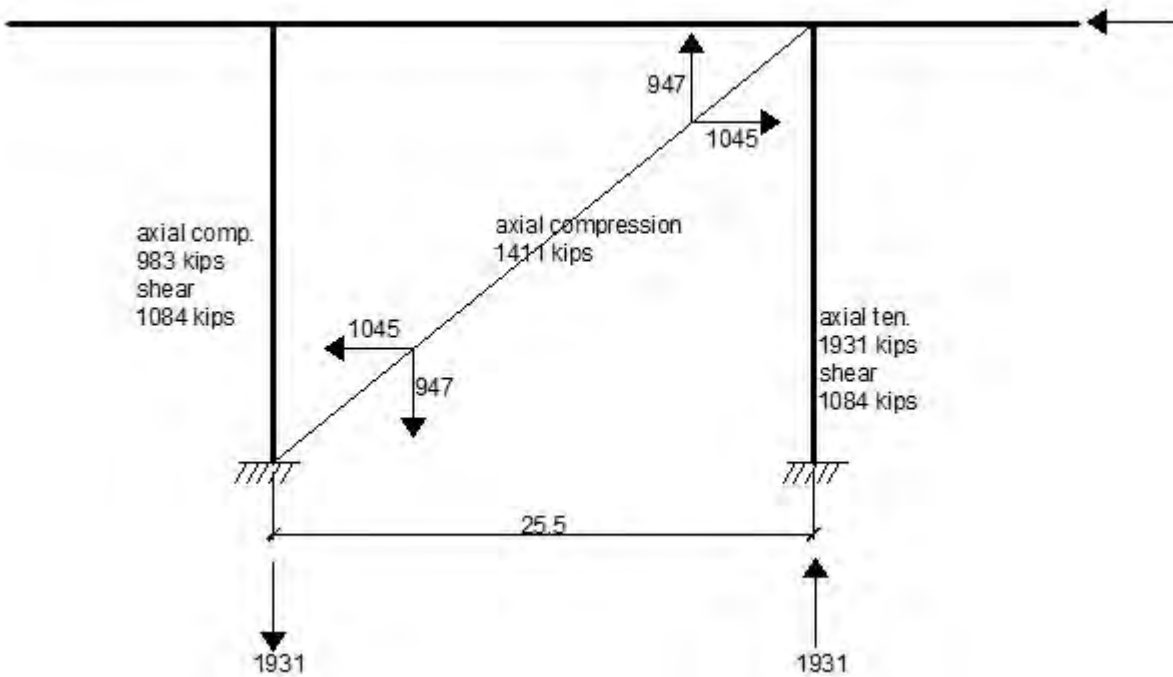
Figure A-4b Reactions at the base and forces in the bridge member when the BRB is in compression

Therefore, the design force for the column under the lateral load can be summarized in table A-1 below (govening cases are hignlighted by the box):

Table A-1 Design force for the column under lateral load

case	column	M(kips*in)	P(kips)	V(kips)
BRB in ten.	left	126891	983	1084
	right	126891	-1837	1084
BRB in comp.	left	126891	-983	1084
	right	126891	1931	1084

To note, the model assumes that the force from the BRB goes directly into the foundation as shown in figure A-5a. However, if there is an eccentricity between the point where the brace and the column workline meet around the foundation, the segment of the column over the length of that eccentricity could be subjected to forces equal to the value of the reactions shown in figure A-5a and A-5b. Therefore,the design forces for the columns would change to the values in table A-2.

Table A-2 Design force for the column under lateral load considering the eccentricity

case	column	M(kips*in)	P(kips)	V(kips)
BRB in ten.	left	126891	1837	2024
	right	126891	-1837	2024
BRB in comp.	left	126891	-1931	2128
	right	126891	1931	2128

The governing design forces for the column is highlighted in the box. To be conservative, the force from table A-2 will be used.

The load that is present in the columns would also need to consider the dead load effect. The distributed dead loads is 15.64 kip/ft, applied on the entire length of the bridge in the longitudinal direction.
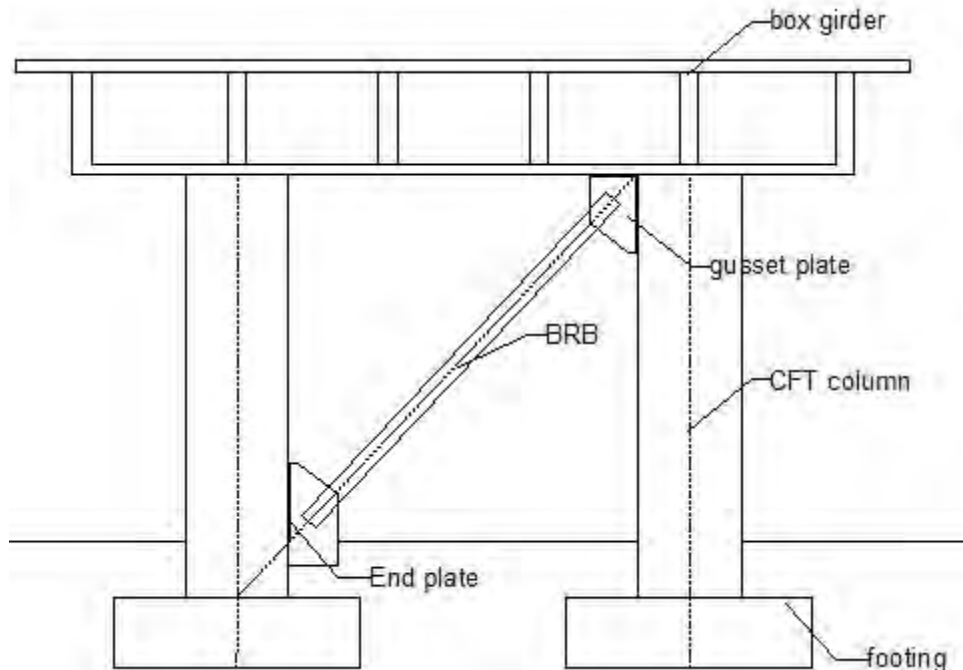
Figure A-5a Idealized geometry of the bridge bent with single inclined braces in the transverse
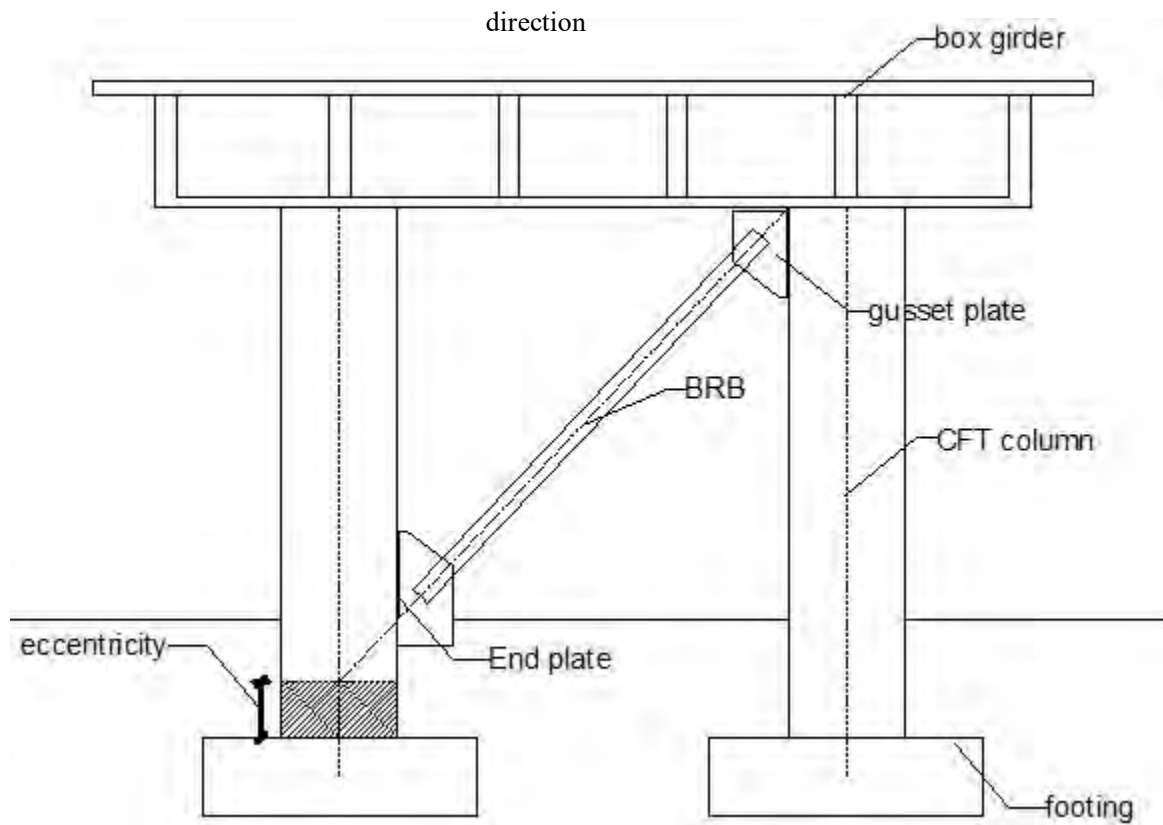
Figure A-5b The bridge bent with single inclined braces in the transverse direction considering a possible eccentricity,e

An estimation of the dead load reaction at the bent is

$$R_b = 2994.68 \qquad\qquad\qquad\qquad\qquad \text{kips}$$

The axial force should be obtained by applying the dead load on the cap beam at the locations of the girders. Here a simplified analysis is done and the force is directly distributed to in the two columns. The BRB is assumed not to take any dead loads.

$$P_d = \frac{R_b}{2} = 1.497 \times 10^3 \qquad\qquad\qquad\qquad \text{kips}$$

Table A-3 shows the design checks for the columns using the values from table A-2 plus the dead loads. The ϕ factors listed when the design strength is calculated are included in the table. The $M_u/M_y+P_u/P_y$ check is tabulated to show the yielding moment strength and axial load interaction capacity. The interaction diagram gives a value greater than 1.0 for both columns because the design approach considered column yield moments not accounting for the presence of axial force. The $M_u/\phi M_n+P_u/\phi P_n$ ratios are all smaller than 1.0, which means the sections are found adequate to resist the force applied.

Table A-3 Force checking for the columns for the single inclined BRB case

My	Mu	Pu	Vu	ΦMn	ΦPn
126891	126891	-3331	2024	187800	-12840
126891	126891	437	2128	187800	9918

ΦVn	Mu/My+Pu/ΦPn	Mu/ΦMn+Pu/ΦPn	Vu/ΦVn
2974.5	1.26	0.94	0.68
2974.5	1.04	0.72	0.72

Design of structural fuse for BRBs in inverted-V case

The configuration of the bridge bent with BRBs in inverted-V in the transverse direction is shown in figure B-6. The distance between the columns, the numbers of the BRBs, the columns size can be subjected to adjustment.

The length of the BRB is
$$L_{cb} = \sqrt{\left(\frac{L_c}{2}\right)^2 + h^2} = 267.202 \qquad in$$

The inclination angle of the BRB with the horizontal axis is
$$\theta_c = atan\left(\frac{2 \cdot h}{L_c}\right) = 1.067$$

$$\cos(\theta_c) = 0.483 \qquad \sin(\theta_c) = 0.876$$

The length yielding ratio fo the BRB is obtained by setting the strain limit, to be attained, when the expected spectrum displacement Δy is reached. The corresponding displacement of the BRB is $\Delta_y \cos\theta$. Noting that 1.5% strain limit is assumed to be conservative here, and larger strain limit can be used. A small strain limit can also be used, however, this would result in a longer yielding core and thus a larger brace section and yielding force to achieve the same target brace stiffness.

$$c_{cb} = \frac{\Delta_y}{0.015 \cdot L_{cb}} \cdot \cos(\theta_c) = 0.085$$

The corresponding displacement of the CFT column when the BRBs yield is

$$\Delta_{fc} = \frac{f_{ybrb} \cdot c_{cb} \cdot L_{cb}}{E_s \cdot \cos(\theta_c)} = 0.069 \qquad in$$

The area of the BRB required to attain the stiffness calculated above is

$$A_{cb} = \Delta_{fc} \cdot \frac{\frac{K_{fuse}}{2}}{f_{ybrb} \cdot \cos(\theta_c)} = 17.178 \qquad in^2$$

The yielding force of the BRB brace is

$$f_{ybrb} \cdot A_{cb} = 721.46 \qquad kips$$
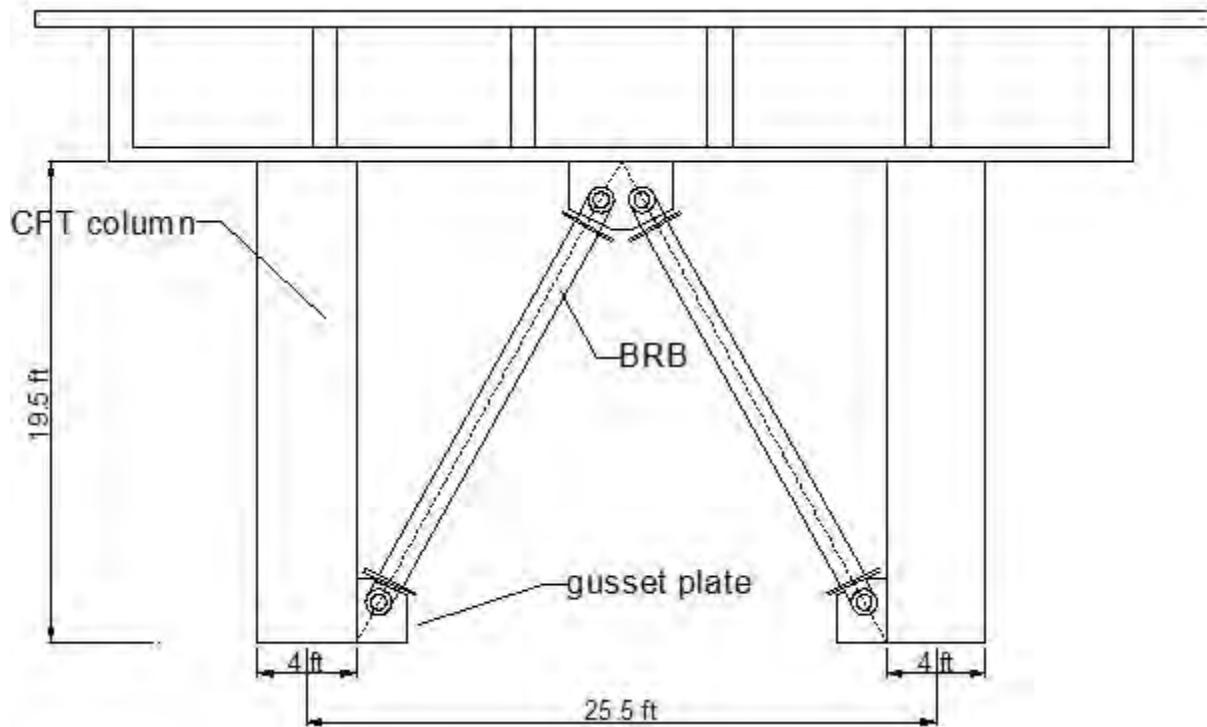
Figure A-6 The elevation of the bridge bent in the transverse direction with chevron BRBs

After the BRB yields, it will enter into the strain hardening stage. The axial force in the BRB will increase, and the strain hardening factors used before for the single inclined BRB case is used to calculate the largest forces that the BRBs can develop under compression or tension forces.

The largest force that can be developed in the BRB subjected to compressive force is

$$\omega\beta \cdot f_{ybrb} \cdot A_{cb} = 1.082 \times 10^3 \qquad\qquad \text{kips}$$

The largest force that can be developed in the BRB subjected to tensile force is

$$\omega \cdot f_{ybrb} \cdot A_{cb} = 973.97 \qquad\qquad \text{kips}$$

The lateral shear resistance provided by the compressive BRBs in inverted-V is

$$V_{cbc} = \omega\beta \cdot f_{ybrb} \cdot \cos(\theta_c) \cdot A_{cb} = 522.46 \qquad\qquad \text{kips}$$

The lateral shear resistance provided by the tensile BRBs in inverted-V is

$$V_{cbt} = \omega \cdot f_{ybrb} \cdot \cos(\theta_c) \cdot A_{cb} = 470.214 \qquad\qquad \text{kips}$$

The maximum axial force added to the CFT columns by the BRB in compression is

$$P_{cbc} = \omega\beta \cdot f_{ybrb} \cdot A_{cb} \cdot \sin(\theta_c) = 947.718 \qquad\qquad \text{kips}$$

The maximum axial force added to the CFT columns by the BRB in tension is

$$P_{cbt} = \omega \cdot f_{ybrb} \cdot A_{cb} \cdot \sin(\theta_c) = 852.946 \qquad\qquad \text{kips}$$

Under the lateral load, the vertical reactions as shown in figure A-7 in the columns are

$$F_{cc} = F_{re} + P_{cbt} = 1.837 \times 10^3 \qquad\qquad \text{kips}$$

$$F_{ct} = F_{re} + P_{cbc} = 1.931 \times 10^3 \qquad\qquad \text{kips}$$

The force demands in the columns for two cases are tabulated in table a-4. The governing design forces are shown in the box. The difference is caused by the eccentricity between the point when

the brace and the column workline meet around the foundatio, similar to what is shown in figure A-5a and A-5b.

Table A-4 shows the design force for the column with and without eccentricity considered.

case	column	M(kips*in)	P(kips)	V(kips)
w/o eccentricity	left	126891	983	1084
	right	126891	-983	1084
w eccentricity	left	126891	1837	1554
	right	126891	-1931	1606

The design checks for the columns in the chevron BRB case is shown in table A-5 plus the dead load effect. The columns are found adequate to resist the force applied.

Table A-5 Force checking for the columns in the chevron BRB case

My	Mu	Pu	Vu	ΦMn	ΦPn
126891	126891	343	1554	187800	9918
126891	126891	-3425	1606	187800	-12840

ΦVn	Mu/My+Pu/ΦPn	Mu/ΦMn+Pu/ΦPn	Vu/ΦVn
2974.5	1.03	0.71	0.52
2974.5	1.27	0.94	0.54
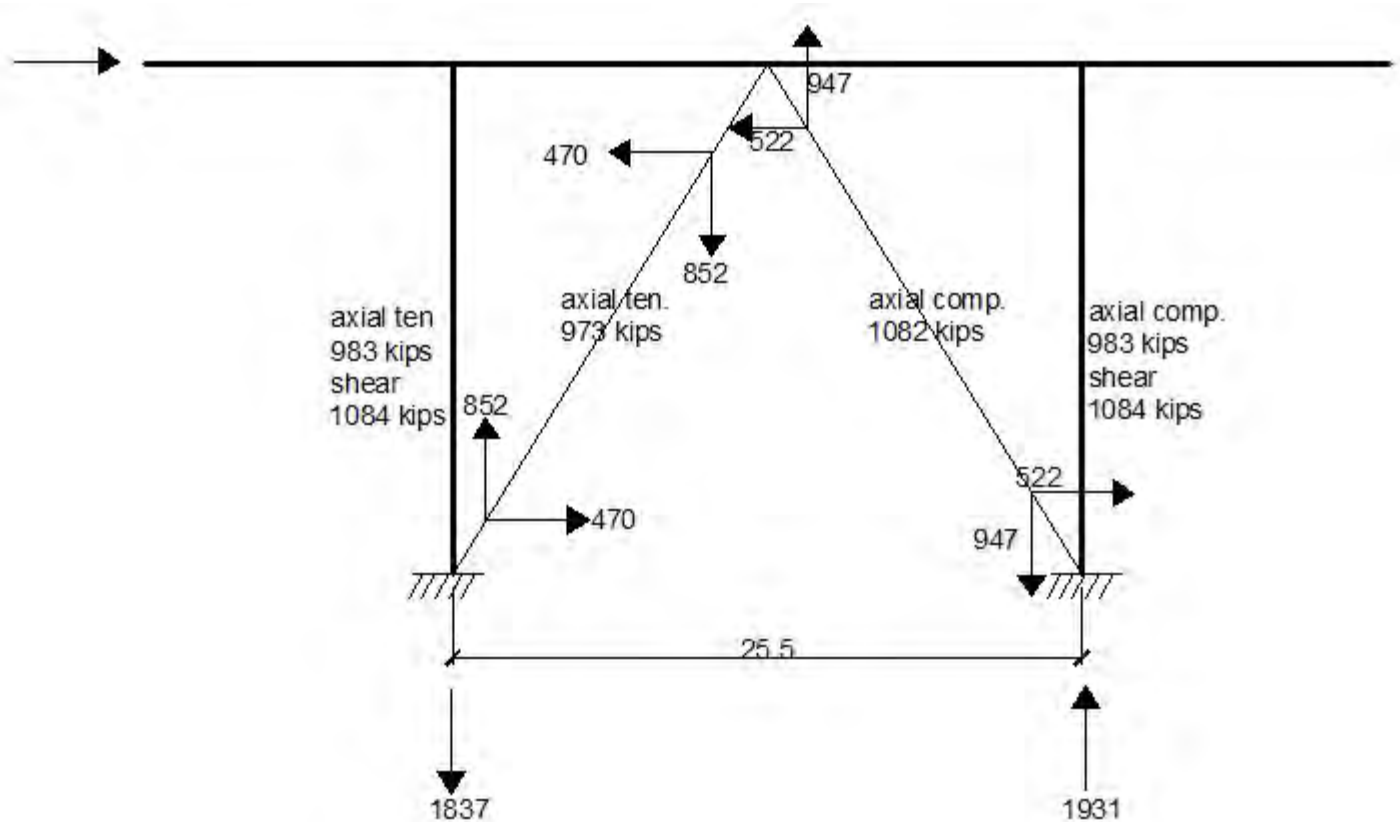
Figure A-7 Reactions at the base and forces in the bridge member for the BRBs in inverted-V case

470

A.2 Box pier bent with BRBs

This design example illustrates how BRBs are designed as structural fuses to limit damage to the bridge bent. The design procedure for box pier (eight CFT columns) with BRBs inserted between the columns, is shown below.

CFT column properties

Start with a trial circular CFT column with the following properties

The height of the bent column	$h = 234$	in
The diameter of the CFT column	$D = 32$	in
The thickness of the steel tube	$t = 0.75$	in
The inside diameter of the concrete infill	$D_c = D - 2 \cdot t = 30.5$	in
The area of the steel tube	$A_s = \pi \cdot \dfrac{\left(D^2 - D_c^2\right)}{4} = 73.631$	in^2
The area of the concrete infill	$A_c = \dfrac{\pi \cdot D_c^2}{4} = 730.617$	in^2
The area of the reinforcement in the infill concrete	$A_{sr} = 0$	in^2
The moment of inertia of the steel tube	$I_s = \pi \cdot \dfrac{\left(D^4 - D_c^4\right)}{64} = 8.993 \times 10^3$	in^4
The moment of inertia of the concrete infill	$I_c = \pi \cdot \dfrac{D^4}{64} = 5.147 \times 10^4$	in^4
The moment of inertia of the reinforcement in the concrete	$I_{sr} = 0$	in^4
The strength of the steel shell using A572 alloy steel plate Gr60	$F_y = 60$	ksi
	$F_u = 75$	ksi
The strength of the infill concrete	$f_c = 4$	ksi
The elastic modulus of concrete	$E_c = \dfrac{57000}{1000} \cdot \sqrt{f_c \cdot 1000} = 3.605 \times 10^3$	ksi
The elastic modulus of steel	$E_s = 29000$	ksi
EI of the CFT column	$EI = E_s \cdot I_s + E_c \cdot I_c = 4.464 \times 10^8$	in^4

Strength calculation

Axial Compressive and tensile strength

Per AISC 2010, the design compressive strength of the CFT section is calculated below using the LRFD approach. Additional information about why AISC equations instead of the AASHTO Bridge Design Specifications can be found in appendix A3.

The stability limit using Width-to-thickness ratio is first checked according to table I1.1 A & B

$$\frac{D}{t} = 42.667 \qquad \text{smaller than} \qquad \lambda_{p1} = 0.15 \cdot \frac{E_s}{F_y} = 72.5 \qquad \text{for compression}$$

$$\lambda_{p2} = 0.09 \cdot \frac{E_s}{F_y} = 43.5 \qquad \text{for flexure}$$

The composite section is categorized as a compact section both under axial force and moment

To calculate the compressive strength, section I2.b is used per AISC2010

For circular section $\qquad C_2 = 0.95$

For compact section $\qquad P_p = F_y \cdot A_s + C_2 \cdot f_c \cdot \left(A_c + A_{sr} \cdot \frac{E_s}{E_c} \right) = 7.194 \times 10^3 \qquad$ kips

$$P_{n0} = P_p$$

To get the effective stiffness of the CFT section, the coefficient C3 is calculated

$$C_3 = 0.6 + 2 \cdot \left(\frac{A_s}{A_c + A_s} \right) = 0.783 \qquad \text{smaller than 0.9, ok}$$

The effective stiffness of the CFT section

$$EI_{eff} = E_s \cdot I_s + 0.5 \cdot E_s \cdot I_{sr} + C_3 \cdot E_c \cdot I_c = 4.061 \times 10^8 \qquad \text{in}^4$$

Check global buckling of the CFT column under axial compression load

The CFT column is fixed at both ends $\qquad K_c = 0.5$

The elastic critical buckling load is determined by using equatioin I2-5 (AISC,2010) with the unsupported lateral length of h/2

$$P_e = \pi^2 \cdot \frac{EI_{eff}}{\left(K_c \cdot \frac{h}{2} \right)^2} = 1.171 \times 10^6 \qquad \text{kips}$$

$$n_1 = \frac{P_{n0}}{P_e} = 6.142 \times 10^{-3} \qquad \text{smaller than 2.25, OK}$$

The axial compression strength of the CFT column is calculated according to equation I2-2 (AISC,2010)

$$P_n = P_{n0} \cdot 0.658^{n_1} = 7.176 \times 10^3 \qquad \text{kips} \qquad \phi_c = 0.75$$

The axial tension strength of the CFT column is determined based on I2-8

$$T_n = F_y \cdot A_s = 4.418 \times 10^3 \qquad \text{kips} \qquad \phi_t = 0.9$$

The strength reduction factor for design is listed on the right side, and not included into the strength calculations at this stage.

Per AISC 2010, shear strength for filled composite members can be determined using the available shear strength of the steel alone. The nominal shear strength for round HSS per AISC 2010 Chapter G, is calculated using the equations listed below. The limit states of shear yielding and buckling is considered. The same equation is provided in the AASHTO Bridge Design Specifications (2010) section 6.12.1.2.3c

The critical shear stress is calculated to be the smaller of

$$F_{cr1} = 1.60 \cdot \frac{E_s}{\sqrt{\frac{h}{D}} \cdot \left(\frac{D}{t}\right)^{\frac{5}{4}}} = 157.353$$

$$F_{cr2} = 0.78 \cdot \frac{E_s}{\left(\frac{D}{t}\right)^{\frac{3}{2}}} = 81.163$$

$$F_{cr3} = 0.6 \cdot F_y = 36$$

therefore, $\quad F_{cr} = F_{cr3}$

The shear strength of the CFT section: $\quad V_n = F_{cr} \cdot \dfrac{A_s}{2} = 1.325 \times 10^3 \qquad$ kips

$$\phi_v = 0.9$$

Flexural strength calculation

Two approaches are identified as appropriate to calculate the flexural strength in AISC (2010), namely, (1) the plastic stress distribution, (2) the strain compatibility method. Per AASHTO Guide Specifications for LRFD Seismic Bridge Design (2009) section 7.6 , the design flexural strength of the composite section is calculated below using a method similiar to the plastic distribution method.

β is the central angle formed between the neutral axis chord line and the center point of the steel shell found by the following recursive equation (unit: rad)

$$\beta = 2.404 \qquad \frac{A_s \cdot F_y + 0.2 \cdot D^2 \cdot f_c \cdot \left[\sin\left(\frac{\beta}{2}\right) - \left(\sin\left(\frac{\beta}{2}\right)\right)^2 \cdot \tan\left(\frac{\beta}{4}\right) \right]}{0.125 \cdot D^2 f_c + D \cdot t \cdot F_y} = \blacksquare \beta \qquad (7.6.2 - 8)$$

The following are parameters shown in figure B-1 for calculating the flexural strength of the CFT section

$$b_c = D \cdot \sin\left(\frac{\beta}{2}\right) = 29.848 \qquad (7.6.2 - 7)$$

$$a = \frac{b_c \cdot \tan\left(\frac{\beta}{4}\right)}{2} = 10.232 \qquad (7.6.2 - 6)$$

$$e_1 = b_c \cdot \left(\frac{1}{2 \cdot \pi - \beta} + \frac{1}{\beta}\right) = 20.111 \qquad (7.6.2 - 4)$$

$$e_2 = b_c \cdot \left[\frac{1}{2 \cdot \pi - \beta} + \frac{b_c^2}{1.5 \cdot \beta \cdot D^2 - 6 \cdot b_c \cdot (0.5 \cdot D - a)} \right] = 17.693 \qquad (7.6.2 - 5)$$

$$C_{r1} = F_y \cdot \beta \cdot D \cdot \frac{t}{2} = 1.731 \times 10^3 \qquad (7.6.2 - 2)$$

$$C_{r2} = f_c \cdot \left[\beta \cdot \frac{D^2}{8} - \frac{b_c \cdot \left(\frac{D}{2} - a \right)}{2} \right] = 886.524 \qquad (7.6.2 - 3)$$

$$\phi_f = 1.0$$

Therefore the plastic strength of the CFT section is

$$M_n = \phi_f \cdot \left(C_{r1} \cdot e_1 + C_{r2} \cdot e_2 \right) = 5.049 \times 10^4 \qquad \text{kips·in}$$

Flexural strength, yielding displacement, and stiffness

The yielding flexural strength is obtained when the extreme point in the steel shell reaches the yielding strain of 0.002. Hand calculation is not performed here; instead this value is obtained from SAP2000 Section Designer.

The yielding flexural strength of the section is $\qquad M_y = 34199 \qquad$ kips·in

The yielding curvature of the CFT column $\qquad \phi_y = 0.00011515 \qquad$ in^{-1}

The yielding displacement of the CFT column $\qquad \Delta_y = 2 \cdot \phi_y \cdot \dfrac{\left(\frac{h}{2} \right)^2}{3} = 1.051 \qquad$ in

The effective stiffness of the CFT column $\qquad K_{col} = \dfrac{2 \cdot M_y}{h \cdot \Delta_y} = 278.153 \qquad \dfrac{\text{kip}}{\text{in}}$

The gross stiffness of the CFT column based on the gross section properties $\qquad K_{gross} = 12 \cdot \dfrac{EI}{h^3} = 418.044 \qquad \dfrac{\text{kip}}{\text{in}}$

The ratio of the effective stiffness over the gross stiffness is $\qquad \dfrac{K_{col}}{K_{gross}} = 0.665$

Fuse stiffness calculation

There are eight CFT columns in the bridge bent, so the total stiffness of the bridge bent is

$$K_{bent} = 8 \cdot K_{col} = 2.225 \times 10^3 \qquad \dfrac{\text{kip}}{\text{in}}$$

Assuming the period of the bridge bent in the transverse direction is in the range of the design spectrum plateau, which is the largest value of the spectrum

$$S_a = 2 \quad g$$

The relationship between the expected displacement of the bridge δe , the acceleration Sa, and the period T is

$$\delta_e = S_a \cdot T^2 \cdot \dfrac{g}{4 \cdot \pi^2}$$

The period of the bridge bent combined with the fuse can be calculated, assuming the expected displacement of the bridge bent to be the yielding displacement of the CFT columns Δ_y.

$$T_s = \sqrt{ \Delta_y \cdot 4 \cdot \dfrac{\pi^2}{S_a \cdot 386} } = 0.232 \qquad s$$

The weight of the superstructure (includes all the dead loads calculated in chaper 4)

$W_{super} = 4692$ kips

The total stiffness of the bridge required to make the period of the bridge to be Ts is

$$K_t = \frac{W_{super} \cdot 4 \cdot \pi^2}{386 \cdot T_s^2} = 8.93 \times 10^3 \qquad \frac{kip}{in}$$

The required stiffness of the fuse is obtained by substracting the stiffness of the bent columns

$$K_{fuse} = K_t - K_{bent} = 6.705 \times 10^3 \qquad \frac{kip}{in}$$

The ratio of the stiffness of the fuse over the bent is

$$\frac{K_{fuse}}{K_{bent}} = 3.013$$

The following demonstrates the necessity of adding fuses to prevent column yielding

The period of the bridge for the bare bent alone is $T = 2\pi \sqrt{\dfrac{m_{super}}{K_{bent}}}$

$$T_b = 2 \cdot \pi \cdot \sqrt{\frac{W_{super}}{386 \cdot K_{bent}}} = 0.464 \qquad s$$

From the acceleration spectrum in figure 4-10, the spectrum acceleration

$S_b = 1.51$ g

The corresponding expected spectrum displacement is

$$\delta_t = S_b \cdot T_b^2 \cdot \frac{386}{4 \cdot \pi^2} = 3.184 \qquad in$$

which is much larger than the expected displacement Δy

$$\frac{\delta_t}{\Delta_y} = 3.03$$

This shows that the added structural fuse is effective to prevent the yielding of the bent columns.

Design of BRBs

Transverse direction

The configuration of one of the bridge bent with inserted BRBs between the columns is shown in figure A-9. There are two bent with the same layout in parallel to each other. Note that, the distance between the columns, the numbers of the BRBs, the columns size will vary from bridge to bridge.

The material used for BRB is A500Gr.B steel with yielding strength requirement of 42 ksi

$f_{ybrb} = 42$ ksi

The clear distance between the CFT columns is 6 ft in this case. There are four BRBs between the adjacent columns. The overhang of the bridge box girder is 3 ft.

$L_c = 6 \cdot 12 = 72$ in

The length of the BRB is

$$L_{brb} = \sqrt{L_c^2 + \left(\frac{h}{4}\right)^2} = 92.77 \qquad \text{in}$$

The inclination angle of the BRB with the horizontal axis is

$$\theta = \text{atan}\left(\frac{\frac{h}{4}}{L_c}\right) = 0.682$$

$$\cos(\theta) = 0.776 \qquad \sin(\theta) = 0.631$$
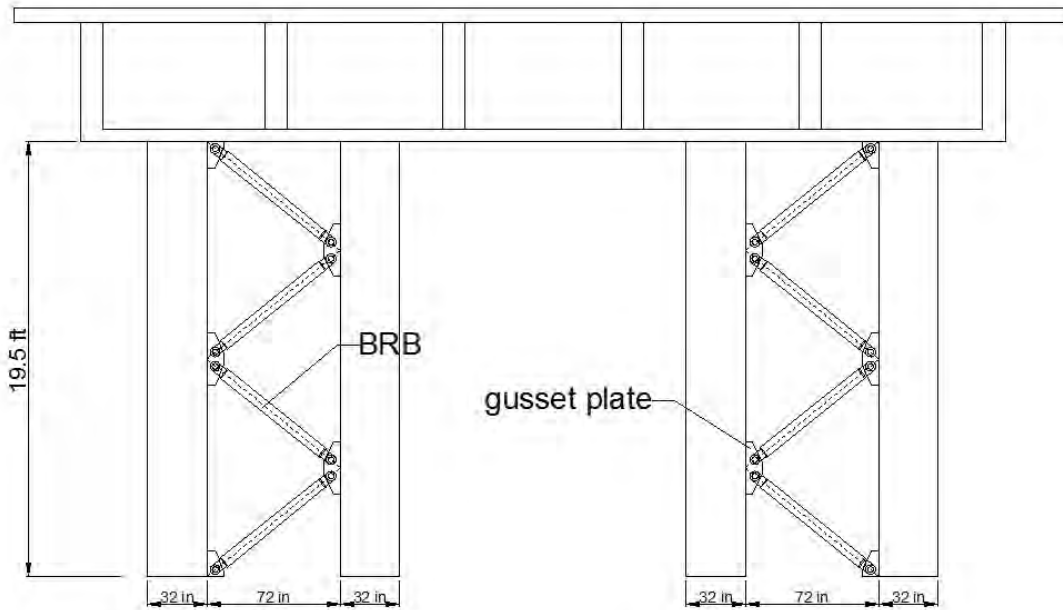
Figure A-9 The elevation view of the bridge bent in the transverse direction with inserted BRBs

A typical BRB consists of a yielding streel core encased to restrain buckling, non-yielding and buckling-restrained transition segments, and non-yielding and unrestrained end zones. When the BRB yields, yielding is limited to the buckling restrained yielding segment. The length of this yielding core is $c_{brb} * L_{brb}$, where c_{brb} is the yielding length ratio, which needs to be calculated.

The yielding length ratio of the BRB is obtained here by having the BRB strain limit to be attained, when the expected spectrum displacement at the top of the bent reach Δy. The corresponding displacement of the BRB is $\Delta_y \cos\theta/4$. Noting that 1.5% strain limit is assumed to be conservative here, and larger strain limit can be used. A small strain limit can also be used, however, this would result in a longer yielding core and thus a larger brace section and yielding force to achieve the same target brace stiffness.

$$c_{brb} = \frac{\frac{\Delta_y}{4}}{0.015 \cdot L_{brb}} \cdot \cos(\theta) = 0.147$$

The corresponding displacement of the CFT column when the BRB yields is

$$\Delta_{fuse} = \frac{4 \cdot f_{ybrb} \cdot c_{brb} \cdot L_{brb}}{E_s \cdot \cos(\theta)} = 0.101 \qquad \text{in}$$

The area of the BRB required to obtain the stiffness calculated above is

476

$$A_{brb} = \Delta_{fuse} \cdot \frac{K_{fuse}}{4 \cdot \left(4 \cdot f_{ybrb} \cdot \sin(\theta) \cdot \dfrac{L_c}{h} \right)} = 5.217 \qquad \text{in}^2$$

The yielding force in the BRB is

$$f_{ybrb} \cdot A_{brb} = 219.126 \qquad \text{kips}$$

After the BRB yields, it will enter into the strain hardening stage. The axial force in the BRB will increase, and the strain hardening factors below are used to calculate the largest forces the BRB can develop under compression or tension forces. To note, strain hardening factors will vary with BRB size and suppliers.

$$\omega\beta = 1.5 \qquad \omega = 1.35$$

The largest force that can be developed in the BRB subjected to compressive force is

$$\omega\beta \cdot f_{ybrb} \cdot A_{brb} = 328.688 \qquad \text{kips}$$

The largest force that can be developed in the BRB subjected to tensile force is

$$\omega \cdot f_{ybrb} \cdot A_{brb} = 295.819 \qquad \text{kips}$$

The overall largest lateral load resistance provided by four BRBs between the adjacent columns

$$V_{bc} = (2 \cdot \omega + 2\omega\beta) \cdot f_{ybrb} \cdot \sin(\theta) \cdot A_{brb} \cdot \frac{L_c}{h} = 242.345 \qquad \text{kips}$$

The overall largest axial force added to the CFT columns by four BRBs between the adjacent column is

$$P_{bc} = (2 \cdot \omega + 2\omega\beta) \cdot f_{ybrb} \cdot \sin(\theta) \cdot A_{brb} = 787.62 \qquad \text{kips}$$

To note, the axial forces from the BRBs are added to the columns at different points.

Longitudinal direction

To be consistent with the transverse direction, the distance between the adjacent columns in the longitudinal direction would still be 6 ft. There are four parallel longitudinal bent as shown in figure A-10.

Since the bridge is designed to have the same increase of the stiffness in both directions, the period and target displacement in each direction would be the same. The columns will reach the target displacement, a.k.a, the yielding displacement Δ_y. The layout of the BRBs between the columns is the same as the ones between the adjacent columns in the transverse direction. Therefore, the design of the BRBs does not change. The BRBs will still have the assumed strain hardening limit of 1.5% when the bridge reached the yielding displacement in the longitudinal direction.

The axial-flexure interaction, and shear capacity check of the columns under the bi-directional earthquake load effect will be checked using the analysis results in Chapter 4.
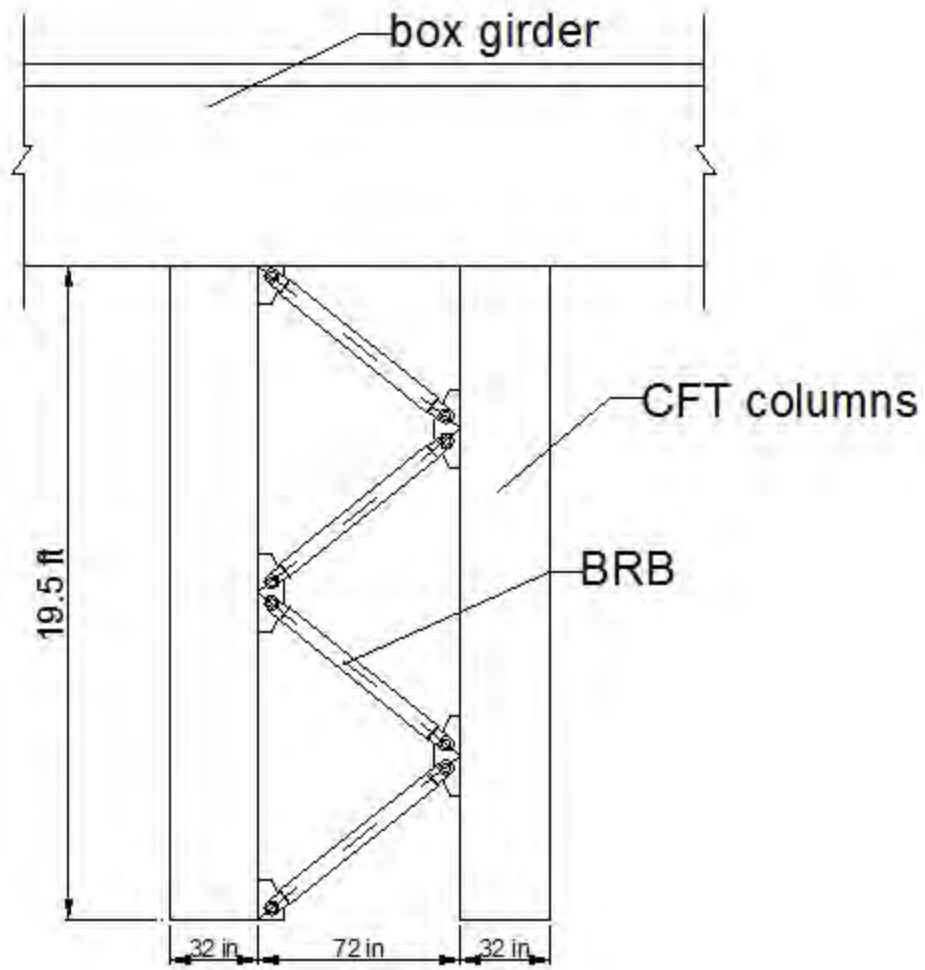
Figure A-10 The elevation view of the bridge bent in the longitudinal direction with inserted BRBs

A.3 Section designer analysis in SAP2000 and comparison with code design values

Some properties of the CFT column used in analyses are obtained using SAP2000's Section Designer (which provides cross-section properties and moment-curvature relationship, using a fiber analysis).   The outside diameter of the section is 48".   The thickness of the steel shell is 1.25".   A grid of 20 by 20 fibers is used for calculating the capacity of the section and plastic hinge analysis.

Table A-6 compares the axial strength of the section per AISC (2010) in Chapter 4, AASHTO (2010) in Appendix B, and the value obtained from section designer.   The tabulated values are those calculated without reduction factors, ϕ.   The value for the axial strength from section designer is obtained for bi-linear material properties, considers no strain hardening. The bi-linear stress-strain curve for A572 Gr 60 steel is shown in Figure A-11.   The yielding strength is 60 ksi, reached at the strain of 0.002069.   The ultimate strain is set to be 0.17, the same as the unmodified A572 Gr60 steel based on the material properties provided by the ASTM A572 for high-strength low-alloy Columbium-Vanadium structural steel.
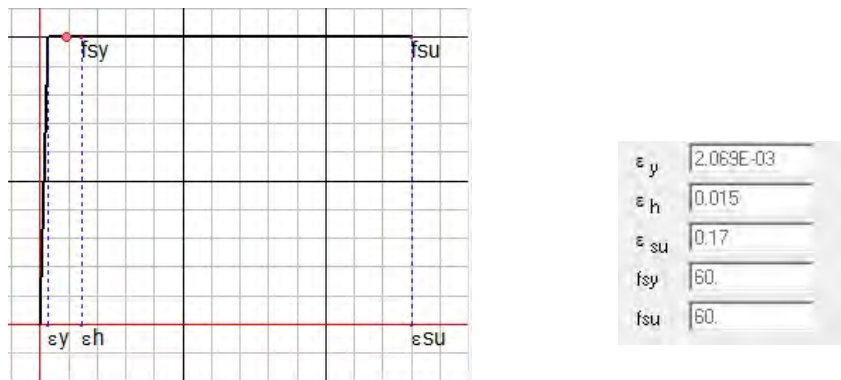
Figure A-11 The bilinear model of the steel stress-strain curve

The concrete tensile strength is not considered in the concrete material properties. Confined concrete model is used here as shown in Figure. A-12. The compressive strength of the concrete is 4 ksi, which is reached at the strain of 0.002219.   Then the compressive strength drops to 2 ksi at the largest strain of 0.02.
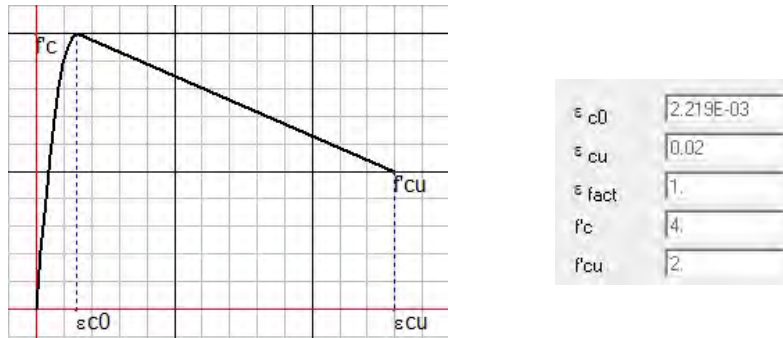
Figure A-12 The confined concrete material stress-strain curve

Table A-6 shows the axial strength under compressive and tensile forces calculated based on the equations from AISC (2010) and AASHTO Bridge Design Specifications (2010). The tensile strength of the section is the same for the two equations from the design codes as f_yA_s.

Table A-6 Comparison of axial strengths obtained from AISC 2010 and from SAP2000 section designer

	Tension	Compression	Difference with Section Designer having 0.85 concrete reduction factors
AISC (2010) (kips)	11020	-17120	4.16%
AASHTO (2010) (kips)	11020	-16470	0.20%
Section Designer ($f_yA_s+ f_cA_c$) for comp. strength (kips)		-17332	
Section Designer ($f_yA_s+0.85 f_cA_c$) for comp. strength (kips)		-16437	

Note that the reduction factor for the concrete compressive strength per AISC (2010) and AASHTO (2010) is 0.95 and 0.85, respectively. Therefore, the compressive strength design value from AISC (2010) is close to the value obtained from Section Designer value calculated without the reduction factor, while the compressive strength design value from AASHTO (2010) is closer to the one with reduction factor.

The value from section designer with the reduction factor is the one retained for the axial strength when performing capacity check. The AASHTO equations to calculate axial strength are identical to those in an older edition of the AISC Specifications; the new AISC equations are assumed to reflect the latest knowledge on this topic and are used here.

A moment curvature curve from Section Designer is calculated using elasto-plastic material models, with steel yielding at F_y=60 ksi and concrete strength of f'$_c$=4 ksi.   The curve is shown in Figure A-13.   The plastic flexural strength is 184 036 kip-in, when the assumed ultimate strain of the concrete of 0.02 is reached.   The moment curvature curve drops due to degradation of concrete strength per Figure A-12.   For comparison, if the concrete was modeled to have no strength degradation, the plastic flexural strength reached would have been 185710 kip-in.
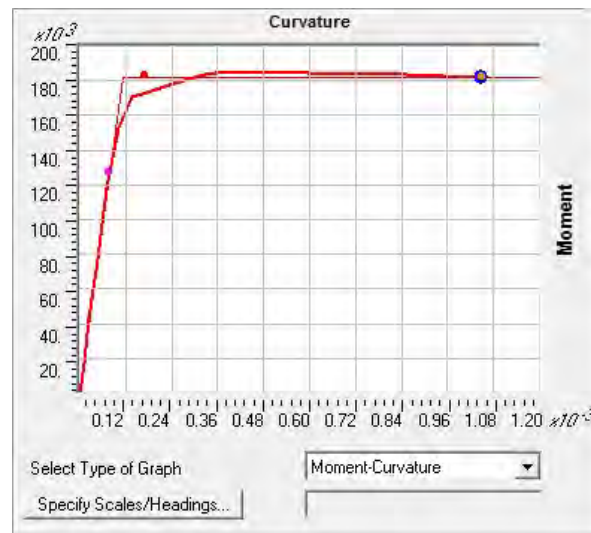
Figure A-13 Moment-curvature curve of the fiber model analysis w/o strain hardening

For design purposes, it is desirable to simplify the actual moment curvature considering strain hardening effects into an equivalent elastic perfectly plastic curve.   In particular, the Caltrans seismic design criteria (2010) specifies that such an idealized bi-linear model can be used to estimate the plastic moment capacity of a member's cross section. For that purpose, the SAP2000 Section Designer includes an option to calculate the flexural strength of the section using what it defines as the "Caltrans idealized model."   It first defines the elastic portion of the idealized curve by a straight line passing through the point when first yielding of the steel shell occurs. The value of the plastic moment is then obtained by balancing the areas between the actual and the idealized moment-curvature curve beyond the first yielding of the steel shell.   Following this procedure, the resulting Caltrans idealized flexural strength in Figure A-13 is 183 328 kip-in.

The design flexural strength of the CFT section per AASHTO is 187800 kip-in (Appendix A.1).   The difference of 2.4% compared with the Caltrans idealized design value is negligible.   The yielding of the CFT section in section designer is set to be at the first yielding of the extreme steel fiber.   The corresponding yielding moment is 126891 kip-in, which is the value used in Appendix B for the structural fuse design.

An alternative way to use Section Designer is to consider material properties having strain hardening.   The stress-strain curve of the steel and concrete material is shown in Figure A-14.   The yielding strength of the steel is 60 ksi, which is reached at the strain of 0.002069. The steel enters the strain hardening stage at the strain of 0.015.   The ultimate tensile strength of the steel material is 75 ksi, which is reached at the strain of 0.11.   The ultimate rupture strain of the steel would be 0.17.
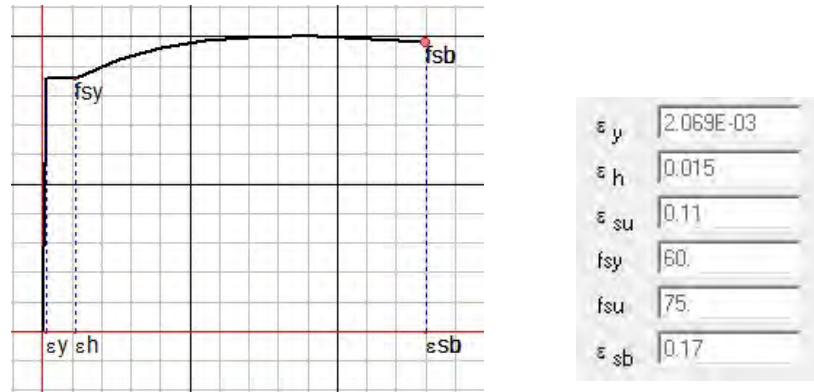
Figure A-14 Steel stress-strain curve considering the strain hardening

The resulting moment curvature curve is obtained as in Figure A-15. The plastic flexural strength is 194147 kip-in, shown as the blue point in Figure A-15 and obtained when the assumed ultimate strain of the concrete of 0.02 is reached. The corresponding Caltrans idealized flexural strength (i.e., calculated per the procedure described above) is 185621 kip-in.   Interestingly, this is within 1.17% of the AASHTO value calculated in Appendix A.1.
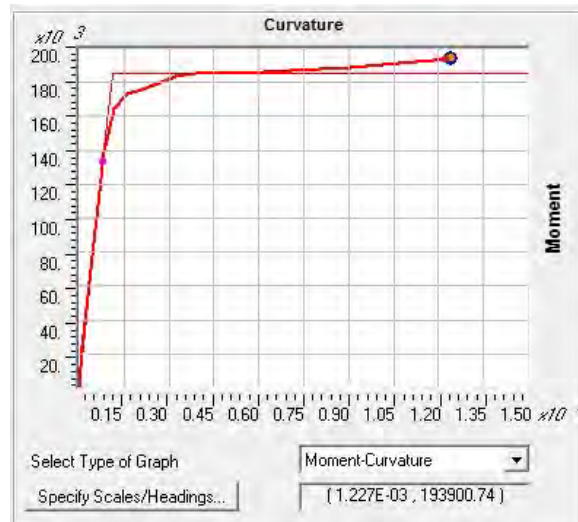
Figure A-15 Moment-curvature curve of the CFT column

Note that the design checks performed by hand calculations use the values from AISC (2010) for axial strength and shear strength and AASHTO for flexural strength. However, when analyses are performed with SAP2000 to check the resulting design, the forces obtained from SAP2000 are compared to the strength values obtained from SAP2000 Section Designer. The flexural strength use the Caltrans idealized flexural strength of 185621 kip-in. The compression strength is -16437 kips, using the value having the concrete reduction factor of 0.85. The tension strength is 11020 kips, the same as the values from the design codes.

Appendix B Anchor rod design calculation sheet

This design example illustrates two example design of the BRBs using anchor rods to conect to the foundation or cap beam. The first one for two column bent with the inverted-V BRBs are designed to be connected (1) at the bottom only to the foundation for the tensile BRB; (2) at the top to the cap beam for both BRBs. The second one for box pier with BRBs are designed to be connected (1) at the bottom only to the foundation for the tensile BRB; (2) at the top to the cap beam for both BRBs.

B.1 Two column bent with Chevron BRBs

(1) Tensile BRB with footing

The force demand is

$V_t := 470.43$ kips $N_t := 853.44$ kips

Use the anchor rod Grade 55

Minimum tensile strength	$F_u := 58$	ksi
Minimum yielding strength	$F_y := 36$	ksi
16 anchor rods are used for this design	$n := 16$	
The diameter of the anchor rod is	$d := 2$	in
The area of the anchor rod is	$A_d := \pi \cdot \dfrac{d^2}{4} = 3.142$	in^2
The bearing area of the anchor rod from table is	$A_{brg} := 5.35$	in^2
The concrete strength is	$f_c := 5$	ksi

ACI 318-08 Appendix D

The steel anchor strength under tension force is $N_s := 0.75 \cdot F_u \cdot A_d = 136.659$ kips

The steel anchor strength under tension force is $V_s := 0.65 \cdot F_u \cdot A_d = 118.438$ kips

The concrete pullout strength of a single anchor rod in tension calculated is according to section D5.3 in ACI318-08

$N_p = \phi_1 \cdot \psi_1 \cdot A_{brg} \cdot 8 \cdot f_c$

where : the concrete cracking parameter $\psi_1 := 1$

         the resistance reduction factor $\phi_1 := 0.75$

$N_p := \phi_1 \cdot \psi_1 \cdot A_{brg} \cdot f_c \cdot 8 = 160.5$ kips

The concrete breakout strength of a single anchor rod in tension calculated is according to section D5.2 in ACI318-08

$$N_b = \phi_2 \cdot \left[16 \cdot \sqrt{f_c \cdot 1000} \cdot \frac{\left(h_{ef}\right)^{\frac{5}{3}}}{1000} \right]$$

where : the resistance reduction factor $\phi_2 := 0.7$

Table B-1 Anchor rod dimensions and areas (Hogan and Thomas, 1994)

Rod Diameter, in.	Rod Area, A_n, in²	Bearing Area, in²
⅝	0.307	0.689
¾	0.442	0.906
⅞	0.601	1.22
1	0.785	1.50
1⅛	0.994	1.81
1¼	1.23	2.24
1½	1.77	3.13
1¾	2.41	4.17
2	3.14	5.35
2¼	3.98	6.69
2½	4.91	8.17
2¾	5.94	9.80
3	7.07	11.4
3¼	8.30	13.3
3½	9.62	15.3
3¾	11.0	17.5
4	12.6	19.9

The embedment length of the anchor rod is $h_{ef} := 30$ in

$$N_b := \phi_2 \cdot 16 \cdot \sqrt{f_c \cdot 1000} \cdot \frac{(h_{ef})^{\frac{5}{3}}}{1000} = 229.389 \qquad \text{kips}$$

The group effect of the anchor rods is considered in the following equation for the concrete breakout strength:

The design horizontal center-to-center distance of the anchor rod in the x-axis direction is

$h_{dis} := 40$ in

The design horizontal center-to-center distance of the anchor rod in the y-axis direction is

$v_{dis} := 40$ in

The layout of the anchor rods group is shown in figure 6-93a, 6-93b.

The projected concrete failure area of the anchor rods group is

$$A_n := (3 \cdot h_{ef} + 3 \cdot h_{dis}) \cdot (3 \cdot h_{ef} + 3 v_{dis}) = 4.41 \times 10^4 \qquad \text{in}^2$$

The projected concrete failure area of a single anchor with an edge distance equal to or greater than $1.5 h_{ef}$ is

$$A_{no} := 9 \cdot h_{ef}^2 = 8.1 \times 10^3 \qquad \text{in}^2$$
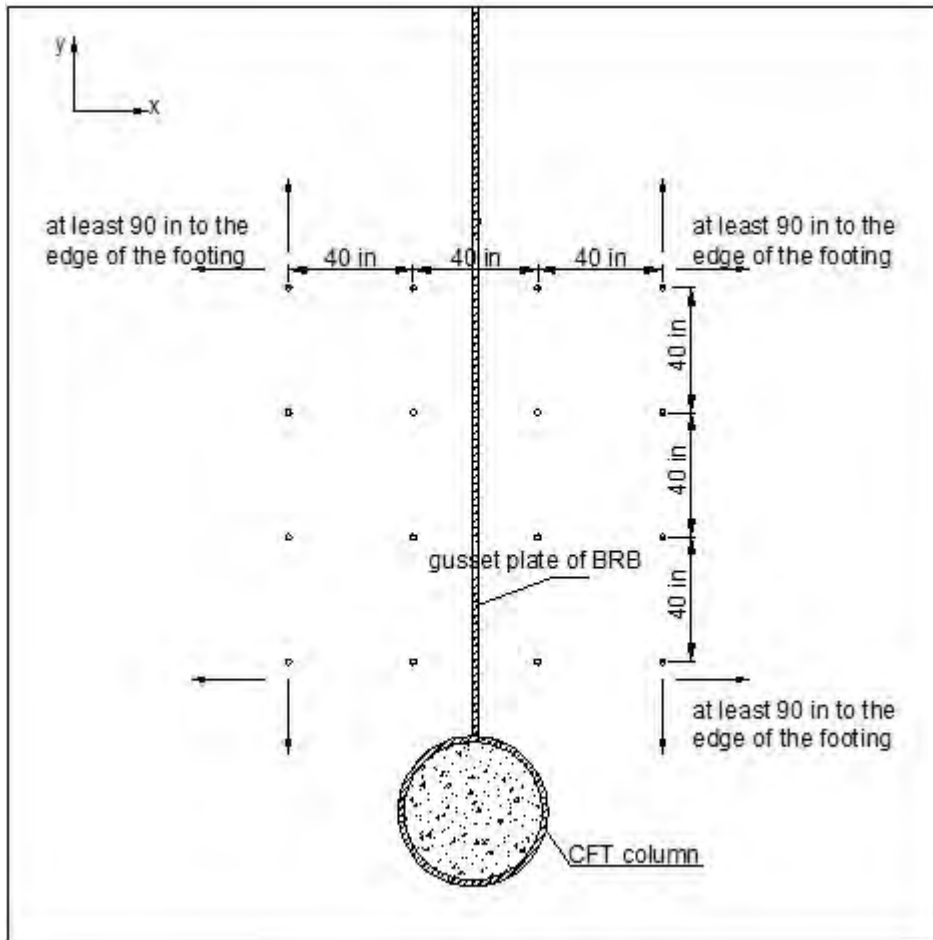
Figure 6-93a The layout of the anchor rods from top view
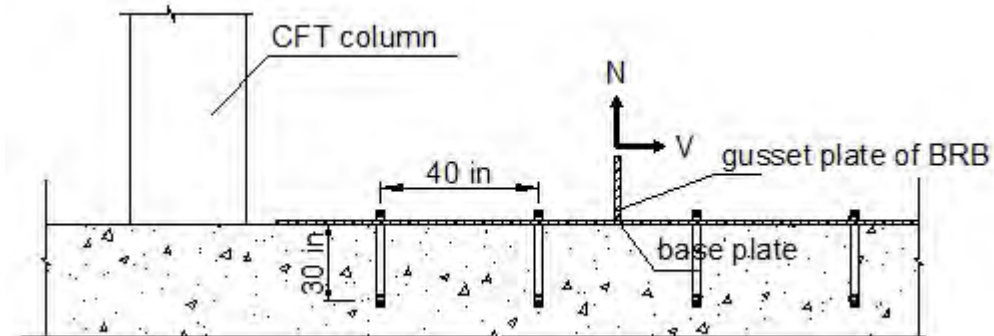
Figure 6-93b The layout of the anchor rods from side section view

The reduced tensile resistance of the anchor rods group is

$$N_{bg} := N_b \cdot \frac{A_n}{A_{no}} = 1.249 \times 10^3 \qquad\qquad \text{kips}$$

Smaller than

$$n \cdot N_b = 3.67 \times 10^3 \qquad\qquad \text{kips}$$

$$n \cdot N_s = 2.187 \times 10^3 \qquad\qquad \text{kips}$$

$$n \cdot N_p = 2.568 \times 10^3 \qquad\qquad \text{kips}$$

The concrete prying out strength of anchor rods group in shear is calculated according to section D6.3 in ACI318-08

$$Vp = k_{cp} \cdot N_{bg}$$

where : the factor for h_{ef} larger than 2.5" $\qquad k_{cp} := 2.0$

$$V_{pg} := k_{cp} \cdot N_{bg} = 2.498 \times 10^3 \qquad\qquad \text{kips}$$

The concrete breakout strength of a single anchor rod in shear is calculated according to section D6.2 in ACI318-08

$$Vb = \phi_3 \cdot 10.4 \cdot \sqrt{d} \cdot \sqrt{f_c \cdot 1000} \cdot \frac{c_1^{1.5}}{1000}$$

where : the resistance reduction factor $\qquad \phi_3 := 0.7$

The side distance of the anchor rod to an edge $\qquad c_1 := 90 \qquad$ in

$$V_b := \phi_3 \cdot 10.4 \cdot \sqrt{d} \cdot \sqrt{f_c \cdot 1000} \cdot \frac{c_1^{1.5}}{1000} = 621.577 \qquad\qquad \text{kips}$$

The projected concrete failure area of the anchor rods group is

$$A_v := (3 \cdot c_1 + 3h_{dis}) \cdot h_{ef} = 1.17 \times 10^4 \qquad\qquad \text{in}^2$$

The projected concrete failure area of a single anchor in a deep member with a distance from edges equal or greater than 1.5 h_{ef} in the direction perpendicular to the shear surface

$$A_{vo} := 3 \cdot c_1 \cdot h_{ef} = 8.1 \times 10^3 \qquad\qquad \text{in}^2$$

The reduced shear strength of the anchor rods group is

$$V_{bg} := V_b \cdot \frac{A_v}{A_{vo}} = 897.834 \qquad\qquad \text{kips}$$

Smaller than $\qquad n \cdot V_b = 9.945 \times 10^3 \qquad\qquad$ kips

$$V_{pg} = 2.498 \times 10^3 \qquad\qquad \text{kips}$$

For the anchor rod group, the interaction of the shear and tension force interaction is checked using the following equation.

$$\left(\frac{V_t}{V_{bg}}\right)^{\frac{5}{3}} + \left(\frac{N_t}{N_{bg}}\right)^{\frac{5}{3}} = 0.871$$

smaller than 1.0, therefore the anchor rod group design is sufficient to resist the forces.

AISC (2010)

AISC (2010) provided the following equation for the shear and tension stress check in a single anchor rod. The available tensile strength of a single anchor rod subjected to combined tension and shear forces shall be determined according to the limit state of tension and shear rupture as follows:

$$R_n = \phi_4 \cdot F_{nt} \cdot A_d$$

where: nominal tensile stress modified to include the effects of shear stress.

$$F_{nt1} = 1.3 \cdot F_{nt} - \frac{F_{nt} \cdot f_s}{0.75 \cdot F_{nv}}$$

the resistance reduction factor is. $\qquad \phi_4 := 0.75$

The nominal tensile stress in the anchor rod $\qquad F_{nt} := 0.75 \cdot F_u = 43.5 \qquad$ ksi

The nominal shear stress in the anchor rod $\qquad F_{nv} := 0.4 \cdot F_u = 23.2 \qquad$ ksi

The shear stress in the anchor rod is $\qquad f_s := \dfrac{V_t}{n \cdot A_d} = 9.359 \qquad$ ksi

The total tension force can be taken by the anchor rod group would be

$$F_{nt1} := 1.3 \cdot F_{nt} - F_{nt} \cdot \frac{f_s}{0.75 \cdot F_{nv}} = 33.153 \qquad \text{ksi}$$

$$F_t := n \, F_{nt1} \cdot A_d \cdot \phi_4 = 1.25 \times 10^3 \qquad \text{kips}$$

The tension force demand is $\qquad N_t = 853.44 \qquad$ kips

The anchor rod group is sufficient to resist the forces per AISC(2010).

(2) Two BRBs top connection with cap beam

The force demand is $V_t := 992$ kips

Use the anchor rod Grade 55

Minimum tensile strength $F_u := 58$ ksi

Minimum yielding strength $F_y := 36$ ksi

16 anchor rods are used for this design $n := 16$

The diameter of the anchor rod is $d := 2$ in

The area of the anchor rod is $A_d := \pi \cdot \dfrac{d^2}{4} = 3.142$ in^2

The bearing area of the anchor rod from table B-1 is $A_{brg} := 5.35$ in^2

The concrete strength is $f_c := 5$ ksi

ACI 318-08 Appendix D

The steel anchor rod strength under tension force is $V_s := 0.65 \cdot F_u \cdot A_d = 118.438$ kips

The concrete breakout strength of a single anchor rod in tension is calculated according to section D5.2 in ACI318-08

$$N_b = \phi_2 \left[16 \cdot \sqrt{f_c \cdot 1000} \cdot \frac{\left(h_{ef} \right)^{\frac{5}{3}}}{1000} \right]$$

where : the resistance reduction factor $\phi_2 := 0.7$

The embedment length of the anchor rod is $h_{ef} := 30$ in

$$N_b := \phi_2 \cdot 16 \cdot \sqrt{f_c \cdot 1000} \cdot \frac{\left(h_{ef} \right)^{\frac{5}{3}}}{1000} = 229.389$$ kips

The group effect of the anchor rod group is considered in the following equation for the concrete breakout strength:

The design horizontal center-to-center distance of the anchor rod in the x-axis direction is

$h_{dis} := 40$ in

The design horizontal center-to-center distance of the anchor rod in the y-axis direction is

$v_{dis} := 40$ in

The layout of the anchor rod group is shown below

The projected concrete failure area of the anchor group is

$A_n := \left(3 \cdot h_{ef} + 3 \cdot h_{dis} \right) \cdot \left(3 \cdot h_{ef} + 3 v_{dis} \right) = 4.41 \times 10^4$ in^2
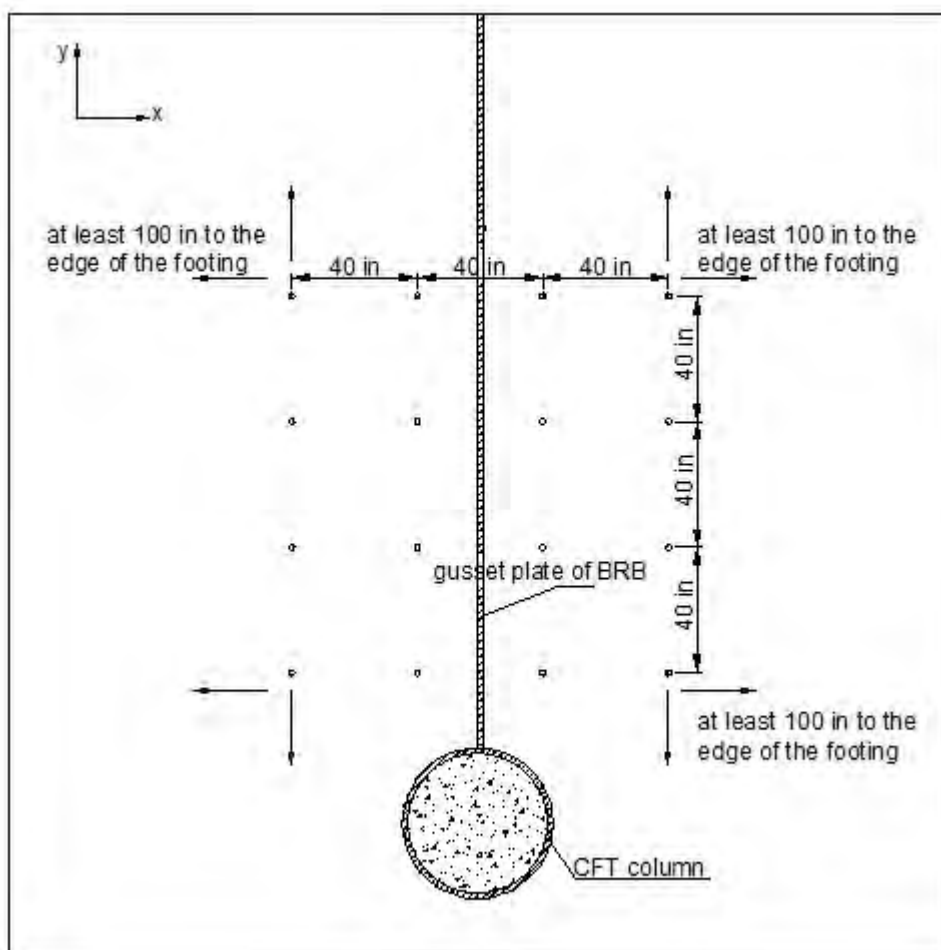
Figure B-1a The layout of the anchor rod from top view(with center-to-center distance change from 90 in to 100 in)
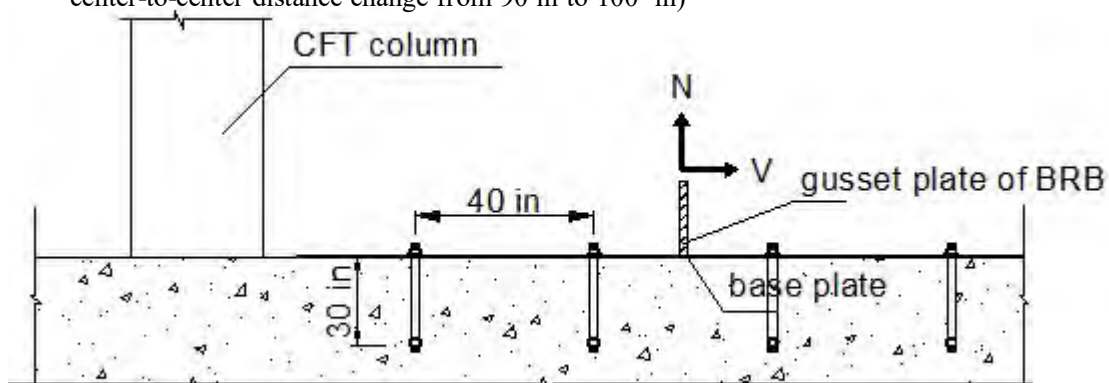
Figure B-2b The layout of the anchor rod from side section view

The projected concrete failure area of a single anchor with an edge distance equal to or greater than $1.5h_{ef}$ is

$$A_{no} := 9 \cdot h_{ef}^2 = 8.1 \times 10^3 \qquad\qquad in^2$$

The reduced tensile resistance of the anchor rod group is

$$N_{bg} := N_b \cdot \frac{A_n}{A_{no}} = 1.249 \times 10^3 \qquad \text{kips}$$

The concrete prying out strength of anchor rod group in shear is calculated according to section D6.3 in ACI318-08

$$Vp = k_{cp} \cdot N_{bg}$$

where : the factor for h_{ef} larger than 2.5" $k_{cp} := 2.0$

$$V_{pg} := k_{cp} \cdot N_{bg} = 2.498 \times 10^3 \qquad \text{kips}$$

The concrete breakout strength of a single anchor rod in shear is calculated according to section D6.2 in ACI318-08

$$Vb = \phi_3 \cdot 10.4 \cdot \sqrt{d} \cdot \sqrt{f_c \cdot 1000} \cdot \frac{c_1^{1.5}}{1000}$$

where : the resistance reduction factor $\phi_3 := 0.7$

The side distance of the anchor rod to an edge $c_1 := 100$ in

$$V_b := \phi_3 \cdot 10.4 \cdot \sqrt{d} \cdot \sqrt{f_c \cdot 1000} \cdot \frac{c_1^{1.5}}{1000} = 728 \qquad \text{kips}$$

The projected concrete failure area of the anchor rod group is

$$A_v := (3 \cdot c_1 + 3h_{dis}) \cdot h_{ef} = 1.26 \times 10^4 \qquad \text{in}^2$$

The projected concrete failure area of a single anchor in a deep member with a distance from edges equal or greater than 1.5 h_{ef} in the direction perpendicular to the shear surface

$$A_{vo} := 3 \cdot c_1 \cdot h_{ef} = 9 \times 10^3 \qquad \text{in}^2$$

The reduced shear strength of the anchor rod group is

$$V_{bg} := V_b \cdot \frac{A_v}{A_{vo}} = 1.019 \times 10^3 \qquad \text{kips}$$

Smaller than $n \cdot V_b = 1.165 \times 10^4 \qquad \text{kips}$

$$V_{pg} = 2.498 \times 10^3 \qquad \text{kips}$$

$$n \cdot V_s = 1.895 \times 10^3 \qquad \text{kips}$$

$$\frac{V_{bg}}{V_t} = 1.027 \qquad \text{OK}$$

AISC (2010)

The nominal shear stress in the anchor rod $F_{nv} := 0.4 \cdot F_u = 23.2 \qquad \text{ksi}$

The shear stress in the anchor rod is $f_s := \frac{V_t}{n \cdot A_d} = 19.735 \qquad \text{ksi}$

$$\frac{F_{nv}}{f_s} = 1.176 \qquad \text{OK}$$

B.2 Box pier with BRBs

The force demand is

$V_t := 186.65$ kips $N_t := 229.54$ kips

Use the anchor rod Grade 55

Minimum tensile strength	$F_u := 58$	ksi
Minimum yielding strength	$F_y := 36$	ksi
6 anchor rods are used for this design	$n := 6$	
The diameter of the anchor rod is	$d := 2$	in
The area of the anchor rod is	$A_d := \pi \cdot \dfrac{d^2}{4} = 3.142$	in^2
The bearing area of the anchor rod from table B-1 is	$A_{brg} := 5.35$	in^2
The concrete strength is	$f_c := 5$	ksi

ACI 318-08 Appendix D

The steel anchor rod strength under tension force is $N_s := 0.75 \cdot F_u \cdot A_d = 136.659$ kips

The steel anchor rod strength under tension force is $V_s := 0.65 \cdot F_u \cdot A_d = 118.438$ kips

The concrete pullout strength of a single anchor rod in tension is calculated according to section D5.3 in ACI318-08

$N_p = \phi_1 \cdot \psi_1 \cdot A_{brg} \cdot 8 \cdot f_c$

where : the concrete cracking parameter $\psi_1 := 1$

         the resistance reduction factor $\phi_1 := 0.75$

$N_p := \phi_1 \cdot \psi_1 \cdot A_{brg} \cdot f_c \cdot 8 = 160.5$ kips

The concrete breakout strength of a single anchor rod in tension is calculated according to section D5.2 in ACI318-08

$$N_b = \phi_2 \cdot \left[16 \cdot \sqrt{f_c \cdot 1000} \cdot \frac{(h_{ef})^{\frac{5}{3}}}{1000} \right]$$

where : the resistance reduction factor $\phi_2 := 0.7$

The embedment length of the anchor rod is $h_{ef} := 20$ in

$$N_b := \phi_2 \cdot 16 \cdot \sqrt{f_c \cdot 1000} \cdot \frac{(h_{ef})^{\frac{5}{3}}}{1000} = 116.704 \quad \text{kips}$$

The group effect of the anchor rod group is considered in the following equation for the concrete breakout strength:

The design horizontal center-to-center distance of the anchor rod in the x-axis direction is

$h_{dis} := 20$ in

The design horizontal center-to-center distance of the anchor rod in the y-axis direction is

$$v_{dis} := 20 \qquad in$$

The layout of the anchor rod group is shown in figure 6-94a, 5-94b.
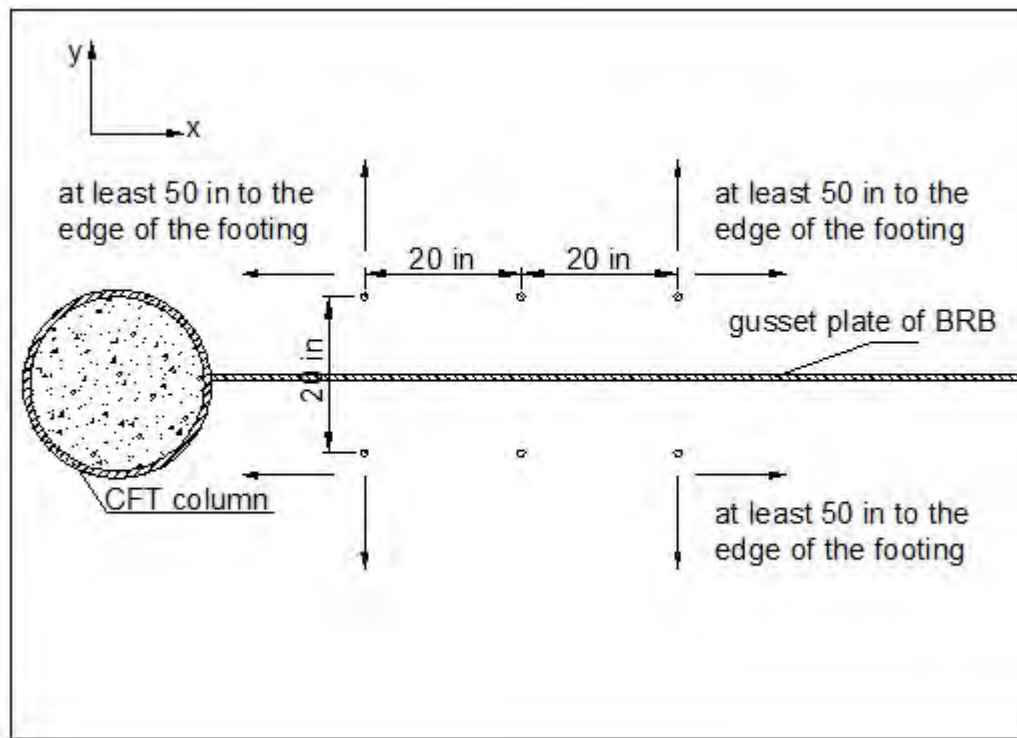
Figure 6-94a The layout of the anchor rod from top view
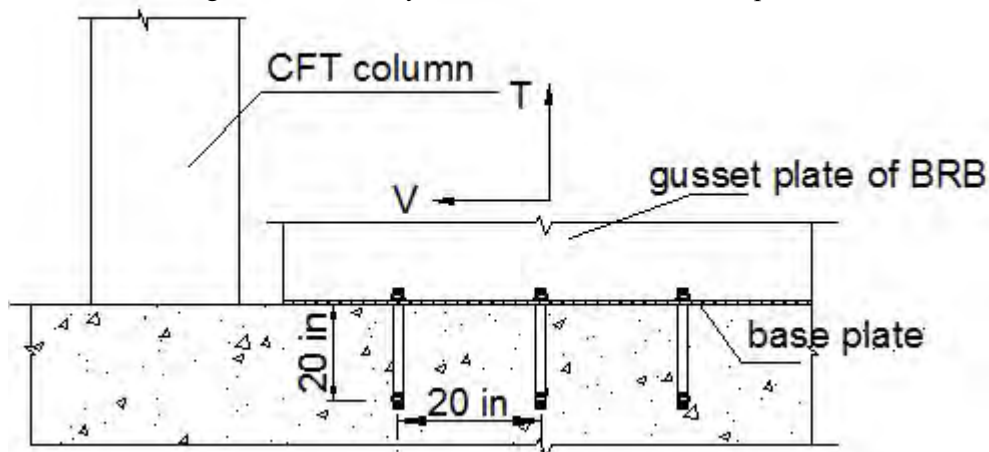
Figure 6-94b The layout of the anchor rod from side section view

The projected concrete failure area of the anchor rod group is

$$A_n := \left(3 \cdot h_{ef} + 2h_{dis}\right) \cdot \left(3 \cdot h_{ef} + 2v_{dis}\right) = 1 \times 10^4 \qquad in^2$$

The projected concrete failure area of a single anchor rod with an edge distance equal to or greater than $1.5h_{ef}$ is

$$A_{no} := 9 \cdot h_{ef}^2 = 3.6 \times 10^3 \qquad in^2$$

The reduced tensile resistance of the anchor rod group is

$$N_{bg} := N_b \cdot \frac{A_n}{A_{no}} = 324.178 \qquad \text{kips}$$

Smaller than $\quad n \cdot N_b = 700.225 \qquad$ kips

$$n \cdot N_s = 819.956 \qquad \text{kips}$$

$$n \cdot N_p = 963 \qquad \text{kips}$$

The concrete prying out strength of the anchor rod group in shear is calculated according to section D6.3 in ACI318-08

$$V_p = \phi k_{cp} \cdot N_{bg}$$

where : the factor for h_{ef} larger than 2.5" $\qquad k_{cp} := 2.0$

$$V_{pg} := k_{cp} \cdot N_{bg} = 648.356 \qquad \text{kips}$$

The concrete breakout strength of a single anchor rod in shear calculated is according to section D6.2 in ACI318-08

$$V_b = \phi \phi_3 \cdot 10.4 \cdot \sqrt{d} \cdot \sqrt{f_c \cdot 1000} \cdot \frac{c_1^{1.5}}{1000}$$

where : the resistance reduction factor $\qquad \phi_3 := 0.7$

The side distance of the anchor rod to an edge in the direction of the applied shear force $\qquad c_1 := 50 \qquad$ in

$$V_b := \phi_3 \cdot 10.4 \cdot \sqrt{d} \cdot \sqrt{f_c \cdot 1000} \cdot \frac{c_1^{1.5}}{1000} = 257.387 \qquad \text{kips}$$

The projected concrete failure area of the anchor rod group is

$$A_v := \left(3 \cdot c_1 + 2 h_{dis}\right) \cdot h_{ef} = 3.8 \times 10^3 \qquad \text{in}^2$$

The projected concrete failure area of a single anchor rod in a deep member with a distance from edges equal or greater than 1.5 h_{ef} in the direction perpendicular to the shear surface

$$A_{vo} := 3 \cdot c_1 \cdot h_{ef} = 3 \times 10^3 \qquad \text{in}^2$$

The reduced shear strength of the anchor rod group is

$$V_{bg} := V_b \cdot \frac{A_v}{A_{vo}} = 326.023 \qquad \text{kips}$$

Smaller than $\quad n \cdot V_b = 1.544 \times 10^3 \qquad$ kips

$$V_{pg} = 648.356 \qquad \text{kips}$$

For the anchor rod group, the interaction of the shear and tension force interaction is checked using the following equation.

$$\left(\frac{V_t}{V_{bg}}\right)^{\frac{5}{3}} + \left(\frac{N_t}{N_{bg}}\right)^{\frac{5}{3}} = 0.957$$

smaller than 1.0, therefore the anchor rod group design is sufficient to resist the forces.

AISC (2010)

AISC (2010) provided the following equation for the shear and tension stress checks in the a single anchor rod. The available tensile strength of a anchor rod subjected to combined tension and shear forces shall be determined according to the limit state of tension and shear rupture as follows:

$$R_n = \phi_4 \cdot F_{nt} \cdot A_d$$

where: nominal tensile stress modified to include the effects of shear stress.

$$F_{nt1} = 1.3 \cdot F_{nt} - \frac{F_{nt} \cdot f_s}{0.75 \cdot F_{nv}}$$

the resistance reduction factor is. $\phi_4 := 0.75$

The nominal tensile stress in the anchor rod $F_{nt} := 0.75 \cdot F_u = 43.5$ ksi

The nominal shear stress in the anchor rod $F_{nv} := 0.4 \cdot F_u = 23.2$ ksi

The shear stress in the anchor rod is $f_s := \dfrac{V_t}{n \cdot A_d} = 9.902$ ksi

The total tension force can be taken by the anchor rod group would be

$$F_{nt1} := 1.3 \cdot F_{nt} - F_{nt} \cdot \frac{f_s}{0.75 \cdot F_{nv}} = 31.795 \qquad \text{ksi}$$

$$F_t := n \, F_{nt1} \cdot A_d \cdot \phi_4 = 449.488 \qquad \text{kips}$$

The tension force demand is $N_t = 229.54$ kips

The anchor rod group is sufficient to resist the forces per AISC(2010).

Appendix C Simplified Benchmark Bridge Modeling and Analyses

Xiaone Wei, Shenshen Zhang

This Appendix provides additional information on the modeling of the simplified benchmark bridge used in the parametric analyses in Chapter 7. Also additional bridge models were built and analyzed to provide more information to understand the EDSs' behavior in bridges. The OpenSees model description is provided in Section C.1. The properties of the simplified bridge models and the resulting displacement demands from the time history analyses are presented in Section C.2.

The work presented in this Appendix was collaboratively done by Xiaone Wei and Shenshen Zhang, with responsibilities divided as follows:

- Xiaone Wei was responsible for: designing all benchmark models; constructing the initial benchmark model in SAP2000 to provide information for Shenshen Zhang to build models in OpenSees; performing analyses and generating analyses results; summarizing all results, comparing results and formulating conclusions

- Shenshen Zhang was responsible for: modeling initial benchmark model in OpenSees; performing analyses and generating analyses results

C.1   Analytical Model Building in OpenSees

C.1.1   Simplified Model Descriptions

The EDS-1 simplified nonskew bridge model in Figure C-1 is used in this section to illustrate how the model is built in SAP2000 and OpenSees. The L-BRB and T-BRB represent the longitudinal and transverse BRBs. The girder indicates the superstructure of the bridge model. The beam and columns are rigid members that connect the girder, BRBs and the base. The bridge mass is distributed at the whole length of the girder. Figure C-2 shows the simplified EDS-2 nonskew bridge model, which is basically modeled in the same way except for different connecting point for the long and short BRBs. Note that the modeling of the initial SAP2000 model is not explained here, since the focus of this section is to explain the models built in OpenSees, which were used to perform the nonlinear time history analyses of all the bridges in Chapter 7 and this Appendix. The initial models in OpenSees were analyzed and the results were verified with the initial SAP2000 models.

The girder and beam are defined by using the element command *elasticBeamColumn*. Areas and moments of inertia were set to be 10^7 in^2 and 10^{12} in^4 to make the member rigid and create a rigid diaphragm, when using the young's modulus of 29000 ksi and shear modulus of 11154 ksi. Note that the element command *rigidLink* in the beam type could also have been used to build these rigid members. Element command *truss* was used to model the columns which serve as the link between the base and the top of the diaphragm. They are also rigid elements defined with elastic uniaxial material, which have large young's modulus value of 10^{12} to model the large stiffness, when the cross sectional area was set to be 1.
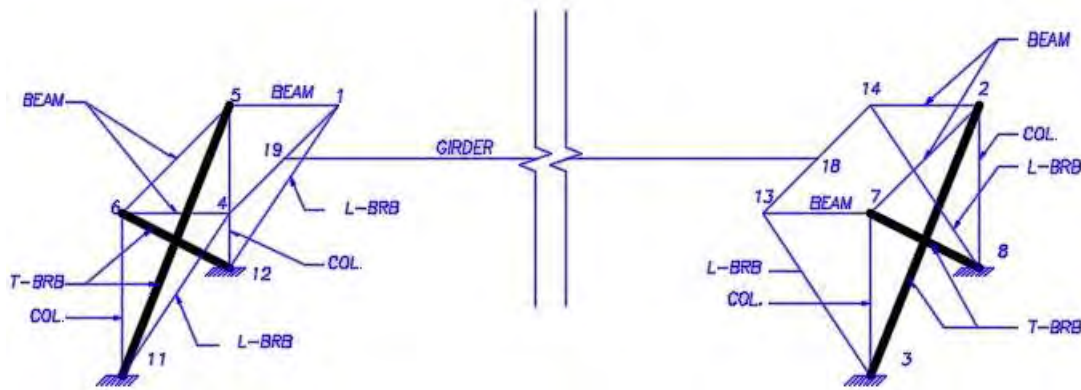
Figure C-1. Simplified EDS-1 nonskew bridge model
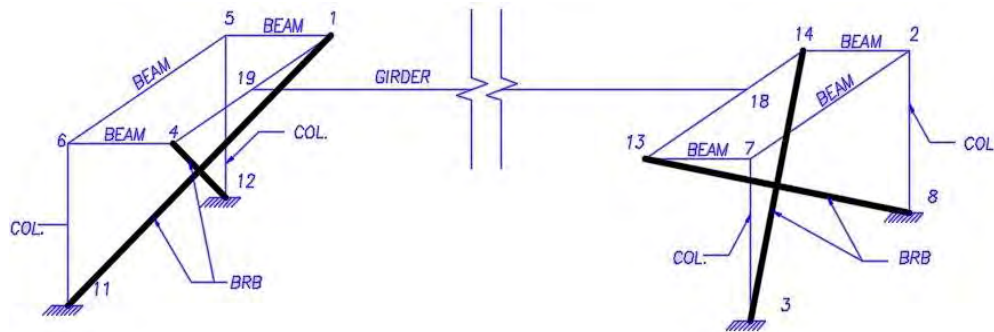
Figure C-2. Simplified EDS-2 nonskew bridge model

Element command *truss* was also used to build BRB members. The *truss* element was constructed by specifying an area and a *UniaxialMaterial* identifier. The material of BRBs was defined to be bilinear. It was found that using the *Elastic-Perfectly Plastic (Elastic PP)* material command alone couldn't define the bilinear material if the material had no strain-hardening after yielding point (i.e. the young's modulus *E* equals to zero in plastic stage as shown in Figure C-3). Therefore the elastic stage was first defined by using the *Elastic PP* material command. For the plateau stage, the *Elastic* material command was used by setting the young's modulus to be very small to achieve the bilinear assumption of the material. *Parallel* Command was then used to create a parallel material object made up of previously-constructed material objects as shown in Figure C-4.

The *ElasticPP* material used young's modulus of 29000 ksi. The yield strain of the *ElasticPP* material is the yield strength of the BRB material of 42 ksi divided by the young's modulus, and the resulting value is 0.00144. The young's modulus of 0.00001 was set for the *Elastic* material (i.e. this is equivalent to setting strain hardening ratio as 0.00001/29000, therefore, the combined material would represent the bilinearity). Note that this is for BRBs with the yield length ratio of 1.0.

When the yield length ratio is smaller than 1.0, the BRB was modeled by maintaining the same length of the BRB member and changing the young's modulus of the *ElasticPP* material with larger values, which can be calculated using the equation below:

$$E_{new} = E_{original}/c \qquad (C\text{-}1)$$

498

where, $E_{original} = 29000$ is the original young's modulus for the real BRB material; c is yielding length ratio.
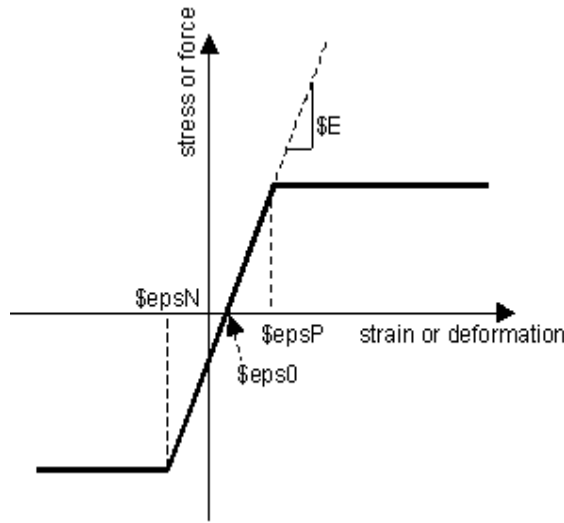
Figure C-3. Material stress-strain curve built in Elastic-Perfectly Plastic command for BRBs;
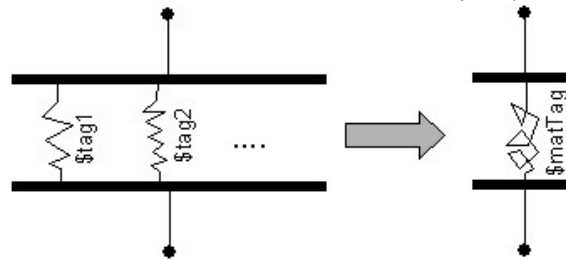
Figure C-4. UniaxialMaterial Command – Parallel material

The *Truss* element command doesn't include Rayleigh damping by default. Since the damping in the model considered Rayleigh damping, therefore, for the BRB members, the Rayleigh damping needs to be activated by adding *"–doRayleigh 1"* at the end of the truss element.

C.1.2 Analyses Definition

For each bridge model, modal analyses, nonlinear pushover analysis, and nonlinear time history analyses were performed. The pushover analyses in the longitudinal and transverse direction gave the yielding strength and displacement of the bridge model in the corresponding directions. The nonlinear time history analyses of each bridge diaphragm model utilized 44 ground motions, and the nonlinear displacement demands under those ground motions were obtained to study dynamic behaviors of the proposed EDSs. In this section, the commands to perform the pushover and time history analyses are explained in Section C.1.2.1 and C.1.2.2, respectively.

C.1.2.1 Pushover Analyses

Joint loads were applied at the level of the girder and beams in the direction for which the pushover analyses were intended to perform. *Plain* pattern with linear manner was used to define the joint loads. The constraints used Lagrange multiplier with the factors *alphaS* and *alphaM* defined as 1.0. A *Plain*

Numberer was used. The System command used *BandGeneral*. The Algorithm command used *ModifiedNewton* to determine the sequence of steps taken to solve the nonlinear residual equation. The Test commands used *EnergyIncr* to construct a convergence test which uses the dot product of the solution vector and norm of the right hand side of the matrix equation to determine if convergence had been reached. Values for the factors *tol* and *iter* in the energy increment option were set to be 10^{-8} and 6, respectively. The analysis command type was *Static*. The *Integrator* command used *DisplacementControl* in the pushover analyses. Node 1 in Figure C-1 was used as the control point for the pushover analyses. The degree of freedom is the direction of the pushover analysis, and 1 and 2 represents X and Y direction, respectively. The displacement increment and the analyses steps were set to be 0.001" and 1000, respectively.

C.1.2.2   Nonlinear Time History Analyses

Nonlinear time history analyses definitions are presented in this section, which include commands for defining Rayleigh damping and time history analyses execution.

C.1.2.2.1   Rayleigh Damping

Mass-stiffness proportional damping, normally refers to as Rayleigh damping, is commonly used in nonlinear dynamic analysis. During formulation, the damping matrix is assumed to be proportional to the mass and initial stiffness matrices as follows:

$$C = \alpha M + \beta K \qquad\qquad (C\text{-}2)$$

where:
- α is the mass-proportional damping coefficient
- β is the stiffness-proportional damping coefficient

In OpenSees, the Rayleigh damping matrix is constructed as below:

$$D = \$alphaM * M + \$betaK * K_{current} + \$betaK_{init} * K_{init} + \$betaK_{comm} * K_{Commit} \qquad (C\text{-}3)$$

where:
- M is the mass matrix
- $K_{current}$, K_{init}, and K_{commit} are the current, initial and committed stiffness matrices

The committed stiffness matrix K_{comm} considers i and (i+1) steps of analysis, and K_i is a tangent stiffness matrix for the i-th step of analysis. This matrix can be used to get the solution for the next analysis step (i+1) but was not updated during iterations for that step of analysis. After solving the (i+1) step of analysis, the tangent stiffness matrix is updated to K_{i+1}. This stiffness matrix is called committed and can be used for the next step of analysis.

The damping coefficients used in Equation C-3 should be given using the following command in OpenSees:

rayleigh $alphaM $betaK $betaKinit $betaKcomm

where:
- $alphaM is the factor applied to elements or nodes mass matrix
- $betaK is the factor applied to elements current stiffness matrix

- $betaK_{init}$ is the factor applied to elements initial stiffness matrix
- $betaK_{comm}$ is the factor applied to elements committed stiffness matrix

In order to figure out which stiffness matrix is better to utilize, different combinations of the damping coefficients were used while all the other setting of the analyses remained the same. Six cases for different mass and stiffness matrix combinations were used and also listed in Table C-1, so as to check the differences of displacement demands:

Table C-1. Results calculated from six analysis cases using different stiffness matrix factors

Displacement	Case 1: K_{comm}	Case 2: K_{curr}	Case 3: K_{init}	Case 4: $M+K_{curr}$	Case 5: $M+K_{init}$	Case 6: $M+K_{comm}$
Max(in)	0.376	0.336	0.376	0.380	0.376	0.380
Min(in)	-0.207	-0.207	-0.207	-0.207	0.207	0.207

There is no difference between Case 4 and Case 6, which indicates that K_{curr} or K_{comm} in Rayleigh damping definition doesn't influence the resulted displacements. The smallest results shown in the table is given by Case 5, which is same as the result obtained from SAP2000 analysis, since only the initial stiffness matrix of the structure is considered. For the purpose of having the equivalent models and being able to verify the results from both software, $M+K_{init}$ combination was chosen for Rayleigh damping definition, which was considered to be more conservative.

The critical modal damping ratio has the following relationship with the natural frequency:

$$\xi_n = \frac{1}{2\omega_n}\alpha + \frac{\omega_n}{2}\beta \qquad\qquad \text{(C-4)}$$

where:
- ξ_n is the critical-damping ratio, in this case, take $\xi_n = 0.05$
- ω_n is the natural frequency ($\omega_n = 2\pi f_n$)

The proportionality factors are obtained by setting the damping ratio for both natural frequencies to be equal, and the eigenvalues from the modal analysis can be used in calculating the natural frequencies (corresponding to the period in the main vibration directions).

$$\alpha = \frac{2\omega_i\omega_j}{(\omega_i+\omega_j)} \qquad\qquad \text{(C-5)}$$

$$\beta = \frac{2\xi}{(\omega_i+\omega_j)} \qquad\qquad \text{(C-6)}$$

C.1.2.2.2   Analysis Execution

Two ground motions in one pair was input at the base of the bridge model in orthogonal directions. *UniformExcitation* pattern command was used to apply the ground motion. The constraints used *Transformation* handler. A *RCM* Numberer was used. The System command used *BandGeneral*. The Algorithm command used *Newton* to determine the sequence of steps taken to solve the nonlinear residual equation. The Test commands used *EnergyIncr* to construct a convergence test which uses the dot product of the solution vector and norm of the right hand side of the matrix equation to determine if convergence had been reached. Values for the factors *tol* and *iter* in the energy increment option were set

to be 10^{-8} and 10, respectively. The analysis command type is *Transient*. The Integrator command used *Newmark* options with the values of gamma and beta to be 0.5 and 0.25, respectively. The time step was set to be 0.0001s for all the ground motions, which was considered small enough. The total number of steps in the time history analyses for a ground motion of 30s was 300000.

C.2   Bridge Model Key Properties and Analyses Results

In Chapter 7 Section 7.3.2.3, the simplified benchmark skew bridges were built to have the same yield displacement and yield strength in the longitudinal and transverse directions as the nonskew bridges. For all the skew bridges, they all correspond to the same equivalent nonskew bridges. In this Section, the bridge models with EDS-1 scheme were designed following different principles, i.e. different yield strength or yield displacement in the longitudinal and transverse directions. As the skew angle changed, the longitudinal stiffness stayed the same, and the skew stiffness in the skew EDS-1 bridge was kept the same as the transverse stiffness in the nonskew EDS-1 bridge. Therefore, each skew bridge (with different skew angles) has its corresponding equivalent nonskew bridges, since the yield strength and yield displacement in the longitudinal and transverse direction changed as the skew angle changed. The bridges' dimensions and properties and also the comparison of the dynamic response between the skew and nonskew bridges with EDS-1 are provided in this Section. In Section C.2.1, the stiffness ratio between the stiffness in the longitudinal and skew direction of the EDS-1 scheme is 1, and the stiffness ratio changed to 2 in Section C.2.2. In Sections C.2.3, the stiffness of the skew and nonskew bridges was designed the same in both the longitudinal and transverse directions. The strength of the skew and nonskew bridges was the same in both the longitudinal and transverse directions in Section C.2.4.

The method to obtain the scale factor for the ground motions is the same as mentioned in Chapter 7. The scale factors of the equivalent nonskew bridges were obtained for each ductility level, and were used in the nonlinear time history analyses for both the skew and its equivalent nonskew bridges. Displacement demands and comparisons between the skew and equivalent nonskew bridges are also presented.

C.2.1   Stiffness Ratio of 1.0 between the stiffness of the EDS-1 in the Longitudinal and Skew Direction

Dimensions and properties of the skew and nonskew bridge with EDS-1 are tabulated in Table C-1, for longitudinal and transverse stiffness ratio of 1.0. The stiffness is 5126.5 kip/in. The BRBs' steel cores have the yielding strength of 42 ksi and the yield length ratio of the steel core's length over the entire length is 1.0. The equivalent nonskew bridges of the skew bridge had the same yield strength and yield displacement in the longitudinal and transverse direction as the skew bridge. The properties of the equivalent nonskew bridges are tabulated in Table C-2. Note that these equivalent nonskew bridges are ideal and only modeled to generate the displacement demands in order to compare to those from the skew bridges. The BRBs' steel cores have different yielding strength as tabulated in Table C-2 and the yield length ratio of the steel core's length over the entire length is 1.0.

Table C-3 shows the displacement demands of the nonskew bridge in Table C-1 and the EDS-1 equivalent nonskew bridges in Table C-2. The equivalent nonskew bridges are presented by the skew angle of its corresponding skew bridges. Since the longitudinal directions of all nonskew equivalent

bridges in Table C-2 have the same yield displacement and yield strength as the nonskew bridge in Table C-1, the displacement demand are the same too. For the nonskew bridge in Table C-1, the displacement demands are the same for the longitudinal and transverse directions, and the values are tabulated in Table C-3. For the nonskew equivalent bridges in Table C-2, the transverse displacement demands are different for each equivalent nonskew bridge and shown in Table C-3, while the longitudinal displacements are the same as the nonskew bridge.

Table C-1 Properties of benchmark simplified EDS-1 skew and nonskew bridges (stiffness ratio of longitudinal/transverse=1.0)

Skew Angle (Degree)	0	15	30	45	60	75
First translational period T_1 (s)	0.20	0.23	0.28	0.37	0.55	1.08
Second translational period T_2 (s)	0.20	0.18	0.16	0.15	0.15	0.14
Longitudinal BRB Cross Sectional Area (in²)	9.00	9.00	9.00	9.00	9.00	9.00
Skew BRB Cross Sectional Area (in²)	9.00	8.85	8.51	8.27	8.22	6.81
Global Yielding Displacement in longitudinal directions (in)	0.209	0.209	0.209	0.209	0.209	0.209
Global Yielding Displacement in transverse directions (in)	0.209	0.231	0.304	0.469	0.843	1.613
Global Yielding Strength in longitudinal direction (kips)	1069.1	1069.1	1069.1	1069.1	1069.1	1069.1
Global Yielding Strength in Transverse direction (kips)	1069.1	1033.3	935.5	801.8	617.3	286.5

Table C-2 Properties of benchmark simplified EDS-1 equivalent nonskew bridges of the skew bridges (stiffness ratio of longitudinal/transverse =1.0)

Corresponding Skew Angle (Degree)	15	30	45	60	75
First translational period T_1 (s)	0.21	0.26	0.35	0.53	1.07
Second translational period T_2 (s)	0.20	0.20	0.20	0.20	0.20
Longitudinal BRB Cross Sectional Area (in²)	9.00	9.00	9.00	9.00	9.00
Skew BRB Cross Sectional Area (in²)	7.87	5.40	3.00	1.286	0.312
Longitudinal BRB core yield strength (ksi)	42.00	42.00	42.00	42.00	42.00
Transverse BRB core yield strength (ksi)	46.42	61.25	94.50	169.74	324.75
Global Yielding Displacement in longitudinal directions (in)	0.209	0.209	0.209	0.209	0.209
Global Yielding Displacement in transverse directions (in)	0.231	0.304	0.469	0.843	1.613
Global Yielding Strength in longitudinal direction (kips)	1069.1	1069.1	1069.1	1069.1	1069.1
Global Yielding Strength in Transverse direction (kips)	1033.3	935.5	801.8	617.3	286.5

The displacement demands of the skew bridges are shown in Table C-4 in both longitudinal and transverse directions. Table C-5 compares skew bridges' displacement demands in both directions (in Table C-4) to the equivalent nonskew bridges (in Table C-3), and the difference in both the longitudinal and transverse direction are shown in percentages. The displacement difference in the longitudinal directions increases as the skew angles increases. In the transverse direction, skew bridge with skew angle of 30 degree has the largest increase in percentage.

Table C-3 Displacement demands of the EDS-1 equivalent nonskew bridges (stiffness ratio of longitudinal/transverse =1.0) (Unit: in)

Ductility	Skew angle of corresponding skew bridge (degree)											
	Nonskew 0°		Equivalent nonskew 15°		Equivalent nonskew 30°		Equivalent nonskew 45°		Equivalent nonskew 60°		Equivalent nonskew 75°	
	Longi.	Trans.	Longi.	Trans.	Longi.	Trans.	Longi.	Trans.	Longi.	Trans.	Longi.	Trans.
2	0.390	0.390	0.390	0.418	0.390	0.48	0.390	0.768	0.390	1.52	8.198	8.198
3	0.66	0.66	0.66	0.673	0.66	0.778	0.66	1.176	0.66	2.358	12.899	12.899
4	0.981	0.981	0.981	1.002	0.981	1.22	0.981	1.702	0.981	3.469	17.877	17.877
5	1.333	1.333	1.333	1.367	1.333	1.669	1.333	2.261	1.333	4.501	23.18	23.18
6	1.634	1.634	1.634	1.731	1.634	2.1	1.634	2.809	1.634	5.362	28.721	28.721

Table C-4 Displacement demands of EDS-1 skew bridges (stiffness ratio of longitudinal/transverse =1.0) (Unit: in)

Ductility	Skew 15°		Skew 30°		Skew 45°		Skew 60°		Skew 75°	
	Longi.	Trans.	Longi.	Trans.	Longi.	Trans.	Longi.	Trans.	Longi.	Trans.
2	0.403	0.421	0.492	0.563	0.518	0.844	0.645	1.461	1.922	7.796
3	0.683	0.687	0.798	0.917	0.931	1.018	1.101	2.427	2.908	11.494
4	0.992	0.998	1.107	1.251	1.271	1.724	1.609	3.493	3.961	15.579
5	1.303	1.353	1.386	1.605	1.622	2.235	2.085	4.455	5.205	20.517
6	1.571	1.667	1.678	1.95	1.971	2.728	2.495	5.41	6.473	25.368

Table C-5 Displacement comparison between the EDS-1 skew bridge and their equivalent nonskew bridges (stiffness ratio of longitudinal/transverse =1.0)

Ductility	Skew 15°		Skew 30°		Skew 45°		Skew 60°		Skew 75°	
	Longi.	Trans.	Longi.	Trans.	Longi.	Trans.	Longi.	Trans.	Longi.	Trans.
2	3.40%	0.80%	26.10%	17.40%	36.30%	9.90%	65.40%	-3.90%	392.60%	-4.90%
3	3.40%	2.00%	20.90%	17.90%	47.00%	-13.40%	66.70%	2.90%	340.30%	-10.90%
4	1.10%	-0.40%	12.90%	2.50%	34.50%	1.30%	64.00%	0.70%	303.70%	-12.90%
5	-2.30%	-1.00%	4.00%	-3.80%	26.70%	-1.20%	56.30%	-1.00%	290.30%	-11.50%
6	-3.80%	-3.70%	2.70%	-7.10%	26.20%	-2.90%	52.70%	0.90%	296.20%	-11.70%

C.2.2 Stiffness Ratio of 2.0 between the stiffness of the EDS-1 in the Longitudinal and Skew Direction

The longitudinal over the transverse stiffness ratio of the EDS-1 was changed to 2 to investigate how it could affect the bridge's dynamic behavior as the skew angle changes. Dimensions and properties of the skew and nonskew bridge with EDS-1 are tabulated in Table C-6. The stiffness in the longitudinal direction is still 5126.5 kip/in. The BRBs' steel cores have the yielding strength of 42 ksi and the yield length ratio of the steel core's length over the entire length is 1.0. The equivalent nonskew bridges of the skew bridges were also built and their properties are tabulated in Table C-7. The BRBs' steel cores have different yielding strength as tabulated in Table C-7 and the yield length ratio of the steel core's length over the entire length is 1.0.

Table C-8 shows the transverse displacement demands of the nonskew bridge in Table C-6 and the EDS-1 equivalent nonskew bridges in Table C-7. The equivalent nonskew bridges are presented by the skew angle of its corresponding skew bridges. Since the longitudinal directions of nonskew bridge in Table C-6 and all the nonskew equivalent bridges in Table C-7 have the same yield displacement and yield

strength as the nonskew bridge in Table C-1, the displacement demands are the same too. The transverse displacements increase as the skew angle of the equivalent nonskew bridges increase.

Table C-6 Properties of benchmark simplified EDS-1 skew and nonskew bridges (stiffness ratio of longitudinal/transverse =2)

Skew Angle (Degree)	0	15	30	45	60	75
First translational period T_1 (s)	0.28	0.29	0.35	0.46	0.67	1.33
Second translational period T_2 (s)	0.20	0.20	0.18	0.17	0.17	0.16
Longitudinal BRB Cross Sectional Area (in²)	9.00	9.00	9.00	9.00	9.00	9.00
Skew BRB Cross Sectional Area (in²)	4.50	4.43	4.25	4.13	4.45	6.78
Global Yielding Displacement in longitudinal directions (in)	0.209	0.209	0.209	0.209	0.209	0.209
Global Yielding Displacement in transverse directions (in)	0.209	0.223	0.274	0.391	0.717	2.436
Global Yielding Strength in longitudinal direction (kips)	1069.1	1069.1	1069.1	1069.1	1069.1	1069.1
Global Yielding Strength in Transverse direction (kips)	534.6	516.7	467.7	400.9	334.1	285.2

Table C-7 Properties of benchmark simplified EDS-1 nonskew equivalent bridges (stiffness ratio of longitudinal/transverse =2)

Corresponding Skew Angle (Degree)	15	30	45	60	75
First translational period T_1 (s)	0.30	0.35	0.45	0.66	1.32
Second translational period T_2 (s)	0.20	0.20	0.20	0.20	0.20
Longitudinal BRB Cross Sectional Area (in²)	9.00	9.00	9.00	9.00	9.00
Skew BRB Cross Sectional Area (in²)	4.06	3.00	1.80	0.81	0.21
Longitudinal BRB core yield strength (ksi)	42.00	42.00	42.00	42.00	42.00
Transverse BRB core yield strength (ksi)	44.96	55.13	78.75	144.38	490.54
Global Yielding Displacement in longitudinal directions (in)	0.209	0.209	0.209	0.209	0.209
Global Yielding Displacement in transverse directions (in)	0.223	0.274	0.391	0.717	2.436
Global Yielding Strength in longitudinal direction (kips)	1069.1	1069.1	1069.1	1069.1	1069.1
Global Yielding Strength in Transverse direction (kips)	516.7	467.7	400.9	334.1	285.2

The displacement demands of the skew bridges are shown in Table C-9 in both longitudinal and transverse directions. Table C-10 compares skew bridges' displacement demands (Table C-9) in both directions to the equivalent nonskew bridges (Table C-8), and the difference in both the longitudinal and transverse direction is shown in percentages. The displacement difference of skew bridge with 75 degrees is the largest. In the transverse direction, skew bridge with skew angle of 30 degree has the largest increase in percentage.

Table C-8 Transverse Displacement demands of the EDS-1 equivalent nonskew bridges (stiffness ratio of longitudinal/transverse =2.0) (Unit: in)

Ductility	Skew angle of corresponding skew bridge (degree)											
	Nonskew 0°		Equivalent nonskew 15°		Equivalent nonskew 30°		Equivalent nonskew 45°		Equivalent nonskew 60°		Equivalent nonskew 75°	
	Longi.	Trans.	Longi.	Trans.	Longi.	Trans.	Longi.	Trans.	Longi.	Trans.	Longi.	Trans.
2	0.390	0.346	0.390	0.361	0.390	0.461	0.390	0.646	0.390	1.299	8.198	4.925
3	0.66	0.593	0.66	0.607	0.66	0.703	0.66	1.02	0.66	2.054	12.899	7.837
4	0.981	0.875	0.981	0.881	0.981	1.027	0.981	1.456	0.981	3.034	17.877	10.626
5	1.333	1.153	1.333	1.185	1.333	1.364	1.333	1.819	1.333	4.002	23.18	13.123
6	1.634	1.416	1.634	1.479	1.634	1.693	1.634	2.2	1.634	4.785	28.721	15.974

Table C-9 Displacement demands of EDS-1 skew bridges (stiffness ratio of longitudinal/transverse =2.0) (Unit: in)

Ductility	Skew 15°		Skew 30°		Skew 45°		Skew 60°		Skew 75°	
	Longi.	Trans.	Longi.	Trans.	Longi.	Trans.	Longi.	Trans.	Longi.	Trans.
2	0.368	0.462	0.339	0.613	0.291	0.794	0.337	1.355	0.803	4.782
3	0.627	0.717	0.577	0.96	0.471	1.19	0.542	2.261	1.277	7.438
4	1.055	1.069	0.87	1.361	0.732	1.644	0.834	3.236	1.765	10.232
5	1.277	1.254	1.194	1.712	1.052	2.111	1.149	4.101	2.322	12.738
6	1.577	1.517	1.483	2.016	1.321	2.577	1.431	4.921	2.829	15.562

Table C-10 Displacement comparison between the EDS-1 skew bridge and their equivalent nonskew bridges (stiffness ratio of longitudinal/transverse =2.0)

Ductility	Skew 15°		Skew 30°		Skew 45°		Skew 60°		Skew 75°	
	Longi.	Trans.	Longi.	Trans.	Longi.	Trans.	Longi.	Trans.	Longi.	Trans.
2	-5.60%	27.80%	-13.20%	33.00%	-25.50%	22.80%	-13.70%	4.30%	105.80%	-2.90%
3	-5.10%	18.20%	-12.60%	36.60%	-28.80%	16.60%	-18.00%	10.10%	93.30%	-5.10%
4	7.50%	21.40%	-11.30%	32.60%	-25.40%	12.90%	-15.00%	6.70%	79.90%	-3.70%
5	-4.20%	5.70%	-10.50%	25.50%	-21.10%	16.10%	-13.80%	2.50%	74.20%	-2.90%
6	-3.50%	2.60%	-9.20%	19.00%	-19.10%	17.10%	-12.40%	2.80%	73.20%	-2.60%

C.2.3 Equal stiffness in the Longitudinal and Transverse Direction

The stiffness in the longitudinal and transverse direction of the skew models was designed to be the same value of 5126.5 kip/in. Dimensions and properties of the skew and nonskew bridge with EDS-1 are tabulated in Table C-11. Only models of bridges with skew angles up to 30 degree can be designed. The BRBs' steel cores have the yielding strength of 42 ksi and the yield length ratio of the steel core's length over the entire length is 1.0. The equivalent nonskew bridges of the skew bridges were also built and their properties are tabulated in Table C-12.   The BRBs' steel cores have different yielding strength as tabulated in Table C-12 and the yield length ratio of the steel core's length over the entire length is 1.0.

Table C-13 shows the displacement demands of the EDS-1 equivalent nonskew bridges in Table C-12. Since the nonskew bridge in Table C-11 and the longitudinal directions of all the nonskew equivalent bridges in Table C-12 have the same yield displacement and yield strength as the nonskew bridge in Table C-1, the displacement demands are the same too. The equivalent nonskew bridges are presented by the skew angle of its corresponding skew bridges.

Table C-11 Properties of benchmark simplified EDS-1 skew and nonskew bridges (equal stiffness in the longitudinal and transverse direction)

Skew Angle (Degree)	0	15	30
First translational period T_1 (s)	0.20	0.22	0.25
Second translational period T_2 (s)	0.20	0.17	0.12
Longitudinal BRB Cross Sectional Area (in²)	9.00	9.00	9.00
Skew BRB Cross Sectional Area (in²)	9.00	10.22	17.01
Global Yielding Displacement in longitudinal directions (in)	0.209	0.209	0.209
Global Yielding Displacement in transverse directions (in)	0.209	0.233	0.361
Global Yielding Strength in longitudinal direction (kips)	1069.1	1069.1	1069.1
Global Yielding Strength in Transverse direction (kips)	1069.1	1193.2	1851.8

Table C-12 Properties of benchmark simplified EDS-1 nonskew equivalent bridges (equal stiffness in longitudinal and transverse directions)

Corresponding Skew Angle (Degree)	15	30
First translational period T_1 (s)	0.20	0.20
Second translational period T_2 (s)	0.20	0.20
Longitudinal BRB Cross Sectional Area (in²)	9.00	9.00
Skew BRB Cross Sectional Area (in²)	9.00	9.00
Longitudinal BRB core yield strength (ksi)	42.00	42.00
Transverse BRB core yield strength (ksi)	46.87	72.75
Global Yielding Displacement in longitudinal directions (in)	0.209	0.209
Global Yielding Displacement in transverse directions (in)	0.233	0.361
Global Yielding Strength in longitudinal direction (kips)	1069.1	1069.1
Global Yielding Strength in Transverse direction (kips)	1193.2	1851.8

Table C-13 Displacement demands of the EDS-1 equivalent nonskew bridges (equal stiffness in longitudinal and transverse directions) (Unit: in)

Ductility	Skew angle of corresponding skew bridge (degree)			
	Equivalent nonskew 15°		Equivalent nonskew 30°	
	Longi.	Trans.	Longi.	Trans.
2	0.390	0.434	0.390	0.674
3	0.66	0.735	0.66	1.141
4	0.981	1.089	0.981	1.688
5	1.333	1.482	1.333	2.297
6	1.634	1.815	1.634	2.815

The displacement demands of the skew bridges are shown in Table C-14 in both longitudinal and transverse directions. Table C-15 compares skew bridges' displacement demands in both directions (Table C-14) to the equivalent nonskew bridges (Table C-13), and the difference in both the longitudinal and transverse direction is shown in percentages. The displacement difference of skew bridge of 30 degrees is larger than the one of 15 degrees in the longitudinal direction, and smaller in the transverse direction.

Table C-14 Displacement demands of EDS-1 skew bridges (equal stiffness in longitudinal and transverse directions) (Unit: in)

Ductility	Skew 15°		Skew 30°	
	Longi.	Trans.	Longi.	Trans.
2	0.434	0.424	0.882	0.615
3	0.706	0.69	1.427	1.016
4	1.024	0.999	1.87	1.468
5	1.338	1.371	2.299	1.886
6	1.6	1.712	2.716	2.38

Table C-15 Displacement comparison between the EDS-1 skew bridge and their equivalent nonskew bridges (equal stiffness in longitudinal and transverse directions)

Ductility	Skew 15°		Skew 30°	
	Longi.	Trans.	Longi.	Trans.
2	11.28%	-2.50%	126.10%	-8.80%
3	6.97%	-6.10%	116.10%	-10.90%
4	4.38%	-8.20%	90.60%	-13.00%
5	0.38%	-7.50%	72.40%	-17.90%
6	-2.08%	-5.60%	66.30%	-15.50%

C.2.4 Equal Strength in the Longitudinal and Transverse Direction

The strength in the longitudinal and transverse direction of the skew models were designed to be 5126.5 kips. Dimensions and properties of the skew and nonskew bridge with EDS-1 are tabulated in Table C-16. Only bridges with skew angles up to 45 degree can be built. The BRBs' steel cores have the yielding strength of 42 ksi and the yield length ratio of the steel core's length over the entire length is 1.0. The equivalent nonskew bridges of the skew bridges were also built and their properties are tabulated in Table C-17. The BRBs' steel cores have different yielding strength as tabulated in Table C-17 and the yield length ratio of the steel core's length over the entire length is 1.0.

Table C-16 Properties of benchmark simplified EDS-1 skew and nonskew bridges (equal strength in longitudinal and transverse directions)

Skew Angle (Degree)	0	15	30	45
First translational period T_1 (s)	0.20	0.23	0.27	0.35
Second translational period T_2 (s)	0.20	0.18	0.15	0.14
Longitudinal BRB Cross Sectional Area (in²)	9.00	9.00	9.00	9.00
Skew BRB Cross Sectional Area (in²)	9.00	9.16	9.72	11.02
Global Yielding Displacement in longitudinal directions (in)	0.209	0.209	0.209	0.209
Global Yielding Displacement in transverse directions (in)	0.209	0.231	0.313	0.521
Global Yielding Strength in longitudinal direction (kips)	1069.1	1069.1	1069.1	1069.1
Global Yielding Strength in Transverse direction (kips)	1069.1	1069.1	1069.1	1069.1

Table C-17 Properties of benchmark simplified EDS-1 nonskew equivalent bridges (equal strength in longitudinal and transverse directions)

Corresponding Skew Angle (Degree)	15	30	45
First translational period T_1 (s)	0.21	0.24	0.32
Second translational period T_2 (s)	0.20	0.20	0.20
Longitudinal BRB Cross Sectional Area (in²)	9.00	9.00	9.00
Skew BRB Cross Sectional Area (in²)	8.13	6.00	3.60
Longitudinal BRB core yield strength (ksi)	42.00	42.00	42.00
Transverse BRB core yield strength (ksi)	46.52	63.00	105.00
Global Yielding Displacement in longitudinal directions (in)	0.209	0.209	0.209
Global Yielding Displacement in transverse directions (in)	0.231	0.313	0.521
Global Yielding Strength in longitudinal direction (kips)	1069.1	1069.1	1069.1
Global Yielding Strength in Transverse direction (kips)	1069.1	1069.1	1069.1

Table C-18 shows the displacement demands of the EDS-1 equivalent nonskew bridges in Table C-17. Since the nonskew bridge in Table C-16 and the longitudinal directions of all the nonskew equivalent bridges in Table C-17 have the same yield displacement and yield strength as the nonskew bridge in Table C-1, the displacement demands are the same too. The equivalent nonskew bridges are presented by the skew angle of its corresponding skew bridges.

The displacement demands of the skew bridges are shown in Table C-19 in both longitudinal and transverse directions. Table C-20 compares skew bridges' displacement demands in both directions (Table C-19) to the equivalent nonskew bridges (Table C-18), and the difference in both the longitudinal and transverse direction is shown in percentages. The displacement difference of skew bridge of 30 degrees is larger than the one of 15 degree in the longitudinal direction, and smaller in the transverse direction for ductility 5 and 6.

Table C-18 Displacement demands of the EDS-1 equivalent nonskew bridges (equal strength in longitudinal and transverse directions) (Unit: in)

Ductility	Skew angle of corresponding skew bridge (degree)			
	Equivalent nonskew 15°		Equivalent nonskew 30°	
	Longi.	Trans.	Longi.	Trans.
2	0.390	0.425	0.390	0.505
3	0.66	0.686	0.66	0.819
4	0.981	1.034	0.981	1.261
5	1.333	1.413	1.333	1.763
6	1.634	1.764	1.634	2.256

Table C-15 and C-20 each represents the displacement difference of the skew bridge from its corresponding equivalent nonskew bridges in both directions. The skew bridges that were designed to have the equal stiffness and strength in Chapter 7 also were analyzed and the responses were also compared between the skew and equivalent nonskew bridges. These three design principles are named as "same stiffness", "same strength", and "same stiffness and strength" for the bridge comparisons in Section C.2.3, C.2.4 and Chapter 7, to distinguish between each other. For skew bridges, the longitudinal displacement difference for the case of "same stiffness and strength" is mostly the smallest, except for

ductility 2 for skew bridge of 15 degrees. The difference in the transverse direction for "same stiffness and strength" is generally between the case of "same stiffness" and "same strength".

Table C-19 Displacement demands of EDS-1 skew bridges (equal strength in longitudinal and transverse directions) (Unit: in)

Ductility	Skew 15°		Skew 30°	
	Longi.	Trans.	Longi.	Trans.
2	0.411	0.423	0.562	0.561
3	0.69	0.69	0.902	0.902
4	1.002	0.994	1.258	1.29
5	1.311	1.363	1.561	1.663
6	1.583	1.684	1.883	2.033

Table C-20 Displacement comparison between the EDS-1 skew bridge and their equivalent nonskew bridges (equal strength in longitudinal and transverse directions)

Ductility	Skew 15°		Skew 30°	
	Longi.	Trans.	Longi.	Trans.
2	5.40%	-0.50%	44.10%	11.10%
3	4.40%	0.50%	36.60%	10.20%
4	2.10%	-3.90%	28.20%	2.20%
5	-1.70%	-3.60%	17.10%	-5.60%
6	-3.10%	-4.50%	15.30%	-9.90%

APPENDIX D   Thermal effect on low-cycle fatigue of BRBs

Luna Ngeljaratan, Xiaone Wei

Section D1 Introduction

D1.1   General

Buckling Restrained Braces (BRBs) are structural components having the ability to provide stable and reliable dissipation of seismic energy through high hysteretic deformations and having large ductility capacity. The main characteristic of BRBs is that they are expected to yield but not buckle either in tension or compression, which makes them highly suitable for dissipating and absorbing energy during earthquakes. There exists many manufacturers of BRBs delivering devices having different designs, but generally their components remains fairly consistent. The main component of BRBs is a yielding steel core plate, resisting the axial force developed in the brace. A casing, typically provides the buckling restraining mechanism against flexural buckling of the yielding core. Finally, a separation gap or de-bonding agent is placed between the steel core and the restraining part, to ensure independent axial deformation of the yielding steel core relative to the restraining part.

Primary BRBs applications to date in US have been in buildings. In bridges, prior research has considered the use of BRBs in trusses and in slab-on-girder bridges, as ductile diaphragms. A design of diaphragms to avoid buckling of diaphragm members was recommended by Itani and Rimal (1996) as well as Zahrai and Bruneau (1998). Tests of BRBs in ductile diaphragm were conducted by Carden et al (2006). Further studies of BRB as ductile diaphragm to resist bidirectional earthquake excitations were conducted by Celik and Bruneau (2011; 2009) proposing BRBs to be connected to abutment, either at the bearing level (on the horizontal side) or on the vertical side. Such an application would require the BRB to span across an expansion joint, and thus be designed to accommodate bridge thermal movements.

In this latter application, BRBs connected to abutments and crossing expansion joints should not only designed to resist significant forces from seismic excitations but would also be expected to expand or contract as a consequence of thermal movements of the bridge. This can be accommodated by various design approaches, but one approach is simply to design the BRB core to undergo those movements without developing low cycle failure. Such expansion and contraction of BRBs due to thermal movements of the bridge following the ambient temperature changes at a specific bridge location would produce cyclic thermal stresses and strains, and the design intent would be to prevent

low-cycle fatigue of the BRB over the design life of bridge, recommended to be taken as 75 years by AASHTO (AASHTO 2012).

A few studies have investigated the fatigue performance of BRBs. In particular, Takeuchi et al (2008), Usami et al (2011) and Wang et al (2012) proposed formulas to predict the energy and deformation capacities of BRBs as well as techniques to improve their low-cycle fatigue. These previous works have not explicitly addressed the low-cycle fatigue demands for BRBs in bridge applications spanning expansion joints and affected by bridge thermal expansion.

The objective of this study was to determine the length of BRBs required to prevent their potential failure due to low-cycle fatigue when they are installed longitudinally across the expansion joint of a bridge and subjected to a history of displacement corresponding to the bridge thermal movements. The target performance is to ensure that the BRBs have a fatigue life exceeding the 75 years design life required by AASHTO. To accomplish this objective, a parametric study was conducted to estimate the low-cycle fatigue life of BRBs due to thermal deformation using temperature data in selected locations across US.

D 1.2   Scope of Work

The scope of work for this study was as follows:

1. Investigate existing and alternative methods capable of estimating fatigue life of steel, specially focusing on the prediction of low-cycle fatigue life of constructional steel.
2. Develop formulas to calculate thermal strains in BRB installed across bridge expansion joints, considering BRB deformation due to thermal expansion considering various analytical assumptions.
3. Evaluate available computer programs to calculate low-cycle fatigue life.
4. Perform low-cycle fatigue life of BRBs installed across bridge expansion joint, considering the temperature variation histories of a number of cities, and different BRB installation temperature, only considering BRB axial strains.
5. Develop a calibration factor for assumed material type of BRB to further investigate the influence of local buckling on BRB fatigue life, using the data from previous BRB experiments.

D 1.3   Organization

This appendix contains six sections, a list of references and three sub appendices, organized as follows. Section D2 briefly describes Buckling-Restrained Braces (BRBs) applications as ductile end diaphragm in bridges and provides a review of low-cycle fatigue principles and theories that would be used in the study of BRBs low-cycle fatigue. Section D3 presents the research

methodology used in this study, together with examples of analysis conducted to assess the fatigue life of BRBs. Section D4 presents a summary of the results obtained on the low-cycle fatigue of BRBs following the method described in Section D3. Section D5 presents the development of a calibration factor necessary to consider the additional strains due to the possibility of local buckling of BRBs which were neglected in estimating fatigue life in Section D4. Section D6 presents the summary of the work and the key conclusions of the study. Sub appendices A and B present detailed results on the low-cycle fatigue life of BRBs estimated using the methods provided in Section D3 for all locations selected for this study. Sub appendix C provides calibration examples for the software used in estimating low-cycle fatigue.

Section D2 Literature Review

D 2.1   Introduction

This section presents a brief description of Buckling-Restrained Braces (BRBs) applications as ductile end diaphragm in bridges and a review of low-cycle fatigue principles and theories that would be used in the study of their low cycle fatigue. This includes descriptions of the various methods for cycle counting and low-cycle fatigue assessments (particularly considering the effect of mean stresses in such calculations). Stress-strain hysteretic models are explained briefly. The methods to predict fatigue lives are reviewed and the linear-cumulative damage procedure is also explained. A brief summary is given at the end of the section explaining the rationale for the selected method used in the research presented in this appendix.

D 2.2   Buckling Restrained Braces (BRBs)

Buckling-restrained braces (BRBs) are a hysteretic-energy dissipation device that can be attached to a structure in order to absorb and to dissipate energy during earthquakes through their cyclic inelastic deformation. However, in North America, they are typically designed as conventional yielding steel structural members, rather than damper.   To date, BRBs as an energy dissipation system have been implemented in buildings (Aiken et al. 2002; Black et al. 2004; Clark et al. 1999; Di Sarno and Manfredi 2010; Fahnestock et al. 2007; Huang et al. 2000; Kiggins and Uang 2006; Kim and Choi 2004; López and Sabelli 2004; Maley et al. 2010; Sabelli et al. 2003; Saeki et al. 1995; Watanabe et al. 1988; Xie 2005) as well as bridges. In bridges, BRBs were initially foreseen to be useful in ductile-end diaphragm in straight bridges and trusses to resist transverse direction earthquake excitation and have been implemented as such in a few bridges.

D 2.2.1 BRBs as Ductile-end Diaphragm on Bridges

In bridge superstructure, diaphragms or cross frames are constructed to transfer the loads from bridge deck to base plate of girder then to bridge supports (bearings). Diaphragms also provide lateral stability during bridge construction. They are generally categorized as intermediate and end diaphragms based on their location along the bridge span. In conventional (non-seismic) design specifications for bridges, the requirements for the design of diaphragm are generally limited to the mention that diaphragms should be installed at a distance less than 25 ft, without any detailed specifications for their strength or stiffness (AASHTO (1992),. In seismic applications, observations made by Itani and Rimal (1996) as well as Zahrai and Bruneau (1998) demonstrate than an adequate design of diaphragms (particularly end diaphragms) is required to transfer lateral seismic loads from bridge decks to supports. Most of the seismic loads are carried by the end diaphragms before they are transferred to support. No recognizing this significant load path can lead to buckling or yielding of the diaphragm members and other consequent bridge damage.

Studies were conducted to develop ductile design of diaphragms by using ductile systems such as shear panels, eccentrically braced frames, triangular-plate added damping, stiffness devices and BRBs (Carden et al. 2006; Zahrai and Bruneau 1999). The application of BRBs as ductile diaphragm was first introduced in straight bridges as a structural fuse to resist seismic loads applied in the transverse direction of the bridge. Carden et al (2006) studied such implementation and reported good axial hysteretic behavior of BRBs. As typically the case in BRBs, the observed BRB compression strength was typically 10–15% higher than tension strength.

The ductile diaphragm concept using BRBs was further developed to make it applicable to resist bidirectional earthquake excitation (Celik and Bruneau 2009). Celik and Bruneau proposed two configurations of end diaphragm system for straight bridges, namely Retrofit Scheme-1 (RS-1) and Retrofit Scheme-2 (RS-2). In RS-1, two pairs of BRBs were installed at each end of a span in a configuration that coincided with the transverse and longitudinal directions. As for RS-2, a single pair of BRBs was installed at each end of a span at an angle that did not coincide with the bridge longitudinal and transverse directions. The results obtained by Celik and Bruneau showed that the proposed configurations were able to resist both transverse and longitudinal seismic effects. This work was then expanded (Celik and Bruneau 2011) to address applications in skewed bridges. The results also demonstrated the possible benefit of using BRBs as ductile seismic fuses in skewed bridges.

The pair of longitudinal BRBs in straight or skewed bridges introduced by Celik and Bruneau (2011; 2009) were proposed to be connected to abutment, either at the bearing level (on the horizontal side) or on the vertical side. Celik and Bruneau recommended that BRBs be connected to the

abutment in series with lock-up devices to allow thermal expansion under normal conditions, but engaged the BRBs during earthquakes; they also noted that the lock-up devices might be neglected if the BRB could be properly sized to accommodate the thermal expansion or contractions of bridges.

D 2.2.2 Fatigue of BRBs

BRBs attached to bridges, oriented in their longitudinal direction and crossing expansion joints, should not only be designed to resist significant forces from seismic excitations but also be expected to experience expansion and contraction as a consequence of thermal movements of the bridge. Under thermal movements, the effective equivalent stress in the yielding core of BRBs may exceed its yield stress (σ_y), which indicates that low cycle fatigue life may be a concern. When failure of steel occurs under repeated displacement cycles at less than 10^4 cycles, this phenomenon is called low-cycle fatigue (Coffin Jr 1962; Lemaitre et al. 1999; Libertiny 1968). Within this displacement regime, the failure mechanism is typically governed by a plastic response sometimes called ductile damage (Libertiny 1968). ASTM E-1049 (2011) defines fatigue life, N_f, as the number of cycles of stress or strain sustained by a material before it fails. In this current study on BRBs in bridge applications, ideally, low-cycle fatigue life should exceed the 75 years of bridge design life specified by ASSHTO (2012) – although, alternatively, plans could be made to periodically replace BRBs having shorter low-cycle fatigue life.

Up to now, only few studies (such as Takeuchi et al (2008), Usami et al (2011) and Wang et al (2012)) have investigated the low cycle fatigue of BRBs. Takeuchi et al (2008), proposed equations to predict the cumulative absorbed energy and deformation c pacities of BRBs based on assumption on their bilinear hysteretic behavior. Usami et al (2011) and Wang et al (2012) conducted experiments to show improvement in the low cycle fatigue performance of BRBs by smoothing the weld toes at both ends of the BRBs (toe-finished method).

However, no study has specifically addressed the low-cycle fatigue of BRBs in bridge applications spanning expansion joints and affected by bridge thermal expansion. As a first step, existing analysis method and general theories of fatigue can be used in a parametric study to provide the low cycle fatigue information needed for the design of BRBs in such applications. The following sections summarize some of the principles commonly used in low-cycle fatigue life assessments.

D 2.3   Fatigue Analysis

D 2.3.1 Fatigue Life Approach

There are at least three approaches commonly used to quantify the fatigue behavior of materials and evaluate fatigue life, namely: (1) the Stress-Life model, commonly known as the

Basquin model (Basquin 1910); (2) the Strain-Life model (Coffin 1954; Manson 1953), and; (3) the energy-based approach (Ellyin and Xia 1993). The Stress-Life approach is also known as the high-cycle fatigue approach and the Strain-Life approach is known as the low-cycle fatigue approach. The Strain-Life approach is suitable for materials subjected to fluctuating stresses greater than the yield stress and causing plastic failure mechanisms Suresh (1998); therefore, it is the approach suitable for the current study on BRBs.

The fatigue life of materials estimated using the Strain-Life approach can be expressed in the form of Strain-Life curve defined in terms of a number of material constants, such as the modulus of elasticity (E), the fatigue strength coefficient(σ_f'), the fatigue strength exponent (b), the fatigue ductility coefficient (ε_f'), the fatigue ductility exponent (c), the cyclic strength coefficient (K') , and the cyclic strain hardening exponent (n'). In this study, the material used for the BRBs was assumed to be ASTM A36. The material properties of ASTM A36 taken in this study were: elastic modulus (E) = 200000 MPa, fatigue strength coefficient (σ_f') = 1014 MPa, fatigue strength exponent (b) =-0.132, fatigue ductility coefficient (ε_f') = 0.271, fatigue ductility exponent (c) = -0.451, cyclic strength coefficient (K') = 1097, and cyclic strain hardening exponent (n')= 0.249 (Higashida et al. 1978). The method used to construct the corresponding Strain-Life curve for this material is presented in Section D3.4.

D 2.3.2 Loading Type

In this study, the low cycle fatigue life of BRBs is a consequence of thermal expansions or contractions of bridges resulting in strains on BRBs, and calculated from actual recorded daily and average temperatures (AccuWeather 2012) for selected locations. The chosen locations as well as the detailed procedures to generate the thermal strain of BRBs from recorded temperature are given in Section D3.5. However, note that the strain histories generated from those temperature changes are characterized as variable amplitude strain loading because the strain ranges (or amplitudes) change in each cycle instead of being of constant amplitude. There exists many references addressing cyclic stress-strain response and fatigue life estimation under variable amplitude loading (Dowling 1971; Polak and Klesnil 1979). Most reviewed by Dowling (1971) who summarized the methods for fatigue life prediction under variable amplitude loading, with an emphasis on the method to perform cycle counting as well as to generate stress-strain hysteresis loop. These are summarized below.

D 2.3.3 Cycle Counting

The first step in fatigue analysis of material subjected to variable amplitude loading consists of breaking the loading history into individual cycles. ASTM E1049 (2011) standardizes the

procedures to obtain such cycles according to various methods, which include level-crossing counting, peak counting, simple-range counting, range-pair counting, and rainflow counting. Dowling (1971) mentioned that the results from the range pair and rainflow counting methods are more appropriate as they also consider the small cycles that contribute to calculation of damages, and indicated that all of the counting methods, with the exception of the range pair and rainflow methods, have been shown to have significant weaknesses.

Ellyn (1993) described that, for uniaxial load, most established fatigue damage parameters were calculated from the cycles identified from the hysteretic loops. The proper method which identified these hysteretic loops within a load, stress, or strain history was Rainflow Counting. This method was first introduced in 1968 by Matsuishi and Endo (1968). In the Rainflow Counting method, cycles are extracted from the variable amplitude loading where each cycle is associated with a closed stress-strain hysteretic loop. This method provides a good representation for cyclic stress-strain response obtained from variable amplitude loading (Polak and Klesnil 1979). The details of the procedure and an example of Rainflow Counting method are given in Section D3.10.1.

D 2.3.4 Stress-Strain Relationship

D 2.3.4.1   Ramberg-Osgood Relationship

A number of hysteretic models have been developed to represent the cyclic behavior of materials. Two commonly categories of models are polygonal hysteretic models and smooth hysteretic models (Sivaselvan and Reinhorn 2000). Among the smooth hysteretic models, some popular ones include the Bouc-Wen model (1967; 1976), the Ozdemir model (1976) and the Ramberg–Osgood model (1943). The Ramberg-Osgood model is a simple mathematical model that can provide a good approximation for stress-strain relationship (Sivaselvan and Reinhorn 2000). One of advantages of this model is its ability to describe hysteretic behavior even when a material is below yielding (Segal and Val 2006). This model exhibits a nonlinear behavior from the beginning (i.e., from zero stress-force level) and forms hysteretic loop under reversal loading from any amplitude. It consists of a power law relation between stress and total strain in which the total strain consists in the sum of elastic and plastic strains. The Ramberg-Osgood relationship is generally represented by the equation below:

$$\varepsilon = \frac{\sigma}{E} + \left(\frac{\sigma}{K'}\right)^{1/n'} \tag{D2.1}$$

D 2.3.4.2   Masing Model

The Masing model is a simple and an effective tool for understanding and describing the hysteretic behavior of many physical systems, and can be used to predict cyclic stress–strain response

under variable amplitude loading conditions. This model has been applied in the fields of material plasticity (Chiang and Beck 1994; Segal and Val 2006; Skelton et al. 1997), structural dynamics and vibrations (Lee and Royston 2000; Segalman 2005), control systems (Webb et al. 2000) and magnetics (Macki et al. 1993). This model defines the cyclic stress–strain curve obtained by multiplying the monotonic curve by a factor of 2, and accounts for Bauschinger effect (Bauschinger 1886).

Masing (1926) observed that each branch of the hysteresis loop was geometrically similar to the monotonic stress-strain curve with a scale factor of two. Upon unloading and taking peak tensile load as the new origin, each element was required to deform through twice its previous equivalent yield stress ($2\sigma_y$). The tension path of the model followed the compression path resulting in a closed hysteresis loop. However, Masing did not provide a formula for general use (Skelton (1997). Therefore, the Masing model was later modified by Morrow (1965). The resulting Morrow equation (which models the Masing behavior) is given in equation D2.2.

$$\Delta\varepsilon = \frac{\Delta\sigma}{E} + 2\left(\frac{\Delta\sigma}{2K'}\right)^{1/n'} \tag{D2.2}$$

An example of how to generate a hysteresis loop using the Ramberg-Osgood and Masing models is provided in Section D3.10.2.

D 2.3.5 Fatigue Life Prediction

D 2.3.5.1   No Mean Stress Correction Model

The initial Basquin model and Coffin-Manson model mentioned in Section D2.3.1 ignore the effect of mean stress on fatigue behaviors (Lin and Chen 2008); therefore, they are offered referred to as "no-mean stress correction" models. Some researchers supported the use of such models in some applications (e.g., Takao and Endo (1969), when the effect of mean stress is negligible in crack initiation and fatigue process. Previous studies (Maeda et al. 1998; Nakagomi et al. 2000) have showed that such models could be applied to BRB core assuming that plastic strain was generally distributed over the entire length of the core plates, that sufficient strain against buckling was provided, and that the core maintained its positive incremental stiffness after yielding.

Generally, the Basquin model (1910) describes the high-cycle, low-strain regime where the nominal strains were elastic as expressed below:

$$\frac{\Delta\varepsilon_e}{2} = \frac{\sigma_f'}{E}\left(2N_f\right)^b \tag{D2.3}$$

whereas the Coffin (1954) and Manson (1953) equation describes the low-cycle, high-strain regime where the nominal strains are plastic as given below :

$$\frac{\Delta \varepsilon_p}{2} = \varepsilon_f'(2N_f)^c \tag{D2.4}$$

These two regimes of elastic and plastic strains are accumulated to give total strain, providing the basic relation between total strain range and cyclic life given in equation D2.5.

$$\frac{\Delta \varepsilon}{2} = \frac{\Delta \epsilon_e}{2} + \frac{\Delta \varepsilon_p}{2} = \frac{\sigma_f'}{E}(2N_f)^b + \varepsilon_f'(2N_f)^c \tag{D2.5}$$

D 2.3.5.2   Mean Stress Correction Model

It has been recognized that mean stress can have a significant influence on fatigue life and that the fatigue process is sensitive to tensile mean stress in both the high-cycle fatigue and low-cycle fatigue regimes (Stephens et al. 2001; Xia et al. 1996). Dowling (1971) reported that, in stress-strain relationship where relatively large mean stresses were present for a significant number of cycles, the fatigue life could not be adequately predicted without considering the effect of mean stress. For cases with low strain amplitudes (<0.005), fatigue life respectively increases or decreases if the mean stress is compressive or tensile (Koh and Stephens 1991). This was confirmed by several researchers (Arcari and Dowling 2012; Chu and Chernenkoff 2001; Maddox 1975; Saal 1972; Wehner and Fatemi 1991). This is because, under uniaxial loading, the fatigue failure mechanism is due to plane separation and mean compressive stress help prevent the separation of planes.

Several methods for predicting the effect of mean stress in fatigue life have been proposed, such as those by Smith (1942), Stulen (1965), Morrow (1968), Topper and Sandor (1970) and Smith-Watson Topper (1970). The Strain-Life based approach models by Morrow as well as by Smith-Watson and Topper, which are the most popular in simple engineering applications (Ince and Glinka 2011; Kwofie and Chandler 2001), are described below.

D 2.3.5.2.1 Smith Watson Topper (SWT) Model

The Smith Watson Topper model (1970), developed to account for mean stress correction, has been reported to give good results for steel and is often recommended for this purpose (Cui 2002; Dowling 2004). In this model, it is assumed that the product of the maximum tensile stress, σ_{max} and the strain amplitude ε_a controls and that a constant fatigue life is obtained if this product remains constant. The Smith Watson Topper model is expressed by the given equation below :

$$\sigma_{max}\varepsilon_a = \frac{(\sigma_f')^2}{E}(2N_f)^{2b} + \varepsilon_f'\sigma_f'(2N_f)^{b+c} \tag{D2.6}$$

where σ_{max} is the maximum stress of a given cycle and $2N_f$ is the number of fatigue life reversals. Note that this method will predict an infinite fatigue life if the maximum tensile stress is zero or negative.

D 2.3.5.2.2 Morrow Model

The Morrow model (1968) assumes that the mean stress had a more significant effect on fatigue life when cycles of elastic strain amplitude dominate. In this model, the mean stress only affects the elastic portion of the strain life. The Morrow model is expressed in the equation below :

$$\frac{\Delta\varepsilon}{2} = \frac{\sigma_f' - \sigma_m}{E}\left(2N_f\right)^b + \varepsilon_f'\left(2N_f\right)^c \tag{D2.7}$$

where σ_m is the mean stress of a given cycle and $2N_f$ is the fatigue life reversals. As is the case for the Smith Watson Topper model, Dowling (2004) also reported that the Morrow mean stress correction is suitable for steel.

D2.3.6 Cumulative Fatigue Damage

Cumulative fatigue damage analysis plays a fundamental role in predicting the fatigue life of materials subjected to variable load histories. Fatemi and Yang (1998) summarized the existing fatigue damage models principally used between the 1970s and 1990s and categorized them into six major model categories, namely: (1) linear damage and linear summation models; (2) nonlinear damage and two-stage linearization models; (3) life curve modification models; (4) crack growth based models; (5) continuum mechanics based models, and; (6) energy-based models. Among these model, the linear damage model which was first proposed by Palmgren (1924) and later mathematical expressed as a linear damage rule by Miner (1945) is the simplest to predict the fatigue life of components subjected to irregular or variable-amplitude loading (Hashin 1980; Johannesson et al. 2005; Lutes and Larsen 1990; Okamura et al. 1979; Svensson 1997; Wu et al. 1997). For steel structures and materials, this method has been popular and used in fatigue life assessment for steel bridges (Li et al. 2001) and to estimate damage accumulation in steel sheets and bars under uniaxial random loading test (Łagoda 2001). This concept had been widely applied in Stress-life approaches; however, it has also been commonly applied to Strain-Life approaches (Takeuchi et al. 2008). As such, the Palmgren-Miner's rule remain widely used in industry and design practice (Taheri et al. 2013; Wirsching and Shehata 1977).

In Palmgren-Miner's model, the damage given by each cycle in a strain history is considered by assuming that percentage of damage contributed by a specific range is independent from that produced over other ranges. Consequently, the failure condition of a material subjected to variable amplitude loading is calculated using equation D2.8. For example, if a material is subjected to a certain number of cycles (or stress reversals) n_i of stress amplitude s_i, and the total number of stress cycles to produce failure at that given amplitude level is N_{fi}, then the material has attained a partial fatigue damage of $D_i = n_i/N_{fi}$. For other stress amplitudes, other partial damage contributions can

be calculated, and summed to produce a total accumulated damage of D, as expressed by equation D2.8.

$$D = \sum_{i=1}^{N} \frac{n_i}{N_{fi}} = 1 \tag{D2.8}$$

It is assumed that failure occurs when $D = 1$. The accuracy of the Palmgren-Miner's rule has often being questioned (Ibrahim and Miller 1979; Miller and Ibrahim 1981; Miller et al. 2013; Miller and Zachariah 1977). First, the assumption that damage accumulates proportionally at all stress levels was deemed to be simplistic, but tests have shown that it is conservative. Second, for high-cycle fatigue, the Palmgren Miner's rule fails to consider damage that may accumulate when damage induced during large amplitude cycles further increases during cycles of amplitude below the fatigue limit (when using a fatigue life curve that has been developed for constant amplitude cycles), which can result in over-estimated life prediction. The consequence of this second issue had been demonstrated in many applications and compensating safety factors are typically used in practical applications to account for this shortcoming (Fatemi and Yang 1998; Gurney 1992; Todinov 2001). However, this is of little consequence in low-cycle fatigue, and usefulness of the simple analytical criterion remains of considerable value (Sobczyk 1987) and is suitable for the applicable considered in this report.

D 2.4 Summary

The application of BRBs in ductile diaphragms of straight or skewed bridges has been shown to provide good hysteretic behavior under seismic load. BRBs oriented in the longitudinal direction of a bridge and crossing an expansion joint could be subjected to low cycle fatigue failure as they experience strains due to the thermal expansion and contractions of the bridge. Therefore, a study is necessary to provide information regarding the low-cycle fatigue life of BRBs and design recommendations in such applications.

The low-cycle fatigue life of BRBs should be calculated using a Strain-Life approach. Considering that the thermal strain history in BRBs would be a variable amplitude loading, strain cycles would be computed using a Rainflow Counting method and the cyclic hysteresis model needed to compute this fatigue life would be generated using Ramberg-Osgood and Masing models. The fatigue life of BRBs can be estimated either by considering or neglecting the mean stress effect (for comparison purposes). The damage caused by cycles at each amplitude can be accumulated using a Palmgren-Miner's rule. Fatigue life is achieved when this damage is equal to 1.0.

Section D3 Methodology

D 3.1 General

The objective of this study was to determine the length of BRBs required to prevent their potential failure due to low-cycle fatigue when they are installed longitudinally across the expansion joint of a bridge and subjected to a history of displacement corresponding to the bridge thermal movements. The target performance is to ensure that the BRBs have a fatigue life exceeding the 75 years design life required by AASHTO. The purposes of this section are to (1) describe the procedure used in collecting the temperature data; (2) describe the research methodology used in this study; and (3) provide examples of the analysis conducted to assess the fatigue life of the BRBs and recommended BRB lengths to meet the target performance objective.

D 3.2 Data

D 3.2.1 Temperature Data

A number of cities were arbitrarily chosen for this study. They were chosen to represent a broad cross-section of seismic regions and scenarios of daily and yearly temperature variations. The selected locations within the United States were Anchorage, Alaska; Boston, Massachussets; Charleston, South Carolina; Los Angeles, California; Memphis, Tennessee; Portland, Oregon; San Francisco, California; and Seattle, Washington. Quebec City in Canada was also chosen due to its wide range of temperature variations within a year and significant seismic sources near the city. The maximum and minimum daily temperatures were collected from Accuweather for the arbitrarily chosen year of 2012 (AccuWeather 2012). Average daily maximum and minimum values were also collected for comparison purposes. The recorded temperature used in the study are presented in Figure D3-1.

D 3.2.2 Material Data

The material used for the BRBs was assumed to be ASTM A36, for which data on the fatigue properties was available. No such information could be found on ASTM A572 Gr 42, but it is believed that there are no significant difference in the fatigue resistance properties of constructional steel over the 36 ksi to 100 ksi yield strength range (H. Mitchell, Director of Technical Assistance, American Institute of Steel Construction, personal communication, September 25, 2013); hence, the Sr-N relationship used in this study would be deemed to also apply to all steels including A572 Gr 42, recognizing that larger bridge thermal displacements would be required to exceed the yield strains; as such, results obtained for A36 steels will be conservative when applied to BRBs with yield cores of other steel grades. The material properties of ASTM A36 BM taken in this fatigue life study for

the model described in Section D2.1 were: elastic modulus (E) = 200000 MPa, fatigue strength coefficient (σ_f') = 1014 MPa, fatigue strength exponent (b) =-0.132, fatigue ductility coefficient (ε_f') = 0.271, fatigue ductility exponent (c) = -0.451, cyclic strength coefficient (K') = 1097, and cyclic strain hardening exponent (n')= 0.249 (Higashida et al, 1978).

Seattle, Washington
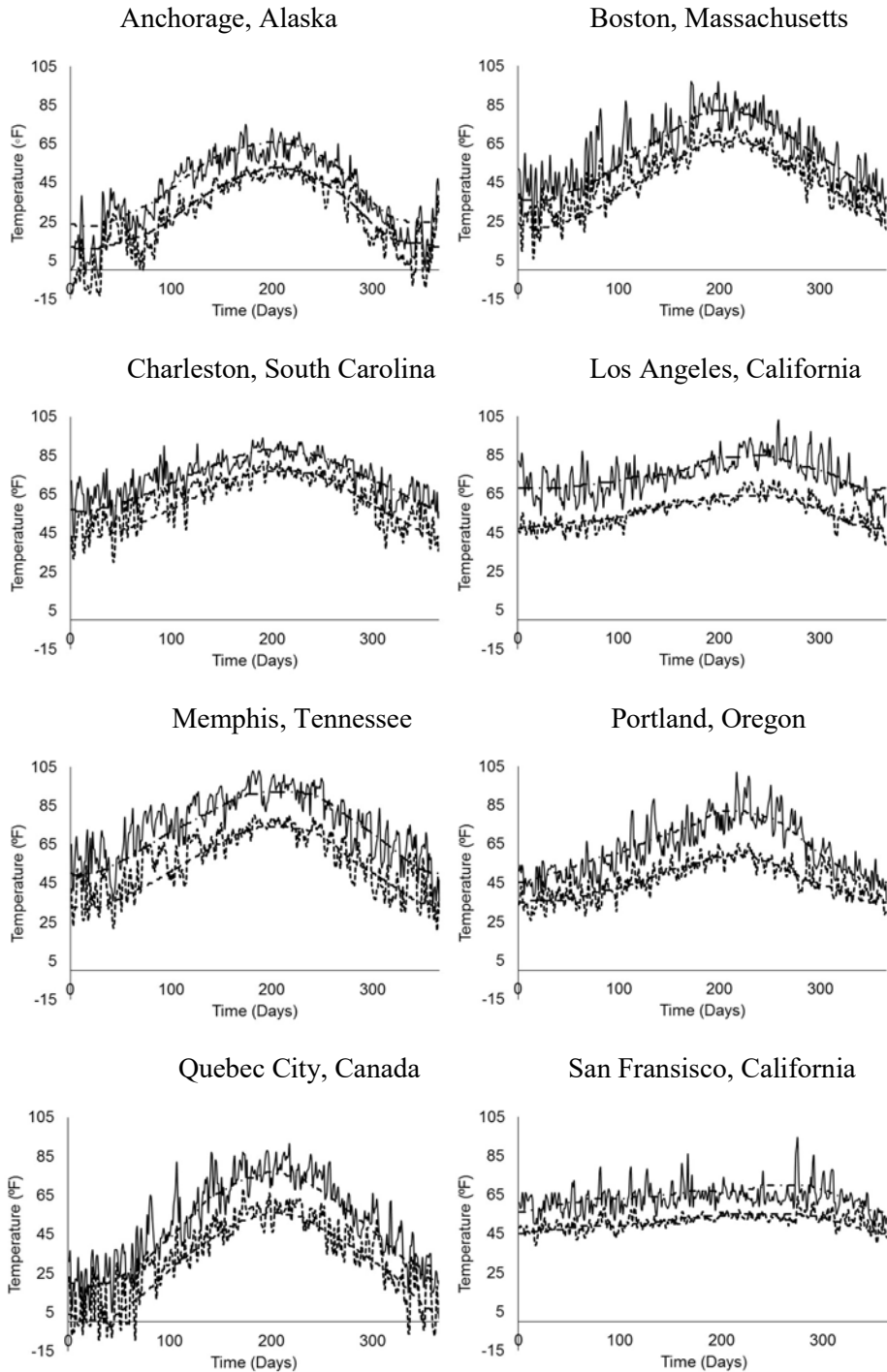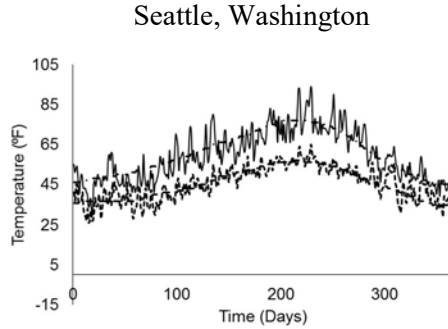
Figure D3- 1 Recorded temperature at selected locations (AccuWeather 2012)

D 3.3   Software

The Fatiga Software–Beta 5 (Fatec Engineering, 2013) was used for conducting the rainflow counting, for calculating the damage produced by each cycle, as well as for estimating the fatigue life of BRB using the proposed method described later in Section D3.6

D 3.4   Strain-Life Curve

The fatigue properties of ASTM A36 were used to generate the Strain-Life curve using the material fatigue parameters presented in Section D2.2 and the equations from Section D2.7. The Strain-Life curve of ASTM A36 is given in Figure D3-2 and the steps to generate it are described below.

The Strain-Life curve provides the relationship between the applied strain amplitude $\left(\frac{\Delta\varepsilon}{2}\right)$ and the fatigue life reversals/reversals to failure $(2N_f)$. In the Strain Life calculations performed here (following the procedure described in Section D2.4), cycles to failure are converted to reversals to failure. One cycle has two reversals; as such, the symbol $2N_f$ is used to represent the fatigue life reversals. To plot the Strain-Life curve, the total strains are first divided into their elastic and plastic parts. Elastic strain amplitude,$\left(\frac{\Delta\varepsilon_e}{2}\right)$, obtained using the Basquin equation described in Section D2.7, is related to $2N_f$ by a linear relationship (in a log-log space) having a slope equal as to the fatigue strength exponent (b), as illustrated by the green line in Figure D3-2. As for plastic strain amplitude $\left(\frac{\Delta\varepsilon_p}{2}\right)$, it is calculated using the Coffin and Manson formula given in Section D2.7, as a linear function of $2N_f$ (again in log-log space) of slope equal to the fatigue ductility exponent (c), as shown by the green line in Figure D3-2. The applied strain amplitude is then obtained by adding the elastic and plastic portions of the strain, this sum corresponding to the red line in Figure D3-2. The life where elastic and plastic components of strain are equal is called the transition fatigue life $(2N_t)$ and for

ASTM A36 it corresponds to 261,100 reversals. Therefore, for lives less than $2N_t$ the deformation is mainly plastic, whereas for lives larger than $2N_t$ the deformation is mainly elastic.

$$2N_t = \left(\frac{\varepsilon_f' E}{\sigma_f'}\right)^{1/(b-c)} = 261100$$
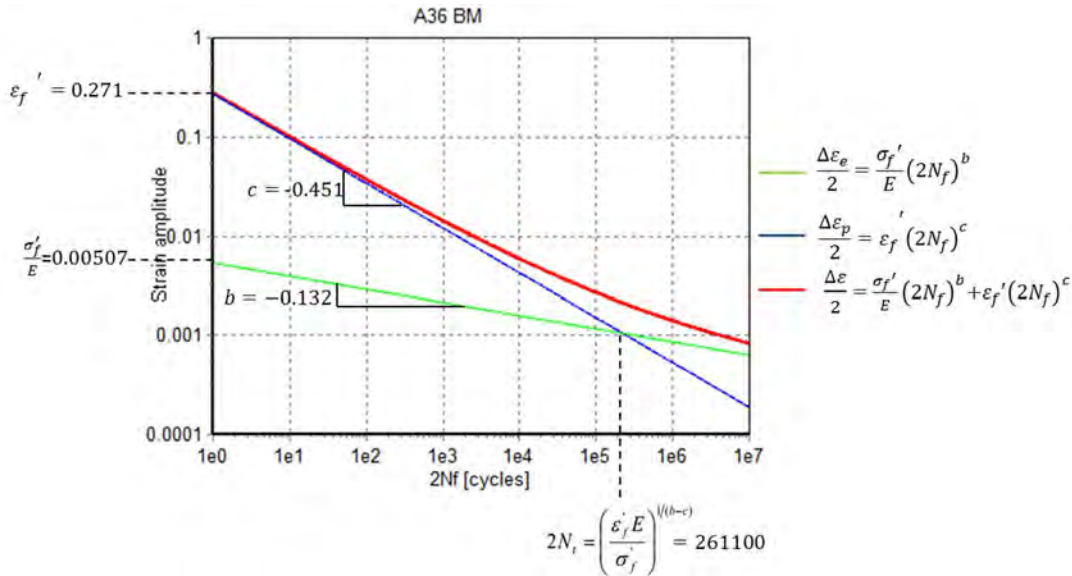
Figure D3-2 Strain-Life curve for ASTM A36

D 3.5 Strain of BRBs

In this study, the bridge superstructure was assumed to be a simply supported steel girder with composite concrete deck, with total span length of L, bridge effective length of L_1 (equal to the distance from the BRB attachment point along the girder to the fixed bearing at the far end of the span), BRB length of L_2, and end-offset length of a, as shown in Figure D3-3. The BRB was installed in the longitudinal direction of the bridge superstructure, connecting the abutment to a point along the bridge girder. The temperature change (Δ_T) was considered uniform along the bridge, and corresponds to the reference temperature (T_r) subtracted by the recorded temperature (T) in one day (a sign convention chosen so that a positive Δ_T would corresponds to tension on the BRB). The reference temperature (T_r) was assumed to be the temperature when the BRB was first installed on the bridge. A number of possible values of T_r were considered in the analyses, ranging between the recorded maximum and minimum temperature at the specific bridge location, and varying by 10°F intervals.
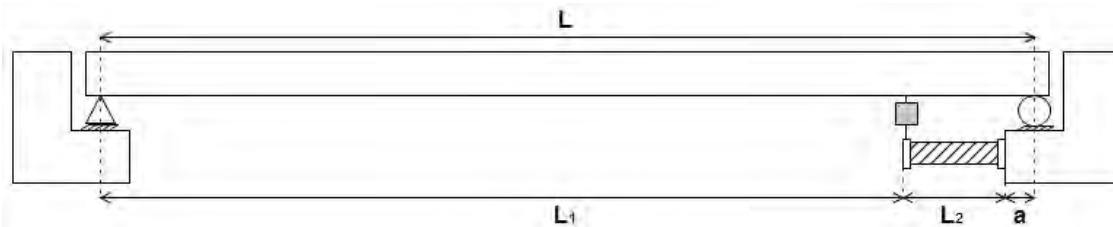
Figure D3-3 BRB connecting the bridge abutment and girder
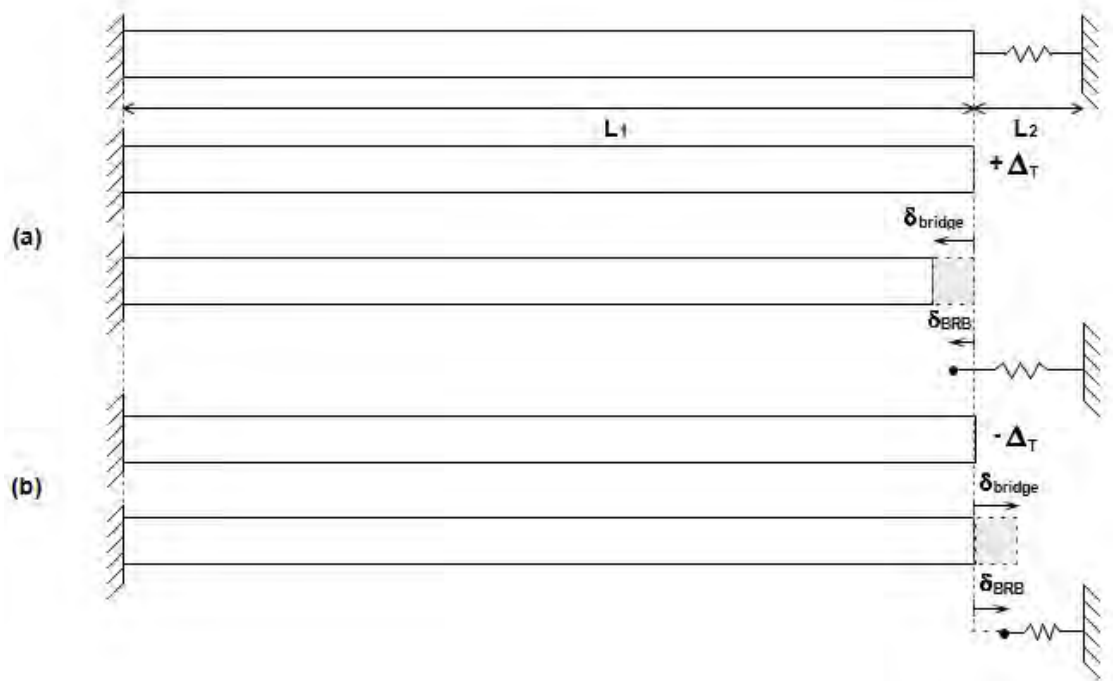
Figure D3-4 Effect of uniform temperature changes at bridge deck on the BRB

Uniform temperature changes (Δ_T) at the bridge cause thermal expansions or contractions on the bridge and BRB, and their effect on the BRB depends on whether the Δ_T is positive or negative. Consider Figure D3-4 where the bridge is free at one end and is subjected to thermal changes Δ_T. Positive Δ_T as shown in Figure D3-4a contracts the bridge with effective length L_1 resulting in elogation on the BRB while negative Δ_T expands the bridge causing the BRB in compression, as shown in Figure D3-4b. Therefore, as the T_r increased, BRB would experience more tensile strains than compressive strains, and vice versa.

To determine the deformation and strain of BRBs due to thermal changes, for the BRB connecting the bridge abutment and girder as shown in Figure D3-3, a number of assumptions are possible. First, the strain in the BRB can be obtained by only considering the displacements due to thermal changes Δ_T of the bridge. More precisely, the effect of thermal changes in deforming the BRB itself can be considered. In this latter case, the stiffness of the BRB would need to be taken into account (considering that the length of the BRB (L_2) consists of its connections, yielding core which was assumed as $0.5\,L_2$, and non-yielding part of the core), as well as its strength, recognizing that the core of the BRB yields at a values of P_y (taken here, for simplicity, to be the product of the yielding core area and its yield stress). Note that thermal changes can cause not only elastic but also plastic deformations on the BRB.

In this section, the BRB thermal deformations in the elastic and plastic ranges are investigated. In each case, expressions are derived considering deformations due to thermal expansion of only the bridge, or both the bridge and BRB. The thermal strain of the BRB (ε_{eq}) is only distributed inside the BRB core with the assumed length of 0.5 L_2 and it can be calculated as:

$$\varepsilon_{eq} = \frac{\delta_{eq}}{0.5\,L_2} = 2\frac{\delta_{eq}}{L_2} \tag{D3-1}$$

where L_2 is the total length of the BRB, and the deformation at equilibrium (δ_{eq}) is the deformation of BRB due to thermal changes. The procedures to generate δ_{eq} are described below. In this study, ratios of $\frac{0.5L_2}{L}$ of 1%, 2%, 3%, 4%, and 5% are considered.

D 3.6   Elastically Calculated Strain History of BRB

D 3.6.1 Case 1: BRB thermal expansion = 0

Consider a BRB subjected to temperature changes (Δ_T) as given in Figure D3-5. As a first approximation, the total span length of bridge, L (equal to $L_1 + L_2$), can be taken to calculate total elongation, rather than adding the BRB elongations to that of the effective length of bridge (which would be equal to the bridge span minus the BRB length, if there was no offset). In this case, thermal expansion of the BRB can be neglected in the analysis. As will be shown in subsequent sections, this expedient approach can provide reasonably conservative results. Note that, here, the offset (a), shown in Figure D3-5a, was taken as zero in all fatigue life calculations, which was equivalent to assuming that span length was equal to the distance to the face of the abutment at the free end, rather than to centerline of the support there.

In this case, the deformation of the BRBs due to thermal changes, as shown in Figure D3-5c, is equal to the expansion of the bridge, and is calculated as:

$$\delta_{eq} = \delta = \alpha_1 \Delta_T L \tag{D3-2}$$

where α_1 is the coefficient of thermal expansion of concrete taken as 0.000006 in/in/°F (Chen and Duan, 2014); and all other parameters have been defined previously. Note that the coefficient of thermal expansion of steel (for the bridge girders) is 0.0000065 in/in/°F (Chen and Duan, 2014), which would have given slightly larger deformations, but the thermal expansion coefficient for concrete was selected based on the arbitrary assumption that the concrete deck cross-section area for the bridge would be larger than the section area of steel girder and may govern thermal elongation. The strain of BRB (ε_{eq}) then can be calculated as given in eq.D3-1.

More precisely, the BRB can be also modeled as an equivalent spring, as shown in Figure D3-6a. The bridge is subjected to Δ_T and the length of the bridge considered deforming due to Δ_T is taken as the effective length L_1, as shown in Figure D3-6.
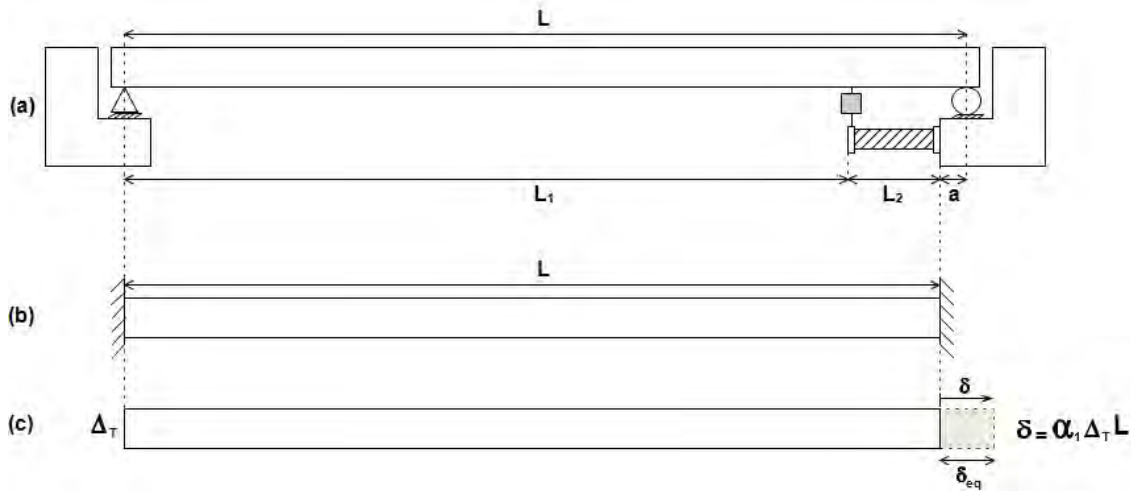
Figure D3-5 Bridge thermal expansion considering the total span L
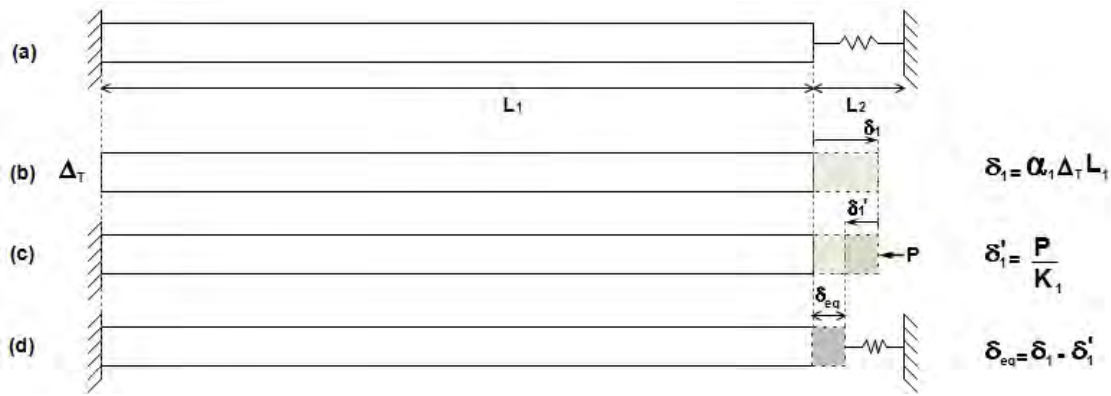
Figure D3-6 Bridge thermal expansion considering the effective span L_1

For this case, the solution can be obtained as follows. First, consider that the free end of the bridge deck is free to deform laterally as shown in Figure D3-6b. Thermal changes (Δ_T) in the bridge result in an expansion of the bridge of δ_1. In this case, deformations of the BRB itself due to Δ_T are neglected; therefore, the BRB's own thermal expansion (δ_2) = 0. Second, due to the bridge stiffness(K_1), an equivalent force (P) pushes the bridge, resisting its thermal expansion, resulting in the lateral deformation δ_1' shown in Figure D3-6c. The deformation at equilibrium is δ_{eq}, given by:

$$\delta_{eq} = \delta_1 - \delta_1'$$
$$= \delta_1 - \frac{P}{K_1}$$

(D3-3)

Since the bridge and BRB are connected in series, the equivalent force P is equal to the total force in the system due to thermal changes:

$$
\begin{aligned}
P &= K_{tot}\delta_1 \\
&= \frac{K_1 K_2}{K_1 + K_2}\delta_1
\end{aligned}
\qquad\text{(D3-4)}
$$

where K_2 is the effective stiffness of BRB. Therefore; the equivalent deformation of the BRB due to thermal changes can be written as :

$$
\begin{aligned}
\delta_{eq} &= \delta_1 - \frac{K_1 K_2}{K_1 + K_2}\delta_1 \frac{1}{K_1} \\
&= \delta_1\left[1 - \frac{K_2}{K_1 + K_2}\right]
\end{aligned}
\qquad\text{(D3-5)}
$$

By substituting equation D3-5 into equation D3-1, the thermal strain of the BRB can be written as:

$$
\varepsilon_{eq} = \frac{\delta_{eq}}{0.5L_2} = 2\alpha_1\Delta_T\frac{L_1}{L_2}\left[1 - \frac{K_2}{K_1 + K_2}\right]
\qquad\text{(D3-6)}
$$

where L_2 is the length of the BRB.

D3.6.2 Case 2: BRB thermal expansion = δ_2

In case 2, thermal changes (Δ_T) are assumed to deform both the bridge and the BRB, producing as δ_1 and δ_2 adding up to a total thermal expansion of δ_{tot}, as shown in Figure D3-7b.
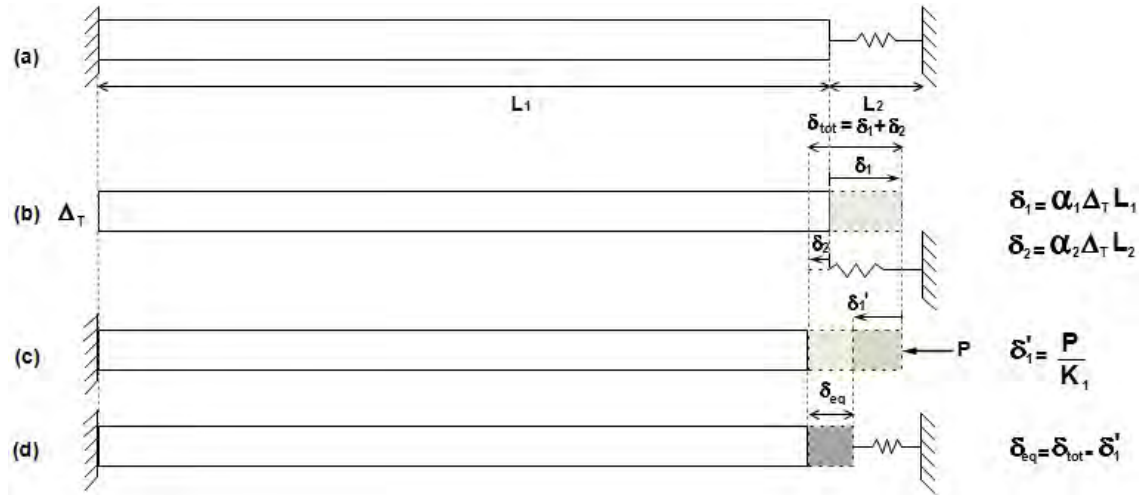
Figure D3-7 Bridge and BRB thermal expansion considering the effective span L_1

From Figure D3-7d the equation for δ_{eq} can be written as:

$$
\begin{aligned}
\delta_{eq} &= \delta_{tot} - \delta_1' \\
&= \delta_{tot} - \frac{P}{K_1}
\end{aligned}
\qquad\text{(D3-7)}
$$

where P is equal to the equivalent force in the system due to total thermal expansions of the bridge and BRB, calculated as :

$$P = K_{tot}\delta_{tot}$$
$$= \frac{K_1 K_2}{K_1 + K_2}\delta_{tot} \tag{D3-8}$$

The deformation at equilibrium then can be written as :

$$\delta_{eq} = \delta_{tot} - \frac{K_1 K_2}{K_1 + K_2}\delta_{tot}\frac{1}{K_1}$$
$$= \delta_{tot}\left[1 - \frac{K_2}{K_1 + K_2}\right] \tag{D3-9}$$

Therefore, the thermal strain of the BRB can be calculated as :

$$\varepsilon_{eq} = \frac{\delta_{eq}}{0.5L_2} = 2\left[\alpha_1 \Delta_T \frac{L_1}{L_2} + \alpha_2 \Delta_T\right]\left[1 - \frac{K_2}{K_1 + K_2}\right] \tag{D3-10}$$

where α_2 is the thermal expansion coefficient of the BRB which is taken as 0.0000065 in/in/°F.

D 3.7   Plastically Calculated Strain History of BRB

D 3.7.1 Case 1: BRB thermal expansion = 0

Similar to Section D3.5.1.1, thermal changes Δ_T are first considered at the bridge deck alone, as shown in Figure D3-8b.
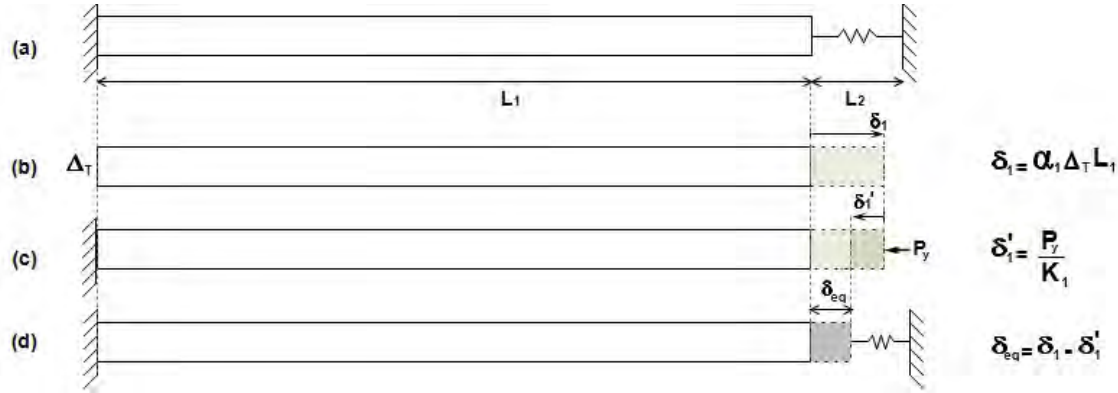
Figure D3-8 Bridge thermal expansion considering the effective span L_1

As before, due to to bridge stiffness (K_1), an equivalent force (P) resists these elongations, resulting in lateral deformation δ_1' under that force. However, when BRB plastic response is taken into account, the equivalent force P is now limited to P_y, equal to the product of the BRB yielding core area and strength. The equivalent deformation (δ_{eq}) is therefore:

$$\delta_{eq} = \delta_1 - \delta_1'$$
$$= \delta_1 - \frac{P_y}{K_1} \tag{D3-11}$$

where P_y is equal to:

$$P_y = A_{ysc}F_y \tag{D3-12}$$

where A_{ysc} is the area of BRB yielding core and F_y is the yielding strength of the BRB taken as 36 ksi for ASTM A36. The deformation at equilibrium then can be written as :

$$\delta_{eq} = \delta_1 - \frac{A_{ysc}F_y}{K_1} \tag{D3-13}$$

and the thermal strain of the BRB is calculated as :

$$\varepsilon_{eq} = \frac{\delta_{eq}}{0.5\,L_2} = 2\left(\alpha_1\Delta_T\frac{L_1}{L_2} - \frac{A_{ysc}F_y}{K_1 L_2}\right) \tag{D3-14}$$

D 3.7.2 Case 2 : BRB thermal expansion = δ_2

Similar to Section D3.5.1.2 of BRB in Elastic Range, thermal changes Δ_T is considered to deform both the bridge deck and the BRB, as shown in Figure D3-9b.
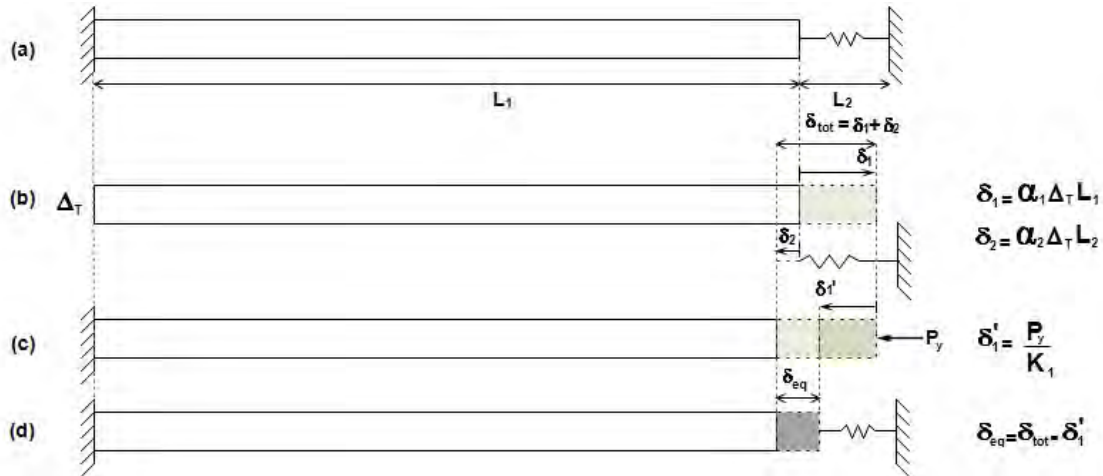
Figure D3-9 Bridge and BRB thermal expansion considering the effective span L_1

As shown in Figure D3-9b, the total deformation due to thermal changes Δ_T is taken as $\delta_1 + \delta_2$. From Figure D3-9d, the equation for δ_{eq} can be written as:

$$\begin{aligned}\delta_{eq} &= \delta_{tot} - \delta_1' \\ &= \delta_{tot} - \frac{P_y}{K_1}\end{aligned} \tag{D3-15}$$

where P_y is the previously defined maximum force that can be obtained from the BRB due to plastic capacity of the of BRB yielding core which is equal to:

$$P_y = A_{ysc}F_y \tag{D3-16}$$

where A_{ysc} is the area of BRB yielding core and F_y is the yielding strength of the BRB core. The total thermal deformation can be written as :

$$\delta_{eq} = \delta_{tot} - \frac{A_{ysc}F_y}{K_1} \tag{D3-17}$$

Therefore, the thermal strain of BRB is calculated as :

$$\varepsilon_{eq} = \frac{\delta_{eq}}{0.5L_2} = 2\left(\alpha_1\Delta_T\frac{L_1}{L_2} + \alpha_2\Delta_T - \frac{A_{ysc}F_y}{K_1L_2}\right) \tag{D3-18}$$

D 3.8 Calculation Example of BRB Thermal Strain

A simple example of BRB thermal strain calculation is provided in this section using the equations generated in the previous part. The results are compared to illustrate how the calculate BRB thermal strain for the various assumptions considered in the Section D3.5.1 and D3.5.2, particularly with regards to modeling the BRBs as either elastic or plastic for the sake of calculating thermal deformations.

In this example, thermal changes (ΔT) are subjected to a bridge with span length of L and they are taken from 10°F to 100°F within 10°F intervals. The ratios of BRB length (L_2) over bridge length are taken as 1%, 2%, 3%, 4% and 5%. Assumptions are made for bridge concrete deck properties such as compressive strength (f_c') as 60 psi, elastic modulus (E_1) is calculated using the formula of $57000\sqrt{f_c'}$ as 4415.201 ksi, thermal expansion coefficient (α_1) = 0.000006 in/in/°F and deck section (A_1) as 3150 in². The material for BRB is ASTM A36 with elastic modulus (E_2) = 200000 MPa (also equal to 29007.54 ksi), yield strength (F_y) = 36 ksi, thermal expansion coefficient (α_2) = 0.0000065 in/in/°F and the yield core area (A_{ysc}) is taken as 4 in².

The thermal strains of BRB calculated from the equations derived in Section D3.5.1 and D3.5.2 are given in Figure D3-10. To illustrate the sensitivity of the results to the various assumptions, an example is taken for a bridge with a ratio of $L_2/L = 3\%$ and for the case of ΔT equal to 40°F. The thermal strains calculated per equations D3-1, D3-6, and D3-10, are 0.0160, 0.0123, and 0.0128; respectively. If calculated by equations D3-14 and D3-18, then the results would be 0.0153 and 0.0158, respectively. From these results, it can be seen that elastically calculated BRB thermal strain (accomplished by neglecting the deformation δ_1' described in Section D3.6.1) given by equation D3-1 is only slightly different from the one calculated plastically using the more precise equation D3-18. Equation D3-1 and equation D3-18 are both retained for further calculations of BRB thermal strain in the rest of this report, recognizing that use of equation D3-1 results in larger strains in the BRB, which will lead to more conservative estimation of low-cycle fatigue life.

(a) $0.5L_2/L = 1\%$

(b) $0.5\,L_2/L = 2\%$

(c) $0.5L_2/L = 3\%$

(d) $0.5L_2/L = 4\%$

(e) $0.5L_2/L = 5\%$
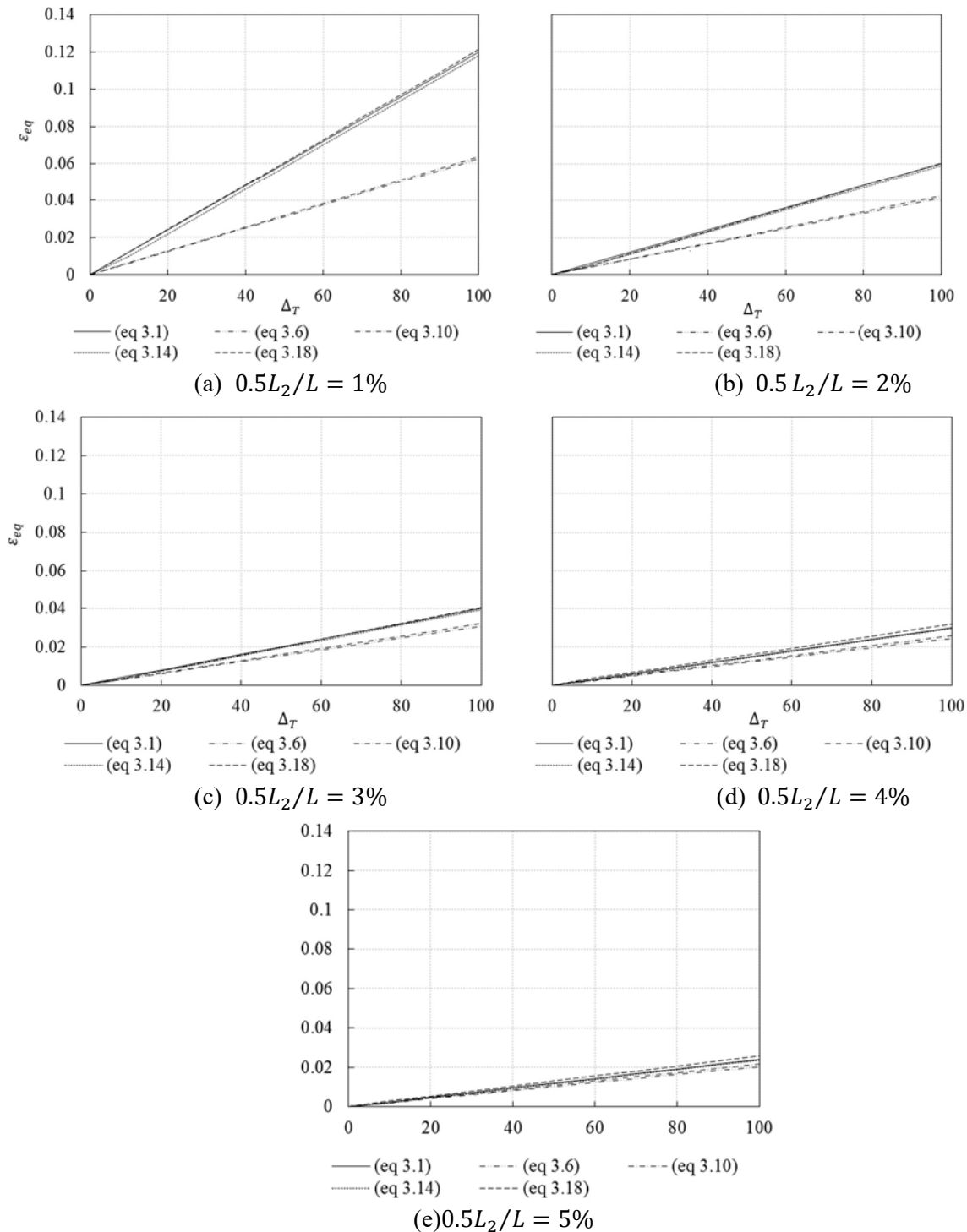
Figure D3-10 Thermal strain of BRB in various temperature changes

D 3.9 BRBs Strain History

BRB strain history corresponding to the temperature histories presented in Section D3.1, were calculated using the thermal strain equations generated in Section D5.1 and D5.2. Note that in

each temperature history, two temperature values were recorded each day (i.e. maximum and minimum daily temperatures), resulting in maximum and minimum BRB thermal strains each day. These daily maximum and minimum strains were then assembled together into one-continuous strain history with 732 data points (there were 366 days in 2012). Examples of BRB strain history are given in Section D4.4.1.

D 3.10 Fatigue Analysis

D 3.10.1   Rainflow Counting

The first step in the fatigue analysis was to break the continuous strain history obtained from the temperature history (as described in Section D2.4) into individual cycles. The cycle counting method chosen for this purpose in this project was the Rainflow Counting method. The total numbers of cycles from the given strain loading history were calculated using the method and the results were typically given in a matrix form or histogram. Here, the rainflow counting method is applied using the Fatiga software and the steps of the procedure (as described by ASTM E-1049) are as follows:

1. Let X denote the range under consideration; Y, the previous range adjacent to X; and S, the starting point in the history.

2. Read the next peak or valley. If out of data, go to Step 6.

3. If there were less than three points, go to Step 1. Form ranges X and Y using the three most recent peaks and valleys that have not been discarded.

4. Compare the absolute values of ranges X and Y :
   (a) If X < Y, go to Step 1.
   (b) If X > Y, go to Step 4.

5. If range Y contains the starting point S, go to Step 5; otherwise, count range Y as one cycle; discard the peak and valley of Y; and go to Step 2.

6. Count range Y as one-half cycle; discard the first point (peak or valley) in range Y; move the starting point to the second point in range Y; and go to Step 2.

7. Count each range that has not been previously counted as one-half cycle.

An example of how to execute the above Rainflow Counting method is given in FigureD 3-10 and the result, given in the form of a Rainflow Matrix, is shown in Figure D3-12. In Figure D3-11 (a), the strain history is given from point A to I (the loading unit is set to unity, for simplicity). In Figure D3-11 (b), the counting is started at point A and the absolute values of range A-B and B-C are compared; as the range B-C is larger; point A is discarded in the history. Range A-B is counted

to give 0.5 cycle and the counting continues starting from point B. A similar approach is following through Figures D3-11 (c), (d), (e) and (f), by comparing ranges of two peaks or valleys and eliminating those instances when the range of 2 points following is larger. The typical discarded point is considered to correspond to one-half cycle, one cycle, or more, depending on how many peaks or valleys preceding that point are eliminated. The total counted number of cycles resulting from this loading history is 4 cycles, with strain ranges forming the cycles tabulated at the bottom of Figure D3-11.
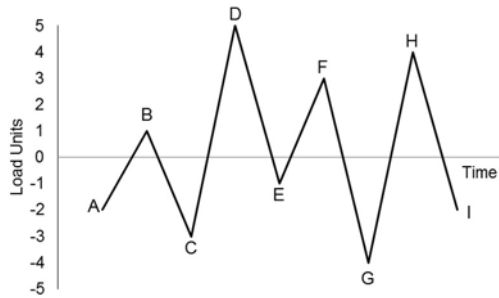
(a)
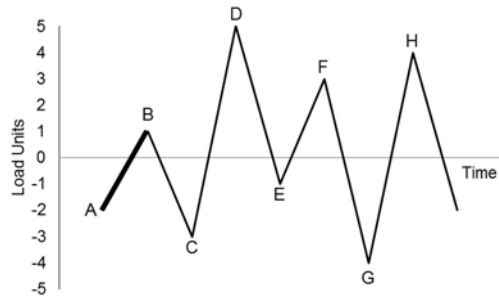
(b)
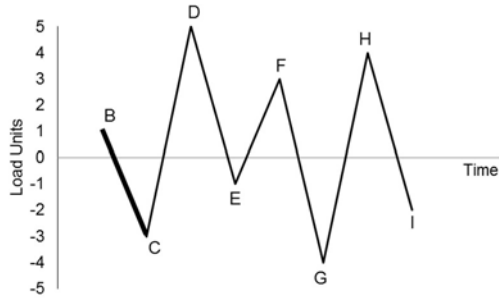
(c)
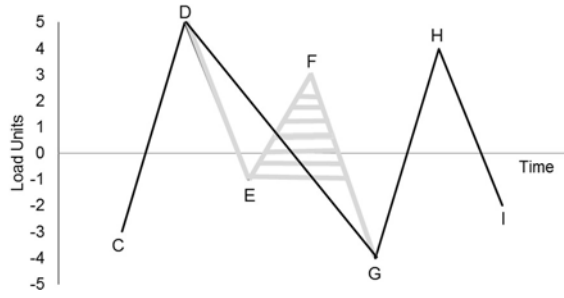
(d)
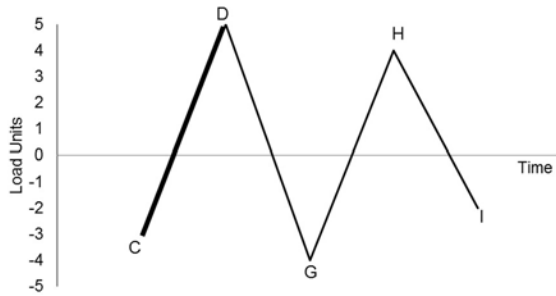
(e)
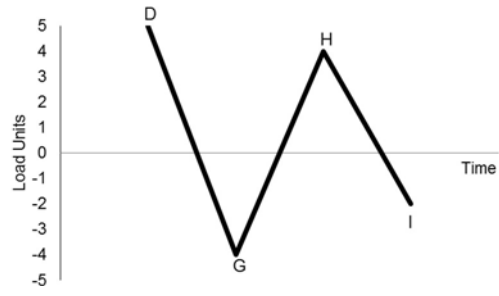
(f)

(1) S = A; Y = |A-B |; X = |B-C|; X > Y. Y contains S, that is, point A. Count |A-B| as one-half cycle and discard point A; S = B. (See Fig. B)

(2) Y = |B-C|; X = |C-D|; X > Y. Y contains S, that is, point B. Count| B-C| as one-half cycle and discard point B; S = C. (See Fig. c)

(3) Y = |C-D|; X = |D-E|; X < Y.

(4) Y = |D-E|; X = |E-F|; X < Y.

(5) Y = |E-F|; X = |F-G|; X > Y. Count |E-F| as one cycle and discard points E and F. (See Fig. d) Note that a cycle is formed by pairing range E-F and a portion of range F-G.)

(6) Y = |C-D|; X = |D-G|; X > Y; Y contains S, that is, point C. Count |C-D| as one-half cycle and discard point C. S = D. (See Fig. e)

(7) Y = |D-G|; X = |G-H|; X < Y.

(8) Y = |G-H|; X = |H-I|; X < Y. End of data.

(9) Count |D-G| as one-half cycle, |G-H| as one-half cycle, and| H-I| as one-half cycle. (See Fig. f)

(10) End of counting.

Range (units)	Cycle Counts	Events
10	0	
9	0.5	D-G
8	1	C-D,G-H
7	0	
6	0.5	H-I
5	0	
4	1.5	B-C,E-F
3	0.5	A-B
2	0	
1	0	

Figure D3-11 Rainflow counting procedures (ASTM E-1049)
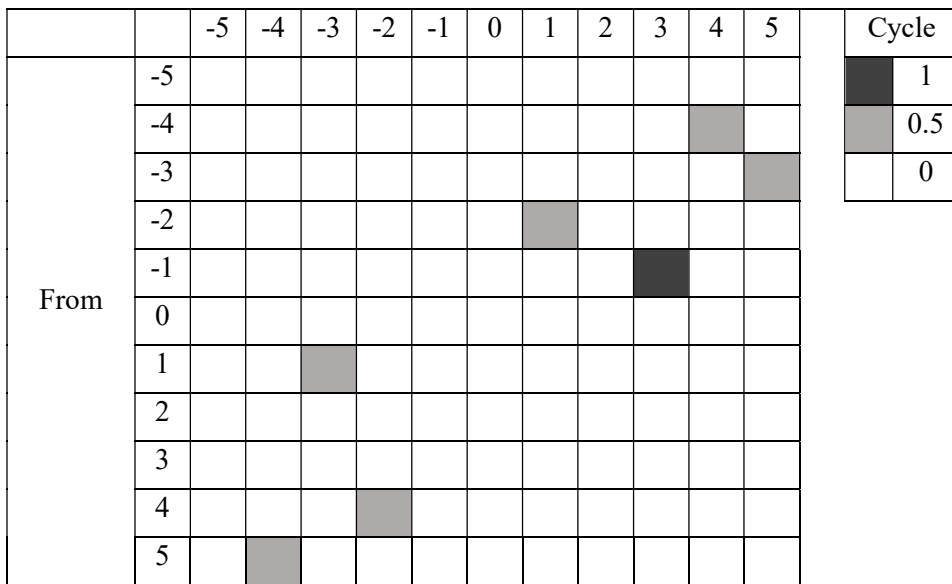
Figure D3-12 Rainflow matrix

D 3.10.2 Stress-Strain Relationship

The Rainflow Counting, described in the previous section, provides the number of cycles that fall within specific strain ranges. The next step in Fatigue analysis is to obtain the stresses associated with those strains, which are needed to estimate the BRB fatigue life using methods that consider the mean stress effect (described further in Section D3.6.3). The parameters used to generate the resulting hysteresis loops include the elastic modulus (E), the cyclic strength coefficient K', and the cyclic strain hardening exponent n'. For ASTM A36, these values were taken as 200,000 MPa, 1097, and 0.249, respectively.

An example of how to generate the stress-strain relationship is given in Table D3-1, with the resulting hysteresis loop given in Figure D3-13. The strain ranges and associated cycles used in this example are based on the Rainflow counting results in Figure D3-11 and the loading unit is taken

as a percent of strain. From Figure D3-13, the first half cycle/inner loop is assumed to follow the stable cyclic stress-strain response expressed by the following Ramberg-Osgood relationship as given in Section D2.3 as:

$$\varepsilon = \frac{\sigma}{E} + \left(\frac{\sigma}{K'}\right)^{1/n'} \tag{D3-19}$$

In this project, the behavior of BRB under variable amplitude-strain loading was assumed to obey Masing behavior (Masing 1926), in that its cyclic stress-strain hysteresis loop was geometrically similar to the monotonic stress-strain curve magnified by a scale factor of two. Therefore, the outer loop shape is different from the Ramberg-Osgood line by approximately a factor of two, following the Masing behavior. Hence, the outer loop shape follows Masing behavior and the relationship between strain range and stress range is expressed by Morrow's equation, namely:

$$\Delta\varepsilon = \frac{\Delta\sigma}{E} + 2\left(\frac{\Delta\sigma}{2K'}\right)^{1/n'} \tag{D3-20}$$

For example, consider points A and B in Table D3-1 forming the inner loop with 0.5 cycle. Note that for the history considered in this example, shown in Figure D3-10a, the initial strain is not zero but -0.02. The stresses at point A and point B are calculated using the Ramberg-Osgood relationship with the results of -403.3 MPa and 333 MPa, respectively. From Rainflow Counting in Figure D3-11, a half-cycle is formed from point B to C with a strain range of 0.04. The stress range from point B to C associated with the strain range of 0.04 is calculated using Morrow's equation as 782.4 MPa. Therefore, the stress at point C is obtained as -449.4 MPa (calculated by subtracting stress at point B from the stress range from point B to C). Similar steps to obtain the stress ranges related to the other strain ranges obtained from Rainflow Counting are conducted using the Morrow equation and the stress at each point is calculated by simply subtracting the stress at the point preceding that referred point from the associated stress ranges between those two points.
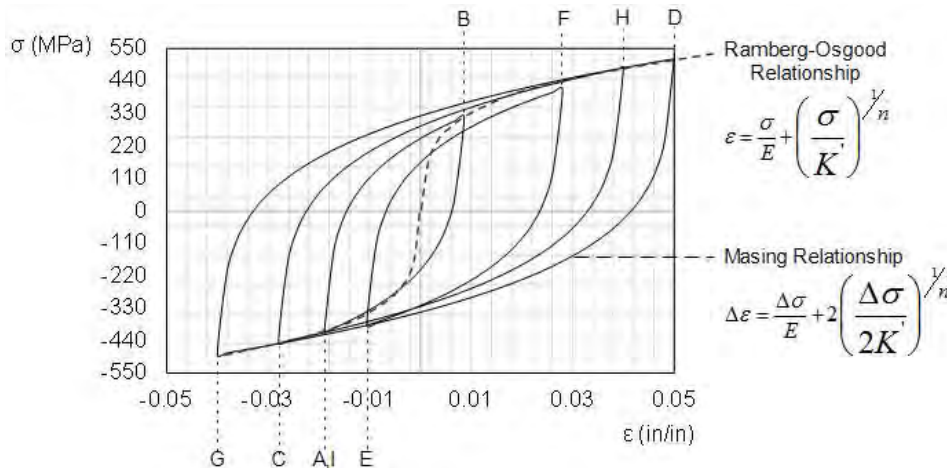
Figure D3-13 Stress-strain hysteresis loop

Table D3- 1 Stress-Strain calculation using Ramberg-Osgood and Masing relationship

Ramberg-Osgood			Hysteretic Loop		
Point	ε	σ (Sampaio et	Point	E	σ (Sampaio et
A	-0.02	-403.3	A	-0.02	-403.3
B	0.01	333	B	0.01	333
E	-0.01	-333	C	-0.03	-449.4
Masing			D	0.05	519.7
Point	$\Delta\varepsilon$	$\Delta\sigma$ (Sampaio et	E	-0.01	-333
A to B	0.03	736.3	F	0.03	449.4
B to C	0.04	782.4	G	-0.04	-484.5
C to D	0.08	969.1	H	0.04	484.5
D to G	0.09	1004.3	I	-0.02	403.3
E to F	0.04	782.4			
G to H	0.08	969.1			
H to I	0.06	887.9			

D3.10.3 Fatigue Life

The three methods described in Section D2.6 were used to calculate the Fatigue Life of BRB, namely the Basquin-Coffin and Manson method, the Smith-Watson and Topper method, and the Morrow method. Recall that the Basquin-Coffin and Manson method neglects the effect of Mean Stress (σ_m), while both the Smith-Watson and Topper method and the Morrow one consider the effect of Mean Stress. An example of fatigue life calculation is presented below using the cycles obtained from the Rainflow Counting example in Section D3.6.1, and the corresponding Stress-Strain relationship obtained as described in Section D3.6.2 and summarized in Table D3-1.

In Table D3-2, total life reversals, $2N_f$, were obtained using the Basquin-Coffin and Manson, Smith-Watson and Topper, or Morrow equations (presented in Section D2.6). The total number of cycles to failure under the specific stress (N_{fi}) for each cycle is then calculated as half of $2N_f$. Damage given by each cycle (D_i) is obtained by dividing the actual number of cycles under the specific stress, n_i, with N_{fi}. The total damage (D) is accumulated using the Palmgren-Miner's rule (presented in Section D2.7) and the Fatigue Life is obtained by dividing the value of 1 by the total damage value. Note that in the Palmgren-Miner's rule, it is assumed that failure occurs when the damage fraction reaches 1; therefore, the value of 1 is also synonymous to attainment of Fatigue Life.

For example, consider the strain range of 0.03 and stress range of 736.4 MPa from point A to B contributing 0.5 cycle, from Table D3-2. By solving the Basquin-Coffin and Manson equation, the resulting value of $2N_f$ is 852 reversals. Consequently, N_{fi}, is 426 reversals (or cycles) to failure if the stress range from point A to B was continuously repeated. The damage for 0.5 cycle of that strain range from point A to B is obtained by dividing 0.5 by 426, resulting in a damage value of

0.00117. Similar steps are taken for all other strain ranges in the strain history, and the total damage D obtained by summing the contributions from each cycle is 0.05497. The Fatigue Life for that repeated strain history is then obtained by the reciprocal of the total damage, namely $1/0.05497 = 18.19$ repetitions (when calculated using the Basquin-Coffin and Manson approach). As per Smith-Watson-Topper and Morrow approaches, the steps taken to calculate the damages for each cycle as well as to estimate the Fatigue Life are similar to those in the Basquin-Coffin and Manson approach. The only difference lies on the formulas used; the Smith-Watson Topper method considers a correction based on the maximum stress (σ_{max}) whereas Morrow method uses mean stress $(\sigma_m)$to estimate the total life reversals of $2N_f$.

Using the above procedures, Fatigue Life for BRBs in bridges for the temperature histories presented in Figure D3-1 are calculated and presented in the next section, for a range of reference temperatures (T_r) and percentages of $\frac{L_{BRB}}{L_{Bridge}}$. The objective is to provide design recommendations on the ratio of $\frac{L_{BRB}}{L_{Bridge}}$ required to achieve the 75 years design life required by AASHTO without the need to replace the BRBs.

Table D3- 2 Example of fatigue life calculation of BRB

				Basquin-Coffin and Manson (*)				
Point	From	To	$\Delta\varepsilon$	$\frac{\Delta\varepsilon}{2}$	$2N_f$	N_{fi}	n_i	$D_i = \frac{n_i}{N_{fi}}$
A to B	-0.02	0.01	0.03	0.015	852.4	426.2	0.5	0.00117
B to C	0.01	-0.03	0.04	0.02	423.2	211.6	0.5	0.00236
C to D	-0.03	0.05	0.08	0.04	81.8	40.9	0.5	0.01221
D to G	0.05	-0.04	0.09	0.045	62.2	31.1	0.5	0.01607
E to F	-0.01	0.03	0.04	0.02	423.2	211.5	1	0.00473
G to H	-0.04	0.04	0.08	0.04	81.8	40.9	0.5	0.01221
H to I	0.04	-0.02	0.06	0.03	160.8	80.4	0.5	0.00622
Fatigue Life, $N_f = 1/D = 18.19$					**Total Damage, D**			**0.05497**

				Smith-Watson and Topper (**)					
Point	From	To	$\Delta\varepsilon$	$\frac{\Delta\varepsilon}{2}$	σ_{max}	$2N_f$	N_{fi}	n_i	$D_i = \frac{n_i}{N_{fi}}$
A to B	-0.02	0.01	0.03	0.015	333	1291.2	645.6	0.5	0.00077
B to C	0.01	-0.03	0.04	0.02	333	755.6	377.8	0.5	0.00132
C to D	-0.03	0.05	0.08	0.04	519.7	95.6	47.8	0.5	0.01046
D to G	0.05	-0.04	0.09	0.045	519.7	77.4	38.7	0.5	0.01291
E to F	-0.01	0.03	0.04	0.02	449.4	435.4	217.7	1	0.00459
G to H	-0.04	0.04	0.08	0.04	484.5	108.4	54.2	0.5	0.00922
H to I	0.04	-0.02	0.06	0.03	484.5	181.7	90.8	0.5	0.0055
Fatigue Life, $N_f = 1/D = 22.37$						**Total Damage, D**			**0.0447**

Morrow (***)									
Point	From	To	$\Delta\varepsilon$	$\dfrac{\Delta\varepsilon}{2}$	σ_m	$2N_f$	N_{fi}	n_i	$D_i = \dfrac{n_i}{N_{fi}}$
A to B	-0.02	0.01	0.03	0.015	-35.1	862.6	431.	0.5	0.00116
B to C	0.01	-0.03	0.04	0.02	-58.1	430	215	0.5	0.00232
C to D	-0.03	0.05	0.08	0.04	35.2	81.4	40.7	0.5	0.01228
D to G	0.05	-0.04	0.09	0.045	17.6	62	31	0.5	0.01612
E to F	-0.01	0.03	0.04	0.02	58.1	416.5	208.	1	0.0048
G to H	-0.04	0.04	0.08	0.04	0	81.8	40.9	0.5	0.01222
H to I	0.04	-0.02	0.06	0.03	35.2	159.7	79.8	0.5	0.00626
Fatigue Life, $N_f = 1/D = 18.19$						**Total Damage, D**			**0.05516**

(*) $\dfrac{\Delta\varepsilon}{2} = \dfrac{\sigma_f'}{E}\left(2N_f\right)^b + \varepsilon_f'\left(2N_f\right)^c$

(***) $\dfrac{\Delta\varepsilon}{2} = \dfrac{\sigma_f' - \sigma_m}{E}\left(2N_f\right)^b + \varepsilon_f'\left(2N_f\right)^c$

(**) $\sigma_{max}\dfrac{\Delta\varepsilon}{2} = \dfrac{\left(\sigma_f'\right)^2}{E}\left(2N_f\right)^{2b} + \varepsilon_f'\sigma_f'\left(2N_f\right)^{b+c}$

Section D4 Analysis Results

D 4.1 General

In this section, the low-cycle fatigue life of BRBs, calculated based on the methods described in Section D3, are presented. An example of how the results are obtained is given for BRBs with thermal strain calculated using the recorded real-temperature data in Memphis, Tennessee, while the complete results for all selected locations are provided in Sub Appendix A. The strain histories calculated using the method which gives more conservative results are provided, as well as their corresponding cycles resulting from the Rainflow counting method. The stress-strain relationship of BRBs generated from Ramberg-Osgood and Morrow equations is also provided. Low-cycle fatigue life results estimated based on the Coffin-Manson and Basquin, Smith-Watson and Topper, as well as Morrow methods are given at the end of the section, along with suggestions on the length of BRBs required to prevent their potential failure due to low-cycle fatigue.

D4.2 Strain of BRBs

The assumptions and formulas used to calculate the thermal strains of BRB are described in Section D3.5 to D3.8. According to Section D3.8, the use of simplified method as given in Equation D3.1 leads to more conservative estimation of low-cycle fatigue life, with only a small difference from the one calculated using the more precise method given in Equation D3.18. Simplified method provided in Equation D3.1 is defined as neglecting the deformation δ_1' resulting from bridge lateral deformation against its thermal deformation due to its stiffness while the precise method given in Equation D3.18 considers the δ_1' as well as the plastic deformation of BRBs due to thermal changes.

For illustration purposes, the low-cycle fatigue life described in Section D4.4 are estimated from thermal strains calculated using both Equations D3.1 and D3.18 while the strain histories in this section is provided only from Equation D3.1.

The strain histories given in Figure D4.1 to D4.8 provide the set of thermal strain histories calculated by Equation D3.1 using recorded real-temperature data for a given year in Memphis, Tennessee. As stated in Section D3.5, for a given set of temperature data, increasing the reference temperature, T_r, causes the BRBs to experience more expansions/elongations and less contractions/shortening (and vice versa). Therefore, as shown in Figure D4.1, BRBs have more tensile strain for $T_r = 100^0$F and more compressive strains for $T_r = 30^0$F. The axis in the continuous thermal strain histories in Figure D4.1 to D4.8 corresponds to 732 data points associated with the strains calculated from recorded maximum and minimum temperature within a year. Also, as shown in Figure D4.1 to D4.8, higher strains in the BRBs are found in the shorter length of BRB or in the smallest ratio between the BRB length and bridge total span length, and vice versa.

Low-cycle fatigue is identified by a small number of cycles with large plastic deformations in which the strain range, $\Delta\varepsilon$ is bigger than $2\varepsilon_y$ (ε_y = yield strain) and $2\varepsilon_y$ is calculated as $2 f_y/E$. As provided in Section 3.2.2, the values of f_y and E for the BRBs are taken as 250 MPa (equivalent to f_y =36 ksi) and 200000 MPa resulting in $2\varepsilon_y = 0.00248$ (0.248% of strain). Strain histories given in Figure D4.1 to 4.8 show that the calculated thermal strains exceed 0.248% of strain (maximum of 9% BRB strain), at least for some cycles, in most of the cases considered in the study, showing that the BRB will at times undergo high plastic strains, leading to the possibility of low-cycle fatigue failure.
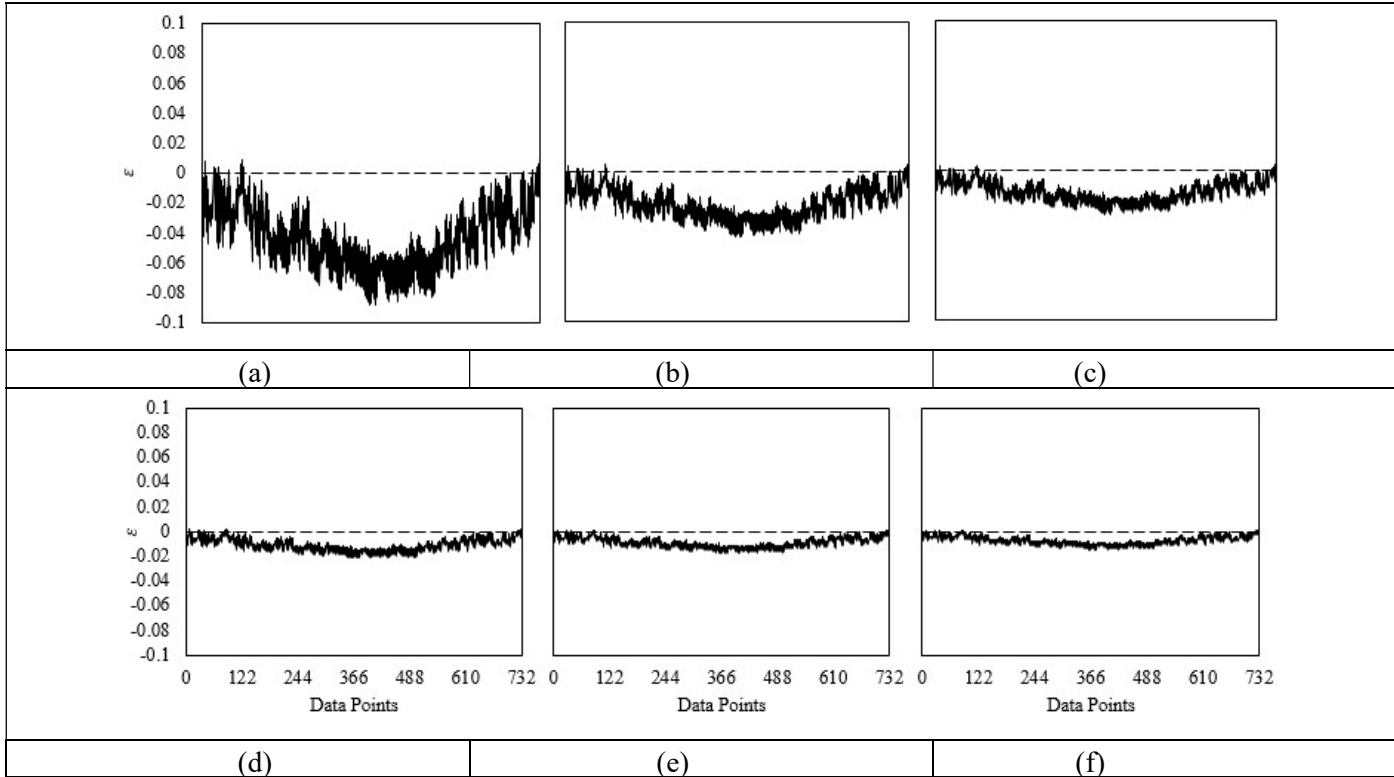
Figure D4-1 Strain histories of BRBs for Memphis, Tennessee with $T_r = 30^0$F for : (a) $L_2/L = 1\%$; (b) $L_2/L = 2\%$; (c) $L_2/L = 3\%$; (d) $L_2/L = 4\%$; (e) $L_2/L = 5\%$; (f) $L_2/L = 6\%$
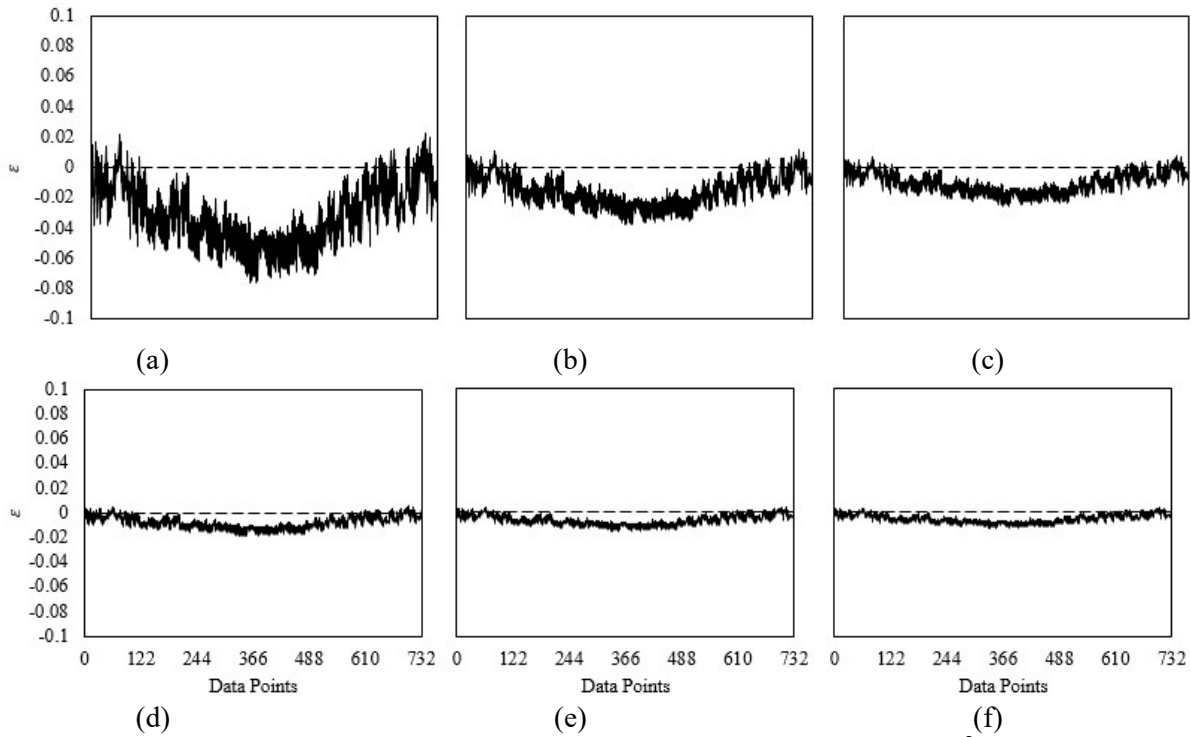
Figure D4-2 Strain histories of BRBs for Memphis, Tennessee with $T_r = 40^0$F for : (a) $L_2/L = 1\%$; (b) $L_2/L = 2\%$; (c) $L_2/L = 3\%$; (d) $L_2/L = 4\%$; (e) $L_2/L = 5\%$; and (f) $L_2/L = 6\%$

542
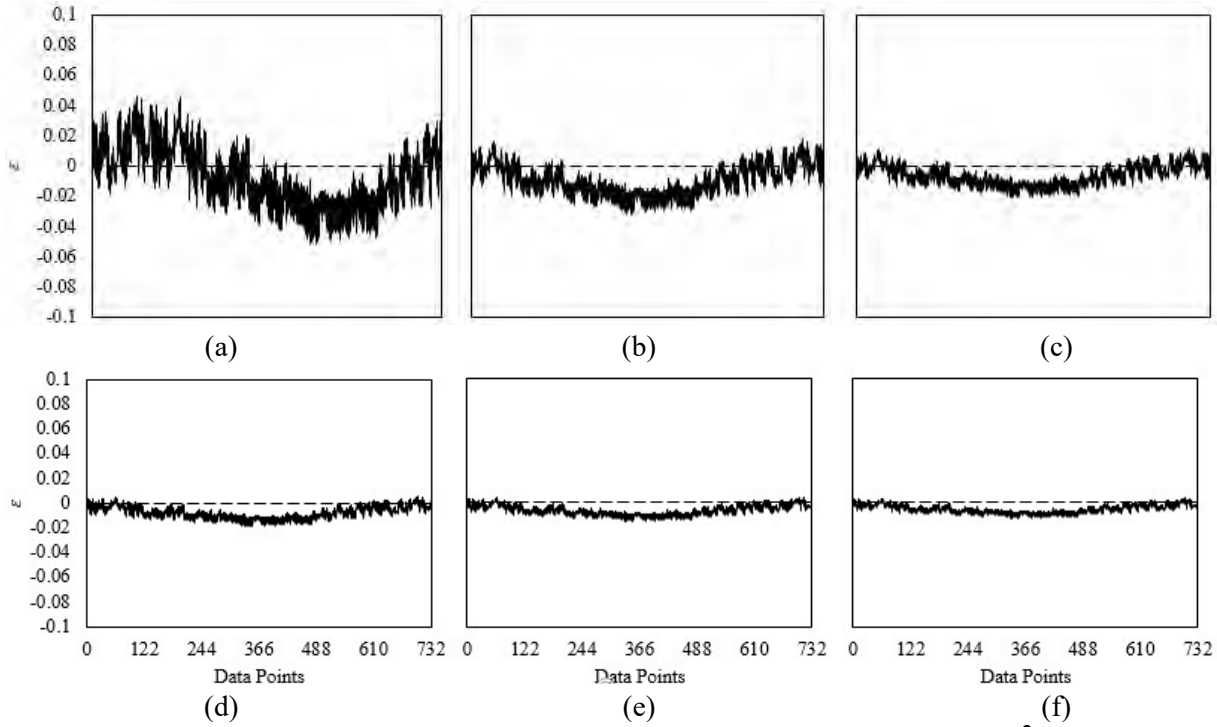
Figure D4-3 Strain histories of BRBs for Memphis, Tennessee with $T_r = 50^0$F for :
(a) $L_2/L = 1\%$; (b) $L_2/L = 2\%$; (c) $L_2/L = 3\%$; (d) $L_2/L = 4\%$; (e) $L_2/L = 5\%$; and
(f) $L_2/L = 6\%$
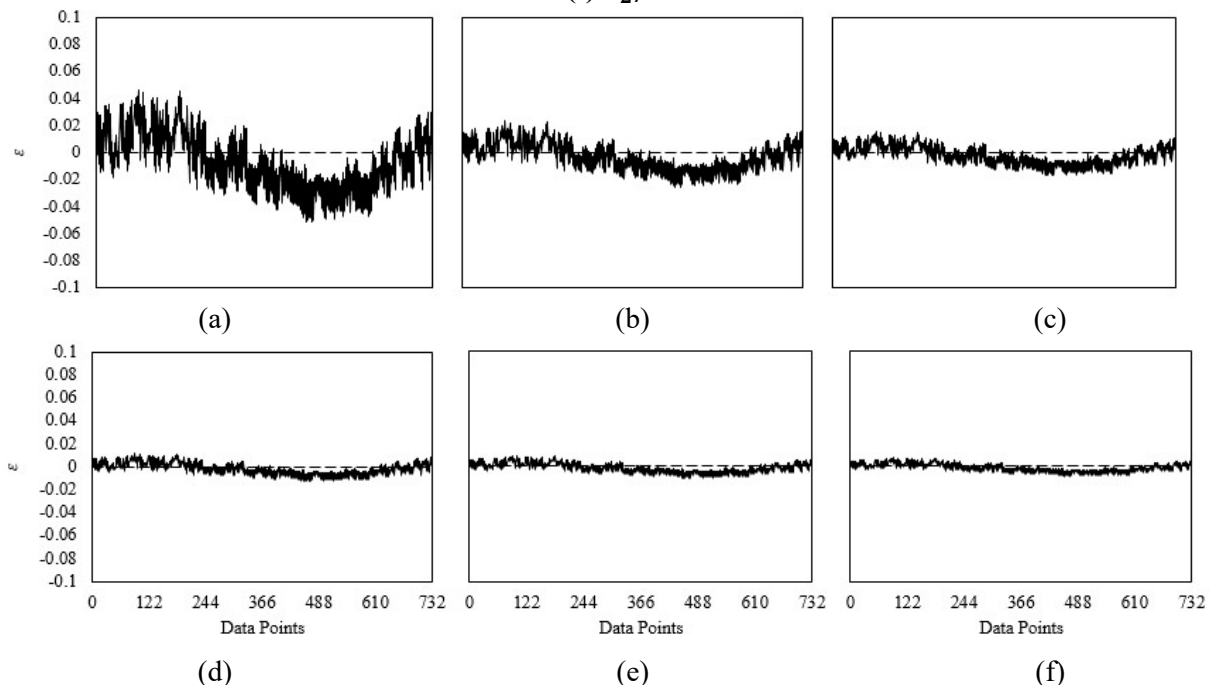
Figure D4-4 Strain histories of BRBs for Memphis, Tennessee with $T_r = 60^0$F for :
(a) $L_2/L = 1\%$; (b) $L_2/L = 2\%$; (c) $L_2/L = 3\%$; (d) $L_2/L = 4\%$; (e) $L_2/L = 5\%$; and
(f) $L_2/L = 6\%$
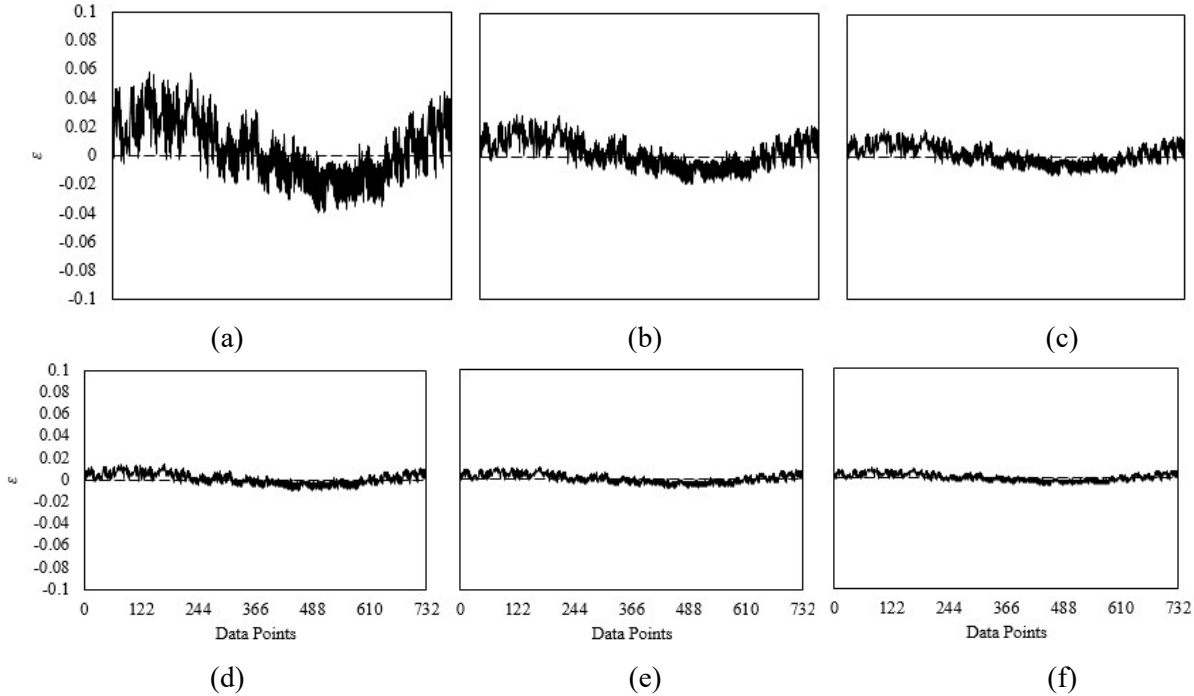
Figure D4-5 Strain histories of BRBs for Memphis, Tennessee with $T_r = 70^0$F for :
(a) $L_2/L = 1\%$; (b) $L_2/L = 2\%$; (c) $L_2/L = 3\%$; (d) $L_2/L = 4\%$; (e) $L_2/L = 5\%$; and
(f) $L_2/L = 6\%$
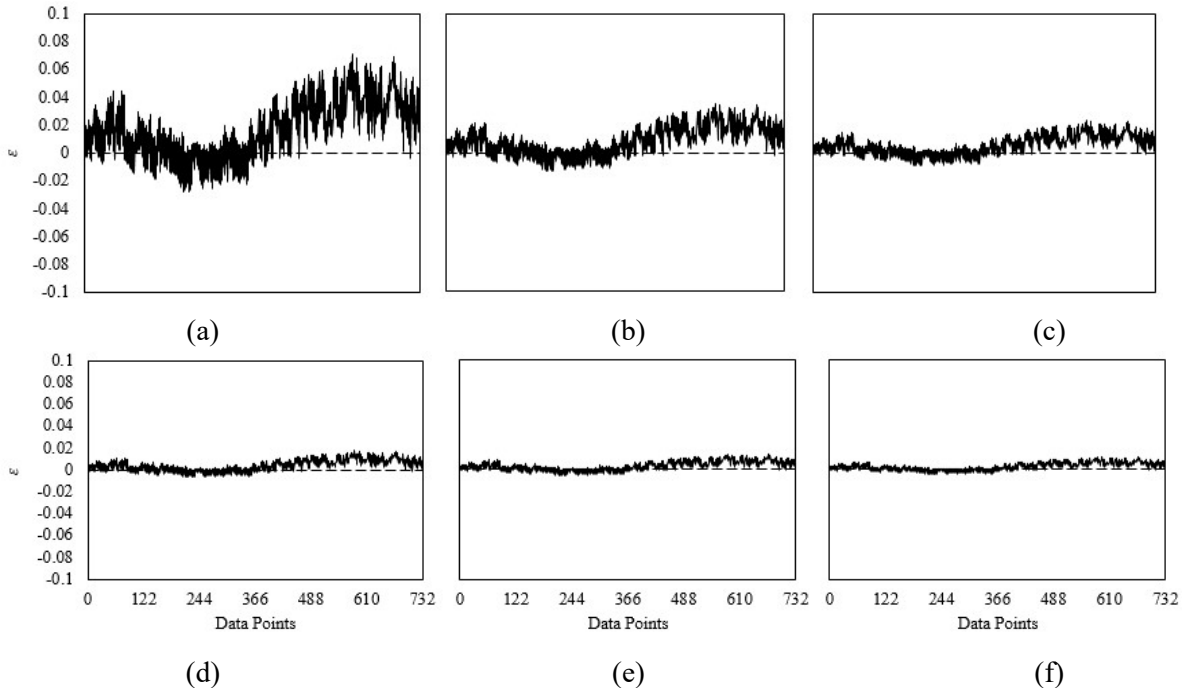
Figure D4-6 Strain histories of BRBs for Memphis, Tennessee with $T_r = 80^0$F for :
(a) $L_2/L = 1\%$; (b) $L_2/L = 2\%$; (c) $L_2/L = 3\%$; (d) $L_2/L = 4\%$; (e) $L_2/L = 5\%$; and (f)
$L_2/L = 6\%$
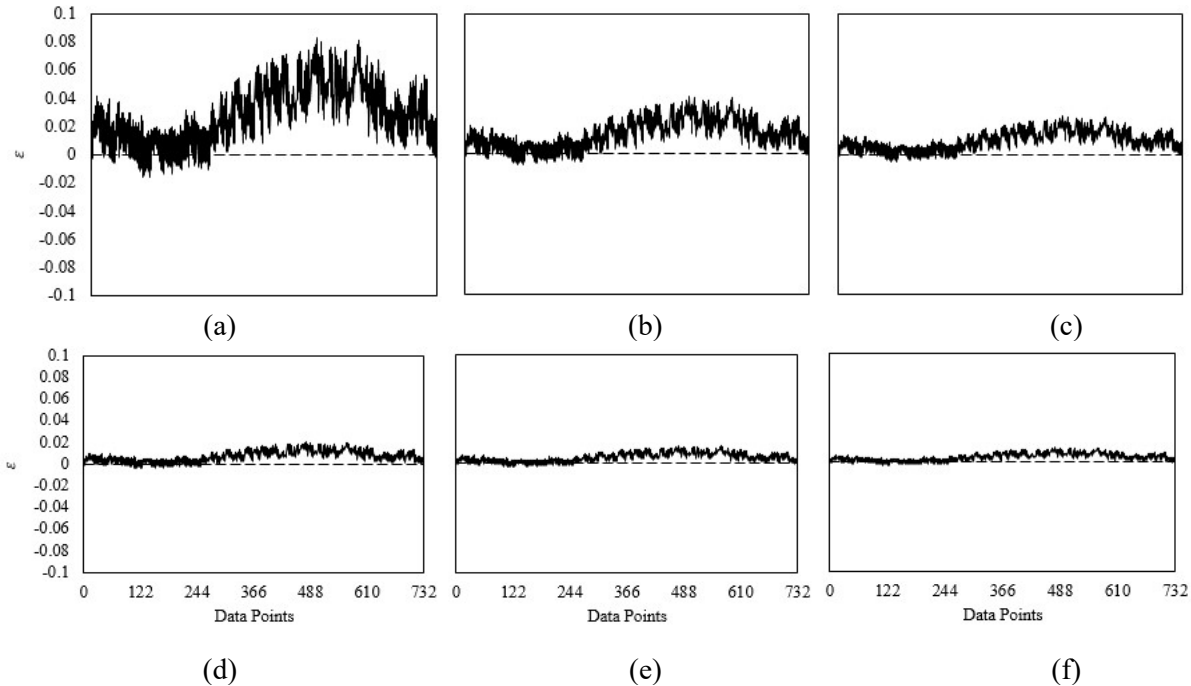
**Figure D4-7 Strain histories of BRBs for Memphis, Tennessee with $T_r = 90^0F$ for :
(a) $L_2/L = 1\%$; (b) $L_2/L = 2\%$; (c) $L_2/L = 3\%$; (d) $L_2/L = 4\%$; (e) $L_2/L = 5\%$; (d)
$L_2/L = 4\%$; and (e) $L_2/L = 6\%$**
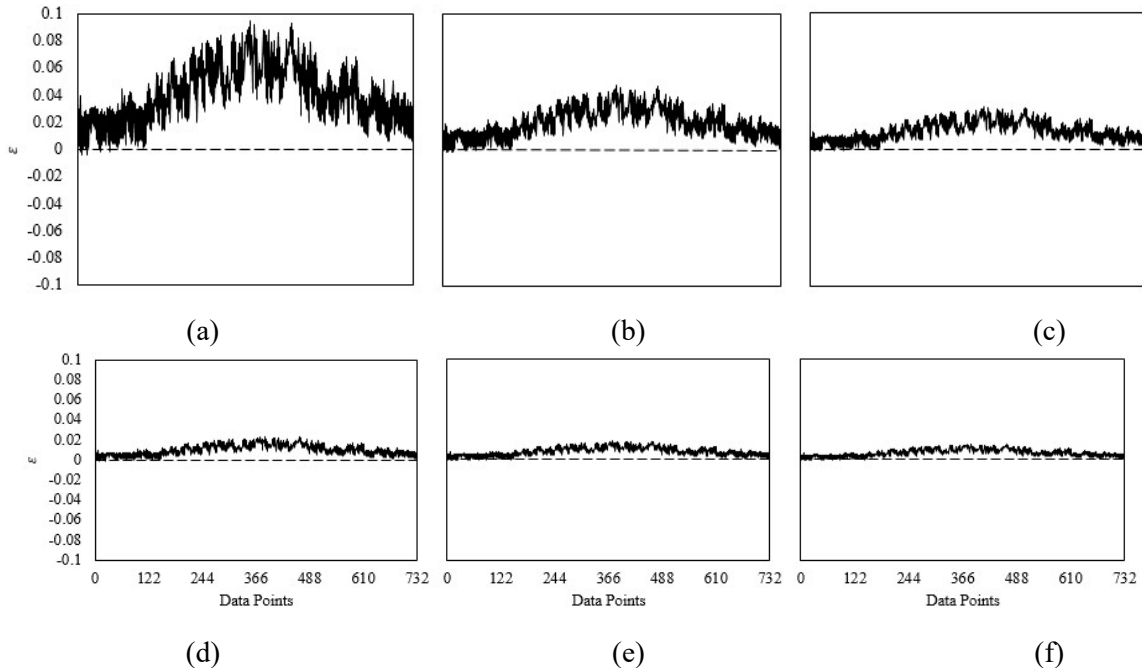
**Figure D4-8 Strain histories of BRBs for Memphis, Tennessee with $T_r = 100^0F$ for :
(a) $L_2/L = 1\%$; (b) $L_2/L = 2\%$; (c) $L_2/L = 3\%$; (d) $L_2/L = 4\%$; (e) $L_2/L = 5\%$; and
(f) $L_2/L = 6\%$**

D 4.3   Cycle Counting

Extracting and counting cycles are the key features in estimating the fatigue life of materials, as these cycles determine the damaging sequence in variable amplitude loading histories. As

described in Section D3.10.1, the strain histories are extracted into individual cycles and the Rainflow counting method is chosen to separate and to count cycles over various strain ranges. Cycles formed from strain histories given in Figure D4-1 to D4-8 are obtained using Rainflow counting method and the results are provided in matrix format as shown in Figure D4-9 to D4-16. The Rainflow matrices given in Figure D4-9 are associated with strain histories in Figure D4-1 and so on.

A total of 361 cycles is counted from strain histories in Figure D4-1 to D4-8 and the results are provided in Rainflow matrix given in Figure D4-9 to D4-16. The ordinate and axis showing in the to-form format in the Rainflow matrix are associated with the strain ranges forming the cycles. For example, Rainflow matrix in Figure D4-9(a) shows that 1 cycle is formed from the strain of 0.01 to the strain of -0.085 giving the strain range, $\Delta\varepsilon = 0.095$. Another example can be seen in the same figure in which 8 cycles are formed from the strain of -0.05 to -0.075 resulting in $\Delta\varepsilon = 0.025$.

The Rainflow matrices show that the cycles counted in higher reference temperature, T_r, are formed in tensile strains and they will be more detrimental to the fatigue life of BRBs compared to the cycles formed in lower T_r. Also, as the length of BRB, L_2, increases, the strain of BRBs declines and it is reflected in the Rainflow matrix by having more cycles at smaller strains for the cases where the ratios of L_2/L increase. These larger cycles at small strain ranges affect the fatigue life of BRBs since their damages will always be more than the damage for an individual smaller cycle.
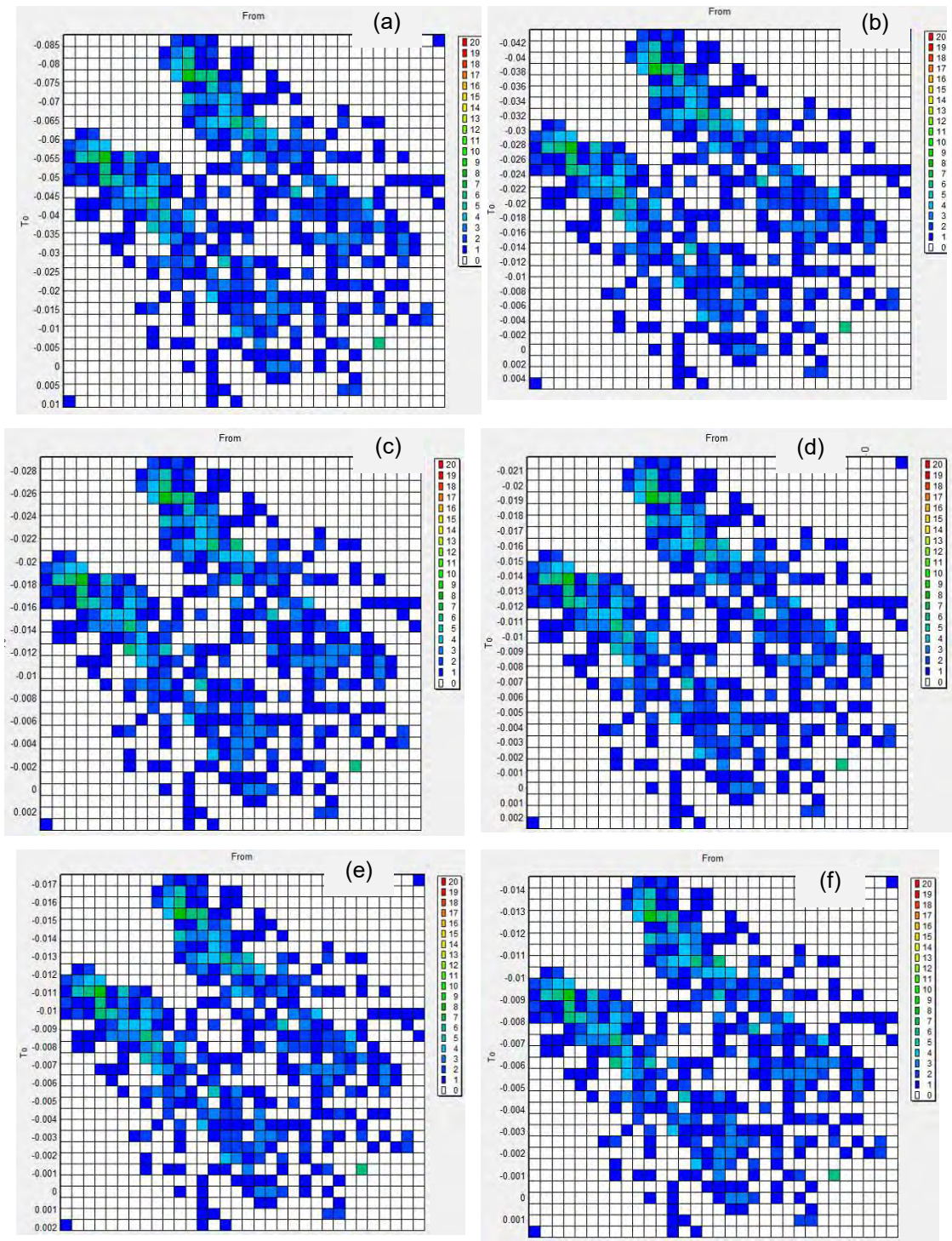
**Figure D4-9 Rainflow matrix of BRBs for Memphis, Tennessee with $T_r = 30^0$F for :
(a) $L_2/L = 1\%$; (b) $L_2/L = 2\%$; (c) $L_2/L = 3\%$; (d) $L_2/L = 4\%$; (e) $L_2/L = 5\%$; (f) $L_2/L = 6\%$**
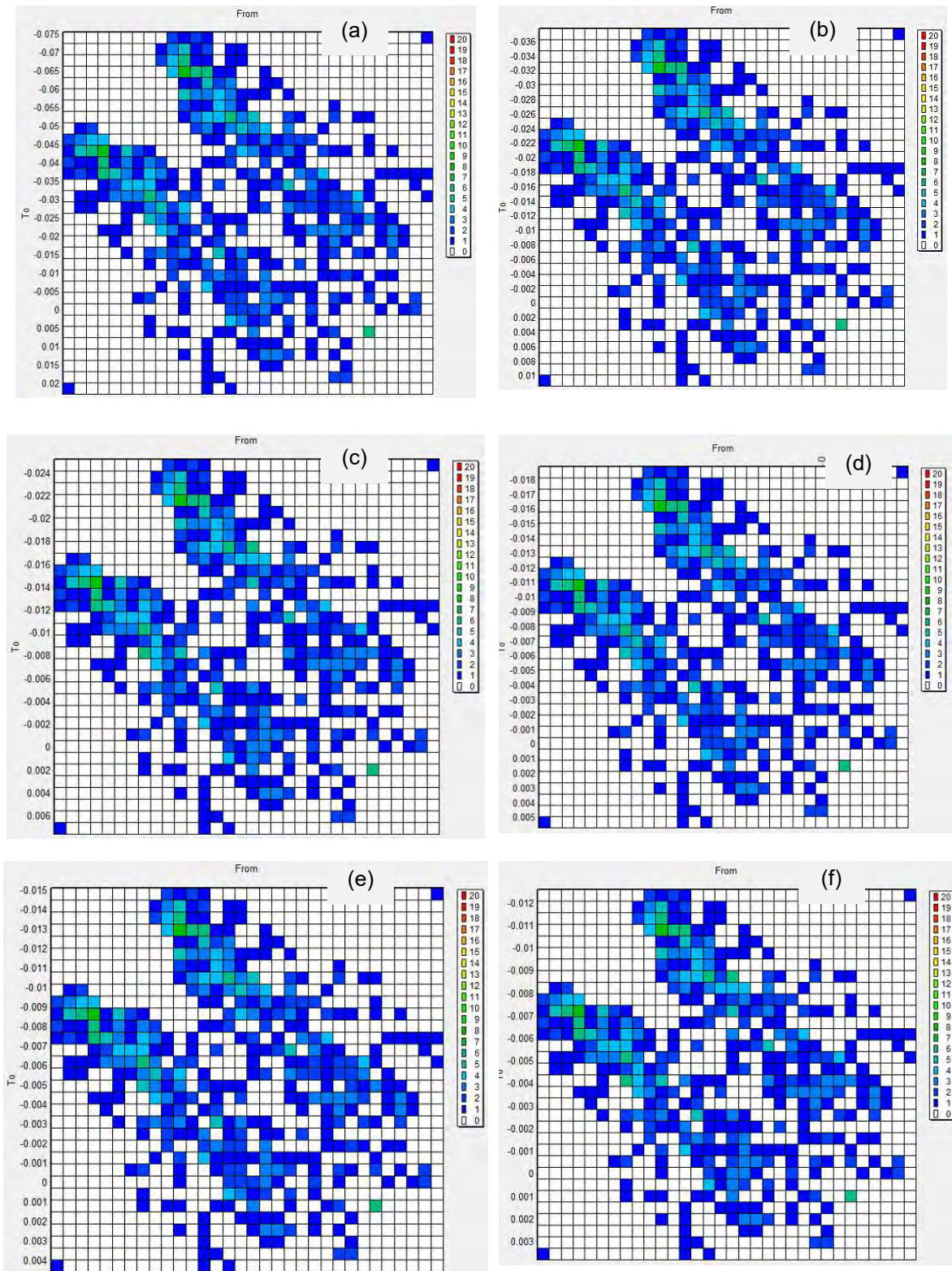
Figure D4-10 Rainflow matrix of BRBs for Memphis, Tennessee with $T_r = 40^0$F for :
(a) $L_2/L = 1\%$; (b) $L_2/L = 2\%$; (c) $L_2/L = 3\%$; (d) $L_2/L = 4\%$; (e) $L_2/L = 5\%$; and (f) $L_2/L = 6\%$
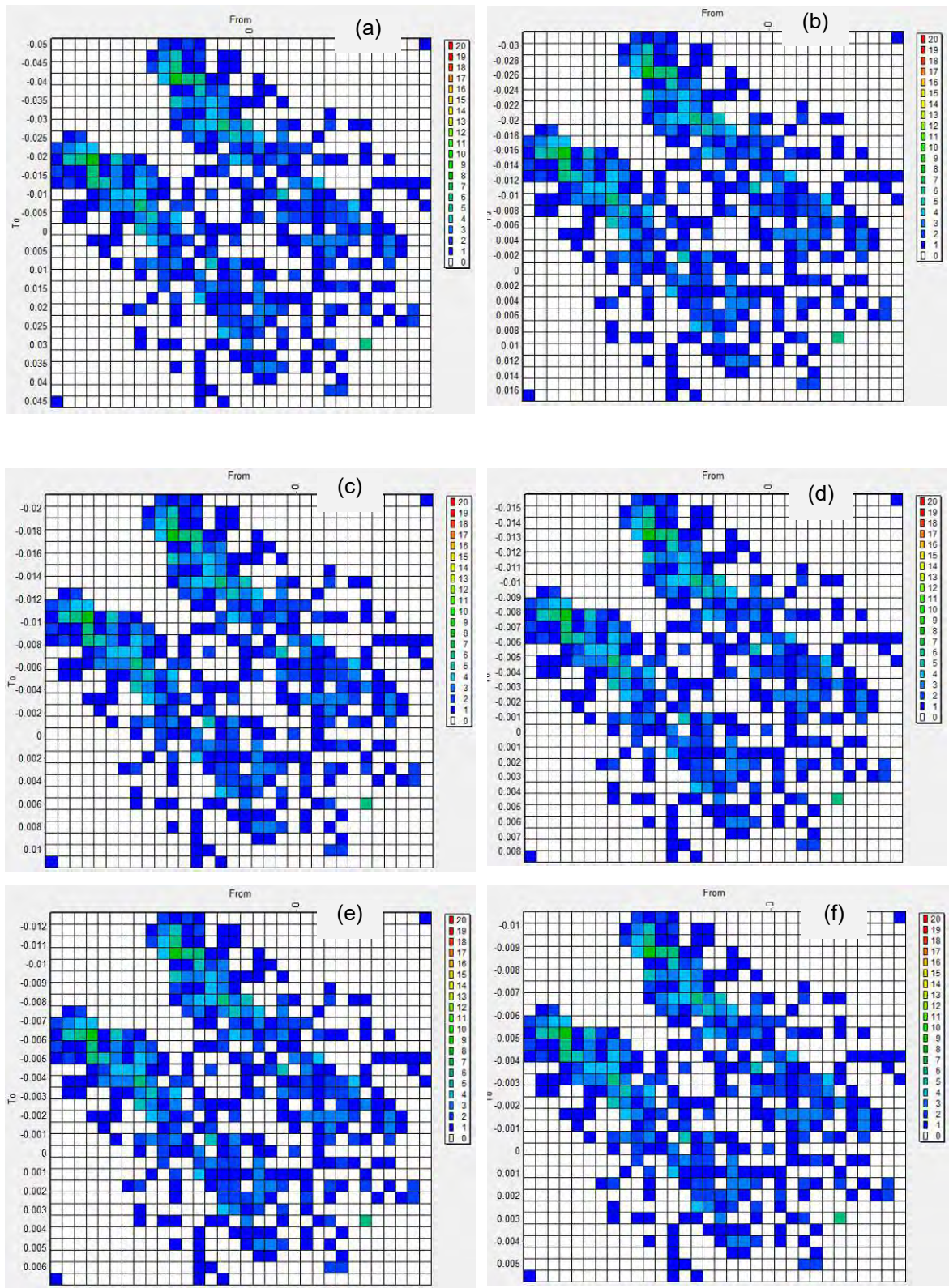
Figure D4-11 Rainflow matrix of BRBs for Memphis, Tennessee with $T_r = 50^0F$ for :
(a) $L_2/L = 1\%$; (b) $L_2/L = 2\%$; (c) $L_2/L = 3\%$; (d) $L_2/L = 4\%$; (e) $L_2/L = 5\%$; and
(f) $L_2/L = 6\%$
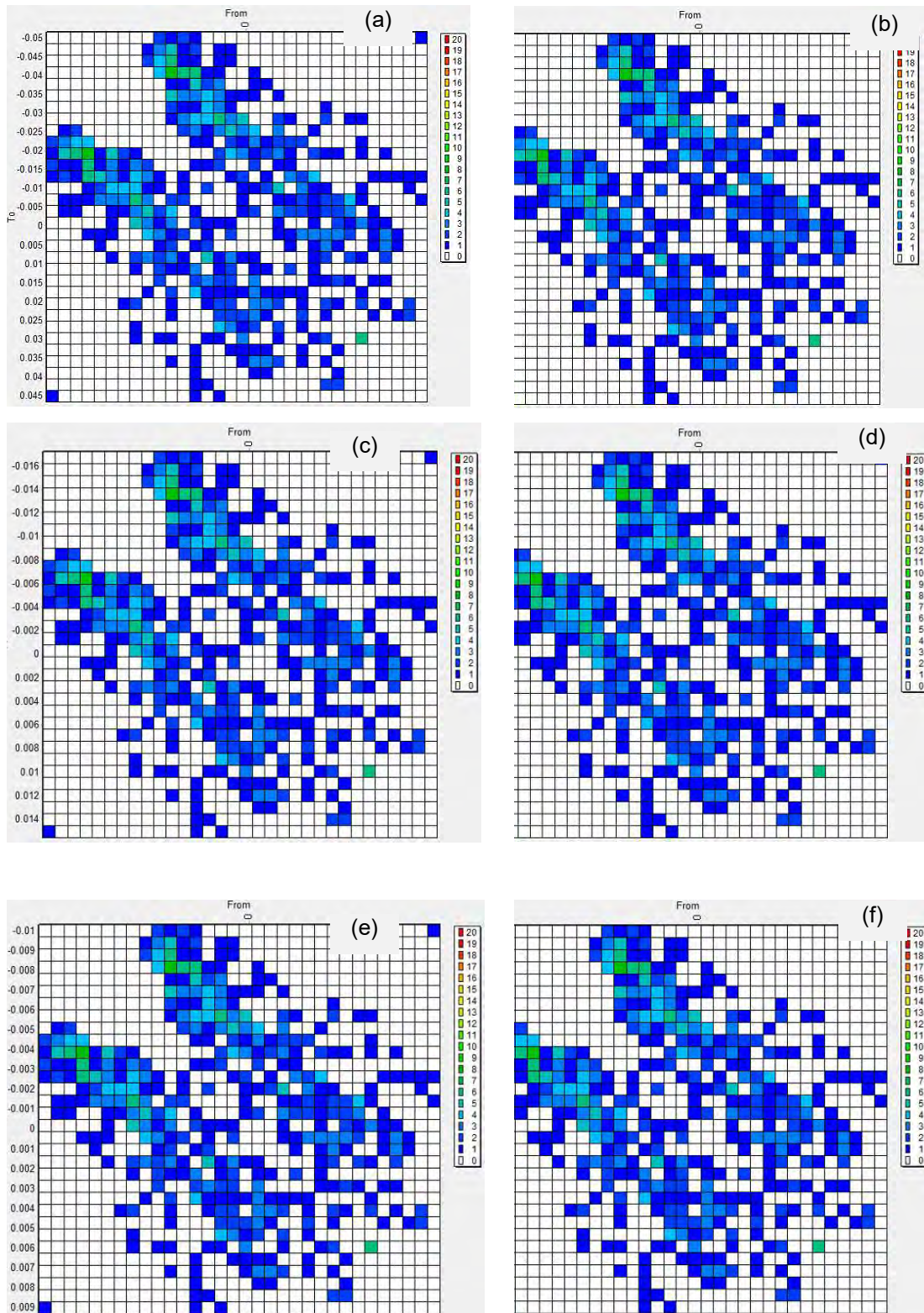
**Figure D4-12 Rainflow matrix of BRBs for Memphis, Tennessee with $T_r = 60^0$F for :
(a) $L_2/L = 1\%$; (b) $L_2/L = 2\%$; (c) $L_2/L = 3\%$; (d) $L_2/L = 4\%$; (e) $L_2/L = 5\%$; and
(f) $L_2/L = 6\%$**
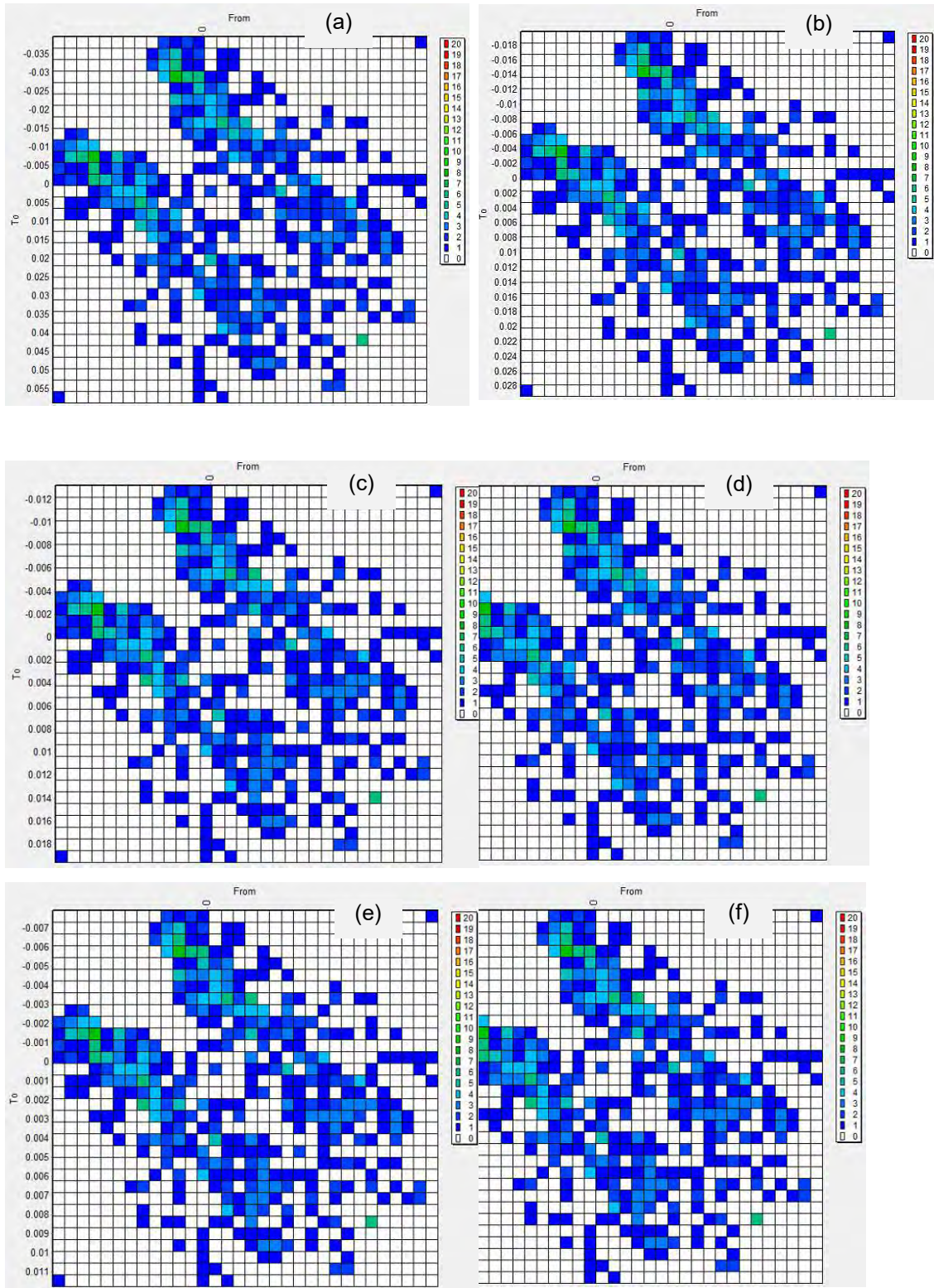
Figure D4-13 Rainflow matrix of BRBs for Memphis, Tennessee with $T_r = 70^0F$ for : (a) $L_2/L = 1\%$; (b) $L_2/L = 2\%$; (c) $L_2/L = 3\%$; (d) $L_2/L = 4\%$; (e) $L_2/L = 5\%$; and (f) $L_2/L = 6\%$
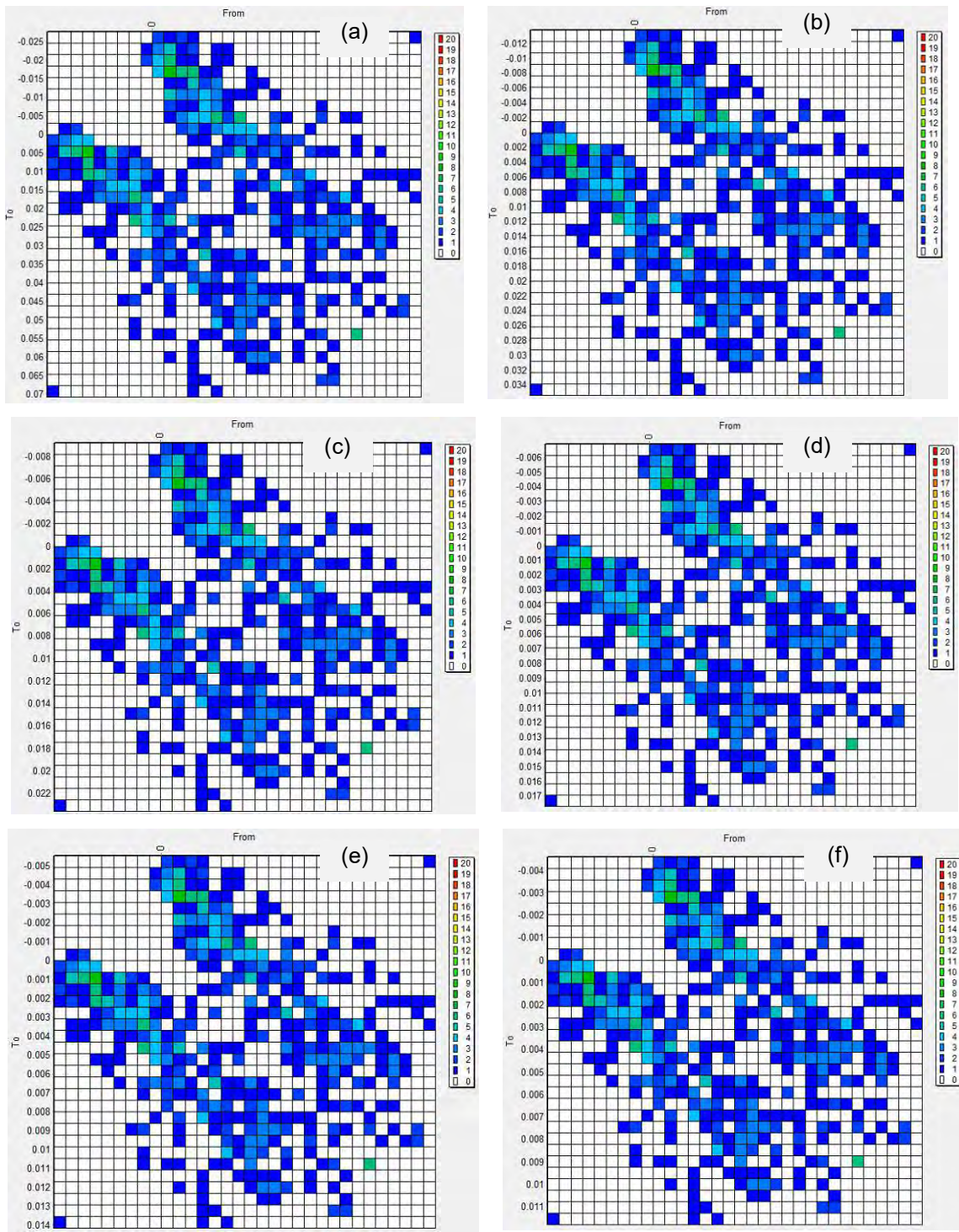
**Figure D4-14 Rainflow matrix of BRBs for Memphis, Tennessee with $T_r = 80^0$F for :
(a) $L_2/L = 1\%$; (b) $L_2/L = 2\%$; (c) $L_2/L = 3\%$; (d) $L_2/L = 4\%$; (e) $L_2/L = 5\%$; (d)
$L_2/L = 4\%$; and (f) $L_2/L = 6\%$**
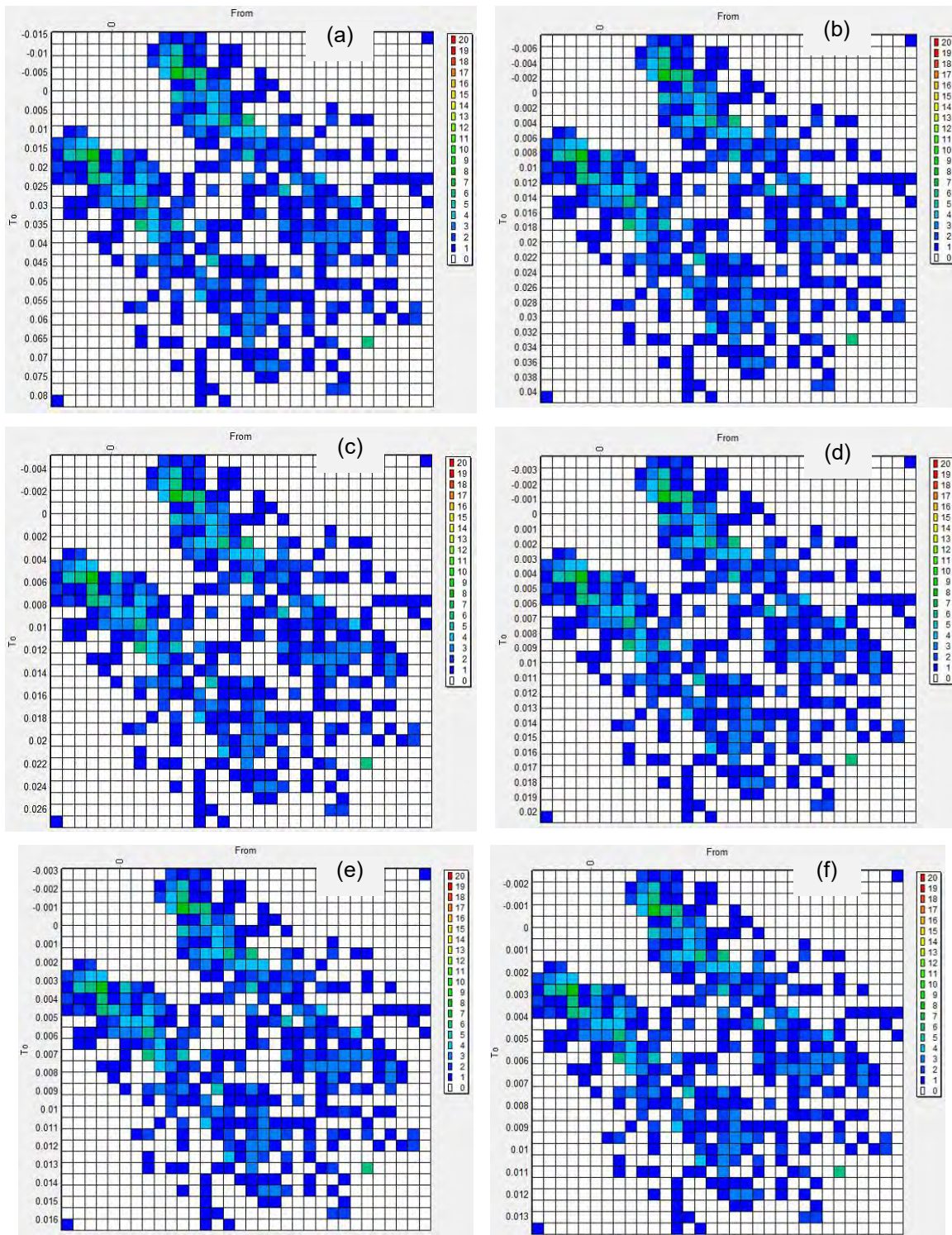
Figure D4-15 Rainflow matrix of BRBs for Memphis, Tennessee with $T_r = 90^0$F for :
(a) $L_2/L = 1\%$; (b) $L_2/L = 2\%$; (c) $L_2/L = 3\%$;(d) $L_2/L = 4\%$; (e) $L_2/L = 5\%$; and
(f) $L_2/L = 6\%$
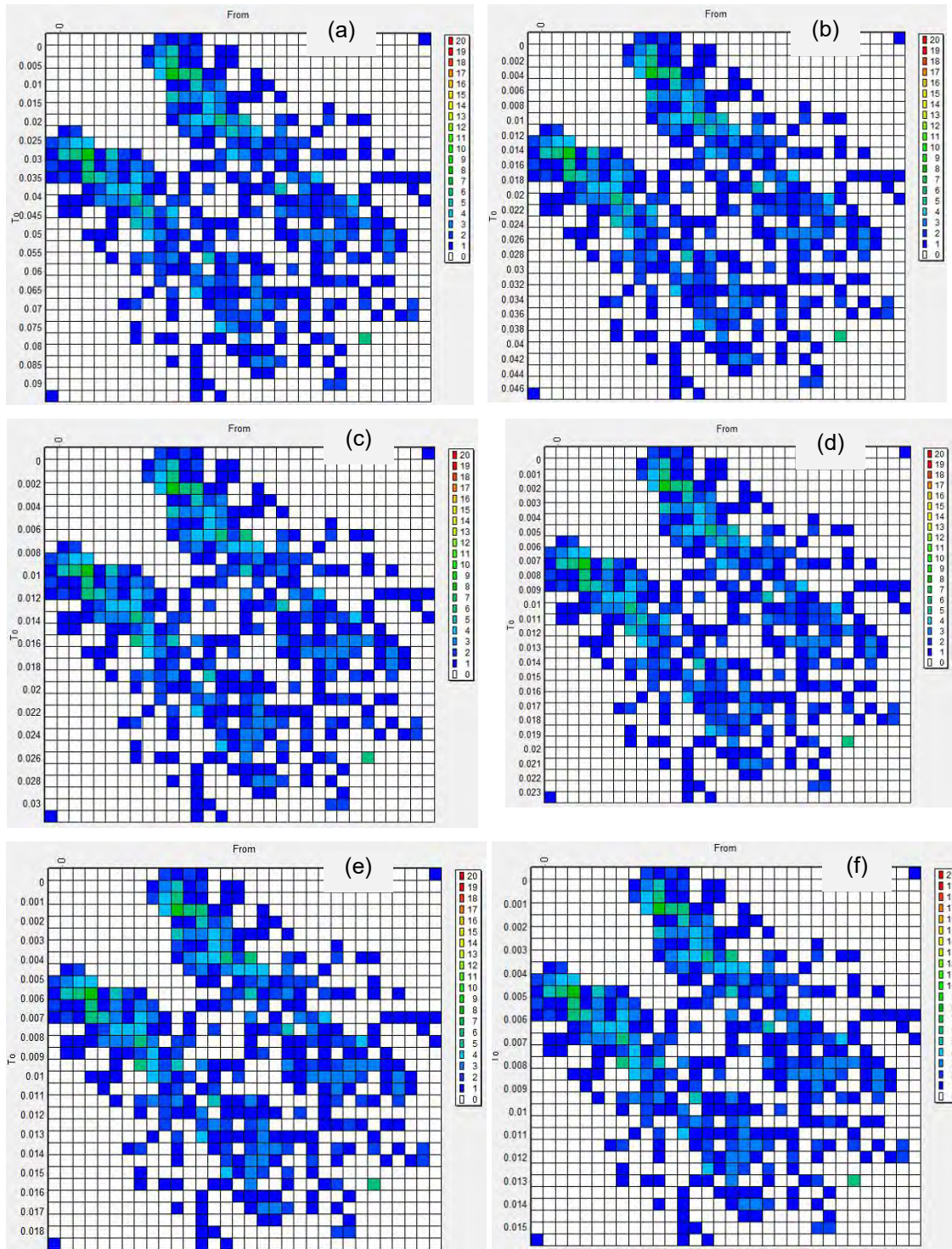
Figure D4-16 Rainflow matrix of BRBs for Memphis, Tennessee with $T_r = 100^0$F for : (a) $L_2/L = 1\%$; (b) $L_2/L = 2\%$; (c) $L_2/L = 3\%$; (d) $L_2/L = 4\%$; (e) $L_2/L = 5\%$; and (f) $L_2/L = 6\%$

D 4.4   Cyclic Stress-Strain Relationship

Cycle identified from the Rainflow counting method, with their associated strain, corresponds to positive or negative stress peaks in which the stress is calculated from the Ramberg-Osgood and Morrow equations, as presented in Section D2.3.4. The BRBs cyclic strain hardening exponent and coefficient which are related to the cyclic and fatigue properties of the ASTM A36 (as given in Section D3.2.2) are used in these equations. The calculated stress with its associated strain is plotted forming a cyclic stress-strain hysteresis loop which defines a single fatigue cycle in stress-strain space. The results of cyclic stress-strain hysteresis loops of BRBs for Memphis, Tennessee are shown in Figure D4.17 to D4.24. These hysteresis loops are associated with thermal strain histories and counted cycles provided in Section D4.2 and D4.3. For example, stress-strain hysteresis loops in Figure D4.17 correspond to thermal strain histories in Figure D4.2 with number of cycles resulted from Rainflow matrix in Figure D4.9, etc.

Figure D4.20(a) shows an example of stress-strain hysteresis loop generated from thermal strain histories in Figure D4.4(a) with counted cycles given in Rainflow matrix in Figure D4.12(a). The hysteresis loop in Figure D4.20(a) shows cyclic behavior of the BRBs at $T_r = 60^0\text{F}$ for the ratio of $L_2/L = 1\%$. The cyclic curve shown in Figure D4.20(a) follows Ramberg-Osgood hysteresis model with the loop shape following the Masing behavior.   The cyclic curve consists of both elastic and plastic strains where the cyclic yield limit in the curve is defined by $\sigma_y = 250$ MPa and $\varepsilon_y = 0.00124$.
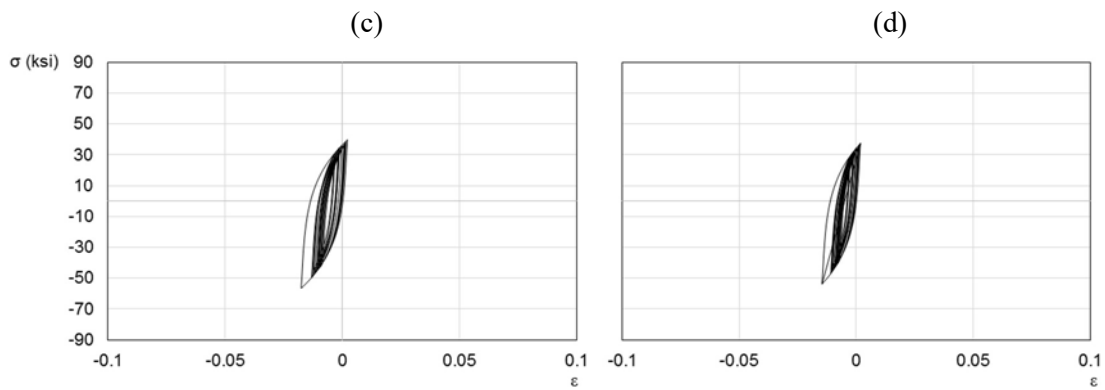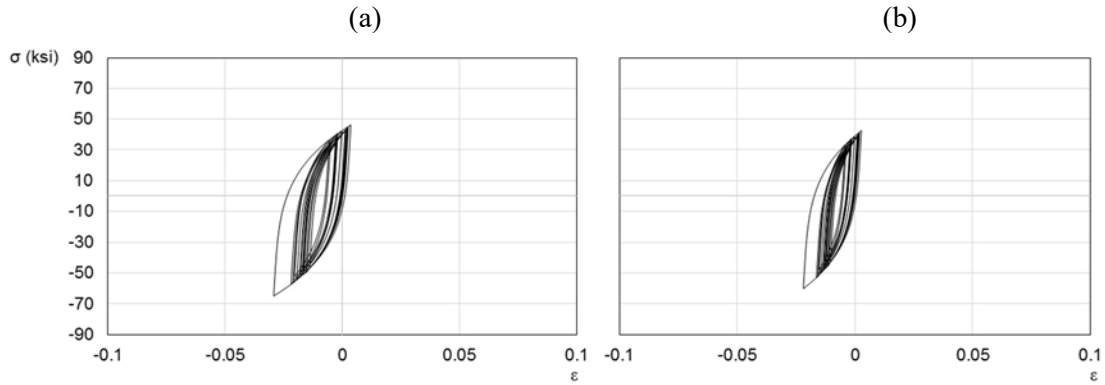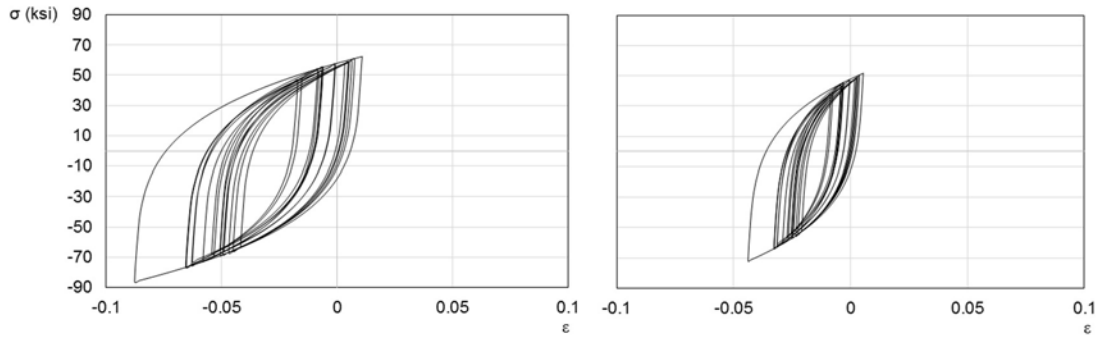
Figure D4-17 Stress-strain Relationship of BRBs for Memphis, Tennessee with $T_r = 30^0$F for : (a) $L_2/L = 1\%$; (b) $L_2/L = 2\%$; (c) $L_2/L = 3\%$; (d) $L_2/L = 4\%$; (e) $L_2/L = 5\%$; and (f) $L_2/L = 6\%$
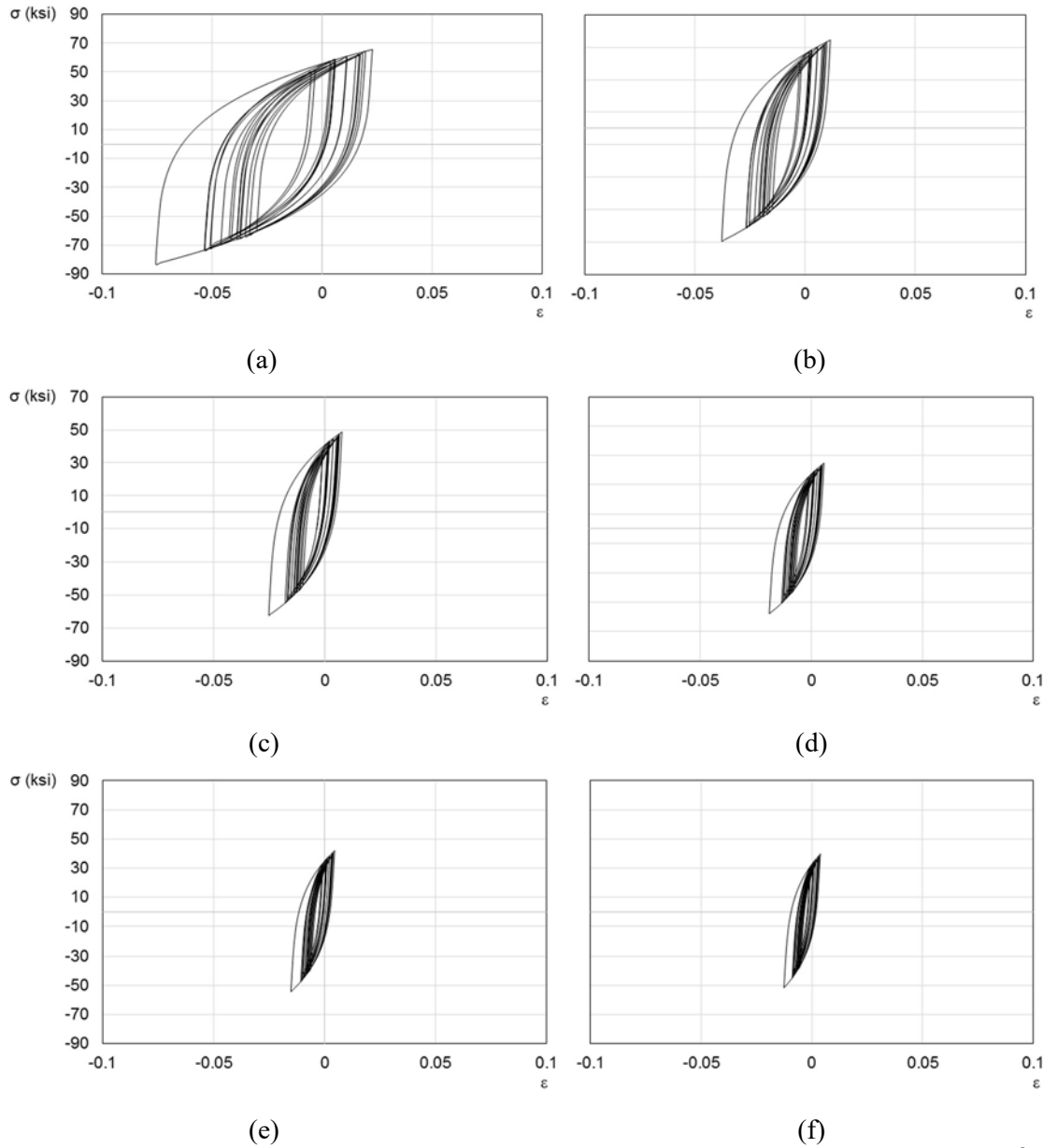
Figure D4-18 Stress-strain Relationship of BRBs for Memphis, Tennessee with $T_r = 40^0F$ for : (a) $L_2/L = 1\%$; (b) $L_2/L = 2\%$; (c) $L_2/L = 3\%$; (d) $L_2/L = 4\%$; (e) $L_2/L = 5\%$; and (f) $L_2/L = 6\%$
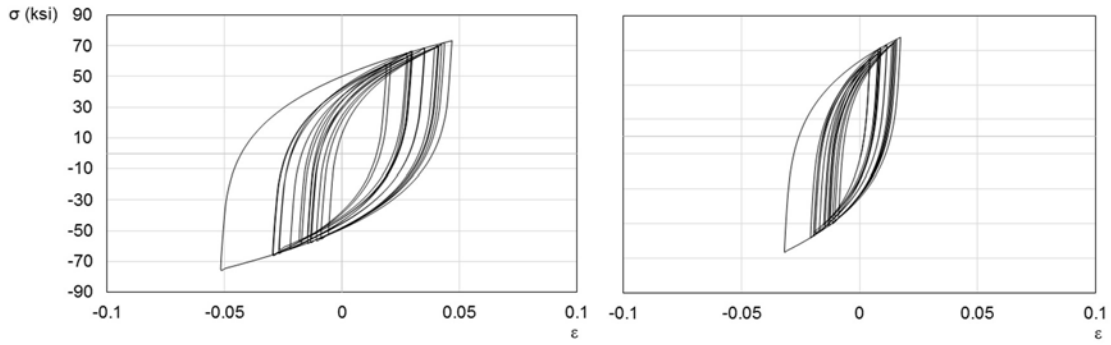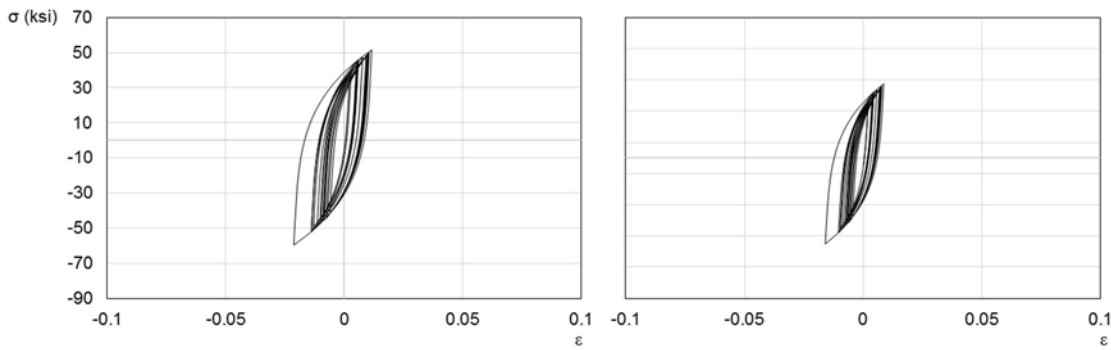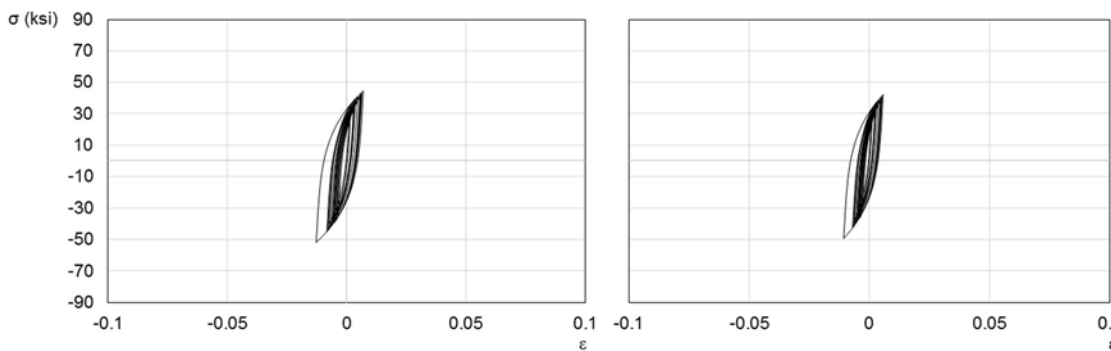
Figure D4-19 Stress-strain Relationship of BRBs for Memphis, Tennessee with $T_r = 50^0F$ for : (a) $L_2/L = 1\%$; (b) $L_2/L = 2\%$; (c) $L_2/L = 3\%$; (d) $L_2/L = 4\%$; (e) $L_2/L = 5\%$; and (f) $L_2/L = 6\%$
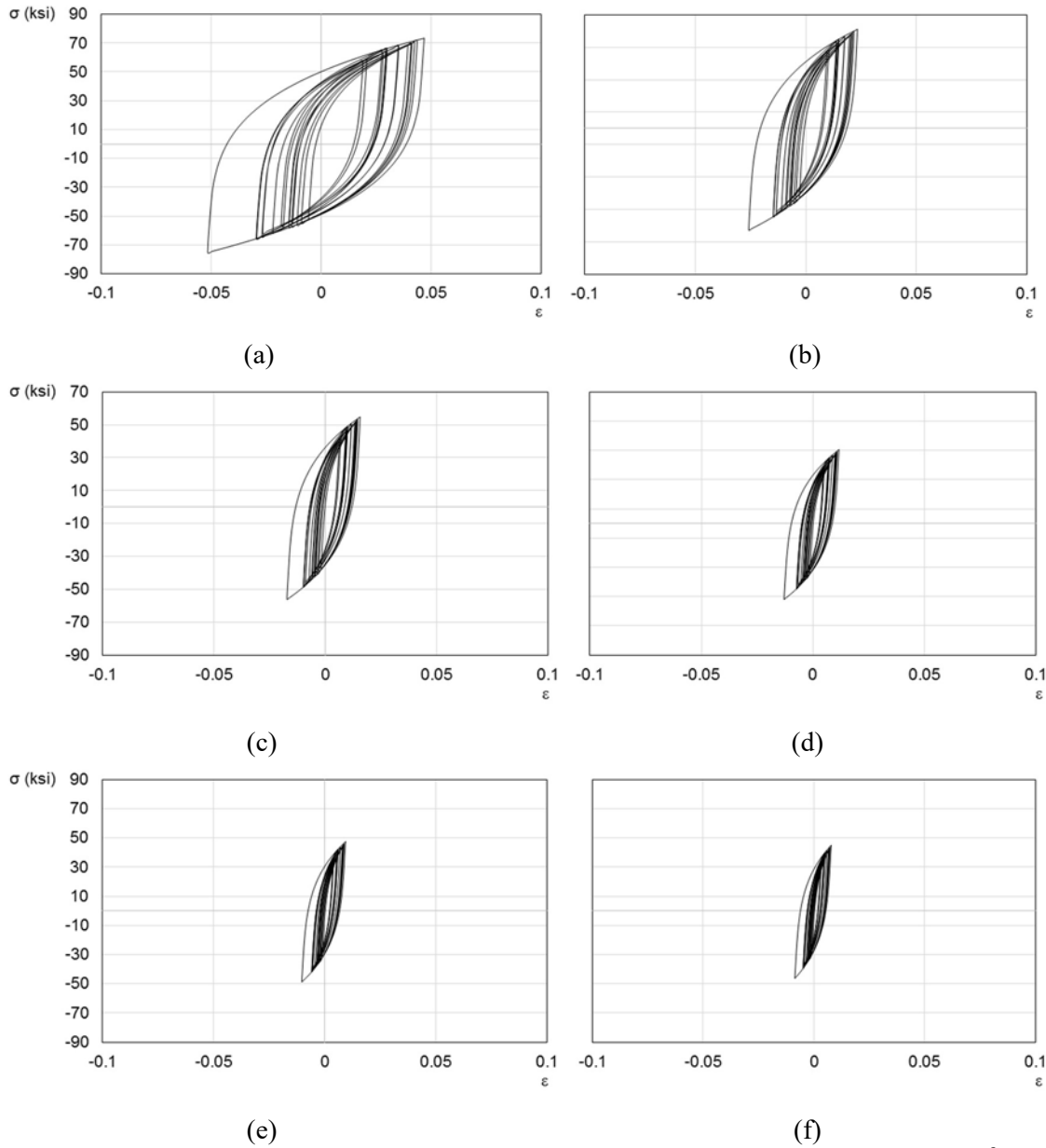
Figure D4-20 Stress-strain Relationship of BRBs for Memphis, Tennessee with $T_r = 60^0\text{F}$
for : (a) $L_2/L = 1\%$; **(b)** $L_2/L = 2\%$; **(c)** $L_2/L = 3\%$; **(d)** $L_2/L = 4\%$; **(e)** $L_2/L = 5\%$; **and (f)**
$L_2/L = 6\%$
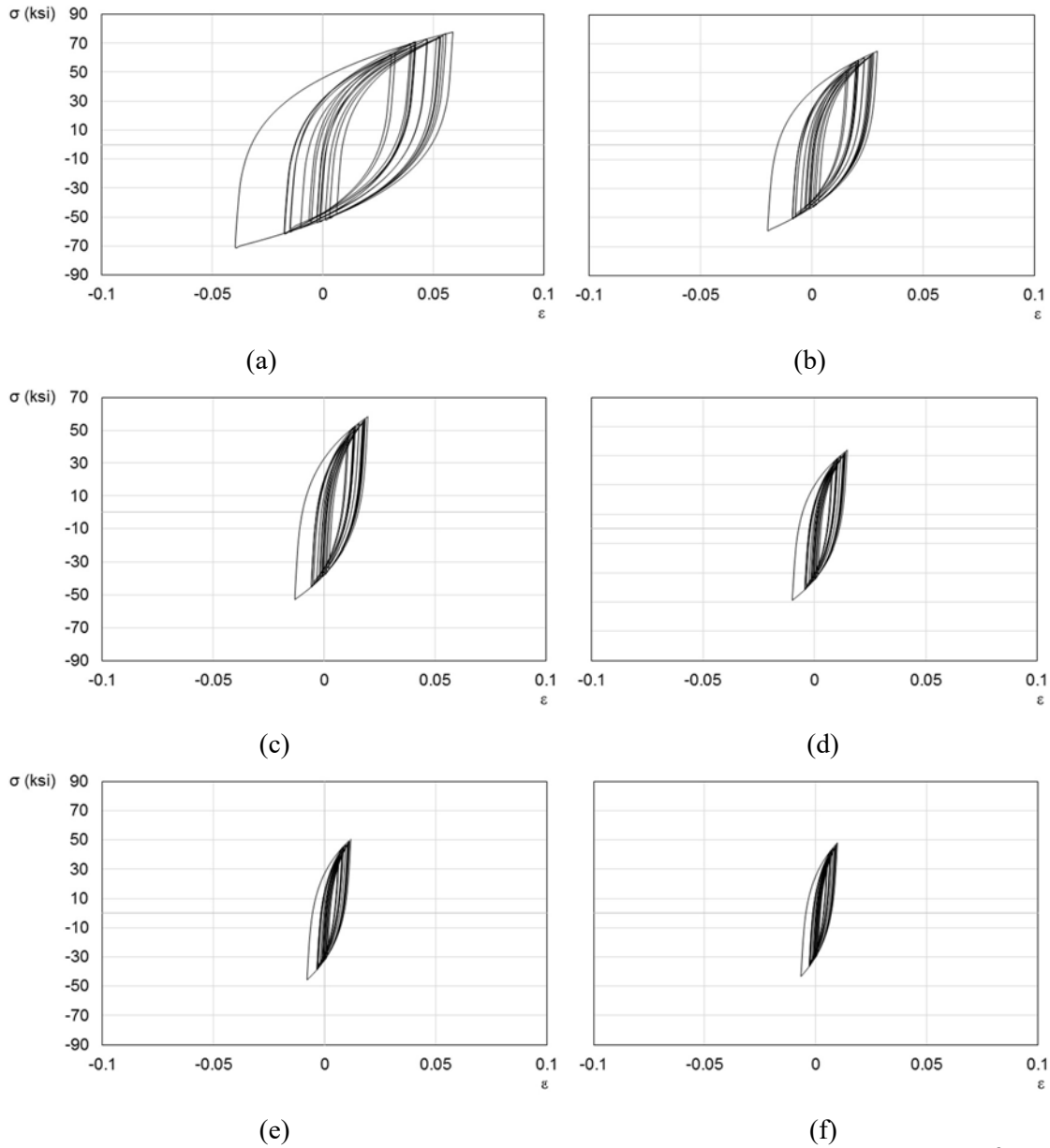
Figure D4-21 Stress-strain Relationship of BRBs for Memphis, Tennessee with $T_r = 70^0F$ for : (a) $L_2/L = 1\%$; (b) $L_2/L = 2\%$; (c) $L_2/L = 3\%$; (d) $L_2/L = 4\%$; (e) $L_2/L = 5\%$; and (f) $L_2/L = 6\%$
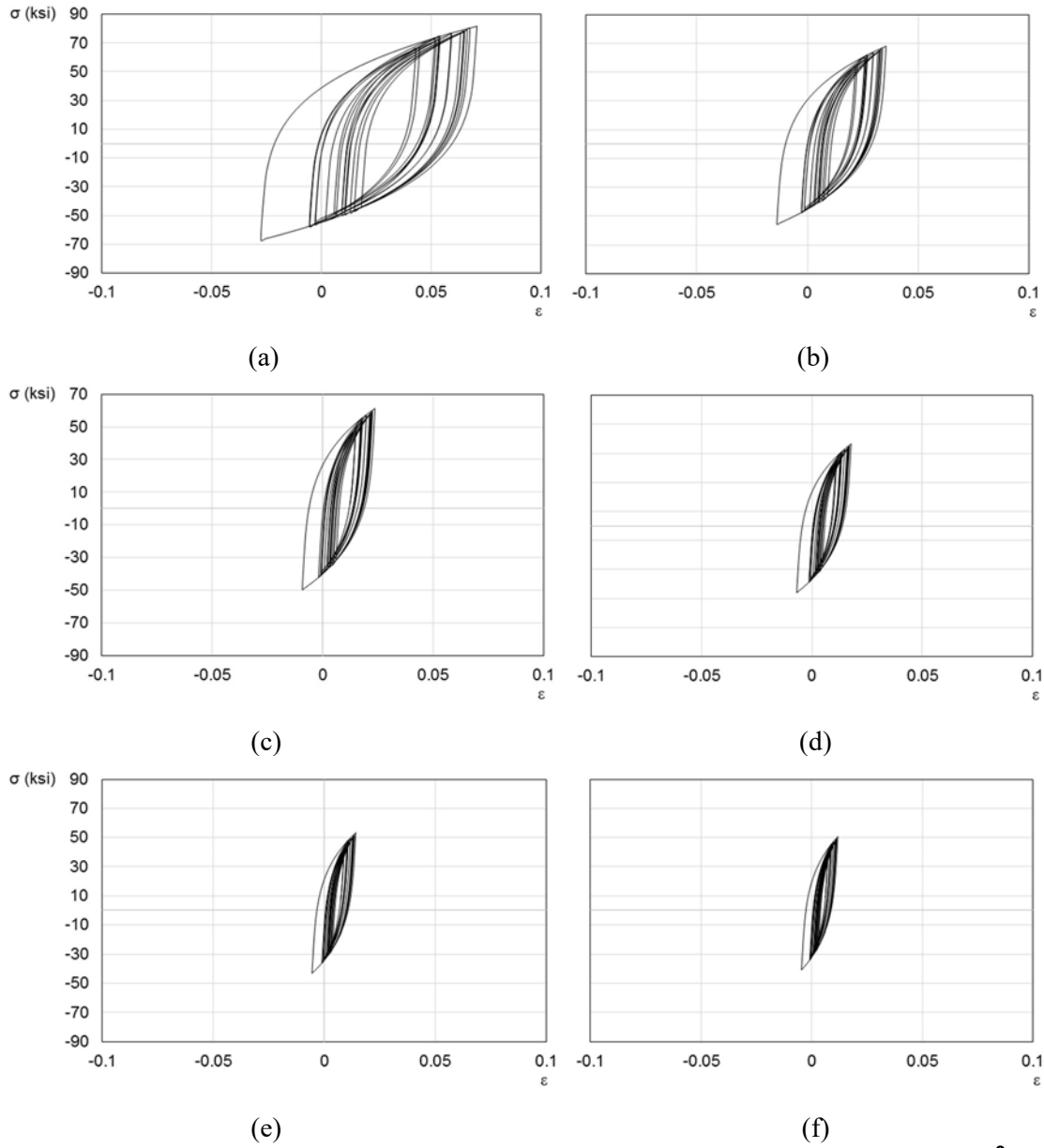
Figure D4-22 Stress-strain Relationship of BRBs for Memphis, Tennessee with $T_r = 80^0$F for : (a) $L_2/L = 1\%$; (b) $L_2/L = 2\%$; (c) $L_2/L = 3\%$; (d) $L_2/L = 4\%$; (e) $L_2/L = 5\%$; and (f) $L_2/L = 6\%$
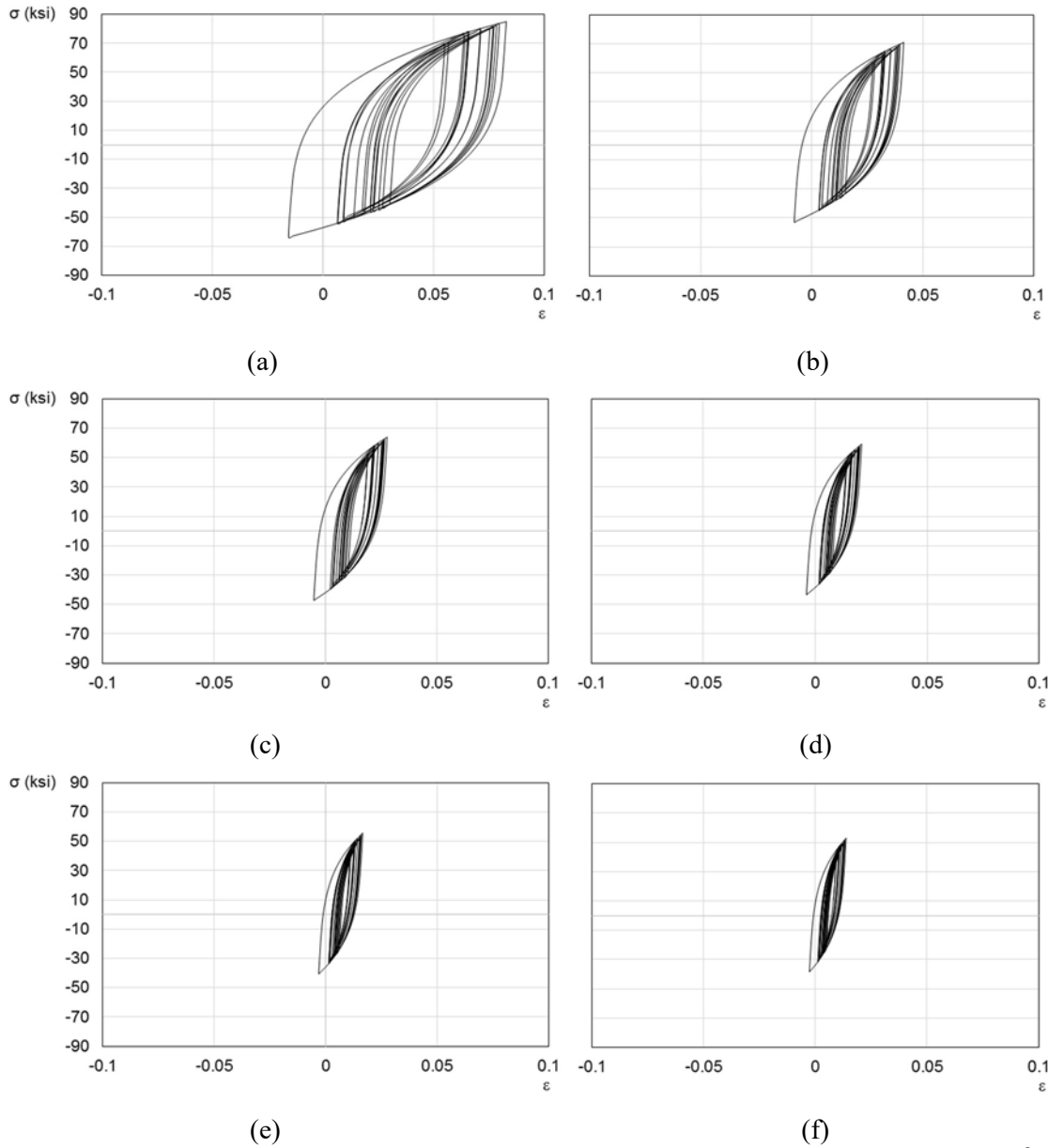
Figure D4-23 Stress-strain Relationship of BRBs for Memphis, Tennessee with $T_r = 90^0 F$ for : (a) $L_2/L = 1\%$; (b) $L_2/L = 2\%$; (c) $L_2/L = 3\%$; (d) $L_2/L = 4\%$; (e) $L_2/L = 5\%$; and (f) $L_2/L = 6\%$

(a)

(b)

(c)

(d)

(e)

(f)
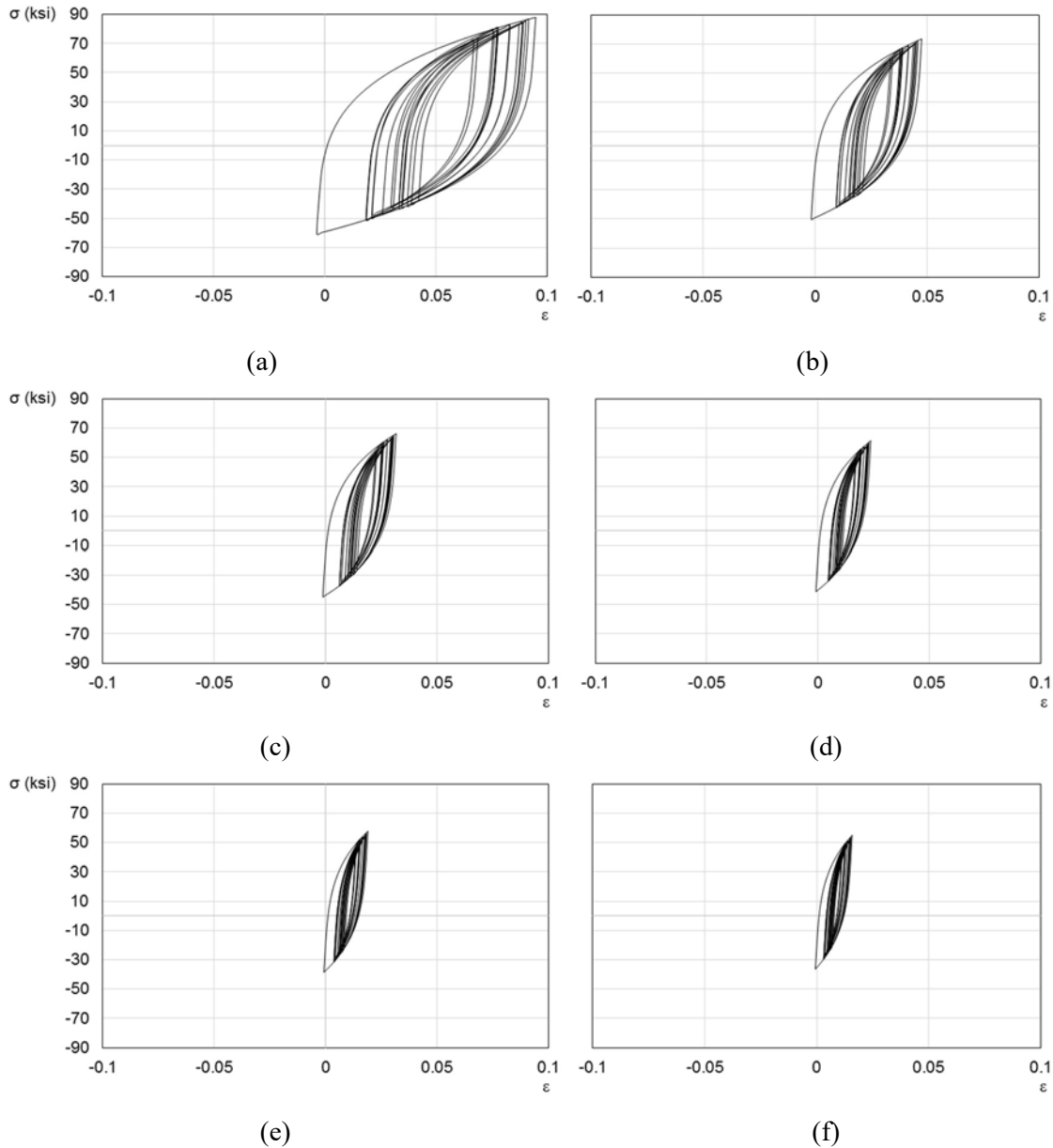
Figure D4-24 Stress-strain Relationship of BRBs for Memphis, Tennessee with $T_r = 100^0F$ for : (a) $L_2/L = 1\%$; (b) $L_2/L = 2\%$; (c) $L_2/L = 3\%$; (d) $L_2/L = 4\%$; (e) $L_2/L = 5\%$; and (f) $L_2/L = 6\%$

D 4.5   Low-cycle Fatigue Life of BRBs

The low-cycle fatigue failure of BRBs can be preliminarily assessed by methods which count the applied cycles of inelastic stress-strain of the base metal (understanding that some correction factor will be required, as described in Section D5). Three methods are chosen to estimate the low-cycle fatigue life of BRBs, considering the effect of mean stress or neglecting it. As described in Section D2.3.5, the Coffin-Manson and Basquin model is chosen as a "no-mean stress correction" model providing the basic relation between total strain range and cyclic life. Smith-Watson and

563

Topper as well as Morrow model are also used as two models to estimate fatigue life in which the fatigue process is sensitive to tensile mean stress in low-cycle fatigue regimes. Palmgren-Miner's rule is used to accumulate the fatigue damage of BRBs by assuming that failure occurs when the damage fraction reaches 1.

Figure D4.25 to D4.32 show the low-cycle fatigue life of the BRBs estimated from thermal strain histories, Rainflow counting method, and cyclic stress-strain hysteresis loop provided in the previous sections. The exact values of fatigue life in Figure D4.25 to D4.32 can be seen in Sub Appendix A for the location of Memphis, Tennessee. Low-cycle fatigue life results in these figures are presented from thermal strain histories calculated using Equations D3.1 and D3.18 to provide the comparison between the BRBs fatigue life estimation using simplified approach (as given in Equation D3.1) and more precise method (as given in Equation D3.18).

An expected design life of BRBs of 75 years, according to the AASHTO specifications, is highlighted by the dashed line shown in the figures. It can be seen that at the ratio of $L_2/L = 6\%$, the fatigue life, N_f, of the BRBs exceeds the 75 years design life required by AASHTO for all cases of reference temperature, T_r, as well as for all three methods of the Coffin-Manson and Basquin, Smith-Watson and Topper, and Morrow considered in this study. Low-cycle fatigue life results in Figure D4.25 to D4.32 also show that the BRBs fatigue life calculated using simplified approach of Equation D3.1 provide more conservative results than the one calculated using Equation D3.18. For example, in Figure D4.32 for $L_2/L = 6\%$, the low-cycle fatigue life of the BRB calculated by Equation D3.1 is 183, 83.9, and 136 years using Coffin-Manson and Basquin, Smith-Watson and Topper, and Morrow methods; respectively. As for low-cycle fatigue life calculated by Equation D3.18, the results are 154, 72.9 and 115 years for all three methods. The low-cycle fatigue life predicted by the more precise method is only approximately 1.7% , 2.6% and 0.8% (with respect to Coffin-Manson and Basquin, Smith-Watson and Topper, and Morrow methods) higher than the one calculated from the simplified approach.

The low-cycle fatigue life results also present that with an increment in T_r, a more conservative/less/shorter fatigue life is obtained using Smith-Watson and Topper compared to Coffin-Manson and Basquin as well as Morrow. Conversely, as the T_r declines, more compressive strains are calculated in BRB resulting in indefinite fatigue life estimated by Smith-Watson and Topper method compared to Coffin-Manson and Basquin or Morrow method. As an example, consider fatigue life at the ratio of $L_2/L = 3\%$ in Figure D4.25 and D4.32 where the thermal strain is calculated using Equation D3.1. The result shows that the increasing of T_r affects the low-cycle fatigue life of BRBs significantly in Smith-Watson and Topper model. In Figure D4.25 where $T_r = 30°F$, the fatigue lives calculated are 183, 3320 and 252 years whereas for $T_r = 100°F$ in Figure

D4.32, the fatigue lives are obtained as 171. 81.9 and 129 years using Coffin-Manson and Basquin, Smith-Watson and Topper, and Morrow methods, respectively. This difference is expected following the description in Section D2.3.5.1 and D2.3.5.2 that Smith-Watson and Topper method predicts an infinite fatigue life if the maximum tensile stress is zero or negative while Morrow method provides more accurate results in compressive loadings. As for Coffin-Manson and Basquin model, it generates almost similar fatigue life with the changing in reference temperature, T_r, since the only parameter in this model affecting the fatigue life is its strain ranges with insignificant variations of strains in each 10°F increment of T_r.

(a)   (b)
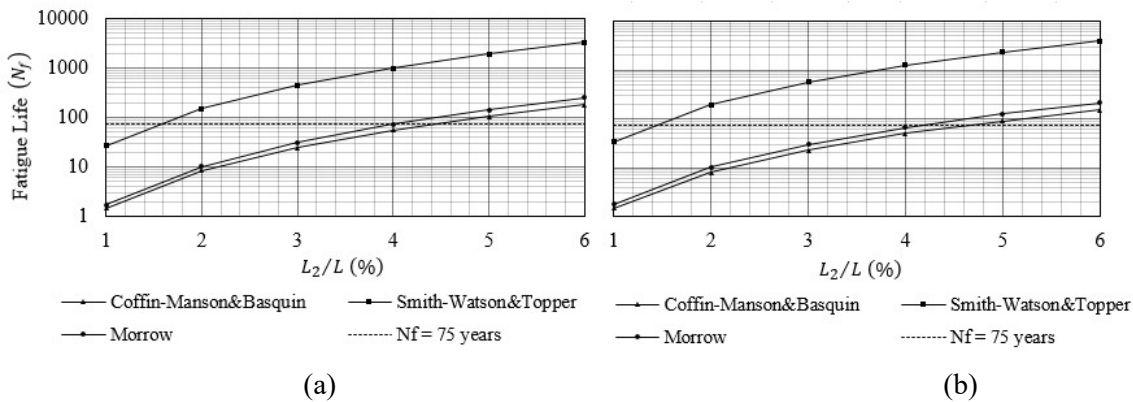
Figure D4-25 Fatigue life of BRBs for Memphis, Tennessee with $T_r = 30°F$ calculated by (a) Eq. D3.1 and (b) Eq. D3.18

(a)   (b)
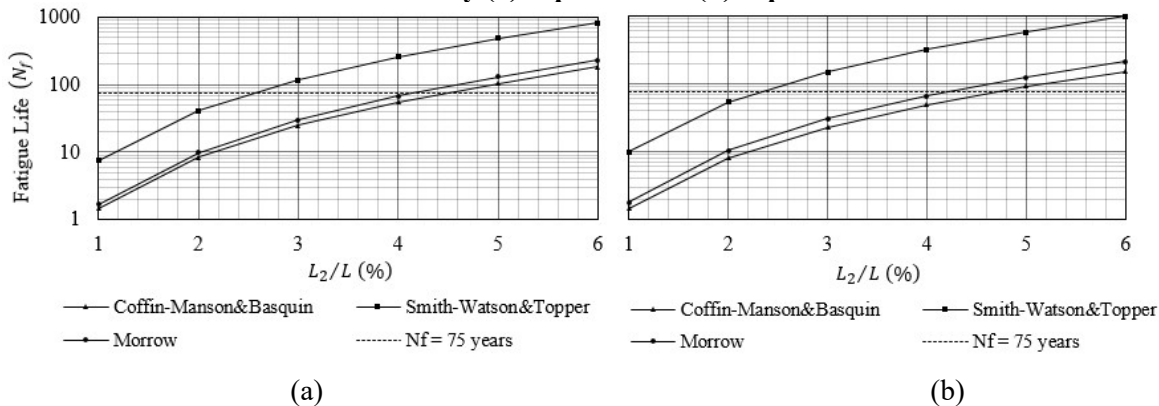
Figure D4-26 Fatigue life of BRBs for Memphis, Tennessee with $T_r = 40°F$ calculated by (a) Eq. D3.1 and (b) Eq. D3.18

(a)   (b)
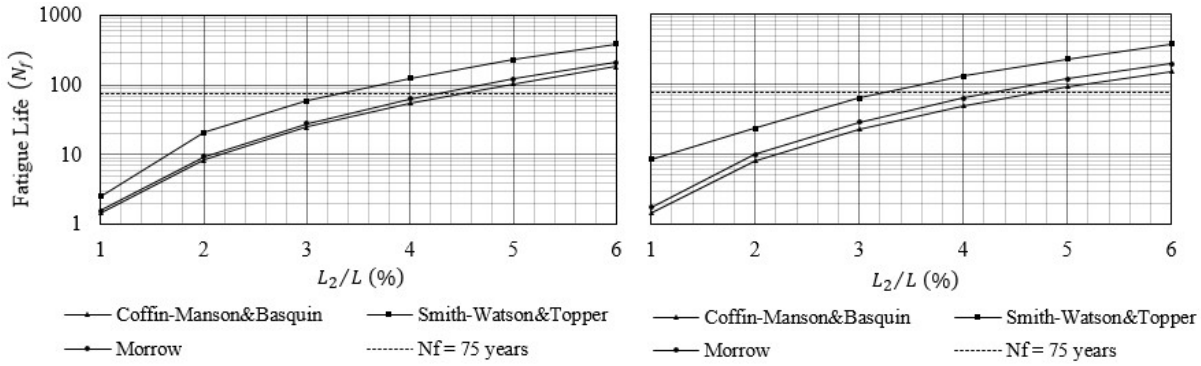
Figure D4- 27 Fatigue life of BRBs for Memphis, Tennessee with $T_r = 50°F$ calculated by (a) Eq. D3.1 and (b) Eq. D3.18

(a)   (b)
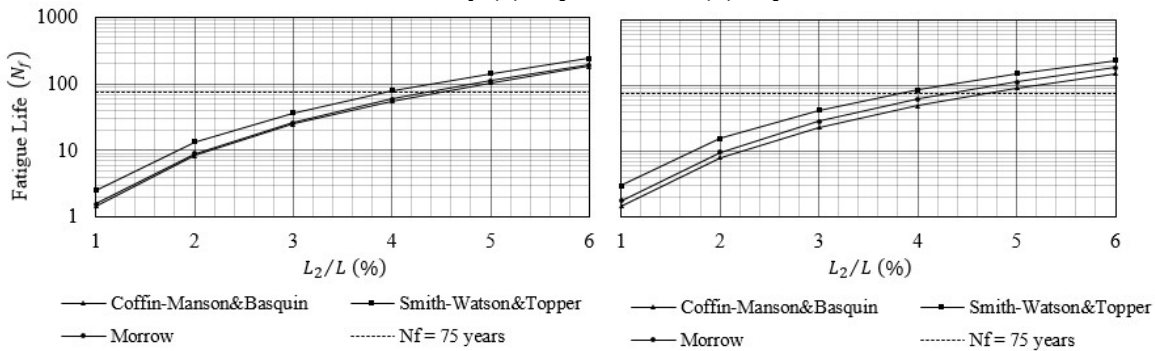
Figure D4-28 Fatigue life of BRBs for Memphis, Tennessee with $T_r = 60°F$ calculated by (a) Eq. D3.1 and (b) Eq. D3.18

(a)   (b)
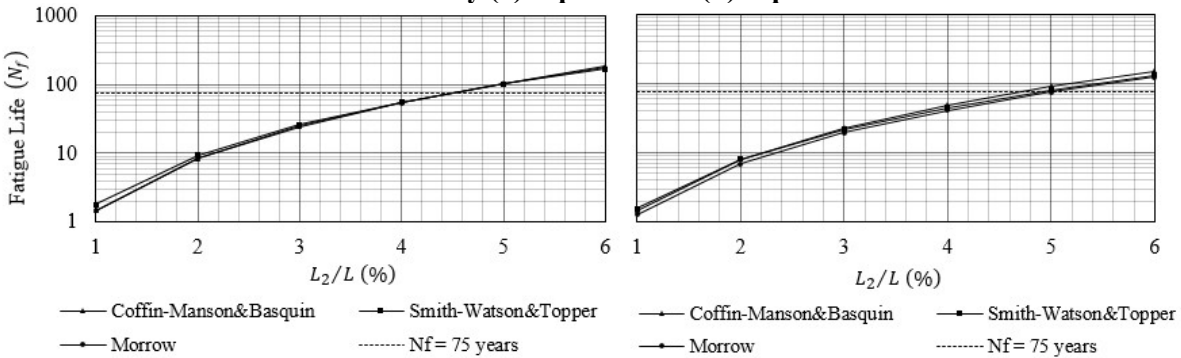
Figure D4-29 Fatigue life of BRBs for Memphis, Tennessee with $T_r = 70°F$ calculated by (a) Eq. D3.1 and (b) Eq. D3.18

566
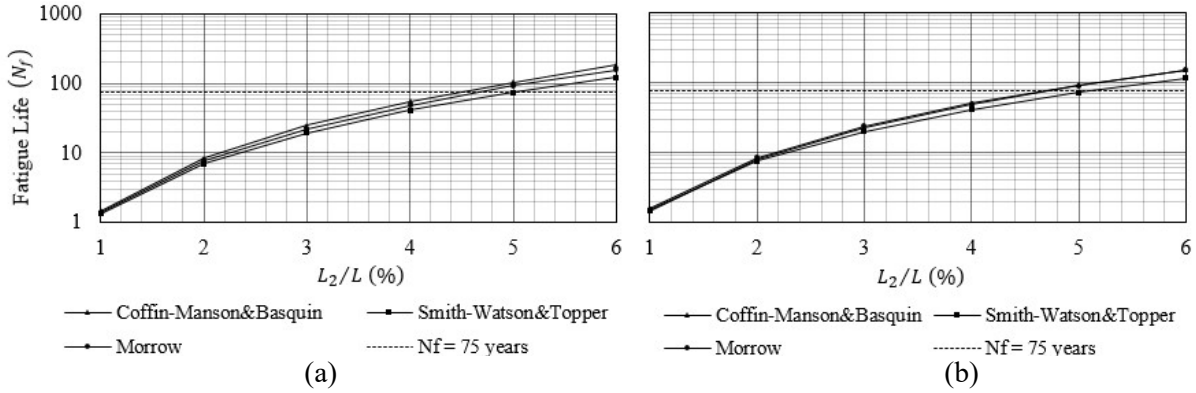
Figure D4-30 Fatigue life of BRBs for Memphis, Tennessee with $T_r = 80°F$ calculated by (a) Eq. D3.1 and (b) Eq. D3.18
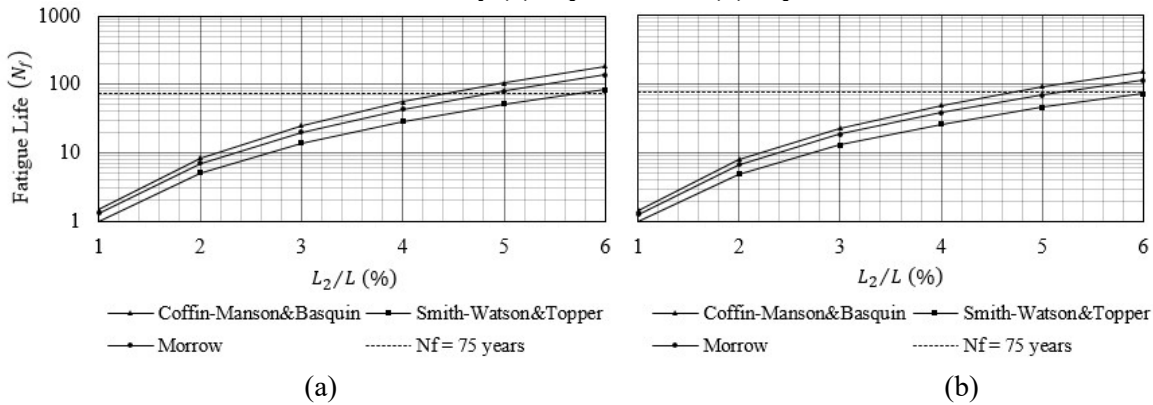
Figure D4-31 Fatigue life of BRBs for Memphis, Tennessee with $T_r = 90°F$ calculated by (a) Eq. D3.1 and (b) Eq. D3.18
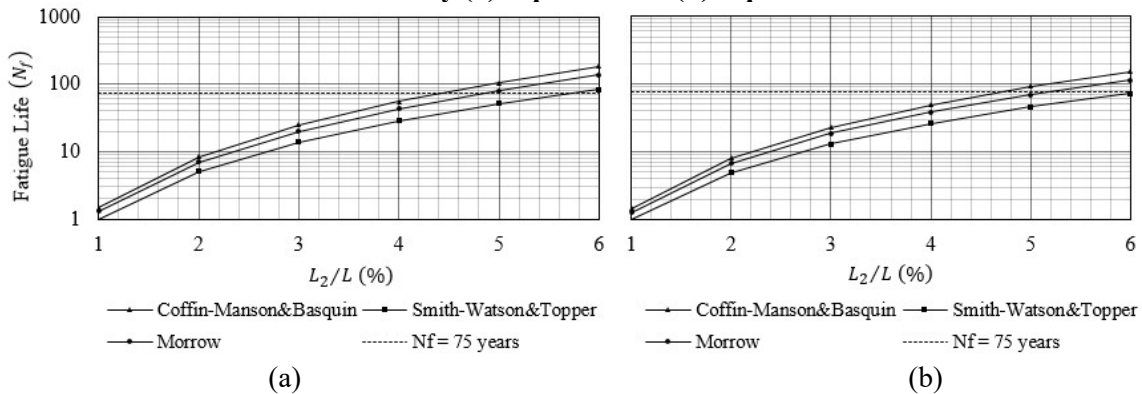
Figure D4-32 Fatigue life of BRBs for Memphis, Tennessee with $T_r = 100°F$ calculated by (a) Eq. D3.1 and (b) Eq. D3.18

Section D 5 Calibration factor based on experimental results

D 5.1 Introduction

As mentioned in Section D2.2.2, some experiments were conducted in the past to assess the low-cycle fatigue behavior of BRBs as an axial-type hysteresis damper for building and bridge applications. These experiments, conducted under strain-controlled loading histories, showed that

the applied strains caused local buckling, that itself produced additional flexural plastic deformations, and eventually fracture from low-cycle fatigue. Some of these experimental results are used in this chapter to develop a calibration factor for the results presented in Section D4, since the results in Section D4 calculated the estimated fatigue life of BRBs based on only its bare steel (for ASTM A36 material properties) neglecting the added strains due to local buckling. In other words, the effect of flexural strains due to local buckling, which adds up to the pure axial strains, was neglected in the calculation of BRBs thermal strains in Section D3. Therefore, a calibration factor is necessary considering that the local buckling of BRBs may reduce the estimated low-cycle fatigue life results presented in Section D4. Note that this calibration factor is expected to depend on how the BRB is fabricated, as this would have an impact on the amplitude of the local buckles in the BRB core. Therefore, since BRBs are not typically tested up to fracture, the calibration factors presented here are only applicable to the type of BRBs used in their development.

In this section, four experimental results of BRBs low-cycle fatigue under constant amplitude loading are presented. These studies are chosen by considering that the mechanical properties of the tested BRBs are closely equivalent to ASTM A36. A description of the tested BRBs is provided as well as their associated number of cycles to failure obtained from the experiments. Since little data is available for the low-cycle fatigue of BRBs under variable amplitude loading (Yamaguchi et al., 2004), the calibration is made only from the constant amplitude loading obtained from the four experiments by Usami et al. (2011), Wang et al. (2012), Akira et al. (2000) and Maeda et al (1998).

D 5.2   Material Properties of the Tested BRBs

As mentioned above, the BRBs in the four experiments considered here had material properties assumed to be closely equivalent to ASTM A36. More specifically, the properties for the two types of JIS steel grades used in these experiments are compared to ASTM 36 steel grade in Table D5.1. The low-cycle fatigue life experiments using SM400A were conducted by Usami et al. (2011) and Wang et al. (2012) whereas steel grade SN400B were used by Akira et al. (2000) and Maeda et al (1998). Note that experiments by Akira et al. (2000) and Maeda et al (1998) also included some BRBs that used a special low-yield steel that can develop 40% elongation at failure and has a different low-cycle fatigue life; therefore, these specimens are neglected here.

Table D5-1 Material properties of ASTM A36, SM400A and SN400B

Experiments by	Steel grade	E (Sampaio et al.)	σ_y (Sampaio et al.)	ε_y
(Higashida et al. 1978)	ASTM A36	200000	250	0.00124
(Usami et al. 2011), (Wang et al. 2012)	SM400A	210000	291	0.00139
(Akira 2000), (Maeda et al. 1998)	SN400B	205000	259	0.00126

D 5.3 Low-cycle Fatigue Experiments of BRBs

D 5.3.1 Description of Tested BRBs

BRBs made from JIS SM400A were tested up to low-cycle fatigue by Usami et al. (2011) and Wang et al. (2012). In the Usami et al. (2011) experimental study, twelve BRB specimens with steel grade SM400A were divided into two groups; in a first group of six BRBs, a special detail to improve low-cycle fatigue failure life was provided by smoothing the weld toes located at both ends of the brace member, while the remaining BRBs were left without such a detail. Wang et al. (2012) conducted experimental and numerical studies of BRBs using two series of BRBs made from SM400A steel. Two specimens with stoppers (named FE-4.0 and FT-3.5), and two without stoppers (called FE-4.0(NS) and FT-3.5(NS)), were tested to investigate the effects of stoppers on BRBs low-cycle fatigue. Here, only the low-cycle fatigue life results from the tested BRBs without the improved details and without stoppers are considered. The geometric dimensions of SM400A which were used in Usami et al. (2011) and Wang et al (2012) are given in Figure D5-1.

Maeda et al. (1998) conducted low-cycle fatigue test of BRBs made from JIS SN400B and from low-yielding steel type of LYP100. Akira (2000) studied the performance limit of BRBs used as hysteresis dampers in building structure by investigating their number of cycles to failure. Three types steel grades were used in the BRBs tested by Akira (2000), namely LYP100, LYP 235 and JIS SN400B. Since only BRBs made of steel having fatigue properties similar to ASTM A36 are of interest here, the results for the low-yielding steel types LYP100 and LYP235 are neglected in this chapter. The geometric dimensions of the BRBs made of JIS SN400B used in Maeda et al. (1998) and Akira (2000) are given in Figure D5-2.

(a)
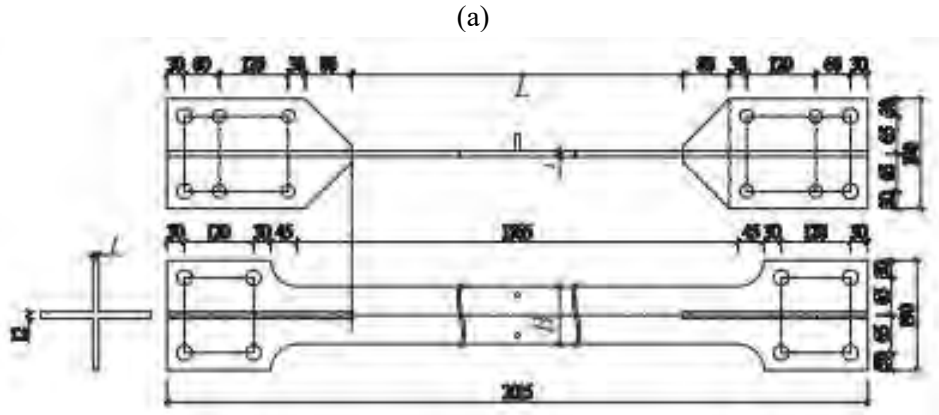
(b)

Figure D5-1 Dimensions of Tested JIS SM400A (in mm unit) :(a) Usami et al. (2011); (b) Wang et al (2012)
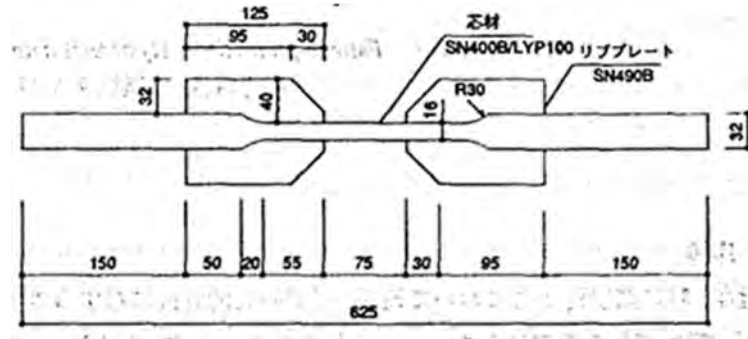
(a)
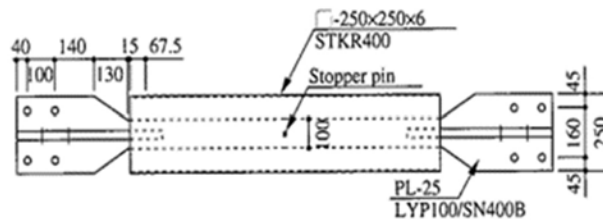
(b)

Figure D5-2 Dimensions of Tested JIS SN400B (in mm unit): (a) Maeda et al. (1998); (b) Akira (2000)

D 5.3.2 Loading Protocol

The low-cycle fatigue experiments of Maeda et al. (1998), Akira (2000), Usami et al. (2011) and Wang et al (2012) were conducted under constant amplitude loading test with the loading protocol shown in Figure D5-3. The experiments were done by first controlling the axial displacement up to the yield portion of BRBs, δ_y. Then, the constant strain amplitude, $\Delta\varepsilon/2$ specified in Table D5.3 was imposed cyclically, starting with tension strains, until the BRBs specimen failed. In each case, the number of cycles to failure were recorded.
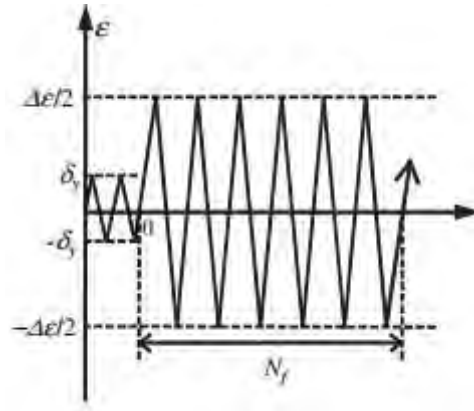
Figure D5-3 Loading protocol of constant amplitude loading test

D 5.3.3 Results

The number of cycles to failure of the BRBs used in the experiments, (N_{f_a}) are given in Table D5.3. The results show (as expected) that increasing strains of the BRBs core from amplitudes of 1% to 4% reduced the number of cycles needed for low-cycle fatigue failure.

D 5.3.4 Comparison with Fatigue Life Estimation using Coffin-Manson method

The number of cycles to failure for the constant strain amplitude, $\Delta\varepsilon/2$ specified in Table D5.3 are then re-calculated using the Coffin-Manson method given in Equation D2.4 using bare steel ASTM A36 fatigue properties (i.e., values of fatigue curve exponent and coefficient, elastic modulus, and plastic stain exponent and coefficient, provided in Section D3.2.2). The ratio between the numbers of cycles to failure obtained in the experiments, N_{f_a}, are then compared to the numbers of cycles to failure calculated using Coffin-Manson, N_{f_b}. The results are provided in Table D5.3. Note that the ratio of N_{f_a}, calculated from experiments over the number of cycles to failure for bare steel, N_{f_b}, is not a constant value.

D 5.4   Calibration Factor for Analysis Results Verified by Experimental Results

In this section, a calibration factor is calculated to modify the low-cycle fatigue life results using bare steel properties obtained in Section D4.5. To establish a correction factor, a regression analysis is first conducted to obtain the linear relationship between the strain amplitude, $\Delta\varepsilon/2$ and the number of failure cycles, N_f, for the experimental results, as well as for the values calculated on bare steel properties using Coffin-Manson equation. From these results, calibration factors are calculated to modify the low-cycle fatigue life results using bare steel properties obtained in Section D4.5.

Table 5- 2 Number of Failure Cycles of BRBs from Constant Amplitude Strain Loading

Experiments by	Specimens	$\Delta\varepsilon/2$	Number of failure cycles (N_f)		N_{fa}/N_{fb}
			Experiment (N_{fa})	Coffin-Manson (N_{fb})	
Maeda et al. 1998	400-D1	0.0072	534	3116	0.17
	400-D2	0.00485	1481	7484	0.20
	400-D3	0.00375	3100	13238	0.23
	400-D4	0.00285	8650	24330	0.35
	400-D5	0.00215	24250	45454	0.53
	400-L1	0.00085	63900	355961	0.18
	400-L2	0.000425	376000	1655977	0.23
	400-L3	0.0003	1140000	3581581	0.32
	400-L4	0.00017	5350000	12655943	0.42
Akira 2000	400-200	0.02	140	1504	0.09
	400-150	0.015	211	2847	0.07
	400-040	0.004	4050	53351	0.07
Usami et al. 2011	FE-1.0	0.01	111	1504	0.07
	FE-2.0	0.02	29	323	0.09
	FE-3.0	0.03	14	132	0.11
Wang et al. 2012	FE-4.0 (NS)	0.04	4	70	0.06
	FT-3.5(NS)	0.035	5	94	0.05

D 5.4.1 Calibration Factor for SM400A

The exponential regression for the SM400A as well as bare steel BRBs are provided in Figure D5-4 to obtain the linear relationship between strain amplitude, $\Delta\varepsilon/2$ and the number of failure cycles, N_f. The equations for the bare steel and SM400A are given as:

Bare steel   : $y = 3068.3e^{-98.14x}$ (D5.1)

SM400A   : $y = 317.27\ e^{-111.8x}$ (D5.2)

A calibration factor, α, is calculated by scaling the straight lines equations (in log-linear space) obtained for the bare steel to be equal to that of SM400A, as :

$$\alpha\ (3068.3e^{-98.14x}) = 317.27\ e^{-111.8x} \qquad (D5.3)$$

To solve this equation, the value of x is taken as 0; therefore, the calibration factor, α, can be calculated as :

$$\alpha = 317.27/3068.3 = 0.103 \approx 0.1$$

The results shown in Figure D5-5 illustrate that the calibrated values match the experimental one at a strain amplitude of 1% and 3%, with standard error of 1% at strain amplitudes of 2%, 3.5% and 4%.

Therefore, the calibration factor obtained by calibration on the SM400A BRBs experimental results, α, is taken as 0.1. Assume that the ratio of $L_2/L= 6\%$ is chosen, then using the calibration factor, $\alpha = 0.1$, the low-cycle fatigue life when using the same ratio of $L_2/L= 6\%$ would now become:

$$N_f = \alpha (75) = 0.1 \times 75 = 7.5 \text{ years}$$

Therefore, the BRBs would have to be periodically replaced, or made longer to achieve the same 75 years' fatigue life.
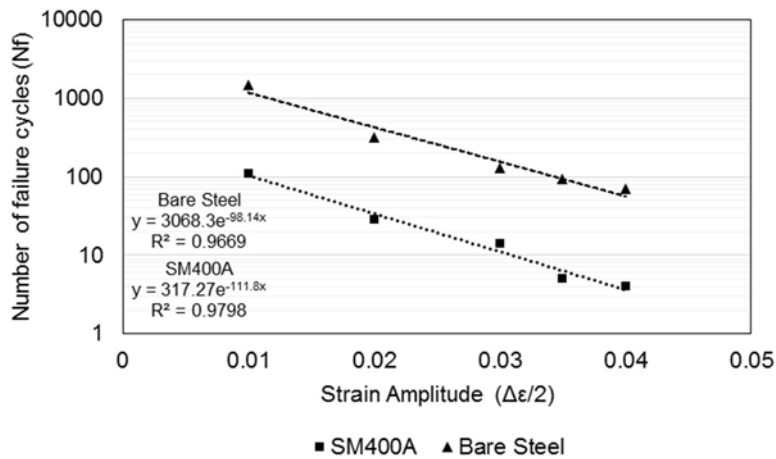
Figure D5-4 Exponential Regression of Bare Steel and SM400A
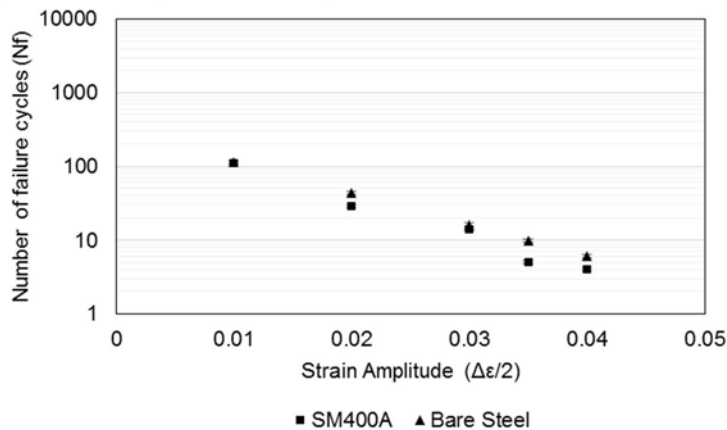
Figure D5-5 Calibrated Number of Failure Cycles of Bare Steel to SM400A

D5.4.2 Calibration Factor for SN400B

D5.4.2.1 Considering Elastic and Plastic Strain Amplitudes

A simple power regression of number of cycles to failure of SN400B from experiment and Coffin-Manson method is given in Figure D5-6. All the strain amplitudes varied from elastic to

plastic strain provided in Table D5.3 are used in the power regression model. The results for the SN400B BRBs compared to ASTM A36 bare steel are given in Figure D5-6 in which the equations for the bare steel and SN400B are given as:

Bare Steel : $y = 0.0552x^{-2.218}$ (D5.4)

SN400B : $y = 0.0022x^{-2.477}$ (D5.5)

Similar to Section D5.4.1, a calibration factor, β, is calculated by taking the equations of straight lines of BRBs to be equal to bare steel, as :

$$\beta\ (0.0552x^{-2.218}) = 0.0022x^{-2.477}$$ (D5.6)

To simplify this equation, the value of x is taken as 1; therefore, the calibration factor, β, can be calculated as :

$$\beta = 0.0022/0.0552 = 0.0398 \approx 0.04$$

Therefore, the calibration factor using low-cycle fatigue life results of SN400B, β, is taken as 0.04. Using the calibration factor, $\beta = 0.04$, the low-cycle fatigue life results of 75 years obtained at the ratio of $L_2/L= 6\%$ is now calibrated as :

$$N_f = \alpha\ (75) = 0.04 \times 75 = 3 \text{ years}$$
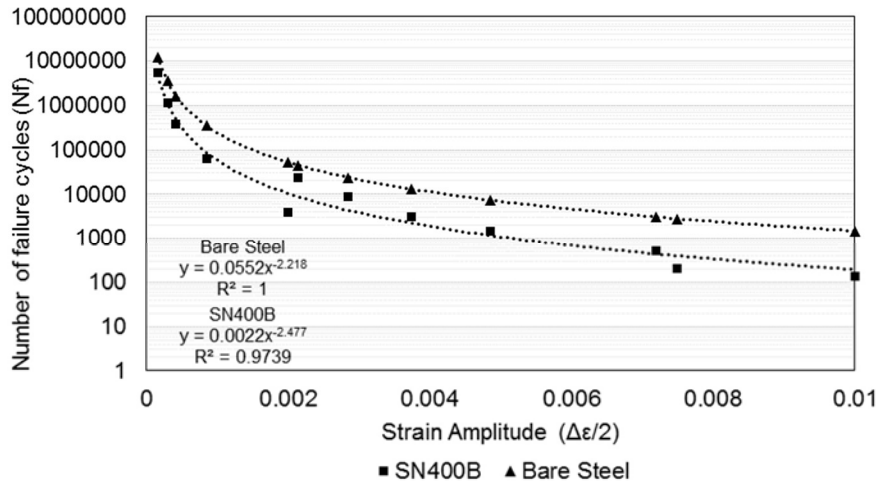
Figure D5-6 Power Regression of SN400B and ASTM A36 considering all strain amplitudes

D5.4.2.2 Considering only Plastic Strain Amplitudes

The regression analysis provided in Figure D5-6 considers all the strain amplitudes including the elastic strain which is less than yield strain of ASTM A36, $\varepsilon_y = 0.00124$. Here, only the plastic strain amplitude is considered in the analysis since it contributes more to the fatigue life of the BRBs. A simple exponential regression of number of cycles to failure of SN400B from experiment and Coffin-Manson method is given in Figure D5-7 and only strain amplitudes which are more than $\varepsilon_y = 0.00124$ in Table D5.3 are used in the regression model.

The equations generated for the SN400B as well as bare steel of ASTM A36 when only plastic strain amplitudes considered are given as:

Bare Steel : $$y = 93471e^{-449.8x} \qquad (D5.7)$$

SN400B : $$y = 31596\ e^{-583.2x} \qquad (D5.8)$$

Similar to Section D5.4.1, a calibration factor, γ, is calculated by taking the equations of straight lines of BRBs to be equal to bare steel, as :

$$\gamma\ (93471e^{-449.8x}) = 31596e^{-583.2x} \qquad (D5.9)$$

To simplify this equation, the value of x is taken as 0; therefore, the calibration factor, γ, can be calculated as :

$$\gamma = 31596/93471 = 0.33 \approx 0.3$$

Therefore, the calibration factor using low-cycle fatigue life results of SN400B when only the plastic strain is considered is taken as 0.3. The results shown in Figure D5-8 illustrate that the calibrated values only match the experimental one at a strain amplitude of 0.285% with the standard error of 1% at the strain amplitudes of 0.2% and 0.3% up to 1%. Using the calibration factor, $\gamma = 0.3$, the low-cycle fatigue life results of 75 years obtained at the ratio of $L_2/L= 6\%$ is now calibrated as :

$$N_f = \gamma\ (75) = 0.3 \times 75 = 23 \text{ years}$$

Therefore, the BRBs would have to be periodically replaced, or made longer to achieve the same 75 years' fatigue life.

The calibration factors calculated using SM400A and SN400B provided in Section D5.4.2.1 and D5.4.2.2 are quite different; for the time being, while awaiting further experimental data, it is advisable to use the calibration factor that gives more conservative results. Therefore, the calibration factor for low-cycle fatigue life obtained for SM400A is used, in which the calibration factor for the bare steel is taken as $\alpha = 0.1$.
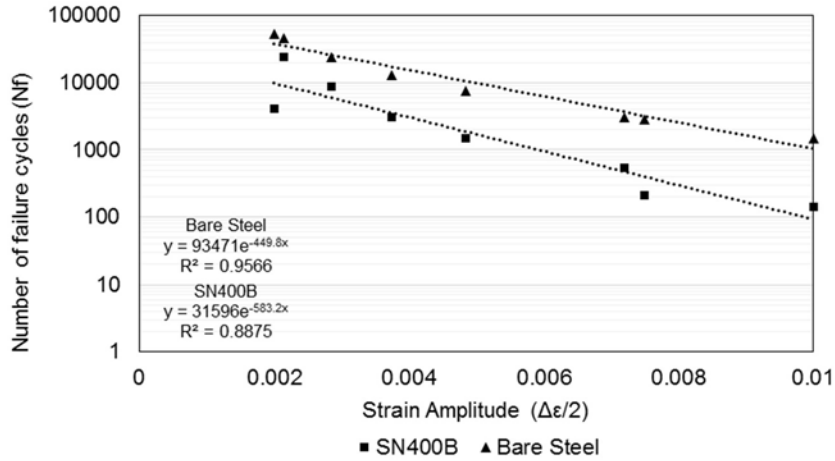
Figure D5-7 Exponential Regression of Bare Steel and SN400B considering only plastic strain amplitude
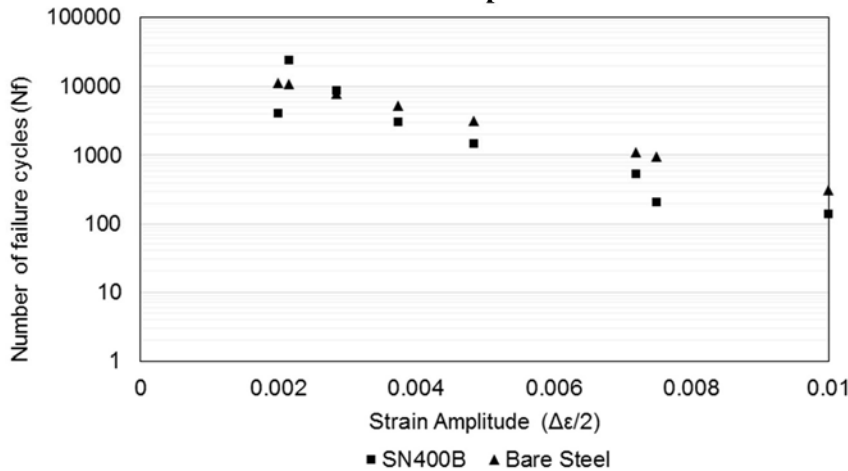
Figure D5-8 Calibrated Number of Failure Cycles of Bare Steel to SN400B

considering only plastic strain amplitude

Section D6 Summary and conclusions

D 6.1   Summary

Fatigue analysis was conducted to estimate the fatigue life of Buckling Restrained Braces installed longitudinally across the expansion joint of a bridge and subjected to a displacement history corresponding to the bridge thermal movements. Typical temperature fluctuation for nine cities located across North America were selected for the study to represent a broad cross-section of seismic regions and scenarios of daily and yearly temperature variations. A reference temperature (T_r) was defined as the temperature when the BRB was installed in the bridge, and analyses considered cases for this value ranging between the maximum and minimum temperature at the specific bridge location and varying by 10°F intervals. The ratios of BRB length over bridge length (L_2/L) considered in calculating BRB thermal strain were taken as 1%, 2%, 3%, 4%, 5% and 6%.

The Strain-Life approach was chosen for fatigue analysis and the strains of BRB corresponding to temperature changes were calculated. Three methods to obtain the fatigue life of BRB were chosen based on whether the mean Stress effect was considered or neglected in estimating the Fatigue Life, namely, the Basquin-Coffin and Manson, Smith-Watson and Topper, and Morrow methods. Based on results from those analyses, design recommendations were made to achieve the 75 years' design life required by AASHTO, so that BRBs could be used in applications across expansion joints (without the need to link them in series with lock-up devices) to accommodate the thermal changes.

The low-cycle fatigue life results in Section D4 in this appendix were estimated using bare steel ASTM A36 fatigue properties. However, to account for the fact that additional strains due to local buckling of BRB cores would reduce the estimated low-cycle fatigue life results given in Section D4, a calibration factor was developed based on previous experiments. Note that such calibration factors are only applicable to the type of BRBs considered in their development.

D 6.2   Conclusions

- As expected, in places where the fluctuation of temperature within a year were more severe (e.g., Memphis, Portland, Oregon; and Quebec City, Canada in this study), the calculated fatigue life of BRB was less compared to places where the yearly temperature variations were small (such as San Francisco and Charleston).

- BRB strains due to thermal effects was calculated with various levels of refinements. It was found that assuming the deformation of BRB due to thermal changes to be equal to the thermal expansion of the bridge (i.e., neglecting force applied to the bridge due to resistance to thermal expansion as well as deformation of BRB due to temperature changes) resulted in slightly larger strains in the BRB and provided more conservative estimation of low-cycle fatigue life of BRB.

- The Smith-Watson and Topper method provided the most conservative low-cycle fatigue life of BRBs made of bare steel ASTM A36 as this method accounted for the tensile mean stress in the low-cycle fatigue regime. Using this method, the ratio of BRB total length over bridge total length, L_2/L, should be of 6% to exceed the 75 years design life as required by AASHTO without suffering from low cycle fatigue (for the worst of all locations and installation temperatures considered).

- Results from previous low-cycle fatigue life experiments conducted on BRBs made from SM400A steel, were used to calibrate the calculated low-cycle fatigue life of bare ASTM A36 steel. As a result, the recommended ratio of BRB total length over bridge length is increased to $L_2/L = 6\%$ to exceed the AASHTO-specified 75 years design life without suffering from low

cycle fatigue (for the worst of all locations and installation temperatures considered). This result is due to the effect of flexural strains introduced by local buckling of the BRB yielding core, which add up to the pure axial strains of that core inside the BRB; this combined effect is accommodated by constructing a longer BRB to reduce the contribution due to axial strains.

- The calibration factor provided in this report is expected to depend on how the BRB is fabricated as this would have an impact on the amplitude of the local buckling inside the BRB core. As such, values should be developed for the various designs offered by BRB manufacturers.

D.7 REFERENCES

AASHTO (1992). "Standard specifications for highway bridges." American Association of State Highway Officials, Washington.

AASHTO, L. (2012). "Bridge Design Specifications, 2012." *American Association of State Highway and Transportation Officials, Washington DC*.

AccuWeather (2012). "Local weather 2012." *http://www.accuweather.com/en*.

Aiken, I. D., Mahin, S. A., and Uriz, P. "Large-scale testing of buckling-restrained braced frames." *Proc., Proceedings, Japan Passive Control Symposium*, 35-44.

Akira, W. (2000). "Fatigue properties of practical-scale unbonded braces." *Nippon steel technical report*, 82(0).

Arcari, A., and Dowling, N. E. (2012). "Modeling mean stress relaxation in variable amplitude loading for 7075-T6511 and 7249-T76511 high strength aluminum alloys." *International Journal of Fatigue*, 42, 238-247.

ASTM (2011). *ASTM E-1049 Standard practices for cycle counting in fatigue analysis*, ASTM International, West Conshohocken, PA.

Basquin, O. (1910). "The exponential law of endurance tests." *Proc ASTM*, 10, 625-630.

Bauschinger, J. (1886). "Mitt. Mech. Tech. Lab. Munchen." 13, 1-115.

Black, C. J., Makris, N., and Aiken, I. D. (2004). "Component testing, seismic evaluation and characterization of buckling-restrained braces." *Journal of Structural Engineering*, 130(6), 880-894.

Bouc, R. "Forced vibration of mechanical systems with hysteresis." *Proc., Proceedings of the Fourth Conference on Non-linear oscillation, Prague, Czechoslovakia*.

Carden, L. P., Itani, A. M., and Buckle, I. G. (2006). "Seismic performance of steel girder bridges with ductile cross frames using buckling-restrained braces." *J.Structural Eng.*, 132, 338-345.

Celik, O., and Bruneau, M. (2011). "Skewed Slab-on-Girder Steel Bridge Superstructures with Bidirectional-Ductile End Diaphragms." *Journal of Bridge Engineering*, 16(2), 207-218.

Celik, O. C., and Bruneau, M. (2009). "Seismic behavior of bidirectional-resistant ductile end diaphragms with buckling restrained braces in straight steel bridges." *Engineering Structures*, 31(2), 380-393.

Chiang, D., and Beck, J. (1994). "A new class of distributed-element models for cyclic plasticity—I. Theory and application." *International journal of solids and structures*, 31(4), 469-484.

Chu, C.-C., and Chernenkoff, R. (2001). "Crack closure-based analysis of fatigue tests with mean stresses." *International journal of fatigue*, 23, 187-194.

Clark, P., Aiken, I., Kasai, K., Ko, E., and Kimura, I. "Design procedures for buildings incorporating hysteretic damping devices." *Proc., Proceedings 68th annual convention*, 355-371.

Coffin Jr, L. (1962). "LOW CYCLE FATIGUE--A REVIEW." General Electric Co. Research Lab., Schenectady, NY.

Coffin, L. (1954). " A study of the effects of cyclic thermal stress on a ductile metal." *Trans ASME* 76, 931-950.

Committee, S. J. (1975). "Technical Report on Fatigue Properties." *SAE J1099, Society of Automotive Engineers, Warrendale, PA*.

Cui, W. (2002). "A state-of-the-art review on fatigue life prediction methods for metal structures." *Journal of marine science and technology*, 7(1), 43-56.

Di Sarno, L., and Manfredi, G. (2010). "Seismic retrofitting with buckling restrained braces: application to an existing non-ductile RC framed building." *Soil Dynamics and Earthquake Engineering*, 30(11), 1279-1297.

Dowling, N. E. (1971). "Fatigue failure predictions for complicated stress-strain histories." DTIC Document.

Dowling, N. E. (2004). "Mean stress effects in stress-life and strain-life fatigue." *Proc., 2nd SAE Brasil International Conference on Fatigue,* Sao Paolo, Brazil.

Ellyin, F., and Xia, Z. (1993). "A general fatigue theory and its application to out-of-phase cyclic loading." *ASME J Eng Mater Technol* 115, 411-416.

Fahnestock, L. A., Sause, R., and Ricles, J. M. (2007). "Seismic response and performance of buckling-restrained braced frames." *Journal of Structural Engineering*, 133(9), 1195-1204.

Fatemi, A., and Yang, L. (1998). "Cumulative fatigue damage and life prediction theories: a survey of the state of the art for homogeneous materials." *International journal of fatigue*, 20(1), 9-34.

Gurney, T. (1992). "Comparative fatigue tests on fillet welded joints under various types of variable amplitude loading."

Hashin, Z. (1980). "A reinterpretation of the Palmgren-Miner rule for fatigue life prediction." *Journal of Applied Mechanics*, 47(2), 324-328.

Higashida, Y., Burk, J. D., and Lawrence, F. V. (1978). "Strain-Controlled Fatigue Behavior of Astm A36 and A514 Grade-F Steels and 5083-0 Aluminum Weld Materials." *Weld J*, 57(11), S334-S344.

Huang, Y., Wada, A., Sugihara, H., Narikawa, M., Takeuchi, T., and Iwata, M. (2000). "Seismic performance of moment resistant steel frame with hysteretic damper." *Behaviour of Steel Structures in Seismic Areas: STESSA*, 403-409.

Ibrahim, M., and Miller, K. (1979). "Determination of fatigue crack initiation life." *Fatigue & Fracture of Engineering Materials & Structures*, 2(4), 351-360.

Ince, A., and Glinka, G. (2011). "A modification of Morrow and Smith–Watson–Topper mean stress correction models." *Fatigue Fract Engng Mater Struc*, 34, 854–867.

Itani, A. M., and Rimal, P. P. (1996). "Seismic analysis and design of modern steel highway connectors." *Earthquake spectra*, 12(2), 275-296.

Iwata, M., and Murai, M. (2006). "Buckling-restrained brace using steel mortar planks; performance evaluation as a hysteretic damper." *Earthquake engineering & structural dynamics*, 35(14), 1807-1826.

Johannesson, P., Svensson, T., and De Mare, J. (2005). "Fatigue life prediction based on variable amplitude tests—methodology." *International Journal of Fatigue*, 27(8), 954-965.

Kiggins, S., and Uang, C.-M. (2006). "Reducing residual drift of buckling-restrained braced frames as a dual system." *Engineering structures*, 28(11), 1525-1532.

Kim, J., and Choi, H. (2004). "Behavior and design of structures with buckling-restrained braces." *Engineering Structures*, 26(6), 693-706.

Koh, S. K., and Stephens, R. I. (1991). "Mean stress effects on low cycle fatigue for a high strength steel." *Fatigue Fracture of Engrg.Mater.and Struct*, 14, 413-428.

Kwofie, S., and Chandler, H. (2001). "Low cycle fatigue under tensile mean stresses where cyclic life extension occurs." *International journal of fatigue*, 23(4), 341-345.

Łagoda, T. (2001). "Energy models for fatigue life estimation under uniaxial random loading. Part II: Verification of the model." *International Journal of Fatigue*, 23(6), 481-489.

Lee, S.-H., and Royston, T. (2000). "Modeling piezoceramic transducer hysteresis in the structural vibration control problem." *The Journal of the Acoustical Society of America*, 108(6), 2843-2855.

Lemaitre, J., Sermage, J., and Desmorat, R. (1999). "A two scale damage concept applied to fatigue." *International Journal of Fracture*, 97(1-4), 67-81.

Li, Z., Chan, T. H., and Ko, J. M. (2001). "Fatigue analysis and life prediction of bridges with structural health monitoring data—Part I: methodology and strategy." *International Journal of Fatigue*, 23(1), 45-53.

Libertiny, G. (1968). "Effect of hydrostatic pressure on the short life fatigue property of an alloy steel." *Proceedings of the Institution of Mechanical Engineers*, 182(3C), 48-64.

Lin, X., and Chen, D. (2008). "Strain controlled cyclic deformation behavior of an extruded magnesium alloy." *Mater Sci Eng A*, 496 (1-2), 106-113.

López, W. A., and Sabelli, R. (2004). "Seismic design of buckling-restrained braced frames." *Steel tips*, 78.

Lutes, L. D., and Larsen, C. E. (1990). "Improved spectral method for variable amplitude fatigue prediction." *Journal of Structural Engineering*, 116(4), 1149-1164.

Macki, J. W., Nistri, P., and Zecca, P. (1993). "Mathematical models for hysteresis." *SIAM review*, 35(1), 94-123.

Maddox, S. (1975). "The effect of mean stress on fatigue crack propagation a literature review." *International Journal of Fracture*, 11(3), 389-408.

Maeda, Y., Nakata, Y., Iwata, M., and Wada, A. (1998). "Fatigue properties of axial-yield type hysteresis dampers." *J.Struct.Constr.Eng.*, 503, 109-115.

Maley, T. J., Sullivan, T. J., and Corte, G. D. (2010). "Development of a displacement-based design method for steel dual systems with buckling-restrained braces and moment-resisting frames." *Journal of Earthquake Engineering*, 14(S1), 106-140.

Manson, S. "Behavior of materials under conditions of thermal stress " *Proc., Heat Transfer Symposium*, University of Michigan.

Masing, G. *Proc., 2nd Int.Congr.Applied Mechanics*, 332-225.

Matsuishi, M., and Endo, T. (1968). "Fatigue of metals subjected to varying stress." *Japan Society of Mechanical Engineers, Fukuoka, Japan*, 37-40.

Miller, K., and Ibrahim, M. (1981). "Damage accumulation during initiation and short crack growth regimes." *Fatigue & Fracture of Engineering Materials & Structures*, 4(3), 263-277.

Miller, K., Mohamed, H., and De Los Rios, E. "Fatigue damage accumulation above and below the fatigue limit." *Proc., EGF1*.

Miller, K., and Zachariah, K. (1977). "Cumulative damage laws for fatigue crack initiation and stage I propagation." *The Journal of Strain Analysis for Engineering Design*, 12(4), 262-270.

Miner, M. A. (1945). "Cumulative damage in fatigue." *Journal of applied mechanics*, 12(3), 159-164.

Morrow, J. (1965). "Cyclic plastic strain energy and fatigue of metals in internal friction, damping, and cyclic plasticity." *ASTM STP*, 378, 45-87.

Morrow, J. (1968). "Fatigue properties of metals." *Fatigue Design Handbook*, Society of Automotive Engineers.

Nakagomi, T., Iwamoto, T., Kamura, H., Shimokawa, H., and Harayama, K. (2000). "Experimental study on fatigue characteristics of flat-bar brace with low yield stress steel stiffened by square steel tube." *J. Struct. Constr. Eng.*, 530, 155-161.

Okamura, H., Sakai, S., and Susuki, I. (1979). "Cumulative fatigue damage under random loads." *Fatigue & Fracture of Engineering Materials & Structures*, 1(4), 409-419.

Özdemir, H. (1976). "Nonlinear transient dynamic analysis of yielding structures." University of California, Berkeley.

Palmgren, A. (1924). "Die lebensdauer von kugellagern." *Zeitschrift des Vereins Deutscher Ingenieure*, 68(14), 339-341.

Polak, J., and Klesnil, M. (1979). "Cyclic plasticity and low cycle fatigue life in variable amplitude loading." *Fatigue & Fracture of Engineering Materials & Structures*, 1(1), 123-133.

Ramberg, W., and Osgood, W. R. (1943). "Description of stress-strain curves by three parameters." National Advisory Committee for Aeronautics, Washington DC.

Saal, H. (1972). "Fatigue crack growth in notched parts with compressive mean load." *Journal of Basic Engineering*, 94(1), 243-247.

Sabelli, R., Mahin, S., and Chang, C. (2003). "Seismic demands on steel braced frame buildings with buckling-restrained braces." *Engineering Structures*, 25(5), 655-666.

Saeki, E., Maeda, Y., Nakamura, H., Midorikawa, M., and Wada, A. (1995). "Experimental study on practical-scale unbonded braces." *Journal of Structural and Constructional Engineering, Architectural Institute of Japan*, 476, 149-158.

Sampaio, R., Maia, N., and Silva, J. (1999). "Damage detection using the frequency-response-function curvature method." *Journal of Sound and Vibration*, 226(5), 1029-1042.

Segal, F., and Val, D. V. (2006). "Energy evaluation for Ramberg–Osgood hysteretic model." *Journal of engineering mechanics*, 132(9), 907-913.

Segalman, D. J. (2005). "A four-parameter Iwan model for lap-type joints." *Journal of applied mechanics*, 72(5), 752-760.

Sivaselvan, M. V., and Reinhorn, A. M. (2000). "Hysteretic models for deteriorating inelastic structures." *Journal of Engineering Mechanics*, 126(6), 633-640.

Skelton, R., Maier, H., and Christ, H.-J. (1997). "The Bauschinger effect, Masing model and the Ramberg–Osgood relation for cyclic deformation in metals." *Materials Science and Engineering: A*, 238(2), 377-390.

Skelton, R. P., Maier, H. J., and Christ, H.-J. (1997). "The Bauschinger effect, Masing model and Ramberg-Osgood relation for cyclic deformatoin in metals." *Materials Science and Engineering*, A238, 377-390.

Smith, J. O. (1942). "The effect of Range of Stress on the fatigue strength of metals." *Bulletion No.334*, University of Illinois, Engineering Experiment Station, Urbana.

Smith, K. N., Watson, P., and Topper, T. H. (1970). "A stress-strain function for the fatigue of metals." *Journal of Materials ASTM*, 5, 767-778.

Sobczyk, K. (1987). "Stochastic models for fatigue damage of materials." *Advances in applied probability*, 652-673.

Stephens, R. I., Fatemi, A., Stephens, A. A., and and Fuchs, H. O. (2001). *Metal Fatigue in Engineering*, John Wiley, New York.

Stephens, R. I., Fatemi, A., Stephens, R. R., and Fuchs, H. O. (2000). *Metal fatigue in engineering*, John Wiley & Sons.

Stulen, F. L. (1965). "Fatigue life data displayed by a single quantity relating alternating and mean stress." Wright-patterson AFB, Ohio, 65-121.

Suresh, S. (1998). *Fatigue of materials*, Cambridge University Press, United Kingdom.

Svensson, T. (1997). "Prediction uncertainties at variable amplitude fatigue." *International Journal of Fatigue*, 19(93), 295-302.

Taheri, S., Vincent, L., and Le-roux, J.-C. (2013). "A New Model for Fatigue Damage Accumulation of Austenitic Stainless Steel Under Variable Amplitude Loading." *Procedia Engineering*, 66, 575-586.

Takao, K., and Endo, T. "Effect of mean stress on the fatigue crack initiation and propagation of a carbon steel." *Proc., Preprint for annual meeting on Japan Society of Mechanical Engineers*, 129-132.

Takeuchi, T., Ida, M., Yamada, S., and Suzuki, K. (2008). "Estimation of cumulative deformation capacity of buckling restrained braces." *Journal of structural engineering*, 134(5), 822-831.

Todinov, M. (2001). "Necessary and sufficient condition for additivity in the sense of the Palmgren–Miner rule." *Computational materials science*, 21(1), 101-110.

Topper, T. H., and Sandor, B. I. (1970). "Effects of mean stress and prestrain on Fatigue damage summation." *ASTM STP*, 462, 93-104.

Usami, T., Wang, C., and Funayama, J. (2011). "Low-cycle fatigue tests of a type of buckling restrained braces." *Procedia Engineering*, 14, 956-964.

Wang, C.-L., Usami, T., and Funayama, J. (2012). "Evaluating the influence of stoppers on the low-cycle fatigue properties of high-performance buckling-restrained braces." *Engineering Structures*, 41, 167-176.

Wang, C.-L., Usami, T., and Funayama, J. (2012). "Improving low-cycle fatigue performance of high-performance buckling-restrained braces by toe-finished method." *Journal of Earthquake Engineering*, 16(8), 1248-1268.

Watanabe, A., Hitomi, Y., Saeki, E., Wada, A., and Fujimoto, M. "Properties of brace encased in buckling-restraining concrete and steel tube." *Proc., Proceedings of Ninth World Conference on Earthquake Engineering*, 719-724.

Webb, G., Kurdila, A., and Lagoudas, D. (2000). "Adaptive hysteresis model for model reference control with actuator hysteresis." *Journal of Guidance, Control, and Dynamics*, 23(3), 459-465.

Wehner, T., and Fatemi, A. (1991). "Effects of mean stress on fatigue behaviour of a hardened carbon steel." *International Journal of Fatigue*, 13(3), 241-248.

Wen, Y.-K. (1976). "Method for random vibration of hysteretic systems." *Journal of the Engineering Mechanics Division*, 102(2), 249-263.

Wirsching, P., and Shehata, A. M. (1977). "Fatigue under wide band random stresses using the rain-flow method." *Journal of engineering materials and technology*, 99(3), 205-211.

Wu, W., Liou, H., and Tse, H. (1997). "Estimation of fatigue damage and fatigue life of components under random loading." *International journal of pressure vessels and piping*, 72(3), 243-249.

Xia, Z., Kujawski, D., and Ellyin, F. (1996). "Effect of mean stress and ratcheting strain on fatigue life of steel." *International Journal of Fatigue*, 18(5), 335-341.

Xie, Q. (2005). "State of the art of buckling-restrained braces in Asia." *Journal of Constructional Steel Research*, 61(6), 727-748.

Zahrai, S. M., and Bruneau, M. (1998). "Impact of diaphragms on seismic response of straight slab-on-girder steel bridges." *Journal of Structural Engineering*, 124(8), 938-947.

Zahrai, S. M., and Bruneau, M. (1999). "Ductile end-diaphragms for seismic retrofit of slab-on-girder steel bridges." *Journal of Structural Engineering*, 125(1), 71-80.

SUB APPENDIX A

Sub Appendix A-1. Fatigue Life of BRB using Coffin-Manson and Basquin method with thermal strain data calculated using Eq D3.2

T_r (°F)	L_2/L (%)	Fatigue Life (Years) Data from Recorded Real Temperature								
		(1)	(2)	(3)	(4)	(5)	(6)	(7)	(8)	(9)
100	1	-	-	-	1.9	1.5	1.9	-	-	-
	2	-	-	-	11.4	8.4	11.0	-	-	-
	3	-	-	-	34.7	24.7	32.5	-	-	-
	4	-	-	-	79.8	55.1	72.5	-	-	-
	5	-	-	-	172.0	105.0	151.1	-	-	-
	6	-	-	-	183.0	183.0	173.9	-	-	-
90	1	-	2.3	4.1	1.9	1.5	1.9	1.3	4.9	2.8
	2	-	13.4	25.3	11.2	8.4	10.8	7.0	30.7	16.9
	3	-	39.0	77.6	33.7	24.7	31.6	19.8	98.4	51.6
	4	-	85.3	178.0	77.6	55.1	70.5	42.8	234.3	118.4
	5	-	174.6	380.4	152.5	105.0	134.0	86.2	514.6	252.7
	6	-	183.0	411.8	183.0	183.0	173.9	109.8	640.5	366.0
80	1	-	2.3	4.1	1.9	1.5	1.9	1.3	4.9	2.8
	2	-	13.1	24.8	11.0	8.4	10.6	7.0	30.7	16.9
	3	-	37.9	75.4	33.1	24.7	31.0	19.8	98.4	51.6
	4	-	83.0	173.1	75.9	55.1	68.9	42.8	234.3	118.4
	5	-	154.8	337.3	148.6	105.0	130.5	86.2	514.6	252.7
	6	-	183.0	411.8	183.0	183.0	173.9	109.8	640.5	366.0
70	1	2.9	2.3	4.0	1.8	1.5	1.8	1.3	4.9	2.8
	2	17.1	12.9	24.4	10.8	8.4	10.5	7.0	30.7	16.9
	3	50.4	37.3	74.1	32.6	24.7	30.5	19.8	98.4	51.6
	4	111.2	81.1	169.2	74.7	55.1	67.8	42.8	234.3	118.4
	5	101.6	150.8	328.6	145.7	105.0	128.1	86.2	514.6	252.7
	6	137.3	183.0	411.8	183.0	183.0	173.9	109.8	640.5	366.0
60	1	2.9	2.2	4.0	1.8	1.5	1.8	1.3	4.9	2.8
	2	17.1	12.7	24.1	10.8	8.4	10.5	7.0	30.7	16.9
	3	50.4	36.6	72.9	32.4	24.7	30.4	19.8	98.4	51.6
	4	111.2	79.8	166.5	74.2	55.1	67.4	42.8	234.3	118.4
	5	101.6	147.9	322.4	144.7	105.0	127.1	86.2	514.6	252.7
	6	137.3	183.0	411.8	174.3	183.0	165.6	109.8	640.5	366.0
50	1	2.9	2.2	4.0	1.8	1.5	1.8	1.3	4.9	2.8
	2	17.1	12.7	24.0	10.8	8.4	10.5	7.0	30.7	16.9
	3	50.4	36.4	72.5	32.4	24.7	30.4	19.8	98.4	51.6
	4	111.2	79.3	165.4	74.2	55.1	67.4	42.8	234.3	118.4
	5	101.6	146.9	320.0	144.7	105.0	127.1	86.2	514.6	252.7
	6	137.3	174.3	392.1	174.3	183.0	165.6	109.8	640.5	366.0

T_r (°F)	L_2/L (%)	(1)	(2)	(3)	(4)	(5)	(6)	(7)	(8)	(9)
		Fatigue Life (Years)								
		Data from Recorded Real Temperature								
40	1	2.9	2.2	4.0	1.8	1.5	1.8	1.3	4.9	2.8
	2	17.1	12.7	24.0	10.8	8.4	10.5	7.0	30.7	16.9
	3	50.4	36.4	72.5	32.4	24.7	30.4	19.8	98.4	51.6
	4	111.2	79.3	165.4	74.2	55.1	67.4	42.8	234.3	118.4
	5	101.6	146.9	320.0	144.7	105.0	127.1	86.2	514.6	252.7
	6	137.3	174.3	392.1	174.3	183.0	165.6	109.8	640.5	366.0
30	1	2.9	2.2	-	-	1.5	1.8	1.3	-	2.8
	2	17.1	12.7	-	-	8.4	10.5	7.0	-	16.9
	3	50.4	36.4	-	-	24.7	30.4	19.8	-	51.6
	4	111.2	79.3	-	-	55.1	67.4	42.8	-	118.4
	5	101.6	146.9	-	-	105.0	127.1	86.2	-	252.7
	6	137.3	174.3	-	-	183.0	165.6	109.8	-	366.0
20	1	2.9	2.2	-	-	-	-	1.3	-	-
	2	17.1	12.7	-	-	-	-	7.0	-	-
	3	50.4	36.4	-	-	-	-	19.8	-	-
	4	111.2	79.3	-	-	-	-	42.8	-	-
	5	101.6	146.9	-	-	-	-	86.2	-	-
	6	137.3	174.3	-	-	-	-	109.8	-	-
10	1	2.9	2.2	-	-	-	-	1.3	-	-
	2	17.1	12.7	-	-	-	-	7.0	-	-
	3	50.4	36.4	-	-	-	-	19.8	-	-
	4	111.2	79.3	-	-	-	-	42.8	-	-
	5	101.6	146.9	-	-	-	-	86.2	-	-
	6	137.3	174.3	-	-	-	-	109.8	-	-
0	1	2.9	-	-	-	-	-	1.3	-	-
	2	17.1	-	-	-	-	-	7.0	-	-
	3	50.4	-	-	-	-	-	19.8	-	-
	4	111.2	-	-	-	-	-	42.8	-	-
	5	101.6	-	-	-	-	-	86.2	-	-
	6	137.3	-	-	-	-	-	109.8	-	-
-10	1	2.9	-	-	-	-	-	-	-	-
	2	17.1	-	-	-	-	-	-	-	-
	3	50.4	-	-	-	-	-	-	-	-
	4	111.2	-	-	-	-	-	-	-	-
	5	101.6	-	-	-	-	-	-	-	-
	6	137.25	-	-	-	-	-	-	-	-

T_r : reference temperature L_2 : total length of BRB L : total span length of bridge

(1) Anchorage, Alaska

(2) Boston, Massachusetts

(3) Charleston, South Carolina

(4) Los Angeles, California

(5) Memphis, Tennessee

(6) Portland, Oregon

(7) Quebec City, Canada

(8) San Fransisco, California

(9) Seattle, Washington

T_r (°F)	L_2/L (%)	(1)	(2)	(3)	(4)	(5)	(6)	(7)	(8)	(9)
					Fatigue Life (Years)					
					Data from Recorded Average Temperature					
100	1	-	-	-	-	-	-	-	-	-
	2	-	-	-	-	-	-	-	-	-
	3	-	-	-	-	-	-	-	-	-
	4	-	-	-	-	-	-	-	-	-
	5	-	-	-	-	-	-	-	-	-
	6	-	-	-	-	-	-	-	-	-
90	1	-	-	-	-	2.4	-	-	-	-
	2	-	-	-	-	15.4	-	-	-	-
	3	-	-	-	-	50.4	-	-	-	-
	4	-	-	-	-	123.8	-	-	-	-
	5	-	-	-	-	284.0	-	-	-	-
	6	-	-	-	-	411.8	-	-	-	-
80	1	-	4.4	7.6	2.4	2.4	2.7	-	-	-
	2	-	29.8	56.5	15.1	15.4	17.4	-	-	-
	3	-	101.7	210.9	50.6	50.4	57.2	-	-	-
	4	-	257.8	578.5	127.3	123.8	141.3	-	-	-
	5	-	594.0	1446.0	302.2	284.0	328.3	-	-	-
	6	-	823.5	1738.5	457.5	411.8	549.0	-	-	-
70	1	-	4.4	7.6	2.4	2.4	2.7	2.5	6.8	4.0
	2	-	29.8	56.5	15.1	15.4	17.4	15.8	51.4	27.0
	3	-	101.7	210.9	50.6	50.4	57.2	50.4	197.9	93.5
	4	-	257.8	578.5	127.3	123.8	141.3	120.7	573.2	242.1
	5	-	594.0	1446.0	302.2	284.0	328.3	267.1	1537.2	586.2
	6	-	823.5	1738.5	457.5	411.8	549.0	457.5	1830.0	823.5
60	1	5.7	4.4	7.6	2.4	2.4	2.7	2.5	6.8	4.0
	2	39.8	29.8	56.5	15.1	15.4	17.4	15.8	51.4	27.0
	3	139.2	101.7	210.9	50.6	50.4	57.2	50.4	197.9	93.5
	4	359.9	257.8	578.5	127.3	123.8	141.3	120.7	573.2	242.1
	5	848.1	594.0	1446.0	302.2	284.0	328.3	267.1	1537.2	586.2
	6	1098.0	823.5	1738.5	457.5	411.8	549.0	457.5	1830.0	823.5
50	1	5.7	4.4	7.6	2.4	2.4	2.7	2.5	6.8	4.0
	2	39.8	29.8	56.5	15.1	15.4	17.4	15.8	51.4	27.0
	3	139.2	101.7	210.9	50.6	50.4	57.2	50.4	197.9	93.5
	4	359.9	257.8	578.5	127.3	123.8	141.3	120.7	573.2	242.1
	5	848.1	594.0	1446.0	302.2	284.0	328.3	267.1	1537.2	586.2
	6	1098.0	823.5	1738.5	457.5	411.8	549.0	457.5	1830.0	823.5

T_r (^{0}F)	L_2/L (%)	(1)	(2)	(3)	(4)	(5)	(6)	(7)	(8)	(9)
		Fatigue Life (Years) Data from Recorded Average Temperature								
40	1	5.7	4.4	-	-	2.4	2.7	2.5	-	4.0
	2	39.8	29.8	-	-	15.4	17.4	15.8	-	27.0
	3	139.2	101.7	-	-	50.4	57.2	50.4	-	93.5
	4	359.9	257.8	-	-	123.8	141.3	120.7	-	242.1
	5	848.1	594.0	-	-	284.0	328.3	267.1	-	586.2
	6	1098.0	823.5	-	-	411.8	549.0	457.5	-	823.5
30	1	5.7	4.4	-	-	-	-	2.5	-	-
	2	39.8	29.8	-	-	-	-	15.8	-	-
	3	139.2	101.7	-	-	-	-	50.4	-	-
	4	359.9	257.8	-	-	-	-	120.7	-	-
	5	848.1	594.0	-	-	-	-	267.1	-	-
	6	1098.0	823.5	-	-	-	-	457.5	-	-
20	1	5.7	-	-	-	-	-	2.5	-	-
	2	39.8	-	-	-	-	-	15.8	-	-
	3	139.2	-	-	-	-	-	50.4	-	-
	4	359.9	-	-	-	-	-	120.7	-	-
	5	848.1	-	-	-	-	-	267.1	-	-
	6	1098.0	-	-	-	-	-	457.5	-	-
10	1	-	-	-	-	-	-	2.5	-	-
	2	-	-	-	-	-	-	15.8	-	-
	3	-	-	-	-	-	-	50.4	-	-
	4	-	-	-	-	-	-	120.7	-	-
	5	-	-	-	-	-	-	267.1	-	-
	6	-	-	-	-	-	-	457.5	-	-
0	1	-	-	-	-	-	-	-	-	-
	2	-	-	-	-	-	-	-	-	-
	3	-	-	-	-	-	-	-	-	-
	4	-	-	-	-	-	-	-	-	-
	5	-	-	-	-	-	-	-	-	-
	6	-	-	-	-	-	-	-	-	-
-10	1	-	-	-	-	-	-	-	-	-
	2	-	-	-	-	-	-	-	-	-
	3	-	-	-	-	-	-	-	-	-
	4	-	-	-	-	-	-	-	-	-
	5	-	-	-	-	-	-	-	-	-
	6	-	-	-	-	-	-	-	-	-

T_r : reference temperature L_2 : total length of BRB L : total span length of bridge

(1) Anchorage, Alaska

(2) Boston, Massachusetts

(3) Charleston, South Carolina

(4) Los Angeles, California

(5) Memphis, Tennessee

(6) Portland, Oregon

(7) Quebec City, Canada

(8) San Fransisco, California

(9) Seattle, Washington

Sub Appendix A-2. Fatigue Life of BRB using Smith-Watson and Topper method with thermal strain data calculated using Eq D3.2

T_r (°F)	L_2/L (%)	**Fatigue Life (Years)** Data from Recorded Real Temperature								
		(1)	(2)	(3)	(4)	(5)	(6)	(7)	(8)	(9)
100	1	-	-	-	1.2	1.0	1.2	-	-	-
	2	-	-	-	6.3	5.1	6.1	-	-	-
	3	-	-	-	17.2	13.7	16.7	-	-	-
	4	-	-	-	36.7	28.6	34.9	-	-	-
	5	-	-	-	46.8	51.3	44.0	-	-	-
	6	-	-	-	58.7	83.9	50.3	-	-	-
90	1	-	1.5	2.6	1.3	1.1	1.3	0.8	2.7	1.7
	2	-	8.0	14.4	7.1	5.8	6.8	4.1	14.7	9.2
	3	-	21.9	40.6	19.9	15.7	18.7	11.0	42.5	25.6
	4	-	45.8	88.0	42.7	33.0	39.4	22.4	92.4	55.0
	5	-	57.7	114.2	63.2	59.5	57.4	27.7	121.5	70.6
	6	-	67.1	142.6	88.9	97.8	62.2	30.2	151.0	83.9
80	1	-	1.8	3.2	1.6	1.3	2.8	0.9	3.1	2.0
	2	-	9.2	17.8	8.6	7.0	7.9	4.5	17.3	10.6
	3	-	25.3	50.7	24.4	19.3	21.9	12.1	50.4	30.1
	4	-	53.3	110.8	53.0	40.7	46.3	24.9	112.7	65.1
	5	-	77.6	166.0	99.2	74.1	85.0	35.4	173.0	97.1
	6	-	84.5	177.8	123.0	123.0	92.3	44.5	204.5	124.5
70	1	1.8	2.1	4.4	2.2	1.8	2.7	1.0	3.9	2.4
	2	9.6	11.3	24.2	12.1	9.5	9.9	5.2	22.1	13.1
	3	26.5	31.1	69.1	35.5	26.1	28.1	13.8	66.4	37.8
	4	51.8	66.0	151.0	79.6	55.3	61.1	28.4	151.0	83.3
	5	57.6	119.7	282.4	152.8	101.0	114.4	50.4	296.1	158.4
	6	58.7	133.3	307.5	229.6	167.0	156.6	59.5	512.5	205.0
60	1	2.1	2.9	6.5	4.0	2.5	2.7	1.2	5.8	3.4
	2	11.2	15.1	36.3	23.3	13.4	15.3	6.3	36.3	19.6
	3	31.0	41.8	105.5	70.3	37.1	45.0	17.0	116.5	59.0
	4	66.2	88.8	234.3	161.6	78.8	100.3	35.4	285.2	134.9
	5	96.9	167.7	444.8	318.1	144.0	192.4	63.1	594.9	263.7
	6	106.7	208.8	730.6	960.0	240.0	360.0	72.0	1878.8	417.5
50	1	2.7	4.1	12.5	7.9	2.5	3.6	1.6	24.8	7.1
	2	14.2	21.6	72.3	77.5	20.9	32.7	8.3	175.2	42.5
	3	39.4	60.1	216.4	252.4	58.6	98.3	22.4	606.0	130.6
	4	83.8	127.0	490.4	629.3	126.0	223.5	46.2	1573.2	301.9
	5	152.9	230.4	950.4	1329	232.0	435.2	82.2	3403.6	596.9
	6	184.5	336.0	1800	9750	390.0	975.0	96.0	240000	1200

Fatigue Life (Years) Data from Recorded Real Temperature										
T_r (°F)	L_2/L (%)	(1)	(2)	(3)	(4)	(5)	(6)	(7)	(8)	(9)
40	1	3.5	4.1	25.9	626.3	7.5	15.5	1.4	616.2	12.2
	2	18.6	33.7	235.5	8088.3	41.0	90.9	11.0	12639.5	115.9
	3	51.7	93.9	730.2	47760.9	117.0	275.5	29.6	78133.3	366.6
	4	110.3	200.2	1713.8	296440.6	257.0	634.9	61.0	510032.6	870.6
	5	201.5	361.2	3461.2	660625.6	484.0	1238.7	108.5	1167524.3	1743.1
	6	260.9	585.0	4875.0	828000.0	828.0	6624.0	117.0	1365000.0	9750.0
30	1	4.9	12.5	-	-	27.2	610.2	3.0	-	117.4
	2	25.8	64.5	-	-	152.0	613.5	15.1	-	783.3
	3	71.6	173.8	-	-	444.0	2059.5	39.7	-	2713.0
	4	171.5	361.3	-	-	992.0	5278.1	80.9	-	7264.7
	5	271.0	640.0	-	-	1910.0	11689.6	141.1	-	16630.3
	6	384.0	828.0	-	-	3320.0	14940.0	165.6	-	20700.0
20	1	4.4	25.8	-	-	-	-	4.2	-	-
	2	36.0	128.8	-	-	-	-	20.6	-	-
	3	99.0	342.4	-	-	-	-	53.9	-	-
	4	207.0	697.5	-	-	-	-	108.5	-	-
	5	372.5	1231.6	-	-	-	-	187.9	-	-
	6	438.8	4150.0	-	-		-	232.4	-	-
10	1	10.7	88.2	-	-	-	-	6.6	-	-
	2	55.0	498.5	-	-	-	-	33.8	-	-
	3	148.4	1538.0	-	-	-	-	91.7	-	-
	4	309.2	3758.3	-	-	-	-	192.1	-	-
	5	548.2	8026.2	-	-	-	-	347.5	-	-
	6	745.2	9960.0	-	-		-	662.4	-	-
0	1	19.5	-	-	-	-	-	14.3	-	-
	2	99.7	-	-	-	-	-	79.6	-	-
	3	270.1	-	-	-	-	-	231.4	-	-
	4	562.0	-	-	-	-	-	512.5	-	-
	5	1013.4	-	-	-	-	-	987.4	-	-
	6	4150.0	-	-	-		-	1162.0	-	-
-10	1	86.1	-	-	-	-	-	-	-	-
	2	578.2	-	-	-	-	-	-	-	-
	3	2099.6	-	-	-	-	-	-	-	-
	4	6102.8	-	-	-	-	-	-	-	-
	5	13881.4	-	-	-	-	-	-	-	-
	6	14940.0	-	-	-	-	-	-	-	-

T_r : reference temperature L_2 : total length of BRB L : total span length of bridge

(1) Anchorage, Alaska   (4) Los Angeles, California   (7) Quebec City, Canada

(2) Boston, Massachusetts   (5) Memphis, Tennessee   (8) San Fransisco, California

(3) Charleston, South Carolina   (6) Portland, Oregon   (9) Seattle, Washington

T_r (°F)	L_2/L (%)	(1)	(2)	(3)	(4)	(5)	(6)	(7)	(8)	(9)
						Fatigue Life (Years) Data from Recorded Average Temperature				
100	1	-	-	-	-	-	-	-	-	-
	2	-	-	-	-	-	-	-	-	-
	3	-	-	-	-	-	-	-	-	-
	4	-	-	-	-	-	-	-	-	-
	5	-	-	-	-	-	-	-	-	-
	6	-	-	-	-	-	-	-	-	-
90	1	-	-	-	-	1.5	-	-	-	-
	2	-	-	-	-	8.1	-	-	-	-
	3	-	-	-	-	23.3	-	-	-	-
	4	-	-	-	-	50.9	-	-	-	-
	5	-	-	-	-	67.1	-	-	-	-
	6	-	-	-	-	83.9	-	-	-	-
80	1	-	2.4	4.6	1.7	1.8	1.8	-	-	-
	2	-	13.6	27.9	9.8	10.1	9.8	-	-	-
	3	-	40.1	86.1	28.8	29.4	28.5	-	-	-
	4	-	90.1	202.3	65.4	65.7	63.5	-	-	-
	5	-	121.5	282.5	89.1	100.9	85.2	-	-	-
	6	-	167.8	377.6	125.9	133.4	109.1	-	-	-
70	1	-	3.0	6.7	2.4	2.6	2.2	1.6	4.3	2.8
	2	-	17.4	40.8	14.0	14.3	12.5	8.6	26.6	16.6
	3	-	52.6	128.1	43.5	42.1	37.4	24.4	85.1	50.4
	4	-	120.6	307.0	103.6	94.6	86.4	53.4	208.6	117.7
	5	-	189.1	501.6	169.5	181.8	137.2	70.1	303.2	165.1
	6	-	266.7	711.3	355.6	225.5	266.7	83.9	587.3	251.7
60	1	3.3	4.3	11.3	5.1	3.8	3.4	1.9	6.9	4.1
	2	19.1	25.2	72.3	32.0	22.0	21.4	10.7	47.7	26.2
	3	57.8	76.4	237.7	105.4	66.4	68.4	31.2	170.8	86.4
	4	133.0	176.1	593.5	266.4	152.8	167.2	69.7	466.6	216.4
	5	182.8	345.7	1260.3	575.7	300.2	345.7	106.4	872.9	371.3
	6	209.8	461.3	2562.5	2562.5	469.7	820.0	133.4	8890.9	800.2
50	1	4.5	6.6	31.4	38.4	6.9	8.2	2.7	56.5	10.3
	2	27.1	39.5	230.2	379.7	41.8	54.0	15.2	571.1	70.0
	3	82.9	122.5	872.6	2012.5	130.8	184.0	44.2	2823.2	244.0
	4	193.4	288.1	2517.6	8003.9	310.4	474.4	97.8	10463.6	643.8
	5	306.7	574.6	6124.9	24472.6	631.0	1045.2	185.9	30989.8	1446.2
	6	400.1	730.6	7306.3	31312.5	1200.0	4175.0	225.5	51250.0	10250.0

T_r (°F)	L_2/L (%)	(1)	(2)	(3)	(4)	(5)	(6)	(7)	(8)	(9)
					Fatigue Life (Years) Data from Recorded Average Temperature					

T_r (°F)	L_2/L (%)	(1)	(2)	(3)	(4)	(5)	(6)	(7)	(8)	(9)
40	1	6.8	11.7	-	-	12.1	40.2	3.9	-	56.0
	2	40.6	72.8	-	-	123.4	338.4	21.6	-	513.7
	3	40.5	230.3	-	-	425.2	1456.2	63.0	-	2374.2
	4	296.0	552.7	-	-	1107.8	4733.7	139.7	-	8222.2
	5	596.4	1131.1	-	-	2445.4	12789.8	265.0	-	22444.4
	6	820.0	2640.0	-	-	3022.5	15600.0	313.1	-	31312.5
30	1	10.8	19.0	-	-	-	-	5.5	-	-
	2	67.7	199.0	-	-	-	-	31.1	-	-
	3	218.5	700.2	-	-	-	-	91.0	-	-
	4	534.1	1850.9	-	-	-	-	202.7	-	-
	5	1108.7	4163.5	-	-	-	-	386.2	-	-
	6	2087.5	5850.0	-	-	-	-	540.0	-	-
20	1	24.6	-	-	-	-	-	5.5	-	-
	2	175.2	-	-	-	-	-	48.6	-	-
	3	632.2	-	-	-	-	-	145.6	-	-
	4	1714.9	-	-	-	-	-	330.4	-	-
	5	3927.3	-	-	-	-	-	640.8	-	-
	6	6000.0	-	-	-	-	-	1072.5	-	-
10	1	-	-	-	-	-	-	17.3	-	-
	2	-	-	-	-	-	-	106.1	-	-
	3	-	-	-	-	-	-	337.7	-	-
	4	-	-	-	-	-	-	816.8	-	-
	5	-	-	-	-	-	-	1686.0	-	-
	6	-	-	-	-	-	-	2070.0	-	-
0	1	-	-	-	-	-	-	-	-	-
	2	-	-	-	-	-	-	-	-	-
	3	-	-	-	-	-	-	-	-	-
	4	-	-	-	-	-	-	-	-	-
	5	-	-	-	-	-	-	-	-	-
	6	-	-	-	-	-	-	-	-	-
-10	1	-	-	-	-	-	-	-	-	-
	2	-	-	-	-	-	-	-	-	-
	3	-	-	-	-	-	-	-	-	-
	4	-	-	-	-	-	-	-	-	-
	5	-	-	-	-	-	-	-	-	-
	6	-	-	-	-	-	-	-	-	-

T_r : reference temperature L_2 : total length of BRB L : total span length of bridge

(1) Anchorage, Alaska

(2) Boston, Massachusetts

(3) Charleston, South Carolina

(4) Los Angeles, California

(5) Memphis, Tennessee

(6) Portland, Oregon

(7) Quebec City, Canada

(8) San Fransisco, California

(9) Seattle, Washington

Sub Appendix A-3. Fatigue Life of BRB using Morrow method
with thermal strain data calculated using Eq D3.2

T_r (^{0}F)	L_2/L (%)	(1)	(2)	(3)	(4)	(5)	(6)	(7)	(8)	(9)
				Fatigue Life (Years) Data from Recorded Real Temperature						
100	1	-	-	-	1.6	1.3	1.7	-	-	-
	2	-	-	-	9.2	7.0	9.2	-	-	-
	3	-	-	-	26.4	19.9	25.3	-	-	-
	4	-	-	-	59.0	42.6	54.9	-	-	-
	5	-	-	-	103.4	80.0	94.3	-	-	-
	6	-	-	-	108.8	136.0	104.3	-	-	-
90	1	-	2.1	3.6	1.7	1.3	1.7	1.1	12.6	2.4
	2	-	11.3	20.8	9.8	7.3	9.3	5.9	79.8	13.7
	3	-	31.6	61.2	28.0	20.9	26.8	16.2	258.0	39.8
	4	-	68.3	138.2	63.4	45.3	58.5	33.7	631.0	89.0
	5	-	117.4	243.8	121.8	84.4	109.3	55.5	1340.0	158.6
	6	-	126.9	272.0	129.6	144.0	115.2	58.9	1800.0	163.2
80	1	-	2.2	3.8	1.7	1.4	2.0	1.1	13.7	2.6
	2	-	11.8	23.8	10.2	7.8	9.9	6.0	86.4	14.4
	3	-	34.0	67.8	30.4	22.3	28.4	17.0	288.0	43.3
	4	-	73.5	155.1	67.7	48.6	61.8	35.2	713.0	97.0
	5	-	137.1	305.4	135.1	92.2	118.6	64.6	1520.0	189.5
	6	-	141.1	326.4	142.3	157.0	127.6	65.3	2100.0	201.6
70	1	2.6	2.3	4.1	1.9	1.5	2.0	1.2	14.8	2.7
	2	14.2	12.7	25.1	10.9	8.3	10.3	6.3	96.6	15.6
	3	40.7	36.5	76.5	33.1	24.2	30.3	17.5	326.0	47.2
	4	90.7	77.6	171.9	78.6	54.6	69.2	36.7	826.0	106.8
	5	68.3	147.1	340.8	150.9	102.0	131.5	67.6	1800.0	215.3
	6	126.9	157.0	372.9	161.3	176.0	136.9	69.7	2350.0	230.6
60	1	2.7	2.3	4.4	2.0	1.6	1.9	1.2	15.8	2.8
	2	15.2	13.2	27.3	12.2	9.0	11.2	6.4	109.0	16.7
	3	43.6	38.6	83.5	37.2	26.4	33.0	18.1	374.0	51.7
	4	97.7	86.2	196.9	86.5	59.0	75.0	39.6	980.0	125.3
	5	179.5	160.1	384.2	170.6	113.0	145.1	72.2	2120.0	242.4
	6	182.4	166.2	400.9	185.3	195.0	156.0	75.3	2700.0	264.0
50	1	2.8	2.5	4.6	2.1	1.6	2.0	1.2	17.6	3.0
	2	16.2	14.7	29.5	13.2	9.4	12.2	6.9	125.0	19.1
	3	47.5	42.4	91.8	41.3	28.1	36.7	19.4	438.0	59.3
	4	103.0	92.6	209.6	97.4	63.4	84.3	41.4	1150.0	139.3
	5	199.7	173.9	426.5	192.6	122.0	164.8	78.5	2510.0	278.1
	6	206.1	180.4	448.5	203.3	213.0	174.3	80.9	3000.0	292.5

T_r (°F)	L_2/L (%)	(1)	(2)	(3)	(4)	(5)	(6)	(7)	(8)	(9)
					Fatigue Life (Years) Data from Recorded Real Temperature					

T_r (°F)	L_2/L (%)	(1)	(2)	(3)	(4)	(5)	(6)	(7)	(8)	(9)
40	1	3.0	2.5	4.8	2.3	1.7	2.2	1.3	19.4	3.2
	2	17.0	15.4	32.4	14.2	9.9	13.2	7.3	143.0	21.2
	3	50.3	44.9	99.7	45.5	29.8	40.5	20.7	507.0	66.9
	4	115.7	99.5	236.3	109.2	68.2	94.6	45.2	1330.0	157.9
	5	213.8	185.1	459.1	218.6	132.0	183.7	84.0	2940.0	314.6
	6	224.9	193.6	484.1	221.8	231.0	189.4	86.2	3400.0	329.2
30	1	3.2	2.7	-	-	1.7	2.3	1.4	20.6	3.5
	2	18.7	15.7	-	-	10.3	13.9	7.6	152.0	22.0
	3	55.1	47.2	-	-	31.7	42.8	22.3	560.0	72.2
	4	124.8	106.4	-	-	72.5	97.7	49.0	1550.0	181.0
	5	232.6	198.5	-	-	143.0	195.5	91.3	3270.0	345.3
	6	241.8	203.3	-	-	252.0	203.5	95.2	3800.0	351.1
20	1	3.2	2.8	-	-	-	-	1.4	-	-
	2	19.7	16.8	-	-	-	-	8.0	-	-
	3	58.8	49.6	-	-	-	-	23.1	-	-
	4	131.8	108.1	-	-	-	-	55.0	-	-
	5	247.2	209.9	-	-	-	-	97.4	-	-
	6	259.5	221.0	-	-	-	-	101.8		-
10	1	3.4	2.8	-	-	-	-	1.5	-	-
	2	20.4	16.8	-	-	-	-	8.5	-	-
	3	62.2	51.1	-	-	-	-	25.2	-	-
	4	140.1	111.8	-	-	-	-	56.3	-	-
	5	265.1	229.4	-	-	-	-	106.7	-	-
	6	269.8	232.6	-	-		-	109.0		-
0	1	3.6	-	-	-	-	-	1.5	-	-
	2	21.2	-	-	-	-	-	8.7	-	-
	3	64.2	-	-	-	-	-	25.5	-	-
	4	143.9	-	-	-	-	-	56.1	-	-
	5	273.7	-	-	-	-	-	110.1	-	-
	6	288.8	-	-	-	-	-	116.3	-	-
-10	1	3.6	-	-	-	-	-	-	-	-
	2	22.2	-	-	-	-	-	-	-	-
	3	68.1	-	-	-	-	-	-	-	-
	4	150.5	-	-	-	-	-	-	-	-
	5	294.2	-	-	-	-	-	-	-	-
	6	310.2	-	-	-	-	-	-	-	-

T_r : reference temperature L_2 : total length of BRB L : total span length of bridge

(1) Anchorage, Alaska   (4) Los Angeles, California   (7) Quebec City, Canada

(2) Boston, Massachusetts   (5) Memphis, Tennessee   (8) San Fransisco, California

(3) Charleston, South Carolina (6) Portland, Oregon   (9) Seattle, Washington

T_r (°F)	L_2/L (%)	(1)	(2)	(3)	(4)	(5)	(6)	(7)	(8)	(9)
		Fatigue Life (Years) Data from Recorded Average Temperature								
100	1	-	-	-	-	-	-	-	-	-
	2	-	-	-	-	-	-	-	-	-
	3	-	-	-	-	-	-	-	-	-
	4	-	-	-	-	-	-	-	-	-
	5	-	-	-	-	-	-	-	-	-
	6		-	-	-	-	-	-	-	-
90	1	-	-	-	-	2.1	-	-	-	-
	2	-	-	-	-	12.3	-	-	-	-
	3	-	-	-	-	37.8	-	-	-	-
	4	-	-	-	-	89.1	-	-	-	-
	5	-	-	-	-	165.7	-	-	-	-
	6	-	-	-	-	181.3	-	-	-	-
80	1	-	3.7	6.4	2.2	2.2	2.4	-	-	-
	2	-	22.9	43.9	12.9	13.2	14.4	-	-	-
	3	-	73.4	153.3	41.0	42.3	44.4	-	-	-
	4	-	183.4	399.2	99.0	100.8	110.0	-	-	-
	5	-	345.6	827.2	191.7	208.2	203.6	-	-	-
	6	-	389.9	906.7	226.7	220.8	235.7	-	-	-
70	1	-	4.0	7.2	2.3	2.3	2.5	2.2	5.7	3.7
	2	-	25.3	51.3	14.8	15.0	15.8	13.1	39.6	23.2
	3	-	84.2	189.5	48.3	47.5	50.7	39.8	146.1	78.2
	4	-	212.2	495.2	120.5	115.7	124.7	93.2	407.7	196.1
	5	-	453.8	1149.4	258.1	242.8	260.6	170.4	881.7	396.4
	6	-	480.0	1344.0	288.0	264.9	288.0	190.4	1088.0	453.3
60	1	4.9	4.3	8.3	2.6	2.5	2.7	2.3	7.3	3.9
	2	31.5	28.8	63.0	17.3	15.9	17.3	14.0	51.1	26.3
	3	104.9	99.3	238.9	58.1	53.8	57.5	44.1	197.0	91.9
	4	265.2	250.8	643.7	149.9	136.8	144.8	104.2	570.0	238.1
	5	518.3	544.1	1506.8	336.0	287.0	318.1	210.7	1421.2	541.1
	6	580.3	608.4	1766.3	372.9	312.9	353.3	230.4	1728.0	624.0
50	1	5.3	4.7	9.6	2.7	2.7	3.1	2.5	8.2	4.5
	2	35.6	32.3	75.3	19.0	18.5	20.1	15.5	68.5	31.9
	3	123.4	114.6	298.7	68.0	62.7	69.4	49.4	285.3	115.6
	4	318.3	304.3	865.7	186.7	161.1	184.1	117.9	842.7	308.9
	5	694.4	668.9	1978.3	403.7	350.1	401.4	245.1	2140.6	718.7
	6	720.0	733.3	2151.1	469.3	370.5	430.2	264.9	2453.1	785.0

T_r (^{0}F)	L_2/L (%)	(1)	(2)	(3)	(4)	(5)	(6)	(7)	(8)	(9)
					Fatigue Life (Years) Data from Recorded Average Temperature					

T_r (^{0}F)	L_2/L (%)	(1)	(2)	(3)	(4)	(5)	(6)	(7)	(8)	(9)
40	1	5.8	5.2	-	-	2.8	3.3	2.6	-	5.0
	2	41.5	37.9	-	-	20.2	23.1	16.7	-	36.3
	3	40.1	139.4	-	-	70.6	80.8	53.9	-	135.8
	4	405.9	359.8	-	-	186.4	216.9	135.5	-	387.4
	5	864.6	795.4	-	-	403.5	475.3	280.2	-	883.9
	6	902.8	877.5	-	-	426.0	487.5	293.3	-	928.9
30	1	6.4	5.5	-	-	-	-	2.8	-	-
	2	46.5	43.0	-	-	-	-	18.5	-	-
	3	174.2	158.3	-	-	-	-	60.9	-	-
	4	478.2	425.0	-	-	-	-	149.0	-	-
	5	1039.4	927.8	-	-	-	-	311.3	-	-
	6	1173.3	968.2	-	-	-	-	331.5	-	-
20	1	7.2	-	-	-	-	-	2.9	-	-
	2	55.6	-	-	-	-	-	20.0	-	-
	3	211.2	-	-	-	-	-	67.0	-	-
	4	560.9	-	-	-	-	-	168.6	-	-
	5	1262.9	-	-	-	-	-	353.2	-	-
	6	1462.5	-	-	-	-	-	377.6	-	-
10	1	-	-	-	-	-	-	3.2	-	-
	2	-	-	-	-	-	-	21.1	-	-
	3	-	-	-	-	-	-	72.8	-	-
	4	-	-	-	-	-	-	184.5	-	-
	5	-	-	-	-	-	-	397.1	-	-
	6		-	-	-	-	-	480.5	-	-
0	1	-	-	-	-	-	-	-	-	-
	2	-	-	-	-	-	-	-	-	-
	3	-	-	-	-	-	-	-	-	-
	4	-	-	-	-	-	-	-	-	-
	5	-	-	-	-	-	-	-	-	-
	6	-	-	-	-	-	-	-	-	-
-10	1	-	-	-	-	-	-	-	-	-
	2	-	-	-	-	-	-	-	-	-
	3	-	-	-	-	-	-	-	-	-
	4	-	-	-	-	-	-	-	-	-
	5	-	-	-	-	-	-	-	-	-
	6	-	-	-	-	-	-	-	-	-

T_r : reference temperature L_2 : total length of BRB L : total span length of bridge

(1) Anchorage, Alaska   (4) Los Angeles, California   (7) Quebec City, Canada

(2) Boston, Massachusetts   (5) Memphis, Tennessee   (8) San Fransisco, California

(3) Charleston, South Carolina   (6) Portland, Oregon   (9) Seattle, Washington

SUB APPENDIX B

Sub Appendix B-1. Fatigue Life of BRB using Coffin-Manson and Basquin method with thermal strain data calculated using Eq D3.18

T_r (°F)	L_2/L (%)	(1)	(2)	(3)	(4)	(5)	(6)	(7)	(8)	(9)
						Fatigue Life (Years) Data from Recorded Real Temperature				
100	1	-	-	-	1.9	1.5	1.9	-	-	-
	2	-	-	-	10.8	8.1	10.5	-	-	-
	3	-	-	-	32.0	23.1	30.1	-	-	-
	4	-	-	-	71.3	49.8	65.0	-	-	-
	5	-	-	-	135.8	92.0	120.4	-	-	-
	6	-	-	-	144.9	154.0	135.9	-	-	-
90	1	-	2.3	4.2	2.0	1.5	2.0	1.2	4.8	2.8
	2	-	13.1	25.0	11.6	8.1	11.1	6.6	29.7	16.4
	3	-	37.0	74.9	34.7	23.1	31.9	18.3	92.4	48.7
	4	-	78.7	166.4	77.7	49.8	69.2	38.3	214.1	108.4
	5	-	143.0	315.9	149.2	92.0	128.6	68.4	418.8	205.8
	6	-	152.2	344.2	154.0	154.0	135.9	81.5	452.9	226.5
80	1	-	2.6	4.7	2.2	1.5	2.5	1.3	5.1	3.0
	2	-	14.4	27.9	13.1	8.1	12.5	7.2	32.1	17.7
	3	-	40.9	83.6	39.6	23.1	36.6	19.9	101.6	53.2
	4	-	87.2	186.2	89.6	49.8	80.4	41.9	238.5	119.8
	5	-	158.5	353.0	173.9	92.0	151.3	75.3	476.5	230.5
	6	-	163.1	362.4	181.2	154.0	181.2	81.5	480.1	244.6
70	1	2.9	2.8	5.2	2.6	1.5	2.5	1.4	5.7	3.5
	2	15.8	15.5	31.5	15.4	8.1	13.8	7.7	36.8	20.9
	3	43.9	44.5	96.1	46.3	23.1	40.4	21.5	118.8	63.6
	4	90.8	95.2	217.6	104.8	49.8	88.8	45.3	283.9	144.3
	5	159.5	173.9	417.8	202.7	92.0	166.7	81.6	572.2	279.9
	6	172.1	181.2	425.8	208.4	154.0	181.2	81.5	588.8	289.9
60	1	3.2	2.8	5.4	2.4	1.5	2.5	1.5	8.1	3.9
	2	16.7	15.7	32.9	14.4	8.1	14.4	8.2	51.6	23.1
	3	49.3	45.0	100.6	43.3	23.1	42.1	23.0	163.3	70.5
	4	102.3	96.6	228.1	97.6	49.8	92.5	48.5	381.6	160.6
	5	180.1	177.0	439.4	188.3	92.0	173.9	87.9	753.3	309.8
	6	190.2	181.2	452.9	199.3	154.0	181.2	90.6	788.1	335.2
50	1	3.4	2.8	5.0	2.1	1.5	2.3	1.5	6.1	3.5
	2	17.4	15.8	30.6	12.4	8.1	13.2	8.1	38.7	20.9
	3	54.2	45.7	93.9	37.0	23.1	38.2	22.6	122.7	62.9
	4	112.9	98.3	214.1	83.4	49.8	83.5	47.9	288.6	142.0
	5	199.6	181.1	412.7	160.5	92.0	156.4	87.2	574.2	274.8
	6	200.2	185.7	452.9	172.1	154.0	181.2	90.6	588.8	289.9

T_r (°F)	L_2/L (%)	(1)	(2)	(3)	(4)	(5)	(6)	(7)	(8)	(9)
					Fatigue Life (Years) Data from Recorded Real Temperature					

T_r (°F)	L_2/L (%)	(1)	(2)	(3)	(4)	(5)	(6)	(7)	(8)	(9)
40	1	3.4	2.8	4.4	1.9	1.5	2.1	1.5	5.0	3.2
	2	19.0	15.5	26.6	11.1	8.1	12.0	7.9	31.4	18.9
	3	53.6	44.6	81.2	32.8	23.1	34.7	22.3	99.2	56.4
	4	112.6	95.9	183.8	73.4	49.8	75.3	47.4	231.5	126.8
	5	200.7	176.0	354.0	141.0	92.0	140.0	86.2	460.0	243.9
	6	201.1	185.7	380.5	149.5	154.0	144.9	90.6	480.1	289.9
30	1	3.4	2.6	-	-	1.5	1.9	1.4	-	3.0
	2	19.0	14.7	-	-	8.1	11.3	7.9	-	17.4
	3	53.9	42.2	-	-	23.1	32.8	22.2	-	52.2
	4	113.2	90.8	-	-	49.8	71.3	47.0	-	117.5
	5	201.7	166.7	-	-	92.0	133.8	85.7	-	226.4
	6	226.5	179.4	-	-	154.0	144.9	90.6	-	244.6
20	1	3.3	2.5	-	-	-	-	1.4	-	-
	2	18.6	14.0	-	-	-	-	7.8	-	-
	3	52.7	40.2	-	-	-	-	21.9	-	-
	4	110.8	86.3	-	-	-	-	46.5	-	-
	5	197.6	158.5	-	-	-	-	84.9	-	-
	6	235.5	176.6	-	-	-	-	90.6	-	-
10	1	3.2	2.4	-	-	-	-	1.4	-	-
	2	18.3	13.6	-	-	-	-	7.7	-	-
	3	51.5	38.9	-	-	-	-	21.5	-	-
	4	108.4	83.5	-	-	-	-	45.6	-	-
	5	193.5	153.3	-	-	-	-	83.1	-	-
	6	235.5	176.6	-	-	-	-	90.6	-	-
0	1	3.1	-	-	-	-	-	1.4	-	-
	2	17.7	-	-	-	-	-	7.5	-	-
	3	49.8	-	-	-	-	-	21.1	-	-
	4	105.0	-	-	-	-	-	44.6	-	-
	5	187.3	-	-	-	-	-	81.2	-	-
	6	226.5	-	-	-	-	-	90.6	-	-
-10	1	3.0	-	-	-	-	-	-	-	-
	2	16.9	-	-	-	-	-	-	-	-
	3	47.8	-	-	-	-	-	-	-	-
	4	100.4	-	-	-	-	-	-	-	-
	5	179.1	-	-	-	-	-	-	-	-
	6	199.3	-	-	-	-	-	-	-	-

T_r : reference temperature L_2 : total length of BRB L : total span length of bridge

(1) Anchorage, Alaska   (4) Los Angeles, California   (7) Quebec City, Canada

(2) Boston, Massachusetts   (5) Memphis, Tennessee   (8) San Fransisco, California

(3) Charleston, South Carolina (6) Portland, Oregon   (9) Seattle, Washington

T_r (°F)	L_2/L (%)	(1)	(2)	(3)	(4)	(5)	(6)	(7)	(8)	(9)
					Fatigue Life (Years) Data from Recorded Average Temperature					
100	1	-	-	-	-	-	-	-	-	-
	2	-	-	-	-	-	-	-	-	-
	3	-	-	-	-	-	-	-	-	-
	4	-	-	-	-	-	-	-	-	-
	5	-	-	-	-	-	-	-	-	-
	6	-	-	-	-	-	-	-	-	-
90	1	-	-	-	-	2.6	-	-	-	-
	2	-	-	-	-	16.0	-	-	-	-
	3	-	-	-	-	50.8	-	-	-	-
	4	-	-	-	-	121.0	-	-	-	-
	5	-	-	-	-	248.0	-	-	-	-
	6	-	-	-	-	271.8	-	-	-	-
80	1	-	4.7	8.7	2.6	2.8	2.9	-	-	-
	2	-	31.2	62.9	16.6	18.0	18.3	-	-	-
	3	-	104.0	225.7	54.2	58.0	59.1	-	-	-
	4	-	256.0	598.1	133.8	140.8	143.1	-	-	-
	5	-	526.9	1317.2	283.0	290.2	298.4	-	-	-
	6	-	543.5	1630.6	298.9	308.0	317.1	-	-	-
70	1	-	5.4	9.0	3.3	2.9	3.4	2.8	7.1	4.8
	2	-	36.8	67.0	21.3	18.1	21.9	17.1	52.8	32.7
	3	-	125.2	248.3	71.4	59.2	72.5	53.5	200.5	113.2
	4	-	314.2	677.2	180.4	144.3	179.2	124.5	566.6	293.2
	5	-	657.6	1533.3	388.0	302.6	381.8	246.0	1368.7	645.2
	6	-	679.4	1721.2	407.6	317.1	398.6	271.8	2264.7	706.6
60	1	6.4	5.3	10.0	3.1	2.9	3.8	3.1	13.3	5.7
	2	42.3	36.1	76.7	20.4	18.3	24.7	19.3	110.1	40.0
	3	139.4	124.3	292.1	67.8	59.7	82.4	61.2	459.3	142.1
	4	333.9	315.3	811.0	169.9	146.6	207.1	144.3	1419.5	374.7
	5	664.8	673.0	1862.6	366.4	306.7	441.5	289.2	3673.8	841.8
	6	724.7	697.5	1902.4	380.5	317.1	452.9	317.1	4529.4	887.8
50	1	6.8	5.3	9.7	2.6	2.9	3.3	2.9	8.4	4.9
	2	45.8	36.2	74.3	16.3	18.4	20.6	18.1	62.6	32.7
	3	154.0	124.7	282.8	53.0	60.0	66.1	57.6	237.6	110.6
	4	379.3	317.6	786.6	130.3	146.6	160.6	136.1	673.7	279.3
	5	774.9	680.2	1811.2	276.8	306.7	331.4	273.7	1626.0	601.0
	6	797.2	697.5	1902.4	317.1	317.1	380.5	294.4	2310.0	670.4

T_r (°F)	L_2/L (%)	(1)	(2)	(3)	(4)	(5)	(6)	(7)	(8)	(9)
					Fatigue Life (Years) Data from Recorded Average Temperature					
40	1	6.4	5.2	-	-	2.7	2.9	2.8	-	4.4
	2	43.7	35.8	-	-	17.1	18.3	17.5	-	28.6
	3	147.4	122.9	-	-	55.1	58.1	55.4	-	95.5
	4	366.5	313.0	-	-	133.8	139.6	131.5	-	239.7
	5	759.5	669.9	-	-	278.9	289.2	263.4	-	512.5
	6	797.2	679.4	-	-	312.5	308.0	294.4	-	634.1
30	1	6.5	5.2	-	-	-	-	2.8	-	-
	2	44.3	35.6	-	-	-	-	17.2	-	-
	3	150.0	122.1	-	-	-	-	54.6	-	-
	4	372.3	310.7	-	-	-	-	129.2	-	-
	5	771.8	681.3	-	-	-	-	261.4	-	-
	6	797.2	697.5	-	-	-	-	294.4	-	-
20	1	6.9	-	-	-	-	-	2.9	-	-
	2	46.7	-	-	-	-	-	18.0	-	-
	3	156.7	-	-	-	-	-	57.2	-	-
	4	385.1	-	-	-	-	-	136.1	-	-
	5	790.3	-	-	-	-	-	272.7	-	-
	6	806.2	-	-	-	-	-	294.4	-	-
10	1	-	-	-	-	-	-	2.9	-	-
	2	-	-	-	-	-	-	17.8	-	-
	3	-	-	-	-	-	-	56.6	-	-
	4	-	-	-	-	-	-	133.8	-	-
	5	-	-	-	-	-	-	270.6	-	-
	6	-	-	-	-	-	-	294.4	-	-
0	1	-	-	-	-	-	-	-	-	-
	2	-	-	-	-	-	-	-	-	-
	3	-	-	-	-	-	-	-	-	-
	4	-	-	-	-	-	-	-	-	-
	5	-	-	-	-	-	-	-	-	-
	6	-	-	-	-	-	-	-	-	-
-10	1	-	-	-	-	-	-	-	-	-
	2	-	-	-	-	-	-	-	-	-
	3	-	-	-	-	-	-	-	-	-
	4	-	-	-	-	-	-	-	-	-
	5	-	-	-	-	-	-	-	-	-
	6	-	-	-	-	-	-	-	-	-

T_r : reference temperature L_2 : total length of BRB L : total span length of bridge

(1) Anchorage, Alaska   (4) Los Angeles, California   (7) Quebec City, Canada

(2) Boston, Massachusetts   (5) Memphis, Tennessee   (8) San Fransisco, California

(3) Charleston, South Carolina   (6) Portland, Oregon   (9) Seattle, Washington

Sub Appendix B-2. Fatigue Life of BRB using Smith-Watson and Topper method with thermal strain data calculated using Eq D3.18

T_r (°F)	L_2/L (%)	Fatigue Life (Years) Data from Recorded Real Temperature								
		(1)	(2)	(3)	(4)	(5)	(6)	(7)	(8)	(9)
100	1	-	-	-	1.2	1.0	1.2			
	2	-	-	-	6.1	5.0	6.0			
	3	-	-	-	16.5	13.1	15.8			
	4	-	-	-	33.6	26.4	31.9			
	5	-	-	-	59.6	46.0	55.8			
	6	-	-	-	62.5	72.9	60.4			
90	1	-	1.6	2.7	1.4	1.2	1.3	0.8	2.7	1.7
	2	-	7.9	14.4	7.2	5.9	6.8	4.0	14.4	9.0
	3	-	21.0	39.8	19.4	15.6	17.9	10.4	40.5	24.6
	4	-	42.6	83.2	40.6	31.7	36.6	20.6	85.9	51.0
	5	-	74.4	149.0	72.9	55.5	64.8	35.1	156.8	91.0
	6	-	83.3	177.0	83.4	88.6	70.9	38.5	177.0	104.1
80	1	-	1.9	3.5	1.8	1.5	3.5	0.9	3.2	2.1
	2	-	9.5	18.8	9.4	7.6	8.4	4.6	17.5	10.8
	3	-	25.1	51.6	26.1	20.2	22.6	11.8	49.7	29.7
	4	-	51.6	108.8	55.6	41.2	46.9	23.5	108.3	62.6
	5	-	90.5	196.3	101.3	72.4	83.8	40.3	201.3	113.1
	6	-	104.2	229.3	126.5	116.0	89.6	43.8	260.6	145.9
70	1	1.8	2.4	5.2	2.1	1.6	2.6	1.1	4.3	2.7
	2	9.0	12.1	28.0	11.8	8.1	8.6	5.3	40.6	14.8
	3	23.5	32.4	78.0	34.2	22.0	24.0	13.8	109.6	41.7
	4	46.6	66.6	167.5	75.5	45.6	51.5	27.6	162.1	90.1
	5	79.2	117.0	302.4	142.6	81.6	95.4	47.6	312.0	166.2
	6	83.3	121.3	369.1	266.0	133.0	133.0	50.6	632.7	210.9
60	1	2.2	2.4	6.6	5.6	3.0	3.3	1.0	7.2	3.3
	2	10.7	12.7	36.2	31.8	15.6	18.0	5.1	45.2	18.7
	3	28.5	34.5	103.5	94.5	42.1	51.7	13.5	145.2	55.7
	4	56.8	71.4	224.5	210.0	86.5	111.8	27.3	350.8	125.4
	5	97.0	127.8	419.6	405.1	153.0	208.0	47.9	726.2	241.7
	6	104.2	177.3	709.3	914.8	247.0	320.2	57.6	2660.0	443.3
50	1	2.9	4.7	17.2	30.0	8.5	13.2	1.6	43.1	9.4
	2	13.5	24.0	96.0	99.0	23.4	40.0	8.4	305.9	55.1
	3	37.2	64.9	278.4	313.5	63.3	116.3	22.0	1033.5	165.7
	4	73.9	132.0	602.3	769.1	131.0	253.5	43.5	2519.4	367.1
	5	125.3	232.7	1131.3	1500.1	232.0	473.3	74.9	5193.4	704.7
	6	128.7	274.4	1829.6	8377.8	377.0	837.8	82.3	91481.5	1646.7

		Fatigue Life (Years) Data from Recorded Real Temperature								
T_r (°F)	L_2/L (%)	(1)	(2)	(3)	(4)	(5)	(6)	(7)	(8)	(9)
40	1	2.9	13.8	88.4	680.4	10.0	22.7	4.1	2805.6	51.1
	2	14.4	37.5	270.2	11999.3	54.1	133.8	10.5	26046.4	161.6
	3	38.2	99.4	808.5	88442.9	151	393.4	27.2	193652.0	485.3
	4	76.4	199.7	1848.8	438069	320	864.0	53.5	969822.6	1077.6
	5	132.4	345.7	3615.1	1994603	582	1618.8	90.8	3969156.6	2049.8
	6	177.3	502.7	4188.9	3326667	998	16633.3	108.9	5026666.7	16755.6
30	1	5.3	15.5	-	-	34.2	613.7	5.0	-	161.4
	2	26.3	78.3	-	-	197	1178.1	16.5	-	1205.8
	3	68.4	203.0	-	-	573	4631.1	42.4	-	4695.0
	4	133.2	400.6	-	-	1260	13465.6	83.0	-	14013.8
	5	224.1	678.4	-	-	2340	31553.3	139.7	-	35556.0
	6	256.1	831.7	-	-	3960	55440.0	166.3	-	41583.3
20	1	13.6	28.4	-	-	-	-	7.2	-	-
	2	35.1	141.8	-	-	-	-	22.2	-	-
	3	89.4	368.9	-	-	-	-	57.1	-	-
	4	172.2	732.9	-	-	-	-	112.5	-	-
	5	285.1	1271.9	-	-	-	-	185.1	-	-
	6	318.4	5544.0	-	-		-	237.6	-	-
10	1	12.5	128.4	-	-	-	-	8.0	-	-
	2	60.9	857.6	-	-	-	-	40.7	-	-
	3	153.5	3162.2	-	-	-	-	107.9	-	-
	4	295.7	8771.9	-	-	-	-	219.6	-	-
	5	487.6	19894.1	-	-	-	-	385.4	-	-
	6	623.8	23760.0	-	-		-	665.3	-	-
0	1	21.6	-	-	-	-	-	16.6	-	-
	2	106.2	-	-	-	-	-	91.4	-	-
	3	272.5	-	-	-	-	-	263.5	-	-
	4	534.8	-	-	-	-	-	571.3	-	-
	5	888.7	-	-	-	-	-	1059.9	-	-
	6	1029.6	-	-	-	-	-	1267.2	-	-
-10	1	95.7	-	-	-	-	-	-	-	-
	2	659.3	-	-	-	-	-	-	-	-
	3	2377.2	-	-	-	-	-	-	-	-
	4	6290.4	-	-	-	-	-	-	-	-
	5	14105.2	-	-	-	-	-	-	-	-
	6	18216.0	-	-	-	-	-	-	-	-

T_r : reference temperature

L_2 : total length of BRB

L : total span length of bridge

(1) Anchorage, Alaska

(2) Boston, Massachusetts

(3) Charleston, South Carolina

(4) Los Angeles, California

(5) Memphis, Tennessee

(6) Portland, Oregon

(7) Quebec City, Canada

(8) San Fransisco, California

(9) Seattle, Washington

T_r (°F)	L_2/L (%)	(1)	(2)	(3)	(4)	(5)	(6)	(7)	(8)	(9)
					Fatigue Life (Years)					
					Data from Recorded Average Temperature					
100	**1**	-	-	-	-	-	-	-	-	-
	2	-	-	-	-	-	-	-	-	-
	3	-	-	-	-	-	-	-	-	-
	4	-	-	-	-	-	-	-	-	-
	5	-	-	-	-	-	-	-	-	-
	6	-	-	-	-	-	-	-	-	-
90	**1**	-	-	-	-	1.6	-	-	-	-
	2	-	-	-	-	8.3	-	-	-	-
	3	-	-	-	-	23.2	-	-	-	-
	4	-	-	-	-	49.1	-	-	-	-
	5	-	-	-	-	89.8	-	-	-	-
	6	-	-	-	-	104.1	-	-	-	-
80	**1**	-	2.5	5.1	1.9	2.0	1.9	-	-	-
	2	-	13.9	29.3	10.6	10.8	10.2	-	-	-
	3	-	40.2	87.9	30.6	30.4	29.0	-	-	-
	4	-	87.0	198.7	67.3	66.0	62.9	-	-	-
	5	-	162.0	382.3	127.5	122.1	117.1	-	-	-
	6	-	208.3	416.6	208.3	156.4	135.4	-	-	-
70	**1**	-	3.3	7.7	3.2	2.9	2.6	1.7	4.7	3.2
	2	-	18.8	45.7	18.7	16.0	14.5	8.9	28.2	18.7
	3	-	54.7	138.4	56.8	45.4	42.4	24.8	89.3	56.2
	4	-	120.9	329.4	132.4	99.3	95.8	52.4	211.5	128.0
	5	-	227.5	633.8	263.8	185.5	185.0	95.2	432.8	250.1
	6	-	281.4	938.1	625.4	284.7	312.7	104.1	1041.4	416.6
60	**1**	3.5	4.9	15.9	8.5	3.5	4.7	2.1	12.4	5.5
	2	19.2	27.7	100.0	55.5	20.0	28.3	11.7	89.8	35.0
	3	54.9	81.1	321.4	185.8	59.3	88.6	32.9	328.7	112.8
	4	116.8	189.8	778.8	470.5	135.5	210.0	70.5	908.5	274.5
	5	212.5	339.7	1602.2	1034.8	259.3	422.8	128.8	2112.5	567.5
	6	249.9	421.8	10545.5	105454.5	620.7	1054.5	156.4	10423.5	1042.4
50	**1**	4.4	5.9	52.8	114.7	10.1	9.9	3.0	194.5	16.7
	2	28.3	34.5	425.6	2208.6	60.4	67.3	16.3	2864.4	115.7
	3	79.2	104.5	1719.8	18314.7	187.4	232.3	45.7	17398.5	404.0
	4	171.5	240.6	5116.1	89076.7	431.9	600.6	97.8	71369.0	1055.3
	5	315.0	467.7	12781.8	337144.2	858.7	1324.5	179.5	226475.9	2337.0
	6	416.9	886.7	15960.0	620666.7	2744.4	26600.0	189.8	527272.7	52727.3

T_r (°F)	L_2/L (%)	(1)	(2)	(3)	(4)	(5)	(6)	(7)	(8)	(9)
		Fatigue Life (Years) Data from Recorded Average Temperature								
40	1	7.4	15.1	-	-	57.9	110.0	3.2	-	143.4
	2	42.1	90.4	-	-	208.9	1145.5	17.5	-	1675.1
	3	121.9	279.8	-	-	711.7	5595.2	49.9	-	8051.8
	4	267.1	643.1	-	-	1785.4	18835.6	108.2	-	26490.5
	5	499.9	1282.2	-	-	3801.4	50748.6	200.1	-	70855.8
	6	738.2	1829.6	-	-	5864.4	73185.2	266.0	-	88666.7
30	1	9.9	98.9	-	-	-	-	6.0	-	-
	2	59.3	363.5	-	-	-	-	32.3	-	-
	3	182.0	1246.6	-	-	-	-	91.8	-	-
	4	416.6	3179.9	-	-	-	-	196.8	-	-
	5	816.9	4658.6	-	-	-	-	361.0	-	-
	6	2660.0	-	-	-	-	-	594.6	-	-
20	1	50.1	-	-	-	-	-	19.7	-	-
	2	350.2	-	-	-	-	-	58.1	-	-
	3	1197.8	-	-	-	-	-	167.0	-	-
	4	2915.3	-	-	-	-	-	363.4	-	-
	5	6044.6	-	-	-	-	-	677.4	-	-
	6	8233.3	-	-	-	-	-	837.8	-	-
10	1	-	-	-	-	-	-	28.2	-	-
	2	-	-	-	-	-	-	173.9	-	-
	3	-	-	-	-	-	-	546.9	-	-
	4	-	-	-	-	-	-	662.1	-	-
	5	-	-	-	-	-	-	2563.1	-	-
	6	-	-	-	-	-	-	4158.3	-	-
0	1	-	-	-	-	-	-	-	-	-
	2	-	-	-	-	-	-	-	-	-
	3	-	-	-	-	-	-	-	-	-
	4	-	-	-	-	-	-	-	-	-
	5	-	-	-	-	-	-	-	-	-
	6	-	-	-	-	-	-	-	-	-
-10	1	-	-	-	-	-	-	-	-	-
	2	-	-	-	-	-	-	-	-	-
	3	-	-	-	-	-	-	-	-	-
	4	-	-	-	-	-	-	-	-	-
	5	-	-	-	-	-	-	-	-	-
	6	-	-	-	-	-	-	-	-	-

T_r : reference temperature L_2 : total length of BRB L : total span length of bridge

(1) Anchorage, Alaska   (4) Los Angeles, California   (7) Quebec City, Canada

(2) Boston, Massachusetts   (5) Memphis, Tennessee   (8) San Fransisco, California

(3) Charleston, South Carolina   (6) Portland, Oregon   (9) Seattle, Washington

Sub Appendix B-3. Fatigue Life of BRB using Morrow method
with thermal strain data calculated using Eq D3.18

T_r (°F)	L_2/L (%)	Fatigue Life (Years) Data from Recorded Real Temperature								
		(1)	(2)	(3)	(4)	(5)	(6)	(7)	(8)	(9)
100	1	-	-	-	1.6	1.3	1.6	-	-	-
	2	-	-	-	8.8	6.8	8.8	-	-	-
	3	-	-	-	24.8	18.6	23.6	-	-	-
	4	-	-	-	52.5	38.7	49.6	-	-	-
	5	-	-	-	95.6	69.7	87.2	-	-	-
	6	-	-	-	105.4	115.0	91.0	-	-	-
90	1	-	2.1	3.6	1.7	1.4	1.7	1.1	3.9	2.4
	2	-	11.2	20.6	9.4	7.5	9.1	5.6	23.1	13.5
	3	-	30.8	60.5	27.3	20.8	25.4	14.9	68.4	37.9
	4	-	63.1	129.4	59.2	43.4	53.2	30.2	153.3	82.3
	5	-	110.5	235.3	112.0	78.8	97.7	52.5	291.1	149.9
	6	-	124.6	258.8	119.1	129.0	109.2	86.2	325.8	162.9
80	1	-	2.3	4.2	2.0	1.6	2.5	1.2	4.3	2.6
	2	-	12.3	23.6	11.3	8.5	10.6	6.0	25.5	14.6
	3	-	35.2	69.7	33.3	24.0	30.0	16.4	78.2	43.1
	4	-	72.2	153.5	73.3	50.4	64.2	35.1	177.7	93.2
	5	-	129.2	283.1	139.0	91.3	117.6	58.9	352.0	177.6
	6	-	138.9	297.7	152.0	152.0	123.5	94.3	396.9	198.5
70	1	2.5	2.5	4.9	1.8	1.3	1.8	1.3	4.9	3.1
	2	13.4	13.7	29.1	10.5	6.9	8.9	6.5	31.1	18.0
	3	35.5	38.7	88.0	31.5	19.4	25.4	17.9	98.5	53.9
	4	72.5	81.8	196.0	69.2	41.3	55.4	36.4	231.0	120.2
	5	121.5	145.2	377.3	132.8	75.6	101.7	63.8	464.2	230.0
	6	134.2	152.0	427.5	152.8	125.0	111.1	95.0	532.0	266.0
60	1	2.8	2.0	4.2	2.4	1.8	2.3	1.0	5.8	2.7
	2	14.3	10.9	25.3	14.5	9.8	12.8	5.3	36.9	16.8
	3	40.5	30.3	75.3	43.3	28.6	37.6	14.2	115.7	47.8
	4	81.8	63.3	168.3	98.5	62.2	82.9	28.9	267.3	107.1
	5	143.2	114.5	319.4	187.9	114.0	154.1	50.9	537.7	207.0
	6	148.8	125.0	347.2	213.9	191.0	171.9	83.3	590.3	236.1
50	1	3.1	2.7	5.3	2.2	1.8	2.3	1.3	6.3	3.5
	2	15.2	15.3	33.5	13.2	9.9	13.2	7.0	41.3	21.2
	3	46.1	44.2	103.2	40.0	28.6	37.9	19.1	133.5	64.9
	4	94.8	96.0	229.0	92.5	63.0	83.3	40.0	316.7	147.5
	5	163.6	177.2	429.3	178.7	118.0	158.2	70.1	629.7	282.3
	6	171.0	191.0	458.4	196.0	196.0	176.4	99.3	687.6	305.6

T_r (°F)	L_2/L (%)	(1)	(2)	(3)	(4)	(5)	(6)	(7)	(8)	(9)
					Fatigue Life (Years) Data from Recorded Real Temperature					
40	1	2.4	2.8	4.9	2.2	1.8	2.3	1.4	5.7	3.4
	2	13.0	16.0	30.1	12.9	10.3	13.2	7.2	37.2	20.8
	3	35.5	44.5	91.7	40.9	30.4	39.4	19.7	118.4	62.5
	4	72.5	96.1	208.7	90.9	66.5	86.6	41.6	284.1	145.0
	5	127.2	174.4	400.2	180.3	126.0	162.8	74.0	572.9	281.3
	6	138.9	196.0	478.2	198.8	213.0	177.5	109.8	627.2	309.7
30	1	3.2	2.8	-	-	1.8	2.2	1.5	-	3.4
	2	18.2	16.0	-	-	10.3	13.5	7.9	-	20.6
	3	51.2	47.3	-	-	30.4	40.1	22.1	-	64.9
	4	106.2	99.4	-	-	66.5	89.7	46.8	-	149.1
	5	183.5	189.0	-	-	126.0	166.6	84.5	-	296.6
	6	191.0	213.0	-	-	213.0	191.7	113.6	-	319.5
20	1	3.4	2.8	-	-	-	-	1.5	-	-
	2	18.8	16.5	-	-	-	-	8.5	-	-
	3	51.7	47.7	-	-	-	-	23.9	-	-
	4	108.8	103.0	-	-	-	-	50.3	-	-
	5	195.0	183.8	-	-	-	-	92.3	-	-
	6	196.0	205.9	-	-	-	-	127.8	-	-
10	1	3.5	2.9	-	-	-	-	1.5	-	-
	2	19.8	16.7	-	-	-	-	8.7	-	-
	3	56.8	48.2	-	-	-	-	24.6	-	-
	4	117.3	111.0	-	-	-	-	51.7	-	-
	5	209.1	188.1	-	-	-	-	106.8	-	-
	6	213.0	198.8	-	-	-	-	134.9	-	-
0	1	3.6	-	-	-	-	-	1.6	-	-
	2	20.8	-	-	-	-	-	8.8	-	-
	3	58.6	-	-	-	-	-	25.3	-	-
	4	121.0	-	-	-	-	-	53.5	-	-
	5	215.8	-	-	-	-	-	97.5	-	-
	6	248.5	-	-	-	-	-	142.0	-	-
-10	1	3.6	-	-	-	-	-	-	-	-
	2	21.1	-	-	-	-	-	-	-	-
	3	59.0	-	-	-	-	-	-	-	-
	4	123.0	-	-	-	-	-	-	-	-
	5	217.5	-	-	-	-	-	-	-	-
	6	248.5	-	-	-	-	-	-	-	-

T_r : reference temperature L_2 : total length of BRB L : total span length of bridge

(1) Anchorage, Alaska   (4) Los Angeles, California   (7) Quebec City, Canada

(2) Boston, Massachusetts   (5) Memphis, Tennessee   (8) San Fransisco, California

(3) Charleston, South Carolina   (6) Portland, Oregon   (9) Seattle, Washington

T_r (°F)	L_2/L (%)	(1)	(2)	(3)	(4)	(5)	(6)	(7)	(8)	(9)
						Fatigue Life (Years) Data from Recorded Average Temperature				
100	1	-	-	-	-	-	-	-	-	-
	2	-	-	-	-	-	-	-	-	-
	3	-	-	-	-	-	-	-	-	-
	4	-	-	-	-	-	-	-	-	-
	5	-	-	-	-	-	-	-	-	-
	6	-	-	-	-	-	-	-	-	-
90	1	-	-	-	-	2.2	-	-	-	-
	2	-	-	-	-	12.7	-	-	-	-
	3	-	-	-	-	37.6	-	-	-	-
	4	-	-	-	-	85.1	-	-	-	-
	5	-	-	-	-	165.2	-	-	-	-
	6	-	-	-	-	191.7	-	-	-	-
80	1	-	3.8	7.1	2.3	2.5	2.5	-	-	-
	2	-	23.6	47.7	14.2	14.7	15.0	-	-	-
	3	-	74.3	160.2	43.2	45.2	45.1	-	-	-
	4	-	174.7	399.6	101.4	104.3	105.2	-	-	-
	5	-	346.9	848.0	204.6	208.8	210.1	-	-	-
	6	-	383.3	958.3	239.6	248.1	239.6	-	-	-
70	1	-	4.6	8.3	3.2	2.6	3.1	2.4	6.1	4.2
	2	-	28.6	57.7	20.1	16.3	18.7	13.9	32.5	27.5
	3	-	93.0	203.8	66.6	51.5	60.5	41.3	100.4	90.4
	4	-	223.6	525.9	162.0	122.5	145.1	94.0	321.0	223.7
	5	-	461.8	1184.2	348.8	251.5	302.5	176.2	670.0	474.9
	6	-	496.2	1389.2	396.9	285.0	347.3	191.7	1228.0	766.7
60	1	5.3	4.8	10.7	3.4	2.2	3.6	2.7	7.3	5.4
	2	32.4	31.8	82.4	23.8	13.7	24.5	16.0	33.0	37.1
	3	103.0	106.4	312.0	79.6	44.7	81.3	49.4	110.0	130.2
	4	236.2	263.7	885.5	205.3	107.1	200.7	112.4	341.6	343.3
	5	458.5	549.0	1911.9	453.9	224.0	431.5	223.9	704.2	781.5
	6	479.2	570.0	2090.0	475.0	250.0	456.0	248.1	1245.1	992.3
50	1	6.0	4.0	9.2	2.3	3.1	2.7	2.7	8.1	5.4
	2	38.7	26.8	74.6	15.4	20.7	17.7	16.8	41.1	38.7
	3	124.5	92.6	304.1	52.4	69.6	58.7	56.7	121.4	136.0
	4	293.8	230.2	829.2	135.3	175.4	144.9	121.3	331.1	368.7
	5	596.4	489.6	1851.1	295.3	365.2	310.9	238.2	698.2	822.0
	6	694.6	520.8	2083.3	347.2	382.0	381.9	266.0	1221.3	1140.0

T_r (^{0}F)	L_2/L (%)	(1)	(2)	(3)	(4)	(5)	(6)	(7)	(8)	(9)
					Fatigue Life (Years) Data from Recorded Average Temperature					
40	1	6.3	5.6	-	-	3.1	3.3	2.1	-	4.0
	2	42.2	40.3	-	-	20.5	22.3	12.9	-	28.4
	3	141.3	141.8	-	-	68.5	75.5	40.0	-	100.7
	4	345.3	370.3	-	-	176.4	203.2	93.4	-	263.3
	5	703.4	770.4	-	-	381.4	407.9	188.6	-	584.3
	6	760.0	840.4	-	-	431.2	458.4	215.3	-	763.9
30	1	5.3	6.3	-	-	-	-	2.8	-	-
	2	36.2	46.7	-	-	-	-	18.1	-	-
	3	124.0	170.2	-	-	-	-	57.6	-	-
	4	308.3	444.6	-	-	-	-	138.2	-	-
	5	642.2	534.4	-	-	-	-	274.3	-	-
	6	694.4	611.2	-	-	-	-	305.6	-	-
20	1	8.3	-	-	-	-	-	3.2	-	-
	2	60.0	-	-	-	-	-	20.5	-	-
	3	213.9	-	-	-	-	-	65.9	-	-
	4	541.5	-	-	-	-	-	160.7	-	-
	5	1068.8	-	-	-	-	-	329.2	-	-
	6	1146.0	-	-	-	-	-	392.0	-	-
10	1	-	-	-	-	-	-	3.3	-	-
	2	-	-	-	-	-	-	22.2	-	-
	3	-	-	-	-	-	-	74.9	-	-
	4	-	-	-	-	-	-	182.9	-	-
	5	-	-	-	-	-	-	374.5	-	-
	6	-	-	-	-	-	-	426.0	-	-
0	1	-	-	-	-	-	-	-	-	-
	2	-	-	-	-	-	-	-	-	-
	3	-	-	-	-	-	-	-	-	-
	4	-	-	-	-	-	-	-	-	-
	5	-	-	-	-	-	-	-	-	-
	6	-	-	-	-	-	-	-	-	-
-10	1	-	-	-	-	-	-	-	-	-
	2	-	-	-	-	-	-	-	-	-
	3	-	-	-	-	-	-	-	-	-
	4	-	-	-	-	-	-	-	-	-
	5	-	-	-	-	-	-	-	-	-
	6	-	-	-	-	-	-	-	-	-

T_r : reference temperature L_2 : total length of BRB L : total span length of bridge

(1) Anchorage, Alaska   (4) Los Angeles, California   (7) Quebec City, Canada

(2) Boston, Massachusetts   (5) Memphis, Tennessee   (8) San Fransisco, California

(3) Charleston, South Carolina   (6) Portland, Oregon   (9) Seattle, Washington

SUB APPENDIX C SOFTWARE VALIDATION

1. Scope of the Validation

Fatiga is a software package to estimate the fatigue life of a material by simply using the fatigue properties of specimens. Fatiga can evaluate either constant or variable amplitude loading histories of a tested specimen by using either the Stress-Life or Strain-Life method. Also within the Fatiga software, there is a variety of structural elements and material properties that can be used either from the software database or by user input. The methodologies in estimating fatigue life in Fatiga are based on Rainflow counting, the linear damage rule known as Miner's rule, as well as the three methods to estimate fatigue life as descripbed in Section 3, i.e Coffin-Manson and Basquin, Smith-Watson and Topper, and Morrow methods.

The validation conducted here uses previous fatigue experiments of some materials which are then compared with the results from Fatiga. For fatigue life estimation considering the effect of mean stress, generating hysteresis loop is conducted manually using Ramberg-Osgood and Masing model as described in Section 3, since a tool for generating stress-strain hysteresis loops is not available in the software. The specific features to be tested are listed in each of the examples and they are presented in Section 3, 4, 5, and 6. Validation of Fatiga is accomplished by comparing the results from Fatiga with the results from reference or from hand calculation results. It is the objective here to show that a negligible difference in results was obtained for the selected test cases, as compared to the results given in Fatiga.

2. Environment

a. Software

The version of Fatiga used in this project was the Fatiga Beta 5 which was downloaded with permission of the software developer, Fatec engineering. Initially, the older version of Fatiga (Fatiga Beta 4) was used in the project, but a serious bug was discovered and reported to the developer, who corrected the error. The bug in Fatiga Beta 4 related to calculation of the damage index given by each cycle, D_i, given as $D_i = \frac{n_i}{2N_{fi}}$ but that was reported in error as $D_i = \frac{n_i}{N_{fi}}$. This bug was caused by the software error in interpreting the life reversals $2N_{fi}$ as cycles to failure N_{fi} and it was fixed in the Beta 5 version of the software. The current version of Fatiga 2014 available for downloading on the website is a demo version and the beta version is not available anymore.

b. Hardware

Fatiga Beta 5 software was installed on a personal computer (notebook) with a single Intel ® Core ™ 2 Duo CPU running at 2.20 GHz with 2.00 GB of memory and local 40 GB hard disk. The notebook operated using Microsoft Windows Vista Home Premium.

3. Example 1

a. Input

Example 1 refers to Stephens (2000) in which the example fatigue life of the strain loading histories given in Figure C-1 is calculated using the Smith-Watson and Topper method. The material used is RQC-100 with properties shown in Table C-1.

Point	Strain
A	0.0069
B	0.003
C	0.0047
D	-0.0024
E	0.004
F	0.0013
G	0.0023
H	-0.0018
I	0.0069
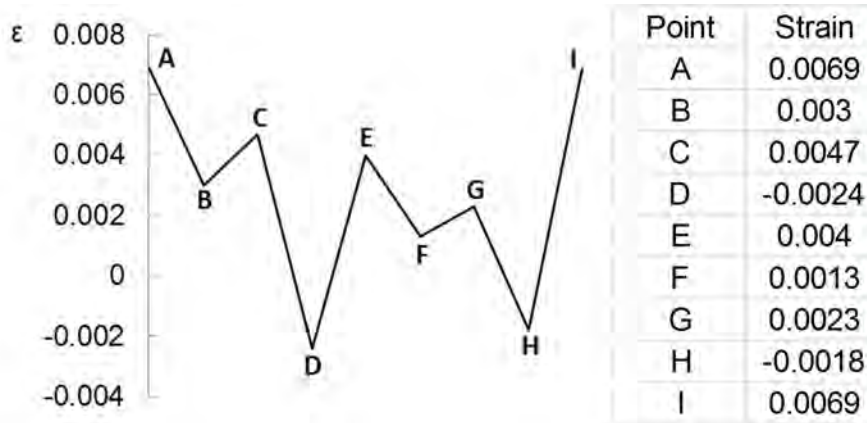
Figure C- 1 Strain loading history (Stephens et al. 2000)

Table C- 1 Material properties of RQC-100

Fatigue strength coefficient	σ_f'	1240 MPa
Fatigue strength exponent	b	-0.07
Fatigue ductility coefficient	ε_f'	0.66
Fatigue ductility exponent	c	-0.69
Elastic modulus	E	200000 MPa
Cyclic strength coefficient	K'	1434
Cyclic strain hardening exponent	n'	0.14

b. Procedures

The loading history shown in Figure C-1 is then extracted into individual cycle using the Rainflow counting method, with the result shown in Table C-2 below.

Table C- 2 Rainflow counting results

Loop	Strain range ($\Delta\varepsilon$)	Cycle (n_i)
A to D	0.0093	1
E to H	0.0058	1
C to B	0.0017	1
G to F	0.001	1

Since the reference calculates the Fatigue Life using the Smith-Watson and Topper method, the stress associated with each point is then manually calculated using the Ramberg-Osgood and Masing method, and the results are shown in Table C-3. The mean stress of the two points forming a loop is also calculated as shown in Table C-3. The hysteresis loop provided in the reference is then compared

to the one generated from manual calculation as shown in Figure C-2. It is shown that the difference of hysteresis loop between the reference and manual calculation is small (approximately 1.48%).

Table C- 3 Stress-Strain Results

Point	ε	σ (MPa) *	σ (MPa) **
A	0.0069	653.15***	653
B	0.003	-98.98	-94
C	0.0047	241.18	248
D	-0.0024	-522.37	-524
E	0.004	501.94	498
F	0.0013	-35.89	-34
G	0.0023	164.51	156
H	-0.0018	-475.41	-479
I	0.0069	653.15	653

Loop	$\Delta\varepsilon$	σ_m(MPa) *	σ_m (MPa) **
A to D	0.0093	653.39	64.5
E to H	0.0058	13.26	9.5
C to B	0.0017	71.10	77
G to F	0.001	64.31	61

*	Manual calculation
**	Reference
***	Calculated using Ramberg-Osgood
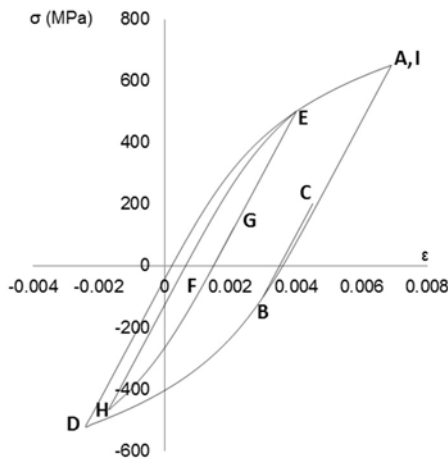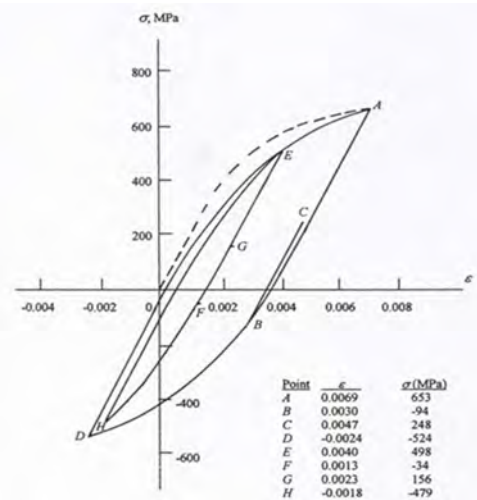
(a)   (b)

Figure C- 2 Stress-strain hysteresis loop from (a) manual calculation (b) reference

c. **Results**

The results of fatigue life estimation calculated using Smith-Watson and Topper method in example 1 are given in Table C-4. The fatigue life for the strain loading shown in Figure C-1 is obtained as 3853.5 reversals, which is a 1.2% difference from the result from the reference which is 3900 reversals.

Table C- 4 Fatigue life calculated using Smith-Watson and Topper method

Point	From	To	$\Delta\varepsilon$	$\dfrac{\Delta\varepsilon}{2}$	σ_{max}	N_{fi}	n_i	$D_i = \dfrac{n_i}{N_{fi}}$
A to D	0.0069	-0.0024	0.009	0.00465	653.15	4133.63	1	0.000242
E to H	0.004	-0.0018	0.005	0.0029	501.94	105340.95	1	0.0000175
B to C	0.0047	0.003	0.001	0.00085	241.18	875578269355	1	6.75E-09
F to G	0.0023	0.0013	0.001	0.0005	164.51	5.96E+13	1	1.49E-11

$N_f^* = 1/D = 3853$ $\qquad\qquad\qquad$ $D = 0.000259$
$N_f^{**} = 3900$ $\qquad\qquad\qquad\qquad\quad$ $^* =$ Fatiga
% difference = 1.2 $\qquad\qquad\qquad\qquad$ $^{**} =$ reference

4. Example 2

a. Input

Example 2 is taken from Committee (1975) in which the tested material is 1020 HR and the strain loading history is as shown in Figure C-3. The properties of 1020 HR used in the test are given in Table C-5.

Point	Strain
1	0.0045
2	-0.002
3	0.004
4	-0.0045
5	0.0025
6	-0.0045
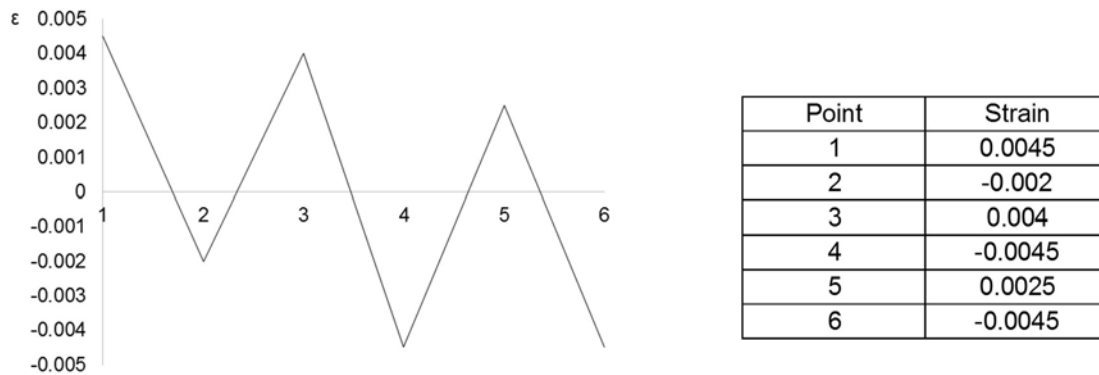
Figure C- 3 Strain loading history (Committee, 1975)

Table C- 5 Material properties of 1020HR

Fatigue strength coefficient	σ_f'	896 MPa
Fatigue strength exponent	b	-0.12
Fatigue ductility coefficient	ε_f'	0.41
Fatigue ductility exponent	c	-0.51
Elastic modulus	E	203395 MPa
Strain hardening coefficient	K'	772
Strain hardening exponent	n'	0.18

b. Procedures

The total number of cycles of the strain loading history shown in Figure C-3 is then calculated using the Rainflow counting method, resulting in three cycles as shown in Table C-6. The stress-strain values as well as the hysteresis loop are calculated manually and they are shown in Table C-7 and Figure C-4.

Table C- 6 Rainflow counting results

Loop	Strain range ($\Delta\varepsilon$)	Cycle (n_i)
1 to 6	0.009	1
3 to 2	0.006	1
5 to 4	0.007	1

Table C- 7 Stress-strain results

Point	ε	σ (MPa) [*]	Point	ε	σ (MPa) [*]
1	0.0045	273.78[**]	4	-0.0045	-273.78
2	-0.002	-231.08	5	0.0025	240.86
3	0.004	263.16	6	-0.0045	-273.78

Loop	$\Delta\varepsilon$	σ_m(MPa) [*]	Loop	$\Delta\varepsilon$	σ_m(MPa) [*]
1 to 6	0.009	0	3 to 2	0.007	16.04
5 to 4	0.006	-16.46			

[*]	Manual calculation
[**]	Calculated using Ramberg-Osgood
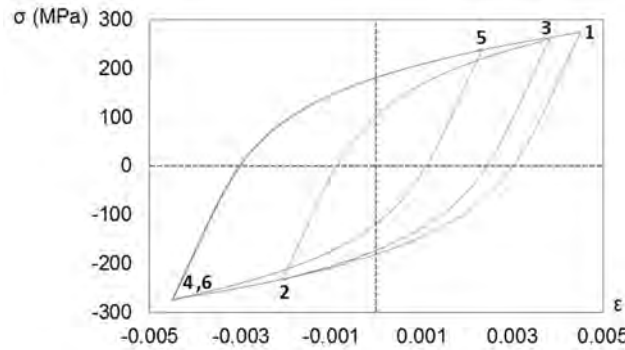
Figure C- 4 Stress-strain hysteresis loop

c. Results

The fatigue life of 1020HR in the reference is calculated using the Morrow method, with a resulting estimated fatigue life of 3862 reversals. The comparison is also calculated manually using the Morrow method as shown in Table C-8, with a total resulting fatigue life of 3932 reversals. The difference between the results from the reference and Fatiga is 1.8%.

Table C- 8 Fatigue life calculated using Morrow method

Point	From	To	$\Delta\varepsilon$	$\dfrac{\Delta\varepsilon}{2}$	σ_m	N_{fi}	n_i	$D_i = \dfrac{n_i}{N_{fi}}$
1 to 6	0.0045	-0.0045	0.009	0.0045	0	7246.38	1	0.000138
5 to 4	0.0025	-0.0045	0.006	0.003	-16.46	14347.20	1	0.0000697
3 to 2	0.004	-0.002	0.007	0.0035	16.04	21459.23	1	0.0000466

$$N_f^* = 1/D = 3932 \qquad\qquad D = 0.0002543$$
$$N_f^{**} = 3862 \qquad\qquad\quad [*] = \text{Fatiga}$$
$$\% \text{ difference} = 1.8 \qquad\qquad [**] = \text{reference}$$

5. Example 3

a. Input

The strain history given in example 3 as shown in Figure C-5 is a created model and the assumed material properties is ASTM A36, the same as the one utilized in the project as described in Section 3. The properties of ASTM A36 are given in Table C-9.

Point	Strain
A	-0.01
B	-0.006
C	-0.008
D	-0.002
E	-0.005
F	0.002
G	-0.001
H	0.006
I	-0.001
J	0.002
K	-0.005
L	-0.002
M	-0.008
N	-0.006
O	-0.01
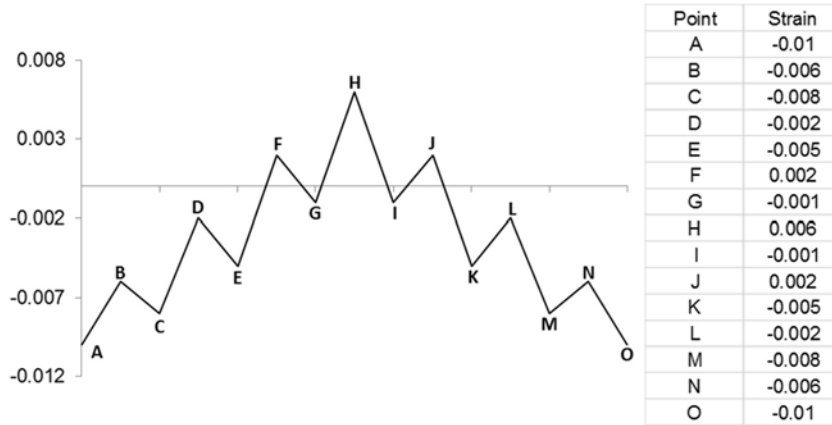
Figure C- 5 Strain loading history

Table C- 9 Material properties of ASTM A36

Fatigue strength coefficient	σ_f'	1014 MPa
Fatigue strength exponent	b	-0.132
Fatigue ductility coefficient	ε_f'	0.271
Fatigue ductility exponent	c	-0.451
Elastic modulus	E	200000 MPa
Strain hardening coefficient	K'	1097
Strain hardening exponent	n'	0.249

b. Procedures

The cycles formed from the loading history given in Figure C-5 are calculated using the Rainflow counting method and the results in Table C-10 show that a total of seven cycles is obtained. The stress associated with strain at each point is given in Table C-11 and the stress-strain hysteresis loop is provided in Figure C-6.
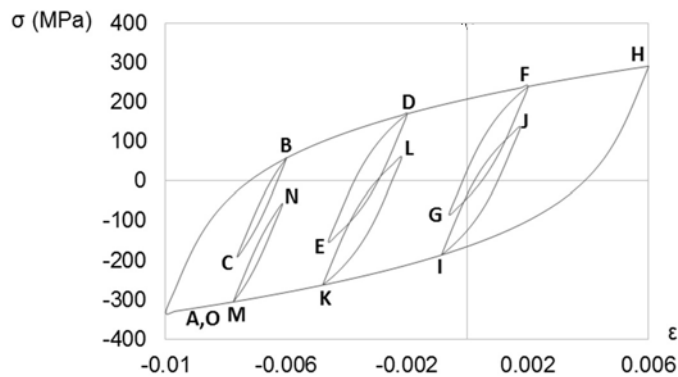
Figure C- 6 Stress-strain hysteresis loop

612

Table C- 10 Rainflow counting results

Loop	Strain range ($\Delta\varepsilon$)	Cycle (n_i)	Loop	Strain range ($\Delta\varepsilon$)	Cycle (n_i)
H to O	0.016	1	I to J	0.003	1
D to E	0.003	1	B to C	0.002	1
K to L	0.003	1	M to N	0.002	1
F to G	0.003	1			

Table C- 11 Stress-strain results

Point	ε	σ (MPa) *	Point	ε	σ (MPa) *
A	-0.01	-332.22**	I	-0.001	22.25
B	-0.006	-57.98	J	0.002	367.11
C	-0.008	-339.02	K	-0.005	-112.94
D	-0.002	195.10	L	-0.002	231.91
E	-0.005	-149.75	M	-0.008	-223.04
F	0.002	367.11	N	-0.006	57.98
G	-0.001	22.25	O	-0.01	-332.22
H	0.006	285.61			

Loop	$\Delta\varepsilon$	σ_m(MPa) *	Loop	$\Delta\varepsilon$	σ_m(MPa) *
H to O	0.016	-23.30	I to J	0.003	194.68
D to E	0.003	22.67	B to C	0.002	-198.50
K to L	0.003	59.48	M to N	0.002	-82.53
F to G	0.003	194.68			

*   Manual calculation

**   Calculated using Ramberg-Osgood

c. Results

The fatigue life in Example 3 is estimated using the Coffin-Manson and Basquin, as well as the Morrow methods. Result from Fatiga given in Table C-12 shows that the fatigue life calculated using the Coffin-Manson and Basquin method is estimated as 2095 reversals, with similar result calculated manually.

Table C- 12 Fatigue life calculated using Coffin-Manson and Basquin method

Point	From	To	$\Delta\varepsilon$	$\Delta\varepsilon$	N_{fi}	n_i	D_i
H to O	0.006	-0.01	0.016	0.008	2147.05	1	0.000466
D to E	-0.002	-0.005	0.003	0.0015	377178.30	1	0.00000265
K to L	-0.005	-0.002	0.003	0.0015	377178.30	1	0.00000265
F to G	0.002	-0.001	0.003	0.0015	377178.30	1	0.00000265
I to J	-0.001	0.002	0.003	0.0015	377178.30	1	0.00000265
B to C	-0.006	-0.008	0.002	0.001	2027475.26	1	0.000000493
M to N	-0.008	-0.006	0.002	0.001	2027475.26	1	0.000000493

$$N_f^* = 1/D = 2095 \qquad\qquad D = 0.000477$$
$$N_f^{**} = 2095 \qquad\qquad * = \text{manual calculation}$$
$$\% \text{ difference} = 0 \qquad\qquad ** = \text{Fatiga}$$

Table C- 13 Fatigue life calculated using Morrow method

Point	From	To	$\Delta\varepsilon$	$\dfrac{\Delta\varepsilon}{2}$	σ_m	N_{fi}	n_i	$D_i = \dfrac{n_i}{N_{fi}}$
H to O	0.006	-0.01	0.016	0.008	-23.30	2175.96	1	0.00046
D to E	-0.002	-0.005	0.003	0.0015	22.67	358456.45	1	0.0000028
K to L	-0.005	-0.002	0.003	0.0015	59.48	330081.71	1	0.0000030
F to G	0.002	-0.001	0.003	0.0015	194.68	245434.75	1	0.0000040
I to J	-0.001	0.002	0.003	0.0015	194.68	245434.75	1	0.0000040
B to C	-0.006	-0.008	0.002	0.001	-198.50	3837876.73	1	0.00000026
M to N	-0.008	-0.006	0.002	0.001	-82.53	2633681.07	1	0.00000038

$$N_f^* = 1/D = 2109 \qquad\qquad D = 0.0002543$$
$$N_f^{**} = 2127 \qquad\qquad\quad {}^* = \text{manual calculation}$$
$$\% \text{ difference} = 0.9 \qquad\qquad {}^{**} = \text{Fatiga}$$

6. Example 4

a. Input

The strain loading history in example 4, shown in Figure C-7, is also a created model and the material properties of ASTM A36 shown in Table C-9 are still being used.

Point	Strain
A	0
B	0.08
C	0.05
D	0.08
E	0.05
F	0.08
G	0.05
H	0.08
I	0
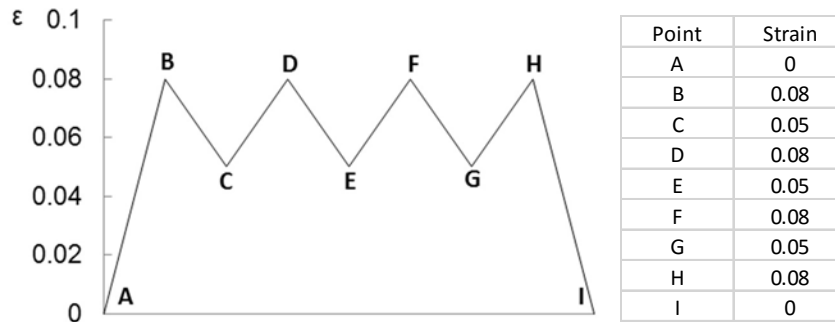
Figure C- 7 Strain loading history

b. Procedures

The Rainflow counting procedure is conducted to extract the strain loading history in Figure C-7 into individual cycles. A total of two cycles are formed, as shown by the stress-stain hysteresis loops in Figure C-8 with the stress-strain values given in Table C-15.

Table C- 14 Rainflow counting results

Loop	$\Delta\varepsilon$	Cycle (n_i)
A to B	0.08	0.5
B to C	0.03	0.5
C to D	0.03	0.5
D to E	0.03	0.5
E to F	0.03	0.5
F to G	0.03	0.5
G to H	0.03	0.5
H to I	0.08	0.5

Table C- 15 Stress-strain results

Point	ε	σ (MPa) *	Point	ε	σ (MPa) *
A	0	0	F	0.08	579.26
B	0.08	579.26**	G	0.05	-165.37
C	0.05	-165.37	H	0.08	579.26
D	0.08	579.26	I	0	0
E	0.05	-165.37			

Loop	$\Delta\varepsilon$	σ_m(MPa) *	Loop	$\Delta\varepsilon$	σ_m(MPa) *
A to B	0.08	289.63	E to F	0.03	206.94
B to C	0.03	206.94	F to G	0.03	206.94
C to D	0.03	206.94	G to H	0.03	206.94
D to E	0.03	206.94	H to I	0.08	289.63

*   Manual calculation

**   Calculated using Ramberg-Osgood
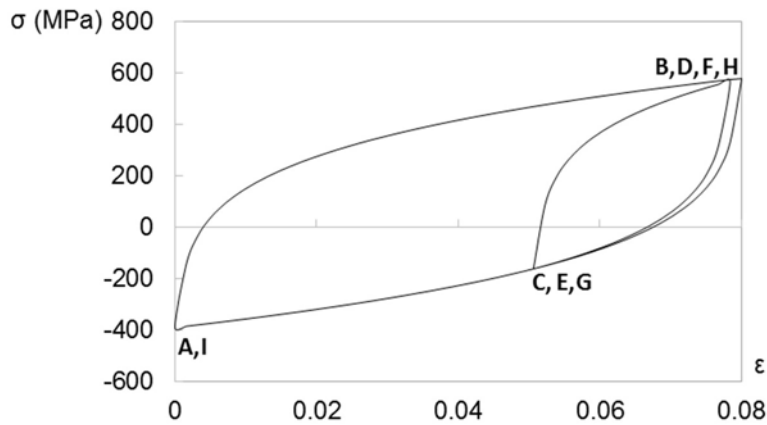
Figure C- 8 Stress-strain hysteresis loop

c. Results

The fatigue life corresponding to the strain loading history given in example 4 is estimated using the Coffin-Manson and Basquin method, the Smith-Watson and Topper method, as well as Morrow method. In table C-16, the calculated fatigue life using the Coffin-Manson and Basquin from Fatiga provides 32.13 reversals whereas manual calculation gives a fatigue life of 32.12 reversals. There is a small difference of 0.03% between the two, which is insignificant. For fatigue life calculated using Smith-Watson and Topper, as shown in Table C-17, there is a 0.4 % difference between the result from Fatiga and manual calculations, in which Fatiga gives the fatigue life as 26.4 reversals whereas manual calculation estimated it as 26.3 reversals. A small percentage of difference is also obtained for the fatigue life results obtained using the Morrow method in Table C-18, in which fatigue life from manual calculation is obtained as 30.4 reversals and Fatiga estimates it as 29.6 reversals.

Table C- 16 Fatigue life calculated using Coffin-Manson and Basquin method

Point	From	To	$\Delta\varepsilon$	$\dfrac{\Delta\varepsilon}{2}$	N_{fi}	n_i	$D_i = \dfrac{n_i}{N_{fi}}$
A to B	0	0.08	0.08	0.04	41.29	0.5	0.024
B to C	0.08	0.05	0.03	0.015	433.94	0.5	0.0069
C to D	0.05	0.08	0.03	0.015	433.94	0.5	0.0069
D to E	0.08	0.05	0.03	0.015	433.94	0.5	0.0069
E to F	0.05	0.08	0.03	0.015	433.94	0.5	0.0069
F to G	0.08	0.05	0.03	0.015	433.94	0.5	0.0069
G to H	0.05	0.08	0.03	0.015	433.94	0.5	0.0069
H to I	0.08	0	0.08	0.04	41.29	0.5	0.024

$$N_f^* = 1/D = 32.12 \qquad\qquad D = 0.031$$
$$N_f^{**} = 32.13 \qquad\qquad {}^* = \text{manual calculation}$$
$$\% \text{ difference} = 0.03 \qquad\qquad {}^{**} = \text{Fatiga}$$

Table C- 17 Fatigue life calculated using Smith-Watson and Topper method

Point	From	To	$\Delta\varepsilon$	$\dfrac{\Delta\varepsilon}{2}$	σ_{max}	N_{fi}	n_i	$D_i = \dfrac{n_i}{N_{fi}}$
A to B	0	0.08	0.08	0.04	579.26	39.65	0.5	0.0252
B to C	0.08	0.05	0.03	0.015	579.26	234.20	0.5	0.013
C to D	0.05	0.08	0.03	0.015	579.26	234.20	0.5	0.013
D to E	0.08	0.05	0.03	0.015	579.26	234.20	0.5	0.013
E to F	0.05	0.08	0.03	0.015	579.26	234.20	0.5	0.013
F to G	0.08	0.05	0.03	0.015	579.26	234.20	0.5	0.013
G to H	0.05	0.08	0.03	0.015	579.26	234.20	0.5	0.013
H to I	0.08	0	0.08	0.04	579.26	39.65	0.5	0.0252

$$N_f^* = 1/D = 26.3 \qquad\qquad D = 0.038$$
$$N_f^{**} = 26.4 \qquad\qquad {}^* = \text{manual calculation}$$
$$\% \text{ difference} = 0.4 \qquad\qquad {}^{**} = \text{Fatiga}$$

Table C- 18 Fatigue life calculated using Morrow method

Point	From	To	$\Delta\varepsilon$	$\dfrac{\Delta\varepsilon}{2}$	σ_m	N_{fi}	n_i	$D_i = \dfrac{n_i}{N_{fi}}$
A to B	0	0.08	0.08	0.04	289.63	39.29	0.5	0.0254
B to C	0.08	0.05	0.03	0.015	206.94	403.39	0.5	0.0074
C to D	0.05	0.08	0.03	0.015	206.94	403.39	0.5	0.0074
D to E	0.08	0.05	0.03	0.015	206.94	403.39	0.5	0.0074
E to F	0.05	0.08	0.03	0.015	206.94	403.39	0.5	0.0074
F to G	0.08	0.05	0.03	0.015	206.94	403.39	0.5	0.0074
G to H	0.05	0.08	0.03	0.015	206.94	403.39	0.5	0.0074
H to I	0.08	0	0.08	0.04	289.63	39.29	0.5	0.0254

$$N_f^* = 1/D = 30.4 \qquad\qquad D = 0.0328$$
$$N_f^{**} = 29.6 \qquad\qquad {}^* = \text{manual calculation}$$
$$\% \text{ difference} = 2.6 \qquad\qquad {}^{**} = \text{Fatiga}$$

Appendix E Reaction Block Design and BRB information

E.1 Reaction block design calculations

The reaction block consists of a base plate, a steel wide flange section, and a gusset plate as shown in Figure E.1. The gusset plates have the same dimensions, thickness and pin hole size. The base plates have the same thickness. The W-sections have the same cross section and length. The base plate dimension and the relative location of the tie-down hole in the base plate is different because of the different center-to-center distance of the holes in the strong floor and the shake table.
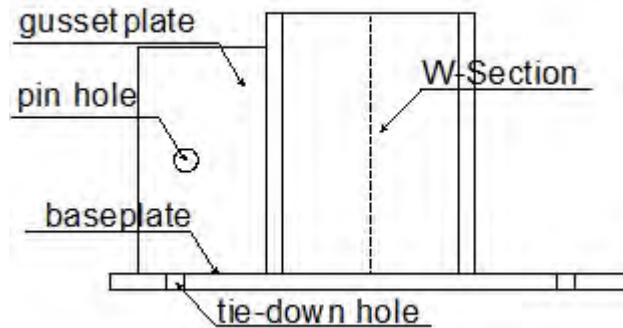
Figure E-1 Reaction Block Configuration

The BRB is connected to the reaction block through the pin connection. Axial force from the BRB is applied to the reaction block (with a small inclination due to the 2" elevation difference between the shake table and the strong floor).

The maximum axial force from the BRB is considerted to be

$F_u := 100$ kips

The BRB's pin to pin length is

$L_b := 100$ in

When the BRB is fully extended in the longitudinal direction of 1.5 times the design displacement and 7" in the transverse direction, the force acting in the longitudinal and transverse direction is

$F_{uv} := 1.976$ kips

$F_{uT} := 6.894$ kips

$F_{uL} := 99.743$ kips

The gusset plate should remain elastic under the applied lateral force that cause the flexural moment on the gusset plate. The W-section, which the gusset plate is connected to, will be subjected to torsion passed on from the gusset plate .
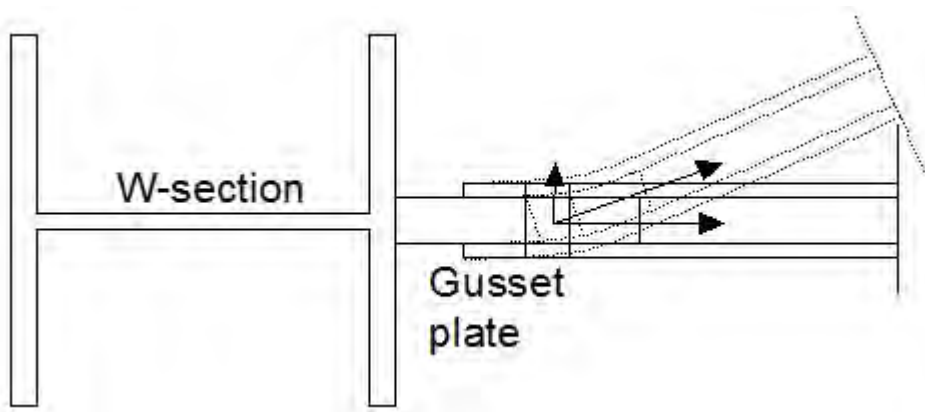
Figure E-2 Deformed gusset plate and BRB's end plate

E.1.1. Gusset plate design

Gusset plate properties:

The yielding and tensile stress of the gusset plate

$$f_{yp} := 50 \qquad\qquad\qquad \text{ksi}$$

$$f_{up} := 65 \qquad\qquad\qquad \text{ksi}$$

The dimensions of the gusset plate is shown in Fig.E.3. The gusset plate has its side A and B connecting to the W-section and the base plate, respectively. Two-sided fillet weld is used for the connection. The pin connecting the gusset plate and BRB's end plate is first designed. Then the gusset plate's strength is checked under the tension or compression force of 100 kips, and the lateral force of 7 kips (to be conservative). For the flexural strength of the gusset plate, yielding at side A or side B with the full lateral load is checked.

The thickness of the gusset plate is

$$t_{gp} := 1.25 \qquad\qquad\qquad \text{in}$$

The pin hole size in the gusset plate (1 17/32 in)

$$d_{hp} := 1 + \frac{17}{32} = 1.531 \qquad\qquad\qquad \text{in}$$

The height of the gusset plate is

$$h_{gp} := 12 \qquad\qquad\qquad \text{in}$$

The diameter of the pin is

$$d_p := 1.5 \qquad\qquad\qquad \text{ksi}$$

The pin use the material of A490, and the shear strength of the A490 when thread is excluded from the shear plane

$$f_{vb} := 75 \qquad\qquad\qquad \text{ksi}$$
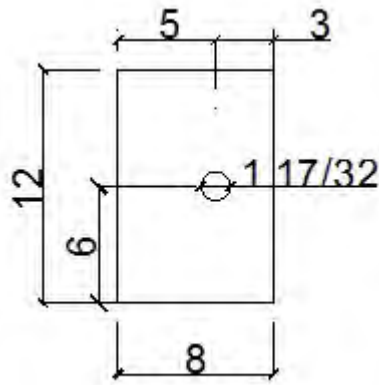
Figure E.3 Dimensions of the gusset plate

The shear strength of the pin, with two shear plane

$$V_{pin} := 2 \cdot 0.75\pi \cdot \frac{d_p^{\ 2} \cdot f_{vb}}{4} = 198.804 \ > 100 \qquad \text{kips}$$

The pin has the diameter of 1.5 in, with A490 material.

E.1.1.1 Gusset plate strength under the tensile force:

The gross and net cross sectional area is

$$A_{gp} := 12 \cdot t_{gp} = 15 \qquad \text{in}^2$$

$$A_{np} := \left(12 - d_{hp}\right) \cdot t_{gp} = 13.086 \qquad \text{in}^2$$

The yield and tensile strength of the gusset plate under tensile force is

$$F_{ytp} := 0.9 \cdot f_{yp} \cdot A_{gp} = 675 \qquad \text{kips}$$

$$F_{ntp} := 0.75 \cdot f_{up} \cdot A_{np} = 637.939 \qquad \text{kips}$$

To prevent the shear tear-out of the gusset plate under tensile force, distance from the edge of the pin hole to the gusset plate's free edge is edge of the plate

$$L_c := 3 - \frac{d_{hp}}{2} = 2.234 \qquad \text{in}$$

The bearing strength of the gusset plate under tensile force is

$$R_{ngp} := 0.75 \cdot 1.2 \cdot f_{up} \cdot L_c \cdot t_{gp} = 163.389 \qquad \text{kips}$$

$$\text{smaller than} \quad 0.75 \cdot 2.4 d_{hp} \cdot t_{gp} \cdot f_{up} = 223.945 \qquad \text{kips}$$

Note that, the requirement of the minimum edge distance for hole size over 1.25 in is: (From Table J3.4 in AISC steel manual (2010)) is not satisfied here

$$3 - 0.5 d_{hp} = 2.234 \ < 1.75 d_{hp} = 2.68 \qquad \text{in}$$

So the bearing strength of the gusset plate under tensile force is 163 kips, which is larger than 100 kips, ok

E.1.1.2 Gusset plate strength under compressive force:

The edge of the pin hole to the fixed edge of the gusset plate

$$l_{gp} := 5 - \frac{d_{hp}}{2} = 4.234 \qquad \qquad \text{in}$$

The gusset plate is attached to the base plate and the W-section at two edges, with the other two free, the K factor is chosen to be 2.1 as shown in Commentary Table C-C2.2 in AISC steel manual

$$\text{k*lgp/r} = 2.1 \cdot l_{gp} \cdot \frac{\sqrt{12}}{t_{gp}} = 24.643 \qquad \qquad \text{ksi}$$

$$\text{smaller than} \qquad 4.71 \cdot \sqrt{\frac{29000}{f_{yp}}} = 113.432 \qquad \qquad \text{ksi}$$

Elastic critical buckling stress is

$$f_e := \pi^2 \cdot \frac{29000}{\left(2 \cdot l_{gp} \cdot \frac{\sqrt{12}}{t_{gp}}\right)^2} = 519.634 \qquad \qquad \text{ksi}$$

The flexrual buckling stress is

$$f_{cr} := 0.658^{\frac{f_{yp}}{f_e}} \cdot f_{yp} = 48.026 \quad \text{I} < f_{yp} = \blacksquare \cdot 50 \qquad \qquad \text{ksi}$$

The compressive strength of the gusset plate under compressive force is

$$P_c := t_{gp} \cdot h_{gp} \cdot f_{cr} \cdot 0.9 = 648.355 \quad > 100 \qquad \qquad \text{kips}$$

E.1.1.3 Plate strength under lateral force:

The flexural yield strength of the gusset plate at side A is

$$M_{ygv} := h_{gp} \cdot \frac{t_{gp}^2 \cdot f_{yp}}{6} = 156.25 \qquad \qquad \text{kip} \cdot \text{in}$$

The flexural yield strength of the gusset plate at side B is

$$M_{ygh} := 8 \cdot \frac{t_{gp}^2 \cdot f_{yp}}{6} = 104.167 \qquad \qquad \text{kip} \cdot \text{in}$$

The moment cause by the lateral force at the surface connecting the W-section is

$$M_v := F_{uT} \cdot 5 = 34.47 \quad < M_{ygv} \qquad \qquad \text{kip} \cdot \text{in}$$

The moment cause by the lateral force at the surface connecting the base plate is

$$M_h := F_{uT} \cdot 6 = 41.364 \quad < M_{ygh} \qquad\qquad \text{kip·in}$$

therefore, if the moment caused by the lateral force is fully taken by the side connecting the W-section, there is enough flexural strength

For the gusset plate design under combined axial force and moment, the equation for the design of beam-column from Equation H1-1a in AISC steel manual is used. Since

$$F_{ytp} = 675 \; > \; P_c = 648.355$$

therefore the tensile strength at side A is larger than compressive strength, the axial and flexural strength interaction is

$$\frac{M_v \cdot 8}{M_{ygv} \cdot 9} + \frac{100}{P_c} = 0.35 \; < 1 \qquad\qquad \text{ok}$$

therefore, if the moment caused by the lateral force is fully taken by side A, there is also enough reserved flexural strength

E.1.2. Gusset plate weld design

The height of the W-section:

$$l_{ws} := 16 \qquad\qquad \text{in}$$

The W-section Properties:

Size W12X96:

$d := 12.7$	in
$b_f := 12.2$	in
$t_f := 0.9$	in
$t_w := 0.55$	in

Young's Modulus: $\qquad\qquad E := 29000 \qquad$ ksi

Yielding strength: $\qquad\qquad f_{ycol} := 50 \qquad$ ksi

Ultimate strength: $\qquad\qquad f_{ucol} := 65 \qquad$ ksi

To calculate the force at the surface between the gusset plate and the base plate and W-section, uniform force method is used below with the following demisions as shown in Figure 4

$$e_c := \frac{d}{2} = 6.35 \qquad\qquad \text{in}$$

$$\alpha_b := 5 \qquad\qquad \text{in}$$

$$r_g := e_c + \alpha_b = 11.35 \qquad\qquad \text{in}$$

The weld between the base plate and the gusset plate need to resist the shear force of

$$H_b := \frac{\alpha_b \cdot F_{uL}}{r_g} = 43.94 \qquad \text{kips}$$

The weld between the base plate and the W-section need to resist the tensile force of

$$H_c := \frac{e_c \cdot F_{uL}}{r_g} = 55.803 \qquad \text{kips}$$

The weld between the gusset plate and the W-section need to resist the flexural moment of

$$M_{gc} := F_{uT} \cdot 5 = 34.47 \qquad \text{kips·in}$$
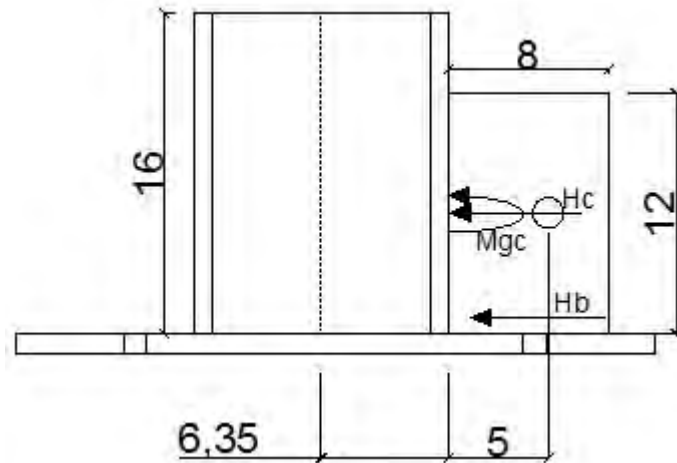
Figure E.4 Gusset plate connection force, Mgc applied at the weak axis of the gusset plate (Mgc applied in the weak axis of the gusset plate)

The requirement of designing the fillet weld is listed below:
1. For the plates with thickness larger than 0.25 in, the largest weld size is (t-1/16) in
2. If the material of the thiner part of the connection over 0.75 in, then the minimum size of fillet weld size is 5/16 in
2. Minimum weld length should be larger than 4a, where a is the weld size
3. Maximum effective length is the weld length, if Lw is smaller than 100a, where a is the weld size
4.If the yield stress of the base metal of the connection is smaller than 60 ksi, use electrode E70

The welds between the W-section, gusset plate and base plate is subjected to FuL, FuT, and Fuv

The weld length between the gusset plate and the base plate is fillet weld of size 5/16 in and length of 7 in; the weld length between the gusset plate and W-section is fillet weld of size 3/8 in and length of 11 in

The weld group strength for the longitudinal force FuL

$$R_{nwL} := 0.85 \cdot (0.75 \cdot 0.707 \cdot 0.3125 \cdot 7 \cdot 2 \cdot 0.6 \cdot 70) + 1.5 \cdot (0.75 \cdot 0.707 \cdot 0.375 \cdot 11 \cdot 2 \cdot 0.6 \cdot 70 \cdot 0.5) = $$

larger than $\quad\quad F_{uL} = 99.743 \quad\quad\quad\quad$ kips

The weld group strength for the vertical force Fuv

$$R_{nwv} := 0.85 \cdot (0.75 \cdot 0.707 \cdot 0.3125 \cdot 7 \cdot 2 \cdot 0.6 \cdot 70 \cdot 0.5) + 1.5 \cdot (0.75 \cdot 0.707 \cdot 0.375 \cdot 11 \cdot 2 \cdot 0.6 \cdot 70) = 317.007$$

larger than $\quad\quad F_{uv} = 1.976 \quad\quad\quad\quad$ kips

The weld group strength for the transverse force FuT

$$R_{nwt} := 0.85 \cdot (0.75 \cdot 0.707 \cdot 0.3125 \cdot 7 \cdot 2 \cdot 0.6 \cdot 70 \cdot 0.5) + 1.5 \cdot (0.75 \cdot 0.707 \cdot 0.375 \cdot 11 \cdot 2 \cdot 0.6 \cdot 70 \cdot 0.5) = 179.20$$

larger than $\quad\quad F_{uT} = 6.894 \quad\quad\quad\quad$ kips

The stress in the weld due to the moment

$$\sigma_m := \frac{M_{gc}}{0.75 \cdot \left[\frac{\left(t_{gp} + 2 \cdot 0.375 \right)^3 - \left(2 \cdot 0.375 \right)^3}{12} \right] \cdot 11} = 6.616 \quad\quad\quad\quad \text{ksi}$$

(equation is from: http://www.mitcalc.com/doc/welding/help/en/welding.htm)

This weld is a transverse loaded weld, and the strength of the weld would be reduced to half, which is

$$f_{ytw} := 0.6 \cdot 70 \cdot 0.5 = 21 \quad\quad\quad\quad\quad\quad\quad\quad\quad\quad \text{ksi}$$

check for the strength of the welds under the combined force

$$\frac{F_{uL}}{R_{nwL}} + \frac{F_{uv}}{R_{nwv}} + \frac{F_{uT}}{R_{nwt}} + \frac{\sigma_m}{f_{ytw}} = 0.812 \quad < 1 \quad\quad \text{ok} \quad \text{(solely taken by the side)}$$

The base metal strength is checked using the force Hb and Hc only considering the force effect of FuL

Check the base metal's shear strength of the gusset plate and the base plate

$$\min\left(0.6 \cdot f_{yp} \cdot t_{gp} \cdot 7, 0.75 \cdot 0.6 \cdot f_{up} \cdot t_{gp} \cdot 7 \right) = 255.937 \quad > H_b \quad\quad\quad\quad \text{kips}$$

Check the base metal's tear-out strength of the W-section

$$\min\left(0.6 \cdot f_{ycol} \cdot t_f \cdot 11, 0.75 \cdot 0.6 \cdot f_{ucol} \cdot t_f \cdot 11 \right) = 289.575 \quad > H_c \quad\quad\quad\quad \text{kips}$$

Figure E.5 show the weld design between the gusset plate and the base plate, and the W-section.
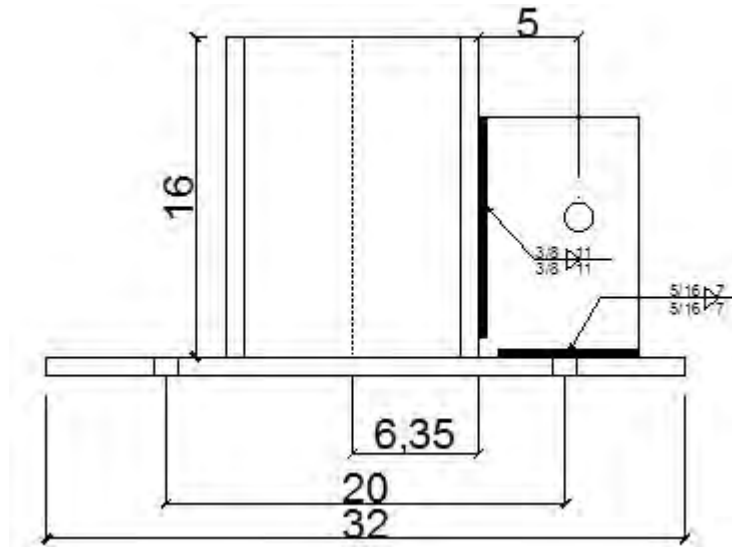
Figure E.5 Weld design between the gusset plate, the steel W-section, and the base plate

E.1.3. Steel W-section strength check

The horizontal tension force applied to the W-section from the weld with gusset plate is assumed to act on the half height of the gusset plate

$$h_{ph} := 6 \qquad\qquad\qquad in$$
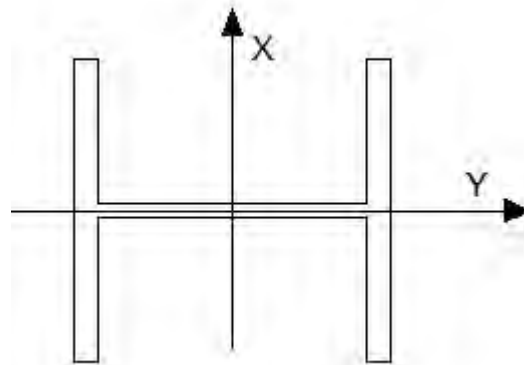
Figure E.6 W-section cross section

The moment demand on the column caused by the tension force Hc and Fuv from the gusset plate through the gusset plate and W-section weld is

$$M_{cx} := H_c \cdot h_{ph} + F_{uv} \cdot 5 = 344.7 \qquad\qquad kip \cdot in$$

The moment demand on the column caused by the transverse force Fut from the gusset plate through the gusset plate and W-section weld is

$$M_{cy} := F_{uT} \cdot \left(\frac{11}{11 + 7}\right) \cdot h_{ph} = 25.278 \qquad\qquad kip \cdot in$$

624

The torsion demand on the column caused by the transverse force Fut from the gusset plate through the gusset plate and W-section weld is

$$T_c := F_{uT} \cdot \left(\frac{11}{11+7}\right) \cdot \left(\frac{d}{2} + 5\right) = 47.818 \qquad \text{kip·in}$$

The sectional properties of the W-shape is obtained from AISC steel manual and design guide 9 Appendix A

Moment of inertia

$$I_x := 833 \qquad \text{in}^4$$

$$I_y := 270 \qquad \text{in}^4$$

Shear modulus
$$G_c := 11200 \qquad \text{ksi}$$

Torsional constant
$$J_c := 6.86 \qquad \text{in}^4$$

Statical moments

$$Q_w := 73.6 \qquad \text{in}^3$$

$$Q_f := 31.3 \qquad \text{in}^3$$

Torsional properties

$$S_{w1} := 98.2 \qquad \text{in}^4$$

$$W_{no} := 35.9 \qquad \text{in}^2$$

$$a := 59.6 \qquad \text{in}$$

The shear stress due to the horizontal force Hc and FuT in the web is

$$\tau_{w1} := H_c \cdot \frac{Q_w}{I_x \cdot t_w} = 8.965 \qquad \text{ksi}$$

$$\tau_{w2} := F_{uT} \cdot \left(\frac{11}{11+7}\right) \cdot \frac{Q_w}{I_y \cdot t_w} = 2.088 \qquad \text{ksi}$$

The shear stress due to the horizontal force Hc and FuT in the flange is

$$\tau_{f1} := H_c \cdot \frac{Q_f}{I_x \cdot t_f} = 2.33 \qquad \text{ksi}$$

$$\tau_{f2} := F_{uT} \cdot \left(\frac{11}{11+7}\right) \cdot \frac{Q_f}{I_y \cdot t_f} = 0.543 \qquad \text{ksi}$$

The normal stress due to the moment Mcx and Mcy in the flange is

$$\sigma_{bx} := \frac{M_{cx}}{I_x} = 0.414 \qquad \text{ksi}$$

$$\sigma_{by} := \frac{M_{cy}}{I_y} = 0.094 \qquad \text{ksi}$$

To calculate the stress in the W-section caused by the torsion, the approach from AISC Design Guide 9- Torsional analysis of structural steel members was used. The W-section under the torsion is assumed as a cantilever beam, and the followship functions are taken from Appendix B, Case 9 with α=0.5

The ratio of the height of W-section to the parameter a is

$$\frac{l_{ws}}{a} = 0.268$$

at the support (z/L=0)

$$\theta \cdot G_c \cdot \frac{J_c}{T_c \cdot l_{ws}} = 0 \qquad\qquad \theta = \blacksquare \cdot 0$$

$$\theta' \cdot G_c \cdot \frac{J_c}{T_c} = 0 \qquad\qquad \theta' = \blacksquare \cdot 0$$

$$\theta'' \cdot G_c \cdot \frac{J_c}{T_c} \cdot a = \blacksquare \cdot 0.05 \qquad\qquad \theta'' = \blacksquare \cdot 0.05 \cdot \frac{T_c}{G_c \cdot J_c}$$

$$\theta''' G_c \cdot \frac{J_c}{T_c} \cdot a^2 = -1 \qquad\qquad \theta''' = \frac{T_c \cdot (-1)}{G_c \cdot a^2 \cdot J_c}$$

The shear stress in the W-section due to pure torsion is

$$\tau_{pt} = \blacksquare \cdot \theta' \cdot G_c \cdot t$$

The shear stress in the W-section's flange due to warping

$$\tau_T := E \cdot \frac{S_{w1}}{t_f} \cdot \frac{T_c}{J_c \cdot G_c \cdot a^2} = 0.554 \qquad\qquad \text{ksi}$$

The normal stress in the W-section's flange due to warping at the flange

$$\sigma_T := E \cdot W_{no} \cdot 0.05 \cdot \frac{T_c}{G_c \cdot J_c} = 32.397 \qquad\qquad \text{ksi}$$

The stress summation from the shear force, moment and torsion applied on the W-section is calculated below:

in the flange:

normal stress

$$\sigma_f := \sigma_T + \sigma_{bx} + \sigma_{by} = 32.905 \qquad\qquad \text{ksi}$$

shear stress

$$\tau_f := \tau_T + \tau_{f1} + \tau_{f2} = 3.427 \qquad\qquad \text{ksi}$$

in the web: only shear stress

$$\tau_{w1} + \tau_{w2} = 11.053 \qquad\qquad \text{ksi}$$

The equivalent stress calcualted from the normal and shear stress in the flange was checked

$$f_{es} := \sqrt{\sigma_f^2 + 3 \cdot \tau_f^2} = 33.436 \ < \ f_{ycol} = 50 \qquad\qquad \text{ksi}$$

E.1.3. Weld design between steel W-section and the base plate

The steel W-section has its flanges and web fillet welded to the base plate. There are tension force, shear force, moment and torsion that should be resisted by the fillet weld between the W-section and the base plate.

The tension force demand due to moment Mcx at the flange weld is

$$F_{wcx} := \frac{M_{cx}}{d - t_f} = 29.212 \qquad \text{kips}$$

The shear force demand at each flange weld is

$$V_{w1} := \frac{F_{uT}}{2} = 3.447 \qquad \text{kips}$$

$$V_{w2} := \frac{H_c}{2} = 27.902 \qquad \text{kips}$$

The shear force in each flange weld due to torsion is

$$V_T := \frac{T_c}{d - t_f} = 4.052 \qquad \text{kips}$$

The fillet weld at the web is assumed to take the shear force Vw2 due to Hc

The thickness of the W-section web and the base plate is 0.55 in and 1.25 in, so the minimum fillet size is 1/4 in.

The length of the W-section's web is

$$d - 2 \cdot t_f = 10.9 \qquad \text{in}$$

Assume the length of the one-side fillet weld is 10 in. The required size of the fillet weld between the W-section web and the base plate is

$$a_{fw} := \frac{V_{w2}}{0.75 \cdot 10 \cdot 0.707 \cdot 0.6 \cdot 70 \cdot 2} = 0.063 \qquad \text{in}$$

Therefore, choose the fillet size to be 0.25 in

The fillet weld at the flange is going to take the shear force Vw1 due to Fut, the tension force Fwcx due to Mcx, the shear force VT due to Tc, the moment due to Mcy. The two-sided fillet weld length is 10 in. The thickness of the W-section flange and the base plate is 0.9 in and 1.5 in, so the minimum fillet size is 5/16 in.

The unit length load in the flange fillet weld is calculated below:

$$f_{vf} := \frac{V_{w1} + V_T}{2 \cdot 10} = 0.375 \qquad \text{kip/in}$$

$$f_{af} := \frac{F_{wcx}}{10} = 2.921 \qquad \text{kip/in}$$

$$f_{bf} := \frac{M_{cy}}{2 \cdot \frac{1}{12} \cdot 10^3} = 0.152 \qquad \text{kip/in}$$

The peak force of a unit length is

$$f_{peak} := \sqrt{\left(f_{af} + f_{bf}\right)^2 + f_{vf}^2} = 3.096 \qquad \text{kip/in}$$

therefore, the size of the weld is

$$\frac{f_{peak}}{0.75 \cdot 0.707 \cdot 0.6 \cdot 70 \cdot 2} = 0.07 \qquad \text{in}$$

The fillet weld between the W-section and the base plate has the size of 5/16 in as shown in Figure E.7.
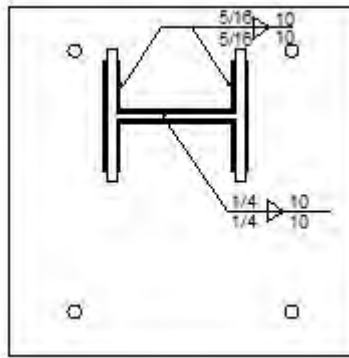
Figure E.7 Fillet welds between the W-section and the base plate

E.1.4. Base plate and anchor rod design

E.1.4.1 Base plate on the strong floor

The base plate and tie-down rod design is different for the reaction block on the strong floor and the shake table. The base plate material is A36, different from the gusset plate.

The yielding and tensile stress of the base plate

$$f_{yb} := 36 \qquad \text{ksi}$$

$$f_{ub} := 58 \qquad \text{ksi}$$

Base Plate No.1 (on the strong floor) Size:

$$A_p := 32 \qquad \text{in}$$
$$B_p := 32 \qquad \text{in}$$

The dimensions of Base Plate No.1 are shown in Figure E.8. The hole distance of 24 in on the strong floor is the same in both directions. The center of the W-section is 6 in from the center of the base plate. (considering the relative location of the holes in the strong floor and the shake table)

Distance of anchor hole on the strong floor:

$$D_h := 24 \qquad \text{in}$$

Tie-down hole center to plate edge distance in both direction are

$$C_{oa} := \frac{A_p - D_h}{2} = 4 \qquad \text{in}$$

$$C_{ob} := \frac{B_p - D_h}{2} = 4 \qquad \text{in}$$
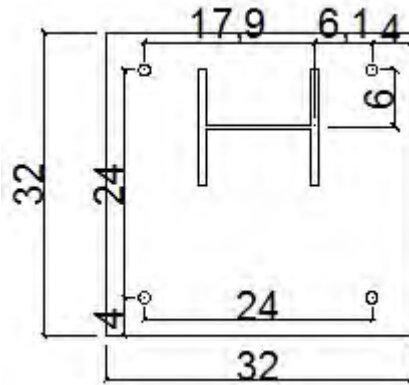
Figure E.8 Base Plate No.1 on the strong floor

The dywigad threadbars are used to connect the reaction block to the strong floor. The maximum jacking stress may not exceed 0.7 fpu.

The size of the threadedbar is

$$d_{dw} := 1 + \frac{3}{8} = 1.375 \qquad \text{in}$$

The nominal cross section area is

$$A_{dw} := 1.58 \qquad \text{in}^2$$

The minimum ultimate tensile strength is

$$f_{dw} := 150 \qquad \text{ksi}$$

The shear strength is

$$f_{dwv} := 0.6 \cdot f_{dw} = 90 \qquad \text{ksi}$$

The pretension force is

$$F_{dw} := 0.7 \cdot f_{dw} \cdot A_{dw} = 165.9 \qquad \text{kips}$$

The friction coefficient is

$$\mu := 0.2$$

The shear force the can be taken by the reaction block is

$$V_{dw} := 4 \cdot F_{dw} \cdot \mu = 132.72 \qquad \text{kips}$$

larger than $\qquad F_{uL} = 99.743 \qquad$ kips

The hole size on the base plate is

$$d_{hdw} := d_{dw} + \frac{3}{16} = 1.563 \qquad \text{in}$$

Assuming the rod's threads are excluded from shear plane

The torsion moment caused by the force from the BRB on the base plate is

$$T_{cb} := F_{uL} \cdot 6 + F_{uT} \cdot \frac{d}{2} = 642.235 \qquad \text{kip·in}$$

The distance from the center of the W-section to the rod is 17 in

The shear stress in the rod is

$$f_{v1} := \frac{F_{uL} + F_{uT}}{4 A_{dw}} + \frac{T_{cb}}{4 \cdot 17 \cdot A_{dw}} = 22.851 \quad < 90 \qquad \text{ksi}$$

The reduced tensile strength of the anchor rod is

$$F_{ntr1} := 1.3 \cdot f_{dw} - \frac{f_{dw} \cdot f_{v1}}{0.75 \cdot f_{dwv}} = 144.221 \qquad \text{ksi}$$

The tensile yield strength of each anchor rod is

$$0.75 \cdot F_{ntr1} \cdot A_{dw} = 170.902 \qquad \text{kips}$$

The shear strength of each anchor rod is

$$0.75 \cdot f_{dwv} \cdot A_{dw} = 106.65 \qquad \text{kips}$$

The maximum force that the hole in the strong floor can take to avoid the concrete fail in punching shear is 182 kips from the Table 5 in the SEESL lab manual, which is larger than the anchor rod's tensile yield strength

The base plate bearing strength at each hole (under tension force shown in Fig.E.9) is

$$R_{n1} := \min\left[0.75 \cdot 1.2 \cdot f_{ub} \cdot \left(C_{oa} - \frac{d_{hdw}}{2} \right) \cdot t_{gp}, 0.75 \cdot 2.4 d_{hdw} \cdot t_{gp} \cdot f_{ub} \right] = 203.906 \quad \text{kips}$$

For slip critical connection, the minimum pretension force of the anchor rod is used

$$0.7 \cdot \left(f_{dw} \cdot A_{dw} \right) = 165.9 \qquad \text{kips}$$

The nominal slip resistance of each anchor rod is

$$R_{ab} := 1 \cdot 0.35 \cdot 1.13 \cdot 1 \cdot 165.9 \cdot 1 = 65.613 \qquad \text{kips}$$

Parameters in the this equation is explained as: mean slip coefficient= 0.35, multiplier for the ratio of the beam installled bolt pretension to the sepcified minimum bolt pretension =1.13, standard size holes =1, number of slip plane =1

After considering the anchor rod steel shear resistance, the base plate bearing strength, the nominal slip resitance ,the shear resistance of the anchor rods group is

$$4 \min\left(0.75 \cdot f_{dw} \cdot A_{dw}, R_{n1}, R_{ab} \right) = 262.454 \qquad \text{kips}$$

larger than $\qquad F_{uL} = 99.743 \qquad$ kips

The distance between the hole and the center of the plate is

$$d_T := 12 \cdot \sqrt{2} = 16.971 \qquad \text{in}$$

The bearing demand of the base plate under torsion is

$$\frac{T_{cb}}{4 \cdot d_T} = 9.461 \qquad \text{kips}$$

The base plate bearing strength at each hole (under torsion shown in Fig. E.9) is

$$R_{n2} := \min\left[0.75 \cdot 1.2 \cdot f_{up} \cdot \left(C_{oa} - \frac{d_{hdw}}{2} \right) \cdot t_{gp} \cdot \sqrt{2}, 0.75 \cdot 2.4 d_{hdw} \cdot t_{gp} \cdot f_{up} \right] = 228.516 \text{ kips}$$

larger than the bearing demand, ok
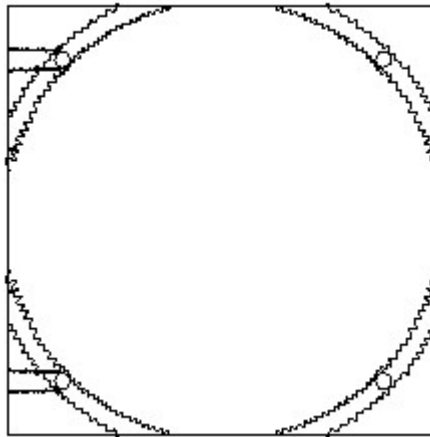
Figure E.9 Possible block shear failure of base plate under tension force and torsion

The design of the base plate is to withstand the horizontal force applied by the BRB. The horizontal force Hc results in the moment in the W-section, the anchor rod connects the base plate to the strong floor so that the base do not tip or fail in concrete bearing. The compressive reaction center line is assumed to correspond to the center of the W-section flange for the moment Mcx, so the distance to the center of the anchor rod is 17.9 in in Figure E.10. The compressive reaction center line is assumed to correspond to the web of the W-section flange for the moment Mcy, so the distance to the center of the anchor rod is 6 in in Figure E.11 (case 1 when the rod close to the W-section is in tension).

The maximum tension force for the anchor rod (closest to the center of the W-section) due to the overturning moment is

$$F_{rd1} := \left(\frac{M_{cx}}{17.9} + \frac{M_{cy}}{6} \right) \cdot 0.5 = 11.735 \qquad \text{kips}$$

smaller than the tensile strength of the anchor rod, ok

The shear force that can be taken by the reaction block (after considring the pretension force) is

$$V_{dwr} := \left[2 \cdot F_{dw} + 2\left(F_{dw} - F_{rd1}\right) \right] \cdot \mu = 128.026 \qquad \text{kips}$$

still larger than FuL
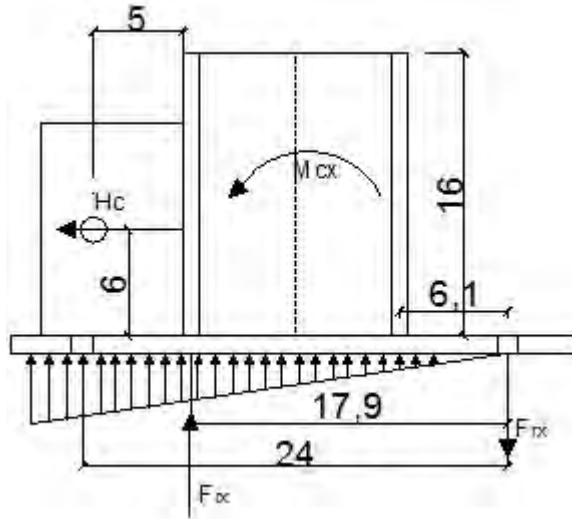
Figure E.10 Base Plate No.1 with moment Mcx and reaction force Frx
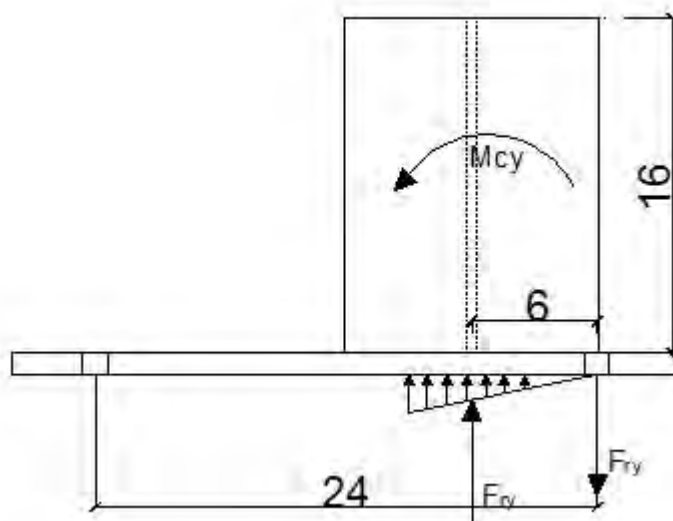
Figure E.11 Base Plate No.1 with moment Mcy and reaction force Fry (case 1)

For another case, when the further rod is in tension under the moment Mcy (Figure E.12), the tension force in the anchor rod is calculated to be

$$F_{rd2} := \left(\frac{M_{cx}}{17.9} + \frac{M_{cy}}{24 - 6} \right) \cdot 0.5 = 10.331 \qquad \text{kips}$$

smaller than Frd1, ok
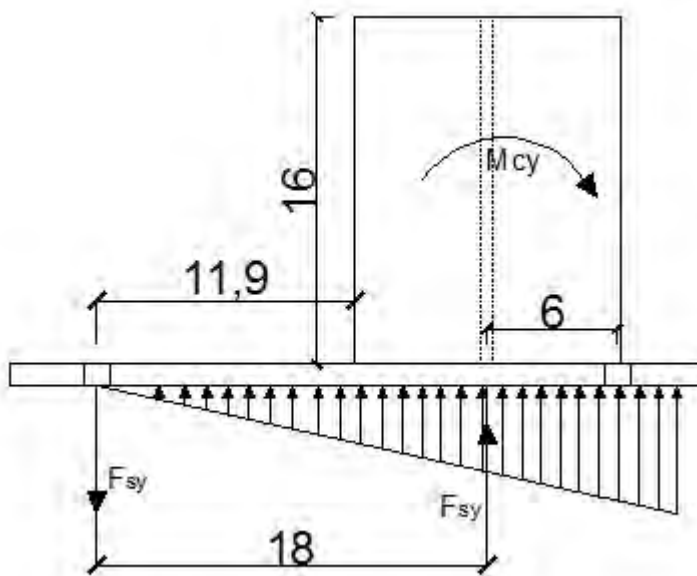
Figure E.12 Base Plate No.1 with moment Mcy and reaction force Fry (case 2)

Check for base plate yielding limit at the tension interface

The thickness of the base plate is

$$t_{bp} := 1.25 \qquad \text{in}$$

The distance between the center of the anchor rod to the center of the column flange is 6.1 in as shown in Figure E.10. The distance between the center of the anchor rod to the center of the column flange is 11.9 in as shown in Figure E.12 (case 2 governs).

For a unit width of base plate, the required bending strength of the base plate can be determined as:

$$M_{pl} := \max\left(F_{rd1} \cdot \frac{6.1}{B_p}, F_{rd2} \cdot \frac{11.9}{B_p} \right) = 3.842 \qquad \text{kips}$$

smaller than the base plate unit flexrural strength

$$0.9 f_{yp} \cdot \frac{t_{bp}^2}{4} = 17.578 \qquad \text{kips} \quad \text{ok}$$

The concrete bearing stress is checked below:

The stress between the concrete and the base plate (case 1) is

$$\sigma_{s1} := \frac{M_{cx} \cdot 2}{17.9 \cdot 32 \cdot (17.9 \cdot 1.5)} + M_{cy} \cdot \frac{2}{6 \cdot 32 \cdot (6 \cdot 1.5)} = 0.074 \qquad \text{ksi}$$

The stress between the concrete and the base plate (case 2) is

$$\sigma_{s2} := \frac{M_{cx} \cdot 2}{17.9 \cdot 32 \cdot (17.9 \cdot 1.5)} + M_{cy} \cdot \frac{2}{18 \cdot 32 \cdot (18 \cdot 1.5)} = 0.048 \qquad \text{ksi}$$

both smaller than the concrete strength of 4 ksi

E.1.4.2 Base plate on the shake table

The design of the base plate No.2 on the shake table follows the same design process as the base plate No.1. The dimensions of base plate 2 is shown in Figure E.13.

Base Plate No.2 (on the shake table) Size:

$A_s := 32$ in

$B_s := 32$ in

The hole distance is different in the two directions is

$D_{s1} := 20$ in

$D_{s2} := 24$ in

The holes in the base plate on the shake table has slotted holes to make sure that the W-section 's strong axis lines up with the centerline of the base plate in case the other side of the W-section is needed to be welded to the gusset plate for tests to save the cost
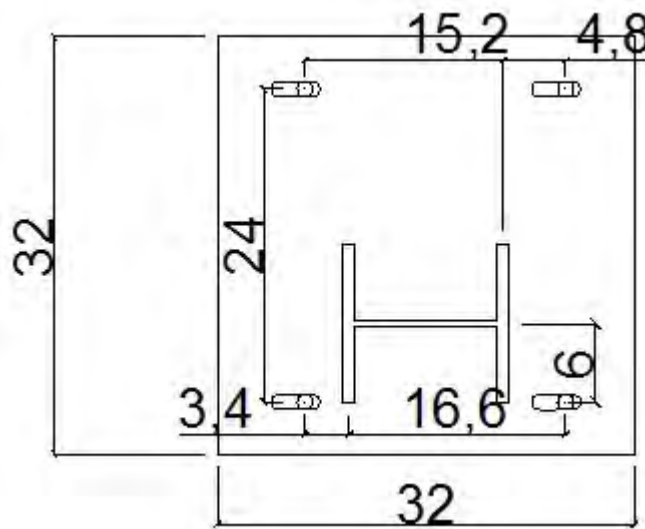
Figure E.13 Base Plate No.2 on the shake table

The threadbars are used to connect the reaction block to the shake table has the same strength as the dywidag bar. The maximum jacking stress may not exceed 0.7 fpu.

The size of the threadedbar is

$d_{tb} := 1.125$ in

The nominal cross section area is

$A_{tb} := 1.25$ in^2

The pretension force is

$F_{tb} := 0.8 \cdot f_{dw} \cdot A_{tb} = 150$ kips

Though the interface between the shake table and the base plate is steel-to-steel. The same friction coefficient of 0.2 is still used.

The shear force the can be taken by the reaction block is

$$V_{tb} := 4 \cdot F_{tb} \cdot \mu = 120 \qquad\qquad \text{kips}$$

larger than 100 kips required

The hole width on the base plate is

$$d_{htb} := d_{tb} + \frac{3}{16} = 1.313 \qquad\qquad \text{in}$$

Assuming the anchor rod's threads are excluded from shear plane

The distance from the center of the base plate to the rod is 15.18 in and 16.07 in. The four anchors rods are assumed to take the same torsion moment. The one closer to the center would have larger shear force.

The shear stress in the threaded rod is

$$f_{v2} := \frac{F_{uL} + F_{uT}}{4 A_{tb}} + \frac{T_{cb}}{4 \cdot 15.18 \cdot A_{tb}} = 29.789 \qquad\qquad \text{ksi}$$

The reduced tensile strength of the threaded rod is

$$F_{ntr2} := 1.3 \cdot f_{dw} - \frac{F_{dw} \cdot f_{v2}}{0.75 \cdot f_{dwv}} = 121.785 \qquad\qquad \text{ksi}$$

The tensile strength of each threaded rod is

$$0.75 \cdot F_{ntr2} \cdot A_{tb} = 114.174 \qquad\qquad \text{kips}$$

The shear strength of each threaded rod is

$$0.75 \cdot f_{dwv} \cdot A_{tb} = 84.375 \qquad\qquad \text{kips}$$

The tensile bearing strength of the base plate is ignored since the hole is a slotted hole.

The distance between the hole and the center of the plate is

$$d_{T2} := 15.18 \qquad\qquad \text{in}$$

The larger bearing demand of the base plate under torsion is

$$\frac{T_c}{4 \cdot d_{T2}} = 0.788 \qquad\qquad \text{kips}$$

The base plate bearing strength at each hole (under torsion shown in Fig.E.9) is

$$R_{ns2} := \min\left[0.75 \cdot 1.2 \cdot f_{ub} \cdot \left(\frac{6 \cdot 15.18}{12} - \frac{d_{htb}}{2} \right) \cdot t_{gp}, \ 0.75 \cdot 2.4 d_{htb} \cdot t_{gp} \cdot f_{ub} \right] = 171.281$$

larger than the bearing demand , ok

The horizontal force Hc results in the moment in the W-section, the anchor rod connects the base plate to the strong floor so that the base do not tip or fail in concrete bearing.

The compressive reaction center line is assumed to correspond to the center of the W-section flange for the moment Mcx.The distance to the center of the anchor rod is 15.2 in in Figure E.14 (The other side has the center of rod to the flange of 16.6 in, does not control). The compressive reaction center line is assumed to correspond to the web of the W-section flange for the moment Mcy, so the distance to the center of the anchor rod is 6 in in Figure E.15 (case 1, the tensile anchor is closer to the reaction block).

The maximum tension force in the threaded rod is

$$F_{rs1} := \left(\frac{M_{cx}}{15.2} + \frac{M_{cy}}{6} \right) \cdot 0.5 = 13.445 \quad < 77.5 \qquad \qquad \text{kips}$$

smaller than the tensile strength of the anchor rod, ok
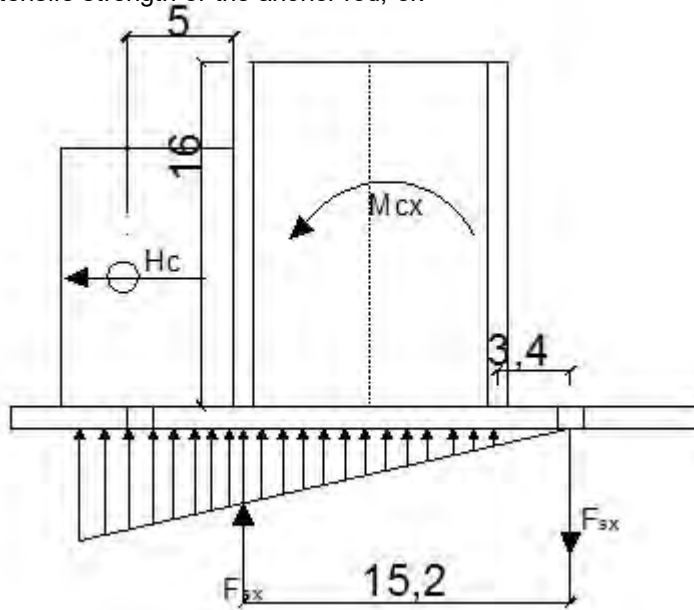
Figure E.14 Base Plate No.2 with moment Mcx and reaction force Fsx

For another case, then the further rod is in tension under the moment Mcy (Figure E.16), the tension force in the anchor rod is calculated to be

$$F_{rs2} := \left(\frac{M_{cx}}{15.2} + \frac{M_{cy}}{24 - 6} \right) \cdot 0.5 = 12.041 \qquad \qquad \text{kips}$$

smaller than Frs1, ok
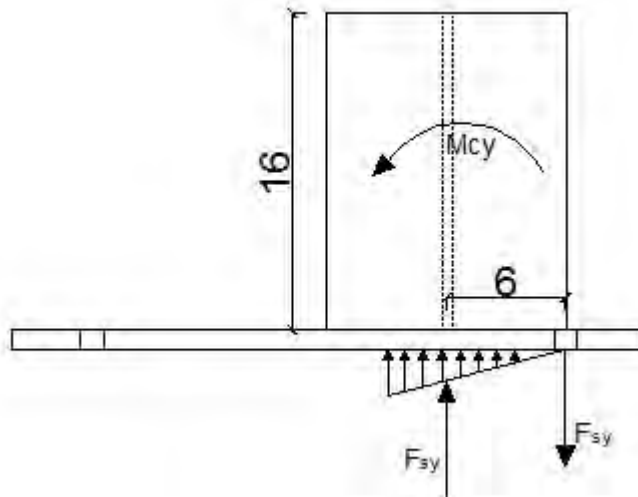
Figure E.15 Base Plate No.2 with moment Mcy and reaction force Fsy (case 1)
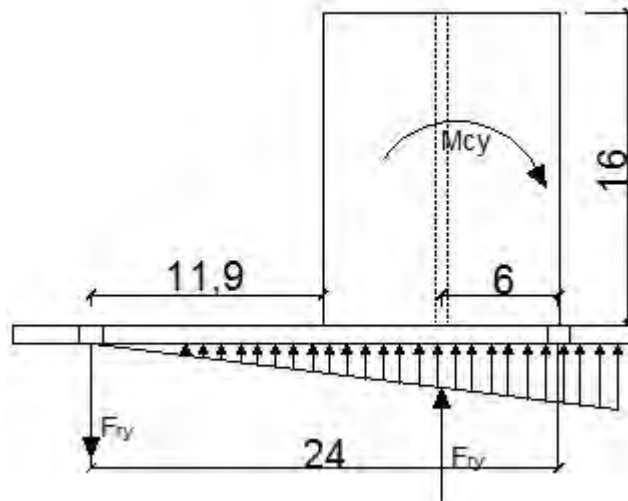
Figure E.16 Base Plate No.2 with moment Mcy and reaction force Fry (case 2)

Check for base plate yielding limit at the tension interface

The thickness of the base plate is the same as No.1 base plate

The distance between the center of the anchor rod to the center of the column flange is 4.35 in as shown in Figure E.14. The distance between the center of the anchor rod to the center of the column flange is 11.9 in as shown in Figure E.16 (case 2 govens).

For a unit width of base plate, the required bending strength of the base plate can be determined as:

$$M_{p2} := \max\left(F_{rs1} \cdot \frac{4.35}{B_p}, F_{rs2} \cdot \frac{11.9}{B_p}\right) = 4.478 \qquad \text{kips}$$

smaller than the base plate unit flexrural strength

$$0.9f_{yp} \cdot \frac{t_{bp}^2}{4} = 17.578 \qquad \text{kips}$$

The concrete bearing stress is checked below:

The stress between the concrete and the base plate (case 1 controls) is

$$\sigma_{d1} := \frac{M_{cx} \cdot 2}{15.2 \cdot 32 \cdot (15.2 \cdot 1.5)} + M_{cy} \cdot \frac{2}{6 \cdot 32 \cdot (6 \cdot 1.5)} = 0.091 \qquad \text{ksi}$$

The configuration of the BRB test setup is shown in Figure E.17 with the BRB test specimen.

(a)

(b)
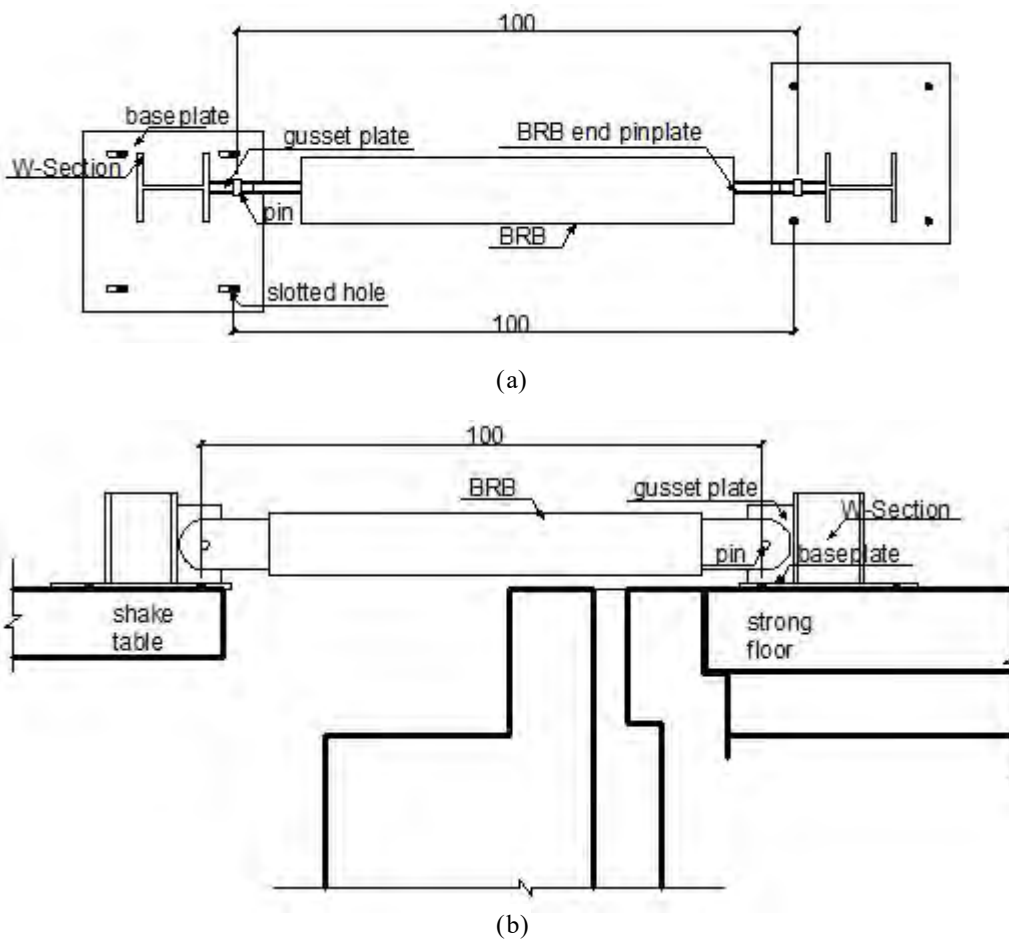
Figure E.17 BRB test setup

E.2 Test BRB drawing details

ALL STRAND WELDS TO BE MADE IN FLAT POSITION
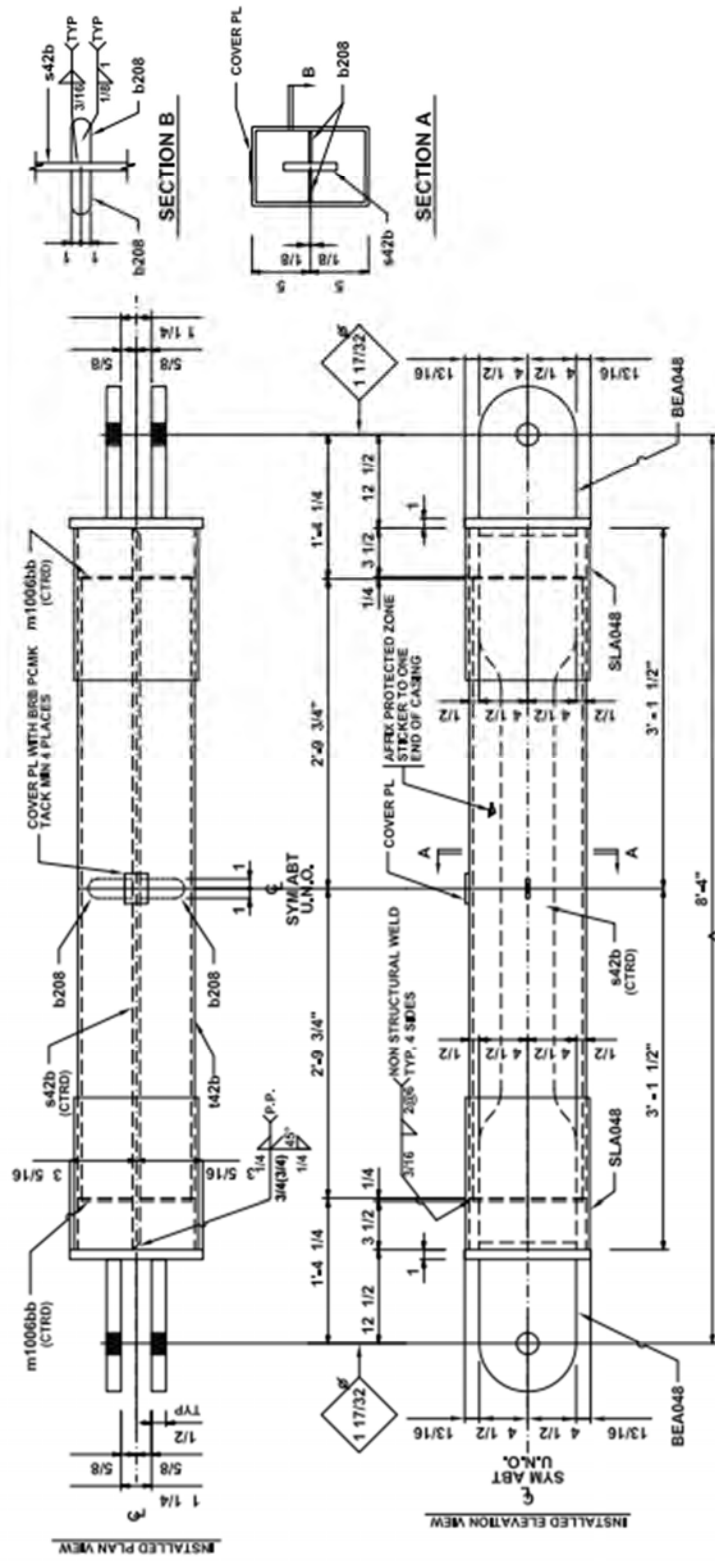
Use pin: Bott. Spacer: f966a

BRACE LOCATION(S)
at, et,

SECTION B

SECTION A

COVER PL

INSTALLED PLAN VIEW

INSTALLED ELEVATION VIEW

SYM ABT. U.N.O.

NON STRUCTURAL WELD TYP, 4 SIDES

AFFIX PROTECTED ZONE STICKER TO ONE END OF CASING

COVER PL WITH BRB PCMK TACK MIN 4 PLACES

8'-4"

4 BRACES PC42b

BILL OF MATERIAL

NO.	PCS.	DESCRIPTION	LENGTH FT.	LENGTH IN.	MARK	REMARKS
4	4	Brace	8	4	PC42b	0
	4	HSS10x6x1/4	5	7 1/2	t42b	A500-Gr B
4	4	FB 3/4 x 9	6	3	s42b	A36-LY
8	8	PL 1/4 x 2	0	2 1/4	b208	A36
8	8	PL 1/4 x 5 5/8	0	9 5/8	m1006bb	A36
8	8	End Pl Assembly			BEA048	See sheet SA048
8	8	Collar Pl Assembly			SLA048	See sheet SA048
-	-	-			-	-

REF:
WORK THIS DWG
W/ DWG NO.: s42b

NO.	DESCRIPTION OF REVISION	DATE	CHECKED BY
	Revised Quantities		
1		1/30/2015	SP
A	Approval	1/28/15	SP

SHOP PLACE PIECE MARK ON LEFT HAND END OF MEMBER AS DETAILED
ERECT MEMBER WITH PIECE MARK TO END SHOWN ON PLACING PLAN

MATERIAL: A36 & AS NOTED   APPROX CONCR.: 0.05 YRDS3 EA
SURFACE PREP.: SP3   APPROX BRACE WT.: 506 LBS EA
SHOP PAINT: STD, SHOP PRIMER   SPACER: f966a

SUBJECT: PC42b – UB-BRB-1
PROJECT: U of Buffalo Test Brace
LOCATION: Location
CUSTOMER: Customer
SS BRB NO.: -
ENG. DWG: ERECTION DWG: DATE: 1/28/2015
DRAWN BY: BP   CHECKED BY: SP   SEQ.:

StarSeismic
WWW.STARSEISMIC.NET
PHONE: 1-435-940-9222
FAX: 1-435-655-0073
6300 N. SAGEWOOD DR
SUITE H #511
PARK CITY UT 84098

JOB NO.: NA   DWG NO.: PC42b

SHOP NOTE: DEBURR ALL CUT EDGES

RADIAL CUT AND
LENGTHS ARE
SAME AS OTHER
SIDE U. N. O.

6-3

1.33

9.255

6.544

6.544

6.544

5

6

3
SYM ABT

1/2
12

1/2
12

1/2
12

Spacer mark: 1966s
Lyz=46.49 In
Total Brace A sc= 1 In^2

BILL OF MATERIAL

4-STRAND PLATES s42b

NO.			LENGTH		MARK	REMARKS
PCS.	DESCRIPTION		FT.	IN.		
4	STRAND PLATES					A36-LY
4	FB 3/4 x 9		6	3	s42b	Heat#PL14101677
						Fysc=46ksi

REF: WORK THIS DWG W/ DWG NO.: PC42b	
1	REVISED Quantities / Paddle Length / Fixed BOM call-out
A	Approval
NO.	DESCRIPTION OF REVISION

1/20/2015 SP	
1/28/2015 SP	
DATE CHECKED BY	

1/2" x 1/2" SNIP

BENT PLATE
(FOR COLLAR)

WELD AFTER STRAND PLATE WELDS

4 SIDES, TYP., SNIP TO BE TOWARDS END PL

3/16

c1006a1

1/4
1/4
6 1/8

1/4 TYP

1/4
1/4
10 1/8

1'-6
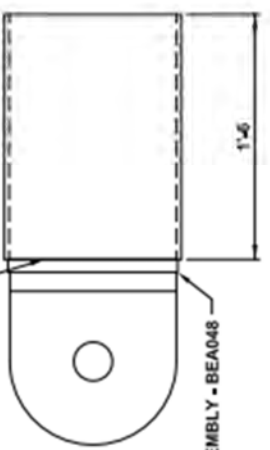
END PLATE ASSEMBLY - BEA048

8 COLLAR PL. ASSEMBLY SLA048

CHECK FOR HOLE ALIGNMENT AFTER WELDING

5/16
3/8(1/4)
0
45°
TYP

1 1/4 (+.030) (-.030)

p048
e1006g

2 11/16
2 11/16

1 17/32"

5 5/16
5 5/16

1
11 1/2
4 1/2

4 1/2
4 1/2

8 END PL. ASSEMBLY BEA048

USE pin: Bolt
Use with braces: PC42b
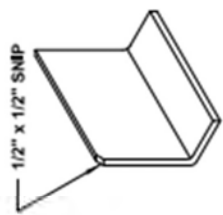
BILL OF MATERIAL

NO. PCS.	DESCRIPTION	LENGTH FT.	IN.	MARK	REMARKS
8	END PL. ASSEMBLY			BEA048	
16	PL 1/2 x 9	1	4	p048	A36 Fyp>38ksi
8	PL 1 x 6 5/8	0	10 5/8	e1006g	A572-Gr 50
8	COLLAR PL. ASSEMBLY			SLA048	
16	PL 1/4 x 18	1	4 1/4	c1006a1	BENT

			REVISED Quantities	
		1/20/15 SP		
		1/28/15 SP	Approval	
NO.	DATE CHECKED BY		DESCRIPTION OF REVISION	

SHOP PLACE PIECE MARK ON LEFT HAND END OF MEMBER AS DETAILED
ERECT MEMBER WITH PIECE MARK TO END SHOWN ON PLACING PLAN
MATERIAL: A36 & AS NOTED   HOLES -   UNLESS NOTED
SURFACE PREP.:   BOLTS -   UNLESS NOTED
SHOP PAINT:

BILL OF MATERIAL

NO. PCS.	DESCRIPTION	LENGTH FT.	IN.	MARK	REMARKS
4	Brace	8	4	PC42c	0
4	HSS10x6x1/4	6	8 1/2	t42c	A500-Gr B
4	FB 3/4 x 5	7	4	s42c	A36-LY
8	PL 1/4 x 2	0	2 1/4	b208	A36
8	m1006bb	0	9 5/8	m1006bb	A36
8	End Pl Assembly	-	-	BEA049	See sheet SA049
8	Collar Pl Assembly	-	-	SLA049	See sheet SA049

SECTION A
SECTION B

COVER PL

INSTALLED PLAN VIEW
INSTALLED ELEVATION VIEW

ALL STRAND WELDS TO BE MADE IN FLAT POSITION
Use pin: Bott. Spacer: f966a
BRACE LOCATION(S)
at, et

COVER PL WITH BRB PCMK (CTRD) TACK MIN 4 PLACES
AFFIX PROTECTED ZONE STICKER TO ONE END OF CASING
NON STRUCTURAL WELD TYP. 4 SIDES
SYM ABT U.N.O.

4 BRACES PC42c

REF: WORK THIS DWG W/ DWG NO.: s42c

NO.	DESCRIPTION OF REVISION	DATE	CHECKED BY
	REVISED Quantities / Strand Width	1/20/15	SP
	Approval	1/28/15	SP

SHOP PLACE PIECE MARK ON LEFT HAND END OF MEMBER AS DETAILED
ERECT MEMBER WITH PIECE MARK TO END SHOWN ON PLACING PLAN
MATERIAL: A36 & AS NOTED   APPROX CONCR.: 0.05 YRDS3 EA
SURFACE PREP.: SP3   APPROX BRACE WT.: 506 LBS EA
SHOP PAINT: STD. SHOP PRIMER   SPACER: f966a

SUBJECT: PC42c – UB-BRB-2
PROJECT: U of Buffalo Test Brace
LOCATION: Location
CUSTOMER: Customer
SS BRB NO.: -
ENG. DWG:
DRAWN BY: BP
ERECTION DWG:
CHECKED BY: SP
DATE: 1/28/2015
SEQ.:

StarSeismic
WWW.STARSEISMIC.NET
PHONE: 1-435-940-9222
FAX: 1-435-655-0073
6300 N. SAGEWOOD DR
SUITE H #511
PARK CITY UT 84098

JOB NO.: NA   DWG NO.: PC42c

Appendix F Concrete filled tube tests specimen and setup design

F.1 Design of test set-up and the specimen of 16" Concrete-filled CHS

F.1.1 Reaction Block

The location of the tab plates is at the height of 10.125" from the bottom of the reaction block. The distance of the bolt hole locations from the edge of the reaction block is shown in Fig. E.1. The design maximum pulling force is

$$F_p := 100 \qquad\qquad \text{kips}$$

Assuming the deformation of the three bolts are proportional as shown in the dashed line in Fig. F.2, the force distribution would also be proportional. The required largest resulting tensile force in the bolt that is farthest from the edge of the reaction block is P. The moment equilibrium for the point O in Fig. F.1 is

$$P \cdot 15 + P \cdot \frac{2 \cdot 10}{3} + P \cdot \frac{1 \cdot 5}{3} = F_p \cdot 10.125$$

$$P := F_p \cdot \frac{10.125}{23.33} = 43.399 \qquad\qquad \text{kips}$$

The diameter of the threaded rods is

$$D_t := 1.125 \qquad\qquad\qquad \text{in}$$

The threaded bolts each was torqued to 600 ft-lb, and the pretension force is calcualted per the torque applied on the bolt (in lubricated condition):

$$P_{pre} := 600 \cdot \frac{12}{0.15 \cdot D_t \cdot 1000} = 42.667 \qquad \text{kips}$$

The yield strength of the bolt is 102.7 kips, which leaves out enough strength (56.5 kips) for the bolt to take the extra tensile load from the overturning of the reaction block.

With six threaded bolts with standard size bolt holes, considering the friction coefficient of 0.35 between the reaction block and the floor beam, the slip resistance strength of the bolted connection is

$$R_s := 1.13 \cdot 0.35 \cdot P_{pre} \cdot 6 = 101.248 \quad 100 \qquad \text{kips}$$

F.1.2 Tab Plates

The material for the two tab plate is A572 Gr50.

The yielding stress of the tab plate is

$$F_{yt} := 50 \qquad\qquad\qquad \text{ksi}$$

The ultimate stress of the tab plate is

$F_{ut} := 65$ ksi
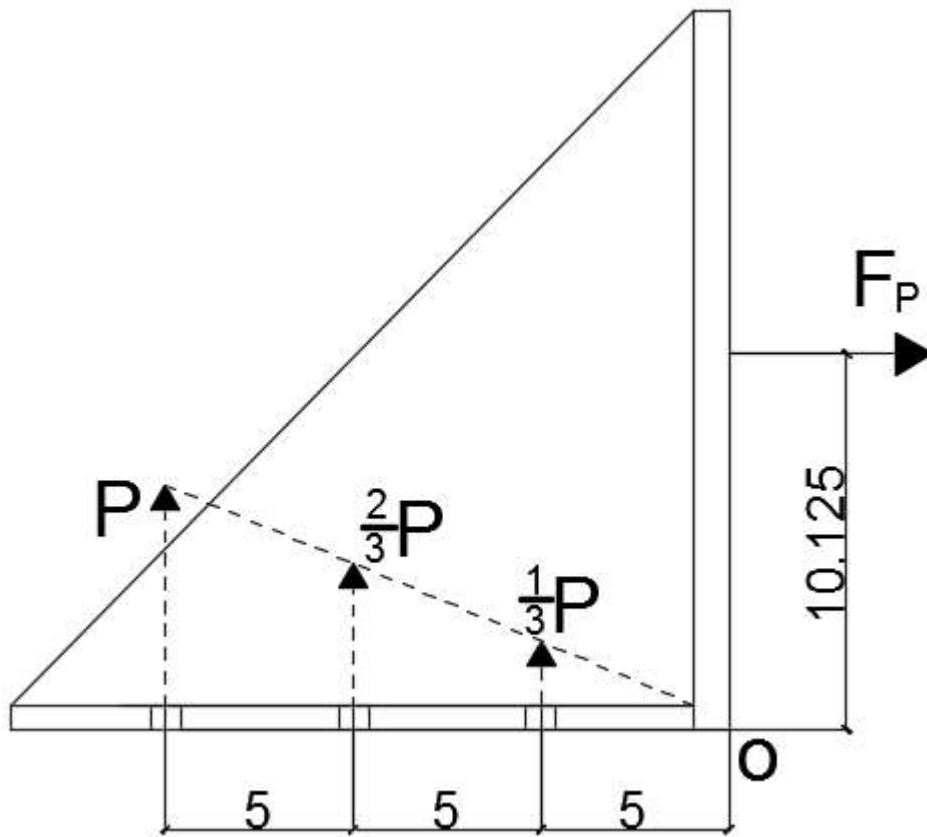
Fig. F.1 Threaded bolts connection between the reaction block and the floor beam

The width of the tab plate is

$L_{pt} := 3$ in

The thickness of the tab plate is

$t_{pt} := 0.375$ in

The yield strength of the tab plate is

$P_{yt} := 0.9 F_{yt} \cdot L_{pt} \cdot t_{pt} = 50.625$ kips

The diameter of the bolt is

$d := 0.75$ in

The diameter of the hole in the tab plate is

$d_h := d + \dfrac{1}{16} = 0.813$ in

The effective net area

$A_{et} := \left(4 - d_h\right) \cdot t_{pt} = 1.195$ in^2
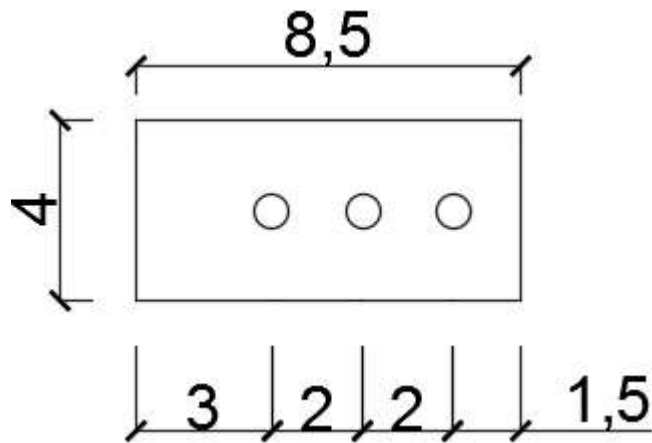
Fig. F.2 Tab plate dimension

The nominal strength of the tab plate in fracture is

$P_{nt} := 0.75 \cdot A_{et} \cdot F_{ut} = 58.271$ kips

The distance from the center of the first bolt to the tab plate's end is

$L_{e1} := 1.5$ in

$L_{c1} := L_{e1} - \dfrac{d_h}{2} = 1.094$ in

The bearing strength of the tab plate at the first bolt is

$R_{nt1} := 1.2 F_{ut} \cdot L_{c1} \cdot t_{pt} = 31.992$ kips
The upper limit is

$2.4 d \cdot t_{pt} \cdot F_{ut} = 43.875 \ > 32$ kips

The distance between the center of the 1st and 2nd, and the 2nd and 3rd bolt is

$L_{e2} := 2$ in
$L_{c2} := L_{e2} - d_h = 1.188$ in
The bearing strength of the tab plate at the second and third bolt is

$R_{nt2} := 1.2 F_{ut} \cdot L_{c2} \cdot t_{pt} = 34.734$ kips
The upper limit is

$2.4 d \cdot t_{pt} \cdot F_{ut} = 43.875 \ > 34.73$ kips

Assuming the bolts sharing load equally, therefore, the nominal bearing strength of the connection is

$R_{nt} := 6 R_{nt1} = 191.953$ kips

The bearing strength of the tab plates is

$R_{bt} := 0.75 R_{nt} = 143.965$ kips

F.1.3 Branch Plate

The material for the branch plate is A572 Gr60.

The yielding stress of the branch plate is

$$F_{yp} := 60 \qquad \text{ksi}$$

The ultimate stress of the branch plate is

$$F_u := 75 \qquad \text{ksi}$$

The width of the branch plate is

$$L_p := 5 \qquad \text{in}$$

The thickness of the branch plate is

$$t_p := 0.25 \qquad \text{in}$$

The yield strength of the plate is

$$P_y := 0.9 F_{yp} \cdot L_p \cdot t_p = 67.5 \qquad \text{kips}$$

The effective net area

$$A_e := (5 - d_h) \cdot t_p = 1.047 \qquad \text{in}^2$$

The nominal strength of the branch plate in fracture is

$$P_{nb} := 0.75 \cdot A_e \cdot F_u = 58.887 \qquad \text{kips}$$
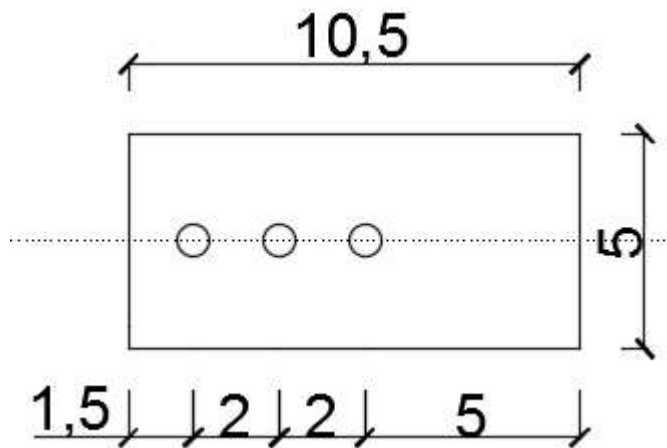
Fig. F.3 Branch plate welded to the 16" tube (weld on the right)

The distance from the center of the first bolt to the branch plate's end is

$$L_{eb1} := 1.5 \qquad \text{in}$$

$$L_{cb1} := L_{eb1} - \frac{d_h}{2} = 1.094 \qquad \text{in}$$

The bearing strength of the branch plate at the first bolt is

$$R_{n1} := 1.2 F_u \cdot L_{cb1} \cdot t_p = 24.609 \qquad \text{kips}$$

The upper limit is

$$2.4d \cdot t_p \cdot F_u = 33.75 \quad > 36.91 \qquad \text{kips}$$

The distance between the center of the 1st and 2nd, and the 2nd and 3rd bolt is

$$L_{eb2} := 2 \qquad\qquad\qquad \text{in}$$

$$L_{cb2} := L_{eb2} - d_h = 1.188 \qquad \text{in}$$

The bearing strength of the branch plate at the second and third bolt is

$$R_{n2} := 1.2F_u \cdot L_{cb2} \cdot t_p = 26.719 \qquad \text{kips}$$

The upper limit is

$$2.4 \cdot d \cdot t_p \cdot F_u = 33.75 \quad > 40.08 \qquad \text{kips}$$

Assuming the bolts sharing load equally, therefore, the nominal bearing strength of the connection is

$$R_n := 3R_{n1} = 73.828 \qquad\qquad \text{kips}$$

The bearing strength of the bolt connection is

$$R_b := 0.75R_n = 55.371 \qquad\qquad \text{kips}$$

The branch plate and the tab plates are connected with slip-resistant bolted connections, which has the bolts torqued to provide pretension force.

The torque in each bolts is 300 ft-lb, and the tensile strength of the bolt is 37.4 kips obtained from the AISC steel construction manual (2010). The slip resistance strength of the bolted connection is

$$R_{sb} := 1.13 \cdot 0.35 \cdot 37.4 \cdot 2 \cdot 3 = 88.75 \qquad \text{kips}$$

Therefore, the bolted connection reaching the force of 89 kips before the bolts slip; after that, the bolted connection between the tab plates and the branch plate is controlled by the failure of the branch plate, which is the net section failure of the plate

$$\min\left(P_y, P_{nb}, R_{sb}\right) = 58.887 \qquad\qquad \text{kips}$$

F.1.4 Fillet Welds

The double-sided fillet welds are designed between the CHS and the branch plates. The size of the fillet weld is

$$w := 0.375 \qquad\qquad\qquad \text{in}$$

The length of the weld is

$$l_w := 3 \qquad\qquad\qquad\qquad \text{in}$$

The weld use E80xx eletrode

$$F_{exx} := 80 \qquad\qquad\qquad\qquad \text{ksi}$$

$$F_w := 0.6 \cdot F_{exx} = 48 \qquad\qquad \text{ksi}$$

The strength of the welds between the branch plate and CHS is

$$R_w := 0.75 \cdot 0.707 \cdot w \cdot l_w \cdot F_w \cdot 2 = 57.267 \quad \text{kips}$$

The double sided fillet weld is designed between the tab plates and the reaction block (or the steel block at the actuator head). The size of the fillet weld is

$$w_t := 0.375 \qquad \text{in}$$

The length of the weld is

$$l_{wt} := 4 \qquad \text{in}$$

The weld use E70xx eletrode

$$F_{exxt} := 70 \qquad \text{ksi}$$

$$F_{wt} := 0.6 \cdot F_{exxt} = 42 \qquad \text{ksi}$$

Note that due to the small distance between the two tab plates, after welding one tab plate, it will be hard to weld the other one with two sided fillet weld. Therefore, the other tab plate only have one side fillet weld. And the strength of the welds between the two tab plates and reaction block (or the steel block at the actuator head) is

$$R_{wt} := 0.75 \cdot 0.707 \cdot w \cdot l_w \cdot F_w \cdot 3 = 85.9 \qquad \text{kips}$$

F.1.5 CHS strength from Ring model

The maximum unit length strength from the Abaqus Ring model assumed A500GrB steel (yield strength of 42 ksi, ultimate strength of 58 ksi) is

$$P_r := 4.03 \qquad \text{kips}$$

When the length of the CHS is chosen as

$$L_{chs} := 3 \qquad \text{in}$$

The predicted strength from the Ring model is

$$P_p := P_r \cdot L_{chs} = 12.09 \qquad \text{kips}$$

When the specimen with branch plate and fillet weld was modeled in Abaqus, the resulted strength when the ultimate strain close to the weld was developed in the CHS, which is 28.7 kips. Note that this strength is obtained from the model with steel material of engineering stress and strain from A500GrB, not the true stress and strain from the coupon test. After the data from the coupon test from the real material is available, new analyses of the specimen model in Abaqus was performed, and the resulting strength is 31.4 kips. For the bolt, weld and branch plate design of the specimen, it is still below those strength.

F.1.6 Modification of strengthening the branch plate

The yielding stress of the strengthening plate is

$$F_{yp1} := 36 \qquad \text{ksi}$$

The ultimate stress of the strengthening plate is

$$F_{u1} := 50 \qquad \text{ksi}$$

The thickness of the strengthening plate is

$$t_s := 0.125 \qquad \text{in}$$

The yield strength of the strengthening plate is

$$P_{ps} := 0.9 F_{yp1} \cdot 8 \cdot t_s = 32.4 \qquad \text{kips}$$

The fracture strengh of the strengthening plate is

$$P_{us} := 0.75 \cdot F_{u1} \cdot (8 - d_h) \cdot t_s = 33.691 \qquad \text{kips}$$
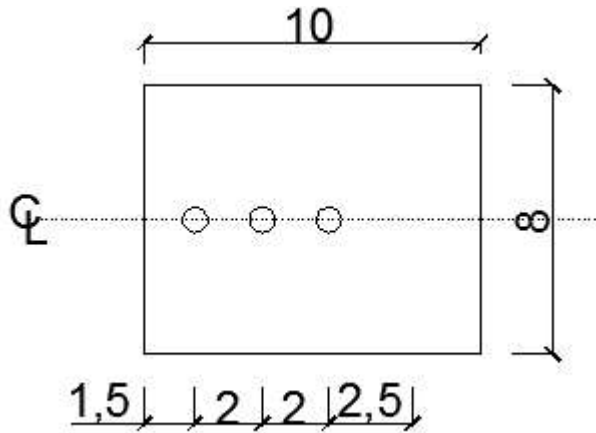
Fig.F.4 Strengthening plate

The size of the fillet weld on both sides of the branch plate is

$$L_{sw} := 10 \qquad \text{in}$$

The strength of the two welds with the width of 1/8" is

$$P_{ws} := 0.75 \cdot \left(0.707 \cdot \frac{1}{8} \cdot L_{sw} \right) \cdot 0.6 \cdot 70 \cdot 2 = 55.676 \qquad \text{kips}$$

which is larger than the yield and fracture strength of the strengthening plate

The strength of the base metal strength check

For the strengthening plate

$$2(0.6 \cdot 36 \cdot 0.125 \cdot 10) = 54 \qquad \text{kips}$$

For the branch plate

$$2 \cdot 0.6 \cdot 50 \cdot 0.125 \cdot 10 = 75 \qquad \text{kips}$$

Therefore, the weld strength is 54 kips

And the weld strength is larger than the yield strength and the fracture strength of the strengthening plate.

The yield strength calculation of the combined plate:

The displacement of the branch plate and the strengthening plate should be the compatible through the weld length. Since the material yield strength of the strengthening plate is smaller, the strengthening plate will yield first, and the corresponding force resisted by the combined plate is

$$P_{ps} + P_y \cdot \frac{36}{60} = 72.9 \qquad \text{kips}$$

649
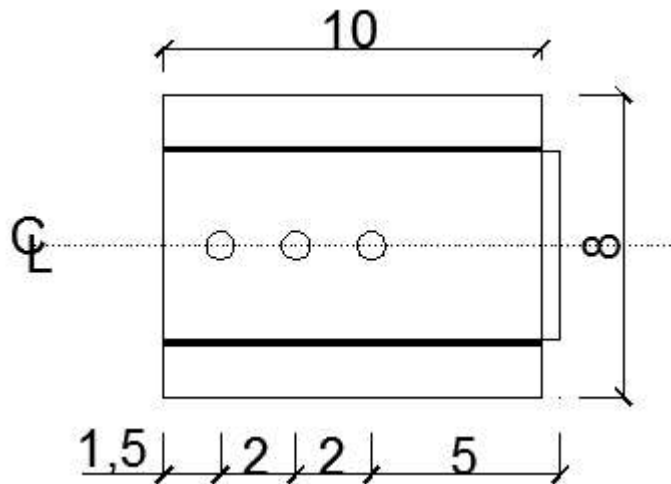
Fig.F.5 Branch plate and strengthening plate assembly

When the branch plate yield, the strain in the shim plate is still at the plateau range of the stress-strain curve. Therefore, when the branch plate yield at the combined part, the yield force would be the two yield force added together

$$P_{yc} := P_y + P_{ps} = 99.9 \qquad\qquad \text{kips}$$

For the part where the branch plate is not connected with the strengthening plate, the yield strength is

$$P_{yc1} := P_y = 67.5 \qquad \text{kips}$$

The fracture strength calculation of the combined plate:

The strain in the strengthening plate will first reach the ultimate strain, and the corresponding stress of the branch plate will be 65 ksi

The nominal strength of the branch plate in fracture is

$$P_{nb1} := 0.75 \cdot A_e \cdot F_{u1} = 39.258 \qquad\qquad \text{kips}$$

The failed facture strength of the combined plate is

$$P_{nb2} := P_{nb} + P_{us} = 92.578 \qquad\qquad \text{kips}$$

The bearing strength calculation of the combined plate:

The distance from the center of the first bolt to the branch plate's end is

$$L_{e3} := 1.5 \qquad\qquad\qquad \text{in}$$

$$L_{c3} := L_{e3} - \frac{d_h}{2} = 1.094 \qquad\qquad\qquad \text{in}$$

The bearing strength of the branch plate at the first bolt is

$$R_{n3} := 1.2 F_u \cdot L_{c3} \cdot t_p = 24.609 \qquad\qquad \text{kips}$$

The upper limit is

$$2.4 d \cdot t_p \cdot F_u = 33.75 \quad > 36.91 \qquad \text{kips}$$

The bearing strength of the strengthening plate at the first bolt is

$$R_{n1s} := 1.2 F_{u1} \cdot L_{c3} \cdot t_s = 8.203 \qquad \text{kips}$$

The upper limit is

$$2.4 d \cdot t_s \cdot F_{u1} = 11.25 \quad > 8.203 \qquad \text{kips}$$

The distance between the center of the 1st and 2nd, and the 2nd and 3rd bolt is

$$L_{e4} := 2 \qquad \qquad \text{in}$$

$$L_{c4} := L_{e4} - d_h = 1.188 \qquad \text{in}$$

The bearing strength of the branch plate at the second and third bolt is

$$R_{n4} := 1.2 F_u \cdot L_{c4} \cdot t_p = 26.719 \qquad \text{kips}$$

The upper limit is

$$2.4 d \cdot t_p \cdot F_u = 33.75 \quad > 40.08 \qquad \text{kips}$$

The bearing strength of the shim plate at the second and third bolt is

$$R_{n2s} := 1.2 F_{u1} \cdot L_{c2} \cdot t_s = 8.906 \qquad \text{kips}$$

The upper limit is

$$2.4 d \cdot t_s \cdot F_{u1} = 11.25 \quad > 8.91 \qquad \text{kips}$$

Therefore, the nominal bearing strength of the connection is

$$R_{nb1} := \left(R_{n3} + R_{n1s} \right) \cdot 3 = 98.438 \qquad \text{kips}$$

Considering the slip resistance of the pre-tensioned bolt connection calculated, which is 88.75 kips, the strength of the bolt connection is

$$R_{b1} := 0.75 R_n = 55.371 \qquad \text{kips}$$

The strength of the weld between the branch plate and HSS is

$$R_{w1} := 77 \qquad \text{kips}$$

Therefore, the controlling force would be

$$P_1 := \min \left(P_{yc1}, P_{yc}, P_{nb1}, R_b, R_w \right) = 39.258 \qquad \text{kips}$$

controlled by the yield of the branch plate, without the shim plate reinforcement. This factor considered the ϕ factor of 0.9, and the yield strength of 60 ksi. With the strain hardening factor of 1.15 and eliminating the ϕ factor, the strength can be resisted by the plate can reach

$$\frac{P \cdot 1.15}{0.9} = 55.454 \qquad \text{kips}$$

Then the failure will be controlled by the weld between the branch plate and the HSS.

F.2 Design of test set-up and the specimen of 9.625" Concrete-filled CHS

F.2.1 Reaction Block

The location of the tab plates is at the height of 10.125" from the bottom of the reaction block. The distance of the bolt hole locations from the edge of the reaction block is shown in Fig. F.1. The design maximum pulling force is

$$F_p := 100 \qquad\qquad \text{kips}$$

Assuming the deformation of the three bolts are proportional as shown in the dashed line in Fig. F.1, the force distribution would also be proportional. The required largest resulting tensile force in the bolt that is farthest from the edge of the reaction block is P. The moment equilibrium for the point O in Fig. F.1 is

$$P \cdot 15 + P \cdot \frac{2 \cdot 10}{3} + P \cdot \frac{1 \cdot 5}{3} = F_p \cdot 10.125$$

$$P := F_p \cdot \frac{10.125}{23.33} = 43.399 \qquad\qquad \text{kips}$$

The diameter of the threaded rods is

$$D_t := 1.125 \qquad\qquad\qquad \text{in}$$

The threaded bolts each was torqued to 600 ft-lb, and the pretension force is calcualted per the torque applied on the bolt (in lubricated condition):

$$P_{pre} := 600 \cdot \frac{12}{0.15 \cdot D_t \cdot 1000} = 42.667 \qquad \text{kips}$$

The yield strength of the bolt is 102.7 kips, which leaves out enough strength (56.5 kips) for the bolt to take the extra tensile load from the overturning of the reaction block.

With six threaded bolts with standard size bolt holes, considering the friction coefficient of 0.35 between the reaction block and the floor beam, the slip resistance strength of the bolted connection is

$$R_s := 1.13 \cdot 0.35 \cdot P_{pre} \cdot 6 = 101.248 \quad 100 \qquad \text{kips}$$

F.2.2 Tab Plates

The material for the two tab plate is A572 Gr50.

The yielding stress of the tab plate is

$$F_{yt} := 50 \qquad\qquad\qquad \text{ksi}$$

The ultimate stress of the tab plate is

$$F_{ut} := 65 \qquad\qquad\qquad \text{ksi}$$

The width of the tab plate is

$L_{pt} := 3$ in

The thickness of the tab plate is

$t_{pt} := 0.375$ in

The yield strength of the tab plate is

$P_{yt} := 0.9 F_{yt} \cdot L_{pt} \cdot t_{pt} = 50.625$ kips

The diameter of the bolt is

$d := 0.75$ in

The diameter of the hole in the tab plate is

$d_h := d + \dfrac{1}{16} = 0.813$ in

The effective net area

$A_{et} := \left(4 - d_h\right) \cdot t_{pt} = 1.195$ in^2

The nominal strength of the tab plate in fracture is

$P_{nt} := 0.75 \cdot A_{et} \cdot F_{ut} = 58.271$ kips

The distance from the center of the first bolt to the tab plate's end is

$L_{e1} := 1.5$ in

$L_{c1} := L_{e1} - \dfrac{d_h}{2} = 1.094$ in

The bearing strength of the tab plate at the first bolt is

$R_{nt1} := 1.2 F_{ut} \cdot L_{c1} \cdot t_{pt} = 31.992$ kips

The upper limit is

$2.4 d \cdot t_{pt} \cdot F_{ut} = 43.875 \; > 32$ kips

The distance between the center of the 1st and 2nd, and the 2nd and 3rd bolt is

$L_{e2} := 2$ in

$L_{c2} := L_{e2} - d_h = 1.188$ in

The bearing strength of the tab plate at the second and third bolt is

$R_{nt2} := 1.2 F_{ut} \cdot L_{c2} \cdot t_{pt} = 34.734$ kips

The upper limit is

$2.4 d \cdot t_{pt} \cdot F_{ut} = 43.875 \; > 34.73$ kips

Assuming the bolts sharing load equally, therefore, the nominal bearing strength of the connection is

$R_{nt} := 6 R_{nt1} = 191.953$ kips

The bearing strength of the tab plates is

$R_{bt} := 0.75 R_{nt} = 143.965$ kips

F.2.3 Branch Plate

The material for the branch plate is A572 Gr60.

The yielding stress of the branch plate is

$F_{yp} := 60$ ksi

The ultimate stress of the branch plate is

$F_u := 75$ ksi

The width of the branch plate is

$L_p := 3$ in

The thickness of the branch plate is

$t_p := 0.375$ in

The yield strength of the plate is

$P_y := 0.9 F_{yp} \cdot L_p \cdot t_p = 60.75$ kips

The effective net area

$A_e := (3 - d_h) \cdot t_p = 0.82$ in^2

The nominal strength of the branch plate in fracture is

$P_{nb} := 0.75 \cdot A_e \cdot F_u = 46.143$ kips
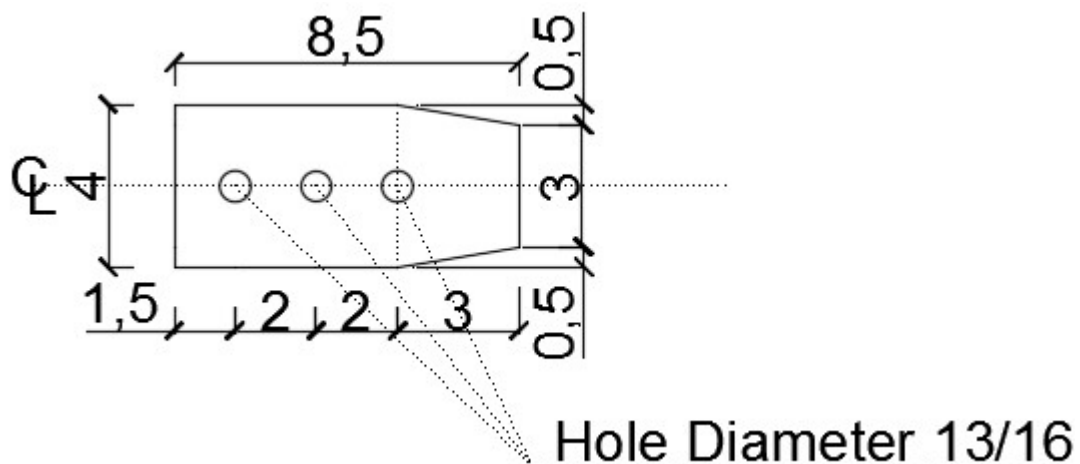
Fig. F.6 Branch plate welded to the 9.625" tube (weld on the right)

The distance from the center of the first bolt to the branch plate's end is

$L_{eb1} := 1.5$ in

$L_{cb1} := L_{eb1} - \dfrac{d_h}{2} = 1.094$ in

The bearing strength of the branch plate at the first bolt is

$$R_{n1} := 1.2 F_u \cdot L_{cb1} \cdot t_p = 36.914 \qquad \text{kips}$$

The upper limit is

$$2.4 d \cdot t_p \cdot F_u = 50.625 \ > 36.91 \qquad \text{kips}$$

The distance between the center of the 1st and 2nd, and the 2nd and 3rd bolt is

$$L_{eb2} := 2 \qquad\qquad \text{in}$$
$$L_{cb2} := L_{eb2} - d_h = 1.188 \qquad \text{in}$$

The bearing strength of the branch plate at the second and third bolt is

$$R_{n2} := 1.2 F_u \cdot L_{cb2} \cdot t_p = 40.078 \qquad \text{kips}$$

The upper limit is

$$2.4 d \cdot t_p \cdot F_u = 50.625 \ > 40.08 \qquad \text{kips}$$

Assuming the bolts sharing load equally, therefore, the nominal bearing strength of the connection is

$$R_n := 3 R_{n1} = 110.742 \qquad \text{kips}$$

The bearing strength of the bolt connection is

$$R_b := 0.75 R_n = 83.057 \qquad \text{kips}$$

The branch plate and the tab plates are connected with slip-resistant bolted connections, which has the bolts torqued to provide pretension force.

The torque in each bolts is 300 ft-lb, and the tensile strength of the bolt is 37.4 kips obtained from the AISC steel construction manual (2010). The slip resistance strength of the bolted connection is

$$R_{sb} := 1.13 \cdot 0.35 \cdot 37.4 \cdot 2 \cdot 3 = 88.75 \qquad \text{kips}$$

Therefore, the bolted connection reaching the force of 89 kips before the bolts slip; after that,the bolted connection between the tab plates and the branch plate is controlled by the failure of the branch plate, which is the net section failure of the plate

$$\min\left(P_y, P_{nb}, R_{sb}\right) = 46.143 \qquad \text{kips}$$

Appendix G Bidirectional ductile diaphragm design in multi-span simply supported bridge

This design example illustrates how BRBs are designed in the bidrectional ductile diaphragm in multi-span simply supported bridge. Note that this design example use metric units.

G.1 Bridge properties

The bridge is a three-span simply supported 40 m span bridge on concrete bents with four 900mm diameter columns (5m tall).

The bridge's single span length is

$$L_s := 40 \qquad\qquad\qquad m$$

The number of columns in each bent are

$$n_c := 4$$

The height of the columns in each bent are

$$h_c := 5 \qquad\qquad\qquad m$$

The mass of the bridge in each span is

$$M := 286000 \qquad\qquad\qquad kg$$

The bridge's superstructure plus the girder stiffness in the transverse direction (perpendicular to the deck's vertical axis) is

$$EI_D := 3.72 \cdot 10^{11} \qquad\qquad N \cdot m^2$$

The concrete bent stiffness in the transverse direction is

$$K_e := 3 \cdot 10^8 \qquad\qquad\qquad N/m$$

The concrete bent stiffness in the longitudinal direction is

$$K_{el} := 7.5 \times 10^7 \qquad\qquad\qquad N/m$$

The girder used is WWF1200x333, and the number of the girder is 4

The girder height is

$$h_g := 1.2 \qquad\qquad\qquad m$$

The thickness of the girder's top and bottom flange is

$$t_f := 0.03 \qquad\qquad\qquad m$$

The height of the girder's web is

$$h_w := h_g - 2 \cdot t_f = 1.14 \qquad\qquad\qquad m$$

The thickness of the girder's web is

$t_w := 0.015875$ m

The steel material's young's modulus is

$E_s := 206000$ MPa

Two girder bearing stiffener plates 1200*100*10 were placed on each side of the girder web. The width and thickness of the stiffener are

$w_s := 0.1$ m

$t_s := 0.01$ m

The total bearing stiffeners' moment of inertia is

$$I_{sy} := t_s \cdot \frac{(2 \cdot w_s + t_w)^3}{12} = 8.384 \times 10^{-6} \qquad m^4$$

The lateral stiffness provided at each girder is

$$K_{gw} := 3 \cdot E_s \cdot \frac{I_{sy} \cdot 10^6}{h_g^3} = 2.998 \times 10^6 \qquad \text{N/m}$$

The lateral stiffness provided the four girders at one end of the bridge span is

$K_g := 4 \cdot K_{gw} = 1.199 \times 10^7$ N/m

The distance between the girders is

$W_g := 2$ m

The yield strength of the stiffener steel is

$F_{yw} := 345$ Mpa

The yield strength of the stiffener at one end of the girder is

$$V_{gs} := F_{yw} \cdot 10^6 \cdot t_s \cdot \frac{(2 \cdot w_s + t_w)^2}{6 h_g} = 2.233 \times 10^4 \qquad \text{N}$$

The yield displacement of the stiffener is

$$\delta_{gs} := \frac{V_{gs}}{K_{gw}} = 7.448 \times 10^{-3} \qquad m$$

The total yield force of the four stiffeners at one end of the bridge span is

$V_{gw} := 4 \cdot V_{gs} = 8.932 \times 10^4$ N

The yield force of the girder link in the model is

$$\frac{V_{gs} \cdot \frac{4}{3}}{\sqrt{\left(\frac{2^2}{2^2 + 1.2^2}\right)}} = 3.472 \times 10^4 \qquad \text{N}$$

G.2 Transverse ductile diaphragm design for the middle span

The design stiffness of the ductile diaphragm in the transverse direction is

$$K_{dt} := 8.76 \cdot 10^7 \qquad\qquad \text{N/m}$$

The ratio between half of the transverse bent stiffness and the transverse ductile diaphragm is

$$\frac{\dfrac{K_e}{2}}{K_{dt}} = 1.712$$

The stiffness of the support spring system at the end of the bridge span (in the transverse direction) is

$$K_n := \frac{1}{\dfrac{1}{\dfrac{K_e}{2}} + \dfrac{1}{K_g + K_{dt}}} = 5.985 \times 10^7$$

$$B_1 := \frac{EI_D \cdot \left(\dfrac{1}{\dfrac{K_e}{2}} + \dfrac{1}{K_g + K_{dt}} \right)}{L_s^{\,3}} = 0.097$$

The first mode period is

$$T_T := 2 \cdot \pi \cdot \sqrt{\frac{M \cdot \left(\dfrac{31}{3024} + 30 \cdot B_1^2 + B_1 \right)}{K_n \cdot B_1 \cdot \left(60 \cdot B_1 + 1 \right)}} = 0.333 \qquad\qquad \text{s}$$

The generalized mass of the first mode is

$$M_{t1} := \frac{M \cdot \left(60 \cdot B_1 + 1 \right)^2}{60 \cdot \left(60 \cdot B_1^2 + 2 \cdot B_1 + \dfrac{31}{1512} \right)} = 2.846 \times 10^5 \qquad\qquad \text{kg}$$

The inclination angle of the BRB in the transverse ductile diaphragm is

$$\alpha := \operatorname{atan}\left(\frac{h_g}{W_g} \right) = 0.54$$

The length of the transverse BRB is

$$L_{bt} := \sqrt{\left(h_g \right)^2 + \left(W_g \right)^2} = 2.332 \qquad\qquad \text{m}$$

The yield strength of the core plate steel in the BRB is

$$f_{yb} := 317.2 \qquad\qquad \text{MPa}$$

The yield length ratio of the transverse BRBs is

$$c_b := 0.6$$

The yield dispalcement of the transverse BRB is

$$\delta_{brb} := L_{bt} \cdot c_b \cdot \frac{f_{yb}}{199480} = 2.225 \times 10^{-3} \qquad m$$

The displacement of the ductile diaphragm with BRBs in the transverse direction when the BRB yields is

$$\delta_{bt} := c_b \cdot L_{bt} \cdot \frac{f_{yb}}{199480 \cdot \cos(\alpha)} = 2.595 \times 10^{-3} \qquad m$$

The yield strength of the transverse diaphragm is

$$V_d := \delta_{bt} \cdot K_{dt} = 2.273 \times 10^5 \qquad N$$

The yield force in the single BRB is (two transverse BRBs in the transverse direction)

$$V_b := \frac{V_d}{2 \cdot \cos(\alpha)} = 1.326 \times 10^5 \qquad N$$

The corresponding force at the girder bearing stiffeners is

$$V_{gy} := \frac{V_d \cdot K_g}{K_{dt}} = 3.112 \times 10^4 \qquad N$$

The total force applied to the bent from the transverse ductile diaphragm and girder stiffeners is

$$V_d + V_{gy} = 2.585 \times 10^5 \qquad N$$

The corresponding transverse displacement at the top of the bent is

$$\delta_{yct} := \frac{V_d + V_{gy}}{\dfrac{K_e}{2}} = 1.723 \times 10^{-3} \qquad m$$

This yield displacement should be smaller than the yield displacement of the columns, which is estimated as

$$\Delta_c := 0.005 \cdot h_c = 0.025 \qquad m$$

The ratio between the yield displacement of the stiffener and ductile diaphragm is

$$\frac{\delta_{gs}}{\delta_{bt}} = 2.87$$

which indicates that when the BRB's ductility goes beyond this ratio, the stiffeners would yield

The yield displacement of the spring system at one end of the bridge span is

$$\delta_t := \delta_{yct} + \delta_{bt} = 4.318 \times 10^{-3} \qquad m$$

G.3 Longitudinal ductile diaphragm design for the middle span

The longitudinal ductile diaphragm was designed to have two different stiffness caes. The stiffness and strength of the ductile diaphragm in the longitudinal and transverse direction are the same.

The design stiffness of the ductile diaphragm in the transverse direction is

$$K_{dl} := 8.76 \cdot 10^7 \qquad\qquad \text{N/m}$$

The stiffness of the support spring system at the end of the bridge span (in the longitudinal direction) is

$$K_{nl} := \frac{1}{\dfrac{1}{\dfrac{K_{el}}{2}} + \dfrac{1}{K_{dl}}} = 2.626 \times 10^7 \qquad\qquad \text{N/m}$$

The longitudinal period is

$$T_L := 2 \cdot \pi \cdot \sqrt{\frac{M}{2 \cdot K_{nl}}} = 0.464 \qquad\qquad \text{s}$$

The inclination angle of the longitudinal BRB with the horizontal direction is

$$\beta := \operatorname{atan}\left(\frac{h_g}{1}\right) = 0.876$$

The length of the longitudinal BRB is

$$L_{bl} := \sqrt{\left(h_g\right)^2 + (1)^2} = 1.562 \qquad\qquad \text{m}$$

The yield length ratio of the longitudinal BRBs is

$$c_{b2} := 0.669$$

The yield dispalcement of the longitudinal BRB is

$$\delta_{bL} := L_{bl} \cdot c_{b2} \cdot \frac{f_{yb}}{199480} = 1.662 \times 10^{-3} \qquad\qquad \text{m}$$

The displacement of the ductile diaphragm with BRBs in the longitudinal direction when the BRB yields is

$$\delta_{blh} := c_{b2} \cdot L_{bl} \cdot \frac{f_{yb}}{199480 \cdot \cos(\beta)} = 2.596 \times 10^{-3} \qquad\qquad \text{m}$$

The yield strength of the longitudinal diaphragm is

$$V_{dL} := \delta_{blh} \cdot K_{dl} = 2.274 \times 10^5 \qquad\qquad \text{N}$$

The yield force of the BRBs in the longitudinal ductile diaphragm is

$$V_{bl} := \frac{V_{dL}}{\cos(\beta)} = 3.552 \times 10^5 \qquad\qquad \text{N}$$

The corresponding longitudinal displacement at the top of the bent is

$$\delta_{ycL} := \frac{V_{dL}}{\dfrac{K_{el}}{2}} = 6.063 \times 10^{-3} \qquad\qquad \text{m}$$

The yield displacement of the spring system at one end of the bridge span is

$$\delta_L := \delta_{ycL} + \delta_{blh} = 8.659 \times 10^{-3} \qquad m$$

Note that this middle span, does not exist in the actual bridge. The abutment at the end spans would add to the bridge's stiffness in the longitudinal direction. Therefore, in the bridge model in Section 10, there are two cases considered for the longitudinal BRBs in order to see the effect of using different longitudinal stiffnesses.

When the longitudinal ductile diaphragm's stiffness is incrased to twice of the stiffness in the transverse ductile diaphragm.

$$K_{nl2} := \cfrac{1}{\cfrac{1}{\cfrac{K_{el}}{2}} + \cfrac{1}{2K_{dl}}} = 3.089 \times 10^7 \qquad N/m$$

$$T_{L2} := 2 \cdot \pi \cdot \sqrt{\frac{M}{2 \cdot K_{nl2}}} = 0.428 \qquad s$$

$$V_{dl2} := 2V_d = 4.547 \times 10^5 \qquad kips$$

$$\delta_{ycL2} := \cfrac{V_{dl2}}{\cfrac{K_{el}}{2}} = 0.012 \qquad m$$

$$\delta_{L2} := \delta_{ycL2} + \delta_{blh} = 0.015 \qquad m$$

G.4 Spectral displacement demands for the middle span

The following figure is the design response spectrum used for this example. For the longitudinal and transverse period, both of the longitudinal and transverse period corresponds to the spectral acceleration on the plateau.

Design Response Spectrum
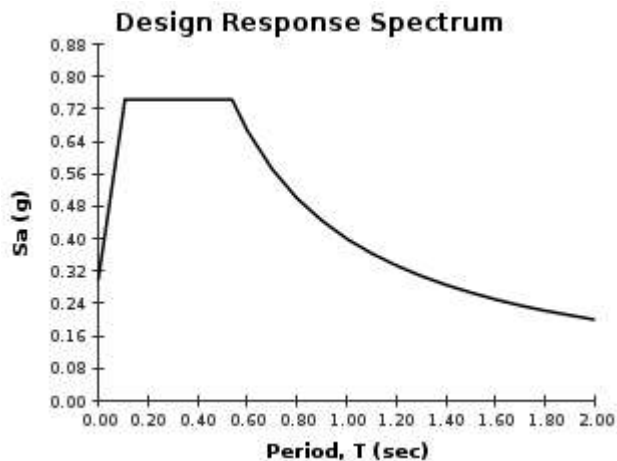
$$S_{at} := 0.74 \quad g$$

$$S_{al} := 0.74 \quad g$$

The displacement demand of the spring system in the transverse direction is

$$\delta_{ut} := \frac{M \cdot S_{at} \cdot 9.8}{M_{t1} \cdot \left(\frac{2 \cdot \pi}{T_T}\right)^2} = 0.021 \qquad \qquad m$$

The ductility of the spring system in the transverse direction is

$$\mu_{st} := \frac{\delta_{ut}}{\delta_t} = 4.748$$

$$\phi_{10} := \frac{38.4 B_1 \cdot L_s^4}{L_s^4 \cdot \left(1 + 38.4 \cdot B_1\right)} = 0.789$$

$$\tau_1 := \frac{\left(1 + 38.4 \cdot B_1\right)\left(60 \cdot B_1 + 1\right)}{38.4 \cdot \left(60 \cdot B_1^2 + 2 \cdot B_1 + \frac{31}{1512}\right)} = 1.077$$

The ductility for the bridge center span's displacement in the transverse direction is

$$\mu_e := 1 + \frac{\mu_{st} - 1}{\phi_{10} \cdot \tau_1} = 5.412$$

The displacement demand of the transverse BRB is

$$\mu_{dt} := \mu_{st} \cdot \left[1 + \frac{\left(K_g + K_{dt}\right)}{\frac{K_e}{2}}\right] - \frac{\left(K_g + K_{dt}\right)}{\frac{K_e}{2}} = 7.236$$

The displacement demand of the spring system in the longitudinal direction is

$$\delta_{ul} := \frac{M \cdot S_{al} \cdot 9.8}{2 K_{nl}} = 0.039 \qquad \qquad m$$

The ductility for the bridge center span's displacement in the longitudinal direction is

$$\mu_{sl} := \frac{\delta_{ul}}{\delta_L} = 4.561$$

The displacement demand of the longitudinal BRB is

$$\mu_{dl} := \mu_{sl} \cdot \left(1 + \frac{K_{dl}}{\frac{K_{el}}{2}}\right) - \frac{K_{dl}}{\frac{K_{el}}{2}} = 12.879$$

$$\delta_{ul2} := \frac{M \cdot S_{al} \cdot 9.8}{2 K_{nl2}} = 0.034 \qquad \qquad m$$

$$\mu_{sl2} := \frac{\delta_{ul2}}{\delta_{L2}} = 2.281$$

$$\mu_{dl2} := \mu_{sl2} \cdot \left(1 + \frac{2 K_{dl}}{\frac{K_{el}}{2}}\right) - \frac{2 K_{dl}}{\frac{K_{el}}{2}} = 8.265$$

MCEER Technical Reports

MCEER publishes technical reports on a variety of subjects written by authors funded through MCEER. These reports are available from both MCEER Publications and the National Technical Information Service (NTIS). Requests for reports should be directed to MCEER Publications, MCEER, University at Buffalo, State University of New York, 133A Ketter Hall, Buffalo, New York 14260. Reports can also be requested through NTIS, P.O. Box 1425, Springfield, Virginia 22151. NTIS accession numbers are shown in parenthesis, if available.

NCEER-87-0001 "First-Year Program in Research, Education and Technology Transfer," 3/5/87, (PB88-134275, A04, MF-A01).

NCEER-87-0002 "Experimental Evaluation of Instantaneous Optimal Algorithms for Structural Control," by R.C. Lin, T.T. Soong and A.M. Reinhorn, 4/20/87, (PB88-134341, A04, MF-A01).

NCEER-87-0003 "Experimentation Using the Earthquake Simulation Facilities at University at Buffalo," by A.M. Reinhorn and R.L. Ketter, not available.

NCEER-87-0004 "The System Characteristics and Performance of a Shaking Table," by J.S. Hwang, K.C. Chang and G.C. Lee, 6/1/87, (PB88-134259, A03, MF-A01). This report is available only through NTIS (see address given above).

NCEER-87-0005 "A Finite Element Formulation for Nonlinear Viscoplastic Material Using a Q Model," by O. Gyebi and G. Dasgupta, 11/2/87, (PB88-213764, A08, MF-A01).

NCEER-87-0006 "Symbolic Manipulation Program (SMP) - Algebraic Codes for Two and Three Dimensional Finite Element Formulations," by X. Lee and G. Dasgupta, 11/9/87, (PB88-218522, A05, MF-A01).

NCEER-87-0007 "Instantaneous Optimal Control Laws for Tall Buildings Under Seismic Excitations," by J.N. Yang, A. Akbarpour and P. Ghaemmaghami, 6/10/87, (PB88-134333, A06, MF-A01). This report is only available through NTIS (see address given above).

NCEER-87-0008 "IDARC: Inelastic Damage Analysis of Reinforced Concrete Frame - Shear-Wall Structures," by Y.J. Park, A.M. Reinhorn and S.K. Kunnath, 7/20/87, (PB88-134325, A09, MF-A01). This report is only available through NTIS (see address given above).

NCEER-87-0009 "Liquefaction Potential for New York State: A Preliminary Report on Sites in Manhattan and Buffalo," by M. Budhu, V. Vijayakumar, R.F. Giese and L. Baumgras, 8/31/87, (PB88-163704, A03, MF-A01). This report is available only through NTIS (see address given above).

NCEER-87-0010 "Vertical and Torsional Vibration of Foundations in Inhomogeneous Media," by A.S. Veletsos and K.W. Dotson, 6/1/87, (PB88-134291, A03, MF-A01). This report is only available through NTIS (see address given above).

NCEER-87-0011 "Seismic Probabilistic Risk Assessment and Seismic Margins Studies for Nuclear Power Plants," by Howard H.M. Hwang, 6/15/87, (PB88-134267, A03, MF-A01). This report is only available through NTIS (see address given above).

NCEER-87-0012 "Parametric Studies of Frequency Response of Secondary Systems Under Ground-Acceleration Excitations," by Y. Yong and Y.K. Lin, 6/10/87, (PB88-134309, A03, MF-A01). This report is only available through NTIS (see address given above).

NCEER-87-0013 "Frequency Response of Secondary Systems Under Seismic Excitation," by J.A. HoLung, J. Cai and Y.K. Lin, 7/31/87, (PB88-134317, A05, MF-A01). This report is only available through NTIS (see address given above).

NCEER-87-0014 "Modelling Earthquake Ground Motions in Seismically Active Regions Using Parametric Time Series Methods," by G.W. Ellis and A.S. Cakmak, 8/25/87, (PB88-134283, A08, MF-A01). This report is only available through NTIS (see address given above).

NCEER-87-0015   "Detection and Assessment of Seismic Structural Damage," by E. DiPasquale and A.S. Cakmak, 8/25/87, (PB88-163712, A05, MF-A01). This report is only available through NTIS (see address given above).

NCEER-87-0016   "Pipeline Experiment at Parkfield, California," by J. Isenberg and E. Richardson, 9/15/87, (PB88-163720, A03, MF-A01). This report is available only through NTIS (see address given above).

NCEER-87-0017   "Digital Simulation of Seismic Ground Motion," by M. Shinozuka, G. Deodatis and T. Harada, 8/31/87, (PB88-155197, A04, MF-A01). This report is available only through NTIS (see address given above).

NCEER-87-0018   "Practical Considerations for Structural Control: System Uncertainty, System Time Delay and Truncation of Small Control Forces," J.N. Yang and A. Akbarpour, 8/10/87, (PB88-163738, A08, MF-A01). This report is only available through NTIS (see address given above).

NCEER-87-0019   "Modal Analysis of Nonclassically Damped Structural Systems Using Canonical Transformation," by J.N. Yang, S. Sarkani and F.X. Long, 9/27/87, (PB88-187851, A04, MF-A01).

NCEER-87-0020   "A Nonstationary Solution in Random Vibration Theory," by J.R. Red-Horse and P.D. Spanos, 11/3/87, (PB88-163746, A03, MF-A01).

NCEER-87-0021   "Horizontal Impedances for Radially Inhomogeneous Viscoelastic Soil Layers," by A.S. Veletsos and K.W. Dotson, 10/15/87, (PB88-150859, A04, MF-A01).

NCEER-87-0022   "Seismic Damage Assessment of Reinforced Concrete Members," by Y.S. Chung, C. Meyer and M. Shinozuka, 10/9/87, (PB88-150867, A05, MF-A01). This report is available only through NTIS (see address given above).

NCEER-87-0023   "Active Structural Control in Civil Engineering," by T.T. Soong, 11/11/87, (PB88-187778, A03, MF-A01).

NCEER-87-0024   "Vertical and Torsional Impedances for Radially Inhomogeneous Viscoelastic Soil Layers," by K.W. Dotson and A.S. Veletsos, 12/87, (PB88-187786, A03, MF-A01).

NCEER-87-0025   "Proceedings from the Symposium on Seismic Hazards, Ground Motions, Soil-Liquefaction and Engineering Practice in Eastern North America," October 20-22, 1987, edited by K.H. Jacob, 12/87, (PB88-188115, A23, MF-A01). This report is available only through NTIS (see address given above).

NCEER-87-0026   "Report on the Whittier-Narrows, California, Earthquake of October 1, 1987," by J. Pantelic and A. Reinhorn, 11/87, (PB88-187752, A03, MF-A01). This report is available only through NTIS (see address given above).

NCEER-87-0027   "Design of a Modular Program for Transient Nonlinear Analysis of Large 3-D Building Structures," by S. Srivastav and J.F. Abel, 12/30/87, (PB88-187950, A05, MF-A01). This report is only available through NTIS (see address given above).

NCEER-87-0028   "Second-Year Program in Research, Education and Technology Transfer," 3/8/88, (PB88-219480, A04, MF-A01).

NCEER-88-0001   "Workshop on Seismic Computer Analysis and Design of Buildings With Interactive Graphics," by W. McGuire, J.F. Abel and C.H. Conley, 1/18/88, (PB88-187760, A03, MF-A01). This report is only available through NTIS (see address given above).

NCEER-88-0002   "Optimal Control of Nonlinear Flexible Structures," by J.N. Yang, F.X. Long and D. Wong, 1/22/88, (PB88-213772, A06, MF-A01).

NCEER-88-0003   "Substructuring Techniques in the Time Domain for Primary-Secondary Structural Systems," by G.D. Manolis and G. Juhn, 2/10/88, (PB88-213780, A04, MF-A01).

NCEER-88-0004   "Iterative Seismic Analysis of Primary-Secondary Systems," by A. Singhal, L.D. Lutes and P.D. Spanos, 2/23/88, (PB88-213798, A04, MF-A01).

NCEER-88-0005   "Stochastic Finite Element Expansion for Random Media," by P.D. Spanos and R. Ghanem, 3/14/88, (PB88-213806, A03, MF-A01).

666

NCEER-88-0006   "Combining Structural Optimization and Structural Control," by F.Y. Cheng and C.P. Pantelides, 1/10/88, (PB88-213814, A05, MF-A01).

NCEER-88-0007   "Seismic Performance Assessment of Code-Designed Structures," by H.H-M. Hwang, J-W. Jaw and H-J. Shau, 3/20/88, (PB88-219423, A04, MF-A01). This report is only available through NTIS (see address given above).

NCEER-88-0008   "Reliability Analysis of Code-Designed Structures Under Natural Hazards," by H.H-M. Hwang, H. Ushiba and M. Shinozuka, 2/29/88, (PB88-229471, A07, MF-A01). This report is only available through NTIS (see address given above).

NCEER-88-0009   "Seismic Fragility Analysis of Shear Wall Structures," by J-W Jaw and H.H-M. Hwang, 4/30/88, (PB89-102867, A04, MF-A01).

NCEER-88-0010   "Base Isolation of a Multi-Story Building Under a Harmonic Ground Motion - A Comparison of Performances of Various Systems," by F-G Fan, G. Ahmadi and I.G. Tadjbakhsh, 5/18/88, (PB89-122238, A06, MF-A01). This report is only available through NTIS (see address given above).

NCEER-88-0011   "Seismic Floor Response Spectra for a Combined System by Green's Functions," by F.M. Lavelle, L.A. Bergman and P.D. Spanos, 5/1/88, (PB89-102875, A03, MF-A01).

NCEER-88-0012   "A New Solution Technique for Randomly Excited Hysteretic Structures," by G.Q. Cai and Y.K. Lin, 5/16/88, (PB89-102883, A03, MF-A01).

NCEER-88-0013   "A Study of Radiation Damping and Soil-Structure Interaction Effects in the Centrifuge," by K. Weissman, supervised by J.H. Prevost, 5/24/88, (PB89-144703, A06, MF-A01).

NCEER-88-0014   "Parameter Identification and Implementation of a Kinematic Plasticity Model for Frictional Soils," by J.H. Prevost and D.V. Griffiths, not available.

NCEER-88-0015   "Two- and Three- Dimensional Dynamic Finite Element Analyses of the Long Valley Dam," by D.V. Griffiths and J.H. Prevost, 6/17/88, (PB89-144711, A04, MF-A01).

NCEER-88-0016   "Damage Assessment of Reinforced Concrete Structures in Eastern United States," by A.M. Reinhorn, M.J. Seidel, S.K. Kunnath and Y.J. Park, 6/15/88, (PB89-122220, A04, MF-A01). This report is only available through NTIS (see address given above).

NCEER-88-0017   "Dynamic Compliance of Vertically Loaded Strip Foundations in Multilayered Viscoelastic Soils," by S. Ahmad and A.S.M. Israil, 6/17/88, (PB89-102891, A04, MF-A01).

NCEER-88-0018   "An Experimental Study of Seismic Structural Response With Added Viscoelastic Dampers," by R.C. Lin, Z. Liang, T.T. Soong and R.H. Zhang, 6/30/88, (PB89-122212, A05, MF-A01). This report is available only through NTIS (see address given above).

NCEER-88-0019   "Experimental Investigation of Primary - Secondary System Interaction," by G.D. Manolis, G. Juhn and A.M. Reinhorn, 5/27/88, (PB89-122204, A04, MF-A01).

NCEER-88-0020   "A Response Spectrum Approach For Analysis of Nonclassically Damped Structures," by J.N. Yang, S. Sarkani and F.X. Long, 4/22/88, (PB89-102909, A04, MF-A01).

NCEER-88-0021   "Seismic Interaction of Structures and Soils: Stochastic Approach," by A.S. Veletsos and A.M. Prasad, 7/21/88, (PB89-122196, A04, MF-A01). This report is only available through NTIS (see address given above).

NCEER-88-0022   "Identification of the Serviceability Limit State and Detection of Seismic Structural Damage," by E. DiPasquale and A.S. Cakmak, 6/15/88, (PB89-122188, A05, MF-A01). This report is available only through NTIS (see address given above).

NCEER-88-0023   "Multi-Hazard Risk Analysis: Case of a Simple Offshore Structure," by B.K. Bhartia and E.H. Vanmarcke, 7/21/88, (PB89-145213, A05, MF-A01).

NCEER-88-0024   "Automated Seismic Design of Reinforced Concrete Buildings," by Y.S. Chung, C. Meyer and M. Shinozuka, 7/5/88, (PB89-122170, A06, MF-A01). This report is available only through NTIS (see address given above).

NCEER-88-0025   "Experimental Study of Active Control of MDOF Structures Under Seismic Excitations," by L.L. Chung, R.C. Lin, T.T. Soong and A.M. Reinhorn, 7/10/88, (PB89-122600, A04, MF-A01).

NCEER-88-0026   "Earthquake Simulation Tests of a Low-Rise Metal Structure," by J.S. Hwang, K.C. Chang, G.C. Lee and R.L. Ketter, 8/1/88, (PB89-102917, A04, MF-A01).

NCEER-88-0027   "Systems Study of Urban Response and Reconstruction Due to Catastrophic Earthquakes," by F. Kozin and H.K. Zhou, 9/22/88, (PB90-162348, A04, MF-A01).

NCEER-88-0028   "Seismic Fragility Analysis of Plane Frame Structures," by H.H-M. Hwang and Y.K. Low, 7/31/88, (PB89-131445, A06, MF-A01).

NCEER-88-0029   "Response Analysis of Stochastic Structures," by A. Kardara, C. Bucher and M. Shinozuka, 9/22/88, (PB89-174429, A04, MF-A01).

NCEER-88-0030   "Nonnormal Accelerations Due to Yielding in a Primary Structure," by D.C.K. Chen and L.D. Lutes, 9/19/88, (PB89-131437, A04, MF-A01).

NCEER-88-0031   "Design Approaches for Soil-Structure Interaction," by A.S. Veletsos, A.M. Prasad and Y. Tang, 12/30/88, (PB89-174437, A03, MF-A01). This report is available only through NTIS (see address given above).

NCEER-88-0032   "A Re-evaluation of Design Spectra for Seismic Damage Control," by C.J. Turkstra and A.G. Tallin, 11/7/88, (PB89-145221, A05, MF-A01).

NCEER-88-0033   "The Behavior and Design of Noncontact Lap Splices Subjected to Repeated Inelastic Tensile Loading," by V.E. Sagan, P. Gergely and R.N. White, 12/8/88, (PB89-163737, A08, MF-A01).

NCEER-88-0034   "Seismic Response of Pile Foundations," by S.M. Mamoon, P.K. Banerjee and S. Ahmad, 11/1/88, (PB89-145239, A04, MF-A01).

NCEER-88-0035   "Modeling of R/C Building Structures With Flexible Floor Diaphragms (IDARC2)," by A.M. Reinhorn, S.K. Kunnath and N. Panahshahi, 9/7/88, (PB89-207153, A07, MF-A01).

NCEER-88-0036   "Solution of the Dam-Reservoir Interaction Problem Using a Combination of FEM, BEM with Particular Integrals, Modal Analysis, and Substructuring," by C-S. Tsai, G.C. Lee and R.L. Ketter, 12/31/88, (PB89-207146, A04, MF-A01).

NCEER-88-0037   "Optimal Placement of Actuators for Structural Control," by F.Y. Cheng and C.P. Pantelides, 8/15/88, (PB89-162846, A05, MF-A01).

NCEER-88-0038   "Teflon Bearings in Aseismic Base Isolation: Experimental Studies and Mathematical Modeling," by A. Mokha, M.C. Constantinou and A.M. Reinhorn, 12/5/88, (PB89-218457, A10, MF-A01). This report is available only through NTIS (see address given above).

NCEER-88-0039   "Seismic Behavior of Flat Slab High-Rise Buildings in the New York City Area," by P. Weidlinger and M. Ettouney, 10/15/88, (PB90-145681, A04, MF-A01).

NCEER-88-0040   "Evaluation of the Earthquake Resistance of Existing Buildings in New York City," by P. Weidlinger and M. Ettouney, 10/15/88, not available.

NCEER-88-0041   "Small-Scale Modeling Techniques for Reinforced Concrete Structures Subjected to Seismic Loads," by W. Kim, A. El-Attar and R.N. White, 11/22/88, (PB89-189625, A05, MF-A01).

NCEER-88-0042   "Modeling Strong Ground Motion from Multiple Event Earthquakes," by G.W. Ellis and A.S. Cakmak, 10/15/88, (PB89-174445, A03, MF-A01).

NCEER-88-0043   "Nonstationary Models of Seismic Ground Acceleration," by M. Grigoriu, S.E. Ruiz and E. Rosenblueth, 7/15/88, (PB89-189617, A04, MF-A01).

NCEER-88-0044   "SARCF User's Guide: Seismic Analysis of Reinforced Concrete Frames," by Y.S. Chung, C. Meyer and M. Shinozuka, 11/9/88, (PB89-174452, A08, MF-A01).

NCEER-88-0045   "First Expert Panel Meeting on Disaster Research and Planning," edited by J. Pantelic and J. Stoyle, 9/15/88, (PB89-174460, A05, MF-A01).

NCEER-88-0046   "Preliminary Studies of the Effect of Degrading Infill Walls on the Nonlinear Seismic Response of Steel Frames," by C.Z. Chrysostomou, P. Gergely and J.F. Abel, 12/19/88, (PB89-208383, A05, MF-A01).

NCEER-88-0047   "Reinforced Concrete Frame Component Testing Facility - Design, Construction, Instrumentation and Operation," by S.P. Pessiki, C. Conley, T. Bond, P. Gergely and R.N. White, 12/16/88, (PB89-174478, A04, MF-A01).

NCEER-89-0001   "Effects of Protective Cushion and Soil Compliancy on the Response of Equipment Within a Seismically Excited Building," by J.A. HoLung, 2/16/89, (PB89-207179, A04, MF-A01).

NCEER-89-0002   "Statistical Evaluation of Response Modification Factors for Reinforced Concrete Structures," by H.H-M. Hwang and J-W. Jaw, 2/17/89, (PB89-207187, A05, MF-A01).

NCEER-89-0003   "Hysteretic Columns Under Random Excitation," by G-Q. Cai and Y.K. Lin, 1/9/89, (PB89-196513, A03, MF-A01).

NCEER-89-0004   "Experimental Study of `Elephant Foot Bulge' Instability of Thin-Walled Metal Tanks," by Z-H. Jia and R.L. Ketter, 2/22/89, (PB89-207195, A03, MF-A01).

NCEER-89-0005   "Experiment on Performance of Buried Pipelines Across San Andreas Fault," by J. Isenberg, E. Richardson and T.D. O'Rourke, 3/10/89, (PB89-218440, A04, MF-A01). This report is available only through NTIS (see address given above).

NCEER-89-0006   "A Knowledge-Based Approach to Structural Design of Earthquake-Resistant Buildings," by M. Subramani, P. Gergely, C.H. Conley, J.F. Abel and A.H. Zaghw, 1/15/89, (PB89-218465, A06, MF-A01).

NCEER-89-0007   "Liquefaction Hazards and Their Effects on Buried Pipelines," by T.D. O'Rourke and P.A. Lane, 2/1/89, (PB89-218481, A09, MF-A01).

NCEER-89-0008   "Fundamentals of System Identification in Structural Dynamics," by H. Imai, C-B. Yun, O. Maruyama and M. Shinozuka, 1/26/89, (PB89-207211, A04, MF-A01).

NCEER-89-0009   "Effects of the 1985 Michoacan Earthquake on Water Systems and Other Buried Lifelines in Mexico," by A.G. Ayala and M.J. O'Rourke, 3/8/89, (PB89-207229, A06, MF-A01).

NCEER-89-R010   "NCEER Bibliography of Earthquake Education Materials," by K.E.K. Ross, Second Revision, 9/1/89, (PB90-125352, A05, MF-A01). This report is replaced by NCEER-92-0018.

NCEER-89-0011   "Inelastic Three-Dimensional Response Analysis of Reinforced Concrete Building Structures (IDARC-3D), Part I - Modeling," by S.K. Kunnath and A.M. Reinhorn, 4/17/89, (PB90-114612, A07, MF-A01). This report is available only through NTIS (see address given above).

NCEER-89-0012   "Recommended Modifications to ATC-14," by C.D. Poland and J.O. Malley, 4/12/89, (PB90-108648, A15, MF-A01).

NCEER-89-0013   "Repair and Strengthening of Beam-to-Column Connections Subjected to Earthquake Loading," by M. Corazao and A.J. Durrani, 2/28/89, (PB90-109885, A06, MF-A01).

NCEER-89-0014   "Program EXKAL2 for Identification of Structural Dynamic Systems," by O. Maruyama, C-B. Yun, M. Hoshiya and M. Shinozuka, 5/19/89, (PB90-109877, A09, MF-A01).

669

NCEER-89-0015   "Response of Frames With Bolted Semi-Rigid Connections, Part I - Experimental Study and Analytical Predictions," by P.J. DiCorso, A.M. Reinhorn, J.R. Dickerson, J.B. Radziminski and W.L. Harper, 6/1/89, not available.

NCEER-89-0016   "ARMA Monte Carlo Simulation in Probabilistic Structural Analysis," by P.D. Spanos and M.P. Mignolet, 7/10/89, (PB90-109893, A03, MF-A01).

NCEER-89-P017   "Preliminary Proceedings from the Conference on Disaster Preparedness - The Place of Earthquake Education in Our Schools," Edited by K.E.K. Ross, 6/23/89, (PB90-108606, A03, MF-A01).

NCEER-89-0017   "Proceedings from the Conference on Disaster Preparedness - The Place of Earthquake Education in Our Schools," Edited by K.E.K. Ross, 12/31/89, (PB90-207895, A012, MF-A02). This report is available only through NTIS (see address given above).

NCEER-89-0018   "Multidimensional Models of Hysteretic Material Behavior for Vibration Analysis of Shape Memory Energy Absorbing Devices, by E.J. Graesser and F.A. Cozzarelli, 6/7/89, (PB90-164146, A04, MF-A01).

NCEER-89-0019   "Nonlinear Dynamic Analysis of Three-Dimensional Base Isolated Structures (3D-BASIS)," by S. Nagarajaiah, A.M. Reinhorn and M.C. Constantinou, 8/3/89, (PB90-161936, A06, MF-A01). This report has been replaced by NCEER-93-0011.

NCEER-89-0020   "Structural Control Considering Time-Rate of Control Forces and Control Rate Constraints," by F.Y. Cheng and C.P. Pantelides, 8/3/89, (PB90-120445, A04, MF-A01).

NCEER-89-0021   "Subsurface Conditions of Memphis and Shelby County," by K.W. Ng, T-S. Chang and H-H.M. Hwang, 7/26/89, (PB90-120437, A03, MF-A01).

NCEER-89-0022   "Seismic Wave Propagation Effects on Straight Jointed Buried Pipelines," by K. Elhmadi and M.J. O'Rourke, 8/24/89, (PB90-162322, A10, MF-A02).

NCEER-89-0023   "Workshop on Serviceability Analysis of Water Delivery Systems," edited by M. Grigoriu, 3/6/89, (PB90-127424, A03, MF-A01).

NCEER-89-0024   "Shaking Table Study of a 1/5 Scale Steel Frame Composed of Tapered Members," by K.C. Chang, J.S. Hwang and G.C. Lee, 9/18/89, (PB90-160169, A04, MF-A01).

NCEER-89-0025   "DYNA1D: A Computer Program for Nonlinear Seismic Site Response Analysis - Technical Documentation," by Jean H. Prevost, 9/14/89, (PB90-161944, A07, MF-A01). This report is available only through NTIS (see address given above).

NCEER-89-0026   "1:4 Scale Model Studies of Active Tendon Systems and Active Mass Dampers for Aseismic Protection," by A.M. Reinhorn, T.T. Soong, R.C. Lin, Y.P. Yang, Y. Fukao, H. Abe and M. Nakai, 9/15/89, (PB90-173246, A10, MF-A02). This report is available only through NTIS (see address given above).

NCEER-89-0027   "Scattering of Waves by Inclusions in a Nonhomogeneous Elastic Half Space Solved by Boundary Element Methods," by P.K. Hadley, A. Askar and A.S. Cakmak, 6/15/89, (PB90-145699, A07, MF-A01).

NCEER-89-0028   "Statistical Evaluation of Deflection Amplification Factors for Reinforced Concrete Structures," by H.H.M. Hwang, J-W. Jaw and A.L. Ch'ng, 8/31/89, (PB90-164633, A05, MF-A01).

NCEER-89-0029   "Bedrock Accelerations in Memphis Area Due to Large New Madrid Earthquakes," by H.H.M. Hwang, C.H.S. Chen and G. Yu, 11/7/89, (PB90-162330, A04, MF-A01).

NCEER-89-0030   "Seismic Behavior and Response Sensitivity of Secondary Structural Systems," by Y.Q. Chen and T.T. Soong, 10/23/89, (PB90-164658, A08, MF-A01).

NCEER-89-0031   "Random Vibration and Reliability Analysis of Primary-Secondary Structural Systems," by Y. Ibrahim, M. Grigoriu and T.T. Soong, 11/10/89, (PB90-161951, A04, MF-A01).

NCEER-89-0032   "Proceedings from the Second U.S. - Japan Workshop on Liquefaction, Large Ground Deformation and Their Effects on Lifelines, September 26-29, 1989," Edited by T.D. O'Rourke and M. Hamada, 12/1/89, (PB90-209388, A22, MF-A03).

NCEER-89-0033   "Deterministic Model for Seismic Damage Evaluation of Reinforced Concrete Structures," by J.M. Bracci, A.M. Reinhorn, J.B. Mander and S.K. Kunnath, 9/27/89, (PB91-108803, A06, MF-A01).

NCEER-89-0034   "On the Relation Between Local and Global Damage Indices," by E. DiPasquale and A.S. Cakmak, 8/15/89, (PB90-173865, A05, MF-A01).

NCEER-89-0035   "Cyclic Undrained Behavior of Nonplastic and Low Plasticity Silts," by A.J. Walker and H.E. Stewart, 7/26/89, (PB90-183518, A10, MF-A01).

NCEER-89-0036   "Liquefaction Potential of Surficial Deposits in the City of Buffalo, New York," by M. Budhu, R. Giese and L. Baumgrass, 1/17/89, (PB90-208455, A04, MF-A01).

NCEER-89-0037   "A Deterministic Assessment of Effects of Ground Motion Incoherence," by A.S. Veletsos and Y. Tang, 7/15/89, (PB90-164294, A03, MF-A01).

NCEER-89-0038   "Workshop on Ground Motion Parameters for Seismic Hazard Mapping," July 17-18, 1989, edited by R.V. Whitman, 12/1/89, (PB90-173923, A04, MF-A01).

NCEER-89-0039   "Seismic Effects on Elevated Transit Lines of the New York City Transit Authority," by C.J. Costantino, C.A. Miller and E. Heymsfield, 12/26/89, (PB90-207887, A06, MF-A01).

NCEER-89-0040   "Centrifugal Modeling of Dynamic Soil-Structure Interaction," by K. Weissman, Supervised by J.H. Prevost, 5/10/89, (PB90-207879, A07, MF-A01).

NCEER-89-0041   "Linearized Identification of Buildings With Cores for Seismic Vulnerability Assessment," by I-K. Ho and A.E. Aktan, 11/1/89, (PB90-251943, A07, MF-A01).

NCEER-90-0001   "Geotechnical and Lifeline Aspects of the October 17, 1989 Loma Prieta Earthquake in San Francisco," by T.D. O'Rourke, H.E. Stewart, F.T. Blackburn and T.S. Dickerman, 1/90, (PB90-208596, A05, MF-A01).

NCEER-90-0002   "Nonnormal Secondary Response Due to Yielding in a Primary Structure," by D.C.K. Chen and L.D. Lutes, 2/28/90, (PB90-251976, A07, MF-A01).

NCEER-90-0003   "Earthquake Education Materials for Grades K-12," by K.E.K. Ross, 4/16/90, (PB91-251984, A05, MF-A05). This report has been replaced by NCEER-92-0018.

NCEER-90-0004   "Catalog of Strong Motion Stations in Eastern North America," by R.W. Busby, 4/3/90, (PB90-251984, A05, MF-A01).

NCEER-90-0005   "NCEER Strong-Motion Data Base: A User Manual for the GeoBase Release (Version 1.0 for the Sun3)," by P. Friberg and K. Jacob, 3/31/90 (PB90-258062, A04, MF-A01).

NCEER-90-0006   "Seismic Hazard Along a Crude Oil Pipeline in the Event of an 1811-1812 Type New Madrid Earthquake," by H.H.M. Hwang and C-H.S. Chen, 4/16/90, (PB90-258054, A04, MF-A01).

NCEER-90-0007   "Site-Specific Response Spectra for Memphis Sheahan Pumping Station," by H.H.M. Hwang and C.S. Lee, 5/15/90, (PB91-108811, A05, MF-A01).

NCEER-90-0008   "Pilot Study on Seismic Vulnerability of Crude Oil Transmission Systems," by T. Ariman, R. Dobry, M. Grigoriu, F. Kozin, M. O'Rourke, T. O'Rourke and M. Shinozuka, 5/25/90, (PB91-108837, A06, MF-A01).

NCEER-90-0009   "A Program to Generate Site Dependent Time Histories: EQGEN," by G.W. Ellis, M. Srinivasan and A.S. Cakmak, 1/30/90, (PB91-108829, A04, MF-A01).

NCEER-90-0010   "Active Isolation for Seismic Protection of Operating Rooms," by M.E. Talbott, Supervised by M. Shinozuka, 6/8/9, (PB91-110205, A05, MF-A01).

NCEER-90-0011   "Program LINEARID for Identification of Linear Structural Dynamic Systems," by C-B. Yun and M. Shinozuka, 6/25/90, (PB91-110312, A08, MF-A01).

NCEER-90-0012   "Two-Dimensional Two-Phase Elasto-Plastic Seismic Response of Earth Dams," by A.N. Yiagos, Supervised by J.H. Prevost, 6/20/90, (PB91-110197, A13, MF-A02).

NCEER-90-0013   "Secondary Systems in Base-Isolated Structures: Experimental Investigation, Stochastic Response and Stochastic Sensitivity," by G.D. Manolis, G. Juhn, M.C. Constantinou and A.M. Reinhorn, 7/1/90, (PB91-110320, A08, MF-A01).

NCEER-90-0014   "Seismic Behavior of Lightly-Reinforced Concrete Column and Beam-Column Joint Details," by S.P. Pessiki, C.H. Conley, P. Gergely and R.N. White, 8/22/90, (PB91-108795, A11, MF-A02).

NCEER-90-0015   "Two Hybrid Control Systems for Building Structures Under Strong Earthquakes," by J.N. Yang and A. Danielians, 6/29/90, (PB91-125393, A04, MF-A01).

NCEER-90-0016   "Instantaneous Optimal Control with Acceleration and Velocity Feedback," by J.N. Yang and Z. Li, 6/29/90, (PB91-125401, A03, MF-A01).

NCEER-90-0017   "Reconnaissance Report on the Northern Iran Earthquake of June 21, 1990," by M. Mehrain, 10/4/90, (PB91-125377, A03, MF-A01).

NCEER-90-0018   "Evaluation of Liquefaction Potential in Memphis and Shelby County," by T.S. Chang, P.S. Tang, C.S. Lee and H. Hwang, 8/10/90, (PB91-125427, A09, MF-A01).

NCEER-90-0019   "Experimental and Analytical Study of a Combined Sliding Disc Bearing and Helical Steel Spring Isolation System," by M.C. Constantinou, A.S. Mokha and A.M. Reinhorn, 10/4/90, (PB91-125385, A06, MF-A01). This report is available only through NTIS (see address given above).

NCEER-90-0020   "Experimental Study and Analytical Prediction of Earthquake Response of a Sliding Isolation System with a Spherical Surface," by A.S. Mokha, M.C. Constantinou and A.M. Reinhorn, 10/11/90, (PB91-125419, A05, MF-A01).

NCEER-90-0021   "Dynamic Interaction Factors for Floating Pile Groups," by G. Gazetas, K. Fan, A. Kaynia and E. Kausel, 9/10/90, (PB91-170381, A05, MF-A01).

NCEER-90-0022   "Evaluation of Seismic Damage Indices for Reinforced Concrete Structures," by S. Rodriguez-Gomez and A.S. Cakmak, 9/30/90, PB91-171322, A06, MF-A01).

NCEER-90-0023   "Study of Site Response at a Selected Memphis Site," by H. Desai, S. Ahmad, E.S. Gazetas and M.R. Oh, 10/11/90, (PB91-196857, A03, MF-A01).

NCEER-90-0024   "A User's Guide to Strongmo: Version 1.0 of NCEER's Strong-Motion Data Access Tool for PCs and Terminals," by P.A. Friberg and C.A.T. Susch, 11/15/90, (PB91-171272, A03, MF-A01).

NCEER-90-0025   "A Three-Dimensional Analytical Study of Spatial Variability of Seismic Ground Motions," by L-L. Hong and A.H.-S. Ang, 10/30/90, (PB91-170399, A09, MF-A01).

NCEER-90-0026   "MUMOID User's Guide - A Program for the Identification of Modal Parameters," by S. Rodriguez-Gomez and E. DiPasquale, 9/30/90, (PB91-171298, A04, MF-A01).

NCEER-90-0027   "SARCF-II User's Guide - Seismic Analysis of Reinforced Concrete Frames," by S. Rodriguez-Gomez, Y.S. Chung and C. Meyer, 9/30/90, (PB91-171280, A05, MF-A01).

NCEER-90-0028   "Viscous Dampers: Testing, Modeling and Application in Vibration and Seismic Isolation," by N. Makris and M.C. Constantinou, 12/20/90 (PB91-190561, A06, MF-A01).

NCEER-90-0029   "Soil Effects on Earthquake Ground Motions in the Memphis Area," by H. Hwang, C.S. Lee, K.W. Ng and T.S. Chang, 8/2/90, (PB91-190751, A05, MF-A01).

NCEER-91-0001   "Proceedings from the Third Japan-U.S. Workshop on Earthquake Resistant Design of Lifeline Facilities and Countermeasures for Soil Liquefaction, December 17-19, 1990," edited by T.D. O'Rourke and M. Hamada, 2/1/91, (PB91-179259, A99, MF-A04).

NCEER-91-0002   "Physical Space Solutions of Non-Proportionally Damped Systems," by M. Tong, Z. Liang and G.C. Lee, 1/15/91, (PB91-179242, A04, MF-A01).

NCEER-91-0003   "Seismic Response of Single Piles and Pile Groups," by K. Fan and G. Gazetas, 1/10/91, (PB92-174994, A04, MF-A01).

NCEER-91-0004   "Damping of Structures: Part 1 - Theory of Complex Damping," by Z. Liang and G. Lee, 10/10/91, (PB92-197235, A12, MF-A03).

NCEER-91-0005   "3D-BASIS - Nonlinear Dynamic Analysis of Three Dimensional Base Isolated Structures: Part II," by S. Nagarajaiah, A.M. Reinhorn and M.C. Constantinou, 2/28/91, (PB91-190553, A07, MF-A01). This report has been replaced by NCEER-93-0011.

NCEER-91-0006   "A Multidimensional Hysteretic Model for Plasticity Deforming Metals in Energy Absorbing Devices," by E.J. Graesser and F.A. Cozzarelli, 4/9/91, (PB92-108364, A04, MF-A01).

NCEER-91-0007   "A Framework for Customizable Knowledge-Based Expert Systems with an Application to a KBES for Evaluating the Seismic Resistance of Existing Buildings," by E.G. Ibarra-Anaya and S.J. Fenves, 4/9/91, (PB91-210930, A08, MF-A01).

NCEER-91-0008   "Nonlinear Analysis of Steel Frames with Semi-Rigid Connections Using the Capacity Spectrum Method," by G.G. Deierlein, S-H. Hsieh, Y-J. Shen and J.F. Abel, 7/2/91, (PB92-113828, A05, MF-A01).

NCEER-91-0009   "Earthquake Education Materials for Grades K-12," by K.E.K. Ross, 4/30/91, (PB91-212142, A06, MF-A01). This report has been replaced by NCEER-92-0018.

NCEER-91-0010   "Phase Wave Velocities and Displacement Phase Differences in a Harmonically Oscillating Pile," by N. Makris and G. Gazetas, 7/8/91, (PB92-108356, A04, MF-A01).

NCEER-91-0011   "Dynamic Characteristics of a Full-Size Five-Story Steel Structure and a 2/5 Scale Model," by K.C. Chang, G.C. Yao, G.C. Lee, D.S. Hao and Y.C. Yeh," 7/2/91, (PB93-116648, A06, MF-A02).

NCEER-91-0012   "Seismic Response of a 2/5 Scale Steel Structure with Added Viscoelastic Dampers," by K.C. Chang, T.T. Soong, S-T. Oh and M.L. Lai, 5/17/91, (PB92-110816, A05, MF-A01).

NCEER-91-0013   "Earthquake Response of Retaining Walls; Full-Scale Testing and Computational Modeling," by S. Alampalli and A-W.M. Elgamal, 6/20/91, not available.

NCEER-91-0014   "3D-BASIS-M: Nonlinear Dynamic Analysis of Multiple Building Base Isolated Structures," by P.C. Tsopelas, S. Nagarajaiah, M.C. Constantinou and A.M. Reinhorn, 5/28/91, (PB92-113885, A09, MF-A02).

NCEER-91-0015   "Evaluation of SEAOC Design Requirements for Sliding Isolated Structures," by D. Theodossiou and M.C. Constantinou, 6/10/91, (PB92-114602, A11, MF-A03).

NCEER-91-0016   "Closed-Loop Modal Testing of a 27-Story Reinforced Concrete Flat Plate-Core Building," by H.R. Somaprasad, T. Toksoy, H. Yoshiyuki and A.E. Aktan, 7/15/91, (PB92-129980, A07, MF-A02).

NCEER-91-0017   "Shake Table Test of a 1/6 Scale Two-Story Lightly Reinforced Concrete Building," by A.G. El-Attar, R.N. White and P. Gergely, 2/28/91, (PB92-222447, A06, MF-A02).

NCEER-91-0018   "Shake Table Test of a 1/8 Scale Three-Story Lightly Reinforced Concrete Building," by A.G. El-Attar, R.N. White and P. Gergely, 2/28/91, (PB93-116630, A08, MF-A02).

NCEER-91-0019   "Transfer Functions for Rigid Rectangular Foundations," by A.S. Veletsos, A.M. Prasad and W.H. Wu, 7/31/91, not available.

673

NCEER-91-0020 "Hybrid Control of Seismic-Excited Nonlinear and Inelastic Structural Systems," by J.N. Yang, Z. Li and A. Danielians, 8/1/91, (PB92-143171, A06, MF-A02).

NCEER-91-0021 "The NCEER-91 Earthquake Catalog: Improved Intensity-Based Magnitudes and Recurrence Relations for U.S. Earthquakes East of New Madrid," by L. Seeber and J.G. Armbruster, 8/28/91, (PB92-176742, A06, MF-A02).

NCEER-91-0022 "Proceedings from the Implementation of Earthquake Planning and Education in Schools: The Need for Change - The Roles of the Changemakers," by K.E.K. Ross and F. Winslow, 7/23/91, (PB92-129998, A12, MF-A03).

NCEER-91-0023 "A Study of Reliability-Based Criteria for Seismic Design of Reinforced Concrete Frame Buildings," by H.H.M. Hwang and H-M. Hsu, 8/10/91, (PB92-140235, A09, MF-A02).

NCEER-91-0024 "Experimental Verification of a Number of Structural System Identification Algorithms," by R.G. Ghanem, H. Gavin and M. Shinozuka, 9/18/91, (PB92-176577, A18, MF-A04).

NCEER-91-0025 "Probabilistic Evaluation of Liquefaction Potential," by H.H.M. Hwang and C.S. Lee," 11/25/91, (PB92-143429, A05, MF-A01).

NCEER-91-0026 "Instantaneous Optimal Control for Linear, Nonlinear and Hysteretic Structures - Stable Controllers," by J.N. Yang and Z. Li, 11/15/91, (PB92-163807, A04, MF-A01).

NCEER-91-0027 "Experimental and Theoretical Study of a Sliding Isolation System for Bridges," by M.C. Constantinou, A. Kartoum, A.M. Reinhorn and P. Bradford, 11/15/91, (PB92-176973, A10, MF-A03).

NCEER-92-0001 "Case Studies of Liquefaction and Lifeline Performance During Past Earthquakes, Volume 1: Japanese Case Studies," Edited by M. Hamada and T. O'Rourke, 2/17/92, (PB92-197243, A18, MF-A04).

NCEER-92-0002 "Case Studies of Liquefaction and Lifeline Performance During Past Earthquakes, Volume 2: United States Case Studies," Edited by T. O'Rourke and M. Hamada, 2/17/92, (PB92-197250, A20, MF-A04).

NCEER-92-0003 "Issues in Earthquake Education," Edited by K. Ross, 2/3/92, (PB92-222389, A07, MF-A02).

NCEER-92-0004 "Proceedings from the First U.S. - Japan Workshop on Earthquake Protective Systems for Bridges," Edited by I.G. Buckle, 2/4/92, (PB94-142239, A99, MF-A06).

NCEER-92-0005 "Seismic Ground Motion from a Haskell-Type Source in a Multiple-Layered Half-Space," A.P. Theoharis, G. Deodatis and M. Shinozuka, 1/2/92, not available.

NCEER-92-0006 "Proceedings from the Site Effects Workshop," Edited by R. Whitman, 2/29/92, (PB92-197201, A04, MF-A01).

NCEER-92-0007 "Engineering Evaluation of Permanent Ground Deformations Due to Seismically-Induced Liquefaction," by M.H. Baziar, R. Dobry and A-W.M. Elgamal, 3/24/92, (PB92-222421, A13, MF-A03).

NCEER-92-0008 "A Procedure for the Seismic Evaluation of Buildings in the Central and Eastern United States," by C.D. Poland and J.O. Malley, 4/2/92, (PB92-222439, A20, MF-A04).

NCEER-92-0009 "Experimental and Analytical Study of a Hybrid Isolation System Using Friction Controllable Sliding Bearings," by M.Q. Feng, S. Fujii and M. Shinozuka, 5/15/92, (PB93-150282, A06, MF-A02).

NCEER-92-0010 "Seismic Resistance of Slab-Column Connections in Existing Non-Ductile Flat-Plate Buildings," by A.J. Durrani and Y. Du, 5/18/92, (PB93-116812, A06, MF-A02).

NCEER-92-0011 "The Hysteretic and Dynamic Behavior of Brick Masonry Walls Upgraded by Ferrocement Coatings Under Cyclic Loading and Strong Simulated Ground Motion," by H. Lee and S.P. Prawel, 5/11/92, not available.

NCEER-92-0012 "Study of Wire Rope Systems for Seismic Protection of Equipment in Buildings," by G.F. Demetriades, M.C. Constantinou and A.M. Reinhorn, 5/20/92, (PB93-116655, A08, MF-A02).

NCEER-92-0013   "Shape Memory Structural Dampers: Material Properties, Design and Seismic Testing," by P.R. Witting and F.A. Cozzarelli, 5/26/92, (PB93-116663, A05, MF-A01).

NCEER-92-0014   "Longitudinal Permanent Ground Deformation Effects on Buried Continuous Pipelines," by M.J. O'Rourke, and C. Nordberg, 6/15/92, (PB93-116671, A08, MF-A02).

NCEER-92-0015   "A Simulation Method for Stationary Gaussian Random Functions Based on the Sampling Theorem," by M. Grigoriu and S. Balopoulou, 6/11/92, (PB93-127496, A05, MF-A01).

NCEER-92-0016   "Gravity-Load-Designed Reinforced Concrete Buildings: Seismic Evaluation of Existing Construction and Detailing Strategies for Improved Seismic Resistance," by G.W. Hoffmann, S.K. Kunnath, A.M. Reinhorn and J.B. Mander, 7/15/92, (PB94-142007, A08, MF-A02).

NCEER-92-0017   "Observations on Water System and Pipeline Performance in the Limón Area of Costa Rica Due to the April 22, 1991 Earthquake," by M. O'Rourke and D. Ballantyne, 6/30/92, (PB93-126811, A06, MF-A02).

NCEER-92-0018   "Fourth Edition of Earthquake Education Materials for Grades K-12," Edited by K.E.K. Ross, 8/10/92, (PB93-114023, A07, MF-A02).

NCEER-92-0019   "Proceedings from the Fourth Japan-U.S. Workshop on Earthquake Resistant Design of Lifeline Facilities and Countermeasures for Soil Liquefaction," Edited by M. Hamada and T.D. O'Rourke, 8/12/92, (PB93-163939, A99, MF-E11).

NCEER-92-0020   "Active Bracing System: A Full Scale Implementation of Active Control," by A.M. Reinhorn, T.T. Soong, R.C. Lin, M.A. Riley, Y.P. Wang, S. Aizawa and M. Higashino, 8/14/92, (PB93-127512, A06, MF-A02).

NCEER-92-0021   "Empirical Analysis of Horizontal Ground Displacement Generated by Liquefaction-Induced Lateral Spreads," by S.F. Bartlett and T.L. Youd, 8/17/92, (PB93-188241, A06, MF-A02).

NCEER-92-0022   "IDARC Version 3.0: Inelastic Damage Analysis of Reinforced Concrete Structures," by S.K. Kunnath, A.M. Reinhorn and R.F. Lobo, 8/31/92, (PB93-227502, A07, MF-A02).

NCEER-92-0023   "A Semi-Empirical Analysis of Strong-Motion Peaks in Terms of Seismic Source, Propagation Path and Local Site Conditions, by M. Kamiyama, M.J. O'Rourke and R. Flores-Berrones, 9/9/92, (PB93-150266, A08, MF-A02).

NCEER-92-0024   "Seismic Behavior of Reinforced Concrete Frame Structures with Nonductile Details, Part I: Summary of Experimental Findings of Full Scale Beam-Column Joint Tests," by A. Beres, R.N. White and P. Gergely, 9/30/92, (PB93-227783, A05, MF-A01).

NCEER-92-0025   "Experimental Results of Repaired and Retrofitted Beam-Column Joint Tests in Lightly Reinforced Concrete Frame Buildings," by A. Beres, S. El-Borgi, R.N. White and P. Gergely, 10/29/92, (PB93-227791, A05, MF-A01).

NCEER-92-0026   "A Generalization of Optimal Control Theory: Linear and Nonlinear Structures," by J.N. Yang, Z. Li and S. Vongchavalitkul, 11/2/92, (PB93-188621, A05, MF-A01).

NCEER-92-0027   "Seismic Resistance of Reinforced Concrete Frame Structures Designed Only for Gravity Loads: Part I - Design and Properties of a One-Third Scale Model Structure," by J.M. Bracci, A.M. Reinhorn and J.B. Mander, 12/1/92, (PB94-104502, A08, MF-A02).

NCEER-92-0028   "Seismic Resistance of Reinforced Concrete Frame Structures Designed Only for Gravity Loads: Part II - Experimental Performance of Subassemblages," by L.E. Aycardi, J.B. Mander and A.M. Reinhorn, 12/1/92, (PB94-104510, A08, MF-A02).

NCEER-92-0029   "Seismic Resistance of Reinforced Concrete Frame Structures Designed Only for Gravity Loads: Part III - Experimental Performance and Analytical Study of a Structural Model," by J.M. Bracci, A.M. Reinhorn and J.B. Mander, 12/1/92, (PB93-227528, A09, MF-A01).

NCEER-92-0030   "Evaluation of Seismic Retrofit of Reinforced Concrete Frame Structures: Part I - Experimental Performance of Retrofitted Subassemblages," by D. Choudhuri, J.B. Mander and A.M. Reinhorn, 12/8/92, (PB93-198307, A07, MF-A02).

NCEER-92-0031   "Evaluation of Seismic Retrofit of Reinforced Concrete Frame Structures: Part II - Experimental Performance and Analytical Study of a Retrofitted Structural Model," by J.M. Bracci, A.M. Reinhorn and J.B. Mander, 12/8/92, (PB93-198315, A09, MF-A03).

NCEER-92-0032   "Experimental and Analytical Investigation of Seismic Response of Structures with Supplemental Fluid Viscous Dampers," by M.C. Constantinou and M.D. Symans, 12/21/92, (PB93-191435, A10, MF-A03). This report is available only through NTIS (see address given above).

NCEER-92-0033   "Reconnaissance Report on the Cairo, Egypt Earthquake of October 12, 1992," by M. Khater, 12/23/92, (PB93-188621, A03, MF-A01).

NCEER-92-0034   "Low-Level Dynamic Characteristics of Four Tall Flat-Plate Buildings in New York City," by H. Gavin, S. Yuan, J. Grossman, E. Pekelis and K. Jacob, 12/28/92, (PB93-188217, A07, MF-A02).

NCEER-93-0001   "An Experimental Study on the Seismic Performance of Brick-Infilled Steel Frames With and Without Retrofit," by J.B. Mander, B. Nair, K. Wojtkowski and J. Ma, 1/29/93, (PB93-227510, A07, MF-A02).

NCEER-93-0002   "Social Accounting for Disaster Preparedness and Recovery Planning," by S. Cole, E. Pantoja and V. Razak, 2/22/93, (PB94-142114, A12, MF-A03).

NCEER-93-0003   "Assessment of 1991 NEHRP Provisions for Nonstructural Components and Recommended Revisions," by T.T. Soong, G. Chen, Z. Wu, R-H. Zhang and M. Grigoriu, 3/1/93, (PB93-188639, A06, MF-A02).

NCEER-93-0004   "Evaluation of Static and Response Spectrum Analysis Procedures of SEAOC/UBC for Seismic Isolated Structures," by C.W. Winters and M.C. Constantinou, 3/23/93, (PB93-198299, A10, MF-A03).

NCEER-93-0005   "Earthquakes in the Northeast - Are We Ignoring the Hazard? A Workshop on Earthquake Science and Safety for Educators," edited by K.E.K. Ross, 4/2/93, (PB94-103066, A09, MF-A02).

NCEER-93-0006   "Inelastic Response of Reinforced Concrete Structures with Viscoelastic Braces," by R.F. Lobo, J.M. Bracci, K.L. Shen, A.M. Reinhorn and T.T. Soong, 4/5/93, (PB93-227486, A05, MF-A02).

NCEER-93-0007   "Seismic Testing of Installation Methods for Computers and Data Processing Equipment," by K. Kosar, T.T. Soong, K.L. Shen, J.A. HoLung and Y.K. Lin, 4/12/93, (PB93-198299, A07, MF-A02).

NCEER-93-0008   "Retrofit of Reinforced Concrete Frames Using Added Dampers," by A. Reinhorn, M. Constantinou and C. Li, not available.

NCEER-93-0009   "Seismic Behavior and Design Guidelines for Steel Frame Structures with Added Viscoelastic Dampers," by K.C. Chang, M.L. Lai, T.T. Soong, D.S. Hao and Y.C. Yeh, 5/1/93, (PB94-141959, A07, MF-A02).

NCEER-93-0010   "Seismic Performance of Shear-Critical Reinforced Concrete Bridge Piers," by J.B. Mander, S.M. Waheed, M.T.A. Chaudhary and S.S. Chen, 5/12/93, (PB93-227494, A08, MF-A02).

NCEER-93-0011   "3D-BASIS-TABS: Computer Program for Nonlinear Dynamic Analysis of Three Dimensional Base Isolated Structures," by S. Nagarajaiah, C. Li, A.M. Reinhorn and M.C. Constantinou, 8/2/93, (PB94-141819, A09, MF-A02).

NCEER-93-0012   "Effects of Hydrocarbon Spills from an Oil Pipeline Break on Ground Water," by O.J. Helweg and H.H.M. Hwang, 8/3/93, (PB94-141942, A06, MF-A02).

NCEER-93-0013   "Simplified Procedures for Seismic Design of Nonstructural Components and Assessment of Current Code Provisions," by M.P. Singh, L.E. Suarez, E.E. Matheu and G.O. Maldonado, 8/4/93, (PB94-141827, A09, MF-A02).

NCEER-93-0014   "An Energy Approach to Seismic Analysis and Design of Secondary Systems," by G. Chen and T.T. Soong, 8/6/93, (PB94-142767, A11, MF-A03).

NCEER-93-0015   "Proceedings from School Sites: Becoming Prepared for Earthquakes - Commemorating the Third Anniversary of the Loma Prieta Earthquake," Edited by F.E. Winslow and K.E.K. Ross, 8/16/93, (PB94-154275, A16, MF-A02).

NCEER-93-0016   "Reconnaissance Report of Damage to Historic Monuments in Cairo, Egypt Following the October 12, 1992 Dahshur Earthquake," by D. Sykora, D. Look, G. Croci, E. Karaesmen and E. Karaesmen, 8/19/93, (PB94-142221, A08, MF-A02).

NCEER-93-0017   "The Island of Guam Earthquake of August 8, 1993," by S.W. Swan and S.K. Harris, 9/30/93, (PB94-141843, A04, MF-A01).

NCEER-93-0018   "Engineering Aspects of the October 12, 1992 Egyptian Earthquake," by A.W. Elgamal, M. Amer, K. Adalier and A. Abul-Fadl, 10/7/93, (PB94-141983, A05, MF-A01).

NCEER-93-0019   "Development of an Earthquake Motion Simulator and its Application in Dynamic Centrifuge Testing," by I. Krstelj, Supervised by J.H. Prevost, 10/23/93, (PB94-181773, A-10, MF-A03).

NCEER-93-0020   "NCEER-Taisei Corporation Research Program on Sliding Seismic Isolation Systems for Bridges: Experimental and Analytical Study of a Friction Pendulum System (FPS)," by M.C. Constantinou, P. Tsopelas, Y-S. Kim and S. Okamoto, 11/1/93, (PB94-142775, A08, MF-A02).

NCEER-93-0021   "Finite Element Modeling of Elastomeric Seismic Isolation Bearings," by L.J. Billings, Supervised by R. Shepherd, 11/8/93, not available.

NCEER-93-0022   "Seismic Vulnerability of Equipment in Critical Facilities: Life-Safety and Operational Consequences," by K. Porter, G.S. Johnson, M.M. Zadeh, C. Scawthorn and S. Eder, 11/24/93, (PB94-181765, A16, MF-A03).

NCEER-93-0023   "Hokkaido Nansei-oki, Japan Earthquake of July 12, 1993, by P.I. Yanev and C.R. Scawthorn, 12/23/93, (PB94-181500, A07, MF-A01).

NCEER-94-0001   "An Evaluation of Seismic Serviceability of Water Supply Networks with Application to the San Francisco Auxiliary Water Supply System," by I. Markov, Supervised by M. Grigoriu and T. O'Rourke, 1/21/94, (PB94-204013, A07, MF-A02).

NCEER-94-0002   "NCEER-Taisei Corporation Research Program on Sliding Seismic Isolation Systems for Bridges: Experimental and Analytical Study of Systems Consisting of Sliding Bearings, Rubber Restoring Force Devices and Fluid Dampers," Volumes I and II, by P. Tsopelas, S. Okamoto, M.C. Constantinou, D. Ozaki and S. Fujii, 2/4/94, (PB94-181740, A09, MF-A02 and PB94-181757, A12, MF-A03).

NCEER-94-0003   "A Markov Model for Local and Global Damage Indices in Seismic Analysis," by S. Rahman and M. Grigoriu, 2/18/94, (PB94-206000, A12, MF-A03).

NCEER-94-0004   "Proceedings from the NCEER Workshop on Seismic Response of Masonry Infills," edited by D.P. Abrams, 3/1/94, (PB94-180783, A07, MF-A02).

NCEER-94-0005   "The Northridge, California Earthquake of January 17, 1994: General Reconnaissance Report," edited by J.D. Goltz, 3/11/94, (PB94-193943, A10, MF-A03).

NCEER-94-0006   "Seismic Energy Based Fatigue Damage Analysis of Bridge Columns: Part I - Evaluation of Seismic Capacity," by G.A. Chang and J.B. Mander, 3/14/94, (PB94-219185, A11, MF-A03).

NCEER-94-0007   "Seismic Isolation of Multi-Story Frame Structures Using Spherical Sliding Isolation Systems," by T.M. Al-Hussaini, V.A. Zayas and M.C. Constantinou, 3/17/94, (PB94-193745, A09, MF-A02).

NCEER-94-0008   "The Northridge, California Earthquake of January 17, 1994: Performance of Highway Bridges," edited by I.G. Buckle, 3/24/94, (PB94-193851, A06, MF-A02).

NCEER-94-0009   "Proceedings of the Third U.S.-Japan Workshop on Earthquake Protective Systems for Bridges," edited by I.G. Buckle and I. Friedland, 3/31/94, (PB94-195815, A99, MF-A06).

NCEER-94-0010   "3D-BASIS-ME: Computer Program for Nonlinear Dynamic Analysis of Seismically Isolated Single and Multiple Structures and Liquid Storage Tanks," by P.C. Tsopelas, M.C. Constantinou and A.M. Reinhorn, 4/12/94, (PB94-204922, A09, MF-A02).

NCEER-94-0011   "The Northridge, California Earthquake of January 17, 1994: Performance of Gas Transmission Pipelines," by T.D. O'Rourke and M.C. Palmer, 5/16/94, (PB94-204989, A05, MF-A01).

NCEER-94-0012   "Feasibility Study of Replacement Procedures and Earthquake Performance Related to Gas Transmission Pipelines," by T.D. O'Rourke and M.C. Palmer, 5/25/94, (PB94-206638, A09, MF-A02).

NCEER-94-0013   "Seismic Energy Based Fatigue Damage Analysis of Bridge Columns: Part II - Evaluation of Seismic Demand," by G.A. Chang and J.B. Mander, 6/1/94, (PB95-18106, A08, MF-A02).

NCEER-94-0014   "NCEER-Taisei Corporation Research Program on Sliding Seismic Isolation Systems for Bridges: Experimental and Analytical Study of a System Consisting of Sliding Bearings and Fluid Restoring Force/Damping Devices," by P. Tsopelas and M.C. Constantinou, 6/13/94, (PB94-219144, A10, MF-A03).

NCEER-94-0015   "Generation of Hazard-Consistent Fragility Curves for Seismic Loss Estimation Studies," by H. Hwang and J-R. Huo, 6/14/94, (PB95-181996, A09, MF-A02).

NCEER-94-0016   "Seismic Study of Building Frames with Added Energy-Absorbing Devices," by W.S. Pong, C.S. Tsai and G.C. Lee, 6/20/94, (PB94-219136, A10, A03).

NCEER-94-0017   "Sliding Mode Control for Seismic-Excited Linear and Nonlinear Civil Engineering Structures," by J. Yang, J. Wu, A. Agrawal and Z. Li, 6/21/94, (PB95-138483, A06, MF-A02).

NCEER-94-0018   "3D-BASIS-TABS Version 2.0: Computer Program for Nonlinear Dynamic Analysis of Three Dimensional Base Isolated Structures," by A.M. Reinhorn, S. Nagarajaiah, M.C. Constantinou, P. Tsopelas and R. Li, 6/22/94, (PB95-182176, A08, MF-A02).

NCEER-94-0019   "Proceedings of the International Workshop on Civil Infrastructure Systems: Application of Intelligent Systems and Advanced Materials on Bridge Systems," Edited by G.C. Lee and K.C. Chang, 7/18/94, (PB95-252474, A20, MF-A04).

NCEER-94-0020   "Study of Seismic Isolation Systems for Computer Floors," by V. Lambrou and M.C. Constantinou, 7/19/94, (PB95-138533, A10, MF-A03).

NCEER-94-0021   "Proceedings of the U.S.-Italian Workshop on Guidelines for Seismic Evaluation and Rehabilitation of Unreinforced Masonry Buildings," Edited by D.P. Abrams and G.M. Calvi, 7/20/94, (PB95-138749, A13, MF-A03).

NCEER-94-0022   "NCEER-Taisei Corporation Research Program on Sliding Seismic Isolation Systems for Bridges: Experimental and Analytical Study of a System Consisting of Lubricated PTFE Sliding Bearings and Mild Steel Dampers," by P. Tsopelas and M.C. Constantinou, 7/22/94, (PB95-182184, A08, MF-A02).

NCEER-94-0023   "Development of Reliability-Based Design Criteria for Buildings Under Seismic Load," by Y.K. Wen, H. Hwang and M. Shinozuka, 8/1/94, (PB95-211934, A08, MF-A02).

NCEER-94-0024   "Experimental Verification of Acceleration Feedback Control Strategies for an Active Tendon System," by S.J. Dyke, B.F. Spencer, Jr., P. Quast, M.K. Sain, D.C. Kaspari, Jr. and T.T. Soong, 8/29/94, (PB95-212320, A05, MF-A01).

NCEER-94-0025   "Seismic Retrofitting Manual for Highway Bridges," Edited by I.G. Buckle and I.F. Friedland, published by the Federal Highway Administration (PB95-212676, A15, MF-A03).

NCEER-94-0026   "Proceedings from the Fifth U.S.-Japan Workshop on Earthquake Resistant Design of Lifeline Facilities and Countermeasures Against Soil Liquefaction," Edited by T.D. O'Rourke and M. Hamada, 11/7/94, (PB95-220802, A99, MF-E08).

NCEER-95-0001 "Experimental and Analytical Investigation of Seismic Retrofit of Structures with Supplemental Damping: Part 1 - Fluid Viscous Damping Devices," by A.M. Reinhorn, C. Li and M.C. Constantinou, 1/3/95, (PB95-266599, A09, MF-A02).

NCEER-95-0002 "Experimental and Analytical Study of Low-Cycle Fatigue Behavior of Semi-Rigid Top-And-Seat Angle Connections," by G. Pekcan, J.B. Mander and S.S. Chen, 1/5/95, (PB95-220042, A07, MF-A02).

NCEER-95-0003 "NCEER-ATC Joint Study on Fragility of Buildings," by T. Anagnos, C. Rojahn and A.S. Kiremidjian, 1/20/95, (PB95-220026, A06, MF-A02).

NCEER-95-0004 "Nonlinear Control Algorithms for Peak Response Reduction," by Z. Wu, T.T. Soong, V. Gattulli and R.C. Lin, 2/16/95, (PB95-220349, A05, MF-A01).

NCEER-95-0005 "Pipeline Replacement Feasibility Study: A Methodology for Minimizing Seismic and Corrosion Risks to Underground Natural Gas Pipelines," by R.T. Eguchi, H.A. Seligson and D.G. Honegger, 3/2/95, (PB95-252326, A06, MF-A02).

NCEER-95-0006 "Evaluation of Seismic Performance of an 11-Story Frame Building During the 1994 Northridge Earthquake," by F. Naeim, R. DiSulio, K. Benuska, A. Reinhorn and C. Li, not available.

NCEER-95-0007 "Prioritization of Bridges for Seismic Retrofitting," by N. Basöz and A.S. Kiremidjian, 4/24/95, (PB95-252300, A08, MF-A02).

NCEER-95-0008 "Method for Developing Motion Damage Relationships for Reinforced Concrete Frames," by A. Singhal and A.S. Kiremidjian, 5/11/95, (PB95-266607, A06, MF-A02).

NCEER-95-0009 "Experimental and Analytical Investigation of Seismic Retrofit of Structures with Supplemental Damping: Part II - Friction Devices," by C. Li and A.M. Reinhorn, 7/6/95, (PB96-128087, A11, MF-A03).

NCEER-95-0010 "Experimental Performance and Analytical Study of a Non-Ductile Reinforced Concrete Frame Structure Retrofitted with Elastomeric Spring Dampers," by G. Pekcan, J.B. Mander and S.S. Chen, 7/14/95, (PB96-137161, A08, MF-A02).

NCEER-95-0011 "Development and Experimental Study of Semi-Active Fluid Damping Devices for Seismic Protection of Structures," by M.D. Symans and M.C. Constantinou, 8/3/95, (PB96-136940, A23, MF-A04).

NCEER-95-0012 "Real-Time Structural Parameter Modification (RSPM): Development of Innervated Structures," by Z. Liang, M. Tong and G.C. Lee, 4/11/95, (PB96-137153, A06, MF-A01).

NCEER-95-0013 "Experimental and Analytical Investigation of Seismic Retrofit of Structures with Supplemental Damping: Part III - Viscous Damping Walls," by A.M. Reinhorn and C. Li, 10/1/95, (PB96-176409, A11, MF-A03).

NCEER-95-0014 "Seismic Fragility Analysis of Equipment and Structures in a Memphis Electric Substation," by J-R. Huo and H.H.M. Hwang, 8/10/95, (PB96-128087, A09, MF-A02).

NCEER-95-0015 "The Hanshin-Awaji Earthquake of January 17, 1995: Performance of Lifelines," Edited by M. Shinozuka, 11/3/95, (PB96-176383, A15, MF-A03).

NCEER-95-0016 "Highway Culvert Performance During Earthquakes," by T.L. Youd and C.J. Beckman, available as NCEER-96-0015.

NCEER-95-0017 "The Hanshin-Awaji Earthquake of January 17, 1995: Performance of Highway Bridges," Edited by I.G. Buckle, 12/1/95, not available.

NCEER-95-0018 "Modeling of Masonry Infill Panels for Structural Analysis," by A.M. Reinhorn, A. Madan, R.E. Valles, Y. Reichmann and J.B. Mander, 12/8/95, (PB97-110886, MF-A01, A06).

NCEER-95-0019 "Optimal Polynomial Control for Linear and Nonlinear Structures," by A.K. Agrawal and J.N. Yang, 12/11/95, (PB96-168737, A07, MF-A02).

NCEER-95-0020   "Retrofit of Non-Ductile Reinforced Concrete Frames Using Friction Dampers," by R.S. Rao, P. Gergely and R.N. White, 12/22/95, (PB97-133508, A10, MF-A02).

NCEER-95-0021   "Parametric Results for Seismic Response of Pile-Supported Bridge Bents," by G. Mylonakis, A. Nikolaou and G. Gazetas, 12/22/95, (PB97-100242, A12, MF-A03).

NCEER-95-0022   "Kinematic Bending Moments in Seismically Stressed Piles," by A. Nikolaou, G. Mylonakis and G. Gazetas, 12/23/95, (PB97-113914, MF-A03, A13).

NCEER-96-0001   "Dynamic Response of Unreinforced Masonry Buildings with Flexible Diaphragms," by A.C. Costley and D.P. Abrams," 10/10/96, (PB97-133573, MF-A03, A15).

NCEER-96-0002   "State of the Art Review: Foundations and Retaining Structures," by I. Po Lam, not available.

NCEER-96-0003   "Ductility of Rectangular Reinforced Concrete Bridge Columns with Moderate Confinement," by N. Wehbe, M. Saiidi, D. Sanders and B. Douglas, 11/7/96, (PB97-133557, A06, MF-A02).

NCEER-96-0004   "Proceedings of the Long-Span Bridge Seismic Research Workshop," edited by I.G. Buckle and I.M. Friedland, not available.

NCEER-96-0005   "Establish Representative Pier Types for Comprehensive Study: Eastern United States," by J. Kulicki and Z. Prucz, 5/28/96, (PB98-119217, A07, MF-A02).

NCEER-96-0006   "Establish Representative Pier Types for Comprehensive Study: Western United States," by R. Imbsen, R.A. Schamber and T.A. Osterkamp, 5/28/96, (PB98-118607, A07, MF-A02).

NCEER-96-0007   "Nonlinear Control Techniques for Dynamical Systems with Uncertain Parameters," by R.G. Ghanem and M.I. Bujakov, 5/27/96, (PB97-100259, A17, MF-A03).

NCEER-96-0008   "Seismic Evaluation of a 30-Year Old Non-Ductile Highway Bridge Pier and Its Retrofit," by J.B. Mander, B. Mahmoodzadegan, S. Bhadra and S.S. Chen, 5/31/96, (PB97-110902, MF-A03, A10).

NCEER-96-0009   "Seismic Performance of a Model Reinforced Concrete Bridge Pier Before and After Retrofit," by J.B. Mander, J.H. Kim and C.A. Ligozio, 5/31/96, (PB97-110910, MF-A02, A10).

NCEER-96-0010   "IDARC2D Version 4.0: A Computer Program for the Inelastic Damage Analysis of Buildings," by R.E. Valles, A.M. Reinhorn, S.K. Kunnath, C. Li and A. Madan, 6/3/96, (PB97-100234, A17, MF-A03).

NCEER-96-0011   "Estimation of the Economic Impact of Multiple Lifeline Disruption: Memphis Light, Gas and Water Division Case Study," by S.E. Chang, H.A. Seligson and R.T. Eguchi, 8/16/96, (PB97-133490, A11, MF-A03).

NCEER-96-0012   "Proceedings from the Sixth Japan-U.S. Workshop on Earthquake Resistant Design of Lifeline Facilities and Countermeasures Against Soil Liquefaction, Edited by M. Hamada and T. O'Rourke, 9/11/96, (PB97-133581, A99, MF-A06).

NCEER-96-0013   "Chemical Hazards, Mitigation and Preparedness in Areas of High Seismic Risk: A Methodology for Estimating the Risk of Post-Earthquake Hazardous Materials Release," by H.A. Seligson, R.T. Eguchi, K.J. Tierney and K. Richmond, 11/7/96, (PB97-133565, MF-A02, A08).

NCEER-96-0014   "Response of Steel Bridge Bearings to Reversed Cyclic Loading," by J.B. Mander, D-K. Kim, S.S. Chen and G.J. Premus, 11/13/96, (PB97-140735, A12, MF-A03).

NCEER-96-0015   "Highway Culvert Performance During Past Earthquakes," by T.L. Youd and C.J. Beckman, 11/25/96, (PB97-133532, A06, MF-A01).

NCEER-97-0001   "Evaluation, Prevention and Mitigation of Pounding Effects in Building Structures," by R.E. Valles and A.M. Reinhorn, 2/20/97, (PB97-159552, A14, MF-A03).

NCEER-97-0002   "Seismic Design Criteria for Bridges and Other Highway Structures," by C. Rojahn, R. Mayes, D.G. Anderson, J. Clark, J.H. Hom, R.V. Nutt and M.J. O'Rourke, 4/30/97, (PB97-194658, A06, MF-A03).

680

NCEER-97-0003   "Proceedings of the U.S.-Italian Workshop on Seismic Evaluation and Retrofit," Edited by D.P. Abrams and G.M. Calvi, 3/19/97, (PB97-194666, A13, MF-A03).

NCEER-97-0004   "Investigation of Seismic Response of Buildings with Linear and Nonlinear Fluid Viscous Dampers," by A.A. Seleemah and M.C. Constantinou, 5/21/97, (PB98-109002, A15, MF-A03).

NCEER-97-0005   "Proceedings of the Workshop on Earthquake Engineering Frontiers in Transportation Facilities," edited by G.C. Lee and I.M. Friedland, 8/29/97, (PB98-128911, A25, MR-A04).

NCEER-97-0006   "Cumulative Seismic Damage of Reinforced Concrete Bridge Piers," by S.K. Kunnath, A. El-Bahy, A. Taylor and W. Stone, 9/2/97, (PB98-108814, A11, MF-A03).

NCEER-97-0007   "Structural Details to Accommodate Seismic Movements of Highway Bridges and Retaining Walls," by R.A. Imbsen, R.A. Schamber, E. Thorkildsen, A. Kartoum, B.T. Martin, T.N. Rosser and J.M. Kulicki, 9/3/97, (PB98-108996, A09, MF-A02).

NCEER-97-0008   "A Method for Earthquake Motion-Damage Relationships with Application to Reinforced Concrete Frames," by A. Singhal and A.S. Kiremidjian, 9/10/97, (PB98-108988, A13, MF-A03).

NCEER-97-0009   "Seismic Analysis and Design of Bridge Abutments Considering Sliding and Rotation," by K. Fishman and R. Richards, Jr., 9/15/97, (PB98-108897, A06, MF-A02).

NCEER-97-0010   "Proceedings of the FHWA/NCEER Workshop on the National Representation of Seismic Ground Motion for New and Existing Highway Facilities," edited by I.M. Friedland, M.S. Power and R.L. Mayes, 9/22/97, (PB98-128903, A21, MF-A04).

NCEER-97-0011   "Seismic Analysis for Design or Retrofit of Gravity Bridge Abutments," by K.L. Fishman, R. Richards, Jr. and R.C. Divito, 10/2/97, (PB98-128937, A08, MF-A02).

NCEER-97-0012   "Evaluation of Simplified Methods of Analysis for Yielding Structures," by P. Tsopelas, M.C. Constantinou, C.A. Kircher and A.S. Whittaker, 10/31/97, (PB98-128929, A10, MF-A03).

NCEER-97-0013   "Seismic Design of Bridge Columns Based on Control and Repairability of Damage," by C-T. Cheng and J.B. Mander, 12/8/97, (PB98-144249, A11, MF-A03).

NCEER-97-0014   "Seismic Resistance of Bridge Piers Based on Damage Avoidance Design," by J.B. Mander and C-T. Cheng, 12/10/97, (PB98-144223, A09, MF-A02).

NCEER-97-0015   "Seismic Response of Nominally Symmetric Systems with Strength Uncertainty," by S. Balopoulou and M. Grigoriu, 12/23/97, (PB98-153422, A11, MF-A03).

NCEER-97-0016   "Evaluation of Seismic Retrofit Methods for Reinforced Concrete Bridge Columns," by T.J. Wipf, F.W. Klaiber and F.M. Russo, 12/28/97, (PB98-144215, A12, MF-A03).

NCEER-97-0017   "Seismic Fragility of Existing Conventional Reinforced Concrete Highway Bridges," by C.L. Mullen and A.S. Cakmak, 12/30/97, (PB98-153406, A08, MF-A02).

NCEER-97-0018   "Loss Asssessment of Memphis Buildings," edited by D.P. Abrams and M. Shinozuka, 12/31/97, (PB98-144231, A13, MF-A03).

NCEER-97-0019   "Seismic Evaluation of Frames with Infill Walls Using Quasi-static Experiments," by K.M. Mosalam, R.N. White and P. Gergely, 12/31/97, (PB98-153455, A07, MF-A02).

NCEER-97-0020   "Seismic Evaluation of Frames with Infill Walls Using Pseudo-dynamic Experiments," by K.M. Mosalam, R.N. White and P. Gergely, 12/31/97, (PB98-153430, A07, MF-A02).

NCEER-97-0021   "Computational Strategies for Frames with Infill Walls: Discrete and Smeared Crack Analyses and Seismic Fragility," by K.M. Mosalam, R.N. White and P. Gergely, 12/31/97, (PB98-153414, A10, MF-A02).

NCEER-97-0022   "Proceedings of the NCEER Workshop on Evaluation of Liquefaction Resistance of Soils," edited by T.L. Youd and I.M. Idriss, 12/31/97, (PB98-155617, A15, MF-A03).

MCEER-98-0001   "Extraction of Nonlinear Hysteretic Properties of Seismically Isolated Bridges from Quick-Release Field Tests," by Q. Chen, B.M. Douglas, E.M. Maragakis and I.G. Buckle, 5/26/98, (PB99-118838, A06, MF-A01).

MCEER-98-0002   "Methodologies for Evaluating the Importance of Highway Bridges," by A. Thomas, S. Eshenaur and J. Kulicki, 5/29/98, (PB99-118846, A10, MF-A02).

MCEER-98-0003   "Capacity Design of Bridge Piers and the Analysis of Overstrength," by J.B. Mander, A. Dutta and P. Goel, 6/1/98, (PB99-118853, A09, MF-A02).

MCEER-98-0004   "Evaluation of Bridge Damage Data from the Loma Prieta and Northridge, California Earthquakes," by N. Basoz and A. Kiremidjian, 6/2/98, (PB99-118861, A15, MF-A03).

MCEER-98-0005   "Screening Guide for Rapid Assessment of Liquefaction Hazard at Highway Bridge Sites," by T. L. Youd, 6/16/98, (PB99-118879, A06, not available on microfiche).

MCEER-98-0006   "Structural Steel and Steel/Concrete Interface Details for Bridges," by P. Ritchie, N. Kauhl and J. Kulicki, 7/13/98, (PB99-118945, A06, MF-A01).

MCEER-98-0007   "Capacity Design and Fatigue Analysis of Confined Concrete Columns," by A. Dutta and J.B. Mander, 7/14/98, (PB99-118960, A14, MF-A03).

MCEER-98-0008   "Proceedings of the Workshop on Performance Criteria for Telecommunication Services Under Earthquake Conditions," edited by A.J. Schiff, 7/15/98, (PB99-118952, A08, MF-A02).

MCEER-98-0009   "Fatigue Analysis of Unconfined Concrete Columns," by J.B. Mander, A. Dutta and J.H. Kim, 9/12/98, (PB99-123655, A10, MF-A02).

MCEER-98-0010   "Centrifuge Modeling of Cyclic Lateral Response of Pile-Cap Systems and Seat-Type Abutments in Dry Sands," by A.D. Gadre and R. Dobry, 10/2/98, (PB99-123606, A13, MF-A03).

MCEER-98-0011   "IDARC-BRIDGE: A Computational Platform for Seismic Damage Assessment of Bridge Structures," by A.M. Reinhorn, V. Simeonov, G. Mylonakis and Y. Reichman, 10/2/98, (PB99-162919, A15, MF-A03).

MCEER-98-0012   "Experimental Investigation of the Dynamic Response of Two Bridges Before and After Retrofitting with Elastomeric Bearings," by D.A. Wendichansky, S.S. Chen and J.B. Mander, 10/2/98, (PB99-162927, A15, MF-A03).

MCEER-98-0013   "Design Procedures for Hinge Restrainers and Hinge Sear Width for Multiple-Frame Bridges," by R. Des Roches and G.L. Fenves, 11/3/98, (PB99-140477, A13, MF-A03).

MCEER-98-0014   "Response Modification Factors for Seismically Isolated Bridges," by M.C. Constantinou and J.K. Quarshie, 11/3/98, (PB99-140485, A14, MF-A03).

MCEER-98-0015   "Proceedings of the U.S.-Italy Workshop on Seismic Protective Systems for Bridges," edited by I.M. Friedland and M.C. Constantinou, 11/3/98, (PB2000-101711, A22, MF-A04).

MCEER-98-0016   "Appropriate Seismic Reliability for Critical Equipment Systems: Recommendations Based on Regional Analysis of Financial and Life Loss," by K. Porter, C. Scawthorn, C. Taylor and N. Blais, 11/10/98, (PB99-157265, A08, MF-A02).

MCEER-98-0017   "Proceedings of the U.S. Japan Joint Seminar on Civil Infrastructure Systems Research," edited by M. Shinozuka and A. Rose, 11/12/98, (PB99-156713, A16, MF-A03).

MCEER-98-0018   "Modeling of Pile Footings and Drilled Shafts for Seismic Design," by I. PoLam, M. Kapuskar and D. Chaudhuri, 12/21/98, (PB99-157257, A09, MF-A02).

MCEER-99-0001   "Seismic Evaluation of a Masonry Infilled Reinforced Concrete Frame by Pseudodynamic Testing," by S.G. Buonopane and R.N. White, 2/16/99, (PB99-162851, A09, MF-A02).

MCEER-99-0002   "Response History Analysis of Structures with Seismic Isolation and Energy Dissipation Systems: Verification Examples for Program SAP2000," by J. Scheller and M.C. Constantinou, 2/22/99, (PB99-162869, A08, MF-A02).

MCEER-99-0003   "Experimental Study on the Seismic Design and Retrofit of Bridge Columns Including Axial Load Effects," by A. Dutta, T. Kokorina and J.B. Mander, 2/22/99, (PB99-162877, A09, MF-A02).

MCEER-99-0004   "Experimental Study of Bridge Elastomeric and Other Isolation and Energy Dissipation Systems with Emphasis on Uplift Prevention and High Velocity Near-source Seismic Excitation," by A. Kasalanati and M. C. Constantinou, 2/26/99, (PB99-162885, A12, MF-A03).

MCEER-99-0005   "Truss Modeling of Reinforced Concrete Shear-flexure Behavior," by J.H. Kim and J.B. Mander, 3/8/99, (PB99-163693, A12, MF-A03).

MCEER-99-0006   "Experimental Investigation and Computational Modeling of Seismic Response of a 1:4 Scale Model Steel Structure with a Load Balancing Supplemental Damping System," by G. Pekcan, J.B. Mander and S.S. Chen, 4/2/99, (PB99-162893, A11, MF-A03).

MCEER-99-0007   "Effect of Vertical Ground Motions on the Structural Response of Highway Bridges," by M.R. Button, C.J. Cronin and R.L. Mayes, 4/10/99, (PB2000-101411, A10, MF-A03).

MCEER-99-0008   "Seismic Reliability Assessment of Critical Facilities: A Handbook, Supporting Documentation, and Model Code Provisions," by G.S. Johnson, R.E. Sheppard, M.D. Quilici, S.J. Eder and C.R. Scawthorn, 4/12/99, (PB2000-101701, A18, MF-A04).

MCEER-99-0009   "Impact Assessment of Selected MCEER Highway Project Research on the Seismic Design of Highway Structures," by C. Rojahn, R. Mayes, D.G. Anderson, J.H. Clark, D'Appolonia Engineering, S. Gloyd and R.V. Nutt, 4/14/99, (PB99-162901, A10, MF-A02).

MCEER-99-0010   "Site Factors and Site Categories in Seismic Codes," by R. Dobry, R. Ramos and M.S. Power, 7/19/99, (PB2000-101705, A08, MF-A02).

MCEER-99-0011   "Restrainer Design Procedures for Multi-Span Simply-Supported Bridges," by M.J. Randall, M. Saiidi, E. Maragakis and T. Isakovic, 7/20/99, (PB2000-101702, A10, MF-A02).

MCEER-99-0012   "Property Modification Factors for Seismic Isolation Bearings," by M.C. Constantinou, P. Tsopelas, A. Kasalanati and E. Wolff, 7/20/99, (PB2000-103387, A11, MF-A03).

MCEER-99-0013   "Critical Seismic Issues for Existing Steel Bridges," by P. Ritchie, N. Kauhl and J. Kulicki, 7/20/99, (PB2000-101697, A09, MF-A02).

MCEER-99-0014   "Nonstructural Damage Database," by A. Kao, T.T. Soong and A. Vender, 7/24/99, (PB2000-101407, A06, MF-A01).

MCEER-99-0015   "Guide to Remedial Measures for Liquefaction Mitigation at Existing Highway Bridge Sites," by H.G. Cooke and J. K. Mitchell, 7/26/99, (PB2000-101703, A11, MF-A03).

MCEER-99-0016   "Proceedings of the MCEER Workshop on Ground Motion Methodologies for the Eastern United States," edited by N. Abrahamson and A. Becker, 8/11/99, (PB2000-103385, A07, MF-A02).

MCEER-99-0017   "Quindío, Colombia Earthquake of January 25, 1999: Reconnaissance Report," by A.P. Asfura and P.J. Flores, 10/4/99, (PB2000-106893, A06, MF-A01).

MCEER-99-0018   "Hysteretic Models for Cyclic Behavior of Deteriorating Inelastic Structures," by M.V. Sivaselvan and A.M. Reinhorn, 11/5/99, (PB2000-103386, A08, MF-A02).

MCEER-99-0019 "Proceedings of the 7th U.S.- Japan Workshop on Earthquake Resistant Design of Lifeline Facilities and Countermeasures Against Soil Liquefaction," edited by T.D. O'Rourke, J.P. Bardet and M. Hamada, 11/19/99, (PB2000-103354, A99, MF-A06).

MCEER-99-0020 "Development of Measurement Capability for Micro-Vibration Evaluations with Application to Chip Fabrication Facilities," by G.C. Lee, Z. Liang, J.W. Song, J.D. Shen and W.C. Liu, 12/1/99, (PB2000-105993, A08, MF-A02).

MCEER-99-0021 "Design and Retrofit Methodology for Building Structures with Supplemental Energy Dissipating Systems," by G. Pekcan, J.B. Mander and S.S. Chen, 12/31/99, (PB2000-105994, A11, MF-A03).

MCEER-00-0001 "The Marmara, Turkey Earthquake of August 17, 1999: Reconnaissance Report," edited by C. Scawthorn; with major contributions by M. Bruneau, R. Eguchi, T. Holzer, G. Johnson, J. Mander, J. Mitchell, W. Mitchell, A. Papageorgiou, C. Scaethorn, and G. Webb, 3/23/00, (PB2000-106200, A11, MF-A03).

MCEER-00-0002 "Proceedings of the MCEER Workshop for Seismic Hazard Mitigation of Health Care Facilities," edited by G.C. Lee, M. Ettouney, M. Grigoriu, J. Hauer and J. Nigg, 3/29/00, (PB2000-106892, A08, MF-A02).

MCEER-00-0003 "The Chi-Chi, Taiwan Earthquake of September 21, 1999: Reconnaissance Report," edited by G.C. Lee and C.H. Loh, with major contributions by G.C. Lee, M. Bruneau, I.G. Buckle, S.E. Chang, P.J. Flores, T.D. O'Rourke, M. Shinozuka, T.T. Soong, C-H. Loh, K-C. Chang, Z-J. Chen, J-S. Hwang, M-L. Lin, G-Y. Liu, K-C. Tsai, G.C. Yao and C-L. Yen, 4/30/00, (PB2001-100980, A10, MF-A02).

MCEER-00-0004 "Seismic Retrofit of End-Sway Frames of Steel Deck-Truss Bridges with a Supplemental Tendon System: Experimental and Analytical Investigation," by G. Pekcan, J.B. Mander and S.S. Chen, 7/1/00, (PB2001-100982, A10, MF-A02).

MCEER-00-0005 "Sliding Fragility of Unrestrained Equipment in Critical Facilities," by W.H. Chong and T.T. Soong, 7/5/00, (PB2001-100983, A08, MF-A02).

MCEER-00-0006 "Seismic Response of Reinforced Concrete Bridge Pier Walls in the Weak Direction," by N. Abo-Shadi, M. Saiidi and D. Sanders, 7/17/00, (PB2001-100981, A17, MF-A03).

MCEER-00-0007 "Low-Cycle Fatigue Behavior of Longitudinal Reinforcement in Reinforced Concrete Bridge Columns," by J. Brown and S.K. Kunnath, 7/23/00, (PB2001-104392, A08, MF-A02).

MCEER-00-0008 "Soil Structure Interaction of Bridges for Seismic Analysis," I. PoLam and H. Law, 9/25/00, (PB2001-105397, A08, MF-A02).

MCEER-00-0009 "Proceedings of the First MCEER Workshop on Mitigation of Earthquake Disaster by Advanced Technologies (MEDAT-1), edited by M. Shinozuka, D.J. Inman and T.D. O'Rourke, 11/10/00, (PB2001-105399, A14, MF-A03).

MCEER-00-0010 "Development and Evaluation of Simplified Procedures for Analysis and Design of Buildings with Passive Energy Dissipation Systems, Revision 01," by O.M. Ramirez, M.C. Constantinou, C.A. Kircher, A.S. Whittaker, M.W. Johnson, J.D. Gomez and C. Chrysostomou, 11/16/01, (PB2001-105523, A23, MF-A04).

MCEER-00-0011 "Dynamic Soil-Foundation-Structure Interaction Analyses of Large Caissons," by C-Y. Chang, C-M. Mok, Z-L. Wang, R. Settgast, F. Waggoner, M.A. Ketchum, H.M. Gonnermann and C-C. Chin, 12/30/00, (PB2001-104373, A07, MF-A02).

MCEER-00-0012 "Experimental Evaluation of Seismic Performance of Bridge Restrainers," by A.G. Vlassis, E.M. Maragakis and M. Saiid Saiidi, 12/30/00, (PB2001-104354, A09, MF-A02).

MCEER-00-0013 "Effect of Spatial Variation of Ground Motion on Highway Structures," by M. Shinozuka, V. Saxena and G. Deodatis, 12/31/00, (PB2001-108755, A13, MF-A03).

MCEER-00-0014 "A Risk-Based Methodology for Assessing the Seismic Performance of Highway Systems," by S.D. Werner, C.E. Taylor, J.E. Moore, II, J.S. Walton and S. Cho, 12/31/00, (PB2001-108756, A14, MF-A03).

MCEER-01-0001 "Experimental Investigation of P-Delta Effects to Collapse During Earthquakes," by D. Vian and M. Bruneau, 6/25/01, (PB2002-100534, A17, MF-A03).

MCEER-01-0002 "Proceedings of the Second MCEER Workshop on Mitigation of Earthquake Disaster by Advanced Technologies (MEDAT-2)," edited by M. Bruneau and D.J. Inman, 7/23/01, (PB2002-100434, A16, MF-A03).

MCEER-01-0003 "Sensitivity Analysis of Dynamic Systems Subjected to Seismic Loads," by C. Roth and M. Grigoriu, 9/18/01, (PB2003-100884, A12, MF-A03).

MCEER-01-0004 "Overcoming Obstacles to Implementing Earthquake Hazard Mitigation Policies: Stage 1 Report," by D.J. Alesch and W.J. Petak, 12/17/01, (PB2002-107949, A07, MF-A02).

MCEER-01-0005 "Updating Real-Time Earthquake Loss Estimates: Methods, Problems and Insights," by C.E. Taylor, S.E. Chang and R.T. Eguchi, 12/17/01, (PB2002-107948, A05, MF-A01).

MCEER-01-0006 "Experimental Investigation and Retrofit of Steel Pile Foundations and Pile Bents Under Cyclic Lateral Loadings," by A. Shama, J. Mander, B. Blabac and S. Chen, 12/31/01, (PB2002-107950, A13, MF-A03).

MCEER-02-0001 "Assessment of Performance of Bolu Viaduct in the 1999 Duzce Earthquake in Turkey" by P.C. Roussis, M.C. Constantinou, M. Erdik, E. Durukal and M. Dicleli, 5/8/02, (PB2003-100883, A08, MF-A02).

MCEER-02-0002 "Seismic Behavior of Rail Counterweight Systems of Elevators in Buildings," by M.P. Singh, Rildova and L.E. Suarez, 5/27/02. (PB2003-100882, A11, MF-A03).

MCEER-02-0003 "Development of Analysis and Design Procedures for Spread Footings," by G. Mylonakis, G. Gazetas, S. Nikolaou and A. Chauncey, 10/02/02, (PB2004-101636, A13, MF-A03, CD-A13).

MCEER-02-0004 "Bare-Earth Algorithms for Use with SAR and LIDAR Digital Elevation Models," by C.K. Huyck, R.T. Eguchi and B. Houshmand, 10/16/02, (PB2004-101637, A07, CD-A07).

MCEER-02-0005 "Review of Energy Dissipation of Compression Members in Concentrically Braced Frames," by K.Lee and M. Bruneau, 10/18/02, (PB2004-101638, A10, CD-A10).

MCEER-03-0001 "Experimental Investigation of Light-Gauge Steel Plate Shear Walls for the Seismic Retrofit of Buildings" by J. Berman and M. Bruneau, 5/2/03, (PB2004-101622, A10, MF-A03, CD-A10).

MCEER-03-0002 "Statistical Analysis of Fragility Curves," by M. Shinozuka, M.Q. Feng, H. Kim, T. Uzawa and T. Ueda, 6/16/03, (PB2004-101849, A09, CD-A09).

MCEER-03-0003 "Proceedings of the Eighth U.S.-Japan Workshop on Earthquake Resistant Design f Lifeline Facilities and Countermeasures Against Liquefaction," edited by M. Hamada, J.P. Bardet and T.D. O'Rourke, 6/30/03, (PB2004-104386, A99, CD-A99).

MCEER-03-0004 "Proceedings of the PRC-US Workshop on Seismic Analysis and Design of Special Bridges," edited by L.C. Fan and G.C. Lee, 7/15/03, (PB2004-104387, A14, CD-A14).

MCEER-03-0005 "Urban Disaster Recovery: A Framework and Simulation Model," by S.B. Miles and S.E. Chang, 7/25/03, (PB2004-104388, A07, CD-A07).

MCEER-03-0006 "Behavior of Underground Piping Joints Due to Static and Dynamic Loading," by R.D. Meis, M. Maragakis and R. Siddharthan, 11/17/03, (PB2005-102194, A13, MF-A03, CD-A00).

MCEER-04-0001 "Experimental Study of Seismic Isolation Systems with Emphasis on Secondary System Response and Verification of Accuracy of Dynamic Response History Analysis Methods," by E. Wolff and M. Constantinou, 1/16/04 (PB2005-102195, A99, MF-E08, CD-A00).

MCEER-04-0002 "Tension, Compression and Cyclic Testing of Engineered Cementitious Composite Materials," by K. Kesner and S.L. Billington, 3/1/04, (PB2005-102196, A08, CD-A08).

MCEER-04-0003   "Cyclic Testing of Braces Laterally Restrained by Steel Studs to Enhance Performance During Earthquakes," by O.C. Celik, J.W. Berman and M. Bruneau, 3/16/04, (PB2005-102197, A13, MF-A03, CD-A00).

MCEER-04-0004   "Methodologies for Post Earthquake Building Damage Detection Using SAR and Optical Remote Sensing: Application to the August 17, 1999 Marmara, Turkey Earthquake," by C.K. Huyck, B.J. Adams, S. Cho, R.T. Eguchi, B. Mansouri and B. Houshmand, 6/15/04, (PB2005-104888, A10, CD-A00).

MCEER-04-0005   "Nonlinear Structural Analysis Towards Collapse Simulation: A Dynamical Systems Approach," by M.V. Sivaselvan and A.M. Reinhorn, 6/16/04, (PB2005-104889, A11, MF-A03, CD-A00).

MCEER-04-0006   "Proceedings of the Second PRC-US Workshop on Seismic Analysis and Design of Special Bridges," edited by G.C. Lee and L.C. Fan, 6/25/04, (PB2005-104890, A16, CD-A00).

MCEER-04-0007   "Seismic Vulnerability Evaluation of Axially Loaded Steel Built-up Laced Members," by K. Lee and M. Bruneau, 6/30/04, (PB2005-104891, A16, CD-A00).

MCEER-04-0008   "Evaluation of Accuracy of Simplified Methods of Analysis and Design of Buildings with Damping Systems for Near-Fault and for Soft-Soil Seismic Motions," by E.A. Pavlou and M.C. Constantinou, 8/16/04, (PB2005-104892, A08, MF-A02, CD-A00).

MCEER-04-0009   "Assessment of Geotechnical Issues in Acute Care Facilities in California," by M. Lew, T.D. O'Rourke, R. Dobry and M. Koch, 9/15/04, (PB2005-104893, A08, CD-A00).

MCEER-04-0010   "Scissor-Jack-Damper Energy Dissipation System," by A.N. Sigaher-Boyle and M.C. Constantinou, 12/1/04 (PB2005-108221).

MCEER-04-0011   "Seismic Retrofit of Bridge Steel Truss Piers Using a Controlled Rocking Approach," by M. Pollino and M. Bruneau, 12/20/04 (PB2006-105795).

MCEER-05-0001   "Experimental and Analytical Studies of Structures Seismically Isolated with an Uplift-Restraint Isolation System," by P.C. Roussis and M.C. Constantinou, 1/10/05 (PB2005-108222).

MCEER-05-0002   "A Versatile Experimentation Model for Study of Structures Near Collapse Applied to Seismic Evaluation of Irregular Structures," by D. Kusumastuti, A.M. Reinhorn and A. Rutenberg, 3/31/05 (PB2006-101523).

MCEER-05-0003   "Proceedings of the Third PRC-US Workshop on Seismic Analysis and Design of Special Bridges," edited by L.C. Fan and G.C. Lee, 4/20/05, (PB2006-105796).

MCEER-05-0004   "Approaches for the Seismic Retrofit of Braced Steel Bridge Piers and Proof-of-Concept Testing of an Eccentrically Braced Frame with Tubular Link," by J.W. Berman and M. Bruneau, 4/21/05 (PB2006-101524).

MCEER-05-0005   "Simulation of Strong Ground Motions for Seismic Fragility Evaluation of Nonstructural Components in Hospitals," by A. Wanitkorkul and A. Filiatrault, 5/26/05 (PB2006-500027).

MCEER-05-0006   "Seismic Safety in California Hospitals: Assessing an Attempt to Accelerate the Replacement or Seismic Retrofit of Older Hospital Facilities," by D.J. Alesch, L.A. Arendt and W.J. Petak, 6/6/05 (PB2006-105794).

MCEER-05-0007   "Development of Seismic Strengthening and Retrofit Strategies for Critical Facilities Using Engineered Cementitious Composite Materials," by K. Kesner and S.L. Billington, 8/29/05 (PB2006-111701).

MCEER-05-0008   "Experimental and Analytical Studies of Base Isolation Systems for Seismic Protection of Power Transformers," by N. Murota, M.Q. Feng and G-Y. Liu, 9/30/05 (PB2006-111702).

MCEER-05-0009   "3D-BASIS-ME-MB: Computer Program for Nonlinear Dynamic Analysis of Seismically Isolated Structures," by P.C. Tsopelas, P.C. Roussis, M.C. Constantinou, R. Buchanan and A.M. Reinhorn, 10/3/05 (PB2006-111703).

MCEER-05-0010   "Steel Plate Shear Walls for Seismic Design and Retrofit of Building Structures," by D. Vian and M. Bruneau, 12/15/05 (PB2006-111704).

MCEER-05-0011 "The Performance-Based Design Paradigm," by M.J. Astrella and A. Whittaker, 12/15/05 (PB2006-111705).

MCEER-06-0001 "Seismic Fragility of Suspended Ceiling Systems," H. Badillo-Almaraz, A.S. Whittaker, A.M. Reinhorn and G.P. Cimellaro, 2/4/06 (PB2006-111706).

MCEER-06-0002 "Multi-Dimensional Fragility of Structures," by G.P. Cimellaro, A.M. Reinhorn and M. Bruneau, 3/1/06 (PB2007-106974, A09, MF-A02, CD A00).

MCEER-06-0003 "Built-Up Shear Links as Energy Dissipators for Seismic Protection of Bridges," by P. Dusicka, A.M. Itani and I.G. Buckle, 3/15/06 (PB2006-111708).

MCEER-06-0004 "Analytical Investigation of the Structural Fuse Concept," by R.E. Vargas and M. Bruneau, 3/16/06 (PB2006-111709).

MCEER-06-0005 "Experimental Investigation of the Structural Fuse Concept," by R.E. Vargas and M. Bruneau, 3/17/06 (PB2006-111710).

MCEER-06-0006 "Further Development of Tubular Eccentrically Braced Frame Links for the Seismic Retrofit of Braced Steel Truss Bridge Piers," by J.W. Berman and M. Bruneau, 3/27/06 (PB2007-105147).

MCEER-06-0007 "REDARS Validation Report," by S. Cho, C.K. Huyck, S. Ghosh and R.T. Eguchi, 8/8/06 (PB2007-106983).

MCEER-06-0008 "Review of Current NDE Technologies for Post-Earthquake Assessment of Retrofitted Bridge Columns," by J.W. Song, Z. Liang and G.C. Lee, 8/21/06 (PB2007-106984).

MCEER-06-0009 "Liquefaction Remediation in Silty Soils Using Dynamic Compaction and Stone Columns," by S. Thevanayagam, G.R. Martin, R. Nashed, T. Shenthan, T. Kanagalingam and N. Ecemis, 8/28/06 (PB2007-106985).

MCEER-06-0010 "Conceptual Design and Experimental Investigation of Polymer Matrix Composite Infill Panels for Seismic Retrofitting," by W. Jung, M. Chiewanichakorn and A.J. Aref, 9/21/06 (PB2007-106986).

MCEER-06-0011 "A Study of the Coupled Horizontal-Vertical Behavior of Elastomeric and Lead-Rubber Seismic Isolation Bearings," by G.P. Warn and A.S. Whittaker, 9/22/06 (PB2007-108679).

MCEER-06-0012 "Proceedings of the Fourth PRC-US Workshop on Seismic Analysis and Design of Special Bridges: Advancing Bridge Technologies in Research, Design, Construction and Preservation," Edited by L.C. Fan, G.C. Lee and L. Ziang, 10/12/06 (PB2007-109042).

MCEER-06-0013 "Cyclic Response and Low Cycle Fatigue Characteristics of Plate Steels," by P. Dusicka, A.M. Itani and I.G. Buckle, 11/1/06 06 (PB2007-106987).

MCEER-06-0014 "Proceedings of the Second US-Taiwan Bridge Engineering Workshop," edited by W.P. Yen, J. Shen, J-Y. Chen and M. Wang, 11/15/06 (PB2008-500041).

MCEER-06-0015 "User Manual and Technical Documentation for the REDARS^{TM} Import Wizard," by S. Cho, S. Ghosh, C.K. Huyck and S.D. Werner, 11/30/06 (PB2007-114766).

MCEER-06-0016 "Hazard Mitigation Strategy and Monitoring Technologies for Urban and Infrastructure Public Buildings: Proceedings of the China-US Workshops," edited by X.Y. Zhou, A.L. Zhang, G.C. Lee and M. Tong, 12/12/06 (PB2008-500018).

MCEER-07-0001 "Static and Kinetic Coefficients of Friction for Rigid Blocks," by C. Kafali, S. Fathali, M. Grigoriu and A.S. Whittaker, 3/20/07 (PB2007-114767).

MCEER-07-0002 "Hazard Mitigation Investment Decision Making: Organizational Response to Legislative Mandate," by L.A. Arendt, D.J. Alesch and W.J. Petak, 4/9/07 (PB2007-114768).

MCEER-07-0003 "Seismic Behavior of Bidirectional-Resistant Ductile End Diaphragms with Unbonded Braces in Straight or Skewed Steel Bridges," by O. Celik and M. Bruneau, 4/11/07 (PB2008-105141).

MCEER-07-0004 "Modeling Pile Behavior in Large Pile Groups Under Lateral Loading," by A.M. Dodds and G.R. Martin, 4/16/07(PB2008-105142).

MCEER-07-0005 "Experimental Investigation of Blast Performance of Seismically Resistant Concrete-Filled Steel Tube Bridge Piers," by S. Fujikura, M. Bruneau and D. Lopez-Garcia, 4/20/07 (PB2008-105143).

MCEER-07-0006 "Seismic Analysis of Conventional and Isolated Liquefied Natural Gas Tanks Using Mechanical Analogs," by I.P. Christovasilis and A.S. Whittaker, 5/1/07, not available.

MCEER-07-0007 "Experimental Seismic Performance Evaluation of Isolation/Restraint Systems for Mechanical Equipment – Part 1: Heavy Equipment Study," by S. Fathali and A. Filiatrault, 6/6/07 (PB2008-105144).

MCEER-07-0008 "Seismic Vulnerability of Timber Bridges and Timber Substructures," by A.A. Sharma, J.B. Mander, I.M. Friedland and D.R. Allicock, 6/7/07 (PB2008-105145).

MCEER-07-0009 "Experimental and Analytical Study of the XY-Friction Pendulum (XY-FP) Bearing for Bridge Applications," by C.C. Marin-Artieda, A.S. Whittaker and M.C. Constantinou, 6/7/07 (PB2008-105191).

MCEER-07-0010 "Proceedings of the PRC-US Earthquake Engineering Forum for Young Researchers," Edited by G.C. Lee and X.Z. Qi, 6/8/07 (PB2008-500058).

MCEER-07-0011 "Design Recommendations for Perforated Steel Plate Shear Walls," by R. Purba and M. Bruneau, 6/18/07, (PB2008-105192).

MCEER-07-0012 "Performance of Seismic Isolation Hardware Under Service and Seismic Loading," by M.C. Constantinou, A.S. Whittaker, Y. Kalpakidis, D.M. Fenz and G.P. Warn, 8/27/07, (PB2008-105193).

MCEER-07-0013 "Experimental Evaluation of the Seismic Performance of Hospital Piping Subassemblies," by E.R. Goodwin, E. Maragakis and A.M. Itani, 9/4/07, (PB2008-105194).

MCEER-07-0014 "A Simulation Model of Urban Disaster Recovery and Resilience: Implementation for the 1994 Northridge Earthquake," by S. Miles and S.E. Chang, 9/7/07, (PB2008-106426).

MCEER-07-0015 "Statistical and Mechanistic Fragility Analysis of Concrete Bridges," by M. Shinozuka, S. Banerjee and S-H. Kim, 9/10/07, (PB2008-106427).

MCEER-07-0016 "Three-Dimensional Modeling of Inelastic Buckling in Frame Structures," by M. Schachter and AM. Reinhorn, 9/13/07, (PB2008-108125).

MCEER-07-0017 "Modeling of Seismic Wave Scattering on Pile Groups and Caissons," by I. Po Lam, H. Law and C.T. Yang, 9/17/07 (PB2008-108150).

MCEER-07-0018 "Bridge Foundations: Modeling Large Pile Groups and Caissons for Seismic Design," by I. Po Lam, H. Law and G.R. Martin (Coordinating Author), 12/1/07 (PB2008-111190).

MCEER-07-0019 "Principles and Performance of Roller Seismic Isolation Bearings for Highway Bridges," by G.C. Lee, Y.C. Ou, Z. Liang, T.C. Niu and J. Song, 12/10/07 (PB2009-110466).

MCEER-07-0020 "Centrifuge Modeling of Permeability and Pinning Reinforcement Effects on Pile Response to Lateral Spreading," by L.L Gonzalez-Lagos, T. Abdoun and R. Dobry, 12/10/07 (PB2008-111191).

MCEER-07-0021 "Damage to the Highway System from the Pisco, Perú Earthquake of August 15, 2007," by J.S. O'Connor, L. Mesa and M. Nykamp, 12/10/07, (PB2008-108126).

MCEER-07-0022 "Experimental Seismic Performance Evaluation of Isolation/Restraint Systems for Mechanical Equipment – Part 2: Light Equipment Study," by S. Fathali and A. Filiatrault, 12/13/07 (PB2008-111192).

MCEER-07-0023 "Fragility Considerations in Highway Bridge Design," by M. Shinozuka, S. Banerjee and S.H. Kim, 12/14/07 (PB2008-111193).

MCEER-07-0024   "Performance Estimates for Seismically Isolated Bridges," by G.P. Warn and A.S. Whittaker, 12/30/07 (PB2008-112230).

MCEER-08-0001   "Seismic Performance of Steel Girder Bridge Superstructures with Conventional Cross Frames," by L.P. Carden, A.M. Itani and I.G. Buckle, 1/7/08, (PB2008-112231).

MCEER-08-0002   "Seismic Performance of Steel Girder Bridge Superstructures with Ductile End Cross Frames with Seismic Isolators," by L.P. Carden, A.M. Itani and I.G. Buckle, 1/7/08 (PB2008-112232).

MCEER-08-0003   "Analytical and Experimental Investigation of a Controlled Rocking Approach for Seismic Protection of Bridge Steel Truss Piers," by M. Pollino and M. Bruneau, 1/21/08 (PB2008-112233).

MCEER-08-0004   "Linking Lifeline Infrastructure Performance and Community Disaster Resilience: Models and Multi-Stakeholder Processes," by S.E. Chang, C. Pasion, K. Tatebe and R. Ahmad, 3/3/08 (PB2008-112234).

MCEER-08-0005   "Modal Analysis of Generally Damped Linear Structures Subjected to Seismic Excitations," by J. Song, Y-L. Chu, Z. Liang and G.C. Lee, 3/4/08 (PB2009-102311).

MCEER-08-0006   "System Performance Under Multi-Hazard Environments," by C. Kafali and M. Grigoriu, 3/4/08 (PB2008-112235).

MCEER-08-0007   "Mechanical Behavior of Multi-Spherical Sliding Bearings," by D.M. Fenz and M.C. Constantinou, 3/6/08 (PB2008-112236).

MCEER-08-0008   "Post-Earthquake Restoration of the Los Angeles Water Supply System," by T.H.P. Tabucchi and R.A. Davidson, 3/7/08 (PB2008-112237).

MCEER-08-0009   "Fragility Analysis of Water Supply Systems," by A. Jacobson and M. Grigoriu, 3/10/08 (PB2009-105545).

MCEER-08-0010   "Experimental Investigation of Full-Scale Two-Story Steel Plate Shear Walls with Reduced Beam Section Connections," by B. Qu, M. Bruneau, C-H. Lin and K-C. Tsai, 3/17/08 (PB2009-106368).

MCEER-08-0011   "Seismic Evaluation and Rehabilitation of Critical Components of Electrical Power Systems," S. Ersoy, B. Feizi, A. Ashrafi and M. Ala Saadeghvaziri, 3/17/08 (PB2009-105546).

MCEER-08-0012   "Seismic Behavior and Design of Boundary Frame Members of Steel Plate Shear Walls," by B. Qu and M. Bruneau, 4/26/08 . (PB2009-106744).

MCEER-08-0013   "Development and Appraisal of a Numerical Cyclic Loading Protocol for Quantifying Building System Performance," by A. Filiatrault, A. Wanitkorkul and M. Constantinou, 4/27/08 (PB2009-107906).

MCEER-08-0014   "Structural and Nonstructural Earthquake Design: The Challenge of Integrating Specialty Areas in Designing Complex, Critical Facilities," by W.J. Petak and D.J. Alesch, 4/30/08 (PB2009-107907).

MCEER-08-0015   "Seismic Performance Evaluation of Water Systems," by Y. Wang and T.D. O'Rourke, 5/5/08 (PB2009-107908).

MCEER-08-0016   "Seismic Response Modeling of Water Supply Systems," by P. Shi and T.D. O'Rourke, 5/5/08 (PB2009-107910).

MCEER-08-0017   "Numerical and Experimental Studies of Self-Centering Post-Tensioned Steel Frames," by D. Wang and A. Filiatrault, 5/12/08 (PB2009-110479).

MCEER-08-0018   "Development, Implementation and Verification of Dynamic Analysis Models for Multi-Spherical Sliding Bearings," by D.M. Fenz and M.C. Constantinou, 8/15/08 (PB2009-107911).

MCEER-08-0019   "Performance Assessment of Conventional and Base Isolated Nuclear Power Plants for Earthquake Blast Loadings," by Y.N. Huang, A.S. Whittaker and N. Luco, 10/28/08 (PB2009-107912).

MCEER-08-0020   "Remote Sensing for Resilient Multi-Hazard Disaster Response – Volume I: Introduction to Damage Assessment Methodologies," by B.J. Adams and R.T. Eguchi, 11/17/08 (PB2010-102695).

MCEER-08-0021   "Remote Sensing for Resilient Multi-Hazard Disaster Response – Volume II: Counting the Number of Collapsed Buildings Using an Object-Oriented Analysis: Case Study of the 2003 Bam Earthquake," by L. Gusella, C.K. Huyck and B.J. Adams, 11/17/08 (PB2010-100925).

MCEER-08-0022   "Remote Sensing for Resilient Multi-Hazard Disaster Response – Volume III: Multi-Sensor Image Fusion Techniques for Robust Neighborhood-Scale Urban Damage Assessment," by B.J. Adams and A. McMillan, 11/17/08 (PB2010-100926).

MCEER-08-0023   "Remote Sensing for Resilient Multi-Hazard Disaster Response – Volume IV: A Study of Multi-Temporal and Multi-Resolution SAR Imagery for Post-Katrina Flood Monitoring in New Orleans," by A. McMillan, J.G. Morley, B.J. Adams and S. Chesworth, 11/17/08 (PB2010-100927).

MCEER-08-0024   "Remote Sensing for Resilient Multi-Hazard Disaster Response – Volume V: Integration of Remote Sensing Imagery and VIEWS^{TM} Field Data for Post-Hurricane Charley Building Damage Assessment," by J.A. Womble, K. Mehta and B.J. Adams, 11/17/08 (PB2009-115532).

MCEER-08-0025   "Building Inventory Compilation for Disaster Management: Application of Remote Sensing and Statistical Modeling," by P. Sarabandi, A.S. Kiremidjian, R.T. Eguchi and B. J. Adams, 11/20/08 (PB2009-110484).

MCEER-08-0026   "New Experimental Capabilities and Loading Protocols for Seismic Qualification and Fragility Assessment of Nonstructural Systems," by R. Retamales, G. Mosqueda, A. Filiatrault and A. Reinhorn, 11/24/08 (PB2009-110485).

MCEER-08-0027   "Effects of Heating and Load History on the Behavior of Lead-Rubber Bearings," by I.V. Kalpakidis and M.C. Constantinou, 12/1/08 (PB2009-115533).

MCEER-08-0028   "Experimental and Analytical Investigation of Blast Performance of Seismically Resistant Bridge Piers," by S.Fujikura and M. Bruneau, 12/8/08 (PB2009-115534).

MCEER-08-0029   "Evolutionary Methodology for Aseismic Decision Support," by Y. Hu and G. Dargush, 12/15/08.

MCEER-08-0030   "Development of a Steel Plate Shear Wall Bridge Pier System Conceived from a Multi-Hazard Perspective," by D. Keller and M. Bruneau, 12/19/08 (PB2010-102696).

MCEER-09-0001   "Modal Analysis of Arbitrarily Damped Three-Dimensional Linear Structures Subjected to Seismic Excitations," by Y.L. Chu, J. Song and G.C. Lee, 1/31/09 (PB2010-100922).

MCEER-09-0002   "Air-Blast Effects on Structural Shapes," by G. Ballantyne, A.S. Whittaker, A.J. Aref and G.F. Dargush, 2/2/09 (PB2010-102697).

MCEER-09-0003   "Water Supply Performance During Earthquakes and Extreme Events," by A.L. Bonneau and T.D. O'Rourke, 2/16/09 (PB2010-100923).

MCEER-09-0004   "Generalized Linear (Mixed) Models of Post-Earthquake Ignitions," by R.A. Davidson, 7/20/09 (PB2010-102698).

MCEER-09-0005   "Seismic Testing of a Full-Scale Two-Story Light-Frame Wood Building: NEESWood Benchmark Test," by I.P. Christovasilis, A. Filiatrault and A. Wanitkorkul, 7/22/09 (PB2012-102401).

MCEER-09-0006   "IDARC2D Version 7.0: A Program for the Inelastic Damage Analysis of Structures," by A.M. Reinhorn, H. Roh, M. Sivaselvan, S.K. Kunnath, R.E. Valles, A. Madan, C. Li, R. Lobo and Y.J. Park, 7/28/09 (PB2010-103199).

MCEER-09-0007   "Enhancements to Hospital Resiliency: Improving Emergency Planning for and Response to Hurricanes," by D.B. Hess and L.A. Arendt, 7/30/09 (PB2010-100924).

690

MCEER-09-0008 "Assessment of Base-Isolated Nuclear Structures for Design and Beyond-Design Basis Earthquake Shaking," by Y.N. Huang, A.S. Whittaker, R.P. Kennedy and R.L. Mayes, 8/20/09 (PB2010-102699).

MCEER-09-0009 "Quantification of Disaster Resilience of Health Care Facilities," by G.P. Cimellaro, C. Fumo, A.M Reinhorn and M. Bruneau, 9/14/09 (PB2010-105384).

MCEER-09-0010 "Performance-Based Assessment and Design of Squat Reinforced Concrete Shear Walls," by C.K. Gulec and A.S. Whittaker, 9/15/09 (PB2010-102700).

MCEER-09-0011 "Proceedings of the Fourth US-Taiwan Bridge Engineering Workshop," edited by W.P. Yen, J.J. Shen, T.M. Lee and R.B. Zheng, 10/27/09 (PB2010-500009).

MCEER-09-0012 "Proceedings of the Special International Workshop on Seismic Connection Details for Segmental Bridge Construction," edited by W. Phillip Yen and George C. Lee, 12/21/09 (PB2012-102402).

MCEER-10-0001 "Direct Displacement Procedure for Performance-Based Seismic Design of Multistory Woodframe Structures," by W. Pang and D. Rosowsky, 4/26/10 (PB2012-102403).

MCEER-10-0002 "Simplified Direct Displacement Design of Six-Story NEESWood Capstone Building and Pre-Test Seismic Performance Assessment," by W. Pang, D. Rosowsky, J. van de Lindt and S. Pei, 5/28/10 (PB2012-102404).

MCEER-10-0003 "Integration of Seismic Protection Systems in Performance-Based Seismic Design of Woodframed Structures," by J.K. Shinde and M.D. Symans, 6/18/10 (PB2012-102405).

MCEER-10-0004 "Modeling and Seismic Evaluation of Nonstructural Components: Testing Frame for Experimental Evaluation of Suspended Ceiling Systems," by A.M. Reinhorn, K.P. Ryu and G. Maddaloni, 6/30/10 (PB2012-102406).

MCEER-10-0005 "Analytical Development and Experimental Validation of a Structural-Fuse Bridge Pier Concept," by S. El-Bahey and M. Bruneau, 10/1/10 (PB2012-102407).

MCEER-10-0006 "A Framework for Defining and Measuring Resilience at the Community Scale: The PEOPLES Resilience Framework," by C.S. Renschler, A.E. Frazier, L.A. Arendt, G.P. Cimellaro, A.M. Reinhorn and M. Bruneau, 10/8/10 (PB2012-102408).

MCEER-10-0007 "Impact of Horizontal Boundary Elements Design on Seismic Behavior of Steel Plate Shear Walls," by R. Purba and M. Bruneau, 11/14/10 (PB2012-102409).

MCEER-10-0008 "Seismic Testing of a Full-Scale Mid-Rise Building: The NEESWood Capstone Test," by S. Pei, J.W. van de Lindt, S.E. Pryor, H. Shimizu, H. Isoda and D.R. Rammer, 12/1/10 (PB2012-102410).

MCEER-10-0009 "Modeling the Effects of Detonations of High Explosives to Inform Blast-Resistant Design," by P. Sherkar, A.S. Whittaker and A.J. Aref, 12/1/10 (PB2012-102411).

MCEER-10-0010 "L'Aquila Earthquake of April 6, 2009 in Italy: Rebuilding a Resilient City to Withstand Multiple Hazards," by G.P. Cimellaro, I.P. Christovasilis, A.M. Reinhorn, A. De Stefano and T. Kirova, 12/29/10.

MCEER-11-0001 "Numerical and Experimental Investigation of the Seismic Response of Light-Frame Wood Structures," by I.P. Christovasilis and A. Filiatrault, 8/8/11 (PB2012-102412).

MCEER-11-0002 "Seismic Design and Analysis of a Precast Segmental Concrete Bridge Model," by M. Anagnostopoulou, A. Filiatrault and A. Aref, 9/15/11.

MCEER-11-0003 'Proceedings of the Workshop on Improving Earthquake Response of Substation Equipment," Edited by A.M. Reinhorn, 9/19/11 (PB2012-102413).

MCEER-11-0004 "LRFD-Based Analysis and Design Procedures for Bridge Bearings and Seismic Isolators," by M.C. Constantinou, I. Kalpakidis, A. Filiatrault and R.A. Ecker Lay, 9/26/11.

MCEER-11-0005 "Experimental Seismic Evaluation, Model Parameterization, and Effects of Cold-Formed Steel-Framed Gypsum Partition Walls on the Seismic Performance of an Essential Facility," by R. Davies, R. Retamales, G. Mosqueda and A. Filiatrault, 10/12/11.

MCEER-11-0006 "Modeling and Seismic Performance Evaluation of High Voltage Transformers and Bushings," by A.M. Reinhorn, K. Oikonomou, H. Roh, A. Schiff and L. Kempner, Jr., 10/3/11.

MCEER-11-0007 "Extreme Load Combinations: A Survey of State Bridge Engineers," by G.C. Lee, Z. Liang, J.J. Shen and J.S. O'Connor, 10/14/11.

MCEER-12-0001 "Simplified Analysis Procedures in Support of Performance Based Seismic Design," by Y.N. Huang and A.S. Whittaker.

MCEER-12-0002 "Seismic Protection of Electrical Transformer Bushing Systems by Stiffening Techniques," by M. Koliou, A. Filiatrault, A.M. Reinhorn and N. Oliveto, 6/1/12.

MCEER-12-0003 "Post-Earthquake Bridge Inspection Guidelines," by J.S. O'Connor and S. Alampalli, 6/8/12.

MCEER-12-0004 "Integrated Design Methodology for Isolated Floor Systems in Single-Degree-of-Freedom Structural Fuse Systems," by S. Cui, M. Bruneau and M.C. Constantinou, 6/13/12.

MCEER-12-0005 "Characterizing the Rotational Components of Earthquake Ground Motion," by D. Basu, A.S. Whittaker and M.C. Constantinou, 6/15/12.

MCEER-12-0006 "Bayesian Fragility for Nonstructural Systems," by C.H. Lee and M.D. Grigoriu, 9/12/12.

MCEER-12-0007 "A Numerical Model for Capturing the In-Plane Seismic Response of Interior Metal Stud Partition Walls," by R.L. Wood and T.C. Hutchinson, 9/12/12.

MCEER-12-0008 "Assessment of Floor Accelerations in Yielding Buildings," by J.D. Wieser, G. Pekcan, A.E. Zaghi, A.M. Itani and E. Maragakis, 10/5/12.

MCEER-13-0001 "Experimental Seismic Study of Pressurized Fire Sprinkler Piping Systems," by Y. Tian, A. Filiatrault and G. Mosqueda, 4/8/13.

MCEER-13-0002 "Enhancing Resource Coordination for Multi-Modal Evacuation Planning," by D.B. Hess, B.W. Conley and C.M. Farrell, 2/8/13.

MCEER-13-0003 "Seismic Response of Base Isolated Buildings Considering Pounding to Moat Walls," by A. Masroor and G. Mosqueda, 2/26/13.

MCEER-13-0004 "Seismic Response Control of Structures Using a Novel Adaptive Passive Negative Stiffness Device," by D.T.R. Pasala, A.A. Sarlis, S. Nagarajaiah, A.M. Reinhorn, M.C. Constantinou and D.P. Taylor, 6/10/13.

MCEER-13-0005 "Negative Stiffness Device for Seismic Protection of Structures," by A.A. Sarlis, D.T.R. Pasala, M.C. Constantinou, A.M. Reinhorn, S. Nagarajaiah and D.P. Taylor, 6/12/13.

MCEER-13-0006 "Emilia Earthquake of May 20, 2012 in Northern Italy: Rebuilding a Resilient Community to Withstand Multiple Hazards," by G.P. Cimellaro, M. Chiriatti, A.M. Reinhorn and L. Tirca, June 30, 2013.

MCEER-13-0007 "Precast Concrete Segmental Components and Systems for Accelerated Bridge Construction in Seismic Regions," by A.J. Aref, G.C. Lee, Y.C. Ou and P. Sideris, with contributions from K.C. Chang, S. Chen, A. Filiatrault and Y. Zhou, June 13, 2013.

MCEER-13-0008 "A Study of U.S. Bridge Failures (1980-2012)," by G.C. Lee, S.B. Mohan, C. Huang and B.N. Fard, June 15, 2013.

MCEER-13-0009 "Development of a Database Framework for Modeling Damaged Bridges," by G.C. Lee, J.C. Qi and C. Huang, June 16, 2013.

MCEER-13-0010   "Model of Triple Friction Pendulum Bearing for General Geometric and Frictional Parameters and for Uplift Conditions," by A.A. Sarlis and M.C. Constantinou, July 1, 2013.

MCEER-13-0011   "Shake Table Testing of Triple Friction Pendulum Isolators under Extreme Conditions," by A.A. Sarlis, M.C. Constantinou and A.M. Reinhorn, July 2, 2013.

MCEER-13-0012   "Theoretical Framework for the Development of MH-LRFD," by G.C. Lee (coordinating author), H.A Capers, Jr., C. Huang, J.M. Kulicki, Z. Liang, T. Murphy, J.J.D. Shen, M. Shinozuka and P.W.H. Yen, July 31, 2013.

MCEER-13-0013   "Seismic Protection of Highway Bridges with Negative Stiffness Devices," by N.K.A. Attary, M.D. Symans, S. Nagarajaiah, A.M. Reinhorn, M.C. Constantinou, A.A. Sarlis, D.T.R. Pasala, and D.P. Taylor, September 3, 2014.

MCEER-14-0001   "Simplified Seismic Collapse Capacity-Based Evaluation and Design of Frame Buildings with and without Supplemental Damping Systems," by M. Hamidia, A. Filiatrault, and A. Aref, May 19, 2014.

MCEER-14-0002   "Comprehensive Analytical Seismic Fragility of Fire Sprinkler Piping Systems," by Siavash Soroushian, Emmanuel "Manos" Maragakis, Arash E. Zaghi, Alicia Echevarria, Yuan Tian and Andre Filiatrault, August 26, 2014.

MCEER-14-0003   "Hybrid Simulation of the Seismic Response of a Steel Moment Frame Building Structure through Collapse," by M. Del Carpio Ramos, G. Mosqueda and D.G. Lignos, October 30, 2014.

MCEER-14-0004   "Blast and Seismic Resistant Concrete-Filled Double Skin Tubes and Modified Steel Jacketed Bridge Columns," by P.P. Fouche and M. Bruneau, June 30, 2015.

MCEER-14-0005   "Seismic Performance of Steel Plate Shear Walls Considering Various Design Approaches," by R. Purba and M. Bruneau, October 31, 2014.

MCEER-14-0006   "Air-Blast Effects on Civil Structures," by Jinwon Shin, Andrew S. Whittaker, Amjad J. Aref and David Cormie, October 30, 2014.

MCEER-14-0007   "Seismic Performance Evaluation of Precast Girders with Field-Cast Ultra High Performance Concrete (UHPC) Connections," by G.C. Lee, C. Huang, J. Song, and J. S. O'Connor, July 31, 2014.

MCEER-14-0008   "Post-Earthquake Fire Resistance of Ductile Concrete-Filled Double-Skin Tube Columns," by Reza Imani, Gilberto Mosqueda and Michel Bruneau, December 1, 2014.

MCEER-14-0009   "Cyclic Inelastic Behavior of Concrete Filled Sandwich Panel Walls Subjected to In-Plane Flexure," by Y. Alzeni and M. Bruneau, December 19, 2014.

MCEER-14-0010   "Analytical and Experimental Investigation of Self-Centering Steel Plate Shear Walls," by D.M. Dowden and M. Bruneau, December 19, 2014.

MCEER-15-0001   "Seismic Analysis of Multi-story Unreinforced Masonry Buildings with Flexible Diaphragms," by J. Aleman, G. Mosqueda and A.S. Whittaker, June 12, 2015.

MCEER-15-0002   "Site Response, Soil-Structure Interaction and Structure-Soil-Structure Interaction for Performance Assessment of Buildings and Nuclear Structures," by C. Bolisetti and A.S. Whittaker, June 15, 2015.

MCEER-15-0003   "Stress Wave Attenuation in Solids for Mitigating Impulsive Loadings," by R. Rafiee-Dehkharghani, A.J. Aref and G. Dargush, August 15, 2015.

MCEER-15-0004   "Computational, Analytical, and Experimental Modeling of Masonry Structures," by K.M. Dolatshahi and A.J. Aref, November 16, 2015.

MCEER-15-0005   "Property Modification Factors for Seismic Isolators: Design Guidance for Buildings," by W.J. McVitty and M.C. Constantinou, June 30, 2015.

MCEER-15-0006   "Seismic Isolation of Nuclear Power Plants using Sliding Bearings," by Manish Kumar, Andrew S. Whittaker and Michael C. Constantinou, December 27, 2015.

MCEER-15-0007   "Quintuple Friction Pendulum Isolator Behavior, Modeling and Validation," by Donghun Lee and Michael C. Constantinou, December 28, 2015.

MCEER-15-0008   "Seismic Isolation of Nuclear Power Plants using Elastomeric Bearings," by Manish Kumar, Andrew S. Whittaker and Michael C. Constantinou, December 29, 2015.

MCEER-16-0001   "Experimental, Numerical and Analytical Studies on the Seismic Response of Steel-Plate Concrete (SC) Composite Shear Walls," by Siamak Epackachi and Andrew S. Whittaker, June 15, 2016.

MCEER-16-0002   "Seismic Demand in Columns of Steel Frames," by Lisa Shrestha and Michel Bruneau, June 17, 2016.

MCEER-16-0003   "Development and Evaluation of Procedures for Analysis and Design of Buildings with Fluidic Self-Centering Systems" by Shoma Kitayama and Michael C. Constantinou, July 21, 2016.

MCEER-16-0004   "Real Time Control of Shake Tables for Nonlinear Hysteretic Systems," by Ki Pung Ryu and Andrei M. Reinhorn, October 22, 2016.

MCEER-16-0006   "Seismic Isolation of High Voltage Electrical Power Transformers," by Kostis Oikonomou, Michael C. Constantinou, Andrei M. Reinhorn and Leon Kemper, Jr., November 2, 2016.

MCEER-16-0007   "Open Space Damping System Theory and Experimental Validation," by Erkan Polat and Michael C. Constantinou, December 13, 2016.

MCEER-16-0008   "Seismic Response of Low Aspect Ratio Reinforced Concrete Walls for Buildings and Safety-Related Nuclear Applications," by Bismarck N. Luna and Andrew S. Whittaker.

MCEER-16-0009   "Buckling Restrained Braces Applications for Superstructure and Substructure Protection in Bridges," by Xiaone Wei and Michel Bruneau, December 28, 2016.